
# The European X-Ray Free-Electron Laser

# Technical design report

Editors:

**Massimo Altarelli, Reinhard Brinkmann, Majed Chergui, Winfried Decking, Barry Dobson, Stefan Düsterer, Gerhard Grübel, Walter Graeff, Heinz Graafsma, Janos Hajdu, Jonathan Marangos, Joachim Pflüger, Harald Redlin, David Riley, Ian Robinson, Jörg Rossbach, Andreas Schwarz, Kai Tiedtke, Thomas Tschentscher, Ivan Vartaniants, Hubertus Wabnitz, Hans Weise, Riko Wichmann, Karl Witte, Andreas Wolf, Michael Wulff, Mikhail Yurkov**

DESY 2006-097 July 2007

Publisher:

DESY XFEL Project Group
European XFEL Project Team
Deutsches Elektronen-Synchrotron
Member of the Helmholtz Association

Notkestrasse 85, 22607 Hamburg
Germany
http://www.xfel.net
E-Mail: xfel-www@desy.de



**ISBN 978-3-935702-17-1**

# Contents

Authors ..... vii

Foreword ..... xiii

Executive summary ..... 1

1 Introduction ..... 11
1.1 Accelerator-based light sources ..... 11
1.2 Free-electron lasers ..... 13
1.3 Historical development of the XFEL ..... 18
References ..... 20

2 TTF/FLASH in the XFEL context ..... 23
2.1 Historical background ..... 23
2.2 TTF FEL, Phase 1 ..... 24
*2.2.1 Accelerator R&D ..... 24*
*2.2.2 FEL research ..... 24*
*2.2.3 Results ..... 25*
*2.2.4 Experience from commissioning procedures ..... 27*
2.3 TTF FEL, Phase 2 – FLASH ..... 27
*2.3.1 Design ..... 27*
*2.3.2 Installation ..... 29*
*2.3.3 Accelerator commissioning ..... 30*
*2.3.4 FEL commissioning ..... 32*
*2.3.5 Experience form the first user operation periods ..... 35*
*2.3.6 Next steps for FLASH ..... 38*
References ..... 39

3 General layout of the XFEL Facility ..... 41
3.1 Introduction ..... 41
3.2 Injector ..... 43
3.3 Linear accelerator ..... 44
3.4 Beam distribution system ..... 45
3.5 Undulators ..... 45
3.6 Photon beamlines ..... 46
3.7 Experimental stations ..... 46
3.8 Schenefeld campus ..... 47

## Contents


4 XFEL accelerator ..... 49
4.1 Overview ..... 49
*4.1.1 Introduction ..... 49*
*4.1.2 Overall layout and choice of parameters ..... 49*
*4.1.3 Operational flexibility and future options ..... 52*
4.2 Linac ..... 56
*4.2.1 Cavities ..... 56*
*4.2.2 Auxiliaries ..... 68*
*4.2.3 Vacuum system ..... 80*
*4.2.4 High power RF system ..... 82*
*4.2.5 Low level radio frequency control ..... 89*
4.3 Injector ..... 96
*4.3.1 General layout ..... 96*
*4.3.2 Experimental status and future developments ..... 99*
*4.3.3 Photocathode laser ..... 99*
4.4 The bunch compressor system and start-to-end simulations ..... 100
*4.4.1 Introduction and layout ..... 100*
*4.4.2 Space charge and coherent synchrotron radiation effects ..... 101*
*4.4.3 RF set-up and tolerances ..... 102*
*4.4.4 Instabilities driven by space charge and coherent synchrotron radiation ..... 104*
*4.4.5 Start-to-end simulation ..... 105*
4.5 Beam optics and dynamics ..... 108
*4.5.1 Main linac ..... 108*
*4.5.2 Post-linac collimation ..... 113*
*4.5.3 Beam distribution and undulators ..... 116*
*4.5.4 Transverse beam stabilisation ..... 117*
4.6 Beam diagnostics ..... 120
*4.6.1 Requirements ..... 120*
*4.6.2 Measurements of projected bunch properties ..... 121*
*4.6.3 Measurement of slice properties ..... 123*
4.7 Technical layout ..... 128
*4.7.1 Warm vacuum system ..... 128*
*4.7.2 Magnets ..... 132*
*4.7.3 Kickers ..... 134*
*4.7.4 Beam dumps ..... 135*

# Contents


4.8 Synchronisation system for the XFEL ..... 139
*4.8.1 Introduction ..... 139*
*4.8.2 Layout of the XFEL synchronisation system ..... 144*
*4.8.3 Distribution of trigger and clock signals ..... 157*
*4.8.4 Synchronisation of the LLRF for the main linac ..... 158*
4.9 Summary of costs and manpower ..... 160
*4.9.1 Costs and manpower requirements of the superconducting linac ..... 162*
References ..... 164

5 Undulators for SASE and spontaneous emission ..... 173
5.1 Overview ..... 173
*5.1.1 Principles of XFEL operation ..... 173*
*5.1.2 Design criteria for the European XFEL ..... 174*
5.2 FEL radiation parameters ..... 176
*5.2.1 Defining undulator parameters ..... 179*
*5.2.2 Radiation parameters of SASE 3 ..... 183*
*5.2.3 Statistical properties of the radiation ..... 184*
*5.2.4 Higher harmonics ..... 185*
5.3 Spontaneous synchrotron radiation ..... 186
*5.3.1 Undulator parameters ..... 186*
*5.3.2 Spontaneous radiation parameters ..... 186*
5.4 Undulators systems ..... 189
*5.4.1 Choice of undulator parameters ..... 189*
*5.4.2 Basic tolerance requirements ..... 193*
*5.4.3 Undulator segments ..... 194*
*5.4.4 Intersections ..... 198*
*5.4.5 Other components ..... 202*
*5.4.6 Implementation of undulator systems ..... 202*
*5.4.7 Summary ..... 204*
5.5 Photon diagnostics of FEL radiation ..... 205
*5.5.1 Trajectory alignment ..... 206*
*5.5.2 Gap adjustment ..... 208*
*5.5.3 Phase tuning ..... 209*
*5.5.4 Hardware setup ..... 210*
*5.5.5 Test at PETRA II ..... 211*
5.6 Future extensions to the European XFEL Facility ..... 213
5.7 Summary of costs and manpower requirements ..... 217
References ..... 218

## Contents


6 Photon beamlines and scientific instruments ..... 225
6.1 Overview of the X-ray systems ..... 226
6.2 Photon beam transport ..... 228
*6.2.1 Photon beamline concept ..... 228*
*6.2.2 X-ray optical elements ..... 230*
*6.2.3 Other beam transport elements ..... 243*
*6.2.4 Description of the beamlines ..... 247*
6.3 Photon beam diagnostics ..... 255
*6.3.1 Characterisation of beam properties ..... 255*
*6.3.2 Online diagnostics ..... 258*
6.4 Scientific instruments ..... 263
*6.4.1 Small Quantum Systems ..... 264*
*6.4.2 High Energy Density matter experiments ..... 282*
*6.4.3 Coherent X-ray scattering and lensless imaging in materials science ..... 303*
*6.4.4 X-ray Photon Correlation Spectroscopy ..... 330*
*6.4.5 X-ray absorption spectroscopy ..... 349*
*6.4.6 Femtosecond diffraction experiments ..... 375*
*6.4.7 Ultra-fast coherent diffraction imaging of single particles, clusters and biomolecules ..... 401*
*6.4.8 Research and development on x-ray instrumentation ..... 441*
6.5 Specific XFEL experiments instrumentation ..... 449
*6.5.1 Sample environment and manipulation ..... 450*
*6.5.2 X-ray optics ..... 453*
*6.5.3 Optical lasers ..... 456*
*6.5.4 Detectors and requirements ..... 465*
6.6 Summary of cost and manpower requirements ..... 486
References ..... 488

7 Infrastructure and auxiliary systems ..... 513
7.1 Site layout and civil construction ..... 513
*7.1.1 Overall site layout ..... 513*
*7.1.2 Civil construction ..... 517*
7.2 Conventional technical infrastructure ..... 536
*7.2.1 Power distribution and power supplies ..... 536*
*7.2.2 Magnet power supplies ..... 538*
*7.2.3 Magnet water cooling and air conditioning ..... 539*
*7.2.4 Heating, ventilation and air conditioning ..... 542*
*7.2.5 Cryogenics ..... 544*

# Contents


*7.2.6 Accelerator Module Test Facility ..... 554*
*7.2.7 Survey and alignment of XFEL ..... 559*
*7.2.8 Installation of components ..... 564*
7.3 Controls and operation ..... 566
*7.3.1 Control systems ..... 566*
*7.3.2 Radiation safety ..... 571*
*7.3.3 General safety ..... 575*
*7.3.4 Personnel interlock ..... 578*
7.4 Summary of costs and manpower requirements ..... 582
References ..... 585

8 Commissioning and operation ..... 589
8.1 General considerations ..... 589
8.2 Transition phase ..... 590
8.3 User operation ..... 591
8.4 Operation budget ..... 592

9 Project management and organisation ..... 597
9.1 Introduction ..... 597
9.2 Internal organisation of the XFEL GmbH ..... 598
*9.2.1 General aspects ..... 598*
*9.2.2 Primary tasks and internal structure of the XFEL GmbH ..... 598*
*9.2.3 Operation of the accelerator complex ..... 602*
*9.2.4 Build-up of the XFEL staff complement ..... 603*
*9.2.5 Status of personnel and recruitment policy ..... 607*
9.3 General project structure and procedures for the construction period ..... 608
*9.3.1 Principles ..... 608*
*9.3.2 Collaboration agreements between contributing institutes and XFEL GmbH ..... 609*
*9.3.3 Project management structure and oversight ..... 610*
*9.3.4 Later operation of the equipment contributed in kind ..... 611*
9.4 Special relationship between the XFEL GmbH and DESY ..... 612
*9.4.1 DESY as contributor to the construction, commissioning and operation of the XFEL facility ..... 612*
*9.4.2 DESY as host for the XFEL GmbH ..... 613*
9.5 Project management ..... 614
*9.5.1 Overview ..... 614*
*9.5.2 Roles and responsibilities within the XFEL project ..... 616*
*9.5.3 Project management tools ..... 617*
References ..... 618

## Contents

10 Cost and time schedule ..... 619
10.1 Total project cost ..... 619
10.2 Risk analysis ..... 622
10.3 Operation cost ..... 624
10.4 Time schedule ..... 625
10.5 Budget profile ..... 627
References ..... 630

# Authors

R. Abela[49], A. Aghababyan[12], M. Altarelli[12], C. Altucci[61], G. Amatuni[10], P. Anfinrud[60], P. Audebert[37], V. Ayvazyan[12], N. Baboi[12], J. Baehr[13], V. Balandin[12], R. Bandelmann[12], J. Becker[12], B. Beutner[20], C. Blome[12], I. Bohnet[12], A. Bolzmann[4], C. Bostedt[57], Y. Bozhko[12], A. Brandt[12], S. Bratos[41], C. Bressler[35], R. Brinkmann[12], O. Brovko[32], H. Brück[12], J.-P. Carneiro[18], S. Casalbuoni[12], M. Castellano[22], P. Castro[12], L. Catani[23], A. Cavalleri[70], S. Celik[12], H. Chapman[39], D. Charalambidis[26], J. Chen[47], M. Chergui[35], S. Choroba[12], A. Cianchi[23], M. Clausen[12], E. Collet[66], H. Danared[54], C. David[49], W. Decking[12], M. Dehler[48], H. Delsim-Hashemi[20], G. Dipirro[22], B. Dobson[8], M. Dohlus[12], S. Duesterer[12], A. Eckhardt[20], H.-J. Eckoldt[12], H. Edwards[18], B. Faatz[12], M. Fajardo[30], A. Fateev[32], J. Feldhaus[12], Y. Filipov[32], K. Floettmann[12], R. Follath[5], B. Fominykh[31], M. French[9], J. Frisch[54], L. Froehlich[20], E. Gadwinkel[12], L. García-Tabarés[38], J.J. Gareta[51], T. Garvey[34], F. Gel'mukhanov[56], U. Gensch[13], C. Gerth[12], M. Goerler[12], N. Golubeva[12], H. Graafsma[12], H.-J. Grabosch[13], W. Graeff[12], O. Grimm[12], B. Griogoryan[10], G. Grübel[12], C. Gutt[12], K. Hacker[12], L. Haenisch[12], U. Hahn[12], J. Hajdu[53,71], J. H. Han[12], M. Hartrott[5], J. Havlicek[12], O. Hensler[12], K. Honkavaara[20], V. Honkimäki[17], T. Hott[12], M.R. Howells[40], M. Huening[12], H. Ihee[1], F.Ö. Ilday[6], R. Ischebeck[53], M. Jablonka[14], E. Jaeschke[5], K. Jensch[12], J.-P. Jensen[12], S. Johnson[49], L. Juha[29], F. Kaerntner[48], R. Kammering[12], H. Kapitza[12], V. Katalev[12], B. Keil[49], S. Khodyachykh[13], R. Kienberger[44], J.-W. Kim[48], Y. Kim[15], K. Klose[12], V. Kocharyan[12], W. Koehler[13], M. Koerfer[12], M. Kollewe[12], Q. Kong[17], W. Kook[12], D. Kostin[12], O. Kozlov[32], D. Kraemer[19], M. Krasilnikov[13], B. Krause[12], O. Krebs[12], J. Krzywinski[28], G. Kube[12], M. Kuhlmann[12], H. Laich[13], R. Lange[12], M. Larsson[72], R.W. Lee[39], A. Leuschner[12], H. Lierl[12], L. Lilje[12], T. Limberg[12], A. Lindenberg[53], D. Lipka[5], F. Loehl[20], K. Ludwig[12], M. Luong[14], C. Magne[14], A. Maquet[33], J. Marangos[7], C. Masciovecchio[16], M. Maslov[24], A. Matheisen[12], E. Matyushevskiy[32], O. Matzen[12], H.-J. May[12], I. McNulty[2], D. McCormick[53], P. Meulen[72], N. Meyners[12], P. Michelato[21], N. Mildner[12], V. Miltchev[20], M. Minty[12], W.-D. Moeller[12], T. Möller[57], L. Monaco[21], M. Nagl[12], O. Napoly[14], G. Neubauer[12], P. Nicolosi[68], A. Nienhaus[12], D. Noelle[12], T. Nunez[12], F. Obier[12], A. Oppelt[13], C. Pagani[21], R. Paparella[14], H.B. Pedersen[45], B. Petersen[12], B. Petrosyan[12], L. Petrosyan[12], A. Petrov[12], J. Pflueger[12], P. Piot[18], A. Plech[63], E. Ploenjes[12], L. Poletto[68], G. Pöplau[64], E. Prat[12], S. Prat[34], J. Prenting[12], D. Proch[12], D. Pugachov[42], H. Quack[59], B. Racky[12], D. Ramert[12], H. Redlin[12], K. Rehlich[12], R. Reininger[52], H. Remde[12], D. Reschke[12], D. Richter[5], M. Richter[50], S. Riemann[13], D. Riley[51], I. Robinson[67], J. Roensch[20], F. Rosmej[65], M. Ross[53], J. Rossbach[20], V. Rybnikov[12], M. Sachwitz[13], E. Saldin[12], W. Sandner[43], J. Schäfer[12], T. Schilcher[49], H. Schlarb[12], M. Schloesser[12], V. Schlott[49], B. Schmidt[12], M. Schmitz[12], P. Schmueser[20], J. Schneider[12], E. Schneidmiller[12], F. Schotte[60], S. Schrader[12], S. Schreiber[12], C. Schroer[58], R. Schuch[3], H. Schulte-Schrepping[12], A. Schwarz[12], M. Seidel[49], J. Sekutowicz[12], P. Seller[9], D. Sellmann[12], F. Senf[5], D. Sertore[21], A. Shabunov[32], S. Simrock[12], W. Singer[12], H. Sinn[2], R. Smith[7], E. Sombrowski[12], A.A. Sorokin[50], E. Springate[9], M. Staack[12], L. Staykov[13], B. Steffen[12], B. Stephenson[2], F. Stephan[13], F. Stulle[48], E. Syresin[32], K. Sytchev[32], V. Sytchev[24], G. Tallents[69], S. Techert[45], N. Tesch[12],

## Authors

H. Thom[13], K. Tiedtke[12], M. Tischer[12], M. Tolan[62], S. Toleikis[12], F. Toral[38], R. Treusch[12], D. Trines[12], V. Tsakanov[10], I. Tsakov[25], T. Tschentscher[12], F.-R. Ullrich[12], U. van Rienen[64], A. Variola[34], I. Vartaniants[12], E. Vogel[12], J. Vogel[17], R. Vuilleumier[41], H. Wabnitz[12], R. Wanzenberg[12], J.S. Wark[70], H. Weddig[12], T. Weiland[11], H. Weise[12], M. Wendt[18], R. Wenndorff[13], R. Wichmann[12], I. Will[43], A. Winter[12], K. Witte[12], K. Wittenburg[12], P. Wochner[47], T. Wohlenberg[12], J. Wojtkiewicz[12], A. Wolf[46], M. Wulff[17], M. Yurkov[12], I. Zagorodnov[12], P. Zambolin[68], K. Zapfe[12], P. Zeitoun[36], V. Ziemann[72], A. Zolotov[12]

1 Advanced Institute of Science and Technology, 373-1, Guseongdong, Yuseonggu, Daejeon, 305-701, Republic of Korea.

2 Advanced Photon Source, Argonne National Laboratory, 9700 South Cass Avenue., Argonne, IL 60439, USA.

3 Atomic Physics Fysikum, Stockholm University, Alba Nova, 10691 Stockholm, Sweden.

4 Bayerische Julius-Maximilians Universität, Inst. f. Theor. Physik u. Astrophysik, Am Hubland, 97074 Würzburg, Germany.

5 BESSY GmbH, Albert-Einstein-Strasse 15, 12489 Berlin, Germany.

6 Bilkent University, Department of Physics, Ankara 06800, Turkey.

7 Blackett Laboratory, Department of Physics, Imperial College, London SW7 2AZ, UK.

8 CCLRC Daresbury Laboratory, Warrington, Cheshire, WA4 4AD, UK.

9 CCLRC Rutherford Appleton Laboratory, Chilton, Didcot, OX11 0QX, UK.

10 Center for the Advancement of Natural Discoveries using Light Emission CANDLE, Acharyan 31, 375040 Yerevan, Armenia.

11 Darmstadt University of Technology, FB18 - Fachgebiet TEMF, Schlossgartenstr. 8,64289 Darmstadt, Germany.

12 Deutsches Elektronen-Synchrotron DESY, Notkestrasse 85, 22607 Hamburg, Germany.

13 Deutsches Elektronen-Synchrotron DESY, Platanenallee 6, 15738 Zeuthen, Germany.

14 DSM/DAPNIA, CEA Saclay, 91191 Gif s/ Yvette, France.

15 Duke University, FEL Laboratory, Durham, NC 27708-0319, USA.

16 Elettra Sincrotrone Trieste, Area Science Park, 34012 Basovizza, Trieste, Italy.

17 ESRF, B.P. 220, 6, rue Jules Horowitz, 38043 Grenoble Cedex, France.

18 Fermi National Accelerator Laboratory, MS 306, P.O. Box 500, Batavia, IL 60510, USA.

19 Gesellschaft für Schwerionenforschung, Planckstr. 1, 64291 Darmstadt, Germany.

20 Hamburg University, Inst. f. Experimentalphysik, Luruper Chaussee 149, 22761 Hamburg, Germany.

21 INFN Milano - LASA, via Fratelli Cervi 201, 20090 Segrate (MI), Italy.

22 INFN-LNF, via E. Fermi 40, I-00044 Frascati, Italy.

23 INFN-Roma2, via della Ricerca Scientifica 1, 00100 Roma, Italy.

24 Inst. High Energy Physics, 142284 Protvino, Moscow Region, Russia.

25 Institute for Nuclear Researches and Nuclear Energy, Tzarigradsko Shaussee Boulevard 72, 1784 Sofia, Bulgaria.

26 Institute of Electronic Structure and Laser, Foundation for Research and Technology, P.O.Box 1527, Vassilika Vouton, 71110 Heraklion, Greece.

27 Institute of Electronic Systems, Faculty of Electronics and Information Technologies, ELHEP Laboratory, Nowowiejska 15/19, Warsaw, Poland.

28 Institute of Physics, Polish Academy of Sciences, Al. Lotnikow 32/46, 02-668 Warsaw, Poland.

29 Institute of Physics, Academy of Science of the Czech Republic, Na Slovance 2, 18221 Praha 8, Czech Republic.

30 Instituto Superior Técnico, Av. Rovisco Pais, 1049-001 Lisbon, Portugal.

31 ITEP Moscow, Bolshaya Cheremushkinskaya, 25, 117218 Moscow, Russia.

32 Joint Inst. for Nuclear Research, 141980 Dubna, Moscow Region, Russia.

33 Laboratoire de Chimie Physique-Matière et Rayonnement, Université Pierre et Marie Curie, 11 Rue Pierre et Marie Curie, 75231 Paris Cedex 05, France.

34 Laboratoire de l'Accelerateur Lineaire, IN2P3-CNRS, Universite de Paris-Sud, B.P. F-91898, Orsay, France.

35 Laboratoire de Spectroscopie Ultrarapide, Institut des Sciences et Ingénierie Chimiques, Ecole Polytechnique Fédérale de Lausanne, EPFL SB ISIC LSU, 1015 Lausanne-Dorigny, Switzerland.

36 Laboratoire d'Optique Applique LOA, ENSTA, Chemin de la Hunière, 91761 Palaiseau Cedex, France.

## Authors


37 Laboratoire pour l'Utilisation des Lasers Intenses LULI, Ecole Polytechnique, 91128 Palaiseau, France.

38 Laboratorio Conjuto de Superconductividad Aplicada CIEMAT/CEDEX, Madrid, Spain.

39 Lawrence Livermore National Laboratory, 7000 East Avenue Livermore, CA 94550, USA.

40 LBNL, 1 Cyclotron Road, Berkeley, CA 94720 USA.

41 LPTL, Université Pierre et Marie Curie, 4 Place Jussieu, 75252 Paris Cedex 05, France.

42 Lund University, MAX-Lab Box 118, 22100 Lund, Sweden.

43 Max-Born-Institut, Max-Born-Str. 2a, 12489 Berlin, Germany.

44 Max-Planck-Institut für Quantenoptik, Hans-Kopfermann-Strasse 1, 85748 Garching, Germany.

45 Max-Planck-Institut für biophysikalische Chemie, Am Faßberg 11, 37077 Göttingen, Germany.

46 Max-Planck-Institut für Kernphysik, Postfach ..., 69029 Heidelberg, Germany.

47 Max-Planck-Institut für Metallforschung, Heisenbergstraße 3, 70569 Stuttgart, Germany.

48 MIT, Department of Electrical Engineering and Computer Science, 77 Massachusetts Avenue, Cambridge, MA 02139, USA.

49 Paul Scherrer Institut, CH-5232 Villigen PSI, Switzerland.

50 Physikalisch Technische Bundesanstalt, Abbestrasse 2-12, 10587 Berlin, Germany.

51 Queen's University, School of Mathematics and Physics, Belfast, BT7 1NN, UK.

52 Scientific Answers & Solutions, 5708 Restal St, Madison, WI 53711, USA.

53 Stanford Linear Accelerator Center, 2575 Sand Hill Road, Menlo Park, CA 94025, USA.

54 Stockholm University, Manne Siegbahn Laboratory, Frescativägen 24, S-104 05 Stockholm, Sweden.

55 Technical University of Lodz, Department of Microelectronics and Computer Science, Al. Politechniki 11, Lodz, Poland.

56 Theoretical Chemistry, Department of Biotechnology, Royal Institute of Technology (KTH), Alba Nova University Center, Roslagstullbacken, 10691 Stockholm, Sweden.

57 TU Berlin, Institut für Atomare Physik, Hardenbergstrasse 36, PN 3-1, 10623 Berlin, Germany.

58 TU Dresden, Department of Physics, 01062 Dresden, Germany.

59 TU Dresden, Institut für Energietechnik, 01062 Dresden, Germany.

60 Ultrafast Biophysical Chemistry Section, NIDDK, National Institutes of Health, Bethesda, MD 20892-0520, USA.

61 Universita “Frederico II” di Napoli, Dipartimento di Scienze Fisiche, Napoli, Italy.

62 Universität Dortmund, Fachbreich Physik, Otto-Hahn Str. 4, 44227 Dortmund, Germany.

63 Universität Konstanz, Fachbreich Physik, Universitätsstr. 10, 78457 Konstanz, Germany.

64 Universität Rostock, Fakultät für Informatik und Elektrotechnik, Institut für Allgemeine Elektrotechnik, A.-Einstein-Str. 2, 18051 Rostock, Germany.

65 Universite de Provence et CNRS, Avenue Escadrille Normandie-Niemen, 13397 Marseille Cedex 20, France.

66 Université de Rennes 1, Institut de Physique, 2 rue du Thabor - CS 46510, 35065 Rennes Cedex, France.

67 University College London, Department of Physics and Astronomy, Gower Street, London WC1E 6BT, UK.

68 University of Padova, Dept. of Information Engineering, via Gradenigo 6/A, 35131 Padova, Italy.

69 University of York, Department of Physics, Heslington, York YO10 5DD, UK.

70 University of Oxford, Department of Physics, Clarendon Laboratory, Parks Road, Oxford OX1 3PU, UK.

71 Uppsala University, Laboratory of Molecular Biophysics, Husargatan 3, P.O. Box 596, 75124 Uppsala, Sweden.

72 Uppsala University, The Svedberg Laboratory, 75121 Uppsala, Sweden.

# Foreword

This report contains a comprehensive technical description of a new international research infrastructure, the European X-Ray Free-Electron Laser (XFEL) Facility. It was written between October 2005 and June 2006 and provides a realistic cost estimate and a compelling assessment of the scientific pay-off. The report has been prepared with the contribution of hundreds of people from many laboratories in Europe and even beyond. Their contributions have been harmonised and merged by many editors, and the whole effort has been coordinated by the European Project Team, generously supported and hosted by the Deutsches Elektronen-Synchrotron (DESY) laboratory.

It is important and worthwhile to mention the large number of scientists and engineers who have contributed to the preparation of this report, not only to fulfil our obligation to acknowledge and thank them for their work, but also to underline that the perspective of this new international research enterprise generates support and enthusiasm in a wide community spread over many countries.

In spite of the rather pressing time schedule, it was possible to subject intermediate versions of the different chapters to two reviews by the Scientific and Technical Issues (STI) Working Group, enlarged by additional experts in accelerator physics and in the scientific use of photons. The support of these review panels provided strong encouragement, and their constructive advice resulted in many improvements to the clarity and completeness of the report. We, therefore, express our gratitude to them as well.

We hope that this report will contribute to communicating our deep conviction that a brilliant source of ultra-short, spatially coherent x-rays is an indispensable component of the European scientific landscape for the forthcoming decades.

The European Project Team

Massimo Altarelli
Reinhard Brinkmann
Thomas Delissen
Andreas Schwarz
Thomas Tschentscher
Karl Witte

Hamburg, July 2006

# Executive summary

## 1 Basic objectives

This report contains a full technical description of the European X-Ray Free-Electron Laser (XFEL) Facility, a new international scientific infrastructure to be built in the north west of Hamburg. The purpose of the facility is to generate *extremely brilliant* (peak brilliance ~ $10^{33}$ photons/s/mm$^2$/mrad$^2$/0.1%BW), *ultra-short* (~ 100 fs) pulses of *spatially coherent* x-rays with wavelengths down to 0.1 nm, and to exploit them for revolutionary scientific experiments in a variety of disciplines spanning physics, chemistry, materials science and biology. The design contains a baseline facility and provisions to facilitate future extensions and improvements, in preparation for further progress in the relevant technologies. The basic process adopted to generate the x-ray pulses is Self-Amplified Spontaneous Emission (SASE), whereby electron bunches are generated in a high-brightness gun, brought to high energy (up to 20 GeV) through a superconducting linear accelerator (linac), and conveyed to long (up to ~200 m) undulators where the x-rays are generated. Five photon beamlines deliver the x-ray pulses to ten experimental stations, where state-of-the-art equipment is available for the experiments.

From this new user facility, novel results of fundamental importance can be expected in materials physics, plasma physics, planet science and astrophysics, chemistry, structural biology and biochemistry, with significant possible impact on technologies such as nuclear fusion, catalysis, combustion (and their environmental aspects), as well as on biomedical and pharmaceutical technologies. Thanks to its superconducting accelerator technology, in spite of competing American and Japanese projects, the European XFEL Facility will allow Europe to keep its leadership in basic and applied science with accelerator-based light sources, a leadership it acquired in the early 90s with the construction and operation of the European Synchrotron Radiation Facility (ESRF) in Grenoble.

## 2 History of the project

The basic technology underlying the European XFEL Facility is the superconducting linac technology, developed by an international collaboration coordinated by the Deutsches Elektronen-Synchrotron (DESY) laboratory in Hamburg, with the initial objective to create a Tera-Electronvolt Superconducting Linear Accelerator (TESLA), an electron-positron linear collider with TeV energy, for particle physics studies, hence, the name TESLA technology. It was soon realised that this type of innovative linac had ideal characteristics for an x-ray free-electron laser. Proposals to build a free-electron laser, first as a side branch of the linear collider, and later as a self-standing facility, were put forward by DESY to the German government. The construction of a test facility (TESLA Test Facility 1, or TTF1) was undertaken, and lasing down to ~90 nm wavelengths was successfully demonstrated in 2000. TESLA Test Facility 2 (TTF2) had the more

ambitious goal to push lasing to 6 nm wavelengths, with a 1 GeV linac. This should be achieved in 2007; in the meantime, acceleration of electrons up to 0.75 GeV resulted in lasing at 32 nm (January 2005) and at 13 nm (April 2006), and a vigorous user programme was started in August 2005 in the experiments hall downstream from the free-electron laser, forming what is now called the Free-electron LASer in Hamburg (FLASH) facility. In 2003, the German government decided to launch the proposal to constitute a European facility for the construction and operation of an x-ray free-electron laser in Hamburg, undertaking the commitment to finance the new facility by providing up to 60% of its construction costs, and up to 40% of the operation costs. The choice of the location in Hamburg is motivated by the possibility of taking advantage of the unique experience and know-how of the DESY Machine Division in the area of superconducting linacs, and of the possibility of gaining first-hand experience on the operation of a free-electron laser (FEL) through the FLASH facility.

# 3 The scientific case and the X-ray FEL international context

All natural sciences benefit from the use of photons (light waves) of different wavelengths to probe the phenomena of nature. The use of infrared, visible and near ultraviolet light has been revolutionised by the invention of gas lasers and of solid-state lasers, with their properties of high brilliance, spatial coherence and, in more recent decades, ultrashort pulses, with duration down to a few femtoseconds or less (1 femtosecond, or 1 fs, equals a billionth of a millionth of a second; light travels a distance of 0.3 μm in 1 fs). This timescale is of particular importance because atoms in molecules and solids oscillate around their equilibrium positions with typical periods of a few hundreds of femtoseconds, and in general, movements of atoms during the rearrangement of their positions in chemical reactions, or phase transformations also occur on such a timescale.

In the range of the ultraviolet, soft x-ray and hard x-ray wavelengths, great progress was achieved by the exploitation of synchrotron radiation, the brilliant emission by electrons or positrons orbiting in a circular accelerator. Synchrotron radiation, however, is far less brilliant than a powerful laser, has a very limited degree of spatial coherence, and it comes typically in pulses of ~ 30 ps = 30,000 fs duration. The objective of the modern projects for the realisation of x-ray free-electron lasers is the extension of the scientific and technological revolution, ushered in by lasers in the visible light range, to the x-ray range, providing spatially coherent pulses of < 100 fs duration, with peak powers of many GW.

As discussed in four international workshops organised between October 2005 and March 2006 in Hamburg, Paris, Copenhagen, and near Oxford, the outstanding properties of the European XFEL beams (coherence, ultra-high brilliance and time structure) and the development of appropriate detectors and instrumentation will allow completely new experiments. A few examples are listed overleaf.

Coherence can be used for holographic and lensless imaging in materials science and biology. Spectacular possibilities open up, as detailed theoretical studies and simulations

predict that, with a single very short and intense coherent x-ray pulse from the XFEL, a diffraction pattern may be recorded from a large macromolecule, a virus, or a cell, without the need for crystalline periodicity. This would eliminate a formidable bottleneck for many systems of high interest, e.g. membrane proteins, viruses and viral genomes. Measurement of the over-sampled x-ray diffraction pattern permits phase retrieval and hence, structure determination. Although individual samples would eventually be destroyed by the very intense x-ray pulse, a three-dimensional data set could be assembled, when copies of a reproducible sample are exposed to the beam one by one.

The high intensity can also be used to produce highly ionised states of atoms, generating in the laboratory, conditions and processes occurring in interstellar gases. In conjunction with the ultra-short pulse duration, it can be exploited in pump-and-probe experiments, where conventional laser pulses (pump) are used to trigger a chemical reaction or a phase transition, and the XFEL pulses (probe), each following the pump pulse with a well determined delay (from ~50 fs up to nanosecond or even μs), provide a “movie” of the atomic displacements and rearrangement of chemical bonds. In this way, catalytic mechanisms in chemical and biochemical reactions can be elucidated, fast reactions (e.g. combustion) can be subject to detailed investigation, nucleation of ordered phases at phase transitions can be imaged, and hitherto inaccessible states of matter can be brought to experimental investigation: if the pump pulse is sufficiently powerful to produce a plasma, the x-ray pulse can still penetrate the highly ionised medium (opaque to visible light) and provide information on the propagation of the shock front, on the time evolution of temperature and pressure distributions and on the equation of state.

As already emphasised, the potential relevance of scientific breakthroughs of this caliber extends beyond basic science, to technologies of essential importance for Europe. It would not be wise to leave a competitive advantage in this field to the United States, where the Linac Coherent Light Source (LCLS) project is well under way at Stanford, and to Japan, where the Spring-8 Compact SASE Source (SCSS) has already in 2006 obtained the financial green light for start-up. Although these projects started already, and are probably going to be completed earlier, the European XFEL adoption of the superconducting accelerator technology allows the production of 30,000 x-ray pulses per second (and possibly even more in the future), compared to the 120 of the LCLS and the 60 of the SCSS. In addition to this decisive technical advantage, reducing the time necessary to complete some experiments by two orders of magnitude, the useful experience acquired with FLASH could considerably benefit the rapid establishment of a successful scientific exploitation. If the European XFEL Facility keeps a schedule comparable to that of the competing projects, it can occupy the leading position in this field.

A European laboratory in Hamburg and Schleswig-Holstein, pursuing excellence in the physics and applications of hard x-ray free-electron laser radiation would be complementary to other projects in Europe emphasising the soft x-ray part of the spectrum, and benefit all of them through the development and sharing of common technologies.

# 4 Layout and performance goals of the facility

The main components of the facility are (see Figure 4.1) the:

- injector;
- linac;
- beam distribution system;
- undulators;
- photon beamlines;
- instruments in the Experiments Hall.

These components are disposed along an essentially linear geometry, 3.4 km long, starting on the DESY campus in the northwest part of the city of Hamburg, and ending in the neighbouring Federal State of Schleswig-Holstein, south of the city of Schenefeld, where the experimental hall is located.

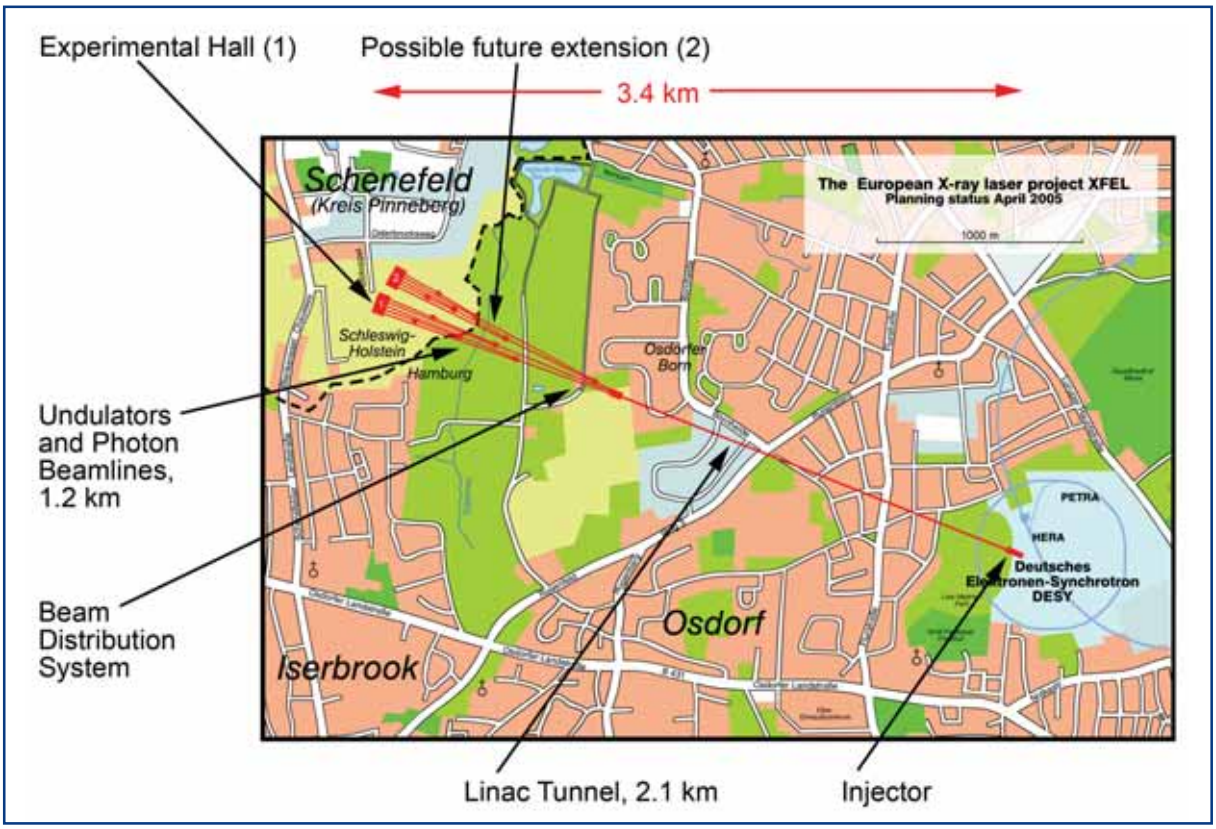


***Figure 4.1*** *Schematic layout of the main components of the European XFEL Facility.*

The basic functions of the main components are schematically described in the following. In the injector, electron bunches are extracted from a solid cathode by a laser beam, accelerated by an electron radio frequency (RF) gun and directed towards the linac with an exit energy of 120 MeV. In the linac, consisting of a 1.6 km long sequence of superconducting accelerating modules, magnets for beam steering and focusing, and diagnostic equipment, the electrons are accelerated to energies of up to 20 GeV (17.5 GeV is the energy foreseen for the standard mode of operation of the XFEL facility). Along the accelerator, two stages of bunch compression are located, to produce the short and very dense electron bunches required to trigger the SASE process. At the end of the linac, the individual electron bunches are channeled down one or the other of two electron beamlines by the beam distribution system (Figure 4.2). Electron bunches channeled down the electron beamline 1 pass through the undulators SASE 1 and SASE 3, producing respectively hard x-ray photons with 0.1 nm wavelength (SASE 1) and softer x-ray photons with 0.4 -1.6 nm wavelength (SASE 3), by the SASE FEL process. After going through SASE 3, electrons are deviated towards a beam dump. Electron bunches channeled through the electron beamline 2 are led through the undulator SASE 2, where hard x-ray photons with wavelengths 0.1-0.4 nm are produced by the SASE process; and then through the undulators U 1 and U 2, before ending in the second beam dump. In U 1 and U 2, very hard x-ray photons (wavelengths down to 0.014 and 0.06 nm, respectively) are generated by the spontaneous emission process. The photons generated by the five undulators are transported through the respective photon beamline to the experimental hall, where they are fed into ten experimental stations. Reducing the electron energy at the end of the accelerator would generate longer wavelengths, in case they are required by some experiments; for example, an electron energy of 10 GeV would correspond to x-rays of 4.9 nm wavelength from the SASE 3 undulator.

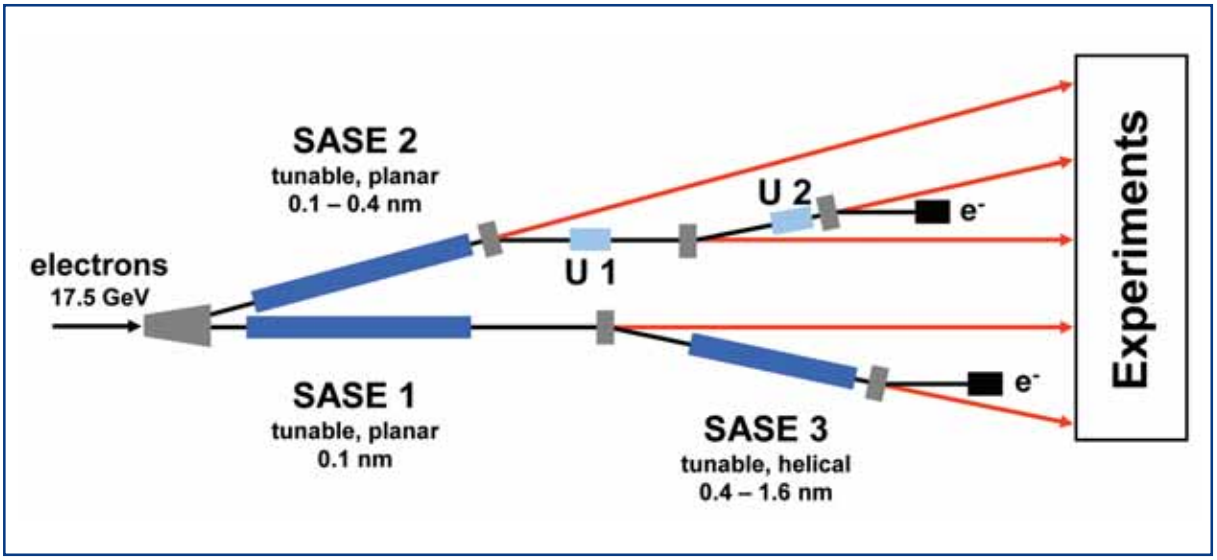


***Figure 4.2*** *Schematic view of the branching of electron (black) and photon (red) beamlines through the different SASE and spontaneous emission undulators. Electron beamlines terminate in the two beam dumps and photon beamlines in the experimental hall.*

## Executive summary

The installation and commissioning of the accelerator, the undulators, beamlines and experimental stations will take place gradually, according to a strategy for the achievement of intermediate and final goals of the facility which was established with the advice of the Scientific and Technical Issues (STI) Working Group.

The first electron beamline and the SASE 1 undulator are going to be installed first. The commissioning of the accelerator and of the SASE 1 undulator, beamline and first station will be pursued, in parallel with installation of the other electron branch, until the first set of intermediate goals (see Table 4.1) is reached.

As recommended by the STI Working Group, the following criteria for the start of operation of the accelerator complex and the SASE radiators and beamlines were adopted:

- The accelerator complex and SASE 1 start operation when on SASE 1 a photon beam is obtained with the intermediate values of Table 4.1, and sufficient equipment is installed and commissioned to perform first scientific experiments.
- SASE 2 starts operation when the same criteria as above are fulfilled, for wavelengths between 0.2 and 0.4 nm.
- SASE 3 starts operation when the same criteria as above are fulfilled, for wavelengths between 2 and 6 nm.

Following the positive experience of the FLASH facility, developments towards the final project goals on all beamlines will proceed in parallel with early user operation, as soon as the criteria stated above are fulfilled.

| Parameter | SASE 1 intermediate values | SASE1 final project values | Units |
|---|---|---|---|
| Wavelength | < 0.2 | 0.1 | nm |
| Peak brilliance | $10^{30}$ | $5\times10^{33}$ | Photons/s/mm$^2$/ mrad$^2$/0.1% BW |
| Dimension at sample (no optics) | < 1.0 | ~ 0.6 | mm$^2$, FWHM |
| Positional stability | 50 | 10 | % of beam size, rms |
| Photon energy stability | ~ 0.1 | ~ 0.1 | % |
| Shot-to-shot intensity fluctuations | Up to a factor 10 | 0.3 – 0.5 | Dimensionless, peak-to-peak |

***Table 4.1*** *Intermediate and final project values for the accelerator and SASE 1 undulator and corresponding photon beamline.*

# 5 Cost, schedule and personnel

## 5.1 Cost of the project

All costs from the project preparation to the commissioning phase (i.e. prior to the start of operation) have to be summed up in order to determine the total project construction cost (TPCC). There will be a period of about 2.5 years during which an overlap of construction, commissioning and operation will occur (see also the discussion of the time schedule and budget profile below). The contributions to the TPCC, summarised in Table 5.1, are:

- The project preparation costs. These are the expenses since the XFEL Memorandum of Understanding (MOU) came into effect (end of 2004), incurred by DESY and by institutes which have concluded collaboration contracts with DESY under the XFEL MoU.
- The construction costs in the proper sense, of the accelerator, the undulators, the photon beamlines, scientific instruments, civil engineering and technical infrastructure of the European XFEL Facility, including capital investment and manpower.
- The cost of commissioning the facility with beam.
- An addition to the personnel cost, in order to take into account allowances for personnel moving from their home country to work at the XFEL company.
- An additional personnel cost overhead, taking account of the XFEL company's management and support costs.

Recurrent costs during the construction in the proper sense (electricity, water, Helium) are not included in the TPCC, since they will be covered by the DESY operation budget free of charge to the XFEL project. Costs related to land acquisition are also not included in the TPCC, since Germany offered to provide the ground free of charge to the project.

| | |
|---|---|
| Project preparation | 38.8 M**€** |
| *Project construction, capital investment* | *736.3 M**€*** |
| *Project construction, personnel* | *250.1 M**€*** |
| **Total construction cost** | **986.4 M€** |
| Beam commissioning | 56.4 M**€** |
| **Total project construction cost** | **1,081.6 M€** |

***Table 5.1*** *Total project cost, including preparation – commissioning phases. All cost figures are on the price basis of the year 2005. - The original Table 5.1 of the TDR has been slightly re-arranged: the additional personnel cost (allowances) and the additional management overhead of the XFEL GmbH, initially shown in separate lines of the table, are now included in the cost for construction and commissioning.*

As described in detail in Chapter 10, the breakdown of this cost between the major components of the facility, is displayed in Figure 5.1.

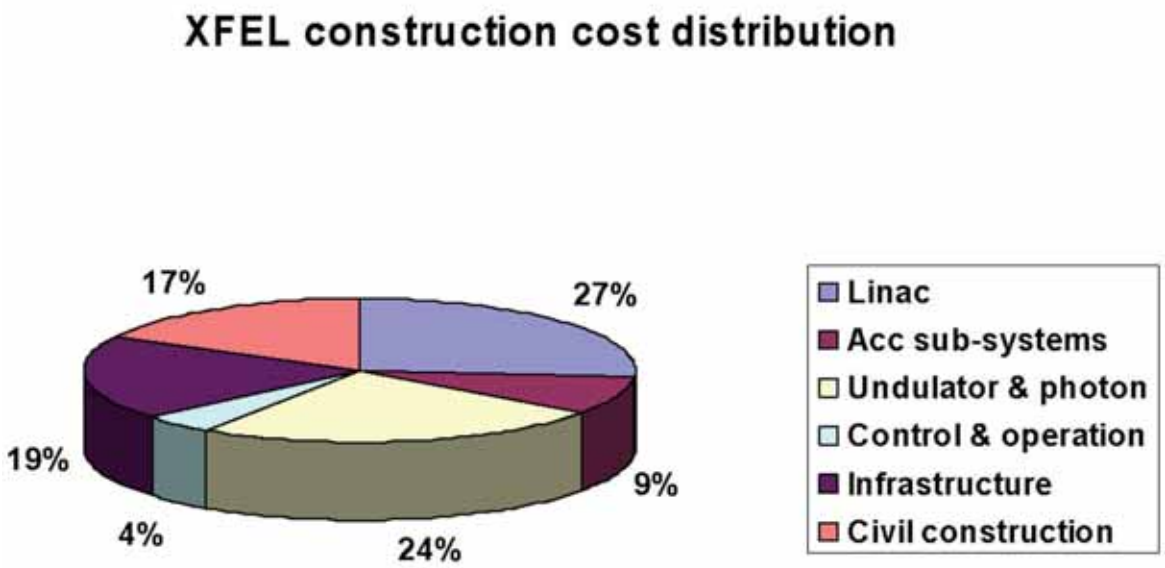


***Figure 5.1*** *Breakdown of the proper construction costs (sum of capital investment and personnel cost) into the work package groups corresponding to the main comnponents of the facility.*

An analysis of the risk of overspend was performed according to guidelines specified by the Full Costing Issues (FCI) subgroup of the Administration and Financial Issues (AFI) Working Group. The resulting risk budget (8% of the proper construction costs) amounts to 78 M**€**, and is the additional figure required to bring the probability of successful completion of the facility within budget to 98%.

The estimated yearly operation costs of the facility, after the end of all construction, are 83.6 M**€**, including all recurrent costs for operation, maintenance and refurbishment, and support of the international user activities, plus a PhD student and a visiting scientists programme.

## 5.2 Project time schedule

The time schedule for the project is presented in Figure 5.2, which assumes that the official start of the project construction is January 2007. For each of the major parts of the facility, phases during construction (which can partially overlap in time) can be defined as:

- design, prototyping and industrialisation;
- fabrication (including pre-series);
- installation;
- commissioning (technical and with beam).

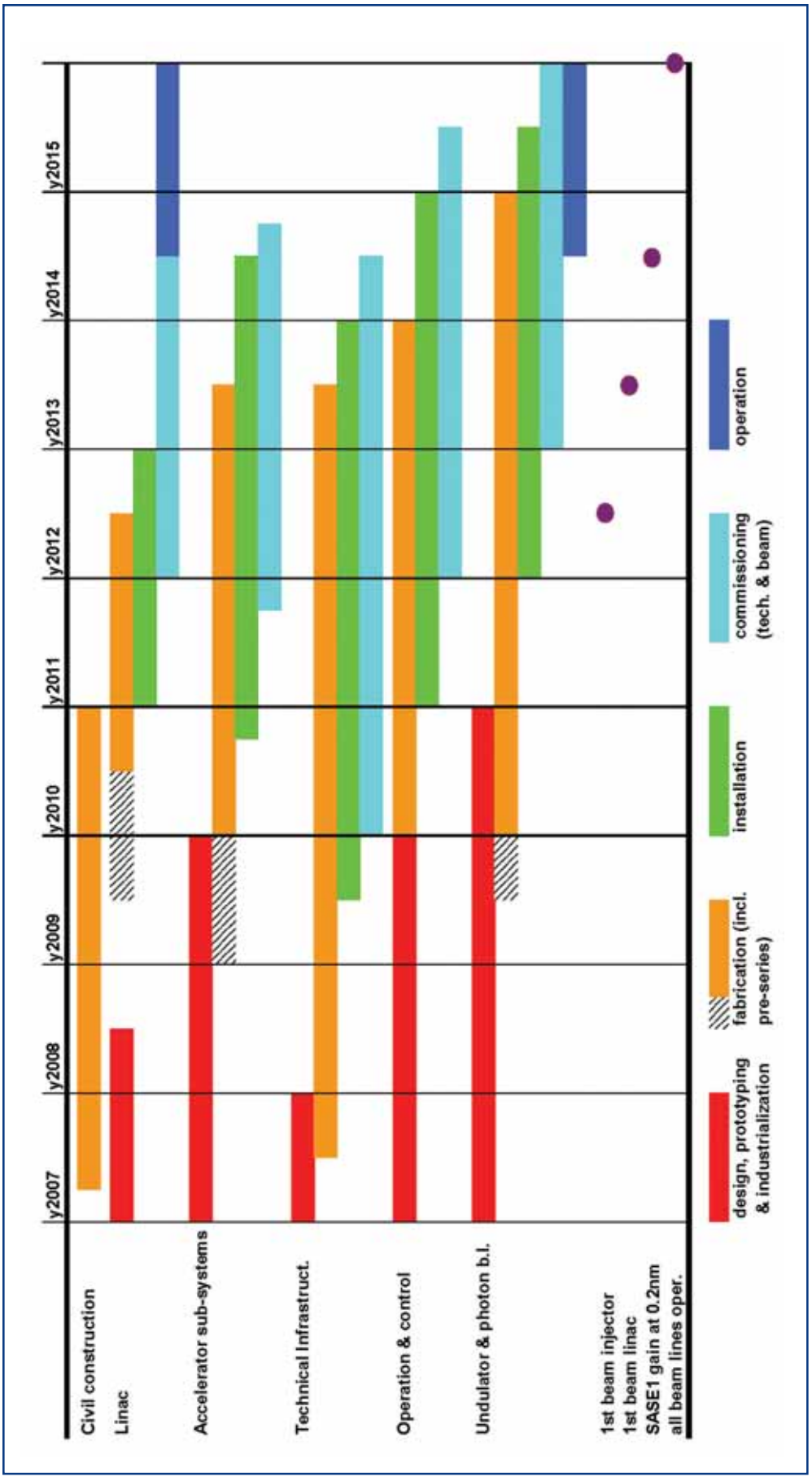


***Figure 5.2*** *Sketch of the schedule for the main components of the facility from start of construction to beginning of operation.*

In summary, the construction schedule provides for the milestone of first beam into the linac to be met 6.5 years after the start of construction. At this point in time, the first branch of beamlines with the SASE 1 undulator will also have been installed. Beam commissioning will then progress until the intermediate performance milestones of SASE 1 radiation are reached, 7.5 years after the start of construction. This beamline will then become operational for first experiments. Commissioning of the other beamlines follows.

## 5.3 Budget profile

With the different contributions to the TPCC as summarised already, the construction time schedule and the operation costs as described in Chapter 8, a complete budget profile for all phases from preparation to operation can be constructed. The result is displayed in Figure 5.3 showing the yearly budget from 2005-2016 on the price basis of the year 2005 (i.e. without applying an escalation to take inflation into account).

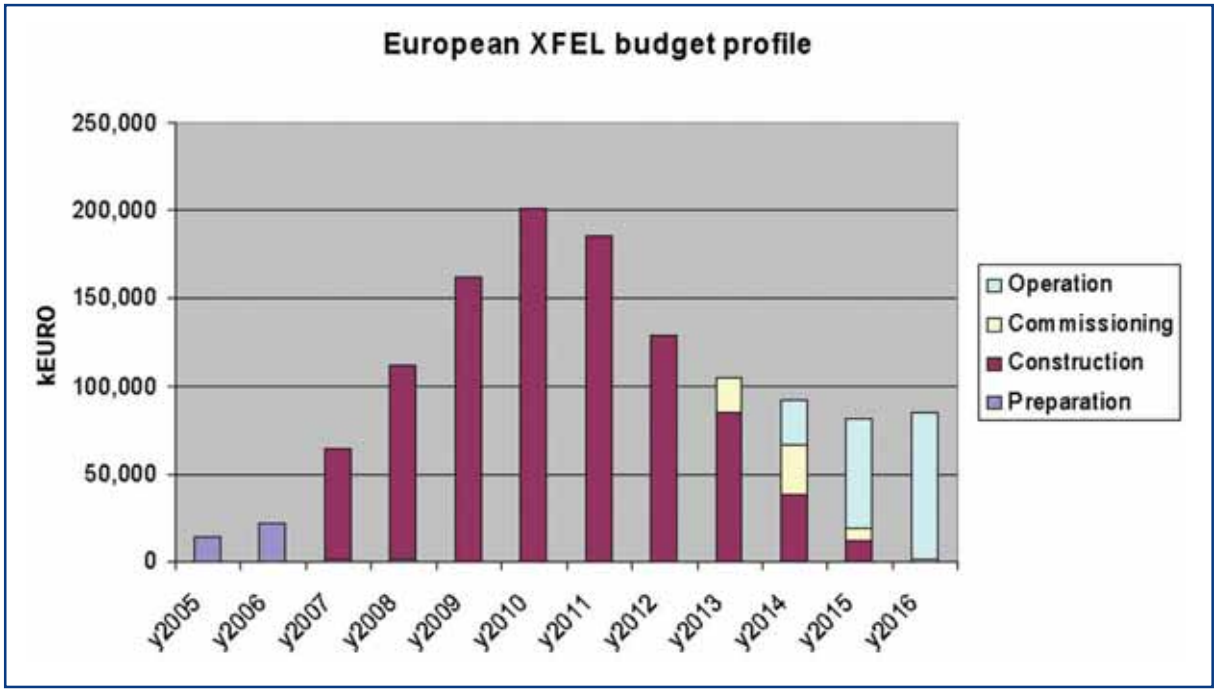


***Figure 5.3*** *Budget profile (sum of capital investment and personnel cost on year 2005 price basis) from preparation to operation phase of the project.*

Personnel costs, as given explicitly in Table 5.1 and implicitly in Figure 5.3 correspond to the cost of the personnel hired by the facility, plus the personnel costs for those work packages of the project, which are provided, as an in-kind contribution, by participating countries' laboratories.

# 1 Introduction

This Technical Design Report of the European X-Ray Free-Electron Laser (XFEL) Facility has been prepared by a large community of scientists and engineers and was edited at Deutsches Elektronen-Synchrotron (DESY) laboratory under the supervision of the European XFEL Project Team.

In September 2004, at the initiative of the German Federal Ministry for Education and Research, a Memorandum of Understanding (MoU) on the preparatory phase of the European XFEL Facility was drafted, and has so far been signed by 13 countries. Under the MoU, an International Steering Committee was created, with the task of overseeing all activities of the preparatory phase of the new European Facility. The International Steering Committee, as foreseen by the MoU, appointed two Working Groups of experts, one on Scientific and Technical Issues (STI), the other on Administrative and Financial Issues (AFI); it also appointed a European Project Team, to be hosted by DESY, with the specific task of preparing all documents necessary for the interested countries to decide to proceed to the Foundation of the European XFEL Facility.

The present report is one of these documents. The following chapters provide a description of the scientific motivations, the background provided by the Tera-Electronvolt Superconducting Linear Accelerator (TESLA) collaboration and the Free-electron LASer in Hamburg (FLASH) facility at DESY (previously known as the VUV-FEL), the physical and technical layout of the new facility, the technical description of the accelerator and of the undulator systems, an indication of the priorities and a technical description of the components of the photon beamlines and the experimental stations.

## 1.1 Accelerator-based light sources

It is evident that light is perhaps the most important tool by which we know the world around us. This is true not only for our everyday experience, but also for the scientific pursuit of an understanding of nature. Experiments using electromagnetic waves, in a range of wavelengths going well beyond the relatively small range of visible light, have played an important role in the development of modern science. Atomic and molecular spectroscopy, i.e. the study of the characteristic wavelengths emitted by matter in the gas phase, has been fundamental in establishing the laws of quantum mechanics and has given us important information on the composition of stars and planets. Röntgen's discovery of x-rays in 1895, and the subsequent demonstration, by von Laue and others in 1911, of x-ray diffraction by crystals laid the foundations of crystallography, by which we can unravel the atomic structure of crystals. Every secondary school student is familiar with Watson and Crick's exploit of 1953, which identified the double helix structure of DNA from the x-ray diffraction work of Franklin and Wilkins, probably the most famous piece of crystallographic work ever.

It is, therefore, hardly surprising that scientists have been eager to obtain the brightest light sources, in order to understand the atomic and electronic structure of matter even

more. In parts of the infrared, in the visible and in the near UV, the invention of the laser has provided an extraordinary tool, which has led to many exciting discoveries and applications. Over a much broader range, encompassing not only the infrared and the visible, but also the whole of the UV and the x-rays to wavelengths well below 0.05 nm, the tool of choice for many scientists is synchrotron radiation (or synchrotron light), i.e. the bright emission of highly collimated electromagnetic waves from electrons (or positrons) orbiting at ultrarelativistic energies in storage rings with diameters of tens to several hundreds of meters (generally called, slightly improperly, “synchrotrons”). In spite of their large dimensions and associated cost, there are some 50 or so storage rings around the world built and operated solely for the purpose of producing light, and more are under construction.

The driving force behind the development of light sources is the optimisation of their brilliance (or spectral brightness), which is the figure of merit of many experiments. Brilliance is defined as a function of frequency given by the number of photons emitted by the source in unit time in a unit solid angle, per unit surface of the source, and in a unit bandwidth of frequencies around the given one. The units in which it is usually expressed are photons/s/mm$^2$/mrad$^2$/0.1% BW, where 0.1% BW denotes a bandwidth of $10^{-3}$ $\omega$ centred around the frequency $\omega$. As one can appreciate from the definition, brilliance puts a premium not only on the photon flux (photons per second in a given bandwidth), but also on the high phase-space density of the photons, i.e. on being radiated out of a small area and with high directional collimation.

The brilliance of available synchrotron sources has been growing at a formidable pace in the last decades, since the first attempts at a systematic exploitation of storage rings as sources of photons for scientific experiments in the 1960s. At that time, some electron storage rings designed and built for nuclear and sub-nuclear physics started to be used parasitically, for some fraction of the time, as sources of photons for experiments in atomic, molecular and solid state physics. These machines are nowadays referred to as “first generation light sources”. The experimental results were so interesting that they stimulated the construction of dedicated rings, designed and optimised to serve exclusively as light sources. Examples of these “second generation” machines are the BESSY I ring in Berlin, the two National Synchrotron Light Source rings in Brookhaven, NY (USA), the SuperACO ring in Orsay, near Paris, and the Photon Factory in Tsukuba (Japan). In the 1990s a new generation of rings started operation. These “third generation” synchrotron sources are characterised by a reduced emittance (i.e. reduced phase-space volume) of the circulating particle beam, and by the extensive use of undulators as radiation sources, with a further increase of the brilliance by several orders of magnitude. Undulators are arrays of magnets, typically 2 to 5 m long, inserted in a straight section of the ring, which produce magnetic force on the drifting electrons and modify their straight trajectory into a zig-zag one, producing a large number of bends with intense radiation emission. Examples of this generation of sources are the European Synchrotron Radiation Facility (ESRF) in Grenoble, the Advanced Light Source in Berkeley, California, Elettra in Trieste, BESSY II in Berlin, Max-II in Lund, Sweden, the Advanced Photon Source, in Argonne, Illinois, Spring 8 in Japan, and the Swiss Light Source in Villigen (CH).

One feature of the storage ring as a light source is that the same electrons turn for hours and hours, going hundreds of thousands and even millions of time per second through the same undulators and dipole magnets. The radiofrequency cavities in the ring give back the radiated energy to the electrons (they typically radiate about 0.1% of their energy at each turn) so that they keep turning and turning. Every times an electron emits a photon, a non-deterministic quantum process, recoil effects perturb its momentum and position. These millions and millions of "random" perturbations per second determine a lower limit to the emittance that the magnetic lattice of the ring can impose on the electrons, i.e. they prevent the phase-space volume of the electrons from being too small. A careful and thorough quantitative analysis shows that it is not possible to substantially lower the emittance of a storage ring below the values achieved in third generation machines. This is the reason why the pursuit for the fourth generation has oriented itself to "single-pass" or "few-passes" machines, where a given electron goes only very few times through an undulator.

## 1.2 Free-electron lasers

At the start of the 21st century, we are witnessing a revolution in synchrotron source intensities, with fourth-generation sources emerging in the form of free-electron lasers (FEL), made possible by recent progress in accelerator technologies, developed in connection with high-energy linear colliders. X-ray FELs (XFELs) have made a new regime of intensities accessible, thus opening up a fundamentally new physical domain.

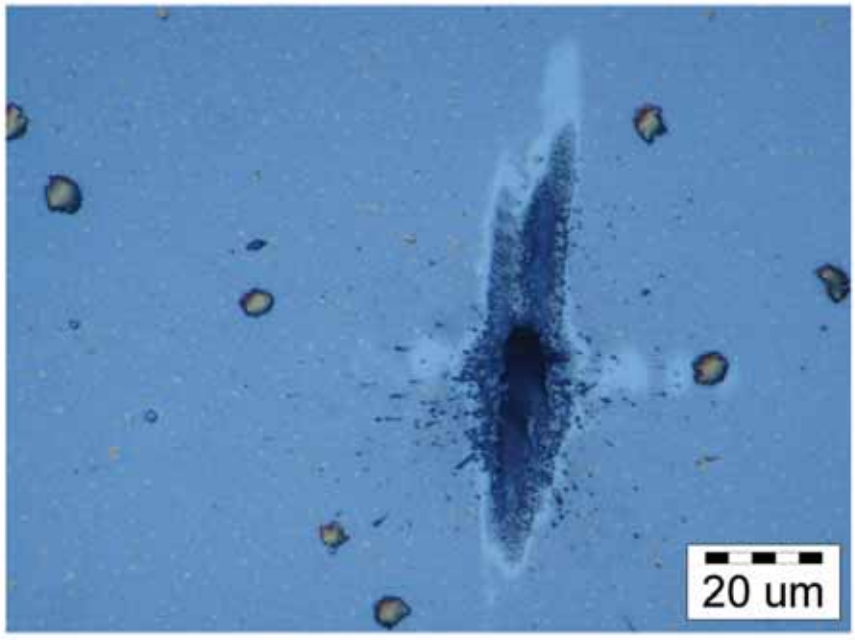


***Figure 1.2.1*** *Interaction of powerful Vacuum Ultraviolet (VUV) radiation with solids* **[1-1]**. *Ablation of Gold target after one pulse of the VUV Self-Amplified Spontaneous Emission (SASE) FEL at the TESLA Test Facility (TTF) at DESY. Radiation wavelength is 98 nm, pulse duration is 40 fs, peak power density is about 100 TW/cm$^2$.*

## Introduction

A new era of synchrotron radiation research has begun with the first user experiments on a VUV FEL based on SASE. Radiation pulses of 98 nm wavelength, with 40 fs pulse duration and a peak power of 1.5 GW, were obtained by the TTF at DESY. Wabnitz et al. reported the first scientific results from this device in **[1-2]**. They illuminated Xenon clusters with high-intensity ($10^{14}$ W/cm$^2$) pulses and observed unexpectedly strong absorption of the VUV radiation. Such a highly nonlinear interaction between light and matter at VUV wavelength range has never been seen before and these fascinating results show the potential of this new class of light sources for scientific research. Further work on FLASH at DESY has been focused on the wavelength range around 80 nm at the request of the second user group. These users studied the ablation of various materials with intense VUV radiation (see Figure1.2.1). FLASH at DESY is currently operating at a wavelength down to 26 nm, and is being extended to cover the soft x-ray spectral range down to wavelengths of 6 nm. Regular user operation started in spring 2005 **[1-3]**.

Compared to present day synchrotron radiation sources, its peak brilliance is more than 100 million times higher (see Figure 1.2.2), the radiation has a high degree of transverse coherence and the pulse duration is reduced from the ~ 100 picoseconds (ps) down to the ~ 10 fs time domain. While modern third generation synchrotron light sources are reaching their fundamental performance limit, recent success in the development of FLASH at DESY has paved the way for the construction of the novel type of light source which will combine most of the positive aspects of both lasers and synchrotrons.

In the following, a slightly more technical description of the physics of FELs is given. The FEL is not, strictly speaking, a laser, i.e. a device based on quantum-mechanical stimulated emission, and its operation is completely described within the framework of classical physics. The FEL is a system consisting of a relativistic electron beam and a radiation field interacting with each other while propagating through an undulator. The FEL is most closely related to vacuum-tube devices. As with vacuum-tube devices, FEL devices can be divided in two classes: amplifiers and oscillators (see Figure 1.2.3). The FEL amplifier is seeded by external radiation, and there is no feedback between the output and input. The FEL oscillator can be considered as an FEL amplifier with a feedback. For an FEL oscillator in the optical wavelength range the feedback is carried out by means of an optical resonator. FELs based on the oscillator principle are limited, on the short-wavelength side, to ultraviolet wavelengths, primarily because of mirror limitations. Free-electron lasing at wavelengths shorter than ultraviolet can be achieved with a single-pass, high-gain FEL amplifier only.

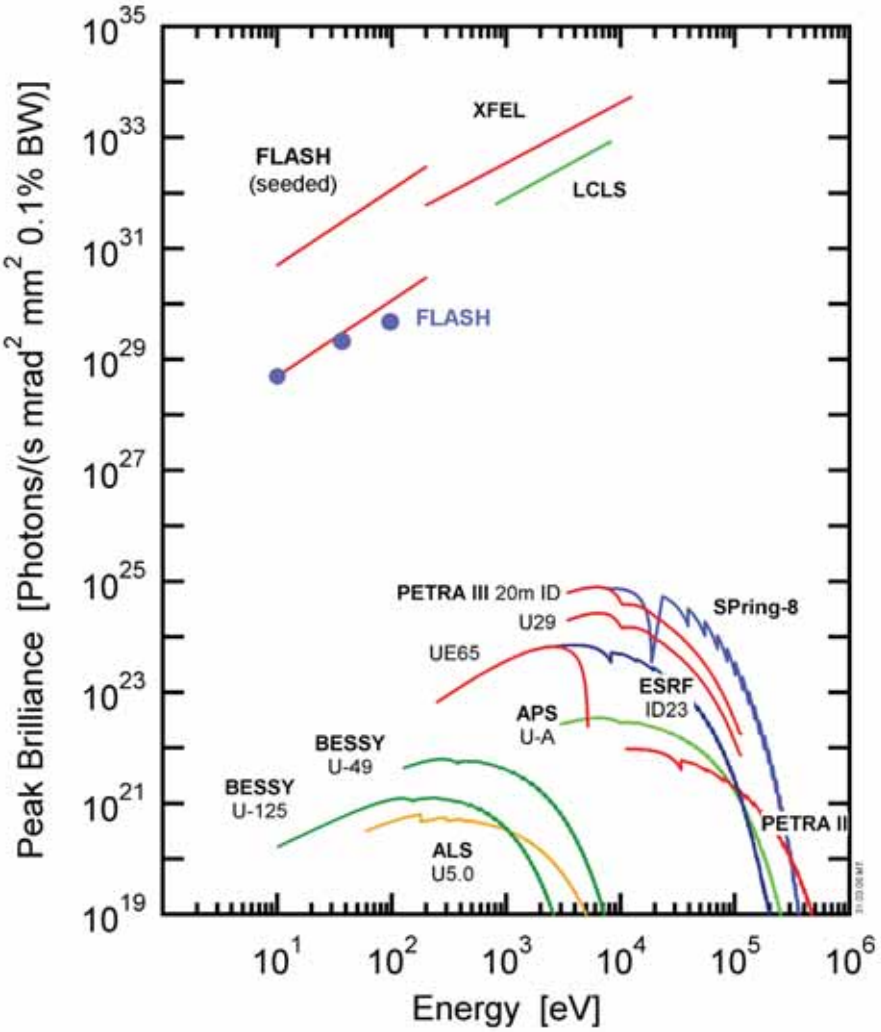


***Figure 1.2.2*** *Peak brilliance of XFELs versus third generation SR light sources. Blue spots show experimental performance of the FLASH at the DESY.*

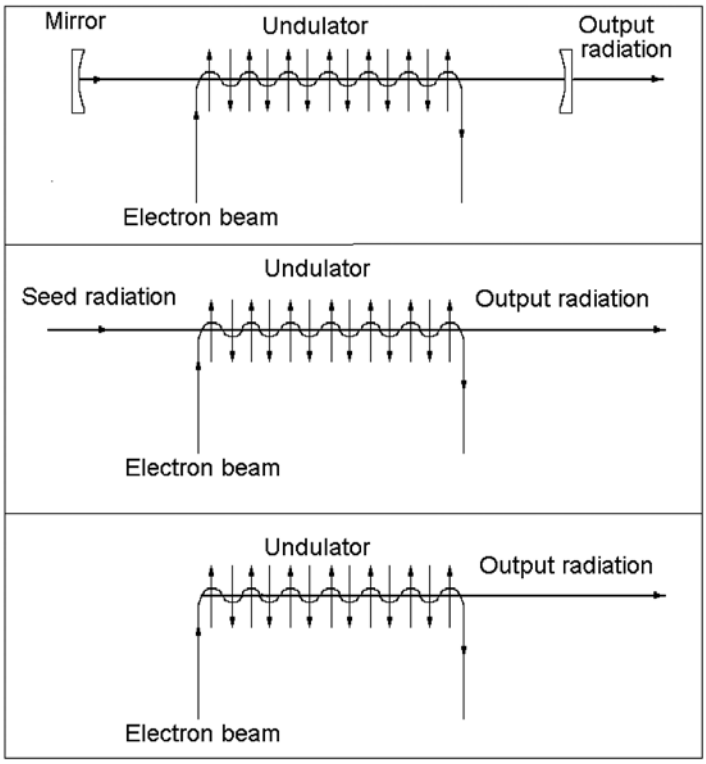


***Figure 1.2.3*** *Free-electron laser configurations: oscillator (top), seeded amplifier (middle), and SASE FEL (bottom).*

The high gain FEL amplifier is an attractively simple device (see Figure 1.2.3). It is a system consisting of a relativistic electron beam and an undulator. At a first glance, this is essentially the setup of a third generation synchrotron radiation source familiar to all users. However, the FEL process is considerably more complicated than the spontaneous emission from relativistic electrons travelling down an undulator. It is essentially a phenomenon that can be described as a radiation-induced collective instability. The basic principle of radiation-induced instability can be described within the standard picture for the generation of synchrotron radiation. Electrons propagate along a sinusoidal path and emit synchrotron radiation in a narrow cone in the forward direction. When an electron beam goes through an undulator, it emits radiation at the resonance wavelength $\lambda = (\lambda_w / 2\gamma^2)(1+K^2)$. Here $\lambda_w$ is the undulator period, $mc^2\,\gamma$ is the electron beam energy, $K=eH_w\,\lambda_w/(2\sqrt{2}\,\pi\,mc)$.

The electromagnetic wave is always faster than the electrons, and a resonant condition occurs when the radiation is ahead of the electrons by a distance $\lambda$ after one undulator period. The fields produced by the moving charges in one part of the electron bunch react on moving charges in another part of the bunch. Thus, we deal with some tail-head instability leading to a growing concentration of particles wherever a small perturbation started to occur.

The FEL collective instability in the electron beam produces an exponential growth (along the undulator) of the modulation of the electron density on the scale of undulator radiation wavelength (micro-bunching). Several conditions must be satisfied for the collective FEL instability to occur. A parameter of crucial importance is the electron beam density in the six-dimensional phase-space. In practice, a (intensity) gain in excess of $10^7$ - $10^8$ can be obtained in the short wavelength regime. At this level of gain, the shot noise of the electron beam is amplified up to complete micro-bunching. In the beginning – without micro-bunching – all the $N$ electrons can be treated as individually radiating charges, and the resulting spontaneous emission power is proportional to $N$. With complete micro-bunching, all electrons radiate almost in phase. This leads to a radiation power growth as $N^2$, and thus, to an amplification of many orders of magnitude with respect to spontaneous emission of the undulator.

Fluctuations of the electron beam current play the role of an input signal to the XFEL. The shot noise corresponds to the fact that photoelectron emission from a cathode is a random process. The emission of electrons from the cathode is believed to be a Poisson process, and from this assumption alone the total fluctuations in current can be deduced. Such random fluctuations in the beam current correspond to an intensity modulation of the beam current at all frequencies simultaneously – including, of course, the frequency to which the undulator is tuned. When the electron beam enters the undulator, the presence of the beam modulation at frequencies close to the resonance frequency initiates the process of radiation.

The actual physical picture of start-up from noise should take into account that the fluctuations of current density in the electron beam are uncorrelated, not only in time, but in space as well. Thus, a large number of transverse radiation modes are excited when the electron beam enters the undulator. These radiation modes have different gain. Obviously, as they progress down the undulator, the high gain modes will increasingly dominate and we can regard the XFEL as a filter, in the sense that it filters the components corresponding to the high gain modes from an arbitrary radiation field. If we consider the undulator radiation from the point of view of paraxial optics, then we immediately see that the high gain modes are associated with radiation propagating along the axis of the undulator, as opposed to radiation propagating at an angle to the axis, which has a low gain. Hence, for a sufficiently long undulator, the emission will emerge in a single (fundamental) transverse mode and the degree of transverse coherence of the output radiation will approach unity.

The amplification bandwidth of a high gain FEL amplifier is determined by the number of undulator periods $N_w$ within one gain length. The gain length is the distance over which the power increases by a factor of e (e=2.718…). Since we study the start-up from shot noise, we assume the input current to have an homogeneous spectral distribution. The spectrum of the transversely coherent fraction of radiation is concentrated within the narrow band, $\Delta\lambda / \lambda = 1 / (2\pi N_w)$. The typical amplification bandwidth of the XFEL is of the order of 0.1%. The electron beam in XFEL transfers enormous peak power. For instance, for typical XFEL parameters (energy of electrons 17.5 GeV and peak current 5 kA), it is about 100 TW. The conversion efficiency of the kinetic energy of electrons into light is in

the order of the amplification bandwidth, therefore, the peak power of X-ray radiation is in the multi-GW range.

## 1.3 Historical development of the XFEL

The origin of the FEL history can be traced to the paper by Pantell, Soncini, and Puthoff **[1-4]**, which contains the first complete set of distinctive features of the FEL: stimulated scattering of the radiation on relativistic electrons moving in the undulator. After the pioneering work of Madey and co-authors **[1-5]** on the first FEL oscillator, and subsequent theoretical work by Kroll and Mc Mullin on the possibility of single-pass gain **[1-6]** the XFEL, which was proposed in 1982, has had more than 20 years of development. The first proposal to use the FEL collective instability to produce optical radiation using a single-pass amplifier starting from shot noise, was published by Kondratenko and Saldin in 1979 **[1-7]**. Single-pass amplification with start-up from noise was also investigated by Bonifacio, Pellegrini, and Narducci **[1-8]**. Following the terminology of quantum lasers (amplified spontaneous emission, ASE), Bonifacio et al. **[1-9]** used the term “self amplified spontaneous emission (SASE)” in connection with an FEL amplifier starting from shot noise. This terminology does not completely correspond to the actual FEL physics (in fact, it is just a vacuum-tube device), but the abbreviation “SASE FEL” has been widely accepted by the physics community.

The first proposal to use the instability in a single-pass amplifier starting from shot noise for a soft (5 nm) XFEL was published by Derbenev, Kondratenko, and Saldin in 1982 **[1-10]**. This proposal envisaged the use of a storage ring to provide the electron beam. At that time, an electron storage ring was the accelerator delivering the highest electron beam quality. Later on, a similar proposal was discussed by Murphy and Pellegrini in 1985 **[1-11]**. However, the limitations on emittance, peak current and energy spread limited the shortest FEL wavelength to about 10 nm.

The next important step was the proposal by Pellegrini, in 1992, of using a recently developed radio frequency (RF) photocathode electron gun coupled to the two-mile Stanford linear accelerator (linac), to produce lasing in the hard x-ray region **[1-12]**. A study group coordinated by Winick developed this concept, calling it the Linac Coherent Light Source (LCLS). This work led many groups to start development of SASE FELs in the infrared to VUV spectral ranges, to demonstrate the concept and develop the technologies necessary to build a linac-based XFEL. First experimental results were obtained in 1997. The SASE FEL theory received some experimental support when the high-gain linear regime of the SASE FEL operation in the infrared range was achieved by Pellegrini and co-workers **[1-13]**. This was the first unambiguous demonstration of the SASE FEL mechanism.

After many years of development, efforts to produce saturated lasing using a SASE FEL started to come to fruition at the start of this century. In September 2000, a group at Argonne National Laboratory (ANL) demonstrated saturation in a visible (390 nm) SASE FEL **[1-14]**. In March 2001, the VISA collaboration, between Brookhaven National Laboratory (BNL), UCLA and the Stanford Linear Accelerator Centre (SLAC), demonstrated lasing to saturation at 830 nm **[1-15]**.

In September 2001, the VUV-FEL at DESY demonstrated lasing to saturation at 98 nm **[1-16]**. In January 2002, saturation was achieved at 82 nm **[1-17]**, and in November 2005 the lasing at 26 nm, the shortest wavelength at which any FEL works, was demonstrated. Recently, the German government, encouraged by these results, launched the proposal of a European collaboration to establish a hard X-ray SASE FEL user facility – the European X-ray Free-Electron Laser Facility at DESY. The US Department of Energy (DOE) has given SLAC the go ahead for the LCLS to be constructed at SLAC. These devices will produce 100 fs x-ray pulses with over 10 GW of peak power **[1-18, 1-19]**, and will be able to produce intensities in the order of $10^{18}$ W/cm$^2$. The main difference between the two projects is the linac: the LCLS will be based on the existing room temperature SLAC Linac; the European XFEL, on the other hand, is foreseeing the construction of a superconducting Linac based on the TESLA technology.

The XFEL based on superconducting accelerator technology will make possible not only a jump in peak brilliance by ten orders of magnitude, but also an increase by five orders of magnitude in average brilliance. The LCLS and European XFEL projects are scheduled to start operation in 2009 and 2013, respectively.

## References

**[1-1]** L. Juha et al., *Ablation of various materials with intense XUV radiation,* Nucl. Instrum. and Methods A 507 (2003) 577.

**[1-2]** H. Wabnitz et al., *Multiple Ionization of Atom Clusters by Intense Soft X-rays from a Free-Electron Laser,* Nature 420 (2002) 482.

**[1-3]** V. Ayvazyan et al., *First operation of a free-electron laser generating GW power radiation at 32 nm wavelength*, Eur. Phys. J. D37 (2006) 297.

**[1-4]** R.H. Pantell, Y. Soncini, and H.E. Puthoff*, Stimulated Photon-Electron Scattering*, IEEE Quantum Electronics 4 (1968) 905.

**[1-5]** D.A.G. Deacon et al., *First Operation of a Free-Electron Laser,* Phys. Rev. Lett. 38 (1977) 892.

**[1-6]** N.M. Kroll and W.A. McMullin, *Stimulated emission from relativistic electrons passing through a spatially periodic transverse magnetic field,* Phys. Rev. A 17 (1978) 300.

**[1-7]** A.M. Kondratenko, E.L. Saldin, *Generation of Coherent Radiation by a Relativistic Electron Beam in an Undulator,* Sov. Phys. Dokl. vol. 24, No. 12 (1979) 986; Part. Accelerators 10 (1980) 207.

**[1-8]** R. Bonifacio, C. Pellegrini and L.M. Narducci, *Collective Instabilities and High-Gain Regime in a Free-Electron Laser,* Opt. Commun. 50 (1984) 373.

**[1-9]** R. Bonifacio, F. Casagrande and L. De Salvo Souza, *Collective Variable Description of a Free-Electron Laser,* Phys. Rev. A 33 (1986) 2836.

**[1-10]** Ya.S. Derbenev, A.M. Kondratenko, and E.L. Saldin, *On the Possibility of Using a Free-Electron Laser for Polarization of Electrons in Storage Rings,* Nucl. Instrum. and Methods 193 (1982) 415.

**[1-11]** J.B. Murphy and C. Pellegrini, *Free electron lasers for the XUV spectral region*, Nucl. Instrum. and Methods A 237 (1985) 159.

**[1-12]** C. Pellegrini, *A 4 to 0.1 nm FEL Based on the SLAC Linac,* Proceedings of the Workshop on Fourth Generation Light Sources, SSRL-SLAC report 92/0.2, (1992), p. 364.

**[1-13]** M. Hogan et al., *Measurements of Gain Larger than 105 at 12 μm in a Self-Amplified Spontaneous-Emission Free-Electron Laser,* Phys. Rev. Lett. 81 (1998) 4867.

**[1-14]** S.V. Milton et al., *Exponential Gain and Saturation of a Self-Amplified Spontaneous Emission Free-Electron Laser*, Science, 292 (2001) 2037.

**[1-15]** A. Tremaine et al., *Characterization of a 800 nm SASE FEL at saturation,* Nucl. Instrum. and Methods A483 (2002) 24.

**[1-16]** V. Ayvazyan et al., *Generation of GW Radiation Pulses from a VUV Free-Electron Laser Operating in the Femtosecond Regime*, Phys. Rev. Lett. 88 (2002) 104802.

**[1-17]** V. Ayvazyan et al., *A new powerful source for coherent VUV radiation: Demonstration of exponential growth and saturation at the TTF free-electron laser,* Eur. Phys. J. D20 (2002) 149.

**[1-18]** P. Audebert et al., *TESLA XFEL: First stage of the X-ray laser laboratory – Technical design report* (R. Brinkmann et al., Eds.), Preprint DESY 2002-167 (see also http://xfel.desy.de).

**[1-19]** The LCLS Design Study Group, *LCLS Design Study Report*, SLAC reports SLAC-R521, Stanford, 1998 (see also http://www-ssrl.slacstanford.edu/lcls/CDR).

# 2 TTF/FLASH in the XFEL context

## 2.1 Historical background

In the early 90s, the Tera-Electronvolt Superconducting Linear Accelerator (TESLA) Test Facility (TTF) was established by the international TESLA collaboration as a test bed for studies of superconducting linac technology for a future linear collider. To this end, work at TTF **[2-1]** was focused on achieving an accelerating gradient around 25 MV/m and on the development of techniques to manufacture such accelerating components in a reliable and cost-effective way. Furthermore, experimental verification of the components' performance in terms of field quality, beam dynamics, reliability, diagnostics tools and control procedures was a key objective.

It was realised very soon, that a superconducting accelerator like TTF would be perfectly suited to drive a free-electron laser (FEL) at wavelengths far below the visible, mainly due to:

- the large iris diameter of the accelerator cavities – wake field effects, eventually degrading the electron beam quality, are very small compared to standard normal conducting cavities;
- its excellent power efficiency – a superconducting linac can be operated at very high duty cycle, up to continous wave operation, a fact that allows for very high average brilliance and for large flexibility in terms of timing structure.

Based on these superior properties, the vision from the very beginning was to develop superconducting FEL technology in a way applicable within a large range of wavelengths, down to the x-ray regime **[2-2]**. As there are no normal incidence mirrors at very short wavelengths, the Self-Amplified Spontaneous Emission (SASE) principle **[2-3, 2-4]** was the most promising concept to adopt.

At that time, the SASE principle was experimentally demonstrated only at wavelengths in the microwave regime **[2-5]**. The direct jump to Ångstrom wavelengths, i.e. a jump by seven orders of magnitude in wavelengths, was considered too ambitious. Thus, a jump by four orders of magnitude was proposed **[2-6]** to reach 100 nm, a wavelength regime where the SASE FEL principle is competitive with other types of lasers. This could be done with the available TTF accelerator by adding a suitable electron source, a bunch compressor, and a 15 m long undulator. This installation was called TTF FEL, Phase 1.

However, besides proving the principle, it was even more important to make scientific use of this new type of radiation source as soon as possible. Thus, in a second phase, the scientifically attractive vacuum ultraviolet (VUV) wavelength range between 6 nm and 40 nm was to be achieved. To this end, the TTF linac had to be upgraded to 1 GeV

maximum beam energy, an additional bunch compressor and a 30 m long undulator had to be installed, and a hall for user experiments had to be built. A proposal **[2-7]** of a two-stage realisation of a SASE FEL user facility based on the TTF, as outlined already, was endorsed by an international advisory committee. This facility was called VUV-FEL. In April 2006, it was renamed as Free-electron LASer in Hamburg (FLASH).

## 2.2 TTF FEL, Phase 1

### 2.2.1 Accelerator R&D

From the very beginning, the overall design of the TESLA superconducting accelerator (linac) was based on nine-cell cavities made from pure Niobium, tuned for the TM010 $\pi$-mode at 1.3 GHz. Eight of such 1.04 m-long elements were assembled into one cryostat module, together with a superconducting magnet package (consisting of quadrupoles, dipole correctors and a beam position monitor), radio frequency (RF) input couplers, and various sensors. While alternative configurations were investigated within the R&D programme at TTF, this general layout was so successful that it has remained unchanged up to now.

At the beginning, the TESLA cavities typically achieved accelerating gradients around 15 MV/m, with considerable fluctuations. The improvement up to the present-day values beyond 35 MV/m was mainly due to intensive research on the treatment of both the bulk and the surface of the Niobium material. Details are given in Section 4.2.1.3 of this report.

### 2.2.2 FEL research

The TTF FEL installation in Phase 1 consisted of a low-emittance, laser-driven RF-gun, a pre-accelerator followed by the first magnetic bunch compressor chicane, two TESLA accelerating modules separated by a second magnetic bunch compressor chicane, and a 15 m long undulator, as illustrated in Figure 2.2.1.

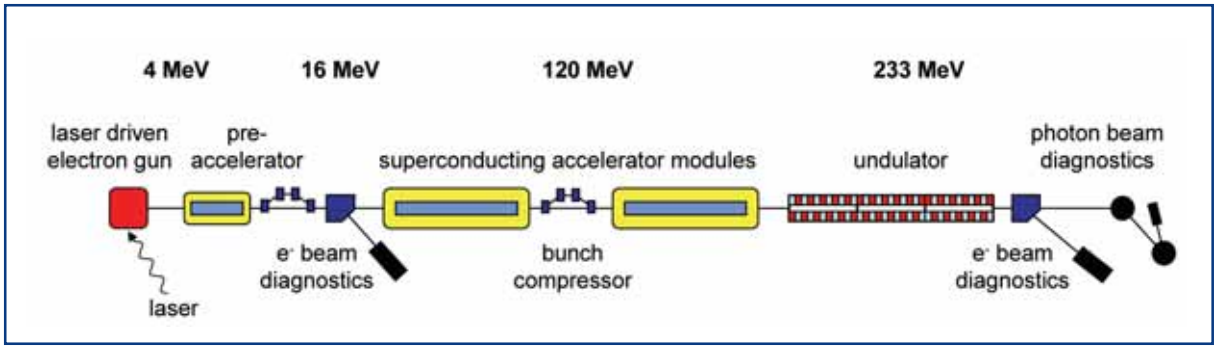


***Figure 2.2.1*** *Schematic layout of Phase 1 of the SASE FEL at the TTF at Deutsches Elektronen Synchrotron Laboratory (DESY), Hamburg. The total length was 100 m.*

The undulator was a permanent-magnet device **[2-8]** with a 12 mm fixed gap and an undulator parameter of K = 1.17. In order to achieve the minimum FEL gain length, the optimum beta function $\beta_{opt} \approx$ 1 m had to be realised inside the undulator. To this end, permanent-magnet quadrupole fields were superimposed on the periodic undulator field

in order to focus the electron beam along the undulator. The undulator system was subdivided into three segments, each 4.5 m long and containing ten quadrupole sections with alternating gradients. The vacuum chamber made from extruded aluminium profiles incorporated ten beam position monitors and ten dipole magnets per segment for orbit steering.

In addition, two pick-up type beam position monitors, and horizontal and vertical wire scanners were installed at the entrance and exit of each undulator segment, with the wire positions aligned with respect to a stretched wire determining a straight reference line. Also, an electron beam collimator was installed in front of the undulator to protect it from radiation damage by electrons with large betatron amplitudes, generated, for instance, by dark current.

### 2.2.3 Results

The TTF FEL, Phase 1 demonstrated a unique femtosecond mode of operation which was not considered at an early design stage of the project **[2-7]**. Due to nonlinear compression and a small local energy spread, a short high-current (3 kA) leading peak (spike) in the bunch density distribution has been produced by the beam formation system **[2-9]**. Despite strong collective effects (of which the most critical was the longitudinal space charge after compression), this spike was bright enough to drive the FEL process up to saturation for wavelengths around 100 nm **[2-10 – 2-12]**. In addition to the possibility for production of high-power femtosecond pulses, this mode of FEL operation demonstrated high stability with respect to drifts of machine parameters.

The TTF FEL, Phase 1 delivering a peak brilliance of $2\times10^{28}$ photons/(s mrad$^2$ mm$^2$ (0.1% bandwidth)) between 80 and 120 nm, was readily used to perform pioneering experiments **[2-13, 2-14]**.

A most important result was the perfect agreement between FEL theory and observation in the wavelength regime around 100 nm **[2-9 – 2-12]**. Figure 2.2.2 shows both the theoretical and experimentally determined gain curve for a wavelength of 98 nm.

By variation of bunch compressors settings it was possible to control the width of the lasing fraction of the electron bunch, resulting in a controlled variation of the radiation pulse length between 30 fs and 100 fs (FWHM). As a consequence, the radiation pulse consisted of only a few optical modes, as seen from single pulse spectra (Figure 2.2.3).

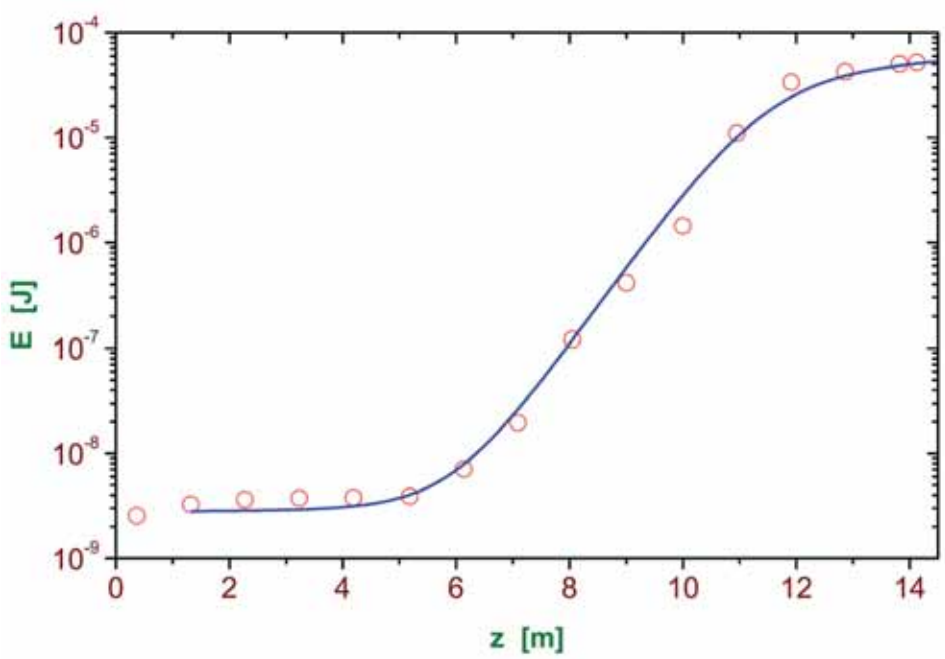


***Figure 2.2.2*** *Average energy in the radiation pulse as a function of the active undulator length at the TTF FEL, Phase 1. Circles: experimental results. Solid curve: numerical simulation using measured electron beam parameters. The wavelength for this measurement was chosen at 98 nm.*

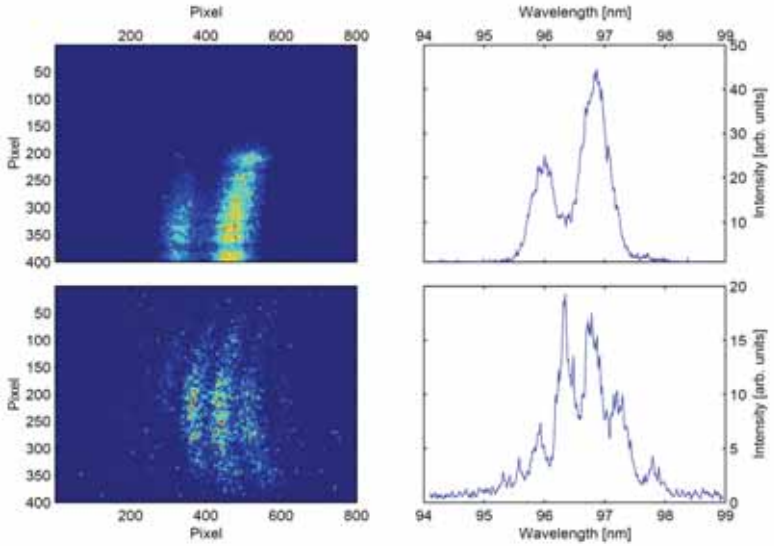


***Figure 2.2.3*** *Spectra from short (top) and long (bottom) FEL pulses, taken at TTF FEL, Phase 1. On the left hand side, the CCD image of the dispersed FEL radiation in the exit plane of the monochromator is shown in a false color code. The dispersive direction is the horizontal one. On the right hand side, the spectra are evaluated quantitatively along the horizontal centre line of the CCD image. The numbers of modes are different: for short pulses (top), there are, on average, 2.6 modes, in the long pulse setting, there are six modes on average.*

### 2.2.4 Experience from commissioning procedures

It took several months from the first observation of spontaneous radiation to the demonstration of lasing. The main reason for this difficulty was insufficient orbit control inside the undulator and incomplete knowledge about the detailed 6D (six-dimensional) phase-space distribution of the electron bunch.

While the combination of undulator field and quadrupole field was a very elegant solution, it left only one way for beam-based alignment of position monitors, namely by changing the beam energy drastically. This procedure turned out to be impractical at TTF FEL, Phase 1 in reality. As the number of free parameters to be varied for finding first lasing is very large, it was extremely important for machine operators to have information on the orbit they could really trust. Therefore, a large number of precisely aligned wire scanners, representing an entirely independent mechanical system for orbit control, turned out to be indispensable.

The most critical step has been to find the onset of laser amplification. For this purpose, a radiation detector equipped with a microchannel plate (MCP) has been used, which features a dynamical range of seven orders of magnitude and covers the entire range of intensities from spontaneous emission up to FEL saturation **[2-15]**. With only little gain present, the FEL beam is hidden in the powerful background of spontaneous undulator radiation. Thus, it was essential that the MCP device was sensitive enough to detect even a few percent of growth in radiation energy. In principle, it should have been possible to achieve a much better suppression of spontaneous background by the insertion of an iris collimating the opening angle seen by the detector. In view of the uncertainty in prediction of the pointing direction of the FEL photon beam, this way was not taken.

While TTF FEL, Phase 1 was running, the design of FLASH was finished in detail, and components were fabricated and tested.

## 2.3 TTF FEL, Phase 2 – FLASH

### 2.3.1 Design

While the original proposal was already published in 1995, the actual start of the installation work for conversion of TTF FEL, Phase 1 into FLASH was in 2002. Based on the experience gained, the design was modified from the original proposal, and a more accurate prediction of beam dynamics and FEL performance could be given. This was described in an update to the 1995 design report **[2-16]**. After commissioning the injector and the first bunch compressor, these predictions could be even more refined **[2-17]**. The key modifications were:

- a larger hall for five photon beamlines and experimental facilities was planned;
- a beamline section giving room for later installation of a seeding option, was inserted;

- during electron beam commissioning, and during beam time dedicated to accelerator research, the electron beam has to be transported down to the beam dump without making any use of the undulator. At TTF FEL, Phase 1, lots of time was wasted in finding a way of keeping the beam losses in the undulator at a tolerable level during such modes of machine operation. Thus, a 100 m long bypass beamline was added to optionally bypass the undulator and seeding section;
- At TTF FEL, Phase 1, off-momentum particles were a source of radiation damage to the undulator, that could not be removed in the straight collimator section. Thus, the collimator for FLASH includes a dispersive dog-leg section;
- the focusing in the undulator section was changed from a superimposed permanent-magnet lattice to electro-magnetic quadrupoles located in the space between the undulator segments. In this way, beam-based alignment can be done without changing beam energy. The minimum average beta function values that can be achieved with this focusing lattice is approximately 4 m. This comes sufficiently close to the optimum beta function of $\beta_{opt} \approx$ 3 m, calculated for FLASH parameters. Except for this modification, the undulator design remained unchanged.

Progress on the TESLA accelerator R&D has been reported in the “TESLA Reports” series (351 reports so far), while the “TESLA-FEL Reports” series is dedicated to FEL-specific work (109 reports by now). In addition, more than 1,000 papers have been published on TTF/FLASH issues since 1993. Figure 2.3.1 illustrates the overall layout of FLASH.

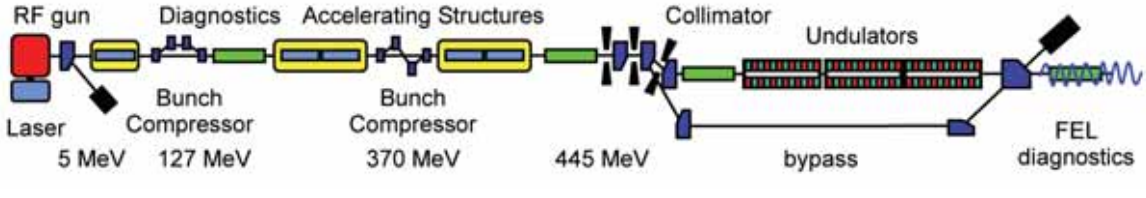


***Figure 2.3.1*** *Schematic layout of Phase 2 of the SASE FEL at the TTF at DESY, Hamburg, now called FLASH. The total length is approximately 330 m (including the experimental hall not shown in the sketch).*

Up to the present time (summer 2006), the maximum beam energy is limited at approximately 730 MeV, since only five TESLA Modules are installed yet, with some cavities limited in gradient.

The new tunnel built to house the additional accelerator modules, the collimator, and the undulator sections, has a circular cross section to mimic the tunnel for a future linear collider and for the X-Ray Free-Electron Laser (XFEL).

Table 2.3.1 shows a few key parameters of FLASH. It is obvious that, in spite of a factor of 1,000 difference in wavelength, the respective requirements on the electron beam invariants for the FLASH and the XFEL do not differ very much.

| Item | FLASH | |
|---|---|---|
| Normalised emittance @ 1 nC | $2\pi$ | mrad mm |
| Peak current | > 2500 | A |
| Nominal bunch charge | 1 | nC |
| Maximum RF pulse repetition rate | 10 | Hz |
| Maximum RF pulse length | 0.8 | ms |
| Maximum number of bunches per RF pulse | 7200 | |
| Total length of vacuum beamlines (including bypass) | 358 | m |
| Number of magnet units (including 99 steerer magnets) | 213 | |
| Number of TESLA cavities (as of June 2006) | 40 | |
| Number of beam diagnostics units | > 146 | |
| Total length of cables | 215 | km |

***Table 2.3.1*** *Key numbers characterising the design of FLASH.*

### 2.3.2 Installation

As indicated in Table 2.3.1, a large number of components had to be installed into the new tunnel. During the course of this work, engineering experience was gained on the installation of SASE FEL components and superconducting accelerator components into a tunnel 5.2 m in diameter:

- Transport and installation of the TESLA Modules and the cryogenic supply lines does not represent a major problem. However, these components determine, to a large extent, the possible arrangements of other components, like klystrons, power supplies and electronics. The lessons from this experience were part of the decision to change the tunnel layout of the XFEL in terms of module mounting. The accelerator modules will be suspended from the ceiling in order to arrange all components requiring maintenance and/or replacement in a much more accessible way.
- Most of the power supplies and electronics to be located inside the tunnel were installed into 32 standard size containers with the advantage that most of the cabling work could be done outside the tunnel. In view of the XFEL, pros and cons of this concept can now be discussed based on hands-on experience. Figure 2.3.2 illustrates the location of these containers within the tunnel cross section.
- The undulator segments, each 4.5 m long, are separated by an insert containing a quadrupole doublet (mounted on micro-movers), a beam position monitor and a pair of wire scanners. These components were all mounted on a granite block and aligned, with respect to each other, to better than 50 µm precision. The overall alignment of all undulator components with respect to one another was supported, and can be monitored, by a stretched wire system.
- Klystron installation inside the tunnel will be a major issue for long accelerator tunnels (XFEL, International Linear Collider (ILC)) and was thus, originally, among the test items. Such a test was abandoned as it would have delayed the FLASH schedule considerably.


***Figure 2.3.2*** *Left: FLASH accelerator tunnel with part of the collimator section and an electronics container visible. Right: The undulator consists of six segments, each 4.5 m long.*

### 2.3.3 Accelerator commissioning

Due to the large number of different components and new as well as ambitious accelerator physics issues, initial commissioning of the machine took several months. Just after it achieved lasing close to the saturation level, first beam was delivered to the users. Even more, it was decided to start user operation without waiting to achieve full performance operation. Although this commissioning philosophy puts some burden on the early users, it seems to be adequate for a new SASE FEL, as it permits users to gain experience and perform experiments as soon as possible while the early user operation periods still allow the accelerator experts to gain knowledge about FEL physics and machine behaviour parasitically. The consequence of the chosen commissioning philosophy is, strictly speaking, that it will take several years to reach the full parameter range.

The first component setting the stage for successful FEL operation is a low-emittance electron source. A dedicated photo-injector has been developed, commissioned and characterised at the Photo-Injector Test Stand (PITZ) at DESY-Zeuthen **[2-18, 2-19]**. Having shown satisfactory performance, the gun was moved and installed into TTF, thus considerably saving commissioning time at TTF.

Commissioning of the entire beamline, some 30 m long, from the photoinjector through the first bunch compression at approximately 125 MeV was the first, major commissioning milestone. The beam dynamics of the dense electron bunch is heavily affected by space-charge forces up to (at least) 100 MeV, thus representing a serious challenge for the commissioning procedure.

The most important result of injector commissioning was the proof that the injector beamline works as theoretically predicted. For measurement of the beam emittance (see Figure 2.3.3), a periodic FODO channel was inserted, permitting a reliable and reproducible determination of beam emittance by four optical transition radiation (OTR) screens, thus eliminating the need for a quadrupole scan.

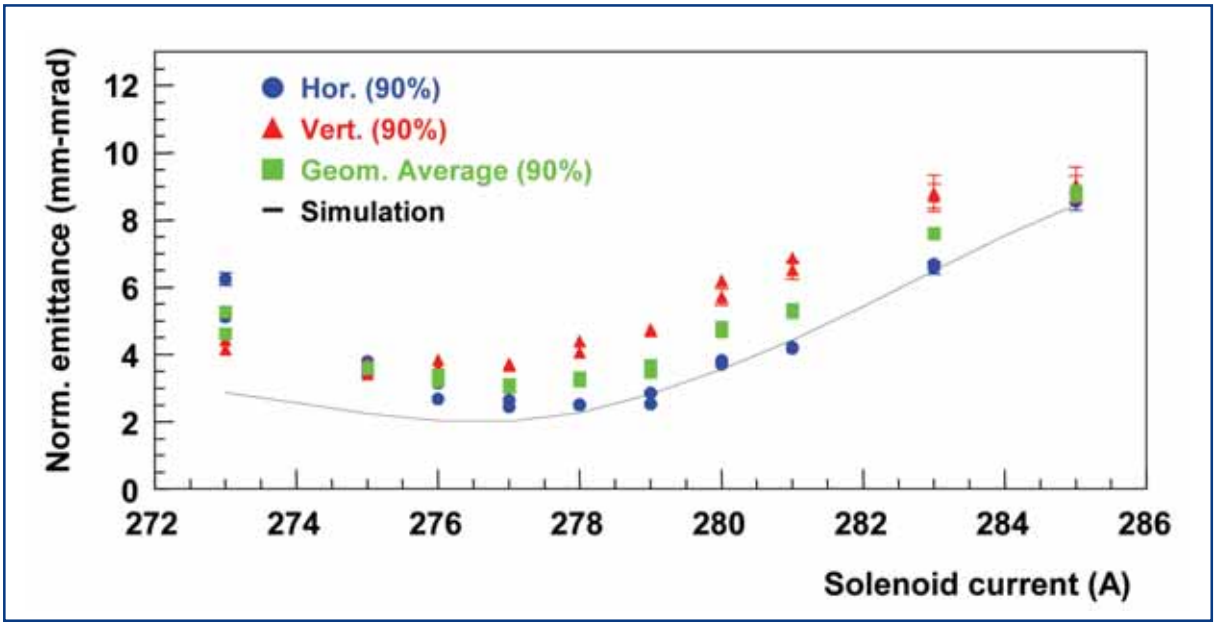


***Figure 2.3.3*** *Measurement of beam emittance at 125 MeV, 1 nC bunch charge, no compression, as a function of the solenoid current at the RF gun. The injector was at its nominal parameters, without further attempts to minimise the emittance. Emittance values quoted contain 90% of the bunch charge.*

When bunch compression was switched on, comparison between measured and calculated beam parameters became much harder, mainly for two reasons:

- With peak currents exceeding 1 kA, space charge forces, and coherent synchrotron radiation (CSR) effects play a leading role in beam dynamics even at beam energies above 100 MeV. According to beam dynamics simulation results, the 6-D phase-space distribution becomes very involved. The control and understanding of beam envelopes becomes very hard as they are no more determined by initial conditions and linear optics only, but also by RF phase settings and bunch charge. In addition, the generation of spurious dispersion was observed, generated, for example, by energy losses due to CSR in the bunch compressors.
- As long as a third harmonic accelerating section is missing (installation at FLASH is scheduled for 2007), the expected longitudinal electron distribution consists of a leading spike about 50 fs long, containing some 10% of the total charge with a peak current exceeding 1 kA, and a long tail with current too small for providing significant FEL gain. According to simulation, this tail has phase-space coordinates quite different from the lasing spike. As most of the diagnostics tools (like wire scanners, OTR screens or beam position monitors) are only able to determine integral properties of the bunch, it is, thus, presently almost impossible to precisely control the orbit and the optics match of the lasing spike.

In spite of these difficulties, it was, nevertheless, possible to determine important properties of the lasing spike with the help of a transverse deflecting cavity (called LOLA). In particular, it was possible to verify the expected longitudinal charge distribution, identify a horizontal offset of the spike with respect to the tail and determine the emittance of the spike. All these values are in reasonable agreement with expectations. A measurement of the longitudinal bunch shape is shown Figure 2.3.4.

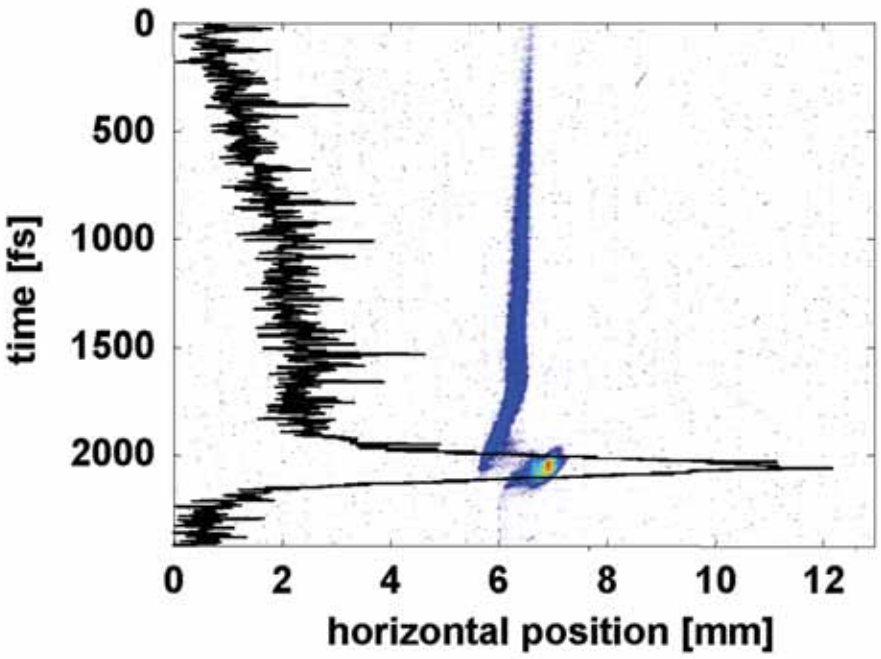


***Figure 2.3.4*** *Longitudinal charge distribution within a single electron bunch of FLASH. In the centre, the image of the bunch on an observation screen is seen. The screen is located downstream of a transverse mode resonator streaking the bunch vertically by a time-dependent field. The horizontal position of electrons is given on the horizontal axis, while the relative longitudinal position inside the bunch is encoded in the vertical coordinate, with the head of the bunch to the bottom. The solid curve shows the charge density projected onto the longitudinal position, i.e. the electron current profile within the bunch. A sharp spike shorter than 120 fs (FWHM) is seen at the head of the bunch, in accordance with beam dynamics calculations.*

### 2.3.4 FEL commissioning

Successful operation of the TTF FEL, Phase 1 in the femtosecond regime and theoretical studies **[2-17]** encouraged us to extend such a mode of operation for shorter wavelengths. It has been found that the beam formation system of the linac can be tuned for production of bunches with a high-peak-current spike driving the FEL process such that FLASH should saturate down to the shortest design wavelength of 6 nm.

Based on the experience from commissioning the TTF FEL, Phase 1 and using similar methods and tools (in particular an MCP detector), first lasing could be established at 32 nm already one week after the first passage of the electron beam through the undulator. Single shot spectra were in agreement with expectations (see Figure 2.3.5),

and, at higher FEL gain approaching the expected saturation regime **[2-20]**, second and third harmonics were observed, as theoretically expected, see Figure 2.3.6.

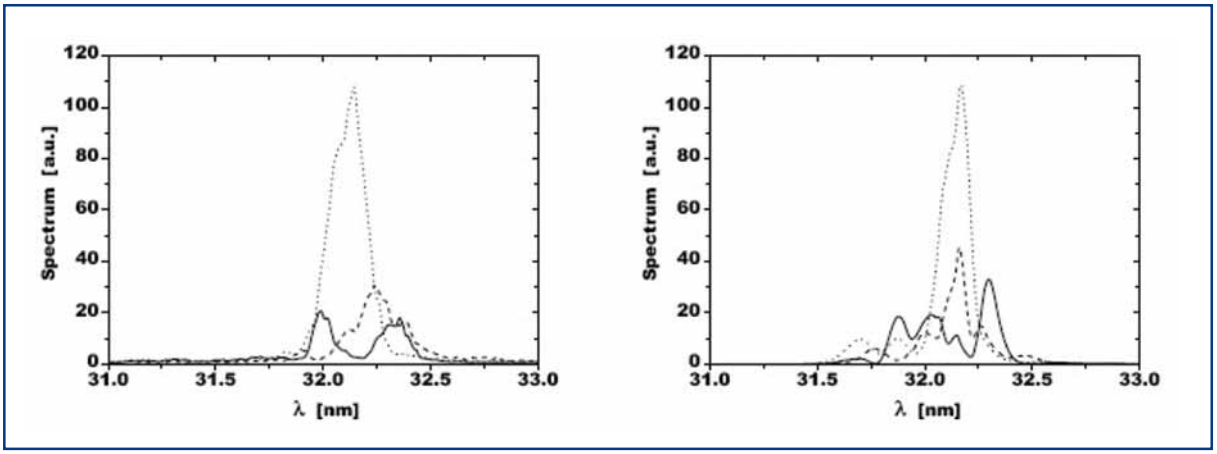


***Figure 2.3.5*** *Three different measured (left) and calculated (right) single-shot spectra of FLASH.*

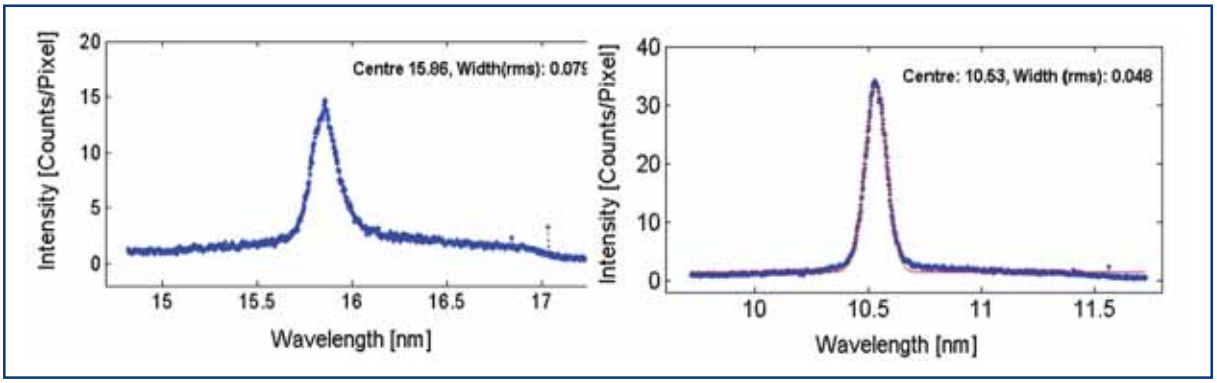


***Figure 2.3.6*** *Second (left) and third (right) harmonics FEL radiation spectra measured at the FLASH facility* **[2-22]**.

From the analysis of single-shot spectra and their fluctuation properties, the FWHM pulse duration of the radiation pulses has been determined at (25 ± 5) fs. The angular divergence of the radiation is almost diffraction limited **[2-20]**. Measurements of the double-slit diffraction patterns indicate a high degree of transverse coherence as well, see Figure 2.3.7. Later on, lasing has been demonstrated in the range of wavelengths from 13.1 nm to 45 nm. The best performance of FLASH has been obtained at the end of the user run in June 2006. At the wavelength of 25.7 nm, the average energy in the radiation pulse was 65 µJ, and peak values were up to 120 µJ (see Figure 2.3.8). At a wavelength of 13.9 nm, the average energy in the radiation pulse was up to 25 µJ. The peak brilliance was $1.5 \times 10^{29}$ and $5 \times 10^{29}$ photons/(s mrad$^2$ mm$^2$ (0.1% bandwidth)) for the wavelengths 25.7 and 13.9 nm, respectively (see Figure 1.2.2), with the accumulated uncertainty being some factor of two. We can conclude that the design goals for the present machine configuration are reached in two key aspects, namely the minimum wavelength (within the limit presently determined by the maximum energy of the accelerator) and the maximum output power: FLASH currently produces GW-level, laser-like VUV radiation pulses on a sub-50 fs scale in agreement with theoretical predictions **[2-17, 2-21]**.

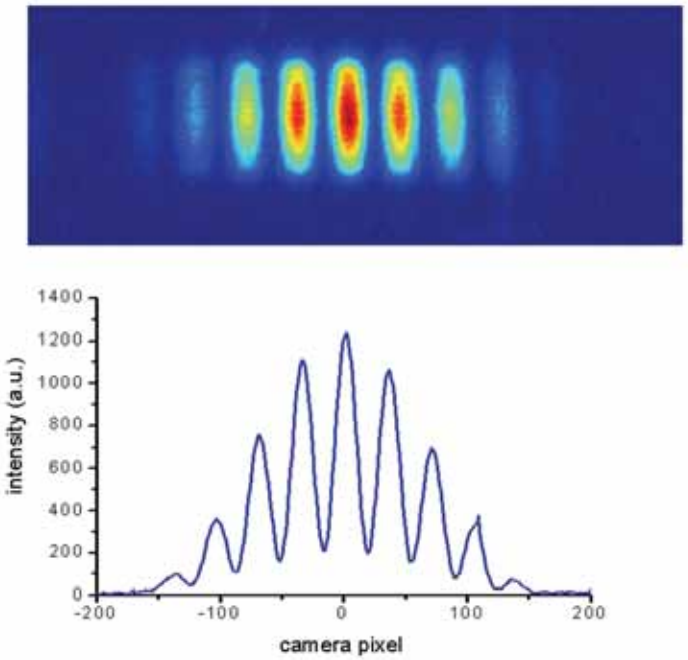


***Figure 2.3.7*** *Double-slit diffraction pattern taken at 25.5 nm. The large modulation depth indicates a considerable level of transverse coherence (unpublished, preliminary data).*

During FEL commissioning, two main difficulties showed up that may have some significance for the XFEL.

### *Beam orbit inside the undulator*

All the efforts made on careful alignment and installation of the undulator did not prevent severe difficulties in establishing a straight electron orbit in the undulator. On one hand, this is due to delayed delivery and insufficient performance of beam position monitors. On the other hand, significant dipole deflections of the electron beam in the undulator section have been observed that cannot be attributed to quadrupole misalignments.

Two sources of such kind of distortions have been identified so far, namely hysteresis dipole field components in the quadrupole magnets and a magnetic stray field generated by uncompensated current leads of PETRA, the latter being a small, though inconvenient, distortion as it depends on the operation status of PETRA and is, thus, time-dependent. However, even after compensation for these effects, dipole deflections of unknown origin are observed. Of course, empirical orbit correction is done but it leaves some ambiguity in the most appropriate procedure in terms of optimising FEL gain. Part of this problem is the fact (mentioned already) that the orbit of the lasing spike does not coincide with the orbit of the total bunch charge.

Another observation that may be related, at least partially, to the orbit issue is the fact that FLASH does not yet routinely reach the ultimate performance in terms of pulse energy.

*Collimation and beam losses in the undulator*

In spite of the presence of a more refined collimator section, it was very difficult to keep beam losses in the undulator below an acceptable limit. Further steps were taken to remove halo particles from the beam: dark current generated in the RF gun was removed as early as possible, namely by a collimator iris at the exit of the RF gun, by a scraper in the dispersive part of the first bunch compressor, and by a fast kicker, thus removing approximately 70% of particles out of phase with the design beam. Nevertheless, wire scanner measurements in the undulator show very broad beam profiles, much wider than consistent with lasing parameters. As mentioned above, such behaviour is expected from space charge effects on beam dynamics, but at FLASH it is very likely that it is further increased by spurious dispersion generated earlier in the machine. Studies on these issues are ongoing.

At any rate, if the orbit in the undulator is well aligned, the collimator system should be able to protect the undulator from all such kinds of badly steered particles, which is not the case. Also, it is obvious that, with parts of the beam covering a large fraction of the available aperture of the undulator vacuum chamber, any kind of investigation on FEL performance becomes very tricky.

Under these circumstances, a novel, glass-fibre-based system for fast radiation dosimetry was indispensable for FEL commissioning. The system consists of a number of radiation-sensitive glass fibres distributed along the undulator. It is capable of indicating amount and location of radiation dose rates every six minutes, keeping the response time of operators reasonably small. The system is backed by traditional TLDs and by a system of fast photomultiplier-based shower counters. These counters are able to resolve individual bunches and allow distinction between beam-induced and dark-current-induced losses.

It is important to note that often perfect FEL user operation conditions were realised at FLASH, with beam losses and radiation dose in the undulator so low that full bunch train operation would be possible. However, these conditions were not sufficiently stable, so that with the machine protection system being in a rudimentary state, running FLASH at its design bunch rate is excluded up to now. It is very likely though, that more studies on beam dynamics and optics will solve the problem. The automatic machine protection system required for operation with long bunch trains is being commissioned. It also includes warning indicators and alarms in case of high losses in the undulators.

### 2.3.5 Experience from the first user operation periods

First user runs were scheduled in the middle of 2005 for wavelengths around 30 nm, just a couple of weeks after FEL gain close to the saturation regime was achieved. For the machine protection reasons mentioned already, the number of bunches per RF pulse was restricted between 1 and 30, depending on the user's request, running at a repetition rate of initially 2, now 5 Hz. The bunch-to-bunch separation time was 1 and 4 µs, again as requested by users. The properties of the photon pulses were routinely monitored in the control room, see Figure 2.3.8.

Quite often, the amount of fluctuation was consistent with the statistics inherent in the SASE process related to the start-up from noise. Under such conditions, smooth user runs were delivered as illustrated in Figure 2.3.9.

However, it also happened frequently, that fluctuations were much larger. Under such conditions, the FEL gain was extremely sensitive on fine tuning of parameters, especially on RF phases, photoinjector-laser settings, and the orbit in the undulator. One issue in this context is that, at the present time, it is not possible to restore SASE without any fine tuning of critical parameters. Even if all subsystems are fully operational, after restoring a previously successful machine setting, typically a few hours of fine tuning are needed to recover full FEL performance. This indicates that the control of some parameters is not precise enough.

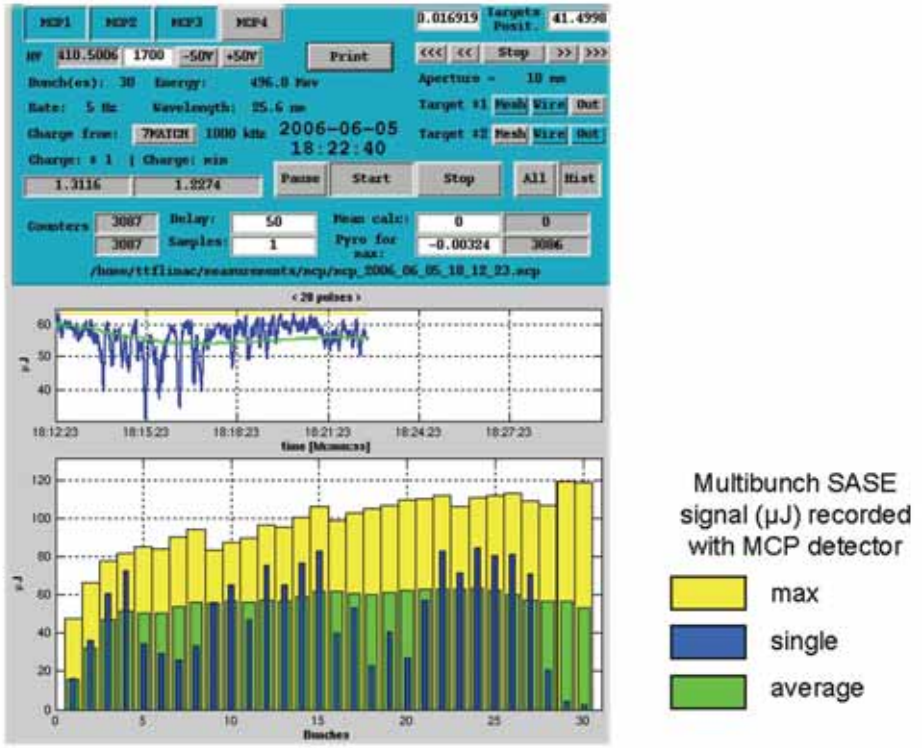


***Figure 2.3.8*** *Photon pulse energies recorded at the end of the user run on 5 June 2006 (image of the control panel of the MCP detector).The radiation wavelength is 25.7 nm, and the pulse train consists of 30 bunches. For each bunch position within the train, the individual energy (blue bar), the maximum energy achieved during the measurement period (yellow bar), and the average value (green bar) are displayed in the bottom window. The window in the middle shows the temporal evolution of the mean energy averaged over all pulses contained within 20 pulse trains (blue line), and the mean energy over the entire measurement period.*

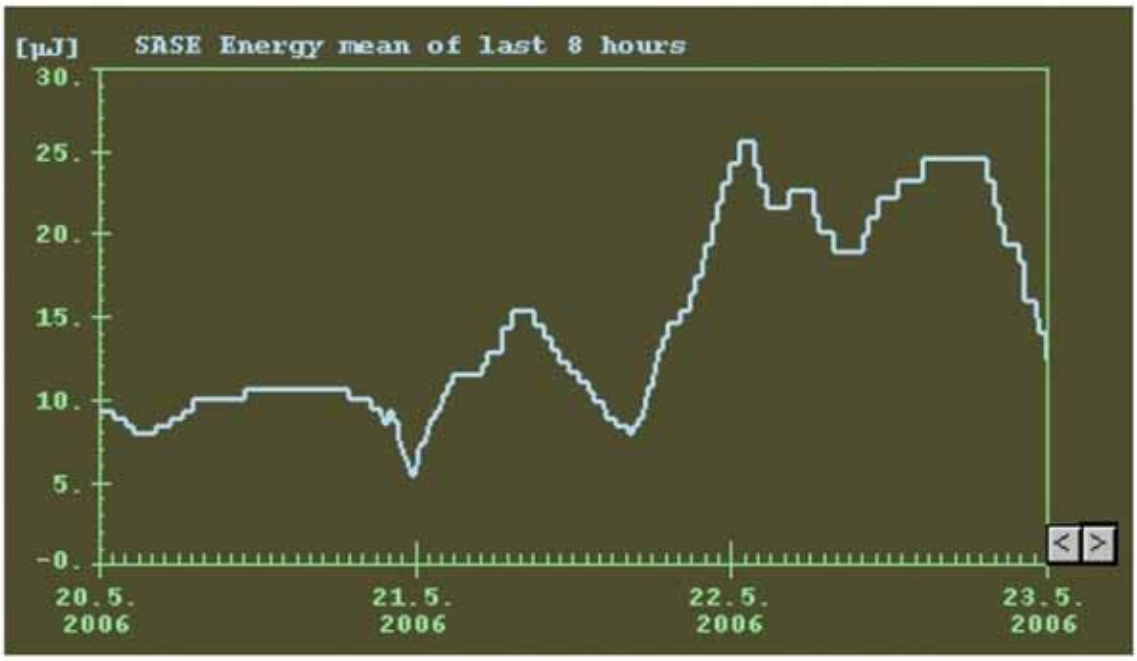


***Figure 2.3.9*** *Example of mean photon pulse energies (averaged over the last eight hours) recorded during three days of a SASE run at 25.6 nm wavelength. On 20-21 May. 10 µJ level of SASE has been delivered to users. On the afternoon of 21 May. SASE intensity has been retuned to the higher level by the request of the new user group.*

The FEL-beam availability during dedicated user time was, on average, over the first weeks of user operation, above 61% (see Figure 2.3.10), an acceptable level for most of the early users.

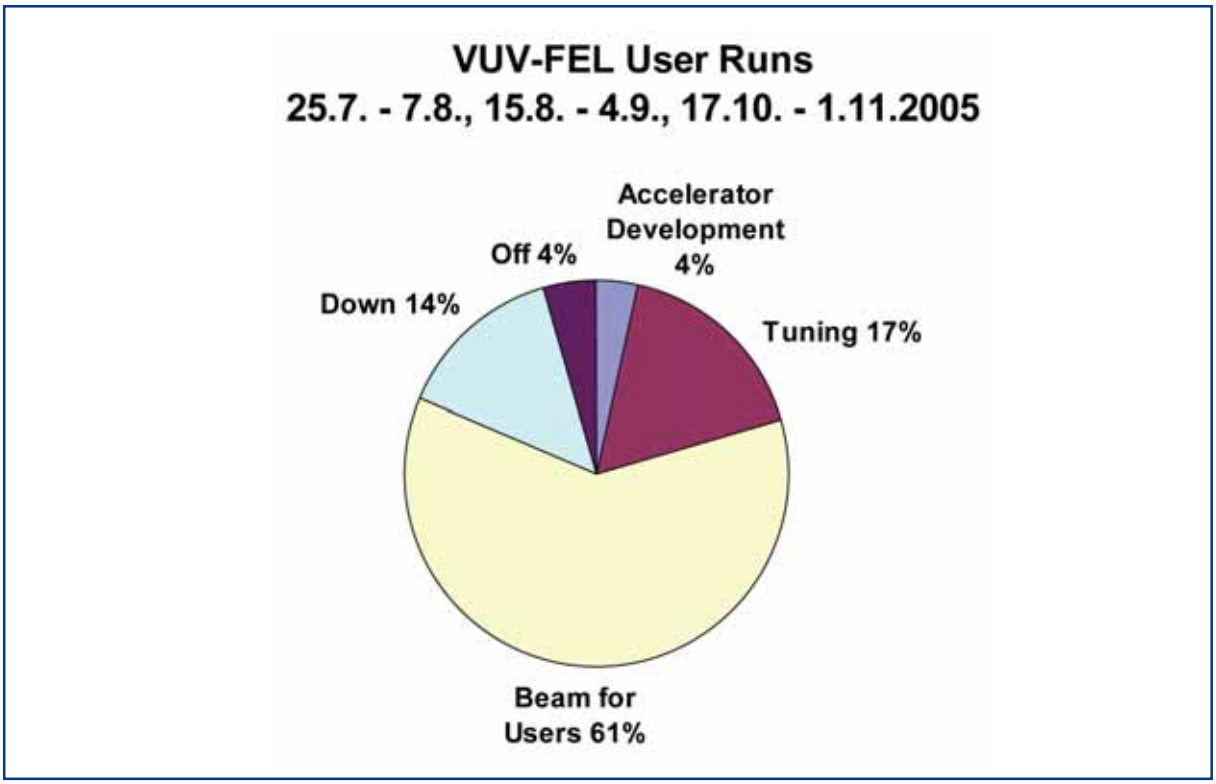


***Figure 2.3.10*** *Beam time availability statistics during early user operation at FLASH.*

### 2.3.6 Next steps for FLASH

Having established basic conditions for user operation at FLASH, a number of further steps must be taken to achieve full performance:

- a number of subsystems must be improved. For instance, the noise of power supplies for steerer magnets must be reduced, the low level RF control must be further stabilised, and the properties of the photoinjector-laser have to be improved;
- the installation of a third harmonic RF system to improve longitudinal phase-space properties of electron bunches;
- the installation of a further TESLA module to reach 1 GeV beam energy;
- the establishment of the FEL operation at wavelengths down to 6 nm (1st harmonic);
- the establishment of fast wavelength tuning. This requires, obviously, improvements in the control and reproducibility of several subsystems;
- operation with a full length of bunch trains;
- installation and commissioning of the self-seeding option at FLASH.

## References


**[2-1]** D.A. Edwards (ed.), *TESLA Test Facility Linac – Design Report*, TESLA 95-01 (1995).

**[2-2]** R. Brinkmann et al., *An X-Ray FEL Laboratory as Part of a Linear Collider Design*, Nucl. Instr. Meth A393, (1997) 86-92.

**[2-3]** A.M. Kondratenko, E.L. Saldin, *Generation of Coherent Radiation by a Relativistic Electron Beam in an Ondulator,* Part. Accelerators 10, (1980) 207.

**[2-4]** R. Bonifacio, C. Pellegrini, L.M. Narducci, *Collective Instabilities and High-Gain Regime in a Free Electron Laser,* Opt. Commun. 50, (1984) 373.

**[2-5]** D. Kirkpatrick, *A high power, 600 µm wavelength free electron laser*, Nucl. Instr. Meth. A285, (1989) 43.

**[2-6]** J. Rossbach, *A VUV Free Electron Laser at the TESLA Test Facility at DESY*, Nucl. Instr. Meth. A375, (1996) 269.

**[2-7]** T. Åberg et al., *A VUV FEL at the TESLA Test Facility at DESY*, TESLA-FEL 95-03 (1995).

**[2-8]** Y.M. Nikitina, J. Pflüger, *Two Novel Undulator Schemes With Quadrupolar Focusing for the VUV FEL at the TESLA Test Facility*, Nucl. Instr. Meth. A 375, (1996) 325.

**[2-9]** M. Dohlus et al., *Start-to-end simulations of SASE FEL at the TESLA Test Facility, phase 1*, Nucl. Instr. Meth. A 530 (2004) 217.

**[2-10]** J. Andruszkow et al., *First Observation of Selfamplified Spontaneous Emission in a Free Electron Laser at 109 nm Wavelength,* Phys. Rev. Lett. 85, (2000) 3825.

**[2-11]** V. Ayvazyan et al., *A New Powerful Source For Coherent VUV Radiation:* Demonstration of Exponential Growth and Saturation at the TTF Free Electron Laser, Eur. Phys. J. D 20, (2002) 149.

**[2-12]** V. Ayvazyan et al., *Generation of GW Radiation Pulses from a VUV Free Electron Laser Operating in the Femtosecond Regime*, Phys. Rev. Lett. 88, (2002) 104802.

**[2-13]** A. Bytchkov et al., *Development of MCP-based photon diagnostics a the TESLA Test Facility at DESY*, Nucl. Instr. Meth. A 528, (2004) 254.

**[2-14]** H. Wabnitz et al., *Multiple Ionization of Atom Clusters by Intense Soft X-rays from a Free-Electron Laser*, Nature 420 (2002) 482.

**[2-15]** L. Juha et al., *Ablation of various materials with intense XUV radiation*, Nucl. Instrum. and Methods A 507 (2003) 577.

**[2-16]** The TESLA Test Facility FEL Team, *SASE FEL at the TESLA Facility, Phase 2*, TESLA-FEL 2002-01.

**[2-17]** E.L. Saldin, E.A. Schneidmiller, M.V. Yurkov, *Expected properties of the radiation from VUV-FEL at DESY (femtosecond mode of operation),* TESLA-FEL 2004-06.

**[2-18]** M. Krasilnikov et al., *Optimizing the PITZ Electron Source for the VUV-FEL*, Proc. EPAC 2004 Conf., Lucerne, Switzerland, 360 (2004).

**[2-19]** S. Schreiber, *Commissioning of the VUV-FEL Injector at TTF*, Proc. EPAC 2004 Conf., Lucerne, Switzerland, 351 (2004).

**[2-20]** V. Ayvazyan, et al., *First operation of a Free-Electron Laser generating GW power radiation at 32 nm wavelength*, Eur. Phys. J. D37 (2006) 297.

**[2-21]** E.L. Saldin, E.A. Schneidmiller, M.V. Yurkov, *Statistical properties of the radiation from VUV FEL at DESY operating at 30~nm wavelength in the femtosecond regime*, Nucl. Instr. Meth. A 562 (2006) 472.

**[2-22]** S. Duesterer et al., *Spectroscopic characterization of vacuum ultraviolet free electron laser pulses*, Opt. Lett. 31 (2006) 1750.

# 3 General layout of the XFEL Facility

## 3.1 Introduction

The present chapter provides an overview of the whole European X-Ray Free-Electron Laser (XFEL) Facility layout, enumerating its main components and describing their position and arrangement on the site. Its purpose is to guide the reader through the much more detailed description of the individual components that follows in the subsequent chapters. For the purpose of this overview, the main components of the facility are the:

- injector;
- linear accelerator (linac);
- beam distribution system;
- undulators;
- photon beamlines;
- experimental stations.

These components are disposed along an essentially linear geometry, 3.4 km long, starting on the Deutsches Elektronen Synchrotron Laboratory (DESY) campus in the north west part of the city of Hamburg, and ending in the neighbouring Federal State of Schleswig-Holstein, south of the city of Schenefeld, where the experimental hall will be located and a lively scientific campus is going to see the light of day (Figure 3.1.1).

The basic functions of the main components are schematically described in the following: In the injector, electron bunches are extracted from a solid cathode by a laser beam, focused and accelerated by an electron radio frequency (RF) gun and directed towards the linac with an exit energy of 120 MeV. In the linac, consisting of a 1.6 km long sequence of superconducting accelerating modules, magnets for beam steering and focusing, and diagnostic equipment, the electrons can be accelerated to energies of up to 20 GeV (17.5 GeV is the energy foreseen for normal operation of the XFEL Facility). At the end of the linac, the individual electron bunches are channelled down one or the other of two electron beamlines by the beam distribution system (Figure 3.1.2).

**General layout of the XFEL Facility**

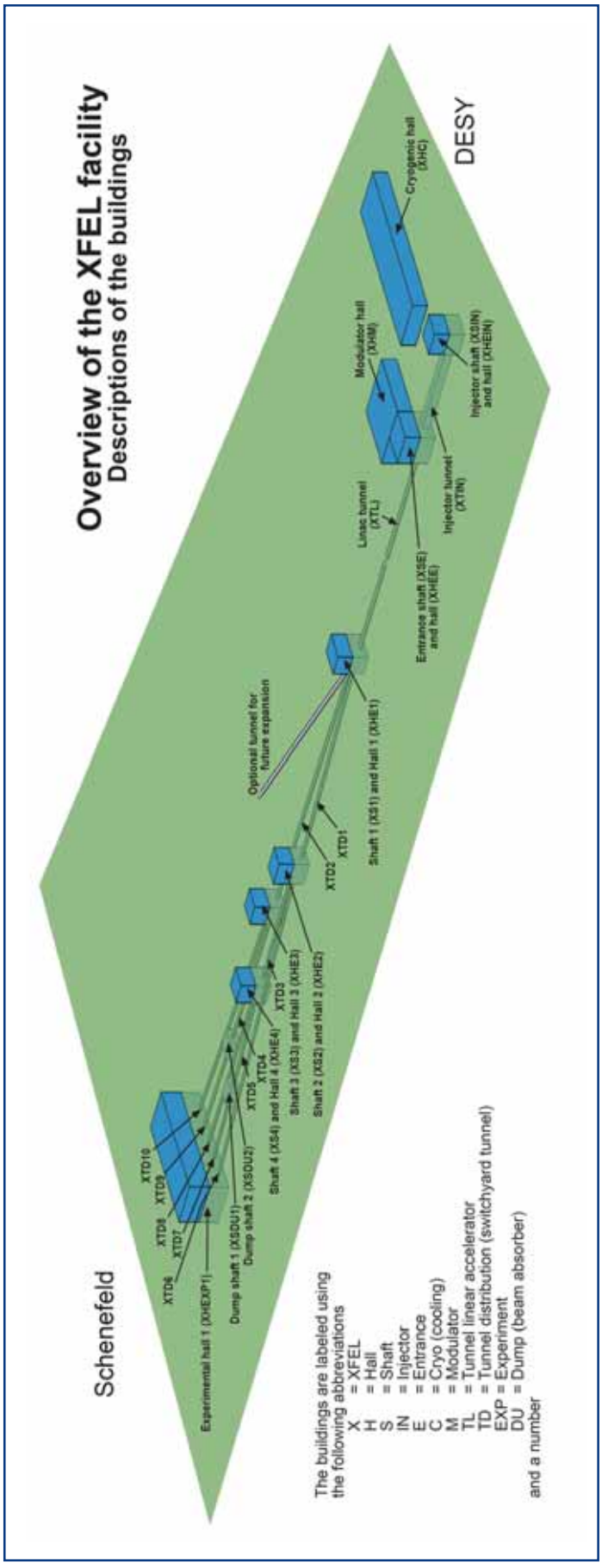


***Figure 3.1.1*** *General layout of the European XFEL Facility, from the injector building on the DESY campus to the experimental hall located in Schenefeld. The branching of tunnels is described in the text.*

Electron bunches channeled down the electron beamline 1 pass through the undulators SASE 1 and SASE 3, producing respectively hard x-ray photons with 0.1 nm wavelength (SASE 1) and softer x-ray photons with 0.4 -1.6 nm wavelength (SASE 3), by the Self-Amplified Spontaneous Emission (SASE) free-electron laser process. After going through SASE 3, electrons are deviated towards a beam dump, composed of a graphic core and a large water-cooled copper block. Electron bunches channeled through the electron beamline 2 are led through the undulator SASE 2, where hard x-ray photons with wavelengths 0.1 - 0.4 nm are produced by the SASE process; and then through the undulators U 1 and U 2, before ending in the second beam dump. In U 1 and U 2, very hard x-ray photons (wavelengths down to 0.025 and 0.009 nm, respectively) are generated by the spontaneous emission process. The photons generated by the five undulators are transported through the respective photon beamline to the experimental hall, where each beamline feeds two experimental stations.

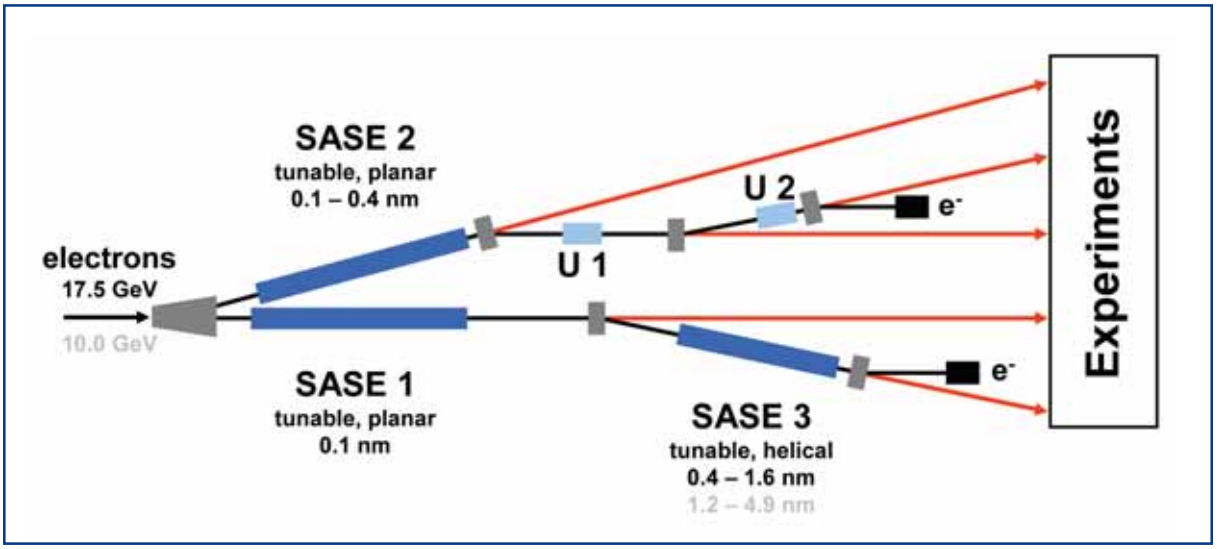


***Figure 3.1.2*** *Schematic view of the branching of electron (black) and photon (red) beamlines through the different SASE and spontaneous emission undulators. Electron beamlines terminate into the two beam dumps, photon beamlines into the experimental hall.*

## 3.2 Injector

The injector is located in a building on the western part of the DESY campus, just inside the PETRA ring perimeter. It is part of a complex of new buildings where also the modulators for the RF system, the cryogenic plant and other technical components are located. The injector building has four underground floors, devoted to housing auxiliary equipment, above the injector itself, located at a depth of about 27 m below the ground. Although the installation of only one injector system is foreseen within the present project, space is foreseen for a second, parallel injector system, located directly above the first one, which could be used later to increase the uptime of the facility for the benefit of the users. The main components of the injector are the gun, composed of a photocathode, from which a visible laser extracts electron bunches, which are then subject to a high accelerating gradient; a system of accelerating cavities which accelerate

the electrons up to 120 MeV; and a series of focusing and diagnostic equipment to ensure the necessary beam quality (low emittance, low energy spread, etc.) which is extremely important for the whole XFEL operation. The total length of the injector is about 66 m, after which the electrons are delivered into the linear accelerator.

## 3.3 Linear accelerator

The linac is located in a tunnel (Figure 3.3.1) which starts from the underground injector building, runs horizontally below the ground, and ends about 2 km further at the location of the beam distribution system. The tunnel, with a diameter of 5.2 m, is horizontal but, since it runs below a slightly sloped ground, is located at a depth below the surface which varies from place to place between 38 m and 15 m. The linac occupies the first 1.6 km of the tunnel. Most of the length is taken by the 116 accelerator modules, each 12 m long, which are necessary to bring the electron energy up to 20 GeV. Further essential components are the two bunch compressors, arrays of magnets with the purpose of shortening the bunch length to about 55 µm, which corresponds to a duration of less than 200 femtosecond. The first bunch compressor is located at the point where the electron energy is 0.5 GeV, the second at the energy of 2.0 GeV.

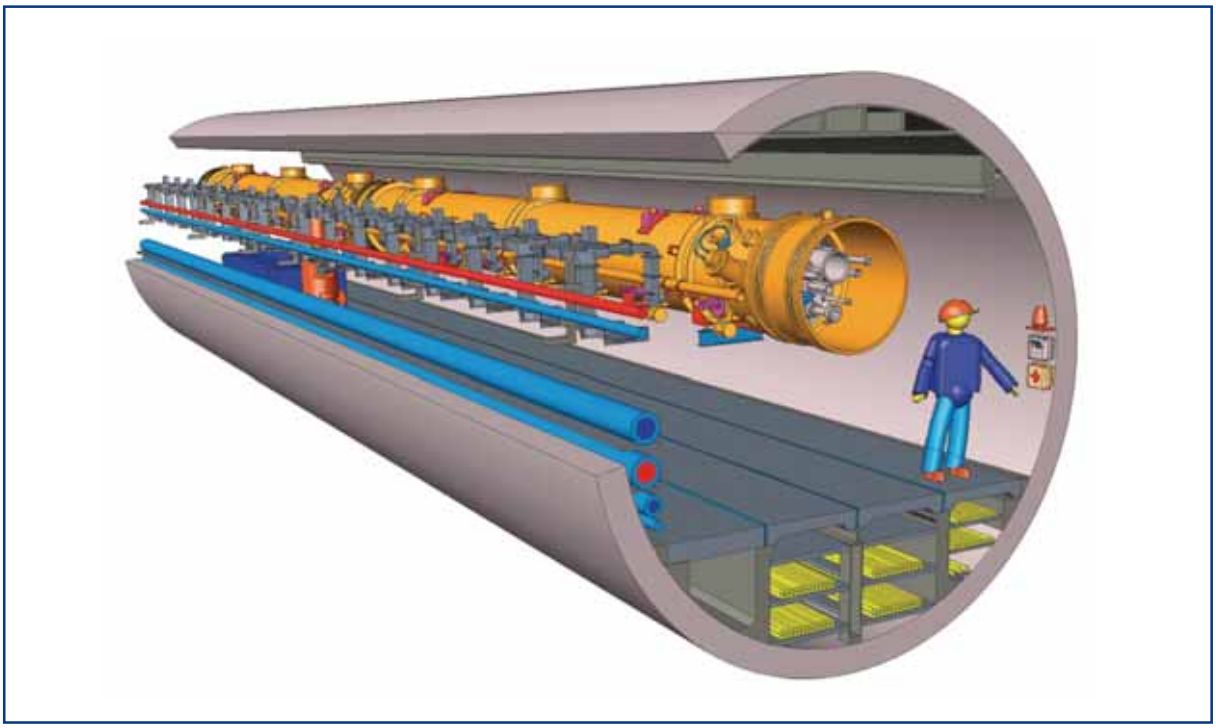

***Figure 3.3.1*** *Schematic section of the linac tunnel. The accelerating modules (yellow) are suspended from the ceiling, for more convenient access and economy of floor space.*

The last 0.4 km of the tunnel are occupied by equipment which has the purpose of delivering a well collimated and aligned beam to the following stages of the FEL and notably to the undulators. It is composed of diagnostic equipment, quadrupole and sextupole magnets and horizontal and vertical kickers.

## 3.4 Beam distribution system

The XFEL linac can produce 10 RF pulses per second, each of 600 μs duration, and each pulse can accelerate a train of up to 3,000 electron bunches, i.e. with a minimum spacing of 200 ns between successive bunches. The users have, in principle, a wide variety of possibilities as the filling pattern can vary from a single or few bunches per train to full trains of 3,000 bunches. Since the facility is meant for simultaneous use of many experimental stations by different groups of users, who may have contradictory requirements, the maximum flexibility corresponds to a system of fast kickers, able to direct individual bunches to one or the other of the two electron beamlines and, therefore, through different sets of undulators.

The system of fast kickers that directs electron bunches through the undulator SASE 1 or SASE 2 (see Figure 3.1.2) is located close to the residential area of Osdorfer Born, a building that provides access to the equipment, which reaches approximately 15 m below the ground. Here, provision of space is made for the later addition of a third possible direction for electron bunches: should it be decided that more experimental stations are needed than the ten initially foreseen, a third tunnel can be added to those of SASE 1 and SASE 2; this transfer tunnel, already realised during construction phase 1, can be used to lead the electrons to an additional series of undulators and experimental stations.

It should be added that downstream along the SASE 1 line, further access to the tunnels is foreseen, to serve the point where electrons are directed through the SASE 3 undulator, while SASE 1 photons continue along their straight path in a separate tunnel. Downstream, along SASE 2, there are also two accesses, one where electrons are deflected to go through the U 1 undulator, and the other where they are further deflected to go through the U 2 undulator.

## 3.5 Undulators

Second- and especially third-generation synchrotron sources make use of undulators, to increase the brilliance of their radiation, and considerable expertise has been gained in the design and construction of these insertion devices. The XFEL's undulators, however, differ from conventional ones in that they have lengths exceeding 100 m (SASE 3) and even 200 m (SASE 1 and SASE 2), and very tight tolerances for alignment and uniformity. In order to respond to these requirements, undulators will consist of 5m long modules, separated by 1.1 m long intersections. In the latter, diagnostic and correction equipment for the electron trajectory are located. The minimum magnetic gap for the SASE undulators is 10 mm, for U 1 and U 2 it is reduced to 6 mm, and all devices can be tuned, by opening the gaps. The undulator segment mechanics have been designed that they can be manufactured economically in large quantities.

## 3.6 Photon beamlines

After leaving the electron bunches at the end of the undulators, the photons are still hundreds of metres away from the experimental stations. They cover this distance by passing through tunnels with a diameter of 4.5 m, at a depth between 6 and 13 m under the ground, which lead the photons to the experimental hall (see Section 3.7). Along this path, various pieces of equipment are located which shape and collimate the beam:

- filtering as much as possible of the considerable spontaneous emission background produced, in addition to the coherent FEL radiation, by the passage of the high energy electrons in the undulators;
- monitoring the position of the beam and, in general, implementing photon diagnostics. The last function is particularly important not only for the user downstream, who needs to have a well characterised beam, but also as an essential tool for diagnostics of the components upstream, such as the alignment of the undulator segments, their proper phasing, etc.

Depending on the purpose and the configuration of the experimental stations downstream, some of the optical elements such as mirrors or monochromators may also be located in the tunnel.

## 3.7 Experimental stations

The experimental stations are located in a dedicated building, which provides access to the underground experimental hall (Figure 3.7.1). In the building, there will be three floors above ground level; with office space on the upper two and preparation laboratories and a lecture hall on the ground floor. The underground part of the building consists of the $50 \times 90$ m$^2$ hall, where the five tunnels corresponding to the five photon beamlines enter, with a distance of 17 m between them, on the 90 m long side. The several experimental stations fed by one beamline must, therefore, occupy a floor space of $15 \times 42$ m$^2$ with a 2 m wide transportation way in between them. The 14 m high ceiling will be equipped with heavy-duty overhead cranes; the height of the ceiling allows the installation of very tall hutches for particular experimental requirements.

It is not possible to summarise, in general terms, the experimental stations' equipment. Their detailed design and configuration is determined by scientific use and can vary considerably. Some applications, such as those exploiting the spatial coherence properties of the beam, generally require a reduction in the number of optical elements or to eliminate them altogether, as they lead to some degradation of the coherence. Other applications may require a very bulky sample environment, or sophisticated microfocus optical devices.

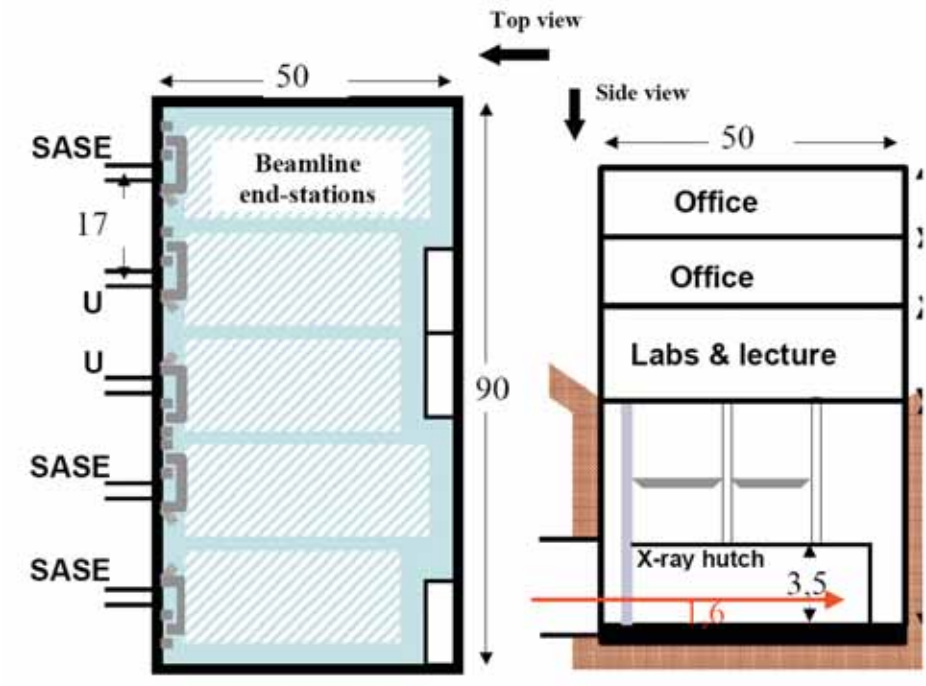


***Figure 3.7.1*** *The floor plan (left) of the experimental hall and a vertical cut through the building (right) showing the three floors above ground level and the underground experimental hall.*

## 3.8 Schenefeld campus

The successful operation of the European XFEL is expected to attract great scientific interest. A large number of scientists will be using it, and will also visit the facility for other purposes, such as attending workshops and conferences, holding discussions with colleagues and visiting laboratories. Partner institutions may wish to have permanent outstations close to the XFEL, similar to the EMBL outstations at DESY and European Synchrotron Radiation Facility (ESRF), or to the Institut de Biologie Structurale (IBS) next to ESRF. It is very likely to become the object of excursions by schools and university classes, or even by the general public with an interest in science. One can, therefore, expect a development of the whole area around the experimental hall buildings, with all the necessary facilities (auditorium, cafeteria, visitor centre, partner institutes' laboratories). An architectural concept is shown in Figure 3.8.1.

***Figure 3.8.1*** *How the Schenefeld research campus might look in the future. The red arrow points to the European XFEL experimental hall building.*

# 4 XFEL accelerator

## 4.1 Overview

### 4.1.1 Introduction

The heart of the accelerator complex is the L-band (1.3 GHz) electron linear accelerator (linac) with a nominal design energy of 20 GeV, operating at an accelerating gradient of 23.6 MV/m. It utilises the advanced superconducting radio fequency (RF) technology which has been successfully developed by the international Tera-Electronvolt Superconducting Linear Accelerator (TESLA) Collaboration, leading to the superconducting Linear Collider technical proposal in 2001 **[4-1]**, and which is routinely in operation at the TESLA Test Facility (TTF) Linac and FLASH at Deutsches Elektronen Synchrotron Laboratory (DESY). The advantages of the superconducting linac technology are: the acceleration of a large number of electron bunches per RF pulse (up to about 3,000); small beam-induced wake fields and the possibility of applying intra-bunch train feedback to provide a stable and high quality beam (Section 4.5); and a large operational flexibility regarding beam time structure and energy, including (as a possible future option) high duty cycle (up to continuous wave (CW)-mode) operation. The linac technology is described in detail in Section 4.2. In the following section, a brief overview of the general layout of the accelerator complex and its parameters and a consideration of operational flexibility and future options are given.

### 4.1.2 Overall layout and choice of parameters

The layout of the accelerator is schematically shown for convenience in Figure 4.1.1 and visualised in a 3D computer drawing in Figure 4.1.2. The electron beam is generated in a laser-driven photocathode RF gun and pre-accelerated in a single superconducting accelerator module (see Section 4.3). The injector is housed in an underground enclosure separate from the linac tunnel, so that it can be commissioned at an early stage, well before installation work in the linac tunnel is completed. Furthermore, there is space foreseen for a completely separate and radiation-shielded second injector, which can be constructed, commissioned and maintained independently from the operation of the first injector.

After transfer to the main accelerator tunnel, the beam is further accelerated by one linac unit (four accelerator modules with eight cavities each, driven by one RF station) to an energy of 0.5 GeV before entering the first bunch compression stage. A third harmonic (3.9 GHz) RF system is foreseen to optimise the longitudinal phase-space properties (Section 4.2.4). After acceleration to 2 GeV with three linac units, the beam enters the second (final) compression stage, after which the bunch peak current has increased to 5 kA, a factor of 100 higher than the initial peak current from the RF gun. Considerable attention to detail has been paid to foreseeing extensive standard and special beam diagnostic tools, to assess the beam phase-space properties after the compression process with high accuracy.

Final acceleration to a nominal maximum beam energy of 20 GeV takes place in the main part of the linac, consisting of 25 RF stations and 100 accelerator modules in total. Downstream from the Linac, a conventional beamline is located, for installation of the beam collimation and trajectory feedback systems, as well as providing and for distribution of the beam into the different undulator beamlines (see Section 4.5), including the connection to a future upgrade of the user facility with more beamlines. A combination of slow and fast switching devices allows generation of bunch trains of different time patterns for different experiments without having to generate and accelerate bunch trains with strongly varying transient beam loading. After having passed through the undulators, the "spent" beam is stopped in radiation-shielded solid absorbers (Section 4.7.4). An additional beam dump is installed in the beam distribution shaft XS1, just upstream from the undulator beamlines. It allows the commission or operation of the accelerator while installation or maintenance work is ongoing in the undulator tunnels.

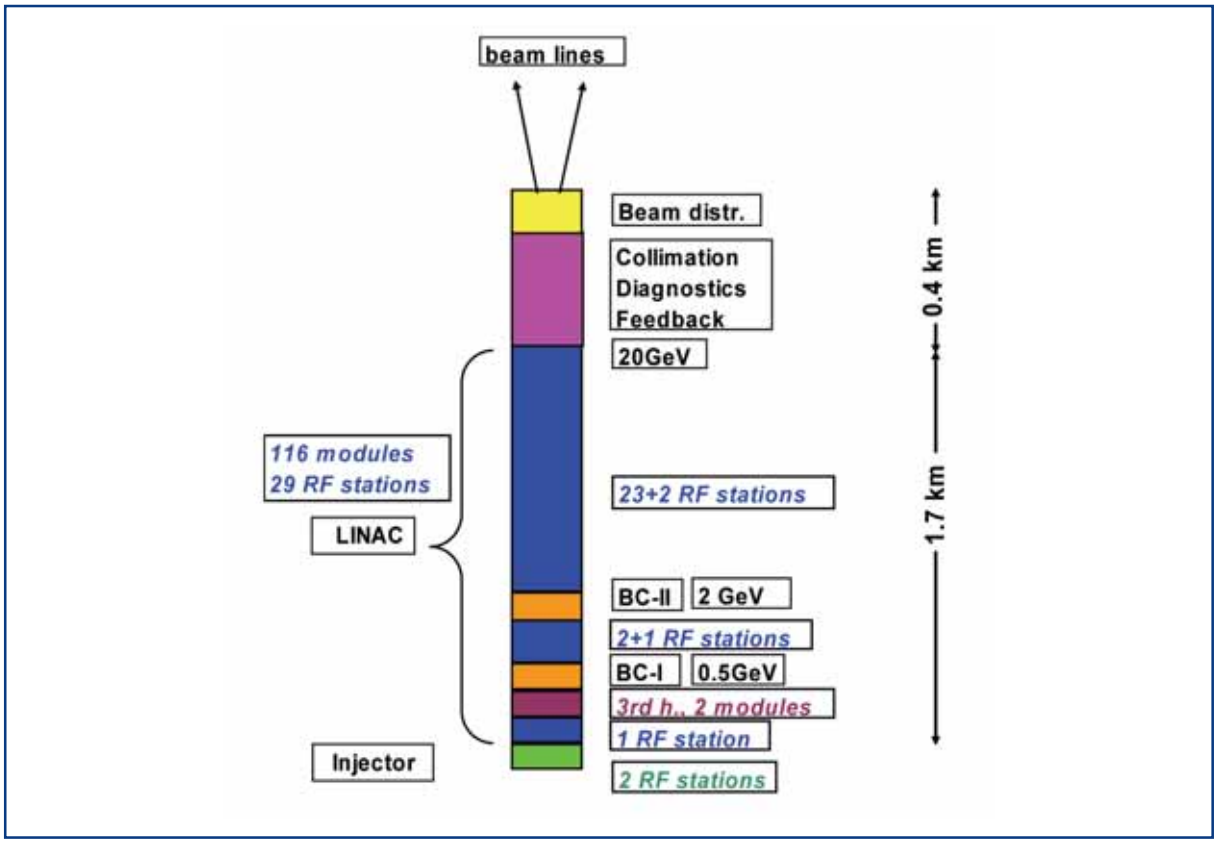


***Figure 4.1.1*** *Schematic layout of the accelerator.*

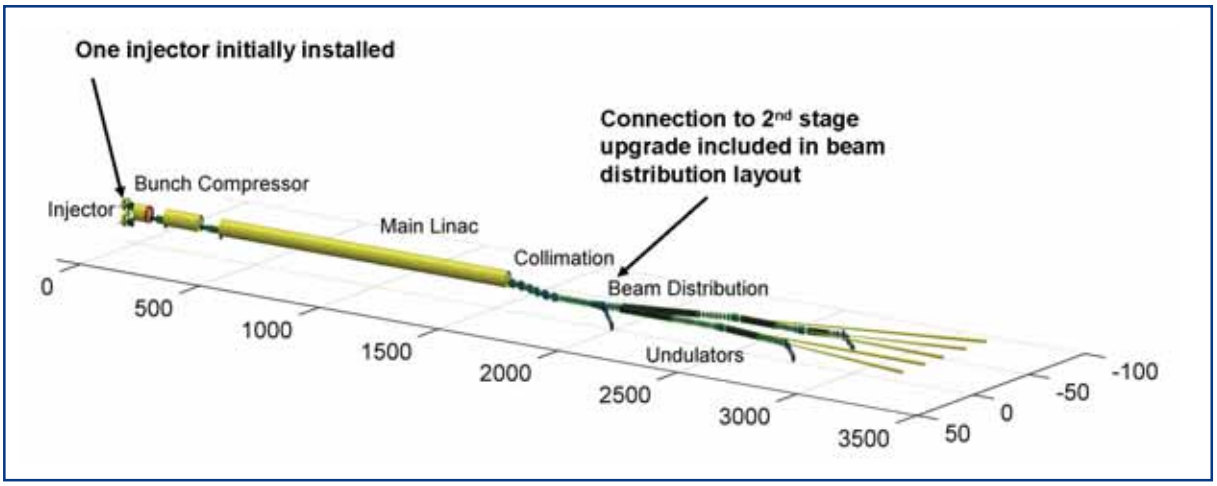


***Figure 4.1.2*** *3-D sketch of the accelerator complex.*

The layout of the linac includes precautions for energy management in case of RF component failure. The section between the two bunch compression stages consists of three RF units with four accelerator modules each, out of which only two have to be active to accelerate the beam to 2 GeV at the design gradient. Likewise, the main section of the linac (from 2 to 20 GeV) has an overhead of two RF stations. This guarantees that in case of an RF unit failure, there is sufficient energy reserve to maintain both the beam energy at the second bunch compressor stage as well as at the end of the linac. Tunnel access for repair of RF stations during scheduled operation time can, thus, be safely avoided. In practice, the reserve stations will not be left idle when not needed. Instead, all available stations will be operated with reduced gradient and in case a station fails, the gradient will be increased in the other sections to keep the beam energy constant.

The main parameters of the accelerator are summarised in Table 4.1.1. The beam energy required for 0.1 nm photon wavelength in the SASE 1 and SASE 2 beamlines is 17.5 GeV. The linac design energy of 20 GeV thus already includes the potential to reach a lower wavelength of about 0.08 nm. The required peak power per RF station is well below the limit of the 10 MW multibeam klystrons (Section 4.2.4). This lower mode is beneficial for highly reliable operation on one hand and potential upgrade of the beam energy or duty cycle on the other (see Section 4.1.3). Likewise, the cryogenic system is laid out with an overhead of 50% (Section 7.2.5) with similar operational benefits.

| | |
|---|---|
| Energy for 0.1nm wavelength *(maximum design energy)* | 17.5 GeV *(20 GeV)* |
| Number of installed accelerator modules | 116 |
| Number of cavities | 928 |
| Acc. gradient (104 active modules) at 20 GeV | 23.6 MV/m |
| Number of installed RF stations | 29 |
| Klystron peak power (26 active stations) | 5.2 MW |
| Loaded quality factor $Q_{ext}$ | $4.6 \times 10^6$ |
| RF pulse length | 1.4 ms |
| Beam pulse length | 0.65ms |
| Repetition rate | 10 Hz |
| Maximum average beam power | 600 kW |
| Unloaded cavity quality factor $Q_0$ | $10^{10}$ |
| 2K cryogenic load (including transfer line losses) | 1.7 kW |
| Maximum number of bunches per pulse *(at 20 GeV)* | 3,250 *(3,000)*[1] |
| Minimum bunch spacing | 200 ns |
| Bunch charge | 1 nC |
| Bunch peak current | 5 kA |
| Emittance (slice) at undulator | 1.4 mm*mrad |
| Energy spread (slice) at undulator | 1 MeV |

***Table 4.1.1*** *Main parameters of the accelerator.*

The specified bunch slice emittance takes into account a 50% dilution budget from the injector to the undulators, significantly higher than the calculated dilution from the bunch compression process. The specified slice energy spread takes into account the intentional beam heating to avoid micro-bunching in the compressor (Section 4.4).

### 4.1.3 Operational flexibility and future options

The single set of basic reference parameters in Table 4.1.1 does not cover the full range of operational flexibility of the linac. There is, within certain limits, a considerable flexibility in operational parameters, based on built-in performance reserves of its technical components.

#### *4.1.3.1 Energy variation*

Operation at lower beam energy, thus extending the photon wavelength range to softer x-rays, is an obvious possibility. Variation of the beam energy will always be done by changing the accelerating gradient in the main part of the linac, i.e. after the bunch compressor, leaving the delicate set-up of the lower energy part of the machine completely untouched. Within a range of ±1.5%, a beam energy variation can be applied even within a bunch train (by appropriate programming of the low level RF system). The beamlines after the linac are designed for this dynamic range.

[1] The limitation to 3,000 bunches at 20 GeV beam energy is related to a maximum load of 300 kW on each of the beam dumps in the initially installed two electron beamlines.

Based on the experience gained with the superconducting TESLA cavities (see Section 4.2.1), it can be realistically expected that the linac can be operated at an accelerating gradient somewhat above the specified design value of 23.6 MV/m at 20 GeV. An increase of the gradient to about 28 MV/m would permit a maximum beam energy of 24 GeV, thus significantly extending the photon wavelength range to harder x-rays, provided that an improved injector beam quality simultaneously becomes available to maintain saturation of the Self-Amplified Spontaneous Emission (SASE) Free-Electron Lasers (FEL) process. The RF system power reserve can cope with the required increase in peak power per station. The cryogenic system also has a certain built-in reserve but, at higher energies, the linac repetition rate will have to be somewhat reduced below the nominal value of 10 Hz (see below). All beamline components downstream from the linac are laid out for a maximum energy of 25 GeV, to avoid the conventional accelerator components becoming a limitation for the energy reach.

#### *4.1.3.2 Repetition rate variation*

In addition to the possibility of higher beam energies, the available reserve in the RF and cryogenic systems can also be used for increasing the linac repetition rate and thus the duty cycle of the pulsed linac. The limitations on repetition rate depend on the energy at which the linac is operated: at lower energy the RF system is the limitation, at higher energy the cryogenic system. In order to illustrate the likely accessible range of maximum repetition rate against energy, these two limitations are plotted in Figure 4.1.3, under the assumption that the RF systems are operated at 80% of their maximum average power capability and the cryogenic plant at 80% of its design 2 K cooling capacity (the assumption of going to 100% of the design values is viewed as unrealistic for a highly reliable and stable operation). It should be noted that in this case an improvement of the injector for higher duty cycle is also necessary.

Higher repetition rates than those shown in Figure 4.1.3. are also possible, if the length of the beam pulse (and thus, the maximum number of bunches per pulse) is reduced. This way, the problem of duty cycle limitation from the injector can also be mitigated. The essential limitation is the maximum pulse rate of the RF power stations, which cannot be arbitrarily increased even if the average power is kept constant. The upper limit for the repetition rate with short pulses is expected to be about 30 Hz at 17.5 GeV beam energy.

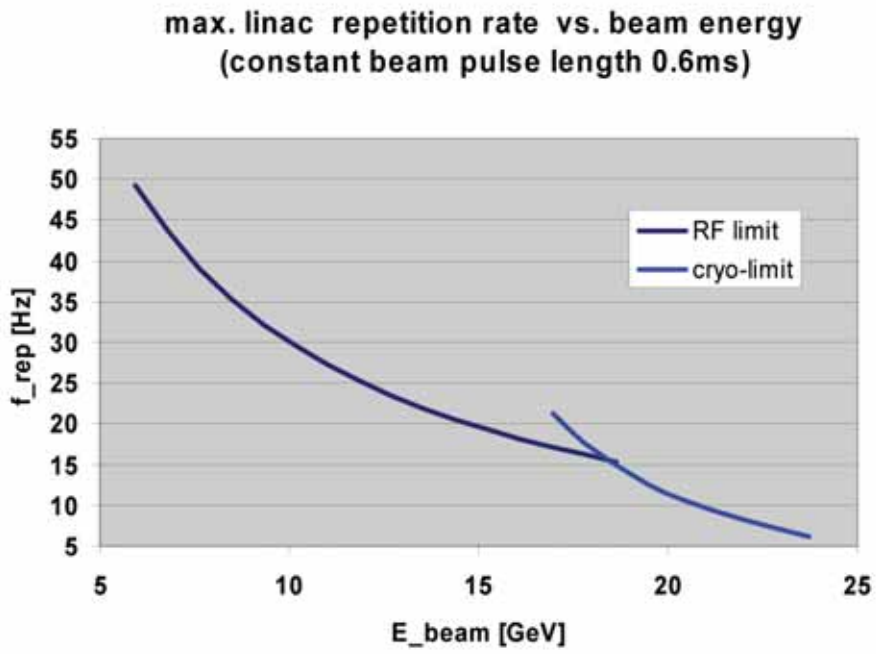


***Figure 4.1.3*** *Limitation of the linac repetition rate as a function of beam energy. A constant beam pulse length of 0.6 ms is assumed.*

### *4.1.3.3 Future option of CW operation*

At sufficiently low beam energy, a 100% duty cycle, i.e. CW, mode of operation is conceivable, an option which is only possible with a superconducting linac. This option is viewed as not being part of the first stage of the X-Ray Free-Electron Laser (XFEL) Facility and can only be briefly discussed here. Continuous wave operation is not a possibility at full energy, because the cryogenic load would become excessive. If, however, experience with the SASE process at short wavelength and improvements of injector performance indicate that the 0.1 nm wavelength regime becomes accessible with electron beam energies around 6-8 GeV, the CW option could be very attractive since it allows optimisation of the beam time structure with experiments' requirements over a very large range. This is illustrated in Figure 4.1.4, where the pulsed machine is compared with a CW linac for the usable average bunch frequency as a function of the maximum bunch frequency which a certain experiment can tolerate (e.g. for detector or sample recovery time reasons). For example: an experiment needs a recovery time of 0.1 ms between photon pulses. With a CW linac, the experiment can operate at the full average bunch (=photon pulse) frequency of 10 kHz, whereas with a pulsed linac of ~1% duty cycle (and in principle maximum possible bunch frequency of 5 MHz), only ~100 Hz of average bunch frequency can actually be used.

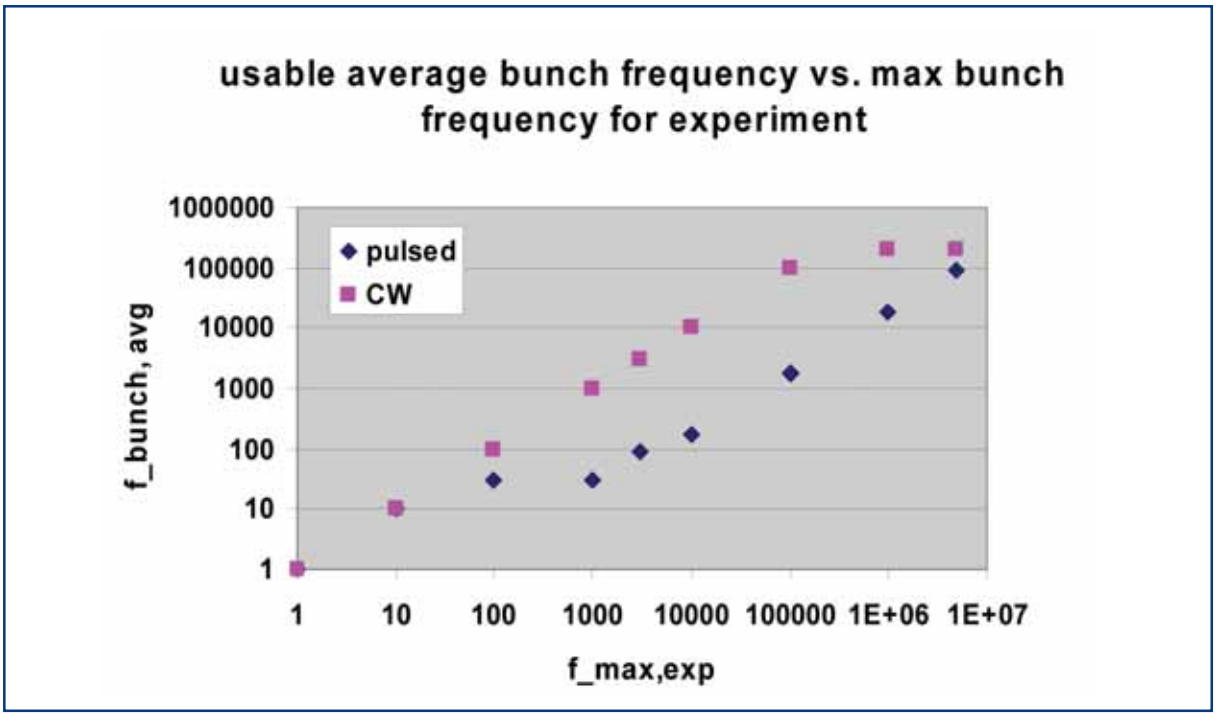


***Figure 4.1.4*** *Usable average bunch frequency against maximum tolerable bunch frequency for an experiment for a CW operation compared to the pulsed XFEL linac (see Section 4.1.3.3).*

A possible set of main parameters for operating the XFEL linac in CW mode is sketched in Table 4.1.2. The 2 K cooling capacity of the cryogenic plant would have to be approximately doubled for this option and a low power CW RF system would have to be added (space in the linac tunnel is available). With today's available technology, this would consist of one inductive output (IOT) device per accelerator module. As a result of the relatively low accelerating gradient, the external quality factor has to be increased by only a moderate factor compared to pulsed operation, cavity detuning due to microphonics is not a serious problem and much of the RF power could be fed to the beam instead of being needed mainly to stabilise the accelerating field.

| | |
|---|---|
| Beam energy | 7 GeV |
| Accelerating gradient | 7.5 MV/m |
| Number of CW RF stations | 116 |
| RF power per accelerator module | ≈20 kW |
| Beam current | 0.18 mA |
| Loaded quality factor $Q_{ext}$ | $2 \times 10^7$ |
| Bunch frequency | 180 kHz |
| Unloaded quality factor $Q_0$ | $2 \cdot 10^{10}$ |
| 2 K cryogenic load | ≈3.5 kW |

***Table 4.1.2*** *Sketch of possible parameters for a future option of operating the linac in CW mode.*

# 4.2 Linac

## 4.2.1 Cavities

### *4.2.1.1 Introduction*

The XFEL accelerating cavity is a nine-cell standing wave structure of about 1 m length whose fundamental TM mode has a frequency of 1,300 MHz. It is identical to the so-called TESLA cavity **[4-1]**, made from solid Niobium, and is bath-cooled by superfluid Helium at 2 K. Each cavity is equipped with: a Helium tank; a tuning system driven by a stepping motor; a coaxial RF power coupler; a pickup probe; and two higher-order mode (HOM) couplers. The superconducting resonators are fabricated from bulk Nobium by electron-beam (EB) welding of deep-drawn half cells. The tubes for the beam pipes and the coupler ports are made by back extrusion and are joined to the cavity by EB welds.

| | | **XFEL** |
|---|---|---|
| Type of accelerating structure | | standing wave |
| Accelerating mode | | TM010, π-mode |
| Fundamental frequency | $f_{RF}$ [MHz] | 1300 |
| Nominal gradient | $E_{acc}$ [MV/m] | 23.6 |
| Quality factor | $Q_0$ | $> 10^{10}$ |
| Active length | $L$ [m] | 1.038 |
| Cell-to-cell coupling | $k_{cc}$ [%] | 1.87 |
| Iris diameter | [mm] | 70 |
| $R/Q$ | [Ω] | 1036 |
| $E_{peak}/E_{acc}$ | | 2.0 |
| $B_{peak}/E_{acc}$ | [mT/MV/m] | 4.26 |
| Tuning range | [kHz] | ± 300 |
| $\Delta f/\Delta L$ | [kHz/mm] | 315 |
| Lorentz-force detuning constant | $K_{Lor}$ [Hz/(MV/m)$^2$] | 1 |
| $Q_{ext}$ of input coupler | | $4.6 \times 10^6$ |
| Cavity bandwidth f/$Q_{ext}$ | [Hz] FWHM | 283 |
| Fill time | [μs] | 780 |
| Number of HOM couplers | | 2 |

***Table 4.2.1*** *Parameters of the nine-cell cavity (note: $R = V^2/P$, where $P$ is the dissipated power and $V$ the peak voltage in the equivalent LCR circuit).*

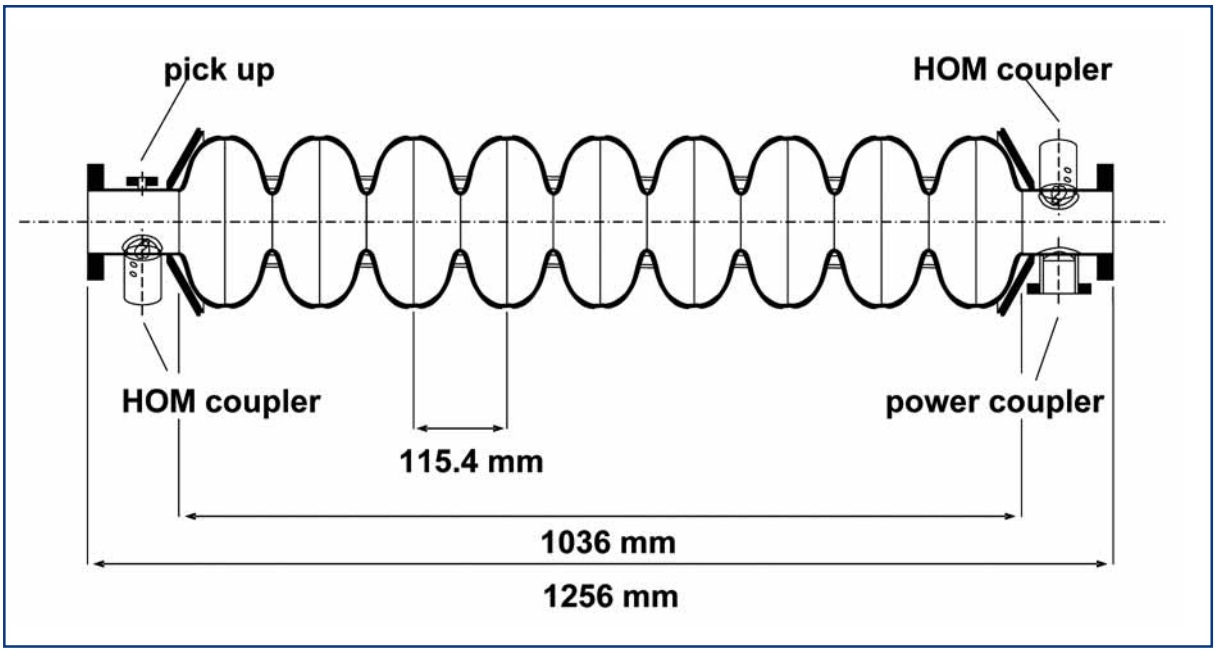


***Figure 4.2.1:*** *Side view of the nine-cell cavity with the main power coupler port (right), the pick up probe (left), and two HOM couplers.*

### *4.2.1.2 Superconducting material and cavity fabrication*

Niobium (Nb) with the highest critical temperature and critical magnetic field of all pure metals ($T_c$=9.2 K; superheating field of approximately 240 mT) is the favourite material for the fabrication of superconducting RF cavities. In addition, Niobium is chemically inert (at room temperature the surface is covered by a protecting pentoxide layer), it can be easily machined and deep drawn, and it is available as bulk and sheet material in any size. The majority of the RF cavities worldwide are formed from Niobium sheet material. There exist superconductors with a higher critical temperature and field, but in practice, cavities based on these materials have shown much inferior performance compared to Niobium cavities. The bulk Niobium is adopted as the material for XFEL cavities.

A high thermal conductivity in the cavity wall is needed (at least 10 W/m K at 2 K) to transfer the dissipated RF power to the liquid Helium coolant. For bulk Niobium cavities this requires Niobium of exceptional purity. The requirements of high purity Niobium are listed in Table 4.2.2.

The residual resistivity ratio (RRR=300 for XFEL cavities) is a common indicator of the purity level. The main interstitially dissolved impurities that act as scattering centres for unpaired electrons and reduce the RRR and therefore, the thermal conductivity, are Oxygen, Nitrogen, Hydrogen and Carbon. Oxygen is dominant due to the high affinity of Niobium to the Oxygen. The influence of Hydrogen on the RRR is not so significant, but the content of Hydrogen should be kept small (less than 3-5 µg/g) to prevent the hydride precipitation and degradation of the Q-value of the high RRR cavities under certain cool down conditions (Hydrogen Q disease).

| Electrical and mechanical properties of Niobium | | Content of the main impurities µg/g | | | |
|---|---|---|---|---|---|
| Residual Resistivity Ratio | > 300 | Ta | ≤ 500 | H | ≤ 2 |
| Grain size | ≈ 50 µm | W | ≤ 50 | O | ≤ 10 |
| Yield strength | > 50 N/mm$^2$ | Mo | ≤ 50 | N | ≤ 10 |
| Tensile strength | > 140 N/mm$^2$ | Ti | ≤ 50 | C | ≤ 10 |
| Elongation at fracture | > 30% | Fe | ≤ 50 | | |
| Vickers hardness HV 10 | ≤ 60 | Ni | ≤ 50 | | |

***Table 4.2.2*** *Technical specification for Niobium applied for the fabrication of 1.3 GHz superconducting cavities.*

Among the metallic impurities, Tantalum (Ta) has the highest concentration (500 µg/g). This element accompanies Niobium in most ores; modern separating methods are based on solvent extraction. The impurity level of 500 µg/g is normally harmless for cavities since Tantalum is a substitutional impurity and does not substantially affect the scattering mechanism. Next in abundance among substitutional impurities are metals such as Tungsten (W), Titanium (Ti), Molybdenum (Mo), Iron (Fe) and Nickel (Ni) usually at the level less than 30-50 µg/g.

Several remeltings in a high vacuum electron beam furnace allow purification of the Niobium ingot. Light elements evaporate during this process. Four to six melting steps are generally necessary to reach the RRR=300 level with few µg/g of interstitial impurities. The content achieved by melting should be maintained during fabrication and treatment.

The Niobium should be free of defects (foreign material inclusions or cracks and laminations) which will initiate a thermal breakdown. For example, Tantalum clusters are dangerous, as they could result in a normal-conducting spot **[4-2]**. An eddy current scanning device for defect diagnostics in Niobium sheets was successfully developed for TTF and will be applied for the XFEL **[4-3]**. A SQUID scanning system could be more sensitive and is currently in development. The acceptance test of the material includes the RRR measurement, microstructure analysis, analysis of interstitial and metallic impurities, hardness measurement, tensile test, examination of the surface roughness and defects diagnostic.

The fabrication procedure of XFEL cavities consists of the deep drawing and EB welding of the parts into a cavity assembly. This procedure is well established and has about 20 years of industrial fabrication experience. Half cells are produced from Niobium discs pressed into shape using a set of dies. The dies are usually fabricated from hard anodised aluminium alloy. For establishing the form of the deep drawing tools, the spring-back of the Niobium sheet material has to be taken into consideration. Deep drawing is sensitive to the mechanical properties of Niobium. In particular, small and uniform grain size (see Table 4.2.2) is essential, unless mono-crystalline sheets can be used (see the end of this section). The Niobium sheet must be annealed to achieve complete re-crystallisation, and to remove lattice defects, without growing large grains. Too large grains would result in a roughening effect during the forming process (“orange peeling”).

If the material is incompletely re-crystallised, it tears during deep drawing. Achieving good mechanical properties for high RRR Niobium requires the proper choice of annealing temperature and time. The final annealing of 2.8 mm thick Niobium sheets occurs normally at 750-800°C in a vacuum oven at a pressure of $10^{-5}$-$10^{-6}$ mbar for 1-2 h. Niobium also has a low degree of work hardening, which is advantageous for mechanical forming. In almost all cases when the proper mechanical properties of the sheet are achieved, cavity parts can be deep drawn to final shape without intermediate annealing. The accuracy of the half cell is controlled by 3D measurement and by sandwiching the half cell between two Niobium plates and measuring the resonance frequency.

The EB welding is done in several steps: The weld parameters are chosen to achieve full penetration. A slightly defocused beam in an elliptic pattern and using 50% beam power during the first weld pass and 100% beam power in the second pass, creates a smooth weld seam. Welding from the inside (RF-side) is recommended, wherever possible. Welds at the equator and iris of cells and at the HOM coupler parts are especially critical because they will be exposed to high magnetic or electric fields. Therefore, a thorough cleaning by ultrasonic degreasing, chemical etching, and ultra pure water rinsing and clean room drying is mandatory; absolutely clean conditions must be assured during welding. Touching the weld preparation area after the last cleaning must be strictly avoided. Since Niobium is a strong getter material for Oxygen, it is important to carry out the EB welds in a sufficiently good vacuum. Tests have shown that RRR300 Niobium has less than 10% RRR degradation by welding at a pressure lower than $5 \times 10^{-5}$ mbar.

Two half cells are joined at the iris with an EB weld to form a dumbbell. This EB welding is usually done from the inside. The next step is the welding of the stiffening ring. The weld shrinkage may lead to a slight deformity of the cell which needs to be corrected. Afterwards, frequency measurements are made on the dumbbells to determine the amount of trimming at the equators.

The dumbbells are visually inspected. Defects and foreign material imprints from previous fabrication steps are removed by grinding. In state-of-the-art EB welding, the iris welds are very smooth, but it is still good practice to also perform the extra step of grinding the iris weld in order to ensure a smooth inner surface in this high electric field region and to avoid geometric field enhancement.

Beam tubes are either purchased as extruded seamless tubes or as rolled from sheet and EB welded. Flanges for the beam tubes are machined. Flanges are located in regions of low magnetic field and can be made from NbTi alloy (about 50%Ti).

After proper cleaning, eight dumbbells and two end group sections are assembled in a precise fixture to carry out the equator welds which are done from the outside. Experience has shown that all equator welds can be done in one production step (one evacuation of the EB chamber) without deterioration of the quality.

Use of an Engineering Data Management System (EDMS) for the complete documentation of the cavity fabrication process and the prompt exchange of all engineering information with the manufacturer will be required. This implies that all documents (inspection

sheets, specifications, drawings, etc.) which are created and maintained during the process of manufacturing the RF cavities, should be made available electronically in the EDMS. The complete information that must be reviewed by the manufacturer and approved by the client will be controlled by the system.

A potentially cost effective and more reliable cavity fabrication approach was recently proposed by colleagues of Jefferson Lab **[4-4, 4-5]**. High purity Niobium sliced directly from EB melted large grain ingot was used instead of Niobium sheets. Several single cell cavities deep drawn and EB welded demonstrated very promising performance. This approach might result in a possible cost saving option for fabrication of XFEL cavities. Several large grain Niobium single cells and 1.3 GHz nine-cell cavities will be produced, treated and RF tested.

#### *4.2.1.3 Cavity preparation*

Based on the standard preparation technique, (a buffered chemical polishing (BCP) followed by high pressure water rinsing), high acceleration gradients up to 30 MV/m were achieved at TTF **[4-6, 4-7]**. Encouraging results in cavity performance of 35-40 MV/m were gained in the cavity preparation with electropolishing in a collaboration of DESY and the KEK laboratories in Japan **[4-8]**. Thus, this newly established process has been chosen as the baseline.

For the XFEL, improved quality control measures for the fabrication of the resonators and the infrastructure for cavity preparation were introduced. The surface preparation relies on the removal of Niobium with electropolishing (EP) only. With this preparation, the post-purification with Titanium at 1,400°C can be avoided which leads to a cost reduction. Easier handling of the cavities due to their more favourable mechanical properties is also and advantage. The only remaining temperature treatment is an 800°C annealing.

The fundamental advantage of superconducting cavities is their extremely low surface resistance at 2 K, leading to RF losses which are five to six orders of magnitude lower than in Copper cavities. The drawback is that even tiny surface contaminations are potentially harmful as they decrease the quality factor and may even lead to a thermal breakdown/quench of the superconductor due to local overheating. Perfect cleaning of the inner cavity surface is of utmost importance. Cavity treatment and assembly is, therefore, carried out in clean rooms conforming to semiconductor standards.

The cavity preparation for the XFEL industrial production is foreseen to be as follows:

- electrochemical removal of a thick Niobium layer (so-called damage layer) of about 150 µm from the inner cavity surface;
- a rinse with particle free/ultra-pure water at high pressure (~100 bar) to remove residues from the electrochemical treatment;
- outside etching of the cavities of about 20 µm;
- ultra-high vacuum annealing at 800°C;
- tuning of the cavity frequency and field profile;

- removal of a thin and final layer of about 30 µm prior to the low power acceptance test done in a vertical dewar;
- rinsing with particle free/ultra-pure water at high pressure (100 bar) to remove surface contaminants;
- assembly of auxiliaries (pick-up probe and HOM pick-up);
- baking at 120°C in an ultra-high vacuum;
- additional six times rinse with high pressure ultra-pure water (100 bar);
- low power acceptance test at 2 K temperature.

Application of the above techniques combined with extremely careful handling of the cavities in a clean-room environment led to acceleration gradients of more than 30 MV/m. The XFEL design gradient of 23.6 MV/m can be reproduced (and likely be exceeded) within one preparation sequence (see Section 4.2.2.4). The latter is an important aspect of the series production, where a cost increase by a reapplied treatment procedure has to be avoided.

**Cavity treatment**

A Niobium layer of in total 180 µm is removed in several steps from the inner cavity surface to obtain good RF performance in the superconducting state. At present, the standard method applied for material removal for XFEL test cavities at DESY is EP. An acid mixture of hydrogen fluoride (HF) (48%), and $H_2SO_4$ >96% mixed in a volume ratio of 1:9 is used. The acid is heated to 30-35°C and a constant voltage of 17 volts is applied between the electrode made from pure aluminum and the cavity body. Closed loop pumping of the acid through the cavity is used. After rinsing with ultra-pure water and drying in a class 100 clean-room, the cavities are annealed at 800°C in an Ultra-High Vacuum (UHV) oven to out-gas possibly dissolved Hydrogen and to relieve mechanical stress, introduced in the Niobium during deep drawing in the cavity fabrication.

After the heat treatment, the cavities are mechanically tuned to adjust the resonance frequency to the design value and to obtain equal field amplitudes in all nine cells. This is followed by a light EP of about 30 µm material removal, a rinse with water at high-pressure (100 bar), and drying in a class 10 clean-room. This surface treatment is followed by the assembly of HOM antennae, the RF pick-up probe, and a provisional input antenna for the low power acceptance test. Even if this is done under controlled clean-room conditions, the cavities are rinsed with high pressure water six times to remove particles that may be introduced during the assembly process. The final acceptance step is an RF test in a super fluid Helium bath cryostat, (the vertical dewar).

**String assembly**

A total of eight superconducting resonators completed by one superconducting quadrupole magnet package are combined to form a module string inside a clean-room. In order to do so, the cavities are disassembled from the test inserts and the field profile and frequency are adjusted before welding the resonators into their individual Helium container. Tank

welding takes place in a normal workshop area. A bead pull system that stays with the cavity until the end of this procedure is installed inside the clean-room to keep the resonator interior as clean as it was during the low power acceptance test. For the string assembly, the provisional input antenna gets replaced by the power coupler. Finally, the cavities are rinsed six times with ultra-pure high pressure water for removing particles that may be introduced during the assembly process.

The interconnection between cavities and the attachment to the quadrupole magnet package with its integrated beam position monitor are made in a class 10 clean-room by insertion of a bellows between the beam pipes of the individual components. During the assembly procedures the working area is monitored by air particle counters. An integral leak check finalises the string assembly before roll-out of the string for module assembly.

**Diagnostic methods and quality control for cavity preparation**

To ensure a reproducible cavity preparation, several diagnostic methods and quality control procedures are installed:

- Control of the ultra-pure water in use for the cavity rinses:

  The main ultra-pure water supply, as well as the point-of-use stations (tap connection), are controlled for particles by online measurements of the particulate contamination, the total oxidable carbon (TOC) content and the resistance of the water.

- The clean-room and process gases (Argon):

  The air and process gases Argon and Nitrogen underlie a general monitoring of particle contamination and air flow conditions (flow speed/flow direction). During the assembly procedures the working area is monitored by additional air particle counters. These data, taken at the point of work, are the basis of quality control of the assembly procedure.

- High pressure rinsing:

  To control the quality and efficiency of the high pressure rinses, the drain water, coming from the inside of the resonator, is conducted through a filter which is examined by a scanning light microscope to identify particulates.

#### *4.2.1.4 Cavity performance*

Radio frequency performance tests on the cavities are a crucial tool for quality control. The performance of the cavities is determined by measuring their “excitation curve”, i.e. the so-called quality factor Q as a function of the accelerating gradient. In first approximation, this quality factor Q is independent of the gradient. In a real cavity the non-perfect superconductor surface leads to a gradient dependence. The low power acceptance test done in a vertical bath cryostat at 2 K temperature includes the measurement of the “excitation curve” with its gradient limit, and the determination of the dark current onset caused by field emission.

### Test setup for the acceptance test

The test infrastructure includes a bath cryostat and its auxiliaries needed to cool down the cavity to 2 K using liquid Helium. The RF measurement setup includes a low level RF feedback system based on a phase locked loop (PLL) to hold the RF generator's signal frequency equal to the resonance frequency of the cavity $f_0$. A solid state continuous wave (CW) 1 kW L-band RF amplifier is used to feed the cavity. Calibrated directional couplers and RF power meters are used to measure the forward, reflected and transmitted RF power. A digital scope, used together with logarithmical amplifiers, detects the signal's pulse shape (see Figures 4.2.2 and 4.2.3). Prior to the measurement, a low power calibration is done. This allows the calculation of the accelerating gradient $E_{acc}$ from the transmitted (probe) power values. The cavity quality factor $Q_0$ is derived from the stored energy, the RF pulse decay time, and the measured RF power coupling coefficients.

During the test, multi-pacting[2] can occur at accelerating gradients of 17-22 MV/m. Conditioning is typically finished in less than half an hour. The usual gradient limitation is a thermal breakdown (called quench) caused by defects or inclusions heating up the cavity surface. X-rays can be produced by field emitted electrons due to a particulate contamination. These electrons are contributing to the dark current in the accelerator and increase the power dissipated inside the cavity. The consequence is a reduction in quality factor and, therefore, the emitted dark current can limit the cavity performance.

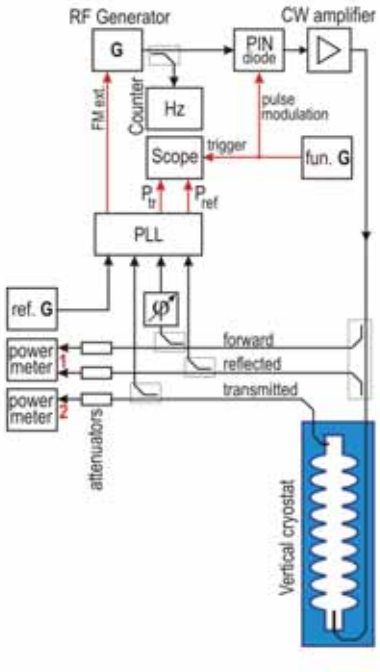


***Figure 4.2.2*** *Vertical cryostat cavity test diagram.*

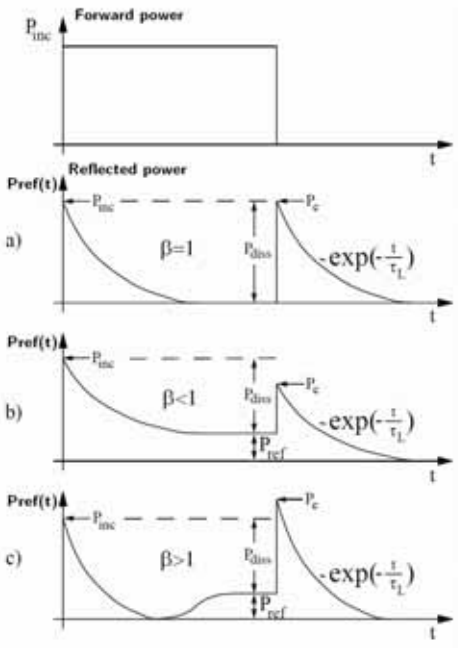


***Figure 4.2.3*** *Forward and reflected RF power pulses.*

[2] Multi-pacting = "Multiple impacting" – electrons emitted from the cavity surface are accelerated and hit the surface yielding secondary electrons. If the secondaries are generated in resonance with the RF frequency, an avalanche is generated. Processing reduces the secondary emission coefficient of the surface.

### Results from acceptance test

As mentioned before, the envisaged XFEL surface preparation is based on EP and 800°C annealing. The classical cavity surface preparation uses a 1400°C post-purification and etching as described in **[4-6, 4-7]**. Electro-polishing offers prospects for significantly higher gradients (Figure 4.2.4) **[4-8, 4-9]**.

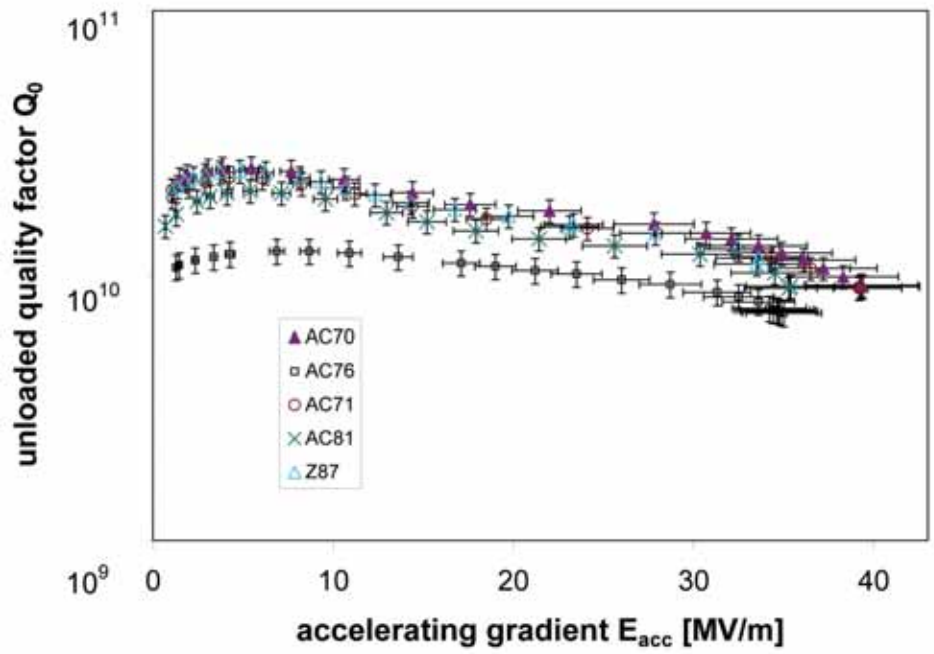


***Figure 4.2.4*** *"Excitation curves" of the best cavities treated with 800°C furnace treatment and EP. The XFEL baseline gradient of 23.4 MV/m is exceeded by a significant margin.*

Comparing the first performance tests on each cavity from both preparation techniques shows that the new XFEL procedure yields an average gradient of 28.4 +/- 3.6 MV/m at $Q_0$ of $10^{10}$, whereas the classical procedure achieves 24.0 +/- 4.8 MV/m.

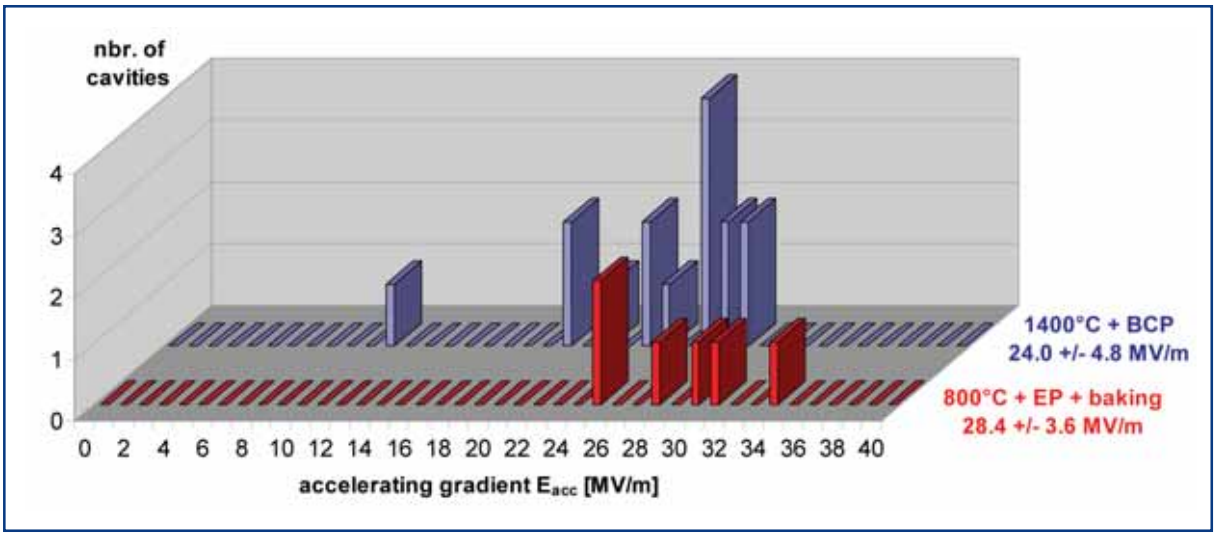


***Figure 4.2.5*** *Comparison of the accelerating gradients at $Q_0=10^{10}$ in the first performance test after the full preparation sequences using etching with post-purification at 1,400°C (blue) and EP with 800°C annealing (red).*

**High power test set-up**

A high power test of each individual cavity is done after assembly of the cavities into the accelerator module cryostats. In addition to that, a fraction of the cavities in production will be tested in an horizontal cryostat cavity test as a cavity qualification test done at 2 K in pulsed RF power mode (CHECHIA, **[4-10]**).

The goal of this test is to measure the performance of a resonator including all its auxiliaries such as main RF power coupler, HOM couplers, tuner and Helium tank. Done either in the completed module or in an horizontal test cryostat, the test conditions are identical with operation conditions in the linac, except for the electron beam.

The test infrastructure includes an L-band klystron to feed the cavity with pulsed RF power up to 1 MW. Calibrated directional couplers and RF power meters are used to measure the forward, reflected and transmitted RF power. A digital scope is used together with logarithmical amplifiers to obtain the signal's pulse shape. Prior to the measurement a low power calibration is done. This allows the calculation of the accelerating gradient $E_{acc}$ from the transmitted (probe) power values. The cavity quality factor $Q_0$ is derived from the stored energy W and the cryogenic losses $P_{loss}$, measured as $Q_0 = 2\pi f_0 W / P_{loss}$.

The cavity operating mode as well as the HOM spectra and quality factors are measured to evaluate the HOM couplers' performance. The variable coupling factor of the main input coupler is checked for the whole antenna movement range and set to the aimed $Q_{load}$ value of $4.6 \times 10^6$.

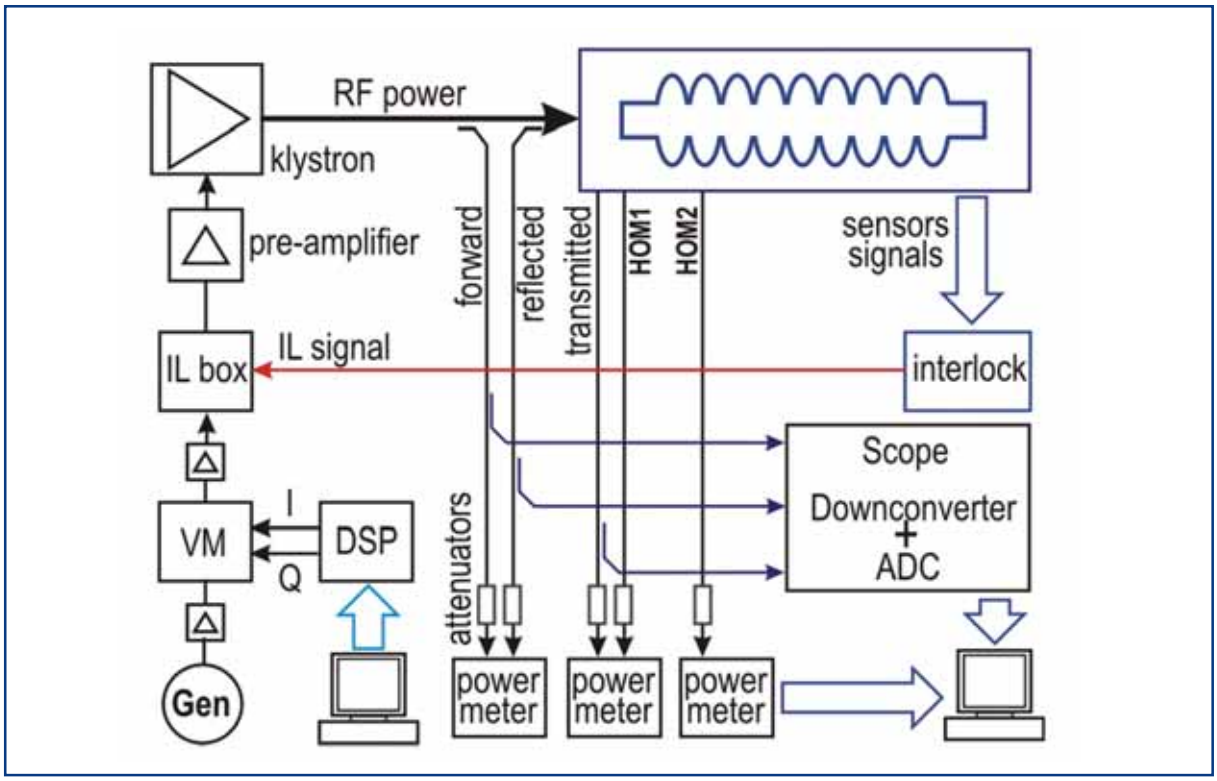


***Figure 4.2.6*** *Horizontal cryostat cavity test diagram.*

The test is done in three major steps:

1 The main RF power coupler is conditioned with the cavity being off resonance; this is done at room temperature.

2 Coupler and cavity are then conditioned with the cavity being on resonance at 2 K.

3 The $Q_0$ vs. $E_{acc}$ measurement is done during 'flat-top' pulse operation; the cavity performance limit is investigated.

The power coupler off-resonance conditioning is carried out for pulse lengths of 20, 50, 100, 200, 400 µs with RF power up to 1 MW, and for pulse lengths of 800 and 1,400 µs up to 600 kW. On-resonance conditioning uses rectangular pulses up to the length of the cavity filling time (780 µs), and for longer pulses (up to 1.4 ms) with a reduced forward power in order to keep the cavity gradient constant during the pulse[3]. During the last stage the cavity quality factor is determined measuring the cryogenic losses at various accelerating gradient values up to the cavity limit. The x-rays associated with the dark current are measured in addition.

[3] Cavity conditioning might include high peak power processing (HPP) done with the pulse lengths of 100-1300 µs up to the cavity breakdown or the 1 MW power limit. The HPP procedure can help to remove the existing cavity electron emitters by applying the short high RF power pulses. **[4-11]**

### High power test results

The accelerating fields achieved in the vertical and the horizontal tests are well correlated **[4-8, 4-6]**. In a few cases a reduced performance was seen, usually caused by field emission. Several cavities improved their performance in the horizontal test because of operation with short (millisecond) pulses instead of the CW operation in the vertical cryostat. The results show that the good performance of the cavities is maintained by taking care to avoid dust contamination during the mounting of the Helium vessel and power coupler. The ultimate performance test of the cavities is done after assembly of the cavity string and their installation into the accelerator module cryostat vessel. The experience obtained at TTF with the accelerator modules is summarised in Figure 4.2.7.

As can be seen, the latest generation accelerator modules (M4 and M5) have operational gradients above the baseline gradient for the XFEL. The expected performance from the acceptance test could be transferred to the fully assembled modules for these modules. For some of the TTF accelerating modules this is not the case. The performance degradation in those modules is partially linked to the different scheme of cavity positioning used as well as to missing quality control procedures in the earlier string and module assemblies.

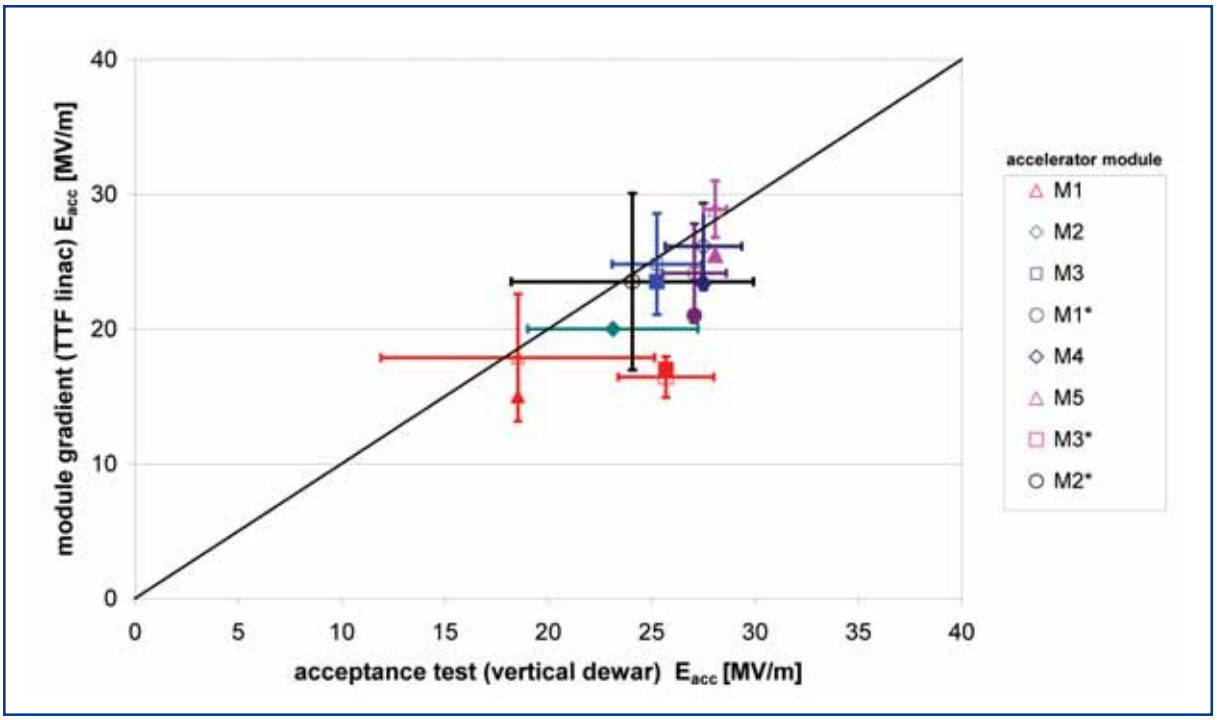


***Figure 4.2.7*** *Performance of the TTF accelerator modules. The plot shows the average maximum gradient in the accelerator modules against the average gradient achieved in the acceptance tests at $Q=10^{10}$ (open symbols). In addition, the operational gradient of the modules is plotted against the acceptance test gradient (closed symbols) which is based on equal RF power feeding.*

## 4.2.2 Auxiliaries

### *4.2.2.1 Main power coupler*

The XFEL linac coaxial RF power input coupler has been developed **[4-12, 4-13]** consisting of a cold section which is mounted on the cavity in the clean-room and closed by a ceramic window, and a warm section which contains the transition from the coaxial line to the waveguide. This section is evacuated and sealed against the air-filled wave guide (WR650) by a second ceramic window (see Figure 4.2.8). The elaborate two-window solution was chosen for additional protection of the cavity against contamination during mounting in the accelerator module, and against a window fracture during linac operation.

Bellows in the inner and outer conductors of the coaxial line of the coupler allow a few mm of motion between the cold mass and the vacuum vessel when the cavities are cooled from room temperature to 2 K. A low thermal conductivity is achieved by using stainless steel pipes and bellows with a 10-30 µm Copper plating at the radio frequency conducting surface. Lower values than the design heat loads of 6 W at 70 K, 0.5 W at 4.5 K and 0.06 W at 2 K have been achieved in practice.

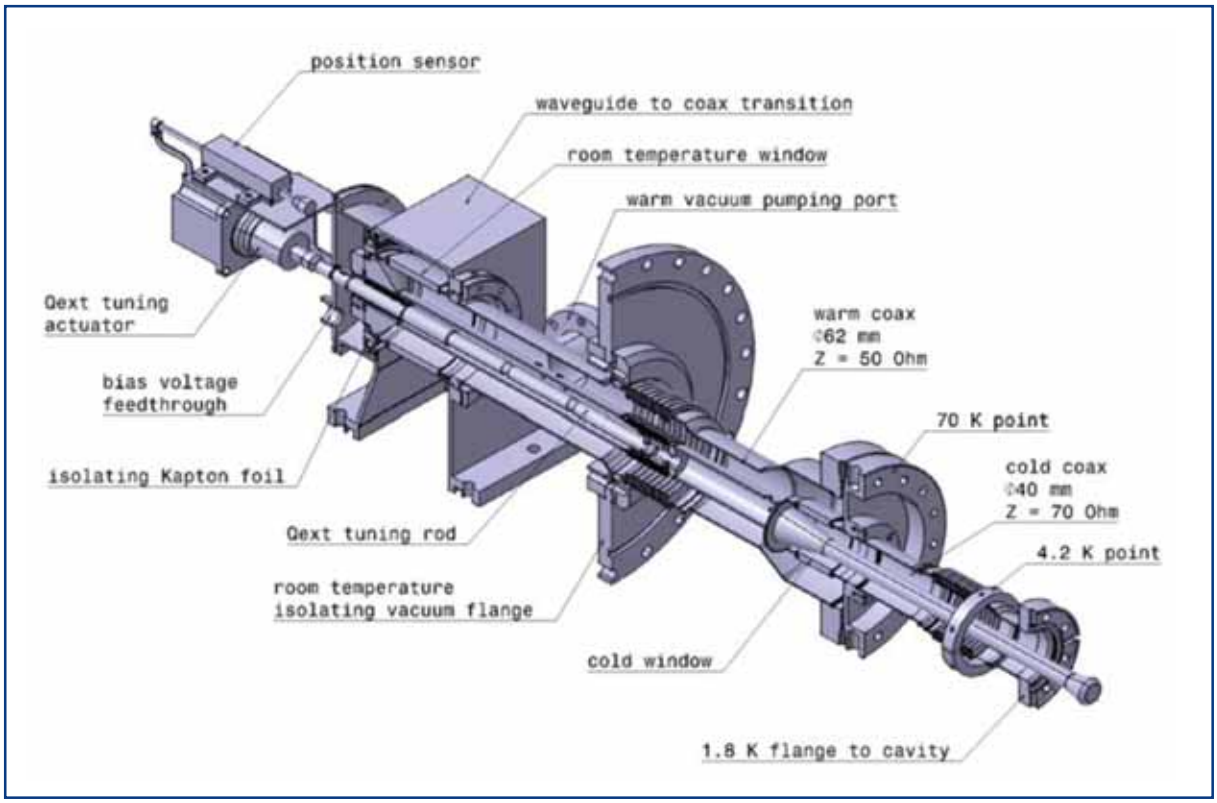


***Figure 4.2.8*** *The coaxial power input coupler for the XFEL linac cavities. The coaxial part is thermally connected to the 4.5 K and 70 K radiation shields of the cryostat. The input antenna is movable to vary $Q_{ext}$ in the range $10^6$ – $10^7$.*

The coupler features two cylindrical $Al_2O_3$ windows which are insensitive to multi-pacting resonances according to the simulations, and are coated with Titanium nitride to reduce the secondary electron emission coefficient **[4-14, 4-15, 4-16]**. The coaxial line is also insensitive to multi-pacting resonances. A further suppression is achieved by applying a DC bias voltage (up to 5 kV) to the inner conductor.

At 20 GeV beam energy, an instantaneous power of 120 kW has to be transmitted to provide a gradient of 23.6 MV/m for a 600 µs long beam pulse of 5 mA. The maximum RF pulse length is 1.38 ms, the filling time of the cavity amounts to 720 µs. The repetition rate is 10 Hz (1.37% duty cycle) and the average power amounts to 1.6 kW. The external quality factor of the coupler is $Q_{ext} = 4.6 \times 10^6$ at 23.6 MV/m. By moving the inner conductor of the coaxial line, $Q_{ext}$ can be varied in the range $10^6$-$10^7$ to cope with different beam loading conditions and to facilitate an in-situ high power processing of the cavities at RF power levels up to 1 MW. This feature has proven to be extremely useful on several occasions to eliminate field emitters that entered the cavities at the last assembly stage. The continuous wave (CW, 100% duty cycle) operation, as an XFEL upgrade option, with an accelerating gradient of 7 MV/m and a beam current of 0.18 mA would need 2.5 kW of CW power for the coupler, including regulation overhead; it will take advantage of using tunable $Q_{ext}$.

All couplers must be conditioned in order to perform according to specifications. During experimental tests at TTF, the couplers were able to transmit up to 1.5 MW of peak pulsed RF power at 2 Hz repetition rate in travelling wave mode on the coupler test stand, and 600 kW at 5 Hz repetition rate in standing wave mode with cavities operated at 35 MV/m in a horizontal test cryostat (2,400 hours of operation, 2.5 kW of average RF power) **[4-8]**.

### *4.2.2.2 Damping of higher-order modes (HOM)*

The spectrum of the electron bunch reaches very high frequencies up to 5 THz due to the short length $\sigma_z$ = 25 µm of the accelerated bunches. The integrated longitudinal loss factor of the accelerator module housing eight nine-cell cavities is 135 V/pC and the total power deposited by the nominal beam (30,000 bunches/s) in an accelerator module is 5.4 W if no resonant excitation takes place **[4-17]**. Its distribution for various frequency ranges is shown in Figure 4.2.9. Two types of devices, HOM couplers and beam pipe absorbers, are proposed for extracting this power from the 2 K environment. Modes below the cut-off frequency of the interconnecting beam tubes (non-propagating part of the spectrum) will be suppressed by the HOM couplers **[4-18]** of which two will be attached to the end beam tubes of each cavity. The HOM couplers, based on the coaxial line technique (Figure 4.2.10) will also suppress non-propagating modes in case of their resonant excitations.

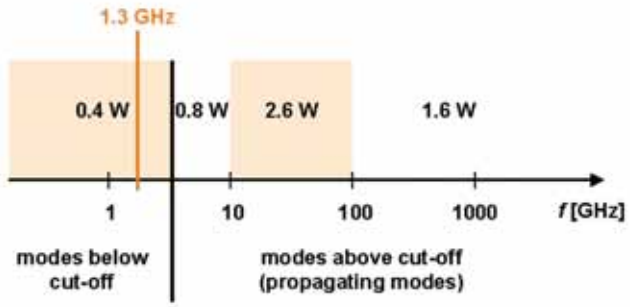


***Figure 4.2.9*** *HOM power distribution against frequency for the nominal pulse operation.*

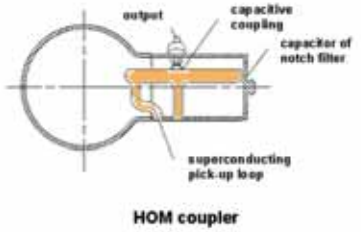


***Figure 4.2.10*** *HOM coupler.*

A large proportion (~80%) of the propagating power will be dissipated in the beam pipe absorbers (Figure 4.2.11) to mitigate additional cryogenic load at 2 K. These devices installed between accelerator modules will absorb the power in the lossy ceramic rings and transfer generated heat to the 70 K environment.

In the beam pipe absorber and HOM coupler designs we take into account a possible upgrade of the XFEL Facility to higher average brilliance by operating it with more bunches in CW or near-CW modes **[4-19]**. For this, the absorber power capability has been specified to be 100 W which will allow for acceleration of up to one million nominal bunches per second. Even for this high power, good heat conductivity of the chosen ceramic keeps the temperature gradient across the ceramic ring below 140 K. Several performed tests confirmed that this gradient does not change the mechanical and RF properties of the absorber. The HOM couplers will be equipped with high heat conductivity feedthroughs (as compared to those used at present for the TTF cavities) allowing their Niobium output probes to be kept in the superconducting state, so avoiding additional cryogenic load at 2 K.

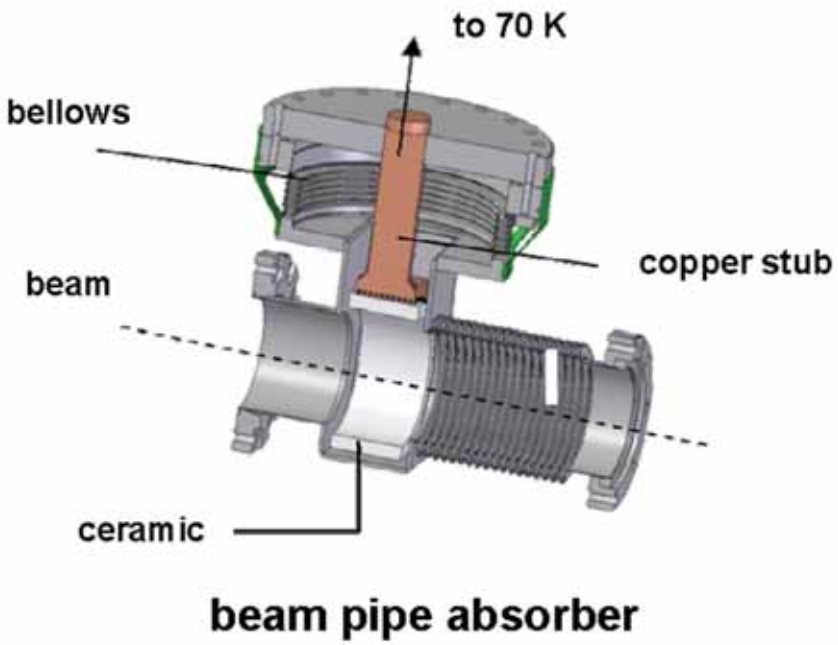


***Figure 4.2.11*** *Layout of the beam pipe absorber.*

### *4.2.2.3 Helium vessel and tuning system*

The cavity is welded into a cylindrical vessel which contains the superfluid Helium needed for cooling and serves as part of the tuning mechanism. The vessel is made from Titanium whose thermal contraction is almost identical to that of Niobium. A Titanium bellows allows the length to be adjusted by the mechanical tuner.

**Slow tuner**

Tuning the cavity to its nominal operating frequency is a challenging task since the cavity length must be adjusted with sub-micron accuracy. The tuning system used at TTF consists of a stepping motor with a gear box and a double lever arm. The moving parts operate at 2 K in a vacuum. The frequency tuning range is about 400 kHz with a resolution of 1 Hz. The tuners in the TTF linac have been working since 1997 with high reliability. The tuner for the XFEL is based on a tuner design used for 1.5 GHz cavities built by CEA Saclay **[4-20, 4-21]**, and being in operation at the ELETTRA and PSI synchrotron light sources. The new design will be stiffer than the TTF tuner, using a double lever with a screw-nut system. In contrast to the TTF design, the cavity is stretched by the tuner. This has the advantage that the piezo elements are compressed under all circumstances (see Figure 4.2.12).

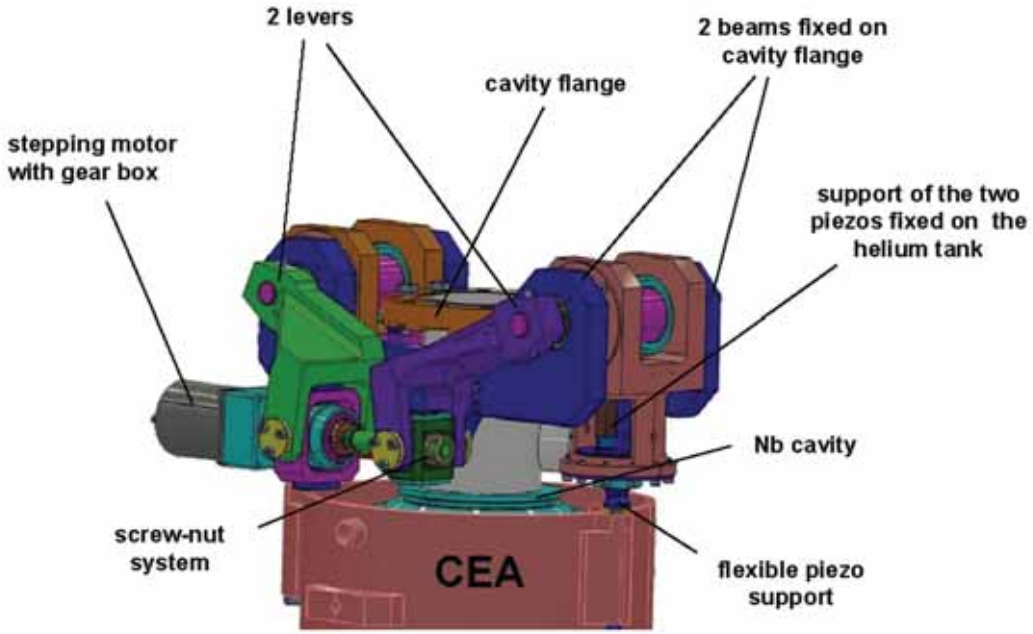


***Figure 4.2.12*** *Overview of the tuner design for the XFEL.*

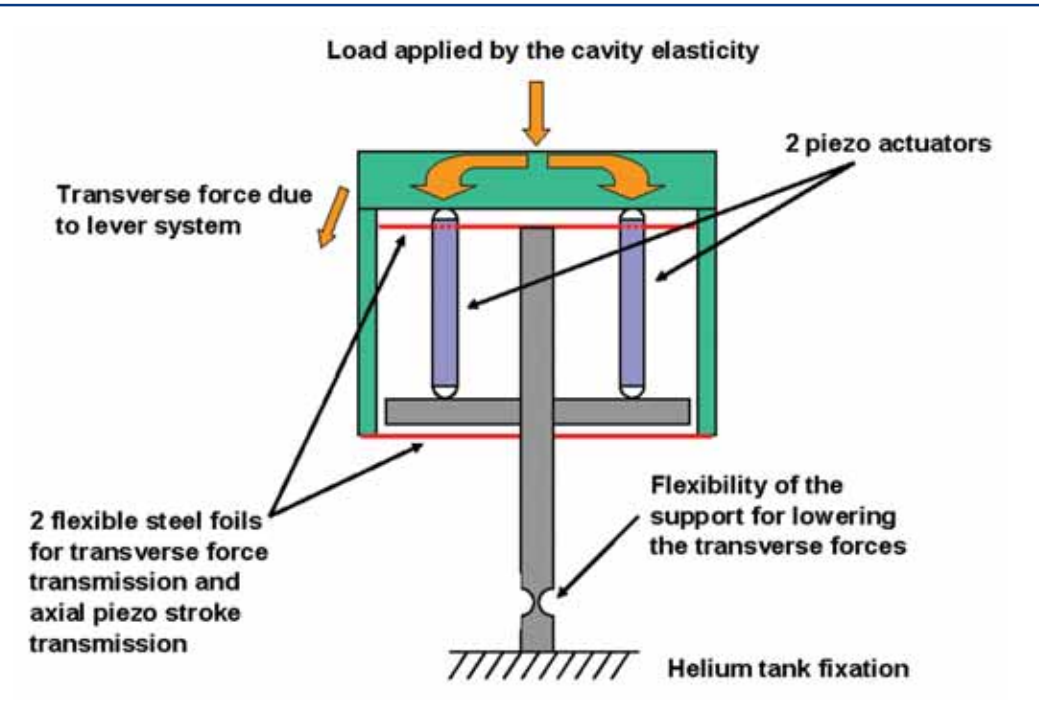


***Figure 4.2.13*** *The principle of operation of the fast piezoelectric elements* **[4-21]**.

**Frequency stability of the cavities within an RF pulse (fast tuner)**

The pulsed operation leads to a time-dependent frequency change of the nine-cell cavities. The stiffening rings joining neighbouring cells are adequate to keep this so-called “Lorentz-force detuning” within tolerable limits up to the nominal XFEL gradient of 23.6 MV/m.

To allow for higher gradients and to further improve frequency stabilisation, the cavity deformation must be compensated for. This approach has been successfully demonstrated using a piezoelectric tuner **[4-8, 4-21]** (see Figure 4.2.14). The result indicates that the present stiffening rings augmented by a piezoelectric tuning system will permit efficient cavity operation for all operation modes of the XFEL. In addition, for lower gradients the frequency of the cavities can be stabilised to a few Hz leading to a better phase stability during the RF pulse **[4-22, 4-23]**.

The principle of the new XFEL tuner is based on the fact that the preload is directly applied on the piezo actuators by the cavity elasticity. No additional force is applied by the support of the piezo elements. With this concept, the preloading of the piezos can be predicted in a more precise way, which is an important improvement compared to the TTF tuner. A prototype system is currently being tested at CEA and DESY.

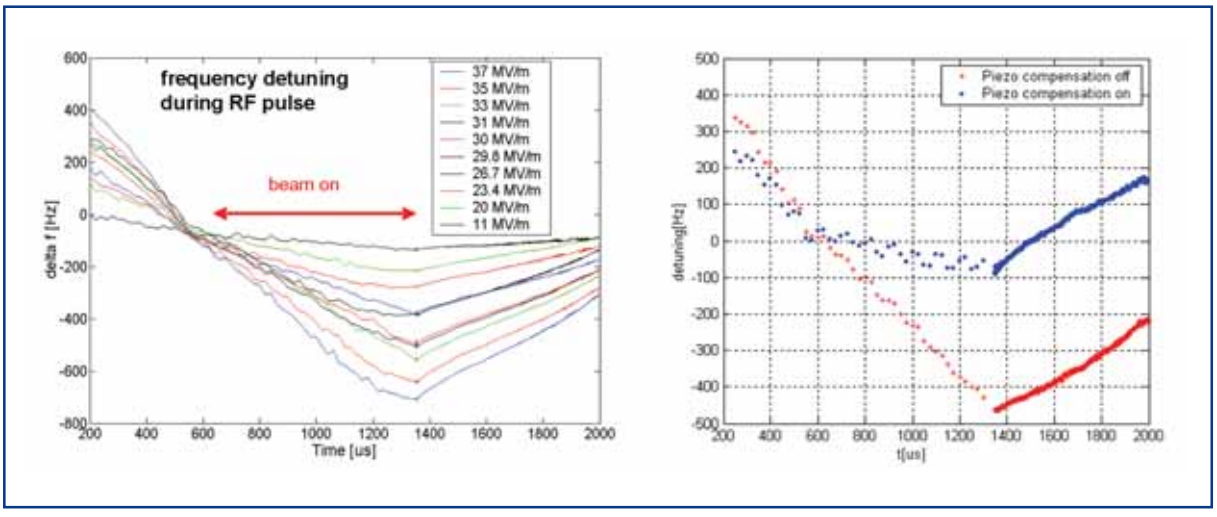


***Figure 4.2.14*** *Lorentz-force detuning in pulsed mode operation at gradients from 11 to 37 MV/m (left). High-power pulsed test at 35 MV/m of an EP nine-cell cavity. The measured detuning during cavity filling and “flat top” at 35 MV/m with and without piezo-electric compensation.*

### *4.2.2.4 Accelerator module (cryomodule)*

The design of the accelerator module described here is based on the third cryomodule generation for the TTF. Two of these so-called type-3 modules have been successfully tested and operated in the TTF linac since March 2003. The length of the type-3 module is 12.2 m, the total weight 7.8 t, (2.8 t for the cold mass and 5 t for the vacuum vessel). Its major components are:

- a Carbon steel vacuum vessel with a standard diameter of 38”;
- a 300 mm Helium Gas-Return-Pipe (GRP) acting as a support structure, together with three adjustable posts on top of the vacuum vessel. The middle post is the fixed-point but, the outer posts can slide in a longitudinal direction, because during-cool down the ends of the 12 m long GRP move by up to 18 mm towards the centre of the module;
- a 2 K forward line transferring single phase Helium, a 2 K two phase line connected to the cavity Helium vessels, a 5-8 K forward and return line, a 40/80 K forward and return line, and a warm-up/cool-down line with capillaries to the bottom of each cavity vessel;
- Aluminum thermal shields with stiff upper parts for 4 K and 40/80 K with 10 layers of super-insulation (MLI) for 4 K and 30 layers for 40/80 K, attached to the support structure;
- eight completed cavities and one beam position monitor (BPM)/magnet unit, attached to the GRP;
- the cavities and BPM/magnet unit can be aligned individually. To keep the cold coupler head of each cavity fixed within 2 mm, each cavity is anchored to a long Invar rod attached to the longitudinal centre of the GRP at the middle post. In addition, the cavity and magnet Helium vessels and GRP are wrapped with 10 layers MLI to reduce the heat transfer in the event of vacuum failure;
- manually operated valves to terminate the beam tube at both ends;
- a HOM-Absorber is part of the beam pipe and installed next to the BPM/magnet unit;
- four C-shaped stainless steel elements clamp a Titanium pad welded to the Helium tank. Rolling needles drastically reduce the longitudinal friction. The cavities are independent from the elongation and contraction of the HeGRP.
- lateral and vertical position the are defined by reference screws. The longitudinal position can be fixed by the use of an Invar rod.

Well defined procedures to prepare the individual components, guide the assembly and installation, and test the linac cryogenic operation of an accelerator module, are available. Already 10 accelerator modules have been built and successfully commissioned for the TTF linac during the last ten years.

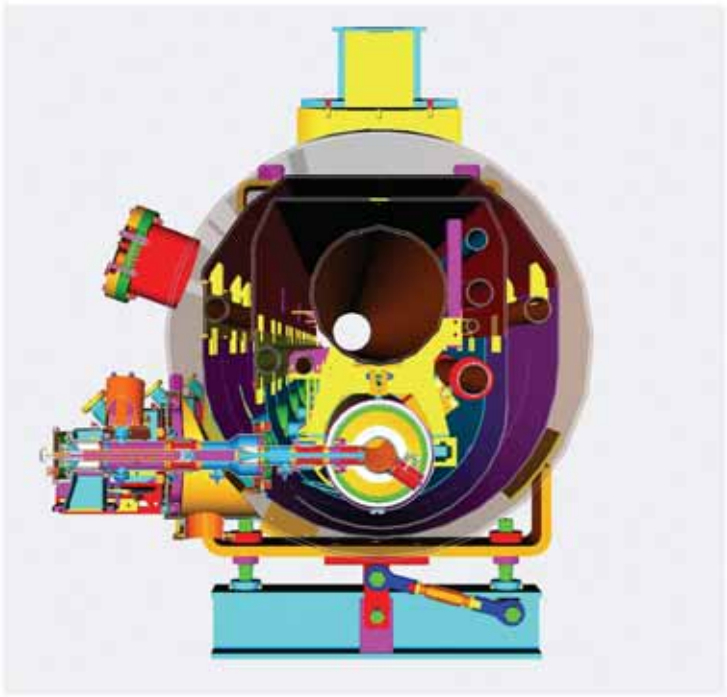

***Figure 4.2.15*** *Cross-section of a type-3 cryomodule.*

The type-3 cryomodule meets nearly all the requirements of the XFEL modules, with the following exceptions:

- the cold magnet will be operated at 2 K (now up to 4 K at TTF) with conduction cooled current leads; the cold magnet and BPM will be one unit; at the XFEL, the 4 K circuit raises up to ~8 K temperature;
- a HOM-Absorber will be placed in module interconnection with 40/80 K cooling; the maximum cooling capacity is laid out for a future CW-operation of the XFEL linac;
- a modified cavity frequency tuner with fast (piezo) tuning will be used;
- the cavity-to-cavity spacing will be corrected to be exactly one RF wavelength. Shortening the cryomodule length by 230 mm allows for an inter-module cavity-to-cavity spacing of a multiple of the RF wavelength.

These necessary modifications are on the way and will be introduced and tested in two further accelerator modules (M8 and M9) of the so-called cryomodule type-3+ in November/December 2006. Industrial studies for the assembly of modules in later series production have been launched.

| Module performance | Module 4 | Module 5 | XFEL specification |
|---|---|---|---|
| **RF gradient** | | | **reached** |
| Design | >24 MV/m | >25 MV/m | 23.6 MV/m |
| Measured | average >26 MV/m | average >29 MV/m | |
| **Dynamic cryo losses 2 K** | | | **reached** |
| 25MV/m 5Hz 500/800µs | | | |
| Design | 3.0 W (Qo=1E10) | 3.0 W (Qo=1E10) | 3.0 W (Qo=1E10) |
| Measured | 2.3 W Qo=1.3E10 | 2.0 W Qo=1.7E10 | |
| **Static cryo losses** | | | **reached** |
| 2K/4K/40-80K | | | |
| Design | 4.2/21.0/12 W | 4.2/21.0/112 W | 4.2/21.0/112 W |
| Estimated | 2.8/13.9/77 W | 2.8/13.9/77 W | |
| Measured | <3.5/13.5/74 W | <3.5/13.5/74 W | |
| **Number of leaks** | 0 | 0 | **reached** |
| He → insulation | 0 | 0 | |
| He → beam pipe | 0 | 0 | |
| Insulation → coupler | 0 | 0 | |
| Insulation → beam pipe | 0 | 0 | |
| Coupler → beam pipe | 0 | 0 | |
| Alignment x/y inside | | | **reached** |
| **Cavities** design x/y | +0.5/-0.5 mm (peak) | +0.5/-0.5 mm (peak) | +-0.5mm (rms) |
| measured x | +0.32/-0.19 mm | +0.35/-0.32 mm | |
| measured y | +0.10/-0.35 mm | +0.2/-0.1 mm | |
| **Magnet/BPM** design | +0.3/-0.3 mm (peak) | +0.3/-0.3 mm (peak) | +-0.3 mm (rms) |
| measured x | +0.10/-0.05 mm | +0.15/-0.05 mm | |
| measured y | +0.35/-0.05 mm | +0.20/-0.05 mm | |
| Alignment z inside | | | **reached** |
| **Coupler antenna** design z within 2 mm | within 2 mm | | within 2 mm |
| Measured z x-ray | within < 2 mm | within <2 mm | |

***Table 4.2.3*** *Comparison of cryomodule type-3 parameters (after two thermal cycles) with the XFEL specifications.*

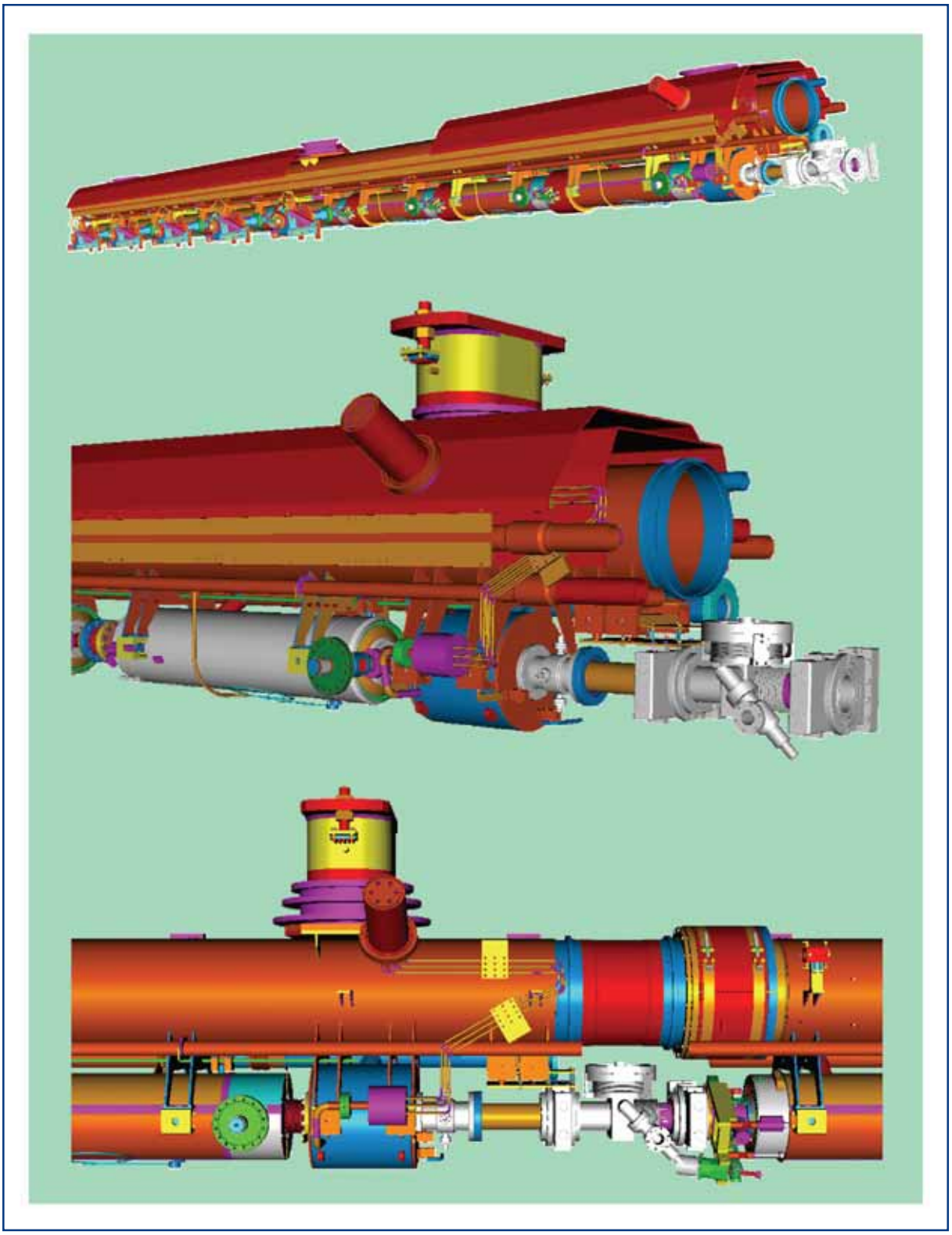

***Figure 4.2.16*** *CAD cut-away view of the type-3+ cryomodule.*
*Top: Cold mass with cavities, BPM/magnet, HOM-Absorber beam pipe valve.*
*Middle: End group of a module.*
*Bottom: Module-to-module connection.*

### *4.2.2.5 XFEL magnet package and cold beam position monitor*

At the downstream end of the cavity string of each XFEL accelerator module, a magnet package and an attached BPM is placed (see Figure 4.2.17). The magnet package contains three independent superconducting magnets: a super-ferric quadrupole magnet, a vertical and a horizontal dipole magnet. A detailed parameter list is given in Table 4.2.4 and Table 4.2.5.

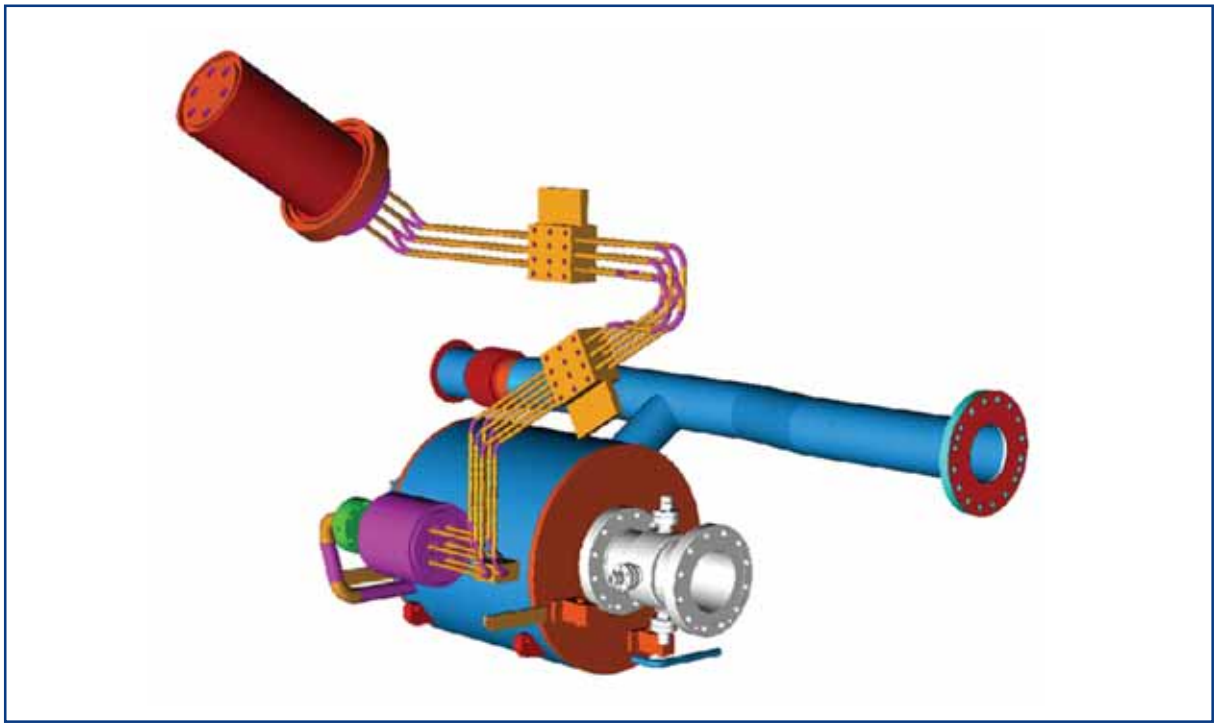

***Figure 4.2.17*** *Schematic view of the magnet package, the BPM and the current leads.*

A super-ferric magnet design has been selected for the quadrupole because a magnet with a low gradient can be best realised with a conventional Iron-based design using a superconducting coil allowing the integration into the 2 K liquid Helium volume in the XFEL accelerator module. The correction magnets are single layer cos-Θ type coils which are directly mounted on the beam pipe. The beam pipe itself is the inner wall of the Helium vessel. In order to avoid flanged connections, the vessel is made of Titanium. This allows welding connections to the cavity tank (also made of Titanium). Iron mirror plates at both magnet ends inside the Helium vessel are included to minimise the stray field outside the magnet and prevent magnetic field penetration into the cavity area. The magnet and cryostat design are done in collaboration with CIEMAT **[4-24]**.

Two different types of BPMs are under discussion: the SACLAY design is described in **[4-25]**, the DESY design is shown in Figure 4.2.17. The connection between the BPM and the magnet package is the same type as the connections between the cavity tanks. The axial space is limited to 170 mm.

### Magnet support and alignment with the BPM

The magnet package is hanging at the 300 mm tube using a bearing system to allow axial movement of about 30 mm during cool-down. The axial position, relative to the central post, is kept constant by connecting the magnet package to the Invar rod. The bearing play is minimised by a spring-loaded support.

For machine operation it is important to know the relative position of the quadrupole with respect to the BPM. The required tolerance for the axis differences is 0.3 mm and it is 3 mrad for the roll angle difference. In order to fulfil these requirements, two dowel pins are used. The position for the boreholes of the dowel pins at the quadrupole flange will be calculated from warm magnetic measurements ($\Delta x$, $\Delta y$ and $\alpha$) and will then be transferred to the quadrupole flange. By this procedure an arbitrary selection of magnet packages and BPMs is possible. To follow this procedure one has to ensure that the deviation of the mechanical and magnetic axes and roll angle of the magnet package is within ±0.4 mm and 6.5 mrad respectively, given by the difference of the bore hole diameter of the BPM flange and the bolt diameter.

| | | **Quadrupole magnet** |
|---|---|---|
| Winding type | | Super-ferric |
| Iron yoke inner diameter | [mm] | 94.4 |
| Iron yoke outer diameter | [mm] | 270 |
| Nominal current | [A] | 50 |
| Nominal gradient | [T/m] | 35 |
| Magnetic length | [mm] | 166.5 |
| Number of turns | | 646 (34x19) |
| Wire diameter (bare/insulated) | [mm] | 0.4/0.438 |
| Copper to superconductor ratio | | 1.35 |
| RRR | | >70 |
| Filament diameter | [micron] | 35 |
| Twist pitch | [mm] | 50 |
| Iron yoke length | [mm] | 140 |
| Coil length | [mm] | 200.6 |
| Stored magnetic energy at 50 A | [J] | 1439 |
| Self inductance | [H] | 1.15 |
| Integrated gradient at 50 A | [T] | 5.828 |
| Integrated b6 at 50 A | $10^{-4}$ × b2 at 30 mm | 1.34 |
| Integrated b10 at 50 A | $10^{-4}$ × b2 at 30 mm | -1.10 |
| Coil peak field | T | 2.47 |
| Integrated gradient at 5 A | T | 0.6284 |
| Integrated b6 at 5 A | $10^{-4}$ × b2 at 30 mm | 0.36 |
| Integrated b10 at 5 A | $10^{-4}$ × b2 at 30 mm | -0.04 |
| Saturation at 50 A (integrated) | % | <5 |

***Table 4.2.4*** *Parameters of the cold superconducting quadrupole magnet.*

| **Dipole magnet** | | **Inner** | **Outer** |
|---|---|---|---|
| Winding type | | cos-Θ | cos-Θ |
| Inner diameter | [mm] | 83.6 | 88.5 |
| Outer diameter | [mm] | 85.66 | 90.56 |
| Nominal current | [A] | 50 | 50 |
| Nominal field | [T] | 0.04 | 0.04 |
| Magnetic length | [mm] | 197.5 | 197.5 |
| Number of turns | | 33 | 34 |
| Wire diameter | [mm] | 0.7/1.03 | 0.7/1.03 |
| Copper to superconductor | | 1.8 | 1.8 |
| RRR | | 100 | 100 |
| Filament diameter | [micron] | 20 | 20 |
| Twist pitch | [mm] | 25 | 25 |
| Iron yoke length | [mm] | 140 | 140 |
| Coil length | [mm] | 230 | 230 |
| Self inductance | [mH] | 0.62 | 0.73 |
| Integrated field at 50 A | [Tm] | 0.0079 | 0.0079 |
| Integrated b3 at 50 A | 10-4 × b1 at 30 mm | 4.14 | -12.66 |
| Integrated b5 at 50 A | $10^{-4}$ × b1 at 30 mm | 119 | 14 |
| Int.field, dip.&quad@50 A | [Tm] | 0.0069 | 0.0068 |
| Saturation at 50 A | [%] | 13 | 14 |

***Table 4.2.5*** *Parameters of the cold superconducting dipole magnet.*

### Current leads

Three pairs of current leads for a maximal current of 50 A are necessary. A design of Copper-coated bronze rods, insulated by Kapton® and embedded in stainless steel tubes is selected. Two thermal heat sinks, one at 4-8 K and one 40-80 K reduce the heat load to the 2 K level (see green parts in Figure 4.2.17). The design is based on a CERN design **[4-26]** used at LHC. The superconducting wires enter the wiring box, which is flanged to the Helium vessel of the magnet package. From here stainless steel is used. The soldered connections of the superconducting wires to the cold ends of the leads are made in the wiring box and the box is closed by welding. In a complicated path the leads are brought out through the two thermal shields, allowing a 30 mm relative movement between the cold and the warm end. The leads are connected by Copper braids to the heat sinks. They end at a flange on the accelerator module where they are connected to ceramic feedthroughs, to which the power supplies are then connected.

## 4.2.3 Vacuum system

The layout of the linac vacuum system of the XFEL is similar to the vacuum system of the TTF linac described in **[4-27]** and **[4-28]**.

### *4.2.3.1 Vacuum requirements*

The requirements for the vacuum system are mainly determined by the goal of reaching high accelerating gradients in the superconducting cavities. Dust particles can act as field emitters and thus, limit the performance of the superconducting cavities. As the 2 K cold cavities are an integral part of the beam pipe they act as huge cryopumps. Therefore, the risk of contaminating the superconducting cavities with particles and condensating gas from other vacuum components during assembly and operation needs to be avoided at all costs. As a consequence, the preparation of all vacuum components includes, in addition to standard UHV procedures, cleaning in a clean-room of at least class 100 to remove particles and the installation of components into the machine under local clean-rooms.

The interaction between beam and residual gas is, however, uncritical and synchrotron radiation is negligible.

### *4.2.3.2 Cold vacuum system*

The superconducting cavities, fabricated from pure Niobium, are surrounded by a Titanium tank filled with superfluid Helium. Eight cavities, a superconducting quadrupole and a beam position monitor are grouped into 12 m long strings, which are assembled in a class 10 clean-room shown in Figure 4.2.16. The cavities are connected via Copper coated bellows without RF-shields. The sealing system has been specially developed and consist of rigid Niobium-Titanium flanges (Nb/Ti55) EB welded to the Niobium cavities and massive aluminium rings as gaskets **[4-29]**. After assembly, the complete string is evacuated, closed off by all-metal manual valves at both ends and inserted into the module tank.

As shown in Figure 4.2.18 the beam pipe interconnection between the accelerator modules consists of a 300 mm long section that incorporates a HOM-Absorber, a bellows and a vacuum pumping port. Every 12 modules, in the area of the module string connection boxes, there will be a connection for continuous pumping of the beam vacuum by sputter ion pumps and all-metal automatic beam valves.

The RF power input coupler attached to each cavity has two ceramic windows, one at a temperature of 70 K and one at room temperature. This design enables complete closure of the cavity in the clean-room by mounting the coupler up to the first window, thus preventing any contamination during further assembly of the module. Additionally, gas and dust are prevented from entering the cavities in case a crack in one of the ceramic windows should occur during operation. The warm coupler parts have a common vacuum for eight couplers of each module which is pumped by a sputter ion pump and a Titanium sublimation pump.

The accelerator module vessels serve as an isolation vacuum once the cavities are cooled down to 2 K. The layout is similar to the HERA design **[4-30]**. The string connection boxes are equipped with a vacuum barrier, which separates the insulating vacuum of the module strings, thus separating vacuum sections of 144 m length.

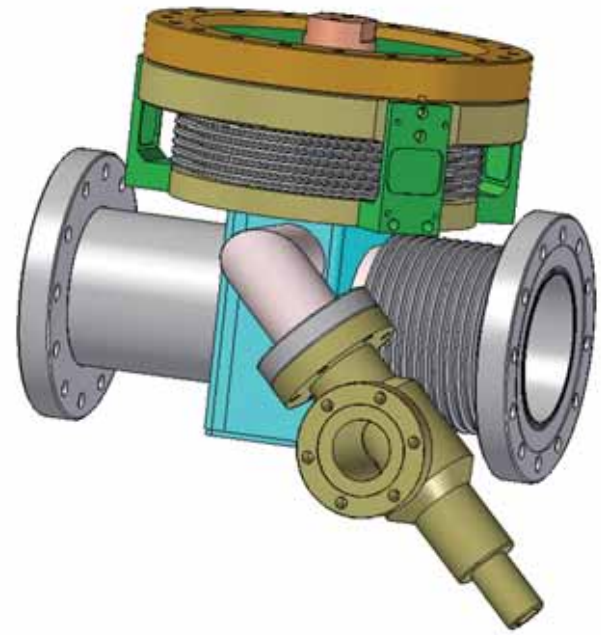

***Figure 4.2.18*** *Module interconnection including the HOM-absorber.*

## 4.2.4 High power RF system

### *4.2.4.1 Introduction*

The XFEL RF system consists of 31 RF stations, 29 for the main linac and two for the injector, and another two if the second injector is added. Each station can provide RF power up to 10 MW peak and 150 kW average at a frequency of 1.3 GHz and distributes the power to a number of cavities in the XFEL main linac, injector and RF gun.

Each RF station comprises a klystron, an HV modulator, which transforms the AC line power to pulsed high voltage power, high voltage pulse cables, a pulse transformer, a waveguide distribution system, a low-level RF system, which controls shape, amplitude and phase of the RF, several auxiliary power supplies for the klystron and the pulse transformer, preamplifier and an interlock and control system, which protects the station and the linac.

Most of the components of the RF stations will be installed in the accelerator tunnel with a separation of 50 m. The exceptions are the modulators which will be installed above ground in a dedicated modulator hall near to one of the linac access shafts. High voltage pulse cables and additional cables for the interlock system connect the components of each station in and outside the tunnel.

The operation parameters, nominal at a linac energy of 20 GeV are listed in Table 4.2.6. Not all optimal values can be achieved at the same time.

At 20 GeV, the linac for the XFEL operates at a gradient of 23.6 MV/m with a repetition rate of 10 Hz. Since the particle beam current is 5 mA, up to 122 kW are required per cavity. The maximum beam pulse duration is 600 µs and the cavity filling time 780 µs.

Thirty-two cavities (four times eight cavities per cryogenic module) will be connected to one klystron by the RF waveguide distribution system. At nominal operation parameters, 3.9 MW are required. Taking into account 6% losses in the waveguide distribution system and a regulation reserve of 15% for phase and amplitude control, the klystron must provide up to 5.2 MW.

| | | Nominal | Maximum |
|---|---|---|---|
| Number of sc cavities in main linac | | 928 | |
| Peak power per cavity | [kW] | 122 | 230 |
| Gradient | [MV/m] | 23.6 | 28.5 |
| Power per 32 cavities | [MW] | 3.9 | 8.3 |
| Power per RF station | [MW] | 5.2 | 10 |
| Number of installed linac RF station | | 29 | |
| Number of active linac RF stations | | 26 | |
| Number of installed injector RF station | | 2 | |
| RF pulse duration | [ms] | 1.38 | 1.5 |
| Repetition rate | [Hz] | 10 | 10 (50) |
| Average klystron beam power | [kW] | 153 | 250 |
| Average RF power during operation | [kW] | 71 | 150 |

***Table 4.2.6*** *RF system requirements.*

In order to match the operation requirements of the different users of the XFEL it is aimed to operate the accelerator and thus the RF system at a higher repetition rate up to 50 Hz by reducing either the RF pulse width or the RF output power at the same time. The limiting factor will be the maximum average klystron beam power.

### *4.2.4.2 RF Power Source*

The RF power source for the XFEL is a 10 MW multi-beam klystron (MBK). By using several smaller electron beams in one klystron envelope instead of a single beam, space charge forces are reduced, thus, leading to higher efficiency and lower klystron cathode voltage in comparison with a single beam klystron of the same output power **[4-31, 4-32]**. The klystron requirements are given in Table 4.2.7.

| | | Nominal | Min./Max |
|---|---|---|---|
| Frequency | [GHz] | 1.3 | 1.3 |
| RF Pulse Duration | [ms] | 1.38 | /1.5 |
| Repetition Rate | [Hz] | 10 | /≈50 (low $P_{peak}$) |
| Cathode Voltage | [kV] | 95 | 120 |
| Beam Current | [A] | 103 | 140 |
| HV Pulse Duration | [ms] | 1.57 | 0.2/1.7 |
| Microperveance | | 3.5 | 3.3/3.7 |
| RF Peak Power | [MW] | 5.2 | 10 |

***Table 4.2.7*** *Klystron parameters.*

Three manufacturers have developed MBKs which meet or almost meet these requirements. Figure 4.2.19 shows the multibeam klystrons TH1801 produced by THALES Electron Devices, VKL 8301 by CPI, and E3736 by Toshiba Electron Devices.

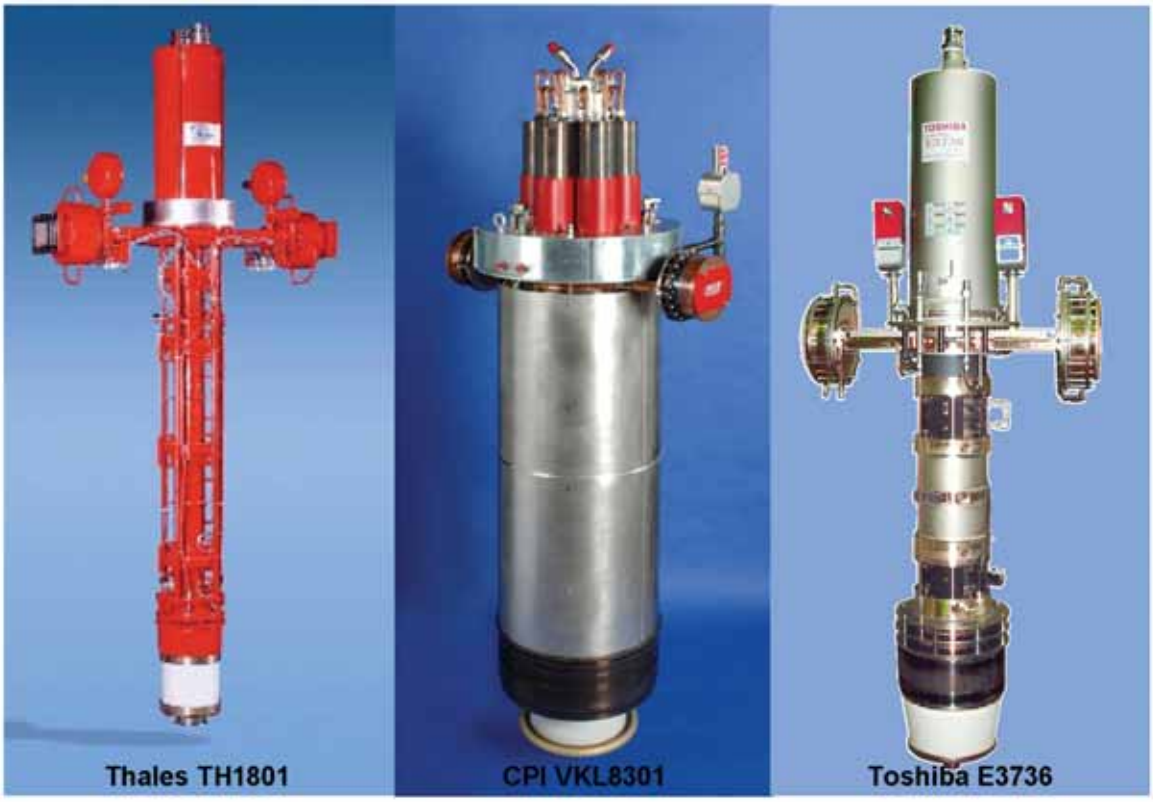


***Figure 4.2.19*** *Thales TH1801, CPI VKL8301, and Toshiba E3736 MBK.*

Two output waveguides are always required to handle the RF power of 2 times 5 MW in the output windows. The total height of each klystron is about 2.5 m. In order to allow horizontal installation in the XFEL tunnel, the klystron must be delivered and installed together with the solenoids on a girder.

Multi beam klystrons have been tested and operated at the TTF at DESY. They achieved an output power of 10 MW with an efficiency of 65%. More detailed information about the individual klystrons can be found in **[4-33 – 4-38]**.

### *4.2.4.3 HV pulse power source (modulator, pulse cable and transformer)*

The HV pulse power source consists of a HV pulse modulator, a 1:12 pulse transformer and HV pulse cables up to 1.5 km length connecting modulator and pulse transformer.

It generates HV pulses of 115 kV of almost rectangular pulse shape required at the klystron cathode. The nominal pulse duration is 1.58 ms and the rise and fall time 200 µs. Already during the leading edge of the high voltage pulse, when the voltage has reached 80% of the flat top level, the klystron can start to generate RF power. Although this part of the RF pulse does not meet the requirements regarding phase and amplitude stability for particle beam acceleration in the accelerator, it can be used to fill the superconducting cavities with RF. The phase change of 320° between 80% and 100% of the klystron voltage can be compensated for by the low level RF control. The flat top ripple should not exceed ±0.5% in order to limit phase and amplitude variations of the klystron RF output during beam acceleration. The pulse-to-pulse stability must be better than ±0.5%. In case of klystron gun sparking, the energy deposited in the spark must be limited to a maximum of 20 J. The requirements are summarised in the Table 4.2.8.

| | | **Nominal** | **Max.** |
|---|---|---|---|
| Modulator pulse voltage/pulse transformer primary | [kV] | 8 | 11 |
| Modulator pulse current voltage/pulse transformer | [kA] | 1.24 | 1.8 |
| Pulse transformer secondary voltage/klystron gun | [kV] | 95 | 132 |
| Pulse transformer secondary current/klystron gun | [A] | 103 | 150 |
| High voltage pulse duration (70% to 70%) | [ms] | 1.58 | 1.7 |
| High voltage rise and fall time (0 to 99%) | [ms] | 0.2 | 0.2 |
| High voltage flat top (99% to 99%) | [ms] | 1.38 | 1.5 |
| Pulse flatness during flat top | [%] | ±0.3 | ±0.5 |
| Pulse-to-pulse voltage fluctuation | [%] | ±0.3 | ±0.5 |
| Energy deposit in klystron in case of gun spark | [J] | <20 | 20 |
| Pulse repetition rate | [Hz] | 10 | 50 |
| Pulse transformer ratio | | 1 :12 | |

***Table 4.2.8*** *HV pulse power source parameters.*

The basic idea of the bouncer modulator is to use a capacitor discharge and compensate for the voltage droop by the linear part of the oscillation of a bouncer circuit. This technical solution is well established and offers high reliability compared to alternative layouts **[4-39]**.

The circuit diagram of the bouncer modulator is sketched in Figure 4.2.20. A HV power supply keeps the 1.4 mF main capacitor C1 charged to the 10 kV level. By closing the switch S1, the capacitor C1 starts to discharge via the pulse transformer into the klystron. The 1:12 transformer converts the 10 kV voltage of the capacitor to the klystron level of

120 kV. After 1.57 ms, switch S1 opens and terminates the pulse. Since the capacitor voltage drops during the pulse, no flat top would be achieved unless a huge capacitor bank storing a large amount of energy could be used. For a droop of 1% a capacitor bank of 29 mF would be required. In order to overcome the disadvantage of a huge capacitor bank the bouncer circuit was added. A circuit consisting of a choke, a capacitor and another switch is connected to the low end of the primary winding of the pulse transformer. By triggering this switch shortly before the main pulse begins, the circuit starts to oscillate. The linear part of the 5 ms long oscillation is then used to compensate for the droop of the main capacitor C1. By this the 19% droop of the 1.4 mF capacitor can be reduced to 1%. A very detailed description of the modulator is given in **[4-40 - 4-44]**.

Within the modulator a special high voltage power supply for charging the main capacitor is required. It has to charge the capacitor to an accurate voltage in order to obtain the same voltage at the klystron from pulse to pulse, and it has to suppress the repetition frequency (up to 50 Hz) load of the mains in order to avoid disturbances of the mains.

The input connection of each power supply is a three-phase grid and the output voltage is 13.5 kV. In order to ensure a high reliability the power supplies will be built in modules of switch mode buck converters or alternatively of series resonant converters.

The power supply regulation is a digital self-learning regulation of the input power, made possible by the high regulation dynamic of the converter supply. In addition, the voltage at the capacitor bank at the firing time of the pulse will be regulated to within 0.1% accuracy. Further information about the power supplies can be found in **[4-45]**.

Several modulators of the bouncer type have been built and are in use at the TTF. The first modulators were built and assembled by Fermilab, USA, and then shipped to DESY. The others were assembled at DESY from units manufactured by industrial companies.

The first modulators made by Fermilab use GTOs and IGBTs as main switches in the pulse generating unit, whereas the newer version of the pulse generating unit built by industry use IGCTs instead. The size of a modulator is 5 m (length) x 2 m (width) x 2.2 m (height).

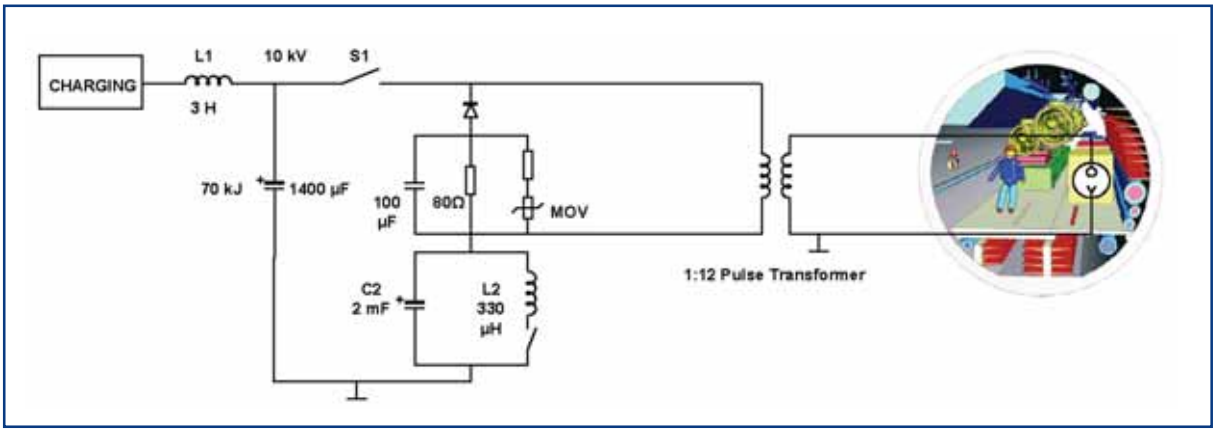


***Figure 4.2.20*** *Circuit diagram of the modulator (schematic).*

A 1:12 pulse transformer transforms the 9.6 kV pulses of the pulse generating unit to 115 kV required by the klystron. The transformers leakage inductance determines the rise time of the HV pulse. The first transformers had a leakage inductance of more than 300 µH whereas the newer ones have less than 200 µH. This meets the specification of rise time of less than 200 µs. The size of the transformer is 3.2 m (length) x 1.2 m (width) x 1.4 m (height), its weight is 6.5 t.

The pulse forming units of the modulators will be installed in the modulator halls at the surface, whereas the pulse transformers will be installed inside the tunnel. Thus, pulse cables with a length of up to 1.7 km must be used for the connection. In order to limit the ohmic power loss to 2%, on average, a current lead of 300 $mm^2$ is required. The wave impedance of the cable must match the impedance of the klystron transformed to the transformers primary side to avoid distortion of the pulse shape. In addition, the skin effect must be minimised. Therefore, four cables in parallel, each of 75 $mm^2$ cross section, 25Ω impedance, and an outer diameter of 30 mm, will be used. The cables are the triaxial type to minimise electromagnetic interference. The inner lead is at high potential (12 kV), the middle cylindrical lead at the potential of the bouncer circuit (±2 kV) and the outer cylindrical lead at ground potential. As insulation material VPE will be used. Additional line matching to the pulse transformer will be done via a RC network. Simulation results and further information on the cable can be found in **[4-46]**.

In case of klystron gun sparking, the modulator's main switch must be opened quickly and must be reliable to limit the energy deposited in the klystron spark to less than 20 J. The energy stored in the transformer leakage inductance and in the power transmission cable will be dissipated in two passive networks, one at the cable end near to the main switch consisting of a reverse diode and a resistor and a second one made up by an 80 Ω resistor across the transformer primary and by a 100 µF capacitor which limits the peak inverse voltage at the primary to 800 V when the main switch is opened.

#### *4.2.4.4 Interlock and control system, preamplifier and auxiliary power supplies*

Although the gain of the klystron is 48 dB and the required drive power is less than 200 W at nominal operation conditions, more power is required if the klystron is operated at lower voltage, e.g. if it is operated at a higher repetition rate than nominal but at the same average power. Taking this into account, a preamplifier with a 1 dB compression point at 650 W is needed. Even at this power level, solid state amplifiers can be used. They will be installed near to the klystrons inside the accelerator tunnel in racks housing the auxiliary power supplies and the interlock system.

Several additional auxiliary power supplies are required for the operation of the klystron and the modulator, e.g. for the klystron focusing solenoid, the klystron filament, the klystron vacuum pump and the pulse transformer core bias. Standard off-the-shelf auxiliary power supplies will be installed together in a rack near to the klystron and the pulse transformer.

The interlock system protects the accelerator and the RF stations in case of malfunction and supports the localisation of faults. Besides the modulator interlock and control system which is an integral part of the modulator, an additional interlock and control system for the RF system's components in the tunnel is required.

It will be based on programmable logic devices which have the advantage that the interlock logic can be modified easily if required. Today, electronic boards based on these devices are fast enough to react within µs. Therefore, no additional hard-wired systems for fast interlock are necessary. Besides system protection and providing start-up and shut-down procedures for the RF stations, the control and interlock system will offer diagnostics functions for the RF systems. It will allow measurement and diagnosis of actual parameters as well as adjustment of set points within certain limits for each RF station and its subsystems; and flexible reaction to different fault conditions. Communication with the accelerator's main control can be accomplished by standardised protocols.

Since each RF station consists of two parts, one in the tunnel and one in the access hall, there will be two interlock units connected to each other by glass fibre cables. Interlock conditions are summarised into categories, each starting a certain action in the other unit, thus, only a limited number of fibres is required. More detailed information on the interlock can be found in **[4-47 - 4-49]**.

The racks housing the preamplifier, auxiliary power supplies and interlock will be shielded by lead, thus protecting the electronic components in these devices from radiation.

Taking into account a maximum input power to the klystron of 250 kW and assuming a combined maximum efficiency of the system of modulator, pulse cable and pulse transformer of 75%, the AC input power is 333 kW. The other tunnel RF components require 17 kW of AC line power. So the total is 350 kW of maximum AC line power per active RF station.

### *4.2.4.5 RF waveguide distribution system*

A linear distribution system is used to branch off equal amounts of power to the individual cavities. Thirty-two cavities (four accelerator modules) are connected to the two output waveguides of a 10 MW multibeam klystron. Directional couplers are foreseen to couple out the required amount of power. During cavity filling, a large amount of RF power is reflected back from the cavity. This also applies after the end of the beam pulse as well as in cases when the linac is operated with low beam current. In order to protect the klystrons against reflected power, a circulator is placed in front of each cavity. Motorised stub tuners are installed between the cavity and the circulator to adjust the cavities' phase and $Q_{load}$. A WR650 waveguide has been chosen for the RF power distributing system. Additional information on the waveguide distribution system can be found in **[4-50, 4-51]**.

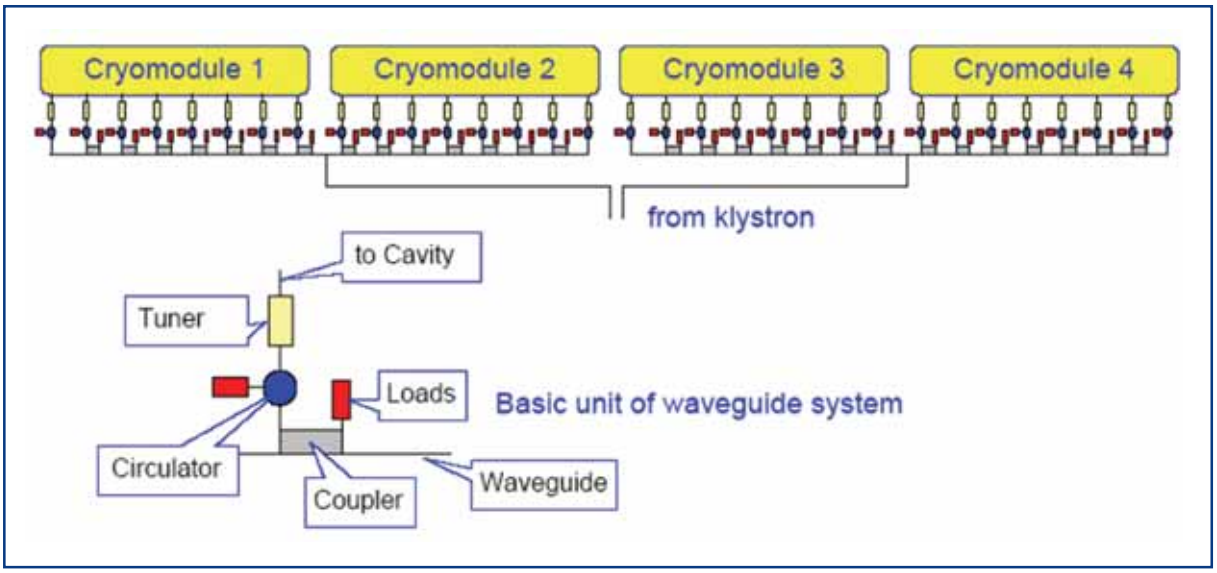


***Figure 4.2.21*** *RF waveguide distribution of one RF station.*

### 4.2.5 Low level radio frequency control

The requirements for RF control systems for the European XFEL are not only defined in terms of the stability of RF amplitude and phase but also with respect to the operability, availability and maintainability of the RF system. The field control of the vector-sum of many cavities driven by one klystron in pulsed mode at high gradients is a challenging task since Lorentz-force detuning, mechanical vibrations (microphonics), and beam-induced field errors must be suppressed by several orders of magnitude. This is accomplished by a combination of local and global feedback and feed-forward control.

Sensors monitor the individual cavity probe signals, together with forward and reflected wave as well as the beam properties. The electron beam energy, beam current and phase, with respect to the external RF master oscillator, are additional input parameters for the low level radio frequency (LLRF) control. Actuators control the incident wave of the klystron and the individual cavities' resonance frequency.

A high degree of automation eases the operability of the large LLRF system. High availability requires robust algorithms, redundancy, and extremely reliable hardware. Sophisticated on-line diagnostics for the LLRF subsystems support maintenance and minimise downtime.

LLRF systems are required for the RF gun, the injector RF systems including the third harmonic cavity, and the accelerator modules in the main linac. The largest RF system installation will be in the linac, with 928 cavities in 116 accelerator modules (where 32 cavities are driven by one 10 MW klystron). The technology for controlling the vector-sum of many cavities driven by one klystron has been demonstrated successfully at the TTF and is presently in operation at Free-electron LASer in Hamburg (FLASH) at DESY. It is a fully digital system providing the capability for feedback and feed-forward, exception handling and extensive build-in diagnostics. However, the full potential of such systems in terms of operability in large scale systems and the reliability required for the XFEL remains to be demonstrated.

### *4.2.5.1 Requirements for RF control*

The requirements for the RF control system are usually defined in terms of phase and amplitude stability of the accelerating field during the 600 µs long flat-top portion of the RF pulse. In addition, operational demands impose further needs on the design of the RF control system.

**Amplitude and phase stability**

The requirements of the RF control system are derived from the desired beam parameters such as bunch-to-bunch and pulse-to-pulse energy spread, the bunch compression in the injector, and the arrival-time of the beam at the undulators. The beam parameters can be translated into the requirements for phase and amplitude of the accelerating field of individual cavities or the vector-sum of several cavities driven by one klystron. The RF systems in the injector of the XFEL require tight field control in the order of 0.01% for the amplitude and 0.01° for the phase. Additional requirements are imposed on the accuracy of the calibration of the vector- sum which must be in the order of 1% for amplitude and 0.5° for phase in presence of ±10° microphonics (see also Section 4.2.5.2).

**Operational requirements**

Besides field stabilisation, the RF control system must provide diagnostics for the calibration of gradient and beam phase, measurement of the loop phase, cavity detuning and control of the cavity frequency tuners. Exception handling capability will be implemented to avoid unnecessary beam loss and to allow for maximum operable gradient.

### *4.2.5.2 Sources of field perturbations*

The LLRF system will suppress field perturbations induced by fluctuations in the resonance frequency of the cavities and fluctuations of the beam current. Changes in resonance frequency result from variations in the cavity shape induced either by mechanical vibrations (microphonics) or by the gradient dependent Lorentz-force caused by the electromagnetic accelerating field inside the cavity.

**Lorentz-force**

The static detuning of a resonator due to Lorentz-force is proportional to the square of the accelerating field. In the case of pulsed RF fields, a time varying cavity detuning – even during the flat-top portion of the RF pulse – can be observed. Mechanical resonances will be excited, whereas the lower the mechanical quality factor and the higher the mechanical resonance frequency (only longitudinal modes should be excited), the less likely is the enhancement of the peak cavity detuning by the Lorentz-force. Stiffening rings at the iris are used to reduce the Lorentz-force detuning constant to below 1 Hz/(MV/m)$^2$ and increase the mechanical resonance frequencies.

**Microphonics**

Mechanical vibrations caused by the accelerator environment (e.g. vacuum pumps at the cryogenics facility) are always present and may be transferred to accelerating structures through cryogenic transfer line, and beam pipe. The frequency spectrum and amplitude of excitation depend strongly on the coupling to the cavities. Measurements at the TTF show typical excitation amplitudes in the order of 5-10 Hz (rms) and frequencies ranging from 0.1 Hz up to a few hundred Hz.

**Beam loading**

The loaded Q is usually chosen for matched conditions, i.e. all of the RF generator power (with the exception of a small amount dissipated in the sc-cavities) is transferred to the beam. In the case of on-crest operation (the electron bunches see the maximum amplitude) the magnitude of the beam-induced voltage is half of the generator-induced voltage. While slow bunch charge fluctuations within the bandwidth of the LLRF system can be controlled, fast fluctuations in the order of a few percent of the bunch charge need not be corrected since the introduced amplitude and phase errors do not exceed the field stability requirements.

### *4.2.5.3 RF control concept and control system architecture*

The basic idea of any RF control system is based on feedback control in which the cavity field vector is measured and compared to the desired set-point. The resulting error vector (the difference between measured field and set-point) is filtered and amplified before modulating the klystron drive and thereby, the incident wave to the cavities. Nevertheless, during pulsed operation, the perturbations from the above mentioned Lorentz-force detuning and beam loading are of a repetitive nature. Thus, the feedback can be supplemented by a feed-forward which compensates the average repetitive error. In addition, the cavity field set-point can be implemented as a table to accommodate the time-varying gradient and phase during cavity filling.

The architecture of a typical RF control system is shown in Figure 4.2.22. A power amplifier provides the RF power necessary for establishing the accelerating fields in the cavities. The cavity field is measured and compared to a set-point. The resulting error signal is amplified and filtered and drives a controller for the incident wave to the cavity. A frequency and phase stable master oscillator and RF distribution system provide the necessary RF reference signals for the cavity field measurements.

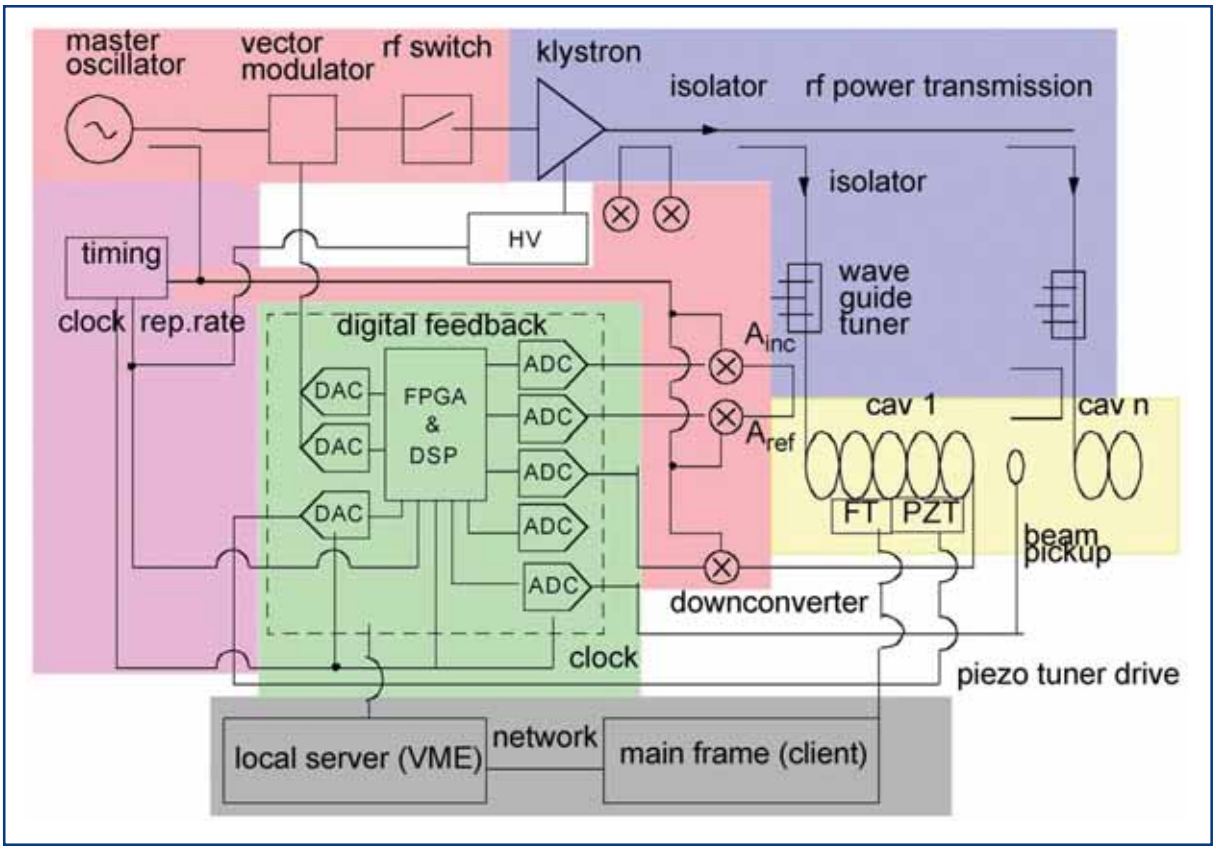


***Figure 4.2.22*** *Typical configuration of an RF control system using digital feedback control.*

The overall design of the RF control system provides:

- control of the cavity resonance frequency. Here the critical issue is the precise measurement of the cavity detuning which can be derived from the relationship of incident and reflected wave or in the pulsed operation mode from the slope of the phase during decay of the cavity field following the RF pulse;
- linearisation of the klystron – since operation close to klystron saturation will result in strong dependence of loop gain with klystron output power;
- remote control of waveguide tuners or phase shifters. In the case of vector-sum control, the phase of the incident wave (and loaded Q) of each cavity must be set independently to compensate for phase errors in the waveguide distribution system;
- exception handling. In case of interlock trips or abnormal operating conditions (wrong loop phase or completely detuned cavity) the control system must ensure safe procedures to protect hardware and avoid unnecessary beam loss.

### *4.2.5.4 Digital RF control*

The use of a digital RF feedback and feed-forward system supports automated operation with minimal operator intervention. A number of algorithms can be used to guarantee best field stability (i.e. lowest possible rms amplitude and phase errors), to allow for fast trip recovery, and to support exception handling. Beam-based feed-forward will further

enhance the field stability. Also important is the automated control of the resonance frequency of the cavities with slow motor-controlled tuners and fast piezo actuator or magneto-strictive element **[4-52]** based tuners for Lorentz-force compensation in pulsed RF systems.

The key elements to be used are modern analogue to digital converters (ADCs), digital to analog converters (DACs), as well as for signal processing, powerful Field Programmable Gate-Array (FPGAs) and digital signal processing (DSPs). Low latencies can be realised – from ADC's clock to DAC output ranging from a few 100 ns to several µs depending on the chosen processor and the complexity of the algorithms. Gigabit Links are used for the high data rates between the large number of analogue I/O channels and the digital processor as well as for communication between various signal processing units **[4-53]**. Typical parameters for the ADCs and DACs are a sample rate of 65-125 MHz at 14-bit resolution (example AD6644). For the signal processing one has the choice of FPGAs with several million gates, including many fast multipliers cores and even with a Power PCs on the same chip such as the Virtex2Pro from Xilinx or the Stratix GX from Altera. More complex algorithms are implemented on slower floating point DSPs, such as the C6701 from Texas Instruments or the SHARC DSP from Analog Devices.

**Present status of the LLRF development**

At the vacuum ultraviolet (VUV)-FEL a DSP-based LLRF system has been commissioned and is now operational. This system does not meet all the requirements of the XFEL for achievable field stability, reliability and operability. The amplitude and phase stability achieved at the VUV-FEL are 0.03% (rms), and 0.03° (rms), respectively, which is sufficient for the main linac of the XFEL but not for the RF system in the injector where an improvement of a factor of 2 to 3 is needed. Areas for improvement are the down-converters for field detection **[4-54, 4-55]** (better linearity and lower noise levels), the number of analogue I/O channels, the latency in the controls loop, and the real-time computing power. The system must also be immune to Single Event Upsets (SEU), i.e. a spontaneous bit flip caused by, for example, radiation. Since a major effort will go into the software development it is important to have a prototype of the hardware to support this. This has been achieved with prototype of an FPGA-based digital controller **[4-56]** which has been evaluated recently during operation of the RF gun. With this platform it will be possible to implement and test new algorithms at FLASH (the VUV-FEL). The new hardware allows for higher sampling rates, thus supporting higher IF frequencies resulting in lower noise levels and lower latency. This hardware is already used at the facilities of the TESLA Technology Collaboration partners which will allow the sharing and exchange of LLRF controls software.

### *4.2.5.5 LLRF studies during the XFEL preparation phase*

**Low level RF system performance (simulations)**

LLRF simulation programmes will be developed to study the expected performance of the RF control system. Feedback and feed-forward algorithms, the response to a cavity quench, or beam current variations, and non-linear gain behaviour of the klystron will be simulated in a Matlab/Simulink environment. In a rather generic way, basic blocks are

defined such as cavity, controller and power source. The simulation programme will be used to compare predicted performance with the actually measured performance and to define the control algorithm to be used in the digital feedback system **[4-57]**. Performance studies include operation at different gradients, and operation close to klystron saturation. If possible the cavity simulation will be implemented on a DSP or FPGA-based system to allow real-time simulation. This will provide a basis for testing the feedback system.

### RF system reliability and tunnel installation

The overall XFEL injector and linac reliability and availability are a serious issue. As far as systems are placed inside the linac tunnel, they must be designed in a robust fashion since they are not accessible during operation. The potential for radiation damage is an added risk. Evaluation of trips or failures, what response results, what action is taken and how long it takes, all result in impact on availability. All these failure modes need to be thought through and possible mitigation considered. Smartly designed redundancy such as a simple feed-forward backing up the complex feedback scheme will be essential to guarantee the required availability. Built-in diagnostics for hardware and software will support preventive maintenance and increase reliability **[4-58]**.

### Exception handling for the RF system

There will be a number of exceptions to normal operation that should be handled as rapidly and transparently as possible in order to maximise the FEL operation time. These exceptions include: cavity trips or quenches, beam current variation, klystron trips, RF out of range, etc. Some of these exceptions can be handled at the RF control level, like in the DSP, while others may need coordination from one station to another, or operation interruption through the Machine Protection System. Lists of exceptions will be developed, strategies for dealing with them worked out, and implication hardware and software specified and designed.

### Waveguide tuner control

In the XFEL, up to 32 cavities (one RF station) will be driven by one klystron. Relative phase and amplitude adjustment between cavities will be provided, in part, by 3-stub tuners at each cavity just before the input power coupler. Tuners will be periodically adjusted by stepping motors based on information gathered by the LLRF system. Conceptual and detailed procedures and control algorithms will be worked out and implemented in hardware and software, with interfaces to LLRF.

### LLRF Finite State Machine server and applications

The goal for the FEL control system is the fully automated operation of the large number of sub-systems. One of the most complex sub-systems is the RF control system. The automation will be implemented in the framework of a Finite State Machine (FSM) which is a well established industrial standard. The FSM concept has been integrated into the control system DOOCS used at the TTF/VUV-FEL to simplify the automation of the accelerator operation. For the XFEL the first step will be the definition of the super-states, sub-states, flows, entry-, during-, and exit-procedures, entry-conditions, timer and event triggered procedures, etc. The next step is the description of the applications to be used

by the FSM. Then the full functionality will be implemented as an FSM server in DOOCS, and the required application programmes will be developed. The basic functions of automation include, for example:

- RF system start-up;
- the setting of the RF system parameters needed for beam operation;
- beam loading compensation;
- cavity detuning;
- adjustment of loaded Q and incident wave;
- exception handling;
- performance optimisation.

### LLRF servers

The LLRF that drives each klystron will be controlled by a FPGA and DSP-based real-time feedback system. The digital signal processing electronics in turn must get their parameters from the LLRF server **[4-59]**. The server software handles: generation of set point and feed-forward tables from basic settings, rotation matrices for I and Q of each cavity, loop phase constant, start-up configuration files, feedback parameters, and exception handler control parameters. Server software and interface to the DSPs and control system need detailed specification and code generation. Other servers relate to local reference oscillators (LO)-generation, RF system calibration, waveguide tuner control, cavity resonance frequency control, the ADC server for measurement of probe, forward and reflected power, and hardware and software diagnostics.

### Local oscillator signal generation

Each RF station will have LO for both basic RF 1.3 GHz frequency generation and for driving the system that supplies down-conversion of the RF monitor signals and sampling gates that produce the I and Q components of the monitored signals. Prototypes have been built but more accurate systems are possible. Investigation and development of better systems for phase-noise and phase drifts are needed.

### Radiation effects on electronics installed in the XFEL linac tunnel

Due to dark currents (from possible field emission in the accelerator cavities) there will be a background radiation (gammas and neutrons) in the XFEL linac tunnel. It is expected that dark current of several microamperes can reach an energy of about 100 MeV before being dumped in the beamline. Similar radiation background can be measured at the positron converter at the Linac II/DESY. This offers the possibility of studying single event effects and total ionising dose effects in electronics similar to the one installed in the XFEL linac tunnel **[4-60, 4-61]**. The main objective is to perform a test which allows learning what type of problems might occur in the XFEL linac tunnel and what shielding and hardware and software design measures can be taken to guarantee reliable performance of the electronics.

### Piezo tuner control

As mentioned already, adaptive feed-forward to control Lorentz-force detuning can be used. Detailed studies at the TTF/FLASH will evaluate the potential for control of the Lorentz-force detuning as well as the control of microphonics.

### Klystron linearisation

Increasing the electron beam energy to more than 20 GeV requires a maximum efficiency of the XFEL linac. The 10 MW klystrons must be operated close to saturation. Due to the non-linearity of the klystron this will lead to a strong dependency of the feedback gain on the klystron output power. A possible solution is the linearisation of the klystron with digital methods such as look-up tables or polynomials. It is desirable to develop an on-line mapping method to correct for klystron ageing. The mapping must be time variable due to the time-varying high voltage during the pulse. The linearisation should work over a large range of high voltage settings.

### Gradient and phase calibration based on beam-induced transients

In order to optimise the LLRF system the transient of a single bunch (1 nC) should be measured **[4-62, 4-63]** with a precision of a few percent. This means that the beam phase can be determined within a few degrees, and the gradient calibration within a few percent. Accuracy can be increased by averaging over many bunches. Lock-in techniques will be studied for further signal noise improvement.

## 4.3 Injector

### 4.3.1 General layout

The injector consists of an RF gun, a standard accelerating module and a diagnostic section. The whole setup is located in the injector tunnel, which is separated from the main linac tunnel by the access shaft XSE. The shielding and personal protection system of the injector tunnel and the integration of a beam dump at the end of the injector, allow the operation of the injector independently of the main linac. The injector building comprises two injector tunnels of which, only one will be equipped with an injector in the beginning. The second tunnel can be used to install a second, redundant injector, or may be used to install a different injector type if, for example, special machine parameters are requested for other operation modes at a later time. Shielding as well as cryogenic supply allow for installation and maintenance work in one injector tunnel while the other injector and the main linac are in operation.

The injector building contains (besides the two injector tunnels) rooms for the installation of the photocathode drive laser, electronic equipment, klystrons, etc. Components are as far as possible installed outside the injector tunnel and are hence, accessible during operation.

From the beam dynamics point of view, the XFEL injector follows in its design the VUV-FEL injector design **[4-64]**. The electron bunch is emitted by a $Cs_2Te$ cathode illuminated by a UV laser pulse in a high accelerating field (60 MV/m on the cathode, corresponding

to 30 MV/m average gradient in the gun cavity) and accelerated up to 6.6 MeV in the normal conducting 1.3 GHz RF gun cavity. The gun cavity is about 0.25 m long (one and a half cells) and is powered by a standard 10 MW klystron. A solenoid, centred 0.4 m downstream of the cathode, focuses the beam into the first accelerator module which is located after a 3 m long drift. Even without a bucking coil the solenoid field on the cathode is negligible. The accelerator module increases the energy to about 120 MeV. The accelerating section is followed by a diagnostics section, consisting of a four-screen transverse emittance measurement section and a dispersive section before the beam dump for energy and energy spread measurements. More details of the injector design can be found in **[4-65]** and **[4-66]**.

Table 4.3.1 summarises the main parameters of the XFEL injector:

| | | |
|---|---|---|
| Charge | 1 | nC |
| Laser pulse length (total) | 20 | ps |
| Laser pulse rise/fall time | 2 | ps |
| Laser spot radius | 1.1 | mm |
| Peak electric field on the cathode | 60 | MV/m |
| Solenoid centre position (with respect to cathode) | 0.41 | m |
| Solenoid peak field | 0.19 | T |
| Accelerator module: | | |
| Gradient cavities 1 - 4 | 7.5 | MV/m |
| Gradient cavities 5 - 8 | 25 | MV/m |

***Table 4.3.1*** *Main XFEL injector parameters.*

Figure 4.3.1 shows the expected evolution of the transverse emittance along the injector with the parameters of Table 4.3.1. The initial kinetic energy of the electrons at the cathode is assumed to be 0.55 eV in this simulation. The final projected emittance is 0.88 mrad mm.

Measurements at the Photo-Injector Test Stand in Zeuthen (PITZ) gun test facility **[4-67, 4-68]** indicate that the kinetic energy of the photoemitted electrons is larger than previously assumed leading to a larger initial emittance. This can be largely compensated for by reducing the initial spot size and re-optimising the focusing parameters into the accelerating module. Figure 4.3.2 shows the final projected emittance of the electron beam after re-optimisation for different initial kinetic energies. The final emittance stays below the design value of 1 mrad mm for kinetic energies below 1 eV.

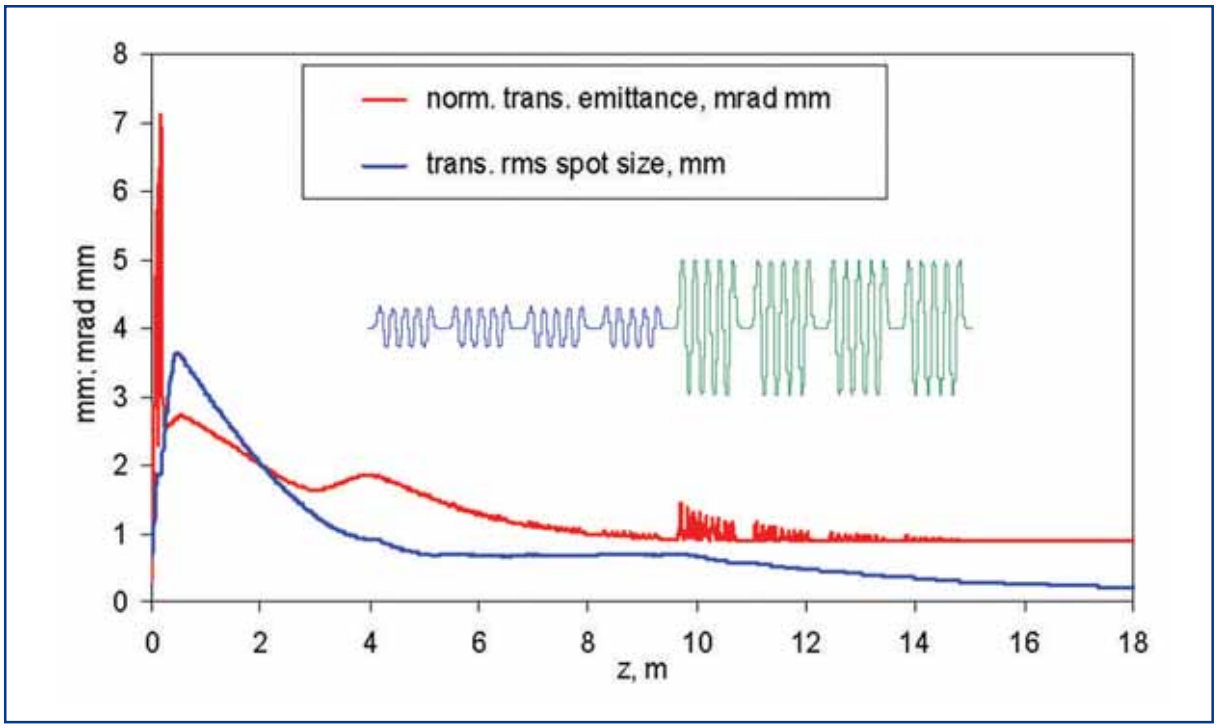


***Figure 4.3.1*** *Evolution of the spot size and the normalised transverse emittance in the XFEL injector. The position and strength of the accelerating field of the superconducting module is also indicated.*

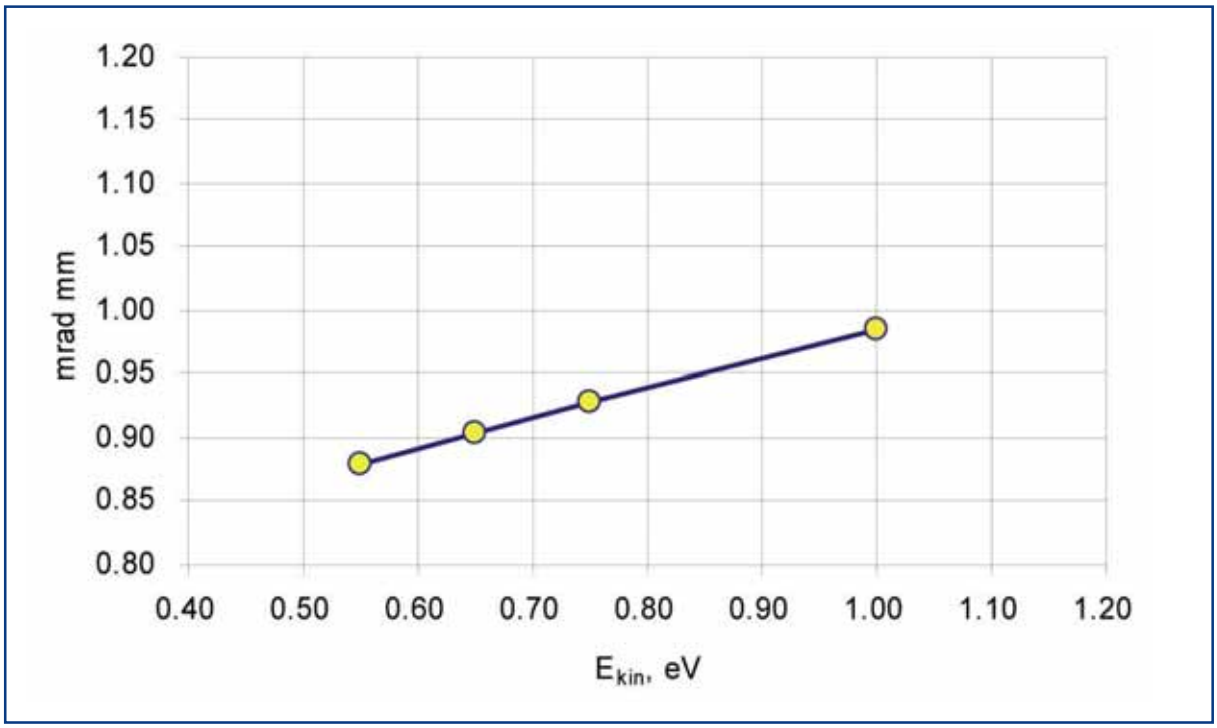


***Figure 4.3.2*** *Final normalised transverse emittance as function of the initial kinetic energy of the photo emitted electrons. A significant increase of the emittance can be avoided by reducing the initial spot size and re-optimising the matching conditions into the accelerator module.*

### 4.3.2 Experimental status and future developments

Transverse core emittance measurements at the photo injector test stand PITZ and at the VUV-FEL yield values of 1.4 mrad mm and below **[4-69 - 4-71]**. The measurements at PITZ are performed directly behind the RF gun cavity at an energy of about 4.5 MeV. The photocathode laser beam is shaped transversely (uniform, circular distribution on the cathode) and longitudinally (trapezoidal, 20 ps length, 4 ps rise/fall time). At the VUV-FEL (FLASH) the optimal longitudinal laser pulse form is not available yet, but the acceleration in the first module improves the emittance compensation mechanism, so that similar emittance values are achieved. Measurements at the VUV-FEL are performed at ~125 MeV beam energy and the photocathode laser beam has a longitudinally Gaussian shape of 4.5 ps rms width. The measurement results of the beam emittance and other beam parameters obtained at PITZ and the VUV-FEL correspond with simulation results and the beam dynamics in the gun and the injector are well understood.

While the measured core emittance values already reach the design slice emittance values for the XFEL at the entrance of the undulator, the design value for the injector has a tighter specification to operate with a sufficient safety margin. To realise the required improvement of the performance, the gradient in the gun cavity has to be increased from the present 42-45 MV/m to 60 MV/m. Additionally, the rise/fall time of the trapezoidal laser pulse should be decreased to 2 ps or below. The development efforts at the test stand PITZ will, hence, focus on these topics in the upcoming years. Other developments concentrate on further improvements in the high duty cycle operation, general stability issues, reduction of dark current and further investigations of the thermal emittance of photocathodes.

### 4.3.3 Photocathode laser

The photocathode laser is based on the laser developed for TTF **[4-72]** and its upgrade for the VUV-FEL **[4-73]**. The laser has been in operation since 1998 providing beam for the TTF linac. Further development of the laser system is continued at PITZ, where new ideas, especially the generation of flat-top laser pulses are studied **[4-74]**. In the present configuration, the laser is based on a diode pumped pulse train oscillator (PTO). The oscillator is synchronised with the master RF. The pulse train generated by the PTO is longer and has a shorter intra-pulse distance than the required electron bunch train structure (27 MHz at the VUV-FEL). A Pockels cell-based pulse picker picks out the required pulse train which is then amplified by a chain of diode-pumped amplifiers. The pulse picker not only gives flexibility in choosing the pulse train structure, it also serves as a fast switch-off mechanism for the MPS. Since the preferred photocathode material $Cs_2Te$ requires radiation in the UV, the infrared light of the laser is quadrupled in frequency by non-linear crystals to 262 nm. The good quantum efficiency of the photocathode (in the order of a few percent) translates into a required laser pulse energy of a few µJ per pulse for a charge of 1 nC. The formation of synchronised picosecond pulses in the PTO is accomplished by an active mode-locking scheme. The key part is an electro-optic phase modulator driven by the 1.3 GHz frequency of the accelerator. It provides a phase stability of the laser pulse in respect to the master RF of less than 0.1°

or 200 fs (rms). This has been confirmed by measurements of the electron beam arrival-time after acceleration at the VUV-FEL **[4-75]**. The shot-to-shot stability in energy of the laser pulses and thus, the electron bunch charge, is 2% (rms) for single pulses and 1% (rms) averaged over a pulse train **[4-64]**. The generation of flat-top laser pulses both in the transverse and longitudinal plane is being successfully tested at PITZ **[4-74]**. Operation of such a system is foreseen at the VUV (FLASH-FEL) in the near future.

## 4.4 The bunch compressor system and start-to-end simulations

### 4.4.1 Introduction and layout

The layout of the bunch compression system **[4-76]** is sketched in Figure 4.4.1. The initially 2 mm (rms) long bunch is compressed in two magnetic chicanes by factors of 20 and five, respectively, to achieve a peak current of 5 kA. The optics of the beamline between the chicanes is optimised to reduce projected emittance growth **[4-77]**. Details about the chicanes proper can be found in **[4-78]**.

The energy chirp injected by running off-crest in the RF upstream of the first chicane is about 10 MeV, roughly compensating the energy contribution by the longitudinal wake fields of all main linac RF structures.

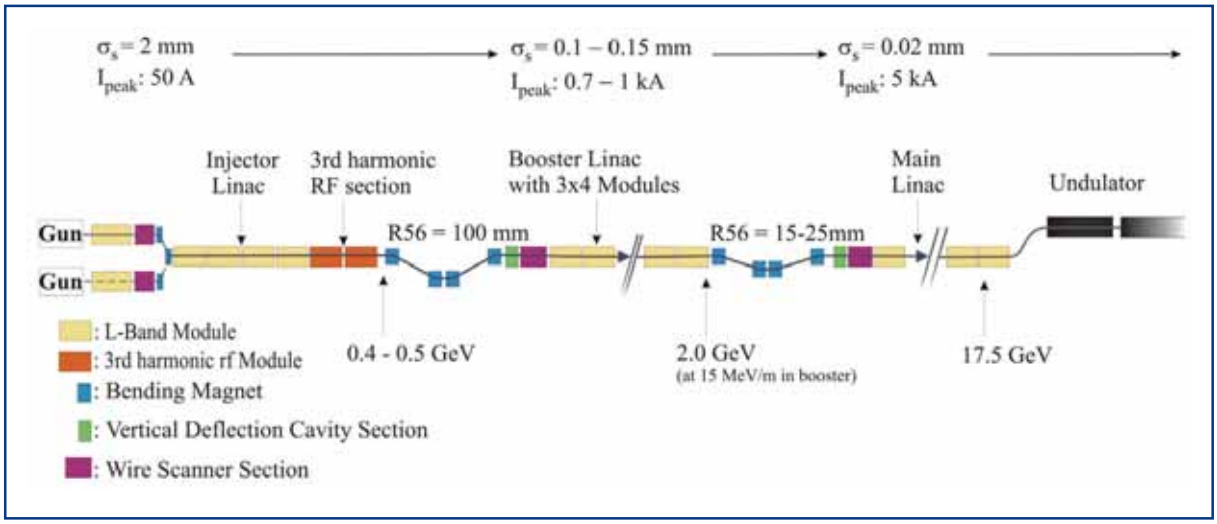


***Figure 4.4.1*** *Sketch of the XFEL bunch compression system.*

A third harmonic RF system is used to optimise the final longitudinal charge distribution **[4-79, 4-80]**. The minimum amplitude is about 90 MeV, corresponding to 16 third-harmonic cavities being operated in one module at 17 MV/m. With a second module, operation at RF working points with much less sensitivity to RF phase jitter becomes possible **[4-81]**.

Downstream of both chicanes, slice emittance and other parameters which vary along the longitudinal position in the bunch can be measured with vertically deflecting RF systems and wire scanner sections allow control of projected emittance and optics. Basic parameters for the bunch compression system are summarised in Table 4.4.1.

| | | |
|---|---|---|
| Beam energy at first chicane | 0.4 … 0.5 | GeV |
| Beam energy at second chicane | 2 | GeV |
| Longitudinal dispersion (R56) of first chicane | ~ -100 | mm |
| R56 of second chicane | -15 … -25 | mm |
| R56 of collimation section | 0.84 | mm |
| Nominal compression factor of first chicane | 20 | |
| Nominal compression factor of second chicane | 5 | |

***Table 4.4.1*** *Parameters for the bunch compression system.*

In the next chapter, results of simulation calculations including coherent synchrotron radiation (CSR) effects, space charge forces and the impact of wake fields are presented. They show the potential of the XFEL for further improvement or, respectively, its safety margin for operation at design values. Operation beyond the design parameters is discussed in two directions: achieving the uppermost number of photons in a single pulse on one hand and reaching the necessary peak current for lasing with a pulse as short as possible with possibly improved transverse emittance on the other.

## 4.4.2 Space charge and coherent synchrotron radiation effects

### *4.4.2.1 Transverse space charge effects*

In low-emittance, high-current electron beams, space charge forces can cause growth of slice emittance and mismatch of slice Twiss parameters, with respect to the design (zero current) optics. Slice emittance growth directly degrades the performance of the SASE-FEL. The generated mismatch complicates accelerator operations because of projected emittance increase and the dependence of transverse dynamics on beam current. Extensive numerical studies were done using the TrackFMN code **[4-82]** and cross-checked with other codes (ASTRA **[4-83]**, CSRtrack **[4-84]**).

With the second compression stage at 2 GeV beam energy and optimised optics in the beamline sections downstream of the compressor chicane, the slice emittance growth (at design parameters) due to transverse space charge is less than 1%. The optical mismatch downstream of the first chicane corresponds to a beating of the $\beta$-function of about 5% if the bunch charge would change by 10%, and less than 1% downstream of the second chicane.

### *4.4.2.2 Coherent synchrotron radiation effects*

The impact of CSR fields on beam emittance in the compressor chicanes was calculated with the code CSRtrack. The left side of Figure 4.4.2 shows the normalised horizontal emittance at the end of the compression system, if the peak current is raised by increasing the bending magnet strength in the second compressor chicane. In the right plot, the bunch charge is lowered and the longitudinal dispersion (R56) of the second chicane increased to keep the 5 kA peak current at the bunch compressor exit. Operating the XFEL like this has two (potential) rewards: The FEL pulse gets shorter and, with even smaller transverse emittance, lasing at shorter wavelengths might be achievable.

For the simulation, a 1 nC beam distribution at the injector exit is scaled in charge. Down to 0.25 nC the slice emittance growth stays within 5%, sufficiently low to profit from smaller emittance at lower bunch charge. The bunch length is reduced to 5 µm.

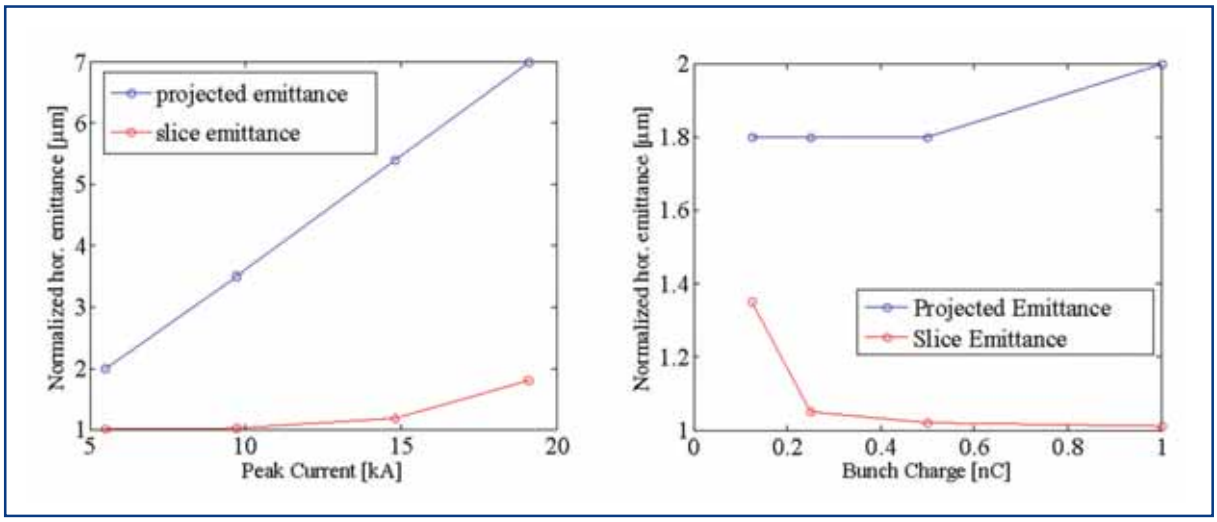


***Figure 4.4.2*** *Normalised horizontal emittance against different peak currents due to different settings of the second bunch compression chicane (left) and against bunch charge for fixed peak current of 5 kA (right).*

### 4.4.3 RF set-up and tolerances

A third harmonic RF system is used to compensate higher order effects of the dispersion and the RF voltage. A procedure to optimise the final longitudinal charge distributions is discussed in **[4-79]**. The amplitudes and phases of the fundamental and the higher harmonic RF system offer four degrees of freedom to adjust the beam energy, the chirp and the second and third derivative of the particle momentum distribution **[4-81]**. The beam energy and the chirp are fixed by the final peak current requirement. Simulations show that only a narrow range of the second derivative settings produces a reasonably symmetric beam profile without spikes.

The third derivative can be adjusted over a wide range without influencing the core of the distribution; it scales mostly with the amplitude of the third harmonic system and can be chosen to optimise RF parameter sensitivities.

Numerical results for a scan of the third derivative are presented in Figure 4.4.3. The amplitude of the fundamental harmonic RF system against the third harmonic RF amplitude is shown as well as sensitivities for the phases and amplitudes of the two RF systems. In the graphs showing sensitivities, the amount of phase or amplitude offset which causes a change of the final peak current by 10% is plotted.

The red curves are calculated for a beam energy of the first chicane of 500 MeV and a compression factor of 20 (and 5 in the second chicane), for the blue curves, the beam energy is 400 MeV and the compression factor 14 (and 7 in the second chicane), to keep space charge forces at the same level.

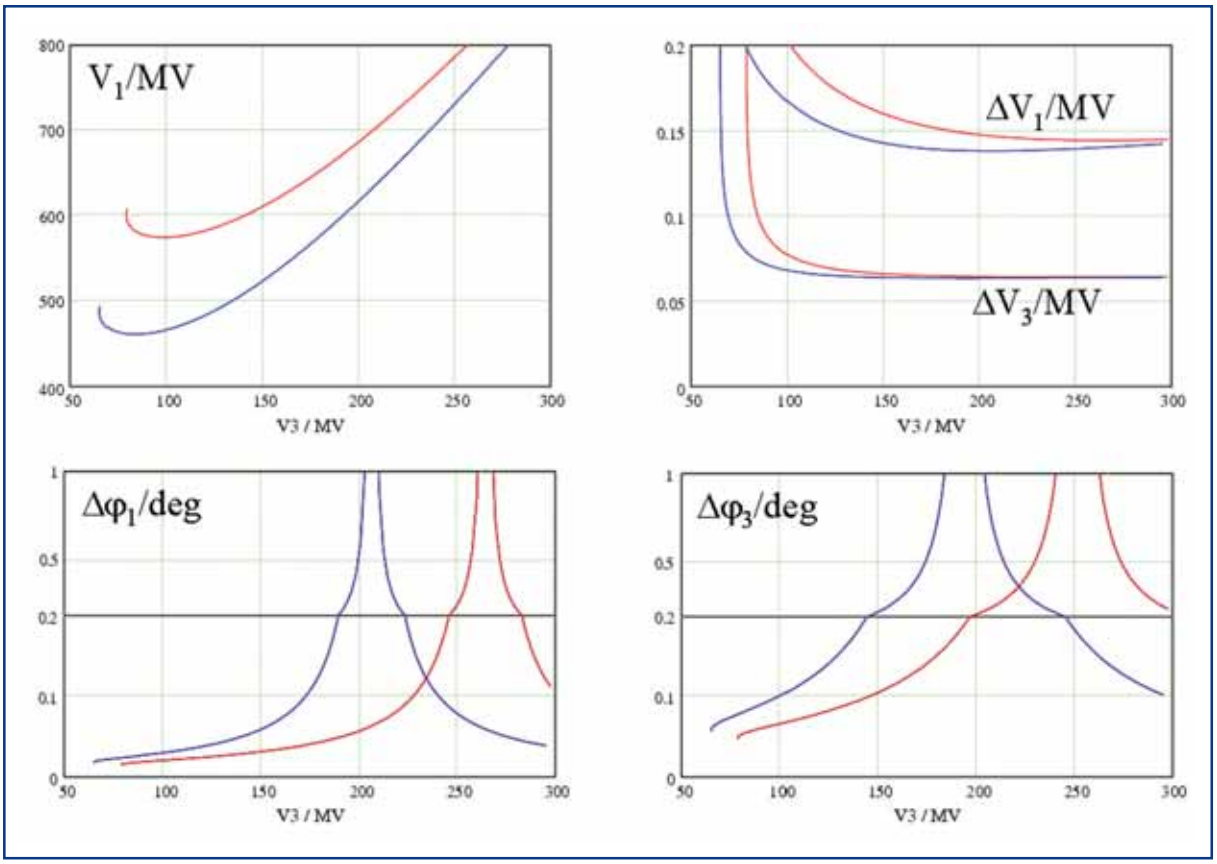


***Figure 4.4.3*** *RF amplitude dependence and amplitude/phase sensitivities for the fundamental mode RF and the third harmonic system. For the red lines, the beam energy at the first chicane is 500 MeV, for the blue ones 400 MeV. The upper left graph shows the amplitude of fundamental harmonic RF system against third harmonic RF amplitude. For the other three graphs, on the vertical axis the amount of phase or amplitude offset which causes a change of the final peak current by 10% is plotted, the horizontal axis shows the amplitude of the third harmonic RF system. Upper right graph: Amplitude sensitivity of both RF systems. Lower left: Phase sensitivity of the fundamental harmonic RF system. Lower right: Phase sensitivity of the third harmonic RF system.*

The phase jitter sensitivity can be reduced by more than an order of magnitude if the third harmonic system is operated with an amplitude of about 200 MV (for the 400 MeV case). At that working point, phase jitter tolerances are of the order of a degree for both RF systems, compared to a few hundredths of a degree for a working point with third harmonic amplitude of about 100 MV. The amplitude jitter tolerances are $3\times10^{-4}$ for the third harmonic RF and $2\times10^{-4}$ for the fundamental mode RF.

At that working point, a cancellation loosens the RF phase jitter tolerances: A change in one of the RF phases causes a change in beam energy and in the induced chirp. The phase jitter sensitivity is reduced if the effectively reduced longitudinal dispersion of the magnet chicane due to the higher beam energy is compensated for by a stronger chirp. An RF system with a single frequency cannot provide this, but for two RF systems such a working point exists.

In general, the relative priorities for peak current and timing stability together with the actual stability of RF amplitudes and phases will determine the RF parameter settings.

### 4.4.4 Instabilities driven by space charge and coherent synchrotron radiation

An initial bunch current ripple can be amplified by the following mechanism: a slight modulation of the initial bunch density profile produces an energy modulation due to longitudinal impedance, caused by CSR and space charge fields. In a bunch compression chicane, the energy modulation creates more density modulation. In a multi-stage bunch compression system, the gain of this amplification can be very high. A limiting factor for this mechanism is the uncorrelated energy spread.

For the calculation of gain curves, a bunch with an initial charge modulation of wavelength $\lambda$ is traced from the gun to the entry of the undulator. The gain is the amplification of the relative modulation amplitude in the simulation.

The gain of the so called 'CSR Instability' was calculated with the 3-D code CSRtrack and found to be < 10 **[4-76]**.

Figure 4.4.4 shows gain curves for the space charge driven instability for different initial random energy spread. The calculated gain at the expected small values for uncorrelated energy spread from the gun (rms < 2 keV) would be sufficient to start amplification from shot noise. With a 'laser heater' **[4-85]** (a magnet chicane approximately two metres long with an undulator magnet which the electron beam traverses together with a laser beam) we can adjust the uncorrelated energy spread between its initial value and up to 40 keV. The initial uncorrelated energy spread must be above 10 keV to limit the modulation of the bunch after the last compressor chicane to less than 1%.

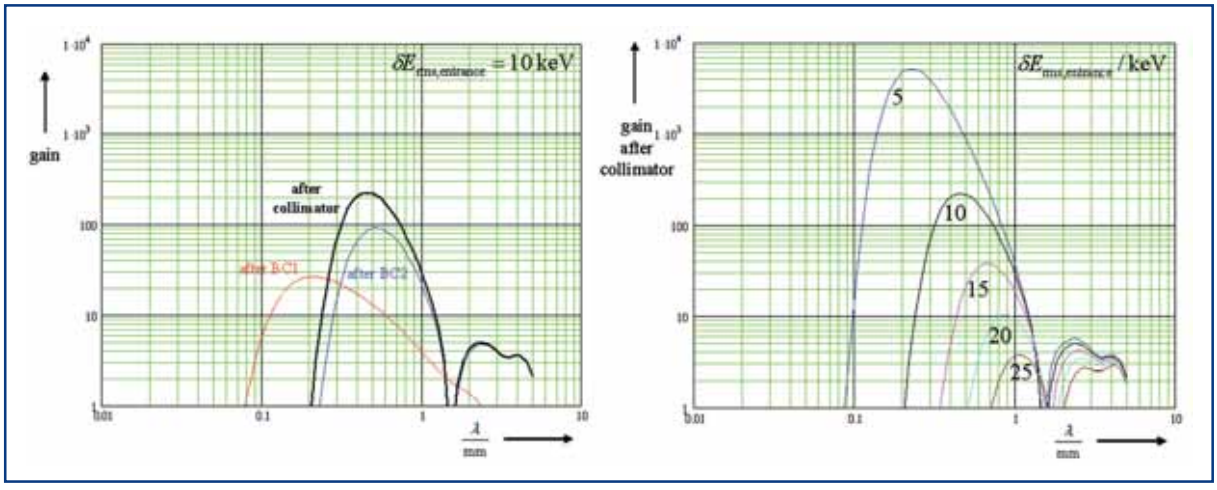


***Figure 4.4.4*** *Gain curves for the space charge driven instability. Left side: Contributions of the sub-sections of the linac for an uncorrelated energy spread of 10 keV. Right side: Overall gain for different uncorrelated energy spreads.*

## 4.4.5 Start-to-end simulation

### *4.4.5.1 Tracking through the accelerator*

In the following we present a start-to-end simulation for the nominal operation parameters. The lattice and the optics were taken directly from the European XFEL reference list **[4-86]**. Parameters for the compression are listed in Table 4.4.2.

| | | |
|---|---|---|
| 1.3 GHz linac phase before first chicane | 1.4 | degree |
| 1.3 GHz linac amplitude before first chicane | 442.85 | MV |
| Third harmonic RF phase | 143.35 | degree |
| Third harmonic RF amplitude | 90.63 | MV |
| Linac phase first chicane to second chicane | 20.0 | degree |
| Linac amplitude first chicane to second chicane | 1596 | MV |
| Longitudinal dispersion (R56) of first chicane | -103.4 | mm |
| R56 of second chicane | -17.6 | mm |

***Table 4.4.2*** *Compression system parameters for start-to-end calculations.*

The beam was traced from the cathode of the RF gun to the entrance of the undulator using different codes in different sections. The straight linac sections are calculated using the space charge code ASTRA if the space charge forces are strong. The impact of weaker space charge forces, for instance in the main linac, are calculated with a semi-analytical model **[4-87]**. The bending sections like chicanes or doglegs are tracked using the 1-D model in the code CSRtrack. Extensive calculations have shown that 3-D calculations yield an only slightly modified result for the nominal parameters. Shielding effects of the CSR fields have been taken into account because they disturb the compensation of projected emittance growth between the two chicanes.

Wake fields for all RF structures are included. The simulation of the SASE process in the next chapter also includes wake field effects.

The beam parameters at the entrance of the undulator are shown in Figure 4.4.5. The peak current is at 5 kA as required and the (normalised) transverse slice emittance in the region where the current is above 2 kA is less than 1 mm-mrad.

The longitudinal phase-space shows that the linear part of the correlated energy spread is approximately zero, as expected. The non-linear kink in the centre of the bunch is generated by space charge forces in the main linac.

The energy spread along the bunch distribution peaks at the centre at 1 MeV, the initial value induced by the laser heater of 10 keV multiplied by the compression factor. The projected emittance is about 1.4 mm-mrad.

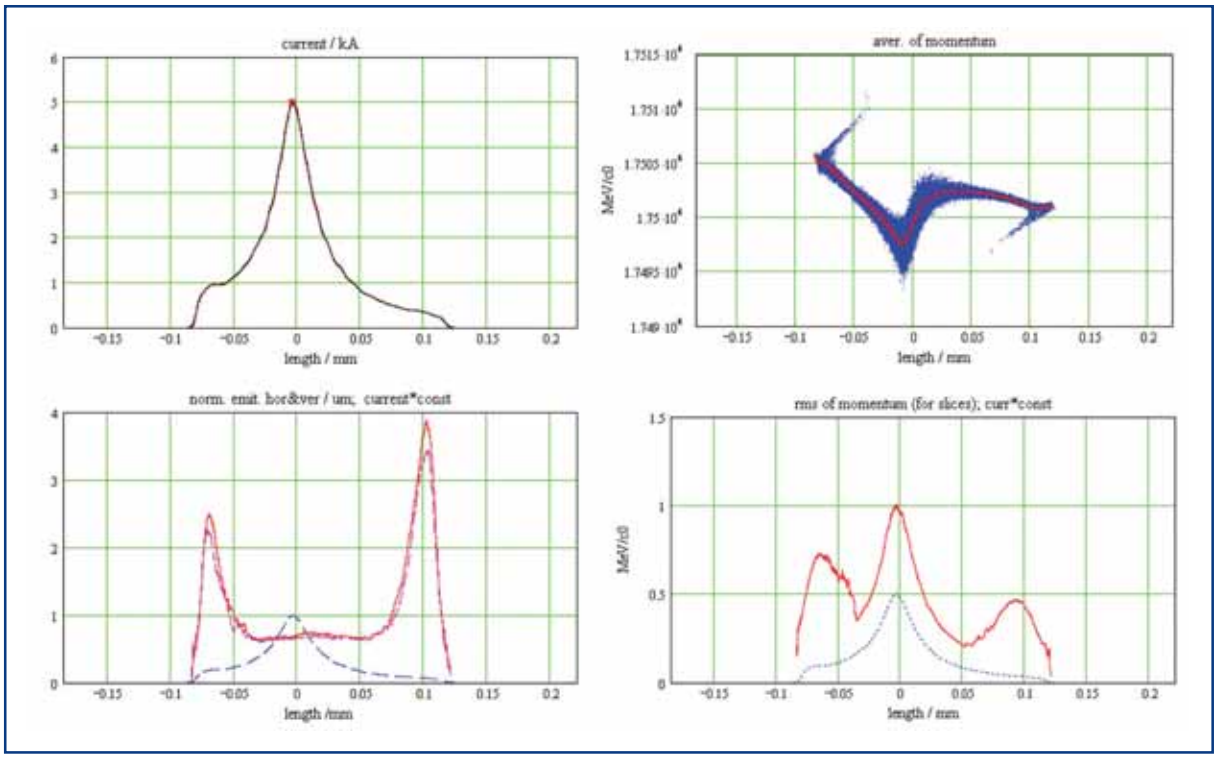


***Figure 4.4.5*** *Beam parameters at the entrance of the SASE undulator.*

### *4.4.5.2 X-Ray FEL Simulations*

**Wake field effects**

For the long undulator, the wake fields in the undulator pipe and intersections have an important effect on the lasing process. The effect of wake fields becomes noticeable as a gain reduction when the variation in energy becomes big compared to the FEL bandwidth, i.e. $\Delta E_{wake}/E > \rho$. In the case of SASE 2, this is true if $\Delta E_{wake} > 41$ keV for a bunch of 1 nC passing through 1 m of the undulator vacuum chamber. This is usually expressed in the notation $\Delta E_{wake} > 41$ keV/(nC m).

There are three major sources of wake fields within the undulator: resistive wall, geometric and surface roughness. Geometrical wake fields arise in variation of the chamber along the undulator. These wake fields were calculated numerically **[4-88]** for the case of elliptical pipe geometry with semi-axes of 3.8 mm and 7.5 mm and for all insertions. The geometric wake for a Gaussian bunch with 25 μm length (rms) introduces an average energy loss of the electrons in the bunch of 12 kV/(nC m), and an energy spread of 4 kV/(nC m).

The resistive wall wake was estimated analytically **[4-90]** for a round pipe with a radius of 3.8 mm. Results for different materials and bunch shapes are shown in Table 4.4.3.

| | | Gaussian bunch Cu/Al | Rectangular bunch Cu/Al |
|---|---|---|---|
| Total energy loss | kV/nC/m | 36/50 | 79/93 |
| Induced energy spread | kV/nC/m | 46/53 | 90/72 |
| Peak energy loss | kV/nC/m | -89/-108 | -256/-243 |

***Table 4.4.3*** *Energy losses due to resistive wall wake field parameters for different bunch shapes.*

Figure 4.4.6 shows the resistive wall (Cu) and geometrical wake potentials and their sum for the bunch in Figure 4.4.5. Surface roughness wake fields **[4-91]** are negligible and are not considered in the SASE FEL simulations presented here.

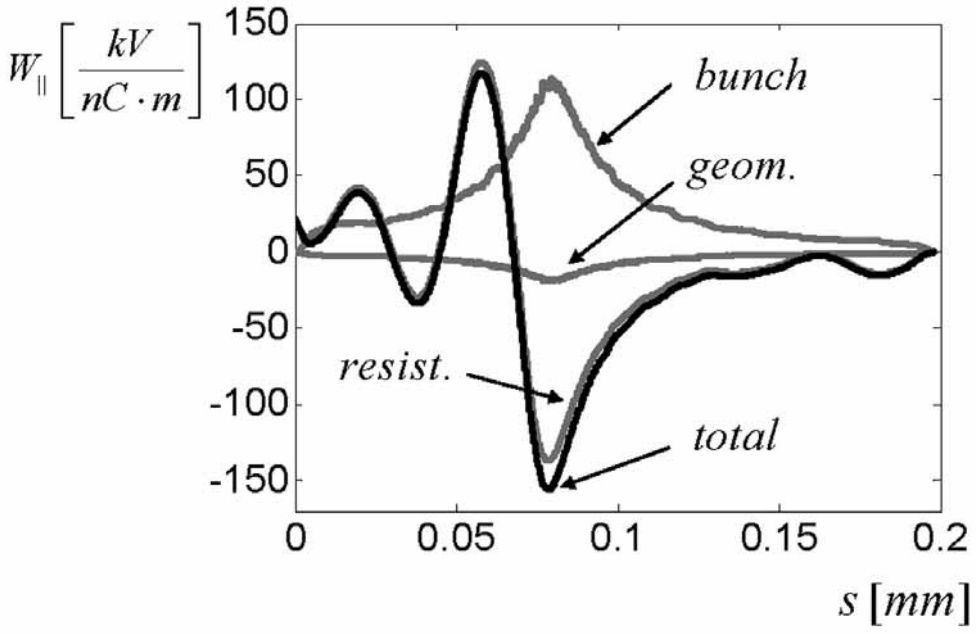


***Figure 4.4.6*** *Energy losses due to resistive wall wake (Cu) and geometrical wake field and their sum.*

### SASE simulations

Figure 4.4.7 and Figure 4.4.8 show the radiation power for the case of the undulator SASE 2, calculated with the code Genesis **[4-92]**. When taking into account wake fields, the peak power is reduced from 80 GW to 50 GW. A linear undulator tapering of the magnet gaps ($\Delta K/K = 4\rho$) compensates the degradation and increases the radiation power up to 90 GW.

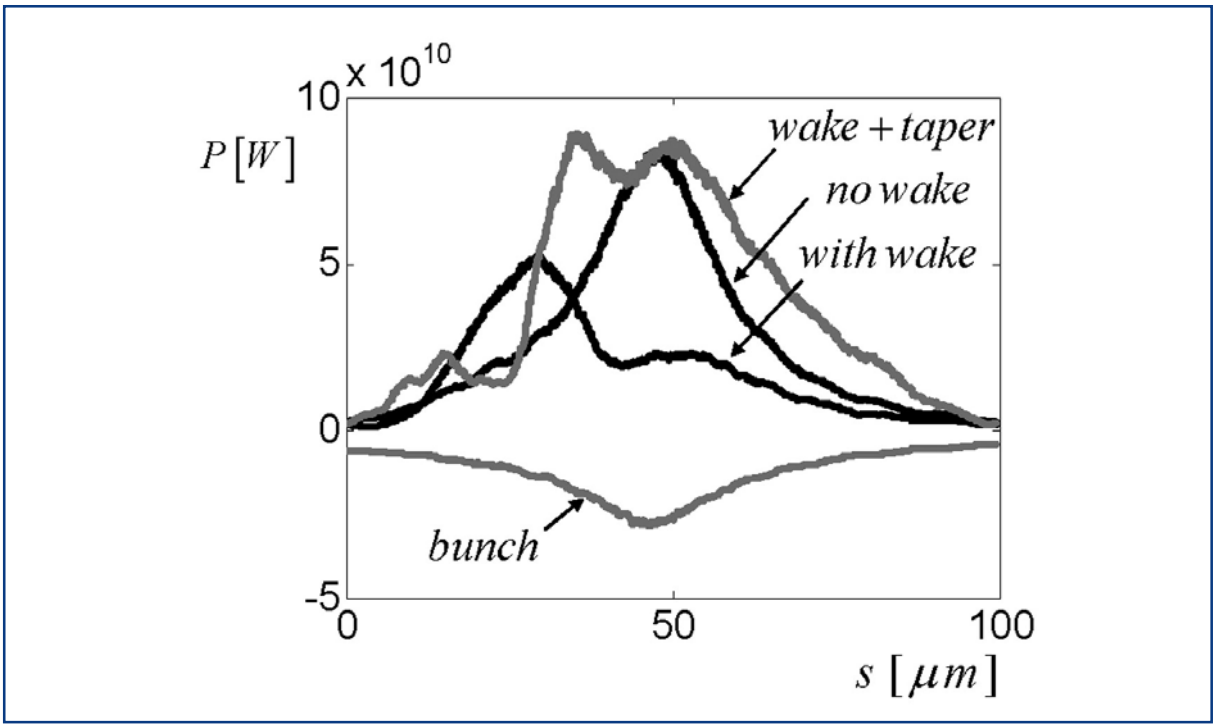


***Figure 4.4.7*** *Radiated power along the pulse at the end of the undulator.*

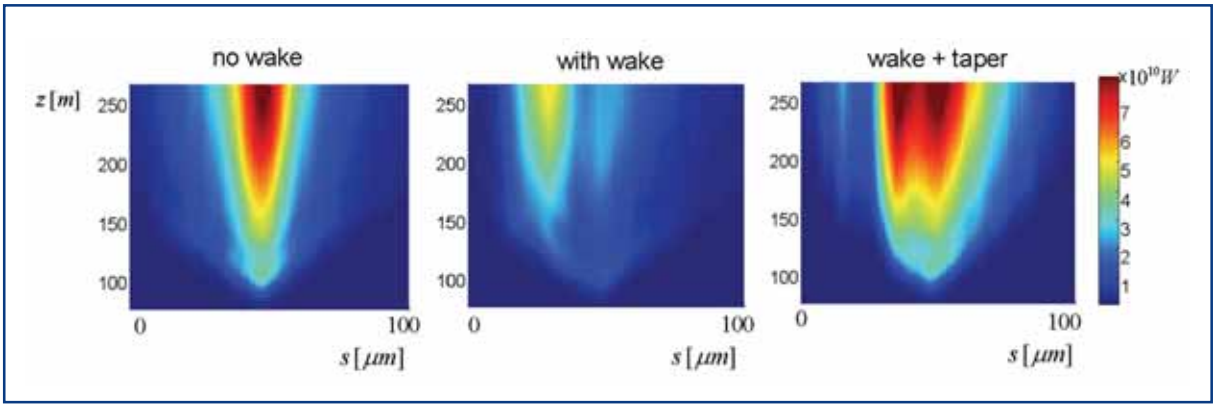


***Figure 4.4.8*** *Evolution of the radiated power pulse along the undulator for the three considered cases.*

The tapering requires an undulator gap variation of 32 μm over 260 m, imposing severe tolerance requirements on the undulator alignment.

## 4.5 Beam optics and dynamics

### 4.5.1 Main linac

The acceleration of the electron beam to the design energy of 20 GeV is performed in the booster linac (0.5-2 GeV) and main linac (2-20 GeV). They are separated by the bunch compression system. The main parameters of the beam at the entrance of each linac are summarised again in Table 4.5.1.

The main linac downstream from the second bunch compression consists of 100 accelerator modules with one quadrupole each forming a FODO cell with 24 m length and a phase advance of 60°. One horizontal or vertical steering magnet per module is foreseen. The booster linac contains six standard FODO cells with average gradient in cavities of about 16 MV/m.

| | | Booster linac | Main linac |
|---|---|---|---|
| Initial energy | GeV | 0.5 | 2 |
| Acceleration gradient | MV/m | 16 | 20.8 |
| Bunch length | μm | 121 | 24 |
| Initial correlated energy spread | % | 1.75 | 0.4 |
| Initial uncorrelated energy spread | % | 0.1 | 0.125 |

***Table 4.5.1*** *Beam parameters at the entrance of booster and main linacs.*

### *4.5.1.1 Single bunch beam dynamics*

The single bunch emittance dilution in linacs is determined by chromatic and transverse wake field effects. In the booster linac these effects are negligible due to the high relative energy gain of the particles compared to their initial energy. The weak wake fields in the superconducting 1.3 GHz accelerating structures and the low chromaticity of the focusing lattice leads to harmless beam dynamics in the main linac as well.

The RF accelerating field and the short range longitudinal wake field leads to an extra negative correlated energy spread (tail particles have lower energy than the head) with rms value of $5\times10^{-4}$ at the end of the main linac. However, the electron bunch has an initial positive correlated energy spread of 0.4% (required for the bunch compression system). This initial energy spread partially cancels the induced correlated energy spread in the main linac, thus, providing an rms relative correlated energy spread at the linac exit (energy 20 GeV) of about $1.2\times10^{-4}$ or absolute rms energy spread of 2.4 MeV (Figure 4.5.1).

The single bunch emittance dilution is mainly caused by the coherent oscillations of the beam due to transverse injection jitter, random cavity tilts and quadrupole misalignments. Cavity and module random misalignments are additional sources of correlated emittance growth due to transverse wake fields exited by off-axis beam trajectory in the accelerating sections. In Table 4.5.2 the rms tolerances to the main linac component misalignments are given.

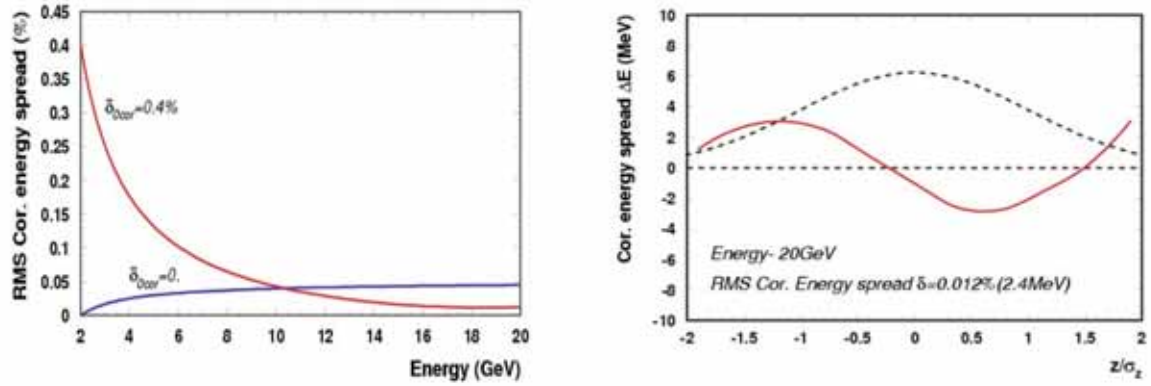


***Figure 4.5.1*** *The rms correlated energy spread along the main linac with (red) and without (blue) initial positive correlated energy spread (left). Absolute correlated energy deviation within the bunch at the linac exit (right).*

| | | |
|---|---|---|
| Injection transverse jitter | 1 σ | |
| Cavity module misalignments | 0.5 | mm |
| Modules Misalignments | 0.5 | mm |
| Correlated 4 modules misalignment | 0.5 | mm |
| Cavity tilts | 0.25 | mrad |
| Quadrupoles module misalignments | 0.5 | mm |
| BPM module misalignments | 0.2 | mm |

***Table 4.5.2*** *Assumed rms misalignment tolerances.*

The left-hand graph in Figure 4.5.2 presents the transverse-wake field caused correlated emittance dilution along the linac for cavity and module misalignments. The results are averaged over 25 random seeds of misalignments and are negligibly small due to weak transverse wake fields in the accelerating sections. In the case of cavity random tilts, the particles experience the transverse Lorenz-force of the accelerating RF field and the beam performs coherent oscillations. The right-hand graph in Figure 4.5.2 presents the correlated and uncorrelated chromatic emittance dilution along the linac caused by the initial energy spread.

The strongest impact of the chromatic effect is observed for a disturbed central trajectory caused by quadrupole misalignments. The steering of the central trajectory is supposed to use one-to-one correction algorithm: the beam trajectory is corrected in each focusing quadrupole to its geometrical axis based on the BPM reading by correction dipole coils incorporated in the previous quadrupole. Figure 4.5.3 presents the disturbed central trajectory of the beam in the main linac for one single random seed of quadrupole misalignment, the corrected trajectory and the resulting uncorrelated and correlated chromatic emittance dilution of the beam.

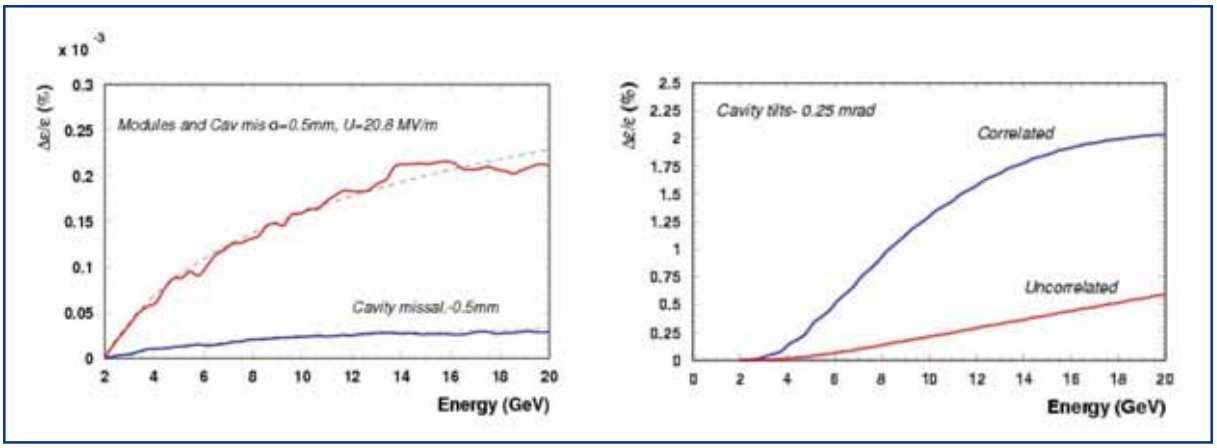


***Figure 4.5.2*** *Wake field caused emittance dilution along the main linac for cavity and modules random misalignments (left). The chromatic emittance dilution along the main linac for cavity random tilts (right).*

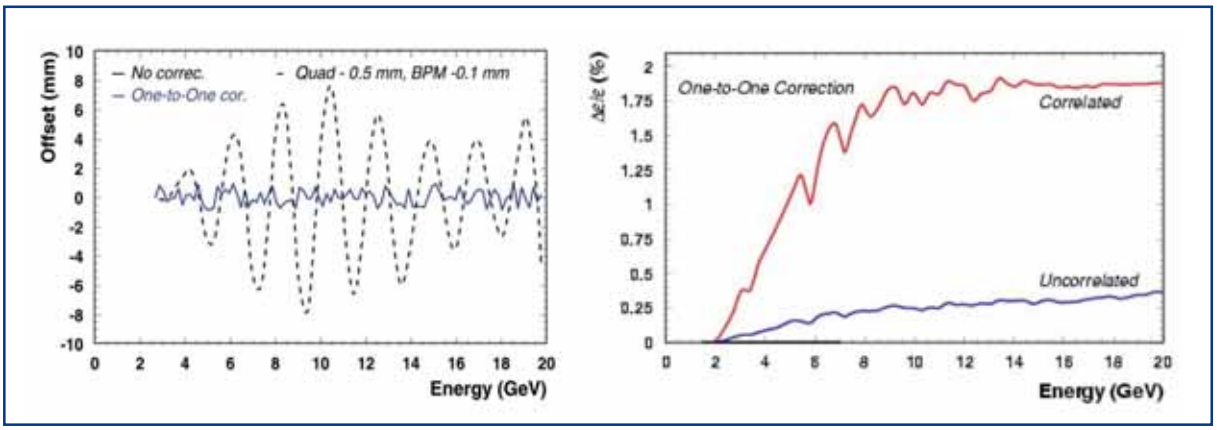


***Figure 4.5.3*** *Coherent betatron oscillation of the beam in the main linac with misaligned quadrupoles and steered trajectory by one-to-one correction algorithm (left). Correlated and uncorrelated emittance dilution along the linac after trajectory steering (right).*

Table 4.5.3 presents the summary of the emittance dilution in the booster and main linac.

| | Booster Linac | Main Linac |
|---|---|---|
| Coherent oscillations | | |
| Uncorrelated | $6\times10^{-6}$ | $2\times10^{-4}$ |
| Correlated | $2\times10^{-3}$ | $1.2\times10^{-3}$ |
| Cavity misalignments | $5\times10^{-6}$ | $3\times10^{-7}$ |
| Modules misalignments | $4\times10^{-5}$ | $2.5\times10^{-6}$ |
| Correlated misalignments (4 modules) | - | $7\times10^{-6}$ |
| Cavity tilt | | |
| Uncorrelated | $5.8\times10^{-5}$ | 0.6% |
| Correlated | 0.6% | 1.9% |
| One-to-one correction | | |
| Uncorrelated | $6.3\times10^{-5}$ | 0.4% |
| Correlated | 1.7% | 2% |
| **Total** | < 3% | < 5% |

***Table 4.5.3*** *Summary of the emittance dilution in booster and main linacs.*

### *4.5.1.2 Multi-bunch beam dynamics*

The effect of the long-range transverse wake field on multiple bunches has been investigated for various cases **[4-93]**. A cavity misalignment of 500 μm rms has been assumed. A typical behaviour of the bunch offset at the end of the linac is shown in Figure 4.5.4. After ≈50 μs a steady state is reached and its value is unchanged as long as the beam trajectory through the linac is unchanged. Moreover, the initial oscillation is largely repetitive and can, thus, be handled by an intra-train feed-forward system.

Figure 4.5.4 shows the average emittance growth along the linac, being only 0.02%, relative to the design slice emittance. The major contribution again comes from the first part of the bunch train. Consequently, the average emittance dilution gets larger for shorter trains, where the steady state is not reached. For high quality beam applications a bunch train of at least 200 bunches should be accelerated, with the first 100 bunches leading to a steady state wake field excitation while the remaining bunches pass the linac almost unperturbed. The unperturbed emittance can be restored by a fast intra-train feed-forward system **[4-94]**.

The longitudinal HOMs lead to an energy spread along the bunch train. As in the transverse case this is strongest for the first part of the bunch train (5.15 MeV rms for a 20 μs bunch train) while the rms energy spread over the whole train is 0.88 MeV. This variation again is repetitive and should be compensated for by the low-level RF system.

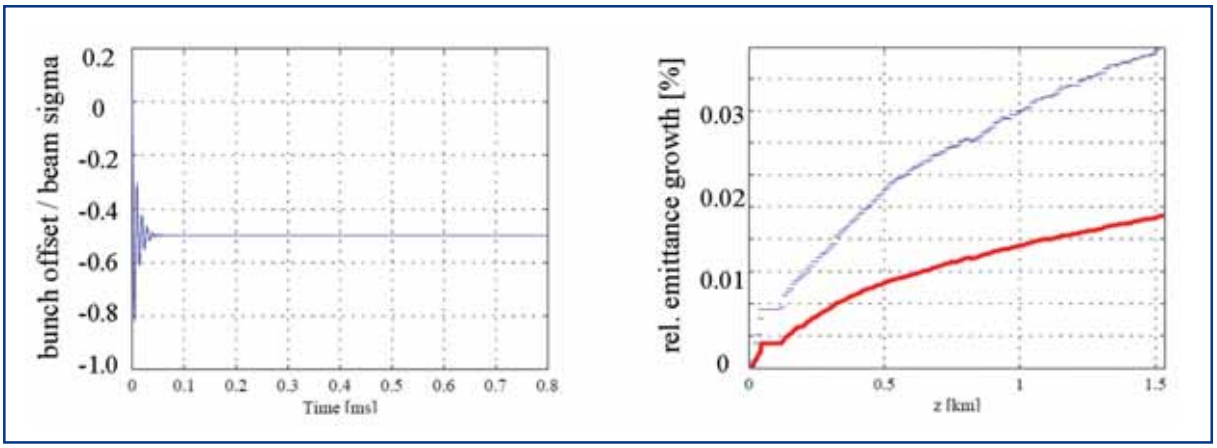


***Figure 4.5.4*** *Simulation results for 20 GeV final energy, 200 ns bunch spacing and 4,000 bunches/train. Left: Bunch offset along a bunch-train. Right: Emittance growth along the linac (red line: average over 100 random seeds, blue line: maximum of standard deviation).*

### 4.5.2 Post-linac collimation

The collimation system simultaneously fulfils several different requirements:

- during routine operation, off-momentum and large amplitude halo particles are removed with high efficiency;
- in case of machine failures, downstream equipment and undulators are protected against mis-steered and off-energy beams, without destroying the collimators in the process;
- the energy acceptance is an important requirement for the optical design of the collimation system. The collimation section is able to accept bunches with different energies (up to ±1.5% from nominal energy) and transport them without any noticeable deterioration.

Figure 4.5.5 shows the optical functions of the post-linac collimation lattice. The system consists of two arcs separated by a phase shifter. It has a dogleg shape. The arcs are identical and each one constitutes a second-order achromat. The collimation section includes matching modules to adapt the optic to the desired upstream and downstream beam behaviour.

The collimation system utilises a spoiler-absorber scheme and is designed as passive, i.e. without an integrated fast emergency extraction system, fast sweeping system or fast beam enlarging system. The spoilers must be able to withstand a direct impact of about 80-100 bunches until a failure is detected and the beam production in the RF gun is switched off. In order to find the minimum tolerable beam-spot size at which a spoiler made from Titanium alloy will survive even in the worst, but theoretically still possible, case when all these bunches will hit it exactly at the same point, the interaction of a bunch with a spoiler was investigated using the EGS4 code. The simulation results show that it is sufficient to have both beta functions above approximately 250 m at the spoiler locations, assuming a normalised emittance of 1.4 μm, beam energy of 20 GeV and bunch charge of 1 nC.

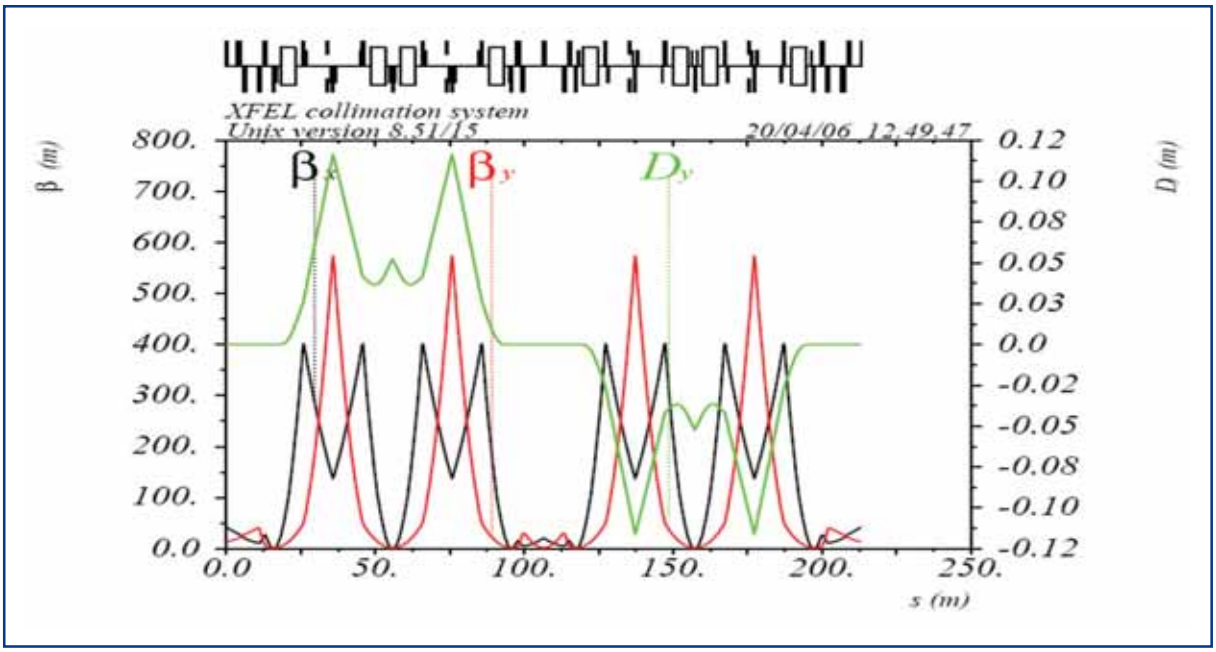


***Figure 4.5.5*** *Optical functions of the collimation system including upstream and downstream matching sections.*

Four spoilers will be used in total, two in each arc. The first arc collimates transverse positions of incoming particles and the second, after a shift of horizontal and vertical phases by 270°, their transverse momenta. The energy collimation and the vertical plane collimation will be done simultaneously, and therefore, the ratio of dispersion to vertical betatron function at spoiler locations is properly adjusted. Collimators are chosen to have circular inner apertures (conical tapered collimators). Analytical and numerical studies have shown that spoilers with inner radii of about 3.8 mm will be able to protect the undulator vacuum chamber (at current stage, assuming that downstream beam transport is linear) and also stop all particles with an energy offset larger than ±3.5%. An example of such investigations is shown in Figure 4.5.6. The initial distribution of the incoming particles was modelled by mono-energetic 4-D slices, with a transverse extension over the radius of the vacuum chamber at the collimator section entrance (the maximum values for transverse momenta were chosen so as to fully populate the acceptance of the transport line). The results are presented as a function of the energy deviation.

The effect of energy offsets, optics nonlinearities and incoming beam mismatches on the evolution of the beam-spot size along the collimation section can be seen in Figure 4.5.7. Simulations show that all particles with transverse offset larger than ≈80 σ (at energy 20 GeV) will be collimated by touching one of the spoilers. All particles with transverse offset smaller than ≈23 σ will pass through the collimation section freely. Some particles with offsets between 23 to 80 Ã are absorbed in the vacuum system of the collimation section.

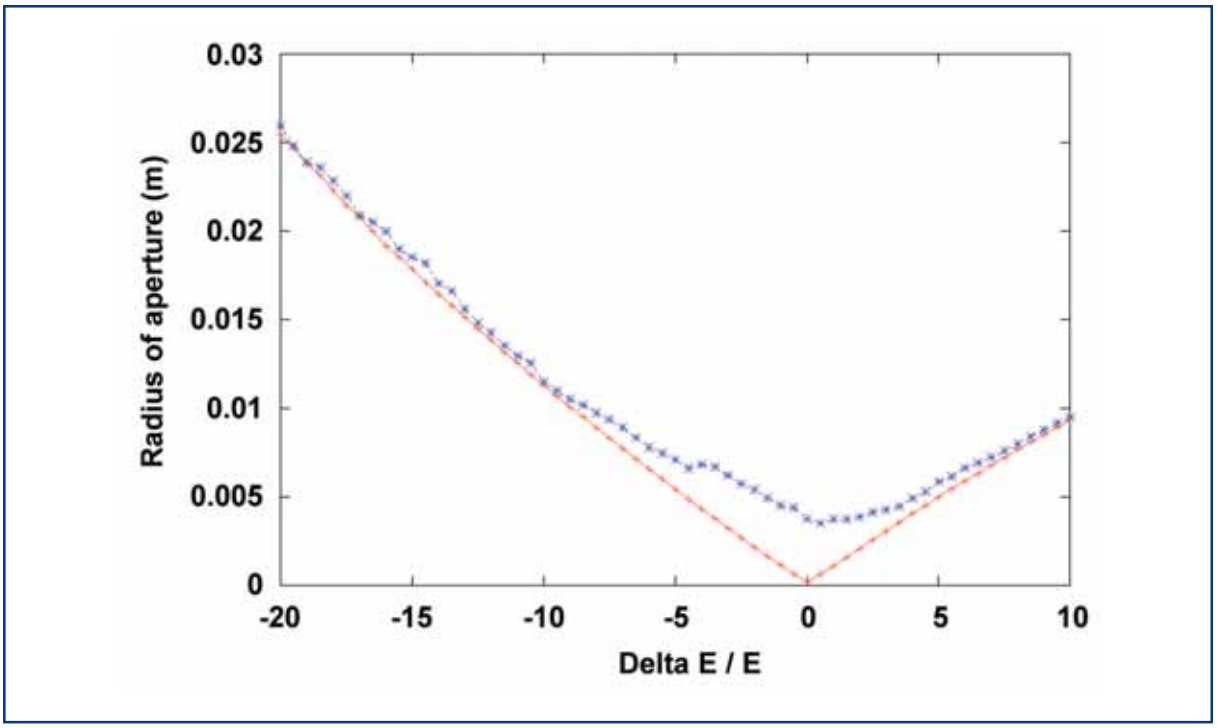


***Figure 4.5.6*** *Blue curve: Aperture radius required to protect the undulator vacuum chamber as a function of the energy deviation. Red curve: Aperture radius required to block the corresponding off-energy fraction of incoming particles in the collimation section.*

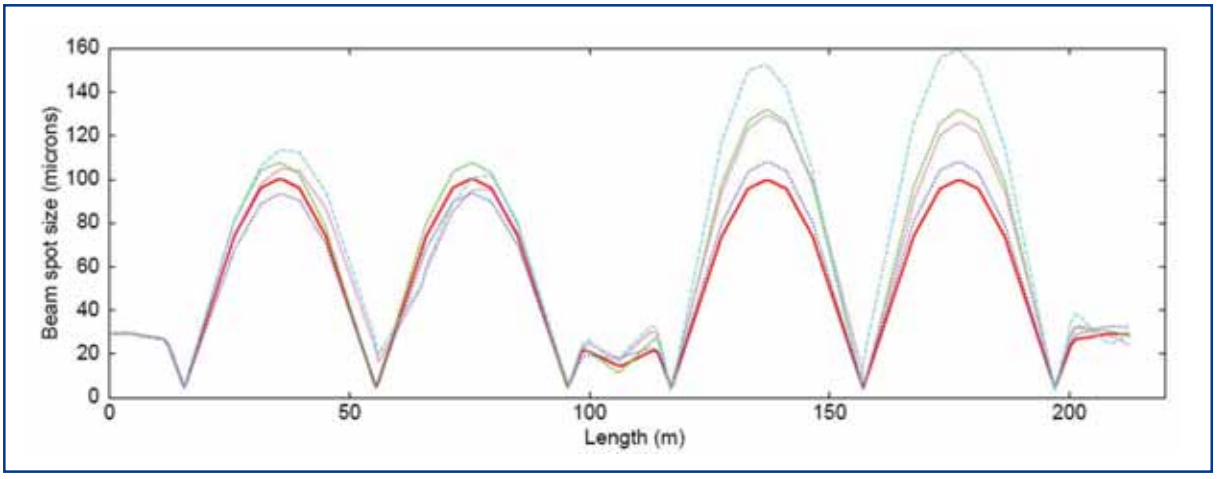


***Figure 4.5.7*** *Evolution of beam-spot size (rms value) along the collimation section. Red curve shows the design spot size (linear theory). All other curves are results extracted from the tracking simulations. A matched Gaussian beam at the entrance with -3% (green) and +3% (blue) energy offsets, with 40 $\sigma$ y-offset (magenta), and with both -3% energy and 40 $\sigma$ y-offsets (light-blue).*

## 4.5.3 Beam distribution and undulators

### *4.5.3.1 Beam distribution*

Operational flexibility for each user is reached by a flexible beam distribution system. This system will allow complete and independent control over the bunch pattern for each electron beamline. The key components of this system are a very stable flat-top kicker for beam distribution into the undulator beamlines and a fast single bunch kicker to kick individual bunches into the beam dump before the beam distribution.

During one pulse, the beam is switched once between the two beamlines by means of the flat-top kicker. While the kicker field is being ramped up, the beam is aborted in the beam dump before the beam distribution with the help of the fast single bunch kicker. Individual bunch patterns are created by aborting 'unwanted' bunches in the beam dump. The beam extraction is realised with a kicker/septum layout, thus reducing the required kick strength for the kicker.

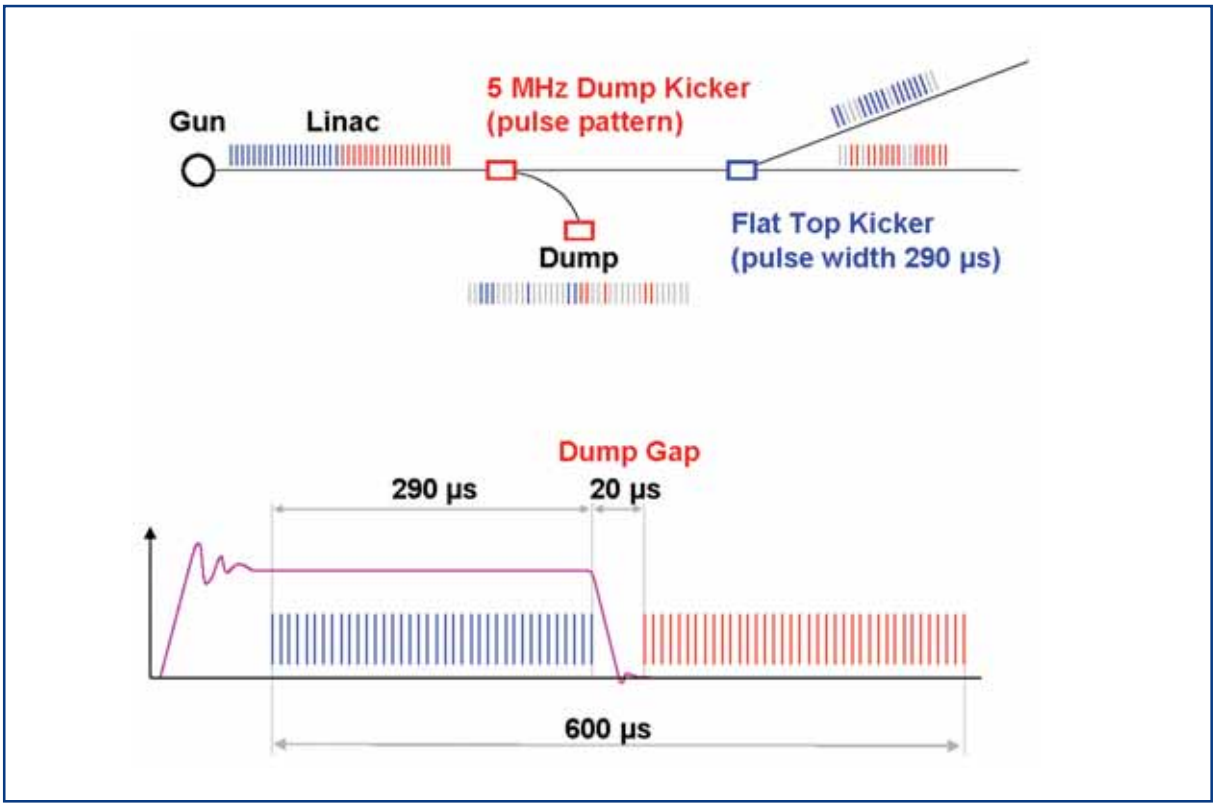


***Figure 4.5.8*** *Beam distribution concept: The linac is operated with a constant beam distribution. Bunches are distributed into the beamlines with a flat-top kicker once per pulse. During the ramp up of this kicker (dump gap is extended in this plot for better visibility) the bunches are aborted in the beam dump, as well as other unwanted bunches out of the train.*

The betatron function in the septum is limited by incoherent synchrotron radiation emittance growth to about 40 m (approximately the same as in the undulator). The upstream collimation protects a downstream aperture of larger than 4.5 mm at this betatron function. Thus, the kicked amplitude at a septum (with 5 mm septum width) is

15 mm, yielding a maximum kicker field of 0.375 mrad or 31 mT×m at 25 GeV. Downstream trajectory stability requirements (< 0.1 $\sigma$) lead to very tight relative amplitude and residual ripple requirements of $5\times10^{-5}$.

The bending sections leading to the five downstream undulators are designed as double-bend achromats with total bending angles between 1.3 and 2.5°. For phase two a deflection of $\approx$ 6.6° is required, which is realised with a triple-bend achromat with dipoles of twice the length. In all bending sections, sextupoles and octupoles provide higher order dispersion correction.

#### *4.5.3.2 Undulator optics*

The electron beam optics in the undulator consist of a simple FODO lattice with a cell length of 12.2 m. The average beta-function in the undulators should be variable between 15 to 45 m, yielding a phase advance between 50 and 15°. The corresponding inverse focal length ranges from 0.12 to 0.04 $m^{-1}$. The vertical focusing due to one 5 m long undulator segment is:

$$\frac{1}{f_y} \approx \frac{1}{2}\left(\frac{e}{p_0}\right)^2 B^2 l.$$

This amounts for B = 1 T and $p_0$ = 6 GeV/c to 0.006 $m^{-1}$. For low electron energies a retuning of the quadrupoles according to the undulator configuration is thus necessary, while for nominal energy the influence of the undulator focusing is negligible.

The beam size in the undulator is about 35 µm, the slice energy spread is 1 MeV (10 keV after the injector). A dispersion of around 25 cm would, thus, lead to a beam size growth of 10%. A much more stringent requirement comes from the ±1.5% energy bandwidth together with the 1/10 $\sigma$ constraint on orbit variations, leading to a residual dispersion of 0.1 mm. This corresponds to an average kick in the quadrupoles (due to orbit errors or quadrupole misalignment) of $\approx$ 15 µrad. SASE operation requires trajectory angles in the order of a few tenths of a µrad, thus yielding the most stringent requirement for the orbit in the undulator. Orbit correction methods based on dispersion-free steering algorithms require a resolution of the dispersion measurement in the order of 10 µm. The collimation system has an energy bandwidth of 6%, leading to a requirement of the BPM resolution in the order of 0.5 µm (if no retuning of the upstream magnet lattice is applied during the measurement/correction).

### 4.5.4 Transverse beam stabilisation

#### *4.5.4.1 Introduction*

First start-to-end simulations of the European XFEL indicate that transverse beam motions in the order of a few tenths of the rms beam sizes seem to be acceptable for stable SASE operation. Moreover, the pointing stability of the photon beam leads to a stability requirement of 0.1$\sigma$ for the electron beam. Such beam stabilities on a micron or even sub-micron level are regularly achieved in today's third generation synchrotron light

sources within a frequency band of $10^{-4}$ Hz up to several hundred Hz using global or local beam feedback systems to actively stabilise the CW-like bunch patterns of storage rings (see for example SLS, ESRF, ALS). The same micron-level beam stability needs to be achieved for a SASE-based user facility like the European XFEL for its proposed bunch structure of 600 µs long bunch trains with bunch distances of 200 ns at a 10 Hz repetition rate. The frequency range from a few Hz up to some kHz, where most of the beam position disturbances are generated by noise sources such as ground motions, cooling water and Helium flow, power supply jitter, switching magnets, RF transients and jitter, photocathode laser jitter and related beam current variations as well as long range wake fields, remains inaccessible for relatively slow closed orbit feedback systems as used in storage rings. Their range of application will be limited to the stabilisation of drifts and low frequency beam motions up to a few Hz. A fast feedback system, however, with a low latency time (preferably < 200 ns) can make use of the long macro pulses of the European XFEL with about 3,000 consecutive bunches to damp beam motions in a frequency range from a few kHz to several hundred kHz applying modern control algorithms in a feedback loop. Both, long range (from bunch train to bunch train) and fast (bunch-by-bunch) repetitive beam movements can be eliminated by adaptive feed-forwards. The basic design considerations and main characteristics of a prototype intra-bunch train feedback (IBFB) system for the European XFEL are introduced in the following section. Such a system is presently developed. It will be tested under “real” SASE conditions at FLASH (VUV-FEL) at DESY and can be considered as the central part of a general beam stabilisation strategy as required for the European XFEL, including electron and photon beam-based diagnostic devices for active stabilisation of the electron beam and critical accelerator components.

### *4.5.4.2 Intra-bunch train feedback system*

The present layout and beam distribution concept of the European XFEL requires only one bunch-by-bunch feedback system for transverse beam stabilisation at the final beam energy of 20 GeV. This system will be located in the beam transport section behind the main linac before the beam distribution system. A schematic view of the IBFB topology is shown in Figure 4.5.9.

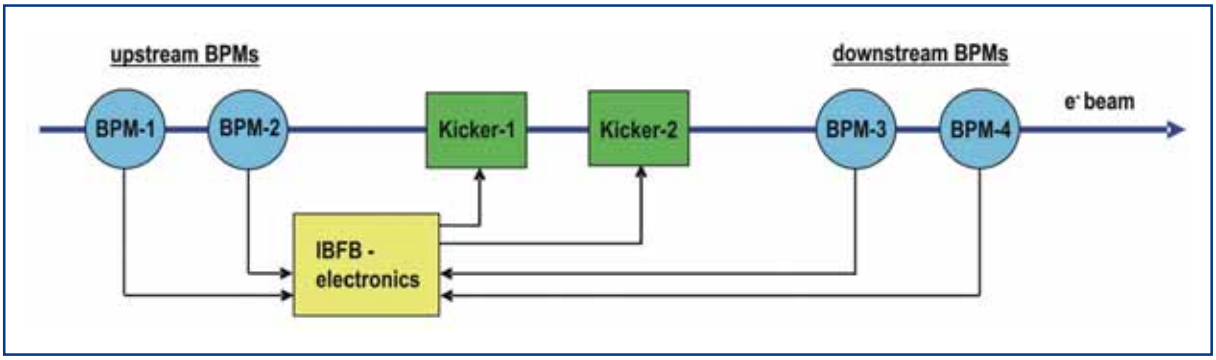


***Figure 4.5.9*** *Topology of IBFB for the European XFEL.*

The IBFB will make use of two upstream and two downstream BPMs for beam position measurements and two fast electromagnetic kickers in between for application of corrections. The proposed topology of using the upstream BPMs for the measurement of the uncorrected beam positions is optimised for lowest latency times through the system, since beam and feedback signals travel in the same direction. The downstream BPMs allow the verification of the feedback model by checking whether the applied kicks lead to the expected corrections. Thus, static and dynamic effects like kicker scaling errors or inaccuracy in the optics model can be detected and eliminated. In the same way, it will be possible to predict long range beam movements from bunch train to bunch train and thus, correct for repetitive disturbances through slow adaptive feed-forwards using look-up tables.

All IBFB components will be installed in the accelerator tunnel. Only short cable connections can be used to keep the system latency time below the bunch-by-bunch distance of 200 ns. The main IBFB components are:

- dedicated strip-line BPMs (at 1.625 GHz) for beam position measurement with a resolution of 1 µm;
- RF front-end for analogue signal conditioning;
- digital electronics including analogue to digital conversion, real-time data processing, calculation of corrections and back-conversion from digital to analogue;
- power electronics and fast electro-magnetic kickers for application of the correction kicks onto the electron beam.

While the strip-line BPM design will be optimised to generate well matched input signals for the RF front-end, the digital part of the system will follow a highly flexible and modular approach by using FPGA-based technology for calculating fast corrections and a set of DSPs for model-based adaptive feed-forwards. In this way, it will be possible to constantly adapt the feedback model in the data processing part of the IBFB to the actual operating conditions of the real accelerator. Interconnection with other complementary feedbacks and accelerator components will be achieved through fibre optic, multi-Gigabit links, like Rocket I/Os, providing the possibility of sharing all relevant information for beam stabilisation on a real-time basis. Beam-based information from the IBFB system could, thus, be used to improve, e.g. low level RF stability. Likewise, real-time data exchange between different electron beam and photon beam position diagnostics may allow efficient cascading of feedbacks and permit the adaptation of feedback models for stable SASE operation.

#### *4.5.4.3 IBFB as an integral part of the XFEL beam stabilisation strategy*

Cascading of beam-based feedbacks and data exchange from different beam diagnostics like electron and photon BPMs have already proven to be the most efficient ways of stabilising the radiation sources of third generation synchrotron radiation facilities. In case of a highly non-linear radiation process like SASE with its noticeable inherent (statistical) fluctuations, it will be even more important to share all relevant information about beam parameters between accelerator sub-systems on a real-time basis. In this

respect, beam stability at an XFEL user facility depends not only on the optimum performance of individual components but more importantly on an efficient matching and integration of all measurement and correction devices as well as critical accelerator sub-systems. It is, therefore, of great importance, that the fields of application and performance ranges of different diagnostics components in terms of bandwidth, resolution, dynamic range, stability and other relevant parameters are well adjusted to each other and that a time-stamped and well correlated view of the accelerator behavior is available on a real-time basis. Standardisation of interfaces including fast data links as well as clear definition of hardware and software concepts are prerequisites for realising such a general beam stabilisation concept. In this way, a vast number of components such as standard electron BPMs and photon beam diagnostics, including the online measurement of photon beam position, intensity, line-width, etc. as well as accelerator sub-systems like timing, low level RF and even gun laser control, can be treated as an integral part of a comprehensive stabilisation strategy, where the IBFB system will not only be used to stabilise the beam position at the location of the SASE radiation sources with highest bandwidth but will also provide important bunch-by-bunch information to support accelerator operation of the European XFEL as a multi-user facility.

## 4.6 Beam diagnostics

### 4.6.1 Requirements

A bunched electron beam of extremely high quality is needed in the XFEL to obtain high gain and saturation in the SASE process at sub-nanometer wavelengths. The specified parameters are given in Table 4.6.1.

| | | |
|---|---|---|
| Bunch length $\sigma_z$ | 20 | µm |
| Peak current I | 5 | kA |
| Relative energy spread $\sigma_E/E$ | $\approx 10^{-4}$ | |
| Orbit deviation in undulator | 3 | µm |
| Directional accuracy in undulator | 0.1 | µrad |
| Arrival-time jitter (rms)[4] | 60 | fs |

***Table 4.6.1*** *Electron beam parameters within a SASE undulator.*

These tight specifications put very demanding requirements on the accelerator and its instrumentation. Special diagnostic tools have to be developed to measure the relevant quantities with sufficient precision. Moreover, feedback systems are indispensable for achieving and stabilising the desired beam quality. The input signals for the feedback loops must be provided by devices that are capable of detecting the deviation of a beam parameter from its nominal value in a non-destructive manner, in order not to disturb the XFEL user operation.

[4] The arrival-time of each bunch can be determined to better than 30 fs.

The beam properties in a single pass machine vary over a wide range during the passage through the machine, thus they have to be measured at various places, resulting in a quite high density of diagnostics all over the machine.

The development of the diagnostics for XFEL will follow the general trend in accelerator instrumentation of using digital systems more intensively and it is planned to use a distributed system of electronics close to the position of the monitor in the beam pipe. These localised stations are then connected to the controls by fast digital interface systems. This should reduce the sensitivity to noise and electromagnetic interference (EMI), but might require more local radiation shielding.

In the following, the various diagnostic instruments are described that are foreseen for the XFEL. Two basic types can be distinguished: dedicated diagnostic instruments for accelerator studies; and optimisation and online diagnostics for monitoring the accelerator performance during XFEL user runs and for providing the input signals to the feedback loops. The former instruments, usually high-resolution systems, may have detrimental effects on the beam quality and may, therefore, be incompatible with user operation of the XFEL.

### 4.6.2 Measurement of projected bunch properties

The XFEL accelerator is a pulsed device, where the characteristics of the electron beam can vary from train to train but also within certain limits inside the train from bunch to bunch. Therefore, each measurement of a beam property has to be treated as a single data point that is connected to one bunch in a certain train. The set of all these data points allows characterisation of the bunch, and correlation of its properties with other bunches. Therefore, single bunch resolution is one main requirement for many diagnostic devices. On the other hand the tolerances, which are ruled by the SASE process, are very tight. An additional complication could be a trend towards decreasing the bunch charge in order to improve emittance, resulting, of course, in a decrease of signal amplitude for the electronics. The following bunch parameters are characterised by means of standard diagnostics.

#### *4.6.2.1 Compression*

Coherent radiation is emitted when the beam traverses a strong dipole field or passes a diffraction radiator. The emitted radiation power is proportional to the square of the bunch form-factor and increases with decreasing bunch length. Variations in the bunch peak current can, therefore, be easily monitored by far-infrared detectors.

At FLASH (VUV-FEL), monitoring the coherent diffraction radiation has become a standard tool to stabilise the RF acceleration phase of the linac.

Future designs will attempt to detect, in a single shot, the frequency spectrum emitted by the electron bunch **[4-95]**. The spectral power carries important information on the source of the longitudinal profile variation and complements the electro-optic data to control the fast longitudinal feedback loops.

#### *4.6.2.2 Beam position*

About 500 BPMs are required along the whole machine. Due to different machine environments (space and beam pipe) different types of BPMs have to be used, and:

- 117 cold BPMs are foreseen in the accelerator modules, either of pick-up type or re-entrant cavity type **[4-96]**;
- striplines and button BPMs similar to the ones used in TTF2 will be used in the warm beamlines;
- in the undulator, the resolution of these standard types is not sufficient. Therefore, cavity BPMs with a resolution about 1 µm are planned for the intersections between the undulator segments;
- special attention has to be put on the BPMs in the dispersive parts of the bunch compressors, since they have to deliver precise information about energy and energy fluctuations in the bunch compressors. The goal is to reach a few µm resolution while measuring wide distributions in a wide, but flat, vacuum chamber.

#### *4.6.2.3 Beam size/emittance*

Emittance is one of the most crucial parameters for the lasing process. Except for adiabatic damping due to the acceleration process, the phase-space volume produced at the injector can only increase during acceleration and beam transport. Therefore, emittance measurement stations have to be available at several positions in the machine, e.g. at the injector, the bunch compressors and after the main linac. All stations will consist of at least four beam size measurement devices, so that the phase ellipse of the beam can be measured without applying quadrupole scans. Usually, the stations are combinations of optical transition radiation (OTR) screens and wire scanners located next to each other. This allows coverage of a wide beam intensity range from machine start-up to long bunch train operation.

Additional tools for monitoring beam size are synchrotron radiation monitors in the bunch compressors and post-undulator beamlines to determine the energy distribution, as well as simple screens to aid machine start-up.

#### *4.6.2.4 Beam intensity*

The beam intensity is measured by current transformers, the so called toroids, which are installed at the beginning and end of each warm section. In addition to the nominal beam current *also* dark current emitted by RF resonators at high gradients is created. Especially dark current from the gun can be transported through the entire machine. Dark current will be monitored before and after dispersive sections and collimators in order to control its transport and optimise the collimation efficiency. Faraday cups for current measurements at the gun and low energy dumps complete the system.

#### *4.6.2.5 Beam loss/radiation dose*

The amount of energy transported within the long bunch trains is very high (up to 65 kJ/ train). Even fractional beam loss can result in severe mechanical damage. Small fractions of the beam or dark current lost in the machine, produce radiation backgrounds and activation that will result in the strongly reduced lifetime of electronics, permanent magnet undulators or other sensitive components. Therefore, loss monitors measuring the dose and protection systems acting on different time scales are required. This ranges from fast interlock systems interrupting the bunch train on the µs level, up to systems watching the integrated dose and finding the hotspots in the machine to prevent long-term damage.

In order to provide signals for the protection systems, about 250 fast beam loss monitors will be installed at critical places along the machine. This network of fast monitors will be accompanied by fibre systems allowing the survey of bigger areas in the machine tunnel.

### 4.6.3 Measurement of slice properties

#### *4.6.3.1 Transverse deflection structure*

The transverse deflecting structure (TDS) is a very multipurpose instrument allowing longitudinal and transverse phase-space analysis with high resolution. The basic idea is simple: the electron bunch is deflected by a rapidly rising electromagnetic field whereby the longitudinal time coordinate inside the bunch is transformed into a spatial coordinate on an observation screen. The system functions in analogy to a conventional oscilloscope tube in which the electrons are deflected by a sawtooth voltage and the time axis of the input pulse appears as the horizontal axis on the screen. In the TDS, the deflecting field is generated by exciting the structure to an eigenmode (TM11-hybrid) exerting a strong transverse force on the electrons. The bunches cross the cavity at zero crossing of the TM wave. The length of the streaked pulse on the screen corresponds directly to the bunch length while the width of the streak is a measure of the beam size and can be used to determine the transverse emittance in the direction perpendicular to the plane of deflection. This emittance can be derived as a function of the longitudinal position in the bunch. Moreover, if the streaked bunch is sent into a spectrometer dipole, the energy of the electrons can be measured as a function of their longitudinal position. An important feature of the TDS is that the RF field is applied in pulsed mode so that an arbitrary bunch in a macro-pulse can be streaked without perturbing the straight trajectory of the other bunches in the train.

**Longitudinal bunch charge distribution**

The longitudinal charge distribution in the compressed electron bunches is one of the most critical quantities. The transverse streak provided by the TDS on an OTR screen is recorded with a CCD camera. At the VUV-FEL a TDS, named LOLA, has been installed in collaboration between Stanford Linear Accelerator Centre (SLAC) and DESY. The structure is 3.6 m long and operated at a frequency of 2.856 GHz with a nominal deflecting voltage of 20 MV. The OTR screen is mounted 10 m downstream from the TDS. Experimental data obtained with the LOLA system are shown in Figure 4.6.1. An excellent time resolution of 20 fs (rms) has been achieved **[4-97]**.

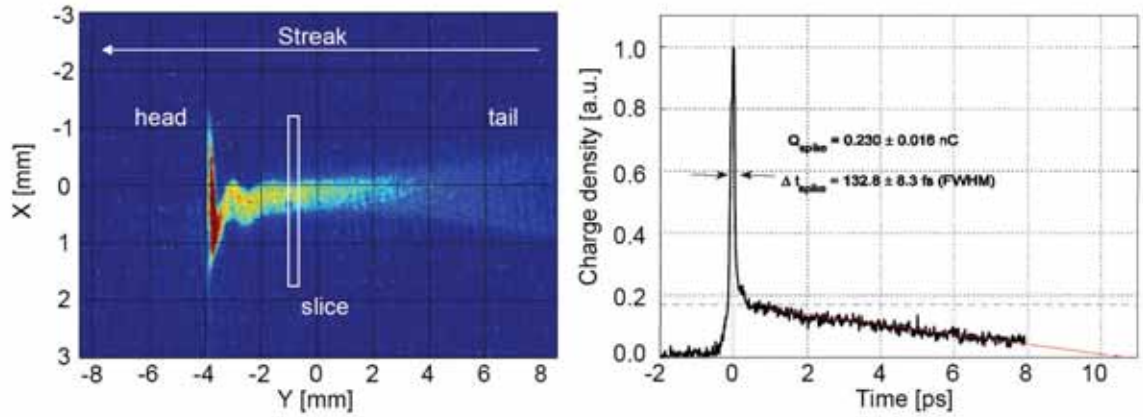


***Figure 4.6.1*** *Image of the beam streaked with the transverse deflecting structure. Strong distortions of the bunch due to collective effects are observed. Right: longitudinal charge profile with a peak current of 1.7 kA. By cutting the beam image into small slices, each representing a time slice of the bunch, the emittance, as a function of the longitudinal position in the bunch, can be determined.*

In the XFEL, TDSs will be in the electron-gun section and downstream of the bunch compressors. The deflecting field is chosen to provide a time resolution of better than 10% of the rms bunch duration. For dedicated studies, the resolution can be improved by increasing the betatron function at the RF structure.

**Determination of slice-emittances**

Ideally, the bunches in the linac should have the shape of an ellipsoid with the z-axis pointing along the flight direction. Coherent effects in the accelerator such as space-charge forces, CSR in the bunch compressor magnets or transverse wake fields in the superconducting cavities may lead to a longitudinal deformation, e.g. to a banana-like shape. In that case, conventional instruments for emittance measurement such as wire scanners or OTR screens equipped with CCD camera readout will yield larger values for the transverse emittance than for undeformed bunches. However, if one were able to subdivide the bunch longitudinally into thin slices, the emittance of any slice should be about the same as in the case of the undeformed bunch. The TDS offers a unique opportunity to determine these slice emittances.

For the emittance measurements a straight beamline comprising several FODO cells with a sufficiently large overall betatron phase advance, is installed between the TDS and the OTR imaging screen. When the quadrupole strengths are kept constant, the determination of the transverse phase-space parameters requires the imaging of the transverse particle density distribution at three (better four for redundancy) different OTR screens with a suitable betatron phase advance in between. A severe constraint is that OTR screens intercepting the electron beam are not possible, since the screen would be damaged by the long bunch train. Therefore, pulsed kicker magnets will be installed at suitable positions, which deflect the bunch to be analysed to off-axis OTR screens **[4-98]**. The slice emittance can then be measured as a function of the longitudinal position in the bunch for an arbitrary bunch in a long train. Measured results from the VUV-FEL are presented in **[4-99]**.

**Energy-position correlation in the bunches**

The TDS also enables the control and tuning of the bunch compression system performance. The streaked bunch is sent into a spectrometer which deflects the electrons in a direction perpendicular to the TDS deflection plane. The two-dimensional particle density distribution on an OTR screen in this dispersive section (the required dispersion is about 1 m) allows measurement of the average energy and the energy spread in each longitudinal slice.

Summarising, the TDS is a most powerful tool for determining the time profile of the bunches and the transverse emittance, the Twiss parameters and the local energy in any slice within the bunch. It must be emphasised, however, that the streaked one to ten bunches are lost for the generation of FEL radiation and must be dumped before the beam enters the main linac. Therefore, this diagnostic device does not allow monitoring of just those bunches which produce the FEL radiation, and it is also not suitable for generating the input signals for feedback systems.

### *4.6.3.2 Online longitudinal bunch diagnostics with electro-optic techniques*

The electro-optic (EO) effect offers the possibility to resolve the time structure of the short electron bunches in a non-destructive manner. The principle is as follows: an EO crystal such as Zinc-Telluride (ZnTe) is mounted at a distance of a few millimetres from the electron beam. The large electric field co-propagating with an electron bunch induces a birefringence in the EO crystal. A linearly polarised optical laser beam acquires an elliptical polarisation when it crosses the birefringent crystal. This elliptical polarisation can be easily detected, for instance in a crossed-polariser setup.

In the electro-optic sampling (EOS) method, the time profile of the electron bunch is sampled by moving ultra-short Titanium-Sapphire laser pulses (typical duration < 20 fs FWHM) in small time steps across the bunch. The bunch shape is obtained from measurements of many bunches. Much more useful for beam diagnostics are single-shot measurements of individual bunches. This is possible in the spectral decoding scheme which is illustrated in Figure 4.6.2.

In this scheme, the Titanium-Sapphire (TiSa) laser pulse which typically contains the wavelength spectrum from 770 to 830 nm, is stretched (chirped) in a dispersive medium to a length of several picoseconds, larger than the electron bunch length. The chirp process is accompanied by a spectral ordering, the long wavelengths being at the head of the stretched pulse and the shorts ones at the tail. The chirped laser pulse overlaps the electron bunch in the ZnTe crystal and the induced birefringence at a given time slice of the bunch, is translated into an elliptical polarisation at the corresponding wavelength slice of the stretched laser pulse. Using a grating spectrometer and a suitable setup of crossed polarisers or quarter wave plates to detect the amount of ellipticity in each wavelength component, the time profile of the electron bunch can be reconstructed.

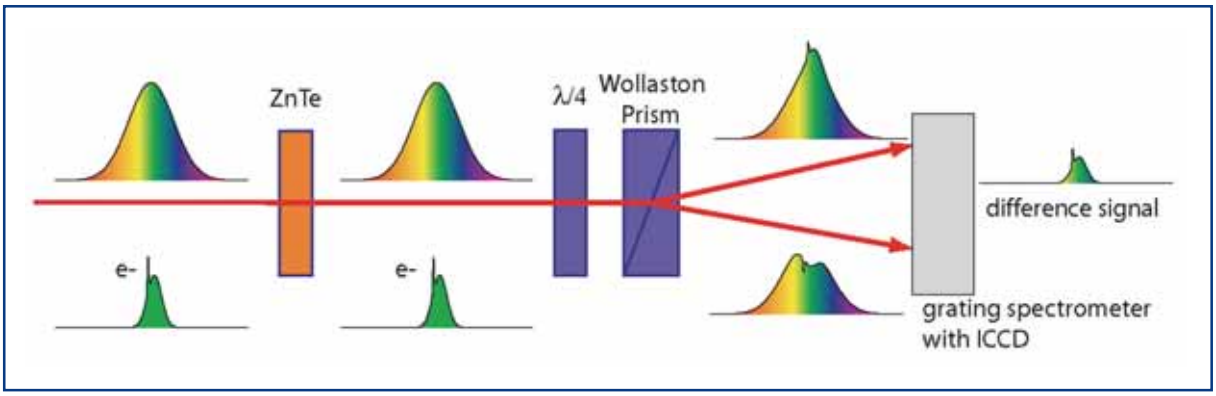


***Figure 4.6.2*** *The spectral decoding scheme for EO reconstruction of the longitudinal charge distribution in an electron bunch. At the top, the stretched linearly polarised TiSa laser pulse is shown. The long wavelength components are at the head of the pulse, the short wavelengths at the tail. The bottom shows the time profile of a typical electron bunch in the linac of the VUV-FEL. In the ZnTe crystal the local electric field at any slice of the bunch is imprinted as an elliptical polarisation onto the corresponding wavelength component of the laser pulse. The reconstruction of the bunch time profile is achieved by spectral analysis of the two polarisation states and subtraction of the two spectra. The spectra can be recorded with a gated intensified CCD camera (ICCD).*

The measured time profiles of several bunches in the linac of the VUV-FEL are shown in Figure 4.6.3. The data from the VUV-FEL illustrate the usefulness of the spectral decoding setup. From the observed bunch shape one can easily judge whether the parameters of the bunch compression system are properly adjusted. Even in the case of optimum bunch compression, one can observe fluctuations in the bunch arrival-time at the EO crystal. The spectral-decoding EO setup is, thus, an excellent real-time monitor for the timing stability of the accelerator **[4-100]**.

Since the repetition rate of the pulsed laser can be precisely synchronised to the RF master oscillator of the machine (timing jitter of less than 20 fs is feasible), the single-shot techniques provide the possibility of determining the arrival-time of each electron bunch at the undulator with a precision of better than 30 fs. This will be of great interest for pump-and-probe experiments at the XFEL.

The intrinsic time resolution of the electro-optic method is limited by the frequency response of the EO crystals. In ZnTe the transverse optical (TO) lattice vibration frequency of 5.3 THz defines a lower limit for the resolvable bunch length of about 80 fs (rms). Of all known EO crystals, gallium phosphide GaP features the highest lattice vibration frequency (11 THz). GaP allows resolving bunch lengths down to 40 fs (rms). As shown above, the transverse deflecting cavity is superior in resolving the width of ultra-short electron bunches, however, it is not suitable for providing timing signals for all bunches in the FEL user operation **[4-101]**.

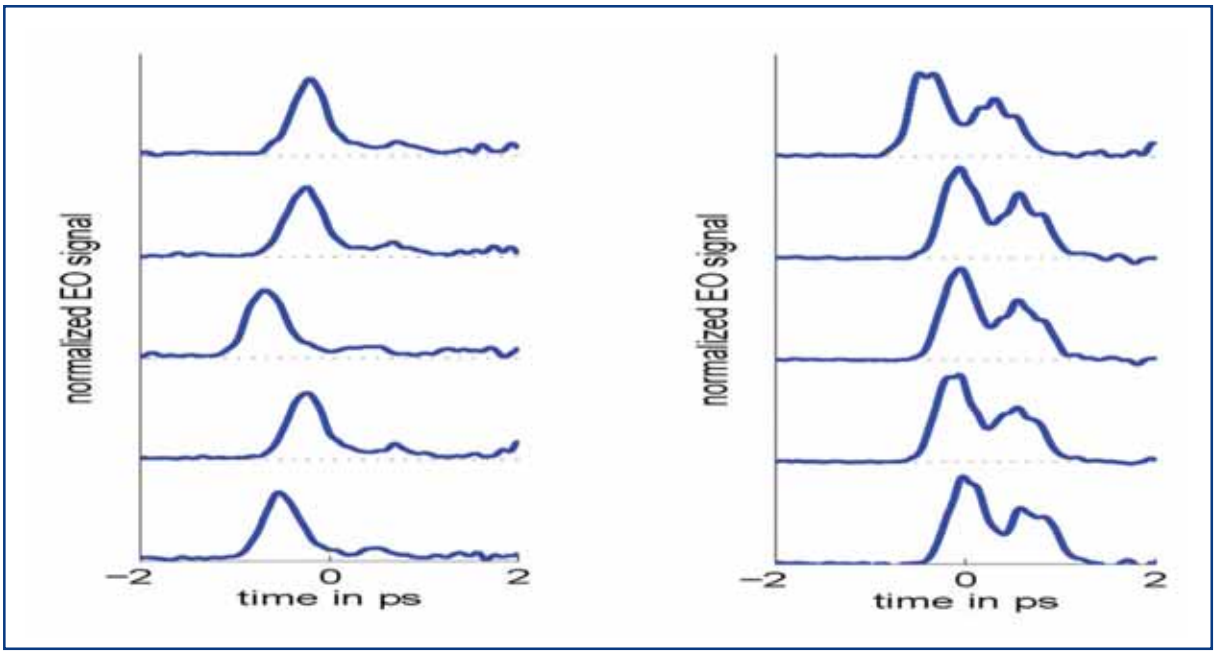


***Figure 4.6.3*** *Time profile of several bunches in the VUV-FEL linac, measured with the spectral decoding technique. Left: bunches with optimum longitudinal compression. Right: bunch shapes obtained with a different setting of the RF phase in the accelerating section preceding the magnetic bunch compressor.*

To detect every bunch in a macro-pulse, a high-speed line camera with processing time of 200 ns is used. The profile information is pre-processed with a field programmable gate array (FPGA) and transferred to a longitudinal intra-pulse-train feedback. Monitoring the longitudinal bunch profile with electro-optic methods is foreseen at the injector (8.5 ps rms) and after the first bunch compressor stage (300 fs rms). After the final compression stage, with 60 fs rms bunch length, the EO technique is at the limit of its resolution.

### *4.6.3.3 Energy spread monitoring*

Synchrotron radiation monitors, that image incoherent synchrotron radiation emitted by dipole magnets and insertion devices, are commonly used in storage rings to monitor the beam profile. In certain dispersive sections of the XFEL, like the bunch compressor or the dump-lines, the transverse beam profile is dominated by the energy spread of the beam. This makes synchrotron radiation monitors excellent candidates for non-destructive measurement of the beam energy and the energy distribution. Planned high precision synchrotron radiation monitors, equipped with fast readout system (line cameras), are listed in Table 4.6.2.

| | | Injector | BC1 | BC2 | Collimator | Dump |
|---|---|---|---|---|---|---|
| Energy | GeV | 0.1 | 0.5 | 2.0 | 17.5 | 17.5 |
| rms Resolution | | $3.0\times10^{-4}$ | $1.7\times10^{-4}$ | $1.6\times10^{-4}$ | $2.4\times10^{-4}$ | $2.4\times10^{-5}$ |
| Dispersion | m | 0.67 | 0.68 | 0.33 | 0.05 | 0.5 |
| Beta-function | m | 8 | 13 | 11 | 2 | 2 |
| Betatron-component of beam size | µm | 200 | 115 | 53 | 12 | 12 |

***Table 4.6.2*** *List of synchrotron radiation monitors to determine the beam energy spread with the capability to record individual bunches in long pulse trains. The rms resolution for the energy profiling is determined by the betatron component (the beam size of a beam with no energy spread) of the transverse beam size.*

To measure the residual energy spread of the beam, OTR screens and special imaging optics are foreseen for use in the commissioning dump-lines, the injector, BC1 and BC2 since these locations provide large dispersion with small beta-function.

# 4.7 Technical layout

## 4.7.1 Warm vacuum systems

The warm vacuum systems of the XFEL consist of four major parts: the injector, bunch compressors (1 and 2), the undulator sections and several beam transport lines which are part of the beam distribution system. An overview of the key aspects of these individual sections is given in Table 4.7.1.

| Section | Length | Issues |
|---|---|---|
| Injector I | 60 m | RF-guns, dust free, high complexity |
| Compressors, diagnostic | 160 m | Flat steel chambers, Copper coating, narrow tolerances |
| Collimator section | 209 m | Precision collimator units, material: Ti |
| Undulator chambers | 713 m | Small aperture, low roughness, high conductivity |
| Beam distribution (e-) | 1.737 m | Optimised for cost, low complexity, Copper pipes |

***Table 4.7.1*** *Overview of warm vacuum sections.*

The requirements for the beam vacuum quality in the XFEL are relaxed as compared to the requirements in a storage ring. Effects which are potentially harmful for the beam include Bremsstrahlung interaction and resulting beam loss, emittance growth from elastic scattering and the fast ion instability which leads to an amplification of orbit deviations along the bunch train.

The fast ion instability is only of importance if the ions generated by one bunch stay long enough in the vicinity of the beam centre to interact with the next bunch. This leads to a threshold condition for the instability which is independent of the residual gas pressure but depends on the bunch distance and the ion mass of the gas molecules **[4-102]**. For

XFEL parameters, only ions with masses beyond M≈100 can be captured by the beam. Such heavy gas species do not occur at relevant partial pressures in accelerator vacuum systems.

The typical gas composition consists of 80% $H_2$ and 20% CO. Since the contribution of Hydrogen is negligible, the Bremsstrahlung scattering rate is roughly estimated using the radiation length of Carbon monoxide, which is $X_0$=320 m under normal conditions. Consequently, at a partial pressure of $P_{CO}=10^{-8}$ mbar, the radiation length is $3\times10^{13}$ m and for a single passage of a 2 km drift length, the fraction of relative beam loss would be below $10^{-10}$. This is less than a single electron from each bunch. Given this low interaction rate, one may already argue that the contribution of gas scattering to the emittance growth is small as well. Indeed, even in the first warm low energy section with $E_{beam}$=120 MeV, where the beam is most sensitive, the relative emittance growth amounts to $5\times10^{-5}$, or emittance doubling would occur only after 600 km drift. On the other hand the above quoted pressure can be achieved easily, at least in the radiation-free transport lines.

#### *4.7.1.1 Injector and bunch compressor*

The RF gun is made from OFHC Copper with very high surface quality requirements. Another critical aspect is the water cooling distribution to keep the spatial temperature distribution within the required tolerances. To obtain a good lifespan from the sensitive cathode, the residual gas pressure has to be kept in the range of $10^{-10}$ mbar. A long-term experience exists at DESY concerning the production of L-band RF guns.

The vacuum chambers in the bunch compressors should exhibit a flat aperture to allow for horizontally varying beam orbits. To obtain the necessary mechanical stability while keeping a reasonable gap height of the dipole magnets, the best choice for the chamber material is stainless steel. The inner surface of the vacuum chambers will be coated with a thin Copper layer to minimise the resistive wall wake field effect. The chambers will be produced from two milled halves which are welded together by laser beam welding, a method which has been established during the production of the bunch compressor chambers for the VUV-FEL. A significant technical challenge is presented by the need to keep sub-millimetre tolerances for the straightness of these chambers with a length of several metres during the welding process.

#### *4.7.1.2 Collimation section*

The major part of the collimation section consists of a beam transport line which will be equipped with Copper tubes and ion getter pumps similar to the beam distribution system. The section contains four collimator units with a tapered round fixed aperture and Titanium blocks as the collimator material. The collimator units will exhibit a similar design to the ones presently in operation at the FLASH (VUV-FEL) (see Figure 4.7.1). There will be a possibility of interchanging up to three different apertures using the appropriate mechanics. Technical measures which allow for precise alignment of the collimator units are of special importance.

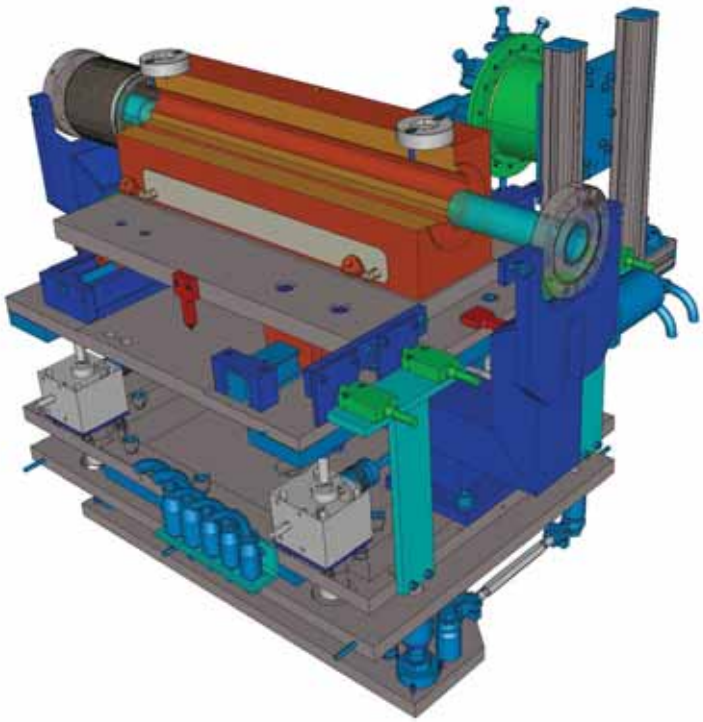

***Figure 4.7.1*** *Cut-away view of the collimator unit presently under operation at the VUV-FEL. The cylindrical part in the centre of the figure contains several tapered circular apertures which can be moved to the beam orbit. The collimator units for the XFEL will closely follow this design, except for different dimensions and choice of material.*

### *4.7.1.3 Beam distribution system*

Roughly 1.7 km of cost-optimised vacuum system for beam distribution has to be built. To limit the resistive wake field effects the vacuum chambers will be produced from Copper with stainless steel flanges. Copper pipes are less expensive than Copper coated steel tubes which present an alternative. An inner diameter of 50 mm has been chosen. The system will be pumped by ion getter pumps with a pumping speed of 60 l/s in a distance of 6 m. In this configuration an average pressure of $5\times10^{-9}$ mbar will be achieved. The power supplies for the getter pumps will be installed in the tunnel.

### *4.7.1.4 Undulator vacuum*

Naturally, the vacuum chamber inside the undulator magnets exhibits a tight aperture. An important design criterion is a small wall thickness in the vertical direction to maximise the beam aperture while keeping an adequate magnet gap height for maximum field strength. Since there is more space available in the horizontal direction, an elliptical shape has been chosen for the chamber geometry. The wider horizontal dimension helps to reduce the amount of spontaneous radiation which is absorbed by the inner chamber walls. The baseline design assumes an elliptical steel tube for the chamber body and two Copper profiles with a water cooling channel which are brazed to both sides of the elliptical profile. The total heating power on the inner wall of the vacuum chamber is dominated by HOM losses and amounts to 2 W/m.

The typical opening angle of the spontaneous radiation is $1/\gamma$ in the vertical plane and $K/\gamma$ horizontally. For example, at 20 GeV this amounts to 25 µrad and 150 µrad for the two planes[5] . It is proposed to protect the beam-pipe from radiation by absorbers which are installed in between the undulator units. With the chosen geometry, shadow angles of 70 µrad and 500 µrad can be achieved. Although the major part of the photons will hit the absorbers there is still a significant fraction in the low energy part of the spectrum with emission angles large enough to reach the beam-pipe. For example, 25% of the photons are radiated at angles beyond $3/\gamma$. Photon induced outgassing occurs for photon energies above ~10 eV which is a small fraction of the critical energy.

The baseline dimensions of the chamber are shown in Figure 4.7.2, including the cross-section of the absorber for spontaneous radiation, which is located in-between two undulators.

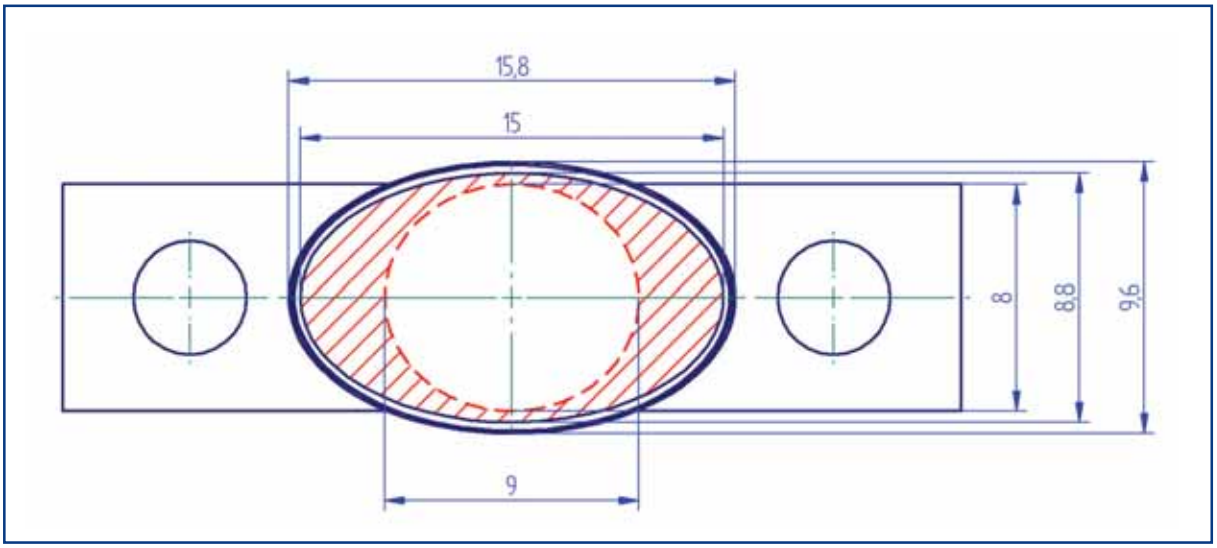


***Figure 4.7.2*** *Cross-section of the undulator beampipe with inner and outer dimensions. The aperture of the radiation absorber is shown as the dashed line.*

To minimise resistive wake field effects, the chamber body will be coated with a Copper or Gold layer. The roughness of the chamber surface should not exceed an rms value of ~300 nm over a wavelength of 1 mm. It has been demonstrated that such values can be achieved in electropolished steel tubes as well as in carefully extruded aluminum tubes.

At the maximum beam energy of 25 GeV, the spontaneous radiation reaches an average level of 8 W/m (beam current 12 µA). Over the length of one undulator unit this amounts to 40 W which will be absorbed by Copper absorbers. The absorbers are also required for shadowing the beam pipe; thereby reducing the photon induced outgassing. The rate of photons produced per unit length in the undulator at 300 kW beam power and a peak field of 1.3 T is $4\times10^{14}$ $m^{-1}s^{-1}$. Assuming that 5% of these photons hit the beam pipe as residual radiation, that leads to an initial radiation-induced outgassing rate of $2\times10^{-11}$ mbar l/s $cm^2$ for steel. In comparison, the thermal outgassing rate without radiation is approximately

[5] The largest K=6 of the SASE 2 undulator has been assumed.

$5\times10^{-12}$ mbar l/s cm$^2$. The vacuum conductance of the narrow pipe is small and amounts to c=0.17 l/s (N2) for one metre length. From this conductance and the volume of the pipe per unit length, a diffusion coefficient of 1.7 m$^2$/s can be computed. The typical relaxation time of pressure bursts in the chamber can be estimated as the diffusion time from the middle of the chamber to the pump. It amounts to 5 seconds. This time is much longer than the repetition time of the bunch trains. Consequently, the pulsed operation of the accelerator will result only in a moderate modulation of the pressure around the average pressure determined from the static diffusion model. The system will be pumped by ion getter pumps installed in the 1.1 m long section between the undulator units. The resulting pressure is dominated by the limited conductance. With the above outgassing rates, an average pressure of $2\times10^{-7}$ mbar is expected for stainless steel. According to the above introductory remarks such relatively high pressures are still very acceptable.

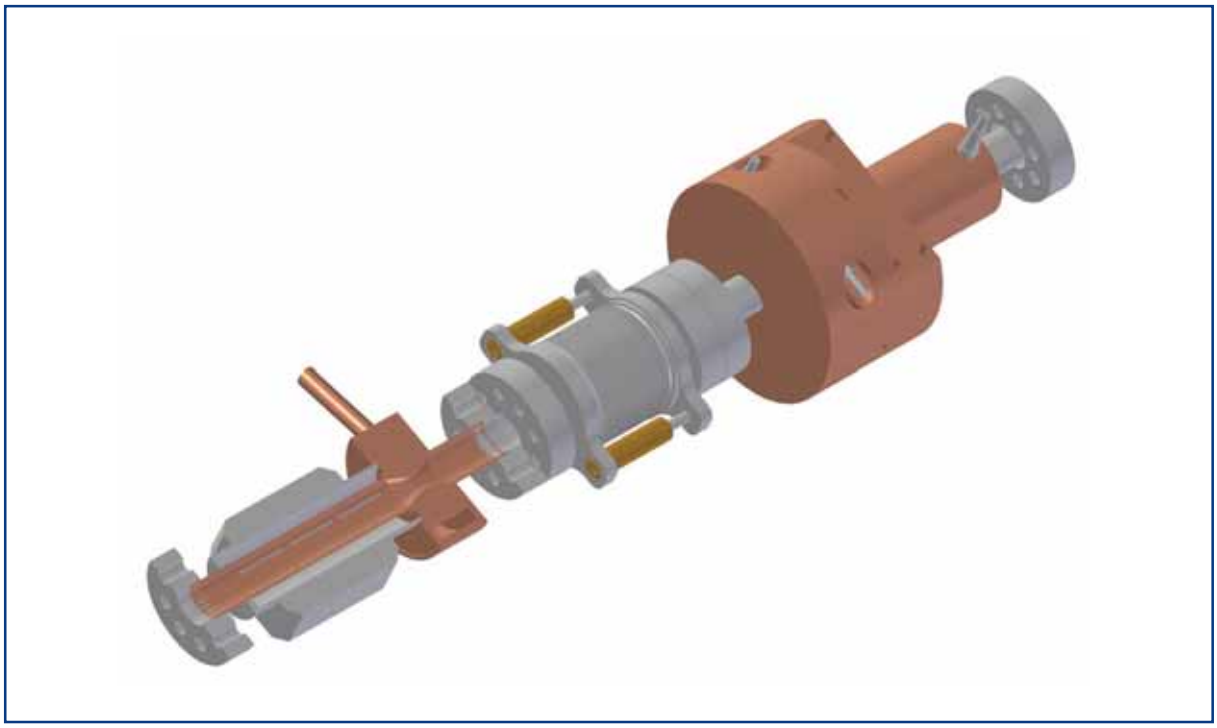

***Figure 4.7.3*** *Intersection beam-pipe between undulators showing RF-shield and pump connection, absorber, bellows unit and cavity BPM (from left).*

### 4.7.2 Magnets

The parameters of the warm dipole and quadrupole magnets are summarised in Tables 4.7.2 and Table 4.7.3 **[4-103]**. Around 60 dipole magnets are used in the bunch compressors, collimation, beam distribution and beam dumps. About 400 quadrupole magnets focus the beam. Subsequent corrector magnets will steer the beam when necessary. The dispersive sections also require about 40 sextupoles and octupoles for higher order corrections. The heavy dipole and quadrupole magnets located in the dump region fit in the maximal geometrical region of 900 mm × 600 mm horizontal and vertical to the beam axis. All other magnets have smaller geometrical size. The dipoles have gap heights of 12 mm, 40 mm, 60 mm and 100 mm respectively, and are of C-type and H-type

shape. Quadrupole and higher order multipole magnets are characterised by standard aperture (diameter) of 12 mm, 40 mm, 60 mm and 100 mm. Magnet yokes do not exceed a length of 5 m to make handling in the tunnel easier.

The magnets will be made of 1 mm laminated steel sheet metal. To minimise the tooling costs, a modular construction system will be worked out for the different types of dipole magnets and quadrupole magnets.

All dipole and quadrupole magnets will have water-cooled Copper coils whereas the correction magnets have air-cooled Copper coils.

| Name | Count | Length m | Gap m | $B_{max}$ T | Current A | Power losses kW | Total weight kg | Water flow rate l/min | Water over heating °C |
|---|---|---|---|---|---|---|---|---|---|
| BA | 4 | 0.3 | 0.04 | 0.667 | 480 | 2.6 | 260 | 1.3 | 28 |
| BI | 6 | 0.5 | 0.04 | 0.31 | 670 | 1.9 | 280 | 2.1 | <15 |
| BF | 1 | 1.0 | 0.04 | 0.931 | 440 | 8.8 | 1800 | 9.1 | 24 |
| BG | 1 | 2.5 | 0.04 | 1.397 | 660 | 39.9 | 4500 | 19.2 | 30 |
| BB | 4 | 0.3 | 0.04 | 1.268 | 900 | 9.2 | 450 | 3.7 | 36 |
| BC | 8 | 5.0 | 0.06 | 0.088 | 120 | 0.8 | 5550 | 0.4 | 31 |
| BE | 6 | 2.5 | 0.06 | 0.730 | 450 | 15.4 | 8450 | 6.1 | 37 |
| BD | 8 | 4.0 | 0.06 | 0.417 | 540 | 20 | 4100 | 11.4 | 24 |
| BV/BW | 14 | 2.5 | 0.06 | 1.456 | 890 | 71.4 | 8450 | 31.1 | 33 |
| BX | 8 | 0.5 | 0.1 | 0.384 | 690 | 10.8 | 515 | 7.3 | 21 |

***Table 4.7.2*** *Main parameters of dipoles.*

| Name | Count | Length m | Bore radius m | $B_{pole}$ T | Current A | Power losses kW | Total weight kg | Water flow rate l/min | Water over heating °C |
|---|---|---|---|---|---|---|---|---|---|
| QI | 28 | 0.25 | 0.02 | 0.05 | 5 | 0.04 | 35 | air cooled | |
| QA | 135 | 0.2 | 0.006 | 0.15 | 40 | 0.05 | 25 | 0.8 | <5 |
| QB | 53 | 0.5 | 0.02 | 0.40 | 170 | 1.9 | 150 | 1.32 | 20 |
| QC | 27 | 0.3 | 0.02 | 0.14 | 60 | 0.16 | 90 | 0.57 | <5 |
| QD | 17 | 0.3 | 0.02 | 0.40 | 170 | 1.3 | 90 | 0.57 | 33 |
| QE/QF | 76/47 | 1.0/0.5 | 0.03 | 1.00 | 390 | 18/10.8 | 1300/600 | 6.3/7.8 | 40/20 |
| QG | 6 | 3.0 | 0.05 | 1.11 | 960 | 77 | 6500 | 44.5 | 35 |
| SEXT | 36 | 0.45 | 0.03 | 0.84 | 450 | 20.6 | 500 | 7.05 | 39 |
| OCT | 6 | 0.4 | 0.03 | 0.47 | 90 | 2.42 | 740 | 1.6 | 22 |

***Table 4.7.3*** *Main parameters of multipoles.*

### 4.7.3 Kickers

Table 4.7.4 gives the parameters for the kicker elements used in the beam distribution system. The kicker magnets are striplines surrounding a sputtered ceramic vacuum chamber. Magnet lengths of between 0.3 and 1 m are foreseen.

| | | **Fast single bunch kicker (for beam dump)** | **Flat-top kicker (for beam distribution)** |
|---|---|---|---|
| Pulse Form | | Burst | Flat top |
| Repetition Rate | Hz | $5\times10^{6}$ | 10 |
| Max. Pulse Width | s | $200\times10^{-9}$ | $300\times10^{-6}$ |
| Rise/Fall Time | s | $< 100\times10^{-9}$ | $\approx 20\times10^{-6}$ |
| Rel. Amplitude Stability | | 0.01 | $5\times10^{-5}$ |
| Relative Residual Ripple | | $5\times10^{-5}$ | $5\times10^{-5}$ |
| Max. int. Field Strength | mT m | 31 | 31 |
| Number of Kickers | | 30 | 10 |
| Pulser Voltage | kV | 8 | 0.3 |
| Pulse Current | A | 100 | 300 |
| Max. Power | kW | 40 | 0.27 |
| Average Power | W | 260 | 270 |

***Table 4.7.4*** *Parameters for the beam distribution system kicker elements.*

The fast pulser prototype is based on Behlke HTS 80-12-UF switches operated in parallel to allow for 5 MHz switching rate. The on/off time of these switches is in the order of 10 ns. Relative amplitude stability of below 0.5% has been measured at TTF for a single switch, while the first 5 MHz prototype shows an amplitude stability of about 3%. Further research and development (R&D) work is planned to improve this below 1%.

The flat-top pulser is based on a capacitor discharge pulser. The accuracy is reached by dividing it into several kicker/pulser systems (say 10), where nine kickers provide most of the amplitude and the tenth is used together with a programmable power supply to correct for the unavoidable systematic voltage drop.

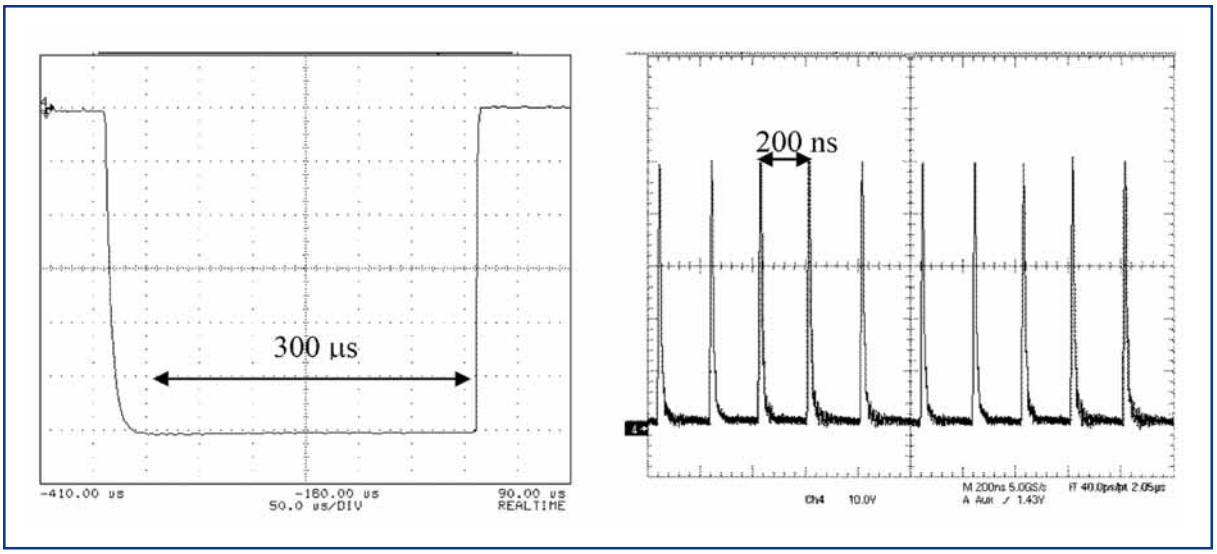


***Figure 4.7.4*** *Left: Pulse current of the flat-top kicker with an amplitude stability of better than 1% over a pulse length of 300 µs. The fall-time is only 5 µs. Right: Pulse form of 5 MHz single-bunch kicker.*

## 4.7.4 Beam dumps

### *4.7.4.1 Requirements and general layout*

In Phase 1 of the XFEL project, the beam can be dumped at three positions downstream of the linac. These main dumps all have the same capabilities as specified by the limits given in Table 4.7.5.

The average power per dump is limited to 300 kW. This allows an operation at the nominal beam parameters (20 GeV, 1500 bunches with 1 nC per beamline, 10 Hz repetition rate). The power limit was chosen so that a solid graphite-based absorber can be used. This approach avoids the complexity and risks of using a liquid (e.g. water) dump system.

| | | |
|---|---|---|
| $E_0$, electron energy | max. 25 | GeV |
| $N_t$, number of electrons per bunch train | max. $2.5 \cdot 10^{13}$ ⇔ | 4µC |
| $I_{ave}$, average beam current | max. 40 | µA |
| $W_t$, energy carried in one bunch train | max. 100 | kJ |
| $P_{ave}$, average beam power | max. 300 | kW |

***Table 4.7.5*** *Parameters of the beam hitting the dump in XSDU1, XSDU2 and XS1.*

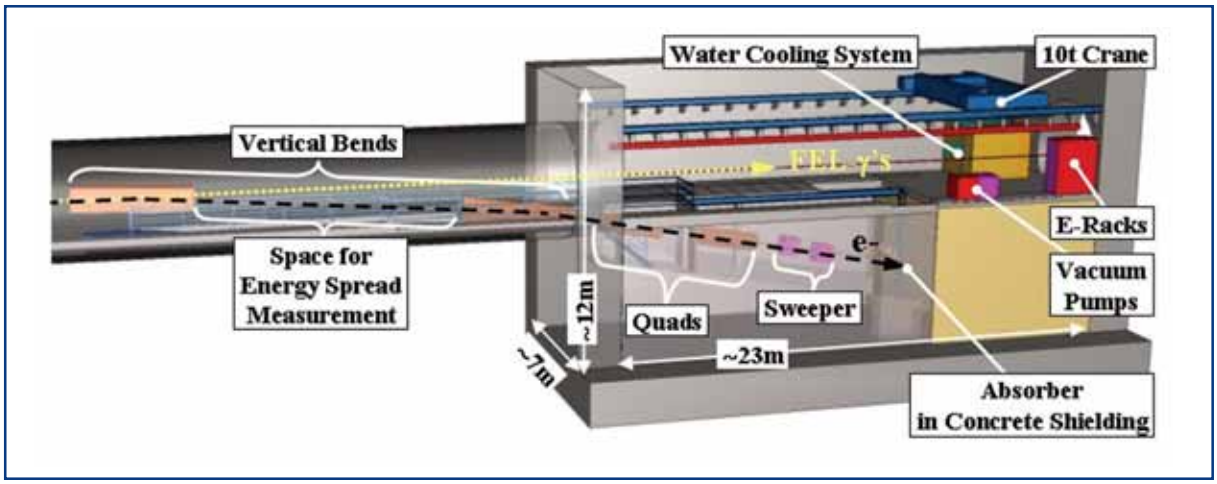


***Figure 4.7.5*** *The main beam dump system in the underground dump building XSDU1.*

Two of the main beam dumps are housed in dedicated buildings (XSDU1 and XSDU2) downstream of the last undulator. During regular FEL operation the electron beam is aborted here after being separated from the FEL photon beams. The third main dump system is implemented at the end of the linac tunnel in the separation building (XS1). This dump will be used during commissioning and in emergency cases. In regular FEL operation mode, this dump takes those bunches which are removed in the process of creating different bunch patterns.

As an example for the overall layout of the dump system, Figure 4.7.5 gives a 3-D sketch of the situation in one of the underground dump buildings (XSDU1). After a 10° vertical bend (15° in XS1) the electron beam is directed onto the absorber. The deflection is provided by a double-bend achromat. On its way two quadrupoles magnify the beam spot size by a factor of 100 up to $\sigma \geq 2$ mm. An issue is the alignment and orbit tolerance of about 0.5 mm in the strong quadrupoles. A slow deflection system (slow-sweeper) distributes the beam bunch train by bunch train (not bunch-by-bunch) circularly with a sweep radius of $R_s$=5 cm at the dump face. Both measures are required for a safe operation in terms of absorber heating, as will be explained in the next section. Before finally entering the absorber, the beam passes through a beam window which separates the beamline vacuum from the low quality vacuum in the absorber section. A second window gives redundancy and as indicated in Figure 4.7.6 offers the possibility of using the intermediate volume for beam profile monitoring by means of gas luminescence.

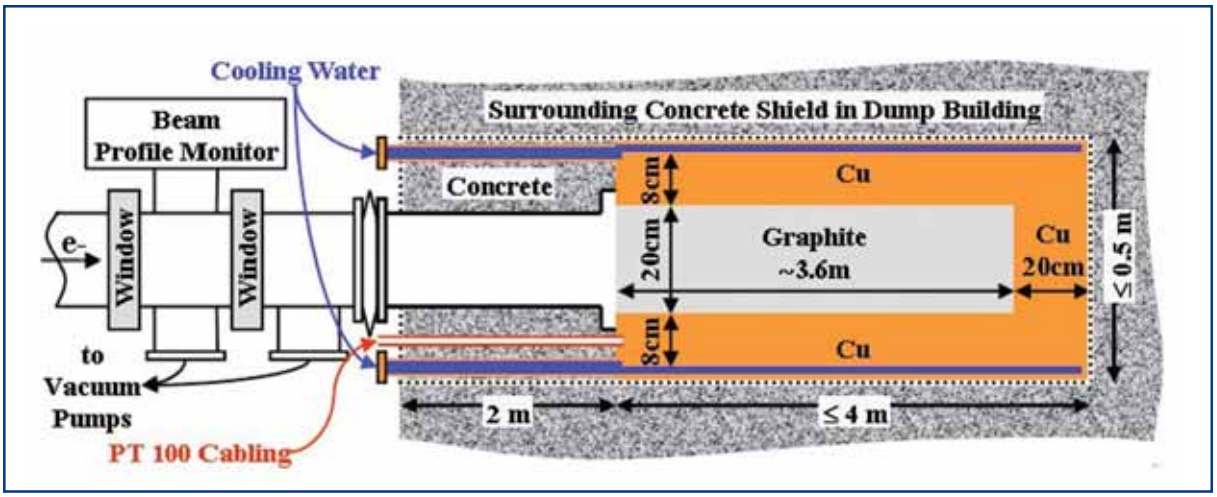


***Figure 4.7.6*** *Layout of the dump module (marked by dotted line) installed in a hole of the surrounding concrete shielding and connected via two windows to the beamline.*

### *4.7.4.2 Description of components*

The cylindrical absorber has a core of 20 cm in diameter, consisting of a 3.6 m ($14.4 \times x_{0,C}$) long graphite section (density 1.7 g/cm$^3$), which is followed by a 20 cm ($13.8 \times x_{0,Cu}$) long Copper tail catcher. The absorption length $x_0$ depends on the material and is, in our case, $x_{0,C}$ = 25 cm for graphite and $x_{0,Cu}$ = 1.4 cm for Copper. Radially this core is surrounded by a layer of 8 cm (5 Molière radii) Copper, which is water-cooled at its circumference and simultaneously serves as a vacuum tight enclosure for the graphite. Less than 1% of the energy of a 25 GeV beam leaks from such an absorber and more than 90% of it is absorbed in the graphite section **[4-104]**.

The largest power dissipation occurs at the shower maximum at a depth of ~1.2 m (25 GeV) and ~0.9 m (7.5 GeV). At $P_{ave}$=300 kW peak power densities of about 1.6 kW/cm at 25 GeV and even 1.8 kW/cm at 7.5 GeV are expected, since the shower is shorter in the latter case. By means of slow circular beam sweeping with a radius of 5 cm, the resulting maximum equilibrium temperature in the graphite (due to heat extraction by radial thermal conduction towards the water-cooled circumference) is kept just below 500°C to 600°C, where graphite tends to oxidise at normal atmospheric conditions. For additional safety and redundancy the graphite is kept under low quality vacuum. Nevertheless, it has to be emphasised that a good ($\leq$ 0.5 W/cm$^2$/K) and long term reliable thermal contact at the radial graphite to Copper boundary plays a vital role for heat extraction. Therefore, brazed connections are aimed for.

Since the sweeping is slow compared to the $\leq$ 1 ms passage time of one bunch train, it does not affect the instantaneous heating produced during the absorption of one train. Thus, for safe operation the impinging beam size has to be kept at $\sigma \geq 2$ mm. In that case the maximum instantaneous temperature jump in graphite is less than 200 K and the dump can withstand the related cyclic mechanical stresses over the long-term (operation period of the XFEL).

For shielding reasons the absorber is placed 2 m deep in a dead-end hole in the surrounding concrete shield, which is part of the building. Therefore, the beam tube, water pipes and temperature sensor cabling need to be extended 2 m in the upstream direction with the intermediate space filled with concrete. With overall dimensions of 6 m in length, 50 cm in diameter and a mass of about 5 t, the front part together with the absorber form the dump module. This unit has to be handled as one part during installation and exchange.

The beam windows need a useful diameter of 200 mm. Each of them is made of a 10 to 15 mm ($<<x_0$) thick graphite ($x_0$=25 cm) disk, which is brazed into a water-cooled Copper frame, which again is brazed to short stainless steel tubes, to which the flange can be welded. The graphite disk has excellent thermal and mechanical properties to withstand the cyclic load induced by the beam and the static load, which is present when one of the adjacent vacuum sections is vented to 1 atm while the other is still pumped. One face of the window will be coated by a thin (~30-50 µm) layer of a suitable material (e.g. pyrolytic graphite) to make the porous graphite window leak tight and its surface suitable to be installed in a particle-free UHV system. Since tests on different window coatings are presently underway, a final choice on the most appropriate coating material has not been made yet. The power dissipation in the window is much less than that in the absorber. Therefore, it does not raise an additional limitation on the incoming beam. A full bunch train (4 µC) with a spot size of $\sigma$ = 2 mm causes an instantaneous temperature rise of only 30 K in the graphite of the window. The average temperature drop, which builds up between the window centre and its cooled circumference at a radius of 10 cm, is again only 30 K when 40 µA of average beam current is homogeneously penetrating along a radius of 3 cm (size of the sweep at the window 2 m upstream of the absorber face).

The cooling water of the edge-cooled absorber takes less than $10^{-3}$ of the primary beam power. Therefore, radiolysis is negligible and activation is a minor problem, but demands a separate cooling circuit of conventional type. This circuit requires a space of about 8 $m^2 \times 2$ m (height) and is placed in the dump building next to the outgoing photon tunnel as shown in Figure 4.7.5. The total amount of water in the circuit is not more than 2 $m^3$. In case of accidental leakage, water flows passively into a container located at the deepest point of the building. After one year of operation (5,000 h) at 300 kW, the activity concentration in the cooling water stays within the legal limits to be drained, except for very short-lived nuclei and the $^7$Be ($t_{1/2}$=53 days) content **[4-105]**. Fortunately not much of the $^7$Be will stay dissolved in the water. Some fraction will attach to the inner surfaces of the cooling circuit and most of it will accumulate in the ion exchanger, where it, treated as a point source, creates a very moderate dose rate of ~2 µSv/h in a 1 m distance without any shielding. Thus, negligible $^7$Be content is expected in the cooling water and the water can be exchanged without problems during regular annual maintenance as required technically, in any case, to retain its quality. Nevertheless, if activity measurements require, the water would be stored for some time to allow for decay.

The activation of soil and ground water close to the dump building will be kept below 10% (DESY planning goal) of the legal limits, if the dump module is shielded by an equivalent 4 m (including the building walls) of normal concrete **[4-105]**. An additional 5.5 m thick

layer of sand, between the building wall and the surface above, results in a publicly accessible area ($\leq$ 0.1mSv/a) there. The dose rate in the downstream photon tunnels and the experimental hall due to escaping muons from the dump is limited by the depth of the dump position and its downward tilted axis. The activity concentration of the tunnel air is tolerable at the outlet above ground, if the air, which resides in gaps within the first 2 m of the concrete shield around the dump is trapped, i.e. cannot couple to the air flow of the vented tunnel. That is why the concrete block, which houses one hole for the dump module in operation and three holes for storing activated faulty ones, is made out of one piece. Nevertheless, where the beam pipe of 200 mm diameter (required by the slow sweep) penetrates the shield, neutrons can go out unshielded. They will activate upstream components and the ambient air as well. Hence, almost the complete ramp area in the dump building is enclosed by a wall and a demountable concrete floor to keep the highly activated air trapped. Access to this area is possible after radiation permit (decay time) and forced ventilation. Exchange of a dump module is expected to be carried out remotely without the necessity to work close to the dump module or the upstream beamline, which has to be removed before the dump module can be pulled out and put into one of the storage holes.

#### *4.7.4.3 Remarks on the dump for the injector*

The dump for the injector will be designed for $E_0 \leq 300$ MeV, $P_{ave} \leq 12$ kW, $I_{ave} \leq 40$ µA and $N_t \leq 2.5\times10^{13}$. A similar layout as presented for the main dump can be chosen. The length of the absorber would be adjusted to about 1.2 m to match with the lower energy. The graphite core can be reduced to a diameter of about 100 mm, since slow sweeping is not required at these power levels. The spot size limit for a full bunch train ($2.5\times10^{13}$ $e^-$) is about $\sigma \geq 1$ mm and fast (intra-bunch train) sweeping may be used, if the beam cannot be sufficiently defocused by optics. A tilted window, coated with an OTR reflecting material, is proposed to integrate a beam profile measurement. This approach may also be used for the main dump, but the required useful aperture of 200 mm is already quite large in that case. Due to the tilt, the actual window size will even exceed this value and the design effort is more challenging with respect to mechanical strength, dissipated power and operating temperatures. Nevertheless, the OTR option will be considered as well for the main dump systems.

## 4.8 Synchronisation system for the XFEL

### 4.8.1 Introduction

Studies of ultra-fast systems, with changes occurring on a timescale of less than 100 fs, are typically carried out with pump-probe laser experiments. Time-dependent phenomena are stimulated by a high-power pump-pulse, for example, with an ultra-fast optical laser or a laser-driven source, and then probed after a defined time delay. By repeating the experiment for different delays, the system changes can be recorded and the underlying dynamics understood. These sorts of experiments require a high level of synchronisation and information about the arrival-time of the pulses.

In the standard setup, shown in Figure 4.8.1, the pump and the probe beam have a common source, so that precise time-delays can be produced with optical path-length differences.

The time-resolution can be as short as a fraction of a femtosecond and is limited only by the overlap of the pump and the probe pulses **[4-106, 4-107]**.

The situation is different for FELs due to the fact that high-energy, high-charge electron beams serve as the driver for the FEL lasing process, and thus, the probe x-ray source is entirely distinct from the optical pump laser source located in the experimental area.

Synchronisation of the electron beam arrival to the arrival of the optical laser pulse with femtosecond precision is highly difficult. Generally, knowledge of the time-difference between the x-ray pulse and the optical laser pulse is sufficient to do pump-probe experiments.

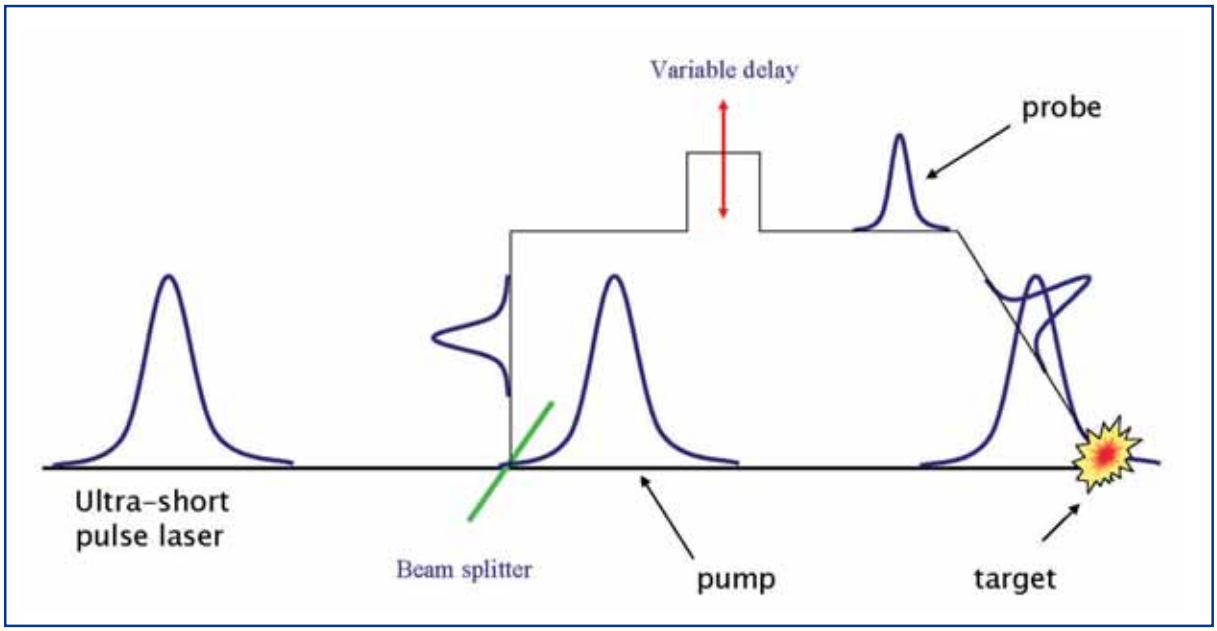


***Figure 4.8.1*** *Layout of a pump-probe experiment using a common source for a pump and probe beam.*

Post-sorting of experimental data according to the difference in the beam arrival-times has been demonstrated at the Sub-Picosecond Pulse Source (SPPS). The electron bunch arrival-time with respect to the optical laser was determined with an electro-optical technique that required transport of the 800 nm short-pulse optical laser over a distance of 150 m **[4-108, 4-109]**. An accuracy of 20-40 fs rms was achieved.

Because the incoherent undulator radiation produced at SPPS is a direct map of the longitudinal beam profile, the measurement of the x-ray pulse arrival-time is limited by the accuracy with which the electron bunch arrival can be determined. For FELs, this is not necessarily the case, because, often, only a small fraction of the bunch will lase. If this fraction is not always the same, then the post-sorting loses accuracy. For a 60 fs rms bunch-duration, a variation of the lasing region by as much as 25 percent, as for example,

in the case of a time-varying transverse-longitudinal tilt, the post-sorting resolution is not better than 15 fs.

Ideally, one would like to measure the arrival-time of the x-ray laser pulse and not just of the electron beam. This requires a geometrical time-sweep technique in which the pump and probe lasers are crossed on a tilted surface or within an interaction volume, so that the timing information is available in the spatial-domain **[4-110, 4-111]**. This technique is, so far, limited by the spatial resolution of the read-out system, which is on the order of 20-40 fs rms (see Section 6.2.2).

### *4.8.1.1 Electron beam stabilisation and arrival-time*

The reliable and stable production of x-ray laser beams with pulse-durations less than 100 fs imposes completely new demands on the synchronisation system for the accelerator and its sub-systems. Phase and amplitude errors of the accelerator RF can cause undesired fluctuations of the electron beam peak-current, change the slice-emittance within the electron bunch, and introduce variation in the arrival-time of the beam at the undulator.

The demanding tolerances on the RF regulation are related to the longitudinal electron beam compression process. The compression is needed because state-of-the-art electron beam sources, RF-photoinjectors, are optimised for the tight requirements on the transverse emittance. The peak current of the RF-photoinjector is, therefore, limited to about 50 A. The beam is longitudinally compressed by introducing an energy-chirp, through off-crest acceleration, into a bunch and then passed through a magnetic chicane. The energy-dependent path-length in the chicane causes a linear shearing of the longitudinal phase-space yielding a shorter bunch at the chicane exit. To achieve 5 kA peak-current, the overall compression-factor, C, must amount to 100 for the XFEL. A deviation of 0.1% in the initial beam energy chirp, however, changes the peak-current at the exit of the last chicane by 10%.

The electron beam arrival-time at the undulator is primarily determined by the time the beam exits the first electron bunch compressor. The time can be approximated by[6]:

$$\sum_t^2 \approx \left(\frac{R_{56}}{c_0}\frac{\sigma_A}{A}\right)^2 + \left(\frac{C-1}{C}\right)^2 \left(\frac{\sigma_\varphi}{c_0 k_{rf}}\right)^2 + \left(\frac{1}{C}\right)^2 \sum_{i,t}^2$$

where R56 = 0.1 m is the momentum compaction of the first chicane BC1, $k_{rf}$ = 27.2 $m^{-1}$ is the RF wave number, $\sigma_A$ and $\sigma_\Phi$ are rms amplitude and phase jitter of the acceleration section prior to BC1, and $c_0$ is the speed of light. $\sum_{t,i}$ denotes the incoming beam arrival-time which is significantly compressed (C>>1).

[6] The contribution of the third harmonic cavity to linearise the longitudinal phase-space is neglected.

A small amplitude deviation of 0.01% of the acceleration field already causes a timing jitter of 33 fs at the undulator. A correlated phase variation of 0.01°, due to a phase change of the local oscillator for the RF down-converter, changes the arrival-time by 21 fs. Electron beam arrival-time stability in the order of a few femtoseconds will, therefore, be extremely difficult, if not impossible to achieve with present day technology of the low-level RF cavity regulation. Furthermore, this example shows that the major challenge of the synchronisation for the XFEL is the large distance of more than 3 km between two of the most critical timing devices: the booster acceleration-section and the pump-probe laser system.

Figure 4.8.2 shows the measured arrival-time stability of the electron beam at the VUV-FEL **[4-112]**. The observed timing-jitter of about 200 fs rms is consistent with the observed amplitude-jitter of the first RF acceleration section and a sensitivity of about 5 ps per percent amplitude variation.

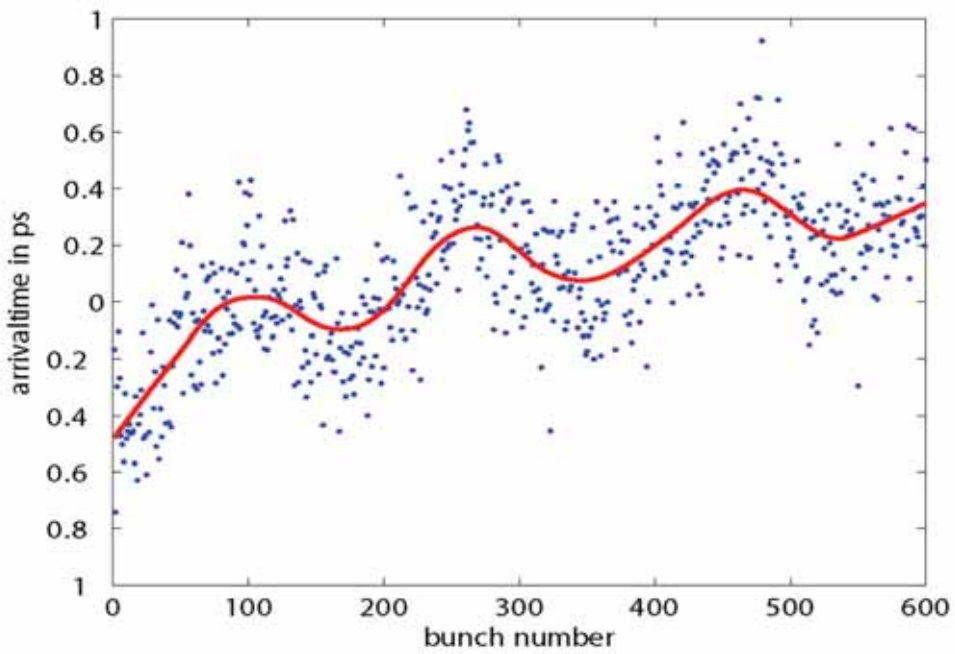


***Figure 4.8.2*** *Timing jitter of the electron beam at the exit of VUV-FEL acceleration linac determined by an electro-optic setup. The rms jitter over five minutes amount to 270 fs, and to 200 fs when the slow drift is removed* **[4-112]**.

### *4.8.1.2 Sub-femtosecond synchronisation*

In the previous section, the difficulties of synchronising the electron bunch and an external reference that serves as a clock for pump-probe lasers has been discussed. To go beyond the limitations of RF system stability, the charge distribution of the electron bunch should not be the relevant carrier of the timing information. This can be achieved with electron-beam manipulation lasers acting on a longitudinally defined sub-ensemble of the electron beam. If the electron beam manipulation occurs downstream of the last bunch-compressor section, then the synchronisation problem is reduced to the locking of the manipulation and the pump laser to one another.

One possibility proposed for the XFEL, based on the use of a femtosecond laser system in conjunction with the x-ray SASE beam, accommodates a technique for the production of attosecond long x-ray pulses **[4-112]**. The basic layout of the attosecond x-ray source is sketched in Figure 4.8.3.

In this scheme, an ultra-short laser pulse is used to modulate the energy of electrons within the femtosecond slice at the manipulation-laser frequency. The manipulation laser pulse has to overlap with the central area of the electron bunch. To modulate the electron beam energy, laser pulse and electron bunch collinearly pass a few-period modulator-undulator tuned to the central wavelength of the laser. The energy-modulation depth and chirp provided by the mJ-level two-cycle laser allows for generation of a single 300 attosecond x-ray pulse. This x-ray pulse is then separated from the SASE radiation of the un-modulated beam using a monochromator. Further details are described in **[4-113]**.

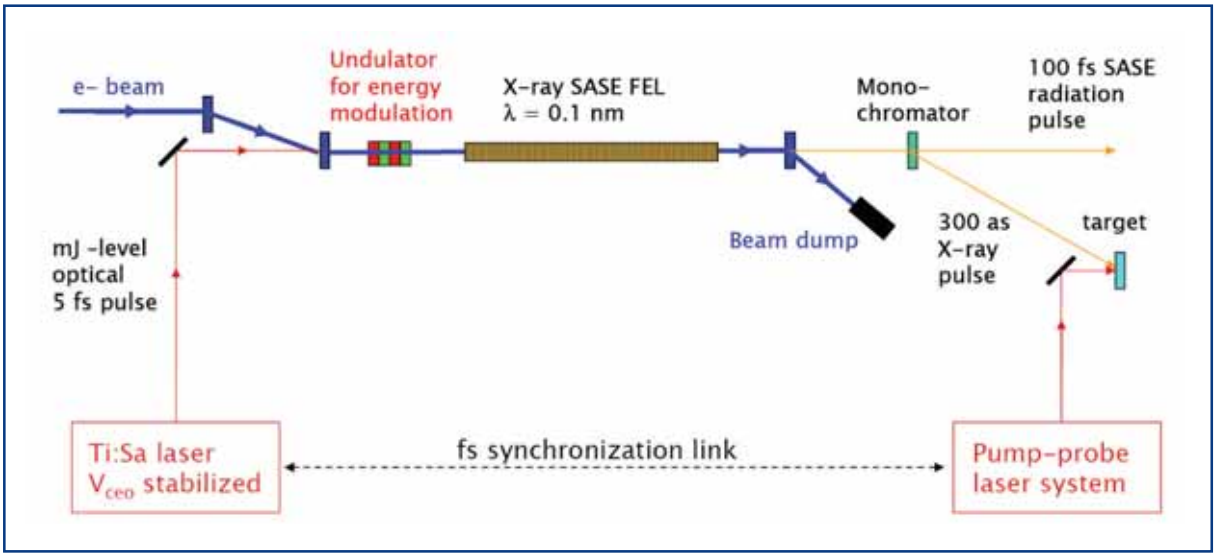


***Figure 4.8.3*** *Scheme of the layout for attosecond x-ray production. The synchronisation of the attosecond pulse is determined by the two-cycle laser and independent of the electron beam arrival. The manipulation and the probe laser have to be locked to one another.*

Unlike the option of post-sorting experimental data, the reliable generation of atto-second x-ray pulses requires the electron bunch to be synchronised to the manipulation laser to within a fraction of the electron bunch duration (~30 fs rms). Furthermore, investigations of physical processes in a pump-probe configuration using the 300 attosecond x-ray pulses, now mean the synchronisation between the two laser systems must be maintained with femtosecond precision. The few-cycle laser will be housed upstream of the SASE undulator at a distance of 1 km to the pump laser located in the experimental hutch.

### *4.8.1.3 Requirements of the XFEL synchronisation system*

The synchronisation system for the XFEL has to meet the following requirements:

- it should serve as a timing reference to the XFEL, providing femtosecond stability between all significant points throughout the facility with small or negligible drifts over days and weeks. This reference system must be self-contained, without the need for recalibrations;
- it must provide RF signals or the possibility to lock ultra-low-noise RF local oscillators to the timing reference at different frequencies;
- it must provide a mechanism to lock various laser systems, as in those used for electron beam generation, beam diagnostics, pump-probe experiments, seeding, and other applications;
- the system stability, robustness, and maintenance should not limit machine availability or delay commissioning;
- the failure modes should be transparent and allow for rapid repair and start-up;
- expenditure should be moderate and cost-effective.

The synchronisation accuracy requirements are only achievable through an optical distribution of the timing signals, even though there is decades more experience with RF-based timing distribution through coaxial cables. This is because the sensitivity of optical phase-detectors far exceeds the capability of RF phase-detection. The robustness of the optical system has yet to be demonstrated, although the potential is present. The constraints and needs of a stable optical synchronisation system must be studied in an accelerator environment. This is why a prototype will be thoroughly developed and tested at FLASH at DESY. Due to the newness of the optical technology and the proven techniques of the RF technology, a hybrid system is a likely choice, in order to exploit the advantages of each.

## 4.8.2 Layout of the XFEL synchronisation system

This section describes the layout and main components of an optical synchronisation system as sketched in Figure 4.8.4. The system was first proposed by the Massachusetts Institute of Technology (MIT) **[4-114, 4-115]** and is currently being developed collaboratively by MIT, Sincrotrone Trieste and DESY.

To provide a stable timing-reference with a master-laser oscillator (MLO), one must lock the laser to a low-noise RF oscillator or to an atomic clock based on an optical frequency standard, as described in Section 4.8.2.1. The MLO under consideration is a mode-locked fibre laser that produces a stream of short optical pulses centred at a wavelength of 1550 nm. The pulse-stream is distributed in a dispersion-managed optical fibre to compensate for the pulse-broadening effects of non-linear dispersion. A fraction of the optical pulse-stream is sent back through the same fibre for stabilisation purposes. By correlating the arrival-time of the return pulses with pulses directly delivered from the MLO, the round-trip time is kept constant by means of a feedback loop that changes the length of the optical fibre.

The possibility of using optical cross-correlation of ultra-short pulses with about 200 fs FWHM duration to stabilise the optical-link provides:

- excellent sensitivity to detect optical path-length variations. A 1% change in the cross-correlation signal between the MLO and the return pulse corresponds to 2 fs difference in the group velocity delay;
- a detection process that is potentially drift-free. The pulse-duration sets an upper-limit on the possible drift because the two pulses must overlap. Furthermore, all critical devices used are optical elements with negligible or very small but controllable thermal dependence.

The laser pulse-stream used to stabilise the optical link also provides the timing information to the accelerator sub-systems. It is important to use a detection mechanism for the accelerator sub-systems that is equivalent to the one used for the fibre link stabilisation. While for cross-correlation, the time-slice with largest derivative of the envelope is used, a measurement of the centre-of-mass of the laser pulse envelope or any other parameter which is rigidly related to the laser-pulse envelope is also an option. To ensure the success of different detection schemes, the frequency spectrum and the output chirp of the laser pulse exiting the MLO have to be sufficiently stable. Thus, currently available commercial fibre lasers are not specified to the extent necessary for this application and one has to expect that these lasers are not optimised for low phase-noise performance.

The longest round-trip time of the laser pulses through optical links in the XFEL Facility is 30 microseconds. Corrections for faster fluctuations of the optical path-length cannot be made and it depends on the short-term stability of the link end-stations how much these uncorrectable path-length fluctuations impact on the final synchronisation precision. The limitation due to the round-trip time will be explored in the near future.

The laser pulses distributed in the facility can be used, in some cases, for a high-accuracy direct timing measurement. For example, the electron beam arrival-time can be detected from a simple pickup with broadband electro-optical modulators (EOMs) developed for the telecommunication industry (see Section 2.2.4). EOMs can also be used to precisely detect the phase of the acceleration RF in superconducting cavities, by sampling the RF with the laser pulse-stream of the timing reference system. Similar techniques allow for measurement of the arrival-time of picosecond-long laser pulses, where optical cross-correlation is difficult to apply.

The second application where optical timing pulses are of great advantage is the synchronisation of various other laser systems used throughout the facility. For example, by frequency doubling the 1550 nm to 775 nm, a regenerative Titan-Sapphire amplifier can be seeded, as proposed for the optical-replica synthesis experiment at the FLASH/ VUV-FEL.

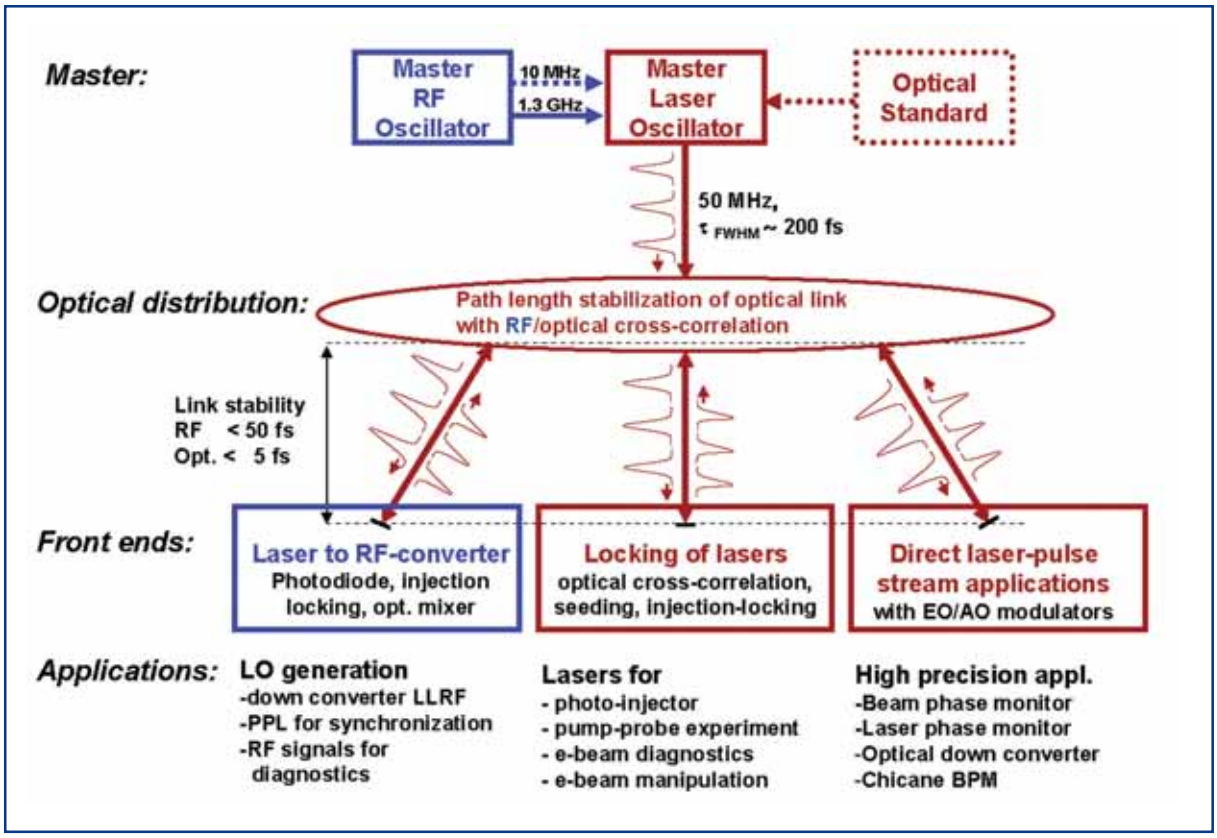


***Figure 4.8.4*** *Scheme of the laser-based synchronisation system for the XFEL. Three levels can be distinguished: the MLO providing a stream of identical optical pulses at a defined repetition rate.The length-stabilised fibre-link distribution to all timing critical devices in the facility and front-ends classified in three different types and their applications.*

Bunch length measurements, for instance, by EOS can be carried out by directly using the optical pulse-stream of the timing system, eliminating the need for an extra laser system. Optical cross-correlation by sum-frequency generation between the optical timing pulses and a laser system providing ultra-short laser pulses allows for precise monitoring or the operation of phase-lock-loops with femtosecond stability **[4-116, 4-117]**. Laser systems can also be synchronised directly through injection-locking, where the master-laser pulse-stream is injected into another mode-locked laser oscillator to be synchronised **[4-118]**.

For the control of the acceleration RF, the optical pulse-stream has to be converted to an RF signal without loss of timing accuracy. Several different techniques providing a clean RF reference are discussed in Section 4.8.2.3.

### *4.8.2.1 Frequency combs*

This section will discuss the issues that go into the choice of mode-locked lasers for timing applications. The following material is a summary of reports about optical mixers and attosecond synchronisation **[4-119, 4-120]**.

Recently, new insight into the frequency and noise characteristics of mode-locked lasers has initiated intense research activities in new directions. In the frequency domain, the pulse-train from the mode-locked laser contains millions of regularly spaced frequency lines, which is often called an optical frequency “comb”. Figure 4.8.5 shows the time-frequency correspondence between the pulse train and the frequency comb.

By stabilising the spacing (repetition frequency) and the offset (carrier envelope offset frequency) of the frequency comb, one can measure an arbitrary optical frequency with unprecedented accuracy. This frequency property of mode-locked lasers has enabled precision frequency spectroscopy and provided a platform for an optical atomic clock **[4-121]**.

Another interesting and important aspect of the pulse trains from mode-locked lasers is their excellent noise performance. Mode-locked lasers can produce extremely low jitter RF-signals as a form of optical pulse trains **[4-122 – 4-124]**. Due to their excellent phase-noise performance, mode-locked lasers are expected to serve as a master clock source for systems requiring stringent synchronisation performance, such as high speed (>GHz), high-resolution optical sampling, analogue to digital converters (ADCs) and large-scale optical clock signal distribution and synchronisation systems, such as those needed for fourth generation light sources and advanced accelerator systems.

The RF-signal is encoded in an optical pulse train, as shown in Figure 4.8.5. By direct photo-detection with a fast photodiode, the optical signal is converted to an electrical signal with frequency components of the fundamental repetition frequency ($f_R$) and its harmonics up to the detector bandwidth. By bandpass filtering the desired frequency component ($nf_R$), we can extract the RF signal from an optical pulse train. Figure 4.8.6 illustrates direct photo-detection for the RF signal regeneration from optical pulse trains.

Although the RF signal encoded as an optical pulse train exhibits an extremely low timing jitter of sub-10 fs levels **[4-123, 4-124]**, the extraction of a clean RF signal from the pulse train is a non-trivial task.

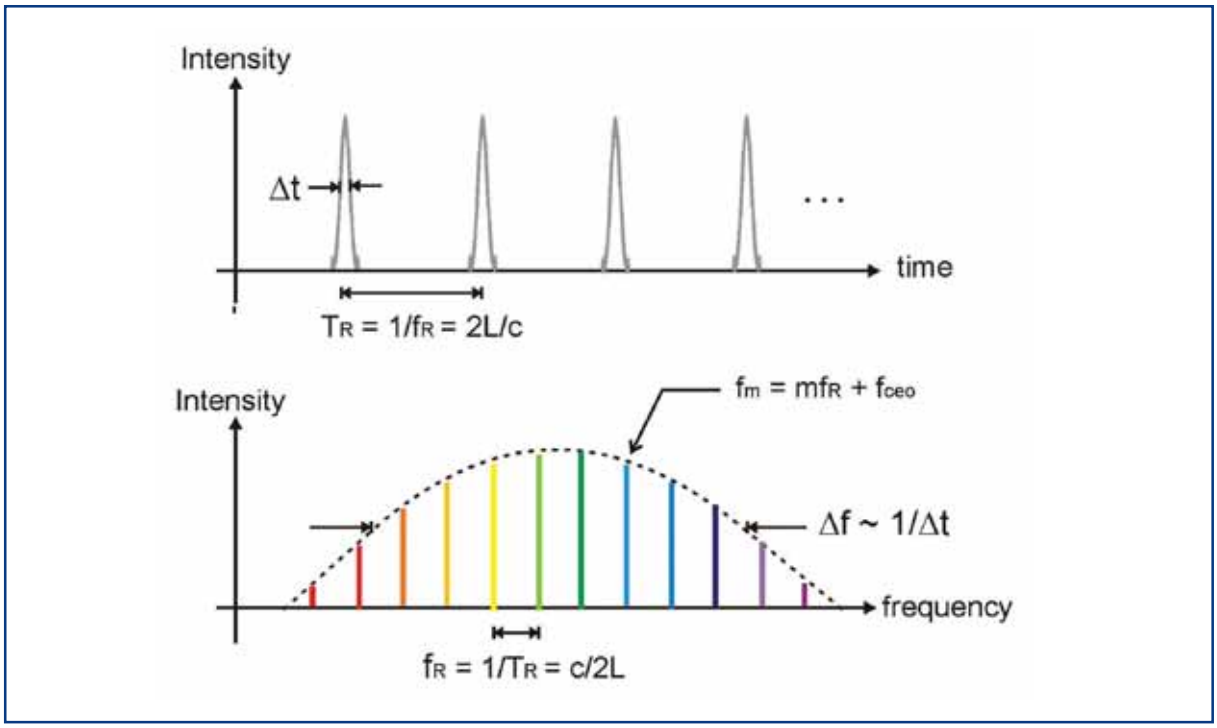


***Figure 4.8.5*** *Time-frequency correspondence between the optical pulse train in the time domain and the frequency comb in the frequency domain. The pulse train has a period of $T_R$, the same as the round-trip time (2 L/c where L is the laser cavity length and c is the velocity of light) in the laser cavity. In the frequency domain, this pulse train corresponds to regularly spaced frequency lines whose bandwidth is inversely proportional to the pulse width ($\Delta f \sim 1/\Delta t$). The spacing corresponds to the repetition frequency $f_R = 1/T_R$, and the whole comb lines are shifted by an offset frequency $f_{ceo}$. Each comb line can be expressed as $f_m = mf_R + f_{ceo}$ (m=integer).*

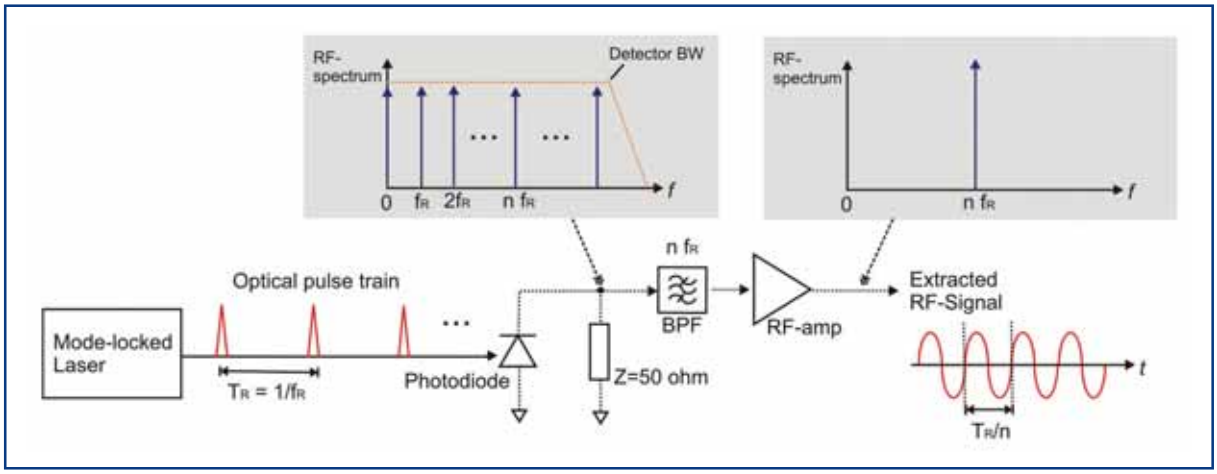


***Figure 4.8.6*** *Direct photo-detection for the RF signal regeneration. The optical pulse train is converted to an electrical signal by a photodiode. By proper bandpass-filtering, we can extract the desired RF signal. BPF: bandpass filter; BW: bandwidth.*

### 4.8.2.2 *Choice of the master-laser oscillator*

Mode-locked fibre lasers are a natural choice for an MLO, because of the ease of coupling into the fibre distribution system, their excellent long-term operating stability, and the well-developed and mature component base available at the optical communications wavelength of 1550 nm. Fibre lasers can generate pulses from picosecond down to 35 fs in duration by simultaneous phase-coherent lasing of multiple longitudinal modes spaced in frequency domain by the pulse repetition rate of the laser.

Mode-locking is initiated by a mechanism providing lower loss (hence, higher net gain) for a pulse than for CW radiation, leading to pulse formation from intra-cavity noise as soon as the laser reaches a certain intra-cavity power **[4-125]**. For passively mode-locked lasers, this is achieved by a real or artificial saturable absorber. Non-linear polarisation evolution in combination with a polariser, serves as an artificial saturable absorber. Non-linear polarisation rotation can occur in an optical fibre when the initial polarisation state is elliptical. The ellipse can be resolved into right- and left-hand circular polarisation components of different intensities. These two circular components then accumulate different non-linear phase shifts related to the intensity dependence of the refractive index (Kerr-effect $n(I) = n_0 + n_2 I$). The polarisation ellipse rotates while maintaining its ellipticity and handedness. An optical fibre is particularly well suited for non-linear polarisation rotation because the small mode diameter leads to high intensities, and thus, to a large non-linear refractive index change. Figure 4.8.7 shows how non-linear polarisation rotation can be used in conjunction with bulk polarisation optics to obtain an artificial saturable absorber.

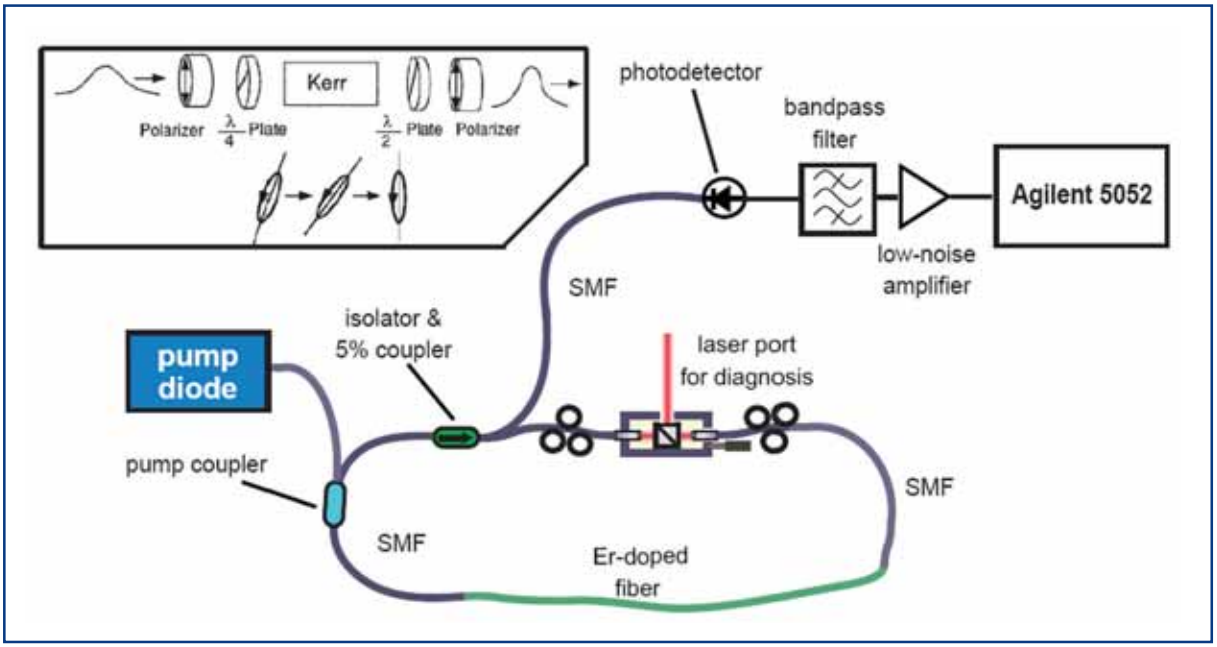


***Figure 4.8.7*** *Scheme of the Erbium-doped fibre laser generating the optical pulse-stream for synchronisation. The Erbium fibre is pumped by commercial diodes at 980 nm wavelength. Passive mode-locking is achieved by an artificial saturable absorber. The inset sketches the polarisation change after the polariser due to Kerr-nonlinearity. A 5% output coupler is used to determine the phase-noise spectrum of the laser-pulse-stream via photo-detection.*

While propagating through the fiber, the polarisation of the intense centre of the pulse is rotated more than that of the wings. Before going through the polariser, a polarisation controller rotates the polarisation such that, the centre of the pulse passes the polariser and the wings are absorbed. The second controller makes the polarisation elliptical before the pulse enters the fibre again.

One of the key features of the MLO is the possibility of generating multiple RF frequencies from the same source with very low phase-noise performance. For offset frequencies above 1 kHz, the intrinsic phase-noise of a free-running fibre laser is comparable to the best commercial microwave oscillators. This is due to the high equivalent microwave Q of the fibre laser, the long upper state lifetime of Erbium (~ ms) which results in the low-pass filtering of pump-power noise for frequencies above 1 kHz. Figure 4.8.8 shows the single-sideband phase-noise spectrum, L(f), of the harmonic at $f_0$=1.3 GHz extracted from the pulse train upon photo-detection and filtering. This phase-noise spectrum can be converted into timing jitter using:

$$\Delta t = \frac{\sqrt{2\int L(f')df'}}{2\pi f_0}$$

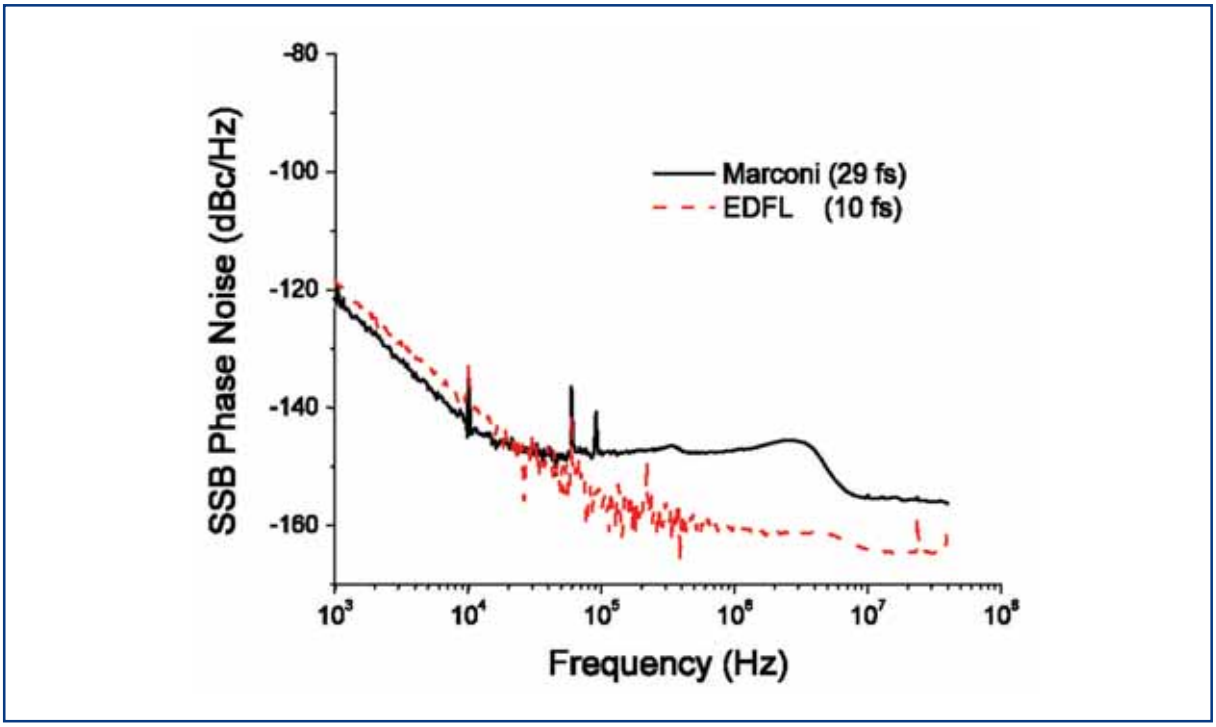


***Figure 4.8.8*** *Single-sideband phase-noise spectrum of the MLO, measured at a frequency of 1.3 GHz. The integrated timing jitter in a band from 1 kHz to half the repletion rate of the oscillator amounts to less than 10 fs, limited by the phase detector. For comparison, a good RF-oscillator (black curve) is also plotted.*

The integrated timing jitter from 1 kHz to the Nyquist bandwidth, i.e., half of the laser repetition rate, is measured at about 10 fs, limited only by the photo-detection process. For comparison, the phase-noise of a very low-noise frequency generator, a Marconi 2041, is also plotted.

At lower offset frequencies, the laser is susceptible to environmental perturbations (microphonics, temperature, etc.). By phase-locking the fibre laser to a low phase-noise commercial RF oscillator, these environmental perturbations can be eliminated. The phase-noise of the locked fibre laser will follow the microwave oscillator for offset frequencies up to the unity gain of the PLL and still has the excellent high-frequency properties of a free-running laser. After photo-detection, a harmonic of the laser repetition rate is picked by a suitable bandpass filter and compared to the reference oscillator in a phase detector. After amplification and filtering, this signal is fed to a piezo-based fibre stretcher incorporated into the laser cavity and it adjusts the repetition rate.

### *4.8.2.3 Laser to RF conversion*

To convert the optical pulse-stream to a clean, high-frequency RF signal (MHz-GHz) with sufficient output power and without the loss of timing accuracy, in the following, three different schemes are discussed.

**Fast photodiodes**

To extract an RF signal with frequency $f = n f_R$, only a fast photodiode, a bandpass-filter tuned to the frequency $f$, and a low-noise amplifier, as shown in Figure 4.8.6, is required. For many applications, this scheme provides the most cost-efficient solution to deliver RF frequencies from 50 MHz up to 10 GHz. The limitations of the photo-detection process in terms of timing stability and drift performance are under investigation.

Recently, it has been shown that the extraction of an RF signal from an optical pulse train using direct photo-detection is limited in precision by excess phase-noise **[4-126]**. The major origin of this excess noise has been identified to be an amplitude-to-phase (AM-to-PM) conversion in the photo-detection process. Figure 4.8.9 shows the AM-to-PM conversion process in the photodiode. The AM-to-PM conversion factor is measured to range typically from 1 to 10 ps/mW **[4-124]**, depending on the bias-voltage and diode types. The amplitude noise of the laser can be converted into a significant amount of phase-noise by this conversion process. Here is one numerical example: if the conversion factor is 1 ps/mW and the applied optical power is 10 mW, the required amplitude regulation is within 0.1% to reach 10-fs jitter level, which is already a challenging requirement.

The sensitivity of AM-to-PM conversion can be significantly reduced by operating the photodiode close to saturation and by the use of additional laser amplitude stabilisation feedback through a fast amplitude modulator. The limitation of the output power delivered by photodiodes puts constraints on the achievable signal-to-noise ratio (SNR) of the regenerated RF signal. Since semiconductor devices typically show high temperature-sensitivity, the use of photodiodes may limit the performance for the long-term stable and drift-free operation of the RF signal regeneration. Theoretical and experimental investigations to explore the limitations on the phase-noise, drift performance and long-term stability of photo-detectors is, therefore, an important part of the near future R&D programme.

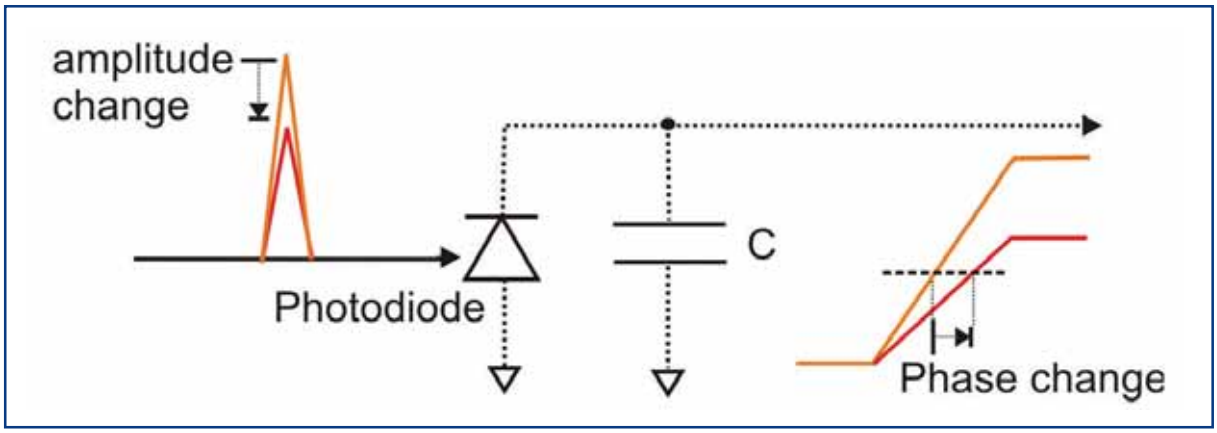


***Figure 4.8.9*** *Conceptual diagram of AM-to-PM conversion through direct photo-detection. Spatial charge distribution in the photodiode induces a change in the capacitance (denoted as C in the figure) of the diode. This results in a change in the phase of the converted electrical signal. By this process, amplitude noise in the optical domain is converted to phase-noise in the electronic domain.*

### Injection locking to low noise oscillators

If simple photo-detection is insufficient to generate an RF signal with the desired stability, it is possible to lock an external voltage controlled oscillator (VCO) to the laser pulse-train. A dielectric resonator oscillator (DRO) optimised for low phase-noise at high offset frequencies is suitable. A very simple and effective approach to achieve the phase locking is to make use of the phase pulling capability of the oscillator and injection lock the DRO.

The dielectric resonator acts as a high-Q bandpass filter. Part of its output is amplified and fed back to the resonator. This loop has to be kept on resonance to achieve a stable output, hence the net phase shift has to be n×360 degrees of the DRO resonance frequency. If a perturbation in the phase balance is introduced by an electronic phase shifter, the DRO will compensate for this shift by changing its centre frequency. The photo-detected laser pulse-train can be directly applied to the high-bandwidth phase shifter. This enhances the quality of the phase-lock significantly compared to applying a sinusoidal wave.

The unity gain can be adjusted by varying the amplitude of the phase perturbation. So this scheme only consists of a photo-detector, a variable attenuator, and the DRO, making it very cost-effective.

The key part is, however, the DRO. It has to have at least comparable high-frequency phase-noise properties to the MLO, as the PLL can only regulate up to a certain frequency (1-10 kHz). Therefore, the RF output signal reflects the DRO phase-noise above the unity gain frequency, while following the timing reference for lower frequencies.

In cooperation with Poseidon Scientific Instruments (PSI), an ultra-low phase-noise DRO has been developed **[4-127]**. The measured timing jitter is less than 4 fs, integrated from 1 kHz to 1 MHz at a frequency of 1.3 GHz (see Figure 4.8.10).The implemented

phase shifter has a bandwidth of 10 GHz. This enables the complete bandwidth transfer of ultra-fast photodiode signal, increasing the locking accuracy. Due to the nature of the process, injection locking is insensitive to offset drifts of the photo-detectors and only weakly sensitive to gain drifts.

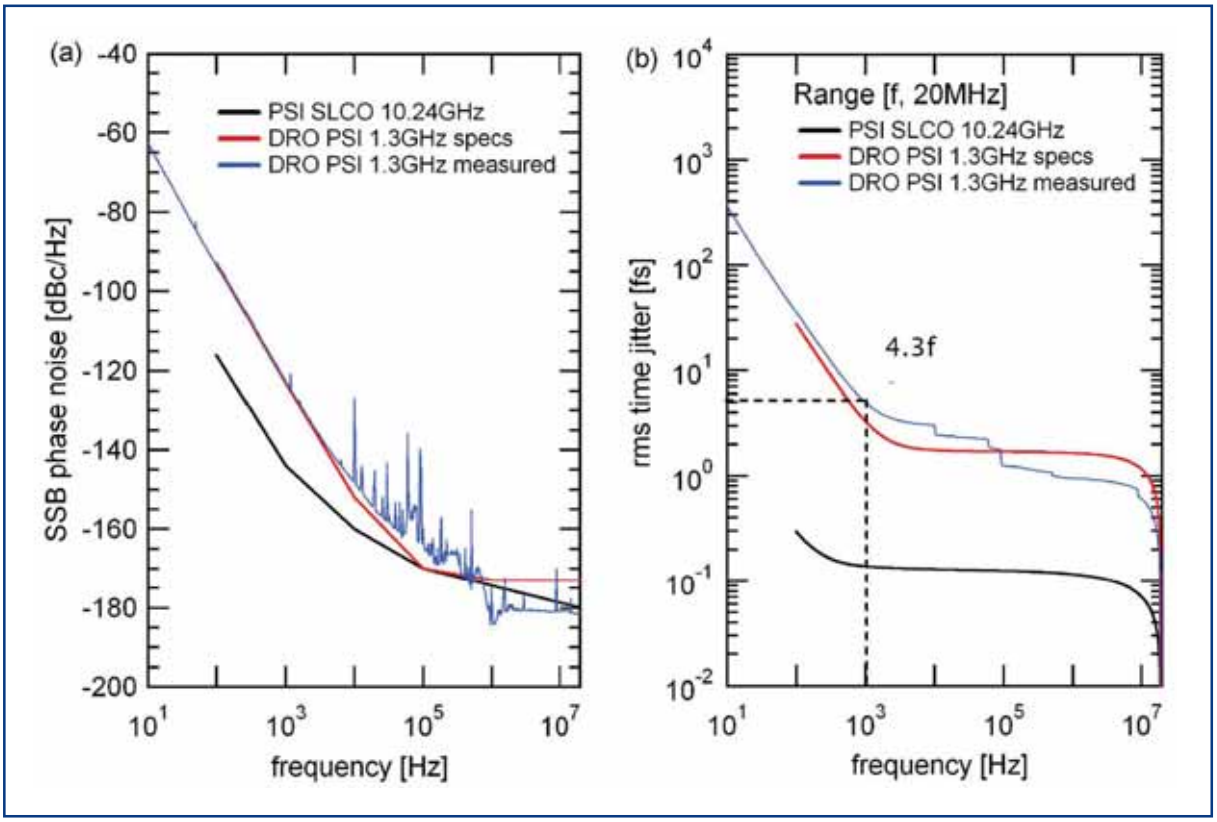


***Figure 4.8.10*** *(a) Single-side band phase-noise spectrum of the DRO produced by PSI. The DRO is a critical component for optical-to-RF conversion schemes. The red and blue curves shows the single-sideband (SSB) specification and measurement. For comparison, the black curve shows the best so far existing RF oscillator (10.24 GHz, Sapphire loaded SLCO from PSI) . (b) Integrated timing jitter between f and 20 MHz.*

### Balanced optical to RF phase detector

An entirely different technique to regenerate an ultra-low noise RF signal from the optical pulse-stream, which does not rely on the phase-detection by photodiodes, instead it uses optical-electrical hybrid PLLs **[4-128]**. As shown in Figure 4.8.11, the continuous wave RF-signal is generated by an ultra-low-jitter VCO as, for example, the DRO described above. The RF phase of the VCO is measured by a low-jitter, and to first order, drift-compensated optical-RF phase detector and regulated with the error signal of the phase detector by a low-noise loop filter.

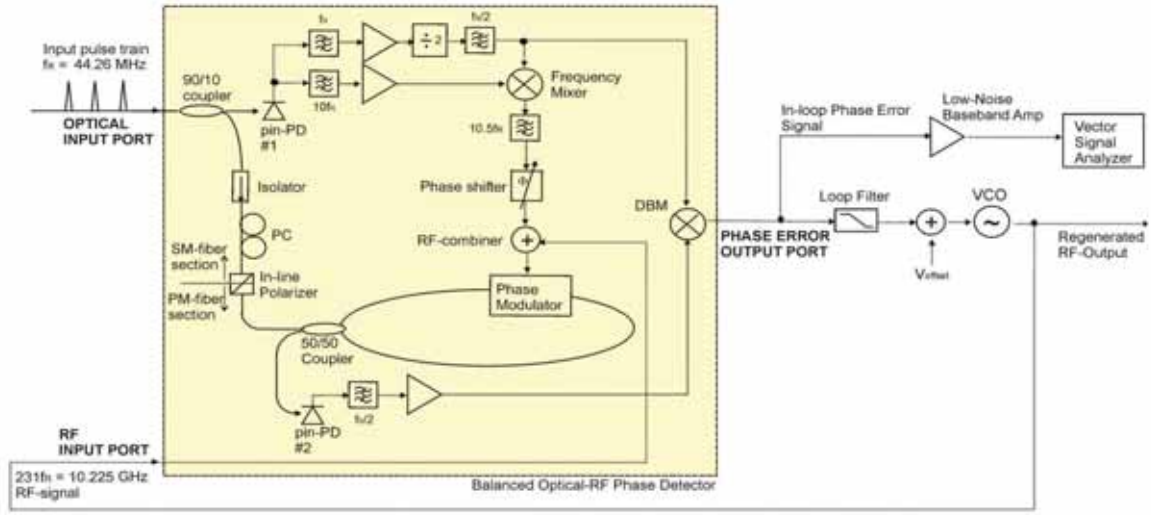


***Figure 4.8.11*** *Schematic setup for RF signal regeneration from an optical pulse train by use of the balanced optical-RF phase detector (yellow box) and a PLL. DBM: double-balanced mixer; PC: polarisation controller; PD: photodiode; PM: polarisation-maintaining; SM: single-mode; VCO: voltage-controlled oscillator. Solid line: optical beam path; dotted line: electric signal path.*

The optical-RF phase detector itself is marked by the yellow box. The photodiode #1 is used to generate a reference signal for a synchronous-detection scheme with half of the repetition frequency ($f_{R/2}$) of the incoming optical pulse-stream. The Sagnac-loop together with the phase-modulator, encodes the phase-error signal of the VCO in the amplitude of the $f_{R/2}$ frequency component detected by the photodiode #2. The mixer down-converts the phase-error signal at $f_{R/2}$ to the baseband through synchronous detection with the reference signal. This baseband signal is the phase error output of the balanced optical-RF phase detector.

A first measurement of the in-loop phase-noise of the balanced optical-to-RF phase detector is shown in Figure 4.8.12.

The voltage signal from the phase error output port was measured with a low-noise preamplifier and vector signal analyser (VSA) converted into SSB phase-noise at 10.225 GHz VCO operation frequency. The black line shows the in-loop phase-noise and the red line is determined by the VSA noise floor. The measurement shows an integrated in-loop timing jitter of 8.8±2.6 fs from 1Hz to 1MHz. The jitter will be significantly improved in the near future by using ultra-low-noise electronics, components with small drifts, and the PSI DROs.

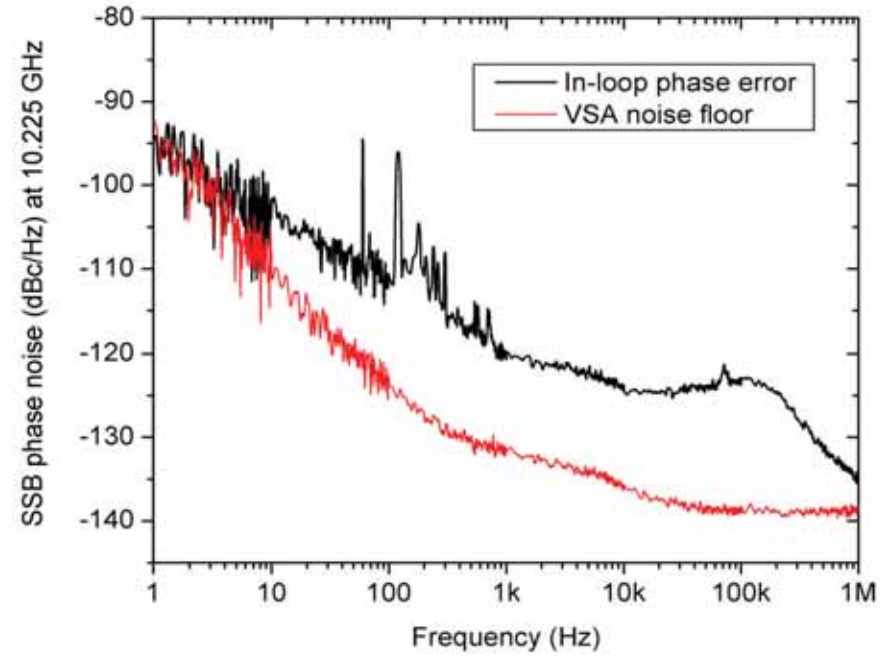


***Figure 4.8.12*** *The SSB in-loop phase-noise spectra at 10.225 GHz. Black line: in-loop phase-noise when it is locked. Red line: VSA noise floor. The integrated timing jitter from 1 Hz to 1 MHz corresponds to 8.8 fs ± 2.6 fs.*

### *4.8.2.4 Fibre length stabilisation: options and first results*

The stabilisation of the fibre transmission line is a crucial part of the optical synchronisation system. The stabilisation system needs to satisfy two aspects:

- it must have enough range to cover the total optical path length change over 3 km for all temperature variations that might occur;
- the resolution of the phase-detector should allow for a stability of ~ 10 fs over long timescales of minutes to hours.

Neither an RF-based system nor optical cross-correlation fulfils both requirements at the same time. Any present day RF mixer will drift with a coefficient of ~200 fs/K (at a frequency of 1.3 GHz), so will not be suitable for long-term stability. It, however, has a dynamic range of several 100 ps, compared to the optical cross-correlation where the range is given by the optical pulse length (~200 fs). Hence, a hybrid system of two feedbacks is required. One coarse RF-based feedback ensures that there is a coarse overlap so the optical cross-correlator can operate.

One of the main features to enable optical cross-correlation, is the dispersion management of the fibre. Since the pulse needs to be short after returning through the fibre, the net dispersion of the fibre link must be zero. This can be accomplished by using matching fibre parts with opposite sign and dispersion slope. When transmitting pulses with a duration of about 200 fs over long distances, higher-order dispersion also needs to be compensated. The choice of wavelength 1550 nm, makes manufacturing optical fibres with these properties possible. These have been available for a few years, driven by the demand of the telecommunications industry.

Another important aspect is the radiation hardness of the optical fibres used in the tunnel. Standard telecommunications fibre uses compounds during manufacturing that darken upon exposure to radiation. There are, however, commercially available fibres featuring significantly lower attenuation per km and dosage. With appropriate shielding of both fibre and localised radiation hotspots (collimators, bunch compressors, etc.), there is no anticipated problem with radiation induced attenuation in the fibre.

A sketch of the fibre link is shown on the left-hand side of Figure 4.8.13. A fraction of the laser light entering the fibre link is reflected back at the end for stabilisation purposes. This, together with laser pulses directly from the MLO, is used to operate the: (a) RF-based feedback and (b) optical cross-correlator. A fibre-stretcher for correcting high frequency perturbations and a delay-line for slower corrections serve as actuators for the feedback.

Tests have been performed with a RF-based feedback at the MIT-Bates laboratory **[4-129]**. In-loop measurements, on the right-hand side of Figure 4.8.13, indicated a stability of 12 fs closed loop over a timescale of 30 seconds, compared to about 60 fs open loop for a 500 m long fibre link. This very promising result shows that an RF-feedback alone is capable of stabilising the link over shorter time-scales on the order of 10 fs. From the measurement result no significant phase-noise degradation of the optical pulse-stream within the accuracy of photo-detection after transmission through the fibre link was observed. A fibre-link stabilisation system including different versions of optical cross-correlation (either by two-photon absorption or second-harmonic generation) is presently under investigation.

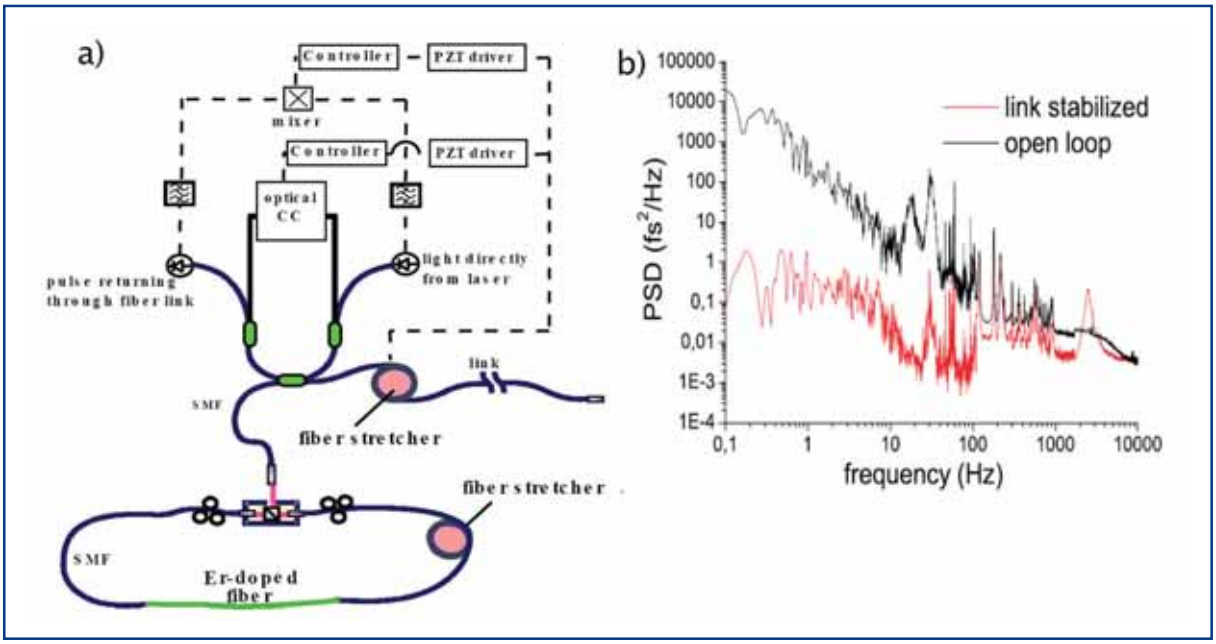


***Figure 4.8.13*** *(a) Scheme of the two feedback fibre link stabilisation system. The coarse fibre link feedback with a large dynamic range is realised by RF means. The high precision and long-term stability is realised by optical cross-correlation. (b) Phase-noise spectrum of open and closed feedback back loop using only RF stabilisation for a 500 m fibre link test at MIT-Bates.*

### *4.8.2.5 Beam phase monitor system*

In collaboration with Sinchrotrone Trieste[7] a compact, high-precision beam arrival-time monitor is being developed (see Figure 4.8.14). The arrival-time is measured by detecting the fast transient signal of a broadband beam pick-up. The pick-up consists of a ring-electrode held by two feed-throughs mounted at opposite sides of the ring. If an electron bunch passes the pick-up, a 200 ps-wide RF pulse is generated with a peak-to-peak voltage of more than 50 V. The large transients of ~0.5 V/ps at the zero-crossing of the signal, permit precise determination of the bunch arrival-time. For that, the beam pickup signal is fed into an EOM with appropriate bandwidth (more than 10 GHz is commercially available). A laser pulse from the optical timing system injected into the EOM at the proper time is sampling the RF pulse transient close to its zero-crossing. In this way the arrival-time of the electron bunch is encoded as an amplitude change into the laser pulse. The amplitude change of the laser pulse is detected by a photodiode and sampled with a fast ADC. Since the laser pulses from the timing system are directly used, no additional devices that may add timing jitter are required.

In first measurements, a resolution of 140 fs could be achieved, limited by readout noise of the photo-diode signal (1% rms). By improving the system components, sub-20 fs resolution seems to be feasible.

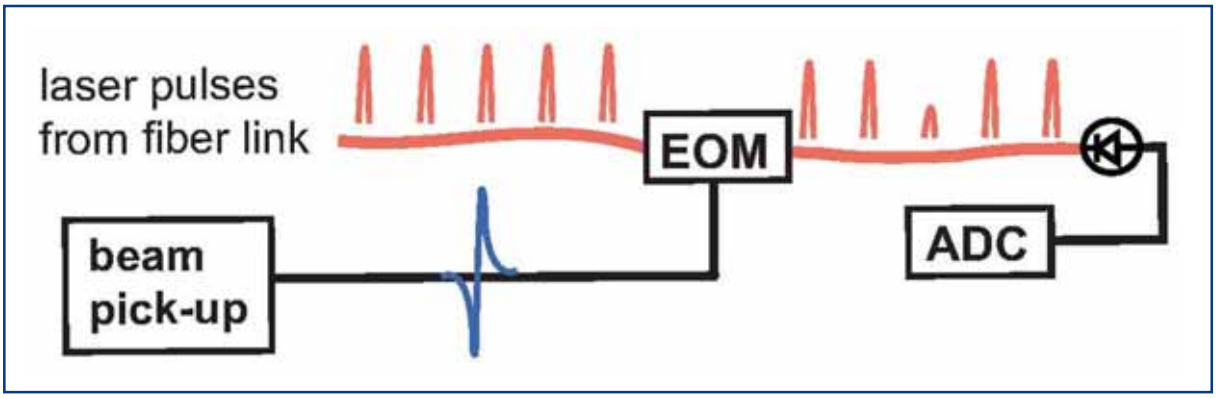


***Figure 4.8.14*** *Schematic setup of a beam arrival-time monitor system.*

A similar setup can be used for an ultra-precise BPM in the dispersive sections. Instead of the circular beam pick-up, used for the beam arrival-time monitor, a strip-line pick-up, mounted perpendicularly to the beam direction, is used. The pulses generated at each end of the strip-line are used as modulation signals for EOMs. The difference in the arrival-time of the pulses is proportional to the beam position along the strip-line.

## 4.8.3 Distribution of trigger and clock signals

The increased sampling rate of present day ADCs imposes significant stability constraints on the clock distribution system. It offers the possibility of direct In-phase/Quadrature (IQ) detection that is limited primarily by the jitter between the clocking frequency of the

[7] Work is funded in part by the EU FP6 contract 011935, EUROFEL.

ADCs and the signal to be sampled. To meet specifications this translates to an allowable timing jitter of less than 10 ps. Clock signals are normally understood as a continuous square-shaped signal used primarily to clock ADCs while a trigger signal indicates the start of an event. The timing of the trigger is much less critical than that of the clock signal, but the distribution is usually combined with the clock using pulse-width modulation.

The clock distribution for the XFEL will be based on readily available optical telecommunication technology that uses an optical fibre similar to the laser-based optical synchronisation system fibre. Clock and trigger signals are generated electronically and transferred to a CW laser by amplitude modulation. The receiver is a photodiode which converts the clock train back into the electronic domain. The demand for picosecond clock and trigger signal stability makes either a direct stabilisation of the optical path length of the fibre or a measurement and subsequent software correction mandatory. A fibre-length stabilisation at the femtosecond-level will be realised anyway to fulfill the demands of the optical synchronisation system. A combination of both systems is, therefore, desirable to reduce R&D effort.

Laser radiation of different wavelengths can propagate without mutual interference through a single optical fibre, enabling multiple channel transmission in optical telecommunication lines. A similar approach is chosen here. The clock distribution system can operate at 1,310 nm which is also a telecom wavelength, thus components are readily available. A wavelength division multiplexer (WDM) coupler is used to combine both the 1,550 nm laser radiation for the synchronisation system and the 1,310 nm radiation for the clock and trigger distribution system. Both wavelengths co-propagate until the end of the link, where a second WDM coupler separates both wavelengths to their respective receivers. These couplers offer an isolation of more than 40dB, so cross-talk between the two channels is negligible. The advantage of such an approach is that both synchronisation and the clock distribution system can operate interference free, but use a common fibre and stabilisation system. The wavelength difference between both channels will lead to a degradation of the link stability for the 1,310 nm system. However, the anticipated stability level is of better than 100 fs. This easily far surpasses the requirements of 10 ps stability for the XFEL clock system.

### 4.8.4 Synchronisation of the LLRF for the main linac

The phase reference system for the main linac must provide the local oscillator signal (f_lo = 1350 MHz) and the RF reference signal (f_ref = 1300 MHz) to the 25 RF stations in the main linac. Each RF station employs more than 100 downconverter channels which require a total RF power in the order of 1 W for local distribution at each RF station. To ensure high availability a redundant distribution system consisting of a coaxial and an optical line will be installed as shown in Figure 4.8.15. In both cases the distribution frequency is 50 MHz and the receiver electronics generates the required frequencies of 1,350 MHz (LO), 1,300 MHz (reference and klystron drive), 50 MHz (from which the ADC clock is derived) and 5 MHz (bunch clock signal).

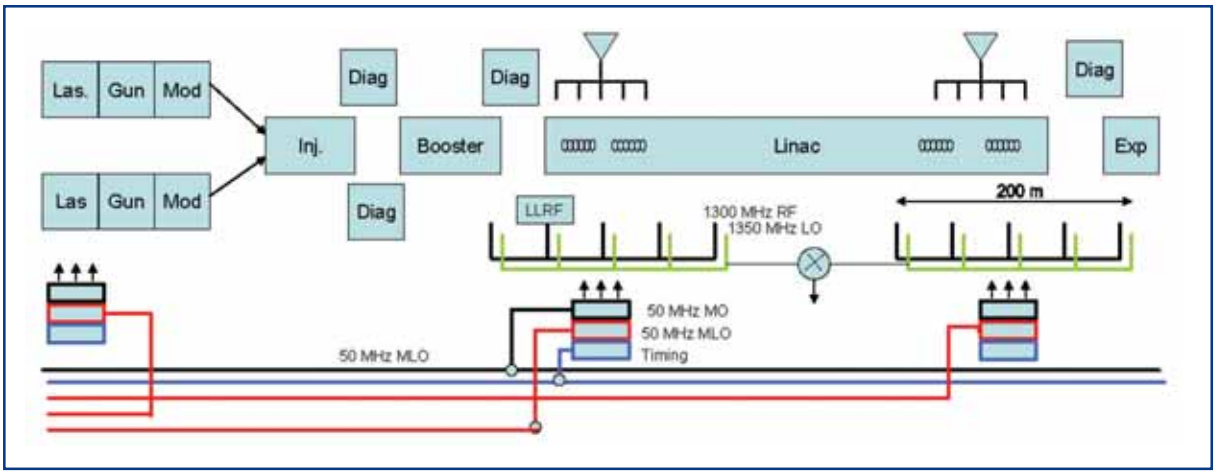


***Figure 4.8.15*** *The phase reference system of the main linac consists of a combination of coaxial and optical distribution systems to a few selected locations in the linac with coaxial sub-distribution for 5-7 RF stations.*

The coaxial system is extremely reliable due to the passive structure, can transport relatively high power levels to many tap points, and provide a reasonable long-term stability in the order of a few ps/km/deg C (consistent with a temperature coefficient of about 1 ppm/deg. C). For the short distances between two RF stations, the required phase stability of the order of 100 fs can be maintained. The fibre optical distribution is superior in stability (with active stabilisation) but provides only point to point connection and requires active RF components to provide the required power level.

The details of the distribution of the RF signals to one RF channel are shown in Figure 4.8.16. In the optical receiver, the 1,300 MHz and 1,350 MHz are generated by filtering of the desired harmonics of the 50 MHz while the harmonics in the coaxial receivers are generated by step recovery diodes or use of PLL loops. The clock signal is synthesised from the 50 MHz distribution signals and requires stability in the order of 5 ps rms. Trigger signals will be distributed through the timing system which will make use of the stability of the optical distribution.

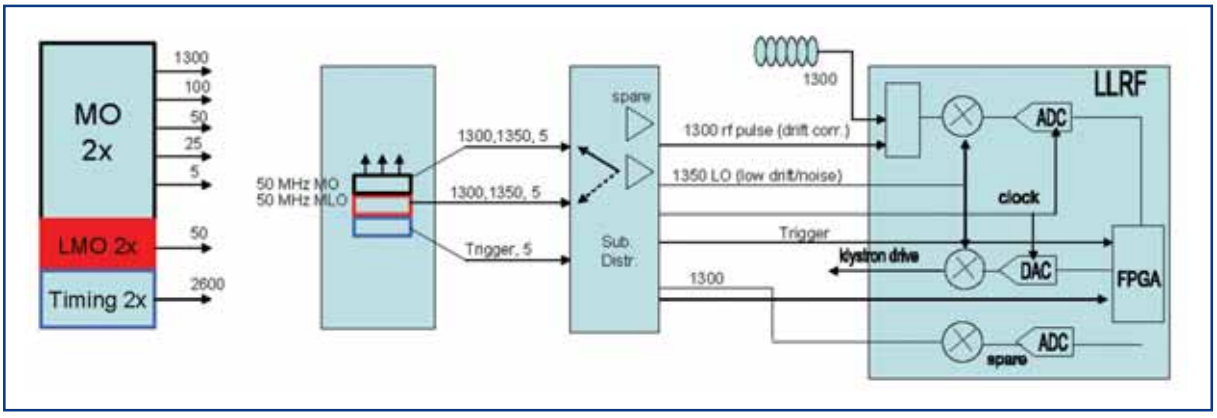


***Figure 4.8.16*** *The receivers for the optical and RF signal generate the required 1,350 MHz, 1,300 MHz, 5 MHz and clock signal (synthesised from the 50 MHz signal) for distribution to several RF stations.*

The sub-distribution of the 1,350 MHz and 1,300 MHz signals are achieved by phase stable 7/8" coaxial lines with a typical stability of better than 1.0 ppm/deg. C as shown in Figure 4.8.17. Redundant receivers and power amplifiers guarantee the required availability. Low cost fibre links with a stability of about 100 fs ensure good long-term stability.

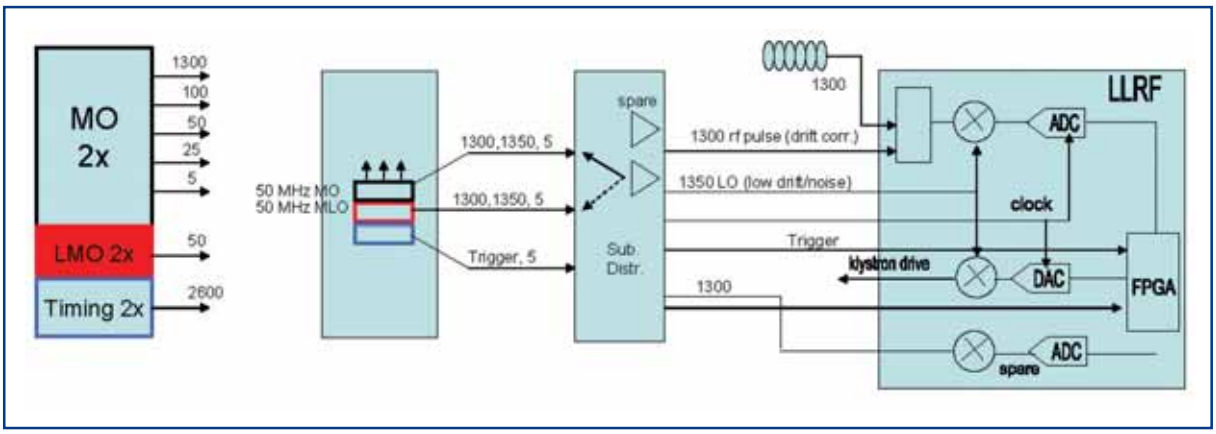


***Figure 4.8.17*** *Subdistribution of the 1350 MHz LO signal (same distribution for 1,300 MHz). The redundant receivers and power amplifiers ensure high availability. Low cost fibre optic references monitor the LO and RF reference stability at each RF station. The RF reference signal is distributed to each downconverter channel to provide on-line calibration.*

## 4.9 Summary of costs and manpower requirements

The capital investment and cost of the personnel necessary to realise the different sections of the accelerator complex as described in Sections 4.1 to 4.8 are summarised in this section. The basis for the cost estimate is the numbers and length of components specified here. For an overview about the total project cost, a description of the methodology of the performed estimate for capital investment, the determination of the costs for personnel and the expected uncertainties, see Chapter 10.

Table 4.9.1 gives a summary of the project cost in terms of capital investment and the cost of personnel for the accelerator complex. The relative distribution of the full costs for the accelerator complex is shown in Figure 4.9.1. The accelerator complex contributes about 35% to the overall capital investment and full costs of the XFEL project, in terms of cost for personnel, close to 40%. Integrated over the entire construction phase, 1,105.8 full-time equivalents (FTE) are required for the accelerator complex.

| | Capital investment [M€] | Personnel cost [M€] | Full cost [M€] |
|---|---|---|---|
| Superconducting linac | 199.69 | 48.64 | 248.32 |
| Injector | 9.38 | 5.87 | 15.25 |
| Bunch compressors | 13.28 | 10.08 | 23.36 |
| Electron beamlines | 38.61 | 20.86 | 59.47 |
| **Total** | **260.96** | **85.45** | **346.41** |

***Table 4.9.1*** *Project cost distribution for major items of the accelerator complex. Values are given for capital investment, personnel costs and full costs in Million-Euro.*

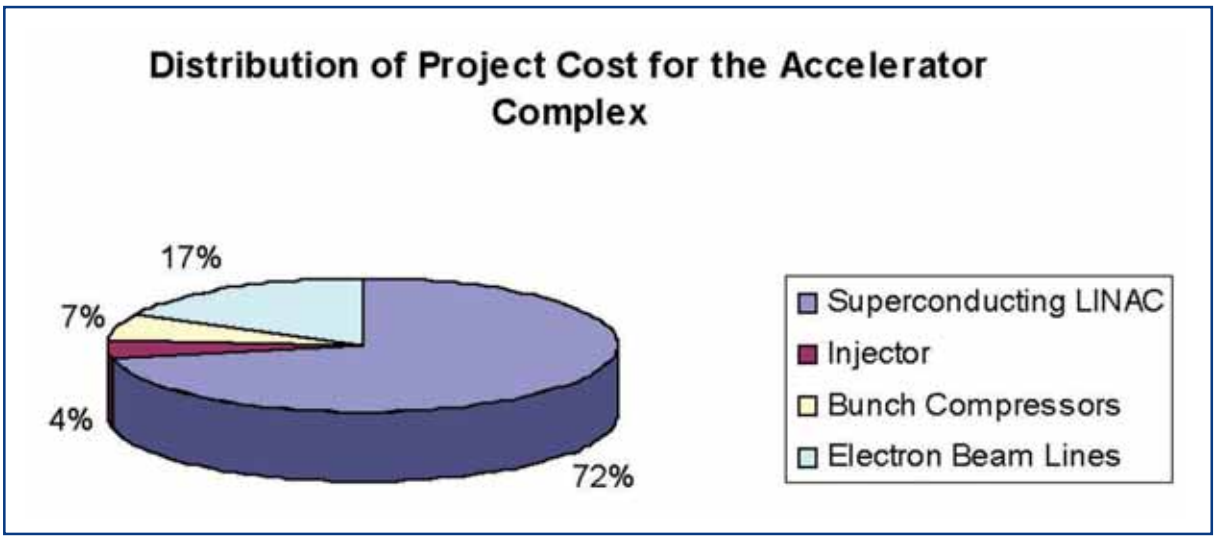


***Figure 4.9.1*** *Relative distribution of full project costs for the accelerator complex.*

The costs summarised in Table 4.9.1 and Figure 4.9.1 include the costs and manpower of the following components:

**Injector:** design and beam physics, electron RF gun and laser system, one accelerator module including the necessary high-power RF (modulator/klystron) and low level RF control components, beam diagnostic elements, beamline magnets and vacuum chambers, laser heater, installation and technical commissioning.

**Bunch compressors:** design and beam physics, beam diagnostic elements, all beamline components, i.e. magnets and vacuum chambers, installation and technical commissioning.

**Electron beamlines:** design and beam physics, collimation system, diagnostic systems, vacuum system and focusing/steering magnets from the end of the linac to the beam dumps (including undulator sections), kicker system for the beam distribution, trajectory stabilisation feedback and beam dumps.

**Superconducting linac:** is the largest item of the accelerator complex contributing close to 72% to its total costs; the cost structure of the superconducting linac is given in the following section.

### 4.9.1 Cost and manpower requirements of the superconducting linac

Table 4.9.2 and Figure 4.9.2 show the individual costs for the major components of the superconducting linac as described in Section 4.2. The individual costs are given in terms of capital investment, personnel costs and the full costs. Integrated over the entire construction phase, 636.8 FTE are required for the superconducting linac.

| | Capital investment [M€] | Personnel cost [M€] | Full cost [M€] |
|---|---|---|---|
| Modules | 24.31 | 7.11 | 31.42 |
| Cavities | 97.54 | 11.05 | 108.59 |
| RF system | 69.81 | 26.08 | 95.88 |
| Vacuum system | 6.44 | 3.91 | 10.36 |
| Beam diagnostic | 1.59 | 0.48 | 2.07 |
| **Total** | **199.69** | **48.64** | **248.32** |

***Table 4.9.2*** *Project cost distribution for major items of the superconducting linac. Values are given for capital investment, personnel costs and full costs in Million-Euro.*

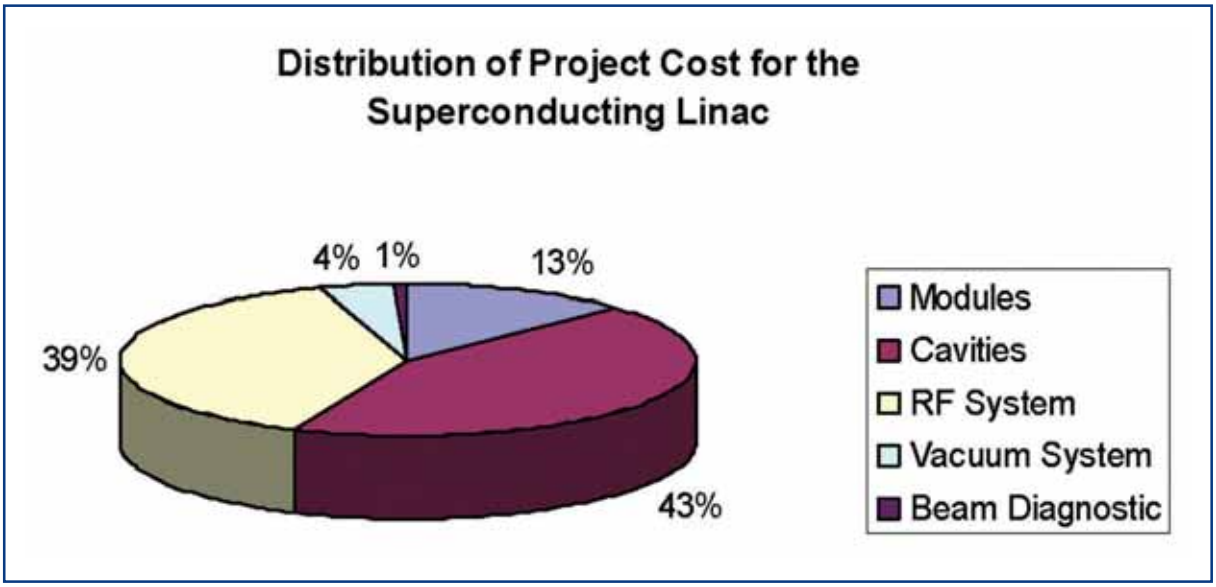


***Figure 4.9.2*** *Relative distribution of full project costs for the superconducting linac.*

The costs summarised in Table 4.9.2 and Figure 4.9.2 include the costs and manpower of the following components.

**Modules:** complete accelerator module cryostat and vacuum vessel, quadrupole magnets, assembly of the module, setup and supervision of fabrication, installation and technical commissioning.

**Cavities:** Niobium material, cavity fabrication and preparation, He tank welding and string assembly, input coupler, higher-order mode coupler, frequency tuner, setup and supervision of fabrication.

**RF system:** RF modulators, power supplies, transformers, klystrons, high voltage pulse cables, waveguide system, low level RF control, setup of fabrication and supervision, component test, installation and technical commissioning.

**Vacuum system:** inter-cavity connections, cold valves, flanges, insulation and RF coupler vacuum systems, vacuum pumps, installation and technical commissioning.

**Beam diagnostic:** beam position monitors.

## References

**[4-1]** R. Brinkmann et al. (eds.), *TESLA Technical Design Report – Part II: The Accelerator*, DESY 2001-011, pp. II-19, March 2001; http://tesla.desy.de

**[4-2]** P. Kneisel, G. Ciovati, G.R. Myneni, W. Singer, X. Singer, D. Proch, T. Carneiro, *Influence of Ta content in high purity niobium on cavity performance*, Proc. Particle Accelerator Conference, USA, Mai 16-20, 2005.

**[4-3]** W. Singer, A. Brinkmann, D. Proch, X. Singer, *Quality requirements and control of high purity niobium for superconducting RF cavities*, Physica C 386 (2003) 379-384.

**[4-4]** G.R. Myneni, *Physical and mechanical properties of single and large crystal high-RRR niobium*, Proc. 12th Workshop on RF Superconductivity, SRF-2005, 10-15 July 2005, Ithaca, USA.

**[4-5]** P. Kneisel, G. Ciovati, G.R. Myneni, J. Sekutowicz, T. Carneiro, *Performance of large grain and single crystal niobium cavities*, Proc. 12th Workshop on RF Superconductivity, SRF- 2005, 10-15 July 2005, Ithaca, USA.

**[4-6]** R. Brinkmann et al. (eds.), *TESLA Technical Design Report – Part II: The Accelerator*, DESY 2001-011, pp. II-27, March 2001.

**[4-7]** B. Aune et al., *Superconducting TESLA Cavities,* Phys. Rev. ST Accel. Beams 3 (2000) 092001.

**[4-8]** L. Lilje, E. Kako, D. Kostin, A. Matheisen, W.-D. Moeller, D. Proch, D. Reschke, K. Saito, P. Schmueser, S. Simrock, K. Suzuki, *Achievement of 35 MV/m in the Superconducting Nine-Cell Cavities for TESLA*, Nucl.Instr.Meth. A524 (2004) p.1-12.

**[4-9]** K. Saito et al., *High gradient performance by electropolishing with 1300 MHz single and multi-cell niobium superconducting cavities*, Proc. 9th Workshop on RF Superconductivity, SRF-1999, Santa Fe, USA, (1999) 288-291.

**[4-10]** J.P. Desvard et al., *Cryogenic and electrical test cryostat for instrumented superconductive RF cavitites (CHECHIA)*, Advances in cryogenic engineering, 41 (1995) 905.

**[4-11]** J. Graber, *High Power Processing Studies of 3 GHz Niobium Superconducting Accelerating Cavities*, Dissertation at the Cornelle University, Ithaca, May 1993.

**[4-12]** W.-D. Moeller for the TESLA Collaboration, *High Power Coupler For The TESLA Test Facility*, Proc. 9th Workshop on RF Superconductivity, SRF-1999, Santa Fe, Vol.2, pp.577-581.

**[4-13]** B. Dwersteg, D. Kostin, M. Lalayan, C. Martens, W.-D. Moeller, *Tesla RF Power Couplers Development at DESY*, Proc. 10th Workshop on RF Superconductivity, SRF-2001, September 6-11, 2001, Tsukuba, Japan, in KEK Proceedings 2003-2, pp.443-447.

**[4-14]** M. Ukkola and P. Yla-Oijala, *Numerical Simulation of Electron Multipacting in TTF III Cold Window with a DC Bias*, Helsinki Institute of Physics, Finland, Technical Report, 2000.

**[4-15]** J. Lorkiewicz, B. Dwersteg, A. Brinkmann, W.-D. Moeller, D. Kostin, M. Lalayan, *Surface TiN Coating of TESLA Couplers at DESY as an Antimultipactor Remedy*, Proc.10th Workshop on RF Superconductivity , SRF-2001, September 6-11, 2001, Tsukuba, Japan, in KEK Proceedings 2003-2, pp.448-452.

**[4-16]** S. Michizono, A. Kinbara et al., *TiN Film Coatings on Alumina Radio Frequency Windows*, J. Vac. Sci. Technol. A 10 (4) 1992.

**[4-17]** M. Dohlus, *3D CSR calculations for XFEL Bunch Compression*, TESLA Collaboration Meeting, DESY-Zeuthen, January 2004; http://www-zeuthen.desy.de/tesla2004/

**[4-18]** J. Sekutowicz, *Higher Order Mode Coupler for TESLA*, Proc. 6th Workshop on RF Superconductivity, October 4-8, SRF-1993, Newport News, Virginia, USA.

**[4-19]** J. Sekutowicz et al., *Proposed Continuous Wave Energy Recovery Operation of an X-Ray Free Electron Laser*, Phys. Rev. ST-AB, vol. 8, January 2005.

**[4-20]** P. Bosland, et al., *Third Harmonic Superconducting Passive Cavities In ELETTRA and SLS,* Proc.11th Workshop on RF Superconductivity , SRF-2003, Lübeck, Germany.

**[4-21]** P. Bosland, Bo Wu, *Mechanical study of the «Saclay piezo tuner» PTS (Piezo Tuning System)*, DAPNIA - CEA Saclay, CARE-Note-2005-004-SRF.

**[4-22]** M. Liepe, W.D. Moeller, S.N. Simrock, *Dynamic Lorentz Force Compensation with a Fast Piezoelectric Tuner*, DESY TESLA-01-03, 2001.

**[4-23]** P. Sekalski, private communication.

**[4-24]** CIEMAT, Research Center for Energy, Environment and Technology, Madrid, Spain.

**[4-25]** M. Juillard, C. Magne, A. Mosnier, B. Phung, *High Resolution BPM for the Next Linear Collider,* Beam Instr.Workshop 2000, Camebridge, Massachusetts, U.S., (2000), p. 259.

**[4-26]** A. Ballerino, *Conduction-cooled 60 a resistive current leads for the LHC dipole correctors*, LHC Project Report 691, March 2001.

**[4-27]** K. Zapfe, *Running experience with the vacuum system of the superconducting linac of the TESLA Test Facility*, Vacuum 73 (2004) 213.

**[4-28]** K. Zapfe, *The vacuum system for the superconducting linac of the TESLA Test Facility*, Vacuum 60 (2001) 51.

**[4-29]** K. Zapfe, F. Herrmann, D. Hubert, P. Schmüser, *A New Flange Design for the Superconducting Cavities for TESLA*, Proc. of the 8th Workshop on RF Superconductivity, Abano Terme, 1997, eds. V. Palmieri and A. Lombardi (INFN, LNL-INFN (Rep) 133/98) 457.

**[4-30]** D. Trines et. al., *The Insulating Vacuum System of the HERA Proton Ring;* Proc. of the XVth Int. Conference on High Energy Accelerators, Hamburg, 1992, ed. J. Roßbach, Int. J. Mod. Phys. A (Proc. Suppl.) 2B (1993) 347.

**[4-31]** C. Bearzatto, M. Bres, G. Faillon, *Advantages of Multiple Beam Klystrons*, ITG Garmisch-Partenkirchen, May 4 to 5, 1992.

**[4-32]** R. Palmer, *Introduction to Cluster Klystrons*, Proc. International Workshop on Pulsed RF Power Sources For Linear Colliders, RF93, Dubna, Protvino, Russia, July 5-9,1993, p. 28.

**[4-33]** A. Beunas, G. Faillon, *10 MW/1.5 ms, L-band multi-beam klystron*, Proc.Conf. Displays and Vacuum Electronics, Garmisch-Partenkirchen, Germany, April 29-30 1998.

**[4-34]** A. Beunas, G. Faillon, S. Choroba, A. Gamp, *A High Efficiency Long Pulse Multi Beam Klystron for the TESLA Linear Collider*, TESLA Report 2001-01.

**[4-35]** H. Bohlen, A. Balkcum, M. Cattelino, L. Cox, M. Cusick, S. Forrest, F. Friedlander, A. Staprans, E. Wright, L. Zitelli, K. Eppley, *Operation of a 1.3GHz, 10MW Multiple Beam Klystron*, Proc. XXII International Linear Accelerator Conference. Linac 2004, Lübeck, Germany, August 16-20, (2004) 693.

**[4-36]** A. Balkcum, E. Wright, H. Bohlen, M. Cattelino, L. Cox, M. Cusick, S. Forrest, F. Friedlander, A. Staprans, L. Zitelli, *Continued Operation of a 1.3GHz Multiple Beam Klystron for TESLA*, Proc. Sixth International Vacuum Electronis Conference, IVEC 2005, Noordwijk, The Netherlands, April 20-22, 2005, p. 505.

**[4-37]** A. Yano, S. Miyake, S. Kazakov, A. Larionov, V. Teriaev, Y.H. Chin, *The Toshiba E3736 Multi-Beam Klystron*, Proccedings of the XXII International Linear Accelerator Conference. Linac 2004, Lübeck, Germany, August 16-20, 2004, p. 706.

**[4-38]** Y.H. Chin, A. Yano, S. Miyake, S. Choroba, *Development of Toshiba L-Band Multi-Beam Klystron for European XFEL Project*, Proceedings of the 2005 Particle Accelerator Conference, PAC05, Knoxville, USA, May 16-20, 2005, p. 3153.

**[4-39]** W. Bothe, Pulse *Generation for TESLA, a Comparison of Various Methods,* TESLA Report 94-21, July 1994.

**[4-40]** H. Pfeffer, C.Jensen, S. Hays, L. Bartelson, *The TESLA Modulator*, TESLA Report 93-30.

**[4-41]** Ed. D.A. Edwards, *The TESLA TEST FACILITY LINAC-Design Report*, Tesla Report 95-01.

**[4-42]** H. Pfeffer, L. Bartelson, K. Bourkland, C. Jensen, Q. Kerns, P. Prieto, G. Saewert. D. Wolff, *A Long Pulse Modulator for Reduced Size and Cost*, Fourth Europ. Particle Accelerator Conf., London 1994.

**[4-43]** H. Pfeffer, L. Bartelson, K. Bourkland, C. Jensen, P. Prieto, G. Saewert, D. Wolff, *A Second Long Pulse Modulator For TESLA Using IGBTs*, Proc. Fifth European Particle Accelerator Conference, EPAC96, Sitges (Barcelona), 10-14 June 1996, p. 2585.

**[4-44]** W. Kaesler, *A Long-Pulse Modulator for the TESLA Test Facility (TTF)*, Proc. XXII International Linear Accelerator Conf., Linac 2004, Lübeck, Germany, August 16-20, (2004) 459.

**[4-45]** H.-J. Eckoldt, N. Heidbrook, *Constant Power TESLA Supplies for the Modulator*, TESLA Report 2000-36.

**[4-46]** H.-J. Eckoldt, *Pulse Cables for TESLA*, TESLA Report 2000-35.

**[4-47]** T. Grevsmühl, S. Choroba, P. Duval, O. Hensler, J. Kahl, F.-R. Kaiser, A. Kretzschmann, H. Leich, K. Rehlich, U. Schwendicke, S. Simrock, S. Weisse, R. Wenndorff, *The RF-Station Interlock for the European X-Ray Laser*, Proc. XXII International Linear Accelerator Conference, Linac 2004, Lübeck, Germany, August 16-20, (2004) 718.

**[4-48]** H. Leich, S. Choroba, P. Duval, T. Grevsmühl, V. Petrosyan, S. Weisse, R. Wenndorff, *An Advanced Interlock Solution for TTF2/XFEL RF Stations*, Proc. 14th IEEE_NPSS Real Time Conference, Stockholm, Sweden, June 4-10, (2005) 36.

**[4-49]** H. Leich, S. Choroba, P. Duval, T. Grevsmühl, A. Kretzschmann, U. Schwendicke, R. Wenndorff, *The Design of a Technical Interlock for TTF2/ XFEL RF Stations*, NEC 2005, XX International Symposium on Nuclear Electronics & Computing (to be published).

**[4-50]** V. Katalev, S. Choroba, *RF Power Distributing Waveguide System for TESLA*, Proceedings of the Russian Particle Accelerator Conference, Rupac 2002, Obninsk, Russia, October 1-4, (2002,) 79.

**[4-51]** V. Katalev, S. Choroba, *Tuning of External Q and Phase for the Cavities of a Superconducting Linear Accelerator*, Proc. XXII International Linear Accelerator Conf., Linac 2004, Lübeck, Germany, August 16-20, (2004) 724.

**[4-52]** P. Sekalski, M. Grecki, C. Albrecht, *Performance of Magnetostrictive Elements at LHe Environment*, MIXDES 2005.

**[4-53]** K.T. Pozniak, R.S. Romaniuk, T. Czarski, W. Giergusiewicz, W. Jalmuzna, K. Olowski, K. Perkuszewski, S. Simrock, *FPGA and optical network based LLRF distributed control system for TESLA-XFEL Linear Accelerator,* Proceedings of SPIE - The International Society for Optical Engineering 5775, pp. 69-77.

**[4-54]** M. Grecki, T. Jezynski, A. Brandt, *Estimation of IQ Vector Components of RF Field - Theory and Implementation*, MIXDES 2005.

**[4-55]** T.A. Filipek, *Frequency Conversion in Field Stabilization System for Application in SC Cavity of Linear Accelerator*, SPIE - COO Warsaw, Poland 2005.

**[4-56]** W. Giergusiewicz, W. JaBmu|na, K. Pozniak, N. Ignashin, M. Grecki, D. Makowski, T. Je|yDki, K. Perkuszewski, K. Czuba, S. Simrock, and R. Romaniuk, *Low latency control board for LLR system – Simcon 3.1*, Photonics Applications in Industry and Research IV, August 2005.

**[4-57]** T. Czarski, K.T. Pozniak, R.S. Romaniuk, S. Simrock, *Cavity parameters identification for TESLA control system development , N*ucl.Instr. and Methods in Physics Research, Section A: Accelerators, Spectrometers, Detectors and Associated Equipment 548 (2003) 283-297.

**[4-58]** T. Jezynski, M. Grecki, *A Performance Diagnostic Tool for the Low Level RF Control System for VUV-FEL*, MIXDES 2005.

**[4-59]** P. Pucyk, T. JezyDski, W. Koprek, T. Czarski, K.T. Pozniak, R.S. Romaniuk, *DOOCS server and client application for FPGA based TESLA cavity controller and simulator,* Proceedings of SPIE - The International Society for Optical Engineering 5775 pp. 52-60.

**[4-60]** D. Makowski, M. Grecki, A. Napieralski, S. Simrock, and B. Mukherjee, *A distributed system for radiation monitoring at linear accelerators*, IEEE Transactions on Nuclear Science (TNS), p. in print, January 2006.

**[4-61]** B. Mukherjee, D. Makowski, and S. Simrock, *Dosimetry of high energy electron linac* produced photoneutrons and the bremsstrahlung gamma rays using TLD-500 and TLD-*700 dosimeter pairs*, Nucl.Instr. and Meth. A 545 (2005) 830-841.

**[4-62]** P. Pawlik, M. Grecki, S. Simrock, *System for High Resolution Detection of Beam Induced Transients in RF Signals*, MIXDES 2005.

**[4-63]** P. Pawlik, M. Grecki, S. Simrock, *Single Bunch Transient Detection for the Beam Phase Measurement in Superconducting Accelerators*, DIPAC 2005, Lyon, France, 6th-8th June 2005.5.Undulators SASE and for Spontaneous Emission.

**[4-64]** S. Schreiber et al., *The Injector of the VUV-FEL at DESY*, Proceedings of FEL 2005, to be published.

**[4-65]** P. Piot et al., C*onceptual design for the XFEL Photoinjector*, DESY TESLA-FEL 01-03, 2001.

**[4-66]** TESLA - Technical Design Report, Part II, TESLA-FEL 01-05, 2001.

**[4-67]** V. Miltchev et al., *Measurements of thermal emittance for cesium telluride photocathodes at PITZ*, Proceedings of FEL 2005, to be published.

**[4-68]** H.-J. Han et al., *Emission Mechanisms in a Photocathode RF Gun*, Proceedings of PAC 2005.

**[4-69]** K. Honkavaara et al., *Electron Beam Characterization at PITZ and the VUV-FEL at DESY*, Proceedings of FEL 2005, to be published.

**[4-70]** K. Honkavaara et al., *Transverse Electron Beam Diagnostics at the VUV-FEL at DESY*, Proceedings of FEL 2005, to be published.

**[4-71]** V. Miltchev, Modelling the Transverse Phase-space and Core Emittance Studies at PITZ, Proceedings of FEL 2005, to be published.

**[4-72]** Will, P. Nickles, W. Sandner, *A Laser System for the TESLA Photo-Injector*, internal design study, Max-Born-Institut, Berlin 1994.

**[4-73]** I. Will, G. Koss, I. Templin, *The upgraded photoinjector laser of the TESLA Test Facility*, Nucl. Instr. and Meth. A 541 (2005) 467-477.

**[4-74]** K. Abrahamyan et al., *Experimental characterization and numerical simulations of the electron source at PITZ,* Nucl. Instr. and Meth. A, in press.

**[4-75]** B. Steffen et al., *Spectral Decoding Electro-Optic Measurements for Longitudinal Bunch Diagnostics at the DESY VUV-FEL*, Proceedings of FEL 2005, to be published.

**[4-76]** V. Balandin et al., *Optimized Bunch Compression System for the European XFEL*. PAC 2005.

**[4-77]** M. Dohlus, T. Limberg, *Impact of Optics on CSR-related Emittance Growth in Bunch Compressor Chicanes*. PAC 2005.

**[4-78]** M. Dohlus, K. Floettmann, Y. Kim, T. Limberg, *Injector and Bunch Compressor for the European XFEL*, EPAC 2004, P. 342-344.

**[4-79]** M. Dohlus, T. Limberg, *XFEL Bunch Compression System Set Up*. Commissioning Workshop, Zeuthen 2005. http://commissioning2005.desy.de/

**[4-80]** P. Piot et al., *Conceptual Design for the XFEL Photoinjector*, DESY TESLA-FEL 01-03, 2001.

**[4-81]** M. Dohlus and T. Limberg, *Bunch Compression Stability Dependence on RF Parameters*, FEL'05, Stanford, CA, 2005.

**[4-82]** V. Balandin and N. Golubeva, *The TrackFMN Program. User's Reference Manual*, unpublished.

**[4-83]** ASTRA; http://www.DESY.de/~mpyflo/Astra_dokumentation/

**[4-84]** M. Dohlus, T. Limberg, *CSRtrack: Faster Calculation of 3D CSR effects*, FEL 2004, 2004.

**[4-85]** E. Saldin, E. Schneidmiller and M. Yurkov, *Nucl. Instrum. Meth*. A **528** (2004) 355.

**[4-86]** http://www.desy.de/xfel-beam/data/component_list.xls

**[4-87]** M. Dohlus, private communication.

**[4-88]** M. Martin and I. Zagorodnov, *Impact of Undulator Wake Fields and Tapering on the European X-Ray FEL Performance*, DESY TESLA-FEL 2005-10.

**[4-89]** K.L.F. Bane and G.V. Stupakov, SLAC-PUB-10707, (2004).

**[4-90]** I.A. Zagorodnov, T. Weiland, *TE/TM field solven for particle beam simulations without numerial Cherenkov radiation,* Physical Review – STAB 8, (2005) 042001.

**[4-91]** M. Dohlus, TESLA 2001-26, (2001).

**[4-92]** S. Reiche, *Genesis 1.3; a fully 3D time-dependent FEL simulation code*, Nucl. Instrum. Methods Phys. Res., Sect. A 429, (1999) 243.

**[4-93]** N. Baboi, *Multi-Bunch Beam Dynamics Studies for the European XFEL*, Proceedings of LINAC 2004, Lübeck.

**[4-94]** N. Baboi, R. Brinkmann, *Higher order mode effects and multi-bunch orbit stability in the TESLA main linac*, DESY-TESLA-2000-28, 2000, Hamburg.

**[4-95]** H. Delsim-Hashemi, *Broadband single shot spectrometer*, Proceedings of the 2005 FEL conference, San Francisco, California.

**[4-96]** M. Juillard, C. Magne, A. Mosnier, B. Phung, high *resolution BPM for the next linear colliders*, 9th Beam Instrumentation Workshop (BIW 2000), Cambridge, Massachusetts, 2000.

**[4-97]** M. Hüning et al., *Observation of femtosecond bunch length using a transverse deflecting structure*, Proceedings of the 2005 FEL conference, San Francisco, California.

**[4-98]** Ch. Gerth, M.Röhrs, H. Schlarb, *Layout of the diagnostic section for the European XFEL*, Proceedings of PAC 2005, Knoxville, Tennessee.

**[4-99]** M. Röhrs et al., *Measurement of Slice-Emittance using a transverse deflecting structure*, Proceedings of the 2005 FEL conference, San Francisco, California.

**[4-100]** B. Steffen et al., *Spectral decoding electro-optic measurements for longitudinal bunch diagnostics at the DESY VEV-FEL,* Proceeding of the 2005 FEL conference, San Francisco, California; A.Cavalieri et al., Phys. Ref. Lett. 94, 114801.

**[4-101]** S. Casalbouni et al., *Numerical Studies on the Electro-Optic Sampling of Revalistic Electron Bunches*, TESLA Report 2005-01.

**[4-102]** T. Raubenheimer, F. Zimmermann, *Fast beam-ion instability I. linear theory and simulation*, Phys.Rev.E 52 (1995) 5487-5497.

**[4-103]** E. Bondarchuk et al., *Technical proposal for a batch of electromagnets for the X-FEL Project*, St. Petersburg, September 2005.

**[4-104]** M. Maslov, V. Sytchev, M. Schmitz, *Layout Considerations on the 25GeV/ 300kW Beam Dump of the XFEL Project, DESY*, (2006) TESLA-FEL Report 2006-05.

**[4-105]** N. Tesch, A. Leuschner, *Sicherheitsbericht zum Strahlenschutz für das Planfest-stellungsverfahren des europäischen Röntgenlasers XFEL*, DESY, 13.4.2005.

**[4-106]** M. Hentschel et al., *Attosecond metrology*, Nature 414, 509-513 (2001).

**[4-107]** E. Goulielmakis et al., *Direct Measurement of Light Waves*, Science, Vol. 305, 1267-1269 (2004).

**[4-108]** A. Cavalieri et al., *Clocking Femtosecond X-ray*, Phys. Ref. Lett. 94, 114801.

**[4-109]** A. Cavalieri, *Electro-optic characterization of femtosecond electron bunches*, PhD-thesis, published by the University of Michigan.

**[4-110]** A. M. Lindberg et al., *Atomic-scale visualization of inertial dynamics*, Science, Vol. 308, 392-395 (2005).

**[4-111]** M. Drescher, DESY Proposal II-02-042 FEL.

**[4-112]** B. Steffen et al., *Spectral decoding electro-optic measurements for longitudinal bunch diagnostics at the DESY VUV-FEL*, Proceedings of the 27th International Free Electron Laser Conference, San Francisco, 2005.

**[4-113]** E.L. Saldin et al., *Terewatt-Scale Sub-10-fs Laser Technology – Key to Generation of GW-Level Attosecond Pulses in X-Ray Free Electron Laser*, DESY Report 04-13, January 2004.

**[4-114]** T. Zwart et al., *The MIT Bates X-ray laser project*, Proceedings of the 2003 Particle Accelerator Conference, Portland (2003).

**[4-115]** J. Kim et al., *Large-scale timing distribution and RF-synchronization for FEL facilities*, Proceedings of the 26th International Free Electron Laser Conference, Trieste, 2004.

**[4-116]** Jun Ye et al., *Sub-10-femtosecond synchronization of two passively mode-locked Ti:sapphire oscillators*, Phy. Rev. A, Vol. 64, 021802(R).

**[4-117]** T.R. Schibli et al., *Attosecond active synchronization of passsive mode-locked lasers by balanced cross correlation*, Optics Letters, Vol. 28, No. 11 (2003) 947-949.

**[4-118]** M. Margalit, et al., *Noise in pulsed injection locking of a passively modelocked laser*, IEEE Journal of Quantum Electronics, Vol. 32, No. 5 (1996) 796-801.

**[4-119]** J. Kim et al., *A Balanced Optical-to-RF Phase Detector for Synchronization and Timing Distribution in XFELs*, Midterm Report for DESY-MIT Synchronisation Project, 40003350-1.

**[4-120]** F.X. Kärtner, *Few-Cycle Laser Source for the Electron Beam Modulation in XFELs on an Attosecond Timing scale and High Harmonic Seed Generation*, internal DESY report, 500040-1.

**[4-121]** S.A. Diddams et al., *An Optical Clock Based on a Single Trapped 199Hg+ Ion*, Science 293 (2001) 825.

**[4-122]** S. Namiki and H.A. Haus, *Noise of the stretched pulse fiber ring laser: Part I-Theory*, IEEE. J. Quantum Electron. 33 (1997) 649.

**[4-123]** J.B. Schlager et al., *Passively mode-locked glass waveguide laser with 14-fs timing jitter*, Opt. Lett. 28 (2003) 2411.

**[4-124]** J. Kim, F.O. Ilday, A. Winter and F.X. Kärtner, *Timing Distribution and RF-Synchronization of Mode-Locked Lasers*, in 2005 Digest of the LEOS Summer Topical Meetings, IEEE, New York, (2005), 149-150.

**[4-125]** L.E. Nelson et al., *Ultrashort-pulse fiber ring laser*, Applied Physics. B 65, (1997) 277-294.

**[4-126]** E.N. Ivanov, S.A. Diddams and L. Hollberg, *Analysis of Noise Mechanisms Limiting the Frequency Stability of Microwave Signals Generated With a Femtosecond Laser*, IEEE J. Sel. Top. Quant. Elec. 9 (2003) 1059-1065.

**[4-127]** Posseidon Scientific Instrument, Report on the 1.3 GHz DRO for DESY.

**[4-128]** J. Kim, F. Ludwig, D. Sheevers, F.Ö. Ilday, J. Burnham, F.X. Kärtner, *A balanced optical-RF phase detector*, Proceedings of the Conference on Lasers and Electro-Optics, Long Beach, 2006.

**[4-129]** A. Winter et al., *High-precision Optical Synchronization System for X-ray Free Electron Lasers*, Proceedings of the 27th International Free Electron Laser Conference, San Francisco, 2005.

# 5 Undulators for SASE and spontaneous emission

## 5.1 Overview

### 5.1.1 Principles of XFEL operation

The free-electron laser (FEL) consists of a relativistic electron beam and a radiation field interacting with each other while propagating through an undulator **[5-1, 5-2]**. The FEL, despite its name, is not actually a laser; it is more closely related to vacuum-tube devices. As with vacuum-tube devices, FEL devices can be divided in two classes: amplifiers and oscillators. The FEL amplifier is a single-pass device. The FEL oscillator can be considered as an FEL amplifier with a feedback. For an FEL oscillator in the optical wavelength range, the feedback is carried out by means of an optical resonator. FELs based on the oscillator principle reach a limit at ultraviolet energies, primarily because of mirror limitations. Free-electron lasing at energies higher than the ultraviolet can be achieved with a single-pass, high-gain FEL amplifier operating in the Self-Amplified Spontaneous Emission (SASE) mode. These are the devices we refer to as X-Ray FELs (XFELs) in the following sections.

In an XFEL, radiation is produced by the electron beam during a single-pass of the undulator **[5-3 – 5-6]**. The amplification process starts from shot noise in the electron beam. During the amplification process a powerful, coherent radiation is produced having a narrow band near the resonance wavelength:

$$\lambda = \frac{\lambda_u}{2\gamma^2}\left(1 + K_{rms}^2\right) \tag{5.1}$$

where $\lambda_u$ is the undulator period, $K_{rms}=eH_{rms}\lambda_u/2\pi m_e c^2$ is the undulator parameter, $H_{rms}$ is the rms-value of the undulator field, $\gamma=E/m_e c^2$ is the relativistic factor, E is the energy of the electron, -e and $m_e$ are the charge and the mass of the electron, respectively, and c is the velocity of light. CGS units are used in this section therefore giving H=B with the relation between rms- and maximum values of $(H_{rms}, B_{rms})=(H_{max}, B_{max})/\alpha$ with $\alpha=1$ for helical magnetic field distribution and $\alpha=2^{1/2}$ for planar sinusoidal (linear) magnetic field distribution.

The electromagnetic wave amplification in the undulator refers to a class of self-consistency problems. It can be separated into two parts: a) solution of the dynamical problem, i.e. finding the motion of the particles under the action of the given electromagnetic fields; b) solution of the electrodynamics problem, i.e. finding the electromagnetic fields generated by a given distribution of charges and currents. To close the loop, the field equations and the equations of motion should be solved simultaneously. Nowadays,

FEL theory has reached a mature status allowing complete description of the FEL process. The optimisation process for the XFELs at the European XFEL Facility has been performed with a combination of analytical techniques **[5-7 – 5-14]**, and simulations with linear and non-linear steady state and time-dependent FEL simulation codes **[5-7, 5-13 – 5-19]**. Comparison of these simulations with experimental results obtained at the Free-electron LASer in Hamburg (FLASH) demonstrated very good agreement, which convinces us that the physical models and simulation tools developed adequately describe the XFEL process **[5-20 – 5-25]**.

### 5.1.2 Design criteria for the European XFEL

The scientific proposals for investigations using XFEL and spontaneous synchrotron radiation presented in Chapter 6 are based on the key properties of this radiation. Namely, on the ultrashort photon pulse duration of approximately 100 fs, on the high degree of coherence, on the outstanding peak brilliance, and last but not least, on the average brilliance **[5-26 – 5-28]**. In the design of the European XFEL Facility and its undulators the requirements with respect to photon energy range and tunability are important. The scientific case shows that most experiments which are not interested in particular resonances, will benefit from using photon energies close to 12.4 keV or slightly above. The design was, therefore, optimised to produce XFEL radiation at 12.4 keV simultaneously at two of the three XFEL undulators. These devices are called SASE 1 and SASE 2. In addition, the present design includes one XFEL for the soft x-ray range (SASE 3) and two undulators for spontaneous synchrotron radiation (U1, U2). SASE 3 corresponds to the demand for FEL radiation in the soft x-ray range and U1 and U2 provide ultrashort, highly coherent x-ray radiation in the 20 to 100 keV range for ultrashort time-scale physics and materials sciences investigations. A sketch of the different undulators and principal elements of the electron beam distribution can be found in Figure 5.1.1, and Table 5.1.1 lists all undulators and their design criteria.

In order to enable experiments over a continuous photon energy range up to 12.4 keV, SASE 2 is designed to be tunable in photon energy by changing the gap height. Tuning by changing the electron energy would be possible in principle, however, this change cannot be done very quickly except for a dynamic range of ± 1.5% (see Section 4.5) and it would affect the operation of all instruments. Tunability by gap variation has consequences for the saturation length (see Section 5.2.1). The tunability of SASE 2 has been set to the range 3.1 to 12.4 keV to limit both the total length and the number of x-ray optics. In contrast, SASE 1 is designed to operate at fixed photon energy of 12.4 keV. Due to the stringent requirements on the electron phase-space volume, XFEL undulators can be placed behind each other only on the condition that the second XFEL radiates at at least four times smaller photon energy. The SASE 3 undulator has been placed behind SASE 1 since the latter operates always at the highest photon energy. In contrast, spontaneously emitting undulators can be placed without problems behind XFELs. The two spontaneous emitting undulators use the spent electron beam of SASE 2. The undulators are planar, hybrid devices with a sinusoidal vertical field, apart from SASE 3 which is designed as an APPLE II device providing circular and linear polarised radiation. SASE 3 is constructed in this manner as there are currently no other means to efficiently generate circular polarised light in this energy region.

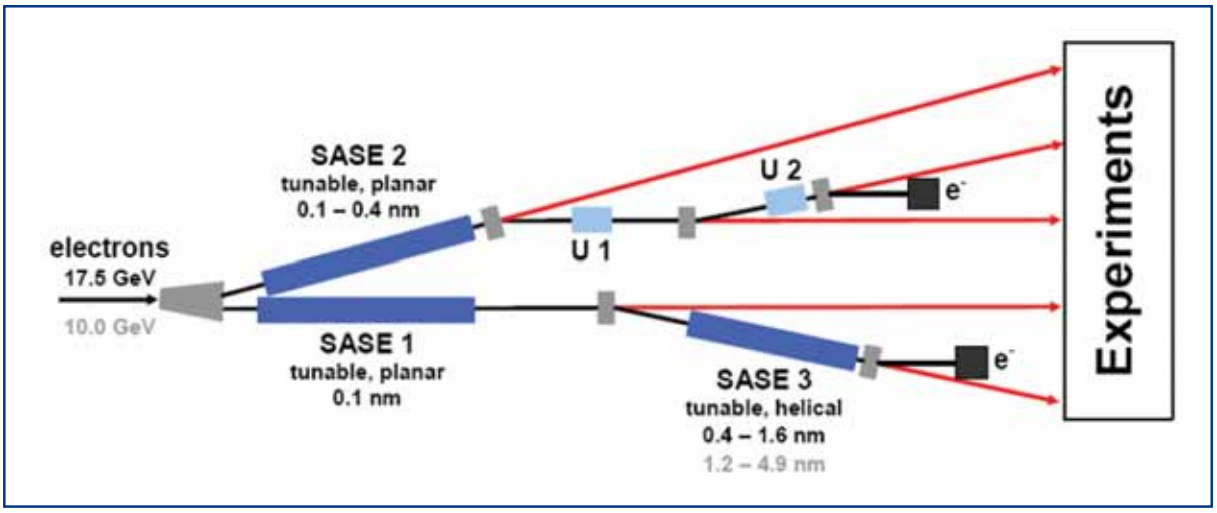


***Figure 5.1.1*** *Schematic overview of the electron beam distribution between accelerator and experimental hall. The two electron beamlines (black) include the five undulator systems for SASE FEL and spontaneous synchrotron radiation, which in turn feed five photon beamlines (red). The distance between the separation into two electron beamlines and the experimental hall is ~1300 m.*

| | Photon energy [keV] | Polarisation | Tunability | Gap variation |
|---|---|---|---|---|
| SASE 1 | 12.4 | Linear | No | Yes |
| SASE 2 | 3.1 – 12.4 | Linear | Yes | Yes |
| SASE 3 | 0.8 – 3.1 (0.25 – 1.0)* | Circular/Linear | Yes | Yes |
| U1, U2 | 20 – 100 | Linear | Yes | Yes |

***Table 5.1.1*** *Design criteria for the five undulators of the European XFEL Facility. The photon energies correspond to an operating energy of the electron beam of 17.5 GeV. The asterisk denotes values for an electron energy of 10 GeV (see text).*

The European XFEL Facility should provide simultaneous operation of different beamlines with independent choice of photon energy. At a fixed energy of the electron beam of 17.5 GeV, independent tuning of the radiation wavelength is performed individually at each beamline by means of changing the undulator gap. In the case of SASE 3, a significant extension of the tunability could be achieved with an electron energy of 10 GeV. In addition, parameters for an additional XFEL for the range 0.2 – 0.8 keV at electron energy of 17.5 GeV are available **[5-29]**.

Starting points for the optimisation of the XFEL sources are the design values for the photon energy ranges, the requirements for photon beam properties, the design parameters of the electron beam, and the restrictions provided by undulator technology. The applied design parameters for the electron beam are compiled in Table 5.1.2. The choice of undulator technology imposes certain restrictions on the optimisation process as well. The discussion of magnetic properties of the undulators is given in Section 5.4.

| | Value | Unit |
|---|---|---|
| Electron energy | 17.5 | GeV |
| Bunch charge | 1 | nC |
| Peak current | 5 | kA |
| Bunch length (rms) | 25 | μm |
| Normalised emittance (rms) | 1.4 | mm mrad |
| Energy spread (rms) | 1.5 | MeV |
| Bunches per RF pulse | 3000 | |
| Repetition rate | 10 | Hz |

***Table 5.1.2*** *Electron beam parameters used for the optimisation of the XFEL sources. The energy 17.5 GeV is already the result of an optimisation as is explained in Section 5.2.1 below.*

## 5.2 FEL radiation parameters

A zero-order estimation of the FEL characteristics is usually performed in the framework of the one-dimensional model in terms of the FEL parameter $\rho_{1D}$ **[5-5]**:

$$\rho_{1D} = \frac{\lambda_u}{4\pi}\left[\frac{4\pi^2 j_o K_{rms}^2 A_{jj}^2}{I_A \lambda_u \gamma^3}\right]^{1/3} . \qquad (5.2)$$

Here $j_0$ is the beam current density, and $I_A=mc^3/e$ =17 kA. The coupling factor $A_{jj}$ is equal to 1 for helical magnetic fields, and $A_{jj}=[J_0(Q)-J_1(Q)]$ for linear fields. Here $J_n$ is the Bessel function of the first kind and $Q=K_{rms}^2/[2(1+K_{rms}^2)]$. Basic characteristics of the SASE FEL are simply estimated in terms of the parameter $\rho_{1D}$ and the number of co-operating electrons $N_c=I/(e\rho_{1D}\omega)$ **[5-7, 5-13]**:

Field gain length: $L_g \approx \lambda_u/(4\pi\rho_{1D})$,

Saturation length: $L_{sat} \approx 10 \times L_g$,

Effective power of shot noise: $\frac{W_{sh}}{\rho_{1D} W_b} = \frac{3}{N_c\sqrt{\pi 1\mathrm{n}N_c}}$ ,

Saturation efficiency: $\rho_{1D}$,

Power gain at saturation: $G = \frac{N_c}{3}\sqrt{\pi 1\mathrm{n}N_c}$ ,

Spectrum bandwidth: $2\rho_{1D}$,

Coherence time at saturation: $\tau_c = \frac{1}{\rho_{1D}\omega}\sqrt{\frac{\pi 1\mathrm{n}N_c}{18}}$ , (5.3)

Here $W_b$=EI/e is the electron beam power, and $\omega=2\pi c/\lambda$ is the frequency of the electromagnetic wave. Although useful for quick qualitative estimations of the parameter range, the one-dimensional approach does not provide reliable quantitative estimates and a complete three-dimensional theory of the FEL amplifier must be used instead.

We assume nearly uniform focusing of the electron beam in the undulator, by using the axisymmetric model of the electron beam to optimise the XFELs (the validity of this approach has been checked later with the actual focusing structure, using a non-axisymmetric model). It is assumed that the transverse distribution function of the electron beam is Gaussian, so that the rms transverse size of the matched beam is $\sigma=(\varepsilon\beta)^{1/2}$, where $\varepsilon=\varepsilon_n/\beta$ is the rms beam emittance and $\beta$ is the focusing beta-function. The energy spread is also assumed to be Gaussian with rms spread $\sigma_E$, and the electron beam has a Gaussian longitudinal profile with rms bunch length $\sigma_z$.

In the framework of the three-dimensional theory, the operation of the FEL amplifier is described by the following parameters: the gain parameter $\Gamma$, the diffraction parameter *B*, the efficiency parameter $\rho$, the space charge parameter $\hat{\Lambda}_p^2$, the energy spread parameter $\hat{\Lambda}_T^2$, and the betatron motion parameter $\hat{k}_\beta$ **[5-7, 5-12]**:

$$\Gamma=\left[I\omega^2\theta_s^2A_{jj}^2/(I_Ac^2\gamma_z^2\gamma)\right]^{1/3},\qquad B=2\Gamma\sigma^2\omega/c,\qquad \rho=c\gamma_z^2\Gamma/\omega,$$
$$\hat{\Lambda}_T^2=(\sigma/E)^2/\rho^2,\qquad \hat{k}_\beta=1/\beta\Gamma,\qquad \hat{\Lambda}_P^2=2c^2/\left(A_{jj}\theta_s\sigma\omega\right)^2. \tag{5.4}$$

Here I is the beam current, $\gamma_z^2=\gamma^2/(1+K_{rms}^2)$, and $\theta_s=K/\gamma$. Note that the 1-D FEL parameter (see above) is $\rho_{1D}=\rho/B^{1/3}$. Typical values of parameters for 12.4 keV XFEL radiation are: $\Gamma^{-1}$~3 m, B~50-120, $\rho\sim1.5\times10^{-3}$, $\hat{\Lambda}_p^2\sim10^{-4}$, $\hat{\Lambda}_T^2$~0.02, and $\hat{k}_\beta$~0.07. An important feature of the parameters space of XFEL is that the space charge field does not influence the FEL process significantly and optimisation of the FEL parameters can be performed by only taking into account diffraction effects, the energy spread in the electron beam and effects of betatron motion.

The amplification process in the FEL amplifier goes through two stages: linear and non-linear. The linear stage lasts over significant fraction of the undulator length (about 80%), and the main target for XFEL optimisation is the field gain length. In the linear high-gain limit the radiation emitted by the electron beam in the undulator can be represented as a set of modes:

$$E_x+iE_y=\int d\omega\,\exp[i\omega(z/c-t)]\sum_{n,k}A_{nk}(\omega)\,\Phi_{nk}(r,\omega)\exp[\,\Lambda_{nk}(\omega)z+in\phi] \tag{5.5}$$

When amplification takes place, the mode configuration in the transverse plane remains unchanged, while the amplitude grows exponentially with the undulator length. Each mode is characterised by the eigenvalue $\Lambda_{nk}(\omega)$ and the field distribution, eigenfunction $\Phi_{nk}(r,\omega)$ in terms of transverse coordinates. At sufficient undulator length, the fundamental $TEM_{00}$ mode is the main contribution to the total radiation power. Thus, an important parameter for XFEL optimisation is the field gain length of the fundamental mode, $L_g=1/\Lambda_{00}$, which gives a good estimate for the expected length of the undulator needed to

reach saturation, $L_{sat}=10\times L_g$. Optimisation of the field gain length has been performed by means of numerical solution of the corresponding eigenvalue equations taking into account all the effects (diffraction, energy spread and emittance) **[5-11, 5-12]**. The performance of modern computers allowed us to perform a complete study of the parameter space of XFEL (which in fact is 11-dimensional). From the practical point of view, it is important to find an absolute minimum of the gain length corresponding to the optimum focusing beta function. For this practically important case,0 the solution of the eigenvalue equation for the field gain length of the fundamental mode and the optimum beta function are rather accurately approximated by **[5-30]**:

$$L_g = 1.67\left(\frac{I_A}{\mathrm{I}}\right)^{1/2}\frac{(\varepsilon_n\lambda_u)^{5/6}}{\lambda^{2/3}}\frac{(1+K_{rms}^2)^{1/3}}{\mathrm{K_{rms}A_{JJ}}}(1+\delta)\,,$$

$$\beta_{\mathrm{opt}} = 11.2\left(\frac{I_A}{\mathrm{I}}\right)^{1/2}\frac{\varepsilon_n^{3/2}\lambda_u^{1/2}}{\lambda K_{rms}A_{JJ}}(1+8\delta)^{-1/3},$$

$$\delta = 131\frac{I_A}{\mathrm{I}}\frac{\varepsilon_n^{5/4}}{\lambda^{1/8}\lambda_u^{9/8}}\frac{\sigma_\gamma^2}{(K_{rms}A_{JJ})^2(1+K_{rms}^2)^{1/8}}\,, \qquad (5.6)$$

for $\sigma_\gamma=\sigma_E/m_ec^2$. Equation (5.6) demonstrates the power of analytical techniques providing a clear interdependence of physical parameters defining operation of the XFEL.

Quantum fluctuations of incoherent undulator radiation are a complicating factor for the optimisation of XFEL parameters. When the electron beam moves in the undulator it also emits incoherent radiation. The mean energy loss of each electron by incoherent radiation is given by:

$$dE/dz = 2r_e^2\gamma^2H(z)^2/3 \qquad (5.7)$$

where $r_e= e^2/m_ec^2$ is the classical radius of the electron. When the relative energy loss of the electron $\Delta E_{SR}/E$ becomes comparable with the FEL bandwidth $\rho B^{-1/3}$, the undulator has to be tapered in order to compensate for this effect and maintain the resonance condition. This tapering is also required due to wake field effects (see Section 4.4.5).

A fundamental limit on the minimal achievable wavelength is imposed by the growth of the uncorrelated energy spread in the electron beam due to the quantum fluctuations of undulator radiation **[5-4, 5-30, 5-31]**. The rate of the energy diffusion is given by **[5-32]**:

$$\frac{d\sigma_\gamma^2}{dz} = \frac{14}{15}\lambda_c{}^2 r_e\gamma^4\kappa_u^2K_{rms}^2F(K_{rms}) \qquad (5.8)$$

where $\lambda_c=\bar{h}/mc$ is the Compton wavelength, $\bar{h}$ is Planck constant, $\kappa_u=2\pi/\lambda_u$, and

$$F(K)=1.42K_{rms}+(1+1.50K_{rms}+0.95K_{rms}{}^2)^{-1} \quad \text{for a helical field,}$$

$$F(K)=1.70K_{rms}+(1+1.88K_{rms}+0.80K_{rms}{}^2)^{-1} \quad \text{for a linear field.} \qquad (5.9)$$

The effect of quantum energy diffusion grows drastically with the energy and imposes a severe limitation on the achievement of very short wavelengths **[5-30]**:

$$\lambda_{\min}^{q}[nm] = \frac{0.4\varepsilon_n[\mu rad]}{I^{3/5}[kA]L_{tot}^{2/5}[m]}. \qquad (5.10)$$

The next step in optimisation of the XFEL parameters is the solution of the initial-value problem, i.e. the calculation of the coefficients $A_{nk}(\omega)$ appearing in (5.5). This has been done by means of a technique reported in **[5-8, 5-10, 5-14]**. At this stage we calculate the degree of transverse coherence of the radiation from the SASE FEL **[5-14, 5-32]**. Calculations show that the degree of transverse coherence of the output radiation at the end of the linear regime is high for all XFELs of the European XFEL Facility.

The final stage of XFEL calculations is the simulation of the FEL process with non-linear simulation codes. We started with the steady-state simulation code FS2R **[5-15]** and Genesis 1.3 **[5-19]** being run in the steady-state mode using as input signal the effective power of the shot noise obtained from the solution of the initial-value problem. Final calculations have been performed with the three-dimensional, time-dependent simulation code FAST **[5-18]**. Final parameters for the XFEL sources have been checked with dedicated runs of the FAST code performing direct simulation of the FEL process for the total number of electrons in the beam. The results have been used for the compilation of Table 5.2.2 of XFEL parameters.

### 5.2.1 Defining undulator parameters

The choice of undulator parameters was based on global optimisation of the parameter space given by (5.6) with additional constraints defined by quantum fluctuations of incoherent radiation (5.8) and the interdependence of undulator parameters defined by state-of-the-art technology. Optimised parameters of the undulators are presented in Table 5.2.1. The choice of the undulator gap and the nominal electron energy is a compromise between the requirements to limit the total undulator length and to preserve the high quality of the XFEL radiation. Figure 5.2.1 shows the dependence of the saturation length on the electron energy for XFEL optimised for 0.1 nm wavelength. One can see that there is definite tendency to shorten the saturation length by reduction of the undulator gap. The optimum electron energy is reduced as well. Reduction of the undulator gap from 10 mm to 6 mm has a benefit in reduction of the saturation length by about 30%. On the other hand, the negative effect of the gap reduction is an increased strength of the wake fields. Although these wake fields are not completely fatal for XFEL operation, their presence significantly complicates the tuning of the machine and results in significant reduction of the parameter space in terms of bunch charge and pulse length. Our studies show that an undulator gap of 10 mm is a value corresponding to tolerable wake fields, acting as a perturbation only (see Section 4.4.5.2). As for the electron energy, the benefit in cost reduction seems to be attractive. However, there exists a severe obstacle: reduction of the electron energy below a certain value leads to significant reduction in the degree of transverse coherence of the radiation for SASE FEL operating at the minimum wavelength around 0.1 nm. The figure of merit defining the

degree of transverse coherence is the diffraction parameter B. When the diffraction parameter is small, the gain of the fundamental mode significantly exceeds the gain of higher modes **[5-7]**. In this case the degree of transverse coherence is limited by the effect of finite spectral width only, but it remains relatively high **[5-14, 5-33]**. At large values of the diffraction parameter, the gain for all modes becomes comparable, and the, mode selection process (5.5) is suppressed. As a result, the degree of transverse coherence of the radiation falls dramatically. Figure 5.2.1 shows the dependence of the diffraction parameter B versus energy for an optimised XFEL. Note that this dependence is universal and does not depend on the undulator gap. For optimised parameters of the FEL amplifier the diffraction parameter scales strongly with energy as $1/E^{5/2}$. At the operating energy of the European XFEL of 17.5 GeV, the value of the diffraction parameter for SASE 1 is about 120, and the degree of transverse coherence of the radiation is about 80%. Operation at lower energy leads to drastic reduction of the degree of transverse coherence **[5-34]**. Figure 5.2.2 shows the simulated saturation lengths for undulators SASE 1 to SASE 3 for the electron energy 17.5 GeV as a function of the wavelength of XFEL radiation.

| | $\lambda$ [nm] | $\lambda_u$ [mm] | g [mm] | $B_{max}$ [T] | K | $\beta$ [m] | $L_{sat}$ [m] |
|---|---|---|---|---|---|---|---|
| SASE 1 | 0.1 | 35.6 | 10 | 1.0 | 3.3 | 32 | 133 |
| SASE 2 | 0.1 | 47.9 | 19 | 0.63 | 2.8 | 45 | 174 |
| | 0.4 | | 10 | 1.37 | 6.1 | 15 | 72 |
| SASE 3 | 0.4 | 80.0 | 23 | 0.44 | 3.3 | 15 | 81 |
| | 1.6 | | 10 | 0.91 | 6.8 | 15 | 50 |
| | 4.9 | | 10 | 0.91 | 6.8 | 15 | 45 |

***Table 5.2.1*** *Undulator parameters as the result of optimisation.*

Detailed calculations of the output parameters of the radiation (temporal and spectral structure, statistical properties) have been performed using the time-dependent simulation code FAST **[5-18]** and taking into account all important physical effects: diffraction, slippage, energy spread and emittance effects. Final numbers have been checked by means of direct simulation of the FEL process with the actual number of electrons using a parallel version of the code FAST operating on a multi-processor computer. Parameters of the radiation from XFEL sources are compiled in Table 5.2.2, and Figures 5.2.3 and 5.2.4 illustrate the radiation properties for SASE 1 operating at a photon energy of 12.4 keV.

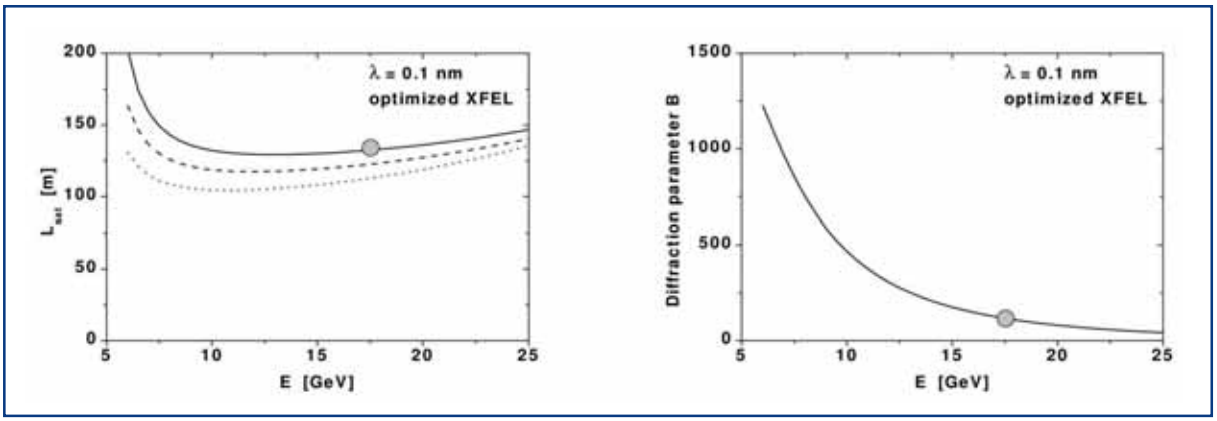


***Figure 5.2.1*** *Left: Saturation length of an XFEL optimised for operation at 0.1 nm. Solid, dashed, and dotted lines correspond to undulator gaps of 10, 8, and 6 mm, respectively. Right: Diffraction parameter B against energy for an optimised XFEL. Circles correspond to the operating point of the European XFEL.*

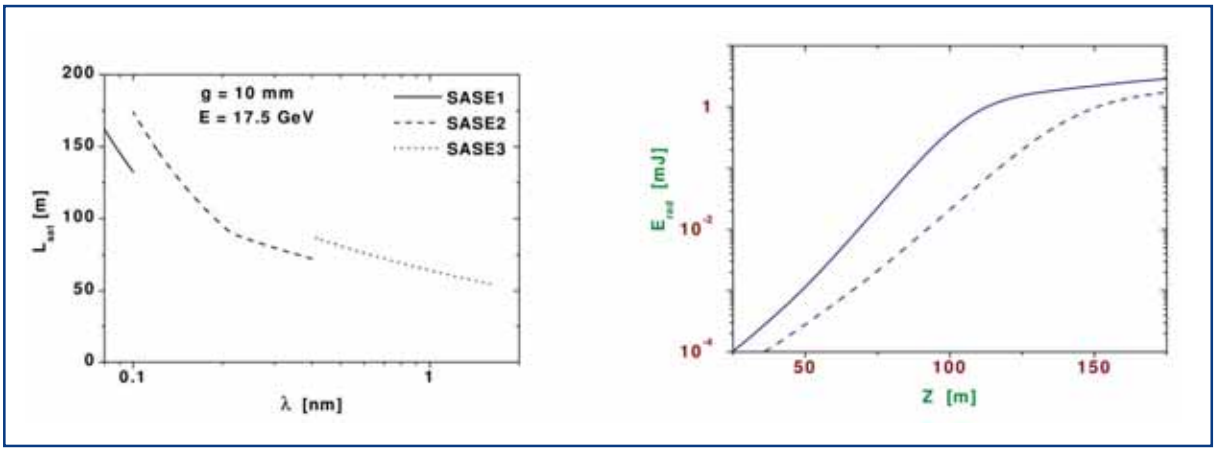


***Figure 5.2.2*** *Saturation length against radiation wavelength for an electron energy of 17.5 GeV. The radiation wavelength is tuned by opening the undulator gap.*

***Figure 5.2.3*** *Average energy in the radiation pulse against magnetic undulator length for SASE 1 (solid line) and SASE 2 (dashed line) operating at 0.1 nm wavelength.*

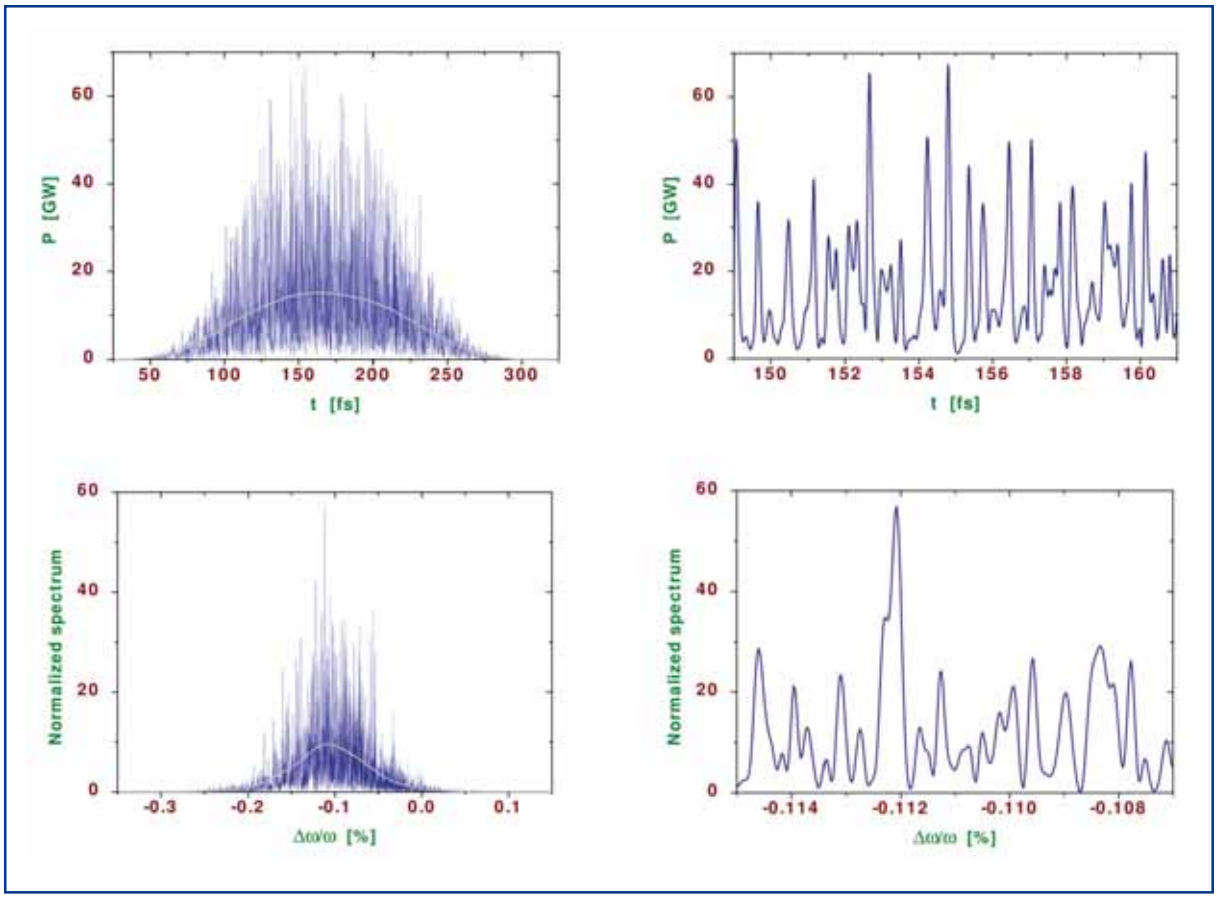


***Figure 5.2.4*** *Temporal (top) and spectral (bottom) structure for 12.4 keV XFEL radiation from SASE 1. Smooth lines indicate averaged profiles. Right side plots show enlarged view of the left plots. The magnetic undulator length is 130 m.*

| | Unit | SASE 1 | SASE 2 | | SASE 3 | | |
|---|---|---|---|---|---|---|---|
| Electron energy | GeV | 17.5 | 17.5 | 17.5 | 17.5 | 17.5 | 10.0 |
| Wavelength | nm | 0.1 | 0.1 | 0.4 | 0.4 | 1.6 | 4.9 |
| Photon energy | keV | 12.4 | 12.4 | 3.1 | 3.1 | 0.8 | 0.25 |
| Peak power | GW | 20 | 20 | 80 | 80 | 130 | 150 |
| Average power | W | 65 | 65 | 260 | 260 | 420 | 490 |
| Photon beam size (FWHM) | µm | 70 | 85 | 55 | 60 | 70 | 90 |
| Photon beam divergence (FWHM) | µrad | 1 | 0.84 | 3.4 | 3.4 | 11.4 | 18 |
| Coherence time | fs | 0.2 | 0.22 | 0.38 | 0.34 | 0.88 | 1.4 |
| Spectral bandwidth | % | 0.08 | 0.08 | 0.18 | 0.2 | 0.3 | 0.65 |
| Pulse duration | fs | 100 | 100 | 100 | 100 | 100 | 100 |
| Photons per pulse | # | $10^{12}$ | $10^{12}$ | $1.6 \times 10^{13}$ | $1.6 \times 10^{13}$ | $1.0 \times 10^{14}$ | $3.7 \times 10^{14}$ |
| Average flux | #/s | $3.0 \times 10^{16}$ | $3.0 \times 10^{16}$ | $4.8 \times 10^{17}$ | $4.8 \times 10^{17}$ | $3.1 \times 10^{18}$ | $1.1 \times 10^{19}$ |
| Peak brilliance | B | $5.0 \times 10^{33}$ | $5.0 \times 10^{33}$ | $2.2 \times 10^{33}$ | $2.0 \times 10^{33}$ | $5.0 \times 10^{32}$ | $1.0 \times 10^{32}$ |
| Average brilliance | B | $1.6 \times 10^{25}$ | $1.6 \times 10^{25}$ | $6.5 \times 10^{24}$ | $5.9 \times 10^{24}$ | $1.4 \times 10^{24}$ | $2.8 \times 10^{23}$ |

***Table 5.2.2*** *XFEL radiation parameters for SASE 1 – SASE 3 as the result of simulations. Brilliance B is given in units of photons/0.1%bw/s/mm$^2$/mrad$^2$.*

### 5.2.2 Radiation parameters of SASE 3

SASE 3 uses the spent electron beam coming from SASE 1. Due to the SASE FEL process in SASE 1, the energy spread of the electron beam increases and is about 8 MeV at the entrance of SASE 3. The XFEL radiation parameters in Table 5.2.2 have been calculated for these parameters, and the saturation length is about 80 m at the radiation wavelength 0.4 nm. In this case the amplification process in SASE 1 is suppressed, e.g. by electron beam manipulation and the energy spread at the entrance of SASE 3 reduces to about 3 MeV. This value corresponds to the initial energy spread plus energy diffusion due to quantum fluctuations of the spontaneous radiation in the SASE 1 undulator. As can be seen in Figure 5.2.5, the saturation length reduces in this case from 80 to 70 m. The relative difference of the energy in the radiation pulse at the project length of SASE 3 (110 m) is about 20% for the cases of SASE 1 on/off.

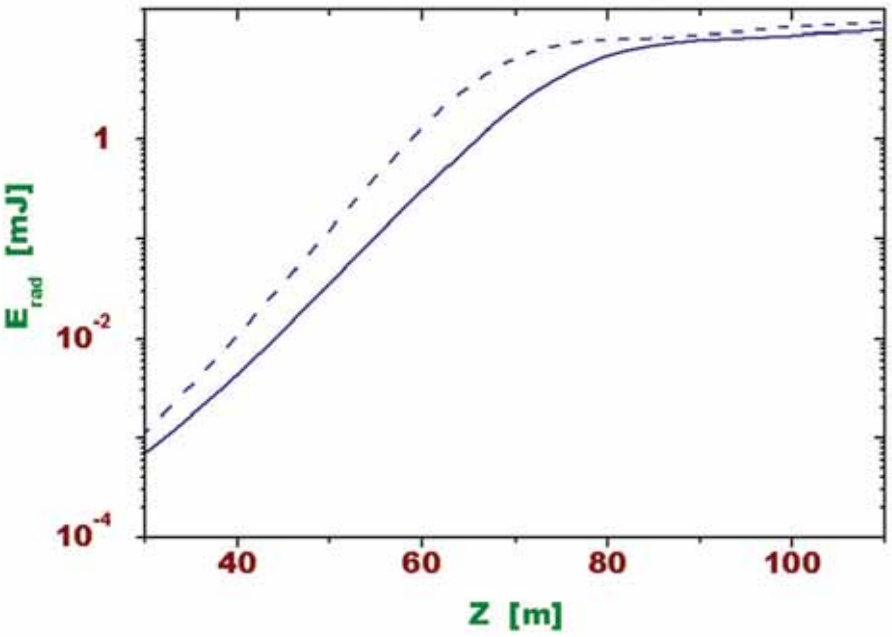


***Figure 5.2.5*** *Average energy in the radiation pulse against magnetic undulator length for SASE 3 operating at 0.4 nm wavelength. Solid and dashed lines correspond to the case of SASE 1 on/off, respectively.*

### 5.2.3 Statistical properties of the radiation

The radiation from SASE FEL operating in the linear regime possesses the typical properties of completely chaotic polarised light **[5-7, 5-13]**. Shot noise in the electron beam is a Gaussian random process; the FEL amplifier, operating in the linear regime, can be considered as a linear filter, which does not change statistics. As a result, radiation is also a Gaussian random process. In this case, the probability distribution of the instantaneous radiation power should be the negative exponential distribution (the notion of instantaneous power refers to a certain moment of time and a point in space, considered over an ensemble of pulses). Also, the finite-time integrals of the instantaneous power (energy in the radiation pulse) and the integrated spectral density (measured after the monochromator) should fluctuate in accordance with the gamma distribution **[5-7, 5-13]**:

$$P(W) = \frac{M^M}{\Gamma(M)} \left( \frac{W}{\langle W \rangle} \right)^{M-1} \frac{1}{\langle W \rangle} \exp\left( -M \frac{W}{\langle W \rangle} \right), \tag{5.11}$$

where $\Gamma$(M) is the gamma function, $M=1/\sigma_w^2$, and $\sigma_w=(\langle(W-\langle W\rangle)^2\rangle)^{1/2}$. The parameter M can be interpreted as the average number of “degrees of freedom” or “modes” in the radiation pulse. Fluctuations reach maximum value at the end of the linear regime. A zero-order estimate for the number of longitudinal modes is $M=\sigma_z/(c\tau_c)$ with $\tau_c$ given by (5.3).

When approaching the saturation point, the statistical properties of the radiation change drastically on a scale of one field gain length **[5-7, 5-13, 5-33, 5-34]**. One useful property of the non-linear regime is the reduction of fluctuations of the radiation energy by about a factor of two with respect to the linear regime. Sensitivity of the radiation pulse energy with respect to jitters of machine parameters is reduced as well. Radiation power in the non-linear regime continues to grow due to the growth of sidebands in the non-linear media. As a result, spectrum broadening occurs. The spectral brightness and the degree of transverse coherence reduce as well. Maximum brightness of the radiation occurs at the undulator length of about ten field gain lengths.

### 5.2.4 Higher harmonics

Radiation of the electron beam in the planar undulator contains a rich harmonic spectrum. This refers to both incoherent and coherent radiation **[5-35 – 5-47]**. The fraction of higher harmonic content is very important for users planning experiments at the European XFEL. On the one hand, higher harmonics constitute a rather harmful background for some classes of experiments; on the other, higher harmonic radiation can significantly extend the operating band of the user facility.

A comprehensive study of the statistical properties of the odd harmonic radiation from SASE FEL has been performed in **[5-46]**, with the time-dependent simulation code FAST **[5-7, 5-18]** upgraded for simulation of non-linear harmonic generation. Application of similarity techniques allowed the derivation of universal formulae for the contribution of the odd harmonics to the total power of SASE FEL operating at saturation. In fact, this contribution is a universal function of the undulator parameter K and the longitudinal velocity spread parameter. For the European XFEL, simulations predict that the relative contribution to the total power of the third and the fifth harmonic is about 1% and 0.03%, respectively. Contribution of higher odd harmonics is at the level of spontaneous emission.

General statistical properties of the odd harmonics of the SASE FEL operating in saturation are as follows. The power of higher harmonics is subject to larger fluctuations than that of the fundamental one. Probability distributions of the instantaneous power of higher harmonics are close to the negative exponential distribution. The coherence time at saturation falls in inverse proportion to the harmonic number, and the relative spectral bandwidth remains constant with harmonic number.

There exists also a mechanism for non-linear generation of the second harmonic **[5-47]**. The contribution of the second harmonic to the total radiation power strongly depends on the value of the diffraction parameter B. Contribution of the second harmonic is expected to be about a fraction of a percent for SASE 3 operating at the wavelength around 1.6 nm, and is practically negligible for SASE 1 operating at 0.1 nm wavelength.

## 5.3 Spontaneous synchrotron radiation

The layout of the XFEL places two long undulators for spontaneous emission behind SASE 2. Although the electron beam performance is degraded by the SASE process, the beam still has a high quality compared to storage rings. Therefore, the minimum undulator gap can be reduced to 6 mm. Due to the small magnetic gap, high fields and consequently large K-values are possible. On axis, the spectrum consists of the well-known peaks of the odd harmonics and the design of the undulators allow for first harmonics in the hard x-ray regime. Furthermore, gap tuning allows coverage of the photon energy range up to nearly 100 keV using first and third harmonic radiation. Of course, the brilliance of spontaneous radiation is several orders of magnitude lower than that of FEL radiation, but its spectral range, time structure with ultrashort pulse durations of the order of <200 fs, and the high degree of coherence makes this radiation very interesting for a variety of experiments [see e.g. **5-48, 5-49**].

### 5.3.1 Undulator parameters

The U1 and U2 undulators will be realised in a similar fashion as the FEL undulators. Due to the length and the small gap the electron beam optics requires a FODO lattice inside the undulator sections the same as for the FEL undulators. The undulators are, therefore, designed to be built out of ten 5 m long segments with 1.1 m intersections between segments. Their magnetic length should be 50 m in order to increase the photon flux. Table 5.3.1 gives the parameters for the U1 and U2 undulators for two gap values. The electron beam parameters given in Table 5.1.2 are also valid for the undulator sections if one includes an increased energy spread of 8 MeV. The beta function in the undulator sections is 15 m.

### 5.3.2 Spontaneous radiation parameters

There are no simulation tools available today which are able to calculate the spontaneous radiation from the proposed undulator. The complexity of the long undulators with intermediate electron beam focusing and the phase problem of the ten segments, do not allow us to use existing tools for calculation of the radiation for the full length of all segments, that is for the full number of nearly 2,000 periods. Since the number of periods is an important parameter that relates directly to radiation properties such as opening angle of radiation and bandwidth, we cannot make an exact prediction of the expected values. Instead, we will give an estimate for the radiation from an incoherent superposition of ten 5 m long segments. This is certainly a lower level approximation. From Table 5.3.2 one observes the radiation parameters for four photon energies. Using the fundamental line, the entire energy range from 20 to 90 keV is accessed with a reasonable variation of the magnetic gap (see also Table 5.3.1). The energy range 20-30 keV is very suitable for diffraction experiments in a classical configuration and for exploiting the time-structure or the coherence of the beam. The energy range from 60 to 90 keV, provided either through the fundamental or by third harmonics radiation, is of high interest to materials science studies, again exploiting the time-structure and the coherence properties. The differences between using fundamental or 3rd harmonic radiation are factors up to 3 in relative

bandwidth and photon flux through an aperture. In Table 5.3.2. we consider only the parameters of the fundamental harmonics, having larger bandwidth and higher photon flux.This table indicates that the flux in photons/pulse will be almost constant over the entire photon energy range. At the same time, the bandwidth narrows by one order of magnitude, the pulse duration is three orders of magnitude shorter, and the coherence improves when comparing it to storage ring sources. Therefore, the increase in brilliance is quite important. The main difference is the angular acceptance. Whereas with synchrotron sources, relatively large angular openings can be accepted due to the proximity of the optical element to the source, here the beam has to be transported ~100 m before the first optical element can be placed into the beam path. Placing a $1\times1$ mm$^2$ aperture at this distance reduces the acceptance to ~1% of the SR case. Figure 5.3.1 shows spectra for spontaneous radiation through this aperture for different settings of the undulator.

| | Unit | 'Closed gap' → 'Opened gap' | | | |
|---|---|---|---|---|---|
| Magnetic gap | mm | 6 | 7.5 | 11.3 | 16.1 |
| Photon energy range first harmonic | keV | 20.2 | 30.6 | 60.1 | 90.1 |
| Photon energy range third harmonic | keV | 60.6 | 92 | - | - |
| Period length | mm | 26 | 26 | 26 | 26 |
| Number of periods per segment | | 192 | 192 | 192 | 192 |
| Number of segments | | 10 | 10 | 10 | 10 |
| Magnetic field | T | 1.24 | 0.95 | 0.54 | 0.28 |
| K- parameter | mm | 3 | 2.3 | 1.3 | 0.7 |

***Table 5.3.1*** *Parameters for U1 and U2 undulators for spontaneous radiation.*

| | Unit | U1/U2 spontaneous synchrotron radiation | | | |
|---|---|---|---|---|---|
| Photon energy | keV | 20.2 | 30.6 | 60.1 | 90.1 |
| Photon beam size (FWHM) | µm | 24.5 | 24.5 | 24.5 | 24.5 |
| Photon beam divergence (FWHM) | µrad | 3.0 | 2.6 | 2.2 | 2.0 |
| Pulse duration (FWHM) | fs | 200 | 200 | 200 | 200 |
| Spectral bandwidth (FWHM) | % | 0.77 | 0.98 | 1.66 | 2.33 |
| Coherence angle | µrad | 0.25 | 0.16 | 0.08 | 0.05 |
| Photons per pulse | # | $1.1\times10^{9}$ | $1.7\times10^{9}$ | $2.5\times10^{9}$ | $1.9\times10^{9}$ |
| Average flux | #/s | $3.4\times10^{13}$ | $5.0\times10^{13}$ | $7.5\times10^{13}$ | $5.6\times10^{13}$ |
| Peak brilliance | B | $3.1\times10^{27}$ | $3.9\times10^{27}$ | $4.3\times10^{27}$ | $2.5\times10^{27}$ |
| Average brilliance | B | $1.8\times10^{19}$ | $2.3\times10^{19}$ | $2.6\times10^{19}$ | $1.5\times10^{19}$ |

***Table 5.3.2*** *Radiation parameters for U1 and U2 radiation at four photon energies calculated using the SPECTRA code* **[5-50]** *for the electron beam parameters given in Table 5.1.2 and an increased energy spread of 8 MeV. Calculations have been performed for $9\times9$ µrad$^2$ angular acceptance. Brilliance is given in units of photons/ 0.1%bw/s/mm$^2$/mrad$^2$.*

In order to estimate if gain due to coherent superposition plays an important role, we have compared the values for 20 keV radiation from an undulator with 5 m coherent superposition length to those obtained for 10 and 20 m long segments. Here, we assume complete phasing and neglect the intersections for electron beam optics. Table 5.3.3 indicates that the flux through an aperture, given in photons per pulse, does not change. The differences in bandwidth and divergence of the beam lead, however, to an increase of the brilliance. We, therefore, do not expect large deviations from our simulations for the spontaneously emitted radiation.

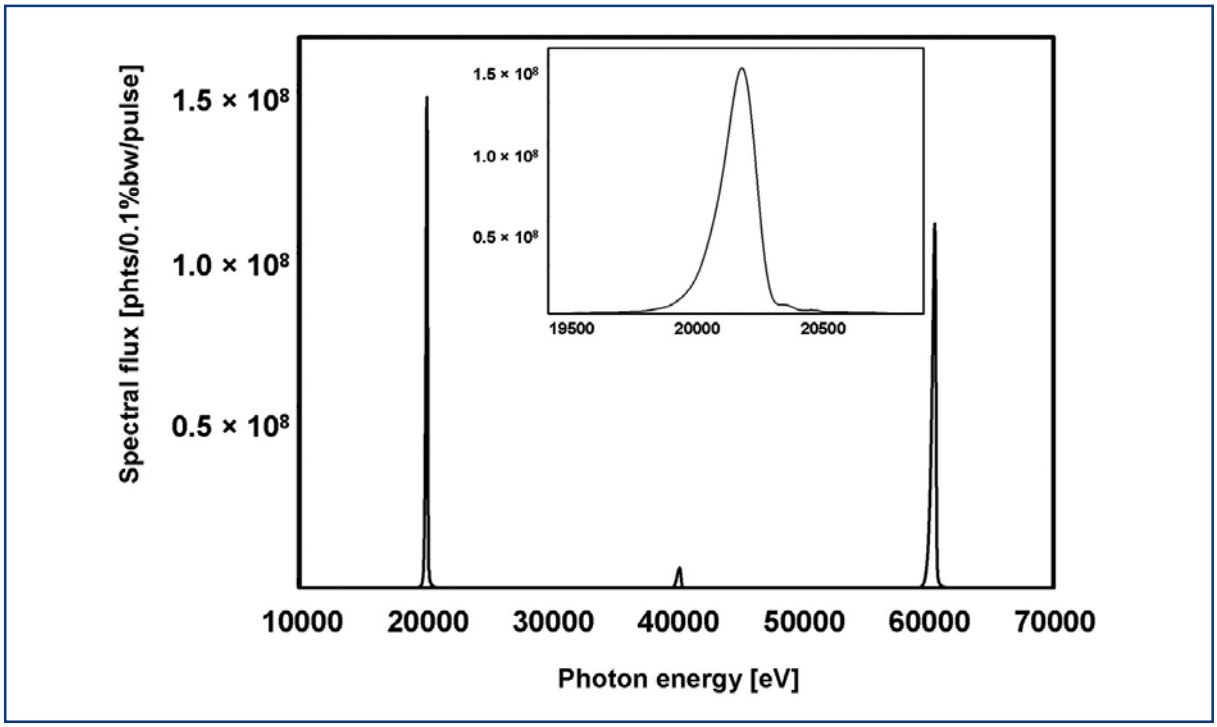


***Figure 5.3.1*** *Spectral flux through an angular aperture of 9×9 μrad² for spontaneous radiation from U1 undulator and a gap of 6 mm. The inset shows the fundamental line that has a bandwidth of 0.77%.*

| | Unit | U1/U2 spontaneous synchrotron radiation | | |
|---|---|---|---|---|
| Length of coherent segments | m | 5 | 10 | 20 |
| Photon beam size (FWHM) | μm | 24.5 | 24.5 | 24.5 |
| Photon beam divergence (FWHM) | μrad | 3.0 | 2.4 | 2.0 |
| Spectral bandwidth (FWHM) | % | 0.77 | 0.64 | 0.57 |
| Photons per pulse | # | $1.1\times10^{9}$ | $1.1\times10^{9}$ | $1.1\times10^{9}$ |
| Average flux | #/s | $3.4\times10^{13}$ | $3.4\times10^{13}$ | $3.4\times10^{13}$ |
| Peak brilliance | B | $3.1\times10^{27}$ | $4.7\times10^{27}$ | $6.4\times10^{27}$ |
| Average brilliance | B | $1.8\times10^{19}$ | $2.8\times10^{19}$ | $3.8\times10^{19}$ |

***Table 5.3.3*** *Radiation parameters from U1/U2 for 20.2 keV calculated using the SPECTRA code* **[5-50]** *for the above parameters and assuming different lengths of the coherently radiating sections. Comparison is done for a total magnetic length of 50 m. Brilliance is given in units of photons/0.1%bw/s/mm²/mrad².*

## 5.4 Undulator systems

The undulator provides the periodic magnetic field which induces the FEL process. Compared to storage ring sources the undulators will be very long as the saturation length is of the order 100 m for x-ray radiation. It is clear that the electron beam requires focusing elements within the undulator section to preserve its lateral size. The electron beam parameters call for a “separate function” undulator, where the periodic magnetic field and the strong focusing are physically separated. The undulator system, thus, consists of undulator segments and separated strong focusing quadrupoles and phase adjusters, beam correctors, position monitors, etc. The European XFEL Facility includes three XFEL undulators and, in addition, two undulators for spontaneously emitted synchrotron radiation as shown in Figure 5.1.1. In the design of the undulators’ systems, no fundamental difference is made between a FEL and a spontaneous undulator system. Therefore, in the following, no special distinction is made, and all undulator systems are treated in the same fashion. In Table 5.4.1 the parameters of the XFELs and spontaneous emitters are summarised.

The undulators described in this section are extremely demanding devices due to their length and their required accuracy. Many components of the undulators have to work together in a complex way. The most delicate and also most expensive items are the magnetic structures. But also the mechanical girders have extreme requirements to stability, precision, and reproducibility. Fortunately, there has been a tremendous development of insertion device technology since undulators have come into use as intense sources of synchrotron radiation 25 years ago. Considerable progress has been made in the design, construction and optimisation of these devices. There are well-established techniques to produce insertion devices with properties that are very close to perfect. Design and construction of undulator systems for the European XFEL will certainly take full advantage of these achievements.

### 5.4.1 Choice of undulator parameters

The basic concept for the layout and design of the undulator systems of the European XFEL is described in Section 5.1.2. For completeness Table 5.4.1 gives an overview of all five undulator systems, their spectral ranges and their parameters. According to this table a total of 116 segments are required for the XFEL. Substantial research and development (R&D) activities are needed to find an economic way to supply this quantity within time, quality and cost limits. These activities are described below. All undulators will be installed in tunnels with a diameter of 5.2 m in case of SASE 1 and SASE 2 and of 4.5 m in the cases of SASE 3, U1 and U2. In Figure 5.4.1 it is shown how a string of three segments would be placed inside the 5.2 m diameter tunnel. Tunnel infrastructure such as air conditioning, cable trays, piping, etc. is omitted. One cell consists of a 5 m long undulator segment and a 1.1 m long intersection. For the transport of undulator segments, a combination of a special transport vehicle similar to those used for magnet transport in accelerator tunnels with air cushions may be used. Fast transport in the XFEL tunnels over distances of several hundred metres at a speed of 2-3 km/h is possible in this way. At the insertion point the air cushions are used to move the segments

in position. Then they are lowered to stable floor plates. In the same fashion insertion devices are moved in DORIS III. If well optimised, an undulator segment may be exchanged in 1-2 hours.

| | $\lambda$ [nm] | $\lambda_u$ [mm] | g [mm] | $B_{max}$ [T] | K | $\beta$ [m] | $L_{sat}^{+}$ [m] | $N_{tot}^{++}$ [m] | $L_{tot}^{+++}$ [m] |
|---|---|---|---|---|---|---|---|---|---|
| SASE 1* | 0.1 | 35.6 | 10 | 1.0 | 3.3 | 32 | 133 | 33 | 201.3 |
| SASE 2* | 0.1 | 48 | 19 | 0.63 | 2.8 | 46 | 174 | 42 | 256.2 |
| | 0.4 | | 10 | 1.37 | 6.1 | 15 | 72 | | |
| SASE 3** | 0.4 | 80.0 | 23 | 0.44 | 3.3 | 15 | 81 | 21 | 128.1 |
| | 1.6 | | 10 | 0.91 | 6.8 | 15 | 50 | | |
| U1/U2*** | 0.06 | 26 | 6 | 1.24 | 3.0 | 15 | - | 10 | 61 |
| | 0.014 | | 16 | 0.28 | 0.7 | 15 | - | | |
| | | | | | | **Total:** | **116** | **707.6** | |

* Planar hybrid undulator.
** Apple II type helical undulator.
*** *Planar hybrid undulators for spontaneous radiation. Wavelength corresponds to first harmonic*
$^{+}$ *Magnetic length without consideration of field errors.*
$^{++}$ *Number of 5m undulator segments plus 20% contingency. Spontaneous emitters have 10 segments each.*
$^{+++}$ *Total system length includes 1.1m long intersection after each undulator segment.*

***Table 5.4.1*** *Parameters of the undulator systems. The electron beam energy is 17.5 GeV.*

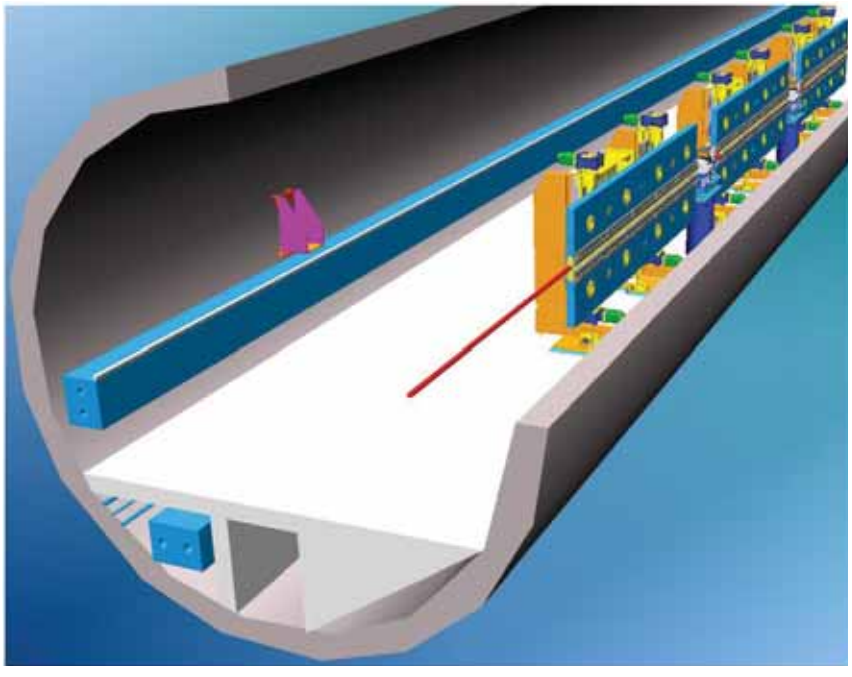

***Figure 5.4.1*** *A string of three cells of an undulator system is shown as it will be installed in a tunnel with a diameter of 5.2 m (SASE 1, SASE 2). Infrastructure such as air conditioning, cable trays, supply media are not included.*

### 5.4.1.1 Magnet technology

Undulators might be built using superconducting magnets, room-temperature electromagnets, or permanent magnets (PMs). These technologies were investigated and discussed in **[5-26, 5-51]**. In 2005, a workshop held at Deutsches Elektronen Synchrotron Laboratory (DESY) discussed the issue again and concluded that, at present, no alternative to PM technology for the large-scale use in undulator systems, such as the European XEL Facility is available. The hybrid design **[5-52]** uses NdFeB permanent magnets and soft Iron parts which concentrate the magnetic flux. For the hybrid design errors are mostly determined by the machined pole faces. In order to produce circularly polarised light, a modified planar pure PM structure was proposed by Sasaki **[5-53]**. With 25 years of development of undulator technology based on PMs, many techniques for error compensation have been developed. Technologically, all problems related to manufacturing of large numbers of undulator segments are solved:

- manufacturing techniques are well established, extensive experience exists;
- the magnet structures are planar, allowing for excellent access for magnetic field measurements and for the insertion of vacuum chambers;
- helical undulators can be built as planar devices as well;
- numerous high-precision magnetic field measuring techniques are available;
- control of field errors can be done using shims or field fine-tuning **[5-54 – 5-56]**.

The design proposal for the undulator systems for the European XFEL will, therefore, be based exclusively on PM technology. For the peak magnetic field the following dependence on material constants $a_1$, $a_2$, $a_3$, magnetic gap $\gamma$ and undulator period $\lambda_u$ is valid:

$$B_{\max}(T) = a_1 \times \exp\left[ a_2 \frac{g}{\lambda_u} + a_3 \left( \frac{g}{\lambda_u} \right)^2 \right]. \qquad (5.12)$$

For a state-of-the-art hybrid undulator made of NdFeB, $a_1$=3.694, $a_2$=-5.068, and $a_3$=1.520 are used. This assumption is valid for NdFeB for $0.1 < g/\lambda_u < 1.0$. The magnetic gap chosen for the XFEL and spontaneous emitters is 10 and 6 mm, respectively.

### 5.4.1.2 Radiation damage

Potential radiation damage of the PM material due to electron, neutron, and hard x-ray bombardment could endanger the required performance of the FEL undulators and, therefore, the performance of XFEL radiation. Until recently experience only existed for IDs in storage rings, where a very high transmission and, therefore, a very low loss rate is enforced by the requirement of long lifetime of the stored electron beam. Under normal operating conditions, no significant radiation damage has been observed **[5-57, 5-58]**. In contrast, not much was known about how PM undulators behave in the radiative environment of a high duty-cycle linac like the one proposed for the European XFEL. Here, the situation is completely different. Although the emittance and beam size are smaller than in storage rings, there might be a significant amount of beam halo and dark

current far outside the phase-space covered by the transverse and longitudinal electron beam emittance. A well-designed collimator system to protect the undulators from being hit by electrons is, therefore, essential. The collimator system is described in Section 4.7.1.2.

Recently, experience has been gained from the operation of the undulator system installed at the FLASH facility at DESY. At FLASH the radiation doses were continuously measured without interruption in a meticulous way over the whole operation time of the undulator at 15 positions equally spaced over the length of the device. Measurements made at the undulator system after de-installation showed that no damage could be detected within an accuracy of $2\times10^{-4}$ after three years of operation and a maximum exposure of 12,000 Gy near the entrance **[5-59]**. An extrapolation to the XFEL based on these data resulted in even higher lifetimes. A coarse lifetime estimate for the magnet material can be made based on the results obtained at the TESLA Test Facility (TTF) facility with the following assumptions:

- we take the result of Okuda **[5-60]** who observed a 9% loss of demagnetisation of NdFeB material for an absorbed dose of 2.5 MGy after electron irradiation, equivalent to 1% for 0.28 MGy;
- the length of the radio frequency (RF) pulses needs to be considered since the radiation dose increases linearly with dark current;
- a factor of 50 accounts for the increased availability of the accelerator compared to the FLASH facility;
- we take the low dose levels at the undulator end for comparison, thus considering the first two segments as additional shielding elements.

Extrapolating thus gives an expected annual dose of 8,000 Gy for the undulators at the European XFEL. This is a worst case estimate and the real irradiation of the magnets will be less due to the following arguments:

- the electron accelerator of the European XFEL has phase-space as well as “energy” collimation. Dark current, therefore, cannot hit the undulator. In addition, the electron beam in the collimator does not point towards the undulator. This is discussed in detail in Section 4.7.1.2;
- the doses at FLASH are integrated over the whole previous life. They include runs with missteered electron beam, high dark current levels or non-optimum collimator adjustments as well. Such conditions contribute significantly to irradiation doses. In this project these unwanted beam conditions can be avoided thanks to the commissioning dump installed in front of the undulators;
- the gap of the FLASH undulator is fixed. In this project the gap can be opened for commissioning and beam optimisation. Thus, the irradiation at these operation modes will be avoided;
- online dosimeters and loss monitors will be installed **[5-61]** giving a clear signal, if the dose level inside the undulator region becomes too high.

The resulting worst case lifetime estimate for 1% demagnetisation is 35 years. This estimate does not include the above relieving arguments. As a result, NdFeB should be fully sufficient as undulator magnetic materials, and the radiation harder magnets samarium and cobalt will not be used. Nevertheless, fast exchange of undulator segments is desirable as a conservative fallback solution in case that radiation damage becomes a problem.

### 5.4.2 Basic tolerance requirements

The line width of FEL radiation is determined by the dimensionless Pierce parameter $\rho_{1D}$ (5.2), which for an XFEL at 0.1 nm amounts to $3\times10^{-4}$. For the undulator system this means that the fundamental wavelength has to be tuned with an accuracy given by:

$$\frac{\Delta\lambda}{\lambda} \leq \rho \,. \tag{5.13}$$

The nature of the FEL process is such that, in order to have an effect on the radiated power, an error has to act over a power gain length, which for the XFEL is in the order of 10 m. Certainly, a conservative requirement would be for (5.13) to be valid for one undulator segment, which is only 5 m long. There are different error sources having an effect on the fundamental line: temperature via the temperature-dependent magnetisation coefficient of the magnet material, vertical alignment via the hyperbolic-cosine field distribution, gap and flatness errors via the exponential field dependence. If all error sources are equally weighted and using

$$\Delta\lambda = \left|\frac{\partial\lambda}{\partial B}\right| \sqrt{\Delta B_{Temp}^2 + \Delta B_{Gap}^2 + \Delta B_{Flat}^2} \tag{5.14}$$

one obtains the values given in Table 5.4.2.

| | | | |
|---|---|---|---|
| Temperature stability (whole system) | $\Delta$T | ± 0.08 | K |
| Alignment (each segment) | $\Delta$Y | ± 100 | µm |
| Gap accuracy (each segment) | $\Delta$g | ± 1 | µm |
| Flatness change of each segment under gap change | $\Delta$g | ± 1 | µm |

***Table 5.4.2*** *Undulator systems tolerances.*

There are two consequences of these requirements:

- the whole undulator system must be in a very well controlled temperature environment. The impact of this requirement on the tunnel layout and air conditioning system will be discussed in Section 7.2.3;
- the geometric tolerances have a strong impact on the mechanical design and requirements on the control system. This will be addressed in the next section.

### 5.4.3 Undulator segments

The huge total length of the undulator section calls for standardisation and an economic design that is optimised for the production of large quantities. Several aspects play a role in long undulator systems for SASE FELs. The total length of an undulator system is much longer than the optimum $\beta$-function for largest FEL gain. External strong focusing is, therefore, needed to keep the $\beta$-function within limits acceptable for the FEL process. The undulator system will be separated into undulator segments and strong focusing quadrupoles. With the single exception that a second working point at 10 GeV electron energy could be established in order to enable access to the soft x-ray regime below 800 eV, the photon energy of the FEL and spontaneous radiation will be changed by gap tuning. This increases the saturation length and leads to a requirement for tunable phase shifters. It could also induce gap dependent field errors. Only four different types of magnet structures are needed for a total of 116 segments. In the design and construction one, therefore, should take advantage of the large numbers by using standardised components wherever possible. Items which will contain as many identical components as possible are:

- the gap separation drive systems, motion control components, motors, servos;
- girders;
- components inside the undulator interruptions, such as phase shifters, corrector magnets and their power supplies, quadrupole magnets, and beam position monitors (BPMs);
- control systems for gap motion and gap dependent excitation of coils, readout of BPMs, etc.;
- vacuum chambers and other vacuum equipment.

Instead of optimising the components for different undulators individually, they will be designed for the most demanding case. For example, mechanical gap separation drive systems and girders will be designed for maximum magnetic forces occurring at the most critical undulator and then adopted for all of them. Phase shifters should be designed to meet the phase shifting requirements at the longest wavelength. This standardisation policy leads to most economical solutions in terms of production, prototyping, operation and maintenance.

#### *5.4.3.1 Support mechanics*

A mechanical design has been worked out, which complies with the accuracy requirements given in the previous section and in addition takes care of boundary conditions specific to the XFEL project, such as tunnel cross-section, transport in the tunnels, exchangeability of undulator segments, fast alignment, escape routes and other safety issues. Since large numbers of devices are required, the effort concentrates on designing one standard system. Critical design parameters were chosen conservatively in order to reduce the risk in fulfilling design performances for each of the segments in an industrial production process.

Figures 5.4.2 and 5.4.3 give a front and rear view of a proposed standard undulator segment for the XFEL. It is flexible enough to accommodate different types of magnetic structures.

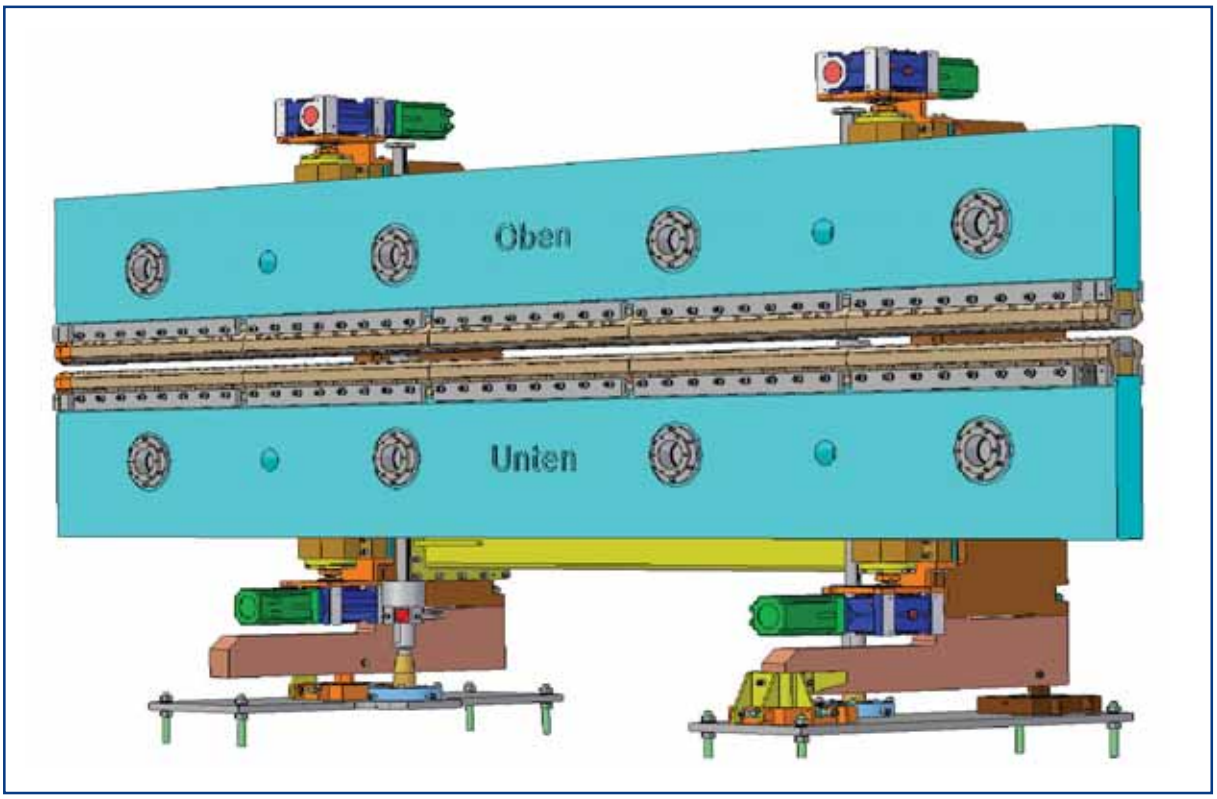


***Figure 5.4.2*** *Front view of a 5 m long undulator segment.*

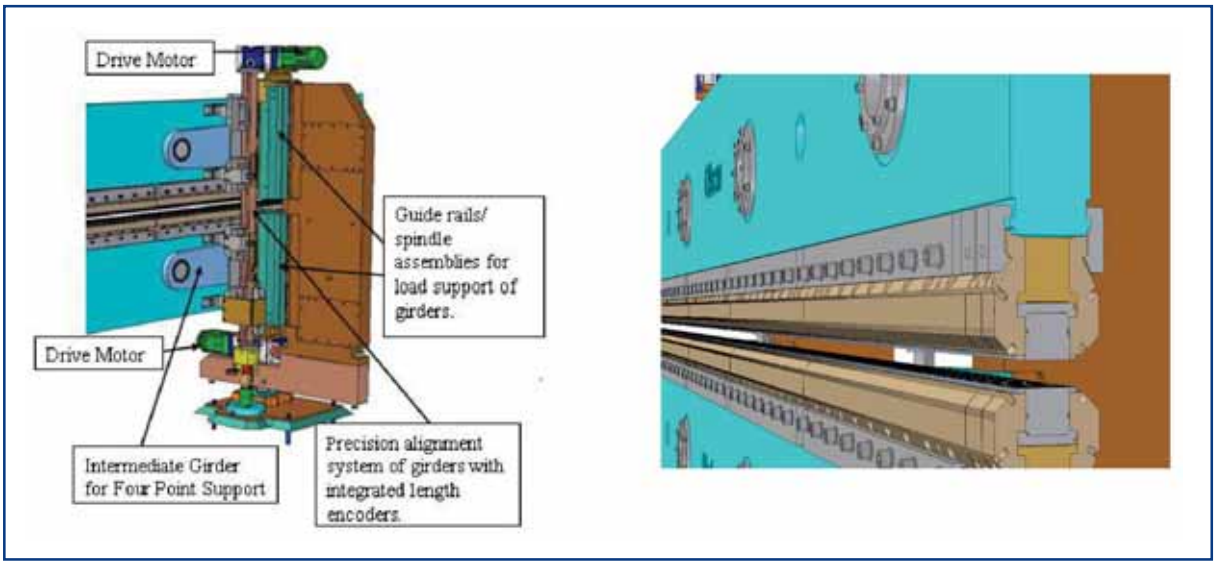


***Figure 5.4.3*** *Rear view showing details of the intermediate girder and the precision alignment system. The support frame has been suppressed to give a better view.*



***Figure 5.4.4*** *Clamping principle of the magnetic structure on the girders.*

There are several points, which deserve being mentioned:

- the girders have a substantial rectangular cross section of 500 by 100 mm to minimise shear deformation, which, in the µm range, dominates over compressive deformation;
- in order to avoid bimetallic bending as a function of temperature on the µm level, the materials for girders and support structures need to be identical. Suitable stainless steel with magnetic permeability smaller than 1.02 (e.g. Type 1.4429) will be taken for magnetic and mechanical stability reasons;
- each girder is supported on four equidistant points as seen in Figure 5.4.2. This reduces the deformation under changing magnetic loads dramatically. Two auxiliary, intermediate girders are needed, which are seen in the rear view in Figure 5.4.3;
- there are four motors, one for each spindle. They are electronically synchronised by a suitable control system;
- the girders are connected to massive guideways and lead screws integrated in the support columns using spherical supports. In this way the magnetic forces are transmitted and a rotational degree of freedom is provided. The exact parallel alignment of top and bottom girder is achieved through a separate guiding system, using movers with preloaded roller bearings free of backlash. This is also shown in Figure 5.4.3. The guiding system also integrates the encoders needed for the high precision position feedback for the four drive motors. Although guiding forces on the guide rails are small, and only originate in residual friction in the supports, their sizes are quite substantial in order to guarantee parallel alignment with high precision.

### *5.4.3.2 Magnetic structures*

The magnet structures are clamped onto the girders. This allows for a girder design which is independent of details of the magnet structure. This is illustrated in Figure 5.4.4. Identical materials are used for the girders and the non-magnetic support parts in order to avoid any bimetallic deformation as a function of temperature.

The mechanical design of the magnetic structure takes advantage of experience gained from the undulator system for the FLASH facility at DESY. Segments of 0.957 m length are used. One is shown in the left of Figure 5.4.5. In addition, end sections made in the same fashion are needed.

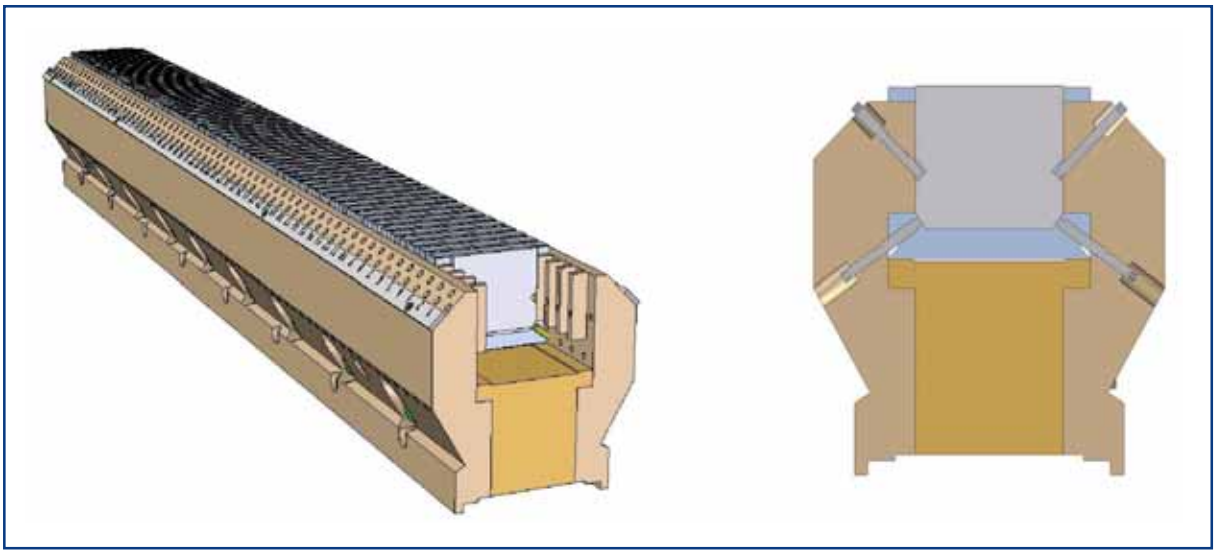

***Figure 5.4.5*** *Left: Assembly of one 0.957 m long magnet segment. The first magnets and poles are not inserted. A 5 m long device uses five segments plus compensation pieces built in exactly the same fashion. Right: Cut through a pole showing the height adjustment principle. The height of a pole can be adjusted by at least ± 0.3 mm and its tilt by about ± 1 mrad. The screws from below are used to lock the pole in position.*

As seen in Figure 5.4.5 there is a comb-like structure with pockets for the magnets and slits for the poles. Magnets and poles are pinned down using worm screws at approximately 45°, which act onto notches in the magnets and poles (compare Figure 5.4.5). For the poles this allows fine adjustment of the height. From the bottom there are counter-screws, which are used to lock a pole in position. The tolerances are chosen in such a way that the overall vertical position can be varied by at least ±0.3 mm and in addition, the tilt of the poles can be adjusted by ±1 mrad by using the right and left adjustment screws. Starting with an initial pole overhang of 0.5 mm the exact adjustment of the poles is done during magnetic measurements. Typical corrections are less than ±0.1 mm. They will be determined using measured magnetic field data and applying the method of “Field fine tuning by Pole Height Adjustment” **[5-56]**.

This method assigns measured field errors to pole height corrections for each pole. A high field quality can be obtained in this way.

### *5.4.3.3 Control system*

There are several requirements on the control system in order to make full use of the capabilities of the undulator system. The control system:

- has to coordinate and synchronise the motion of the four motors of an undulator segment with high precision. The gap should be adjusted with an accuracy of less than 1µm. In addition, operational safety such as proper recognition of equipment failure, breaking of cables, loss of synchronisation, etc. has to be guaranteed;
- has to allow for synchronisation of additional components, for example current settings of corrector coils, gap values for phase shifter settings, etc. It should be possible to implement these corrections in a flexible manner;

- must be modular and easily extendable: It must provide control of the whole undulator system, i.e. synchronisation of many individual cells;
- should be designed for a life time of 15-20 years minimum;
- should be designed for high reliability and availability of components;
- makes use of industrial standards and components wherever possible.

A concept has been developed which is in accordance with these requirements. It is based on components manufactured by Beckhoff Industrie Elektronik, Germany using the TwinCAT software package. A variety of different components are available off the shelf such as: servo controllers, stepping motor controllers, analogue to digital converts (ADCs), digital to analogue converters (DACs), digital I/O modules, etc. They are widely used in industrial applications such as numerical machining, automation, robotics, handling systems, etc. Vendor independent fieldbus systems such as SERCOS or EtherCAT can be used. There are very fast solutions for triggering and synchronisation of an arbitrary number of components in a system. So the requirements mentioned above can be fulfilled.

As a predecessor for an XFEL control system, the so-called Motion Control Test Undulator (MTU) has been setup at DESY to get hands-on experience using these components. An old decommissioned wiggler was refurbished using four motors and components now proposed for the XFEL. It was demonstrated, that the 'In Position' gap with enabled feedback can be controlled with an accuracy of 0.2 µm. Mechanical play and backlash, although detectable in the spindles, were fully compensated for by the encoder feedback. The synchronisation works reliably and the hardware allows for the synchronisation of external components as well. Because of this encouraging experience it now serves as a template for the control system for the XFEL prototype undulator segments.

### 5.4.4 Intersections

Between two adjacent undulator segments there is an intersection unit which contains a phase shifter, corrector coils and an adjustable quadrupole. Currently electromagnetic (EM) phase shifters using a three magnet chicane are foreseen **[5-62]**. In the same fashion, conventional EM quadrupoles mounted on horizontal/vertical remotely controlled movers are planned. The current time and cost planning foresees the use of EM technology for these devices. However, in the following two sections, alternative designs based on PM technology are discussed. This effort is driven by the goal of avoiding any source of heat in the undulator section in order not to jeopardise temperature stability, to make components in the intersection as short and compact as possible, to have a handle to control fringe fields and to have sufficient accuracy for adjustments of the quadrupole centre and its strength. There is yet another difference: EM quadrupoles are structures which completely enclose the electron beam. The insertion of a vacuum chamber after the calibration measurements is therefore problematic. In order to insert the vacuum chamber, three alternatives exist: Either the quadrupole has to be opened and closed; the chamber has to be welded in situ; or magnetic measurements must be made with the

chamber already in place. Each of these procedures jeopardises precision on the µm scale and/or complicates magnetic measurements and/or is difficult to perform in a clean room environment, which is required for the vacuum components of the XFEL. Planar permanent magnet quadrupoles (PPMQs) on the other hand are open to one side and may just be moved over the beam pipe. Here this problem does not exist.

### *5.4.4.1 Planar permanent magnet versus electro magnetic quadrupoles*

An alternative to a conventional EM quadrupole is the PPMQ principle. It is an array of four magnetised parallelepipeds (see Figure 5.4.6). It is a modification of a proposal by Tatchyn **[5-63]**. A strong quadrupolar field is created in the centre of the PM array, which coincides with the beam axis. Two pairs of magnets, separated by a gap, are arranged as shown in Figure 5.4.6. The top and bottom separation distance may be changed independently by moving the blocks along the Z-direction symmetrically to the Y-axis. In this way, the gradient and the exact vertical centre position can be adjusted. These relations are shown in the contour plot in Figure 5.4.7 for European XFEL parameters. The gap is 12 mm. A maximum integrated gradient of about 8 T and a vertical centre adjustability of ±1 mm are required. Magnet dimensions are given in Figure 5.4.7 as well. It is seen that vertical centre adjustment capability requires some compromise with the integrated gradient, which has to be smaller than the maximum achievable one. 12 T is possible, at the cost of almost no adjustability. At 7.8 T the required adjustment range of ±1 mm is possible. Since the strength is proportional to the magnet length, a small increase might be needed to reach exactly 8 T. Horizontal centre adjustment is trivial: all four magnets may be moved by the desired amount along the Z-direction.

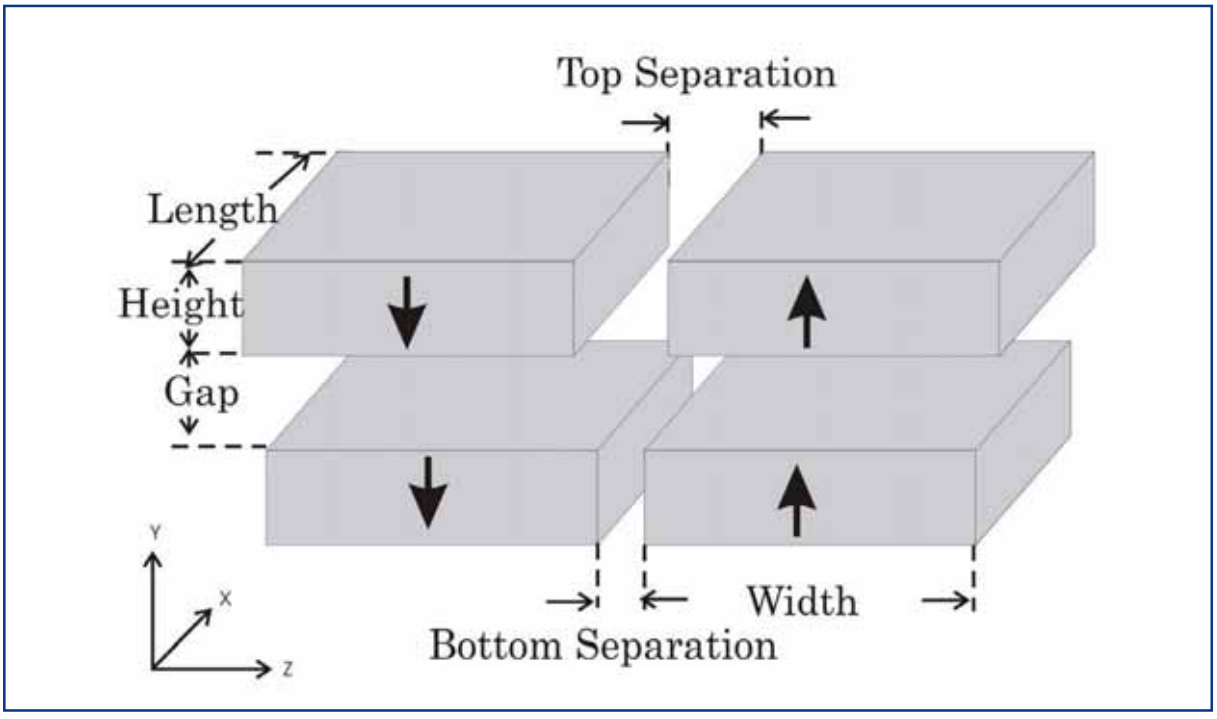


***Figure 5.4.6*** *Principle of a PPMQ.*

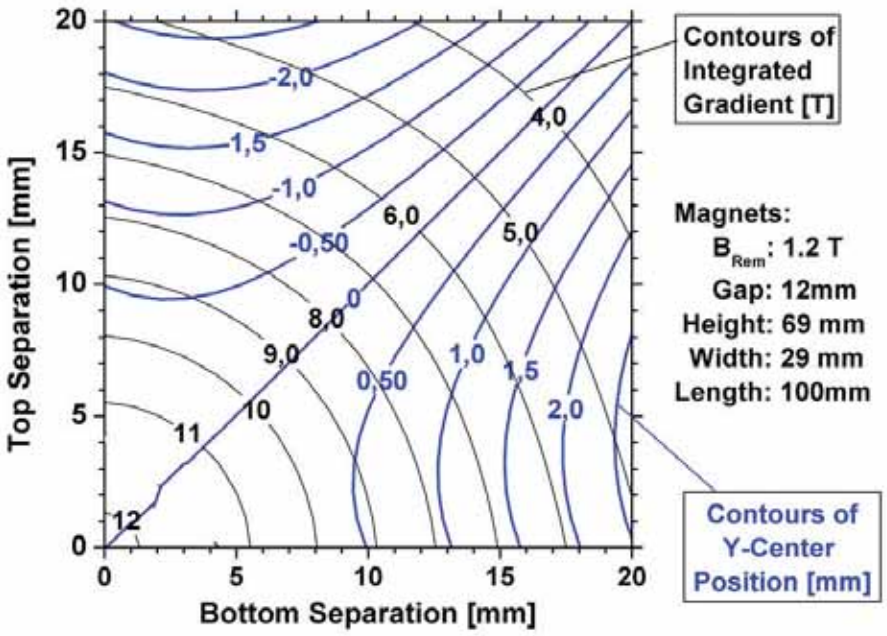


***Figure 5.4.7*** *Contour plot of the field gradient and the position of the vertical centre as function of top and bottom separations.*

The good field area is about ±1.5 mm which is sufficient for an electron beam with an RMS beam size of typically 25 µm. Although it looks exotic, the PPMQ principle was heavily and successfully used in the undulator for the FEL at the TTF Phase 1 (TTF1) at 300 MeV. Magnet arrays similar to those in Figure 5.4.6 were superimposed to the field of a PM undulator **[5-64]**. A total of 30 planar PM quadrupoles were integrated in the 15 m long undulator section. Each quadrupole had an integrated strength of about 1.7 T. They were arranged to form a FODO lattice superimposed to the periodic field of the undulator. An average beta function in the whole 15 m long undulator section of 1 m has been achieved in this way. Adjustment and alignment of the quadrupoles were done in a similar fashion as discussed above **[5-64, 5-65]**.

A PPMQ requires four precisely remotely controlled motorised axes. It may replace an EM quadrupole mounted on movable supports for beam steering as was described in **[5-27]**. This puts the additional mechanical effort for the PPMQ into perspective. The mechanical effort for a PPMQ is still larger than for an EM quadrupole on movable supports, but to compensate no power supply and cooling infrastructure is needed. So the cost difference is moderate. In the long-term, the operating cost of the PPMQ solution is, however, much lower anyway.

For the XFEL, control of the quadrupole centre positions with an accuracy of 1 µm is required. Whether the PPMQ principle meets this requirement depends not only on the stability, reproducibility and hysteresis of the permanent magnet material but also on the accuracy of the mechanical components used to move the magnets. This is subject to a detailed study. Assuming that these requirements can be fulfilled, each PPMQ can be

mapped out individually and with high precision in the same fashion as shown in Figure 5.4.7. In this way all errors can be individually characterised. Gradient and centre position can then be adjusted exactly by using these data.

It needs to be emphasised, that EM quadrupoles do not meet the above stability requirements a priori. Experience gained at FLASH has shown that differences in the coercive field of the Iron become visible at low excitation of the Iron and give rise to dipole components. As a consequence the magnetic centre moves by 50 µm and more depending on the current excitation and the magnetic history. The magnetic centre errors decrease with increasing current excitation. Special quadrupole designs using soft magnetic materials with very low coercive field, high permeability and sufficient saturation polarisation are needed. Such materials are used for special electro-mechanic applications such as actuators with low sticking effect, relays or low loss transformers. In a separate effort, EM quadrupoles using these materials are under development. A careful analysis and comparison of the PPMQ and the EM version will be performed before a final decision can be made.

### *5.4.4.2 Electromagnetic versus permanent magnetic phase shifters*

In undulator systems with variable gaps, phase shifters are needed to exactly adjust the phase between segments so that constructive superposition of the emitted light occurs. The simplest one is a three magnet EM chicane. This solution was proposed in **[5-27]** and is described in detail in **[5-62]**. Drawbacks are hysteresis and asymmetries in the magnets, especially in the central one, space requirements and stray fields.

Figure 5.4.8 shows a sketch of a PM phase shifter, which avoids most of these drawbacks. It uses a zero potential yoke made of soft Iron, PMs and poles in a similar configuration as in the case of a hybrid undulator. The full centre magnets excite flux in the poles next to them with the same strength but opposite sign. So the field integral is always balanced. Additional magnets between poles and the zero potential yoke can be used to enhance the pole strength. Slight vertical movement of these magnets can be used for error correction. In addition the zero potential yoke very effectively terminates the field and avoids stray fields outside the phase shifter. Its strength is controlled via the gap. Parameters were calculated for an application in SASE 3 at minimum gap lasing at 1.6 nm, which is the worst case. Here, a total length (L) of 230 mm is needed. With a 30 mm thick Iron yoke and 9.5 mm long poles a peak field of 1.22 T at a gap of 10 mm can be obtained. With this shifter the phase can be delayed by $2.47 \times 2\pi = 15.5$ rad at 1.6 nm, which allows continuous phase adjustments over the whole wavelength range from 0.4 to 1.6 nm. During operation the phase shifter has to be moved with the gap in a synchronised fashion.

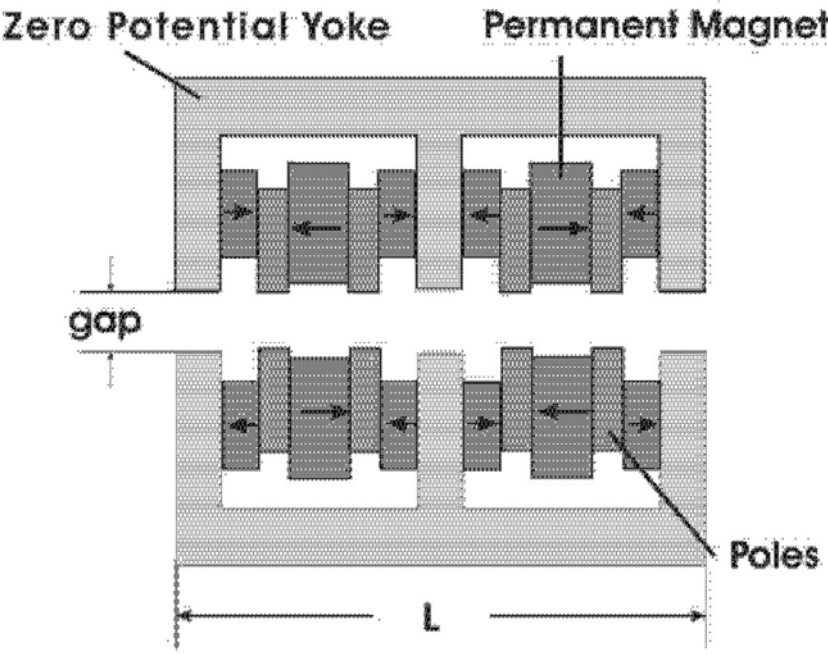


***Figure 5.4.8*** *Proposed PM phase shifter. The soft Iron zero potential yoke avoids stray fields. The strength can be adjusted by changing the gap. The length (L) is about 200 mm.*

### 5.4.5 Other components

For fine correction of residual field integral errors as a function of the gap, horizontal/ vertical air coils are planned. They will be excited by a gap dependent current. Their maximum steering field integral is about 0.2 Tmm. Expected corrections, however, are much smaller, less than 0.05 Tmm. Air coils with similar properties, which are under development for the PETRA-III insertion devices, may be used for this purpose.

### 5.4.6 Implementation of undulator systems

The XFEL requires five undulator systems with the parameters shown in Table 5.4.1 to be operational by 2012/13. The scope of the whole construction effort is large and without precedent: the total magnetic length indicated in Table 5.4.1 is about three to four times that of a state-of-the-art third generation synchrotron radiation source such as APS, European Synchrotron Radiation Facility (ESRF) or Spring8.

Large scale production with heavy involvement of industrial partners will be an important part of the construction effort. Presently, there are very few vendors who have dedicated experience in building insertion devices mainly for use in storage rings. These are single items individually tailored to user requirements and are, therefore, quite expensive. But serial production, i.e. the production of a large number of identical or almost identical devices will be a mandatory aspect of the construction of the XFEL undulator systems. Vendors with suitable experience and capacity for large scale production of undulators do not yet exist. Vendor qualification is, therefore, essential to get qualified industrial partners involved.

It is proposed to procure 'ready to use' undulator segments. Although some conditions and the total amount of work has changed compared to earlier estimates **[5-27]** this basic idea will be pursued and is the basis for further R&D activities, which can be subdivided into three steps:

**Step 1** includes the definition and creation of a technological basis with involvement of industrial partners. This step is heavily affected by prior experience with the FLASH and includes:

- development of concepts for the mechanical design and motion control, which fully comply with XFEL requirements;
- construction of the first generation of prototypes, which in parallel are used for vendor qualification;
- development of fast and robust magnetic measurement techniques, which can be used in an industrial environment and are suited for large scale production;
- the first industrial study to elaborate on large scale production issues.

Some of these activities have already been started: a mechanical design and motion control concept, which has been described in this contribution, will be the basis for the first prototypes. They were built in 2006 as a first step to qualify vendors. In parallel, a new dedicated XFEL magnetic lab will be set up to develop magnetic measurement techniques. They are the prerequisites for the next step.

For step 2, there will be full involvement of industry including magnetic measurements and tuning. **Step 2** includes:

- incorporation of any design changes and imput from step 1;
- production of a second generation of prototypes, including the full production cycle;
- a second industrial study, which will be the basis for setting up large scale production.

**Step 3** is the production phase and is planned to last for almost five years. It starts immediately after step 2 (but only if step 2 has been completed successfully). At this stage, the large scale production starts. Details will strongly depend on the experience gained during prototyping. However, the following points will be important:

- the placement of contracts;
- the planning of production capacities;
- the planning of production sites;
- work flow logistics;
- quality management, QA/QC procedures;
- a definition of the acceptance test;
- the start of serial production;
- the ramp up of production capacity.

A tentative time schedule, assuming that the undulator concept can be realised as described previously is shown in Table 5.4.3. The R&D phase, including two generations of prototypes (according to steps 1 and 2) has already started and will take in total four years. By 2010 everything is assumed to be ready for serial production. The SASE 1 system will be the first to become operational at the end of 2012, so has been started first. After its installation, commissioning of the XFEL will start. The SASE 2 system can be installed during the commissioning phase of SASE 1, and will become operational by the end of 2013. Therefore, it may be started with a delay of one year. The spontaneous systems U1 and U2 should be constructed and installed in parallel to SASE 2. For SASE 1, SASE 2, U1 and U2 the installation in the tunnels can be done parallel to the production since there is no beam in the tunnel. For SASE 3 this is different. This system will need much more construction effort. It is, therefore, postponed and will not become available before the end of 2014. Since SASE 1 is fully operational at this time, the installation will have to be done in a short shutdown of three months. There are no problems anticipated due to the short installation period of SASE 3. The time consuming installation of beamline components, such as vacuum chambers, intersections, etc. can be done previously in a shutdown. The SASE 3 undulator segments themselves will be installed quickly, since they are designed appropriately (see above). This will help to cut down installation time.

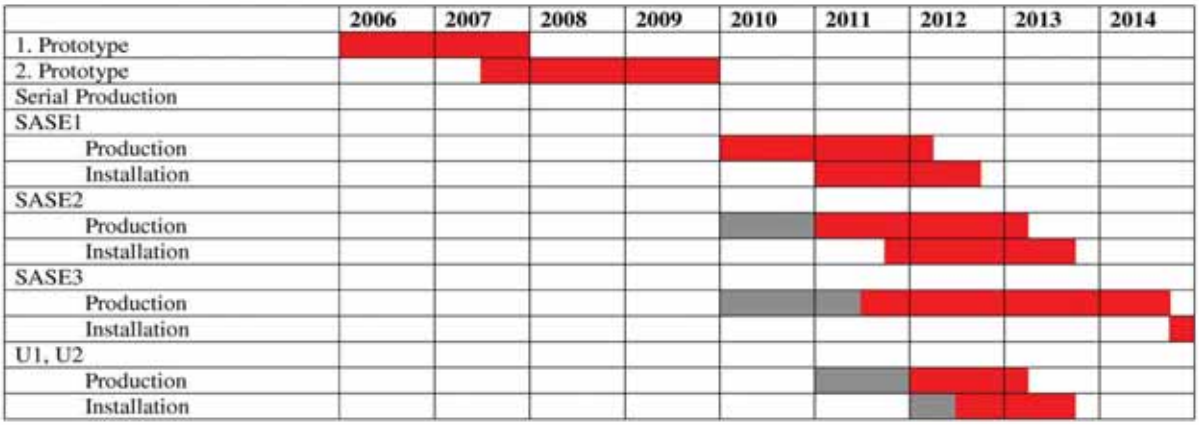


***Table 5.4.3*** *Tentative time schedule for undulator development and production for the XFEL. Start of operation is end of 2012.*

## 5.4.7 Summary

An update and overview over the undulator systems for the XFEL has been given. There are not only stringent tolerance requirements on the undulator systems for the XFEL, the construction of the large number of devices itself is also without precedent. A dedicated R&D programme, including the construction of prototypes, is being launched to provide the technological basis, to involve industry and qualify vendors. This R&D programme is the prerequisite for an effective serial production, which may start by 2010. The XFEL project is planned to start electron beam operation during years 2012/13. The last undulator system will be completed two years later. In this time frame the undulator systems have to be produced in the required numbers, in time, to budget and with sufficient quality.

## 5.5 Photon diagnostics of FEL radiation

FEL as well as spontaneous undulators of the XFEL, are multi-segmented systems with up to 42 single undulator cells. Alignment and commissioning of the numerous undulator cells along the XFEL beamline presents a serious challenge to measurement techniques based on electron beam (see Section 4.6 and **[5-66 – 5-68]**). Therefore, photon diagnostics provide an essential tool for commissioning and operation of the undulator cells independently of the electron-beam-based alignment procedure. Both methods will complement one another since the latter gives no insight into the magnetic gap or the phase match of adjacent undulator segments. Photon diagnostics have successfully been used at the TTF **[5-69]**, FLASH **[5-70, 5-71]**, the LEUTL FEL **[5-72]**, and has been proposed for the Linac Coherent Light Source (LCLS) project **[5-73, 5-74]**.

The concept of the photon-beam-based alignment procedure is based on variable gap undulator segments which allow the sampling of the spontaneous radiation of each segment individually by opening the gap of all other devices. With simultaneous measurement of photon beam position and angle, this radiation will be analysed with a special diagnostic station in order to:

- optimise angle and position of the electron beam trajectory;
- adjust the K-parameter of all undulator segments; and
- adjust the phase match between adjacent undulator segments.

In the following, the x-ray diagnostics for undulator system SASE 1 is discussed as a prototype representative for all beamlines. It is located about 460 m downstream of the last undulator cell (Figure 5.5.1) and allows characterising the radiation of an entire undulator system or individual segments and can be used for photon-beam-based alignment. It consists of a crystal monochromator as a principal unit, an imaging optics and different detector systems such as a CCD array, pin diodes, and a calorimeter. Since all undulators will be equipped with a gap drive, individual segments can be selected for diagnosis by switching off, i.e. opening the gap of all the other segments. This concept of only one common diagnostics for all undulator cells avoids a multiple installation of identical diagnostic devices which all would have to be calibrated against each other. In fact it facilitates a precise alignment and setup of the whole undulator system.

By observing only a limited area on the CCD it serves as a “virtual aperture”, i.e. within the full area of the CCD array the angular acceptance can be set at time of data evaluation. However, an upper limit of 40 µrad (FWHM) is given by an aperture of 8 mm placed at the end of the last undulator (see Section 4.7.1.4). By a proper selection of the angular acceptance, one can get rid of Doppler-shifted higher harmonic and at the same time become less sensitive to electron divergence and beam direction jitter.

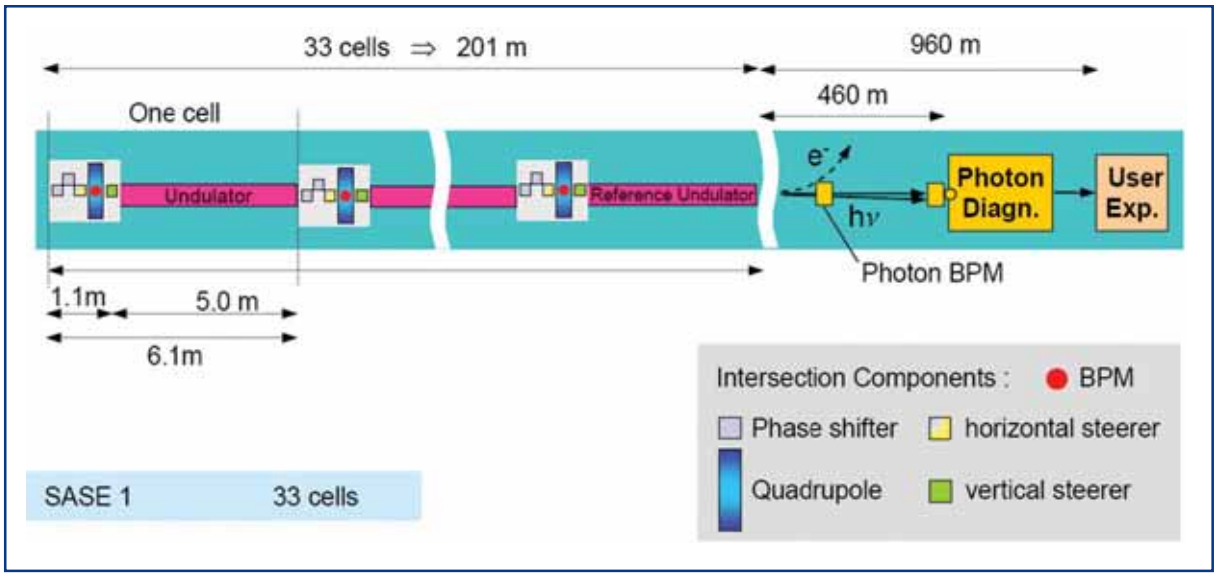


***Figure 5.5.1*** *Schematic layout of a XFEL beamline with photon diagnostics station.*

Fluctuations of electron beam parameters like electron charge and energy can be determined by a differential measurement technique. Following the concept proposed by B.X. Yang **[5-74]** the radiation from two undulator cells in parallel can be used: the last segment as a reference device (reference undulator) and one of the segments to be tested (test undulator). A steering magnet in the intersection upstream of the reference undulator deflects the electron beam horizontally by ~35µrad, so that the x-ray beam emitted from this undulator is well separated from the main axis, but allowed to pass the crystal monochromator of the diagnostic station. The x-ray beams from both segments are collected separately by the CCD array; hence, the radiation of the reference undulator can be used for normalisation.

Wave front calculations have been performed for the parameters of SASE 1 using SRW **[5-75]**, in order to estimate the properties of the undulator radiation of one or two segments observed at the diagnostic station. For ease of comparison, all calculations have been performed for an observation point 660 m downstream of the source. Table 5.5.1 summarises the corresponding photon beam parameters for the spontaneous radiation of one undulator segment. Three major diagnostic issues relate to a proper setup of the undulator cells, namely trajectory alignment, gap adjustment, and phase tuning. These are discussed in the following sections.

### 5.5.1 Trajectory alignment

It has been shown **[5-76]** that a random rms quadrupole offset of 1 µm will lead to a FEL gain reduction of ~10%. This value, corresponding to a second field integral of $I_2 = 83$ Tmm$^2$, is also considered as an upper limit of the trajectory displacement within a single undulator segment. The resulting requirement for angular trajectory alignment within a 5 m long undulator segment is 0.2 µrad. Spontaneous radiation of the first, third or fifth harmonic can be used for the different alignment aspects depending on the required accuracy. The top part of Figure 5.5.2 shows the energy spectrum of the first harmonics of a single SASE 1 undulator segment for an electron beam with the nominal

emittance. As expected, the emittance influence is still small for the (spontaneous) spectrum of the first harmonics. The lower part of Figure 5.5.2 displays spatial distributions for slightly different observation energies of the fundamental undulator peak. Detuning of the observation energy towards lower values leads to a broadening accompanied by a splitting of the intensity cone towards a ring. Detuning by 0.3% to higher energies (Figure 5.5.2c) leads to a considerable narrowing of the radiation cone, however, at the expense of lower intensity. The centre of gravity for all three intensity distributions in Figure 5.5.2 is on the beam axis independent of observing the radiation on- or off-crest of the undulator spectrum. Therefore, the photon beam axis and also the mean undulator trajectory, can be detected independently of a possibly incorrect gap setting. A still smaller spot size is obtained for higher harmonics of the undulator radiation.

| | | |
|---|---|---|
| Fundamental wavelength | 0.1 | nm |
| Fundamental photon energy | 12.4 | keV |
| Opening angle of fundamental σ | 3.2 | μrad |
| Footprint at 200 m (rms) | 0.6 | mm |
| Footprint at 600 m (rms) | 2.1 | mm |

***Table 5.5.1*** *Photon beam parameters for the spontaneous radiation of one undulator segment. The electron beam energy is 17.5 GeV.*

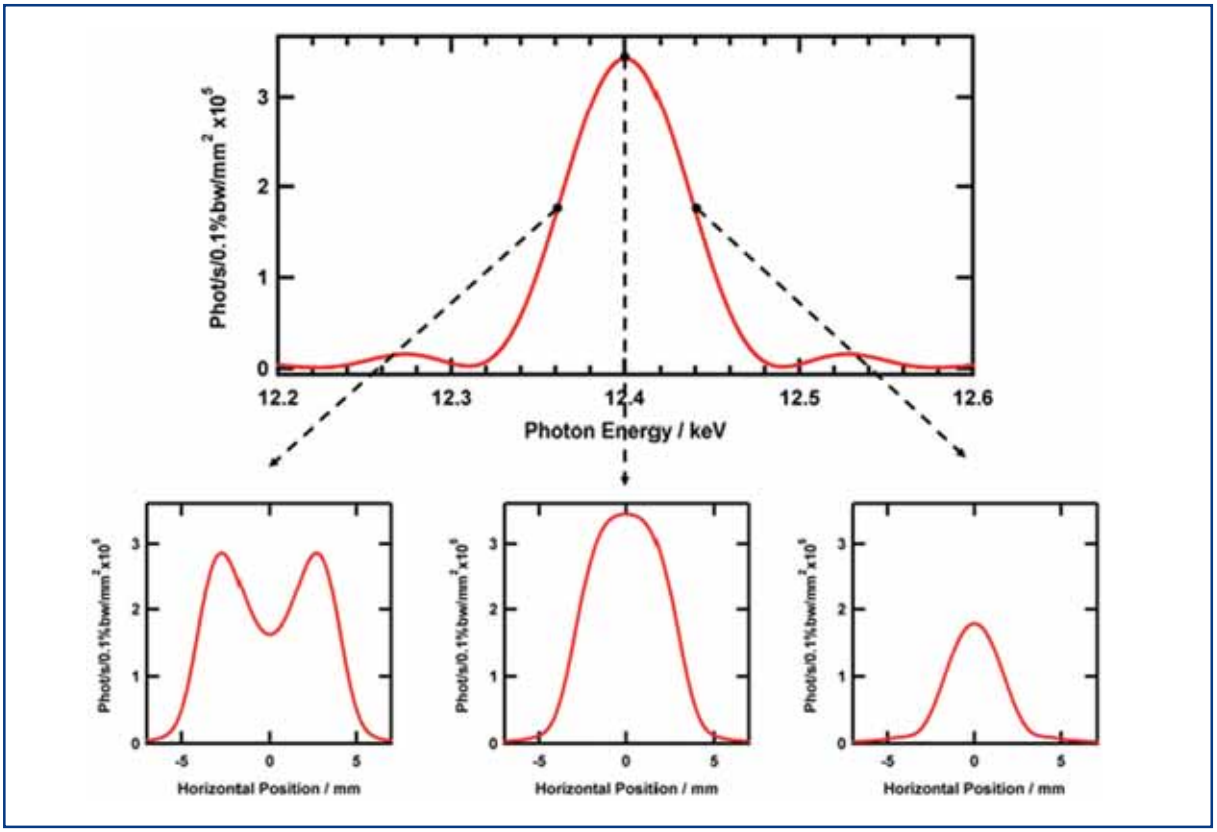


***Figure 5.5.2*** *Top part: Energy spectrum of the spontaneous radiation of a single 5 m long undulator segment of SASE 1 at a wavelength of ~0.1nm. Lower part (a–c): Profile of the circular beam expected for different observation energies (12.36, 12.40, 12.44 keV) in the vicinity of the undulator peak (arrows).*

Assuming a mean spatial line width of ~5.8 mm, an accuracy of ~2% of the FWHM (working with the first harmonic) or, correspondingly, 130 µm of the obtained spatial distribution, has to be achieved in order to cope with the specified angular resolution of 0.2 µrad. The setup described below will meet this requirement. The analysis of the photon spot as a single footprint of the electron trajectory through the undulator cannot distinguish between a shifted and a tilted orbit. Two photon BPMs will be installed between the undulator exit and the diagnostic station, which can be operated continuously without interference with a user experiment (Section 6.3).

### 5.5.2 Gap adjustment

One way to adjust the gap of each undulator segment is to take an energy spectrum whose centre of gravity defines the energy position of the undulator harmonics for the present gap value, which then has to be adjusted. The uncertainty in the measured fundamental energy has to be smaller than the $\rho$-parameter ($4 \times 10^{-4}$), i.e. ~8 eV. Alternatively, the gap can be optimised by maximising the intensity at the desired photon energy which is then kept fixed. Corresponding to the $\rho$-parameter, the precision requirement for the gap adjustment is in the order of ~3 µm. Figure 5.5.3 displays the intensity obtained for fixed observation energy at the fundamental as a function of the gap detuning from its nominal value. It can be seen that the observed intensity varies considerably with a small gap misalignment. This method will work much faster than the first approach. Gap tuning of all undulator segments one by one will result in identical fundamental energies of all cells. A tiny taper of the gap along the entire undulator system, which is required to optimise the SASE intensity, has to be fine-tuned subsequently.

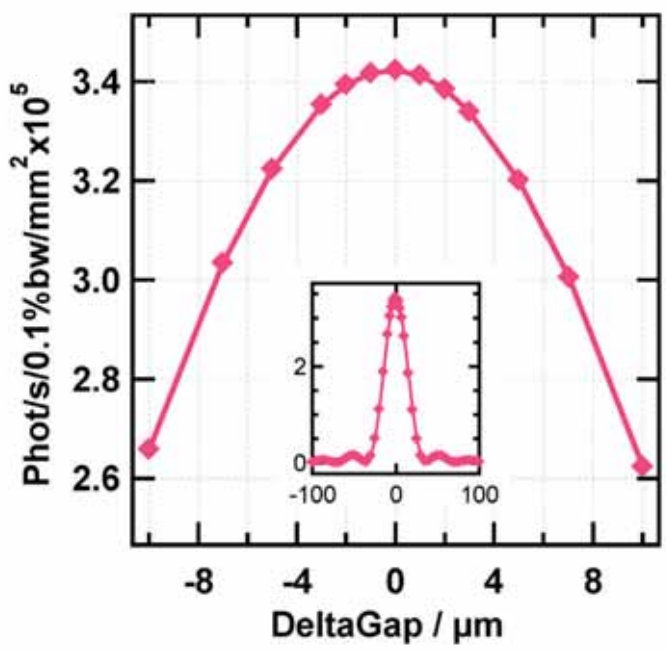


***Figure 5.5.3*** *Photon intensity as function of gap detuning for a constant observation energy of 12.4 keV (first harm.); the reference gap corresponds to the open gap position (10 mm).*

### 5.5.3 Phase tuning

Changing the undulator gap will result in a change of the phase relation between two adjacent segments. In order to compensate for the wavelength dependent phasing condition, a phase shifter is installed in the intersection module (Section 5.4.4). It consists of a three-magnet chicane which is powered by a gap-dependent current, and delays the electron beam so that the radiation from the following segment is in phase with that of the previous for all wavelengths. The adjustment of the optical phase has to be assured with an accuracy of only ~1%, i.e. a few degrees **[5-77]**. The determination of the correct phase is based on observing the radiation of two successive undulator segments. The phase relation affects the energy spectrum as well as the spatial distribution of the composed radiation. For complete phase match, the undulator line peaks at $E_{fund}$: In case of fully destructive interference, the undulator spectrum shows intensity maxima below and above that value. The spatial radiation distribution at $E = E_{fund}$ is cone-like in the matched phase condition, whereas the radiation is emitted in a ring in the destructively interfering case. The easiest way to monitor the phase is to observe the photon intensity at constant energy $E_{obs} = E_{fund}$ while shifting the optical phase in the electron chicane. The detected photon flux shows cosine dependence with a peak-to-peak amplitude ratio of ~700 for a phase advance from $\pi$ to $2\pi$ (Figure 5.5.4). This will be sufficient to tune the optical phase within the required accuracy.

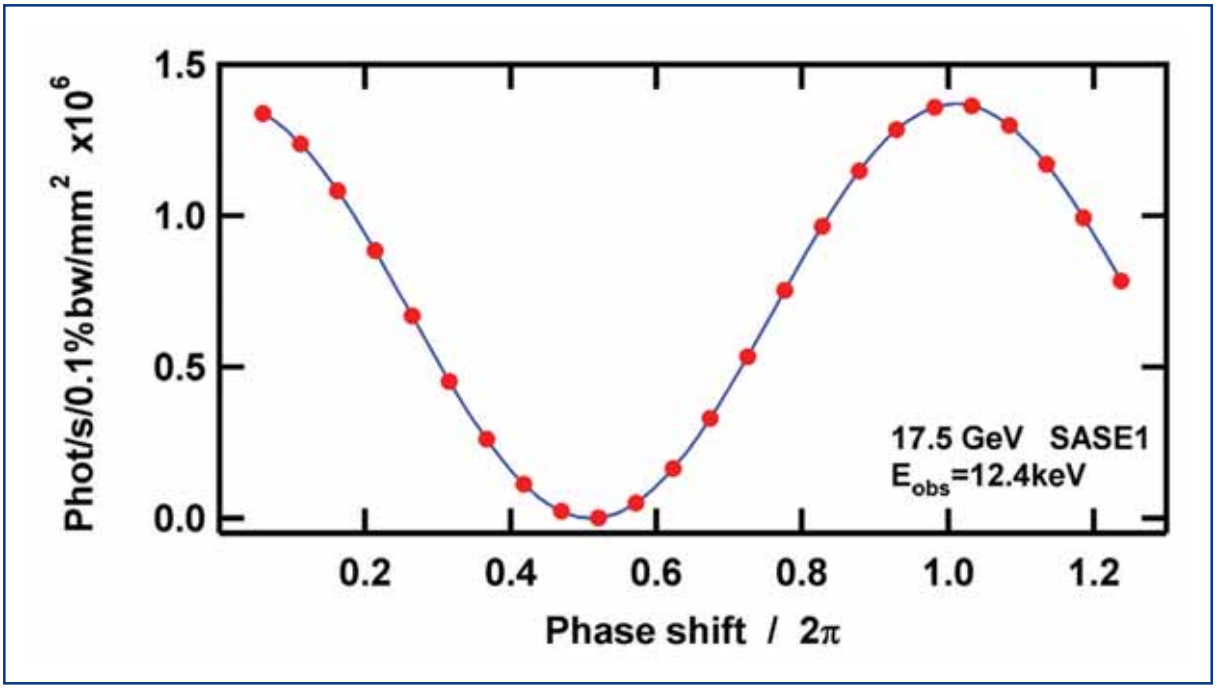


***Figure 5.5.4*** *Simulation of the phase dependent intensity variation using the SRW code. While changing the operating conditions from an anti- to a phased mode one observes a difference in intensity by a factor of 700.*

### 5.5.4 Hardware setup

The photon diagnostic station consists of three parts: the photon beam position monitors, the central imaging station, and a detector unit for observation of integral properties. Photon BPMs will be used in conjunction with the imaging station to precisely align the trajectories of all undulator segments, in particular to distinguish between transversal and angular displacement. Position-sensitive ionisation chambers are present state-of-the-art photon monitors in terms of resolution and are most appropriate for this application as they do not directly interact with the beam (see Section 6.2). The primary part of the photon diagnostic station will image the central cone of the monochromatic beam of the test and reference undulator in parallel. It will be possible to observe an image at the energy of the first and fifth harmonic of the XFEL undulator through two different view ports. A field of view with a diameter of 50 mm is needed in order to disentangle the radiation cones of both the reference and the test undulator and to determine their FWHM and shape. The undulator beam will be monchromatised using a single crystal Laue-case setup similar to that used at the PETRA-undulator beamline at DESY as shown in Figure 5.5.5. There will be two fixed view ports in order to observe the first and fifth harmonic of the undulator by only rotating the crystal. The observation of two angles allows the determination of an absolute energy scale.

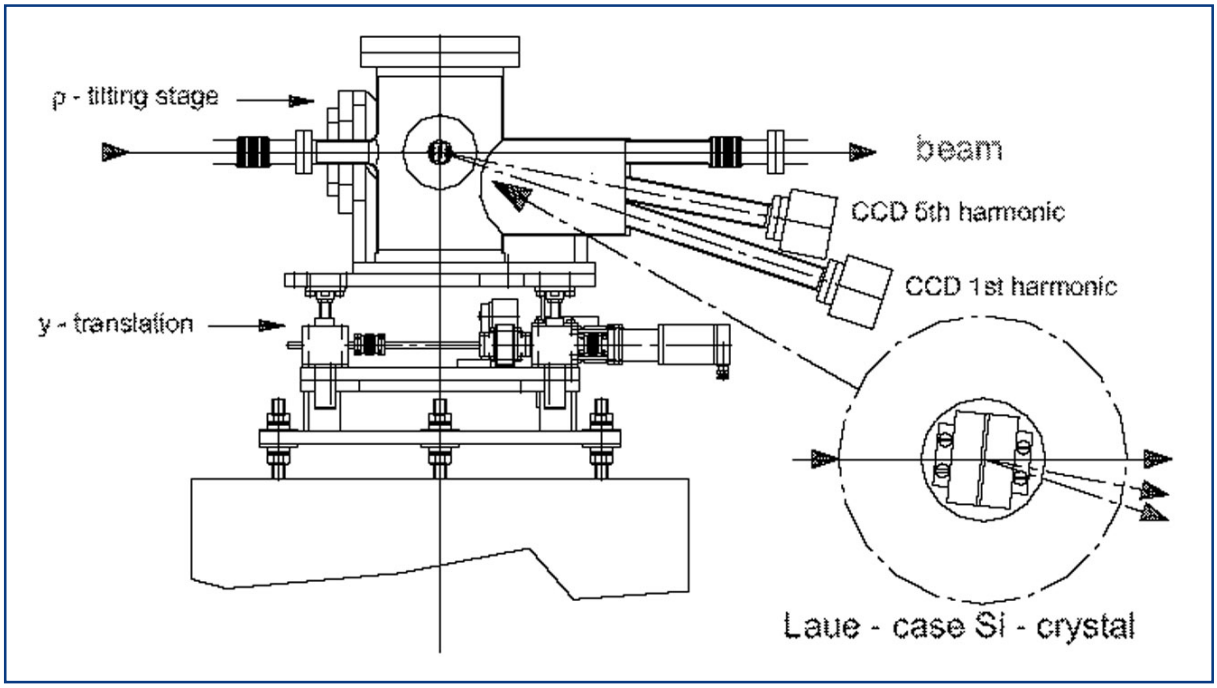


***Figure 5.5.5*** *Schematic view of the diagnostic station setup. A Laue-case Silicon crystal monchromatises the undulator radiation. The central cone will be observed at two photon energies (first and fifth harmonics) through fibre optic view ports coated with fluorescent screens.*

Experience with a similar setup at the PETRA beamline (Section 5.5.5) with the PETRA storage ring at DESY running at 12 GeV positron energy, shows that the images obtained by a thin Laue-case crystal with a thickness of 200 µm provide a clear picture without additional spots and high energy background. The Laue-case setup is favourable due to

the small Bragg angles of 5.49° and 9.17° required for the fifth harmonic using Si (3 3 3) and for the first harmonic with Si (1 1 1), respectively.

An imaging system is proposed using a Laue-case crystal to monochromatise the central cone of the test and reference undulator, projecting them onto a fluorescent screen attached directly onto a fibre optic taper. The fluorescent screen will be either directly coated onto the fibre or be a thin film screen attached to it. This taper is part of a fibre optic vacuum window. At the airside of this window, a CCD chip will be directly bonded onto the fibre. Assuming a field of view of 50 $mm^2$ and the need for a 12 $\mu m^2$ pixel size (16-bit resolution requirement), a taper with an imaging ratio of 2:1 (screens side: CCD side) will be installed. The overall resolution of the system using a 2,048 $\times$ 2,048 pixel CCD will be 24 $\mu m^2$ /pixel. An option will be replacing the fluorescent screen coating at the fibre end by a doping of the fibre end.

Present day 16-bit resolution CCD systems are driven with a maximum pixel clock of 50 kHz, due to an increase in readout noise at higher clock rates. The dark current in a cooled CCD system is negligible at exposure times in the seconds range. Under these conditions, the setup will be able to provide an image every 20 s. A 12-bit system would provide an image in 1 s or faster, but the dynamic range is too limited to observe the effect of phasing two undulator segments without changing the exposure time. Integral beam properties of both the spontaneous and SASE radiation will be determined in a second station.

### 5.5.5 Test at PETRA II

First tests of the basic diagnostic scheme have been successfully performed at the PETRA-II storage ring operating at 12 GeV **[5-78, 5-79]**. Here, a similar setup using BPMs for stabilisation and a cryogenically cooled Silicon crystal in Laue geometry in combination with a fluorescent screen and CCD imager, have been used for emittance measurements. Figure 5.5.6 shows a set of images of the first harmonic of the undulator for a variation of the undulator gap from 18 to 21 mm, corresponding to 21.23 keV at 18.8 mm. Gaussian fits to horizontal lines through the centre of mass in all images provide the standard deviation of the measured intensity distributions in the horizontal plane. The images are processed in order to obtain the standard deviation of the width of the photon beam. The results are depicted in Figure 5.5.7. For each image, the integrated intensity, the shape of the horizontal beam profile through the centre of mass (kurtosis), and the variance values, are determined and plotted against the gap setting. Figure 5.5.7 shows that only at the gap setting yielding the maximum intensity, does the profile have a true Gaussian shape and coincide with the smallest variance, corresponding to the smallest FWHM of the profile.

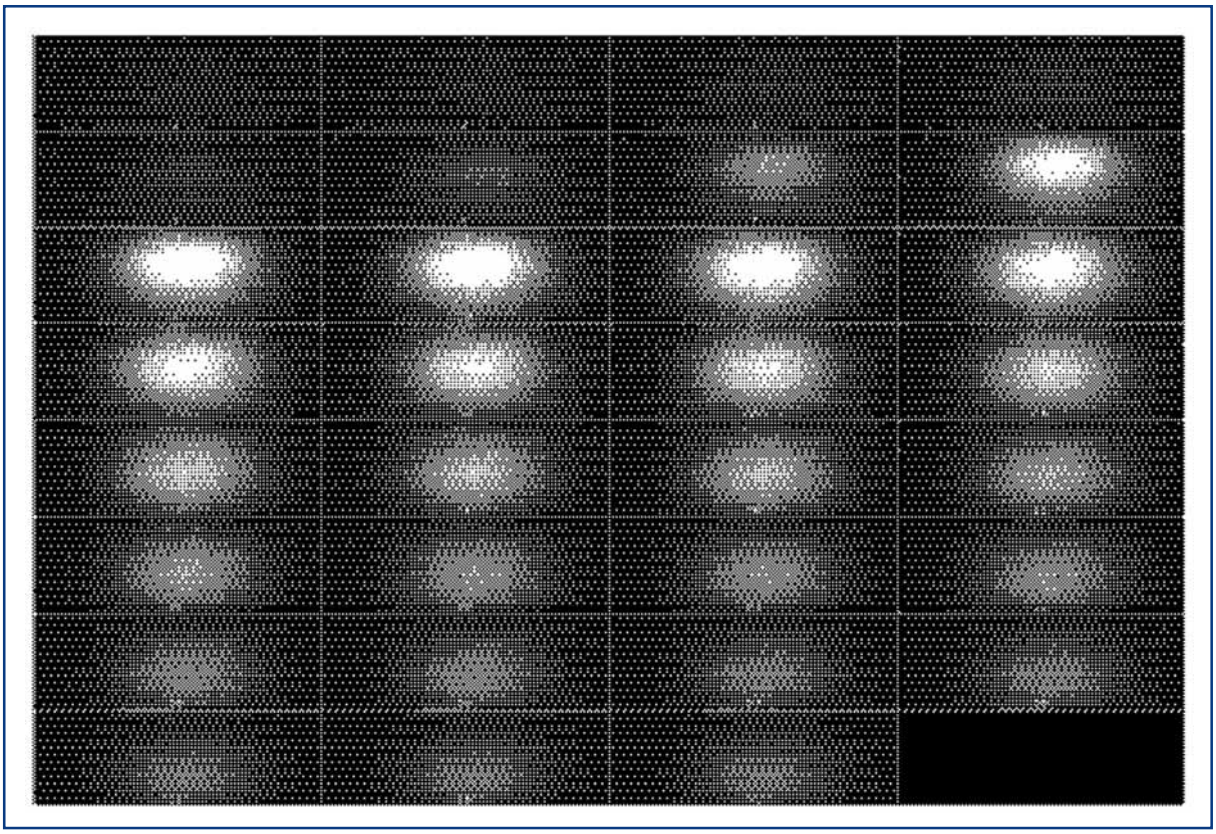

***Figure 5.5.6*** *Set of images taken with a fixed exposure time showing the monochromatised photon beam at a fixed crystal setting corresponding to a photon energy of the first undulator harmonic of 21.23 keV. The setting of the undulator gap ranges from 18 mm to 21 mm magnetic gap in steps of 0.1 mm (top left image #1 at 18 mm, bottom right image #31 at 21 mm).*

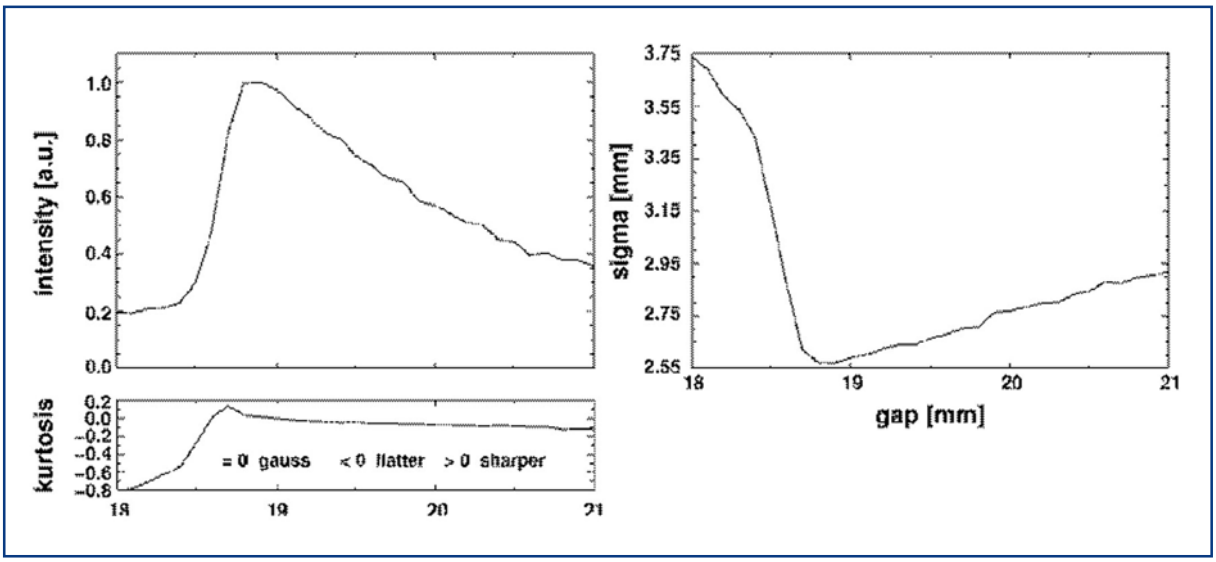


***Figure 5.5.7*** *Left: integrated intensity in each image and the Gauss-likeliness of the line shape of a horizontal cut through the centre of mass in each image. Right: calculated variance of all line scans.*

## 5.6 Future extensions to the European XFEL Facility

The present Technical Design Report describes the basic option of the European XFEL Facility. However, during our design work we foresee physical and technical solutions which will allow significant performance enhancements without significant changes to the infrastructure and hardware. These potential extensions are high-power (sub-TW level) mode of operation, two-colour mode of operation (frequency doubler), and attosecond mode of operation **[5-80]**. The present concept of undulator can be easily modified for operation in high- power and two-colour modes of operation (as illustrated in Figure 5.6.1). Both schemes are realised in a simple way by replacement of one of the undulator modules by a dispersion section, and essentially use the feature of a small energy spread in the electron beam allowing effective enhancement of the beam bunching. Application of the undulator tapering in the final part of the undulator allows production of ultra-high power radiation pulses. Figure 5.6.2 shows the temporal structure of the radiation pulse for SASE 2 undulator tuned to high power mode of operation.

In its simplest configuration, the frequency doubler consists of an input undulator, and an output undulator separated by a dispersion section (see Figure 5.6.1) **[5-81]**. After passing through the dispersion section, the bunched beam has not only a fundamental radiation frequency component, but also considerable intensity in its harmonics. It is possible to have an input undulator operating at one frequency, and an output undulator operating at double this frequency. The radiation in the output undulator will then be excited by the harmonic component in the electron beam, and the FEL will operate as a combination of frequency multiplier and amplifier.

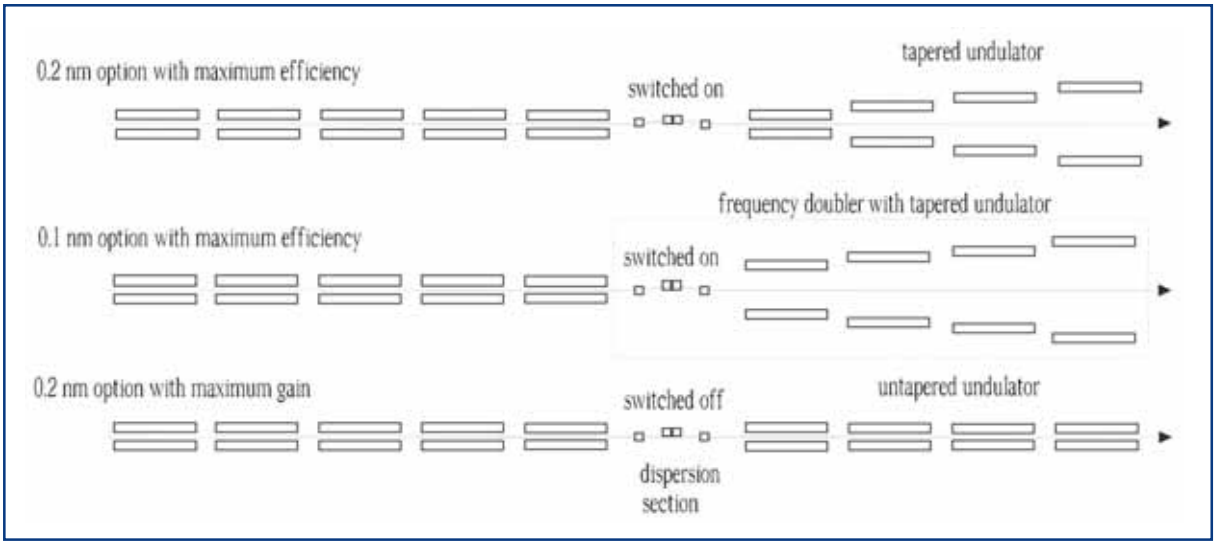


***Figure 5.6.1*** *Three different modes of operation of SASE undulator. Top: high power option; middle: frequency doubler; bottom: standard SASE. Only one type of undulator magnet structure is used. The radiation wavelength will be tuned by changing the gap* **[5-80].**

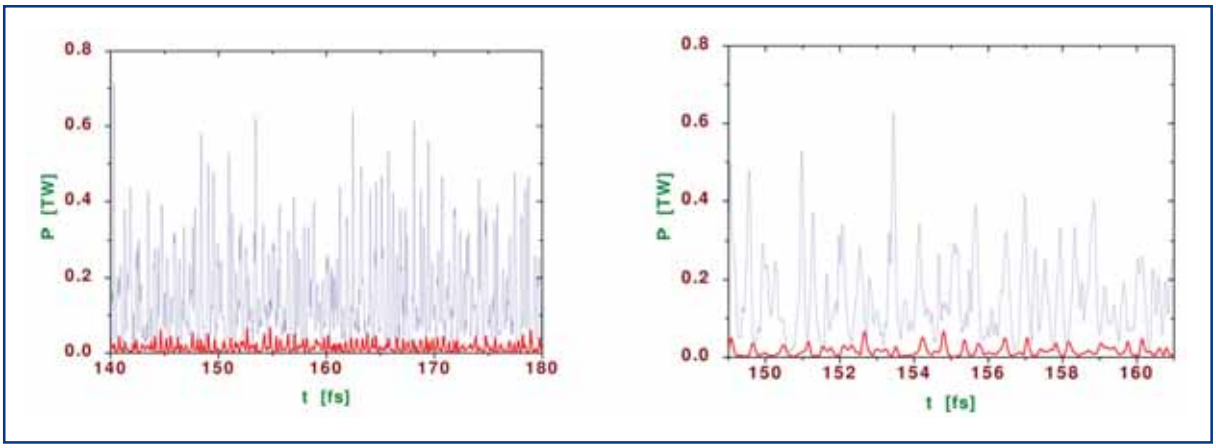


***Figure 5.6.2*** *Temporal structure of the radiation pulse for SASE 2 at 0.2 nm tuned for high power mode of operation. Right plot shows enlarged view of the left plot. The red line shows radiation pulse for the basic option (see Figure 5.2.4). The undulator length is 150 m.*

A technique for the production of attosecond x-ray pulses is based on the use of x-ray SASE FEL combined with a femtosecond laser system **[5-82, 5-83]** (see Figure 5.6.3). An ultrashort laser pulse is used to modulate the energy of electrons within the femtosecond slice of the electron bunch at the seed laser frequency. The seed laser pulse will be timed to overlap with the central area of the electron bunch. It serves as a seed for a modulator which consists of a short (a few periods) undulator. Following the energy modulator the beam enters the x-ray undulator. The process of amplification of radiation in this undulator develops in the same way as in a conventional x-ray SASE FEL: fluctuations of the electron beam current serve as the input signal. The proposed scheme for the generation of attosecond pulses is based on frequency-chirping the SASE radiation pulse. When an electron beam traverses an undulator, it emits radiation at the resonance wavelength $\lambda=\lambda_u(1+K_{rms}^2)/(2\gamma^2)$. The laser-driven sinusoidal energy chirp produces a correlated frequency chirp of the resonant radiation $\delta\omega/\omega=2\delta\gamma/\gamma$. After the undulator, the radiation is passed through a crystal monochromator which selects a narrow bandwidth. Since the radiation frequency is correlated to the longitudinal position within the beam, a short temporal radiation pulse is transmitted through the monochromator. A modification of the attosecond XFEL concept uses undulator detuning for selection and amplification of ultra-high power attosecond pulses (see Figure5.6.4 **[5-83]**).

The attosecond x-ray pulse is naturally synchronised with its femosecond optical pulse which opens a unique perspective for pump-probe experiments with sub-femtosecond resolution. It is important that the attosecond scheme is based on the nominal XFEL parameters, and operates in a “parasitic” mode, not interfering with the main mode of the XFEL operation. It can be realised with minimum additional efforts. The machine design should foresee the space for the installation of a modulator undulator and a view port for the input optical system. Many of the components of the required laser system can be achieved with technology which is currently being developed for applications other than the attosecond x-ray source.

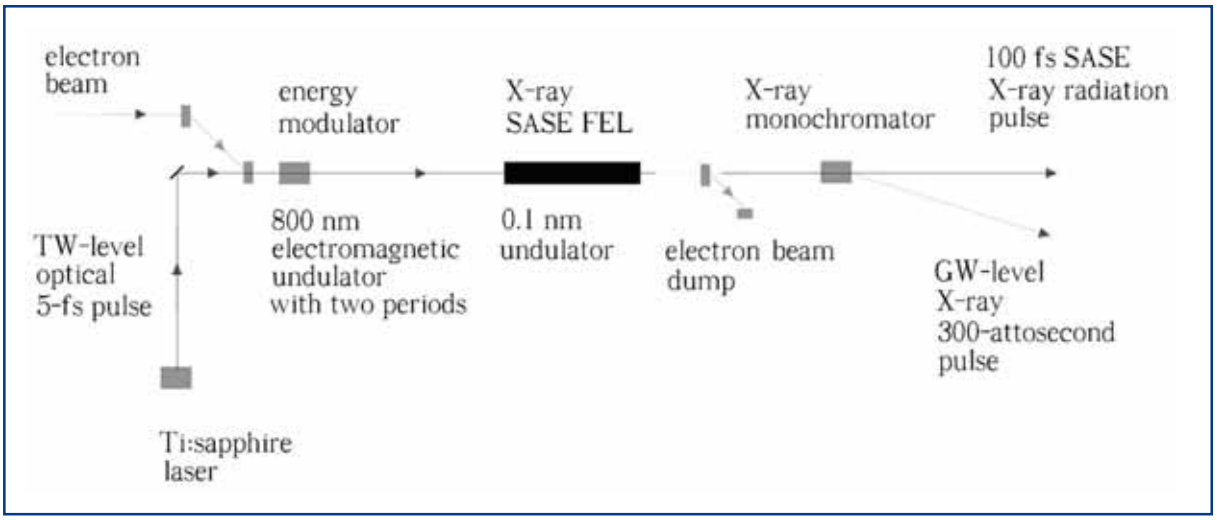


***Figure 5.6.3*** *Schematic diagram of attosecond x-ray source* **[5-82]**.

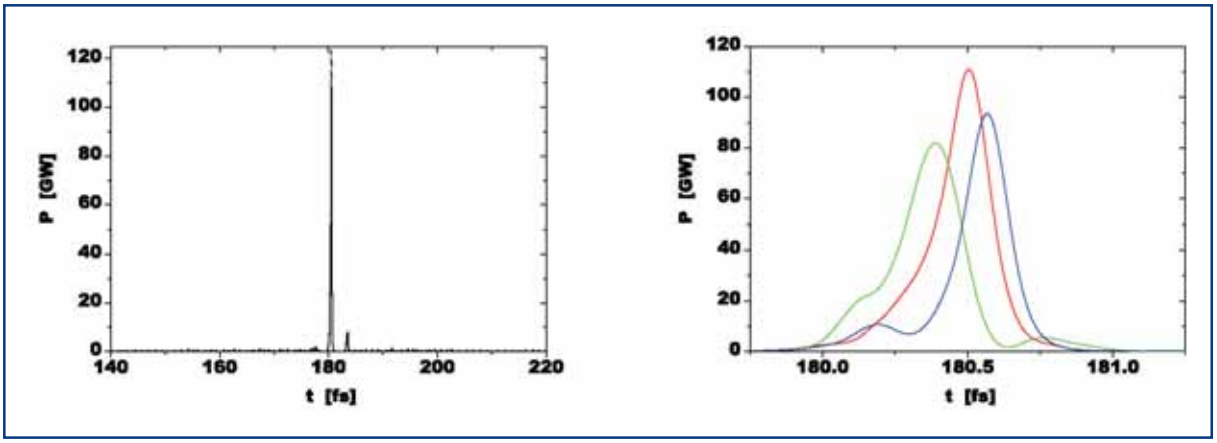


***Figure 5.6.4*** *Temporal structure of the radiation pulse from an ultra-high power attosecond XFEL* **[5-83]**. *Right plot shows enlarged fraction of a central peak. The lines correspond to three different shots.*

A single pass x-ray SASE FEL can be modified as proposed in **[5-84, 5-85]** to significantly reduce the bandwidth and the fluctuations of the output radiation. The modified scheme consists of two undulators with an x-ray monochromator located between them. The first undulator operates in the linear regime of amplification starting from the shot noise, and the output radiation has the usual SASE properties. After the first undulator, the electron beam is guided through a bypass and the x-ray beam enters the monochromator which selects a narrow band of radiation. At the entrance of the second undulator, the monochromatic x-ray beam is combined with the electron beam and is amplified up to the saturation level. The scheme is shown in Figure 5.6.5.

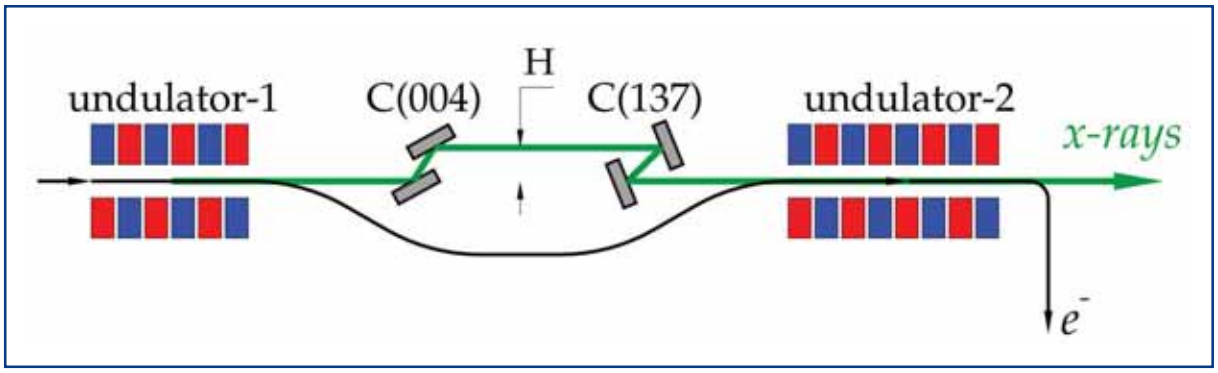


***Figure 5.6.5*** *Schematic layout of the two-stage FEL with the SASE FEL (left), a monochromator and electron debuncher (middle) and an amplifier (right)* **[5-85]**.

Possible extensions of the European XFEL should foresee both extension of the quality of the photon beam properties, and extension of the number of user stations which can operate simultaneously (or, quasi-simultaneously). An x-ray photon beam from a SASE FEL undulator is in principle a single user tool, just like an optical laser. Therefore, the operation and amortisation cost cannot be easily spread over many simultaneous experiments. To avoid prohibitive cost for each experiment, a perspective extension of XFEL laboratory has been proposed **[5-80]**. In this scenario all electrons will be guided into only one electron beamline including three undulator systems and the dump (Figure 5.6.6).

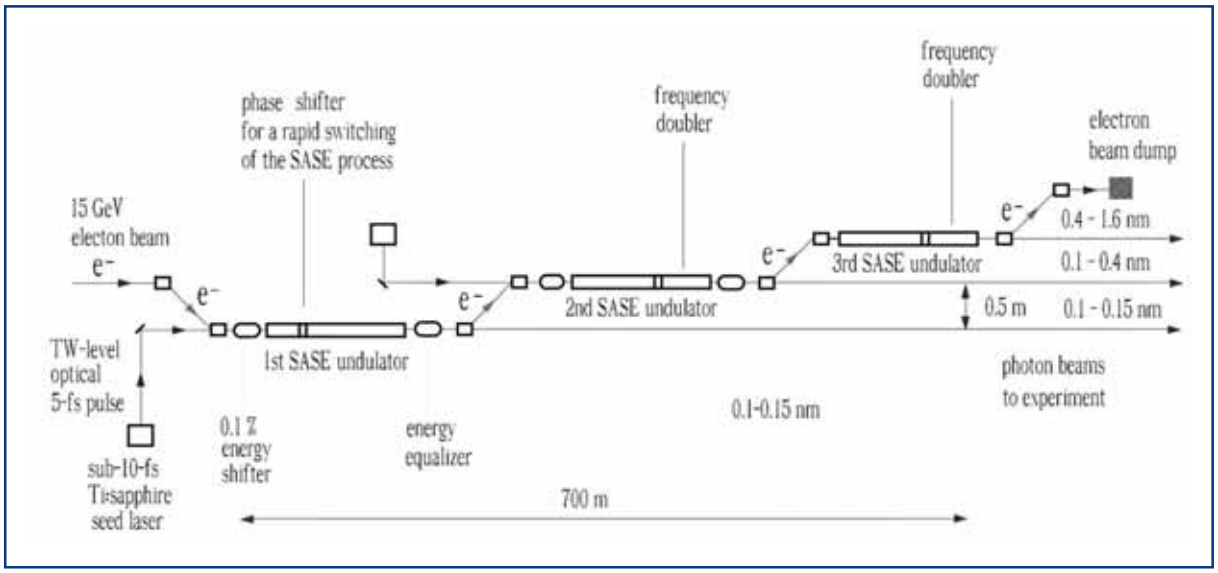


***Figure 5.6.6*** *Sketch of an x-ray SASE FEL source providing multi-user capability* **[5-80]**.

Using a 0.1% electron (photon) energy shifter in a SASE undulator, it is possible to rapidly turn off the FEL gain, thereby enabling users to switch effectively from one XFEL to another. This technique could provide quasi-simultaneous operation of all three XFELs in one electron beamline. Using a photon beam distribution system based on movable optics could thus enable many independent beamlines to work in parallel, thereby providing much more time for user experiments. The present layout of the European

XFEL would accommodate such an extension, and an appropriate increase of the tunnel diameter has been included in the project.

## 5.7 Summary of costs and manpower requirements

The capital investment and cost of the personnel necessary to build the undulator system as described in the previous sections of this chapter are summarised in this section. The basis for the cost estimate is the system layout and the parameters specified here. For an overview about the total project cost, a description of the methodology of the performed estimate for capital investment, the determination of the costs for personnel and the expected uncertainties, see Chapter 10.

Table 5.7.1 gives a summary of the project cost in terms of capital investment and the cost of personnel for the undulator systems. The undulator systems contribute about 10% to the overall project cost. Integrated over the entire construction phase, 149 Full-Time Equivalents (FTE) are required for the undulator system.

| | **Capital Investment [M€]** | **Personnel Cost [M€]** | **Full Cost [M€]** |
|---|---|---|---|
| Undulator Systems | 56.52 | 12.10 | 68.62 |

**Table 5.7.1** *Capital investment, personnel costs and full costs in Million-Euro for the undulator system.*

**Undulator system:** design, construction, magnetic measurement, installation and commissioning of the undulators systems SASE 1 to 3 and U1 and U2 with mechanical support, magnetic structures, motion control, and FEL simulation software. Undulator systems are composed of a certain number of undulator segments and the required instrumentation for electron beam fine correction placed in the intersections between segments. The number of segments is determined by the longest saturation length for the design range of photon energies. Undulators for spontaneous radiation have been designed to be ten segments long.

## References

**[5-1]** R.H. Pantell, Y. Soncini, and H.E. Putthoff, *Stimulated Photon-Electron Scattering*, IEEE J. Quant. Electr. 11 (1968) 905.

**[5-2]** J.M.J. Madey, *Stimulated Emission of Bremsstrahlung in a Periodic Magnetic Field*, J. Appl. Phys. 43 (1972) 3014.

**[5-3]** A.M. Kondratenko and E.L. Saldin, *Generation of Coherent Radiation by a Relativistic Electron Beam in an Undulator*, Part. Accelerators 10 (1980) 207.

**[5-4]** Ya.S. Derbenev, A.M. Kondratenko and E.L. Saldin, *On the Possibility of Using a Free-Electron Laser for Polarisation of Electrons in Storage Rings*, Nucl. Instrum. and Methods 193 (1982) 415.

**[5-5]** R. Bonifacio, C. Pellegrini and L.M. Narducci, *Collective Instabilities and High-Gain Regime in a Free-Electron Laser*, Opt. Commun. 50 (1984) 373.

**[5-6]** J.B. Murphy and C. Pellegrini, *Free electron lasers for the XUV spectral region*, Nucl. Instrum. and Methods A 237 (1985) 159.

**[5-7]** E.L. Saldin, E.A. Schneidmiller, M.V. Yurkov, *The Physics of Free Electron Lasers*, Springer-Verlag, Berlin (1999).

**[5-8]** K.J. Kim, *Three-Dimensional Analysis of Coherent Amplification and Self-Amplified Spontaneous Emission in Free-Electron Lasers*, Phys. Rev. Lett. 57 (1986) 1871.

**[5-9]** J.M. Wang and L.H. Yu, *A transient analysis of a bunched beam free electron laser*, Nucl. Instrum. and Methods A 250 (1986) 484.

**[5-10]** S. Krinsky and L.H. Yu, *Output power in guided modes for amplified spontaneous emission in a single-pass free-electron laser*, Phys. Rev. A 35 (1987) 3406.

**[5-11]** M. Xie, *Exact and variational solutions of 3D eigenmodes in high gain FELs*, Nucl. Instrum. and Methods A 445 (2000) 59.

**[5-12]** E.L. Saldin, E.A. Schneidmiller and M.V. Yurkov, *The general solution of the eigenvalue problem for a high-gain FEL*, Nucl. Instrum. and Methods A 475 (2001) 86.

**[5-13]** E.L. Saldin, E.A. Schneidmiller and M.V. Yurkov, *Statistical properties of radiation from VUV and X-ray free electron laser*, Opt. Commun. 148 (1998) 383.

**[5-14]** E.L. Saldin, E.A. Schneidmiller and M.V. Yurkov, *Diffraction effects in the self-amplified spontaneous emission FEL*, Opt. Commun. 186 (2000) 185.

**[5-15]** E.L. Saldin, E.A. Schneidmiller and M.V. Yurkov, *Nonlinear simulations of FEL amplifier with an axisymmetric electron beam*, Opt. Commun. 95 (1993) 14.

**[5-16]** E.L. Saldin, E.A. Schneidmiller, and M.V. Yurkov, *Simulation studies of a 6 nm Free Electron Laser at the TESLA test facility starting from noise*, Nucl. Instrum. and Methods A 393 (1997) 157.

**[5-17]** P. Pierini and W. Fawley, *Shot noise startup of the 6 nm SASE FEL at the TESLA test facility*, Nucl. Instrum. and Methods A 375 (1996) 332.

**[5-18]** E.L. Saldin, E.A. Schneidmiller, and M.V. Yurkov, *FAST: a three-dimensional time-dependent FEL simulation code*, Nucl. Instrum. and Methods A 429 (1999) 233.

**[5-19]** S. Reiche, *GENESIS 1.3: a fully 3D time-dependent FEL simulation code*, Nucl. Instrum. and Methods A 429 (1999) 243.

**[5-20]** V. Ayvazyan et al., *Generation of GW Radiation Pulses from a VUV Free-Electron Laser Operating in the Femtosecond Regime*, Phys. Rev. Lett. 88 (2002) 104802.

**[5-21]** V. Ayvazyan et al., *A new powerful source for coherent VUV radiation: Demonstration of exponential growth and saturation at the TTF free-electron laser*, Eur. Phys. J. D 20 (2002) 149.

**[5-22]** M. Dohlus et al., *Start-to-end simulations of SASE FEL at the TESLA Test Facility, phase 1*, Nucl. Instrum. and Methods A 530 (2004) 217.

**[5-23]** E.L. Saldin, E.A. Schneidmiller, M.V. Yurkov, *Expected Properties of the Radiation from VUV-FEL at DESY (Femtosecond Mode of Operation)*, TESLA-FEL report 2004-06, DESY, Hamburg (2004).

**[5-24]** E.L. Saldin, E.A. Schneidmiller, M.V. Yurkov, *Statistical Properties of the Radiation from VUV FEL at DESY Operating at 30 nm Wavelength in the Femtosecond Regime*, DESY report 2005-239, DESY, Hamburg (2005).

**[5-25]** V. Ayvazyan et al., *First operation of a free-electron laser generating GW power radiation at 32 nm wavelength*, Eur. Phys. J. D 37 (2006) 297.

**[5-26]** *Conceptual Design of 500 GeV e+e- Linear Collider with Integrated X-ray Facility*, R. Brinkmann et al.(Eds.), DESY report 97-048, DESY, Hamburg (1997).

**[5-27]** *TESLA Technical Design Report Part V, The X-ray Free Electron Laser*, G. Materlik, T. Tschentscher (Eds.), DESY report 2001-011, DESY, Hamburg (2001), http://tesla.desy.de/new_pages/0000_TESLA_Project.html

**[5-28]** *TESLA XFEL Technical Design Report Supplement*, R. Brinkmann, B. Faatz, K. Flöttmann, J. Rossbach, J. Schneider, H. Schulte-Schrepping D. Trines, T. Tschentscher, H. Weise (Eds.), DESY report 2002-167, DESY, Hamburg (2002), http://tesla.desy.de/new_pages/0000_TESLA_Project.html

**[5-29]** E.L. Saldin, E.A. Schneidmiller and M.V. Yurkov, *The Potential for Extending the Spectral Range Accessible to the European X-ray Free Electron Laser in the Direction of Longer Wavelengths*, TESLA FEL report 2004-05, DESY, Hamburg (2004).

**[5-30]** E.L. Saldin, E. A. Schneidmiller, and M.V. Yurkov, *Design formulas for short-wavelength FELs*, Opt. Commun. 235 (2004) 415.

**[5-31]** J. Rossbach, E.L. Saldin, E.A. Schneidmiller and M.V. Yurkov, *Interdependence of parameters of an X-ray FEL*, Nucl. Instrum. and Methods A 374 (1996) 401.

**[5-32]** E.L. Saldin, E.A. Schneidmiller, and M.V. Yurkov, *Calculation of energy diffusion in an electron beam due to quantum fluctuations of undulator radiation*, Nucl. Instrum. and Methods A 381 (1996) 545.

**[5-33]** E.L. Saldin, E.A. Schneidmiller and M.V. Yurkov, *Coherence properties of the radiation from SASE FEL*, Nucl. Instrum. and Methods A 507 (2003) 106.

**[5-34]** E.L. Saldin, E.A. Schneidmiller and M.V. Yurkov, *Coherence properties of the radiation from X-ray free-electron laser*. Proceedings of the FEL 2006 Conference, Berlin.

**[5-35]** M. Schmitt and C. Elliot, *Even-harmonic generation in free-electron lasers*, Phys. Rev. A 34 (1986) 6.

**[5-36]** R. Bonifacio, L. De Salvo, and P. Pierini, *Large harmonic bunching in a high-gain free-electron laser*, Nucl. Instrum. and Methods A 293 (1990) 627.

**[5-37]** W.M. Fawley et al., *Large harmonic bunching in a high-gain free-electron laser*, Proc. IEEE Part. Acc. Conf., (1995) 219.

**[5-38]** H. Freund, S. Biedron and S. Milton, *Nonlinear harmonic generation and proposed experimental verification in SASE FELs*, Nucl. Instrum. and Methods A 445 (2000) 53.

**[5-39]** H. Freund, S. Biedron and S. Milton, *Nonlinear Harmonic Generation in Free-electron Lasers*, IEEE J. Quant. Electr. 36 (2000) 275.

**[5-40]** S. Biedron et al., *Measurements of nonlinear harmonic generation at the Advanced Photon Source's SASE FEL*, Nucl. Instrum. and Methods A 483 (2002) 94.

**[5-41]** S. Biedron et al., *Impact of electron beam quality on nonlinear harmonic generation in high-gain free-electron lasers*, Phys. Rev. ST 5 (2002) 030701.

**[5-42]** Z. Huang and K. Kim, *Three-dimensional analysis of harmonic generation in high-gain free-electron lasers*, Phys. Rev. E 62 (2000) 7295.

**[5-43]** Z. Huang and K. Kim, *Nonlinear harmonic generation of coherent amplification and self-amplified spontaneous emission*, Nucl. Instrum. and Methods A 475 (2001) 112.

**[5-44]** A. Tremaine et al., *Experimental Characterization of Nonlinear Harmonic Radiation from a Visible Self-Amplified Spontaneous Emission Free-Electron Laser at Saturation*, Phys. Rev. Lett. 88 (2002) 204801.

**[5-45]** W. Brefeld et al., *Scheme for time-resolved experiments based on the use of statistical properties of the third harmonic of the SASE FEL radiation*, Nucl. Instrum. and Methods A 507 (2003) 431.

**[5-46]** E.L. Saldin, E.A. Schneidmiller and M.V. Yurkov, *Properties of the Odd Harmonics of the Radiation from SASE FEL with a Planar Undulator*, Phys. Rev. ST 9(2006) 030702.

**[5-47]** G. Geloni, E.L. Saldin, E.A. Schneidmiller and M.V. Yurkov, *Exact Solution for the Second Harmonic Generation in XFELs*, DESY report 2005-137, DESY, Hamburg (2005).

**[5-48]** A.L. Cavalieri et al., *Clocking Femtosecond X-rays*, Phys. Rev. Lett. 94 (2005) 114801.

**[5-49]** A.M. Lindenberg et al., *Atomic-Scale Visualization of Inertial Dynamics*, Science 308 (2005) 392.

**[5-50]** T. Tanaka, H. Kitamura, *SPECTRA: a synchrotron radiation calculation code*, J. Synchrotron Rad. 8 (2001) 1221.

**[5-51]** P. Elleaume, J. Chavanne, B. Faatz, *Design considerations for an 1 Angstroem SASE undulator*, Nucl. Instrum. and Methods A 455 (2000) 503.

**[5-52]** K. Halbach, Nucl. Instrum. and Methods 187 (1987) 109.

**[5-53]** S. Sasaki, *Analyses for a planar variably-polarizing undulator*, Nucl. Instrum. and Methods A 347 (1994) 83.

**[5-54]** J. Chavanne and P. Elleaume, Synchrotron Radiation News 8 (1995) 18-22.

**[5-55]** I. Vasserman and E.R. Moog, *A passive scheme for ID end correction*, Rev. Sci. Instr. 66 (1995) 1943.

**[5-56]** J. Pflüger, H. Lu, T. Teichmann, *Field fine tuning by pole height adjustment for the undulator of the TTF–FEL,* Nucl. Instrum. and Methods A 429 (1999) 386.

**[5-57]** J. Pflüger, G. Heintze, I. Vasserman, *Search for possible radiation damage on a NdFeB permanent magnet structure after two years of operation*, Rev. Sci. Instr. 66 (1995) 1946.

**[5-58]** E.R. Moog, P.K. Den Hartog, E.J. Semones, P.K. Job, Proc. of the 10th National US conference on Synchrotron Radiation Instrumentation , CP417 (1997) 219.

**[5-59]** J. Pflüger, B. Faatz, M. Tischer, T. Vielitz, *Radiation exposure and magnetic performance of the undulator system for the VUV FEL at the TESLA Test Facility Phase-1 after 3 years of operation*, Nucl. Instrum. and Methods A 507 (2003) 186.

**[5-60]** S. Okuda, K. Okashi, N. Kobayashi, *Effects of electron-beam and ã-ray irradiation on the magnetic flux of Nd-Fe-B and Sm-Co permanent magnets*, Nucl. Instrum. and Methods B 94 (1994) 227.

**[5-61]** H. Henschel, M. Körfer, K. Wittenburg, F. Wulf, *Fiberoptic radiation sensing system for TESLA*, TESLA report 2000-26, DESY, Hamburg (2000).

**[5-62]** J. Pflüger, M. Tischer, *A Prototype Phase Shifter for the Undulator Systems at the TESLA X-ray FEL*, TESLA-FEL 2000-08 report, DESY, Hamburg (2000), http://tesla.desy.de/new_pages/0000_TESLA_Project.html

**[5-63]** R. Tatchyn, *Selected applications of planar permanent magnet multipoles in FEL insertion device design*, Nucl. Instrum. and Methods A 341 (1994) 449.

**[5-64]** J. Pflüger, Y. Nikitina, *Planar undulator schemes with strong focusing properties for the VUV-FEL at the TESLA test facility*, Nucl. Instr. and Methods A 381 (1996) 554.

**[5-65]** J. Pflüger, H. Lu, D. Köster, T. Teichmann, *Magnetic measurements on the undulator prototype for the VUV-FEL at the TESLA Test Facility*, Nucl. Instrum. and Methods A 407 (1998) 386.

**[5-66]** B. Faatz, *Beam Based Alignment of the TESLA X-Ray FEL Undulator*, TESLA-FEL report 1997-05, DESY, Hamburg (1997).

**[5-67]** P. Castro, *TTF FEL Beam-based Alignment by Dispersion Correction Using Micado Algorithm*, TESLA-FEL report 1997-05, DESY, Hamburg (1997).

**[5-68]** P. Emma, *Electron Phase Slip in an Undulator with Dipole Field and BPM Errors*, SLAC-TN-05-034, LCLS-TN-00-14, SLAC, Stanford (2000).

**[5-69]** R. Treusch et al., *Development of photon beam diagnostics for VUV radiation from a SASE FEL*, Nucl. Instrum. and Methods A 445 (2000) 456.

**[5-70]** K. Tiedtke et al., *The SASE FEL at DESY: Photon Beam Diagnostics for the User Facility*, Proceedings SRI2003, San Francisco, AIP Conf. Proc. 705 (2004) 588.

**[5-71]** R. Treusch, *Photon Diagnostics for the VUV-FEL*, HASYLAB Annual Report 2005, DESY, Hamburg (2005) 159-164.

**[5-72]** E. Gluskin et al., *The magnetic and diagnostic systems for the Advanced Photon Source self-amplified spontaneously emitting FEL*, Nucl. Instrum. and Methods A 429 (1999) 358.

**[5-73]** E. Gluskin, P. Illinski, N. Vinokurov, *Predicted performance of the LCLS X-ray diagnostics*, LCLS-TN-00-13, SLAC, Stanford (2000).

**[5-74]** B.X. Yang, *High resolution undulator measurements using angle-integrated spontaneous radiation*, Proceedings PAC05, Knoxville, Tennesse ( 2005).

**[5-75]** O. Chubar, P. Elleaume, SRW, Version 3.7, ESRF 1997–2000.

**[5-76]** B. Faatz, J. Pflüger, *Field Accuracy Requirements for the Undulator Systems of the X-Ray FEL's at TESLA*, TESLA-FEL report 2000-14, DESY, Hamburg (2000).

**[5-77]** B. Faatz, Private communication.

**[5-78]** U. Hahn, H. Schulte-Schrepping, *Emittance Measurements at the PETRA Undulator Beamline*, HASYLAB Jahresbericht 2001, DESY, Hamburg (2001) 105.

**[5-79]** U. Hahn, H. Schulte-Schrepping, *Crystal monochromator based emittance measure-ments at the PETRA undulator beamline*, SRI 2003 conference, San Francisco, AIP Conf. Proc. 705 (2003) 533.

**[5-80]** E.L. Saldin, E.A. Schneidmiller and M.V. Yurkov, *The Potential for the Development of the X-Ray Free Electron Laser*, TESLA-FEL report 2004-02, DESY, Hamburg (2004).

**[5-81]** J. Feldhaus et al., *Efficient frequency doubler for the soft X-ray SASE FEL at the TESLA Test Facility*, Nucl. Instrum. and Methods A 528 (2004) 471.

**[5-82]** E.L. Saldin, E.A. Schneidmiller and M.V. Yurkov, *Terawatt-scale sub-10-fs laser technology – key to generation of GW-level attosecond pulses in X-ray free electron laser*, Opt. Commun. 237 (2004) 153.

**[5-83]** E.L. Saldin, E.A. Schneidmiller and M.V. Yurkov, *A new technique to generate 100 GW-level attosecond X-ray pulses from the X-ray SASE FELs*, Opt. Commun. 239 (2004) 161.

**[5-84]** J. Feldhaus et al., *Possible application of X-ray optical elements for reducing the spectral bandwidth of an X-ray SASE FEL*, Opt. Commun. 140 (1997) 341.

**[5-85]** E.L. Saldin, E.A. Schneidmiller, Yu.V. Shvyd'ko and M.V. Yurkov, *X-ray FEL with a meV bandwidth*, Nucl. Instrum. and Methods A 475 (2001) 357.

# 6 Photon beamlines and scientific instruments

The high photon number per pulse, ultra-short pulse duration and high coherence of x-ray free-electron laser (FEL) radiation provide the opportunity to apply new x-ray experimental techniques, thereby enabling new areas of scientific investigation. In this chapter we will describe the x-ray instrumentation for the European X-Ray Free-Electron Laser (XFEL). This includes, in particular, a description of the various scientific domains and the main requirements for experiments in these areas.

The scientific case for an x-ray FEL was discussed previously in the context of the Linac Coherent Light Source (LCLS) project in Stanford, and reported in September 2000 (*LCLS: the first experiments* **[6-1]**); and also in the context of the Tera-Electronvolt Superconducting Linear Accelerator (TESLA) project (for a linear collider with integrated x-ray laser), and reported in the corresponding Technical Design Report (TDR) **[6-2]** in spring 2001. In preparing the present report, these previous efforts were of course taken into account as a starting point, but it was felt that enough time had passed and that sufficient new experience had been acquired with experiments and equipment at projects such as the Sub-Picosecond Pulse Source (SPPS) in Stanford, the "Free-electron LASer in Hamburg (FLASH)" vacuum ultraviolet (VUV)-FEL at Deutsches Elektronen Synchrotron Laboratory (DESY), and at other sources, to warrant an in-depth new consideration of the scientific perspectives and the accompanying requirements for instrumentation. In order to get as wide a European basis as possible, consultation of the scientific community was organised by holding four XFEL workshops at different locations in Europe:

- Diffraction, Crystallography and Imaging at the European XFEL, October 28/29, 2005, DESY, Hamburg, Germany.
- European XFEL Workshop on High Energy Density Science and Non-linear X-ray Processes, November 28/29, 2005 École de Chimie de Paris, Paris, France.
- Ultra-fast Time-Dependent X-ray Experiments at the European XFEL, January 20/21, 2006 Danish Academy of Sciences, Copenhagen, Denmark.
- Detectors for the European XFEL March 28/29, 2006, by the Rutherford Laboratory, Abingdon, UK.

The first three workshops concentrated on the validation of the radiation parameters chosen for the various undulator branches, on the scientific cases and the specific instrumentation requirements; the last workshop centred on the development of area detectors suitable for the XFEL. Most importantly, the workshops were very useful for identifying leading European scientists who became natural "spokespersons" for a given scientific field. These scientists have been editors of the majority of the material presented in this chapter, soliciting, coordinating and organising the contributions of

many authors. It is, therefore, fair to say that XFEL is the product of an international collaboration widely distributed across Europe.

Section 6.1 presents an overview of the x-ray installations that will be described in more detail in later sections. Section 6.2 describes the XFEL photon beam transport from the undulators to the experimental hall, including x-ray optical elements which are part of the scientific instruments. A possible layout of the photon beam transport of the five beamlines is presented. Section 6.3 describes the photon beam diagnostics to be installed in the beamlines and near the instruments, in order to allow the required measurement of the XFEL radiation parameters: most of these diagnostics will be provided on a pulse-by-pulse basis. Section 6.4 describes the various scientific domains and their experimental proposals. The latter have been analysed to define the requirements for the instruments to be installed at the European XFEL. A schematic of these instruments concludes each of the scientific areas. Section 6.5 describes instrumentation where specific developments are required for XFEL, in particular the areas of sample manipulation and environment, x-ray optics, optical lasers and x-ray detectors. Section 6.6 concludes the chapter with a summary of cost and manpower requirements.

## 6.1 Overview of the X-Ray systems

The European XFEL features five x-ray sources: Three long undulators, operated in the Self-Amplified Spontaneous Emission (SASE) mode, provide XFEL radiation in the photon energy range from 0.25 to 12.4 keV. Two further undulators provide spontaneously emitted synchrotron radiation at higher photon energies, from 20 to 100 keV. For each of these x-ray sources, a beamline guides the x-ray beam to the experimental hall, where the instruments for scientific experiments are located. The first installation phase of the European XFEL described in this report includes the installation of ten instruments (see Chapter 1). These instruments will be distributed on five photon beamlines. Since XFEL features a relatively small number of photon beamlines, each of them needs to serve more than one application or x-ray technique. This is in contrast to beamlines at storage ring sources and will lead to a more complex design of the beamlines. Another feature of European XFEL is that electron bunches can be prepared and distributed according to the needs of the experiment. The specific electron beam parameters could be the time pattern, the electron energy (and, therefore, the photon energy) or even more sophisticated parameters of the x-ray pulse. The flexibility of linear accelerators (linacs) is straightforward to exploit for an installation which features only one undulator, such as the FLASH facility at DESY. At the European XFEL it is envisioned that the five undulators and photon beamlines will operate quasi-simultaneously (see Section 5.1), so it is important that the electron beam parameter variation does not lead to a conflict in the operation of the various instruments.

One advantage of the European XFEL is its ability to accelerate a large number of electron bunches per second. The time pattern for fully loaded bunch trains is shown in Figure 6.1.1. Using fast switches in the beam distribution (compare Section 4.5.3.1) it will be possible to distribute a specific bunch pattern into the two electron beamlines, thus enabling operation with from 1 to 3,000 bunches per bunch train. The undulators located

in the same electron beamline branch (two in beamline 1, three in beamline 2) will all receive the same electron bunch pattern. The instruments at these beamlines will operate more independently by the use of fast shutters upstream of the experimental stations, operating with a repetition rate of at least 10 Hz.

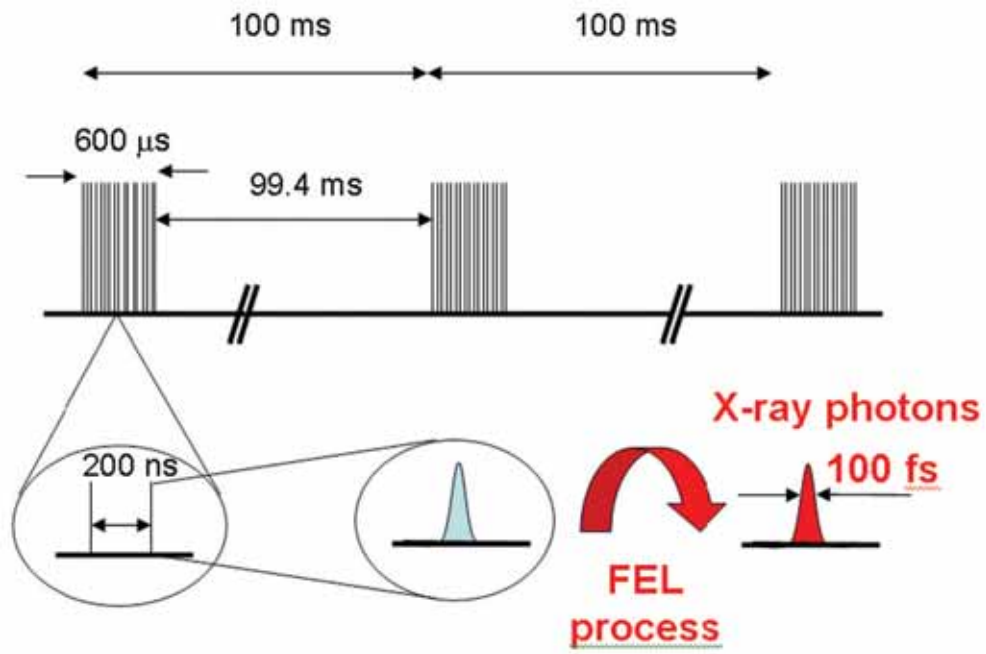


***Figure 6.1.1*** *Electron bunch time pattern with 10 Hz repetition rate and up to 3,000 bunches in a 0.6 ms long bunch train. The separation of electron bunches within a train is 200 ns for full loading. The duration of electron bunches is ~200 fs and the non-linear FEL process reduces the duration of the photon pulses to ~100 fs.*

| Beamline | X-ray features | Proposed instruments |
|---|---|---|
| SASE 1 | ~12 keV<br>High coherence<br>High flux<br>3rd harmonic | PCS 1 – X-ray Photon Correlation Spectroscopy<br>FDE 1 – Femtosecond Diffraction Experiments<br>SPB 1 – Single Particles and Biomolecules |
| SASE 2 | 3.1 – 12.4 keV<br>High coherence<br>High flux | CXI 1 – Coherent X-ray Imaging<br>HED 2 – High Energy Density<br>XAS 2 – X-ray Absorption Spectroscopy |
| SASE 3 | 0.25 – 3.1 keV<br>High coherence<br>High flux<br>3rd harmonic | HED 1 – High Energy Density<br>SQS 1 – Small Quantum Systems<br>XAS 1 – X-ray Absorption Spectroscopy<br>SQS 2 – Small Quantum Systems<br>PCS 2 – X-ray Photon Correlation Spectroscopy<br>CXI 2 – Coherent X-ray Imaging |
| U 1, U 2 | 15* – 90 keV | FDE 2 – Femtosecond Diffraction Experiments<br>CXI 3 – Coherent X-ray Imaging<br>RAD 1 – Research And Development |

* This value of the lowest photon energy requires small modification of the U1 design presented in Chapter 5.

***Table 6.1.1*** *A possible distribution of scientific instruments discussed in Section 6.4 on the photon beamlines. Main x-ray features of the five beamlines are indicated.*

In the present stage of the European XFEL, a strong scientific case has been established. In Section 6.4, the requirement for instruments for scientific applications are discussed. However, no decision has been made yet on which ten out of the 15 instruments presented in Section 6.4 will be realised. This decision has to be prepared by the scientific advisory bodies of the European XFEL in the forthcoming 12 months. In order to give a proper description and costing of the facility in this report, we have evaluated all the proposed instruments and analysed their photon beamline requirements. The instruments have been allocated to the most appropriate beamline (see Table 6.1.1) leading to a beamline design described in Section 6.2.4. It is assumed that the overall concept of the photon beamlines will not change drastically if the final instrument configuration differs from the proposal presented here.

## 6.2 Photon beam transport

### 6.2.1 Photon beamline concept

The photon beam transport for the European XFEL is different from existing light sources due to the specific properties of FEL radiation. Most importantly, a large distance between undulator source and optical elements accepting the FEL beam is required. It allows the beam size to increase, thus reducing the enormous peak power. Also grazing incidence geometries are needed to spread out the beam footprint, requiring long drift paths to achieve sufficient beam separation. Due to the long distances involved, undulators, beam transport elements and instruments are located in different buildings. The undulators and beamlines will be located in tunnels which will impose transverse and longitudinal constraints (see Table 6.2.1). The limited number of beamlines requires a very flexible photon beam transport design since different instruments with different requirements may be installed on the beamlines. Needless to say, the beam transport between undulator and experiments hall must preserve the important XFEL photon beam parameters; namely time structure, flux, and coherence.

Although differences exist between the two hard x-ray FELs, the soft x-ray FEL, and the two x-ray-spontaneous synchrotron radiation beamlines, a modular design of the photon beamlines has been chosen. In the following we introduce the most important elements of this design. A more detailed discussion of each component is given later. For clarity we will focus our description mainly on the XFEL beamline SASE 1. A similar description (with slightly varying parameters) can be given for each of the beamlines (see Table 6.2.1 and Sections 6.2.4.1 – 6.2.4.5).

SASE 1 is equipped with a 200 m long undulator system and aims at the production of 12.4 keV FEL radiation. In the present design the undulator is followed by a 193 m long drift section preserved for future “undulator options”. Several options have been discussed, but are not included in this first installation phase. Examples are self-seeding schemes, laser manipulation of the x-ray beam, two-colour insertion devices, or additional undulators segments for achieving lasing at higher photon energy than originally foreseen. After this section, the electron beam will be separated from the photon beam and will be deflected towards the next undulator. Where the separated

electron beam comes close to the tunnel periphery, a shaft building is located from which two tunnels continue. In case of the terminating undulator (SASE 3, U2), the electron beam will be bent down into an electron beam dump located in an underground hall. Since it is expected that shafts and dump halls will exhibit slightly different ground motions than the neighbouring tunnels, beamline elements requiring exact positioning (e.g. position monitors, mirrors, or monochromators) cannot be located in or near these tunnel "interruptions". The layout with separate tunnel sections has the additional function of allowing access to some of the tunnels for work on beamline elements, while the facility is in operation.

| | SASE 1 | SASE 2 | SASE 3 | U 1 | U 2 |
|---|---|---|---|---|---|
| Electron beam separation | 220 | 129 | 143 | 91 | 110 |
| Intermediate shaft/dump building | 385-415 | 215-245 | 155-180 | 195-225 | 135-160 |
| Primary photon beam diagnostics | 330-450 | 180-300 | 140-200 | 150-240 | 125-180 |
| *Bremsstrahlung* beam stop | 500 | 500 | 250 | 280 | 200 |
| Monochromator | 500 | 500 | 250-350 | 280 | 200 |
| Experiments hall | 960 | 910 | 400 | 590 | 295 |

***Table 6.2.1*** *Distances (in metres) of components from the end of the undulator for each of the five beamlines. Where appropriate, the start and end points of the units are indicated.*

The first beamline element is a combined unit of $10^4$ gas attenuators and beam position monitors located in the vicinity of the shafts and dump halls. The gas absorber system will allow controlled adjustment of the photon flux over four orders of magnitude. Just before and behind the gas absorber, there are two non-invasive photon diagnostic tools: i) X-ray Gas Monitor Detectors (XGMDs) to measure the absolute photon flux; ii) Beam Position Monitors (BPMs), to image the transverse position and direction of the photon beam. These photon beam diagnostics systems will be described in Section 6.3. The following photon diagnostic station is primarily dedicated to photon beam-based alignment for the undulator segments (see Section 5.5). The next element in each of the beamlines is a *Bremsstrahlung* beam stop. A photon beam offset of 50 mm, followed by a collimator with an approximate opening of 10 mm, is required to prevent *Bremsstrahlung* radiation entering the experimental hall, both for radiation protection and signal background reduction. Two complementary schemes are envisaged: For experiments requiring maximum flux, a double-mirror fixed-exit system will be used to generate the offset, while experiments requiring an energy resolution better than the natural bandwidth of the SASE radiation, use crystal or grating monochromators. Perfect crystal monochromators are furthermore expected to preserve wavefronts better than mirrors and are, therefore, the preferred optical element to transport the beam in coherent beam or extreme focusing applications.

For beamlines requiring focused beams, optical elements will be needed at distances appropriate for the required demagnification. For moderate focusing (spot sizes ~100µm, demagnification near unity) focusing elements will be placed in the photon beam transport section. Further mirrors and crystal optics could be employed nearer to the experimental hall to guide the photon beams to separate instruments. The beamlines end at a safety shutter in front of the experimental hall.

## 6.2.2 X-ray optical elements

### *6.2.2.1 Mirrors*

X-ray mirrors will be widely used for the XFEL. They provide high reflectivity and are achromatic tools to distribute the beams to the various experimental stations. In addition, they can be used to focus the x-ray beam and, by using the reflectivity cut-off for higher photon energies, allow reduction of higher harmonic radiation. The requirements for mirrors for XFEL radiation (discussed below) will apply to all kinds of mirrors used for beam distribution in flat geometry or, for focusing, in pre-shaped or dynamically bent geometries. A specific example is the double-mirror system to provide a fixed beam offset of 50 mm at the *Bremsstrahlung* beam stop. The distance (see Table 6.2.1) of these first mirrors to the undulator, of 500 m and 250 m in the cases of SASE 1, SASE 2 and SASE 3, respectively, is a compromise between reduction of photon fluence on the optical surface of the mirrors and available lengths of ultra-high precision mirrors, which in turn limits the acceptable photon beam size. The discussion of the resulting energy deposition on the mirror surfaces (see Section 6.2.2) gives confidence that mirrors in the chosen geometry will withstand the intense radiation safely.

The mirrors will be operated at angles below the critical angle (angle where total external reflection occurs), which depends both on the wavelength and the mirror surface material. For the 12 keV case, highly polished Silicon substrates with Carbon coating at a glancing angle of 2 mrad are proposed for the mirrors. The critical angle $\alpha_c$ of Carbon for this photon energy is 2.44 mrad generating an energy cut-off at ~15 keV. For the opening angle of FEL radiation of ~1 µrad (FWHM) and a distance of the mirror system of 500 m a 0.7 m long mirror could, thus, accept 6-s of the beam, which will include the full coherent beam. For lower photon energies, the opening angle increases, leading to the requirement of larger mirror surfaces. This will be a problem in the case of SASE 2 where an opening of 3.4 µrad at 3.1 keV FEL radiation and assuming identical configuration of the mirror leads to a 6-s mirror length of ~2.2 m. Mirrors of this length cannot be manufactured at the precision required for the XFEL (see below) and other solutions have to be found here.

**Surface finish and figure errors**

Since the mirrors are always in the beam (except when perfect crystals are used instead, see Section 6.2.2.2), they must preserve the wave front of the incident radiation to allow proper focusing and to maintain the coherence properties of the FEL sources. Estimates of the mirror requirements are generally based on models and ray-tracing codes for incoherent light sources. Since the FEL has a significant degree of coherence, one, in principle, needs to perform simulations of the effect of the mirror for the partially coherent

beam. These could be either analytical simulations **[6-3]** or wave front propagation codes. The latter are routinely used for visible light propagation simulation, but are not yet available in full for x-ray radiation. Current understanding of the corresponding requirements on figure error and micro-roughness of mirror surfaces is, therefore, incomplete.

As a starting point for surface figure error, one can assume a value of 10% of the corresponding FEL radiation full angle (0.1 µrad at 12.4 keV). However, simulations indicate that if the maximum focal spot increase which can be tolerated is 10%, figure errors should be an order of magnitude smaller **[6-4]**. Ray-tracing seems to generate similar values. Figure 6.2.1 shows simulation results of focus and wave front deformation for two slope errors using the SHADOW code. The simulations neglect the influence of diffraction due to finite mirror lengths. For focusing experiments, where a beam divergence in the order of 1 mrad is acceptable, a Kirkpatrick Baez (KB)-mirror system in front of the sample could be used in addition to the upstream mirrors. In Figure 6.2.2 ray-tracing results for additional KB mirrors at 1 and 2 metres in front of the sample are shown. For a slope error of 0.01 µrad on all four mirrors, a sub-micron focus with an almost flat wave front is obtained. If the quality of the upstream double bounce mirrors is reduced to 0.1 µrad, but with the KB pair remaining at 0.01 µrad, a focus size in the sub-micron range can still be achieved, however, the wave front distortion will be in the Angstrom range. Recent measurements, however, show that the requirement on figure errors reduces strongly (~1 µrad) for a 20% spot size increase **[6-5]**, in a situation, similar to the XFEL, of long-source-to-mirror distances and strong focusing.

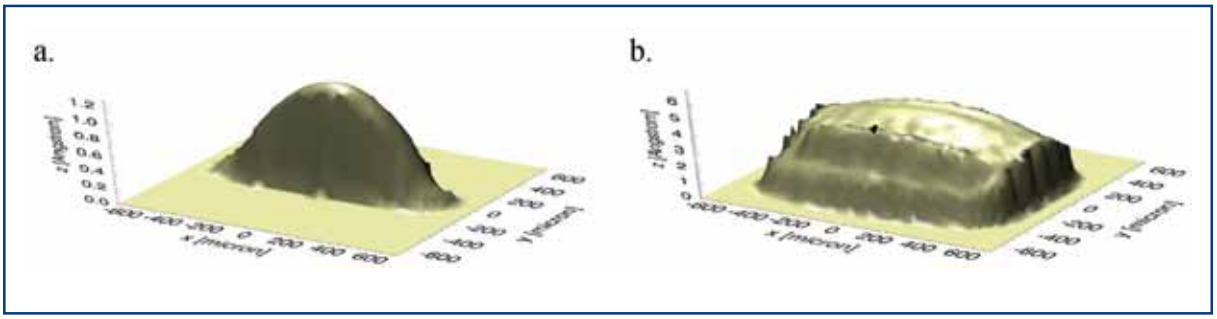


***Figure 6.2.1*** *Ray-tracing results for the double-mirror system at 500 m from the source. The x- and y-axes are the beam dimensions in horizontal and vertical direction. The z-axis shows the relative path lengths in Angstroms. With a slope error of 0.01 µrad rms (a) the beam essentially retains a undistorted spherical wave front and can be focused by bending one of the mirrors to about 70 µm FHWM in y-direction, very close to the source limited spot size. The unfocused direction is 750 µm FWHM. With a figure error of 0.1 µrad; (b), the wave front is distorted on the Angstrom level and the focusing in y-direction is much less effective (FWHM y: 400 µm, x: 820 µm).*

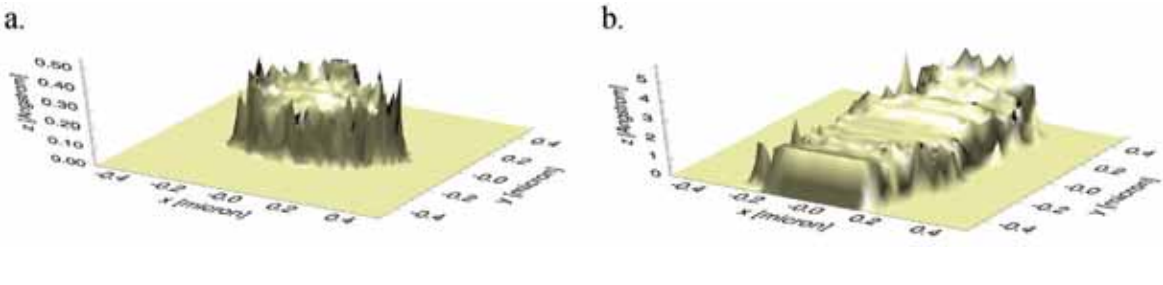


***Figure 6.2.2*** *Ray-tracing of focus and wave front deformation for the case of extreme focusing using KB-mirrors in front of the sample. 0.01 µrad (a) and 0.1 µrad (b) rms slope errors have been assumed for the double-mirror system at 500 m.*

At these accuracy levels the reduction of gravitational sag is important, but the symmetric beam of the FEL will allow horizontal reflection which essentially eliminates this problem. Given the XFEL output, heat deformation of the first mirror has to be expected which might be compensated for by operating the second mirror as an adaptive optic element. In a different application this mirror could be used to focus the beam in one direction. In addition to the figure error, the micro-roughness of the mirrors leads to scattering, thus, producing a wider, less collimated background in addition to the focal spot. Roughness in the order of 0.1 nm seems, at present, to be acceptable for most of the experiments.

State-of-the-art manufacturing achieves rms values of 0.09 nm micro-roughness and 0.3 µrad tangential slope errors for 0.5 m long mirrors (compare Figure 6.2.3). For plane mirrors, the radius was measured to be >240 km. Conventional metrology tools for verifying the optical surfaces, like long trace profilers and interferometers, are already close to their resolution limit because of the use of optical wavelengths. Therefore, the implementation of in-situ wave front sensors is required for improved characterisation of the performance of optical elements (see Section 6.3.1). It should be noted here that during recent years, a discussion started aimed at a better definition of mirror performance. The limiting process in mirror fabrication is metrology, measuring either local roughness or averaged slope errors. In a surface displacement power spectrum, these measurements make two non-overlapping areas. Specification of an x-ray mirror is usually done by values for roughness and slope error without correlating the two parameters. Furthermore, in x-ray applications it is not fully understood how the correlation of the two parameters influences the x-ray beam properties and therefore, the experimental observation. In this field more Research and Development (R&D) will be required in the forthcoming years to properly specify mirrors for XFEL applications.

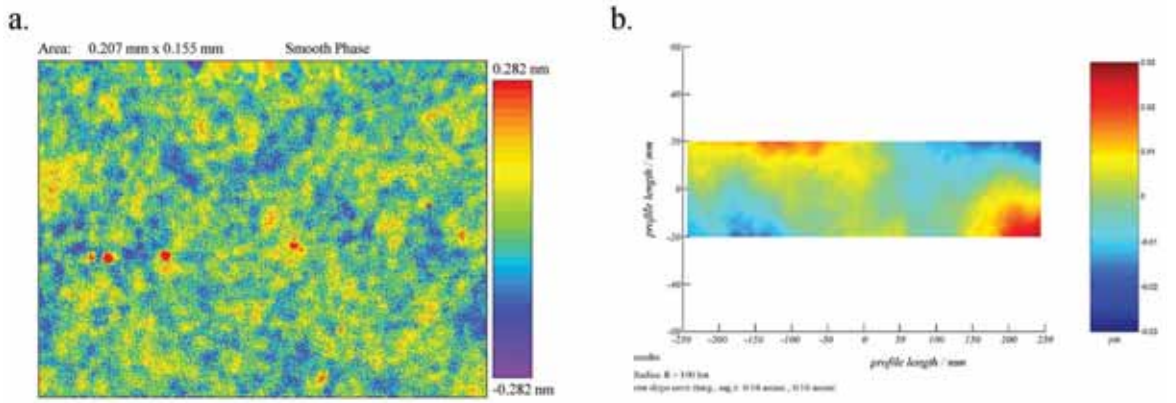


***Figure 6.2.3*** *Micro-interferometric measurement (a) and long trace profilometry (b) of a 0.5 m long plane mirror for a beamline at the Free-Electron LASer in Hamburg (FLASH) facility at DESY manufactured by Zeiss, Oberkochen. rms values of the surface roughness, tangential and sagittal slope errors are 0.09 nm, 0.3 and 0.6 µrad, respectively.*

### Power dissipation

Due to the limited number of electron bunches per second, the average power load on the mirrors is very reasonable. In the case of SASE 1, with 72 W average power of the FEL radiation, and a reflectivity of 0.9, there is an average power density of ~50 mW/mm$^2$ at the mirror surface. The additional power due to spontaneous synchrotron radiation is estimated to be of the same order of magnitude. The particular time structure of the XFEL with up to 3,000 pulses within a period of 0.6 ms does, however, complicate the situation. The power density within this pulse train could be as high as ~8 W/mm$^2$. At third generation synchrotron sources, power densities up to several 100 W/mm$^2$ are currently handled by monochromator crystals with cryo-cooling schemes. Research and development is required to evaluate if these schemes can be equally applied to the long mirrors of the XFEL with their tight tolerances in figure error.

While the average power is still moderate, the peak power within a single pulse will be in the GW range. At these values, the principal problem may no longer be thermal distortion, but rather the possibility of ablation of the mirror surface, causing permanent damage. Ablation will depend on the radiation dose per pulse, which we will quantify as the energy absorbed per atom per pulse. To estimate the dose, we calculate the energy absorbed in the volume defined by the projected beam area $A_{proj}$. on the optical element and one attenuation length $l_{att}$, i.e. the depth into the material measured along the surface normal where the radiation intensity falls to 1/e of its value at the surface. Normalised to one atom, this energy corresponds to the atomic dose near the surface: $D_A = E_{pulse}(1\text{-}R)/A_{proj.}1_{att}n_A$, where $E_{pulse}$ is the energy in one radiation pulse, $R$ is the reflectivity and $n_A$ denotes the element specific density of atoms. In Table 6.2.2 we calculate the dose near the surface for some of the mirror configurations at the XFEL.

| | Unit | SASE 1 | SASE 1 | SASE 3 | SASE 3 |
|---|---|---|---|---|---|
| Photon energy | keV | 12.4 | 12.4 | 3.1 | 0.8 |
| Pulse energy | mJ | 2 | 2 | 8 | 13 |
| Projected beam area | mm2 | 100 | 100 | 57 | 640 |
| Mirror coating | | Si | C | C | C |
| Grazing angle | mrad | 2 | 2 | 10 | 10 |
| Projected fluence | $J/cm^2$ | $2.0\times10^{-3}$ | $2.0\times10^{-3}$ | $1.4\times10^{-2}$ | $2.0\times10^{-3}$ |
| $n_A$ | $cm^{-3}$ | $5.0\times10^{22}$ | $1.1\times10^{23}$ | $1.1\times10^{23}$ | $1.1\times10^{23}$ |
| (1-R) | | $2.57\times10^{-2}$ | $1.98\times10^{-3}$ | 0.54 | $7.46\times10^{-2}$ |
| $L_{att}$ | cm | $5.30\times10^{-7}$ | $5.77\times10^{-7}$ | $1.06\times10^{-5}$ | $3.28\times10^{-7}$ |
| Surface dose | eV/atom | $1.2\times10^{-2}$ | $3.9\times10^{-4}$ | $4.0\times10^{-2}$ | $2.5\times10^{-2}$ |

***Table 6.2.2*** *Parameters for first mirrors and calculation of absorbed dose per XFEL pulse. The reflectivity and attenuation length data have been taken from the CXRO tables* **[6-6]***.*

A surface dose of 0.01 eV/atom is a limiting dose below which no damage is expected **[6-7]**. The values of Table 6.2.2 indicate that for the XFEL in the SASE 1 and SASE 2 cases, the surface dose is about one order of magnitude below this limit, when using Carbon coatings. We, therefore, do not expect any damage mechanisms to be important. However, higher Z materials, such as Silicon, may already pose a problem. In the case of SASE 3, the calculated doses reach up to values of 0.01 eV/atom. There are experimental indications for the EUV regime that damage sets in only at significantly higher doses. However, further detailed studies to determine accurate damage threshold data are required **[6-8]**. Additionally, one will have to evaluate if there are cumulative effects that may cause damage over several thousands of pulses. The neglect of non-linear effects in the above considerations of potential damage by power load is, to some extent, supported by the absence of non-linear interaction during the operation of mirrors for FEL radiation at FLASH. Detailed investigations are underway to study the interaction of XFEL radiation with optical surfaces **[6-8]**.

### *6.2.2.2 Crystal monochromators*

X-ray crystal monochromators will be required to reduce the 0.1% bandwidth of the FEL for various applications, in particular for spectroscopy. In addition, they can be used to match the radiation bandwidth to the one accepted by the sample in a diffraction experiment, which also reduces unwanted heating of the sample. The diffraction limited bandwidth is $1.4\times10^{-4}$ for the Silicon (111)-reflection and $6\times10^{-5}$ for the Diamond (111)-reflection. The energy resolution can be as small as a few $10^{-7}$ for high-order reflections but could be limited by time-dependent temperature gradients in the crystal. Diffraction by crystals creates relatively large deflection angles, which may be useful for distributing the beam to various instruments inside the experimental hall. Single crystals cannot deflect the full XFEL bandwidth at a particular Bragg angle.

In the following, Silicon and Diamond crystals will be described, as they have shown the highest prospect of fulfilling the requirements for XFEL sources. Whereas Silicon crystals can be grown to high perfection standards, Diamond has the advantages of higher heat conductivity and high damage threshold, thus, achieving good performance at high power loads. In this respect, isotopically enriched Silicon-28 ($^{28}$Si) could be an ideal material because of its enhanced thermal conductivity, see the heat load discussion below.

### Silicon and Diamond crystals

Comparing Diamond and Silicon single crystals, one finds that the Diamond (111) reflection is similar to Silicon (220) except for the absorption thickness, which is more than one order of magnitude larger for Diamond **[6-9]**. Therefore, not only are the reflection properties of Diamond better, i.e. the peak reflectivity is (slightly) higher, but also less heat is absorbed. Beryllium, which is superior in this respect, cannot yet be grown as a dislocation-free crystal. In the best case it has a mosaic spread of 200 µrad. Silicon, on the other hand, is absolutely dislocation-free, while Diamond single crystals are only locally perfect **[6-10]**, although development of larger perfect Diamond crystal is showing promising progress. The Silicon (111) reflection provides a good matching ($\omega_H$ =22 µrad at 12.4 keV) for synchrotron beams, but only higher order reflections have a Darwin width small enough to match the XFEL beam divergence (1 µrad (FWHM) at 12.4 keV). This means that the reciprocal space element selected by a perfect crystal out of a spectrally wide, but well collimated beam will be anisotropic, typically with its long axis parallel to the beam direction. This situation is radically different from laboratory or even synchrotron radiation conditions. The choice between Silicon and Diamond will depend on the degree of crystal perfection that is needed, the actual heat loads and radiation damage considerations, as discussed below.

### Heat load simulations

For Silicon crystal monochromators at third generation light sources, the average heat load limit is already reached in certain cases. For higher heat loads it is essential to develop schemes to maintain the monochromator performance. The thermal deformation of the crystal induced by heat load depends on the figure of merit $\alpha/k$, where $\alpha$ and $k$ are, respectively, the thermal expansion coefficient and the thermal conductivity. This ratio is strongly temperature dependent for Silicon and Diamond. At liquid Nitrogen temperature or even lower, $\alpha/k$ could be several orders of magnitude lower than at room temperature. Possible solutions to improve the performance of crystal monochromators are using crystals with lower $\alpha/k$ than Silicon, or using enhanced cooling techniques (higher cooling efficiency or lower temperature of the coolant). Diamond has lower $\alpha/k$ than natural Silicon in a wide temperature range, and is a good candidate. Presently, Silicon crystal monochromators are made of natural Silicon ($^{nat}$Si), which is composed of three stable isotopes: Silicon-28 (92% natural abundance), Silicon-29 (4.7% natural abundance), Silicon-30 (3.3% natural abundance). By purifying Silicon to 99.9% Silicon-28 ($^{28}$Si), the phonon mean free path increases, thereby significantly improving the thermal conductivity. The thermal conductivity is enhanced by 60% at room temperature, by a factor of 2.4 at liquid Nitrogen temperature (77K), and by a factor of 6 at 20 K. The maximum thermal conductivity (30 kW/m/K) of $^{28}$Si at 20 K is 2.5 times higher than that of Diamond. Silicon-

28 ($^{28}$Si) cooled by liquid Helium could be an ideal crystal monochromator for both its perfect crystalline structure and thermal properties. Also, $^{28}$Si is available from semiconductor industries where it is used to reduce the chip temperature. Figure 6.2.4 shows $k$, $\alpha$ and the specific heat $C_p$ versus temperature for Diamond IIa, and both $^{nat}$Si and $^{28}$Si **[6-11]**.

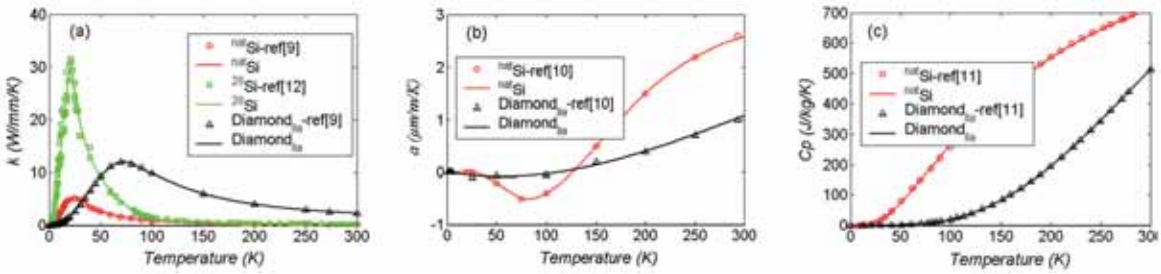


***Figure 6.2.4*** *Thermal conductivity (a) thermal expansion coefficient (b) and specific heat (c) of $^{nat}$Si, $^{28}$Si and Diamond IIa* **[6-11]**.

The response of cryogenically-cooled crystals to the heat deposition during a train of XFEL pulses has been studied by finite element modelling **[6-11]**. Results show the increase of crystal temperature during the pulse train, followed by a sharp decrease after the train. The repetition rate of 10 Hz does not lead to accumulated effects. For an energy Q = 2 J, deposited during the pulse train, the temperature variation at two locations of the crystal and the change in the slope errors are depicted in Figure 6.2.5. The geometry of the crystals studied here is a block of 120×60×60 mm$^3$ for $^{nat}$Si, 20×20×20 mm$^3$ for both $^{28}$Si and Diamond IIa. The crystals are cooled on five surfaces in order to maximise the cooling surface area. The Diamond crystal is cooled by liquid Nitrogen ($h_{cv}$=0.005 W/mm$^2$/K, $T_f$=77 K). The $^{nat}$Si and $^{28}$Si crystals are cooled by liquid Helium ($h_{cv}$=0.005 W/mm$^2$/K, $T_f$=8 K). X-ray beam size is 2×2 mm$^2$ with an incident angle of $\theta_{Bragg}$=14°. The peak values of the thermal slope error and the maximum temperature are summarised in Table 6.2.3 for the three crystals as a function of deposited energy Q. In conclusion, $^{28}$Si crystals cooled by liquid Helium offer thermal slope errors comparable to Diamond crystals for pulse train energies up to 2 J. Therefore, $^{28}$Si crystal monochromators could be an interesting alternative to Diamond for applications where a perfect crystalline structure is needed. It is clear that liquid Helium cooling of crystals has not yet been established and needs a dedicated R&D effort.

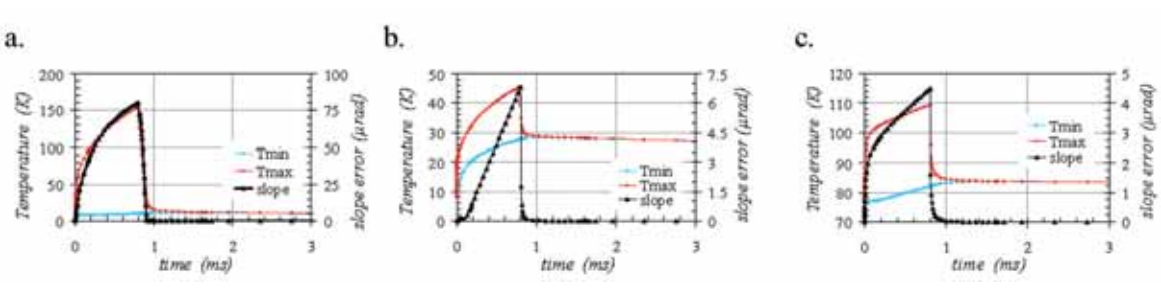


***Figure 6.2.5*** *Temperature and slope error variation during the course of a pulse train for (a) $^{nat}$Si, (b) $^{28}$Si, and (c) Diamond crystals (Q=2 J).*

| Crystal | Cooling | Q [J] | $P_{mean}$ [W] | $T_{max}$ [K] | $slope_{PV}$ [µrad] |
|---|---|---|---|---|---|
| | | 2 | 20 | 109 | 4.5 |
| Diamond IIa | Liquid Nitrogen | 3 | 30 | 129 | 11 |
| (20×20×20 mm³) | (77 K) | 5 | 50 | 178 | 41 |
| | | 10 | 100 | 380 | 346 |
| | | 2 | 20 | 46 | 6.8 |
| Single-isotope $^{28}$Si | Liquid Helium | 3 | 30 | 69 | 26 |
| (20×20×20 mm³) | (8 K) | 4 | 40 | 147 | 69 |
| | | 5 | 50 | 360 | 346 |
| | | 1 | 10 | 44 | 3 |
| Natural Silicon | Liquid Helium | 1.5 | 15 | 77 | 23 |
| (120×60×60 mm³) | (8 K) | 2 | 20 | 155 | 80 |
| | | 3 | 30 | 406 | 566 |

***Table 6.2.3*** *Calculated maximum temperature and peak-to-valley thermal slope error in three crystals at different pulse train energy values Q.*

**Time structure after monochromatisation**

Another point to be addressed is the effect of monochromatisation on the time structure of the XFEL pulse of 100 fs duration and its pulse substructure with coherent radiation bursts of ~0.3 fs duration. The x-ray pulse duration is in the order of the time needed for the pulse to traverse an extinction length (for perfect crystals) or an absorption length (for mosaic crystals). By definition of Bragg's law, the path difference of an x-ray beam is precisely one wavelength per lattice plane with respect to the beam reflected at the crystal surface. Thus, the time delay per lattice plane is $\lambda/c$ where $c$ is the speed of light. Consequently, pulse broadening might occur. Indeed, a simulation investigating the response of a Laue-case monochromator crystal in dynamical diffraction theory has shown a broadening of a $\delta$-pulse **[6-12 – 6-14]**. The crystal reflection acts as a frequency filter and thus, has a broader response in the time domain. However, the simulation suggests that this broadening mainly changes the duration of the bursts to 2-3 fs, but leaves the overall pulse duration of 100 fs effectively unchanged. The simulation also shows that the amplitudes normalised to the average amplitude follow the same statistical law as the incident beam, namely the Rayleigh distribution. Further R&D is needed to implement dynamical diffraction into wave front propagation codes for complete description of time-dependent effects in diffraction.

### *6.2.2.3 Grating monochromators*

For soft x-rays produced at SASE 3, grating monochromators have to be used in order to reduce the bandwidth of FEL radiation for spectroscopy applications. It is proposed to use a plane grating monochromator design originally conceived in 2001 for a soft x-ray beamline at the TESLA XFEL **[6-15]**. This monochromator operates in the photon energy range 0.5-3 keV, provides a resolution of $10^4$ and is able to accept the high power levels of XFEL radiation. Its total length is in the order 120 m, thereby requiring integration of the

monochromator in the photon beamline. Figure 6.2.6 shows the optical design which requires only minor modification.

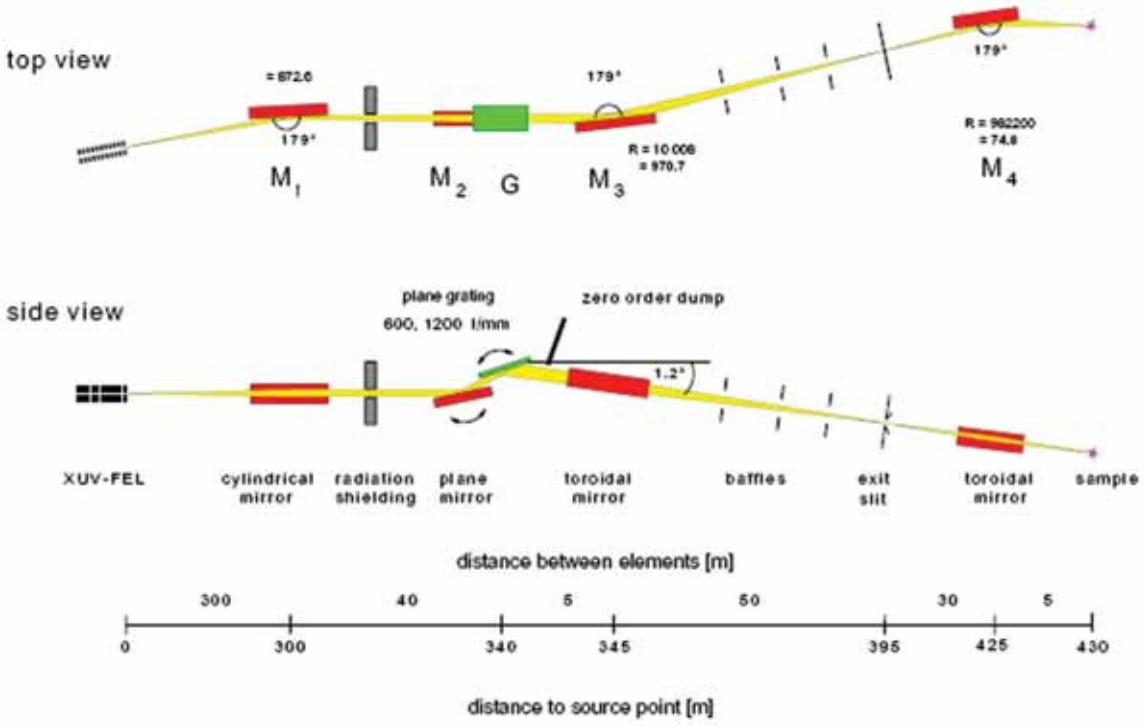


***Figure 6.2.6*** *Optical design for a high power XUV-plane grating monochromator* **[6-15]**.

### *6.2.2.4 Focusing optics*

For a number of experiments, focusing the x-ray beam to a small spot is desirable to increase the photon density at the sample position. This means that the lens apertures should be as large as the beam to collect as many photons as possible. If the optics are illuminated with a fully coherent beam, the focused spot size will no longer depend on the source size or the demagnification factor. It will be diffraction-limited in the case of perfect optics and aberration-limited in the case of a non-perfect optics. Focusing x-ray optics can be divided in three classes; all have their advantages and drawbacks depending on the specific application, photon energy, achievable spot size, aperture, and robustness: (i) reflective, (ii) refractive, and (iii) diffractive. (Waveguides have also been used successfully to produce very small hard x-ray spot sizes **[6-16]**, but due to their small working distance and relative inefficiency compared to other focusing optics they are not likely to find widespread application at XFEL sources). A brief review on the present state-of-the-art for hard x-ray nano-focusing and the future potential with respect to the specific requirements in the context of the XFEL, will be given. This is summarised in Table 6.2.4.

| | KB mirrors | NFLs (refractive lenses) | KB mirrors |
|---|---|---|---|
| Achieved focal spot [nm] | 36×48 (15 keV, mirror **[6-17]**);47×55 (21 keV, **[6-19]**) 45 (24 keV, ML **[6-18]**) | | ~150 (8 keV **[6-20]**; 12.7 keV **[6-21]**) |
| Aperture [µm] | 100×100 | 30×40 | 50 - 300 (circular) |
| Efficiency | Close to 100% | 20% | Typically 10% |
| Thermal stability | Good | Excellent | Poor (transmission) Good (reflection) |
| Diffraction limited | No | No | Yes |
| 1 mm apertures | Difficult | Not applicable | Possible |

***Table 6.2.4*** *Current performances of hard x-ray extreme focusing optics.*

### Mirrors

High resolution x-ray mirrors are usually built in KB geometry. Significant progress has been made in the past year, the best spot sizes are on the order of 50 nm for single surface mirrors **[6-17]** and multilayer mirrors **[6-18]**. Typical apertures are 100 µm, which is matched to the transverse coherence lengths of third generation insertion device beamlines. The performance is still limited by the figure errors of the mirror surfaces. So far, no diffraction-limited resolution has been achieved, but metrology and surface machining are continuously improving, so that this may be possible in the near future. Damage by the high thermal loads of the XFEL seems unlikely, as the power is distributed over a large footprint of a bulk substrate, but even slight thermal deformations would deteriorate the focusing capabilities. A scaling up of the present apertures to collect the whole coherent flux of the source will be very difficult, especially when high (or even diffraction-limited) resolution is required, as the length of the mirror substrates has to increase. In this respect, using multilayer mirrors is probably the more promising approach as it requires much shorter lengths due to the higher reflection angles.

### Refractive lenses

Refractive lenses are, in several respects, promising candidates for focusing hard x-rays at the XFEL. In comparison with mirrors they offer the advantage of a straight beam path. Additionally, the focus size is adjustable, because x-ray lenses are compound devices: single refractive lenses with long focal lengths can be arranged in a stack to form an effective lens with short focal length and therefore, a strong demagnification. A disadvantage of these systems is their chromaticity leading to different focal spots for different photon energies. The loss in coherence due to the passage through a large number of surfaces may also be an important consideration.

### A. Moderate focusing by refractive lenses

Moderate focusing to beam spots the same size as the source or collimation of the beam can be achieved for the well collimated XFEL radiation by using one or several stacked Beryllium lenses. Since the lenses are chromatic, one has to foresee several lenses or stacks of lenses for the different photon energies. A high resolution table with the corresponding translations and rotations will be installed in the photon beamlines.

### B. Extreme focusing by refractive lenses

The focal length of rotationally parabolic refractive lenses is currently limited to about 300 mm. This also limits the diffraction limited spot size of these optics, since it scales approximately with the square root of the focal length. Currently, small focal distances, i.e., f<10 mm, are realised by so-called nano-focusing lenses (NFLs) made of Silicon or Diamond (see Figure 6.2.7). For NFLs, focal spots as small as 15 nm are predicted **[6-19]**. Further reduction of the spot size using refractive optics requires the use of adiabatically focusing lenses that are predicted to focus about $10^8$ photons per pulse to about 5 nm **[6-22]**, resulting in a gain of $8\times10^6$. In view of their application at an XFEL beamline, the following issues have to be addressed for refractive lenses.

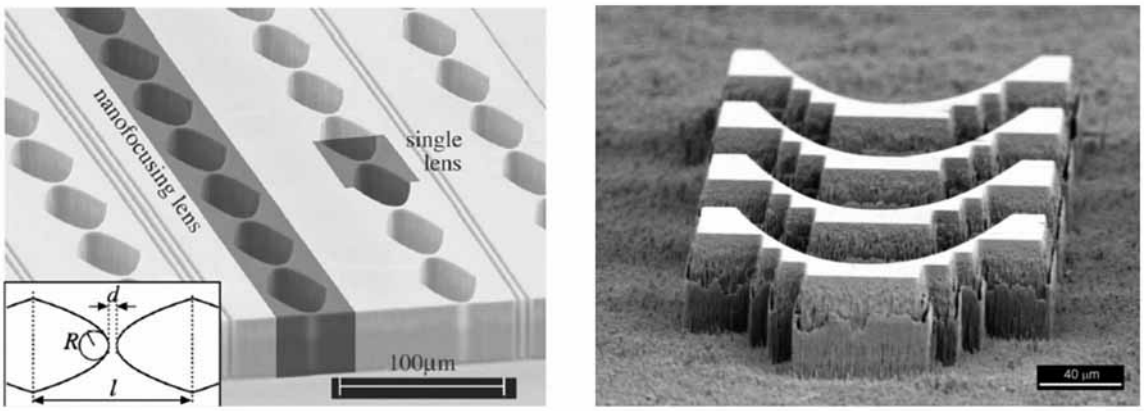


***Figure 6.2.7*** *Left: NFLs made by electron beam lithography and reactive ion etching of Silicon* **[6-19]***. Right: Diamond planar refractive lenses fabricated using a similar technique* **[6-23]***.*

*Expected optical performance*

To focus most of the monochromatic XFEL pulse to dimensions ~100 nm, rotationally parabolic refractive lenses made of Beryllium may be well suited. Table 6.2.5 summarises the expected focus properties for three different lens sets. Beryllium lenses are ideally suited for x-ray energies around E=12.4 keV (SASE 1), but can be operated down to about 5 keV (at SASE 2). For harder x-rays up to several 100 keV, refractive lenses made of different materials have been successfully used. This is of particular interest for focusing the spontaneous radiation from U 1 and U 2 **[6-24]**. For experiments requiring extremely small focal spot size, in general, the preservation of the wave front is of great importance. Experimental verifications of the wave front properties in the focus of a refractive lens are ongoing.

*Radiation damage*

Model calculations suggest that low-Z elements will be stable under irradiation with hard x-rays **[6-25]**. The maximal dose for Beryllium per pulse (assuming $10^{12}$ photons/pulse) at 12 keV gives ~$10^{-5}$ eV/atom, well below the estimated surface dose of 0.01 eV/atom for damage (see Section 6.1.2.1). For Carbon (e.g., Diamond), the maximum dose is four times higher than for Beryllium, but following the above considerations, Diamond is expected to be stable in the XFEL beam, too.

*Heat load*

The average power expected for the SASE 1 undulator at the XFEL is about 72 W at 12.4 keV. Assuming a lateral beam size of 800 µm (FWHM) at the experiment, more than half of the radiation is expected to fall onto the aperture of a Beryllium lens. At this energy, about 3.6% of the incident power is absorbed in the first lens, corresponding to 2.3 W. Overall, 59 W are dissipated in the third set of lenses described in Table 6.2.5. On average, this corresponds to about 0.3 W per lens. Refractive lenses have been used in some synchrotron installations for years under very demanding conditions, e.g. for white beam collimation, without observing damage **[6-26]**.

*Chromaticity*

Due to the quadratic dependence of the refractive index for hard x-rays on the x-ray wavelength, refractive lenses are strongly chromatic. Optimal performance can only be reached for monochromatic x-rays, i. e. $\Delta E/E<10^{-4}$. The natural width of the SASE radiation ($\Delta E/E\sim10^{-3}$) will be focused to an interval along the optical axis that is about one order of magnitude larger than the depth of focus, effectively broadening the focus to several 100 nm. If this is not acceptable for a given experiment, a reduction of the bandwidth using a crystal monochromator may be required.

| N | Unit | 100 | 150 | 200 |
|---|---|---|---|---|
| $D_{eff}$ | µm | 485 | 430 | 409 |
| f | mm | 480 | 345 | 289 |
| N A | | $5.1\times10^{-4}$ | $6.2\times10^{-4}$ | $7.1\times10^{-4}$ |
| Demagnification | | 1/2100 | 1/2900 | 1/3450 |
| $d_t$ | nm | 73 | 60 | 53 |
| Coherent spot size | $nm^2$ | 732 | 602 | 532 |
| Spontaneous spot size | $nm^2$ | 852 | 652 | 572 |
| $\sigma_p$ | % | 14.4 | 10.6 | 9.2 |
| Photons/pulse in focus | | $7.0\times10^{10}$ | $5.3\times10^{10}$ | $4.6\times10^{10}$ |
| Gain | | $1.7\times10^{7}$ | $2.0\times10^{7}$ | $2.3\times10^{7}$ |

***Table 6.2.5*** *Expected performance of Beryllium parabolic refractive x-ray lenses for focusing SASE 1 pulses at an energy of 12.4 keV. An undulator to experiment distance of 1000 m, a source size of 70×70 µm², a fluence of $10^{12}$ ph/pulse, and a beam size of 800 µm (FWHM) at the scientific instrument are assumed. For the Beryllium lenses, a radius of curvature of R = 200 µm, a geometric aperture $2R_0$ = 890 µm, and a minimum thickness d = 10 µm is chosen in accord with current technology. N is the number of single lenses, $D_{eff}$ the effective aperture, f the focal length, NA the numerical aperture, $d_t$ the diffraction limited spot size (FWHM), and $\sigma_p$ the effective lens cross-section* **[6-27]**.

### Diffractive optics

At present, the best resolution for x-ray focusing is obtained by using diffractive optics such as Fresnel or Multilayer-Laue Zone Plates (ZPs). Zone Plates have demonstrated a resolution beyond 30 nm **[6-28]**. The ultimate resolution of a ZP is in the order of the smallest, outermost zone width, meaning that nanolithography processes with sufficient resolution have to be applied. State-of-the-art electron-beam lithography and multilayer deposition tools are capable of placing the diffracting structures with lateral placement accuracies of a few nanometres, i.e. within a fraction of the outermost zone width. As a consequence, the wave front precision is controlled within a fraction of a wavelength, and diffraction-limited resolution is routinely achieved when sufficient transverse and longitudinal coherence is provided. Efficient focusing of hard x-rays by ZPs is more difficult because the zone structures must be sufficiently dense and thick to provide a phase-shift near $\pi$ for best diffraction efficiency. The zone structures are typically made from heavy metals, and they must be on the order of 1 μm thick for hard x-ray focusing. Due to the difficulty in fabricating such high aspect ratio (10:1 or higher) structures, ZPs fabricated by electron beam lithography have been limited to a resolution of about 100 nm in the hard x-ray region **[6-20]**. Recent improvements in fabrication technology will soon allow reaching 50 nm or better **[6-29]** with commercially available devices. Increasing the aperture of these devices towards 1 mm is already possible. It should also be mentioned that diffractive optical elements with more complex functionality such as twin spot zone plates **[6-30]** or computer-generated holograms **[6-31]** can also be made. This unique feature can have very interesting applications in the context of holography and other assisted phase retrieval experiments. Multilayer-Laue ZPs offer the opportunity to reach a resolution beyond 10 nm with efficiency greater 30% **[6-28]**. Only 1-D focusing has been demonstrated so far by these devices, however, fabricating them with large zone aspect ratios is not difficult, thus they can have significant efficiency for hard x-rays.

One drawback of lithographic ZPs is that they are usually fabricated on thin transmitting substrates such as Silicon Nitride membranes, typically 100 nm in thickness. While these membranes only interact weakly with the incident beam, they have poor thermal conductivity. In addition, the heavy materials used to fabricate the zones, while thermally very stable, absorb a significant proportion of the incident beam. Consequently, the lifetime of ZPs may turn as short as a single x-ray pulse.

The possibility of combining the robustness of reflective optics with the diffraction-limited focusing of diffractive optics could be provided by using either multilayer based or crystal based Bragg-Fresnel lenses. They consist of a zone plate pattern etched into a reflecting surface. Although these elements are not used much at present, they can be made with small outermost zone width and large apertures **[6-32]**. A disadvantage of Bragg-Fresnel lenses is that both the focus location and angle depend on the photon energy. Nonetheless, these devices may turn out to be an attractive alternative to presently considered solutions.

#### 6.2.2.5 *Transport of high harmonic radiation*

Several experiments require the use of higher harmonic radiation in pump-probe experiments using the fundamental radiation as the pump. According to Chapter 5, the intensities of third harmonic radiation are at the level of 1% of the fundamental line and fifth harmonic radiation is still at a level of 0.03% of the fundamental line intensity. In case of SASE 1, photon energies could be as high as 37 keV whereas for SASE 2, an energy range of 12 to 24 keV can easily be covered by the third harmonic. Even for SASE 3 it is possible to use the third harmonics of 3.1 keV in experiments combining soft and hard x-ray beams. The major difficulty to transport harmonic radiation to the experiments is the double-mirror system required to stop *Bremsstrahlung* and other background radiation. Due to the cut-off in photon energy at ~15 keV, these mirrors will not transport harmonic radiation in the standard configuration. By coating the mirrors with higher Z materials, one can shift the cut-off to higher photon energies, but the absorbed power is increased too. As an example, coating with Gold will shift the cut-off for 2 mrad grazing angle to >30 keV. At the same time, Gold has a very high reflectivity for photon energies up to ~12 keV at this grazing angle, thus, limiting the surface dose due to the fundamental FEL line to ~$3\times10^{-4}$ eV/atom ($\sigma_s$=$2.47\times10^{-20}$ cm$^2$/atom at 11.8 keV).

Complete separation of fundamental and harmonic radiation can be achieved using a monochromator tuned to reflect harmonic radiation, while at the same time transmitting the fundamental order. For example, the third harmonic of SASE 1 at 0.033 nm is transported by the Diamond (111)-reflection with a Bragg angle $\theta_{Bragg}$= 4.6°, a Darwin width of 4.6 µrad and a corresponding energy resolution of $\Delta E/E\sim6\times10^{-5}$. In comparison to the normal operation (reflection of the fundamental with $\Delta E/E\sim10^{-4}$), the heat load imposed on the crystal due to the full absorption of the fundamental is increased by only ~10%. Therefore, the discussion of heat load effects in Section 6.2.2.2 is also applicable for the transport of higher harmonic orders.

### 6.2.3 Other beam transport elements

In addition to the optical elements discussed in the previous section, the photon beam transport includes other elements required for control and diagnostics of the x-ray beam and for vacuum control purposes.

#### 6.2.3.1 *Safety shutter*

Safety shutters are required to enable access to the downstream beamline area. They will be installed in the SASE 1, SASE 2 and U 1 beamlines to enable access to the photon beamline section between the access shafts and the experimental hall while continuing electron beam operation. The main purpose of the safety shutter is to block the x-ray radiation, including remaining *Bremsstrahlung* radiation propagating down the beamline. Usage of the safety shutter requires to fully open the undulator gap, as these shutters cannot be designed to withstand the average and peak power load of undulator or SASE operation. A second shutter of this type will be implemented in front of the experiments hall to enable access to the downstream experimental areas. The design of the safety shutter will include rigid as well as movable absorber elements to block the *Bremsstrahlung* at 17.5 GeV.

### 6.2.3.2 Slit system

In front of the first two mirrors a slit system will be implemented. The slit system will limit the power load on the mirrors by reducing the transmitted beam size and therefore, significantly reducing the transmission of unwanted spontaneous undulator emission. In Figure 6.2.8 the design of the high-power slit system designed for the PETRA-III facility is shown **[6-33]**. This design fulfils the requirements for an XFEL beamline and could be implemented with minor modifications.

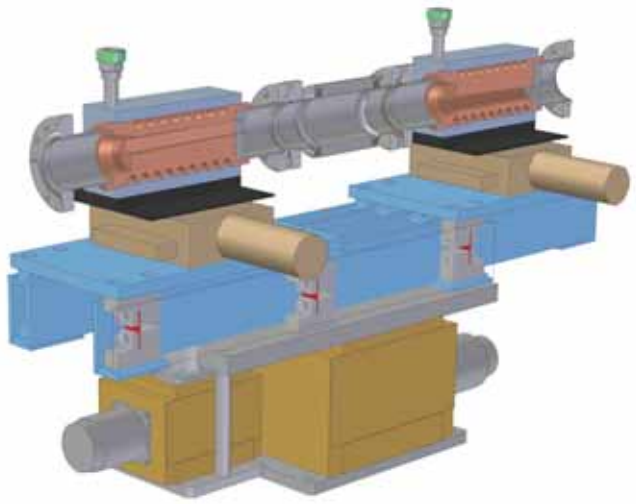

***Figure 6.2.8*** *High-power slit system designed for PETRA-III.*

### 6.2.3.3 Gas absorber system

At the FLASH facility, a gas absorber system based on single photon absorption in a gas, is in routine operation to attenuate the photon pulse intensity on user demand. Among other applications, the reduction of the photon intensity without changing the focusing geometry was found very useful in experiments investigating strong field phenomena. The absorber system consists mainly of a 15 m long gas-filled pipe, together with two differential pumping units (see Figure 6.2.9) to guarantee the ultra-high vacuum in the rest of the beamline. A similar set-up is foreseen to be implemented in all beamlines at the XFEL. In the hard x-ray regime the gas pipe needs to be elongated to 100 m and the maximum pressure will be in the mbar-range due to the reduced atomic cross-sections. As an instructive example, the transmission at 0.1 nm for four different pressures of Xenon is given in Figure 6.2.10(a.). It can be seen that in the range from 0.1-0.4 nm, an attenuation of $10^4$ is always feasible by adjusting the pressure. The same holds for the soft x-ray regime (0.4-6 nm), where an absorption length of 30 m is sufficient, see Figure 6.2.10(b.). To reduce the consumption of Xenon gas, a recirculation scheme is envisaged.

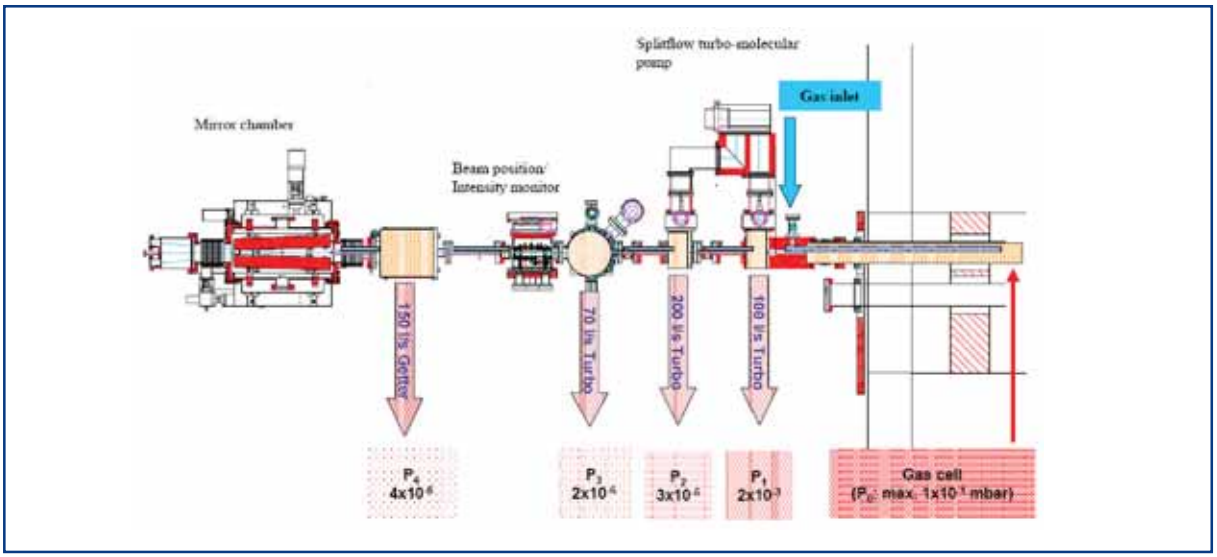


***Figure 6.2.9*** *Differential pumping unit used at FLASH for the transition from the gas-filled attenuator pipe to the ultra-high vacuum beam tube.*

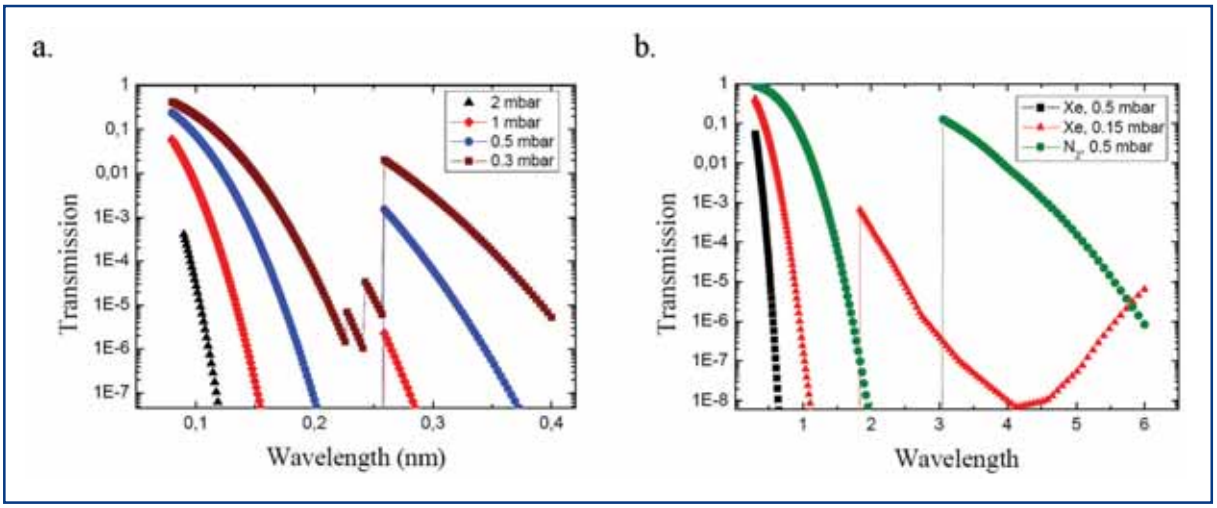


***Figure 6.2.10*** *Transmission of x-ray radiation through a gas-filled attenuator section. In (a.) results for the case of SASE 1 and SASE 2 and a 100 m long gas-absorber filled with Xenon gas at 4 pressures are shown. (b.) shows results for SASE 3 with a 30 m long attenuator at various pressures of Xenon and Nitrogen ($N_2$).*

### *6.2.3.4 Fast shutter for pulse selection*

During the first experiments at the FLASH facility, a significant fraction of users needed to irradiate samples with only one FEL photon pulse at the repetition rate of the bunch train or even below that. Examples are experiments where the sample is significantly modified during the photon-sample interaction, but no continuous renewal of the sample is available, e.g. in solid target experiments. At FLASH this demand is met by a single shot shutter, see Figure 6.2.11. The XFEL will provide a bunch distribution scheme that allows sending only the bunch pattern requested by an experiment into one of the electron beamlines. However, if operating more than one experiment at this electron beamline, a fast shutter is considered useful for the selection of x-ray pulse trains to be accepted by

a specific instrument. The operation of the user instruments, therefore, could significantly benefit from such a device. The XFEL version of such a fast shutter needs to operate at the pulse train repetition rate of 10 Hz with possibility for even faster repetition rates. Furthermore, the shutter will be designed to withstand full bunch trains.

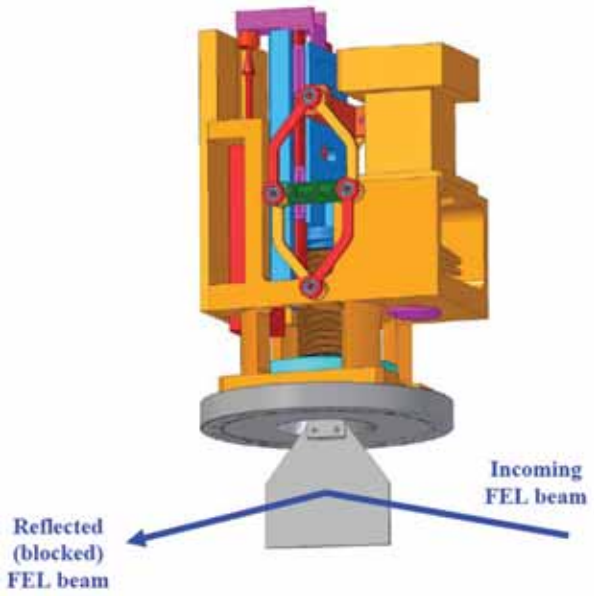


***Figure 6.2.11*** *Fast shutter at the FLASH facility.*

### *6.2.3.5 Beamline vacuum system*

An average pressure of $10^{-7}$ mbar is targeted. This pressure range is determined by the acceptable absorption of the photon beam and by the operation and lifetime of ion-pumps. Differential pumping for a windowless operation of the beamline is mandatory. A vacuum system free of dust particles is necessary to avoid destructive effects on the coherence at the surfaces of mirrors and monochromators. This means all cleaning and mounting of devices has to be done in a class 100 clean room environment. The design and assembly of the beamline instruments have to take this requirement into account. To avoid contamination of surfaces, a Hydrocarbon-free vacuum (partial pressures of Hydrocarbons < $10^{-3}$ of the total pressure) is needed.

The layout of the vacuum structure distinguishes between SASE beamlines, which are longer and carry beams with high peak powers, and beamlines for spontaneous radiation. Typically, five vacuum sections are proposed, separated by valves: The first valve close to the particle beam should be an all-metal valve, while for the others, Viton sealed valves are preferred. This is because of simplicity, the particle-free operation, and the possible short closing times of these devices. The pressure demand for mirror and monochromator chambers will be in the $10^{-9}$ mbar range to minimise contamination. A beam pipe diameter of 100 mm is chosen to reduce the number of pumps along the beamline. Ion pumps with nominal pumping speed of 75 l/s installed at a distance of 30 m will result in an average pressure of <$10^{-7}$ mbar. The pressure difference at mirror and monochromator chambers will result from the differential pumping.

The first valve in the beamline (linac valve) has no protection against synchrotron radiation. This means it can only be closed when the related undulator is not radiating, e.g. the magnetic gap of all undulator elements is open or no electron beam is accelerated. All other section valves and the beam shutter are protected by the photon shutter. The two differential pumping stages of the absorption cell need a special operation and safety system. The accidental venting of large beamline parts with a long pumping time to restore the vacuum has to be prevented.

## 6.2.4 Description of the beamlines

### *6.2.4.1 SASE 1 – X-ray FEL radiation*

This beamline is dedicated to the transport of hard x-ray radiation at photon energies near 12.4 keV. The undulator is not gap tuneable in that its length has been optimised for closed gap and photon energy of 12.4 keV at the nominal electron energy of 17.5 GeV. The SASE 1 beamline is most requested for ultrafast time-resolved diffraction experiments and for non-resonant x-ray photon correlation experiments, both operating at fixed photon energy. For diffraction on crystals, the XFEL bandwidth is too large and monochromatisation to $\Delta E/E \sim 10^{-4}$ will be required. The requirements are the same for correlation experiments, in this case to increase the longitudinal coherence length. Diffraction experiments on non-crystalline matter, single particles and bio-molecules can accept a much larger bandwidth. Therefore, these experiments do not require additional monochromatisation, and in addition, some of them, in particular those on single particles or molecules, will require the maximum achievable photon flux at the sample.

Therefore, two requirements exist and it is proposed to build the beamline with the capability to use either double-crystal or double-mirror optics, both in a fixed-exit geometry. Following these optical elements, a collimator with a 10 mm hole is required to stop *Bremsstrahlung* radiation. Moderate focusing with a demagnification near unity requires placing focusing elements near the first optical elements. Due to their high flexibility a stack of Beryllium lenses will be used here. A (compound) refractive lens has the advantage of being in-line and can be fast removed from or inserted into the beam. It can also be used for both bandwidth options, although the effect of focal length variation due to the chromaticity of the lens needs to be considered in the case of natural bandwidth ($\sim 10^{-3}$). For applications requiring the best possible preservation of wavefronts, e.g. in extreme focusing applications, no focusing will be used in the photon beam transport section and the lens is removed from the beam. In order to distribute the x-ray beam to spatially separated instruments inside the experimental hall, the photon transport is split into three lines. By means of two subsequent mirrors operating at a grazing angle of 2 mrad, a horizontal deflection angle of 8 mrad in relation to the direct beam is achieved. In this way, a horizontal separation of each of the three beams of 1.6 m at the entrance to the experimental hall can be achieved. Figure 6.2.12 shows a sketch of the photon beam transport system for the SASE 1 beamline. The figure shows the possibilitey of separating the XFEL beam to three beamlines by using mirrors to be inserted into the photon path. In Table 6.2.6 the main optical elements of the SASE 1 beamline are listed.

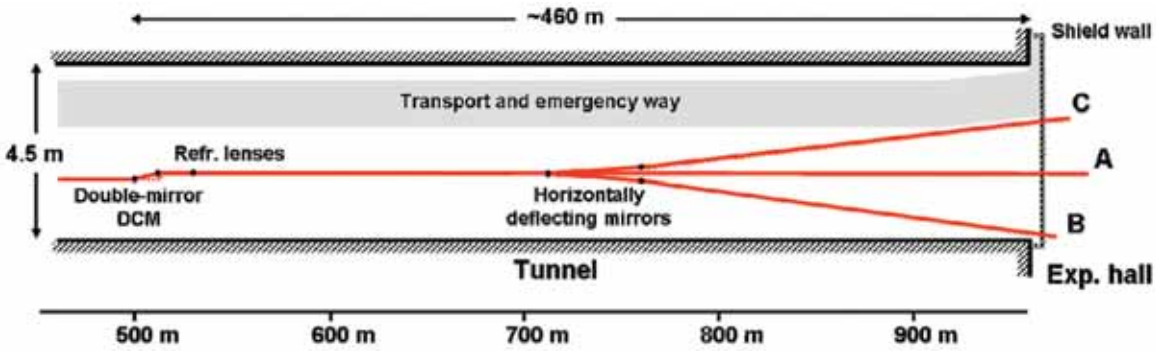


***Figure 6.2.12*** *Schematic layout of the SASE 1 beamline section from 500 m downstream to the end of the undulator at the experimental hall , including major optical elements.*

| Name/ Line | Device | Distance [m] | Task |
|---|---|---|---|
| A1 | Mirror | 500 | Plane mirror reflecting in horizontal geometry with a grazing angle of 2 mrad. Carbon coating reduces the surface dose for this mirror. Retraction is enabled for double-crystal monochromator operation. |
| A2 | Mirror | 512.5 | Second mirror for back-reflecting beam to parallel orientation at an offset of 50 mm from the incident beam. This mirror could be built as an adaptive optics to either compensate for heat load deformation of the mirror A1 or focus the beam horizontally. |
| A3 | DCM | 515 | Double-crystal monochromator to achieve the identical offset. Retraction is enabled for double-mirror operation. The monochromator allows operation at ~12 keV and for third harmonic radiation. |
| A | BS stop | 520 | Collimation against propagation of *Bremsstrahlung* radiation. |
| A4 | Refractive lenses | 530 | For moderate focusing at the instruments and demagnification near unity refractive lenses will be used. They can be removed for transport of unfocused beam. |
| B1, C1 | Mirrors | 735 | This is an assembly of two mirrors that can be placed alternatively in the FEL beam. They reflect, in horizontal geometry, the beam into two different directions for Lines B and C. Grazing angles are 2 mrad. In a third option, the beam passes without reflection for Line A. |
| B2, C2 | Mirrors | 785 | To increase the horizontal offset a second set of mirrors is used in the two side lines. Grazing angles are 2 mrad. The location is chosen to achieve a maximum offset of 1.6 m at the end of the tunnel for each of the side lines with respect to the central line. |
| A, B, C | | 960 | End of the tunnel and start of the experiments hall. |
| B | | 975 | Instrument for diffraction experiments using side beam B. |
| C | | 980 | Instrument for single particle diffraction at side beam C. |
| A | | 985 | Instrument for photon correlation experiments using central beam A. |

***Table 6.2.6*** *List of optical elements in the SASE 1 beamline. Components belong to the central line A or the side lines B and C. The longitudinal distances are given with respect to the end of the undulator.*

### 6.2.4.2 SASE 2 – Tunable X-ray FEL radiation

This beamline is dedicated to the transport of hard x-ray radiation in the photon energy range from 3 to 12 keV. The undulator is gap tunable in that its length has been optimised for a gap opening of 19 mm and photon energy of 12.4 keV at the nominal electron energy of 17.5 GeV. The SASE 2 beamline is requested for experiments carried out over a rather wide photon energy range. The interest is in specific absorption edges and resonances; one may also want to exploit the change of the absorption cross-section, e.g. in high energy density investigations. Tuning the photon energy in a small range is enabled by electron energy changing on short timescales. Monochromatisation to a bandwidth $\Delta E/E \sim 10^{-4}$ will be required in spectroscopy experiments. Also, coherent diffraction experiments, aimed at measuring large Q values, require monochromatisation of the XFEL beam in order to increase the longitudinal coherence length to the order of 1 µm. For coherent diffraction experiments the use of perfect crystals could provide the best solution to preserve the wave front properties of the XFEL beam as required for high resolution imaging (see Section 6.2.2). High energy density science experiments require the maximum achievable photon flux at the sample and usually do not need monochromatisation. Therefore, the situation resembles that of SASE 1 and a similar design of the first optics module including a double-mirror and a double-crystal monochromator is proposed. Following these optics, a collimator with a 10 mm hole is required to stop *Bremsstrahlung* radiation. To achieve moderate focusing with demagnification near unity focusing elements also need to be placed here. Refractive lenses are available for the upper part of the x-ray spectrum but will not work for photon energies <5 keV (see Section 6.2.2.4). For the photon energy range 3-5 keV, the second mirror of the double-mirror system will be replaced by a toroid. In order to distribute the x-ray beam to spatially separated instruments inside the experimental hall, the photon transport is split in to three lines. By means of two subsequent mirrors operating at a grazing angle of 2 mrad, a horizontal deflection angle of 8 mrad with respect to the direct beam is achieved for each of the side lines. In this way, a horizontal separation of the three beams by 1.6 m at the entrance to the experimental hall can be achieved. Figure 6.2.13 shows a sketch of the photon beam transport system for the SASE 2 beamline. The figure shows the possibility of distributing the XFEL beam to three beamlines by using mirrors to be inserted into the photon path. In Table 6.2.7 the main optical elements of the SASE 2 beamline are listed.

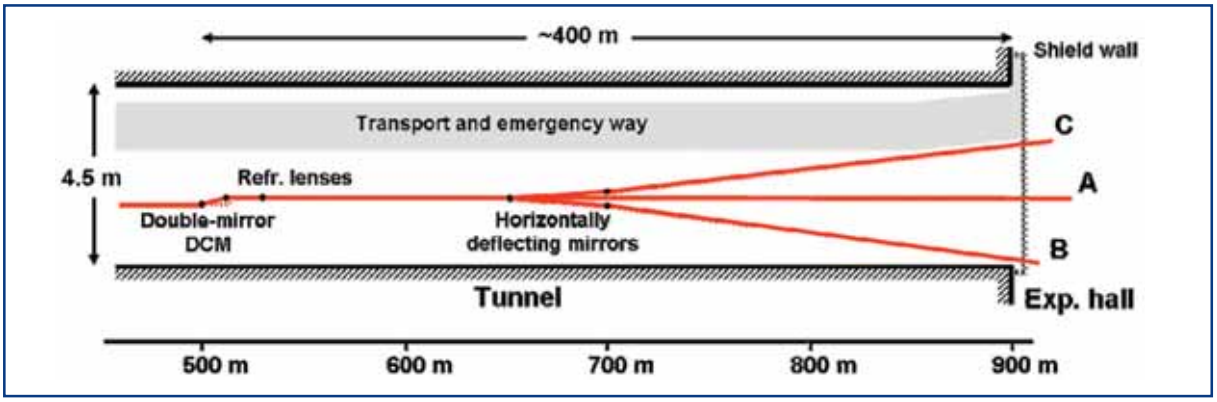


***Figure 6.2.13*** *Schematic layout of the SASE 2 beamline section from 500 m downstream to the end of the undulator at the experimental hall , including major optical elements.*

| Name/ Line | Device | Distance [m] | Task |
|---|---|---|---|
| A1 | Mirror | 500 | Plane mirror reflecting in horizontal geometry with a grazing angle of 2 mrad. Carbon coating reduces the surface dose for this mirror. Retraction is enabled for double-crystal monochromator operation. |
| A2 | Mirror | 512.5 | Second mirror for back-reflecting beam to parallel orientation at an offset of 50 mm from the incident beam. This mirror could be build as an adaptive optics to either compensate for heat load deformation of the first mirror A1 or focus the beam horizontally. In order to achieve focusing in both directions, a second, exchangeable mirror with toroidal shape is available. |
| A3 | DCM | 515 | Double-crystal monochromator to achieve the identical offset. Retraction is enabled for double-mirror operation. The monochromator allows reflection at photon energies of 6-12 keV. |
| A | BS stop | 520 | Collimation against propagation of *Bremsstrahlung* radiation. |
| A4 | Refractive lenses | 530 | For moderate focusing at the instruments and demagnification near unity refractive lenses will be used. Removable for transport of unfocused beam. |
| B1, C1 | Mirrors | 675 | This is an assembly of two mirrors that can be placed alternatively in the FEL beam. They reflect, in horizontal geometry, the beam into two different directions for Lines A and C. Grazing angles are 2 mrad. In a third option, the beam passes without reflection for Line B. |
| B2, C2 | Mirrors | 725 | To increase the horizontal offset a second set of mirrors is used in the two side lines. Grazing angles are 2 mrad. The location is chosen to achieve a maximum offset of 1.6 m at the end of the tunnel for each of the side lines with respect to the central line. |
| A, B, C | | 900 | End of the tunnel and start of the experimental hall. |
| B | | 920 | Instrument for high energy density experiments using side beam B. |
| C | | 915 | Instrument for x-ray absorption using side beam C. |
| A | | 930 | Instrument for coherent x-ray imaging experiments using central beam A. |

***Table 6.2.7*** *List of optical elements in the SASE 2 beamline. Components belong to the central line A or the side lines B and C. The longitudinal distances are given with respect to the end of the undulator.*

### *6.2.4.3 SASE 3 – Tunable Soft X-ray FEL radiation*

This beamline is dedicated to the transport of soft x-ray radiation in the photon energy range from 250 up to 3,100 eV. The extended tunability of this beamline is enabled by a combination of gap and energy tuning. For the nominal electron energy of 17.5 GeV, gap tuning provides access to a photon energy range of 775 to 3,100 eV. For a reduced electron energy of 10 GeV, the photon energy range of 250 to 1,000 eV is provided.

Several of the scientific experiments proposed for this photon energy range have requested a monochromatisation better than the linewidth of the FEL radiation. A resolution of the order $\Delta E/E \sim 10^{-4}$ over the entire photon energy range fulfils most of the experiment requirements. To cope with the high power levels of the FEL radiation, all elements of the monochromator need to operate in very grazing geometry. The whole system, therefore, becomes rather long and can neither simply be integrated into the experimental station nor switched in and out of the beam. In Section 6.2.2.3 a plane grating monochromator designed for the specific radiation properties of the SASE 3 beamlines is presented. Its optical layout has been shown in Figure 6.2.6.

It is, therefore, proposed that the photon beam transport of the SASE 3 beamline includes two lines. Line A uses only mirrors to preserve the high photon flux. Some of these mirrors are curved to fulfil the requirements of the experiments with respect to focal spot sizes at the instruments. Line B includes a PGM, plane-grating monochromator using two or more gratings to cover the entire photon energy range. Figure 6.2.14 shows a sketch of the photon beam transport system for the SASE 3 beamline. The figure shows the possibility of distributing the two beams to two beamlines each by using mirrors to be inserted into the photon path. For the case of SASE 3, it is assumed that grazing angles of 10 mrad can be used. In Table 6.2.8 the main optical elements of the SASE 3 beamline are listed.

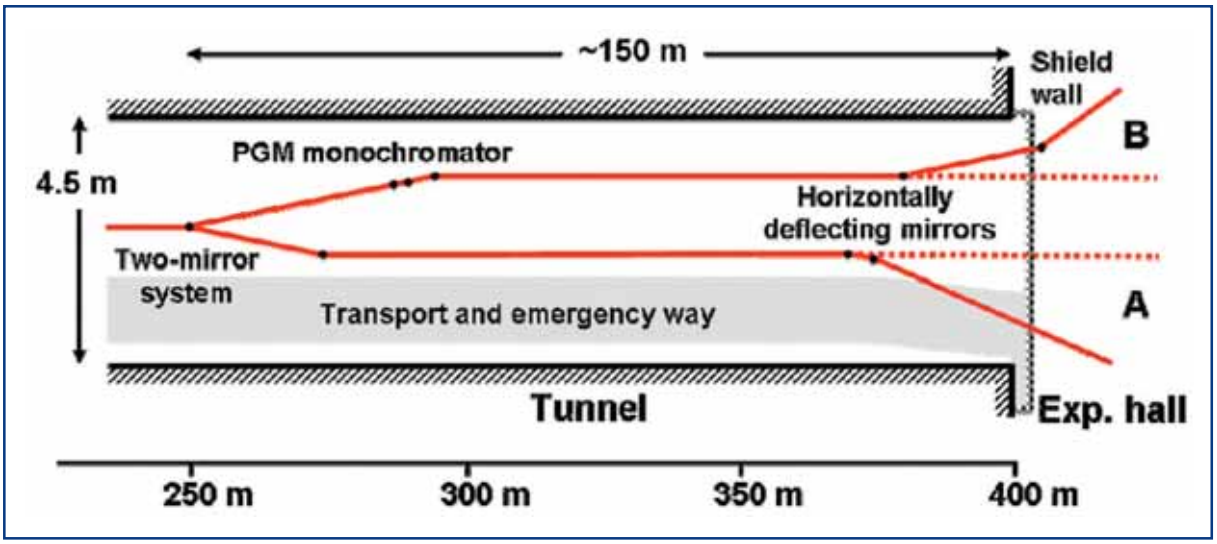


***Figure 6.2.14*** *Schematic layout of the SASE 3 beamline including major optical elements. The longitudinal scale has been increased by a factor of two compared to Figures 6.2.12 and 6.2.13.*

| Name/ Line | Device | Distance [m] | Task |
|---|---|---|---|
| A1, B1 | Mirror | 250 | Assembly of two mirrors to be placed alternatively in the FEL beam. They reflect the beam in horizontal geometry into the Lines A and B. Different mirrors will be used for this task:<br>A1. plane mirror reflects towards the second mirror.<br>B1. cylindrical mirror in order to adapt vertical divergence to the monochromator needs. |
| A2 | Mirror | 275 | Back-reflecting beam to parallel orientation. This mirror would possibly be built as an adaptive optics to both, compensate heat load deformation of the mirror A1 or to focus the beam horizontally. In order to achieve focusing in both directions, this mirror needs to have toroidal shape. |
| A, B | BS stop | 280 | Collimation against propagation of *Bremsstrahlung* radiation. |
| B2 | Mirror | 290 | A vertically reflecting plane mirror in front of the grating allows for a variable deflection angle so that the angles of incidence and diffraction at the grating can be set independently. |
| B | Grating | 290 | At least two gratings are required for the photon energy range 500-3100 eV. The grating operates in vertical reflection geometry. |
| B3 | Mirror | 295 | Horizontally reflecting, toroidal mirror to focus virtual image onto exit slit. |
| B | Exit slit | 345 | Exit slit of the monochromator. |
| A3 | Mirror | 370 | Distribution mirror that can be removed from the beam. Using a grazing angle of 10 mrad this mirror could achieve a displacement of the beam of 1,000 mm in the experimental hall. |
| A4 | Mirror | 375 | This second mirror would generate an offset of 1,900 mm. Using focusing one aims for a demagnification near 1. |
| B4 | Mirror | 380 | Toroidal mirror to refocus the exit slit at the sample position in a 1:1 geometry. |
| B5 | Mirror | 405 | Flat mirror to achieve horizontal offset from straight beam. If placing here the toroidal mirror refocusing the exit slit increases the demagnification of ~6. In this case a flat mirror needs to be placed as mirror B4 in this line. |
| A, B | | 400 | End of the tunnel and start of the experimental hall. |
| B | | 410, 425 | Instruments for experiments using high spectral resolution. |
| A | | 420, 435 | Instruments for experiments using high flux. |

***Table 6.2.8*** *List of optical elements in the SASE 3 beamline. Components belong to line A, containing only mirrors, or to the monochromator line B. The longitudinal distances are given with respect to the end of the undulator.*

### *6.2.4.4 U 1 – Tunable and high energy x-ray synchrotron radiation*

This beamline is very similar to U2, described next, with due consideration of the different distance to the experiment hall.

### 6.2.4.5 *U 2 – Tunable and high energy x-ray synchrotron radiation*

This beamline is dedicated to the transport of spontaneously emitted synchrotron radiation. The undulator can be tuned in the fundamental from ~20 up to 90 keV. Compared to the XFEL radiation, the intensity is reduced by ~$10^3$ in number of photons per pulse. This will ease all power considerations for x-ray optics, so that they need no further discussion. However, due to the small source size and the large distances, the spontaneous radiation is highly coherent. The coherent flux and the ultra-short duration of 200 fs need to be preserved by the beamline optics. Since the spontaneous radiation also has a larger angular opening than FEL radiation, the angular acceptance of the beamline, or the collimation of the x-ray beam, determines the intensity of the x-ray pulses. In Section 5.3 the intensity and spectral properties of spontaneous radiation are given for an angular aperture of 9×9 μrad$^2$. The scientific instruments to be located at this beamline will, in particular, make use of the high coherent flux at high photon energies and of the ultra-short pulse duration in combination with an increased bandwidth of $\Delta E/E \sim 10^{-2}$. Finally, for the x-ray optics R&D programme, this beamline will provide the highly brilliant radiation required to investigate particular aspects of optical elements, e.g. figure and roughness performance or temporal response of crystal monochromators.

These experimental requirements can be divided in to two groups: The first group needs perfect crystal optics to transport the coherent radiation to the corresponding instrument. The limitation in bandwidth will not be a disadvantage for these experiments, since the monochromatisation improves the longitudinal coherence. The second group are experiments requiring large bandwidth for diffraction and will require mirror optics to collect maximum flux and maintain the large bandwidth. For the relatively high photon energies, the grazing angles of mirrors, even if coated with high Z materials, are very small. For the reduced intensity at this beamline also multilayers optics is of interest, providing larger deflection angles. Similarly to the FEL beamlines, a *Bremsstrahlung* beam stop is required, and an arrangement similar to the one proposed for SASE 1 and SASE 2 is adopted. Using a double-mirror double-crystal arrangement in fixed-exit geometry allows placing a collimator for *Bremsstrahlung* radiation. Separation of the two lines for the two scientific instruments is achieved by a multilayer crystal followed by a refractive lens. The diffraction instrument is expected to operate at a fixed photon energy between 15 and 25 keV. The deflection angle and specific multilayer parameters, therefore, can be determined according to technical feasibility. Figure 6.2.15 shows a sketch of the photon beam transport system for the U2 beamline. For the case of U2 it is assumed that grazing angles of 2 mrad can be used. In Table 6.2.9 the main optical elements of the U2 beamline are listed.

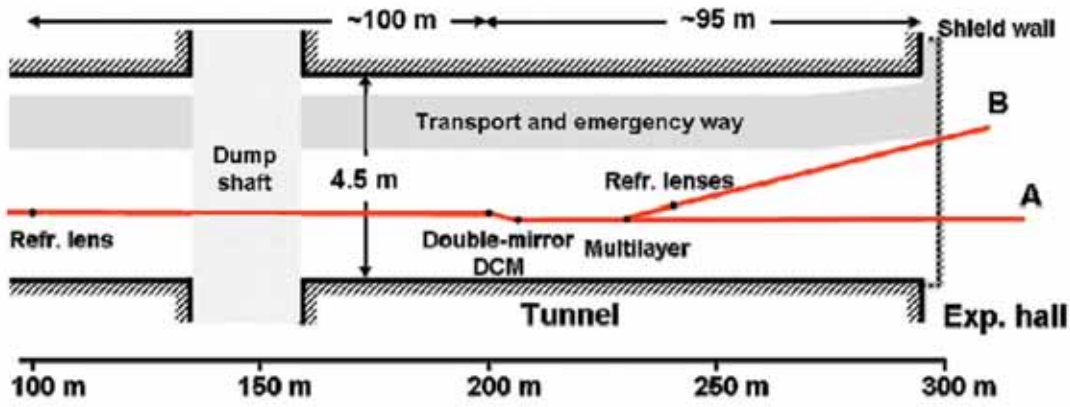


***Figure 6.2.15*** *Schematic layout of the U2 beamline including major optical elements. The location of the refractive lens for beam collimation is also shown.*

| Name/ Line | Device | Distance [m] | Task |
|---|---|---|---|
| A1 | Refractive lens | 100 | Collimation of the radiation cone to maintain high flux and large bandwidth. Retractable for transport of unfocused beam. |
| A1 | Mirror | 200 | Plane mirror reflecting in horizontal geometry with a grazing angle of 2 mrad. High Z materials are required to achieve high reflectivity. Retraction is enabled for double-crystal monochromator operation. |
| A2 | Mirror | 212.5 | Second mirror for back-reflecting beam to parallel orientation at an offset of 50 mm from the incident beam. This mirror could be built as an adaptive optics to either compensate heat load deformation of the first mirror A1 or focus the beam horizontally. |
| A3 | DCM | 215 | Double-crystal monochromator to achieve the identical offset. Retraction is enabled for double-mirror operation. The monochromator allows reflection at photon energies of 15-100 keV using several crystals/reflections. |
| A | BS stop | 220 | Collimation against propagation of *Bremsstrahlung* radiation. |
| B1 | Multilayer | 230 | Deflection of the beam towards Line B for diffraction studies. Retractable for straight transport in Line A. |
| B2 | Refractive lenses | 240 | Moderate focusing at the instrument in a 4:1 focusing geometry. Removable for transport of unfocused beam. |
| A,B | | 295 | End of the tunnel and start of experimental hall. |
| A | | 305 | Instrument for x-ray optics development using central beam A. |
| A | | 315 | Instrument for coherent x-ray imaging experiments using central beam A. |
| B | | 310 | Instrument for large bandwidth diffraction using side beam B. |

***Table 6.2.9*** *List of optical elements in the U2 beamline. Components belong to the central line A or the side line B. The longitudinal distances are relative to the end of the undulator.*

## 6.3 Photon beam diagnostics

Besides the photon-beam-based alignment of the undulators described in Section 5.5, photon beam diagnostics will be an essential tool for the commissioning and operation of the XFEL photon beamlines. Since photon diagnostics has successfully been used in the VUV wavelength range at the TESLA Test Facility (TTF) **[6-34]** and at FLASH **[6-35, 6-36]**, to a large extent the same concepts will be adapted for the x-ray regime. Ideal photon diagnostics techniques for the XFEL cover the full dynamic range of about seven orders of magnitude from spontaneous emission to SASE XFEL radiation in saturation, are suitable for single-pulse measurements (response time < minimum bunch spacing = 200ns), exhibit low degradation under radiation exposure in the x-ray regime, and must be ultra-high vacuum compatible. In the following sections two basic types of photon diagnostics will be described:

- diagnostics for the general characterisation and optimisation of SASE XFEL process and photon beam transport up to the scientific instruments;
- online (that is pulse-by-pulse) monitoring of crucial beam parameters like pulse intensity and pointing stability for user experiments and machine feedback.

### 6.3.1 Characterisation of beam properties

This section describes invasive diagnostics devices which cannot be used for online monitoring, but yield important information for the commissioning of the machine and photon beamlines. These devices will be located either in the primary photon beam diagnostic section (see Section 6.2.1) or will be integrated in the scientific instruments inside the experimental hall.

#### *6.3.1.1 Intensity*

Different kind of detectors such as gas-monitor-detector (see Section 6.3.2), micro-channel-plate (MCP)-based detector **[6-37]**, pin diode and calorimeter will be used to measure the intensity from spontaneous undulator emission when trying to achieve SASE gain or optimising saturation. Since the latter two detectors work within a limited dynamic range and not in parallel with user experiments, they will only be used for cross-calibration and during commissioning of the XFEL sources. MCP-based detectors cover a dynamical range of seven orders of magnitude and are in routine operation at the FLASH facility for optimisation of the FEL radiation. Figure 6.3.1 shows a schematic drawing of the device. The detector uses a thin Gold wire (50 µm diameter) or alternatively a Gold mesh with 65% transmission to reflect part of the FEL beam onto a calibrated MCP. Keeping the MCP in the low gain regime, one can determine the SASE gain with respect to spontaneous emission knowing the applied MCP voltage. By using an optimised geometry with small reflection angles and materials with higher reflectivity in the x-ray regime, one will be able to extend the capabilities of the MCP-based detector from the VUV wavelength range to x-rays. However, since the mesh or wire produces unwanted diffraction resulting in an inhomogeneous intensity distribution at the sample position, this device is not suitable for online monitoring of the intensity while operating user experiments.

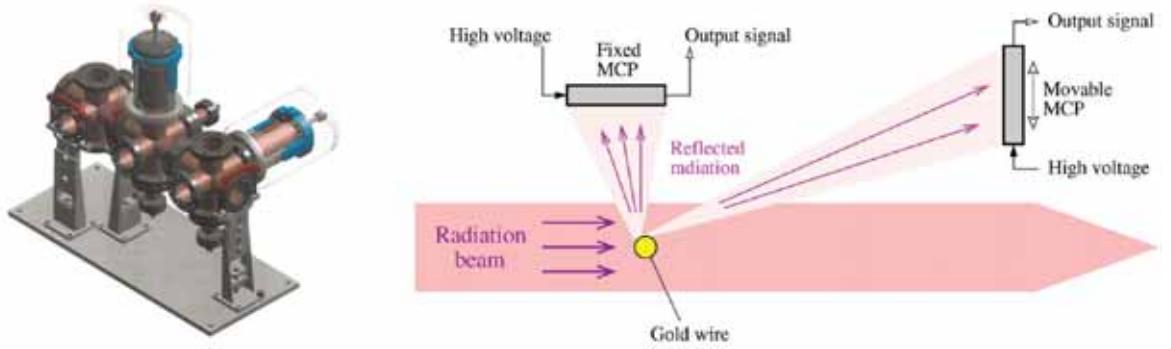


***Figure 6.3.1*** *Scheme of the MCP-based detector which is routinely operating at FLASH.*

### *6.3.1.3 Spectral characterisation*

Spectral characterisation of the photon beam provides essential information for the optimisation of the SASE process and user experiments. Spectral beam properties can be used to cross-check the mean electron energy and determine the bandwidth of the FEL beam as well as the content of higher harmonics. Furthermore, the spectral distribution yields the number of modes in the pulse and can be used to estimate the pulse length **[6-38]**. Two techniques to determine the spectral distribution are proposed; an analyser based on a bent crystal scheme **[6-11]** will be able to disperse the collimated FEL beam and project the spectral distribution onto a linear array detector. This scheme has to be adapted to the bandwidth and towards single-shot use. Since this detection scheme is not transparent, we additionally propose a new non-invasive method based on photoelectron spectroscopy **[6-39]**.

### *6.3.1.4 Wave front measurement*

The quality of the wave front of the coherent XFEL beam has a direct impact on the performance of several kinds of experiments. For example, a distorted wave front will lead to a loss in resolution for phase contrast imaging experiments or a degradation of the focusing and thereby, a loss in the available intensity for high field experiments. As discussed in Section 6.2.2, the requirements on slope error of optical elements for XFEL radiation are very demanding. The shape and slope error budgets of the reflecting elements surfaces required to preserve the wave front over a size of several millimetres are beyond what can be bought today. In fact, the metrology tools available are one of the most severe limitations in the mirror fabrication process. Moreover, even a perfect mirror or monochromator surface may be distorted in the beam either by thermal load or by the mounting itself. This is why it is necessary to develop techniques to measure the distortions of x-ray wave fronts in-situ. A precise knowledge of the wave fronts could then be a basis for learning about the properties of the source itself, to test and improve the optical components, and may even serve to compensate for errors in the illuminating x-ray wave.

A prototype Shack-Hartmann wave front sensor has already been successfully used to characterise the beam wave front and the focusing of beamline BL2 at FLASH **[6-40]**. Another approach to perform in-situ metrology in the hard x-ray regime has been developed at the Paul Scherrer Institute in Switzerland. The x-ray interferometer consists of a phase grating as a beam splitter and an absorption grating as a transmission mask for the detector. The device is able to measure wave front shape gradients corresponding to radii of curvature as large as several dozens of metres, with a lateral resolution of a few microns. This allows detection of wave front distortions of approximately $10^{-12}$ m or $\lambda/100$. The device was used with 12.4 keV x-rays to measure the slope error and height profile of multilayer mirrors **[6-41]** and Beryllium refractive lenses **[6-42]**. A similar setup could be used at the XFEL to investigate the quality of beamline optics under the extreme conditions of this machine.

#### *6.3.1.4 Focus characterisation*

A key point for the understanding and theoretical description of non-linear processes in the focused high intensity FEL beam is their dependence on irradiance. Therefore, among other quantities like pulse energy and duration, the determination of the spot size becomes essential. Conventional methods like knife-edge **[6-43]** and fluorescent screen technique **[6-44 – 6-47]** are limited to spatial resolution in the order of 1 to 2 µm and furthermore, will not withstand the irradiance level of the focused XFEL beam. Therefore, for the focus characterisation of the different XFEL beamlines, we intend to employ two techniques: The first based on wave front measurements (see above) and the second a novel method using atomic photoionisation **[6-48]**. Both methods have been successfully applied to determine the spot size of the microfocus beamline BL2 at FLASH. The latter one is based on a saturation effect upon photoionisation of rare gases and manifests itself by a sub-linear increase of the ion yield with increasing photon number per pulse (Figure 6.3.2). The effect is due to a considerable reduction of target atoms within the interaction zone by ionisation with single photon pulse and becomes stronger with decreasing beam cross-section. Since the cross-sections in the 10 keV range are many orders of magnitude lower compared to the VUV, this method will be of particular interest for spot sizes of 1 µm and below.

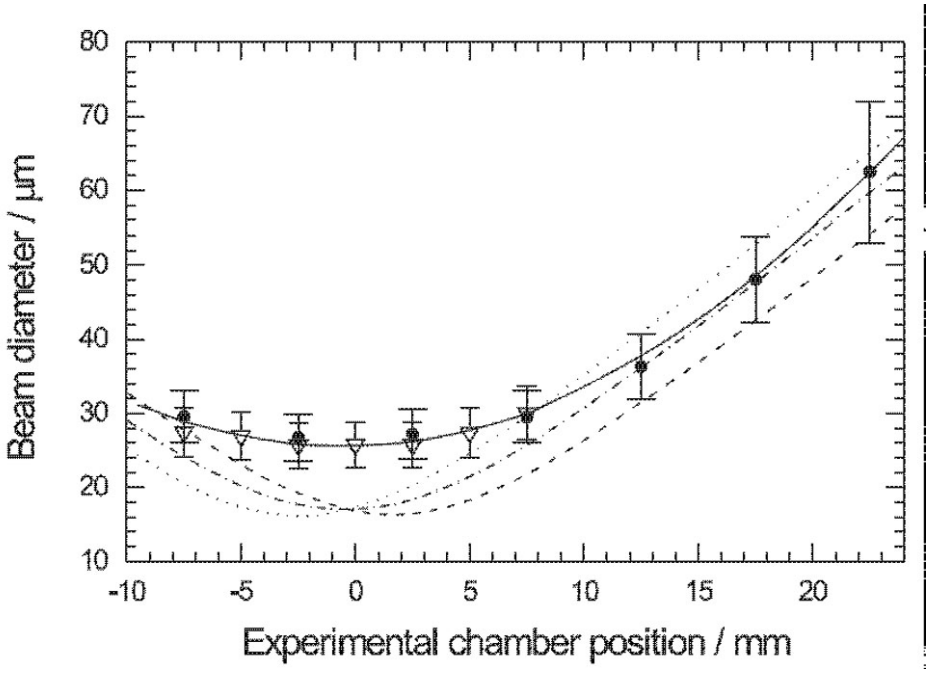


***Figure 6.3.2*** *Photon beam diameter measured at different positions around the focus position of BL2 at FLASH using a novel technique based on atomic photoionisation (taken from* **[6-48]***). The solid line represents a polynomial fit curve. The broken lines display ray-tracing simulations for horizontal (dashed line) and vertical direction (dotted line) and the mean of both (dashed-dotted line).*

## 6.3.2 Online diagnostics

Most user experiments need online information about important beam parameters, such as intensity and timing. This requires the use of diagnostic tools which operate in parallel and in a non-destructive way. Furthermore, due to the SASE-specific shot-to-shot fluctuations, it is mandatory to use pulse-resolved diagnostics. Since all detection schemes described in the following sections are based on the ionisation of gas, they will be placed in the differential pumping units in the gas attenuator section (see Section 6.2.3.3) to allow windowless operation at the required pressure level.

### *6.3.2.1 Online intensity monitors*

Nearly all experiments require a determination of the photon flux, respectively the energy content in the radiation pulse. Thus, online monitoring of the pulse energy is mandatory for free-electron lasers. At FLASH a gas-monitor-detector (GMD) is in routine operation, measuring the photon flux of the highly intense and strongly-pulsed VUV radiation in absolute terms **[6-49, 6-50]** . The detector is based on the atomic photoionisation of a rare gas or Nitrogen at low particle density in the range of $10^{11}$ $cm^{-3}$ which is about five orders lower than for classical ionisation chambers. The advantages are obvious: the detector is indestructible and almost transparent. Thus, the GMD can be used as a permanently operating device. Figure 6.3.3 shows visualisation of the pulse energy measurement over a sequence of pulses performed at FLASH at a wavelength of 32 nm.

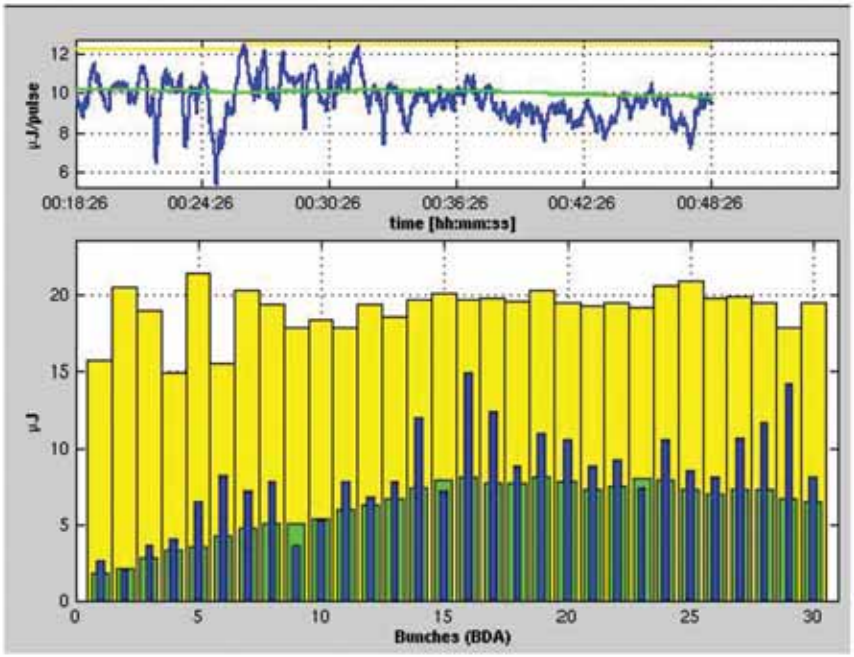


***Figure 6.3.3*** *Diagnostic panel in the control system of FLASH showing the yield of the gas-monitor detector. Top: Averaged ion signal. Bottom: Pulse-resolved electron signal for 30 FEL pulses at 1MHz repetition rate within one pulse train.*

Since the low photoionisation cross-sections in the x-ray regime are challenging for such a detector scheme, a prototype system for femtosecond x-ray pulses has been developed in close cooperation between DESY and the Physikalisch-Technische Bundesanstalt (PTB) in Berlin. After design and construction, the prototype has been successfully characterised and calibrated in the PTB laboratory at the electron storage ring BESSY II in Berlin **[6-51]**. In collaboration with the LCLS, first tests measurements **[6-52]** with femtosecond x-ray pulses at a photon energy of 9.4 keV have been performed at the Sub-Picosecond Pulse Source (SPPS) in Stanford.

A scheme of the XGMD and the responsivity as a function of photon energy is shown in Figure 6.3.4. Photoions are extracted by an electric field and, in contrast to former GMDs, detected by an amplifying open electron multiplier with a sensitive area of 2×2 $cm^2$ and a maximum gain in the order of $10^6$. The system is optimised and tested for absolute ion collection/detection efficiency and linearity for up to $10^6$ ions per pulse. For reliable operation of the multiplier, the target gas pressure measured by use of a calibrated spinning rotor vacuum gauge has to be below $10^{-1}$ Pa. Xenon is chosen as the target gas due to its comparably high photoionisation cross-section in the x-ray regime **[6-6]**. By applying an additional electric field distribution along the photon beam by means of an aperture system, the effective length of interaction volume can be extended to about 20 cm. The aim of the design is to detect 10 to 100 ions per pulse amplified to a pulse charge of about 10 pC and will allow for pulse-resolved measurements for x-ray pulses exceeding $10^7$ photons.

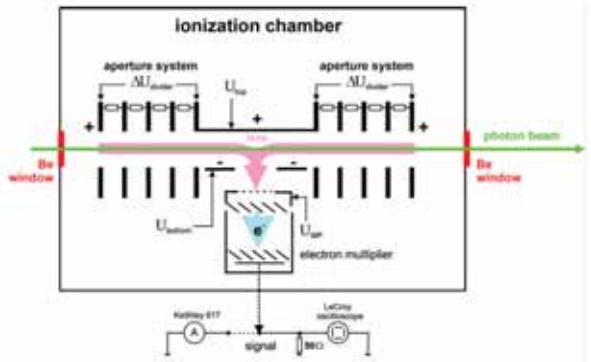


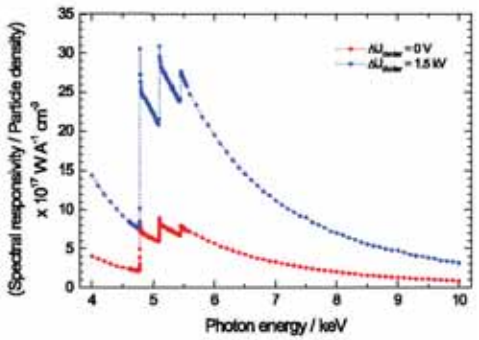


***Figure 6.3.4*** *Left: Schematics of the XGMD. Details are given in* **[6-52]***. Right: Spectral responsivity of the XGMD normalised to the xenon particle density with (blue) and without (red) additional ion collection along the photon beam.*

The X-GMD based on the photoionisation of Xenon atoms is a reliable tool for the quantitative detection of femtosecond x-ray pulses with more than $10^7$ (and up to $10^{15}$) photons per pulse. Its time resolution (well below 100 ns) is dominated by the ion time-of-flight distribution of differently charged ionic fragments. The measurement uncertainties in absolute terms might be improved from currently 15% to 5%. Pulse-to-pulse instabilities are expected to be dominated by photoion signal statistics and are less than 1% for pulses of more than $10^{10}$ photons.

### *6.3.2.2 Time domain properties*

An important target in the characterisation of the FEL radiation properties is the direct measurement of the x-ray pulse duration. Based on theoretical considerations the pulse length can be estimated by measuring the spectral distribution and the statistics of the pulse energies **[6-38]**. However, definitive measurements of the pulse length in the time domain are needed to prove the theoretical concepts. The proposed measurement methods are based on cross-correlation between optical laser and FEL pulses. To avoid systematic errors due to the jitter between laser and FEL, correlation experiments have to be designed in a way to deliver the pulse duration within a single shot. Experiments performed at SPPS have shown single-shot cross-correlation measurements using ultra-fast non-thermal melting of crystalline surfaces allow measuring pulse durations of the order 100 fs and relative timing of the two pulses **[6-54]**. Since the set-up is not transparent and distorts the x-ray pulse, it can not be used as an online diagnostic.

Two other single-shot laser/x-ray cross-correlation methods are currently being investigated to provide the same information without destroying the beam. Experimental validation in the x-ray regime is still missing. The first one uses the spectral broadening of photo-electrons, ionised by x-rays in the field of a strong laser of 800 nm wavelength **[6-55]**. The use of the extremely rapid photo-effect guarantees a temporal resolution of better than 1 fs. By realising different delays at different locations, temporal information is projected onto a spatial coordinate; thus, with an imaging electron spectrometer an arbitrary delay can be measured on a shot-to-shot basis. By evaluating the signal width on the detector the pulse duration can be determined as well. An instrument of this type

has been installed at FLASH and has demonstrated the feasibility of the concept. An extension to the higher photon energies of the XFEL is straightforward because the correlation mechanism does not depend on specific atomic resonances but works with any photon energy exceeding the ionisation energy of an atomic shell. As the spectral broadening scales with the electron momentum, the cross-correlation becomes more efficient at higher photon energies. Figure 6.3.5 shows that the width of the spectral broadening is distinctively larger compared to the line width of the FEL and thus, easily detectable. Consequently, a laser intensity of $10^{12}$ W/cm$^2$, as currently used at FLASH, will suffice for the temporal characterisation of the XFEL pulses.

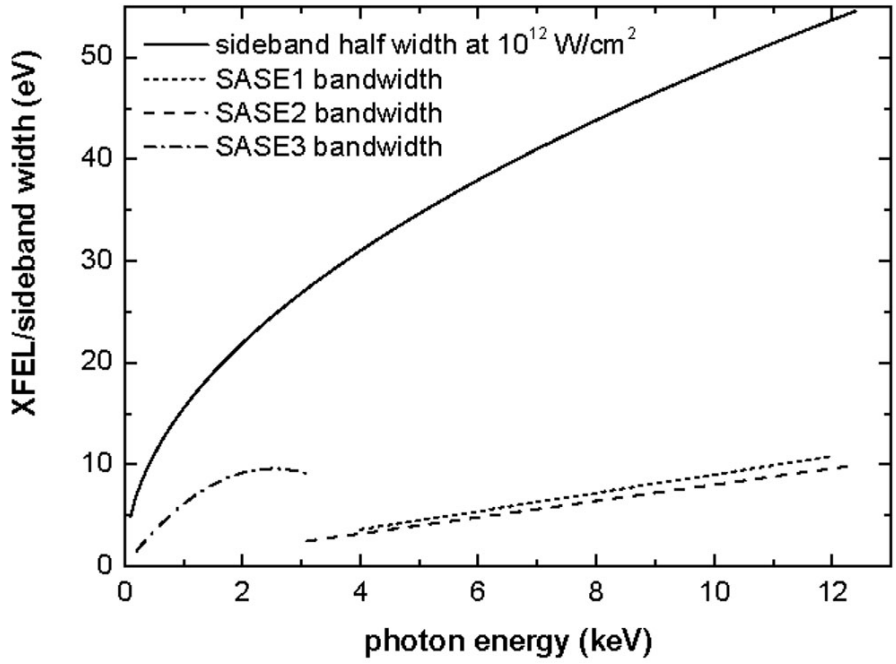


***Figure 6.3.5*** *Calculated spectral sideband half-width at $10^{12}$ W/cm$^2$ laser intensity in comparison with expected bandwidths of various XFEL branches.*

The second method measures an Auger line by detecting the Auger electrons by a time-of-flight (TOF) detector. An additional dressing field provided by a laser pulse will lead to the generation of sideband features due to *free-free transitions* (stimulated inverse *Bremsstrahlung*). The (first) sideband will be separated from the main Auger line by $E_L=h\omega=1.6$ eV at a laser central wavelength of $\lambda=780$ nm (Ti:Sa). The use of an Auger line is ideal as the features of the line are independent from the spectral properties of the exciting x-ray pulse, whereas a photoelectron line would mimic the broad spectrum of the x-ray pulse. The $KL_{23}L_3$ line in Argon, for example, has a width of ~1 eV at around ~800 eV. The temporal distribution of the Auger electrons carries the information about the duration of the x-ray pulse convoluted with the Auger decay time (which is known from literature to be around 1 fs so that it is significantly shorter than the x-ray pulse duration).

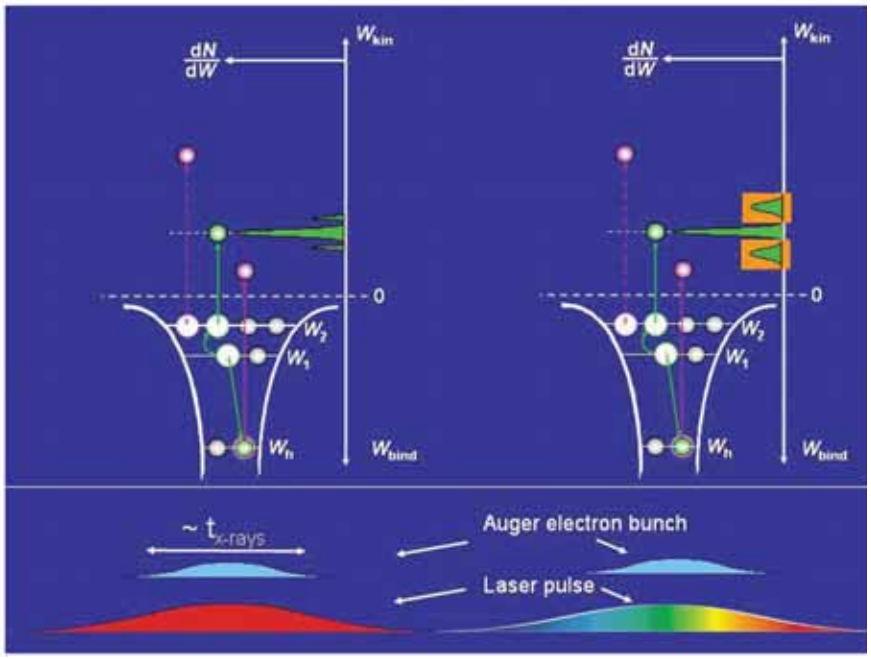


***Figure 6.3.6*** *Schematics of producing sidebands of Auger electron lines produced by the dressing field of a laser pulse with and without chirp, respectively.*

The idea is that the laser pulse providing the dressing field carries a significant linear chirp **[6-56]**. As different temporal portions of the Auger electron bunch interfere with different portions of the laser pulse, they will 'feel' different frequencies $\omega$ resulting in different energy shifts (EL). This leads to a broadening of the sideband which – in the case of a chirp-free electric field – would mimic the main band (see Figure 6.2.6). Given a linear chirp of 1 eV ($\lambda$=500-1,000 nm) in a laser pulse with $\Delta\tau$ = 300 fs this would lead to a 0.25 eV broadening of the Auger-sideband line for an x-ray pulse duration of 80 fs, which is detectable. Thus, the method can also provide the pulse duration on the 100 fs level as well as the jitter between the optical laser and the XFEL.

### *6.3.2.3 Beam position monitor*

The spatial and angular stability of the XFEL radiation will be important for undulator alignment (see Section 5.5) as well as for photon beam transport to user end stations. In addition, the operation of the machine feedback system could be enhanced by the incorporation of x-ray beam position monitors (XBPM) along with the e-beam position monitors. Blade type XBPMs are current state-of-the-art for third generation synchrotron facilities and *white* beam. Blade XBPMs based on photoelectron emission from the blade material are capable to withstand the high power of undulator radiation. Since the information of the beam position is obtained from the halo of the undulator radiation, these detectors cannot be used without affecting the photon beam. Instead, XBPMs based on the detection of electrons/ions generated by the photon beam in the residual gas volume, are considered the best candidates for the XFEL. Residual gas XBPM (RGXBPM) will have no solid elements intersecting the beam. This indirect detection

scheme yields a wide dynamic range and will directly detect the centre of gravity of the photon beam. Residual gas beam profile monitors were first developed to provide beam profile measurements at charged particle accelerators **[6-57]**.

An RGXBPM prototype (see Figure 6.3.7) has been developed and tested **[6-58]**. It consists of an ion chamber in which ions or electrons drift in an homogenous electrical field towards an MCP, which produces an image of the profile on a phosphor screen. This image is transferred by a fibre optic onto a directly coupled CCD camera. The prototype of the RGXBPM has been tested at FLASH and at the DORIS-III beamline BW3 to show the feasibility of the concept. In order to comply with the requirements at the XFEL, the resolution of the device has to be improved by one order of magnitude. Ongoing R&D efforts concentrate on the optimisation of the electrical field distribution inside the detector. At the XFEL, two position monitors will be installed in the differential pumping unit at both ends of the gas attenuator. With a distance of 100 m between the monitors, a spatial and angular resolution of 10 µm and 0.1 µrad, respectively, can be expected.

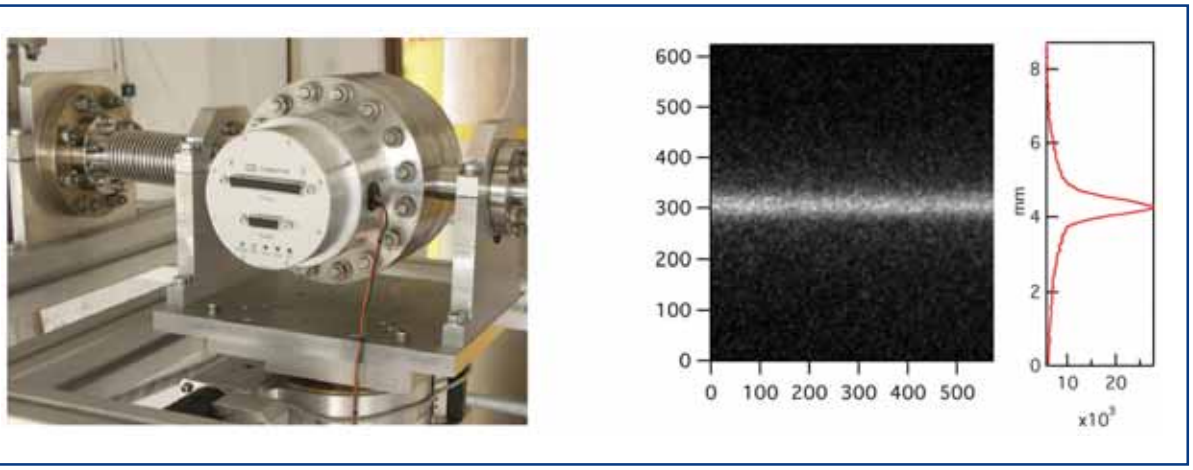


***Figure 6.3.7*** *Left: Prototype of the RGXBPM. Right: Image of the beam profile together with the corresponding integrated profile obtained at BW3, DESY, at a residual gas pressure of $3\times10^{-7}$ mbar, an MCP gain of $3\times10^{4}$, and for a CCD exposure time of 300 ms.*

## 6.4 Scientific instruments

This section contains the experiment proposals and the instrumentation requirements of seven broad scientific domains or experimental techniques, and a programme for R&D on x-ray instrumentation. It is largely the result of a wide consultation of the scientific community. After outlining the new science which is made possible by the European XFEL and the corresponding requirements for the experimental stations, an attempt is made to condense these requirements in a proposal for a schematic beamline layout. The hope is that the common format of these layouts should help the comparison and the analysis of complementarities among the various instruments.

## 6.4.1 Small Quantum Systems

### *6.4.1.1 Scientific case*

In the following sections we present the scientific case for XFEL experiments on Small Quantum Systems: atoms, molecules and clusters. These subjects were discussed at a workshop held in Paris in November 2005, and resulted in a number of concrete proposals for experiments to be performed at XFEL in the first few years of operation. The proposed experiments are divided into:

- linear processes, where there is only a single x-ray photon involved in the process, and, in some cases, a weak probe auxiliary field; and
- non-linear experiments, where there are two x-ray photons or an x-ray photon plus a photon from a strong pump laser field.

**Linear processes**

**I. Inner shell ionisation in atomic ions**

Multiply-charged ions determine the behaviour of hot media that exist both in astrophysical and technical environments. Especially under astrophysical conditions they are often exposed to x-ray radiation fields, so it is important to understand their interaction with high-energy photons. Modelling of absorption and emission spectra often lack sufficiently precise atomic data **[6-59]**. Apart from astrophysics, plasma physics requires precise photoionisation cross-sections for multi-electron ions in the x-ray range. Especially for heavier elements, these ions have a complicated multi-electron structure and are characterised by strong quantum-mechanical correlation effects; hence, the absorption processes frequently involve several interacting electrons. An example is given by the photoionisation resonances that determine the energy dependence of the photoionisation cross-section for many-electron species. The theoretical methods for predicting dynamical processes in systems with more than three electrons are presently undergoing intense development. For improving their reliability, experimental data are needed that probe the parameter spaces of both electron number and nuclear charge, as is possible in measurements on multi-charged ions.

The European XFEL offers new access to these studies as a radiation source strongly exceeding the spectral and temporal photon densities available so far. In addition, using the full pulse train capability of the European XFEL (compare Figure 6.1.1), the average photon flux will be considerably higher than at current soft x-ray sources. Thus, compared to standard neutral targets, ion storage techniques using trapped samples at rest or stored ion beams can be applied to perform single-event studies, even at the small densities to which these devices are limited. Typical densities in traps and beams are usually in the range $10^5$ to ~$10^9$ $cm^{-3}$, at least six orders of magnitude smaller than for gas targets. Two types of experiments are planned for atomic ions: First, collinear merged beam experiments offer the opportunity of absolute cross-section measurements of x-ray single-ionisation processes for a wide range of ion charge states. Second, ion trap experiments offer the possibility of following the sequential ionisation, starting from lower charge states, in strong x-ray radiation fields.

The high brilliance of XFEL photon sources combined with efficiently trapped highly-charged ions, will facilitate selective photon excitation of states in few-electron ions for the first time. These excitations in highly charged few-electron ions will test the most advanced atomic structure calculations, including huge relativistic corrections and non-pertubative quantum electrodynamics in extremely strong fields. The compact electron beam ion trap (EBIT) can produce and trap $10^7$ selected highly-charged ions in a volume of 100 $\mu m^2 \times 10$ mm which is a good match with the x-ray beam properties from the FEL. A scheme for experiments could be to direct the FEL beam of broad bandwidth directly into the EBIT and monitor the induced emission by x-ray spectrometers. Alternatively, fluorescence radiation can be monitored using a narrow-band monochromatic FEL x-ray beam that excites the trapped ions. Furthermore, two-photon excitation using counter-propagating XFEL beams might be implemented, which would result in a tremendous improvement of resolution by Doppler-free spectroscopy. For all these experiments, the opportunity to measure radiation from the trap itself is crucial.

We plan accurate spectroscopy of selected Lithium-like and Helium-like ions, such as $Bi^{80+}$ and $U^{89,90+}$. In Lithium-like Uranium the $2s\text{-}2p_{1/2}$ splitting of around 280 eV should be measured to better than 0.01eV to determine higher order loops in the Lamb-shift correction. A resolution of $10^4$ should be possible at these energies **[6-60]**. At much higher energy, the measurement of the 4.1 keV splitting of $2s\text{-}2p_{3/2}$ in $U^{89+}$, should be done where the accuracy so far is only 0.26 eV. The final aim would be a relative accuracy of $10^{-6}$ in these transition energies, but already, $10^{-5}$ would increase the level of precision considerably. To reach that, an extremely high spectral definition of the XFEL beam will be necessary and in addition, sympathetic/laser cooling of the trapped ions is required. A related application would be to very accurately measure the hyperfine splitting of inner-shell states in ions with nuclear spin, e.g. 1 eV in $2s_{1/2}$ of $^{235}U^{89+}$, in order to determine nuclear magnetisations of different isotopes. Note that the high spectral resolution will alter the temporal distribution of the x-ray pulse and lead to lengthening at the highest resolution. These effects are not expected to disturb the above proposed experiments.

We also propose to perform for the first time “optical pumping” experiments in the x-ray regime by using an EBIT and an FEL. This requires either a circular polarised XFEL beam or a highly monochromatic, linear polarised XFEL beam. Since the Zeeman sub-levels in the EBIT trapping field of 10T would be split by only $10^{-3}$ eV we propose to use circular polarised FEL radiation. In this case, the natural bandwidth of the XFEL of less than 1% should be sufficient to carry out the experiments. For example, with the positive circular polarised 280 eV XFEL photons ($\sigma_+$ light) interacting with the $^{238}U^{89+}$ trapped ions parallel to the magnetic field direction, only the 2s, m=+1/2 state would be populated. This experiment would allow, for the first time, polarisation of trapped, highly charged ions and to perform Zeeman spectroscopy on few-electron ions, e.g. to measure their g-factors. Using ions with nuclear spin, a polarisation of the nuclear magnetic moment can be reached via the hyperfine interaction.

### II. X-ray photons scattered at trapped ion crystals

A unique state of matter that could be imaged with XFEL photons is strongly coupled ion plasmas (Coulomb crystals) in a Penning trap or Paul trap configuration. The equilibrium

dynamics of Coulomb crystals could be studied, and, due to the low ion temperature, ultra-high resolution photon spectroscopy could be performed on transitions only accessible with XFEL photons.

At low temperature, a system of particles with the same charge (q) under the influence of an external confining force (One Component Plasma) liquefies or crystallises (forms Coulomb crystals). For a given harmonic external confining force, the interparticle distance in a Coulomb crystal becomes larger then the Wigner-Seitz radius r, which typically, is in the order of 15 µm, thus, giving densities of $n=3\times10^7$ ions/cm$^3$. A charged plasma of this type, unlike a neutral plasma, can exist at thermal equilibrium. The properties, in particular the equation of state, of infinite one-component Coulomb matter are well understood theoretically and the crystallisation point is known to be near $\gamma=170$, where the universal parameter $\gamma=q^2/rkT$ is the ratio of Coulomb to thermal energy kT. The fact that the parameter is universal also means that highly-charged ion plasmas can become strongly coupled and crystallise at higher temperatures than a singly charged ion plasma of comparable density, and that they are similar to high density plasmas at much higher temperature (e.g. in white dwarfs). Coulomb crystals of singly charged ions have been produced experimentally with laser cooling in electromagnetic ion traps (e.g. at the National Institute of Standards and Technology (NIST) and the Max-Planck-Institut (MPI) for Quantum Optics), and conditions for multiply-charged ion crystallisation have been established using a sympathetic cooling scheme at Lawrence Livermore National Laboratory (LLNL). The strongly coupled plasma condition will be achieved via sympathetic cooling with laser-cooled singly charged ions. In brief, first 9Be+ ions are caught and confined in the trap. These ions are electronically cooled, initially with a tuned circuit and then laser cooled using the resonance transition near 313 nm. Highly charged ions are then merged into the cold Be+ plasma, energy is exchanged by collisions and the kinetic energy of the highly charged ions is reduced to around 1 K. A value of $\gamma$ of over $10^3$ can thus, be reached with ions of q~50.

The highly charged ion crystalline phase can be imaged in fluorescence using transitions accessible with XFEL photons and a focusing element for x-rays. A synchronisation of XFEL photon pulses with the trap parameters and the image detector and with a probe laser to monitor the Be+ plasma temperature will cover the evolution from a non-equilibrium state, into a fully thermal equilibrated state as function of time (ms scale). The focusing condition of the XFEL photon beam will furthermore allow selective heating of, for example, the centrifugally separated highly charged ion cloud, thus creating a distortion of the equilibrium. Measurements of the line width of cooling transition in the Be+ ions as a function of time will allow conclusions about the phonon transport in the strongly coupled plasma components. Follow-up experiments could include high-energy XFEL photons capable of ionising an inner-shell selectively in the highly charged ions. Mixed plasmas with different Coulomb couplings can be created by using different ion components.

Results of this research will be beneficial to condensed matter physics, to the understanding of stellar interiors (for example, white dwarfs), and essential for high-resolution spectroscopy experiments. If one reaches an ion temperature of 10 K, the relative Doppler spread is down to $10^{-7}$.

### III. Molecular dynamics following x-ray photoionisation

Molecules are an important observatory tool for understanding colder astrophysical media and research on molecular regions close to strong radiation sources requires a good understanding of the cross-sections for x-ray induced processes and their products. For polyatomic molecules, several neutral products are often generated following electronic excitation or ionisation by x-ray absorption. The dynamics of the fragmentation process are best revealed by analysing the chemical nature of the final products and their relative momentum by counting techniques in event-based photoabsorption studies. For single-event fragmentation studies, the counting and imaging of neutral reaction products has been proven to be very efficient using fast-moving target systems, from which all break-up fragments are sent into a narrow cone in the forward direction with high offset kinetic energy. Using an energetic beam as the target, hence, allows universal and efficient detection of neutral fragments, in contrast to a target at rest where the fragments would have near-thermal energies and would be emitted in unpredictable directions. Fast-beam fragment imaging has been strongly developed over recent years for molecular ion beams. Beam storage techniques have been developed to control the vibrational and rotational excitation of the energetic molecular ion beam, thus, allowing studies with a well defined initial state distribution.

The high, pulsed photon intensities at the XFEL make it possible to perform x-ray photoabsorption experiments on molecular ion beams which are extremely dilute, but fast moving, target systems. These experiments, thus, produce single-event images of the fragmentation of polyatomic molecular systems following x-ray absorption and yield fragment branching ratios, fragment energies and momentum correlations between different fragments. As a particular field of study, one can consider the fragmentation of polyaromatic hydrocarbon (PAH) molecules that are observed in molecular clouds among others close to active galactic nuclei; such processes can be studied in fast-beam fragmentation studies with PAH cations. In addition, the analysis of neutral fragment channels following x-ray excitation and ionisation of smaller polyatomic molecules such as, for example, $H_2O^+$ and $H_3O^+$, is of great interest for fundamental dynamics in highly excited molecules, as such smaller systems lend themselves to direct comparisons between experimental and theoretical results. Simultaneous imaging and mass measurement of heavy fragments, as produced in interactions with PAH beams, is being intensely developed at present and will find new applications in these proposed XFEL experiments.

### IV. Cluster experiments

Clusters represent an intermediate state of matter between large molecules and solids, having the same local density as a solid but the same average density as a gas. They offer a unique opportunity to study how the light-matter interaction evolves as the size of the target increases. The interactions of clusters with intense infrared laser pulses have been found to be extremely energetic. Ions with energies up to 1 MeV **[6-61]**, and multi-keV electron energies **[6-62 – 6-64]** have been observed. The ions are much more energetic and stripped to much higher charge states than would be obtained from atoms or small molecules irradiated at the same intensity.

However, the physics of the interaction changes dramatically at short wavelengths. Whereas in the infrared, the ponderomotive energy (i.e. the kinetic energy of the electron oscillations in the rapidly varying radiation field, $e^2E_0^2/4m\omega^2$) is considerable (600 eV at $10^{16}$ Wcm$^{-2}$) and electron motion in the field is large compared to the cluster size, at x-ray wavelengths, the ponderomotive energy is much less than 1 eV and electron motion is negligible. In the x-ray regime, single-photon ionisation of core electrons can occur, inner shell holes can be created and ionisation starts at much lower intensities than with infrared radiation, where tunnelling or multiphoton ionisation occur. In the infrared, the most heat is deposited in the cluster at three times the critical electron density of $10^{21}$ cm$^{-3}$ (the critical electron density at a given frequency $\omega$ is the density $n_c$ for which $\omega=[4\pi n_c e^2/m]^{1/2}$). In contrast, at x-ray wavelengths the critical electron densities of $10^{25}$-$10^{29}$ cm$^{-3}$ will not be reached. This may lead one to expect that only weak coupling to clusters will occur. However, experiments with 100 nm radiation at DESY **[6-65]**, which measured 400 eV ions, as well as theoretical calculations, show that existing models for the optical region cannot simply be extrapolated down to x-ray wavelengths. Experimental tests of cluster fragmentation in XFEL beams of very high intensity are now needed.

To investigate the heating processes in clusters at short wavelengths, measurements will be made of ion and electron energies, ion charge states and x-ray spectra as a function of wavelength. Infrared laser radiation will then be used to probe the expansion following heating by the XFEL pulse. It was shown recently that ion energies and charge states can be maximised when the infrared probe pulse is timed to arrive when the electron density inside the cluster reaches a certain critical electron density after initiation of the heating by a pump pulse **[6-66]**. By measuring the optimum pump-probe delay for various target and pulse parameters, the expansion of the cluster can thus be mapped out.

XFEL radiation also offers a unique opportunity to investigate the structure-property relationship of reduced dimensional materials, in particular of size-selected atomic clusters. For these systems, typically containing less than 100 atoms, the cluster properties depend directly on the number of atoms in the structure. For example, the chemical reactivity can change by orders of magnitude with the addition or removal of individual atoms. Being very interesting material systems with a pronounced structure-property relationship, clusters and nanocrystals are bridging the gap between the atom and a bulk crystal. They are promising candidates for novel applications ranging from catalysis to magnetic storage and optoelectronic devices. Cluster research with the XFEL yields various opportunities of great importance.

The investigation of the electronic and geometric structure of size-selected atomic clusters has made significant progress over the last years. New experimental set-ups and powerful cluster sources as recently developed in the cluster consortium (lead by the University of Rostock) allowed first investigations of shallow core levels. The European XFEL will open the door to core level photoemission experiments on size-selected clusters in the gas phase. These experiments will be a unique possibility to unveil the electronic and geometric structure of clusters.

## Non-linear processes

### V. Multiphoton studies in the x-ray spectral region

The foreseen beam parameters at the European XFEL open up the perspective of non-linear optics in the x-ray spectral region. Here, we consider processes involving non-linear ionisation. Given that the photon energy ranges from 200 eV to 15 keV, even for extremely focused intensities up to $10^{18}$ W/cm$^2$, the ponderomotive energy $U_P=e^2E_0^2/4m\omega^2$ is much smaller than the photon energy and the ionisation potential. It follows that multiphoton (MP) (and not tunnelling ) processes govern ionisation transitions. Because of the high photon energy, only inner-shells can be MP ionised (for outer shells, Above-Threshold Ionisation (ATI) can also be considered).

The K-shell two photon ionisation (TPI) cross-section scales as $Z^{-6}$ (Figure 6.4.1). Reasonable intensities for the observation of K-shell TPI range from $10^{12}$ W/cm$^2$, for the light elements, to $10^{16}$ W/cm$^2$ for Z~35 (mean ionisation rate: ~10 ions/s). Saturation intensities range from $10^{17}$ W/cm$^2$ to $10^{21}$ W/cm$^2$, correspondingly. An unavoidable process is of course single photon outer-shell ionisation. For the 100 fs pulse duration of the XFEL, this will be the dominant ionisation process by several orders of magnitude, screening the TPI unless TPI is observed in highly stripped Hydrogen- or Helium-like ions.

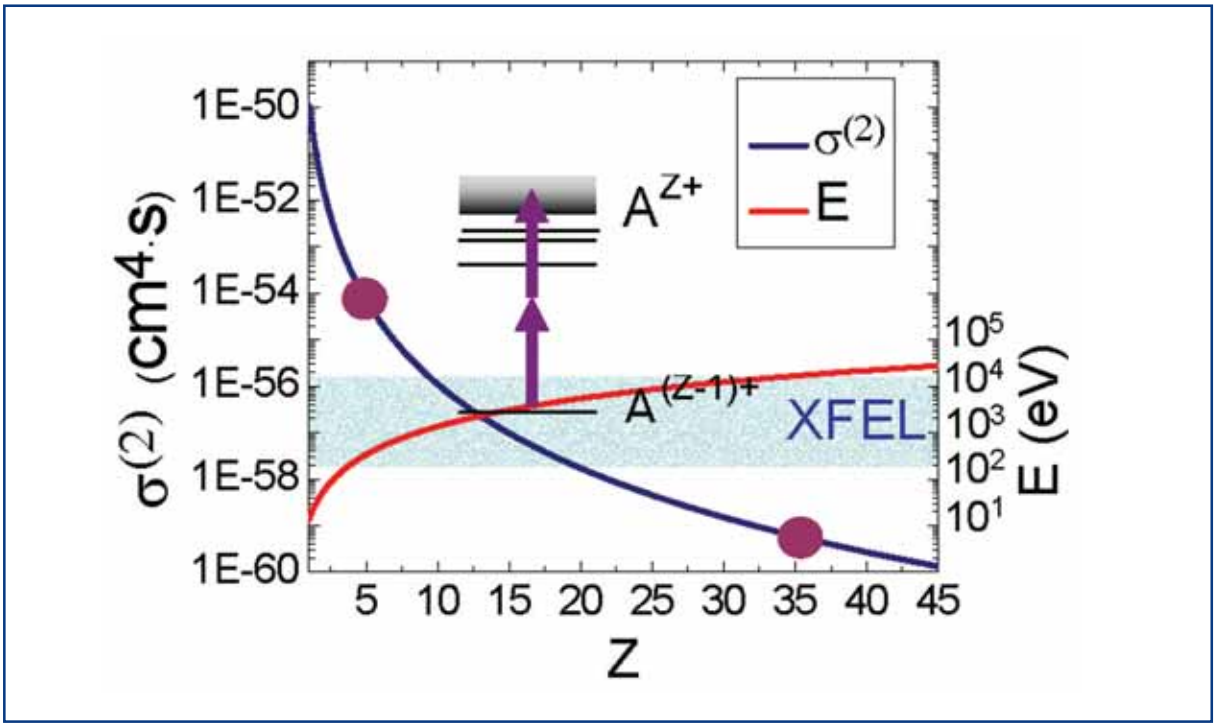


***Figure 6.4.1*** *Z dependence of the TPI cross-section and the binding energy in Hydrogenlike ions.*

Once x-ray multiphoton processes have been established, they can be used for several interesting applications. Two examples are mentioned below: Due to the non-linearity of the process, MPI provides 3-D spatial selectivity in the focused geometries required for its observation. Thus, it becomes appropriate for 3-D spatially resolved analytical applications, such as MP-XRF, MP-XPS and MP-Auger diagnostics. An even more

important application is the use of MPI processes for the temporal characterisation of the XFEL radiation. It is well known that rigorous short pulse diagnostics require non-linear processes induced solely by the radiation to be characterised. Recent achievements in attosecond pulse metrology demonstrated the feasibility of approaches (based on non-linear autocorrelation) and instrumentation (autocorrelators) for the XUV spectral range (see, for example, **[6-67 – 6-70]**). These techniques are, in a straightforward way, extendable to shorter wavelengths for the benefit of XFEL beam diagnostics.

Alternatively, a “two-colour” version of this characterisation method can be envisaged, considering atomic systems submitted simultaneously to a strong pulse of x-ray radiation from the XFEL source and to an intense pulse of radiation from an optical (or infrared (IR)) laser; the atoms can experience radiative transitions involving continuum states that are “dressed” by the laser field. In the test-case of the single-photon ionisation of atomic species via the absorption of one x-ray photon from the XFEL, the photoelectron spectrum is significantly modified in the presence of the laser. It is expected that the photoelectron peak will be depleted and that a set of new peaks, termed “sidebands”, will appear. These peaks, equally spaced with interval $\hbar\omega_L$ where $\omega_L$ is the laser frequency, are located symmetrically on each side of the primary photoelectron line, as they result from the absorption or the stimulated emission of photons from the laser field. It turns out that, by monitoring the magnitude of the sidebands when varying the time delay between the XFEL and laser pulses, one can characterise the temporal properties of the XFEL pulse itself. We note that this implies that the temporal jitter in the SASE emission process is controlled, as well as the spatial overlap between the two beams. Using these experiments in a single-shot fashion enables measurement of the temporal properties of the XFEL pulses, such as, for example, measuring the jitter between optical laser and XFEL pulse or the duration of the XFEL pulse. Two proposals to carry out such measurements as a time domain diagnostic are discussed in Section 6.3.2.2.

Such spectra would represent a new type of ATI measurement, which continue to be thoroughly studied as they represent a paradigm for highly non-linear optical processes in atoms. The determination of the respective magnitudes and of the angular distributions of the associated photoelectron peaks, provide most useful data on the response of atoms to strong external fields. Until now, ATI was explored either in a single-colour scheme via the multiphoton absorption of IR laser radiation or in multi-colour schemes, with a comb of higher harmonics combined with the pump laser. Here, with the highly monochromatic XFEL radiation, the new possibility arises of observing the absorption of a single high frequency photon combined with the exchange of laser photons. This is in contrast with the case of harmonic sources in which it is difficult to single one frequency out of the comb. Again, measurements of the magnitudes and of angle-resolved cross-sections would provide new sets of data that will be relevant in the more general context of strong field atomic physics.

**VI. Dynamics of aligned small molecules and molecular wave packet dynamics**

As also will be discussed in Section 6.4.6, the time-resolved investigation of molecules in the gas phase becomes feasible using XFEL radiation. Here, we are proposing studies of laser-aligned small molecules in the gas phase. By laser aligning we can go from

ensemble averaging to preferred orientation and can, thus, improve the information content of the measurable diffraction pattern. This can be seen as: (a) a stepping stone to single-molecule imaging of larger molecules as it will help address the timescales of x-ray induced Coulomb explosion; and (b) important fundamental molecular science, permitting us to follow the full dynamics of structural change in chemical reactions. Studies on gas-phase molecules in this range would require an ultra-short aligning laser pulse (e.g. Titanium-Sapphire pulse) followed at a variable delay by the XFEL pulse whose diffraction pattern is recorded in order to extract the structure of the molecular species. Different projections of the diffraction pattern or different polarisation axes of the X-pulse, as compared to that of the IR-laser pulse, could also be applied to retrieve 3-D diffraction patterns. The dynamics of molecular alignment or of other photo-induced reactions, possibly triggered by the IR-laser pulse, could be investigated. In addition to measuring the scattered x-ray photons, we propose that the momentum distribution of the x-ray produced photoelectrons should also be measured as this will carry the signature of the molecular structure due to the scattering of the outgoing electrons from other atomic centres in the molecule.

The spatial alignment of molecules can be regarded as a special case of population of coherent rotational states of the molecule. In a similar way one can also consider population of coherent vibration states, applying an IR short-pulse pump laser; and subsequently uses the XFEL radiation as the probe pulse (see Figure 6.4.2). The coherent mixing of vibrational states results in a non-stationary state or nuclear wave packet (WP) which evolves with time and depends on the phase, intensity and shape of the IR field. IR-x-ray pump-probe spectroscopy is a proper tool to study the dynamic of proton transfer in systems with Hydrogen bonding patterns (for example, water). Thus, the spatial confinement of the WP allows it to be selectively excited to the proton transfer well, thereby offering the possibility to map out of the molecular potential along the Hydrogen bond. Another topic of general and fundamental interest is the dynamics of the proton transfer in vibronically coupled core-hole states localised on different sites; this occurs for example in the Glyoxalmonoxime molecule. Through the crossing of the potentials, the proton transfer is accompanied by core-hole hopping. Moreover, x-ray photoionisation of laser-driven molecules offers a unique opportunity to study the electronic recoil effect, which is enhanced through the large size of the laser-induced nuclear WP. Finally, the WP revival caused by the anharmonicity allows the anharmonical shift to be resolved by making use of the one-to-one correspondence between the dynamics of the nuclear WP and the shape of the x-ray probe spectrum. In all these studies, the relative phase of the pump IR radiation strongly affects the x-ray probe spectra, as the WP trajectory is sensitive to this phase.

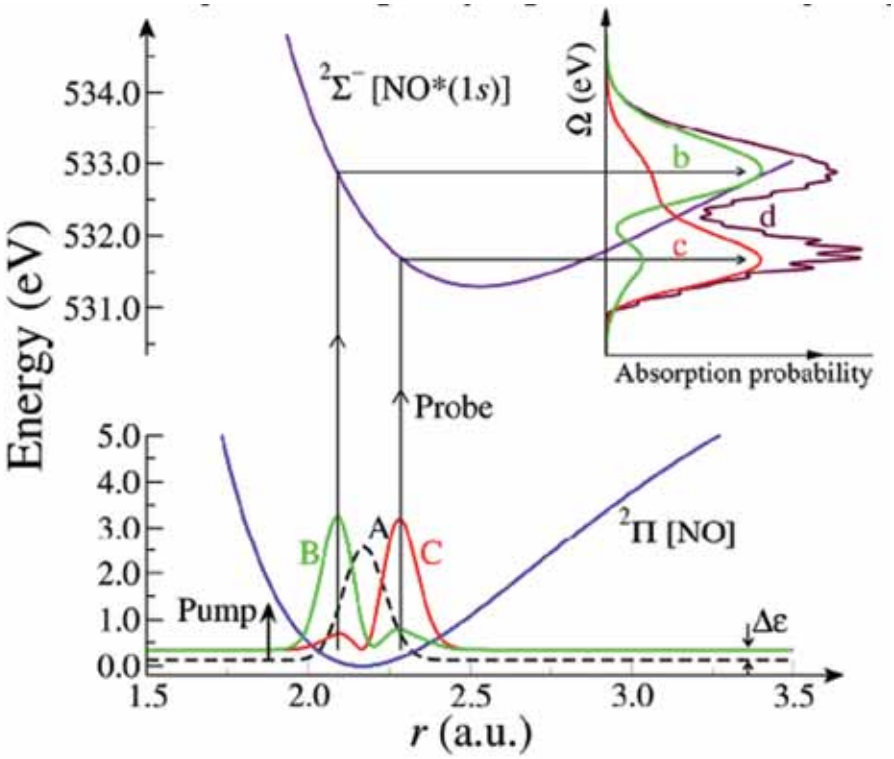


***Figure 6.4.2*** *Example showing how the shape of the vibrational wavepacket in the ground state of the NO molecule affects the lineshape of the O K-edge absorption.*

Regarding the general requirements in order to clock photochemical processes, time and spatial resolution of pump-probe measurements must be considered. The observation of motion in real systems needs rather high spatial resolution through a good localisation of the wave packet. Thus, the formation of the nuclear WP deserves special attention: the degree of localisation depends on the intensity, and on the shape of IR pulse. The localisation of the wave packet requires the coherent excitation of many vibrational levels; this makes it necessary to apply IR intensities of about $10^{12}$-$10^{14}$ W/cm². Moreover, the spread of the WP during its evolution must be rather small.

The key to achieving the necessary time resolution is a sufficiently short duration of less than 100 fs for the x-ray probe pulse. Slicing or compression techniques have already been proposed to shorten x-ray pulses to the desired region of 10-50 fs **[6-71 – 6-72]**. As the WP evolution depends on the phase of the IR field, the probe signal may become position sensitive and mixing would lead to de-phasing effects. To avoid such de-phasing, the spot size of the x-ray beam has to be kept at the size of the IR wavelength.

### VII. Time-resolved photo-fragmentation of small molecules

Photo-fragmention studies using an IR pump pulse and a following x-ray probe pulse give access to new classes of experimental studies focused at the direct observation of spatial structures in molecular systems. Experiments are essentially based on the use of ultra-short (e.g. Titanium-Sapphire) laser pulses synchronised with femtosecond (fs) XFEL pulses. The following example applies one of the experimental methods available.

A broad range of molecular species may be investigated using these techniques, however, in each case sufficiently specific and realistic quantities would need to be considered in order to outline the required experimental parameters in more detail.

By following an idea first reported by U. Becker et al. **[6-73]**, it would be interesting to investigate the breaking dynamics of molecular bonds such as NO in the $N_2O$ molecule. In such a molecule, in fact, the Oxygen atom occupies a side position, which implies an asymmetry even in the inner shell binding energy of the two Nitrogen atoms, the central and terminal ones, respectively. In particular, the 1s binding energies of the two Nitrogen atoms are split by 3.93 eV, the central Nitrogen line being situated at about 409 eV and the terminal-atom line being centred at about 413 eV. The two lines are very well resolvable in spectroscopic experiments, having an FWHM of 0.7 eV and 0.54 eV, respectively. The N-line spectral splitting disappears once the NO bond is broken and the molecule is dissociated into an Oxygen atom and a $N_2$ molecule. We propose to use a pump-probe scheme in which an intense ultra-short pump beam induces multiphoton bond breaking in the molecule; and an ultra-short 400-420 eV XFEL pulse then photoionises the fragment at a variable delay. By means of photoelectron spectroscopy, the dynamics of bond breaking can be studied by monitoring the transition from the double to the single line associated to the N 1s shell as a function of the delay time.

### *6.4.1.2 Instrument requirements*

From the specific needs of the experiments described above main requirements for the investigation of Small Quantum Systems (SQSs) can be derived. They concern the performance of the light source, the diagnostic equipment of the beamlines and their infrastructure. The needs for the experiments described in this section correspond most closely to the projected SASE 3 beamline for soft x-rays. The reason for using soft x-rays comes from the desire to study atomic or molecular excitations occurring in this photon energy range and from the perspective of studying non-linear multiphoton processes. Since the cross-section for these processes decreases strongly with increasing photon energy, the chances of carrying out such experiments are best for the soft x-ray regime. Furthermore, some users wish to study the interaction with circularly polarised x-ray radiation, again (naturally) available only from SASE 3.

**Spectral radiation properties**

Required photon energies vary from 250 eV to around 4100 eV. The lower edge is purely determined by the availability at the European XFEL. The XFEL experiments will, in a sense, be an x-ray continuation of work currently started at smaller photon energies (VUV and XUV). The upper edge corresponds to the L-shell fine structure in highly stripped $U^{89+}$. Most of the proposed experiments do not require a monochromator, but can accept the natural bandwidth of the FEL of 0.7% (250 eV) to 0.2% (3000 eV). Where spectroscopy at specific resonances or energy levels is proposed, an energy resolution of $10^{-4}$-$10^{-3}$ is required. Such resolution is possible because of the proposed monochromator of the SASE 3 beamline. In the case of the proposed investigation of highly stripped high-Z atoms (Experiment II. in Section 6.4.1.1), a resolution as good as $10^{-5}$, in some cases even a near $10^{-5}$, has been requested. This very high resolution monochromator will

require a specific R&D effort, in particular in view of the high intensities. The temporal radiation properties will be affected by the use of high spectral resolution. A second reason to use a monochromator could be to reduce the higher harmonic contents. In particular, two-and-higher order multi-photon experiments are sensitive to photons at two or three times the energy and leading to single-photon ionisation events (Experiment V. in Section 6.4.1.1). For these experiments a reduction of higher harmonics of better than $10^6$ seems to be required. Since calculations show that the natural radiation exhibits a ratio of $10^2$-$10^3$, the realisation of far better suppression of higher order harmonics by means of optics and filters could be a real challenge.

### Beam dimensions

The requested x-ray beam size is determined, in most cases, by the typical size of the sample of 100 µm which is the cross-section of the x-ray beam with an atomic, molecular or cluster jet. At this beam size the intensity will increase to ~$10^{15}$ W/cm$^2$. For merged ion beam experiments (I. and III.) good overlap of x-ray and ion beams over ~0.5 m is required. For 100 µm spot size, the Rayleigh length will be sufficiently long to achieve this value. Experiments V. and VI. benefit from higher intensity and therefore need tighter focusing in order to reach intensities of ~$10^{17}$ W/cm$^2$ and beyond. If one could reach spot sizes of 1 µm or even smaller diameters, intensities beyond $10^{19}$ W/cm$^2$ could be possible which may become important for the non-linear experiments.

### Time domain requirements

Due to intrinsically small cross-sections, many of the experiments are luminosity limited. That means they require the maximum available photon flux and the highest achievable repetition rate. However, due to limitations in the detection channels (see the following discussion) the favourable bunch spacing for most of the experiments is in the regime 1 up to 20 µs. For Experiments I.-IV. investigating linear processes, the planned x-ray pulse duration of the order 100 fs will be largely sufficient. Beyond that the non-linear Experiments V.-VII. would greatly benefit from a reduced pulse duration down to <30 fs. All experiments investigating non-linear effects will suffer from the spike structure of the XFEL radiation. Simulations of the temporal distribution show that XFEL radiation at 250 eV still has many uncorrelated spikes (compare Figure 6.4.3). Monochromatisation will smooth this structure, therefore providing improved conditions.

### Photon diagnostics requirements

All experiments will need diagnostic equipment regarding the measurement of the photon beam intensity on a pulse-to-pulse basis. In addition to the integrated photon number required by all experiments, those experiments investigating non-linear effects may require measurement of the temporal intensity distribution for each FEL pulse. This need arises from the dependence of the linear effects as a function of intensity (W/cm$^2$) and not of flux. The techniques to determine spectral and temporal information on a pulse-to-pulse basis are yet to be developed. In some cases the measurement intensity and some temporal properties for each pulse may already allow the identification of linear and non-linear contributions by using the dependence of measured process rates. Since most experiments will use optically thin samples, the transmitted beam can be used for

various diagnostics. To achieve the small spot sizes, diagnostics of the beam spot location and spatial distribution at the sample location is required.

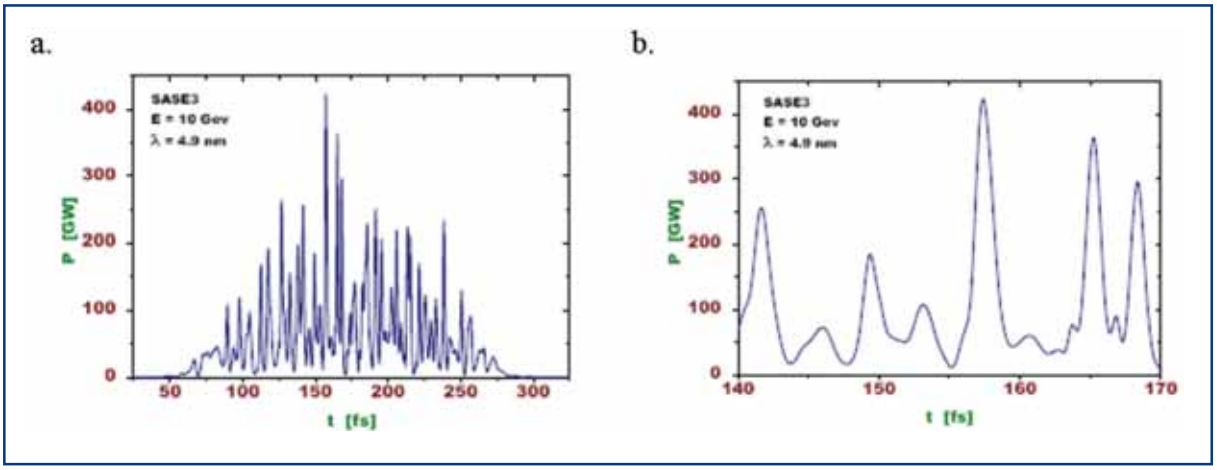


***Figure 6.4.3*** *Simulation of the temporal distribution of 4.9 nm radiation from SASE 3 at 10 GeV. (a) is the entire pulse and (b) shows a slice of 30 fs.*

### Sample manipulation and environment

Many of the experiments will apply atomic, molecular or cluster beam techniques. Some of these sample injection systems operate at relatively high pressure (e.g. for rotational cooling of molecules or cluster formation) and as a consequence, the base pressure in experimental chamber may reach the $10^{-5}$ mbar level. Therefore, careful design of differential pumping stages for connection to the photon beamline needs to be considered. On the other hand, experiments may investigate extremely dilute samples, therefore, requiring partial pressure as low as $10^{-11}$ mbar. In these experiments, differential pumping is required to improve experiments vacuum against beamline vacuum.

Experiments in this scientific field will investigate ions over a large variety of masses (atoms, molecules and clusters) and charges (highly charged atomic ions). In addition to gas beam techniques, the use of ion storage techniques is proposed here. These could be ion trap techniques, such as EBIT or Penning trap, to store ion samples at rest or stored fast ion beams, which may be used in merged (collinear) or crossed beam geometry (see Figure 6.4.4). In order to efficiently carry out experiments using an ion trap or an electrostatic storage ring, it would be beneficial to make these infrastructures available at the XFEL. The footprint required for an ion trap set-up is of the order $5\times5$ m$^2$ and that of an ion storage ring is estimated to be in the order $15\times15$ m$^2$. It has to be noted that groups working in this field often operate their own, specific vacuum chambers. One should foresee the possibility of placing these chambers at a non-occupied vacuum port of the SQS instrument.

### Detector requirements

Depending on the experiment, different detection techniques will be applied. Common to most experiments is particle detection, either electrons or ions. Time-of-flight techniques will be applied for energy measurement of the particles putting a constraint on the maximum repetition rate of the experiment. Typical flight times extend up to µs making

1 MHz operation desirable. To achieve very good energy resolution, retarding schemes will be used leading to particles flight times in the order 10 µs, thus, limiting the repetition rate to ~50 kHz. In combination with 2-D particle detectors, spatial and energy (3-D) resolving detectors can be applied for fragment imaging. In some cases, x-ray emission spectroscopy will be used and spectrometers, possibly even having high time-resolution by using ultrafast x-ray streak cameras (XSC), will be required. In addition, special detector arrangements like the COLTRIMS detector for multi-hit ion and electron coincidence detection will be used.

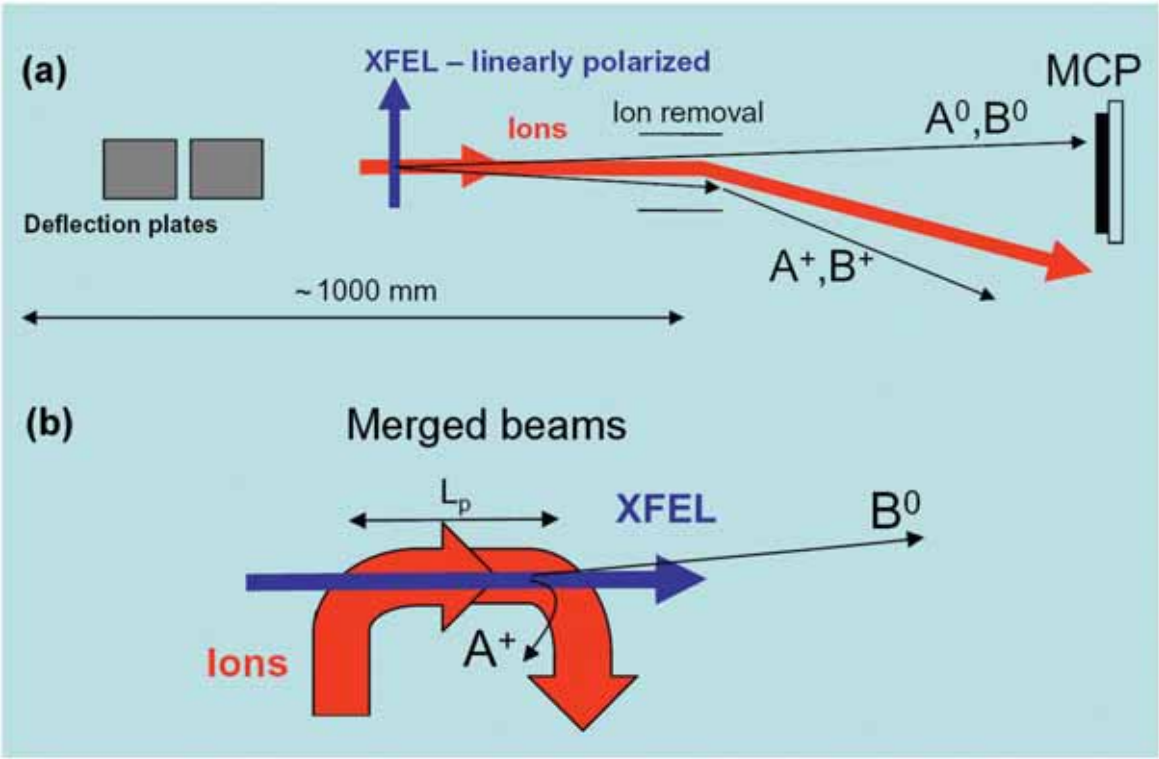


***Figure 6.4.4*** *Schematic arrangements for fast-beam molecular fragment imaging using (a) crossed ion and photon beams or (b) merged beams.*

### Visible laser requirements

An important feature of many of the experiments in this field is the requirement for a synchronised high power ultra-fast IR or visible laser. Starting from a fundamental wavelength at ~800 nm (e.g. Titanium:Sapphire) it should provide wavelength from the fourth harmonic (200 nm) up to the deep infrared (10 µm; requires some R&D). High energy of 1-3 mJ should be provided for fundamental and harmonics, whereas Experiment VI. asks for large range tunability by optical parametric tuning. In this case, one will have to live with 10 µJ. A contrast ratio of larger than $10^5$ is requested and the repetition rate should allow us to follow that of the FEL pulses. It is likely that a trade-off between laser pulse energy and repetition rate will have to be applied. For this class of experiments a pulse duration better then 50 fs and precise synchronisation with the FEL beam in the order of ~10 fs are required. If such synchronisation will not be possible, diagnostic tools to measure the time delay to similar accuracy are required.

### *6.4.1.3 Realisation of the instruments*

According to their requirements, the SQS experiments need to be carried out at the SASE 3 beamline (see Section 6.2.4.3 for a description). SASE 3 enables photon energies from 250 up to 3,100 eV. For higher photon energies the saturation length of the FEL, at given project parameters, will exceed the undulator length. Those experiments requiring photon energies from 3,000 to 4,100 eV may have to be carried out at the SASE 2 beamline (see Section 6.2.4.2). The SASE 3 beamline could features two beam tubes: one for a monochromatic beam with a resolution of about 104 and one using only mirrors to guide the beam. Selection of the beam path is achieved by a set of two movable mirrors. The optics in both lines should not affect the polarisation of the XFEL radiation, thus, linear and circular polarisation can be selected by setting the undulator accordingly. It is not considered possible to bring the monochromatic and the mirror beam to the same location. The specific requirements of the SQS experiments, therefore, ask for two different instruments, described below.

**SQS 1: Monochromatic beam**

The proposed PGM monochromator design for the SASE 3 beamline (see Section 6.2.2.3) should provide a monochromaticity of the order $10^{-4}$ over the entire photon energy range from 500-3,000 eV. This resolution is required to carry out, for example, the inner-shell ionisation experiments of highly charged ions described in Section 6.4.1.1, Experiment II. Other spectroscopy-type experiments, investigating specific energy levels, will also use this instrument. The typical transmission of the monochromator is in the order of a few percent. Therefore, the SQS 1 instrument will not be suitable for experiments requiring the highest intensities. The requirement of a monochromaticity of $10^{-4}$ up to $10^{-5}$ cannot be fulfilled using the proposed, versatile monochromator design. For the SASE 3 photon energy range, such a resolution would require a specific R&D programme.

Two mirrors at a grazing angle in the order 10 mrad will be used to deflect the beam away from the forward beam direction. At the chosen sample location inside the experimental hall a focal spot size of the x-ray beam of ~100 µm will be available. This focus is achieved by using the mirrors within the monochromator design, i.e. by refocusing the exit slit onto the sample. If higher intensities will be required for the experiments, stronger demagnification of the monochromator exit slit will be needed. In this case the focusing mirror must move closer to the sample.

The following elements belong to the SQS 1 instrument inside the experimental hall. They are also depicted in the schematic layout of that instrument in Figure 6.4.5 and are listed in Table 6.4.1. Collimating apertures or a slit system will be placed in front of the experimental chamber to clean the beam from scattering. A gas photon flux monitor (see Section 6.3.2.1) will follow before a differential pumping section separates the beamline from the UHV vacuum chamber for experiments. For the energy range of this beamline, vacuum separation by means of windows is unlikely. The sample chamber will be equipped with systems for atom, molecule, or cluster beam production. We foresee sufficient pumping power to work at relatively high target densities of up to $10^{22}/cm^{-3}$. Experiments to investigate electrons and/or particles and detectors operating in the TOF

mode will be used. X-ray emission spectrometers could complement particle detection. Angular resolution may be used, at least in one direction. This vacuum chamber can be removed and space of 4×5 $m^2$ is foreseen to install specific sample manipulation schemes like ion traps or mass-selected cluster apparatus.

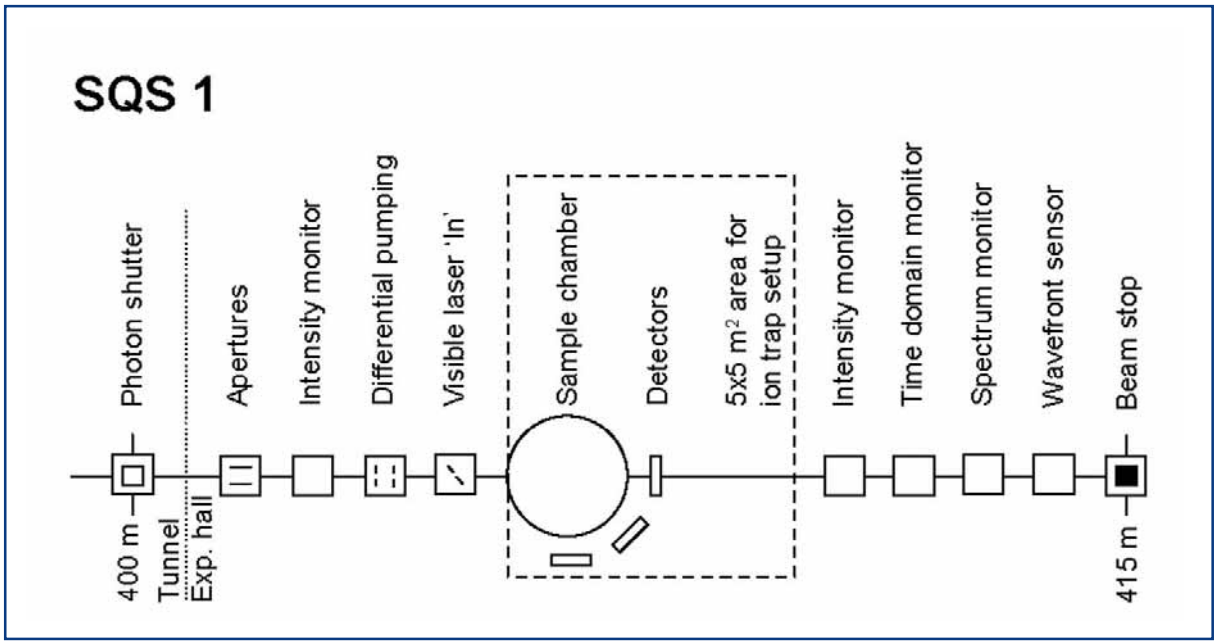


***Figure 6.4.5*** *Schematic layout of components of the SQS 1 station for monochromatic beam use. Distances are given in relation to the end of the undulator.*

Most of the experiments will absorb only a fraction of the incident beam intensity. It is, therefore, intended to use the transmitted beam for the purpose of diagnostics. A second gas monitor detector will be used to measure the transmission. At SQS 1 the spectral measurement is restricted to measurements of the higher harmonic content. Diagnostics of time-domain properties should deliver the arrival-time required for pump-probe experiments using the visible laser. Finally, spatial measurements are required to determine beam location and spatial distribution. Since these measurements are usually destructive they will be carried out in a dedicated set-up at the end of the line and before the beam stop.

The use of visible laser radiation at the SQS 1 instrument will be possible through distribution from the central laser room. The laser will be coupled into the vacuum in front of the sample chamber. Using mirrors with a central aperture, the laser beam can propagate collinear with the XFEL beam.

| Item | Purpose | Specification |
|---|---|---|
| Slits/apertures | Beam definition,<br>beam halo cleaning | 1 µm accuracy,<br>0.25 µm repeatability |
| Intensity monitor | Measurement of incident photon flux | Transmissive (<5% absorption),<br>single pulse measurement,<br>relative accuracy $<10^{-3}$ |
| Differential pumping | Separation of beamline and experiments vacuum | $10^4$ step for all elements |
| Laser inlet | Port-to-couple visible laser radiation into experimental chamber | Mirror with central hole, retractable |
| Sample chamber | Prepare and position samples,<br>mounting of detectors,<br>preparation for high gas loads | UHV,<br>high pumping speed,<br>x-y-z positioning |
| Detectors | Measurement of secondary particles,<br>energy measurement,<br>x-ray emission yields. | TOF for electrons/ions,<br>imaging detector,<br>x-ray spectrometer |
| Intensity monitor | Measurement of incident photon flux | Transmissive (<5% absorption),<br>single pulse measurement,<br>relative accuracy $<10^{-3}$ |
| Spectral monitor | Measurement of harmonic content | single pulse measurement,<br>relative accuracy $<10^{-3}$ |
| Time monitor | Measurement time domain properties | Single pulse measurement |
| Spatial monitor | Measurement of spatial distribution,<br>focus size | Single pulse measurement |
| Ion trap | | 5×5 $m^2$ area |
| Alignment unit | Positioning and position verification | Permanently operating, accuracy<br>~100 µm |
| Lead hutch | Radiation protection | 5×10×4 $m^3$ (W×L×H),<br>± 1° thermal stability |
| Control hutch | Operation of the instrument | Working environment<br>(Noise, temperature, light) |

***Table 6.4.1*** *Elements and specifications of the SQS 1 instrument.*

### SQS 2: High intensity beam

The SQS 2 instrument uses only mirrors for beam guiding. In this way much higher intensities can be achieved at the sample position to carry out e.g. the multiphoton studies in the x-ray spectral region described in Section 6.4.1.1, Experiment V. Other non-linear type experiments, investigating one- and two-colour phenomena will also use this instrument. The beam transport line for “mirror-only” of the SASE 3 beamline provides the options for unfocused and moderately focused beams (compare Figure 6.2.14). This beam is transported to a first vacuum port at this instrument, where micron, or even sub-microm, focusing will be possible. For a demagnification ratio of ~100, intensities as high as $10^{19}$ W/cm2 might be achievable. Sub-microm focusing requires dedicated optics near the sample and a beam transport which preserves the wavefront. This will be best achieved using flat mirrors. However, the unfocused beam of the SASE 3 beamline in the experimental hall has a size of 1.4-7.2 mm (FWHM) for photon

energies of 3.1-0.25 keV, respectively. It is, therefore, considered very difficult building one focusing element that could be used for all photon energies. Since the instrument should feature only one single beam direction, using in-line optics, e.g. zone plates, is proposed. Using two deflecting mirrors a second port could be made available for experiments using the same instrument (compare Figure 6.4.6 and Table 6.4.2). Focusing to spot sizes ~100 µm will be achieved by using one of the offset mirrors.

Both ports will be equipped with similar instrumentation. Collimating apertures or a slit system will be placed in front of the experimental chamber to clean the beam from scattering. A gas photon flux monitor (see Section 6.3.2.1) will follow before a differential pumping section separates the beamline from the UHV system for the experiments. At the 100 µm port, the use of a dedicated vacuum chamber or an ion trap should be possible. In a more detailed layout of the instrument it has to be investigated if an ion beam storage ring can be accommodated at this station. It would require an area of ~15×15 $m^2$ and this is likely to exceed the available surface area. At the 1 µm port, a similar sample chamber as the one described for the SQS 1 station will be used. It will allow experiments using atom, molecule or cluster beams. This vacuum chamber can be removed and space of 2×3 $m^2$ is foreseen for sample environment installations. Most of the experiments will absorb only a fraction of the incident beam intensity. It is, therefore, intended to use the transmitted beam for the purpose of diagnostics. A second gas monitor detector will be used to measure the transmission. At SQS 2 the spectral diagnostics determines mean photon energy, bandwidth, and higher harmonic content of the radiation. Diagnostics of time-domain properties should deliver the arrival-time required for pump-probe experiments using the visible laser. Finally, spatial measurements are required to determine beam location and spatial distribution. Since these measurements are usually destructive, they will be carried out in a dedicated set-up at the end of the line and before the beam stop.

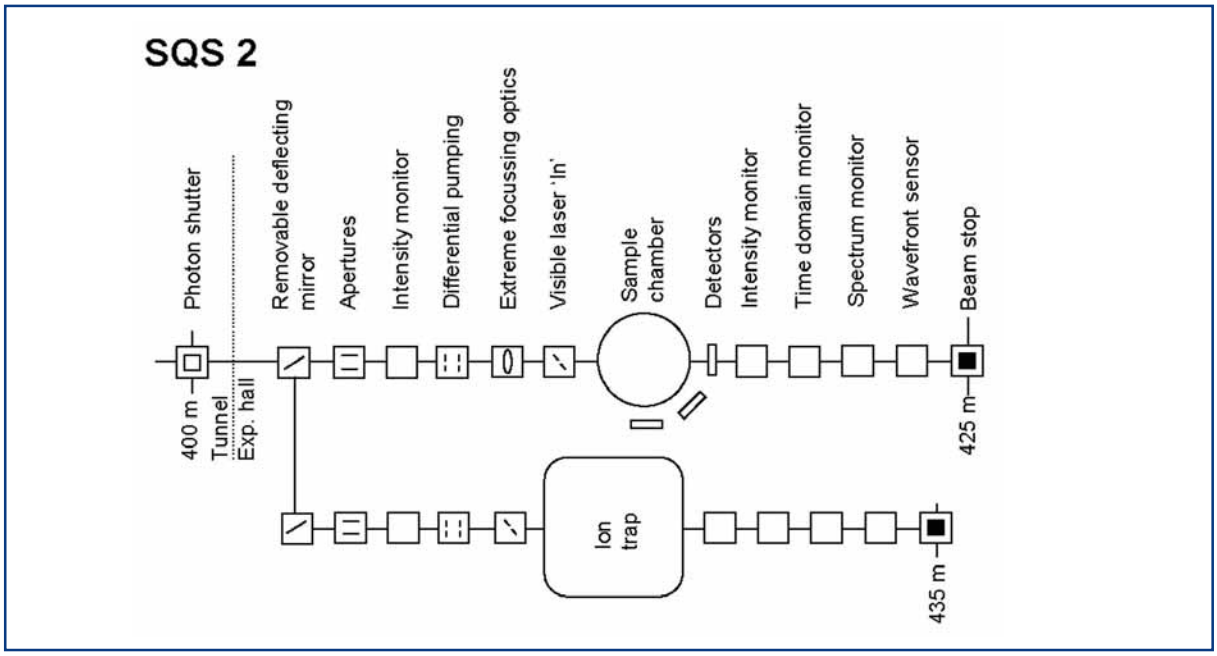


***Figure 6.4.6*** *Schematic layout of the SQS 2 station for "full" beam. The beam is directed either to the dedicated ion trap or a strong focusing optic, e.g. for studies of non-linear effects in atom, molecule or cluster beams.*

The use of visible laser radiation at both ports of the SQS 2 instrument will be possible through distribution from the independent laser room. The laser will be coupled into the vacuum in front of the sample chamber. Using mirrors with a central aperture the laser beam can propagate collinear with the XFEL beam.

| Item | Purpose | Specification |
|---|---|---|
| Deflection mirror | Beam distribution to both ports, deflection angle 20 mrad | 0.5 µrad angular stability, 0.2 µrad figure error, 0.1 nm surface roughness |
| Deflection mirror | Deflection angle 20 mrad | 0.5 µrad angular stability, 0.2 µrad figure error, 0.1 nm surface roughness |
| Slits/Apertures | Beam definition, beam halo cleaning | 1 µm accuracy, 0.25 µm repeatability |
| Intensity monitor | Measurement of incident photon flux | Transmissive (<5% absorption), single pulse measurement, relative accuracy $<10^{-3}$ |
| Differential pumping | Separation of beamline and experiments vacuum | $10^4$ step for all elements |
| Focusing optics | ~1 µm focusing for 0.25-3 keV | 0.1 µrad angular stability |
| Laser inlet | Port-to-couple visible laser radiation into experimental chamber | Mirror with central hole, retractable |
| Sample chamber | Prepare and position samples, mounting of detectors, preparation for high gas loads | UHV, high pumping speed, x-y-z positioning |
| Detectors | Measurement of secondary particles, energy measurement, x-ray emission yields. | TOF for electrons/ions, imaging detector, x-ray spectrometer |
| Intensity monitor | Measurement of incident photon flux | Transmissive (<5% absorption), single pulse measurement, relative accuracy $<10^{-3}$ |
| Spectral monitor | Measurement of harmonic content | Single pulse measurement, relative accuracy $<10^{-3}$ |
| Time monitor | Measurement time domain properties | Single pulse measurement |
| Spatial monitor | Measurement of spatial distribution, focus size | Single pulse measurement |
| Ion trap | | $5\times5$ m$^2$ area |
| Alignment unit | Positioning and position verification | Permanently operating, accuracy ~100 µm |
| Lead hutch | Radiation protection | $10\times15\times4$ m$^3$ (W×L×H), ± 1° thermal stability |
| Control hutch | Operation of the instrument | Working environment (Noise, temperature, light) |

***Table 6.4.2*** *Elements and specifications of the SQS 2 instrument.*

## 6.4.2 High Energy Density matter experiments

### *6.4.2.1 Scientific case*

In 2003, two reports **[6-74, 6-75]** by the US National Academy of Science highlighted the field of High Energy Density (HED) physics as an important area for future research. This regime of matter is defined so that the energy density exceeds ~ $10^{11}$ $Jm^{-3}$ (equivalent to a pressure of ~100 GPa). The regime of interest can be seen on the left-hand side of Figure 6.4.7, where we show the temperature-density phase-space for Hydrogen. Here we see that, for example, a solid density foil heated to a temperature of several eV would qualify. There are a variety of reasons for the widespread interest in HED physics. Further, the figure illustrate that conditions considered in the warm dense matter (WDM) regime occur in the cores of giant planets; for example, Jupiter's core is believed to be at a pressure of ~8000 GPa and a temperature in excess of 16,000 K. Moreover, other astrophysical objects such as accretion disks and astrophysical jets are in the hot dense matter (HDM) part of the HED regime **[6-76]**. On Earth, an important example is an inertial fusion capsule, the conditions for which are indicated as spherical compressions in the figure.

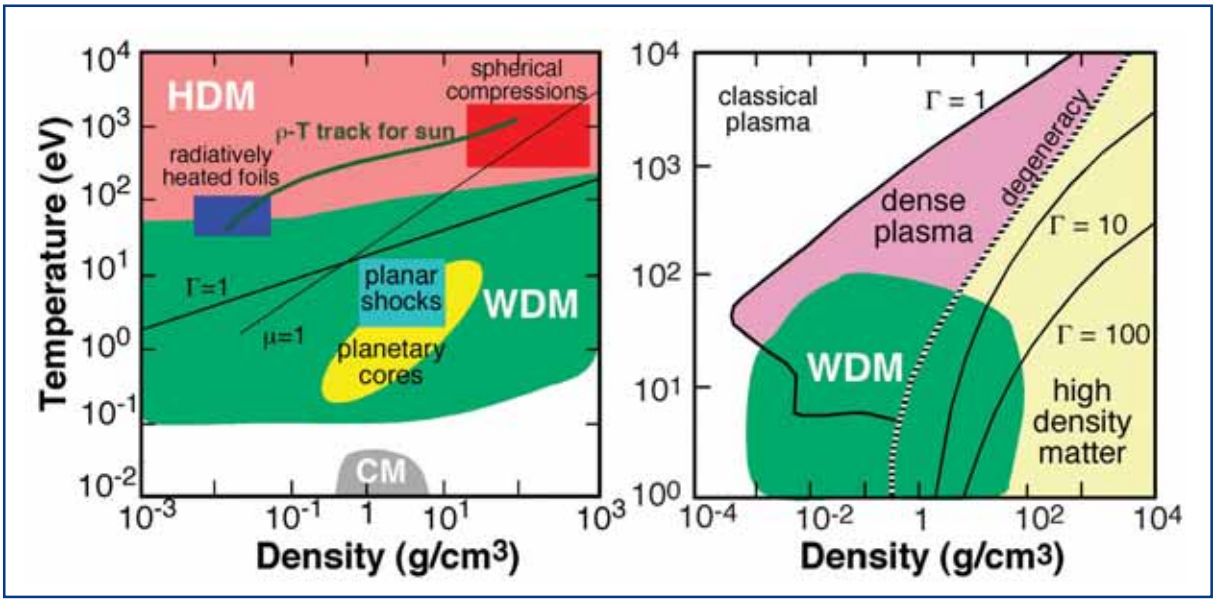


***Figure 6.4.7*** *Temperature-density phase-space diagrams for Hydrogen (left) and Aluminium (right) illustrating the various regions of matter relevant to the discussion of the HED regime. The hot dense matter and warm dense matter regions are indicated along with various examples of areas of application.*

Therefore, the HED regime, separated in HDM and WDM regions covers a vast part of phase-space, but importantly is not described by condensed matter approaches, a regime indicated by the "CM" at the bottom of the figure. In the right hand side of Figure 6.4.7 we show the temperature-density phase-space for Aluminium where it can be seen that there are some important physical characteristics to the WDM region. Firstly, the electrons are partially degenerate. The point at which degeneracy plays a role is indicated by the dashed line that cuts through the WDM region. As we see, for much of the WDM regime we cannot assume $kT<<E_F$ which is why condensed matter theoretical techniques are not suitable for describing this regime.

Note the $\Gamma$ curves, where $\Gamma$ is the ion-ion strong coupling parameter defined as $(Zxe)^2/R_i kT$ and represents the ratio of Coulomb energy between ions of average separation $R_i$ and their thermal energy. When $\Gamma_{ii}$ is of order unity, the ions are strongly correlated and perturbative plasma physics models are not applicable. Clearly this is a regime where theoretical modelling is not straightforward. It is also a regime where good experimental data is in short supply. The problem is illustrated in Figure 6.4.8, which shows the comparison between two models of the equation of state (EOS) which predict the pressure for a given density and temperature. The contours represent the percentage disagreement in the pressure for the two models of the EOS that are both as physically justified. Our full understanding of large planet formation and structure as well as the trajectory of inertial fusion capsule, depends on a better understanding of matter in the WDM and HDM regimes. There are currently experiments, using existing facilities, that can explore various aspects of the physics of HED matter **[6-76]**. These include Z-pinches, ion beams, short-pulse and high energy lasers. These all have their own advantages and limitations. Below, we discuss prospects for the XFEL, highlighting its own unique capabilities as both a creator and probe of HED matter. We shall see that, especially when combined with optical laser facilities, there is the prospect of a powerful and flexible research tool.

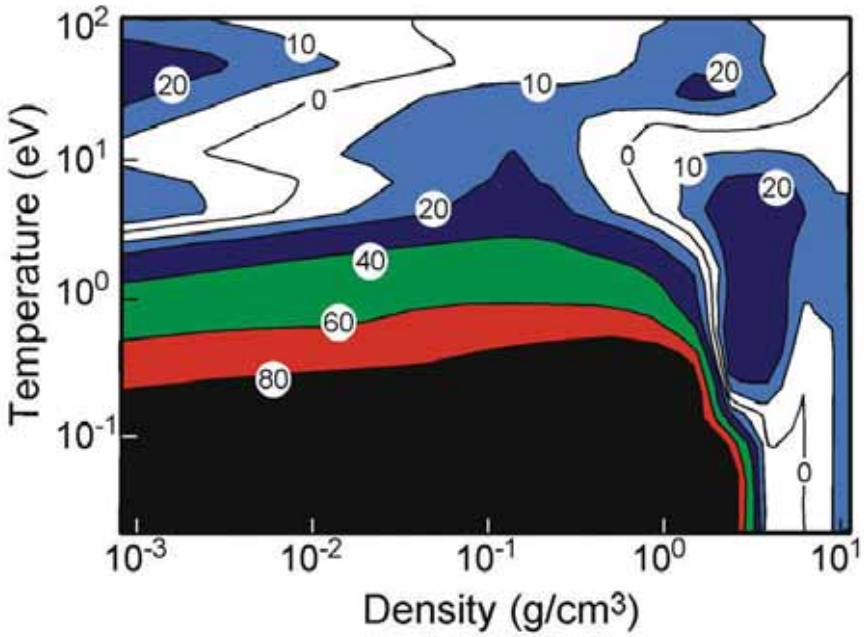


***Figure 6.4.8*** *Contour map of discrepancies in percent between models of the EOS for Aluminium.*

### Prospects for XFEL radiation

The XFEL radiation will be above the plasma frequency of all possible densities that can be created and can penetrate a sample, heating it uniformly to create well-defined conditions that in many cases have not previously been available. As an example we show in Figure 6.4.9 the heating of an Aluminium sample with the proposed SASE 3 beam at 3.1 keV. In this example we assumed a focal spot of 60 μm, and it is envisaged that

much tighter focusing and thus, higher temperatures will be available. We can see that the conditions across the foil are very uniform, with the temperature of ~6-10 eV corresponding to a deposited energy density of $7\times10^{11}$ $Jm^{-3}$. As we will note later on, even higher energy densities (above $10^{14}$ $Jm^{-3}$) can, in fact, be created with the proposed XFEL beam parameters. The beam will be able to probe the internal structure of a sample in, for example, x-ray Thomson scatter experiments, giving unprecedented access to detailed physics at high density, where physics issues such as degeneracy and strong coupling come into play. Both as a creator and probe of HED samples, the XFEL has properties that will allow many detailed and previously impossible experiments. An initial list of proposed experiments and their technical requirements follows in the next sections.

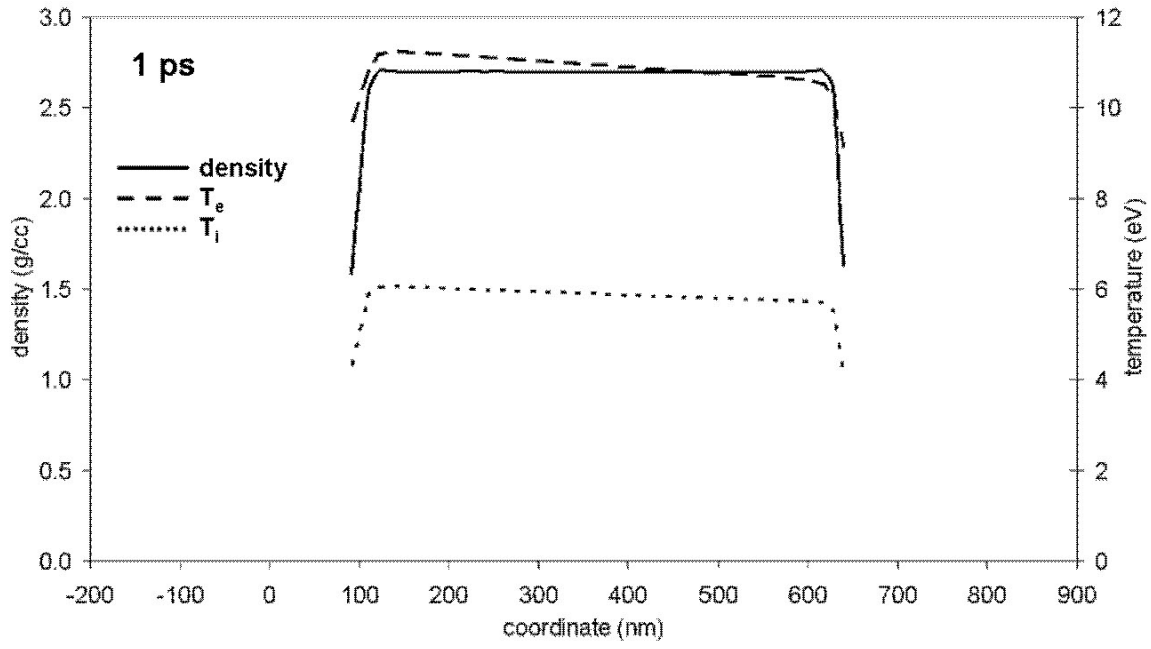


***Figure 6.4.9*** *Density and temperature of an XFEL heated Aluminium foil, 1 ps after heating. The foil is 0.55 µm thick and is heated by 3.1 keV radiation.*

### Proposed experiments

The working group discussed several experimental proposals that would form the core of the initial experimental campaign classified into four broad categories:

- production and diagnosis of WDM;
- High Pressure States (HPS);
- production and diagnosis of HED Matter;
- plasma Spectroscopy (PS).

In the following sections we discuss these proposals. This is not an exhaustive list, giving only a reasonable flavour of the work discussed and proposed.

### I. Warm dense matter experiments

As we saw, in Figure 6.4.9, it will be possible to create samples in the WDM regime, away from the shock Hugoniot. More importantly, they will be uniform well-defined samples. With monitoring of the incident, scattered and transmitted energy, we will obtain a measure of the absorbed energy density, so that meaningful comparison of theory and simulation can be made with experiment.

There will be several measurements that can be performed. If we heat a sample, such as the one depicted in Figure 6.4.9, with the XFEL, the timescale is short enough to give us essentially isochoric heating, depending on the intensity from ~1 eV to well over 100 eV. This will be followed by isentropic expansion, the trajectory for which will depend on the EOS. With a short pulse optical probe laser we can use techniques such as Fourier Domain Interferometry (FDI) **[6-77]** to get a very clear picture of the expansion velocity with time. Optical reflectivity measurements of the surface will be able to determine the conductivity of the sample. With the expansion well characterised and the knowledge that the sample is heated uniformly, the hydrodynamic conditions of density and temperature can be characterised and meaningful comparison to simulations performed.

A unique and productive class of experiment will use the XFEL as both pump and probe. We will separate a portion of the XFEL beam by use of grazing angle reflectors (~0.5° for C at 3keV), allowing us to use a portion of the XFEL beam as a time-delayed probe to measure the x-ray absorption for HDM where there are important effects on the energy level structure of the atoms and ions in the system. For dense plasmas where the strong coupling parameter between ions, $\Gamma_{ii}$, is much larger than unity, these effects are difficult to model theoretically **[6-78]**.

The XFEL is particularly suited to experiments on x-ray Thomson scattering. As the heating of the solid occurs, the electron density and temperature will evolve rapidly. This will affect the spectral signature of the scattering from the free and weakly bound electrons. Obtaining the scatter spectrum with, for example, intensity will be an important test of simulation. A more controlled approach will be to use a pump-probe technique, often by use of an optical laser to generate a preformed uniform sample from a thin foil. The point is well illustrated by Figure 6.4.10, which shows simulated x-ray scattering spectra for a WDM sample. The non-collective scatter is not model-dependent and by looking at both bound and free contributions, the electron density and temperature can be deduced. The forward, collective scatter does depend on whether local field corrections are applied to the free electron contributions. With such data we would be carrying out definitive experiments on fundamental issues in plasma physics, but good data will rely heavily on the availability of a very bright, narrow band x-ray scatter source with short duration, which is why the XFEL so neatly and uniquely fits the bill.

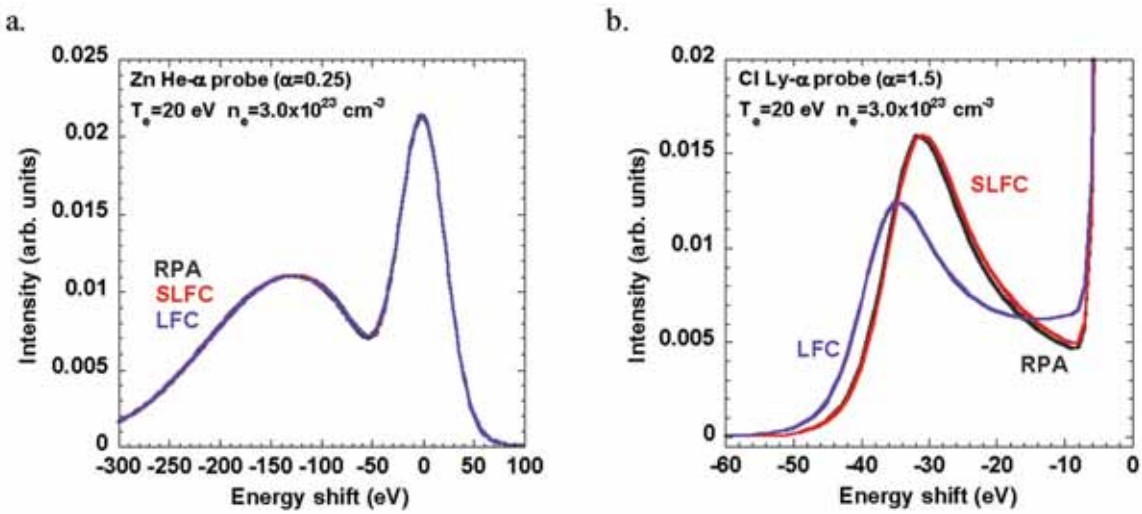


***Figure 6.4.10:*** *Sample x-ray scattering structure factors. In (a) we see that the backscatter case ($\alpha$<1) is not model dependent but can be used to diagnose temperature. The forward (collective regime, $\alpha$>1) scatter (b) is model dependent.*

An important issue in the development of WDM experiments is equilibration **[6-79]**. As it is the electrons that are photo-excited by the absorption of x-rays these will be initially not described by a Maxwell-Boltzmann velocity distribution at a well-defined temperature. They transfer energy to ions via collisions in the matter; in Figure 6.4.9 we see the ions lag behind in temperature when the Spitzer-Brysk electron-ion collision rates are used. However, the use of a simple formulation for the electron-ion collision rate will be incorrect as the bound states of the ion will play a dominant role in the thermalisation process when the density is high and the temperature is low. For example, the sample starts as a solid with a lattice structure and the timescale for the ions to loosen their lattice-like arrangement may be several picoseconds.

One way in which we can probe the microscopic structure of the sample is to use angle-resolved x-ray scattering **[6-80]**. For example, we propose to use the SASE 3 beam at 3.1 keV to heat the sample. There are also second and third harmonics of the beam at about $10^{-3}$-$10^{-2}$ of fundamental intensity. By developing techniques for separating these, it should be possible to pump with the fundamental and probe with the harmonics. Although there are reduced photon numbers in the harmonics this will still be sufficient to provide accurate measurements. Further, the higher energy harmonics reduces absorption so that the scattered signal is not diminished nor does it perturb the sample. In this way, we propose to probe the evolution of the ion-ion structure of the sample as it is heated to WDM conditions **[6-81]**.

### II. Bragg diffraction from surfaces

In particular, HED experiments aim to investigate the interaction of the intense XFEL radiation with the samples. The onset of plasma formation is of importance, however, to other techniques and an in-depth understanding of these processes is a key element in our ability to estimate the damage in optical components. The latest experiments at the

FLASH facility at DESY have shown that a multilayer mirror can still function when irradiated at fluences far exceeding the conventional damage threshold, provided the pulses are short enough so that damage only occurs after the pulse has ended. However, this damage occurs on a single shot. Of particular importance is the investigation of processes by which matter is damaged in a cumulative manner. Recent molecular dynamics simulations by Mazevet et al. **[6-82]** have indicated that when the electrons in a solid are heated to a few eV, the timescale for the ions to move out of a lattice structure is several picoseconds. With the keV photon regime available at the XFEL, the principal mechanism of energy absorption will be inner shell photo-ionisation (the emission from the ions might be used as an observable). Some of the ions evolving from this single photon absorption process may lead to damage. An investigation of the structural processes following absorption of x-ray photons at much higher fluence will provide the necessary input for modelling such single photon damage processes. By comparing intense IR laser and XFEL radiation it will be possible to study the differences in energy transfer to the ions for both types of radiation.

In this proposal the instantaneous change of properties of solid samples irradiated by intense, femtosecond x-ray radiation will be investigated by Bragg diffraction. With sample crystals thinner than the extinction depth, diffraction will be observable, both in Bragg or Laue geometry and, indeed, furthermore, diffuse scattering could also be monitored. Measurements will be carried out as a function of XFEL radiation intensity and time-resolved using split-and-delay techniques of the XFEL beam.

**III. Magnetic field generation and probing**

This project is related to the idea of fast ignitor fusion, in which an ultra-high intensity laser pulse interacts with a compressed fusion pellet and the fast electrons generated ignite the core of the compressed fuel **[6-83]** to achieve ignition with much lower compression (and thus more hydrodynamic stability) than would be achieved with conventional laser-fusion. An important part of this concept is the generation of ultra-high magnetic fields, in the order of 100 T, in the interaction **[6-84]**. These fields are short-lived and exist over a small spatial scale and so are difficult to probe.

It is proposed that, with the XFEL synchronised to an ultra-short pulse (<100 fs) optical laser, capable of intensity $>10^{18}$ W/cm$^2$ on target, the XFEL can act as a probe of the high density plasma regime where the magnetic fields exist. By probing the laser-heated sample with an XFEL beam, the propagation of the electron beam into the solid can be observed. This can be carried out normal to the interaction direction of the optical beam by the use of narrow slab targets. As the electron beam propagates, the ionisation of the solid leads to changes in the refractive index leading to refraction effects that can be measured interferometrically.

With current technology, it is possible to build an interferometer that operates in the keV x-ray regime. Such an instrument would enable interferometric measurements of the electron density in the interaction region, in the same manner as has been achieved optically and in the soft x-ray regime. If a light beam is well polarised, then, on passing through the magnetic field generated, the plane of polarisation can be rotated by the

Faraday effect if the propagation is parallel/anti-parallel to the field direction or by the Cotton-Mouton effect if it is normal to the field. These techniques have previously been used to measure magnetic fields in laser-plasmas with optical probing. With an XFEL we can probe the high density regime well above the optical laser critical density. Further, it is possible that polarisation-dependent absorption changes will be easier to observe in the x-ray signal than a rotation of the polarisation. In this regime, the gradients in the plasma are high and, for example, the $\nabla N \times \nabla T$ magnetic field generation mechanism may lead to very high fields.

### IV. High energy density experiments and plasma spectroscopy

Focusing the XFEL beam to less than 5 µm, will make it possible to reach intensities on target in excess of $10^{17}$ W/cm$^2$. This will make it possible to heat solid density samples to temperatures in excess of 300 eV with pressures in the 1 Gbar range. As for the WDM cases, we can use optical reflection spectroscopy, such as FDI, to diagnose the expansion of the plasma. At this temperature, the emission in the keV photon region can be detected with crystal spectroscopy and we expect to be able to observe some important spectroscopic effects such as line merging and continuum lowering effects on K-shell spectra at very high plasma densities in well defined samples – this latter criterion being most difficult to achieve in present-day laser-plasma experiments. One important type of experiment, not available with any other facility, will be to pump electronic transitions of ions in a dense plasma, making use of the tunable XFEL photon energy. This is illustrated schematically in Figure 6.4.11. and is a very important type of experiment as it will allow the investigation of the effect of plasma environment on transition rates between states. This is something that is expected to be important in the formation of emission spectra, but is, at present, very difficult to include in collisional-radiative models because there are no existing data. In Figure 6.4.12 we can see a simulation carried out assuming an Aluminium target is heated with an IR laser pulse to form a uniaxially constrained plume and at some later time a particular transition is pumped by the XFEL tuned to the transition energy. As the upper state is populated, collisions redistribute the electrons to other bound levels of the Helium-like ion and ionisation forms H-like ions. The rate at which this happens and hence, the resultant spectrum depends on the plasma electron density, which can be determined experimentally.

For this type of experiment to work, it is important that the pumping rate of the transitions during the pulse exceeds the rate of spontaneous decay and auto-ionisation of ~$10^{12}$-$10^{14}$s$^{-1}$. For the high brightness XFEL, radiation pump rates well in excess of this will be possible.

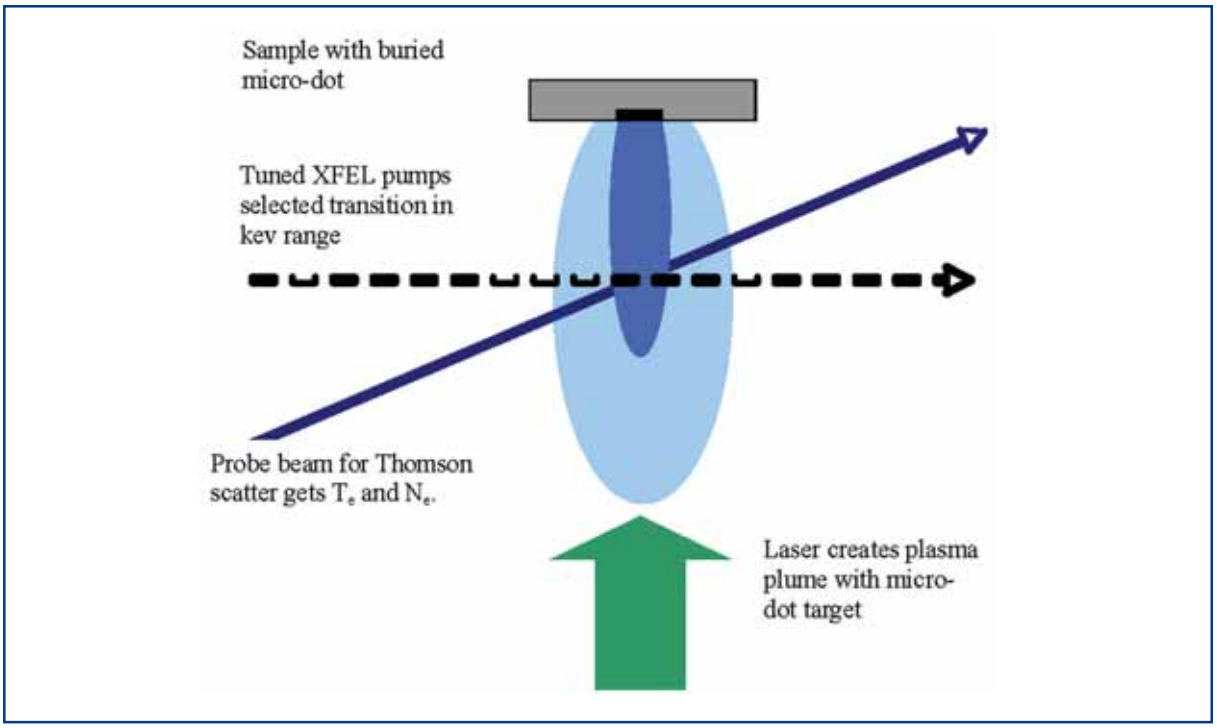


***Figure 6.4.11*** *Experimental arrangement for spectroscopy experiments. The burial of a microdot in a matrix helps to better define the plasma conditions at the time and place of excitation by the XFEL pump. Time- and space-resolved spectroscopy will be used to diagnose the emission.*

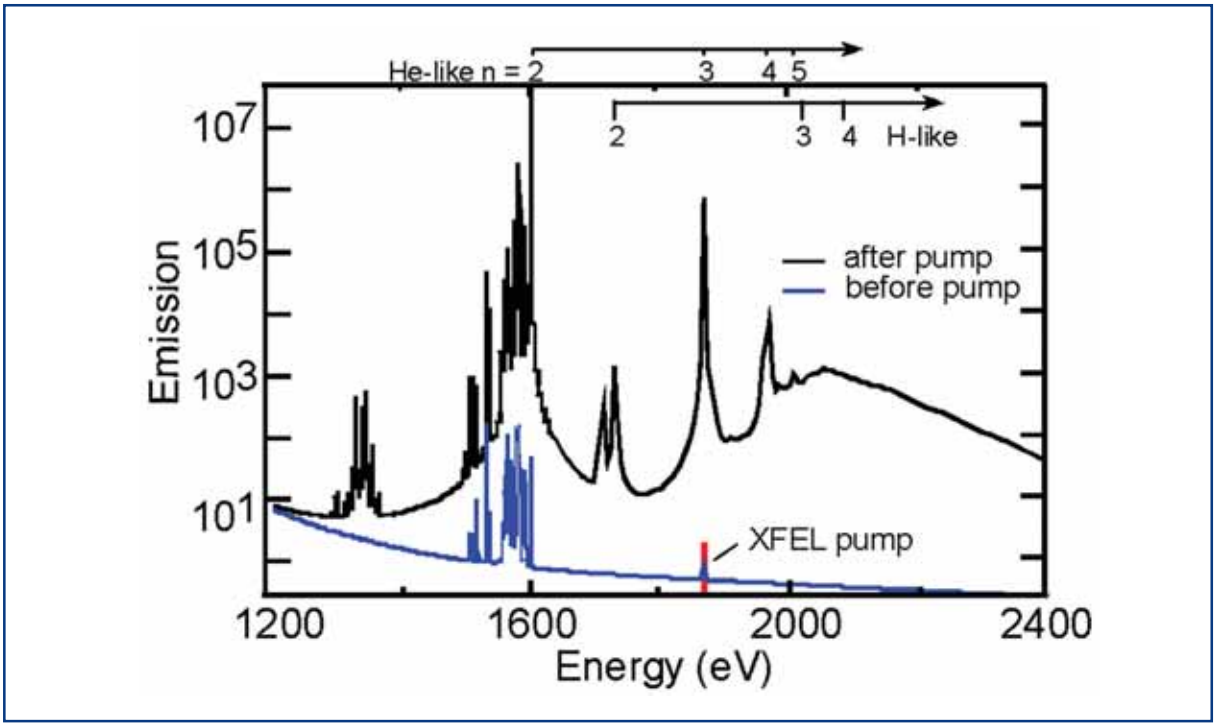


***Figure 6.4.12*** *Simulation of change to emission spectrum for an Aluminium plasma pumped with an XFEL tuned to 1,869 eV in order to pump the Helium-like $1s^2$-1s3p transition.*

### V. Hollow ion emission

The XFEL radiation will enable the creation of hollow ion (HI) states, i.e., atoms/ions with vacancies in the inner core shells, in dense plasmas with atomic population densities more than 10 orders of magnitude higher than in traditional laser-produced plasma experiments. The subsequent x-ray emission, which will escape the extremely high-density plasmas without detrimental absorption, will allow new and innovative studies of atomic systems in intense Coulomb fields and importantly, can form the basis for a diagnostic of the local plasma conditions **[6-85]**.

The simulation of the emission from atoms and ions provides one of the most unambiguous and powerful methods for the understanding of basic phenomena in laboratory and astrophysical plasmas **[6-86 – 6-90]**. An important underlying assumption is that atomic physics is sufficiently well known to accurately predict the spectral signatures. In high-density plasmas, however, particle correlations will alter the statistical mechanics of the free and bound states so that the internal states of the system are dependent on the plasma parameters: Continuum lowering, energy level modification and altered spontaneous transition may occur **[6-91]**. In the extreme case of WDM **[6-92]**, the modifications of the outer bound electrons are so strong, that a perturbative approach for predicting the emission from these shells is not possible. Furthermore, there exists no theory to predict the modification of the internal structure that in the limit leads to complete disappearance, which is mandatory for calculating the corresponding spectroscopy for these extreme states. However, although these extreme states play a role in many high energy density experiments, creating WDM in a manner that can be quantified is not readily available.

X-ray transitions of HIs, i.e., $K^0L^n \rightarrow K^1L^{n-1}+h\nu$, connect the most strongly bound states in these systems **[6-93]**. WDM effects can, therefore, be studied as perturbations to these stable transitions. The basic scheme for a relevant pump-probe experiment is shown in Figure 6.4.11, where a visible laser creates a dense plasma on a picoseconds timescale that is then probed by the 100 fs duration XFEL pulse. The time-dependent simulation of the radiative properties using the MARIA-code **[6-94]** involves population kinetics together with radiation physics. Figure 6.4.13 shows the time-dependent line emission of Magnesium from this pump-probe experiment. Figure 6.4.13 (a) shows a simulation where all processes are included except photoionisation processes from and to the states $K^0L^2$, $K^0L^1M^1$, $K^0L^3$, $K^0L^2M^1$, while Figure 6.4.13 (b) contains all processes.

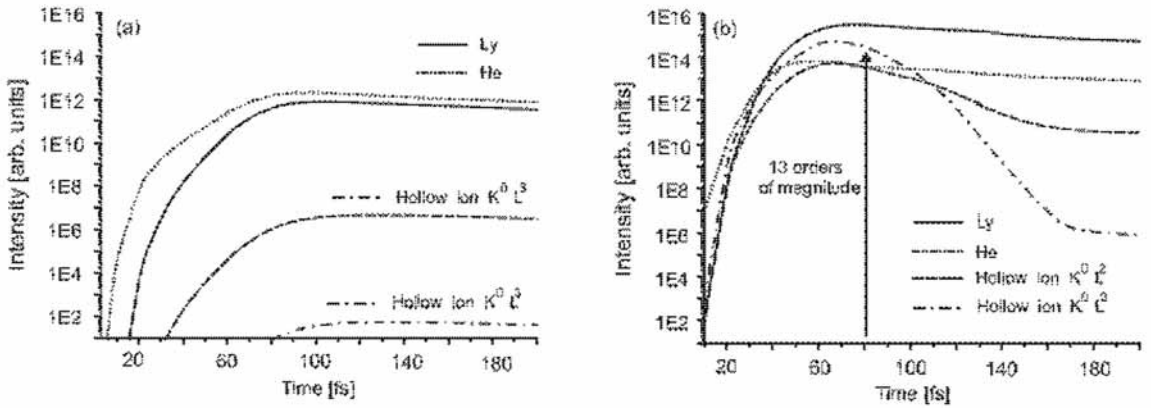


***Figure 6.4.13*** *Simulation of the transient line emission of magnesium ions in a pump-probe driven configuration using the MARIA code* **[6-25]***. The transitions depicted are: Hydrogen-like 1s-2p (Ly$_\alpha$), Helium-like 1s2-1s2p (He$_\alpha$), and the HI transitions $K^0L^2 \rightarrow K^1L^1$, $K^0L^3 \rightarrow K^1L^2$. Parameters for the simulation were: $n_e=10^{21}$ cm$^{-3}$, $kT_e=30$ eV, $L_{eff}=30$ µm, $I=9.2x10^{16}$ W/cm$^2$, $\tau_{XFEL}=100$ fs, $E=3.1$ keV, $\Delta E=6.2$ eV. (a) without photoionisation channels from and to the states $K^0L^2$, $K^0L^1M^1$, $K^0L^3$, $K^0L^2M^1$, (b) with all photoionisation channels.*

The comparison illustrates the essential phenomena: inner-shell photo-ionisations from autoionising levels are the most important channels. Due to large autoionising rates – ~$10^{12}$-$10^{15}$ s$^{-1}$ – the HI states rapidly decay, however, the 100 fs x-ray pulse is sufficiently intense to initiate a chain reaction of inner-shell driven processes before destruction by autoionisation. As can be seen from the Figure 6.4.13 the x-ray pulse increases the HI emission by more than 13 orders of magnitude **[6-85]** to the level of the resonance line intensity (compare with Ly$_\alpha$), which is well known to be observable **[6-95]**. That the x-ray pulse drives a sequence of photoionisation processes efficiently, can be seen from the intensity rise of Ly$_\alpha$. That is, the dominant radiative process from the outer shell is photoionisation: $K^0L^2+h\nu \rightarrow K^0L^1+e$.

We now consider potential diagnostic applications of HI spectroscopy: First, we note that the standard application of Stark broadening for density diagnostics may be difficult as the interaction of intense radiation fields with the ions will result in a strong broadening of line transitions **[6-96]**. In low-density plasmas, this will limit the possible spectral resolution. Indeed, we find that for $I \approx 10^{13}$ W/cm$^2$ considerable broadening occurs, while an intensity of $I=10^{12}$ W/cm$^2$ the spectral resolution is radiation field limited to $\Delta\lambda/\lambda \sim 5\times10^{-4}$. However, it is important that the XFEL pulse initiates HI emissions where the relative intensity of the HI transitions $K^0L^n \rightarrow K^1L^{n-1}+h\nu$ provide information about the electron temperature and <Z> **[6-85]**. This in-situ diagnostic information for the weakly coupled regime also provides time-resolved information in the strongly coupled plasma regime. That the emission is strong only during the XFEL pulse and will have observable intensity indicates that we have a temperature-sensitive diagnostic of HED systems, with a 100 ps temporal resolution. Moreover, compared to usual optical femtosecond-laser pulses, which create hot electrons that effect the radiative properties employed for diagnostics, the XFEL pulse does not create hot electrons as it is in the classical regime with a small parameter $I\lambda^2$ **[6-97]**.

### VI. Radiation hydrodynamics and "forest fire" experiments

Radiation hydrodynamics is a subject of extreme interest in astrophysics **[6-76]**. In recent years, there has been a concerted effort to test ideas about astrophysical plasmas **[6-98]** with experiments in the laboratory, so called laboratory astrophysics. It has been proposed that by focusing a high-power short-pulse optical laser into a gaseous cluster target **[6-99]**, a strong blast wave can be created in which radiation transport may play a key role. It was proposed that if such a target were to be produced, the XFEL beam would be used to modify the parameters by photo-ionisation of the region ahead of the blast wave. The effects on the propagation of the blast wave (for example, the production of various types of instability due to pre-ionisation) would then be a test of the simulations that are naturally complex as they involve hydrodynamics coupled to radiation transport. Such an experiment would require not only a high-power short-pulse for creation of the blast wave but an ancillary probe pulse for carrying optical interferometry of the blast region. Gas jet targets for the creation of cluster targets will also be needed, and the technology is readily available.

One type of experiment that may benefit from the short wavelength and duration of the XFEL is the investigation of so-called "forest fire" phenomena **[6-100]**. This is an effect that is predicted, but experimentally untested. It should occur when a dielectric is exposed to a high intensity optical pulse of only a few cycles duration – perhaps a 10 fs IR pulse. The usual avalanche mechanism of ionisation; where multi-photon ionisation free a few "seed" electrons, absorb energy by inverse *Bremsstrahlung* and then, when they are energetic enough, ionise further electrons across the band-gap, cannot occur on such a short timescale. Despite this, it is seen (**6-87**, and references cited therein) that the refractive index of dielectrics such as fused Silica, can be altered permanently by pulses of 30-50 fs at intensities well below the expected threshold.

The "forest fire" idea is that ionisation is enhanced locally when an electron is initially removed from a nucleus, for example, in a rare gas cluster under IR laser irradiation. What is predicted to happen is that, in the so called "tunneling regime" when the ionisation potential, $I_p$, is much smaller than the ponderomotive potential, $U_p$, the tunneling rate for electrons to escape is proportional to $\exp(1/E_0 \cos\omega t)$, where $E_0$ is the amplitude of the electric field applied by the laser. If the electric field due to a "hole" created by initial removal of an electron is added, we see an exponential enhancement of the ionisation rate locally.

It is then predicted that small "islands" of ionisation will form and spread in a manner reminiscent of forest fires – hence the name. The spatial scale will be sub-micron and thus, it will be suitable to use the XFEL as a probe of the microscopic structure by, for example, angularly resolved Mie scattering from clusters.

### VII. High pressure states of matter

Our current understanding of the fundamental physics of shock compression in condensed matter is still far from complete. Over the past few years there has been some progress made by using nanosecond sources of x-rays to probe crystals compressed using high-power optical lasers **[6-101]**, however the ultimate time-scales of the essential physics of

interest – i.e. phase transformation, dislocation generation and flow, and plastic relaxation, occurs on the picosecond, or sub-picosecond level: a regime that can only be accessed by the XFEL. Thus, there is still a long way to go in developing this understanding. The XFEL provides a unique source for such experiments. With keV photons in a well collimated beam, it is ideally suited to probing shocks driven by optical lasers.

What we propose is that a nanosecond laser with ~100 J per pulse is used to generate shocks in single-crystal solid samples (e.g. single crystals of Copper to study plasticity (as there is no phase transition before shock-melt), Iron to study shock-induced Martensitic transitions, Lead to study shock-melting, etc). Optical reflection techniques such as Velocity Interferometry System for Any Reflector (VISAR) can be used to diagnose the shock speed and particle velocity on exit of the shock, thus providing traditional Hugoniot data. The XFEL beam will provide a means to probe the structure of the material after compression in the bulk of the sample. The excellent time resolution available will allow the observation of changes in structure due to phase changes to be recorded in unprecedented detail, and, importantly, on a timescale shorter than a phonon period. For example, the $\alpha$-$\varepsilon$ phase transition in Iron (body-centred cubic to hexagonal close-packed) has been observed in laser-shocked sample **[6-102]**. Molecular dynamics simulations suggest this occurs in ~1 ps timescale, longer than the XFEL pulse duration, but far shorter than the resolution that laser-plasma sources afford. The high flux of the XFEL beam will allow not only the traditional Bragg diffraction peaks to be observed, but the small angle and diffuse scattering (for example, from stacking faults) will be observable, adding more detail to our picture of materials under pressure and high strain rates. In particular, we believe it will be possible to directly measure stacking fault densities during shock compression, something that has hitherto been unobtainable, despite the fact that high transient dislocation densities are thought to be the means by which plastic deformation can occur on such short time-scales. In Figure 6.4.14(a) we see an example of an experiment that can be used to determine directly the compression profile in a shock wave. The spatial coherence of the source will be evident in features caused by refraction in the very steep gradients of the shock front. Some sample data using laser produced x-ray sources is seen in Figure 6.4.14(b.). With an XFEL, unprecedented temporal resolution will allow the compression, speed of the shock, and with VISAR, the particle velocity to be determined simultaneously. With pulse shaping capability added, it will be possible to investigate isentropic compressions as well as shock Hugoniots.

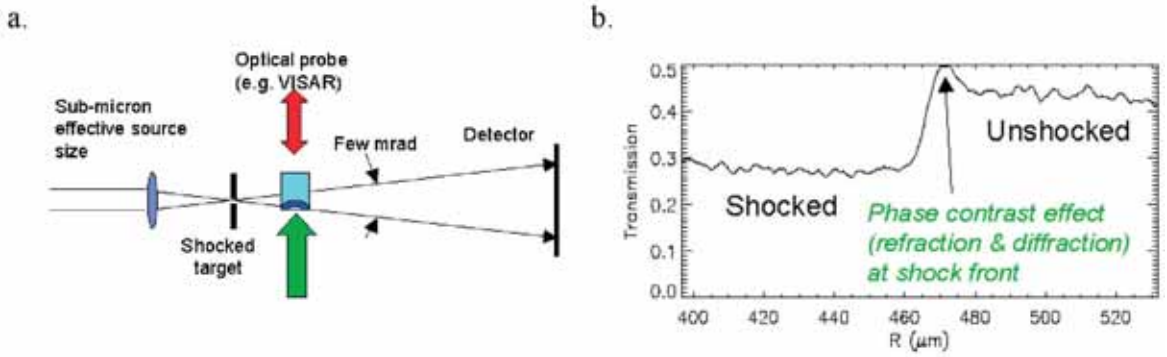


***Figure 6.4.14*** *Schematic of shock wave probing experiment (a). (b) shows a point projection profile of a shock front taken with a 10 micron x-ray source. Phase contrast effects are evident at the shock front. Using spatially coherent XFEL radiation, phase contrast effects will provide more information.*

### *6.4.2.2 Instrument requirements*

From the specific needs of the experiments described above the main requirements for an instrument for investigation of HED matter can be derived. They concern the performance of the light source, the diagnostic equipment of the beamlines and their infrastructure. The experiments described in this section require tunable XFEL radiation of a relatively wide spectral range from ~0.6 to 12 keV. None of the European XFEL beamlines provides the entire photon energy range in the fundamental and the use of SASE 2 and SASE 3 beamlines is proposed instead.

**Spectral radiation properties**

Experiments in this field ask for nearly the entire photon energy range provided at the European XFEL Facility. Whereas the lower photon energies will mainly be used in experiments investigating the interaction of intense radiation with matter (Experiments I., III. and IV. above), the request for hard x-ray radiation follows from the needs in diffraction experiments to investigate structural properties of plasmas following laser heating or pressure shocks (Experiments IV. and V.). Also, plasma diagnostics using Thomson scattering techniques will benefit from higher photon energies (Experiments I. and IV). Real tunability is required in the plasma spectroscopy and hollow ion experiments where specific transitions will be investigated (Experiments VI. and V.). For these experiments, a range from 0.65 to 6.5 keV has been requested. In most experiments the natural bandwidth of XFEL radiation will be sufficient. Even for spectroscopy purposes this resolution should be sufficient, so that no monochromators are requested. Reduction or selection of higher order harmonics is a different topic that requires attention for these experiments. Higher harmonic content may be reduced to reasonable values using mirror cut-offs. Selection, however, requires spectral dispersion using gratings, i.e., for the soft x-ray regime, or very thin crystals in transmission geometry. Whereas the soft x-ray case has been investigated already, a separation of hard x-rays will require some R&D.

### Beam dimensions

The requested x-ray beam size is determined, in most cases, by required intensity and the combination with visible laser beams. Typical beam sizes at the sample position are 1, 10, or 100 µm to reach the different intensity levels. If experiments use visible laser imaging or excitation, one has to take the spatial resolution of the visible laser beam of a few microns into account. Focusing below 1 µm will further enhance the available intensity, but diagnostics of such sub-micron plasmas will be extremely challenging.

### Time domain requirements

These experiments will fully exploit the 100 fs time structure of XFEL radiation. It is, however, expected that the substructure of the pulses will not influence the excitation and probing processes. Since the HED experiments are usually destructive, such that the sample evaporates after being irradiated by the XFEL beam or the high-intensity visible laser beam, sample replacement is expected to be a time-determining parameter (see below). Synchronisation is generally linked to the use of visible lasers and will be discussed in the corresponding section. However, a synchronisation of ~100 fs will be required for the operation of x-ray streak cameras (XSC).

### Photon diagnostics requirements

All experiments will need good diagnostic equipment to measure the photon beam intensity on a pulse-to-pulse basis. To estimate the intensity in $W/cm^2$ at the sample with a high degree of confidence, one must also consider the measurement of the pulse duration and of the spatial properties at the focus. The spectral diagnostics should provide the mean photon energy and the content of higher harmonic radiation. All measurement must be available on a pulse-to-pulse basis.

### Sample manipulation and environment

Samples are thin foils of varying materials for the WDM experiments, thicker slab-like samples varying materials for the HDM and higher pressure experiments, and gas jets for the radiation hydrodynamics experiments. Many of the proposed experiments will require multiple shots to be taken, both to gather a scan of a particular parameter (for example, intensity on target) and to collect sufficient signal photons in experiments where the signal may be weak (for example, scattering). In the case of solids it will be necessary to move the sample to expose a fresh surface. Using the repetition rate of 1-10 Hz for the XFEL, we will need to be able to move the sample quickly but also maintain the alignment, in particular the focal spot size in the case where tight focusing onto target is required. It is possible to design automated systems that use a three-point triangulation in 3-D to define the plane in which a flat foil sits **[6-103]**. It can then move the foil automatically to maintain the exposed part at a fixed focal plane for the incident beam. The only constraint is that the system assumes that the surface is flat. It is clear that, depending on the nature of the experiment, some methods of moving targets into position and monitoring their position relative to the focal plane of the XFEL and/or the optical laser systems will need to be developed.

A capability for insertion of fresh targets without breaking vacuum will also be required. For some experiments, the presence of surface contaminants, such as oxide layers, will be undesirable as they may modify the interaction with the XFEL or the optical probe laser (as in FDI **[6-77]**). Since oxide layers can form very rapidly, some target preparation facilities close to the target area will be needed. Potentially target "cleaning" may need to be carried out in-situ, e.g. low fluence ablation of the top layers or RF cleaning (as sometimes used for compression gratings in laser systems **[6-104]**). In these experiments differential pumping is required to improve experiments vacuum against beamline vacuum.

**Detector requirements**

It is clear that x-ray spectroscopy plays a significant role in several experiments, i.e., in the class of experiments proposed above under Topics I., III., IV., and V., and it makes sense to have common facilities. High resolution x-ray spectrometers based on crystals are available with resolutions from ~$10^3$ to in excess of $10^4$. In order to achieve high signal fluxes with single shot, one should employ either spherically or toroidally curved crystals **[6-105]** which will have a high flux gathering power and, in addition, can be used for imaging of the plasma where appropriate. These crystals should be coupled to CCD detection systems that are efficient in the keV x-ray region and have good pixel resolution of ~10 µm. Detectors with 2K×2K pixels are commercially available, but frame rates larger than 10 Hz for 16-bit dynamics should be targeted. In the keV photon region this gives single photon detection capability.

Furthermore, emission in the XUV regime will be of interest for the same group of experiments. There are high efficiency XUV spectrometers that operate with variable line-space gratings to give a flat field of spectral focusing suitable for use with a back-thinned CCD as detector **[6-106]**. These spectrometers can operate in the 300-2,000 eV regime and can achieve spectral resolutions up to ~$10^3$.

If small single-pulse signal levels are expected, integration over more than one pulse may be required. In these cases, the background noise of the CCD detectors will limit the signal-to-noise ratio if one does not cool the CCD chip. This can be done fairly routinely to 80°C. However, if the CCD sits inside the vacuum, as is often the case, cooling using water or cold gas is required. There is also a problem of condensation, of ice or hydrocarbon, onto the chip that may cause damage, so it is essential to prevent this. The use of "cold fingers" with liquid Nitrogen ($N_2$) as a coolant prior to cooling the chip, may serve to "clean" up the vacuum by causing condensation onto the "cold finger".

To allow time-resolved investigation of emission, e.g. in Experiments I., IV., and V., the use of streak cameras is proposed. Using these detectors it is important to improve the time-resolution, efficiency and stability of these systems. The required R&D work of ultrafast XSCs will be described in Section 6.5.4.

**Visible laser requirements**

Many of the experiments outlined in this section make use of optical laser pulses synchronised to the XFEL beam. In some experiments, the optical pulse is used either to

generate a sample to be probed or pumped by the XFEL, e.g. in III., IV., V., VI. and VII.; in others it is the optical pulse that probes the XFEL generated sample, e.g. in I. and IV. The required lasers can be distinguished by their energy. For probing XFEL-generated plasmas, ultra-short pulses (~30 fs) with energy of about 10 mJ are required. Operated at 1 to 10 kHz, this laser system can also be used for high-order harmonic generation (HHG) radiation. High contrast of ~$10^{10}$ between the main pulse and ASE emission is required for "clean" interaction with the sample.

For experiments where the optical laser pumps the sample on ultra-short timescales, a sub-100 fs laser with energy capability of 10 J per pulse will be desirable. This is possible using the same laser front-end as for the above system, but with a much reduced repetition rate of ~10 Hz **[6-107]**. Basically, the difference would be additional amplifier stages. The beam size is likely to be 5-10 cm diameter and focusing off-axis parabolas will be required to focus to >$10^{19}$ $Wcm^{-2}$. An important requirement will be suppression of pre-pulses, as ASE and non-linear chirp components would deposit energy onto the surface prior to the main pulse. A viable method to reach this suppression has been conversion to second harmonic requiring large area (5-10 cm diameter) second harmonic crystals with sub-mm thickness and high optical quality.

The third system would deliver up to 100 J sub-nanosecond pulses at 10 Hz repetition rate for generation of shocks in condensed matter as proposed in Section 6.4.2.1, Experiment VII. above. A fibre front-end is desirable to shape the pulse in order to optimise the pressure front. This technology currently exists and adaptive optics can be used to ensure a good quality of beam profile. This is important if uniform conditions are to be generated over a focal spot away from tight focus. To this end, beam relay optics and smoothing technology (eg phase ZPs) will be required. It may be possible that the requirements for sub-100 fs and sub-nanosecond can be fulfilled by a single laser system. Current chirped pulse amplification (CPA) technology, used to generate 30 fs pulses, requires the laser to generate a 'stretched' pulse of sub-nanosecond duration. If this is used as the long pulse option, all that is required subsequently is amplification to high energy. However, since versatility should be maintained and noting that, for some experiments, both types of beam will be required simultaneously, it is currently considered better to have the two systems independent of each other. In addition to the operational aspect, it is unlikely that two dedicated systems are more expensive than a single system capable of doing everything.

The optical lasers providing sub-100 fs pulses require precise synchronisation with the FEL beam in the order of ~10 fs. If such synchronisation will not be possible, diagnostic tools to measure the time delay to similar accuracy are required.

### *6.4.2.3 Realisation of the instrument*

From their requirements, the HED experiments require two instruments: one at SASE 3 (HED 1 – Tunable soft x-rays) and the other at SASE 2 (HED 2 – Tunable hard x-rays). The SASE 3 beamline enables experiments at photon energies up to 3,100 eV. Those experiments requiring higher photon energies, i.e. 3.1 to 6.5 keV for HI spectroscopy and ~12.4 keV for diffraction measurements in proposals I., II., IV., and VII. will be best placed

at the SASE 2 beamline. For both instruments additional monochromatisation is not necessary and beam transport using mirrors only will be considered. The corresponding beam transports in the SASE 2 and SASE 3 beamlines have been described in Section 6.2.4.2 and 6.2.4.3, respectively. Both instruments will require focusing the XFEL radiation. Moderate focusing to beam sizes in the order 100 µm is achieved by using a focusing element near the location of the off-set mirrors. Further focusing to 10 µm and smaller beam sizes will be integrated in the instruments and is described below. An important requirement of the design of the SASE 3 beamline is the ability to carry out pump-probe experiments using first and third harmonic radiation. This requires the transport of radiation with photon energies as high as 9.3 keV to the experimental hall. Due to the cut-off by the mirrors (operating at 10 mrad grazing angle at SASE 3), a set of different mirrors is likely to be required here. For SASE 2 this requirement applies only to the lowest photon energies of 3-4 keV.

**HED 1: Tunable soft x-rays**

Two mirrors at a grazing angle of the order 10 mrad will be used to deflect the beam away from the forward beam direction. At the chosen sample location inside the experimental hall, a focal spot size of the x-ray beam of ~100 µm will be available. This focus is achieved by using one of the offset mirrors. To enable focusing in the order 10 µm, it is proposed to use one of the beam deflection mirrors with a demagnification of 20. For micron or sub-micron focusing, special optics need to be employed that are positioned very close to the sample, providing a demagnification of 100 or higher. The HED 1 instrument will be required to carry out a large part of the experiments investigating the interaction of intense high energy radiation with matter described in Section 6.4.2.1, I., III., IV., and V. In addition to x-ray emission, many of these experiments use optical diagnostics.

The following elements belong to the HED 1 instrument inside the experimental hall. They are also depicted in the schematic layout of that instrument in Figure 6.4.15 and are listed in Table 6.4.3. Collimating apertures in front of the experimental chamber remove scattered radiation from the beam. A gas photon flux monitor (see Section 6.3.2.1) will follow before a differential pumping section separates the beamline from the UHV vacuum chamber for experiments. Given the energy range of this beamline, vacuum separation by means of windows is very unlikely.

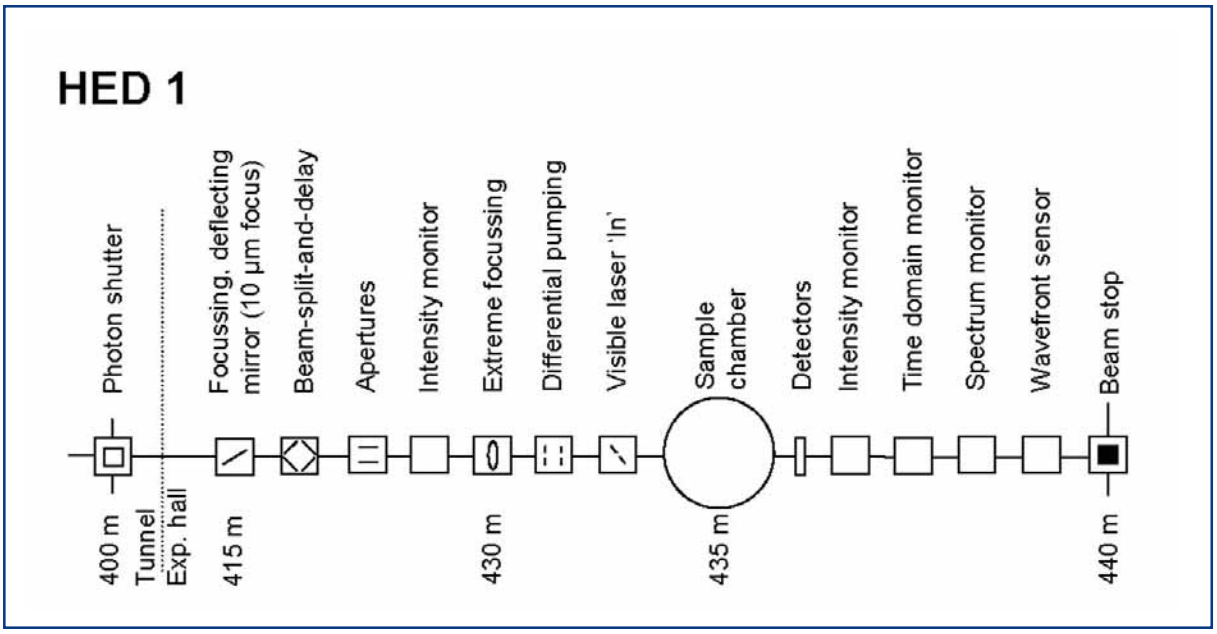


***Figure 6.4.15*** *Schematic layout of the HED 1 station, intended to be located at the SASE 3 beamline. The beam is directed straight to the sample chamber. Various focusing options will be available.*

The sample chamber will be equipped with a high-accuracy sample manipulator allowing x-y-z movements and rotation around two perpendicular axes. The chamber has to be capable of reaching $10^{-8}$ mbar for experiments sensitive to surface contamination. Sample loading from external chambers needs to be accommodated. For experiments using high target densities of up to $10^{22}$ $cm^{-3}$ and high background pressure, sufficient vacuum pumping power will be necessary.

Most experiments will use photon detection by x-rays or visible light. However, particle detection using mass spectroscopy of neutral particles and electron TOF techniques should also be possible. The most important photon detection technique is x-ray emission. A variety of scattering angles should be realisable by the vacuum chamber design, in particular one needs to implement spectrometers that can observe in both a forward and backward direction, relative to the XFEL propagation, to perform detailed balance measurements. Due to the horizontal polarisation the vacuum chamber design should allow horizontal and vertical scattering.

Experiments can absorb significant fractions of the incident beam intensity. It is, however, intended to place most photon beam diagnostics in the transmitted beam. A second gas monitor detector will be used to measure the transmission. The spectral measurement should provide mean photon energy, bandwidth, and higher harmonic content on a pulse-by-pulse basis. Measurement of the detailed spectral, i.e. the width and distribution of spikes, is performed upon request only. Diagnostics of time domain properties should provide the arrival-times of the XFEL and the visible laser required for pump-probe experiments using the visible laser. Finally, spatial measurements must be made to determine the beam location and its spatial distribution. Since these spatial measurements are usually destructive, they will be carried out on a dedicated set-up at the end of the beamline and before the beam stop.

| Item | Purpose | Specification |
|---|---|---|
| Deflection mirror | Beam separation from straight line, deflection angle 20 mrad, focusing to ~10 µm (optional) | 0.1 µrad angular stability, 0.3 µrad figure error, 0.1 nm surface roughness |
| Beam-split-and-delay | Beam splitting (first/first; first/third), delay (first and third) | First harmonic in (un)equal parts, First/third separation, $-10^2$-$10^6$ fs adjustable delay |
| Focusing optics | ≤1 µm focusing for 0.8-3.1 keV | 0.1 µrad angular stability |
| Slits/apertures | Beam definition, beam halo cleaning | 1 µm accuracy, 0.25 µm repeatability |
| Intensity monitor | Measurement of incident photon flux | Transmissive (<5% absorption), single pulse measurement, relative accuracy $<10^{-3}$ |
| Differential pumping | Separation of beamline and experiments vacuum | $10^4$ step for all elements |
| Laser inlet | Port to couple visible laser radiation into experimental chamber | Mirror with central hole, retractable |
| Sample chamber | Sample positioning and orientation, systems to verify sample alignment, prevision of sample preparation, preparation for high gas loads, mounting of detectors | x-y-z move (0.25/1 µm), two rotations (0.25/1 mdeg), optical microscope, UHV conditions, high pumping speed |
| Detectors | Angle-, space-resolved x-ray emission | XUV – x-ray ranges, high efficiency, no scanning spectrometers |
| X-ray streak camera | Time-resolved detection | XUV – x-ray ranges, time resolution ~100 fs, stable, highly efficient |
| X-diffraction detector | Bragg diffraction and diffuse scattering from third harmonics (9.3 keV) | 2-D detector, 1K×1K |
| Intensity monitor | Measurement of incident photon flux | Transmissive (<5% absorption), single pulse measurement, relative accuracy $<10^{-3}$ |
| Spectral monitor | Measurement of mean energy, bandwidth and harmonic content | Single pulse measurement, relative accuracy $<10^{-3}$ |
| Time monitor | Measurement time domain properties | Single pulse measurement |
| Spatial monitor | Measurement of spatial distribution, focus size | Single pulse measurement |
| Alignment unit | Positioning and position verification | Permanently operating, accuracy ~100 µm |
| Lead hutch | Radiation protection, temperature stabilisation, laser protection | 5×12×3 $m^3$ (W×L×H), ± 1° thermal stability |
| Control hutch | Operation of the instrument | Working environment (Noise, temperature, light) |

***Table 6.4.3*** *Elements and specifications of the HED 1 instrument.*

The availability of very intense visible laser radiation will form a critical boundary condition for HED 1. Receiving beam from the independent laser room the laser will be coupled into the vacuum in front of the sample chamber. Using mirrors with a central aperture the laser beam can propagate collinear with the XFEL beam. Further, input ports are needed for experiments where the visible laser is used as a diagnostics tool.

**HED 2: Tunable hard x-rays**

The HED 2 instrument will bear a strong resemblance to HED 1, the difference being that it is positioned at SASE 2 and is designed for hard x-rays. This instrument will be required for the part of the experimental programme to investigate the structural response of matter following deposition of energy and during the formation of plasmas described in Section 6.4.2.1, Experiments I., II., IV.,VI. and VII. In addition, the investigation of HIs (Section 6.4.2.1, Experiment V.) extends into the hard x-ray range.

Since mirrors provide only shallow deflection angles in the order 4 mrad, a gallery of two mirrors is proposed to generate a reasonable offset from the straight beam. These are installed in the photon beam transport section inside the tunnels. Using the SASE 2 beamline lens system, a focal spot size of the x-ray beam of ~100 µm will be available in the experimental hall. Focusing in the order of 10 µm can be achieved by using a compound refractive lens about 100 m in front of the experiment. For micron or sub-micron focusing, special optics need to be employed positioned approximately 5-10 m upstream of the sample chamber, thus providing a demagnification of 100 and higher.

The following elements belong to the HED 2 instrument inside the experimental hall. They are also depicted in the schematic layout of that instrument in Figure 6.4.16 and are listed in Table 6.4.4. Collimating apertures or a slit system will be placed in front of the experimental chamber to remove scattered radiation from the beam.

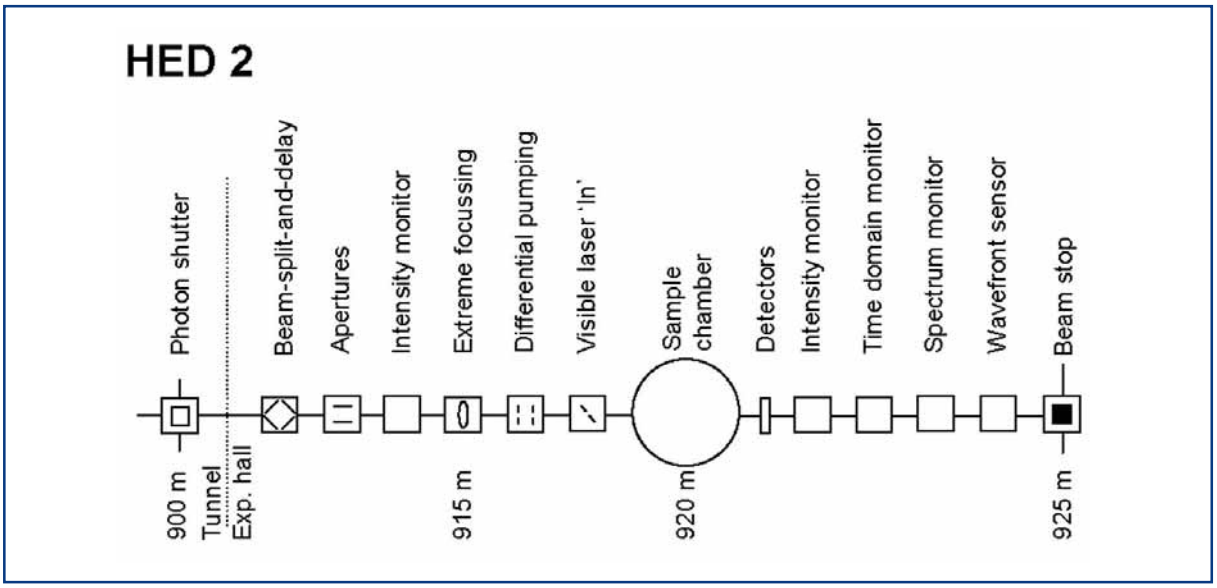


***Figure 6.4.16*** *Schematic layout of the HED 2 station, proposed to be located at the SASE 2 beamline. The beam is directed straight to the sample chamber. Various focusing options will be available.*

| Item | Purpose | Specification |
|---|---|---|
| Deflection mirror | Beam separation from straight line, deflection angle 12 mrad achieved by 4-mirror gallery | 0.1 µrad angular stability, 0.3 µrad figure error, 0.1 nm surface roughness |
| Beam-split-and-delay | Beam splitting (first/first; first/third), delay (first and third) | First harmonic in (un)equal parts, First/third separation, $-10^2$-$10^6$ fs adjustable delay |
| Focusing optics | ≤1 µm focusing for 3.1-12.4 keV, (e.g. CRL system with variable lens number) | 0.1 µrad angular stability |
| Slits/apertures | Beam definition,beam halo cleaning | 1 µm accuracy, 0.25 µm repeatability |
| Intensity monitor | Measurement of incident photon flux | Transmissive (<5% absorption), single pulse measurement, relative accuracy $<10^{-3}$ |
| Differential pumping | Separation of beamline and experiments vacuum | $10^4$ step for all elements |
| Laser inlet | Port to couple visible laser radiation into experimental chamber | mirror with central hole, retractable |
| Sample chamber | Sample positioning and orientation, systems to verify sample alignment, prevision of sample preparation, preparation for high gas loads, mounting of detectors | x-y-z move (0.25/1 µm), two rotations (0.25/1 mdeg), optical microscope, UHV conditions, high pumping speed |
| Detectors | Angle-, space-resolved x-ray emission | XUV – x-ray ranges, high efficiency, no scanning spectrometers |
| X-ray streak camera | Time-resolved detection | XUV – x-ray ranges, time resolution ~100 fs, stable, highly efficient |
| X-diffraction detector | Bragg diffraction and diffuse scattering (3.1-12.4 keV; possibly third harmonics) | 2-D detector, 1K×1K |
| Intensity monitor | Measurement of incident photon flux | Transmissive (<5% absorption), single pulse measurement, relative accuracy $<10^{-3}$ |
| Spectral monitor | Measurement of mean energy, bandwidth and harmonic content | single pulse measurement, relative accuracy $<10^{-3}$ |
| Time monitor | Measurement time domain properties | Single pulse measurement |
| Spatial monitor | Measurement of spatial distribution, focus size | Single pulse measurement |
| Alignment unit | Positioning and position verification | Permanently operating, accuracy ~100 µm |
| Lead hutch | Radiation protection, temperature stabilisation, laser protection | 5×12×3 $m^3$ (W×L×H), ± 1° thermal stability |
| Laser hutch | ~100 J, sub-ns laser system | 5×12×3 $m^3$ (W×L×H), ± 1° thermal stability |
| Control hutch | Operation of the instrument | Working environment (Noise, temperature, light) |



***Table 6.4.4*** *Elements and specifications of the HED 2 instrument.*

An x-ray gas photon flux monitor (see Section 6.3.2.1) will follow before a differential pumping section separates the beamline from the UHV vacuum chamber for experiments. For the energy range of this beamline, vacuum separation by means of windows may be possible and needs to be investigated.

The sample chamber will be equipped with a high-accuracy sample manipulator allowing x-y-z movements and rotation around two perpendicular axes. Since hard x-rays probe the bulk, these experiments are intrinsically less sensitive to surface contamination than the ones at HED 1; however, the chamber should be capable of reaching $10^{-8}$ mbar. For experiments using high target densities of up to $10^{22}$ $cm^{-3}$ and high background pressure, sufficient vacuum pumping power will be necessary. Most experiments will use photon detection by x-rays or visible light. The most important photon detection techniques are x-ray emission and diffraction in forward direction. For x-ray emission, a variety of scattering angles should be realisable by the vacuum chamber design, in particular, one needs to implement spectrometers that can observe in both a forward and backward direction, relative to the XFEL propagation, to perform detailed balance measurements. Due to the horizontal polarisation, the vacuum chamber design should allow horizontal and vertical scattering. For diffraction experiments, forward scattering will be most important and 2-D detectors will be particularly important for diffuse scattering experiments.

Experiments can absorb significant proportions of the incident beam photon flux. It is, however, intended to place most photon beam diagnostics in the transmitted beam. A second gas monitor detector will be used in transmission geometry upstream of the sample to measure the incident photon flux. The spectral measurement should provide mean photon energy, bandwidth, and higher harmonic content on a pulse-by-pulse basis. Measurement of the detailed spectral properties, i.e. the width and distribution of spikes, is performed upon request only.

Diagnostics of time domain properties should provide the arrival-times of the XFEL and the visible laser required for pump-probe experiments using the visible laser. Finally, spatial measurements must be made to determine the beam location and its spatial distribution. Since spatial measurements are usually destructive they will be carried out in a dedicated setup at the end of the line and before the beam stop.

The availability of very intense visible laser radiation will form a critical boundary condition for HED 2, as it does for HED 1. Receiving beam from the independent laser room the laser will be coupled into the vacuum in front of the sample chamber. Using mirrors with a central aperture the laser beam can propagate collinear with the XFEL beam. Further, input ports are needed for experiments where the visible laser is used as a diagnostics tool.

### 6.4.3 Coherent X-ray scattering and lensless imaging in materials science

Most of the material presented in this section is derived from the discussions in the working group “Imaging, Phase Retrieval and Image Reconstruction” at the Workshop on Diffraction, Crystallography and Imaging at the European XFEL, which took place on October 28 and 29, 2005 at DESY.

### *6.4.3.1 Scientific case*

Coherent x-ray Diffraction Imaging (CXDI) is a rapidly advancing form of lensless microscopy that was opened up by the realisation that oversampled diffraction patterns can be inverted to obtain real-space images. The possibility was first pointed out by D. Sayre **[6-108]** but not demonstrated until 1999 by Miao et al. **[6-109]**. The phase information of the diffraction pattern, which is lost in its recording, is embedded in a sufficiently oversampled diffraction pattern, because this is intimately related to the Fourier transform of the object under investigation. The inversion of diffraction back to an image has been proven to be unique in two or higher dimensions, except for "pathological" cases of internal symmetry of the object or its diffraction pattern **[6-110, 6-111]**. Computational methods of performing the inversion, under very general constraints (for example, finite support of a sample, positivity of electron density, etc.) are an active area of development; they are often based on the iterative Hybrid Input-Output (HIO) method introduced in the 1980s by Fienup **[6-112]**.

Lensless imaging using coherent x-rays is an attractive alternative to electron microscopy because of better penetration of the electromagnetic waves in materials of interest; also, multiple scattering effects can be neglected, so that the first Born approximation can be safely used. In many cases, x-rays are less damaging to the sample than electrons and, in either case, the collection of a diffraction pattern is inherently more efficient than the use of lenses **[6-113]**. If the diffraction can be reliably inverted by computation, the method could be routinely used to reveal the structure of materials on the nanometre scale, far beyond the resolution of the traditional light microscope. The holographic method of combining a reference wave is an alternative way to perform the inversion **[6-114]**.

Lensless imaging is also well suited to the unique capabilities of the XFEL. According to recent theoretical calculations **[6-115]**, the incoming beam will have nearly full transverse coherence (80% transverse coherence, with a beam of a few $mm^2$ section; see also Section 5.2.2). Other unique properties of the XFEL, such as the high peak brilliance (we expect $10^{12}$ coherent photons in a single pulse) and ultra-short pulse time structure (100 fs pulses separated by 200 ns), allow us to consider applications of CXDI to structural analysis of nanometre-scale particles, inaccessible using third-generation undulator sources. The opportunity to study dynamics at such resolutions and on the sub-picosecond timescale with the XFEL, opens up entirely new research horizons.

In the last few years we have witnessed rapid development of CXDI techniques. Our experience is based, at the moment, on experiments that utilise the coherence properties of third generation synchrotron sources. The coherent scattering volume at these sources is mainly determined by the source size and distance from the source and is, typically, about 10 µm in the horizontal direction and 100 µm in the vertical direction for 10 keV x-ray energy and 50 m downstream from the source. The longitudinal coherence length is determined by the available monochromator and can reach ~1 µm. The coherent flux is determined by the brilliance of the storage ring and is typically $10^{12}$ ph/s in the pink beam. First, a very short overview of the results obtained using CXDI at these sources will be presented, and then some possible future experiments and the necessary technical requirements for the XFEL will be discussed.

### Present status – Limitations at third generation sources

At the moment, the development of coherent x-ray scattering can be divided into two distinct parts: One is based on Bragg scattering of the incoming coherent beam on small crystals; the other is using the forward scattering geometry for non-crystalline objects. Both applications have their own advantages and limitations. In the case of Bragg diffraction, scattering angles are typically far away from the direct beam, so the whole diffraction pattern can be measured without the need of a beamstop, and there is no contribution from the beam-defining slits in the recorded diffraction pattern. On the other hand, scattering from non-periodic objects can be done only in the forward scattering geometry, making the use of a beamstop in front of the detector unavoidable. As a result, there is a certain amount of missing information in the reciprocal space for small q-values in this scattering geometry. Using the Bragg approach, it is easier to scan a sufficient region of reciprocal space with a 2-D detector to fully obtain 3-D information about the object. This can be done, for example, by fine angular scans near Bragg peak or by energy scans. In the case of scattering from non-crystalline objects, 3-D reconstruction is performed by measuring several diffraction patterns at different projection angles as in tomography and then reconstructing the object by iterative methods.

The following examples show that coherent x-ray diffraction of small crystals can provide us with information such as the crystal shape, internal structure and deformation field. Coherent x-ray diffraction imaging was applied to study 3-D structure of micrometre-sized Gold particles (see Figure 6.4.17) **[6-116, 6-117]**. The 3-D real-space density corresponding to the reconstructed phase and measured amplitude of the CXDI pattern is shown in Figure 6.4.17. The internal density contrast is in the form of bright and dark bands oriented parallel to both the [111] and [11-1] directions in the images. The [111] bands have a width of 50 nm, a period of 100 nm and a lateral extent of 600 nm, both within the section and between adjacent sections. The [11-1] bands have the same width and are slightly less extended. These features were interpreted to be deformation bands associated with sample preparation. The dark region of the band presumably corresponds to material with twinned stacking that would diffract in a direction different from the (11-1) imaging direction. Such bands are known to occur in soft fcc metals and are attributed to recrystallisation following slippage along [111] planes during deformation **[6-118]**.

In the above example, special care was taken to grow unstrained crystals. However, it can be shown, under very general conditions **[6-119]**, that if a coherent x-ray beam is scattered on a strained crystal, then the local symmetry around each Bragg peak is broken and the effect will be stronger at higher-order reflections. In the following example, equilibrium shapes of Lead nano-crystals were investigated **[6-120]**. First, the shape of the crystals was reconstructed from the measured coherent diffraction patterns (Figure 6.4.18) and, in addition, the projection of the strain field on the scattering vector Q was reconstructed (Figure 6.4.19).

The resolution obtained in this experiment was estimated to be 40 nm, and the main limiting factors were the incoming flux (the measurement time was 150 s per frame) and the detector sensitivity. We believe that the XFEL can substantially improve resolution by providing $10^{12}$ coherent photons in one pulse.

One of the most exciting applications of coherent XFEL beams in future will be the studies of quantum systems (quantum dots and quantum wires). This will be discussed in detail later in this chapter. Some initial experience and understanding of how coherent x-ray diffraction can be applied to quantum dot samples was obtained in **[6-121]** and **[6-122]**.

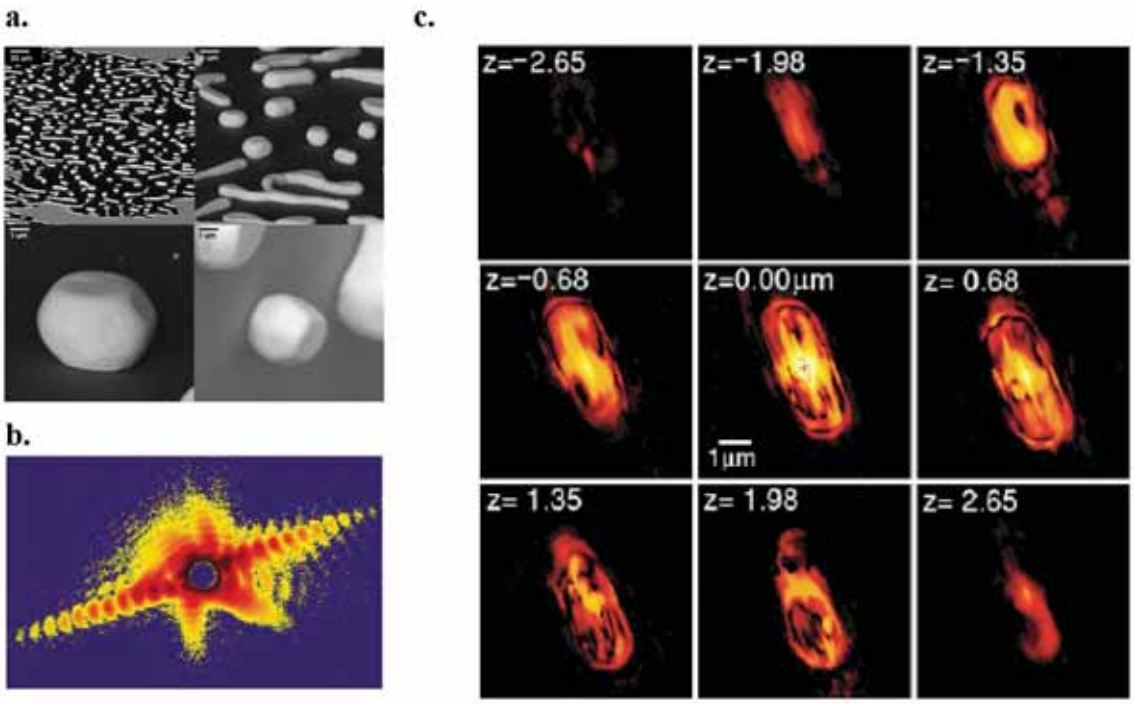


***Figure 6.4.17*** *(a) Scanning Electron Microscope (SEM) image of Gold particles that are obtained after annealing at 950°C for 70 hours; (b) coherent x-ray diffraction pattern from one of these crystals; (c) the 2-D slices through the best fit 3-D reconstructed density, separated as labelled.*

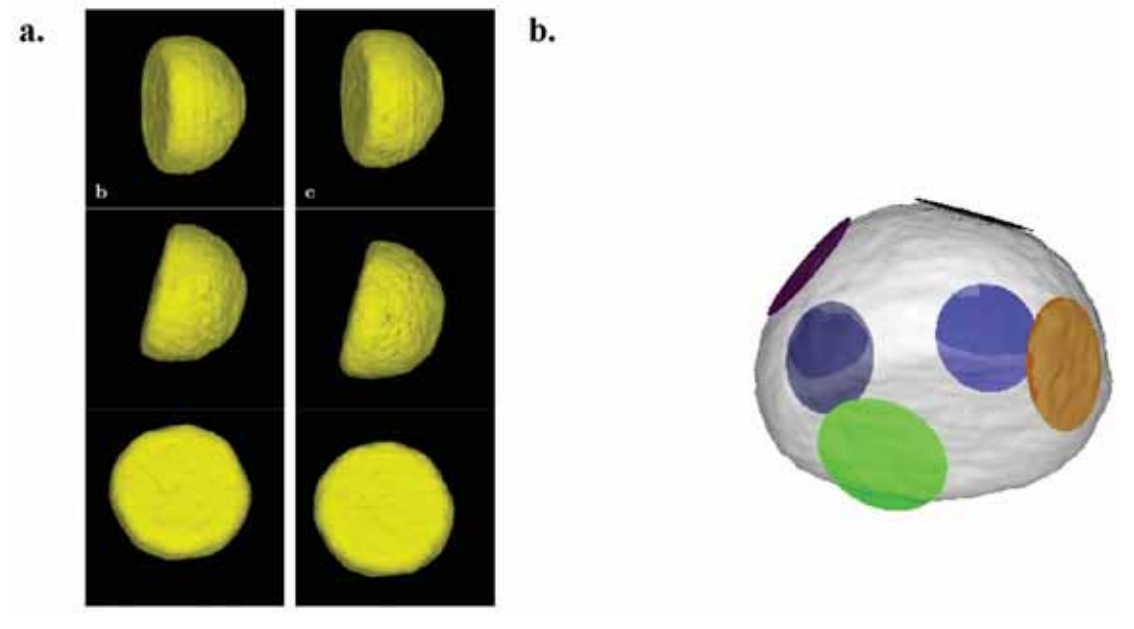


***Figure 6.4.18*** *(a) Surface plots of Lead reconstructed shapes. Left and right column corresponds to two best reconstructions; (b) 3-D view of (a) showing the fitted facet planes of the equilibrium crystal shape.*

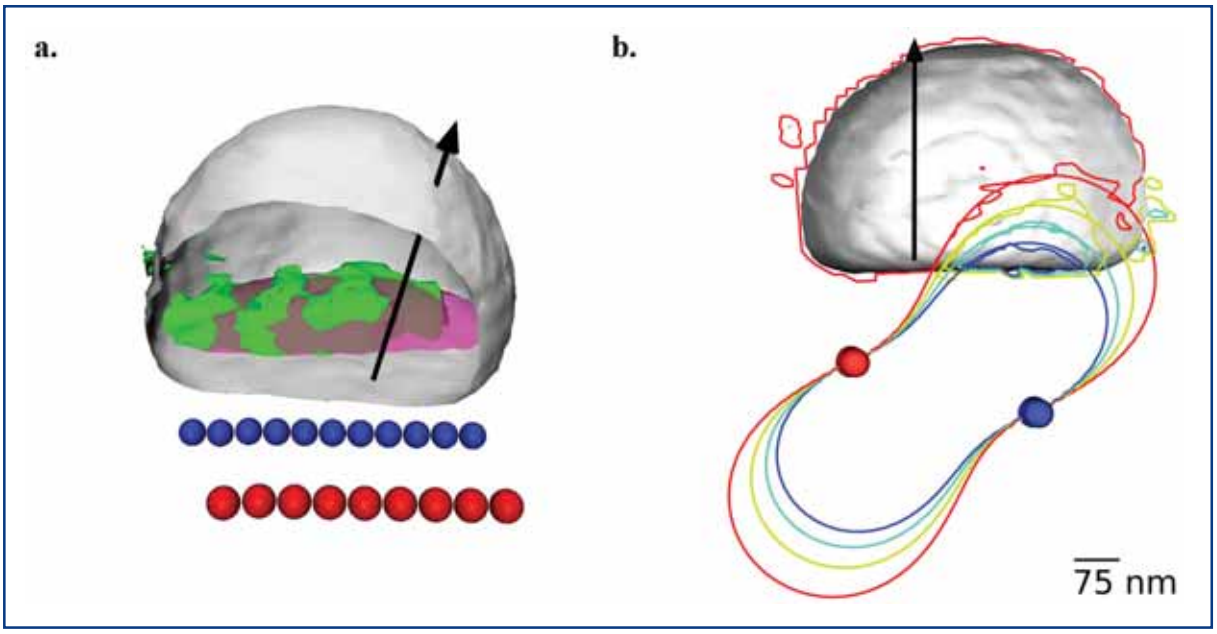


***Figure 6.4.19*** *(a) Single isosurface of the phase and the best fit superimposed on a cut-away image of the crystal density. The point defect lines used to generate the fit (dots) and the direction of Q (arrow) are also illustrated; (b) contour map of the cross section of the reconstructed phase of the complex density function on a plane passing through the middle of the nanocrystal. Smooth lines are the corresponding contours of the projection function* $\vec{Q} \cdot u(r)$*, where u(r) is the strain field calculated for two rows of point defects (balls) of opposite sign. Both sets of contours have spacing of 0.24 rad.*

In the experiment **[6-121]**, performed on a periodic array of Germanium islands on Silicon, the diffracted intensities show all the main features predicted **[6-122]**. However, it contains also a strong "diffuse" scattered intensity that, in a coherent beam, consists of the complicated speckle pattern due to inhomogenities of individual quantum dots. Here, measurements on single quantum dots are expected to provide a much "cleaner" diffraction pattern. We also think that 2-D periodic quantum dot structures could be an important step towards single molecule imaging.

It is clear that CXDI, especially with harder x-rays, is quite photon "hungry": the coherent flux per spatially and temporally coherent mode scales as the inverse third power of the photon energy. Moreover, pushing coherent scattering techniques to study nano-sized samples is even more demanding, as the number of elastically scattered photons decreases as the sample volume. The large coherent flux provided by XFEL will be crucial for the success of these experiments.

Coherent diffraction x-ray imaging experiments are also possible using the predominantly **forward scattering** by non-crystalline objects. The single molecule imaging experiment is the most challenging example of this. Scattering in the forward direction is determined by the electron density distribution of the sample. First results on 3-D reconstruction using coherently scattered diffraction patterns that were used for phasing were reported in 1999 in **[6-123]**. A 3-D reconstruction has been carried out on a specially prepared test Nickel sample using a series of 31 2-D diffraction patterns recorded from the sample with the rotation angles ranging from -75° to 75° in 5° increments. The resolution obtained in this experiment was estimated to reach 50 nm.

Recently, 3-D reconstruction with resolution 10 nm ×10 nm ×40 nm on a test sample using soft x-rays with energy 750 eV (1.65 nm wavelength) has been reported **[6-124]** (see also Section 6.4.7).

**X-ray holography** offers a complementary approach to iterative recovery of the object phase. Holography uses a well-defined reference wave mutually coherent with the scattered object wave to encode the phase in the coherent diffraction pattern from the object. The complex amplitude of the object wave is recovered from the recorded hologram, down to the sign of the phase, by a single (non-iterative) numerical calculation. Various optical geometries for holographic imaging have been demonstrated with soft x-ray lasers **[6-125, 6-126]**, undulator sources **[6-114, 6-127 – 6-130]**, and hard x-ray undulators **[6-131]**. The reference wave can be planar or curved; under appropriate conditions, a curved wave aids unique recovery of the phase **[6-132]**. As with CDXI, the recoverable object resolution is limited by the signal-to-noise ratio of the interference fringes recorded at the greatest momentum transfer Q in the coherent diffraction pattern. In holography experiments to date, this has been restricted to the maximum Q of the reference wave that can be produced by x-ray optics such as pinholes or ZP lenses. This currently corresponds to an object resolution of about 50 nm; this can be expected to improve to 15 nm **[6-133]** and possibly to as high as 1 nm as x-ray optics continue to improve **[6-134, 6-135]**. Figure 6.4.20 is an example of a reconstructed x-ray hologram showing magnetic contrast using a coplanar pinhole to form the reference wave.

Fortuitously, the experimental set-up and optics used for x-ray holography are readily shared with those used for CXDI in the forward-scattering direction. Consequently, it is practical to record holographic interference fringes (i.e. with a mutually coherent reference wave) out to the momentum transfer permitted by the optics, simultaneously with the reference-less coherent diffraction at higher momentum transfer than the hologram fringes. This two-pronged approach is promising because the phase provided directly by the reference wave can be used to improve the speed and accuracy of iterative phase retrieval of the reference-less coherent diffraction at high momentum transfer **[6-136]**. The recoverable resolution in this scheme, therefore, is not limited by the x-ray optics used to form the reference wave and thus, the hologram alone.

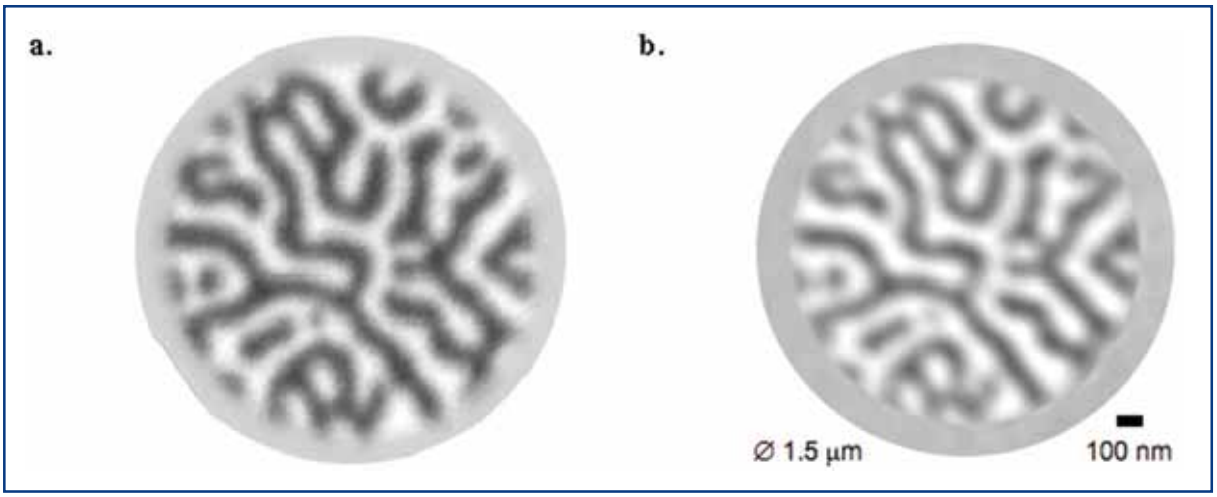


***Figure 6.4.20*** *(a) Scanning transmission x-ray microscope image of a CoPt multilayer containing labyrinthine magnetic domains; (b) reconstructed Fourier transform hologram of the sample, recorded at the BESSY UE56-SGM beamline. In both cases, the difference between opposite helicities of circularly polarised light is shown to reveal the magnetic domains* **[6-114]***.*

### Applications of the XFEL

### I. Nanomaterials

Today's high technology industry demands increasing miniaturisation of device structures, mainly for integrated circuits in the semiconductor industry, but also of magnetic, optical and biological sensors. There has been a strong interest, recently, in the manufacturing and characterisation of structures on a nanometre scale, with the hope that the material properties of nanostructures can be tailored by changing their size, via quantum size effects. One important area is the development of next-generation magnetic storage media. Recent developments in this field are currently pushing the magnetic bit size below 100 nm. There has been considerable impact on our understanding of the growth and structural properties of nanostructures through the use of scanning microscopy techniques, which enable us to achieve atomic resolution in real-space structural determination. However, similar experimental techniques to obtain element specific electronic structure information on a nanometre scale are still lacking.

Despite the fact that many of the fascinating properties of nanoparticles can be exploited only for an ensemble of many particles, it may be of interest to study **properties of a single particle**. This would be of particular interest for in-situ studies of catalytic or magnetic behavior. Alternatively, investigating ensembles requires non-interacting particles with exactly the same size in order to obtain information about a single particle.

In the following, a possible application of the European XFEL for structural investigations of nanocrystalline compounds in the form of single particles are presented. Rough estimates show that single bunch exposures of nanocrystalline materials with diameters of 100 nm to the focused beam will produce a diffraction pattern with enough statistics for phase retrieval. The proposed XFEL Facility will, therefore, be of great interest for structural studies of two different classes of nanomaterials. The first class includes

nanocrystals, i.e. materials with particle size in the range up to some 50 nm. Important groups of these materials are metal alloys and special ceramics based on oxides **[6-137]**. A common trend in modern material science is the adsorption of organic and metal-organic molecules onto the surface of nanocrystalline particles. The second class of materials comprises the extremely fine particles of clays and clay minerals. These materials usually do show translation periodicity; however, they are, in many cases, highly disordered.

Due to their small size, these materials cannot, at present, be investigated by single crystal x-ray diffraction techniques. For the detailed structural analysis of single crystals, it is important to obtain integral Bragg intensities with high reliability. Therefore, it is necessary to establish a highly precise monitoring system for photon flux, coherence and wavelength. An estimate of the sample sizes and exposure times that takes sample damage into account, based on a rough comparison to experiments at the European Synchrotron Radiation Facility (ESRF), shows that for a crystal of $100\times100\times100$ nm$^3$ size and the focused XFEL beam, diffracted intensities from a single bunch would provide a signal allowing the structure to be solved with sufficient accuracy. The information obtained from these data will be sufficient to determine the structure accurately (Bragg peaks) and the degree of disorder (continuous diffuse scattering). Ideally, if the whole crystal will be coherently illuminated, scattered intensity will produce a continuous diffraction pattern with high statistics that can be inverted and give the detailed structure of the defects in the crystal.

If sample degradation due to radiation-induced damage turns out to be tolerable, much smaller samples will be feasible, offering the exciting prospect of studying individual single nano-crystalline particles with x-ray diffraction techniques. With increasing sample size and respective beam diameter, the timescale is reduced correspondingly. If, for example, 1 $\mu$m resolution is considered sufficient for the determination of the local structure fluctuation, a thin needle or flat sample of larger overall dimensions can be sampled with a primary beam size of 1 $\mu$m diameter. In this case, an exposure of 600 ns is sufficient to record the diffuse scattering in a single orientation.

Particularly, for single crystal diffraction of crystals with strongly **fluctuating properties**, the sample stability is of crucial importance. Whether samples will be stable under the intense XFEL beam cannot, at present, be answered with any degree of certainty.

One of the important targets in this area of research are **quantum dot** structures. Progress in nanoscience and nanotechnology requires tools to investigate the structure of objects both on the mesoscopic and atomic levels. This is especially relevant in semiconductor devices based on heterostructures, where one big challenge is the investigation of individual nanostructures, which is important to quantify differences in self-assembled structures and to correlate these differences with the particular nanostructure location on the sample. This will be increasingly important for nanostructures embedded into electronic devices.

Using coherent nanometre-focused XFEL beams targeted on such samples could answer questions that cannot be solved with present levels of technology. Combining

real-space mapping with nanometre resolution and coherent x-ray diffraction experiments could provide information about the size, shape, strain, and chemical composition of individual nanostructures after a single pulse exposure.

Spatially resolved CXDI from low-dimensional systems will play an important role in the understanding of the structure, fabrication, and functionality of many nanomaterials. The advancement of CXDI will have wide-ranging applications including the investigation of self-assembled and semiconductor nanostructures, surfaces and interfaces, extended defects, granular materials and many other systems.

An important field of semiconductor nanoscience research nowadays is investigation of single islands and few coupled islands to obtain their electronic properties. For this purpose, micro-photoluminescence (μ-PL) and photocurrent spectroscopy have been applied to measure transitions in neutral and charged single excitons **[6-138]**, mainly in InGaAs/GaAs quantum dot systems. For the interpretation of the results, model calculations based on the structure of the islands (size, shape, composition and strain profile and existence of facets) are performed **[6-138 – 6-140]**. Due to fluctuations in the quantum dot ensemble, which are difficult to quantify, these models usually contain free parameters, rendering the simulations ambiguous to a certain extent **[6-138]**. Being able to determine the structural parameters of a single island, and correlate the results to μ-PL and photocurrent results at **the same island** would considerably further this field. Transmission electron microscopy (TEM) and cross-section scanning tunnel microscopy (STM) cannot be used for this purpose, as these methods are destructive and do not allow preparation of a specific quantum dot for analysis. Using focused XFEL beams will make it feasible.

X-ray diffraction (XRD) has proven a powerful tool for the determination of composition and strain distribution in nanostructures. Several methods have been established, based on measuring the diffuse intensity distribution with high resolution in reciprocal space **[6-141 – 6-148]**. While conventional local probe techniques such as TEM typically reach lattice parameter resolutions about $\Delta a/a = 10^{-2}$, XRD experiments easily reach values of $\Delta a/a = 10^{-3}$ to $10^{-4}$. So far, large ensembles of typically $10^5$ to $10^6$ nanostructures have been investigated by XRD, providing statistically well-averaged properties with a spatial resolution in the nanometre range for the **average object** under investigation. Focused XFEL beams, allowing high spatial resolution in addition to the high reciprocal space resolution, make the analysis for a **specific nanostructure** on the sample feasible. Considering the typical dimensions, an area with an extension of not more than about 100 nm has to be illuminated.

There has been considerable progress in recent years with x-ray focusing devices, and several groups have demonstrated focus sizes around, or even below, 100 nm **[6-149 – 6-155]**. Using XFEL beams will be beneficial because, due to the high degree of coherence, diffraction-limited focusing can be achieved, providing the smallest possible focus size and preserving full coherence across the beam.

One of the possible projects on XFEL can be the further development of the coherent x-ray diffraction imaging technique, with its application to single islands of semiconductors

coherently grown on a substrate (like SiGe dots on Silicon). One of the most important outcomes of the whole project will be model-free determination of the anisotropic strain distribution in a single island (including buried ones), and in the substrate.

### II. 3D structural characterisation of mesoscale systems

Investigating the meso- or nanoscale properties of hard materials has become a focus of the hard condensed matter community. In contrast to the atomic and macroscopic scale, our understanding of the structure on this scale is less mature. In particular, models tend to be based on average properties, despite the fact that the materials are often very heterogeneous on this scale. As an example, the macroscopic properties of metals such as strength or fatigue are governed by the properties of grains and dislocation structures and their interactions. The properties of the objects vary by orders of magnitude depending on factors such as size and crystallographic orientation. Present structural techniques cannot characterise this heterogeneity.

Neutron diffraction lacks the spatial resolution for observing the “building blocks”. Electron microscopy, on the other hand, probes only the surface. As such, it can be used only for “post mortem” on sectioned samples. The dynamics cannot be probed, and interactions between objects cannot be observed directly. Also, heterogeneous structures tend to be truly three-dimensional, and sections can be misleading. Only recently, with third generation x-ray sources, has it become possible to get static information from each individual grain of micrometre size **[6-156]**. We believe that using CXDI and the power of XFEL we can investigate structural properties of mesoscale systems in three dimensions with nanometre resolution. Some applications to metal and ceramic systems are described in the following paragraphs.

**Metals.** Typical metal structures are presented in Figure 6.4.21, displaying the four inherent length scales: Grain structures in well annealed metals have typical sizes of 1 – 100 $\mu$m and are very homogeneous, as can be seen in Figure 6.4.21(a). Application of stress leads to deformation and the formation of individual dislocations at length scales 0.1 - 1 $\mu$m (Figure 6.4.21(b)). Increasing the deformation leads to dislocation structures at the few micrometer scale (Figure 6.4.21(c)). Upon annealing, new nuclei are formed which grow from the matrix and show no dislocations (Figure 6.4.21(d)). The processes of deformation and annealing are important in the “life” of every material, and it is evident that dynamic, e.g. time-resolved, data will help in understanding the underlying processes. Such data can only relate to the bulk of the material, as the surface is non-representative due to stress relaxation, dislocation migration, pinning on surface grooves, etc. The following specific questions of vital interest motivate such 3-D structural investigations to include:

- How do dislocation structures emerge from individual dislocations?
- How do grains and dislocation structures deform?
- Nucleation: Where in the deformed material do nuclei form, and what are the orientation relationships between nuclei and the sites at which they form? What is the nucleation mechanism?

- Growth: How do the nuclei grow – what is the kinetics as a function of the relative orientations of the nuclei and the surrounding dislocation structures? Does the morphology of the dislocation structure play a role? How are the various types of dislocation structures actually absorbed into the moving interface of the nuclei?

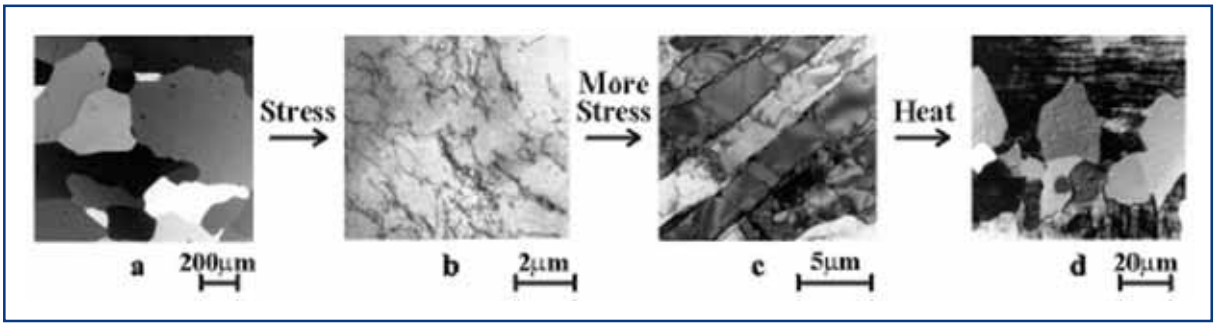


***Figure 6.4.21*** *Metal structures as observed by non-x-ray microscopy. The micrographs correspond to snapshots in time for random locations after exposure to stress and heat. No direct information about dynamics can, thus, be obtained using this method. (a) A well annealed grain structure shows evidence of tangled dislocations after some deformation (b) With more deformation these form into dislocation structures (c) Upon annealing, new nuclei form and grow from this deformed matrix (d) (from* **[6-2]***).*

These topics have been addressed in much detail by traditional means, but answers have been elusive. The XFEL combined with CXDI should be able to provide answers to some of these questions. Furthermore, combined dynamic investigations will be possible on three of the inherent length-scales: those of the sample, grain and dislocation structure. Hence, such data will be instrumental in the development of global models that bridge the length scales; in other words, in anchoring the macroscopic properties of interest to engineers to the mesoscale properties. The case for (industrial) alloys is similar, with the addition that the simultaneous use of tomography will be helpful in mapping and identifying secondary phases, inclusions, etc.

**Ceramics.** Modern ceramics tend to be heterogeneous partly because non-equilibrium parts of phase diagrams are used and partly because function/cost considerations dictate the use of several components (multilayers and inclusions). The kinetics of the reactions, phase transformations, etc. depend on the local environment of the grains, whether in the form of powders or sintered pellets. Again, surface studies are non-representative as the diffusion mechanisms are different. By providing local-scale information, ceramics processing will take a major step away from the present state of trial-and-error.

The study of grain dynamics with the XFEL source combined with CXDI, will allow the kinetics of the individual grains to be observed without locating the grains' exact positions. This will be a substitute for conventional in-situ powder diffraction. "Single crystal" structure refinements are applied here. In this way, a statistical study can be performed based on groups of grains with specific volume, orientation and/or stoichiometric properties. Furthermore, reactions between neighbouring grains can be observed directly by high-resolution mapping. The resolution of a few nanometres fits well with the grain size of many powders. The combination of diffraction and imaging is especially

attractive in this case, since the structure and density of the various grains are often unknown.

### III. Dynamic processes and time-resolved investigations of fluctuations

One potential of the XFEL lies in the ability to measure the **time-evolution** of transient structures on the 200 ns timescale of the XFEL pulse spacing. The 100 fs exposure time of a single bunch might catch a spontaneous fluctuation on that timescale. It is estimated that crystalline objects 10 nm across would give measurable diffraction patterns, and objects 100 nm across would be measurable during a single XFEL pulse. This type of application requires all the special properties of the XFEL: a coherent beam for the imaging, intensity because of the minute object size, and the short time structure for time-resolved experiments. In this regard, CXDI experiments could also take advantage of pump-probe methods being developed for other XFEL experiments such as X-ray Photon Correlation Spectroscopy (XPCS).

Another possible application of coherent femtosecond x-ray pulses will be for study of the surface dynamics. Consider a **crystal surface with an area** of only a few square micrometres. The coherent XFEL produces enough photons to fully characterise such an area in one bunch train, thus in < 1 ms. It will, thus, be possible to see step dynamics on the timescale of successive bunch trains (~100 ms). The dynamics can be caused either by statistical fluctuations or by growth or etching. This imaging would not only be faster than is currently possible, but could also be applied to systems under high gas pressure or at high temperature, or to surfaces buried under a solid or liquid, for which there are no alternative techniques. On a much slower time and larger length scale, a Silicon wafer has been imaged in this way during the etching of the native oxide **[6-157]**.

Of considerable scientific interest are the **spontaneously nucleated clusters of a crystalline solid** in an aqueous solution close to saturation. Time-resolved experiments with the XFEL would permit testing of the microscopic theory of classical nucleation, which has not been possible before. According to theory, solute molecules randomly associate into clusters with a thermodynamic equilibrium distribution, so that the largest clusters are the scarcest (Figure 6.4.22). Once a cluster exceeds the critical nucleus size, it becomes thermodynamically stable and grows into a macroscopic crystal. In standard nucleation theory, a smooth size distribution of small crystallites is assumed to be present up to the critical nucleus size. However, one can imagine that in reality, the size distribution is not smooth, but that certain sizes are preferred. In the case of 2-D nucleation on metal surfaces, such magic clusters have been observed using STM **[6-158]**. The sub-critical nuclei may also have a shape or structure that deviates substantially from that of the bulk crystals that eventually grow out of them. Since we are interested in atomic scale fluctuations upon a large background of parent material, it is advantageous to concentrate the beam onto a reasonably small sample volume in the order of a 1 $\mu m^3$ in order to improve statistics.

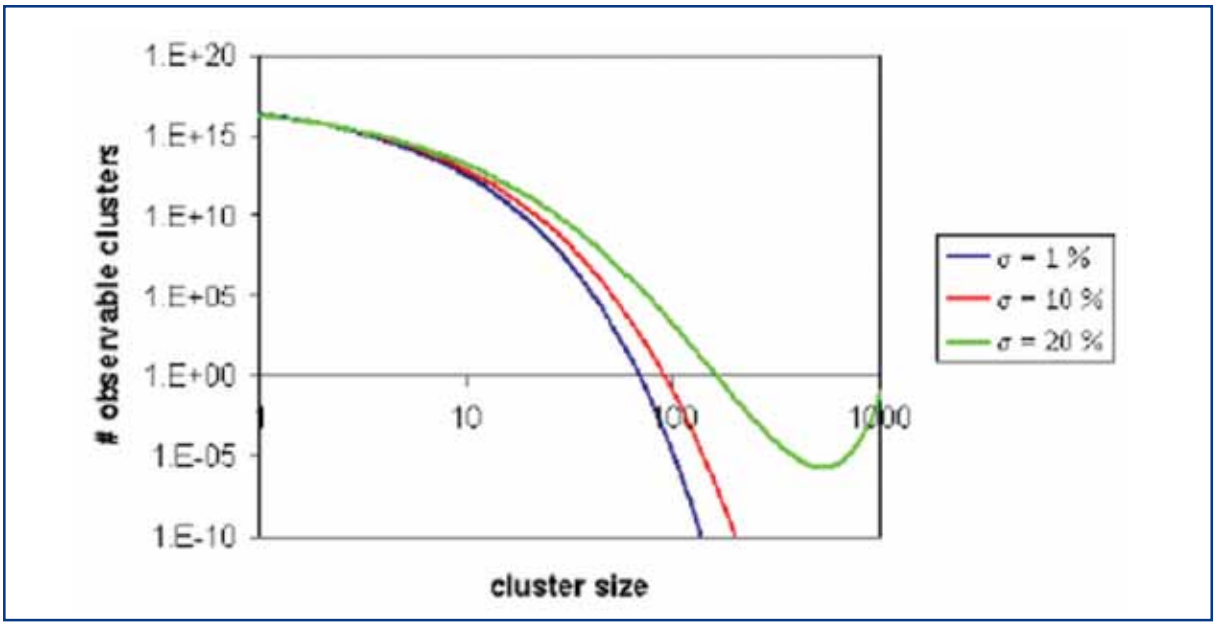


***Figure 6.4.22*** *An estimated cluster-size distribution as a function of supersaturation $\sigma$ according to standard nucleation theory. Only a few clusters exist at an appreciable size.*

Possible systems for study, fall into the general category of **crystalline fluctuations in disordered matter**, induced by some excitation such as temperature. For metals research, suitable examples are the local ordering of a binary alloy above its critical temperature or composition fluctuations in amorphous metal alloys. Alexander and McTague **[6-159]** proposed there would be BCC phase fluctuations in liquid FCC metals. These have been confirmed by simulations by Shen and Oxtoby **[6-160]** and by Klein **[6-161]**.

Fluctuations in aqueous solution are also of interest. Concentrated salt solutions, close to saturation are expected to have critical fluctuations of the crystalline phase. When these “pre-critical” nuclei become sufficiently large, they nucleate into actual crystals. The expected timescale of the fluctuations will depend enormously on the degree of supersaturation, which can be controlled by temperature, for instance. The 100 fs pulse of the European XFEL will be easily short enough to obtain snapshots of them. There is also a large field of study of binary mixtures of fluids that show phase separation into ordered structures that could be detected by diffraction. Self-assembling molecular and biological systems might also be accessible if there is a characteristic length scale established that would lead to diffraction.

In some cases, the fluctuations will be rare events with a characteristic signature of a particular Bragg angle where the parent crystal structure diffracts. Here, the experiment would be run at the highest framing rate that the detector bank can achieve, with a corresponding rate of single XFEL pulses, synchronised to the readout. The data stream would be monitored for “trigger” events such as the appearance of speckles more intense than some threshold. This is analogous to the measurement strategy used in high-energy physics. Only the data immediately before and after such triggers would need to be saved for subsequent analysis. These measurements could also be performed with high-energy spontaneous radiation for sampling of a larger volume.

Other cases would produce a continuous stream of speckle snapshots, uncorrelated between frames because the fluctuations would be too fast. Statistical analysis of the distribution of speckles on each frame would be used to obtain the higher-order correlation functions of the nascent ordering under investigation. Presently, theoretical work **[6-162]** has started to extract the interesting higher-order correlations, e.g. three-point correlation functions. Theoretical considerations combined with conventional coherent diffraction data, obtained from amorphous alloys for example, could be used to anticipate the kinds of correlations that might be interesting in a given system. Very good statistical evaluation of these higher-order correlation functions could be obtained by automated processing of the data stream. The experiment would then consist of varying the sample temperature or composition systematically. Special detector readout schemes or streak camera methods might be introduced to observe the lifetime of these fluctuations.

To illustrate the kind of data that might be obtained with a snapshot experiment during a pre-crystallisation fluctuation, we calculated the diffraction pattern of a $10^3$ atom cluster from a MD simulation of freezing, shown in Figure 6.4.23. The amplitude of its Fourier transform, shown in Figure 6.4.24, represents the square root of the intensity that would be measured with a single European XFEL pulse. Because this is oversampled, it should be directly phasable, and hence, invertible to (projection) images of the fluctuation. The size of the simulation represents a volume of less than $(10\ \text{nm})^3$, which is slightly less than can be achieved with focusing. A similar fluctuation within a larger volume will give the same signal, but more structured background.

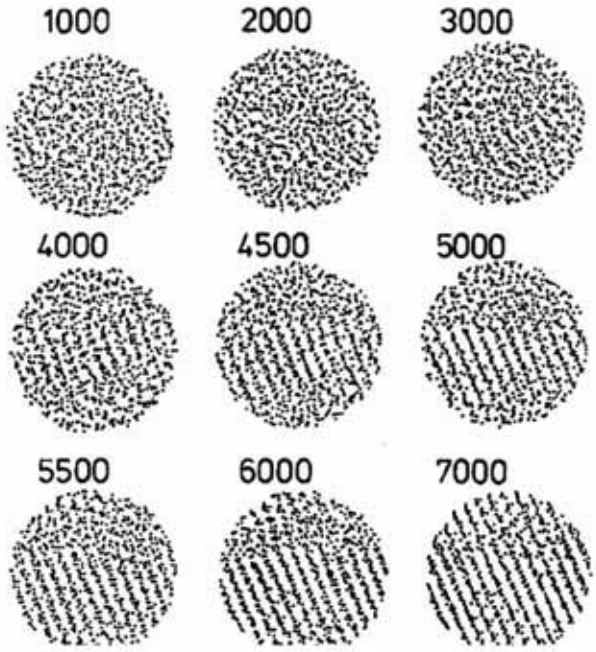


***Figure 6.4.23*** *Molecular dynamics simulation of freezing of a Lennard-Jones liquid of 864 atoms as a function of time steps after a temperature jump* **[6-162]**.

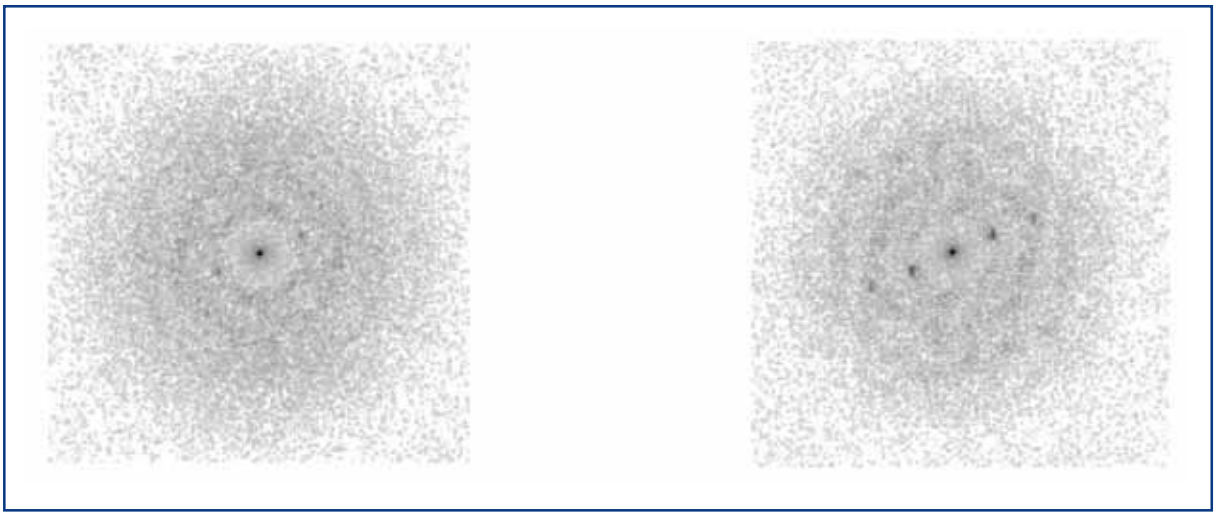

***Figure 6.4.24*** *Simulated diffraction patterns of the atomic distributions simulated in Figure 6.4.23, for the 1,000th (left) and 5,000th (right) time step.*

**IV. Dynamics processes in metals and ceramics**

The understanding of reactions during materials processing will have a new basis when experimental data and correspondingly refined modelling at spatial resolution below 1 µm and temporal resolution below 1 µs become available. Real-time small-angle x-ray scattering analysis may further be performed to analyse dissolution or coarsening of precipitates or pores with sizes smaller than ~1 µm, whereas the opening and closing of larger pores formed, for example, during creep, or close to a crack tip, may be measured using radiography under varying external load. Thus, comprehensive 3-D pictures of local microstructures may be derived with information content close to that obtained by the use of electron microscopy. A few examples from prominent areas have been selected below and indicate that time-resolved hard x-ray measurements at the XFEL can improve, to a great extent, the present-day knowledge of processing technologies. This applies equally well to techniques not mentioned yet, like extrusion, powder processing, sintering, cutting, carburising, rapid solidification, and joining. Even extremely fast processes like brittle cracking or fast deformation of materials by shock waves can be analysed.

**Real-time investigation of welding.** The high intensity and repetition rate of XFEL pulses will allow new and innovative real-time analysis of fast materials processing. For example, the in-situ study of fast formation and deformation of grains, as well as precipitation reactions during welding, will become feasible. This will greatly increase our basic understanding of the formation of microstructures in welds, which is regarded as an excellent basis for improving this joining technology. Time-resolved hard x-ray measurements at the XFEL laboratory are expected to greatly improve our knowledge of further processing technologies.

**Precipitates and pores.** The anticipated time resolution will allow the analysis of extremely fast growth and shrinkage of precipitates or pores. These effects may occur, for example, near crack tips, during melting, during solidification and fast cooling of droplets in powder processing, or during laser treatments of surfaces with local melting

and fast cooling afterwards. Further novel analysis will be based on the extreme photon flux of beams with areas even less than 1 $\mu m^2$ which may allow tomographic small angle x-ray scattering investigations to be performed simultaneously with grain mapping so that spatial variations of sizes and number densities of precipitates and pores may be derived. Such analysis will, for example, significantly improve our basic understanding of failure mechanisms of materials around crack tips or the incoherent formation of creep pores in alloys and ceramics **[6-163]**.

**Ultra-short pulse laser interactions with matter.** The interactions of high power, short-pulse lasers with materials have recently aroused a lot of interest in both the scientific community **[6-164, 6-165]** and the technological arena **[6-166 – 6-169]**. On the one hand, understanding of the fundamental processes and basic mechanisms such as energy transfer from laser field to material, energy transport and subsequent athermal or thermal modifications in the material are largely lacking. On the other hand, technological processes such as laser drilling **[6-170]** and cutting, machining **[6-169]** and peening, and laser ablation for thin film deposition **[6-166]** have now been developed as alternative and replacing technologies for conventional processes. Laser damage in optical materials **[6-170]** presents a technological roadblock to high-tech processing of materials.

Given the femtosecond time structure and extremely high brilliance of XFEL sources, the dynamics of ultra-short pulse laser interaction with matter may now be explored experimentally by using a variety of time-resolved and spatially-resolved techniques. These include diffraction, imaging, and a whole host of spectroscopic methods to capture and record modifications in crystal structure, phase transformation **[6-171, 6-172]**, morphology and microstructure evolution, which occur during the time the material "sees" the laser light. Such dynamical data will in turn help to verify existing models and to construct new and better models of laser-matter interaction processes. These advances will further our basic understanding of laser-based technologies and help us to improve and develop them for future material processing and fabrication.

One of the possible applications can be a study of a short pulse laser ablation that is a promising process for nanoscience applications due to the low threshold for material removal from surfaces. In the laser-ablation process, solid material transforms into an unsteady phase initiated by a rapid deposition of energy. Different pathways for non-thermal excitation can be present for very short laser pulses **[6-166]**. In a recent paper **[6-173]**, an ablation of Gold particles of nanometre size induced by optical femtosecond excitation from a laser was studied. However, the time resolution for this study was limited by the pulse structure of the third generation synchrotron source ESRF in this case). One could extend these studies on the XFEL Facility when the ablation process can be studied with femtosecond resolution. In addition, if the analysis of the paper **[6-173]** was based on modelling of small angle scattering data collected from a large amount of particles, we could foresee a similar experiment using XFEL pulses focused on a single particle that will give enough diffracted intensity to reconstruct the shape of the nanoparticle before and after interaction with optical pulse.

### 6.4.3.2 *Instrument requirements*

The experiments described above lead to requirements for an instrument for scientific applications using Coherent x-ray Imaging (CXI). They concern the performance of the light source, of the optical elements and the diagnostic equipment, of the sample environment, and of detectors. The experiments described in this section require tunable XFEL radiation of a relatively wide spectral range from ~0.6 to 12 keV. Here, 12 keV radiation is requested due to its penetration in bulk investigations. Diffraction and imaging techniques will be applied at this photon energy. Investigations of magnetic systems or resonant scattering in the hard x-ray regime lead to the request for tunable radiation in the range ~3-11 keV. Full-field imaging experiments would employ 12 keV radiation in combination with a high-resolution in-line camera system. This in-line detector will need to be as large as possible an array (if possible, 4K×4K), optically coupled to an optimised fluorescent screen. The field of view is limited by the array size and the optical magnification and should not be compromised. Smaller photon energies around 1 keV will be used to investigate the structure and time evolution of nanostructures in the 20-50 nm range. For these particle sizes, 1 keV radiation provides sufficient penetration, but in general samples will not be isolated and surrounded by a vacuum. Otherwise, they would be studied using electron microscopy. Instead we want to be able to access objects growing in-situ, in contact with a liquid (e.g. water). We propose to use the Grazing Incidence Small Angle X-ray Scattering (GISAXS) Geometry, thus, avoiding the penetration problem. Another possibility is to use samples supported by very thin Silicon Nitride membranes and investigated in transmission geometry. Tunable beam energy around 0.5-1.0 keV will also be needed for the L-edges of 3d transition metals in very thin samples. Another application is the investigation of biological matter, preferably in the water window (0.28–0.5 keV), with enhanced contrast between water and organic materials. None of the European XFEL beamlines provides the entire photon energy range in the fundamental and the use of SASE 2 and SASE 3 beamlines is proposed instead. For materials science applications, such as those discussed in Section 6.4.3.1, Case III., the use of very hard x-rays at energies 60-90 keV is requested. The high photon energies are required to achieve sufficient penetration. Since, at these photon energies, the Ewald sphere of diffraction becomes almost flat, the experiments are well suited to investigations of diffuse scattering planes. These experiments will use the spontaneously emitted synchrotron radiation of U1 which also exhibits a very high degree of coherence.

The relative merits of x-ray microscopy methods suited to XFEL sources are compared in Table 6.4.5. Coherent full-field transmission x-ray imaging, x-ray holography, and CXDI, are described in the table. Holography provides the full complex amplitude of the object in one reconstruction step, whereas lensless CXDI is promising for obtaining the highest spatial resolution.

| | Full-field | Holography | CXDI |
|---|---|---|---|
| Resolution limit | optics | reference | detector |
| Feasible resolution | ~10 nm | ~10 nm | ~ 1 nm |
| Optics required | yes | yes | no |
| Coherence required | no | yes | yes |
| Focusing required | yes | no | no |
| Reference required | no | yes | no |
| Direct method | yes | no (one step) | no (iterative) |
| Phase retrieval needed | no (in focus) | yes (one step) | yes |
| Twin image problem | no (in focus) | no (unless inline) | no |
| Signal dynamic range | low | high | high |
| Compatible with CXDI | no | yes | |

***Table 6.4.5*** *Relative merits and requirements of coherent full-field transmission x-ray imaging, x-ray holography, and CXDI.*

### Spectral radiation properties

The degree of spatial coherence is often considered to be better using soft x-rays, but according to the design, the European XFEL will be fully coherent at all energies. The coherent flux is certainly higher for soft x-rays for a given source brilliance (cubic scaling, as mentioned above). It may be that lasing will be achieved faster for somewhat smaller photon energy, so there is interest in designing experiments operating at about 3 keV. In addition, energies in this range appear optimal for imaging of small biological specimens, based on a comparison of estimated radiation damage versus resolution in electron microscopy, x-ray microscopy, and x-ray crystallography data **[6-174]**. CXDI experiments designed to operate at intermediate, as well as hard x-ray, energies will have to take into account the impact on the optics and detector configuration. Many experiments can be carried out with the natural 0.08% bandwidth of the undulator because of the inherently small size of the diffracting object, but it will probably be worth having an optional Si(111) monochromator for the possible situations where the undulator is not up to specification or for large samples. It will be important to foresee a real-time diagnostics of the undulator performance.

### X-ray optics requirements

In previous reports, the term **coherence preserving optics** had been used to describe the quality of optical elements when used with the almost fully coherent radiation of the XFEL. This term is somewhat misleading, as an optical element – no matter how strong its aberrations and distortions – cannot degrade the coherence of the radiation, meaning that it will not reduce the visibility of any diffraction or interference experiment. However, experiments aiming to retrieve amplitude and phase right after an object require a well-defined phase of the incoming wave front. While this phase is well known for a coherently illuminated, aberration-free, perfect optic, an imperfect optic will introduce wave front distortions which are usually unknown and thus, hard to correct for. Therefore, the term **wave front preserving** or **diffraction limited** seems to be more appropriate to describe

optical elements, in particular with respect to the precision required for nanometre-scale CXDI. Results with diffraction-limited focusing by diffractive lenses at the 15 nm scale are promising in this case **[6-27]**. In fact, the condition to yield a well-defined "clean" wavefront may turn out to be more relevant for optics than the ability to achieve the smallest spot sizes. A situation, where the wave front illuminating the sample is unknown or, even worse, changes in time, must be avoided for the CXI experiments.

The requested beamsize in most experiments will be in the order of 0.1-1 µm. This is needed to limit the sample volume so that not too many fluctuations are sensed, and to concentrate the flux on the region of interest. The average heat load on the sample is not expected to be a serious problem because this is the same as at existing sources, but there will be considerable power levels over the duration of the pulse which could cause plasma formation. However, it seems unlikely that a crystalline nucleus would be completely disrupted on the timescale of the XFEL pulse duration. Further discussion on this topic and theoretical input on the "meaning" of temperature will certainly be needed.

**Time domain requirements**

These experiments do not make explicit use of the ultra-short pulse duration. However, to model the interaction of the intense radiation with the samples, the fluctuation of the pulse duration will need to be kept small compared to 100 fs timescale. Many experiments will require only single pulses at a 10-50 Hz repetition rate as the intense radiation leads to the requirements of sample exchange between exposures. Experiments investigating the time evolution of sample structure over a long period after initial excitation, envisage using the high repetition rate during the x-ray pulse trains. In this way, time information could be obtained in steps of ~200 ns over a period of 0.6 ms. Likely a logarithmic distribution of time steps is sufficient. These experiments require samples withstanding the energy dissipation over at least the period of the pulse train. This could be either specific 'radiation hard' materials or measurements where the incident photon flux is reduced, e.g. by introducing a monochromator or even an absorber. It is, therefore, the intention to use a variety of pulse patterns from single pulses up to several hundreds of x-ray pulses per electron bunch train.

**Photon diagnostics requirements**

All experiments will be in need of pulse-by-pulse diagnostic to determine photon flux, beam position and focus spot size at the sample position. Furthermore, it needs to be verified that the wavefront is stable in time. The spectral diagnostics should provide the mean photon energy and the content of higher harmonic radiation.

**Sample manipulation and environment**

In the experiments envisaged at the XFEL laboratory, the sample size of interest is envisaged to be below one micron. To collect diffraction data and to manipulate such small samples with extreme resolution, it will be necessary to set up high resolution microscopes integrated to the diffractometer. This could be a present-day optical, Scanning Electron Microscope (SEM) or Atomic Force Microscope (AFM) that will be useful for identifying and aligning the sample on the diffractometer. The sample stage will need a single high precision axis for tomography. Supporting samples on a membrane

might work; if the membrane is blown away, the damage would be local and a second shot could be placed on an adjacent region. A square centimetre of sample will be enough for a million shots with ten microns spacing.

Injection of a jet of liquid into the vacuum of the beamline is a method that should work but will severely limit the range of samples available. It might be possible to design a windowless flow cell in which a liquid is held in place by capillary forces. This might be made to work in vacuum in some cases, but is certainly compatible with a Helium environment. Levitated samples, either electrostatically or magnetically, may be used. Using a sample in a gas stream is another option. One should consider the option of not preparing individual particles at all. The particles could be blown through the x-ray beam in a highly diluted gas stream. This could be similar to the sample environment planned for the single molecule station. New techniques will have to be developed to synchronise the movement of such small particles with the x-ray beam and the detection system. One would obtain a series of diffraction patterns at random orientation of different particles, each recorded with a fully transversely coherent x-ray beam. Analytical techniques that have been established for electron diffraction will have to be applied here to analyse the diffraction patterns in order to obtain structural information about the samples. It will be advantageous to have a system for aligning particles in the focus of the beam at least in one direction that will be an important factor for diffraction pattern sorting.

For most of the experiments proposed here, using windows around the sample in the focused beam should be avoided. The window material would become vaporised along with the sample. The use of windows could be possible for unfocused or attenuated beams but special care has to be taken for their quality. The possible restrictions could arise from the availability of x-ray windows. Ideally, a beamline should be windowless so as not to interfere with the coherent wavefront. However, for practical reasons, thin windows could be used in the unfocused beam, before the optics, for example, or in the detector system. Silicon nitride membranes can be fabricated as thin as 50 nm, are radiation-hard, amorphous, and contribute little undesired scattering (especially for hard x-rays). If kept under a few millimetres square, they can also support an air-vacuum interface such as a vacuum interface or a detector entrance window. Differential pumping could be viable, for example between a Helium sample environment and the machine vacuum. This might be relatively easy to achieve, given the very large distances involved.

Since for 12 keV radiation, windows can be allowed, user experiments could bring their own sample environment. Standard interchangeable sample environments (eg baby chambers) should be provided in addition. For experiments at magnetic resonances (3-12 keV), in-vacuum magnet- and cryosystems will be needed.

The 1 keV instrument will differ from the 12keV instrument in having a single vacuum system throughout, with no windows, including the detector chambers. A clever design of the vacuum system would allow plenty of in-vacuum motorised stages to mount optics at various distances. Perhaps there could be several sample stages at different distances from a fixed detector bank. Each one would have to have several translation stages packed close together to mount various optics. A good vacuum design needs to be

flexible in allowing quick access for adjustments. Heating and cooling at the sample will be important as well as magnetic fields inside the vacuum.

### Detector requirements

It is envisaged that the different experimental stations would correspond to the different detector configurations. Since the whole experiment is a snapshot (or series of snapshots), there will be no use for angular scanning using single-point detectors. Only a complete diffraction pattern or complete image would be useful, so the detectors will be parallel, possibly massively parallel (>$10^9$ pixels). The detectors will have to be optimised for a given class of samples that would define the experimental station. Ideally, the detectors should be able to distinguish each x-ray pulse of the XFEL. These experiments make high demands of two-dimensional x-ray detectors in terms of pixel number and size. The realisation of such detectors requires a specific R&D effort that will be described in Section 6.5.4. In Section 6.5.4.1 the specific detector requirements for the CXI instruments will be described. There will be a wide bank of parallel detectors at a few metres distance to see diffraction fringes from objects up to 10 µm in size (100 µm would be hard). A sophisticated system of (conical) collimators in front of the detector bank is needed for a clean scattered signal.

Imaging experiments at fixed photon energy, e.g. at 12 keV, require a high-resolution in-line camera system to record the images. The detector format will need to be as large as possible an array (4K×4K), optically coupled to an optimised fluorescent screen. The optical detector must be optimised for stability, linearity, reproducible background, but not so much for quantum efficiency.

### Visible laser requirements

In this field of application no specific requirement for use of visible lasers for pump-probe experiments has yet been formulated. However, it is assumed that the experiments will need an ultra-fast laser to drive excitations of samples to be followed using the techniques described above. Visible ultra-fast lasers will be centrally provided for all instruments. The distribution of laser radiation to the instruments for CXI experiments can be designed at a later stage. The same applies to specific requirements, e.g. wavelength tunability. The instruments will foresee provision of these future options.

### Other requirements

One important question is available computer power. On modern computers, 3-D Fast Fourier Transform (FFT) calculations for 1,024×1,024×1,024 data points can take about 10 seconds. Taking into account that for the full reconstruction several thousands iterations will be needed the time required for 3-D reconstruction of such a data set is ~14 hrs at present. Such durations could become a serious limitation for operating with big data sets. The hope is that in the coming years the data storage and processing time capabilities will improve considerably.

### *6.4.3.3 Realisation of the instrument*

From their requirements, the CXI experiments ask for three instruments at SASE 3 (CXI 1 – Tunable soft x-rays), at SASE 2 (CXI 2 – Tunable hard x-rays) and at U 1 (CXI 3 – High energy x-ray spontaneous radiation). The SASE 3 beamline enables experiments in the range 0.28 to 1.0 keV and thus, covers the water window for investigation of biological specimen and the L-edges of the 3d transition metals for investigation of magnetic phenomena. At 1 keV, good conditions for investigation of nanocrystals are provided. Experiments requiring higher photon energies, i.e. 3-6 keV for M–edge investigations in actinides, 6-11 keV for L-edge investigations of rare earth elements and ~12.4 keV for bulk investigations, will be carried out at the SASE 2 beamline. Monochromatisation by using perfect crystals will be optional for the hard x-ray regime only. For beam transport, only mirrors will be used. The corresponding beam transports in the SASE 2, SASE 3 and U1 beamlines have been described in Sections. 6.2.4.2 to 6.2.4.4, respectively. All instruments will require focusing of the x-ray beam. Moderate focusing to beam sizes of the order 100 µm is achieved by using a focusing element near the location of the off-set mirrors. Extreme focusing to 0.1–1 µm beam size requires extremely short focal length and therefore needs to be integrated into the instruments.

**CXI 1: Tunable soft x-rays**

Since this experiment is most sensitive to alteration of the wave front by imperfect optics, it should be installed in the beam that comes directly from the offset mirrors, which have to be in the beamline for radiation protection reasons. Having 100 µm focusing provided through the second of these mirrors, the main focusing requirement of the instrument is to achieve much smaller spots.

The following elements belong to the CXI 1 instrument inside the experimental hall. They are depicted in the schematic layout of that instrument in Figure 6.4.25 and are described in Table 6.4.6. Collimating apertures or a slit system will be placed in front of the experimental chamber to define the beam size and to remove scattering from the incident x-ray beam. A gas photon flux monitor (see Section 6.3.2.1) will follow before a differential pumping section separates the beamline from the UHV vacuum chamber for experiments. For the energy range of this beamline, vacuum separation by means of windows is unlikely.

To achieve extreme focusing a special 0.1–1 µm focusing optics will integrated into the instrument. In this case the upstream beamline optics will use only flat mirrors in order to minimise wavefront errors. In-line optics that can be moved in and out will be an advantage. It will be integrated in the sample environment system so that the distance between optics and sample can be fitted to the proper focal distance of the optics. The sample chamber will be equipped with a high accuracy sample manipulator allowing x-y-z movements and rotation around two perpendicular axes. The chamber has to be capable of reaching $10^{-8}$ mbar for experiments requiring in-situ sample preparation and for samples sensitive to surface contamination. Sample loading from external chambers needs to be foreseen. Diffraction should be collected by a large 2-D area detector in the forward direction. It will be necessary to be able to vary the distance between sample and detector.

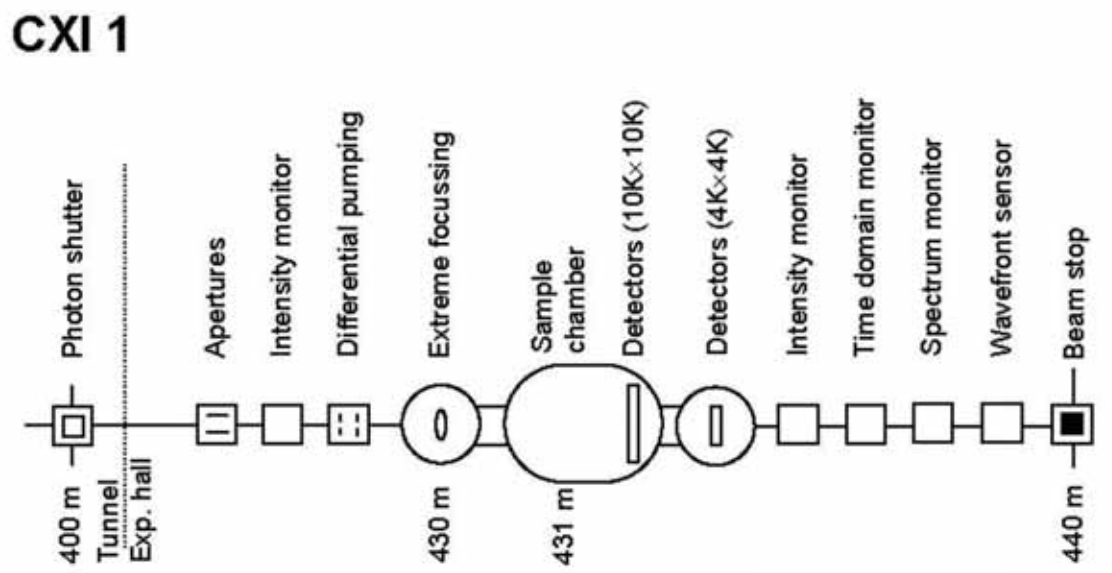


***Figure 6.4.25*** *Schematic layout of the CXI 1 instrument at the SASE 3 beamline. Variation in the distances between optics-sample-detector is foreseen.*

Experiments can absorb a significant proportion of the incident beam. It is, however, proposed to place most photon beam diagnostics in the transmitted beam. A second gas monitor detector will be used to measure the transmission. The spectral measurement should provide mean photon energy, bandwidth, and higher harmonic content on a pulse-by-pulse basis. Measurement of the detailed spectral properties, i.e. the width and distribution of spikes, is only performed upon request. Diagnostics of time domain properties should deliver the arrival-time required for pump-probe experiments using the visible laser. Finally, spatial measurements determine the beam location and its spatial distribution. Since these measurements are usually destructive they will be carried out in a dedicated setup at the end of the line and before the beam stop.

| Item | Purpose | Specification |
|---|---|---|
| Slits/apertures | Beam definition,<br>beam halo cleaning | 0.25 µm accuracy,<br>1 µm repeatability |
| Intensity monitor | Measurement of incident photon flux | Transmissive (<5% absorption),<br>single pulse measurement,<br>relative accuracy $<10^{-3}$ |
| Differential pumping | Separation of beamline and experiments vacuum | $10^4$ steps for all elements |
| Focusing optics | Extreme focusing for 0.28-1.0 keV | 0.1 µrad angular stability |
| Sample chamber | Sample positioning and orientation,<br>systems to verify sample alignment,<br>provision of sample preparation | x-y-z move (0.25/1 µm),<br>two rotations (0.25/1 mdeg),<br>optical microscope,<br>UHV conditions |
| Detector | Measurement of forward scatting in imaging experiments | 2-D, 4K×4K pixels,<br>10×10 µm pixel size,<br>central hole or beamstop |
| Detector | Measurement of diffraction for CXDI experiments | 2-D, 10K×10K pixels,<br>0.1×0.1 $mrad^2$ pixel res. |
| Intensity monitor | Measurement of transmitted photon flux | Transmissive (<5% absorption),<br>single pulse measurement,<br>relative accuracy $<10^{-3}$ |
| Spectral monitor | Measurement of mean energy,<br>bandwidth, and harmonic content | Single pulse measurement,<br>relative accuracy $<10^{-3}$ |
| Spatial monitor | Measurement of spatial distribution,<br>focus size | Single pulse measurement |
| Alignment unit | Positioning and position verification | Permanently operating,<br>accuracy ~100 µm |
| Lead hutch | Radiation protection,<br>temperature stabilisation,<br>laser protection | 4×10×3.5 $m^3$ (W×L×H),<br>±0.5° thermal stability |
| Control hutch | Operation of the instrument | Working environment<br>(noise, temperature, light) |

***Table 6.4.6*** *Elements and specifications of the CXI 1 instrument.*

### CXI 2: Tunable hard x-rays

The CXI 2 instrument is designed for hard x-rays and could best be located at the SASE 2 beamline. Due to the coherence requirements, it should, again, be placed in the beam that comes directly from the offset mirrors. Having 100 µm focusing provided through the second of these mirrors, the main requirement of the instrument is to achieve much smaller spots. The use of a monochromatised beam with a bandwidth ~$10^{-4}$ is possible due to the double-crystal monochromator in the SASE 2 beamline.

The following elements belong to the CXI 2 instrument inside the experimental hall. They are depicted in the schematic layout of that instrument in Figure 6.4.26 and are described in Table 6.4.7. Collimating apertures or a slit system will be placed in front of the experimental chamber for beam definition and to reduce scattered radiation from the x-ray beam. A gas photon flux monitor (see Section 6.3.2.1) will follow before a differential pumping section separates the beamline from the UHV vacuum chamber for experiments.

For this energy range, vacuum separation by means of Beryllium or Diamond windows is another possibility. Great care has to be taken in the perfection of these windows is another possibility to preserve the wavefront properties.

To achieve extreme focusing, a special 0.1–1 µm focusing optics will be integrated into the instrument. In this case the upstream beamline optics will use only flat mirrors to minimise wavefront errors. In-line optics that can be moved in and out will be an advantage. The use of a pair of mirrors in KB geometry is another possibility. The optics are integrated in the sample environment system so that the distance between optics and sample can be fitted to the proper focal distance of the optics. The sample chamber will be equipped with a high accuracy sample manipulator allowing x-y-z movements and rotation around two perpendicular axes. The chamber has to be capable of reaching $10^{-8}$ mbar for experiments requiring in-situ sample preparation or being sensitive to surface contamination. Sample loading from external chambers needs to be foreseen. Diffraction in the forward direction should be collected by a large 2-D area detector. It will be necessary to be able to vary the distance between sample and detector. Again, Beryllium windows could become useful and the flight path may be realised in Helium to reduce absorption.

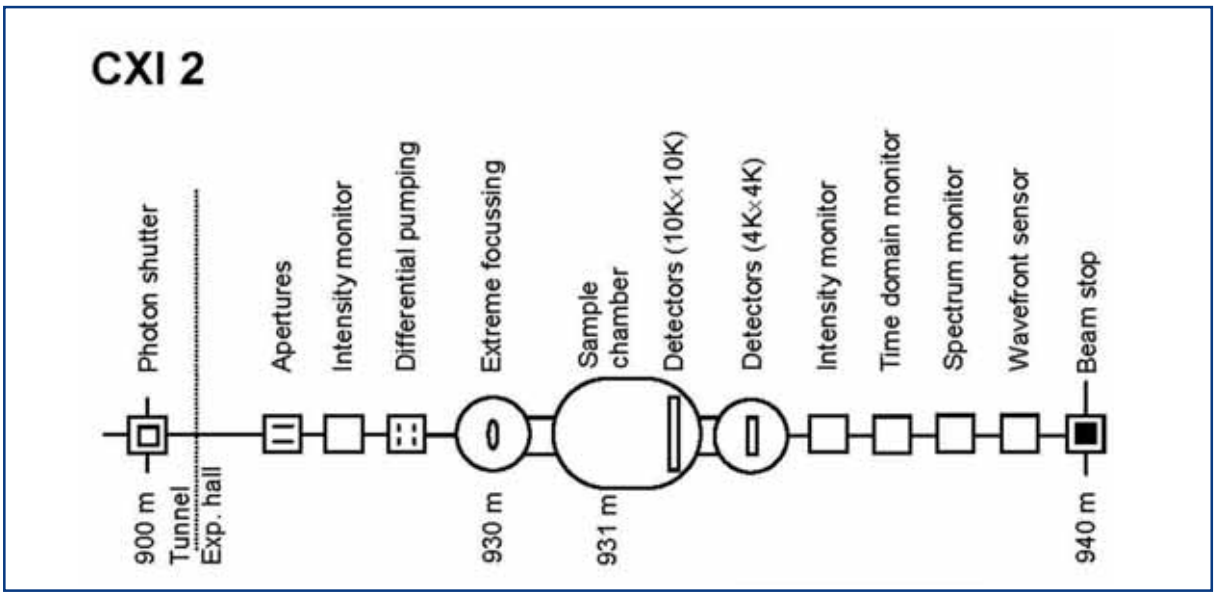


***Figure 6.4.26*** *Schematic layout of the CXI 2 instrument at the SASE 2 beamline. Variation in the distances between optics-sample-detector is foreseen.*

| Item | Purpose | Specification |
|---|---|---|
| Slits/apertures | Beam definition,<br>beam halo cleaning | 0.25 µm accuracy,<br>1 µm repeatability |
| Intensity monitor | Measurement of incident photon flux | Transmissive (<5% absorption),<br>single pulse measurement,<br>relative accuracy $<10^{-3}$ |
| Differential pumping | Separation of beamline and experiments vacuum | $10^4$ steps for all elements |
| Focusing optics | Extreme focusing for 3.1-12.0 keV | 0.1 µrad angular stability |
| Sample chamber | Sample positioning and orientation,<br>systems to verify sample alignment,<br>provision of sample preparation | x-y-z move (0.25/1 µm),<br>two rotations (0.25/1 mdeg),<br>optical microscope,<br>UHV conditions |
| Detector | Measurement of forward scatting in imaging experiments | 2-D, 4K×4K pixels,<br>10×10 µm pixel size,<br>central hole or beamstop |
| Detector | Measurement of diffraction for CXDI experiments | 2-D, 10K×10K pixels,<br>0.1×0.1 $mrad^2$ pixel res. |
| Intensity monitor | Measurement of transmitted photon flux | transmissive (<5% absorption),<br>single pulse measurement,<br>relative accuracy $<10^{-3}$ |
| Spectral monitor | Measurement of mean energy,<br>bandwidth, and harmonic content | Single pulse measurement,<br>relative accuracy $<10^{-3}$ |
| Spatial monitor | Measurement of spatial distribution,<br>focus size | Single pulse measurement |
| Alignment unit | Positioning and position verification | Permanently operating,<br>accuracy ~100 µm |
| Lead hutch | Radiation protection,<br>temperature stabilisation,<br>laser protection | 4´10´3.5 $m^3$ (W×L×H),<br>±0.5° thermal stability |
| Control hutch | Operation of the instrument | Working environment<br>(noise, temperature, light) |

***Table 6.4.7*** *Elements and specifications of the CXI 2 instrument.*

Experiments can absorb a significant proportion of the incident beam. It is, however, proposed to place most photon beam diagnostics in the transmitted beam. A second gas monitor detector will be used to measure the transmission. The spectral measurement should provide mean photon energy, bandwidth, and higher harmonic content on a pulse-by-pulse basis. Measurement of the detailed spectral properties, i.e. the width and distribution of spikes, is only performed upon request. Diagnostics of time domain properties should deliver the arrival-time required for pump-probe experiments using the visible laser. Finally, spatial measurements determine the beam location and its spatial distribution. Since these measurements are usually destructive they will be carried out in a dedicated setup at the end of the line and before the beam stop.

### CXI 3: High energy x-ray spontaneous radiation

The CXI 3 instrument will be located at the spontaneous undulator beamline U 1, therefore, relaxed conditions with respect to the energy dissipation in the optics exist.

The instrument is optimised for operation with high energy photons in the range 50-90 keV. As the requirement for preservation of coherence equally applies to this instrument, it should be located in the beam that comes directly from the offset monochromator. The use of a monochromator instead of mirrors follows from the difficulty of obtaining high reflectivity at these photon energies. The collimating Beryllium lens in the beginning of the U 1 beamline will have some influence on the coherence properties and may need to be removed.

The following elements belong to the CXI 3 instrument inside the experimental hall. They are depicted in the schematic layout of that instrument in Figure 6.4.27 and are described in Table 6.4.8.

Collimating apertures or a slit system will be placed in front of the experimental chamber for beam definition and to reduce scattered radiation from the x-ray beam. A photon flux monitor (this could be a solid-state system in this case) follows. At these photon energies the beamline vacuum ends at the flux monitor. Polished Beryllium or Diamond can be used for vacuum window purposes.

To achieve extreme focusing, a special 0.1–1 µm focusing optics will be integrated into the instrument. One will have to investigate whether multilayer KB or refractive lens optics better preserve coherence and wavefront properties. The distance to the sample can be fitted to the proper focal distance of the optics. The sample will be mounted on a diffractometer including a detector arm for off-axis geometries. The diffractometer supports mounting of sample environments like cryogenic, heating or pressure cells.

Photon beam diagnostics of the transmitted beam provides photon flux and a wavefront sensor will be available for adjustment and verification of the micron focal spot.

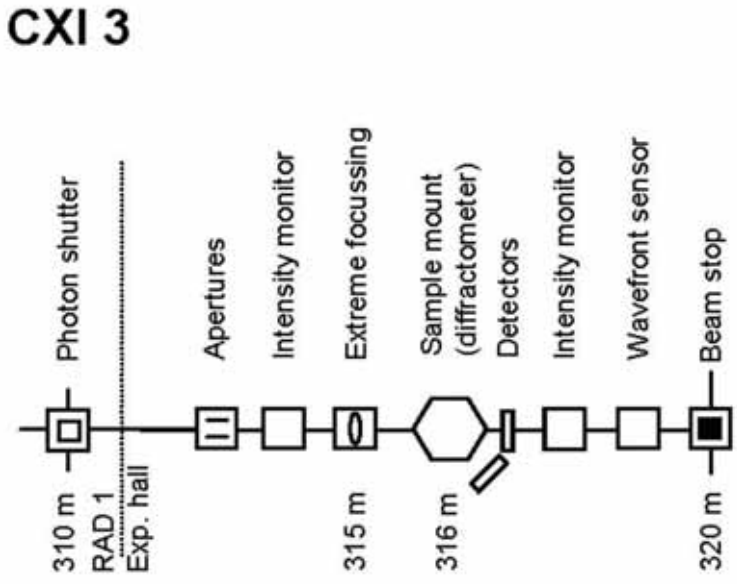


***Figure 6.4.27*** *Schematic layout of the CXI 3 instrument at the U 1 beamline. This instrument is located behind the RAD 1 instrument and distances are given in relation to the undulator end.*

| Item | Purpose | Specification |
|---|---|---|
| Slits/apertures | Beam definition,<br>beam halo cleaning | 0.25 µm accuracy,<br>1 µm repeatability |
| Intensity monitor | Measurement of incident photon flux | Transmissive (<5% absorption),<br>single pulse measurement,<br>relative accuracy $<10^{-3}$ |
| Focusing optics | Sub-µm focusing for 50-90 keV | 0.1 µrad angular stability |
| Sample mount | Sample positioning and orientation,<br>systems to verify sample alignment,<br>provision of sample preparation | x-y-z move (0.25/1 µm),<br>two rotations (0.25/1 mdeg),<br>optical microscope |
| Detector | Measurement of forward scattering<br>and diffraction | 2-D, 4K×4K pixels,<br>10×10 µm pixel size,<br>central hole or beamstop,<br>mounted on diffract. arm |
| Intensity monitor | Measurement of transmitted photon<br>flux | Transmissive (<5% absorption),<br>single pulse measurement,<br>relative accuracy $<10^{-3}$ |
| Wavefront sensor | Verification of wavefront errors;<br>Adjustment of sub-µm optics | |
| Alignment unit | Positioning and position verification | Permanently operating,<br>accuracy ~100 µm |
| Lead hutch | Radiation protection,<br>temperature stabilisation,<br>laser protection | 4×10×3.5 $m^3$ (W×L×H),<br>±1° thermal stability |
| Control hutch | Operation of the instrument | Working environment<br>(noise, temperature, light) |

***Table 6.4.8*** *Elements and specifications of the CXI 3 instrument.*

### 6.4.4 X-Ray Photon Correlation Spectroscopy

Coherent x-rays are particularly well suited for the study of nanoscale dynamics using x-ray photon correlation spectroscopy. The study of fast (t << 1 µs) dynamics (at large momentum transfers Q) was, up to now, restricted to the energy domain (inelastic) techniques. With the XFEL and its unprecedented peak brilliance and high degree of coherence one will be able to study fast dynamics in the time domain which is of outmost importance for a wide variety of phenomena **[6-175]**. Coherence preserving optics coupled with fast 2-D detectors will be essential to the success of this technique at the XFEL.

#### *6.4.4.1 Scientific case*

Complex nanoscale dynamics is an omnipresent phenomenon which is investigated at the frontier of condensed matter research. It comprises a multitude of collective processes such as the visco-elastic flow in liquids, polymer dynamics, protein folding, crystalline phase transitions or the switching of domains. The involved timescales range from femtoseconds to seconds. Slow processes (t >1 µs) are, in favourable cases, accessible via conventional XPCS at third generation synchrotron radiation sources **[6-176]**. The study of fast (t << 1 µs) dynamics (at large momentum transfers Q) is,

however, restricted, up to now, to the energy domain (inelastic) techniques. This, however, will change with the new FEL sources providing extremely brilliant (B>$10^{33}$ ph/s/mm$^2$/mrad$^2$/0.1% bw) and highly coherent x-ray beams. For the first time one will be able to study fast dynamics in the time domain, thus giving direct access to the dynamic response function S(Q,t), instead of S(Q,$\omega$), which is of central importance for a variety of phenomena such as fast non-equilibrium dynamics initiated e.g. by a short pump pulse.

XPCS measures the temporal changes in speckle patterns produced when coherent light is scattered by a disordered system. Today's third generation synchrotron light sources can measure the low frequency dynamics ($10^6$ Hz to $10^{-3}$ Hz) in a Q range from, typically, $10^{-3}$ Å$^{-1}$ up to several Å$^{-1}$. X-ray Photon Correlation Spectroscopy is, in particular, complementary to Dynamic Light Scattering (DLS) or Photon Correlation Spectroscopy (PCS) with visible coherent light which also probes slow dynamics ($\omega < 10^6$ Hz) but can cover only the long wavelength Q < $10^{-3}$ Å$^{-1}$ regime. X-ray Photon Correlation Spectroscopy is furthermore, not subject to multiple scattering, a phenomenon frequently complicating the analysis of PCS data in optically opaque systems. Neutron-based techniques (inelastic and quasi-elastic neutron scattering, neutron spin-echo) or Inelastic X-ray Scattering (IXS) on the other hand, can access the same Q range as storage-ring based XPCS but probe the dynamic properties of matter at high frequencies from, typically, $10^{14}$ Hz down to about $10^8$ Hz. The XFEL with its coherent flux increased by nine orders of magnitude, will allow, for the first time, coverage of dynamics up to about $10^{13}$ Hz at large Q. This is illustrated in Figure 6.4.28 showing frequency-wavevector space covered by a selection of relevant methods. There is a wide variety of problems to be addressed (see, for example, **[6-177, 6-178]**) and some prominent examples are summarised in the experimental programme.

### Experimental programme

Coherence is one of the most prominent features of XFEL radiation. A comprehensive understanding of its coherence and correlation properties is not only of fundamental interest but a necessary condition for coherence-based experiments. A characterisation of the coherence properties is thus mandatory before proceeding to time domain experiments.

### I. Coherence and correlations

The methodology of characterising coherence properties in terms of correlation functions is theoretically well developed and experimentally established by the optical laser community. We propose to setup and carry out an experimental programme aimed at studying first- and higher-order correlation functions, which allows one to determine not only the spatial and temporal coherence parameters (including the coherent flux) but also provides insight into the mode structure, photon statistics (bunching/antibunching) and possible non-Gaussian properties of the source. The programme will involve single (100 fs) shot Young's Double Slit experiments and (Hanbury-Brown Twiss type) intensity-intensity correlation experiments. The results will be fundamental to the tuning and upgrade programme of the facility since the results are directly comparable with FEL simulations that predict the mode structure and the degree of coherence. The expected

high degree of coherence will also open a route to non-Gaussian dynamics (e.g. intermittent dynamics in complex fluids **[6-179]**) via higher order time correlation functions.

### II. Study of glassy dynamics

Many liquids, when rapidly cooled below their freezing points, form metastable glassy or amorphous phases. This applies for a wide variety of materials including metallic alloys, oxides such as Silica, polymeric materials, and many others. Regardless of their importance, glassy materials are probably among the least understood materials at a fundamental level. Conventional equilibrium statistical mechanics does not predict the existence of the amorphous state, whereas it can explain most other states of matter, even quite exotic ones like superconductivity and superfluidity. Understanding visco-elastic effects in glassy materials is, thus, an important topic of fundamental research.

Glassy materials can be classified by the nature of their dynamics. In a typical glass-forming system, the viscosity increases exponentially by many orders of magnitude as temperature is lowered, until viscous flow processes are effectively frozen. Methods such as DLS or NMR have helped to characterise the relevant relaxation processes such as the primary (a) relaxation processes with timescales associated with viscosity. Other, faster (b) processes are also observed near the glass transition **[6-180]**. The nature and role of these processes are still under debate and discussed, for example, in the framework of mode coupling theory **[6-180, 6-181]**.

Experiments set up to study the transition require slow rates to look for the underlying thermodynamic phase transition but still need to be fast enough to avoid crystallisation. Light scattering, neutron scattering, and recently inelastic x-ray scattering **[6-182]** have examined phonon-like modes in these systems and have seen important changes near the glass transition. But measurement times are long, making the systems difficult and frequently even impossible to study with inelastic techniques in particular when the relevant timescales fall below the 1 MHz regime (see also Figure 6.4.28).

X-ray Photon Correlation Spectroscopy measures the time constants of a system as a function of wave vector and gives direct information on the dynamics. The region of Q and t covered by XPCS is very important for the understanding of the nature of the dynamics in glass forming systems both on the atomic and nanoscale. It is proposed to undertake studies spanning a very large range of timescales ($l0^{-12}$ to $10^{3}$ s) in order to observe the evolution of the dynamics from liquid to glassy behaviour as the temperature is lowered. There are many possible candidates for study, such as $B_20_3$. This is a random-network glass with well understood macroscopic properties **[6-183]**, and on which complementary Raman **[6-184]** and neutron scattering **[6-185]** studies have been performed. Its low electron density helps to minimise adiabatic heating by the beam. In order to cover the very large range in timescales different experimental set-ups (see below) will need to be applied.

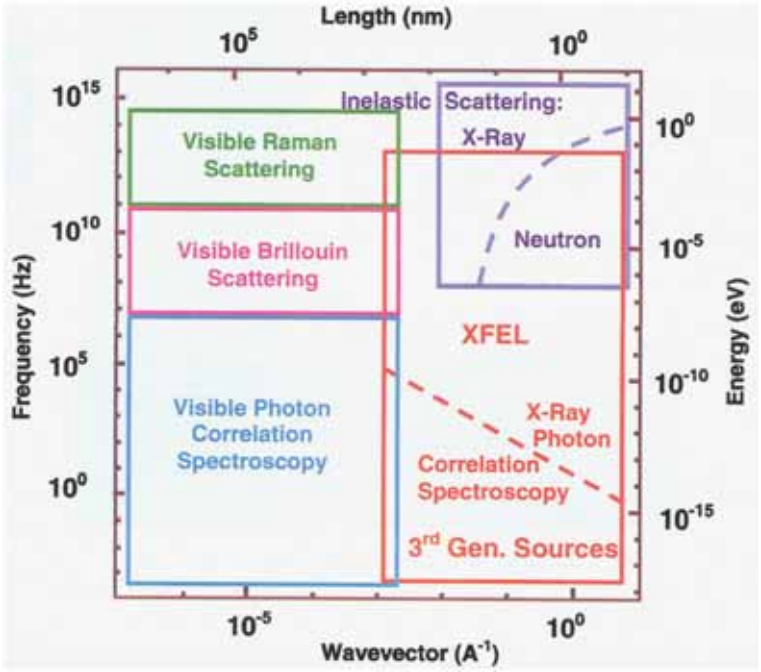


***Figure 6.4.28*** *Frequency-wavevector space covered by different experimental techniques. X-ray Photon Correlation Spectroscopy can operate at large Q and cover slow dynamics at third generation sources and fast dynamics at XFEL sources.*

### III. Phonon spectroscopy

X-ray Photon Correlation Spectroscopy can access density fluctuations allowing experiments related to phonon spectroscopy that can be done today with inelastic x-ray and neutron scattering. However, since the dynamics is measured directly in the time domain, one can access the full timescale from picoseconds to nanoseconds and longer in a single experiment. Moreover, there is the opportunity to examine higher order correlation functions from a cross-correlation analysis of the speckle pattern. While traditional inelastic scattering experiments are limited to density-density correlations, picosecond-XPCS could shine new light on short time dynamics, where coordinated motions of several molecules become important, e.g. during a crystallisation process.

However, even with the extremely high brilliance of the XFEL, it will not be possible to observe equilibrium dynamics of phonons directly (maybe with the exception of extremely strong acoustic phonons very close to a Bragg peak) since the average scattered intensity per speckle will be much less than one count per pulse **[6-186]**. Therefore, one has to add many speckle patterns before a correlation analysis can be done. This will average out random thermal fluctuations. Instead, one will observe phonons that are coherently excited, e.g. by a first x-ray pulse. Typically, a first pulse will generate a hot spot in the sample in the order of the beam size and x-ray attenuation length. A delayed pulse will then reveal insights into the thermal transport processes. To generate a smaller hot spot, a focused laser beam can be also used as a pump. A way to introduce distortions on an even smaller length scale is the use of standing x-ray waves. One could either place the sample in the standing wave field of a Bragg reflection or use x-ray

transient grating spectroscopy, where the coherent beam is split up and a standing x-ray pattern is generated by crossing these two beams.

### IV. Surface XPCS with an XFEL

Surface XPCS experiments at third generation storage sources have been performed successfully in the past and surface dynamics has been investigated on a variety of systems such as membranes, polymer films or bulk liquids. Surface XPCS, in combination with the x-ray standing wave technique, allows, for example, the study of fluctuations of buried interfaces. However, the nanometer length scale of surface dynamics is not accessible due to the limited coherent photon flux. Here, the XFEL provides exciting new possibilities. We will give an estimate of the expected timescales and count rates of surface XPCS experiments at an XFEL for capillary wave dynamics on three model liquids: water, liquid Mercury and liquid Glycerol.

**Water:** At Q = 0.1 Å$^{-1}$ the capillary waves on liquid water are overdamped waves with a correlation function $g_1(t)\sim\exp(-t/t_0)$. Continuum hydrodynamics yields a value of the relaxation time of $t_0 \approx 2.5\text{x}10^{-11}$ s which is 100 times longer than the 100 fs pulse width and 10000 times shorter than the pulse separation of 200 ns. Therefore, a delay line unit (see below) is mandatory for measuring relaxation times in this time region.

Assuming a delay line efficiency of 1% one can operate with two pulses carrying about $10^{11}$ photons each. If the detector subtends a solid angle $\Delta\Omega$ the intensity scattered into the detector can be estimated via **[6-187]**:

$$I = \frac{\Delta\Omega}{A}\frac{d\sigma}{\mathrm{d}\Omega} = I_0 \times \frac{\Delta\Omega}{A} \times L_x L_y \times \frac{\left|k_0^2(1-n^2)\right|^2}{16\pi^2} \times \left|T(k_1)\right|^2 \left|T(k_2)\right|^2 S(Q)\,, \qquad (6.2)$$

where A describes the beam area, $I_0$ the intensity of the incoming beam and $(d\sigma/d\Omega)$ the diffuse scattering cross section. $L_xL_y$ denotes the illuminated area, $k_0$ the x-ray wave number, n the index of refraction and $T(k_i)$ the transmission factors of the incident and exit beams, respectively. S(Q) is the capillary wave scattering function which can be approximated for grazing incidence geometry as $S(Q) \approx k_B T/2\pi\gamma Q^2$ where $\gamma$ denotes the surface tension. For incident angles below the critical angle of total external reflection, the number of photons scattered per (split) XFEL pulse at Q =0.1 Å$^{-1}$ into a detector area of $50 \times 50$ µm$^2$ at 1 m distance is $4\times10^{-4}$. With 3,000 pulses and 10 Hz repetition rate, one will detect about 12 photons per second. Thus, within minutes sufficient statistics should be obtained. At Q = 1 Å$^{-1}$ the count rate is 0.12 ph/s; at Q = 0.01 Å$^{-1}$ one finds 1,200 ph/s.

In the energy domain the overdamped correlation function would yield a Lorentzian energy spectrum centred at $\omega = 0$ with a width $\Delta$E of ca. 20 µeV for Q = 0.1 Å$^{-1}$. This energy broadening would be difficult to resolve with inelastic x-ray scattering.

**Liquid Mercury:** Liquid metals show interesting surface structures such as an atomic layering parallel to the free surface (liquid Mercury). Therefore, the capillary wave dynamics at small length scales is of special interest as the continuum hydrodynamics may be strongly affected by the layering properties of metal atoms at the surface. Up to

Q=0.2 $Å^{-1}$, continuum hydrodynamics is predicting propagating capillary waves on a liquid Mercury surface. Capillary waves with larger Q values are overdamped. The combination of high surface tension, low viscosity and high density makes the capillary wave dynamics on liquid Mercury faster than that of water. Moreover, the large value of the surface tension decreases the x-ray scattering cross-section considerably. For Q = 0.1 $Å^{-1}$ the expected relaxation time is $5\times10^{-13}$ s ($\Delta E$ = 1.3 meV) and the estimated countrate is about 0.18 ph/s.

**Liquid Glycerol:** Glycerol is a typical glass former and the viscosity strongly depends on temperature. At room temperature the viscosity of Glycerol is three orders of magnitude larger than that of water implying a considerably slower dynamics. Liquid Glycerol at -10°C has a viscosity of 35 Pa s. The capillary waves are overdamped and the relaxation time at Q = 1 $Å^{-1}$ is 100 ns. One can, thus, operate in a time regime without need for a delay line unit and can use $10^{13}$ photons per pulse. As the surface tension of liquid Glycerol is similar to water, the scattering cross-section will be very similar. Just by inspecting the numbers it seems that nanometer scale surface dynamics should be observable at least with liquid Glycerol. For Q = 0.1 $Å^{-1}$, the relaxation time is $10^{-6}$ s ($\Delta E = 6.6´10^{-7}$ meV) and the number of scattered photons into a $50\times50$ $\mu m^2$ aperture at 1 m distance is about 1,680 ph/s. We note that all these experiments are luminosity limited and the given estimates assume, in fact, the use of all 3,000 bunches in a 600 µs bunch train repeated at a 10 Hz repetition rate. Open questions to be investigated further are beam damage and the influence of bulk hydrodynamics **[6-188]** at large Q. The onset of non-classical behavior is a fundamental issue that is of interest for all liquids.

### V. Time-resolved magnetic scattering

Magnetic x-ray speckle has been observed in a variety of systems **[6-189]**. More recently it has been shown that magnetic stripe domains can be imaged with a coherent soft x-ray beam **[6-190]**. Sensitivity to magnetism in the CoPt multilayer stemmed from tuning the beam energy to the Co L3 absorption edge at 778 eV ($\lambda$=1.6 nm). A reference aperture in the sample allowed retrieval of the real-space structure of the sample by simple Fourier transformation and a resolution of 50 nm was achieved. Provided there is enough intensity, the temporal fluctuations of spins and magnetic domains can be studied by recording the intensity changes at one given point (or Q value) in the scattering pattern as a function of time. Specific to magnetic scattering experiments is the necessity to tune the incident beam energy to distinct absorption edges in the material in order to achieve or increase the sensitivity to the magnetic states or bands. The best suited absorption edges ($M_{4,5}$) in rare-earth systems and in 3d transition metals ($L_{2,3}$) would require circularly polarised, soft x-rays as provided by the SASE 3 undulator. As the ultimate size resolution is set by the wavelength of the scattered radiation, XPCS in the soft energy domain will allow the study of domain dynamics down to domain sizes of several nm in 3d transition metals, exploiting 2p-3d scattering resonances, and in rare-earth compounds, exploiting the 3d-4f processes. As the coherent scattering is sensitive to the individual domain pattern (beyond statistical averages), critical dynamics can be probed on a nanometre length scale down to timescales in the nanosecond and sub-nanosecond range. This opens up new routes to the investigation of domain fluctuations in the vicinity of the (Curie or Neel) transition temperature. Whether or not thin film magnetic systems

will be able to withstand the full XFEL beam will need to be explored in detail. First estimates indicate that this will be a very serious issue.

### VI. Non-equilibrium dynamics

When a disordered homogeneous material is rapidly brought to a new set of conditions, corresponding, for example, to the coexistence of two equilibrium phases, a spatial pattern of domains of the two phases develops. A change of conditions can, for example, be accomplished by a rapid quench from a high temperature to a low one below the miscibility gap. The result of such a quench is the creation of a microstructure of interconnecting domains. These domains grow in order to minimise the areas of the domain walls that separate the phases.

When the average domain size R(t) at time t is large compared to all other relevant length scales except for the dimension L of the system itself, the system looks invariant if all lengths are measured in units of that domain size. The time dependence of the average domain size can typically be described in terms of an exponent n, such that $R \sim t^n$. This scaling hypothesis applies to a large range of systems. For example, for systems described by a non-conserved scalar order parameter the growth exponent is found to be n=1/2. This applies, for example, Ising systems with spin-flip dynamics, binary alloys undergoing an order–disorder transformation or some magnetic materials. For other systems with conserved order parameter and with diffusion being the only growth parameter one finds n=1/3. This applies for the conserved Ising model and, for example, binary alloys undergoing phase separation. Information on the statistics of fluctuations about this average behaviour (which differs from classical fluctuation statistics) is, however, scarce because conventional methods are not easily applicable since (by the nature of the process) the absolute time matters. A time domain method, such as XPCS, can address such processes as has been shown in recent prototype experiments **[6-191, 6-192]**. Here, fluctuations about the average intensity can be quantified by means of a two time ($t_1$, $t_2$) intensity correlation function.

$$C(Q,t_1,t_2) = \frac{\langle I(t_1)I(t_2)\rangle - \langle I(t_1)\rangle\langle I(t_2)\rangle}{\left[\langle I^2(t_1)\rangle - \langle I(t_1)\rangle^2\right]^{1/2}\left[\langle I^2(t_2)\rangle - \langle I(t_2)\rangle^2\right]^{1/2}} \qquad (6.3)$$

Figure 6.4.29 shows a contour plot of a two-time correlation function for the example discussed in **[6-17]**. Values of C for each contour and the directions of the alternative coordinates $t_{mean}=(t_1+t_2)/2$ and $\Delta t$ are indicated. It is readily observed that the lagtime $\tau = \Delta t/2$ increases as a function of increasing absolute time $t_{mean}$, thus, showing that the dynamics is getting slower as a function of $t_{mean}$. It was shown in the experiment that the correlation times actually obey a scaling law in agreement with the model expectations. Similar experiments were carried out in phase-separating AlLi alloys and analysed successfully in terms of two-time correlation functions **[6-192]**. It is evident that the XFEL will allow the study of the early (short-time) stages of these processes. The XPCS pump-probe configuration will be ideally suited for any type, but in particular fast, non-equilibrium process. The pump or trigger source for reactions or transformations may comprise optical lasers, the XFEL, a Terahertz source, pulsed electric and magnetic fields and/or others.

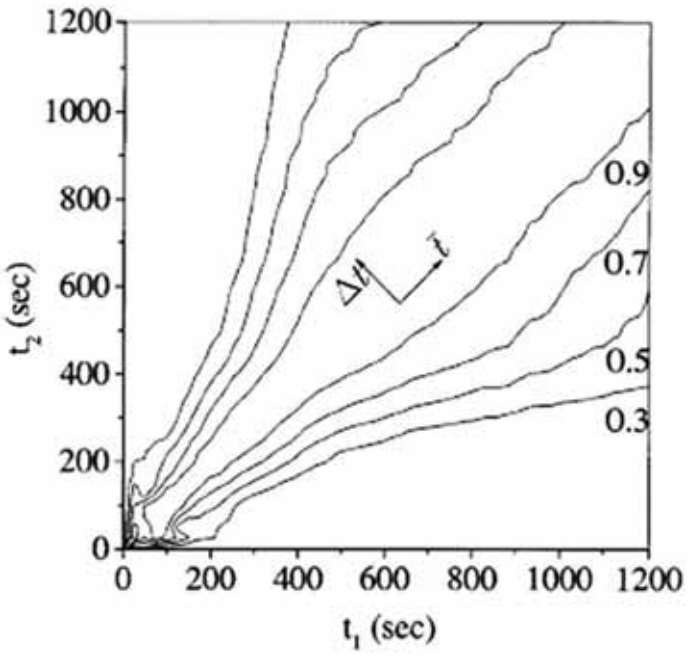


***Figure 6.4.29*** *Contour plot of two-time correlation function at Q=0.01 Å$^{-1}$ in borsilicate glass after a quench to 963K. $\Delta t$ refers to the lagtime and t= $t_{mean}$=($t_1$+$t_2$)/2* **[6-191]**.

### XPCS technique

X-ray Photon Correlation Spectroscopy probes the dynamic properties of matter by analysing the temporal correlations between photons scattered by the material. Correlations of the scattered intensity can be quantified via the normalised time correlation function:

$$g(t) = \frac{\langle n(t)n(t+\tau)\rangle}{\langle n\rangle^2} \qquad (6.4)$$

where n(t) is the number of detected photons at time t and the brackets denote the time average. X-ray Photon Correlation Spectroscopy requires the sample to be illuminated coherently. Thus an intense x-ray beam with sufficiently large transverse $\xi_t$ and longitudinal $\xi_l$ coherence length is required. The longitudinal coherence length $\xi_l = \lambda^2/\Delta\lambda$ depends on the monochromaticity of the beam. With an intrinsic bandwidth of ≈ 0.1% one finds $\xi_l$ = 100 nm. Larger longitudinal coherence lengths can be achieved by monochromatisation. This estimate of the longitudinal coherence length agrees to within a factor of 2 with the results of simulations for the SASE process that yield a coherence time between 0.2 fs and 0.22 fs for $\lambda$=0.1 nm. The longitudinal coherence length must be larger or equal to the maximum path length difference in the sample under investigation. Thus, $\xi_l$ sets a limit for the largest accessible momentum transfer Q. The transverse coherence length is usually determined by the source size $\sigma$, the wavelength $\lambda$ and the distance to the source R via $\xi_t$ » ($\lambda$/2) (R/$\sigma$). For the XFEL, the beam can be expected to be largely spatially coherent, and $\xi_t$ corresponds to the beam size. The flux of coherent

x-rays is proportional to the source brilliance B via $F_c = (\lambda/2)^2 \times B$. The high coherent x-ray flux from the XFEL will allow XPCS measurements at higher frequency $\omega$ and on a greater variety of materials, overlapping with energy-domain measurements using neutron and x-ray inelastic scattering. Time-domain XPCS measurements will provide truly complementary information for understanding relaxational processes (e.g. often associated with the 'central peak' in inelastic scattering). The accessible time windows will naturally be influenced by the time structure of the XFEL (see also Figure 6.1.1). To exploit the unique features of the XFEL, we propose the development of an instrument with the capability for three types of XPCS techniques:

- Using the very high time-averaged coherent x-ray flux from the XFEL to carry out XPCS measurements over timescales from $10^{-1}$ to $10^{3}$ seconds or between 200 ns and 600 μs by recording a sequence of speckle patterns ('sequential' technique).
- Using the extremely high-peak coherent x-ray flux from the XFEL to carry out XPCS measurements over timescales from $10^{-12}$ to $10^{-8}$ seconds using a 'split-pulse' technique.
- The 'pump-probe' technique is based on a comparison of two speckle patterns. One taken before the pump pulse hits the sample and a second one taken at time $\Delta t$ after the pump pulse has excited the sample.

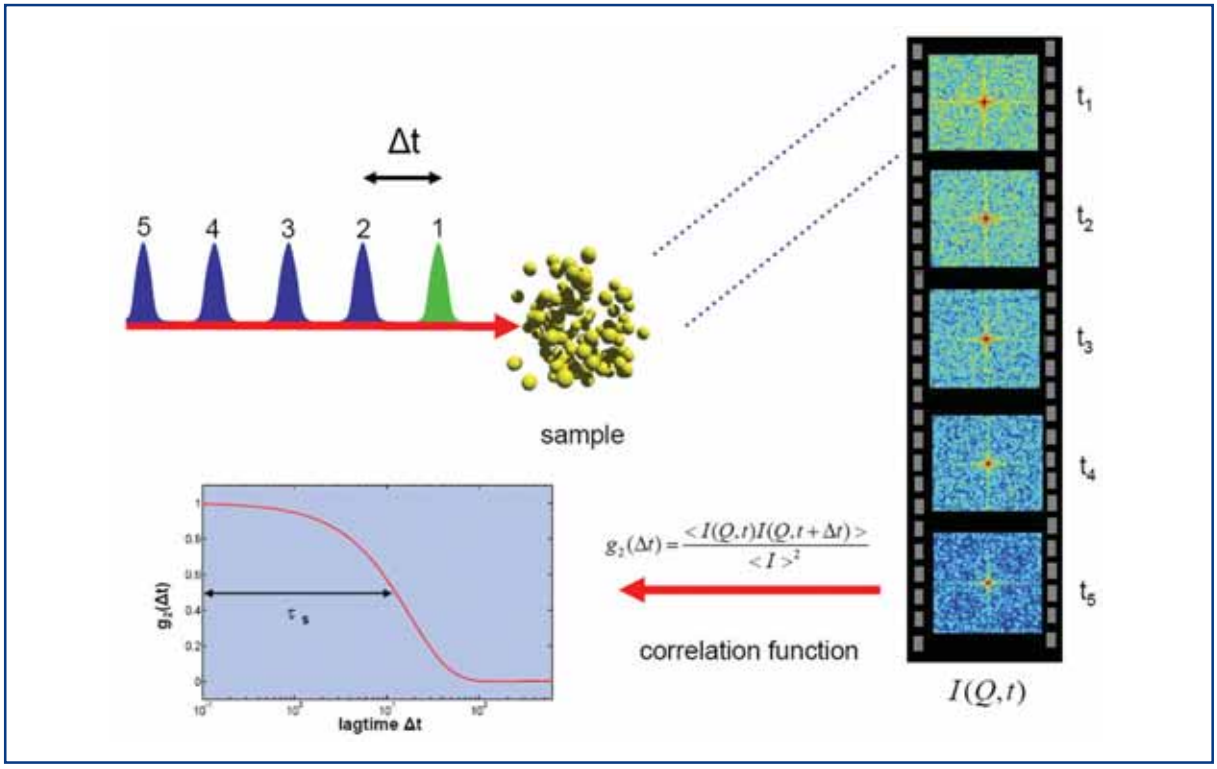


***Figure 6.4.30*** *Illustration of the XPCS sequential technique.*

**Sequential technique:** Important aspects of the microscopic dynamics of systems occur on relatively long timescales, e.g. longer than 0.1 s. This means that it will be possible to employ the very high time-averaged coherent x-ray flux from the XFEL, averaged over the 0.1 s bunch duration, to investigate the dynamics using XPCS data collection and analysis techniques that are similar to those used now. Such an experiment consists of collecting a sequence of speckle patterns on an area detector (see Figure 6.4.30). From an analysis of these sequences, correlation times from a few repetition times up to many minutes can be measured. The advantage of the XFEL will be in higher signal rates than currently available. The specific time structure of the XFEL will also allow the recording of dynamic data within the 600 µs long macro-bunches. The shortest time will be given by the micro-bunch separation of 200 ns. It might turn out to be favourable to divide up this time window in logarithmic time bins, thus, requiring a 2-D detector to operate at a 5 MHz frame rate but only with a limited number of frames to be stored.

**Split-pulse technique:** The short pulse duration of the XFEL will allow the extension of XPCS studies to much faster timescales than currently possible. For example, to understand the dynamics in glass-forming systems at the nanoscale, it will be important to carry out studies spanning a very large range of timescales ($10^{-12}$ to $10^{3}$ s) in order to observe the evolution of the dynamics from liquid to glassy behavior as the temperature is lowered. In order to probe timescales between $10^{-12}$ and $10^{-8}$ s, we propose the development of a split-pulse technique (Figure 6.4.31), taking advantage of the instantaneous brilliance of the XFEL. The concept of the technique is to split each x-ray pulse into two equal-intensity pulses separated in time, but propagating along the same path. The scattering from the two pulses will then be collected during the same exposure of an area detector. If the sample is static on the timescale of the two pulses, the contrast in the summed speckle pattern will be the same as that from a single pulse. If the sample evolves on this timescale, the summed speckle pattern will have lower contrast. Thus, by analysing a set of such patterns, each for a different time delay, the correlation times of the system can be measured, on timescales down to the pulse duration. A pulse splitter with a path length difference variable from $3 \times 10^{-4}$ to 3 m would give delay times from about $10^{-12}$ to $10^{-8}$ seconds. Longer time delays between pulses may be possible using two electron bunches in the FEL.

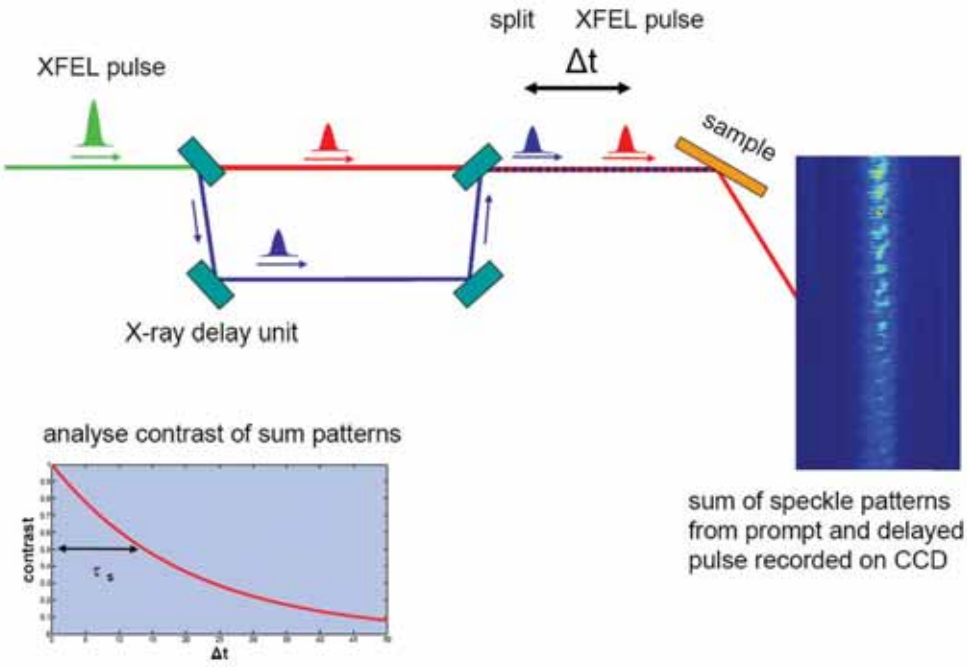


***Figure 6.4.31*** *Illustration of the XPCS split-pulse technique.*

**Pump-probe technique:** The XPCS pump-probe technique (Figure 6.4.32) compares two speckle patterns: one before exposing the sample to a pump pulse with a second pattern taken a time interval $\Delta t$ after the pump pulse. The pump sources for reactions and transformations may comprise optical lasers, the XFEL, a Terahertz source, pulsed electric and magnetic fields, shock waves, and/or others. This allows us to address timescales between 100 fs and typically, 200 ns or longer. This configuration can be used to explore the timescales for magnetisation processes, phase transitions in ferroelectrics, surface dynamics and, for example, during pulsed laser deposition or internal motions in proteins. In principle one could also combine the pump pulse with the above described split-pulse technique.

### Beam damage issues

The pulsed structure of the XFEL presents an important issue for the design of a beamline optimised for XPCS measurements, because of potential sample heating by the beam. For dynamics studies, one would like to avoid heating the sample by more than a few degrees during the measurement. For a pulsed source, two regimes must be considered: a) Adiabatic heating by each pulse, over timescales too small for significant heat flow, so that the temperature rise is determined by the heat capacity of the material; and b) steady-state heating by the time-averaged power in a train of pulses.

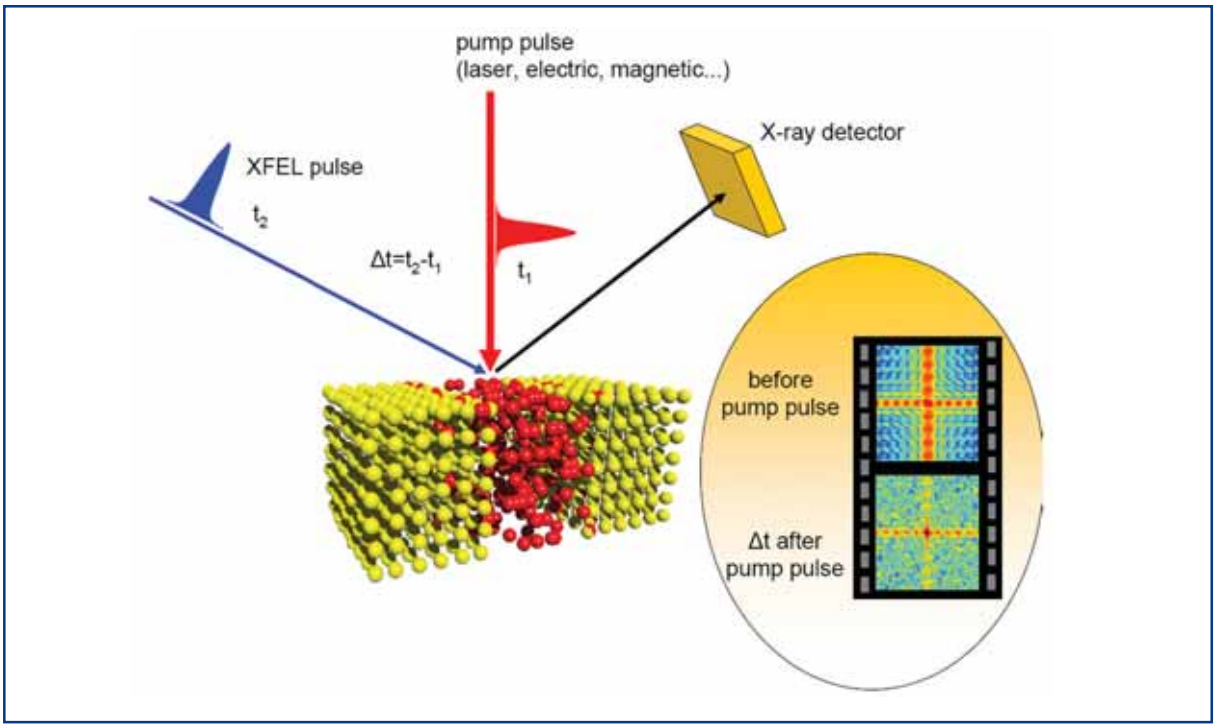


***Figure 6.4.32*** *Illustration of the XPCS pump-probe technique.*

In this second limit, the temperature rise is given by a balance of energy flow into and out of the sample volume. The ratio of the thermal time constant for heat dissipation to the pulse spacing determines whether the adiabatic or steady-state temperature rise is larger. Figure 6.4.33 illustrates the temperature response at the beginning of a pulse train in each of these limits.

The amount of sample heating in the adiabatic case can be evaluated using an analysis developed for the LCLS case **[6-179]**. Figure 6.4.34 shows a comparison of the quantities $N_{MIN}$ (the minimum required number of photons per pulse to give sufficient signal per speckle), $N_{MAX}$ (the maximum tolerable photons per pulse to avoid sample disturbance) and $N_{AVAIL}$ (the available photons per pulse). These are plotted as a function of sample composition for two energies, using $\Delta T_{MAX}$ = 1 K, a beam area of $10^{-4}$ $cm^2$, and two types of samples (having relatively narrow or broad scattering). The calculation predicts that XPCS will be feasible when the value of $N_{MIN}$ is lower than both $N_{MAX}$ and $N_{AVAIL}$ (shaded areas). The result depends strongly on sample composition and photon energy. Because of the order-of-magnitude uncertainty in several quantities, these calculations do not provide exact limits, but do indicate that feasibility will depend upon photon energy, sample composition and scattering power.

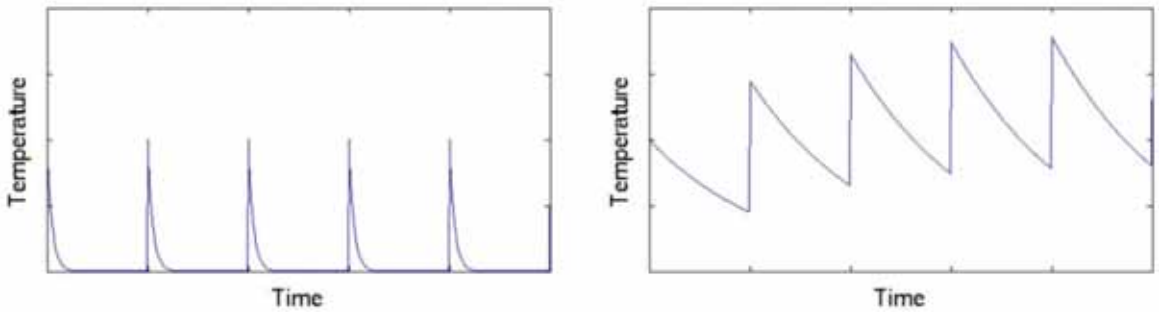


***Figure 6.4.33*** *Schematic temperature response to a pulse train, for samples with a thermal time constant that is a) smaller or b) larger than the pulse spacing.*

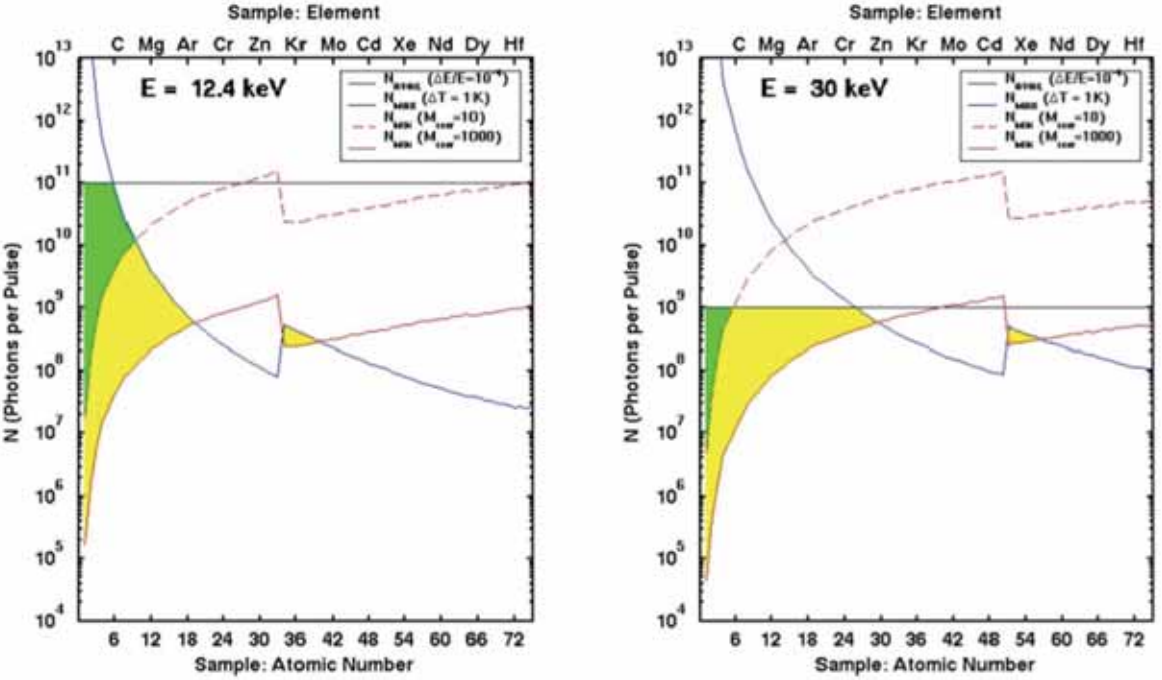


***Figure 6.4.34*** *Comparison of the calculated number of photons per pulse available from the XFEL ($N_{AVAIL}$), the number tolerable due to beam heating of the sample ($N_{MAX}$), and the number required for XPCS ($N_{MIN}$) for two types of samples, corresponding to a typical liquid or glass ($M_{corr}$ = 10) or to nanoscale clusters in a polymer blend ($M_{corr}$ = 1,000), as a function of sample composition, at 12.4 (left) and 30 (right) keV photon energies. Experiments are feasible in the shaded regions (see also* **[6-179]***).*

The relatively short time between pulses at the XFEL (200 ns) compared with LCLS (8 ms) means that steady-state sample heating must also be considered for the XFEL. Here. we present an analysis based on a simple transmission geometry, where the penetration depth of the x-rays is larger than the beam diameter. The illuminated sample volume is thus, a cylinder having the diameter of the beam, d.

We consider conduction transverse to the beam direction as the primary energy flow out of the sample. A thermal time constant can be calculated that is the ratio of the adiabatic

temperature rise per unit deposited energy, to the steady-state temperature rise per unit deposited power. This is given by $\tau \approx d^2 \log(d_0/d)/8D_{th}$, where $d_0$ is the outer diameter of the thermal diffusion zone and $D_{th}$ is the thermal diffusivity. Table 6.4.9 shows values of $\tau$ calculated for various sample materials, taking $d_0$ to be twice the absorption length at 12.4 keV. The time constant is smaller for smaller beam diameters. For highly conductive materials such as Gold or Copper, the thermal time constant can be less than the XFEL pulse spacing (200 ns). However, for most materials, the thermal time constant is larger than 200 ns, indicating that the steady-state temperature rise will be larger than the adiabatic temperature rise if the sample is exposed to every pulse.

| Material | $D_{th}$ [$cm^2/s$] | $\tau$ (d=25 µm) [µs] | $\tau$ (d=10 µm) [µs] |
|---|---|---|---|
| Au | 1.32 | 0.40 | 0.063 |
| Cu | 1.12 | 0.46 | 0.074 |
| Al | 0.84 | 2.9 | 0.60 |
| $Al_2O_3$ | 0.072 | 35 | 7.1 |
| $SiO_2$ glass | 0.003 | 890 | 180 |
| $H_2O$ liquid | 0.0014 | 3200 | 590 |

***Table 6.4.9*** *Thermal time constants $\tau$ for various materials, taking $d_0$ twice the absorption length at 12.4 keV. Here d is the beam size and $D_{th}=k / C_p$ the thermal diffusivity.*

### *6.4.4.2 Instrument requirements*

The experiments described above lead to requirements for an instrument for scientific applications using XPCS techniques. They concern the performance of the light source, the optical elements and the diagnostic equipment, the sample environment, and detectors. The experiments described in this section request mostly hard x-ray XFEL radiation at ~12 keV photon energy. For some experiments one wants to apply third harmonic radiation at considerably higher photon energy, thereby reducing the beam damage. In addition, for investigations of magnetism, tunable radiation around characteristic energies of magnetic materials are of interest. These are the $L_{2,3}$-edges of the transition metals (0.4 – 1.0 keV) and the $M_{4,5}$-edges of the rare-earth elements (0.9 – 1.5 keV). The full photon energy range of 0.4-12 keV in the fundamental FEL line and ~30 keV using higher harmonics will not be provided by any of the European XFEL beamlines solely. The use of SASE 1 and SASE 3 beamlines is proposed instead.

**Spectral radiation properties**

To improve the longitudinal coherence, and thereby, the accessible Q-range, monochromatisation of the incident radiation to the level $\Delta E/E \leq 10^{-4}$ needs to be achieved. Use of such a monochromator will at the same time increase the observable contrast in the scattering pattern and reduce the beam damage in the sample. For the hard x-ray case double-reflection fixed exit geometry will be used to maintain flexibility in the setup. The selection of third harmonic radiation will be achieved as well by this

monochromator. For soft x-rays, the grating monochromator will have to be used to achieve the requested resolution. In selection of the optical elements of the monochromators great care has to be taken not to disturb the transverse coherence properties of the XFEL radiation.

### X-ray optics requirements

Crucial for any coherence-based technique is the conservation of the x-ray wavefront by the first mirrors and the monochromator. It has been simulated for the hard x-ray case that a figure error in the range of 1 µrad would distort the beam at the instrument considerably. The target value for the figure error of the mirrors should be substantially better than 0.1 µrad. A similar stringent requirement holds for the monochromator crystals. The asymmetry angle between crystal planes and surface should be less than 0.1 µrad. To compensate figure errors resulting from heat load and gravitational sag, the second mirror should have a local active correction mechanism.

The most challenging request for optics comes from the proposed use of x-ray beam splitters for these experiments. A beam-splitter/delay-line unit will comprise up to eight perfect crystals providing a path length difference between the two split pulses between 1 ps and 10 ns.

The beamsize at the sample will be determined by the experiments, in particular the sample geometry. Therefore, focusing the XFEL beam to a spot size in the order 10-100 µm should be enabled.

### Time domain requirements

These experiments probe dynamics on a huge timescale from $10^{-12}$ s up to several seconds. This can be achieved by exploiting the sequential and split-pulse techniques proposed in the previous section. The split-pulse and pump-probe techniques make use of the 100 fs pulse duration of the XFEL pulses. Whereas the split-pulse technique defines its own timescale by using one single pulse, the pump-probe technique uses two different sources and, therefore, requires synchronisation of the two sources. The synchronisation should be significantly better than the anticipated time resolution of ~100 fs. For the same reason the fluctuation of the pulse duration must be small compared to the 100 fs timescale. In addition, a synchronisation of 100 fs will be required for the operation of x-ray streak cameras.

It is anticipated that a variety of pulse patterns from single pulses at 10 Hz repetition rate up to several hundreds of x-ray pulses per electron bunch train will be used. A particular request comes from the sequential technique where it is possible to use the time pattern of the accelerator to probe timescales from 200 ns (shortest bunch distance) up to 600 µs (duration of bunch train).

### Photon diagnostics requirements

All experiments will need good diagnostic equipment for the measurement of the photon beam intensity on a pulse-to-pulse basis. To further estimate the intensity in W/cm$^2$ at the sample with a high degree of confidence, the measurement of the pulse duration and of

the spatial properties at the focus are important. Since monochromators are used the measurement of the mean photon energy is not required and spectral diagnostics should provide the content of higher harmonic radiation only. All measurements must be available on a pulse-to-pulse basis.

**Sample manipulation and environment**

Sample mounting and sample environments should allow for x-y-z linear movements (1µm repeatability and 0.25 µm resolution) and angular degrees of freedom (1/1,000 ° repeatability, 1/4,000 ° resolution.). The hard x-ray instrument could be placed in vacuum or even in air if windows are used as a vacuum interface. The windows should receive only the unfocused beam, meaning they should be mounted near the local optics. The soft x-ray instrument will differ from the other one in requiring a single vacuum system throughout, with no windows, including the detector chambers. A clever design of the vacuum system should allow variation of the distance to the detectors. For the soft x-ray experiments at magnetic resonances in-vacuum magnet- and cryosystems will be needed.

**Detector requirements**

These experiments make high demands on two-dimensional x-ray detectors in terms of frame rate, pixel number and pixel size. The realisation of such detectors requires a specific R&D effort that will be described in Section 6.5.4. The specific detector requirements for the XPCS instruments can be found in Section 6.5.4.1.

In addition, an ultrafast x-ray streak camera will be required for calibration of the x-ray beam split and delay line unit and point detectors for alignment and fixed-Q measurements.

**Visible laser requirements**

Visible lasers will be applied in pump-probe experiments. A wavelength tunable system providing pulse durations in the order of 30 fs and pulse energy up to 1 mJ at 800 nm will allow the carrying out of the experiments proposed in this area. Synchronisation to the x-ray beam in the order of the pulse duration or pulse-to-pulse measurements of the jitter is requested.

### *6.4.4.3 Realisation of the instrument*

The XPCS experiments require two instruments at SASE 1 (PCS 1 – Hard x-rays) and at SASE 3 (PCS 2 – Tunable soft x-rays). For a description of the SASE 1 and SASE 3 beamlines see Sections 6.2.4.1 and 6.2.4.3, respectively. The bulk of experiments will be carried out at SASE 1 using hard x-rays at fixed photon energy. All experiments discussed in Section 6.4.4.1 under topics I.-IV. and VI. will use hard x-rays at fixed photon energy.

For some of these experiments it might be of interest to use third harmonic radiation; and PCS 1 foresees the possibility of using this photon energy for the sample location. The PCS 1 instrument will operate using a double-bounce fixed exit monochromator built into the SASE 1 beamline. Since this monochromator is positioned in front of the offset

mirrors operation of the PCS 1 instrument without mirrors is enabled. The experiments investigating magnetism will be carried out at the PCS 2 instrument at the SASE 3 beamline using the built-in monochromator. The PGM monochromator of the SASE 3 beamline needs to be optimised in order not to disturb the wavefronts. Both instruments will require focusing the XFEL radiation.

Moderate focusing to beam sizes in the order of 100 µm is achieved by using a focusing element inside the corresponding beamlines. For the PCS 1 instrument this is likely to be compound refractive lenses (CRLs). By varying the location of the lenses, focal spots from 10-100 µm can be easily achieved. For the PCS 2 instrument refocusing of the monochromator exit slit is used to focus the beam at the sample location. Depending on the position of the focusing element, beam sizes from <10 to 100 µm can be achieved.

**PCS 1: Hard x-rays**

The following elements belong to the PCS 1 instrument inside the experimental hall. They are depicted in the schematic layout of that instrument in Figure 6.4.35 and are described in Table 6.4.10. The first part of the instrument includes specific optical elements for this instrument, like the beam-splitter-and-delay unit. This unit comprises up to eight perfect crystals providing a path length difference between the two split pulses between 1 ps and 10 ns. In addition, provision for additional focusing optics and/or a monochromator for $\Delta E/E <$ few $10^{-4}$ is made.

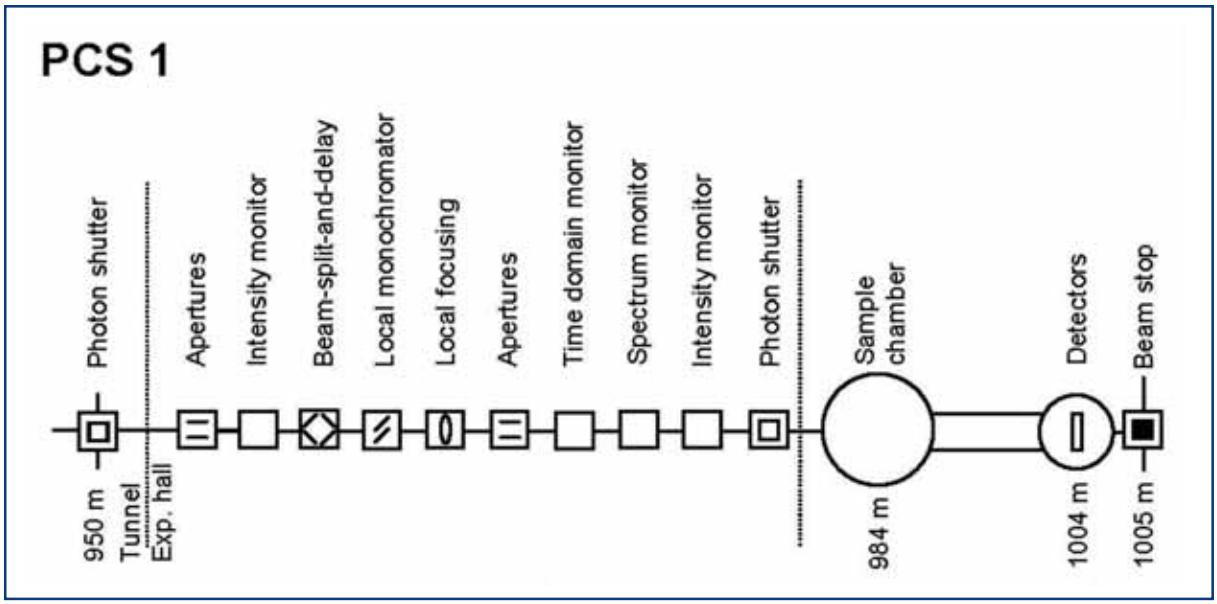


***Figure 6.4.35*** *Schematic layout of the PCS 1 instrument at the SASE 1 beamline. For this instrument diagnostics will be placed entirely upstream of the sample. The distance sample-detector can be varied.*

| Item | Purpose | Specification |
|---|---|---|
| Slits/apertures | Beam definition,<br>beam halo cleaning | 0.25 µm accuracy,<br>1 µm repeatability |
| Intensity monitor | Measurement of incident photon flux | Transmissive (<5% absorption),<br>single pulse measurement,<br>relative accuracy $<10^{-3}$ |
| Beam-split-and-delay | Splitting fund. line into equal parts,<br>delay 1 ps to 10 ns | High optical accuracy to maintain wavefront and x-ray pulse duration |
| Monochromator | Optics: Bandwidth < few $10^{-5}$ | 0.1 µrad angular stability,<br>0.1 mrad asymmetry error |
| Focusing optics | Optics: Extreme focusing (< 10 µm) | 0.1 µrad angular stability |
| Slits/apertures | Beam definition,beam halo cleaning | 0.25 µm accuracy,<br>1 µm repeatability |
| Time domain monitor | Measurements of x-ray arrival-time with respect to visible laser,<br>x-ray streak camera | |
| Spectrum monitor | Measurement high harmonic content | Single pulse measurement,<br>relative accuracy $<10^{-3}$ |
| Intensity monitor | Measurement of incident photon flux | Transmissive (<5% absorption),<br>single pulse measurement,<br>relative accuracy $<10^{-3}$ |
| Sample chamber | Sample positioning and orientation, | x-y-z move (0.25/1 µm),<br>two rotations (0.25/1 mdeg) |
| Detector | Measurement of diffraction pattern | 2-D, 5K×5K pixels,<br>80×80 µm$^2$ pixel size, |
| Alignment unit | Positioning and position verification | Permanently operating,<br>accuracy ~100 µm |
| Lead hutch | Radiation protection optics unit,<br>temperature stabilisation,<br>laser protection | 2×10×3.5 m$^3$ (W×L×H),<br>±0.5° thermal stability |
| Lead hutch | Radiation protection,<br>temperature stabilisation,<br>laser protection | 4×22×3.5 m$^3$ (W×L×H),<br>±0.5° thermal stability |
| Control hutch | Operation of the instrument | Working environment<br>(noise, temperature, light) |

***Table 6.4.10*** **Elements and specifications of the PCS 1 instrument.**

The final slit/aperture module should provide tuneable collimation with 1µm repeatability and 0.25 µm resolution. These elements are bracketed by two diagnostics units and a beamshutter separates the optics section from the experiments hutch which is assumed to have a minimum length of 22 m. The sample environment allows for linear movements (1µm repeatability and 0.25 µm resolution) and angular degrees of freedom (1/1,000 ° repeatability, 1/4000 ° resolution.). The sample to detector distance should be as large as 20 m. The detector equipment comprises fast point detectors, a streak camera and fast 2-D detector(s). A laser system for pump-probe experiments will also be required.

### PCS 2: Tunable soft x-rays

The following elements belong to the PCS 2 instrument inside the experimental hall. They are depicted in the schematic layout of that instrument in Figure 6.4.36 and are described in Table 6.4.11. The first element is a deflecting mirror that can be operated either as a flat mirror, using the focusing optics of the beamline, or as a focusing element, in order to achieve focusing of ~10 µm spot size. Next, the beam-splitter-and-delay unit is placed. For this photon energy it must be based on grating optics. A path length difference between the two split pulses between 1 ps and 10 ns is envisioned. Following an aperture and various diagnostics tools, including an x-ray streak camera for diagnostics of the beam-split-and-delay unit, a differential pumping section separates the beamline for the sample vacuum chamber. The use of windows will not be possible for this instrument. The sample environment allows for linear movements (1µm repeatability and 0.25 µm resolution) and angular degrees of freedom (1/1,000 ° repeatability, 1/4,000 ° resolution.). The sample to detector distance should be as large as 15 m. The detector equipment comprises fast point detectors and fast 2-D detector(s). A laser system for pump-probe experiments should be foreseen.

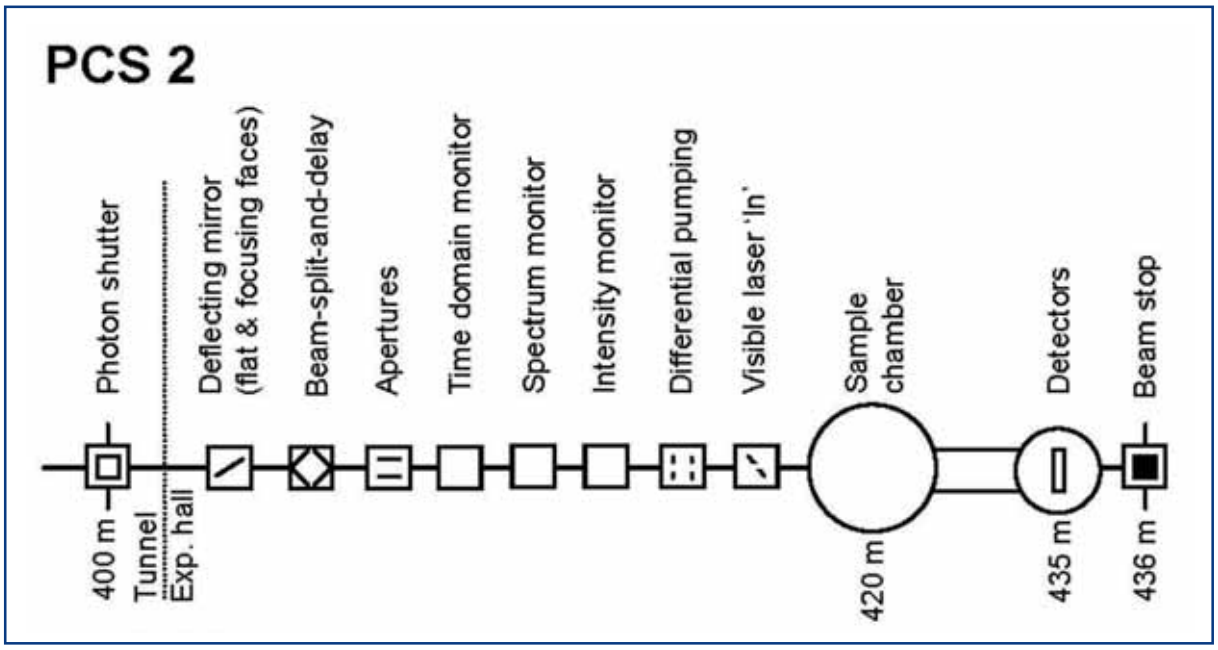


***Figure 6.4.36*** *Schematic layout of the PCS 2 instrument at the SASE 3 beamline. For this instrument diagnostics will be placed entirely upstream of the sample. The distance sample-detector can be varied.*

| Item | Purpose | Specification |
|---|---|---|
| Deflecting mirror | Flat, if using beamline focusing optics, curved for ~10 µm focusing | 0.1 µrad angular stability, 0.1 µrad figure error, 0.1 nm surface roughness |
| Beam-split-and-delay | Splitting fundamental line into equal parts, delay 1 ps to 10 ns | High optical accuracy to maintain wavefront and x-ray pulse duration |
| Slits/apertures | Beam definition, beam halo cleaning | 0.25 µm accuracy, 1 µm repeatability |
| Time domain monitor | Measurements of x-ray arrival-time x-ray with respect to visible laser, x-ray streak camera | |
| Spectrum monitor | Measurement of high harmonic content | Single pulse measurement, relative accuracy $<10^{-3}$ |
| Intensity monitor | Measurement of incident photon flux | Transmissive (<5% absorption), single pulse measurement, relative accuracy $<10^{-3}$ |
| Sample chamber | Sample positioning and orientation | x-y-z move (0.25/1 µm), two rotations (0.25/1 mdeg) |
| Detector | Measurement of diffraction pattern | 2-D, 5K×5K pixels, 80×80 µm$^2$ pixel size |
| Alignment unit | Positioning and position verification | Permanently operating, accuracy ~100 µm |
| Lead hutch | Radiation protection, temperature stabilisation, laser protection | 4×22×3.5 m$^3$ (W×L×H), ±0.5° thermal stability |
| Control hutch | Operation of the instrument | Working environment (noise, temperature, light) |

***Table 6.4.11*** *Elements and specifications of the PCS 2 instrument.*

## 6.4.5 X-ray absorption spectroscopy

### *6.4.5.1 Scientific case*

The development of femtosecond lasers brought entirely new possibilities into the practice of time-resolved spectroscopy, both for the UV-VIS and IR-Raman spectroscopies **[6-193]**. In addition, it has boosted the capabilities of non-linear spectroscopies beyond what could be imagined before their advent. With the implementation of femtosecond laser spectroscopies, it became possible to conduct observations on timescales that are shorter than single nuclear oscillation periods in molecules, liquids, solids, surfaces, interfaces and proteins.

The pump-probe scheme has been a revolutionary tool for observing real-time motion of bound states of small diatomic molecules in the gas phase and of elementary chemical reactions taking place in their unbound states **[6-194]**. The realisation of these experimental possibilities requires not only adequate time resolution for probing vibrations, but also excitation mechanisms suitable for initiating molecular motion in a phase-coherent (i.e., synchronised) manner in order to “observe” the transient structures **[6-194, 6-195]**. This

is the basis of **wave packet** dynamics that has brought about a description of the time evolution of systems in terms of **dynamics** rather than **kinetics**, which was, till then, the rule among chemists and biochemists. The implementation of pump-probe techniques and that of other ultrafast laser techniques to the study of systems of even greater complexity has occurred throughout the 1990's **[6-196 – 6-201]**, with the study of elementary reactions in gas phase organic molecules **[6-194]**, in liquids **[6-202]**, solids **[6-203 – 6-205]** and biological molecules **[6-198 – 6-201]**.

However, because of their wavelength, optical pulses cannot retrieve structural information. The structural information from femtosecond optical pump-probe experiments could only be obtained in the case of small diatomic or triatomic molecules in the gas phase, for which an **a-priori** knowledge of the potential energy surfaces is available **[6-194]**. This is usually not the case for larger assemblies of atoms (e.g. polyatomic molecules), and a further degree of complexity is added to the problem if we are dealing with condensed phases or biological samples, since intermolecular coordinates come into play.

In order to overcome these limitations, an extension of pump-probe techniques to the case where the probe pulse is in the x-ray domain has been considered and attempted by many since the mid-1990's **[6-206 – 6-212]**. Conceptually, the methods of ultrafast x-ray diffraction and x-ray absorption are similar to ultrafast optical pump-probe experiments, provided sufficiently short pulses of x-rays are available.

While the above stresses the possibility of **capturing transient structure**, it should also be underlined that any physical, chemical or biochemical transformation in matter (whether or not induced by light) is a consequence of a **redistribution of charges** (in particular, electrons) of the species constituting the system under study. Therefore, a technique is highly desired which, in addition to capturing **molecular or crystalline structures**, can also unravel the underlying **electronic structure changes** that drive the former ones. **X-ray absorption spectroscopy (XAS)** is such an approach, and with the advent of the XFEL, it will deliver an unsurpassed degree of insight into many physical and chemical phenomena.

Chapter V of the 2001 TDR **[6-213]** presented a very complete and comprehensive account of the scientific questions that could be dealt with the XFEL, in a broad range of systems: atoms, molecules and clusters, plasmas, condensed matter, materials, surfaces and interfaces, chemical systems, and biological systems, as well as in non-linear phenomena. The purpose of the present scientific case is to discuss technical issues related to x-ray absorption spectroscopy at the XFEL, in the light of recent scientific achievements with picosecond x-ray pulses at third generation synchrotrons **[6-211, 6-212, 6-214 – 6-225]**, and to present new scientific issues in chemistry, biology and condensed matter physics, which can only be addressed using x-ray spectroscopy as a method and an XFEL as a tool, and that were not covered in the TDR 2001. In this sense, the present study is an add-on to the 2001 TDR, and it can be updated whenever new scientific questions are raised.

**Why x-ray absorption spectroscopy ?**

The reasons that make XAS a particularly attractive technique for probing the electronic and geometric structure in a large class of systems are:

- It can be implemented in any type of media: gases, liquids, solids (amorphous or ordered), and biological samples. This allows, among other things, for a renewal of the sample, especially for time-resolved studies at the XFEL where sample damage may occur due to the high x-ray and/or optical laser flux.
- It is highly selective, since one studies one type of atom specifically, e.g., the physically, chemically or biochemically significant one, by simply tuning into its characteristic absorption edges.
- With X-ray Absorption Near Edge Spectroscopy (XANES) and Extended X-ray Absorption Fine Structure (EXAFS), one mainly probes the local structure in the immediate vicinity of the atom of interest. For time-resolved experiments in the femtosecond time domain, this is sufficient. Indeed, a typical timescale for the motion of matter is given by the velocity of sound: 0.03-0.1 nm/100 fs. This distance scale is exactly the one that is significant in chemical, biological and condensed matter physical phenomena. Since short timescales correspond to short distance scales, XANES and EXAFS are ideal structural tools in the femtosecond time regime of the XFEL.
- The precision of structural determination by EXAFS is on the order of $10^{-3}$ – $10^{-4}$ nm **[6-226 – 6-228]**, which is ideal for observing transient structures resulting from the photo-induced reaction.
- XANES looks at the valence orbitals of the atom of interest, which are precisely those involved in bond formation, bond breaking and bond transformation. Thus, one can detect the underlying electronic changes that drive the structural ones. In particular, the degree of oxidation of an atom and the occupancy of its valence orbitals are reported by XANES. In addition, for atoms embedded in an ordered atomic environment, the selection rules of core transitions can be altered by the local symmetry, so that structural information can also be retrieved.
- Using polarised x-ray pulses and laser-aligned samples permits the measurement of orientation-dependent spectra.
- It can detect optically silent species, which may result from a photoinduced process.
- Variants of x-ray absorption spectroscopy, such as linear and circular dichroism and spin-sensitive XAS, are now well established tools for the study of magnetic phenomena.

*Why x-ray absorption spectroscopy at an XFEL?*

The dramatic increase in flux and time resolution brought about by XFELs as compared to third generation synchrotron sources, will not merely be another breakthrough in technical achievement, but also allows us to truly envision new science. In terms of flux, we are on the verge of the revolution brought about by the discovery of lasers in the optical domain. In the following the feasibility of time-resolved XAS experiments at an XFEL source are discussed.

*Tunability and energy resolution*

By definition, XAS requires a tuneable source. Furthermore, since one wants to resolve fine structure, an energy resolution of $\Delta E/E \approx 10^{-4}$ is desired. Apart from synchrotrons, that are limited in pulse duration to tens of picoseconds, there exist no sources of tuneable **femtosecond** x-ray pulses, in particular in the hard x-ray domain **[6-212]**. The XFEL is the only one that will be able to provide this tunability, as femtosecond lab-based sources cannot provide it, and seem far from reaching this regime. SASE 2 and SASE 3 cover the region between 1.6 and 0.1 nm, which is ideal for accessing the core excitations of most light and heavy elements. Considering energy resolution, the SASE 2 and SASE 3 will have an energy resolution of $8\times10^{-4}$ to $1.8\times10^{-3}$, which is not sufficient for detailed XAS studies. This resolution can be improved by adding a monochromator. However, considerations of tunability and energy resolution cannot be disentangled from those of flux, which we now discuss.

*Flux considerations*

The calculation of the flux necessary to carry out a time resolved XAS experiment on transition metal compounds in a solution of first-row elements (e.g., water, hexane, and several other organic solvents), was already carried out in **[6-212]**. Figure 6.4.37 shows the required number of incident x-ray photons per data point to measure a transient EXAFS signal with unity signal-to-noise ratio. The calculations assume a 10% photolysis of the sample, and EXAFS changes are in the order of 1% relative to the absorption edge jump. Recent measurements of picosecond transient XAFS spectra of three different compounds **[6-223, 6-224, 6-229]** in aqueous solutions (consisting of three different elemental absorption edges) nicely confirm the results shown in Figure 6.4.37, when scaling the measured signal-to-noise (S/N) and excitation yields to the generic values used for the figure.

While these calculations indicate that a rather modest pulsed x-ray source is sufficient to measure transient structural changes via XAS, the need for more intense and shorter x-radiation to investigate new phenomena in the gas phase, in condensed phases and in biological systems (e.g., wavepacket dynamics) via XAS can only be underscored. One can evaluate the same parameter as in Figure 6.4.37, for the case of gas phase (with density $10^{11}$ $cm^{-3}$) and liquid phase samples (1mM aqueous solutions), and the results confirm that the corresponding experiments can be performed at the XFEL, some of them even with the spontaneous undulators sources.

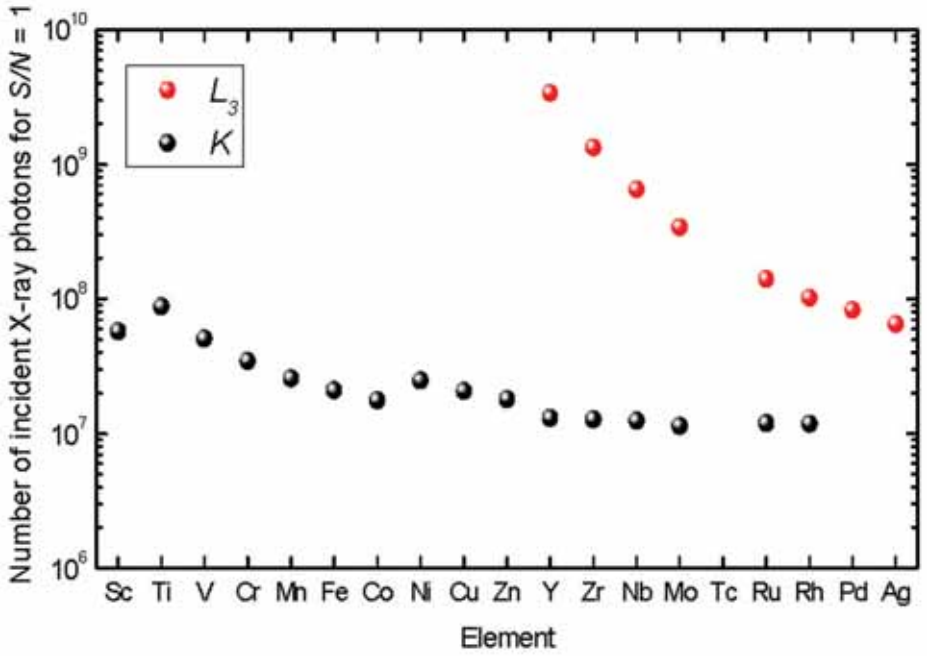


***Figure 6.4.37*** *Required number of incoming x-ray photons to observe time-resolved EXAFS of transition metal compounds in $H_2O$ solution with a signal-to-noise ratio S/N = 1, assuming a laser photolysis yield of 10% and an EXAFS modulation change of 1 % relative to the absorption edge jump of the selected element. From* **[6-212]**.

*Time resolution*

The achievement of femtosecond time resolution with lasers at the beginning of the 1980s allowed physicists and chemists to describe the behaviour of their systems in the language of **dynamics** (i.e. motion of bodies) rather than that of **kinetics** (evolution of populations), thus bringing an unprecedented level of insight into a host of phenomena (physical, chemical and biochemical) in a broad range of systems, from molecules to solids and proteins.

The 100 fs (and hopefully, even shorter) pulse width of the XFEL radiation, will provide us with the ability to detect molecular motion in general and molecular vibrations and phonons in a large class of systems, just as it is possible with femtosecond lasers by the observation of wave packet dynamics. However, the major difference with optical spectroscopy is that with x-rays, the actual structural details of the system can be captured in a **direct** fashion.

Just as in any pump-probe experiment, when the two laser pulses do not have the same colour, group velocity mismatch (GVM) introduces a temporal walk-off between the pulses, which in the case of ultrashort optical and x-ray pulses, is quite significant. Indeed, for a typical medium having an index of refraction of 1.5 in the optical domain, the GVM amounts to 1.6 fs/µm. For a sample thickness of 200 µm, this corresponds to 320 fs! It is, therefore, important to envision pump and probe geometries that overcome this limitation, in particular cross-beam geometries, eventually combined with specific

sample geometries (e.g. line laser excitation of the sample, with x-ray probing along the excitation line).

*Time structure*

The bunch structure of the XFEL provides bunch trains at 10 Hz repetition rate, each consisting of up to 3,000 electron bunches at a repetition rate of 5 MHz (although, as explained in Chapter 4, one can deliver different time structures at the beamlines by a combination of slow and fast kickers in the beam distribution system). The commercial amplified femtosecond laser pulses run at either 1-5 kHz or at 50-300 kHz. Alternatively, unamplified oscillators run at 80 MHz or in cavity-dumped configuration at 1-5 MHz. The latter option seems quite suitable for a pump-probe experiment, but unamplified lasers have weaker energy/pulse than amplified ones. In addition, due to the 10 Hz repetition rate of the bunch trains, the laser pulses between bunch trains are lost, whichever laser repetition rate is used.

Finally, the choice of one or the other laser systems will be determined by the configuration of the experiment, and on the number of species that can be photolysed by the laser.

### Experimental programme

What are the scientific issues which cannot be solved by present day technology, and require XAS at an XFEL? Several very exciting scientific issues were already presented in the TDR 2001**[6-213]**, but here we will be more specific and address issues that: a) concentrate on time-resolved studies; b) require XAS as an experimental method. The following examples are far from being exhaustive and mainly reflect the interest of the authors. It is obvious that entire fields are left out, that could later be added, if additional contributions are made to this text.

### I. Atomic physics

*Measurement of energy shifts of ionised atoms*

Electrons in atoms and molecules are correlated, making the binding energy of an individual electron a function of its entire atomic environment. A change to this environment, such as the application of an external field or the removal of even a weakly bound valence electron, affects the entire system, including the deeply bound core-levels. This makes the energy levels within a single atom sensitive to the configuration, or simply the presence, of other electrons within the atom. Since the wavefunction of valence electrons partly extends deep into the ion core, their charge screening can even affect inner-shell electrons: Cubaynes et. al. **[6-230]** has shown that the binding energy of 2*p* (*L*-shell) electrons in Sodium changes by 2 eV, or about 5%, when the single 3*s* valence electron is excited to the 3*p* level. The influence of a valence electron extends even to the *K* shell: Comparison of measurements in Carbon ions from **[6-231, 6-232]** shows that the energy of transitions involving the *K* shell (1*s*-2*p* transition in C) differs by several electronvolts for differently charged ions.

While these effects have been known for a long time theoretically, their experimental observation only starts to appear now **[6-223, 6-224]**. Yet, with the development of time-resolved x-ray spectroscopy, they regain a special importance, since photoexcitation of an atom within a molecule, also affects the energetics of its core shells. This point was recognised in the recent picosecond XAS study of photoexcited coordination chemistry compounds **[6-223]**, and it calls for a careful examination of the core level shifts upon excitation of valence electrons. This needs to be investigated first in the case of atomic species, and the XFEL, with its high flux and short pulses, is an ideal tool in this respect. Furthermore, the option of using attosecond pulses may one day allow observation of the core level energetic shift in real-time.

*Dynamics and evolution of plasmas*

Plasma diagnosis will greatly benefit from the penetration power of x-rays, allowing the retrieval of information from the volume even for solid-density plasmas. Also, in order to obtain important plasma parameters, like temperature, density, charge state, and collective behaviour of dense, strongly-coupled plasmas, XAS is a very promising approach. It has already been implemented using a lab-based source of picosecond soft x-ray pulses to probe the evolution of an Aluminium plasma over the $L_{2,3}$ absorption edges **[6-233]**. However, the picosecond resolution of this experiment was not sufficient to capture the initial instants of the generation of the high energy density matter that is formed prior to the plasma. With the femtosecond pulses of the XFEL, it will be possible to map the full evolution of the plasma from its birth, by detecting the species in their various ionisation states, and how these change with time. Furthermore, the density distribution of different ionisation stages of atomic species can be determined by absorption contrast imaging. This possibility, based on the coherence of the x-ray beam, can be applied for imaging the plasma region, to obtain information about the density distribution for all plasmas one could produce.

X-ray diagnostic tools based on time-resolved XAS in the femtosecond regime would provide the first direct measurement of microscopic parameters of solid–density plasma, which could be used to properly interpret measurements of thermal and electrical conductivity, equation of state and opacity found in astrophysical environments as well as in virtually all plasma production devices.

**II. Molecular and chemical physics**

Just as with the advent of femtosecond lasers, chemistry is an area where some of the most spectacular achievements of the XFEL are anticipated, one of the major reasons being the importance of structural determination in the description of chemical reaction dynamics, but also the nature and vectorial properties of charge redistribution in chemical systems. Both types of information can be very well captured by ultrafast XAS. Here, we present a few cases where such studies can bring about important new insights into chemical dynamics, even in the case of small molecules.

*Non-adiabatic dynamics of molecules*

The first demonstrations of the power of ultrafast optical spectroscopy, which also marked the field of Femtochemistry, came from the study of gas phase small molecules **[6-194]**. The observation of intramolecular motion was possible by detecting their **wave packet** dynamics. Wave packets result from the coherent (synchronous) excitation of several molecular vibrational (but electronic, rotational, or phonon levels in solids are also possible) levels, while structural information was retrieved by relating the probe wavelengths to the difference potentials between the states involved in the probe transition. The demonstration of the observation of wave packet dynamics probed by soft x-ray femtosecond pulses from a high harmonic source was made by Leone and co-workers **[6-234, 6-235]**.

Aside from being ideal tools to establish techniques and concepts, there are still a number of pending issues in small (and large) molecules, related to the nature of **non-adiabatic couplings [6-236]**, which give rise to avoided crossing of potential curves. The non-adiabatic coupling matrix elements derive from the terms neglected in the Born-Oppenheimer description of electronic states of molecules.

They can arise from different types of coupling terms: spin-orbit, Coriolis, electrostatic, etc. Non-adiabatic couplings are the rule rather than the exception in molecular and condensed matter systems, and they are at the core of energy redistribution and chemical processes. Their full understanding in small molecules may help refine their description in larger molecules, and even in condensed phases, where they play a crucial role.

A particularly interesting example in this respect, is the case of NaI, which we believe is an ideal system for an experiment with the XFEL. Figure 6.4.38 shows its potential curves. The ground state has ionic $Na^{+}I^{-}$ character, it crosses the first excited state, which has covalent character at an internuclear distance of ~0.69 nm, giving rise to an avoided crossing, which results in the upper and lower adiabatic potential curves shown in Figure 6.4.38.

Impulsive excitation of the upper state gives rise to formation of a wave packet (Gaussian on the left hand side of Figure 6.4.38), which evolves on the excited state adiabatic potential curve, with a period of 0.9-1.2 ps (black dots in Figure 6.4.39). In this evolution, as the Na-I distance stretches, the system goes from a covalent character to an ionic one, i.e. an electron transfer occurs from the Sodium atom to the Iodine atom, around the distance of the avoided crossing (dashed line in Figure 6.4.39). In addition, because of the coupling between the two potential curves, part of the wave packet crosses over from the bound excited state potential to the dissociative continuum of the ground state potential, resulting in a damping of the wave packet in the excited state adiabatic potential (black dots in Figure 6.4.39) and a bullet like generation of Sodium and Iodine atomic fragments on the ground state adiabatic potential (open squares in Figure 6.4.39).

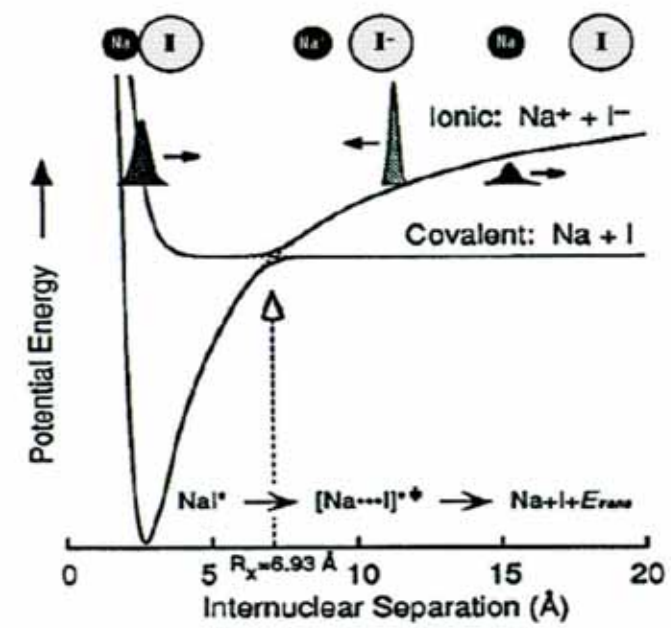


***Figure 6.4.38*** *Potential curves of the NaI molecule and principle of the pump-probe experiment. Femtosecond excitation creates a vibrational wave packet (Gaussian on the left) in the excited state, which will then evolve between the left and right turning points. In so doing, the wave packet passes by the point of crossing and part of it leaks via the dissociative channel giving Sodium and Iodine neutral fragments. After ref* **[6-194]**.

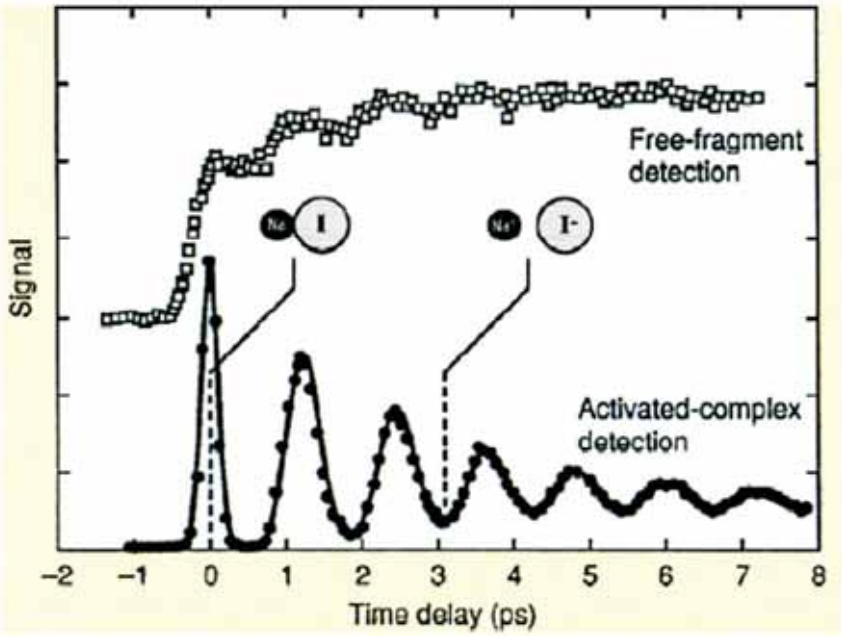


***Figure 6.4.39*** *Wave packet dynamics evolution on the excited state adiabatic potential of NaI (black dots), observed in a pump-probe experiment. Atomic Sodium fragments detected on the dissociative channel of the ground state adiabatic potential curve (Figure 6.4.38). After* **[6-194]**.

This molecule represents an ideal opportunity to understand the fundamentals of the coupling of nuclear and electron motion. Indeed, the time resolution of the XFEL is sufficient to resolve the vibrational coherences observed in the optical pump-probe experiment (Figure 6.4.39). In addition, by recording the time dependent EXAFS signal at the L edges of I near 4.5 keV, one can determine the internuclear distance with high precision, at each instant. More exciting is the fact that by recording the XANES of the Iodine and Sodium (in the soft x-ray domain) atoms, one can record the change of the ionisation state of these atoms, since for the Iodine atom a hole exists in the 5p valence orbital, which disappears in the $I^-$ form, while for the Sodium atom, the 4s electron will disappear upon formation of the $Na^+$ ion. The exciting part of XANES at the XFEL is that it can also determine the degree of electron transfer and its distance (and time) range around the crossing point. These experiments at the XFEL will deliver an unprecedented degree of detail into the non-adiabatic processes, where electron and nuclear motion go together.

*Solvation dynamics*

Most chemical reactions and biological functions take place in solutions. This simple fact has galvanised a tremendous research effort aimed at elucidating the effects of the solvent on the chemical or biochemical reactivity. A complete understanding of liquid chemistry requires knowledge of the detailed molecular pathways that are involved in the reaction dynamics. The elucidation of a set of unifying principles describing chemical dynamics in liquids represents a challenge to both experimentalists and theoreticians **[6-196, 6-202, 6-237 – 6-243]**. The amorphous and dynamic nature of the liquid state leads to reaction systems of exceptional complexity.

Any chemical or photochemical reaction in the condensed phase starts off by a redistribution of charge in the chromophore. This, obviously, applies to photoinduced processes, with the advantage that light offers a clean way to selectively trigger reactions, both in energy and in time. While the redistribution of charge modifies the field of forces within the molecule and leads to its transformation (e.g. via bond breaking, isomerisation, etc.), it also changes the field of forces between the molecule and the solvent species, forcing the latter to rearrange on a timescale that may be shorter or concurrent with that of intramolecular reorganisation. The rearrangement of the solvent species is termed "**solvation dynamics**" (see Figure 6.4.40). It has been much studied by ultrafast laser techniques since the 1980s in a wide variety of solvents **[6-196, 6-202, 6-238 – 6-240, 6-244]**. The central role of solvation dynamics in chemistry and biology is obvious, since the solvent species are not just "spectator" species, but are part of the chemical or biological process. This concerns both steric and electrostatic effects **[6-237, 6-245 – 6-248]**. For example, it is well established that the structure of water around proteins plays a crucial role in their function, to the point that the layer of water around them is thought of as an integral part of the protein **[6-244]**.

Since the solute is excited instantaneously, the solvent species find themselves at time t=0 in a relatively high energy configuration due to the change of field of forces. Subsequently, they begin to move and rearrange to reach their new equilibrium configuration (Figure 6.4.40). This motion includes both translational and rotational

rearrangements. The solvation process typically exhibits a multiexponential decay with timescales of <200 fs, several hundred femtoseconds and a few picoseconds to several tens of picosecond, depending on the solvent. This description, however, is already the source of some ambiguity.

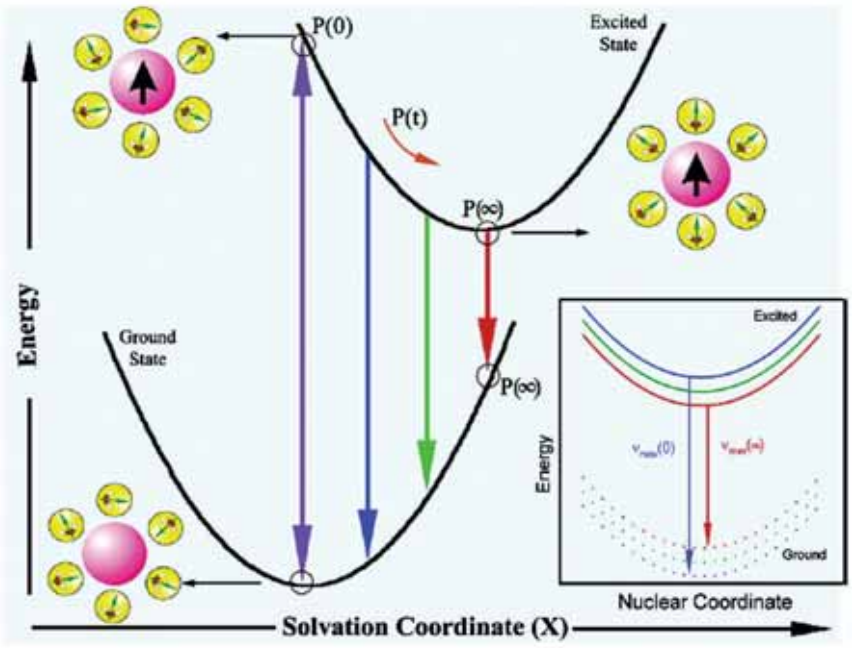


***Figure 6.4.40*** *Schematic illustration of the potential energy surfaces involved in solvation dynamics, showing the water orientational motions along the solvation coordinate together with instantaneous polarisation P. As an inset we show the change in potential energy along the intramolecular nuclear coordinate. As solvation proceeds, the energy of the solute decreases, giving rise to a red shift of the fluorescence spectrum.*

Indeed, so far, all the techniques that have been implemented to study solvation dynamics suffer from three shortcomings: a) they all rely on the use of dye molecules, which due to their shape, already form a specific solvent shell in their ground state. Therefore, the solvent response in the excited state is, to a certain extent, probe-molecule specific, since the dynamics that one observes on ultrashort timescales in the excited state reflect a departure from the initial structure; b) particularly at the shortest timescales, it is difficult to disentangle the high frequency intramolecular and intermolecular contributions; c) only optical methods have so far been used, which are unique in delivering time-domain information about the energetics of the system, but no visualisation of the solvent shell structure around the solute. This last point concerns not only the structural changes during the dynamics, but also after the rearrangement has taken place. The microscopic structural details are of importance, especially at short times, in part because they represent the most energy consuming part of the solvation process **[6-239]**, and correspond to the transition from an “inertial” regime to a “diffusive” one.

In order to visualise the solvation **structural** dynamics in real-time, femtosecond XAS is an ideal approach since it allows: a) a direct visualisation of solvent structures before,

during and after the dynamics; b) the monitoring of the electronic structure changes (by XANES) induced by the laser excitation and; c) the use of atomic ions as probe species, which are usually optically silent, but offer the great advantage of being free from internal modes, so only intermolecular changes are observed.

A successful experiment has already been carried out using the 100 ps pulses at the SLS **[6-229]**. The experiment consisted of exciting the $I^-$ ion in water, to remove the electron and probing the electronic structure of the Iodine atom and the solvent structural changes around it by XANES and EXAFS, respectively. The data show entirely novel results, in that it was found that the solvent shell dramatically changes upon electron abstraction and transfers electron density back to the $I^0$ atom. However, this experiment only captured the **before** and **after** situations within hundreds of picoseconds. As mentioned above, crucial for a full description of solvation dynamics is the observation of the actual process of solvent rearrangement, and how it influences the charge redistribution within the solute. The time resolution of the XFEL of $\leq$100 fs should be sufficient to time-resolve the structural changes of the solvent shell in most solvents, including water **[6-240, 6-249]**.

Finally, any study that delivers the structural details of the solvent environment around a solute and its rearrangement as a function of time, establishes the use of the solute as a probe of solvent structure and dynamics in different physical and thermodynamical states: supercritical, supercooled, at interfaces, etc., for which a number of questions remain unanswered. In consequence, it opens a host of new opportunities for the study of liquid state dynamics in different media.

*Chemical dynamics in liquids*

The solvent shell also plays a crucial role in hindering or affecting the pathways of chemical channels of molecules, and in creating new ones. It is also a thermal contact, which removes energy from the excited species to the rest of the bath. A schematic representation of the processes that are induced in a solvated molecule by light excitation, is shown in Figure 6.4.41.

One of the most studied systems is the case of the $I_2$ molecule in liquids, and the various processes affecting it have been studied over the 1980s and 1990s in different media (liquids, rare gas matrices, high pressure gases and clusters) **[6-194, 6-250, 6-251]**. All of the ultrafast studies have so far been probing the intramolecular motion of the molecule and the way it is affected by the environment, but a clear understanding of the way the solvent cage affects the photochemical reaction dynamics goes by a direct visualisation of the cage response itself. Experimental studies and theoretical simulations **[6-251]** have shown that the first impact of the Iodine fragments on the solvent species occurs within 100-300 fs and takes up most of the energy involved in the reaction. It is followed by a rearrangement of the cage which occurs on the timescale of picoseconds and is affected by energy flow from the molecule to the bath. These processes can only be observed by XAS using the femtosecond x-ray pulses, which will be provided by the XFEL.

*Coordination chemistry*

Controlled electron transfer (ET) and charge separation in molecules are essential requirements for efficient storage and conversion of energy by chemical means, as well as for operation of nanoscale devices such as molecular conductors, rectifiers, transistors, memories, or non-linear optical materials **[6-252 – 6-255]**. Several approaches to molecular electronics use conceptually similar transmission of electronic effects, e.g. through coulombic interactions between mixed-valence complexes **[6-256]** or redox-induced valence tautomerism, whereby information is stored in distinct states of bistable molecules **[6-257, 6-258]**. Biological energy and information conversion provide further inspiration, since directional, long-range ET is the physical basis of photosynthesis, while charge-separation helps to drive retinal isomerisation in the process of vision **[6-259]**. Further progress towards molecular devices requires the development of systems capable of exact timing and switching of the rate and direction of the ET, and the underlying structural rearrangements involved within this. The rates of electron transfer are as important for efficient and error-free operation of molecular devices, as they are, for example, in plant photosynthesis. One of the purpose of XAS studies at the XFEL is to **obtain new and comprehensive understanding of electron transfer and charge separation** in metal-based molecular complexes and also, in multicomponent metal-based molecular assemblies (Donor Bridge Acceptor type), which can be envisioned as functional materials for specific applications.

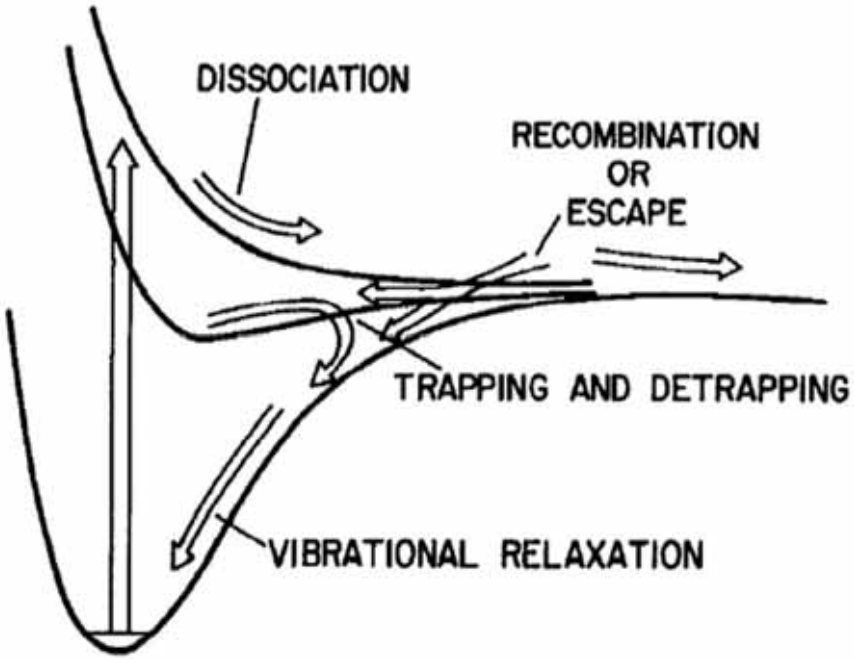


***Figure 6.4.41*** *Processes of photodissociation and geminate recombination of a molecule in solution. Typical timescales for dissociation are <1 ps, 1-10 ps for recombination or escape,100-3,000 ps for trapping or detrapping, and 50-5,000 ps for vibrational relaxation The vertical arrow repre-sents the initial light absorption. After* **[6-250]**.

Coordination chemistry compounds are among the most promising molecules for performing the above functions, and are the object of intense studies at present. In particular, ultrafast (femtosecond-picosecond) spectroscopy is used to investigate intra- and intermolecular ET, especially using UV-Vis transient absorption spectroscopy, UV pump/IR probe techniques, and time-resolved resonance Raman techniques. Vibrational spectroscopies (IR and Raman) provide a high degree of insight into the direction and nature of the electron transfer, by visualising the mode frequency changes of specific chromophores upon oxidation or reduction, but they are limited in time resolution, at best ~0.5 ps, and in their ability to detect low frequency modes, which often are the relevant ones. Optical pump-probe transient absorption spectroscopy easily reaches the few femtoseconds time-resolution, but it cannot detect the nature and direction of the ET. Finally, none of these ultrafast spectroscopic techniques deliver information about the excited state molecular structure, which is particularly important if one wants to analyse and rationalise ET, and eventually, design new compounds for optimal ET.

For the study of ET in metal-based molecular complexes, one needs a technique that: a) allows a direct visualisation of molecular structures both before, during and after the dynamics; b) allows monitoring of the electronic structure changes induced by the laser excitation; and c) can be implemented in disordered media, in particular, liquids. X-ray Absorption Spectroscopy is ideal in this respect and implementing it in a pump-probe configuration has recently been accomplished by Bressler, Chergui and their co-workers with 50-100 ps resolution on metal-based molecular complexes **[6-217, 6-223, 6-229, 6-260]**. Their results fully establish the technique on a routine basis for metal-based complexes in the picosecond time domain, and allow a systematic investigation of ET processes in this class of systems. However, the time resolution of tens of picosecond is not sufficient to fully resolve the dynamics of intramolecular ET processes, which occur on a timescale of $\leq$1 ps **[6-261, 6-262]**, nor to capture the details of the ultrafast energy relaxation cascade, which also occurs on hundreds of femtoseconds to a few picoseconds, and imply successive stages of structural rearrangement. This is where the utility of the femtosecond resolution at the XFEL comes in. Although seemingly paradoxical, the probing of transient structures in these (and other) molecular systems should be easier with femtosecond x-ray pulses than with picosecond ones, since the vibrational coherence imparted by the pump laser to the ensemble of molecules in the samples is preserved up to picoseconds in most systems.

An example of such potential functional materials are metal-diimine complexes, which are ideal for vectorial electron or energy transfer. In particular, M(II)-diimine square planar complexes (M=Pd, Pt) with a variety of anionic donor ligands, represent a perfect class of Donor-Bridge-Acceptor complexes, which may lead to long-lived separation of charge in the excited state of the metallo-organic chromophore **[6-263, 6-264]**. In order to reach this regime, the strategy is to avoid fast back-ET by introducing an energy barrier that results from facile structural reorganisation following the primary photoinduced ET.

In M(II) diimine bis-thiolate complexes (Figure 6.4.42), light-induced electron transfer from the donor thiolate part to the diimine part produces a charge-separated excited state. This process is accompanied by a structural reorganisation probably involving

formation of a 3-electron S-Pt-S bond, which hinders back-ET, while the stability of the S-S bridge can be controlled by varying the nature of the R groups. Time-resolved optical studies and vibrational spectroscopies can only indirectly infer the decrease of electron density at the R-ligands and do not capture the ultrafast formation of the S-S bridge in the excited state. Both of these processes can be detected in a direct fashion by XAS of the photoexcited compound at the XFEL.

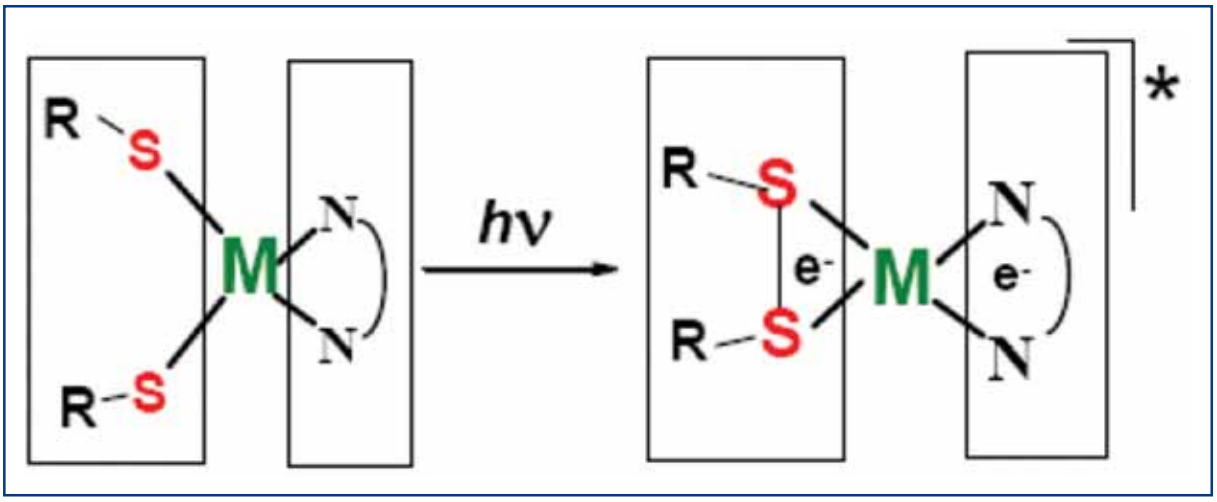


***Figure 6.4.42*** *Metal(II) diimine bis-thiolate complex: M = Pt, Pd or Ni, N)"N represents the diimine, and typical R groups are: H, -$OCH_3$, -$N(CH_3)_2$, $NO_2$.*

### III. Biology

The importance of structure in biology is best expressed by this citation of F. Crick, the co-discoverer of the double helix structure of DNA: "If you want to understand function, study structure". The tremendous development of protein crystallography over the past 40 years is a result of the need to "understand function". But it is clear that observing the evolution of structure in biological systems, rather than just static structure, offers another dimension of insight. At the core of any biological function are chemical reactions, which at the molecular level, occur on the timescale of femtoseconds to picoseconds. There is another reason why studying biological systems at the shortest timescales is necessary: these systems perform their function with high efficiency and high selectivity, and unravelling the details of the underlying mechanisms at the molecular level, may help design biomimetic functional materials for various applications. The femtosecond resolution of the XFEL combined with XAS is an ideal tool in this respect. Model systems on which these concepts can best be demonstrated are heme proteins.

Heme proteins, such as hemo- and myoglobin, are involved in a variety of physiologically important biochemical reactions such as electron transfer, diatomic molecule storage and transport and catalysis. The heme group is a planar chromophore containing a coordination metal atom (in general, Iron), which is able to bind small diatomic and triatomic molecules such as NO, CO, $O_2$, CN, $H_2O$ and $H_2S$. The investigation of heme proteins by time-resolved Laue diffraction is extensively described in Section 6.4.6. However, some of the scientific questions about the dynamics of these systems, in

particular the electronic rearrangements in the metal d-orbitals that take place when the metal atom undergoes a spin transition upon ligand dissociation, can only be dealt with using XAS with the femtosecond resolution of the XFEL. Indeed, the ultrafast electronic structure changes in the metal d-orbitals **[6-265 – 6-269]** can be visualised by XANES, while the ultrafast structural changes associated with the multimode behaviour **[6-270, 6- 271]** can be visualised by EXAFS.

### IV. Condensed matter physics and materials science

*Luminescent materials*

A wide variety of technologically important luminescent solids depend critically on the interaction between impurity ions and the surrounding local structure of a host material. Well known examples include ultrafast laser crystals such as Ti:$Al_2O_3$ or Ruby **[6-272]**. Thanks to this element specificity, femtosecond NEXAFS and EXAFS of the optically active impurity ion can offer a direct observation of the coupling between electronic and vibronic degrees of freedom in such systems, allowing us to gain a better understanding of the basic science underlying the luminescence process. Also interesting are “co-doped” luminescent crystals where energy transfer between different dopant species is important **[6-273]**.

*Order-disorder phase transitions and data storage*

Present-day multimedia strongly rely on rewritable phase-change optical memories. $Ge_2Sb_2Te_5$ (GST), the material of choice in DVD-RAM, has controversial structural properties and probably consists of well-defined rigid building blocks that are randomly oriented in space **[6-274]**. Laser-induced amorphisation results in drastic shortening of covalent bonds and a decrease in the mean-square relative displacement, demonstrating a substantial increase in the degree of short-range ordering, in sharp contrast to the amorphisation of typical covalently bonded solids. This novel order-disorder transition is due to a modification of the coordination geometry of Germanium atoms without rupture of strong covalent bonds, as schematically shown in Figure 6.4.43. It is this unique two-state nature of the transformation that ensures fast DVD performance and repeatable switching over ten million cycles.

The phenomenology of phase-change optical recording is simple. An initially amorphous as-deposited GST layer is crystallised by exposure to a laser beam of intensity sufficient to heat the material to a temperature slightly above the glass-transition temperature.

A subsequent exposure to an intense and short laser pulse melts the GST which is then converted into the amorphous state on quenching. A recorded bit is an amorphised mark against the crystalline background. The reversibility of the crystallisation-amorphisation process allows fabrication of rewritable memory.

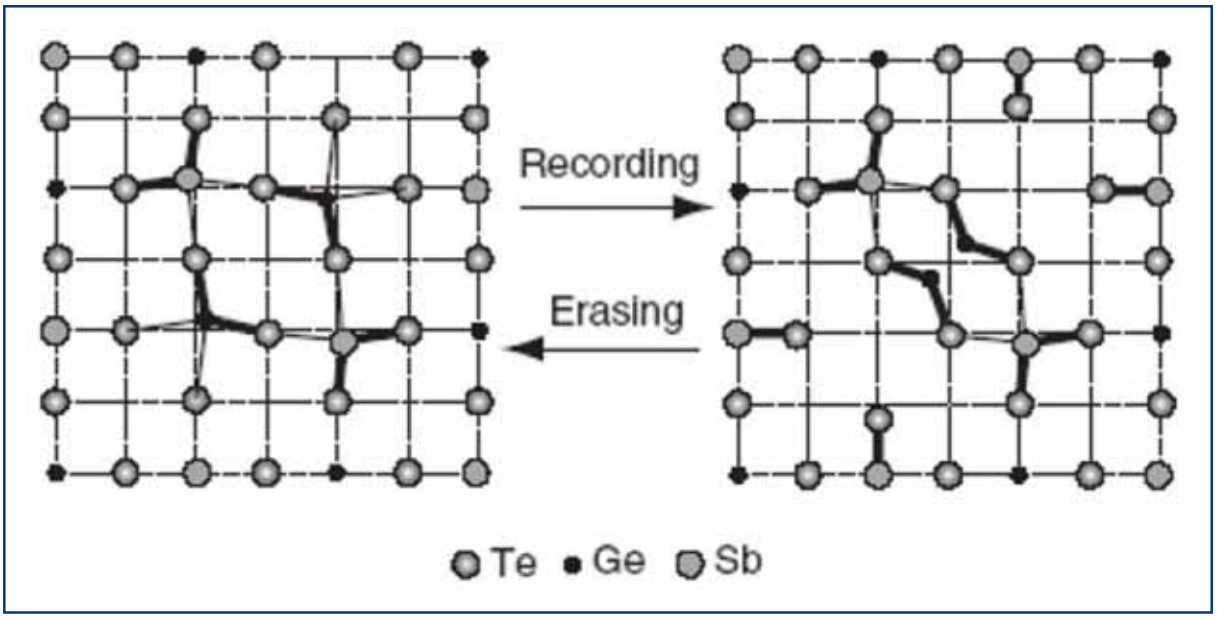


***Figure 6.4.43*** *Schematics of medium-range-order changes in the structure of GST upon reversible amorphisation-crystallisation. The umbrella-flip of Germanium atoms from the initially distorted rocksalt structure in the crystalline state (left) results in a shortening of Sb-Te bonds and subsequent distortions in the Te fcc sublattice (amorphisation) (right).*

An ideal tool for investigating the local structure of a material and its changes on the atomic scale independent of the state of the material (crystalline or amorphous) is XAS, which is already being used in a steady-state mode **[6-274 – 6-276]**. However, the timescales of the structural changes have never been measured. In addition, although it is generally assumed that the role of a laser pulse is to simply heat the material, it seems that electronic excitation creates non-equilibrium charge carriers that are crucial for the weakening and subsequent rupture of the subsystem of weaker Ge-Te bonds **[6-274]**. Such electronic structure changes occur on very short timescales (a few femtoseconds) and can be detected by XANES as done in non-thermal melting phenomena in solids **[6-219, 6-222]**.

The XFEL is an ideal tool to study the order-disorder phase transitions because: a) it provides the right time resolution to capture the atomic motion in real-time; b) for the same reasons as in the case of the luminescent materials, and since the sample is modified after each laser shot, the high flux per pulse at the XFEL makes these experiments feasible in a truly “single-shot” configuration, in which a narrow range of energies (set by the bandwidth of the source and a dispersive energy analyser) and times (set by the geometry of the experiment) can be probed with adequate statistics using a single XFEL pulse.

*Magnetic phenomena*

The study of magnetisation dynamics in thin films and nano/microstructures is motivated by applications in data storage and electronics, but also by the exciting fundamental physics that is involved. Magnetisation dynamics takes place over a large range of

timescales, from some hundreds of femtoseconds up to years. At nanosecond timescales and above, magnetisation reversal in thin films takes place by nucleation of reversed domains and a subsequent propagation of domain walls. Below this regime, from some picoseconds up to nanoseconds, the dynamics is governed by the Landau-Lifshitz-Gilbert (LLG) equation which describes the precessional motion of the magnetisation around the direction of the effective field and the subsequent damping of this motion. This precessional motion can be used to obtain a coherent switching of the magnetisation direction of micron-sized magnetic structures in less than 200 ps **[6-277, 6-278]**, using magnetic pulses applied in the direction perpendicular to the easy axis of magnetisation. Even faster reversal, of the order of picoseconds or below, can be obtained using polarised lasers through the so-called inverse Faraday effect **[6-279, 6-280]**. At these very short timescales thermal effects induced by absorption of the photons, start to play a role and electron-electron and electron-phonon interactions **[6-281]** have to be taken into account.

Time-resolved studies of magnetisation dynamics have already been performed using the time-structure of synchrotron x-rays, with both space-integrated **[6-282]** and imaging techniques **[6-283 – 6-285]**. A pump-probe technique was used for these studies and the temporal resolution was limited to the sub-nanosecond time domain. Using the much shorter and intense x-ray pulses of the XFEL opens up the possibility of studying phenomena like the ones mentioned above, which until now are only accessible with laser beams. The advantage of x-rays over lasers is that they can provide element-selectivity through X-ray Magnetic Circular Dichroism in XAS **[6-284]**, and very high spatial resolution can be obtained if they are combined with x-ray microscopy techniques. This allows the ultrafast magnetisation dynamics in the different layers of multilayered magnetic systems (important for applications) to be studied separately. Also, the role of the spin and orbital magnetic moments of different elements in alloys and compounds on the magnetisation reversal can be studied separately.

*Warm dense matter*

Warm dense matter refers to the thermodynamic regime of matter at temperatures above ~1 eV with densities near that of solids (1-10 g/cm$^3$) (see also Section 6.4.2). Although such states of matter are fairly common in astrophysical bodies, their study on earth is limited by the experimental difficulty of making even basic quantitative measurements. Recently, some progress has been made in using ultrafast pump-probe soft x-ray absorption to study matter approaching this regime **[6-219, 6-222]**. In these experiments, the warm dense matter is created by a femtosecond laser that rapidly heats a thin foil target, generating, for a short time, very high temperatures in the inertially confined foil. A picosecond synchrotron x-ray pulse then probes the x-ray absorption in the vicinity of a characteristic edge, providing information on the electronic and structural condition of the foil as a function of time.

The high temporal resolution of the XFEL will allow the carrying out of such experiments in the femtosecond regime, opening up exciting opportunities to study the high-energy density non-equilibrium coupling between the laser-excited electrons and the initially very cold atomic lattice. This would manifest itself as very short (sub-picoseconds)

dynamics in the near-edge spectral features, as the symmetry features of the solid are destroyed as energy is transferred to the ions, and the occupancy of valence orbitals is changed. In addition, the changes in bond distances and coordination numbers can be captured by ultrafast EXAFS.

One difficulty in these measurements is that the creation of warm dense matter is irreversible, meaning the sample must be replaced between each x-ray pulse. The high flux per pulse and short temporal duration of the SASE beamlines at the XFEL make these experiments feasible in a truly "single-shot" configuration, in which a narrow range of energies (set by the bandwidth of the source and a dispersive energy analyser) and times (set by the geometry of the experiment) can be probed with adequate statistics using a single pulse from the XFEL. As an example, consider a Chromium foil target. The Chromium K-edge is located at approximately 6 keV. Assuming a 0.08% bandwidth from one of the hard x-ray SASE beamlines, the bandwidth at the Chromium K-edge is approximately 5 eV, which is enough energy range to cover the edge shift from neutral Chromium to $Cr^{+}$, as well as the more dramatic pre-edge features of higher valence Chromium. X-rays from the undulator first encounter a bent crystal, set to both focus the beam in one dimension onto the sample and to disperse spectrally the x-rays transmitted through the sample. Thus, a detector placed behind the sample sees along one spatial dimension the transmission spectrum of the foil for each x-ray pulse. Temporal dispersion can be accomplished similarly, by using a large angle between the laser pump pulse and the x-ray probe pulse along the unfocused axis of the x-ray beam. The detector would then see a 2-D x-ray image behind the sample, with one spatial axis representing x-ray wavelength and the other pump-probe delay time, all in a single x-ray shot. Estimates using the XFEL performance goals yield a signal-to-noise ratio of approximately $10^3$ per shot assuming ideal detectors and optics and a 1 ps time window. At the expense of photon number, the spontaneous emission beamlines can offer a wider spectral range.

**Advanced implementation of XAS at the European XFEL facility**

The possibility of the European XFEL tuning the photon energy very fast using an energy modulation of the electron beam invites an attractive solution for ultrafast studies. For less demanding samples, e.g., moderately concentrated liquid solutions, we can exploit a combination of Quick EXAFS (QEXAFS) with the time structure of the XFEL: a QEXAFS monochromator (Figure 6.4.44) synchronised to the sequence of x-ray pulses produced by the train of electron bunches with one RF pulse (every 200 ns for about 0.6 ms) could select a different energy for each single pulse, eventually covering an entire EXAFS scan (with $\Delta E$ = 0.1-1 keV) in 0.2-1 eV steps at 10 Hz repetition rate.

Current QEXAFS monochromators can operate at 40 Hz and cover about 1-1.5° scan angle, which translates into about 1 keV tunability range at 10 keV photon energy. This translates into a 40 eV scan range per millisecond or about 24 eV over the sequence of x-ray pulses from one pulse train. By increasing the angular speed of the monochromator, one might be able to increase this range considerably, thus, enabling measurement of a full XAFS spectrum within 0.6 ms. Since the bandwidth of the FEL line alone is not sufficient to provide the complete XAFS spectrum, an energy chirp of the electrons within one bunch train is required. Synchronisation of the QEXAFS monochromator to the arrival of x-ray pulses to better than 100 µs is further required.

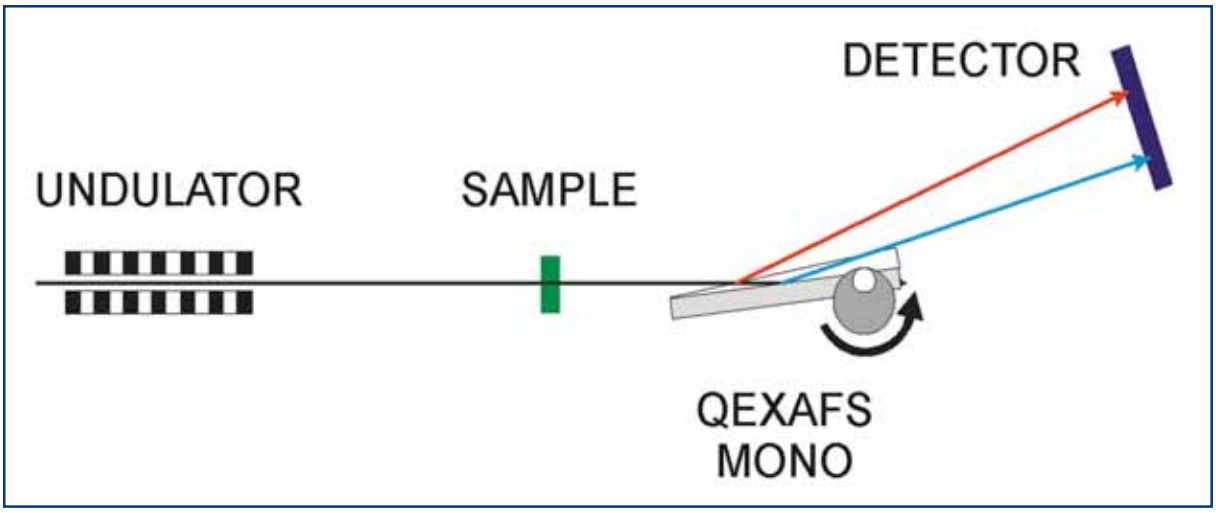


***Figure 6.4.44*** *Synchronising a QEXAFS monochromator with the pulse sequence of the XFEL could allow the measurement of an entire XAFS spectrum within one single train of x-ray pulses (lasting about 0.6 ms) in transmission mode. The rotating Bragg crystal will, thus, deflect different energies at different angles. The spectrum can be collected with a slow detector.*

Since the beam deflected by the QEXAFS monochromator would also point in a different direction, an imaging detector could record the signal from an entire bunch train reducing the requirement for fast readout to the bunch train repetition rate of 10 Hz. Since the incident signal varies it has to be measured pulse-by-pulse for normalisation purposes. A concern is the detector acceptance in terms of x-ray quanta. Starting from the high incident photon number of $10^9$ – $10^{12}$ and a reduction of only $10^2$ – $10^3$ due to bandwidth reduction and sample transmission, a large number of photons hit the detector. In a clever geometric arrangement one single pulse (for one single energy step) could cover about 1,000×10 pixels of the detector, thus entering a regime where detectors with maximised well-depth could work.

To circumvent this difficulty in a second setup, spectroscopy detection of fluorescent radiation is proposed (Figure 6.4.45). Here, the incident radiation is spectrally dispersed using the QEXAFS monochromator already in front of the homogenous sample. The pump laser could co-propagate with the x-ray beam using a mirror that rotates together with the Bragg crystal such that overlap in space and time can be perfectly maintained. X-ray fluorescence from the sample needs to be recorded using a spatially resolving spectrometer. In consequence, the spatial distribution of recorded fluorescence photons is a function of the incident x-ray energy, and can be converted into an XAS spectrum. As for the previous method normalisation of the incident photon flux for every single pulse is required. Another method could exploit the angular distribution of the incident rays using an array of Soller slits to distinguish between scattered light from different locations. In building the energy- and space-resolving spectrometer, it should be possible to determine the incident and emitted photon energy simultaneously, thus allowing measurement of shifts or broadening in the x-ray emission lines.

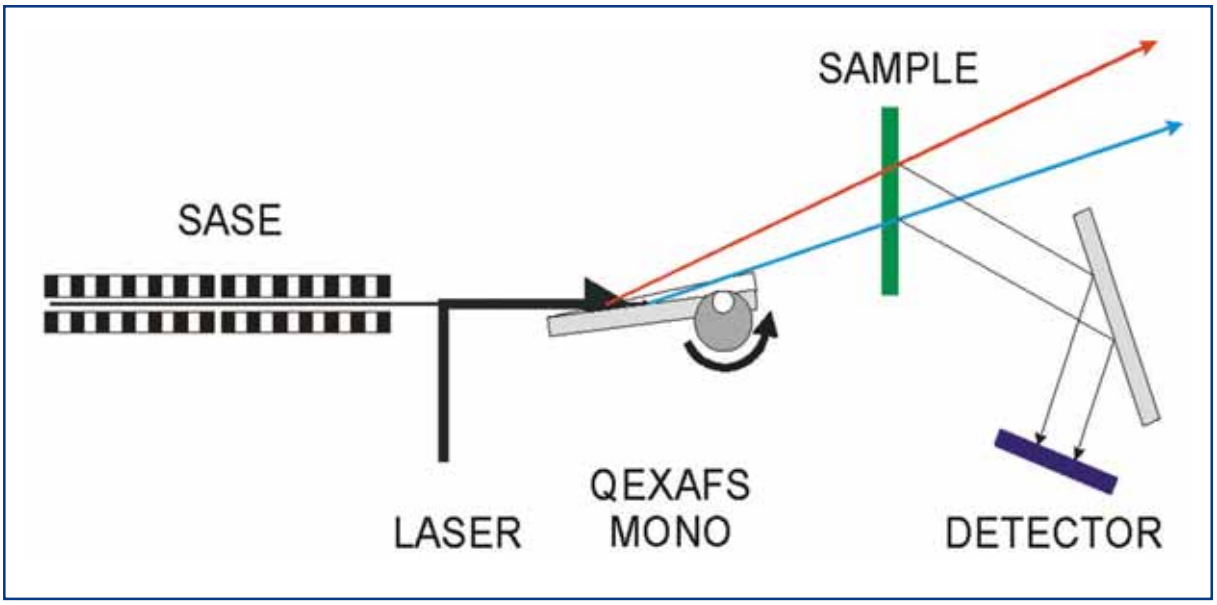


***Figure. 6.4.45*** *The rotating Bragg crystal deflects different energies at different angles, and a co-rotating laser mirror will ensure continued overlap between both laser and x-ray beams on the sample. X-ray fluorescence is collected spatially resolved using crystal spectrometers.*

### *6.4.5.2 Instrument requirements*

The experiments described above lead to requirements of an instrument for scientific applications using XAS. They concern the performance of the light source, the optical elements and the diagnostic equipment, the sample environment, and the detectors. The scientific cases presented call for beamlines suitable to spectroscopy, thus, with a sufficient energy resolution and tunability range. For XANES investigations the intrinsic tunability of about 6% is certainly sufficient, this translates into about 50 eV near 0.8 keV and about 700 eV near 12 keV. EXAFS studies sometimes require a tunability range of about 1 keV, and both SASE 2 and SASE 3 will offer this capability. The SASE 2 and SASE 3 insertion devices will cover the energy range of 3-12 keV and 0.8 – 3 keV respectively. The dedicated beamlines have to concentrate on a specific energy range, given by the characteristics of the monochromating systems.

**Spectral radiation properties**

The measurements require an energy resolution in the order of $\Delta E/E \sim 10^{-4}$. This resolution is about 10-100 times better than the natural bandwidth of the XFEL radiation in the required photon energy range. The monochromatisation is usually achieved in the incident beam, but can, in principle, also be achieved using a dispersive element in the beam transmitted by the sample. However, the latter method increases the absorption of x-ray photons in the sample accordingly. The natural bandwidth in special cases provides enough of an energy range to investigate significant features in the XANES spectra using single x-ray pulses. For the entire XAFS information an energy range of 10% is required.

To implement advanced schemes to tune the photon energy very fast using the QEXAFS scheme (compare Section 6.4.5.1), the availability of the non-monochromatised beam has to be anticipated.

### X-ray optics requirements

Although the technique does not require coherence, the coherence properties and wavefront errors of the x-ray beam can become crucial in these experiments. The reason is the required normalisation of the incident photon flux at the sample position. If coherence effects lead to variation of this photon flux in space or, even worse, in time, the normalisation will become very difficult. With respect to the monochromator crystals one needs to keep the error in asymmetry very small in order to avoid tilting the wavefront and thereby modifying the time pattern at the sample position.

The beamsize at the sample will be determined by the experiments, in particular the sample geometry. Therefore, focusing in the XFEL beam to spot sizes the order 100 µm should be enabled.

### Time domain requirements

These experiments probe dynamics on the ultrafast timescale using pump-probe techniques. Pumping is usually achieved using an ultrafast visible laser. The synchronisation should be significantly better than the anticipated time resolution of ~100 fs. For the same reason the fluctuation of the pulse duration must be small compared to the 100 fs timescale.

It is anticipated that a variety of pulse patterns from single pulses at 10 Hz repetition rate up to several thousands of x-ray pulses per electron bunch train will be used.

### Photon diagnostics requirements

The short- and long-term stability of the x-rays is of extreme importance for the quality of the experiments. The position stability of the emitted x-rays and even their spatial distribution should be monitored. Furthermore, all experiments will need diagnostic equipment for the measurement of the photon flux on a pulse-to-pulse basis. Since monochromators are used, the measurement of the mean photon energy is not required and spectral diagnostics should provide the content of higher harmonic radiation only. All measurements must be available on a pulse-to-pulse basis.

### Sample manipulation and environment

The issue of sample handling under the high flux of the XFEL can be a serious problem, but it obviously depends on the type of experiments one is conducting. At this stage, we can say that concerning liquid samples (molecules or ions in solution, biological systems in solution, pure liquids, etc.), there are no serious challenges because the sample can be refreshed after each pair of laser-x-ray pulses (provided we have sufficient sample), as is already done in picosecond XAS experiments **[6-218]**.

For solid samples, the high XFEL flux may provide the solution since one can work in a single shot regime. Alternatively, given the relatively low repetition rate of the x-ray

source, a shaker can be used to refresh the sample by moving another spot into the focus region. It is clear that specific solutions have to be implemented for each type of experiment.

The hard x-ray instrument could be placed in a vacuum or even in air if windows are used as a vacuum interface. The windows should receive only the unfocused beam, meaning they should be mounted near the local optics. The soft x-ray instrument will differ from the hard x-ray one in requiring a single vacuum system throughout, with no windows, including the detector chambers. For the soft x-ray experiments at magnetic resonances, in-vacuum magnet- and cryosystems will be needed.

**Detector requirements**

The great advantage of XAS, as compared to other x-ray techniques, is that it does not rely on large area detectors, where read out time can be a serious problem for a high repetition rate experiment. In that sense, pump-probe experiments based on XAS are very similar to the analogue transient absorption experiments in the optical domain, and many of the detection methods can and have been implemented in time-resolved XAS experiments **[6-218, 6-286]**. The extension to XFEL-based experiments is, however, not straightforward, because one needs to detect in the order of $10^9 – 10^{11}$ photons of 10 keV energy within a 100 fs pulse, in any given experiment. We usually rely on the linearity of the detector for the given range of pulse intensities. For example, semiconductor photodiodes have proven their worth over a wide range of incident intensities, i.e., from single photon counting up to $10^5$ photons within a 100 ps long x-ray pulse. The large carrier densities created in such a detector by an XFEL pulse will limit their use, although using large area photodiodes far away from the focus may relax these conditions considerably. Today, quasi white-light from Synchrotron Radiation (SR) Undulators achieves about $10^{10}$ photons within a 100 ps long pulse, and these sources may be used as a basis for assessing the utility of sensitive and linear detectors. In an alternative setup, x-ray fluorescence detection using spectroscopic techniques relaxes the detector requirements with respect to photons per time-interval considerably.

**Visible laser requirements**

Visible lasers will be applied in pump-probe experiments. A wavelength tunable system providing pulse durations in the order of 30 fs and pulse energy up to 1 mJ at 800 nm will allow the carrying out of the experiments proposed in this area. Using Optical Parametric Amplification (OPA) schemes a wavelength range of ~200 to 1500 nm should be available at the instrument. Synchronisation to the x-ray beam of the order of the pulse duration or pulse-to-pulse measurements of the jitter is requested.

### *6.4.5.3 Realisation of the instrument*

For their realisation, the XAS experiments require two instruments at SASE 3 (XAS 1 – Tunable soft x-rays) and at SASE 2 (XAS 2 – Tunable hard x-rays). For a description of the SASE 2 and SASE 3 beamlines, see Sections 6.2.4.2 and 6.2.4.3, respectively. Experiments discussed in Section 6.4.5.1 under Topics I.-IV. will be carried out at these instruments depending on the element under investigation. As XAS is a local probe, the

absorption edge of the corresponding element determines the photon energy to be used. Since all experiments require monochromatisation, one might use the monochromators installed in the SASE 3 and SASE 2 beamlines. However, advanced schemes also require receiving the full beam at the instrument and applying monochromatisation in the vicinity of the sample. Both instruments will require moderate focusing of the XFEL radiation to beam sizes in the order of 100 µm achieved by using a focusing element inside the corresponding beamlines. For the XAS 1 instrument refocusing of the monochromator exit slit is used to focus the beam at the sample location. For the XAS 2 instrument the focusing element will likely be Beryllium lenses.

**XAS 1: Tunable soft x-rays**

The following elements belong to the XAS 1 instrument inside the experimental hall. They are depicted in the schematic layout of that instrument in Figure 6.4.46 and are described in Table 6.4.12. A deflecting mirror provides the necessary beam offset for the instrument. Using a demagnification of 1 with respect to the exit slit of the monochromator, a beam spot of ~100 µm can be achieved. Following a slit/aperture unit, time and photon flux monitors follow. A differential pumping section separates the beamline from the sample. Also, the QEXAFS monochromator is installed after the differential pumping section. Between sample and monochromator an photon flux monitor is required to enable a pulse-to-pulse photon flux measurement. The sample environment includes the possibility of mounting spectrometers for fluorescent detection. Behind the sample chamber another photon flux and spectral monitor follows.

The sample environment allows for linear movements (1µm repeatability and 0.25 µm resolution) and angular degrees of freedom (1/1,000° repeatability, 1/4,000° resolution). The detector equipment comprises fast point detectors, space-resolved x-ray emission spectrometers and 2-D detector(s). A laser system including an OPA system for provision of widely tunable visible laser radiation is available.

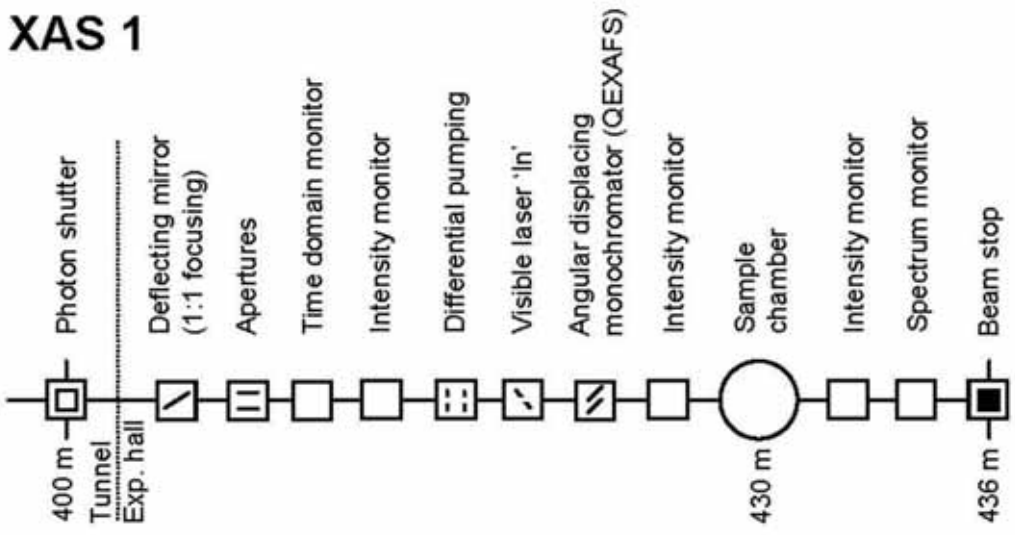


***Figure 6.4.46*** *Schematic layout of the XAS 1 instrument at the SASE 3 beamline. Distances are given in relation to the end of the undulator.*

| Item | Purpose | Specification |
|---|---|---|
| Deflecting optics | Horizontal deflection by 20 mrad, 1:1 focusing of monochromator exit | 0.1 µrad angular stability, 0.3 µrad figure error, 0.1 nm surface roughness |
| Slits/apertures | Beam definition, beam halo cleaning | 0.25 µm accuracy, 1 µm repeatability |
| Time domain monitor | Measurements of x-ray arrival-time x-ray with respect to visible laser | |
| Intensity monitor | Measurement of incident photon flux | Transmissive (<5% absorption), single pulse measurement, relative accuracy $<10^{-3}$ |
| Differential pumping | Separation of beamline and instrument | |
| Monochromator | Angular displacing monochromator (QEXAFS) | 0.1 µrad angular stability, 0.1 mrad asymmetry error |
| Intensity monitor | Measurement of photon flux behind dispersive element | Transmissive (<5% absorption), single pulse measurement, relative accuracy $<10^{-3}$ |
| Sample chamber | Sample positioning and orientation | x-y-z move (0.25/1 µm), two rotations (0.25/1 mdeg) |
| Detector | Measurement of transmitted radiation | 2-D, 2K×2K, 10-30 Hz |
| XES spectrometer | Space-resolved detection of x-ray emission from the sample | In-vacuum, 10-30 Hz frame rate |
| Intensity monitor | Measurement of transmitted photon flux | Transmissive (<5% absorption), single pulse measurement, relative accuracy $<10^{-3}$ |
| Spectrum monitor | Measurement of high harmonic content | Single pulse measurement, relative accuracy $<10^{-3}$ |
| Alignment unit | Positioning and position verification | Permanently operating, accuracy ~100 µm |
| Lead hutch | Radiation protection, temperature stabilisation, laser protection | 4×8×3.5 $m^3$ (W×L×H), ±1° thermal stability |
| Control hutch | Operation of the instrument | Working environment (noise, temperature, light) |

***Table 6.4.12*** *Elements and specifications of the XAS 1 instrument.*

### XAS 2: Tunable hard x-rays

For hard x-rays no significant offset can be achieved for short distances, thus, a deflecting mirror assembly inside the SASE 2 beamline tunnel and about 100 m upstream of the experimental hall is used for horizontal deflection. The XAS 2 instrument resembles XAS 1 very much. Only the first deflecting mirror inside the experimental hall can be avoided. The instrument is about 500 m further away from the end of the undulator. Due to the higher photon energies Beryllium windows might become usable. However, since the instrument is supposed to cover the entire photon energy range from 3-12 keV, a differential pumping section will be of advantage. Figure 6.4.47 depicts the principal setup of XAS 2 and a description of these elements can be found in Table 6.4.13. Further details are given in the section before on XAS 1.

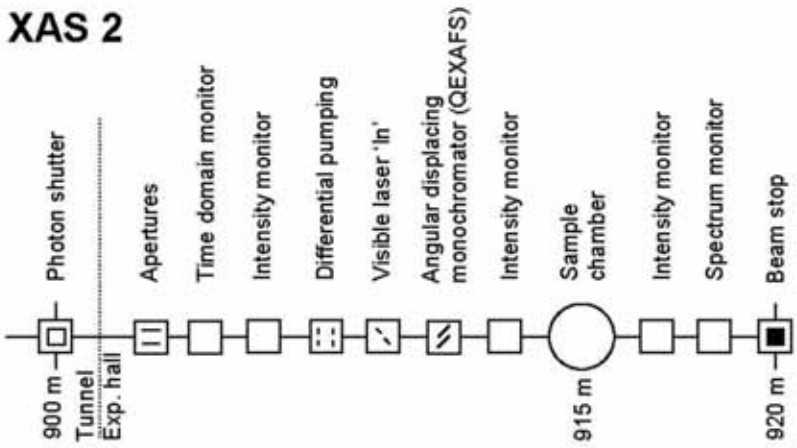


***Figure 6.4.47*** *Schematic layout of the XAS 2 instrument at the SASE 2 beamline. Distances are given with respect to the end of the undulator.*

| Item | Purpose | Specification |
|---|---|---|
| Slits/apertures | Beam definition,<br>beam halo cleaning | 0.25 µm accuracy,<br>1 µm repeatability |
| Time domain monitor | Measurements of x-ray arrival-time x-ray with respect to visible laser | |
| Intensity monitor | Measurement of incident photon flux | Transmissive (<5% absorption), single pulse measurement, relative accuracy $<10^{-3}$ |
| Differential pumping | Separation of beamline and instrument | |
| Monochromator | Angular displacing monochromator (QEXAFS) | 0.1 µrad angular stability,<br>0.1 mrad asymmetry error |
| Intensity monitor | Measurement of photon flux behind dispersive element | Transmissive (<5% absorption), single pulse measurement, relative accuracy $<10^{-3}$ |
| Sample chamber | Sample positioning and orientation, | x-y-z move (0.25/1 µm),<br>two rotations (0.25/1 mdeg) |
| Detector | Measurement of transmitted radiation | 2-D, 2K×2K, 10-30 Hz |
| XES spectrometer | Space-resolved detection of x-ray emission from the sample | In-vacuum,<br>10-30 Hz frame rate |
| Intensity monitor | Measurement of transmitted photon flux | Transmissive (<5% absorption), single pulse measurement, relative accuracy $<10^{-3}$ |
| Spectrum monitor | Measurement of high harmonic content | Single pulse measurement, relative accuracy $<10^{-3}$ |
| Alignment unit | Positioning and position verification | Permanently operating,<br>accuracy ~100 µm |
| Lead hutch | Radiation protection,<br>temperature stabilisation,<br>laser protection | 4×8×3.5 $m^3$ (W×L×H),<br>±1° thermal stability |
| Control hutch | Operation of the instrument | Working environment<br>(noise, temperature, light) |



***Table 6.4.13*** *Elements and specifications of the XAS 2 instrument.*

### 6.4.6 Femtosecond diffraction experiments

It has always been a dream of chemists and physicists to film the making of new molecules and structures to gain a deeper understanding of the parameters in the process. In fact how do atoms and molecules combine to form new molecules or structures? What is driving the transformation? How long does it take? Which atoms are involved? Does the environment catalyse the reaction? These questions are not easy to answer since the primary time steps in chemical and physical transformations are ultrashort, typically on the timescale of molecular vibrations. For example, in the symmetric stretch mode in water, the Hydrogen atoms vibrate along the O-H axis in 9.1 fs. And the heavier Iodine molecule oscillates with a 156 fs period. Femtosecond optical spectroscopy has provided a wealth of information about the timescales in femtochemistry but the long wavelength of light, 200-700 nm, precludes spatial information on the atomic length scale. Ultrafast electron diffraction (UED), on the other hand, can probe chemical reactions in the gas phase with 1 ps resolution, but the strong scattering of electrons makes is difficult to use UED in condensed matter, which is an important drawback since most biological and industrial processes take place in a condensed environment.

The European XFEL Facility will deliver extremely intense, 100 fs long pulses of x-rays that will become a fantastic new tool for studies in femtochemistry. The pulse is expected to contain $1 \times 10^{12}$ photons in a 0.1% bandwidth at 12.4 keV. By comparison, beamline ID09 at ESRF produces $1 \times 10^{10}$ photons in a 3% bandwidth at 15 keV in 100 ps. XFEL radiation is, thus, likely to revolutionise time-resolved studies: a 1,000-fold shorter pulse length, a 100-fold increase in single-pulse intensity and a 30-fold reduction in bandwidth. Simulations indicate that high-quality diffraction patterns from a protein and a liquid can be acquired in one single pulse. These exceptional parameters will lead to new experiments and groundbreaking discoveries.

#### *6.4.6.1 Scientific case*

The aim of pump-probe diffraction experiments with XFEL radiation is to visualise how matter rearranges during chemical or physical reactions with femtosecond resolution. One of the most striking pump-probe experiments with third-generation synchrotrons is Laue diffraction from myoglobin. Using single-pulse Laue diffraction at ESRF and the Advanced Photon Source (APS), it is possible to film, with 100 ps time resolution, the trajectories of CO molecules and the associated structural relaxations as they photodetach from the heme group and migrate towards the solvent. The advantage of working with crystals is substantial: if the non-excited structure is known, the Fourier difference maps determine the change in the electron density in three dimensions and without the need for a model. The maps probe, in principle, the induced changes in position for **all** atoms in the crystal, and this method is complementary to spectroscopy, that probes the local environment around a metal atom (Section 6.4.5(II.)). The unique feature required of the investigated proteins is that they retain their functionality in the crystalline state. This is due to the intrinsic softness of proteins and their large size, so that most residues are located far from the boundaries of the unit cell. There are limits, however, and hemoglobin is one of the best examples. Alternatively, such relaxations can be studied

by small-angle-scattering SAXS but the information content is limited to one-dimensional maps that need interpretation. There is, however, great interest in SAXS since many systems, including membrane proteins, that cannot be crystallised, become accessible.

Further examples of application of ultrafast diffraction concern small molecules, whether in the gas or liquid phase, or in the solid state. In the solid state, detailed information on the structural evolution following excitation by a pump laser can be obtained by applying techniques such as time-resolved powder diffraction. With the short and intense x-ray pulses provided by the XFEL it will be possible to follow intra- and intermolecular structural relaxation processes which are connected to vibrational redistribution processes or to investigate the structure of ultrashort living intermediates (as excitonic states in organic dyes). Further opportunities are provided by resonant (anomalous) diffraction, which has a special sensitivity to electronic properties, and may be used to monitor electronic phase transitions on a fast timescale.

### Experimental programme

#### I. Ultrafast diffraction from molecules in the gas phase

Molecular structural dynamics in the gas phase has already been studied by time-resolved electron diffraction with a temporal resolution approaching 1 ps and spatial resolution better than 0.001 nm **[6-287 – 6-289]**. Electrons are well suited for the gas phase due to its relatively high scattering intensity over x-rays. In general the scattering intensity of electrons is six orders of magnitude stronger than that of x-rays **[6-290, 6-291]**. Since the number of electrons per pulse used in a typical time-resolved electron diffraction is ~$10^4$ at 1 kHz operation **[6-288]**, one needs $10^{12}$ (= $10^4 \times 10^6 \times 10^2$) x-ray photons per pulse at 10 Hz operation to make up for the deficiency of the scattering intensity and the repetition rate. Therefore, once the XFEL comes on stage with its $10^{12}$ photons per pulse, it should be possible to study gas phase structural dynamics by time-resolved x-ray diffraction under similar conditions to time-resolved electron diffraction (a pressure of 1 – 10 torr in the scattering volume). What would be the advantages and disadvantages over time-resolved electron diffraction? Gas-phase time-resolved x-ray diffraction from an XFEL will have a time resolution limited by the x-ray pulse width, that is, about 100 fs. This time resolution is not only 10 times better than state-of-the-art electron diffraction, it also reaches the time window of molecular vibration. This means that the movement of atoms in a molecule can be filmed literally in real time. In addition, electrons are charged and hence, affected by small amounts of positive ions generated as by-products in most pump-and-probe experiments. This causes some baseline drift and complicates the data analysis **[6-292]**. X-rays do not suffer from this problem. The real disadvantage of x-ray diffraction, apart from the poor sensitivity to the lightest atomic species, is that inelastic scattering increases with the scattering angle whereas the situation is reversed in electron diffraction. This means that the usable q-range is inherently limited for x-ray diffraction even if a sufficient number of x-ray photons are provided. Typically, there is no usable elastic scattering for q values larger than 10 $Å^{-1}$. By contrast, the available q-range in electron diffraction is only limited by the electron flux. To summarise, time-resolved x-ray diffraction is feasible when we consider the photon-counting statistics. The diffraction signal from the gas phase dynamics is supposed to be

much simpler than that from solutions, where solvent molecules also contribute. Therefore, gas-phase reactions should be studied prior to liquid-phase reactions for practical reasons.

*Scientific applications*

All molecular systems that have been studied by time-resolved electron diffraction can be revisited by time-resolved XFEL diffraction. Among the simplest molecular systems would be diatomic molecules such as NaI and $I_2$. These systems have been intensively studied by femtosecond optical spectroscopy, and they would be a natural first target for time-resolved x-ray diffraction in the gas phase. In addition, the electron diffraction signal in the femtosecond regime has been simulated for these systems **[6-293, 6-294]**. As shown in Figure 6.4.48, once a ground state Iodine molecule is excited to a repulsive excited state, the distance between the two atoms will expand and the Iodine molecule will eventually dissociate into two Iodine atoms. The wavepacket motion along the vibrational dissociation of the two atoms can be mapped out by x-ray diffraction in real time if sub-picosecond time resolution becomes available.

After acquiring full control of the relevant parameters for pump-probe experiments on diatomic molecules, more challenging targets could be considered: polyatomic molecules, e.g. the haloalkanes such as $CF_2I_2$, $CH_2I_2$, and $C_2F_4I_2$, organometallic such as $Fe(CO)_5$ and $(C_5H_5)Co(CO)_2$, and hydrocarbons such as pyridine ($C_5H_5N$) and cyclohexadiene ($C_6H_8$). It has been shown that a sufficient gas pressure can be easily obtained for these molecules. Due to the insufficient time resolution of electron diffraction, limited to a few picoseconds, the real-time movement of atoms could not be captured, but only the molecular structures of transient intermediates were obtained so far. For example, picosecond electron diffraction studies on ring-shaped molecules such as pyridine and cyclohexadiene showed that the ring is opened upon excitation at 267 nm, but it could not be determined whether the ring is broken in a symmetric or asymmetric fashion. If we can follow atomic motions in real time, this very initial movement can be captured. In addition, one can film intramolecular vibrational energy redistribution, which will affect the bond lengths and angles of an intermediate as a function of time. If the excitation pulse is linearly polarised, the excited molecules will tend to align their transition dipole moment along the polarisation. Femtosecond time resolution should readily observe this excitation anisotropy.

Clusters of atoms or molecules are even more challenging. These systems have been studied by time-resolved electron diffraction **[6-295]**, but only with microsecond time resolution determined by the flight time after a nozzle. Time-resolved x-ray diffraction should be able to follow the phase transition within a cluster and clarify the relationship between the structural parameters and the phase transition.

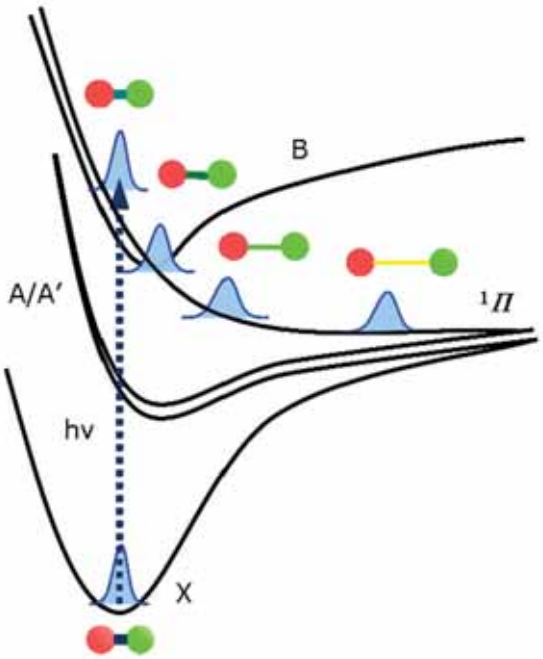


***Figure 6.4.48*** *Schematic view of the potential energy surfaces for ground and excited states of a diatomic molecule and the evolution of vibrational wavefunctions after photoexcitation.*

### II. Liquid-phase photochemistry

The chemistry in solution phase is an important field of research as many biological and industrial reactions take place in solution. Time-resolved x-ray diffraction in liquid phase photochemistry has already been very successful in synchrotron-based experiments **[6-296 – 6-298]**, where it can determine molecular structures of intermediates in solution to a time resolution of 100 ps, limited by the x-ray pulse width from storage rings. In recent experiments, fairly complex reactions with up to six reaction channels in parallel were studied. Better time resolution has been demonstrated with laser-driven plasma sources **[6-299]** and at SPPS **[6-300]**, but the number of x-ray photons per pulse was not sufficient for liquid-phase dynamics, and only solid samples where the structural information is gathered from one or two reflections, were considered. In a typical time-resolved x-ray diffraction experiment, halide-containing solutes such as $Br_2$, $I_2$ $HgBr_2$, $HgI_2$, $CH_2I_2$ and $C_2H_4I_2$ are dissolved in liquids like methanol ($CH_3OH$) or tetrachloromethane ($CCl_4$). In the analysis of x-ray diffraction with 100 ps time resolution, the signal from a laser-excited solution could be decomposed into three principal components: the solute-only term, the solute-solvent cross term, and the solvent-only term; the analysis was aided by using Molecular Dynamics (MD) simulations for equilibrium. This approach was valid because the time resolution of 100 ps was much slower than the nuclear motions, and the system returns to equilibrium within 100 ps. With the femtosecond time resolution expected from the XFEL, the decomposition and the assumption of quasi-equilibrium are no longer valid, which actually means that the XFEL will open a completely new field of research.

*Scientific applications*

The solutes studied so far by 100-ps time-resolved x-ray diffraction in solution include diatomic molecules such as $I_2$ and $Br_2$, and haloalkanes such as $CH_2I_2$, $C_2H_4I_2$, and $CHI_3$. The heavy atoms such as Iodine increased the contrast against the solvent. Unlike a molecule in the gas phase, a solute in solution is surrounded by numerous solvent molecules. The presence of the solvent often alters the reaction pathways through the cage effect. Picosecond resolution allowed observation of these reaction pathways by tracking the structure of the transient intermediates during the course of the reaction, but the real interplay between the solute and solvent is beyond reach. As in the gas phase, femtosecond resolution in XFEL diffraction should allow the observation of the initial motions of the wavepacket once created in the excited state by a laser photon.

Once again, a diatomic molecule such as $I_2$ would be a good example. As shown in Figure 6.4.49, once an $I_2$ molecule is excited, the two Iodine atoms will start to separate, but will soon hit surrounding solvent molecules. Therefore, most of them geminately recombine to form a wavepacket either in the hot ground state or in the A/A' state. The lifetime of the A/A' state was long enough to be captured with picosecond time resolution, but the vibrational cooling of the hot ground state was marginally observed. The femtosecond resolution with the XFEL should allow the follow-up of the vibrational cooling. Vibrational cooling is one of two fundamental ways in which molecules in solution can induce the surrounding molecules to rearrange. The other way, which is also critical to solution chemistry, is through solvation.

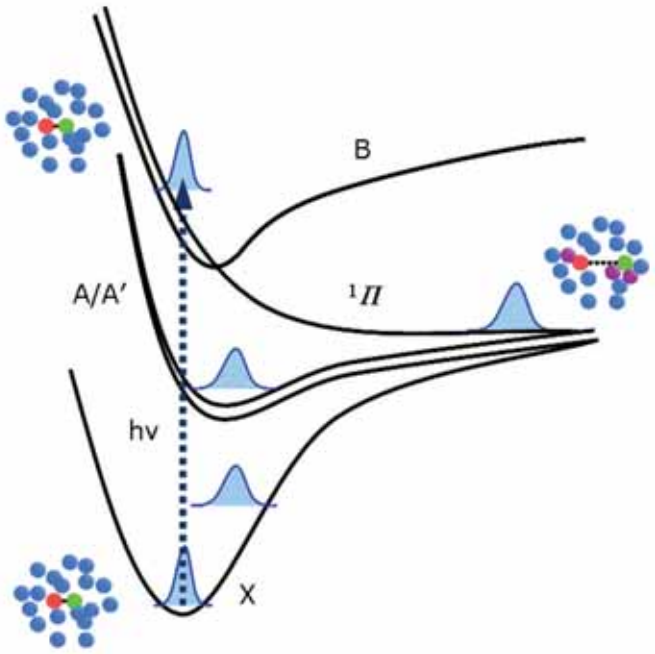


***Figure 6.4.49*** *Same diagram as Figure 6.4.48, but for $I_2$ molecules in solution.*

Molecular dynamics simulations of the photo-dissociation of $I_2$ in $CCl_4$ can define timescales for structural processes, as shown in Figure 6.4.50. Upon photon absorption, Iodine is put into the short-lived excited B-state that decays through a near conical intersection to a dissociative triplet p state. The Iodine can then dissociate completely or the two atoms are trapped by the solvent cage, which leads to geminate recombination. The photo-excitation of $I_2$ in liquid $CCl_4$ induced by a 100 fs laser pulse at 520 nm leads in the simulation to Iodine atoms hitting the cage in 320 fs at a separation of 0.7 nm and with a speed of 1,115 m/s.

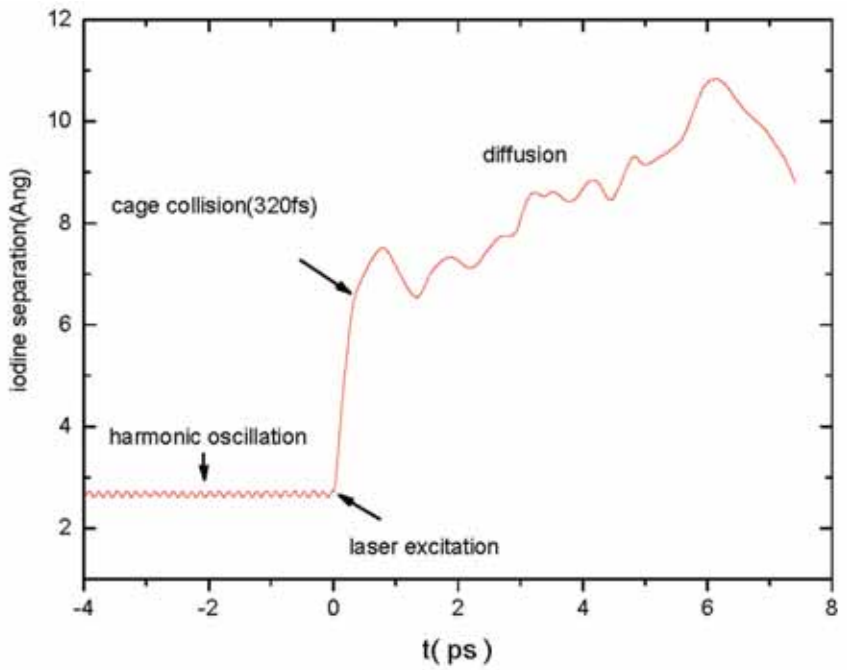


***Figure 6.4.50*** *MD simulation of the Iodine-Iodine distance for a dissociating Iodine pair.*

Turning to polyatomic molecules, a femtosecond laser pulse can initiate an electronic transition in a dye molecule such as Coumarin 153 dissolved in a polar solvent such as methanol (see Figure 6.4.51). The solute has zero dipole moment in its ground state ($S_0$), but a large dipole in its excited electronic state ($S_1$). This electronic transition is rapid as compared to nuclear motions in the solvent, the excited state is initially prepared with a solvation environment that is characteristic of equilibrium $S_0$, not $S_1$. Over time the solvent reorganises along the solvation coordinate in order to lower the solvation energy in the excited state **[6-301]**. This solvation dynamics can be followed by femtosecond x-ray diffraction.

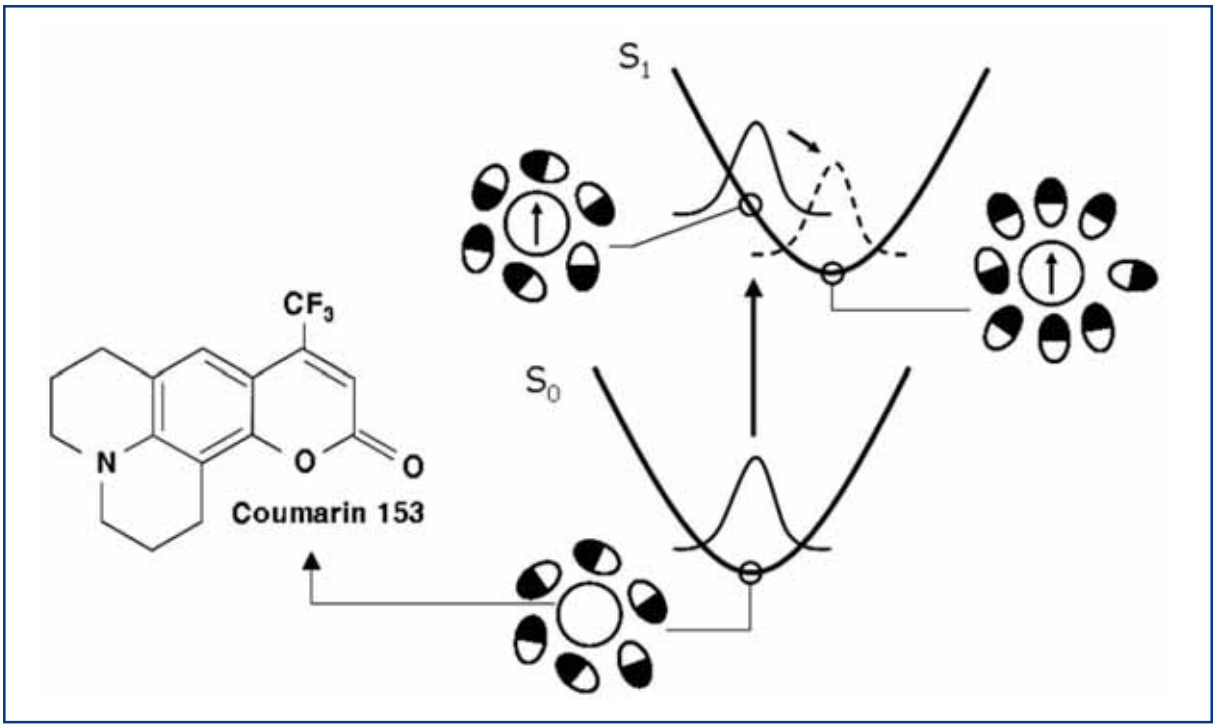


***Figure 6.4.51*** *Illustration of the role of dipoles in the solvation of Coumarin 153.*

Another interesting subject would be real-time observation of isomerisation in solution. For example, it is speculated that the angle between the two naphthyl groups of 1,1'-binaphthyl is changed by about 40° upon excitation from the ground to the first excited singlet state (see Figure 6.4.52). Since the surrounding solvent molecules have to be pushed out in the process, the time for this process is tens of picoseconds and depends on the viscosity of solvent, as demonstrated by time-resolved spectroscopy **[6-302]**. Femtosecond time resolution should be sufficient to follow this kinetics in real time.

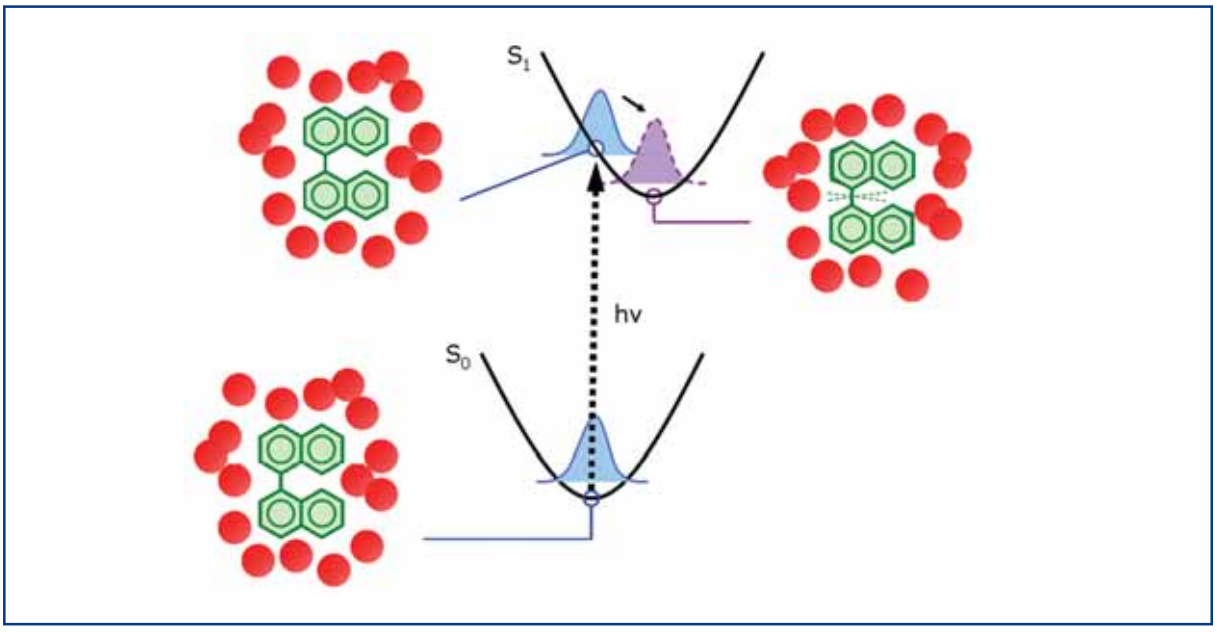


***Figure 6.4.52*** *Illustration of the solvent rearrangement around 1.1' - Binaphtyl.*

### III. Femtosecond time-resolved Laue crystallography of proteins

A detailed mechanistic understanding of how proteins function requires knowledge not only of their static structures, but also of how their structures evolve as they execute their designed function. Recently, the technique of picosecond time-resolved x-ray crystallography was developed and used to visualise, with near-atomic resolution, structural changes in myoglobin as it evolved from the carboxy to the deoxy state **[6-303, 6-304]**. This transition was triggered with picosecond laser pulses and probed with picosecond x-ray pulses. This "pump-probe" approach recovered time-resolved diffraction "snapshots" whose corresponding structures were stitched together into movies that unveiled protein structure changes and ligand migration in real time. The driving force for this structural transition resides in a photolysis-induced displacement of the heme Iron, which moves 0.03 nm or 0.036 nm in the proximal direction. Correlated displacements of the heme, the protein backbone, and other side chains are evident throughout the protein at 100 ps, the earliest time accessible to synchrotron x-ray pulses. Figure 6.4.53 shows structural changes in wild-type MbCO determined 100 ps after photolysis. To enhance the visibility of weak features in the figure, the electron density was mapped non-linearly to color brightness. The most dramatic changes occur within the area enclosed by the white box, but smaller changes are evident over the entire dimensions of the protein. To witness how this piston-like Iron motion drives the structural changes observed in the 100-ps snapshot requires a significantly improved time resolution.

We know from time-resolved IR measurements that the fastest internal motion in photolysed MbCO is the rotation and trapping of CO in the primary docking site. Two trajectories were resolved with time constants of 200 and 500 fs, respectively. We would not expect to resolve the ligand orientation with x-ray crystallography, so around 200 fs time resolution should be more than sufficient to visualise the response of the protein to the ligand translocation event. The doming of the heme along with ligand translocation to the primary docking site triggers a so-called "protein quake" **[6-305]** whose propagation could be resolved for the first time. The biomechanical coupling of the heme doming to the tertiary conformation of Mb is presumably similar to that in hemoglobin, which undergoes a quaternary structure transition that leads to cooperative binding of Oxygen. Being able to explore these processes on the femtosecond timescale promises to help unveil the pistons, levers, wheels, and gears of biology.

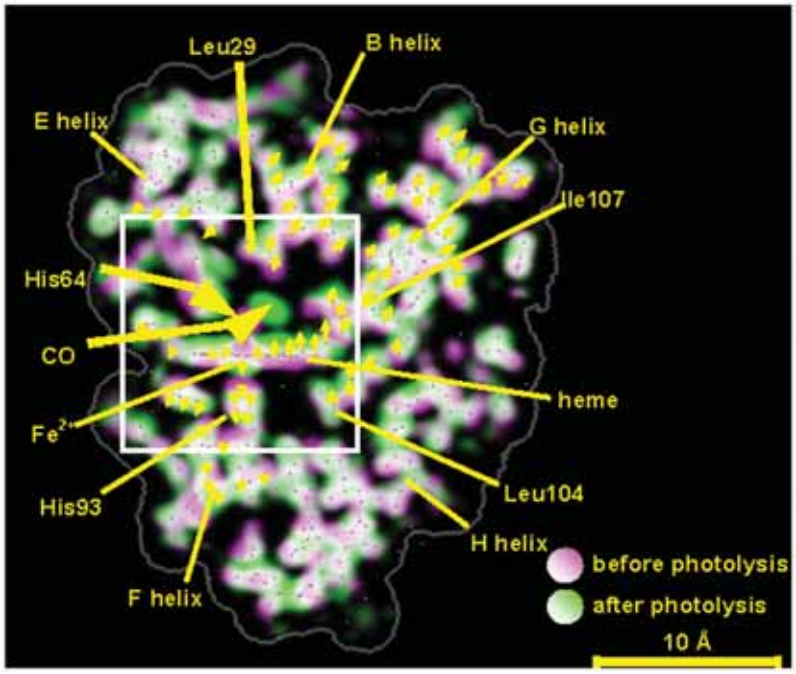


***Figure 6.4.53*** *Structural changes in wild-type MbCO determined 100 ps after photolysis. Electron density differences in wild-type MbCO presented as a colour-coded superposition of the density ascribed to the ground (magenta) and photolysed (green) states. Where magenta and green overlap, they blend to white. The direction of motion, as indicated by arrows, follows the magenta-to-green colour gradient.*

### IV. Solid-phase photochemistry

The solid state is a rich arena of phenomena taking place on sub-picosecond timescales, and the XFEL is particularly suited for their investigation, as a complementary probe to ultrafast visible and IR lasers. In particular, photo-induced phase transitions provide a convenient way to set the zero of the timescale by triggering phenomena with a very short (~fs) laser pulse. The relatively high density of target atoms in solid matter allow the use of various techniques and examples of application of powder diffraction as well as resonant soft x-ray diffraction. These are described here.

Photo-induced effects in the solid state may start as local order-disorder processes (as a consequence of ultrafast structural relaxation pathways), and amplify to cooperative phenomena which can finally trigger structural reorganisation processes in the bulk. This behaviour has been found in the structural response function of pigments and dyes like organic molecular crystals or organic charge-transfer systems (1-D organic mixed stack compounds). They are also the underlying mechanism of other kinds of photo-induced solid state reactions (like photodimerisation and photopolymerisation). Detailed information on the structural evolution can be obtained by applying time-resolved x-ray diffraction both with single-crystal and powder-diffraction techniques. With the short and intense x-ray pulses provided by the XFEL it will be possible to follow intra- and intermolecular structural relaxation processes which are connected to vibrational redistribution processes or to investigate the structure of ultrashort-living intermediates (as excitonic states in organic dyes).

X-ray powder diffraction is a method for x-ray structure determination that has proven versatile and powerful in many applications, albeit having a reduced resolving power and efficiency. Applications from the areas of material sciences and chemistry take advantage of the fact that sample preparation for powder diffraction is much easier. There is no need to grow single crystals of considerable size and crystal quality. Furthermore, powder diffraction enables the investigation of several phases of the material at once using Rietveld refinement methods. With respect to the proposed experiments using FEL radiation, a further important advantage is that powder diffraction allows the collection of the entire structural information simultaneously, that is without the need to rotate or scan parts of the experimental setup. Therefore, single shot experiments become feasible. Figure 6.4.54 shows the radial distribution of a powder diffraction patter of bis-(methylammonium) manganese chloride (MAMC) before and following photoexcitation.

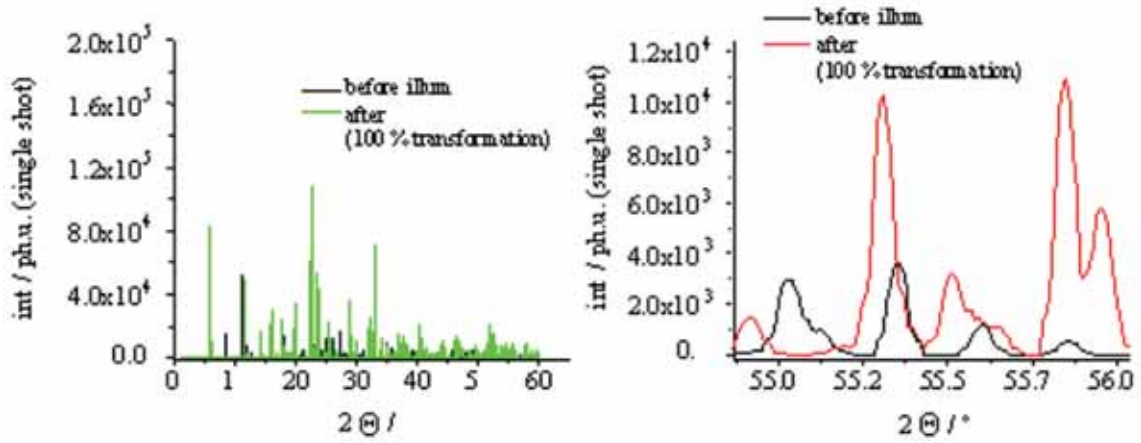


***Figure 6.4.54*** *Radial distribution function of powder diffraction of MAMC upon photo-excitation (assumed to be 100%) in the case of bulk transformation. The simulation shows the variation of the diffraction pattern before and after the photo excited phase transition.*

Another interesting possibility is the study of diffuse scattering induced by cooperative excitations. Cooperative interactions play a central role in many photoactive solids. The structural relaxation of the excited electronic states is not localised on individual molecules but entails many molecules in a “domino” or “cascading” effect. The first step is usually the formation of nano-domains which is followed by long-range order in 3-D. This gives rise to diffuse scattering that probes the deviation from the average periodic structure of the crystal. These deviations in structure appear on very short time-scales 0.1 to a few picoseconds and the signal amplitude is typically at least five orders of magnitude lower than Bragg reflections. It gives direct information about the nature (1-D - 3-D), the size and the dynamics of self-trapped excitations. The aim of these experiments is to see how these non-linear excitations form and propagate in the crystal.

Figure 6.4.55 shows a simulation of the time-evolution of a photo-induced plane in MAMC upon photo-excitation in the UV absorbing subunit of the molecule. The simulated angular intensity distribution of the diffusive scatter signal spans an angular range of 0.08 rad over which was integrated the angular intensity distribution. Applying classical

simulations, the angular frequency of the photoexcited motion was calculated to be $2\pi\nu = 3.24\times10^{12}$ $s^{-1}$ with a damping factor to about $\gamma = 3\times10^{11}$ $s^{-1}$. The displacement factor for this motion was determined to be about $\underline{u} = 10^{-4}$ nm in a potential which was calculated by density functional theory with a B3Lyp functional.

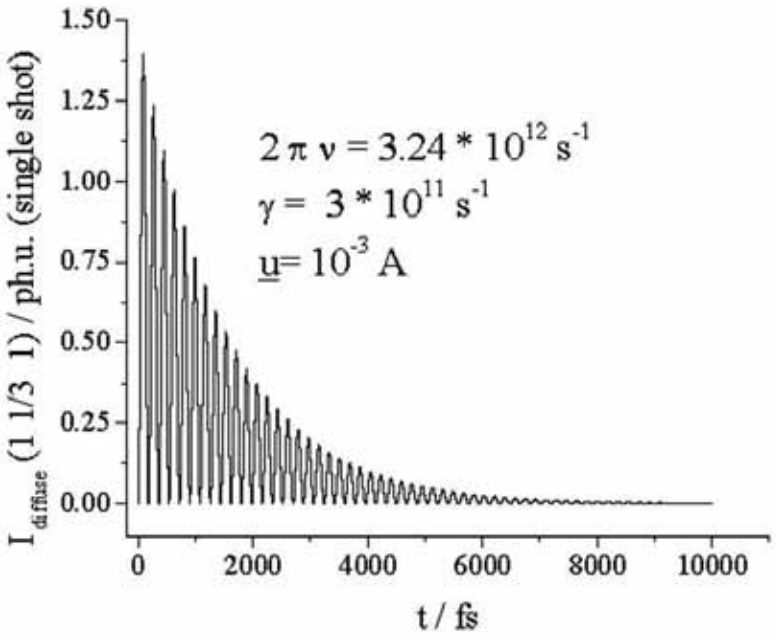


***Figure 6.4.55*** *Proposed time-evolution of a photo-induced plane [1 1/3 1] in MAMC upon photo-excitation in the UV absorbing sub-unit of the molecule.*

### V. Photo-induced transitions in solid-state materials

Photo-induced phase transformations are a new way to manipulate matter by light, with the possibility of ultra-fast switching between two macroscopic states. In some unconventional photo-active materials, the structural distortions are not localised on one molecule, but involve a number of them that aggregate into nano-domains in 0.1- 1 ps. If a sufficient number of nanodomains is created by the laser, the crystal switches to a new phase in 1 100 ps. These cooperative phenomena take place in highly-correlated materials such as charge-transfer complexes (neutral to ionic transition), mixed-valence chains and oxides.

*Charge-transfer materials*

Recent investigation of the photo-induced neutral to ionic transformation in the charge transfer compound TTF-CA illustrate how the changes in the diffraction pattern indicate a macroscopic 3-D structural self-organisation on the 100 ps timescale **[6-306]**. Present results indicate that photo-induced disordering processes can occur at the sub picosecond timescale. Molecular crystals where the phase transitions are driven by coherent molecular motion are likely to be of great interest in the future. Such coherent phonons where investigated in Bismuth by 100 fs X- ray diffraction **[6-307]**. In the simple Bismuth structure, the intensity of one or two Bragg reflections makes it possible to observe the

atomic reorganisation with laser driven plasma sources. However, for more complex materials such as molecular crystals where coherent oscillations are also observed **[6-308]**, the structure analysis will require a large number of Bragg reflections to be measured in real time, which is currently not possible. Ideally, it would be possible to observe the change in electronic structure before atomic reorganisation occurs (sub-picosecond), and then watch the evolving structural relaxation on longer timescales. This will make it possible to observe adiabatic compared to non-adiabatic processes, thus shedding light on the subtle coupling between electronic and structural degrees of freedom.

Diffuse scattering from the compound TTF-CA has been observed experimentally and is concentrated in planes resulting from the one-dimensional periodic nature of fluctuations **[6-308]**. The shape and intensity of the diffuse scattering signal depends on the correlation between molecules and there interaction range **[6-309]**: when the 1-D structure is formed, diffuse planes appear; with 3-D coupling setting in, this signal condenses onto the Bragg reflections and disappears. The time resolved change in shape and intensity will, thereby, provide information on the mechanism driving the transformation from localised excitation to the macroscopic domain.

*Charge-orbital ordering*

The phenomenon of charge/orbital-ordering in strongly correlated electron systems consists of the “crystallisation” of valence charges and/or sometimes orbital alignments **[6-310]**. Strong electron-electron repulsion gives rise to angstrom-scale charge super-lattices, which are not necessarily commensurate with the atomic lattice. Such CO/OO states are often observed in insulating phases of strongly correlated electron systems, which are sometimes in subtle competition with “hidden” metallic or super-conducting states. Systems of particular interest include CMR manganites, High-Tc Cuprates, Nickelates and Cobaltates.

Charge ordering phenomena have been studied statically with a variety of scattering techniques, ranging from neutron to electron diffraction and, most recently, with resonant x-ray scattering **[6-311]**. Particularly interesting and controversial is the relationship that such electronic super-structure formation has with the atomic-structural degree of freedom (CDW formation, Jahn-Teller distortions and the like), and the extent to which atomic arrangements dictate the stability of charge-ordered insulators.

Resonant x-ray scattering to study CO states has been statistically shown to be most effective at the L-edges of the transition metal **[6-312]**, where: (1) the scattering cross section is enhanced; (2) important sensitivity to magnetically dichroic effects is observed; and (3) the final state of the x-ray transition coincides with the same 3d states of the transition metal that participate to the orbital ordering **[6-313]**. Yet, these static techniques become less insightful in the vicinity of critical points, where the rapid fluctuations that dominate the physics are averaged out, appearing only in weak inelastic reflections. The study of these phenomena in the time domain overcomes these problems, clarifying the nature of dynamic couplings between various degrees of freedom of the system.

To the extent that such ordered phases are sensitive to chemical doping, they are also susceptible to photo-doping and are found to undergo photo-induced phase transitions **[6-314, 6-315]**. The case of $VO_2$, a spin Peierls compound with a prominent insulator-metal transition, was recently studied. Ultrafast experiments combined mid-IR excitation and probing with femtosecond soft x-ray absorption **[6-316]** and femtosecond x-ray diffraction **[6-308]**. Most importantly for the type of experiments proposed here, it was shown how the analysis of the fundamental timescale for a photo-induced phase transition can help in establishing a hierarchy of events between electronic and structural degrees of freedom in a correlated electron system **[6-317]**.

To study these effects we propose optical pump, soft x-ray probe measurements of charge-ordering disordering dynamics (compare Figure 6.4.56). Improved sensitivity to the very weak signal from the valence charges can be obtained by measuring resonantly at the transition metal L-edges (0.5 – 0.9 keV), or at the Oxygen K-edge at 0.54 keV to study the rearrangement of Oxygen-containing molecules in the lattice. The proposal is to study two types of photo-induced excitation shown in Figure 6.4.56. First, impulsive excitation of electron-hole pairs across the bandgap using near-infrared light is an ultrafast analogue to the process of chemical doping. A second class of experiments is the coherent excitation of metal-Oxygen optic phonons with mid-infrared light. Experiments would actually cover a variety of techniques, like time-resolved diffraction, XAS or XPCS.

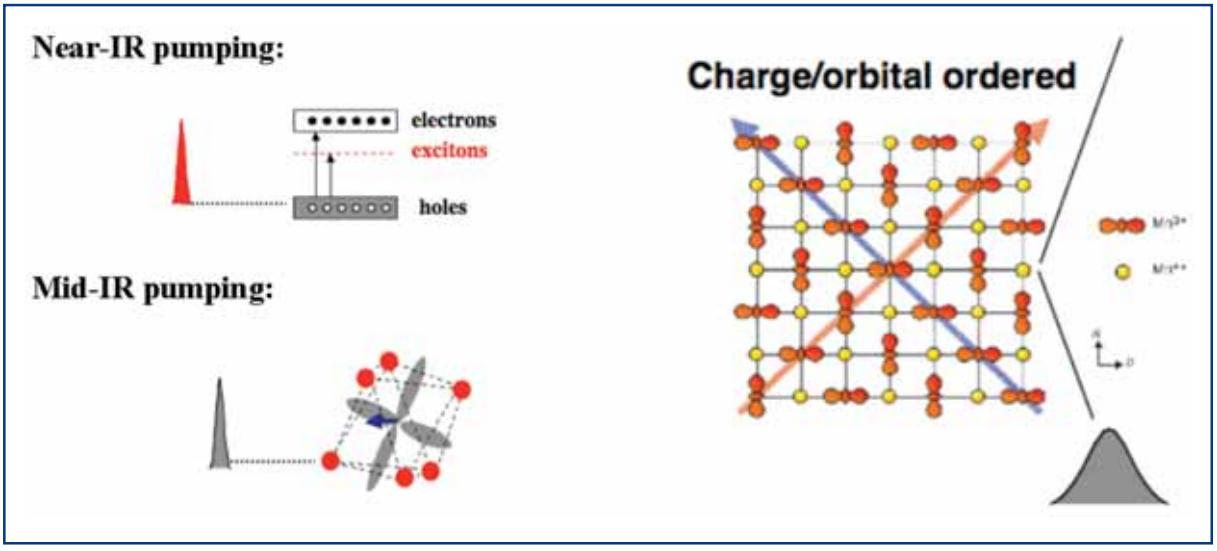


***Figure 6.4.56*** *Pumping (left) and probing (right) charge/orbital ordered crystals using time-resolved techniques and resonant x-ray energies.*

### VI. Investigation of the solid-liquid phase transition and nanoscale materials

The transition from the crystalline to the liquid state, from order to disorder, has attracted great attention over the past 100 years, and has recently served as a testing ground for the development of ultrafast x-ray-based techniques. Much theoretical work has focused on the timescales and mechanisms by which this transition occurs. In some cases, one may view the melting process as an example of a chemical reaction occurring on a macroscopic length scale, in which light-induced changes in the potential energy surface of the solid lead to rapid atomic-scale movement. Many questions remain: What is the

structure of the non-equilibrium liquid state? How does it evolve towards that of the equilibrium liquid (of higher density)? And how does the eventual recrystallisation process occur? These are important questions with respect to semiconductor processing and micro-machining. Ultrafast x-ray pulses produced by the XFEL would allow one to capture snapshots of the disordered liquid state and how it evolves. Measurements to date have focused on a limited number of high-Z materials. The European XFEL enables experiments in low-Z materials, for example, probing femtosecond dynamics in liquid Carbon, of important astrophysical interest, or the dynamics of the ice to liquid water transition following infrared vibrational excitation of the solid.

Recent measurements at the SPPS have probed optically induced liquid state dynamics in the semiconductor InSb **[6-300]**. Measurements have captured the first steps in the solid to liquid transition, during the first few hundred femtoseconds after excitation. Figure 6.4.57 shows two single-shot images of the x-ray diffracted intensity, conducted in a cross-beam geometry so that a range of times around t=0 are measured in a single shot. Time runs from left to right according to the temporal axis shown. In the top image, the x-rays probe the static material. In the lower image, a femtosecond laser pulse drives the transition from solid to liquid and one observes a rapid change in the diffracted x-ray intensity.

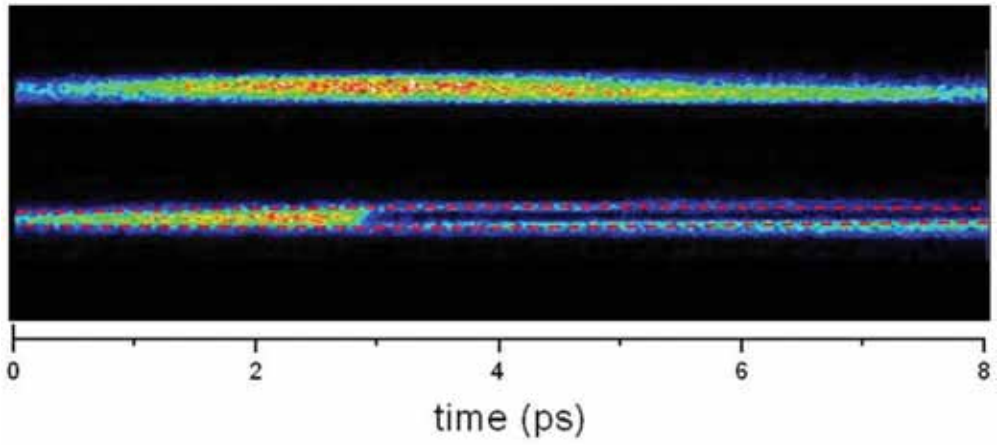


***Figure 6.4.57*** *X-ray diffraction images from InSb surface taken at SPPS. The timescale is determined by the cross-beam geometry of visible laser and x-rays. The top image is taken without a laser and the bottom shows the strong decrease in reflectivity at ~2.3 ps due to non-thermal melting following laser excitation.*

The melting dynamics and structural transformations discussed here are important to understand the functioning of nanoscale materials like semiconductor nanocrystals, known to exhibit important size-dependent properties of great technological interest. There is a natural interest in the structural dynamics of nanomaterials connected with applications in photoexcitation phenomena. Pulsed excitation is used in photonic materials to take advantage of ultrafast relaxations. On the other hand the understanding of static structure and interactions can also profit enormously from experiments, where the equilibrium structure is driven out of equilibrium, allowing to determine the dynamics and intermediate steps of structural and energetic relaxations. It has been observed that

the ultrafast timescale for a phase transition in nanoparticles induces new channels of structure formation, such as a non-thermal ablation and strong near-field effects in plasmonic materials **[6-318]**. However, the investigation of structural dynamics of nanoscale materials is severely limited at present. XFEL radiation can provide the high excitation levels and the spatial and temporal resolution to investigate structural dynamics, in particular during primary steps of structure formation, at a much better accuracy than presently achieved.

### Femtosecond diffraction techniques

Time-resolved x-ray diffraction experiments in the ultrafast timescale are performed in the pump-probe modus where a **reaction** is initiated by a pump pulse and the temporal evolution of this reaction is probed using an x-ray probe pulse. The timescale is established by the delay between pump and probe pulses and the use of (hard) x-rays allows the investigation of structural evolution (at atomic resolution). With the notable exception of the experiments on single particles or molecules, discussed in Section 6.4.7, given the weak scattering of x-rays from atoms, it is generally mandatory to work with ensembles of sample entities in order to enhance the signal and shorten the exposure time. The ultrafast initiation of a bulk sample will normally be done using femtosecond visible laser pulses, but one should keep in mind that the intensity levels achieved by XFEL radiation might allow triggering electronic reactions directly with x-rays. The laser pulse excites a subset of molecules in the sample, typically 1 in 1,000, and the diffraction from a delayed x-ray pulse probes the spatial evolution at that delay. If the reaction is reversible, the experiment can be repeated after a suitable delay, the delay depending on the reaction time and the time needed to cool the sample. In irreversible reactions, specific data acquisition methods have to be applied or the sample has to be exchanged between shots. By collecting structural information at many time delays, for example from 100 fs to 1 ms in nanosecond-steps, this sequence of spatial snapshots can be stitched together to make a movie of the structural processes following photoexcitation.

In ultrafast time-resolved experiments, the time resolution is usually determined by the convolution of the x-ray and visible laser pulse durations and their relative jitter. For the 100 fs XFEL pulses, 30 fs visible laser pulses, which are readily available commercially, and zero timing jitter, one obtains 104 fs as the time resolution, thereby insignificantly broadening the XFEL pulse duration. However, in this regime more subtle effects contribute to broadening of the time resolution. One contribution is the speed of optical light in condensed matter lower than the speed of x-rays. Considering a diffraction experiment in water with the x-rays transmitted through a thin sheet of water perpendicular to the beam. The speed of light is reduced from $3.0\times10^8$ m/s in air (vacuum) to $2.25\times10^8$ m/s in water (n = 1.33). Due to the different velocities the time resolution will, in general, reduce with increasing sample thickness. Let's consider a collinear beam experiment with 100 fs x-ray pulses and 30 fs laser pulses. Initially, the laser pulse is placed at the midpoint of the rising edge of the x-ray pulse. The nominal time delay is the time difference between the centres of the pulses, +50 fs. In the sample, the x-ray pulse will first catch up and finally overtake the laser pulse. After 400 fs, the visible laser pulse will be at the trailing edge of the x-ray pulse which means that the x-ray pulse is now 50 fs

**ahead** of the laser pulse and no longer probing the excited state. 400 fs corresponds to a sample thickness of 120 µm. Time-resolved diffraction experiments in transmission, which is normally used with area detectors, aiming for a time resolution of the order of 100 fs will, therefore, require thin samples of ~ 25 µm. These thin samples limit the observable count rates.

*Gas phase diffraction*

A conventional pump and probe scheme can be used where a femtosecond laser pulse initiates the reaction and a femtosecond XFEL pulse probes the structural dynamics (see Figure 6.4.58). The diffraction pattern is recorded using a 2-D area detector. The laser and x-ray beam have to be co-linear to minimise the spatial and temporal mismatch between the pump and the probe. The gas vapour can be supplied through a nozzle connected to a heated sample reservoir **[6-287]**. Typically, the pressure just outside the nozzle is about 5 torr when the backing pressure is about 100 torr. In this condition, the ambient pressure inside the vacuum chamber can be as high as $10^{-3}$ torr. To maintain a good vacuum in adjacent chambers, differential pumping should be employed. For electron diffraction, the carrier gas that is normally used in time-resolved spectroscopic experiments cannot be used any more because the carrier gas also contributes to the diffraction, thereby increasing the background and hence, degrading the signal to noise. However, for x-ray diffraction, a low Z carrier gas such as Helium might be used because of its relative low scattering power against atoms with higher Z. Clusters of atoms or molecules can be obtained by using special nozzles and a sufficiently high backing pressure.

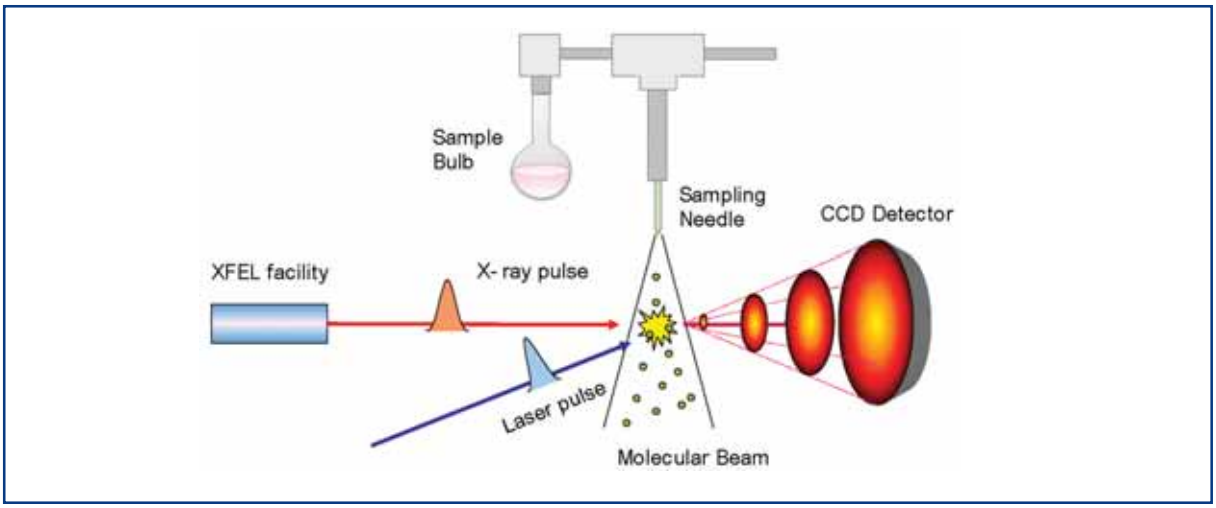


***Figure 6.4.58*** *Schematics of a gas phase diffraction experiment.*

*Liquid scattering*

The experimental setup used for picosecond liquid-phase x-ray diffraction used at present-day x-ray sources should be transferable to femtosecond x-ray diffraction with the XFEL. The pump-probe scheme is shown in Figure 6.4.59. The velocity mismatch between the pump laser and probe x-rays discussed above can be minimised by using a non-collinear geometry for x-rays and laser and restricting the probed sample volume. Concerning the sample cell system, two different setups have been used: a capillary-

based system and an open-jet one. In the first system, the solution is circulated through a quartz capillary (0.3 mm diameter) to provide a stable flow. In the open-jet system, the capillary is removed and a stable jet is produced by a high-pressure slit nozzle (slit, 0.3 mm, Kyburz) at a speed ensuring the refreshment of probe volume for every laser pulse. The open jet system has the advantage over the capillary system that the scattering from the capillary materials is absent, which reduces the background substantially and increases the signal to noise ratio. The lower background also increases the accuracy of the normalisation process. If the whole setting can be housed in a Helium chamber or a vacuum chamber, the background from the air can be greatly reduced.

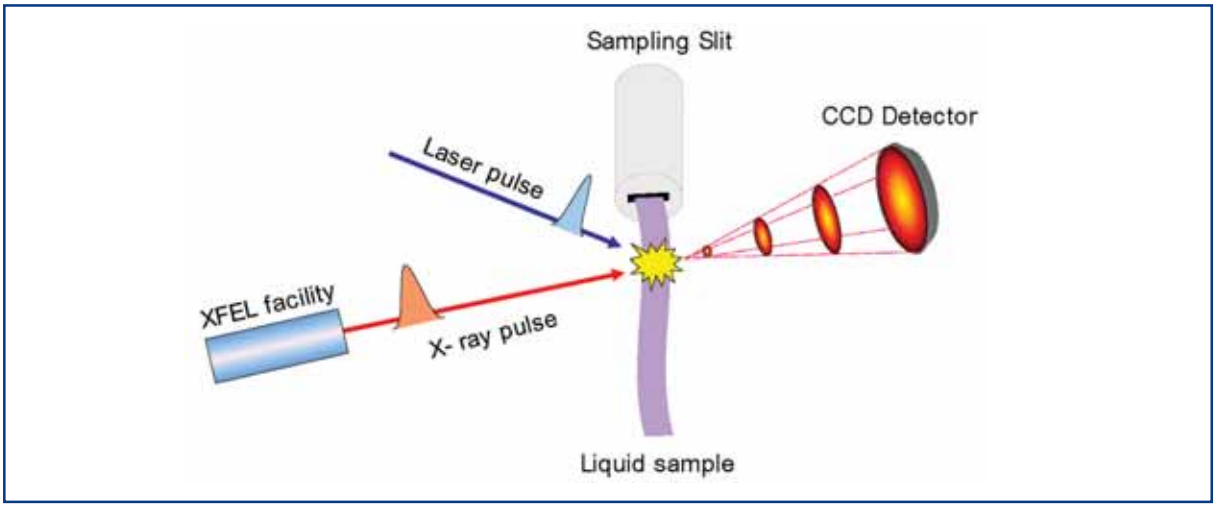


***Figure 6.4.59*** *Schematics of a liquid phase diffraction experiment.*

What is the prospect of filming chemical reactions in solution using single pulses of x-rays? What signal to noise ratio can one expect from having $10^{12}$ photons in one pulse? These questions are important as the technique requires high-quality images for time stamping where every image is recorded together with the actual laser/x-ray delay. In the following, the signal from a newly formed Iodine molecule surrounded by liquid $CCl_4$ will be calculated, taken 1 ps after recombination. Experience with liquid diffraction experiments on beamline ID09 at the ESRF enables calculations of the intensity distribution S(Q, t) for chemical reactions in liquids. The excess energy between the Frank-Condon state and the dissociation limit is 0.83 eV and this energy is transferred to the solvent in less than 1 ps. When the molecule is reformed at the dissociation energy 1.55 eV, the molecule is highly excited and oscillates between 0.23 and 0.4 nm. It is assumed that the excess energy decays exponentially with a 10 ps time constant. We can then determine the size of the molecule at its inner and outer turning points as a function of time. The turning points dominate the ensemble average and the molecular form factor can be approximated by the sum of these extreme states. The 0.1 $mm^3$ liquid $CCl_4$ contains $1.0\times10^{16}$ molecules and we assume a ratio $I_2$* to $CCl_4$ molecules of 1: 1,000 after laser dissociation. The photon flux of the x-ray pulse is $10^{12}$ phts/pulse and the energy is 12.4 keV. The diffracted signal is recorded using an area detector. The ratio of scattered to incoming photons is $2.65\times10^{-5}$ over the q-range 0-10 $Å^{-1}$. The calculated structure-factor difference (excited minus non-excited solution) is shown in Figure 6.4.60(a.) and (b.) for 1 ps and 25 ps,

respectively. One observes that Iodine dominates the early signal while the solvent dominates the late signal. This effect comes from energy conservation in the x-ray volume on short timescales: when the Iodine signal decreases in the recombination process, the solvent becomes thermally excited. On the ultrafast timescale, this temperature rise takes place at constant volume (and density). For the liquid peak the detected signal shows photon flux of 12,000 photons/pixel/pulse (64×64 μm$^2$ pixel area). The distribution has axial symmetry and needs to be ring-integrated in order to obtain sufficient sensitivity for the difference signal. Figure 6.4.60(c.) shows the Iodine and solvent signals after integration. The situation changes when the axial symmetry of the image is used to ring-integrate the intensity. The counting noise from the solvent background is about sqrt (5×10$^6$) = 2,236, so for a signal level of ~ 4,000, the S/N ratio is ~2. The conclusion is that every single image can be recorded separately with a time stamp, at the frequency of the macro-bunch train, i.e. 10 Hz. The images can then be sorted in time bins and averaged to improve the S/N ratio. Finally, the simulation shows that the diffracted intensity is proportional to the flux density (ph/m$^2$/pulse) times the number of x-ray illuminated molecules in the sample. For a thin sheet of liquid, the scattered intensity is, thus, independent of the focal spot dimension. Given the extreme power density in the XFEL beam, it may be advantageous in some cases to work with the unfocused beam of 0.8-1 mm diameter.

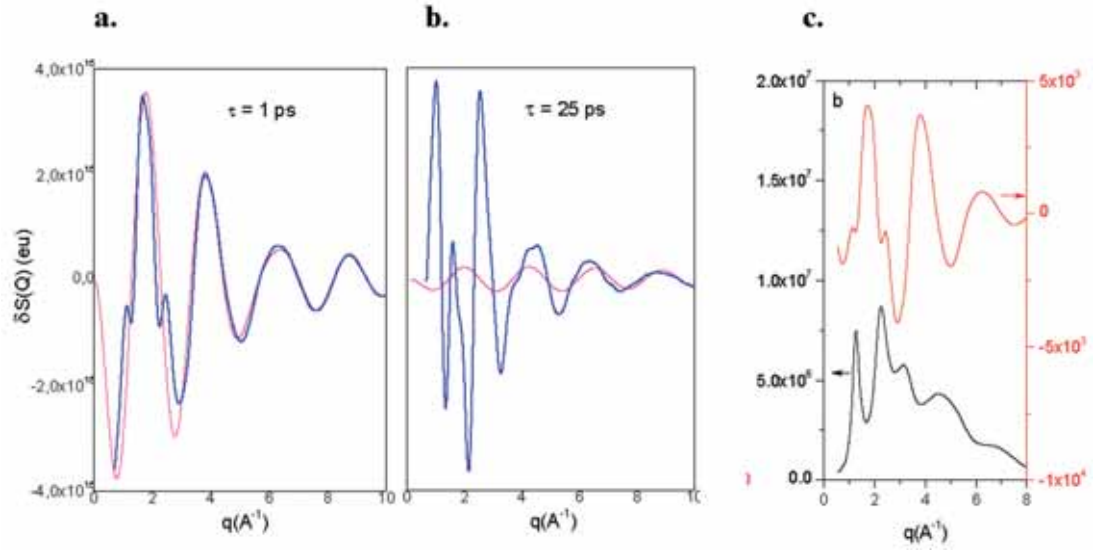


***Figure 6.4.60*** *Simulated difference oscillations from the recombination of $I_2$ for 1 ps (a.) and 25 ps (b.) time delay. The blue curves show the total signal, solute and solvent, the red curves show only Iodine. In (c.) the corresponding detector partial count rates for solution (black) and Iodine (red) for 1 ps delay after radial integration are given.*

*Laue diffraction techniques*

Hard x-ray pulses generated by an XFEL are expected to be about 1,000 times shorter and contain 100 times more photons than those generated by synchrotrons. Such pulse characteristics would provide an unprecedented opportunity to investigate protein function on the chemical timescale at near-atomic resolution. However, to effectively exploit x-ray pulses from an XFEL, there are numerous issues that require careful consideration.

**X-ray heating:** A single XFEL pulse delivered to a protein crystal would deposit sufficient energy to increase the temperature of the probed volume by about 10°C, if focused to a spot of 100 μm diameter. Since the energy is deposited in only 100 fs, a time far faster than that required for the crystal lattice to respond, the diffraction image would be minimally influenced by this T jump. On the other hand, how a crystal responds to this localised stress at longer times is not yet known. In any event, the cool-down period between successive x-ray pulses would have to be sufficient to dissipate this excess energy, and would probably restrict Laue experiments to repetition frequencies no higher than 3.3 Hz. The fact that the XFEL repetition frequency is limited to 10 Hz would not be a liability for Laue crystallography.

**Shot-by-shot x-ray pulse characterisation:** To take full advantage of ultrashort x-ray pulses, it is crucial that the laser be tightly synchronised with the XFEL pulse. The most advanced electronic phase-locked-loop cannot maintain synchronisation any better than a few hundred femtoseconds. Consequently, it is crucial to develop the ability to make single-shot measurements of the time difference so each diffraction image can be assigned an appropriate time stamp. That time stamp should be determined with sub-100 fs precision. Shot-to-shot intensity fluctuations of the primary beam can be tolerated, provided each diffraction pattern contains enough Bragg reflections to calculate a global scale factor. The number of reflections obtained with spontaneous undulator radiation is more than sufficient, but for XFEL radiation, the number of observed reflections will depend on sample mosaicity. Moreover, when using the SASE beam to record diffraction images, it will be crucial that the SASE spectrum either be reproducible on a shot-by-shot basis, or be measured on a shot-by-shot basis. (Changes in the spectral distribution lead to intensity changes of individual Bragg reflections that cannot be distinguished from structurally-induced changes.)

**X-ray photon energy:** The optimal x-ray energy for Laue crystallography would maximise the structural information achieved with the minimum amount of beam time. When the crystal lifetime is determined by x-ray radiation damage, the figure of merit is the number of photons detected, divided by the dose to the crystal. If laser radiation damage limits the crystal lifetime, the figure of merit is the number of photons detected, divided by the number of laser pulses required to collect the data. Using synchrotron radiation, it is the x-ray dose that limits the crystal lifetime, so the optimal x-ray energy is about 15 keV. When photolysing the protein crystal with 100 fs laser pulses, it is likely that the laser pulse will be more damaging to the crystal, so the optimal x-ray energy would be lower, where the diffraction efficiency is higher. Operating the XFEL at 12.4 keV is likely near the optimum for femtosecond time-resolved Laue crystallography.

**Time-resolution limitations due to pump-probe geometry:** Myoglobin crystals investigated at ESRF are optically very dense, and when photolysed near the peak of the Q-band absorption, the laser penetration depth is less than 100 microns. To address the severe mismatch between the x-ray and laser penetration depths, an orthogonal pump-probe geometry (see Figure 6.4.61) is adopted, in which the laser beam is focused from above and the x-ray beam probes the laser-illuminated edge of the crystal. This geometry requires precise positioning of the crystal surface at the intersection of the laser and x-ray pulses.

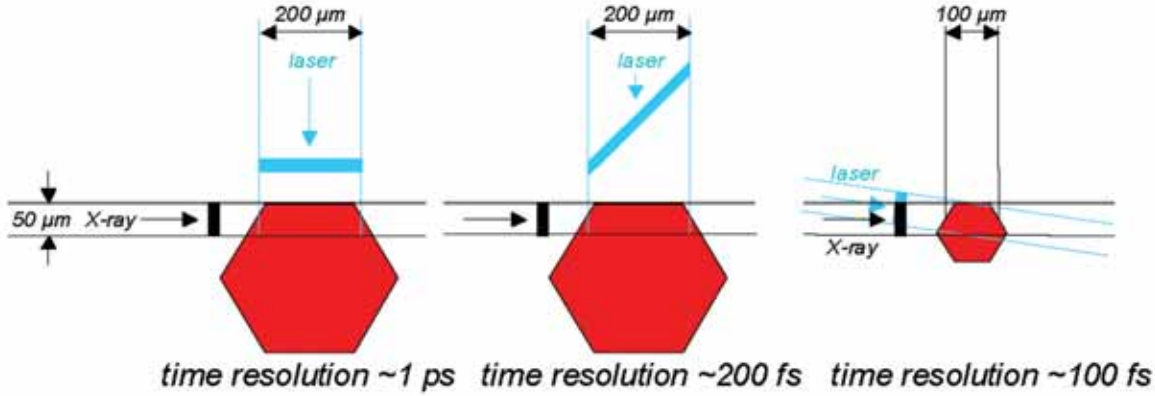


***Figure 6.4.61*** *Geometry considerations for the time resolution in different pump-probe geometries for a typically sized hexagonal myoglobin crystal. Orthogonal laser excitation significantly limits the time resolution, unless the wavefront of the laser beam is tilted by 45°. The best time resolution is obtained by collinear excitation limited by sample thickness due to velocity mismatch.*

The orthogonal pump-probe geometry optimises the spatial overlap between the pump and probe pulses, not their temporal overlap. For example, a 200 µm x-ray path length through a crystal photolysed from above would smear out the time resolution by nearly 700 fs. To mitigate this problem, it is possible to use dispersive or diffractive optics to incline the wave front of the laser beam so that the photons arrive at the surface of the crystal at the appropriate time. With this configuration, one still suffers smearing of the time resolution because the laser penetrates the crystal in a transverse dimension to the x-ray beam. If the vertical size of the x-ray beam was set to 50 µm using slits positioned near the sample, the time resolution could be improved to better than 200 fs. With these modifications, the orthogonal geometry can be employed with minimal sacrifice to the experimental time resolution.

**Spontaneous compared to XFEL radiation:** The spontaneous radiation provided at the European XFEL would be comparable in photon number to that achieved on ID09B at the ESRF. A bandwidth of ~1% is achieveable (see Section 5.3.) and if the electron bunch were in addition energy chirped, this bandwidth might even be broadened. With such a source, a complete set of data would require about 31 angular settings over a range of 60°. Because the spontaneous radiation is much more divergent than XFEL radiation, focusing optics would probably be needed to deliver the x-ray beam to the sample.

Using the monochromatic XFEL beam would require approximately 200 angular settings over a range of 60° (assuming 0.08% bandwidth and no mosaicity). The actual number of images required with XFEL radiation would depend on the degree of crystal mosaicity, with lower mosaicity requiring more images. With XFEL radiation, the dynamic range of the detector would have to be much higher than is currently available. Compared to synchrotron radiation, the XFEL radiation bandwidth is 30 times narrower and its photon flux is 100 times greater. Consequently, the brightness of the diffraction spots would be 3,000 times greater, and many spots would probably saturate the detector. If the XFEL

beam had to be attenuated to avoid saturation, the data collection efficiency in this mode would be compromised.

The spontaneous radiation approach to Laue data collection would be relatively straightforward. However, the XFEL radiation approach, if done well, has the potential to provide higher quality diffraction data. At this stage, we would prefer to develop both methodologies, and assess experimentally which approach achieves the best results.

**Detector characteristics:** To maximise the signal-to-noise ratio of the diffraction images, it would be desirable to have a large area detector that can be read with 16-bit resolution at the pump-probe repetition frequency. Larger is better because the intensity of diffuse scattering decreases as the square of the distance, but the intensity of the diffraction spot remains essentially constant (provided the spot dimensions are determined by the point-spread function of the detector, not the mosaic spread of the crystal).

### *6.4.6.2 Instrument requirements*

The experiments described above lead to requirements for an instrument for scientific applications using Femtosecond Diffraction Experiments (FDE). They concern the performance of the light source, the optical elements and the diagnostic equipment, the sample environment, and the detectors. The scientific cases presented request beamlines suitable for diffraction experiments at hard x-rays using 12.4 keV photon energy. Either intense XFEL radiation or spontaneously emitted synchrotron radiation is employed in these experiments and the incident bandwidth should be adapted to the sample system under investigation. Since the experiments do not require photon energy variation, the corresponding instruments should be located at the SASE 1 beamline for XFEL radiation and at the U 1 beamline for spontaneous radiation. A particular experiment (case V. in Section 6.4.6.1) has expressed an interest in using soft x-ray radiation for resonant experiments at the transition metal L-edges. This experiment requires use of the SASE 3 beamline and a reduced incident bandwidth of $\Delta E/E \sim 10^{-4}$. We propose that the XAS 1 instrument, described in Section 6.4.5.3, should provide the additional capability to carry out such studies. Due to the small signal changes to be observed the instruments require very good stabilisation and/or the tools to measure fluctuation of x-ray and visible laser parameters.

**Spectral radiation properties**

The gas phase and liquid experiments (Cases I. and II., Section 6.4.6.1) can perfectly accept the natural bandwidth of the XFEL or spontaneous radiation. Due to the small observable signal changes accuracy in the order of $10^{-4}$ is needed in mean energy or envelope of the energy distribution. Pulse-by-pulse measurement and single pulse data storage will ease this requirement slightly. However, high stabilisation is required for experiments on extremely dilute samples where the integration of scattering patterns is needed (e.g. gas phase molecules).

Laue diffraction experiments (Case III., Section 6.4.6.1) request photon energies around 12 keV and a bandwidth of 3% as ideal parameters. The large bandwidth can be achieved only by electron beam manipulation techniques like energy chirping, thus

affecting other beamlines. Instead one could use more angular settings to cover the full reciprocal space. The energy distribution of the unmonochromatised XFEL radiation needs to be monitored for single pulses since changes in the spectral distribution lead to intensity changes of individual Bragg reflections that cannot be distinguished from structurally-induced changes.

For single-crystal and crystalline material investigations (Cases IV.-VI., Section 6.4.6.1) typically, a reduced bandwidth of $10^{-4}$ is requested. The reduced bandwidth raises the resolution of the measurement and reduces energy dissipation in the samples. The larger natural bandwidth has the advantage, however, that photo-induced variations of the lattice parameter can be observed over a larger range. Its use, therefore, should be enabled by the instrument design.

**X-ray optics requirements**

No specific requests have been made in this domain. A beam size of 30-100 microns is required in many of the crystalline samples in order to match the sample size or the volume with visible laser penetration. In the case of fluids one may envisage the use of the full unfocused beam. However, large x-ray beam areas require large visible laser spots and significantly raise the requirements of the visible laser beam with respect to homogeneity and parallelism.

For x-ray pump-x-ray probe experiments, a beam-split-and-delay optics is requested. This optical element should allow the XFEL beam to be split into equal parts, e.g. for auto-correlation measurements, and also with a high ratio of ~9:1, e.g. for pump-probe experiments. A path length difference between the two split pulses of between 100 fs and a few 100 ps is required.

**Time domain requirements**

These experiments probe dynamics on the ultrafast timescale using pump-probe techniques. Pumping is usually achieved using an ultrafast visible laser. The synchronisation should be significantly better than the anticipated time resolution of ~100 fs. For the same reason the fluctuation of the pulse duration must be small compared to the 100 fs timescale. It is anticipated that a variety of pulse patterns from single pulses at less than 10 Hz repetition rate (Case III., Section 6.4.6.1) up to several hundreds of x-ray pulses per electron bunch train will be used. The 600 µs long pulse train offers, in principle, the opportunity to follow the structural evolution of the sample time-resolved over a relatively long period with a resolution of 200 ns. Such experiments may require logarithmic distribution of pulses and rely on samples not sensitive to x-ray damage.

**Photon diagnostics requirements**

The short- and long-term stability of the x-rays is of extreme importance for the quality of the experiments. The position stability of the emitted x-rays and even their spatial distribution should be monitored. Furthermore, all experiments will need diagnostic equipment to measure the photon flux on a pulse-to-pulse basis. In cases where monochromators are used, the measurement of the mean photon energy is not required

and spectral diagnostics should provide the content of higher harmonic radiation only. In many cases the samples are optically thin for x-rays and the transmitted radiation can be used for diagnostic purposes. All measurements must be available on a pulse-to-pulse basis.

### Sample manipulation and environment

For gas phase and liquid scattering the sample is refreshed at the repetition rate of the x-ray pulses and no particular difficulties are expected. For crystalline samples, techniques for refreshing the probed sample volume at the repetition rate of the x-ray pulses have to be foreseen. When limiting the repetition rate for pump-probe experiments this is most easily achieved by using sample movement. Another possibility is to steer x-ray and visible laser beams together over the sample (see Section 6.4.5.1). The latter method needs a development programme to provide the required overlap and accuracy.

As a sample environment vacuum, air or Helium can be used. Vacuum chambers, connected via differential pumping will be required for the gas phase measurements. They should be able to reach $10^{-4}$ mbar. Open liquid jets operated in a vacuum or under a Helium atmosphere allow significant reduction of background with respect to an air environment. For solids investigation, a four-axes diffractometer with the possibility to mount samples in air, under Helium pressure, or in vacuum is required. The load capacity of the diffractometer must accept mounting of pressure- or cryosystems.

### Detector requirements

The detector requirements for diffraction from disordered matter, e.g. gases or liquids and crystals, differs largely, leading to two different sets of parameters discussed in Section 6.5.4.1. Crucially important is the possibility of detecting a large number of x-ray photons per pixels and maintaining at the same time, the possibility of detecting very few photons. Simulations done for liquids indicate that $10^4$ photons can easily hit one detector element using present-day geometries and commercially available pixel sizes. For crystalline samples, even higher photon numbers need to be expected. For crystals, the possibility of studying diffuse scattering at the same time leads to the request for a very large dynamic range. Significant scattering can be observed at larger Q, respectively at large angles. Therefore, the detector systems should allow coverage of an angular range up to 60°.

### Visible laser requirements

Visible lasers will be applied in pump-probe experiments. A wavelength tunable system providing pulse durations in the order of 30 fs and pulse energy up to 1 mJ at 800 nm, will allow the experiments proposed in this area to be carried out. Using OPA schemes a wavelength range of ~200 to 1500 nm should be available at the instrument. Synchronisation to the x-ray beam of the order of the pulse duration or pulse-to-pulse measurements of the jitter is requested.

### *6.4.3.2 Realisation of the instrument*

From their requirements, the FDE experiments ask for two instruments at SASE 1 (FDE 1 – Hard XFEL radiation) and at U 1 (FDE 2 – Hard x-ray spontaneous radiation). For a description of the SASE 1 and U 1 beamlines, see Sections 6.2.4.1 and 6.2.4.4, respectively. Experiments discussed in Section 6.4.6.1 under Topics I.-VI. will be carried out at these instruments. Most of the requirements and proposed implementations are identical for the two instruments. The major difference is the enhanced flux for the FDE 1 instrument by a factor of $10^3$. For XFEL radiation, monochromatisation by use of crystal monochromators will be applied in the majority of experiments. However, some experiments will use the maximum available flux and therefore, omit monochromatisation. The SASE 1 beamline with its double-mirror double-crystal setup provides both kinds of radiation to the instruments. For FDE 2 using spontaneous radiation, no monochromatisation will be used since the experiments apply the full bandwidth. In order to collect the large angular cone a collimating optic, probably a refractive lens, needs to be installed as close as possible to the source in U 1.

Both instruments will require moderate focusing of the XFEL radiation to beam sizes in the order of 100 µm, achieved by using a focusing element inside the corresponding beamlines. Whereas, for the FDE 1 instrument a demagnification near unity can be applied, for FDE 2 one needs to take the collimating optics at ~100 m from the source into account.

**FDE 1: Hard XFEL radiation**

Since, for hard x-rays, no significant offset can be achieved for short distances, a deflecting mirror assembly inside the SASE 1 beamline tunnel, about 100 m upstream of the experimental hall, is used for horizontal deflection. The following elements belong to the FDE 1 instrument inside the experimental hall. They are depicted in the schematic layout of that instrument in Figure 6.4.62 and are described in Table 6.4.14.

The first part of the instrument includes specific optical elements for this instrument, most importantly the beam-splitter-and-delay unit. Next, defining apertures, a photon flux monitor and a differential pumping section come in front of the sample. The vacuum system of the beam transport can be intercepted here by a Beryllium window or can be connected to the sample vacuum chamber. The sample environment includes linear x-y-z movements (1µm repeatability and 0.25 µm resolution) and two angular degrees of freedom (1/1,000° repeatability, 1/4,000° resolution). Vertical scattering geometry is chosen for the diffractometer due to the horizontal polarisation of the radiation. Behind the chamber, a 2-D area detector with variable distance to the sample is mounted. On a circle segment, a 1-D detector is mounted covering a large angular range with high angular resolution and ~$10^4$ pixels. The forward direction is kept free and photon flux, spectral and time domain diagnostics follow. At the instrument a laser system is available, including the required diagnostics elements and an OPA system for provision of widely tunable visible laser radiation.

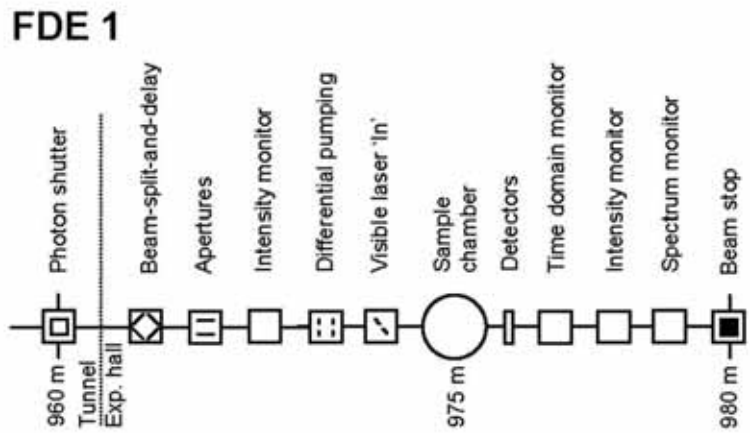


***Figure 6.4.62*** *Schematic layout of the FDE 1 instrument at the SASE 1 beamline. Distances are given in relation to the end of the undulator.*

| Item | Purpose | Specification |
|---|---|---|
| Beam-split-and-delay | Splitting into equal or unequal parts, delay 100 fs to 300 ps | High optical accuracy to maintain x-ray duration |
| Slits/apertures | Beam definition, beam halo cleaning | 0.25 µm accuracy, 1 µm repeatability |
| Intensity monitor | Measurement of incident photon flux | Transmissive (<5% absorption), single pulse measurement, relative accuracy $<10^{-3}$ |
| Differential pumping | Separation of beamline and instrument | |
| Sample chamber | Sample positioning and orientation<br>Vacuum capability for gas phase | x-y-z move (0.25/1 µm), two rotations (0.25/1 mdeg),<br>10 mbar |
| Detector | 2-D patterns for gases and liquids, 1-D pattern for powders and crystals | 2K×2K, 1 MHz,10K, 5 MHz |
| Intensity monitor | Measurement of transmitted photon flux | Transmissive (<5% absorption), single pulse measurement, relative accuracy $<10^{-3}$ |
| Time domain monitor | Measurements of x-ray arrival-time x-ray with respect to visible laser | |
| Spectrum monitor | Measurement of distribution | Single pulse measurement, relative accuracy $<10^{-3}$ |
| Alignment unit | Positioning and position verification | Permanently operating, Accuracy ~100 µm |
| Lead hutch | Radiation protection, temperature stabilisation, laser protection | 4×10×3.5 $m^3$ (W×L×H), ±0.5° thermal stability |
| Control hutch | Operation of the instrument | Working environment (noise, temperature, light) |

***Table 6.4.14*** *Elements and specifications of the FDE 1 instrument.*

### FDE 2: Hard x-ray spontaneous radiation

Since spontaneous radiation is less intense, a multilayer is proposed to deflect the beam horizontally whilst maintaining the large bandwidth at the same time. The multilayer is located about 60 m upstream of the experimental hall. The following elements belong to the FDE 2 instrument inside the experimental hall. They are depicted in the schematic layout of that instrument in Figure 6.4.63 and are described in Table 6.4.15. The instrument includes defining apertures and a photon flux monitor in front of the sample. The vacuum system of the beam transport is ended by a Beryllium window. The sample mounting includes linear x-y-z movements (1µm repeatability and 0.25 µm resolution) and two angular degrees of freedom (1/1,000° repeatability, 1/4,000° resolution). Samples can be investigated in an air or Helium environment. The sample mount supports high loads for measurements in different environments, e.g. cryogenic, high pressure or high temperature. Vertical scattering geometry is chosen for the diffractometer due to the horizontal polarisation of the radiation. Behind the sample mount a CCD 2-D area detector with variable distance to the sample is mounted and a fast 1-D detector on a circle segment to cover the full space angle. The forward direction is kept free and photon flux, spectral and time domain diagnostics follows. At the instrument a laser system is available, including the required diagnostics elements and an OPA system for provision of widely tunable visible laser radiation.

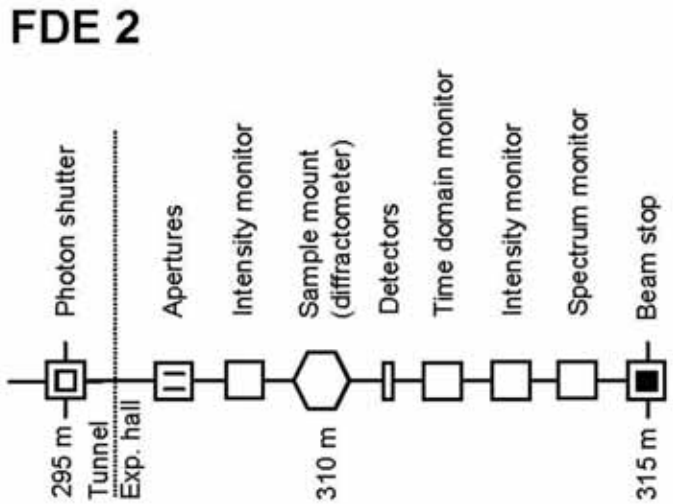


***Figure 6.4.63*** *Schematic layout of the FDE 2 instrument at the U 1 beamline. Distances are given with respect to the end of the undulator.*

| Item | Purpose | Specification |
|---|---|---|
| Slits/apertures | Beam definition, beam halo cleaning | 0.25 µm accuracy,1 µm repeatability |
| Intensity monitor | Measurement of incident photon flux | Transmissive (<5% absorption), single pulse measurement, relative accuracy $<10^{-3}$ |
| Differential pumping | Separation of beamline and instrument | |
| Sample mount | Diffractometer, air or Helium environment | x-y-z move (0.25/1 µm), two rotations (0.25/1 mdeg), 100 kg load |
| Detector | 2-D patterns<br>1-D pattern for powders and crystals | 2K×2K, 10-30Hz, e.g. CCD<br>10K, 5 MHz |
| Intensity monitor | Measurement of transmitted photon flux | Transmissive (<5% absorption), single pulse measurement, relative accuracy $<10^{-3}$ |
| Time domain monitor | Measurements of x-ray arrival-time x-ray with respect to visible laser | |
| Spectrum monitor | Measurement of distribution | Single pulse measurement, relative accuracy $<10^{-3}$ |
| Alignment unit | Positioning and position verification | Permanently operating, accuracy ~100 µm |
| Lead hutch | Radiation protection, temperature stabilisation, laser protection | 4×8×3.5 $m^3$ (W×L×H), ±1° thermal stability |
| Control hutch | Operation of the instrument | Working environment (noise, temperature, light) |

***Table 6.4.15*** *Elements and specifications of the FDE 2 instrument.*

## 6.4.7 Ultra-fast coherent diffraction imaging of single particles, clusters and biomolecules

### *6.4.7.1 Scientific case*

**Summary**

Theoretical studies and simulations predict that with a very short and very intense coherent x-ray pulse, a single diffraction pattern may be recorded from a large macromolecule, a virus, or a cell without the need for crystalline periodicity **[6-319 – 6-322]**. Measurement of the oversampled x-ray diffraction pattern permits phase retrieval and hence, structure determination **[6-323 – 6-330]**. Although individual samples will be destroyed by the very intense x-ray pulse, a three-dimensional data set could be assembled when copies of a reproducible sample are exposed to the beam one by one **[6-331]**. The challenges in carrying out such an experiment requires an interdisciplinary approach, drawing upon structural biology, atomic and plasma physics, mathematics, statistics, and XFEL physics. The potential for breakthrough science in this area is great with impact not only in the biological areas but in any other area of science and technology where structural information with very high spatial and temporal resolution is valuable.

## Experimental programme

Much of what we know about the detailed structure of biomolecules, including proteins and DNA and RNA, has come through the use of x-ray diffraction. Conventional synchrotron radiation has revolutionised this field in the past two decades, enabling study of larger and more complex systems at increasingly high levels of resolution and on smaller (often micron-sized) samples. The key to this great success has been the use of Bragg diffraction from the multiple copies of molecules that are oriented and aligned in a single crystal. However, there are classes of proteins (as well as many other types of materials) that are difficult or impossible to crystallise, including membrane and many glycoproteins, for which a high resolution means of structure determination would be invaluable.

The development of XFELs promises to open up new areas in the life sciences by allowing diffraction imaging of virtually any macromolecule, protein complex, or virus without the need for crystallisation. The same technique can also be applied to study the structure of other nano-sized particles, for example, clusters. This technique, at present only simulated on a computer, represents a formidable scientific and technical challenge.

Before guiding the reader into a more detailed description of the experimental programme, we need to survey boundary conditions and the available parameter space within which these new developments are expected to take place.

## Background for ultra-fast imaging

The scientific case for the ultra-fast imaging of single particles, cluster, and biomolecules is based on published theoretical studies and simulations **[6-319 – 6-322, 6-332, 6-333]**, and is supported by recent experimental results (discussed below) from the first soft x-ray free-electron laser, the FLASH facility at DESY.

Diffraction imaging is elegant in its experimental simplicity: a coherent x-ray beam illuminates the sample and the far-field diffraction pattern of the object is recorded on an area detector. However, radiation damage significantly limits the resolution of conventional imaging experiments. Damage is caused by energy deposited into the sample by the probes used for imaging (photons, electrons, neutrons, etc.). Cooling can slow down sample deterioration, but it cannot eliminate damage-induced sample movement **during** conventional measurements **[6-334, 6-335, 6-380]**. Ultra-short x-ray pulses from XFELs offer the possibility to extend the conventional damage limits, and will allow the imaging of non-crystalline biological (and other) materials. For proteins, simulations based on MD **[6-319, 6-320, 6-336]**, hydrodynamic **[6-337]**, and plasma models **[6-322]** indicate that if very short (100 fs or less) and very intense x-ray pulses are available ($\geq 10^4$ photons/nm$^2$ on the sample), then a single scattering pattern could be recorded from a single protein molecule in the gas phase before radiation damage manifests itself and ultimately destroys the sample (see Figure 6.4.64).

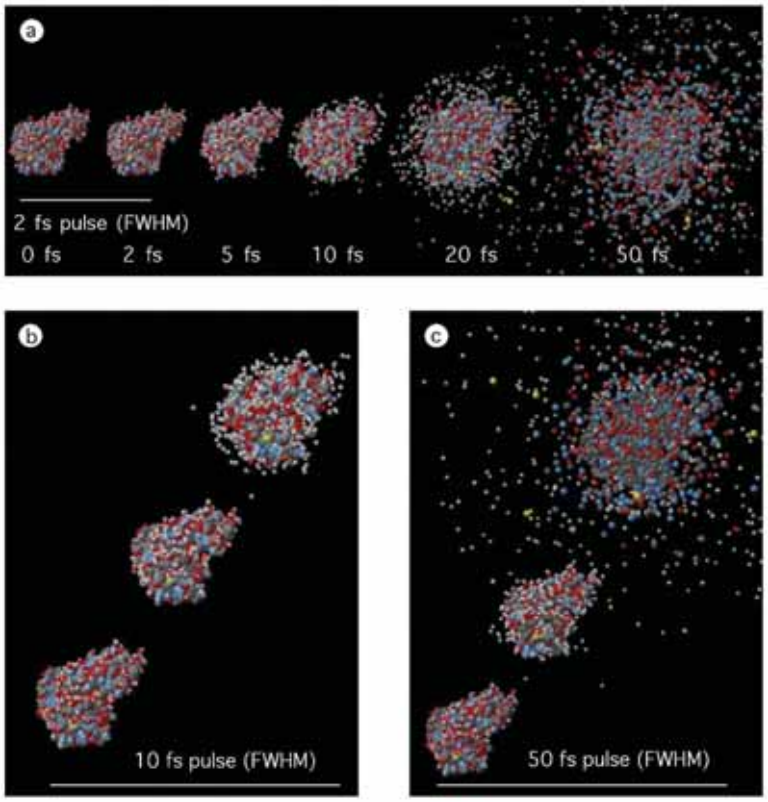


***Figure 6.4.64*** *MD simulation of radiation-induced Coulomb explosion of a small protein (lysozyme). White balls: H, Grey: C, Blue: N, Red: O, Yellow: S. Integrated x-ray intensity: $3\times10^{12}$ (12 keV) photons/100 nm diameter spot (corresponding to $3.8 \times 10^{8}$ photons/nm$^2$, or $3.8 \times 10^{6}$ photons/Å$^2$ on the sample) in all cases. (a) Protein exposed to a 2 fs FWHM x-ray pulse, and disintegration followed in time. The atomic positions in the first two structures (before and after the pulse) are practically identical at this pulse length due to an inertial delay in the explosion. (b) Lysozyme exposed to the same number of photons as in (a) but the pulse FWHM is now 10 fs. The images show the structure at the beginning, in the middle and near the end of the x-ray pulse. (c) Behaviour of the protein during a 50 fs FWHM x-ray pulse. It is also apparent from the figure that during the Coulomb explosion, Hydrogen ions and highly ionised sulphurs are the first to escape the immediate vicinity of the protein (at 12 keV, the photoelectric cross-section for Sulphur is about 50 times larger than that for Carbon). Based on* **[6-319]**.

Only a small fraction of the x-rays that fall on the sample will actually interact with the molecule. The “useful” photons are those that scatter elastically and produce the diffraction pattern. However, the dominant interaction is K-shell photoionisation of the atoms in the molecule, which leads to damage. Photoionisation releases an electron with energy close to the incident photon energy (around 12 keV for 0.1 nm radiation). Several femtoseconds later, the K-shell holes of the non-Hydrogenic atoms (C, N, O, etc.) decay, mainly by emitting Auger electrons with relatively low energies 250 – 500 eV. In biologically relevant elements (C, N, O, S, P), a single absorbed x-ray photon leads to more than a single ionisation event in this way. The photoelectrons and the Auger electrons have different energies, and are released at different times. Early on in an exposure, most of these electrons escape the molecule. The escaping electrons leave behind a net positive charge. This charge can grow large enough during an exposure for

the less energetic Auger electrons to become electrostatically trapped in the molecule. The more energetic photoelectrons become trapped later and only in larger molecules. Both escaping and trapped photoelectrons produce secondary electrons through collisional ionisation of atoms. The escaping photoelectrons produce, at most, a few secondaries, while trapped Auger and photoelectrons produce the majority of the secondaries. This has been modelled in detail for large (and cold) Carbon samples by Ziaja et al. **[6-338 – 6-341]**, and for water clusters by Timneanu et al. **[6-342]**. Figure 6.4.64 illustrates conditions near the physical limits for imaging **[6-319]**. For the two shorter x-ray pulses only very small changes in the atomic positions have had time to develop during the exposure (Figures 6.4.64(a.) and (b.)) although most of the atoms in the sample became photoionised. The life-times of K-shell core holes in biologically relevant elements (C, O, N) is long (around 10 fs), and as a consequence, very little Auger emission takes place in the sample during exposures that are shorter than about 10 fs (discussed below).

Resolution in these diffraction experiments does not depend on sample quality in the same way as in conventional crystallography, but is a function of radiation intensity, pulse duration, wavelength, and the extent of ionisation and sample movement during the exposure **[6-319 – 6-322, 6-336]**.

There is an additional component that will influence the final resolution of a 3-D diffraction data set. Each particle (macromolecule) is exposed to the beam only once, and disintegrates at the end of this process. The diffraction pattern, so recorded, encodes a two-dimensional projection image of the sample (and this may provide sufficient information for some applications). Three-dimensional imaging requires more than one view from the sample. In addition, the signal-to-noise ratio of raw diffraction images will probably be insufficient for a high-resolution reconstruction, and it will be necessary to obtain a redundant data set so that averaging can enhance the signal. Note that one could extend the depth of view from a single exposure by various holographic techniques based on external or internal reference beams, but a full 3-D reconstruction will most likely require **reproducible samples** exposed to the beam one-by one, and in different orientations. A “reproducible sample” (e.g. purified proteins) may contain heterogeneities, different subgroups of sample, and distinct conformers of the molecule. How reproducible a “reproducible sample” is and how well we can distinguish between similar and dissimilar structures will affect resolution through a B-factor-like component.

Conventional “single molecule” electron cryo-microscopy **[6-343, 6-344]** faces similar challenges as those described here. The basic requirement for reconstruction and/or signal averaging from many diffraction images is the ability to tell whether two noisy diffraction patterns represent the same view of the sample or two different views **[6-331]**. With this knowledge, averaging techniques can be used to enhance the signal and extend the resolution in a redundant data set. A 3-D diffraction reconstruction from a number of different exposures and views can take various routes. Techniques from “single molecule” electron cryo-microscopy **[6-344]** can be adapted here for determining the relative orientation of the images and for merging a large number of noisy 2-D diffraction patterns.

In the next stage, phases are derived from the 3-D diffraction pattern. In principle, there is a direct way to determine the phases required for the conversion using an approach called “oversampling” (for a recent review see **[6-345]**), and this has now been used successfully in a number of experiments **[6-327 – 6-329, 6-346 – 6-348]**. Practical algorithms exist **[6-328]** that are very robust and allow *ab initio* reconstruction of 3-D structures.

There is a need for “containerless packaging” so that only the sample of interest is imaged. We will also need sensitive detection of diffraction patterns with noise levels less than a single photon per pixel (discussed below), and the development of advanced reconstruction algorithms for orienting **[6-331]**, averaging, and inverting the diffraction images into the real-space molecule **[6-328, 6-329]**.

**Photon-matter interactions on ultra-short timescales and at high x-ray intensities**

Energy absorption is a subject of interest in practically all applications of XFELs, from biological imaging to creating astrophysical conditions in the laboratory. Imaging of single particles and biomolecules is based on the use of extremely intense and extremely short x-ray pulses to limit radiation-induced changes **during** the exposure so that high quality structural data is collected before significant changes take place in the sample (Figure 6.4.64). Single molecule imaging experiments at XFELs represent the high-end of today’s high-energy density science. In a focused beam of an XFEL, more than 100 eV/atom will be deposited into the sample within a few femtoseconds, and this will turn the sample into a plasma at some point. The question is when and how?

Under extreme conditions in an intense photon field, electrons can be stripped rapidly from an atom. At optical frequencies, the corresponding high-field regime begins to occur at intensities of about $10^{14\text{-}15}$ W/cm$^2$, where some of the new atomic physics and plasma physics phenomena have been observed. At around $10^{18}$ W/cm$^2$, relativistic effects fully enter the dynamics of electrons in the optical frequency domain. The high-field regime in optical frequencies is well known but it is completely unexplored at x-ray frequencies (no experiments have so far been possible due to a lack of suitably intense x-ray sources). X-rays have three to four orders of magnitude higher frequencies than optical light, and as a consequence, the high-field limits for x-rays are expected to be much higher than those for the slower optical frequencies. Various estimates suggest that field ionisation becomes significant at around $10^{22\text{-}23}$ W/cm$^2$, and relativistic effects will dominate the picture at around $10^{26}$ W/cm$^2$. These numbers are very high compared to expected intensities of mildly focused pulses from an XFEL ($10^{16\text{-}17}$ W/cm$^2$). However, a highly focused x-ray beam (<100 nm focal spot) with more than $10^{12}$ photons in a pulse, and at pulse durations shorter than about 5 fs, will approach the high-field limits for x-rays. A quantum mechanical analysis of the electric field induced tunneling indicates that atoms may become stabilised against ionisation under these conditions in a high-frequency x-ray field **[6-349]**. There are no experimental data near this regime and expected stabilisation effects and other non-linear effects are not included in current damage models.

It is important to point out that other major components of the mechanism of damage formation are also different at optical and x-ray frequencies. At optical frequencies, outer shell processes dominate the ionisation of a sample; while at x-ray frequencies, inner shell processes take over (photoemission followed by Auger emission/x-ray fluorescence, shake-up and shake-off excitations, etc.). Inverse Bremsstrahlung absorption is significant at optical frequencies, while it is small at x-ray frequencies. These properties will affect the evolution of Coulomb explosions, and are responsible for differences in the heating of electrons, atoms and ions in the sample during (and after) a short exposure.

### A. Physics of damage formation with x-rays

At 12 keV x-ray energy (~0.1 nm wavelength), the photoelectric cross-section of Carbon is about 10 times higher than its elastic scattering cross-section, making the **photoelectric effect** the primary source of damage. During this process a photon is absorbed and an electron is ejected usually from a low-lying orbital of the atom (about 95% of the photoelectric events remove K-shell electrons from Carbon, Nitrogen, Oxygen and Sulphur), producing a hollow ion with an unstable electronic configuration. Relaxation is achieved through a higher shell electron falling into the vacant orbital. In heavy elements, this usually gives rise to x-ray fluorescence, while in light elements, the electron falling into the lower orbital is more likely to give up its energy to another electron, which is then ejected in the **Auger process**. Auger emission is predominant in light elements like Carbon, Nitrogen, Oxygen and Sulphur (99-95%), thus, most photoelectric events ultimately remove two electrons from these elements. These two electrons have **different energies**, and are released at **different times**. Relevant K-hole lifetimes can be determined from Auger line-widths, and are 11.1 fs (Carbon), 9.3 fs (Nitrogen), 6.6 fs (Oxygen) and 1.3 fs (Sulphur). Note that the chemical environment of an atom will influence Auger life times to some degree. **Shake-up and shake-off excitations** (multiple ionisation following inner shell ionisation, see, for example **[6-350]**), initial- and final-state configuration interaction and interference between different decay channels will modulate this picture. Here again, the chemical environment of an atom will influence shake-effects to some degree. The release of the unbound electron “competes” with Auger electrons. When the first electron velocity is low (at low x-ray energies), the slow electron can interact with the other (valence) electrons on its way out and exchange energy. If the energy of the first electron is above some threshold, the sudden approximation is valid, and in general terms, less shake-up will happen. We expect this to be the case with primary photoelectrons of about 12 keV energies, and expect only a small shake-up fraction (about 10%, **[6-350]**). **Inelastic scattering** represents a direct momentum transfer from an x-ray photon to an electron, so that the x-ray photon is scattered with an altered energy. If the energy taken up by a bound electron is greater than its shell binding energy, the atom will be ionised. The inelastic cross-section of Carbon, Nitrogen and Oxygen is around 3% of the corresponding photoelectric cross-sections, whereas the inelastic cross section of Hydrogen is much higher than its photoelectric cross-section. Electrons ejected from atoms during exposure propagate through the sample, and cause further ionisation by eliciting **secondary electron cascades**. The extent of ionisation through this mechanism will depend on the size of the sample. Photoelectrons released by x-rays of 0.1 nm wavelength are fast (66 nm/fs), and

they can escape from small samples early in an exposure. In contrast, Auger electrons are slow (9.5 nm/fs) for Carbon and it is likely that they will thermalise even in a small sample. A detailed description of secondary electron cascades initiated by an electron with impact energies between 0.1 and 10 keV has been published **[6-338 – 6-341]**. In **late phases** of an exposure, a significant fraction of the emitted electrons will not be able to escape the increased positive potential of the sample. **Trapped electrons** will increase the kinetic energy of the sample through **thermal equilibration**; while at the same time, they will also slow down the Coulomb explosion of the sample by **partially screening** the positively charged protein core (all plasmas start cold and dense and become hot later). These opposing effects are explicitly incorporated into the damage models of Bergh et al. **[6-322]**, Hau-Riege at al. **[6-337]**, and Jurek et al. **[6-336]**, and are balanced by simplifying assumptions in the model of Neutze at al. **[6-319]**. Finally, a **transient radiation hardening of the sample** can be expected **during very short exposures**. The dominant interaction of hard x-rays with atoms is through K-shell photoionisation. This process creates hollow ions with one or both of the K-electrons expelled from the atom. The probability of photoionisation by x-rays in hollow ions is expected to be smaller than in relaxed ions or intact atoms. This short-lived "ionisation-resistance" lasts until outer shell electrons fill the vacant K-hole(s), and one may, thus, expect increased stability during short exposures (≤10-20 fs).

### B. Modelling damage formation and sample dynamics

A number of damage models have been developed during the past few years **[6-319, 6-320, 6-322, 6-336 – 6-342, 6-350]**. Computer simulations using four different models are in general agreement with each other, and suggest that the structure of a molecule could be determined by judicious choice of FEL pulse length, intensity and wavelength before it is stripped by electrons, and is destroyed in a Coulomb explosion.

**The MD model of Neutze et al. [6-319]** describes x-ray induced damage stochastically based on the probability of a photoelectric or inelastic event. The force field incorporates Morse potentials for the description of chemical bonds, thereby enabling bonds with sufficiently high energy to break. For water, a simple point charge model was used and adapted in the same manner. The instantaneous probability of ionisation of atom $j$ at time $t$ is calculated as the product of its photoelectric cross section, and the time-dependent intensity of the x-ray pulse, $I(t)$. Auger emission is modeled as a stochastic exponential decay to reproduce appropriate K-hole lifetimes. The direction of photo-emission is distributed according to a random deviate which follows a Gaussian distribution. A recoil velocity for the ionised atom due to inelastic scattering or the emission of a photo- or Auger electron is calculated from energy and momentum conservation. For inelastically scattered photons, the angle of deflection is determined by a random deviate following a Rayleigh distribution. For each inelastic scattering event, the electron's recoil energy is calculated, and in cases when this is greater than the binding energy of the electron, ionisation is modelled (this approximation was deemed sufficient for light elements with weakly bound electrons). An inventory is kept of all electrons in the sample, and changes in the photoelectric, elastic and inelastic scattering cross-sections are computed for all atoms, hollow ions and relaxed ions in 50 attosecond periods during exposure.

**The hydrodynamic (HD) model of Hau-Riege et al. [6-337]** includes the trapping of photoelectrons but does not treat atomicity explicitly. This model can be applied to both very small and very large samples (millimetres) while MD models are limited to macromolecules because of computing costs. The basic assumption of the HD model is that the sample can be described by a liquid-like continuum of matter rather than considering individual atoms. This gives a simplified description of the average effects of x-ray material interaction and atomic motion, which then permits calculations even on very big samples. The model further assumes that the particle is spherically symmetric, reducing the mathematical model to **one dimension plus time**. The model assumes that the motion of the atoms within the molecule is solely in the radial direction. The electrons and the atoms are treated as separate, structureless, fluids that interact through the Coulomb force and ionisation processes. The short-range electron-electron interactions are treated as a hydrodynamic pressure, and the long-range electron-electron and electron-ion Coulomb interactions are determined from the continuous net charge of the electrons and ions. In this model, all forces act radially. The model further assumes that the trapped electrons are thermalised among themselves, and that they are inertia-free, so that they quickly relax to a force-free spatial equilibrium. Finally, the x-ray matter interaction, atomic ionisation processes, and energy of the trapped electrons are described by time-dependent rate equations. The model shows that at later phases in an exposure, trapped electrons quickly relax in energy and position to form a cloud around the positive ions, leaving a neutral core and a positively charged outer shell (similar to Debye shielding). It is this positively charged outer shell that peels off first, and the Coulomb explosion then “burns” from the outside towards the inside (similar behaviour can be observed in the other models). In the inner core, there is hardly any ion motion but the high electron temperature leads to ionisation and blurring of the electron density. It is this latter effect that requires short pulse lengths to overcome damage.

Two further models have been published recently to include electron-electron, electron-atom, and electron-ion interactions:

**MD with explicit electrons of Jurek et al. [6-336]** – an MD/Monte Carlo (MDMC) model. This model extends the GROMACS-based MD model of Neutze et al. **[6-319]** by including explicit electrons in the simulations. Numerical modelling is based on the non-relativistic classical equation of motion. Quantum processes are taken into account by the respective cross-sections. Just like the first MD model, this model also includes photon-electron, photon-atom, and photon-ion cross-sections in addition to a description of the atom-atom, atom-ion, ion-ion, interactions. The MDMC model extends this by explicitly treating electron-atom, electron-ion, and electron-electron interactions. The model gives very detailed information on the movement of all atoms and electrons in and around the sample. A disadvantage of the model is that it is extremely demanding on computing power, and this limits its use to small samples only (a couple of thousand atoms).

**MD with implicit electrons [6-322]** – a MD/continuum electron (MDCE) model. This model uses a plasma approximation for the description of electrons released and trapped in the sample, and extends the GROMACS-based model of Neutze et al. **[6-319]**

to include the effect of screening by free electrons through the inclusion of an electron gas. The electrons are approximated by a classical gas, and the electron distribution is calculated iteratively from the Poisson-Boltzmann equation. Simulations of water clusters reveal the details of the explosion dynamics, as well as the evolution of the free electron gas during the beam exposure. Inclusion of the electron gas in the model slows down the Coulomb explosion. Hydrogen atoms leave the sample faster than Oxygen atoms, leading to a double layer of positive ions. A considerable electron density is located between these two layers. The fact that protons leave much faster than the Oxygen means that the heavy part of the sample stays intact somewhat longer than the sample as a whole. A disadvantage of this model is its demand on computing power due to complex grid calculations when simulating larger samples.

While these models are significantly different from each other, they all come up with similar predictions.

### C. Calculated scattering patterns for single molecules and particles

Radiation damage causes changes to atomic scattering factors (mainly through ionisations) and also to atomic positions. The creation of a large number of positive charges in close proximity within the sample results in a rise in the electrostatic energy of the sample, which drives its eventual explosion (Figure 6.4.64). The degree of conversion of potential energy into kinetic energy during the x-ray exposure is inertia limited, and as a consequence, strongly depends on the duration of the pulse and on the forces that develop. During the 2 fs pulse in Figure 6.4.64(a.), there was insufficient time for the kinetic energy to grow appreciably. In contrast, by the completion of the 50 fs pulse (Figure 6.4.64(c.)), the kinetic energy of the sample had surpassed its potential energy, and the explosion of the sample was already well underway during the exposure.

The effect of ionisation and ionisation-induced sample movement on the diffraction pattern can be calculated exactly at any point along the simulated trajectories. For unpolarised x-rays, the mean number of elastically scattered photons $I(\mathbf{u},\Omega)$ from a molecule illuminated by a plane wave, to be detected by an idealised detector pixel of a projected solid angle $\Omega$ centred at a positional vector $\mathbf{u}$, is given by

$$I(\mathbf{u},\Omega) = 1/2(1+\cos^2 2\theta)\Omega r_e^2 \int_{-\infty}^{\infty} \mathrm{I}(t) \left| \sum_j f_j(t) \exp\{i\Delta\mathbf{k}(\mathbf{u})\cdot\mathbf{x}_j(t)\} \right|^2 dt \quad , \qquad 6.5)$$

where $r_e$ is the classical electron radius; $\mathrm{I}(t)$ is the intensity of the x-ray pulse; $f_j(t)$ is the atomic scattering factor for the $j^{th}$ atom as a function of time; $\mathbf{x}_j(t)$ is the position of this atom as a function of time; and $\Delta\mathbf{k}$ is the change in the wave vector of the x-ray photon when scattered through $2\theta$ radians towards the pixel centred at $\mathbf{u}$.

Radiation damage interferes with the atomic scattering factors $f_j(t)$ and the atomic positions $\mathbf{x}_j(t)$. Damage-induced changes in the scattering pattern, and the structural information, which can be recovered from the sample during an exposure can, thus, be quantified. Assessment of damage-induced changes in the diffraction pattern is based on the calculated differences between scattering from a sample that suffers radiation damage ($I_{real}$), and scattering from a hypothetical sample that suffers no radiation damage ($I_{ideal}$) over the same time period. The damage-induced error in the integrated

diffraction pattern can thus be described by a weighted average agreement factor ($R$) between the two patterns as defined below:

$$R = \sum_{u} \left| \frac{K^{-1}\sqrt{I_{real}{}^{(u)}} - \sqrt{I_{ideal}{}^{(u)}}}{\sum_{u'} \sqrt{I_{ideal}{}^{(u')}}} \right| \quad , \qquad K = \frac{\sum_{u} \sqrt{I_{real}{}^{(u)}}}{\sum_{u} \sqrt{I_{ideal}{}^{(u)}}} \quad . \tag{6.6}$$

$I_{\mathrm{real}}(\mathrm{u})$ is derived from the time-dependent atomic coordinates, $\mathbf{x}_{\mathrm{j}}(\mathrm{t})$, and scattering factors, $f_{\mathrm{j}}(\mathrm{t})$, of a sample exploding in the x-ray pulse, while $I_{\mathrm{ideal}}(\mathrm{u})$ is determined from a reference molecular dynamics simulation of an unexposed sample. $R$ provides information on the extent to which the elastically scattered radiation is perturbed by x-ray-induced damage and provides a direct assessment of data quality ($R$ = 0 is ideal, larger $R$ means larger errors). Scaling factor K describes the relative scattering power of the sample. Macromolecular crystal structures in the Protein Data Bank have crystallographic R-factors of about 20%. Many of the structures, especially those collected earlier on photographic film, represent data sets with merging R-factors in the 5% to 15% range. Taking the latter value as an arbitrary upper limit, we regard damage as acceptable if $R \leq 15\%$

### D. The landscape of damage tolerance

The four published damage models are fairly different in what they include and what they neglect in their description of atoms, ions, electrons and their interactions with an intense x-ray pulse, but all models arrive at surprisingly similar results on pulse, fluence, and wavelength requirements for diffraction imaging. Here, we pick one of these models **[6-319]** to illustrate the available phase-space for high-resolution imaging of single macromolecules. Figures 6.4.65 and 6.4.66 show the landscape of damage tolerance in a broad parameter space around the expected pulse parameters of XFELs. Figure 6.4.65 gives calculated R-values for a protein molecule (lysozyme, see also Figure 6.4.64) exposed to 12 keV x-rays. Damage-induced error is plotted as a function of pulse length and intensity. Figure 6.4.66 shows that data quality improves with increasing x-ray energies. This is due to a favourable change with wavelength of the ratios of elastic, inelastic and photoelectric cross-sections in biologically relevant elements. Figure 6.4.67 illustrates the calculated scattering intensities for a large macromolecule, Rubisco **[6-351]**, at various points along the grey contour line (R = 15%) of Figure 6.4.65.

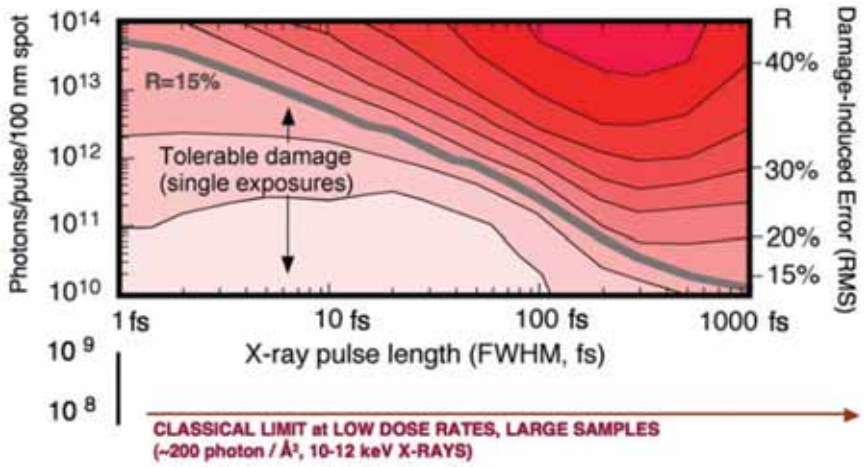


***Figure 6.4.65*** *The landscape of damage tolerance as a function of pulse length and intensity. The figure shows contour plots of the expected damage-induced errors (R) in integrated diffraction patterns as a function of pulse duration and photon intensity for 12 keV x-rays. The weighted average R-factor describes the extent to which the information content of elastically scattered x-rays is degraded due to radiation damage during the exposure (0% = no change in the structure, 67% = structure randomised). We regard damage as acceptable if R ≤ 15%, and this value is shown as a grey contour line in the figure.*

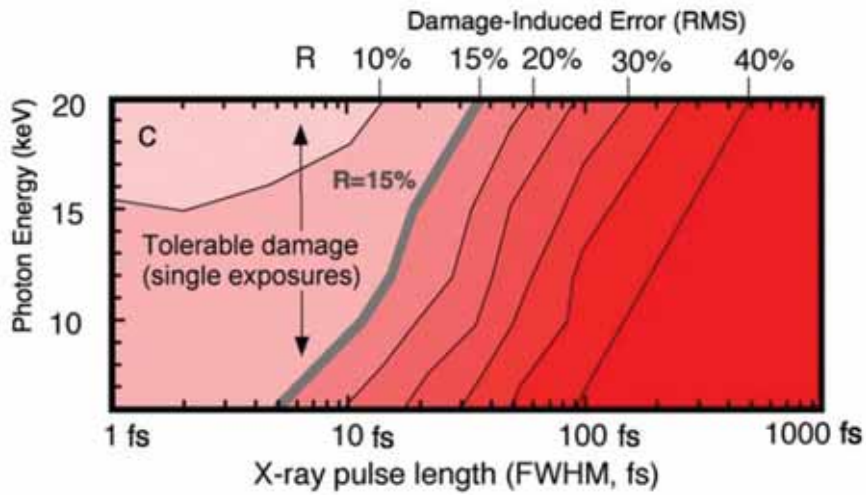


***Figure 6.4.66*** *The landscape of damage tolerance as a function of x-ray energy and pulse length. The figure shows contour plots of expected damage-induced errors (R) as a function of x-ray energy when the total number of elastic scattering events per Carbon atom is held constant ($I_{tot} = 1.33\times10^{12}$ for 6 keV; $1.85\times10^{12}$ for 8 keV; $2.36\times10^{12}$ for 10 keV; $3.0\times10^{12}$ for 12 keV; $3.96\times10^{12}$ for 15 keV; and $6.0\times10^{12}$ for 20 keV x-ray photons/100 nm diameter). The weighted average R-factor describes the extent to which the information content of elastically scattered x-rays is degraded due to radiation damage during the exposure. We regard damage as acceptable if R ≤ 15%, and this value is shown as a grey contour line in the figure.*

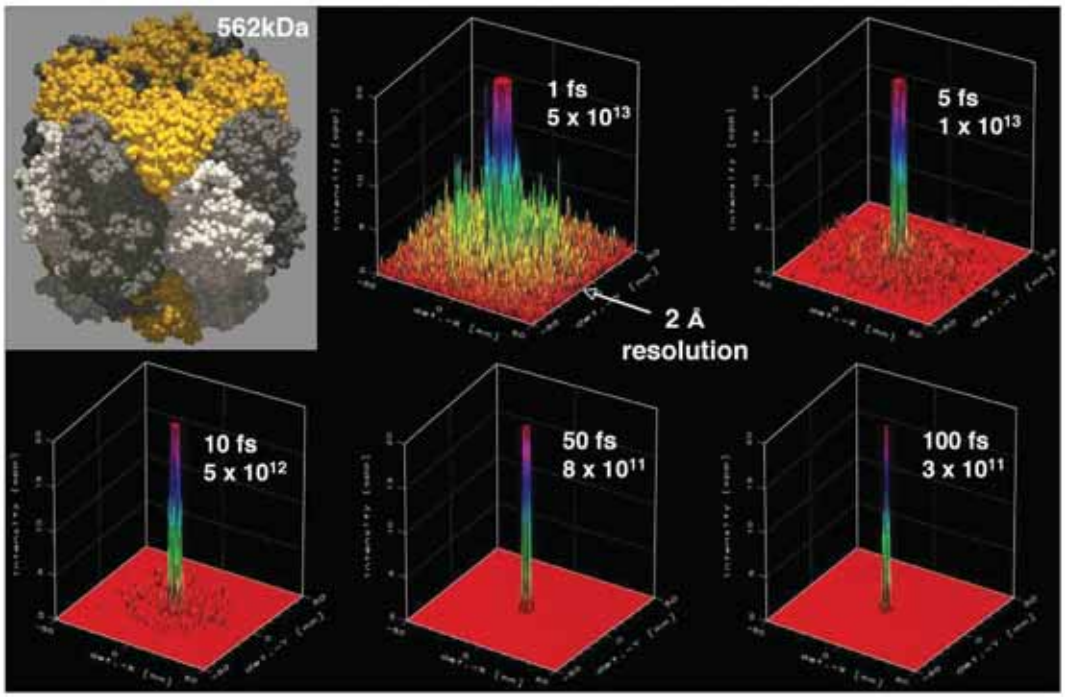


***Figure 6.4.67*** *Expected scattering patterns for a large macromolecule, Rubisco, with 15% damage-induced error. The figure shows calculated diffraction patterns with 1, 5, 10, 50 and 100 fs long pulses, at pulse intensities at the corresponding points along the grey contour line (R = 15%) of Figure 6.4.66.*

The data show that very short and very intense pulses may permit atomic resolution imaging of this macromolecule. During such short and intense pulses (1-10 fs), numerous K-holes may be present at any one time, reducing the photoelectric cross-sections of atoms in which they were produced, and thereby temporarily lowering the total number of primary ionisation events in the sample with x-rays. This effect can make the system radiation hardened to photoionisation during very short exposures. In addition, very short exposures can reduce Auger emission. If the pulse is shorter than the Auger decay time of the atom (i.e. shorter than around 10 fs for Carbon, Nitrogen, Oxygen), then significant Auger emission from these atoms will only happen after the passage of the x-ray pulse. This reduces damage during the exposure, as compared to longer pulses.

*Achievable resolution as a function of pulse parameters and object size*

A combination of results from the hydrodynamic continuum model **[6-337]** with the image classification model of Huldt et al. **[6-331]** allows one to map out the landscape of imaging resolution, molecule size and pulse requirements **[6-352]**. The results are shown in Figure 6.4.68, which show that it will be possible to image single molecules at very high resolutions with very short pulse durations (atomic resolution with pulses less than about 5-10 fs).

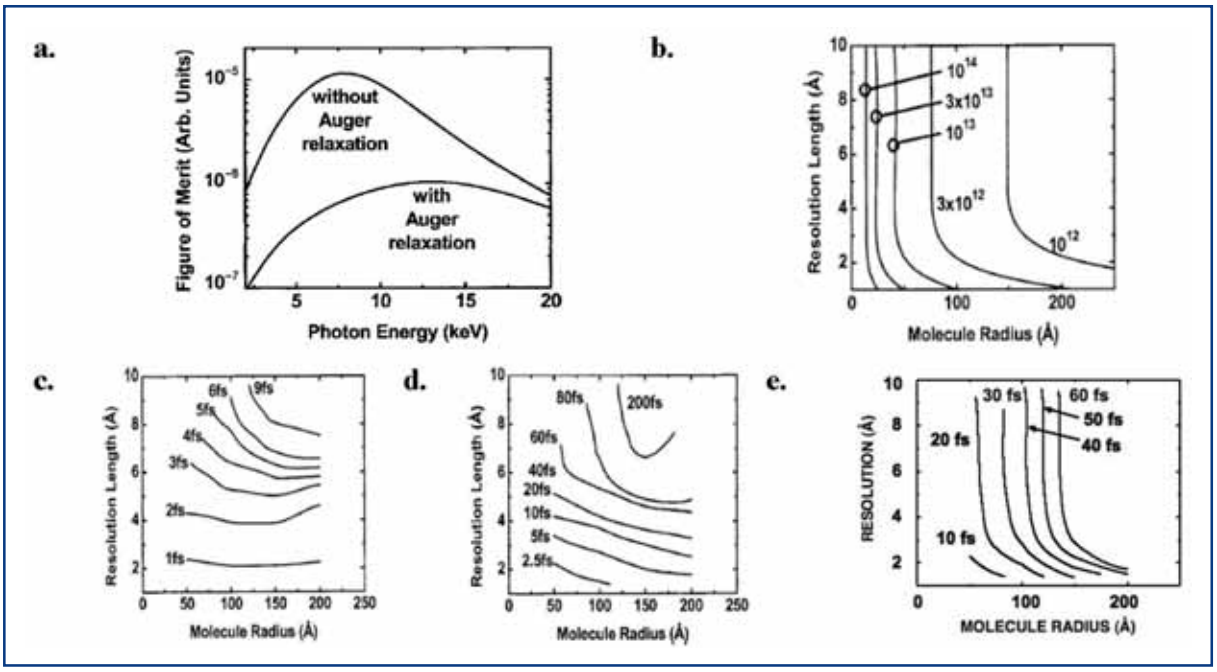


***Figure 6.4.68*** *Resolution compared to radius for different x-ray fluences: (a) Figure of merit (FOM) for imaging conditions as a function of photon energy; (b) x-ray fluence requirements to classify 2-D diffraction patterns of biological molecules according to their orientation with 90% certainty. The curves are labelled with the x-ray fluence in units of photons in a 100 nm spot; (c) plot of achievable resolution compared to molecule size for various pulse durations as limited by damage and classification. Atomic resolution imaging is achievable with pulse durations less than 5 fs and fluences greater than $10^{12}$ photons per 0.1 micron spot size; (d) pulse duration requirements are significantly relaxed for samples that give 10 times larger scattering signal (e.g. viruses or nanocrystals); (e) the use of a tamper and diffraction pattern repair can give similarly dramatic increases in pulse length for single particles.*

First, the optimal photon energy for diffraction imaging was estimated by maximising a FOM, defined as the ratio of signal minus noise to the radiation damage. As shown in Figure 6.4.68(a.), for pulses shorter than the Auger decay time (~10 fs for Carbon), the optimum photon energy is 8 keV, and for longer pulses it is 13 keV, although the peak FOM is much smaller.

Figure 6.4.68(b.) shows the required x-ray fluence versus image resolution length and particle radius, required to achieve a large enough diffraction signal to classify the patterns. Figure 6.4.68(c.) shows the pulse length requirements for x-ray imaging biological molecules with 12 keV photons, assuming no pre-orientation of the molecules. When the fluence requirements are relaxed by orienting molecules with laser fields, using nanocrystals containing only a small number of molecules, or helical molecules, or icosahedral virus particles, up to 10-20 times longer pulses can be tolerated, see Figure 6.4.68(d.).

The physical models of the interaction of a small particle with the XFEL beam have led to insights that offer additional ways to obtain high-resolution information with longer pulses. One such insight is that a tamper can be used to slow down the motion of atoms

during the interaction with the pulse. The tamper may be a small water or Helium drop that surrounds the molecule, and which has a total mass comparable to that of the molecule. Modern electrospray techniques can precisely control the amount of solvent left around the molecule and can be used to select an optimum layer thickness.

Models show that as the molecule becomes charged by the ejection of photoelectrons, the positive charge is confined to the surface, by the ejection of photoelectrons, with a thickness of a Debye length. This layer is ejected first from the particle, and the Coulomb explosion proceeds from the outside in. A rarefaction wave propagates in from the surface at the sound speed, and hence, the centre of the particle undergoes destruction later. The tamper is, hence, a sacrificial layer that preserves the structure of the molecule it contains. However, even with a tamper, the atoms at the centre of the particle quickly become ionised and are surrounded by hot free electrons. Since the x-rays scatter from electrons, the diffraction pattern is substantially modified by this effect. A strict figure of merit, such as used above, does not allow us to tolerate this effect. But since most of the charge is still localised around atoms, structural information is still present. It has been found **[6-353]** that the diffraction pattern can be “repaired” to overcome the effects of ionisation.

The repair strategy assumes that the stoichiometry of the molecule is known and that the ionisation occurs randomly and homogeneously. The method essentially filters the diffraction pattern to correct for the change in atomic scattering factors due to ionisation. The cross-terms, or the effect of different atoms being ionised differently is not compensated for, but it is found in simulations that the simple filtering has a dramatic effect and can correct for 90% of the damage. When coupled with the tamper, this leads to pulse durations about 10 times longer (i.e. on the order of 50 fs), as shown in Figure 6.4.68(e). Experiments with XFEL pulses are required to test these concepts.

**E. Finding image orientations, averaging, and building up a 3-D data set**

Three-dimensional diffraction imaging will be performed by collecting a large number of noisy coherent x-ray diffraction patterns from a supply of identical particles. One diffraction pattern is collected per particle and the particles have random and unknown orientations. Image reconstruction requires: (1) image orientation and assembly of a 3-D data set; (2) signal averaging to reduce the effects of photon shot noise, radiation damage and any other experimental noise source; and (3) phase retrieval. The methods of reconstructing a 3-D image from a number of noisy diffraction patterns of random and unknown orientation are inspired by methods employed in single-particle electron cryo-microscopy **[6-343, 6-344]**.

The greatest challenge is likely to lie in the signal-to-noise ratio of the diffraction images. The inherent power spectral density of the spatial distributions of matter lead to a rapid decrease in intensity with scattering angle (corresponding to increasing resolution). Molecule variability and incoherent scattering increase the noise, particularly at high scattering angles. At the same time, the incident number of photons should be kept to a minimum in order to reduce radiation damage. Therefore, it is crucial that the data set be redundant, and that we locate and average those redundancies to increase the signal-to-noise ratio.

Statistical studies have shown that a signal of less than one photon per pixel would be sufficient to correlate diffraction images of identical particles presenting the same view, assuming photon noise only **6-[331]**. Correlation-based methods to average and orient large numbers of noisy, randomly oriented real-space images have been successfully developed in the electron microscopy community **[6-343, 6-344]**. Diffraction patterns are first classified into classes of like-orientation so that they can be averaged to increase the signal relative to noise **[6-331]**.

The average signal per diffraction pattern at the highest resolution, required for classification, is found to be much less than one photon per pixel, and an incident fluence of $10^8$ ph/nm$^2$ is sufficient to achieve atomic resolution for particles greater than 15 nm radius **[6-331]**. Averaged diffraction patterns must be oriented in relation to each other in 3-D Fourier space, which may be achieved by the method of common lines (Figure 6.4.69), a technique widely used in electron microscopy, where the micrographs represent planar sections through the centre of the molecular transform. Diffraction images are different and represent spherical sections. Each pair of images will intersect with each other in an arc that also passes through the origin of the molecular transform (Figure 6.4.70).

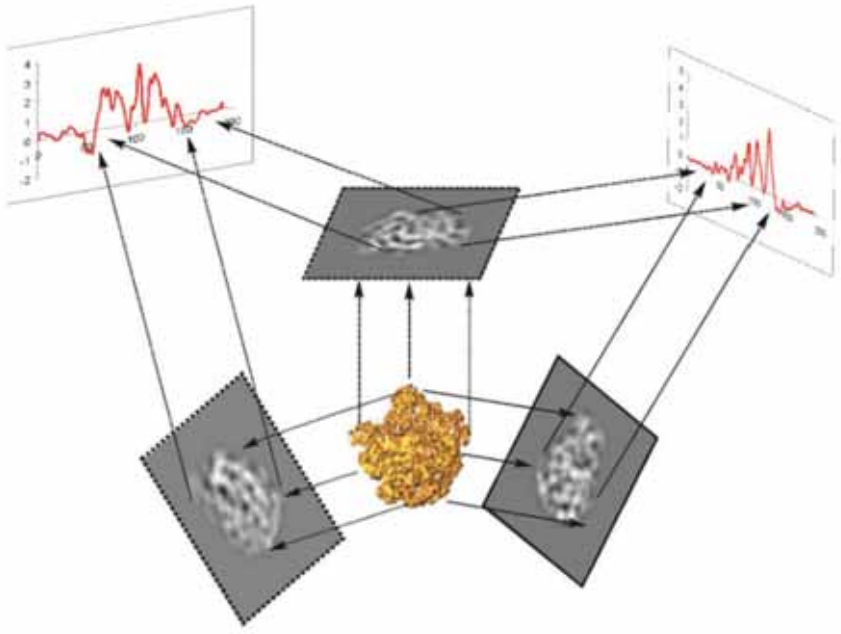

***Figure 6.4.69*** *Three-dimensional reconstruction in electron microscopy/tomography [26]. A 3-D data set can be assembled from individual images based on the common lines projection theorem. The common line is a hinge axis in tomography.*

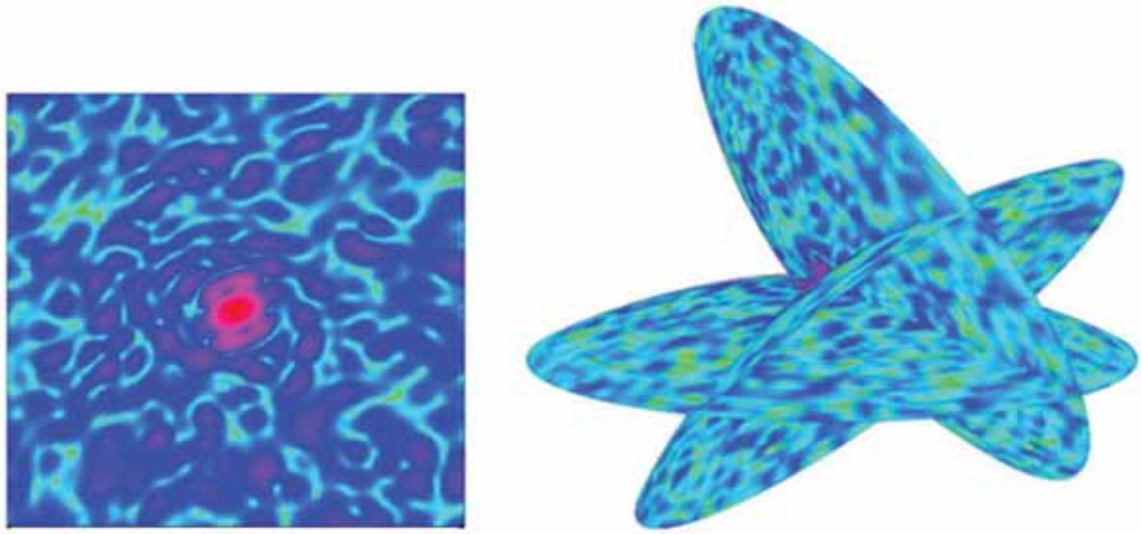

***Figure 6.4.70*** *Intersection of diffraction images along common arcs in diffraction space. The figure on the left shows a predicted diffraction image for lysozyme. The figure on the right shows three different diffraction images of lysozyme intersecting along common arcs in diffraction space. Each arc gives a three-dimensional fix* **[6-331]**.

If the signal is strong enough for the line of intersection to be found in two averaged images, it will then be possible to establish the relative orientation of these images. We note that due to the curvature of the sections (especially at x-ray wavelengths), the common arc will provide a 3-D fix rather than a hinge-axis. Moreover, the centric symmetry of the modulus of the molecular transform ensures that we obtain two independent repeats of the common lines in the two images. This feature provides redundancy for determining sample orientation, and is unique to diffraction images (Figure 6.4.71).

### F. Laser alignment of molecules

As a further possibility, it may be feasible to record 3-D diffraction data sets of molecules using longer pulse durations and lower fluence by using a polarised laser to orient the molecule (or a number of molecules) and assist the data assembly. Diffraction data would be collected tomographically by rotating the polarisation of the laser once enough signal has been accommodated at a particular orientation. A linearly polarised AC laser field will induce a torque on a molecule that has an anisotropy in its polarisability (usually due to its non-spherical shape).

Without damping (as is the case of molecules in a vacuum) the molecule will oscillate with a period that depends on its moment of inertia, the polarisability anisotropy and laser intensity. This oscillation time is calculated to be 1 to 10 ns for small proteins to large complexes **[6-354]**. If the rise time of the intensity experienced by the passing molecule is sufficiently slower than the oscillation period, alignment will be induced adiabatically and the molecule will orient along the direction of the electric field vector without oscillating **[6-355]**.

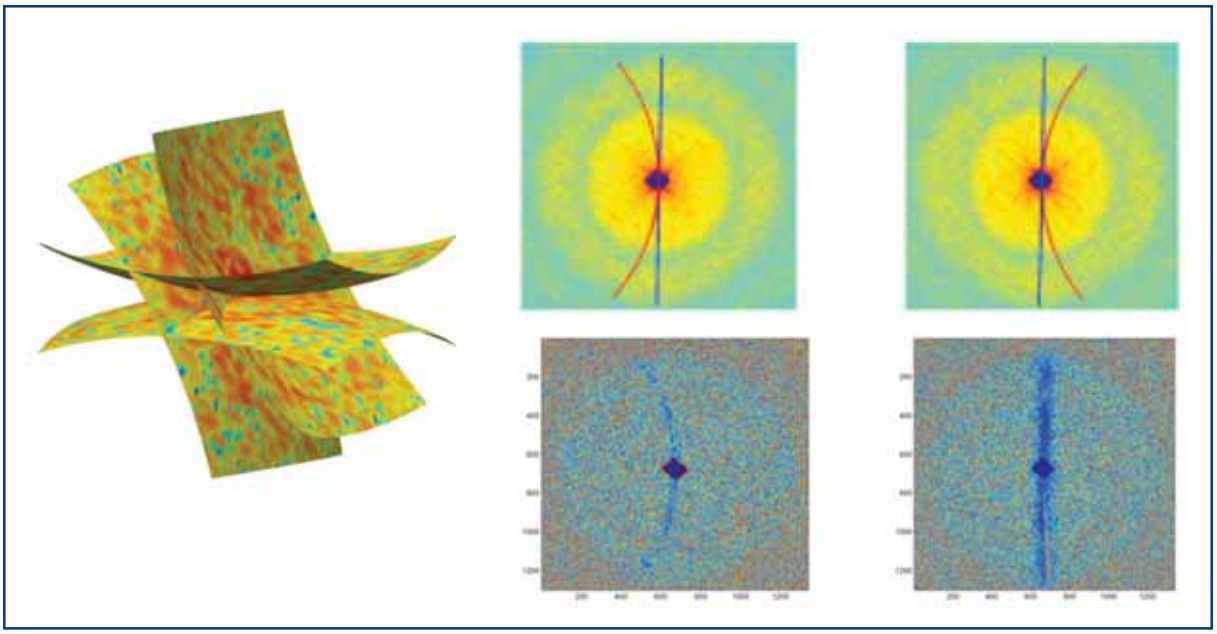

***Figure 6.4.71*** *Intersection of two Ewald spheres with their centrosymmetric opposites. Centrosymmetry gives an extra intersect as there are two common arcs of intersection in each diffraction pattern (upper row). The images in the middle show the expected arcs of intersections in two diffraction patterns from the experimental pyramid x-ray diffraction data set from Figure 6.4.68. Images in the bottom row show these very lines of intersections when the experimentally obtained patterns are subtracted from each other pair-wise* **[6-356]**.

The rise in intensity can be achieved simply by shaping the beam intensity (a Gaussian profile will suffice) with a length scale that depends on the particle velocity, to achieve rise times of about 100 ns. The degree of alignment depends on thermal fluctuations. The equipartition theorem applied to a harmonic oscillator results in the alignment error varying as the inverse of the square root of the laser power and molecule temperature.

The rotational temperature can be brought down to a few Kelvin by the supersonic expansion of the molecule into vacuum that occurs in the injection process, which should result in alignments of 1° to 10° for proteins such as lysozyme under adiabatic conditions **[6-354]**. This requires an intense laser field, on the order of $10^9$ W/cm$^2$, which should be in the near infrared, far from vibrational resonances in the molecule.

The interaction energy of the molecule with the laser beam is the same for a molecule aligned parallel or antiparallel to the field axis and only a DC electrostatic field can break this symmetry. Nevertheless, recent work has shown that an image can be reconstructed from a diffraction pattern that is an average of these two directions **[6-357]**. Alignment of molecules along all three axes (with a sense ambiguity in each direction) has been achieved with high fields and simple inorganic molecules using elliptically polarised laser fields **[6-356]**.

The achievable image resolution will be limited by the degree of alignment, and in general for a length of the molecule of $L$ and a standard deviation in the angle of orientation of $\Delta\theta$, the resolution will be about $L\,\Delta\theta/2$. For small proteins, such as lysozyme, which are only

*L* = 4.5 nm long, a misalignment of 10° gives a blurring of about 0.4 nm. More experimental studies are required to determine what degree of alignment is possible and the required laser parameters.

Larger particles require much less laser intensity due to their larger polarisabilities (tobacco mosaic virus particles can be aligned in water with static fields **[6-348]**). However, they must be aligned with far greater precision for a given image resolution, which is harder due to the rotational temperature. Thus, for large single particles, which will give large diffraction signals, laser alignment may be used **for reducing the number of classes needed to classify a pattern**. Laser alignment will provide a useful platform for developing techniques of single-particle diffraction imaging using the characteristics of pulses in the first stages of XFEL development, allowing us to achieve scientifically relevant results and to better validate models of the interaction of molecules with XFEL pulses.

### G. Methods for phasing

A number of methods exist for recovering phases for objects that have a finite size, or "support". These include oversampling of continuous molecular transforms **[6-323, 6-324, 6-326, 6-359, 6-360]**, holographic imaging methods **[6-361 – 6-364]**, holographic data evaluation methods **[6-362, 6-365]**, classical methods of crystallography, and techniques for phase extension from lower resolution electron/x-ray cryo-microscopy images.

The past few years have seen the development of robust algorithms in solving the phase problem through oversampling the diffraction pattern, and this seems to be a most promising technique for the future. The 3-D diffraction transform of a non-periodic particle is continuous. Only the diffraction amplitudes are sampled at discrete points by the pixellated detector and the process of classification.

The measured diffraction intensities are proportional to the modulus squared of the Fourier transform of the wave exiting the object. On their own, these diffraction intensities are insufficient to back-transform to form an image in real space. That inversion requires knowledge of both the diffraction intensity and phase. If the diffraction pattern intensities are sampled finely enough, it is possible to solve this problem for the diffraction pattern phases **[6-323, 6-324, 6-326, 6-359, 6-360]**.

The solution to this non-linear inversion problem is usually obtained iteratively by sequentially enforcing known constraints in reciprocal space and in real space. Specifically, in real space we assert that the image has zero scattering strength outside the area of the object's boundary (called its "support") **[6-324]**, whilst in reciprocal space, the squared modulus of the Fourier transform of the image must equal the measured diffraction intensities. Such algorithms have now been used successfully for image reconstruction in x-ray diffraction experiments **[6-326, 6-329, 6-330, 6-348]**. An example of a reconstructed 3-D image is shown in Figure 6.4.72.

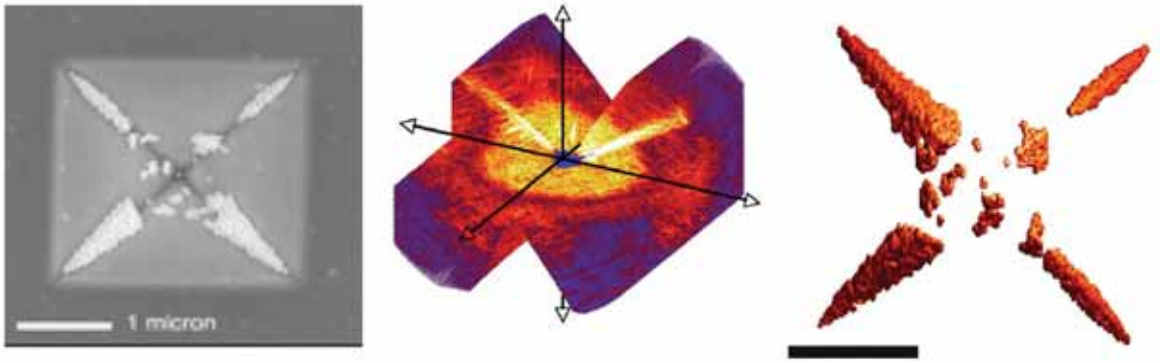


***Figure 6.4.72*** *Coherent diffraction imaging and image reconstruction* **[6-366]**. *Three-dimensional diffraction data (middle) recorded from a test object (left), consisting of 50-nm diameter Gold balls on a Silicon-Nitride pyramid-shaped membrane, at a wavelength of 1.6 nm, and a rendering of the ab initio 3-D image (right) reconstructed from the diffraction intensities to a resolution of 10 nm. The diffraction data were obtained by rotating the specimen in 1° increments from -70° to +70°, and then interpolated onto a $1{,}024^3$-element array. A quadrant of the diffraction data set has been removed for visualisation in the central rendering of the 3-D diffraction intensities. The Gold balls seen in the rendering of the 3-D reconstructed image on the right fill the inside edges of the Silicon-Nitride pyramid. The scale bar is 1 micron.*

The algorithms usually require that the support of the object be known *a priori*, and the closer the support to the actual object boundary, the better the reconstruction. The algorithm called SHRINKWRAP successively refines an estimate of the support from a current estimate of the image **[6-328, 6-329]**. This algorithm does not require the support to be known and is remarkably robust at finding the smallest image support that contains the majority of the image intensity.

Another programme that has been used successfully to phase experimental data is SPEDEN **[6-321]**. This uses a constrained conjugate gradient solver to find the amplitudes of 3-D Gaussian blobs whose calculated diffraction intensities match the measurements while also minimising cost functions based on constraints (including a low-resolution target, 2-D projections or known phases). The algorithm finds the optimal image that fits all the constraints and, since it only ever performs calculations from real to Fourier space, it never needs to interpolate data onto a regular grid.

However, as a local optimiser, it does not have as large a volume of convergence as the iterative transform algorithms and it may be used in XFEL imaging as a way to refine images produced by SHRINKWRAP and avoid artifacts due to missing data.

### Overview of the experimental programme

There is a general class of experiments that utilises the short time structure and the potential for very high intensities of the XFEL beam, and leads up to the exciting new regime in imaging outlined in the first sections.

It is immediately clear that small crystals, nanoclusters and 2-D crystals can already be studied at very high time resolution with low photon intensities from the beginning. In the following sections we will outline some exciting biological problems that become doable this way. Note that the saturation of the beam plays only a secondary role in these experiments, but will be important later.

It was emphasised in the introduction that damage by the incident radiation is the ultimate limit to the resolution of imaging techniques in biological molecules. It is ~ $2\times10^4$ photons/nm$^2$ at 10 keV incident photon energy. The primary damage is caused by the ~10 keV photoelectrons and the ~250 eV Auger electrons that are absorbed in the sample, causing secondary ionisation and, eventually, chemical damage. It is accepted wisdom that the damage in electron microscopy is about 1,000 times more benign with large samples than damage with x-rays.

This would imply that single particle imaging techniques would yield 10-fold lower resolution by x-ray scattering. There are, however, three mitigating factors in favour of x-rays: First, the scattering geometry of x-rays allows large angle data collection and the clean and simple geometry avoids distortions in the image. Second, if small particles can be used, the primary photoelectrons deposit only a small fraction of their energy and the damage should be ameliorated by ~20-40 fold. Third, time honoured techniques of attaching heavy atoms to clusters should increase the signal-to-noise ratio of single particle images.

In order to utilise the advantages outlined in the previous paragraph, two additional developments are needed: focusing of the beam to about 0.1 µm and the development of single particle injection techniques. The latter is well advanced in this partnership. We anticipate that very mildly ionised droplets will be injected into the focused beam just in time.

When mild focusing of the beam becomes available, e.g. the focusing of the projected $10^{12}$ photons in one pulse into a focal diameter of 0.5 µm, giving a flux of $2\times10^6$ photons/nm$^2$ at the focus, single particle images can be obtained using averaging techniques similar to those used in electron microscopy. This should open the door to virus structures, including their genomes, to the study of membrane proteins, to very high time resolution studies of other, known structures.

In summary, we will argue here that new and exciting biological problems will be open for investigation from the first day the beam becomes available. We foresee that our interim technical efforts in sample handling, attaching proteins to viruses and developing algorithms for single particle imaging will fully complement developments with the source. The experiments outlined represent major research lines far beyond the limits of currently available methodologies. We also hope that new research areas may emerge in a field as explosive as biology today by the time the XFEL becomes available. Shortening the pulse length would be a key improvement in all planned applications, including those described in the biological proposal. With shorter pulses, tighter focusing, very fast detectors and development of accurate injection techniques, biomolecular imaging should reach the extreme regime outlined in the theoretical part of this proposal.

### I. Nanocrystals

These are open periodic structures with sub-micron dimensions. All macroscopic crystals start as nanocrystals. X-ray lasers may offer completely new avenues for structural studies on nanocrystalline samples. No such studies are currently possible. When a crystal is small, the Bragg peaks are broadened and the intensity between the Bragg peaks is not negligible. Both the Bragg peaks and the intensity between the peaks carries structural information. The oversampled diffraction pattern visible between Bragg peaks can directly provide phase information.

### II. Two-dimensional crystals of macromolecules

Various estimates show that the number of different membrane proteins in various genomes is similar to the number of soluble proteins, yet there are only a small number of structures known today for integral membrane proteins as compared to well over 30,000 structures for soluble proteins. An understanding of the structure-function relationships in membrane proteins would make invaluable contributions to biochemistry, physiology and medicine, and would produce a substantial socio-economical impact (about 70% of all known drugs target membrane proteins).

Two-dimensional crystals of membrane proteins may be obtained from a number of membrane proteins, e.g. by epitaxial crystal growth methods. The intensity of the scattered x-rays, even from a small 2-D array, can be considerable with XFEL pulses. Integration of the diffraction rods requires images with different sample orientations to be recorded, and this could be achieved by merging data from several randomly oriented samples. This procedure could provide structural data on membrane proteins in bilayers.

### III. Closed nanoclusters for structural studies

In contrast to nanocrystals (which are small but open periodic structures with translational symmetry), the nanoclusters we refer to here are closed structures, which may be periodic (like oligomeric proteins or the capsids of virus particles) but have no translational symmetry. Such nanoclusters come in very well defined sizes or can be made to make up well defined sizes and geometries.

We are developing procedures for assembling proteins of choice into regular nanoclusters for subsequent structural studies. Methods are available for the specific attachment of target proteins onto the surface of regular templates, e.g. icosahedral virus capsids. These methods will be applied to structural studies on soluble and membrane proteins at FELs. Assembling protein molecules into nanoclusters will increase the intensity of scattered radiation from otherwise small proteins. We wish to use modified viruses to construct well defined nanoclusters of a number of different proteins, including membrane proteins.

Expected outcome: structures for “uncrystallisable” proteins attached to the surface of regular templates.

### IV. Virus structures and the structure of viral genomes

No high-resolution structure is available for any genome today. Small spherical viruses are among the simplest replicating systems in biology, yet the packing of the nucleic acid inside the capsid, and the factors affecting viral assembly, stability and disassembly are still not understood. Only a superficial picture is available today on the packing of the genetic material in intact viruses. This is due to the fact that in most viruses, the outer protein shell obeys the space group symmetry, while the inner material does not.

As a consequence, the image of the otherwise tightly packed nucleic acid inside the virion is rotationally averaged over some angular range. From images collected, we propose reconstruction to recover the structure of the inner part (the genome) of the virus. Further experiments will focus on the assembly/disassembly of the virus.

Of particular interest are viruses that cannot be crystallised (e.g. human immunodeficiency virus, herpes simplex virus, and many others). X-ray studies on viral particles in the gas phase (or in vitreous ice) could open up ways to capture elusive intermediates within the "life cycle" of a virus. An understanding of the functional dynamics of viruses may offer a means of interferring with infection. Experiments will capture dynamic events, e.g. steps in the assembly and disassembly of the virus, and studies on key initial steps in a viral infection.

### V. Structural studies on single protein molecules

The need for crystals for high-resolution structural studies is a serious limitation today. Currently, this excludes a very large proportion (>60%) of proteins from detailed structural determination, and hinders progress in the area of structural genomics. Structures accessible today for analysis do not represent a random selection of proteins, and knowledge gained on "crystallisable" structures may not automatically translate into knowledge about "non-crystallisable" structures.

When sufficiently short pulses and a reasonable high pulse intensity become available in the focus, studies on large single individual molecules (probably with molecular masses in excess of 100,000 dalton) may become routinely possible.

### VI. New horizons in time-resolved experiments

Biological function is a four-dimensional property. Time-resolved studies on structure, function and dynamics with x-ray lasers could cover catalysis, protein folding, nucleic acid folding, the assembly/disassembly of biomolecular complexes, viral uncoating, viral infections and so on. Such studies will first become possible on nanoclusters and nanocrystals as they require less stringent beam parameters than studies of single molecules. Later on, these experiments may be extended to individual biomolecules or cells.

*Photochemical reactions*

Marriage of femtosecond laser spectroscopy with femtosecond time-resolved structural studies will be possible.

*Diffusion triggering, stop-flow studies*

While certain key reactions in life are photochemical, most enzymes participate in diffusion-dominated processes with their reactants and partners. Time-resolved structural studies on diffusive processes in crystalline enzymes are difficult due to problems with mixing enzyme and reactant. Structural studies are only possible on intermediates which accumulate transiently in the crystal during a reaction. This requires a relatively fast binding followed by a relatively slow reaction. Due to the generally lower activity of crystalline enzymes, uniform catalysis can often be triggered by diffusing reagents (e.g. substrates) into crystals.

However, the speed of diffusion and ligand binding sets an upper limit to the speed of reactions which can be analysed this way. Past results show, that in an average-sized protein crystal, half saturation binding with small ligands can be reached within about a minute. One obvious possibility for lowering diffusion barriers is to reduce the sample size, get rid of the crystal, and use **stopped-flow** type mixing techniques for time-resolved experiments, where the sample can be sprayed into the beam after certain “aging” times following rapid mixing.

This can be done on purified proteins, nanoclusters or nanocrystalline slurries of enzymes instead of diffusing reactants into large single crystals. With very small samples, the vast majority of solution kinetic techniques and methodologies will suddenly become available for time-resolved structural investigations. We foresee that container-free sample handling methods based on spraying techniques, will open up new horizons here.

## VII. Atomic clusters and nanocrystals

Another field of application is the investigation of atomic clusters’ and nanocrystals’ structures. Research on these systems has become a very important and active field of interdisciplinary interest in recent years **[6-367]**. They allow the study of how macroscopic properties of matter are formed through the assembly of their microscopic units. The transition from the atom to the solid is not a smooth transition at all but rather interesting variations can occur. The size of the clusters is a new parameter, which can be used to control their properties, namely geometrical and electronic structure, magnetic properties and chemical reactivity. A thorough understanding of these properties is also of fundamental interest for applications of clusters since they hold great promise in, for example, microelectronics and photocatalysis. The precise knowledge of the cluster geometry, i.e. the positions of the individual atoms, is essential for a detailed understand of many open questions in cluster research. X-ray scattering as a direct imaging technique would be an ideal tool for structure determination, since most of the present techniques are indirect tools. The application of time-resolved structure determination for these systems will immediately lead to new scientific applications, e.g. in photocatalysis.

Compared to biomolecules the situation is somewhat simpler: Many of these nanometre-size particles have some crystalline order which results in a concentration and enhancement of scattered light into Bragg-type peaks. Furthermore, the heavy elements in clusters scatter much more efficiently than light elements which are the basis of

biomolecules. The prospects and limits are discussed in recent theoretical studies **[6-320, 6-336]**. With 10 fs-long pulses it is possible to obtain scattering patterns for 200 atoms C clusters with sufficient quality before notable structure deformation sets in. A particle density of $1\times10^7$ cluster ions/cm$^3$ is needed in order to get one ion per interaction volume, if a volume of $0.3\times0.3\times10^4$ µm$^3$ is assumed. This is somewhat higher than what can be obtained with radio frequency traps with a rather large volume **[6-368]**. Further, and similar to the case of biomolecules, imaging of clusters and nanocrystals is directly linked to issues of radiation damage, plasma formation and laser cluster interaction. Recent experiments with FLASH unveil the complicated and interesting many-body dynamics of clusters **[6-369, 6-371]** irradiated by intense femtosecond-pulses. Initial experiments with the FLASH FEL at DESY operating at 32 nm, demonstrated the feasibility of single shot scattering measurements of nanometre-size clusters **[6-371]**. Some of this work on clusters can be regarded as model studies of radiation damage in bulk materials and biomolecules.

### First results

*Demonstration of flash-diffraction imaging using a soft XFEL*

The first experimental verification of the principle of coherent flash-diffraction imaging has recently been performed at the FLASH facility **[6-330]**. The results show that an interpretable diffraction pattern can be obtained before the sample turns into plasma when exposed to an intense 25 fs-long photon pulse at 32 nm wavelength (Figure 6.4.73). In these experiments the beam was focused to a peak intensity of up to $10^{14}$ W/cm$^2$. We estimate that the absorbed energy density was approximately 20 eV/atom in the Silicon nitride and that the material **reached a temperature of about $6\times10^4$ K before vaporising**.

Significantly, the image obtained by phase retrieval and inversion of the diffraction pattern shows no discernible sign of damage, and the object can be reconstructed up to the resolution limit of the detector (62 nm with 32 nm photons). Damage occurs only after the pulse traverses the sample. A second exposure shows scattering from the hole that was created by the first pulse. These results provide the first experimental evidence for the basic principle of flash imaging, and this is the very technique we expect to lead to atomic resolution studies when hard XFELs become available.

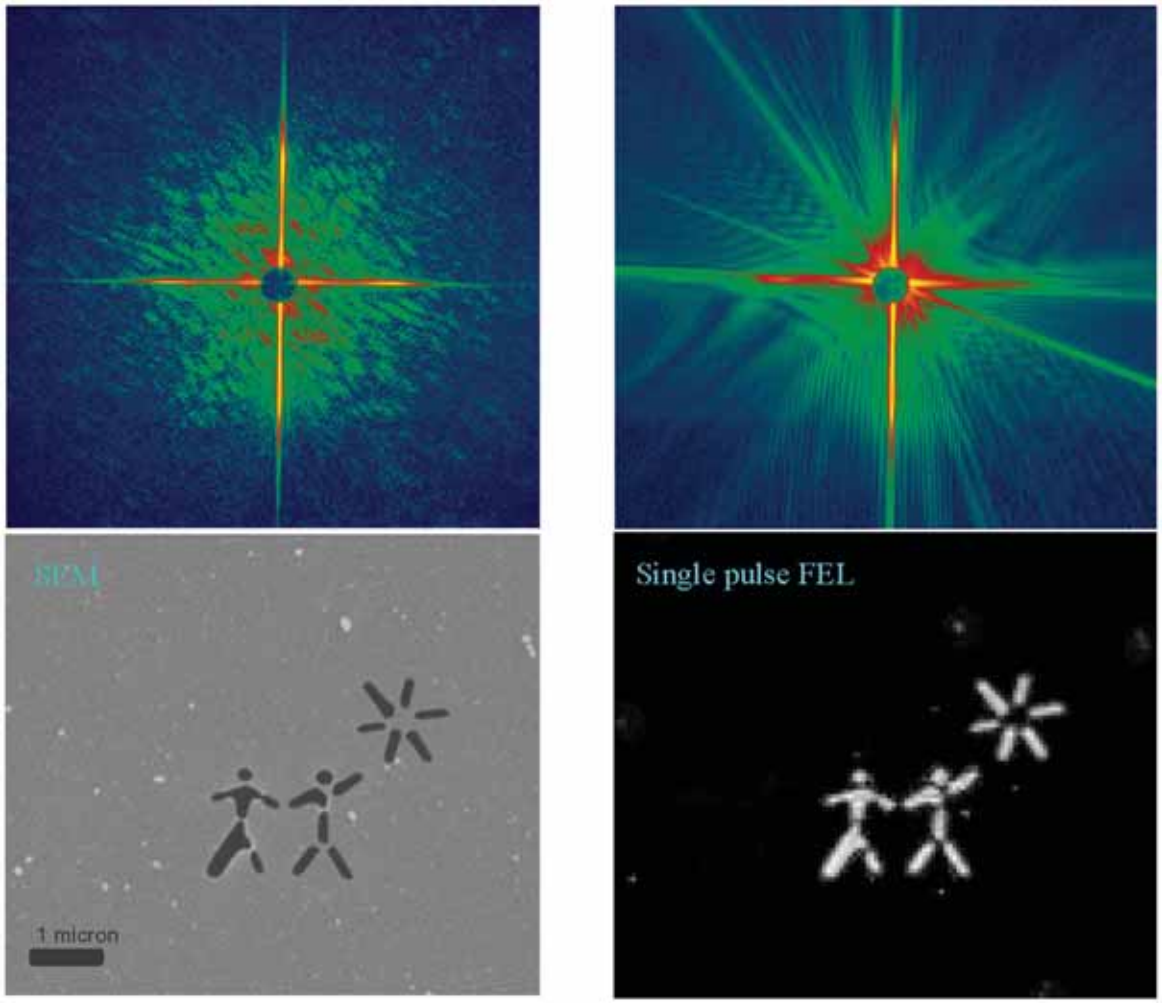


***Figure 6.4.73*** *Demonstration of single-pulse coherent diffraction imaging at 32 nm wavelength (February 2006). Top left: A diffraction pattern recorded with a single 25 fs-long FEL pulse at 32 nm wavelength from a test object placed in the 20 micron focus of BL2 at the FLASH facility of DESY (peak intensity: up to $10^{14}$ W/cm$^2$). We estimate that the absorbed energy density is approximately 20 eV/atom in the Silicon Nitride and that the material reached a temperature of about $6\times10^4$ K before vaporising. Top right: The diffraction pattern recorded on the second pulse some 20 seconds later, showing diffraction from the hole in the sample created by the first pulse. The sample was a pattern cut into a 20 nm thick Silicon Nitride membrane, shown at the bottom left from SEM. Bottom right: The image reconstructed to the resolution limit of the detector at 32 nm wavelength (corresponding to 62 nm resolution) from the single-shot diffraction pattern using the SHRINKWRAP phase retrieval algorithm. The algorithm only used the measured diffraction intensities and the knowledge that the diffraction pattern was over-sampled. We did not use the SEM image in the reconstruction.* **[6-330]**

*Ultra-fast transmittance and reflectance data from FLASH*

Other supporting data show that transmission and reflectance by solids remain **linear** up to $10^{14}$ W/cm$^2$ (the maximum that could be reached so far at the FLASH facility, absorbed energy in $SiO_2$: about 100 eV/atom), provided that this energy is deposited in the sample in a very short photon pulse (~30 femtoseconds at FLASH) **[6-372 – 6-374]**. The sample turns into a plasma, and it is destroyed **after** interaction with the intense photon pulse.

Similar studies show that the reflectivity of mirror surfaces (single component Silicon or Graphite, and multilayer mirrors made of Silicon and Carbon) remain constant over a very wide intensity range when interacting with a very short pulse from the soft XFEL of DESY. These mirrors work perfectly **once** near normal beam geometry even in a focused FEL pulse at $10^{14}$ W/cm$^2$ at 32 nm wavelength **[6-353, 6-372 – 6-374]**. Angularly resolved reflection data show that the period of the Si-C multilayer mirror changed as little as 0.3 nm **during the pulse [6-353]** but the surface was destroyed **after** interaction with the intense photon pulse (Figure 6.4.74), in line with our expectations.

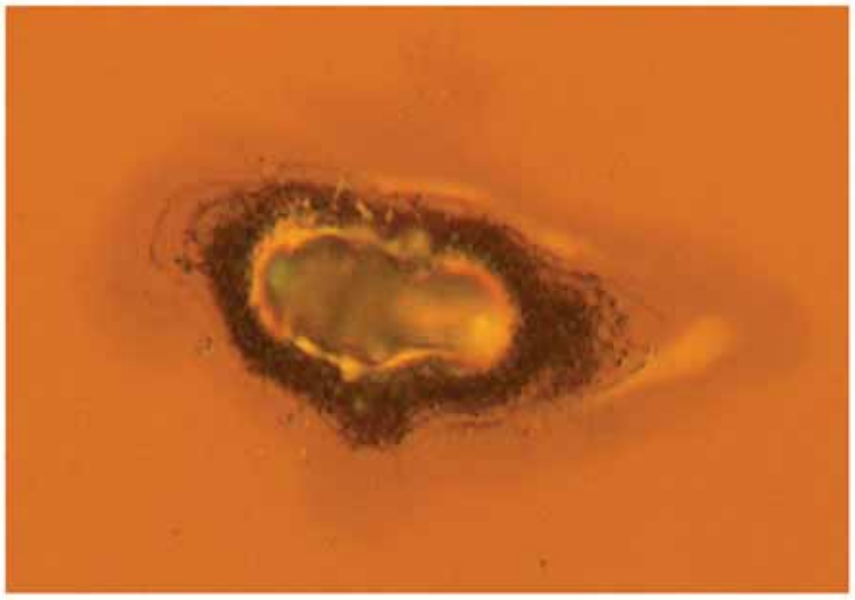

***Figure 6.4.74*** *Nomarski photograph of a Si-C multilayer mirror after interaction with an intense pulse of the FLASH soft x-ray laser at DESY. Wavelength: 32 nm, focal spot size: ~20 micrometer, energy density: ~$10^{14}$ W/cm$^2$. The damage seen here developed after interaction with the intense photon pulse* **[6-353, 6-369 – 6-371]**.

### *6.4.3.2 Instrument requirements*

The experiments described above lead to requirements for an instrument for scientific applications of imaging of Single Particle, clusters and Biomolecules (SPB). They concern the performance of the light source, the optical elements and the diagnostic equipment, the sample environment, and the detectors. The scientific cases presented required beamlines suitable for diffraction experiments at hard x-rays using 12.4 keV photon energy. Extremely intense XFEL radiation will be required in these experiments. Since the experiments do not require photon energy variation, the corresponding instruments should be located at the SASE 1 beamline for XFEL radiation.

The experiment consists of an apparatus to perform coherent x-ray diffraction imaging, and image reconstruction by phasing over-sampled diffraction patterns. The apparatus will include optics to focus the beam onto the sample to provide the necessary x-ray fluence together with pulse compression, as necessary. Samples will not survive the interaction with the focused XFEL beam, so we can consider three fundamental classes of experiment:

(i) 3-D diffraction imaging of reproducible structures;

(ii) 2-D imaging of single objects (like small living cells); and

(iii) 3-D diffraction imaging of single objects at low fluence.

Within these classes of experiment, we can consider variations, such as simultaneous (or time delayed) imaging of objects, imaging of reproducible structures in three-dimensions, imaging nanocrystals of different shapes, and imaging of two-dimensional (membrane protein) crystals. The third class listed above requires the unique coherence properties of the XFEL, and would be undertaken as a development step towards (ii) as well as providing learning that will be brought back to high-brightness third-generation sources.

Note that, while a single diffraction pattern as recorded in scheme (ii) is two-dimensional, this information exists on the Ewald sphere in reciprocal space **and indeed does contain information of spatial frequencies in the depth direction**. This is manifested by the ability to computationally focus through the object, by numerically propagating the complex-valued wavefield that is the retrieved image **[6-366]**. The depth resolution is simply the depth of field of the imaging system, given by $\lambda/NA^2$, where NA is the numerical aperture of the detector. For $\lambda$ = 0.15 nm, NA = 0.3, the depth resolution is 1.6 nm, compared with a transverse resolution of 0.5 nm.

### Spectral radiation properties

In most cases the experiments will exploit the natural bandwidth of XFEL radiation. In the case of large particles, i.e. 1 µm, the longitudinal coherence length needs to be increased to enable coherent diffraction at large Q values. Perfect crystal double-reflection fixed-exit monochromators providing a relative bandwidth of $0.5\text{-}1\times10^{-4}$ will be needed here. Such monochromators can be introduced in the beam path without interference with other beamline elements. Higher harmonic radiation at the level of $10^{-2}$, compared to fundamental radiation, is not expected to cause a problem. For particular experiments third harmonic radiation may be useful since its use strongly reduces sample damage.

### X-ray optics requirements

The beam from the XFEL will be focused to a variable spot diameter 0.1 to 10 microns (variable), depending on the overall sample size and desired x-ray fluence at the sample (some experiments can use larger diameter beams, including the unfocused beam). This requirement could be achieved by a Kirkpatrick-Baez mirror pair, or a grazing ellipsoidal mirror. No prefocusing optic would be used, and ideally, the number of beam-directing mirrors should be minimised. A given required spot size dictates a demagnification factor

of the optic, which forms a demagnified image of the source. The optic-to-focal spot distance is equal to the source-to-optic distance multiplied by the demagnification, and so larger working distances can be achieved by placing the experiment further from the source. This has the added advantage of allowing larger aperture optics (since the unfocused beam is bigger) and hence, reduced fluence on the optical surfaces. For the small foci the stability of beam pointing becomes critical and needs to be minimised. A stability <10% spot size is wishful for the experiments using single shot on gases or solid samples. For the tomography experiments a stability clearly better than 10% is required.

The pulse duration will eventually need to be shortened, which could be achieved either by source modifications or by x-ray pulse compression, using, for example, strained crystal diffraction **[6-375]** or asymmetric multilayer gratings. Our current estimates are that pulses shorter than 50 fs with more than $10^{11}$ photons/pulse are required for realistic single-particle imaging.

Other optical elements include apertures placed in the beam to block unwanted scatter from the beamline. These apertures will be larger than the direct beam. Also called guard slits, these have to be positioned and manufactured very carefully to prevent rather than contribute to the problem. Slits with “soft” edges can be made from wedges of perfect Silicon crystals (as one particular option). The innermost edge is transparent, slowly becoming opaque. This apodises the diffraction pattern by removing high-spatial frequency from the slit structure. With coherent beams, several slits can be placed so that their edges are positioned in the node of the weak scattering pattern formed by the upstream edge.

### Time domain requirements

The experiments will be performed in single shot operation mode, i.e. with single pulses and repetition rates of 10-50 Hz. The tomography experiments require conditions with very little sample damage (i.e. an attenuated beam) and could be performed using x-ray pulse repetition up to MHz employing pulse trains. Since no ultra fast pump-probe experiments are planned, an accuracy of x-ray arrival at the instrument in the order of a few picoseconds is completely sufficient.

### Photon diagnostics requirements

All experiments will require shot-to-shot diagnostics on intensity fluctuations, spectral profiles, pulse shapes and pulse lengths. The strong focusing eases many of the requirements of x-ray beam diagnostics. Most important are the flux and the spatial distribution at the focus. For reaching the smallest (100 nm) foci, sophisticated diagnostics for adjustment and performance verification is required. The samples are optically thin for x-rays and the transmitted radiation can be used for diagnostic purposes. All measurements must be feasible on a pulse-to-pulse basis.

### Sample manipulation and environment

Since the quantities of material in the sample under study will be minute, there should be very little other matter in the beam path, and therefore, the sample (and indeed the entire experimental apparatus) will be in ultra-high vacuum similar to conditions in conventional

electron microscopy. The interaction chamber will house the sample manipulation and injection hardware, instrumentation for various diagnostics, and an in-vacuum area detector system to record the diffraction images (Figure 6.4.75).

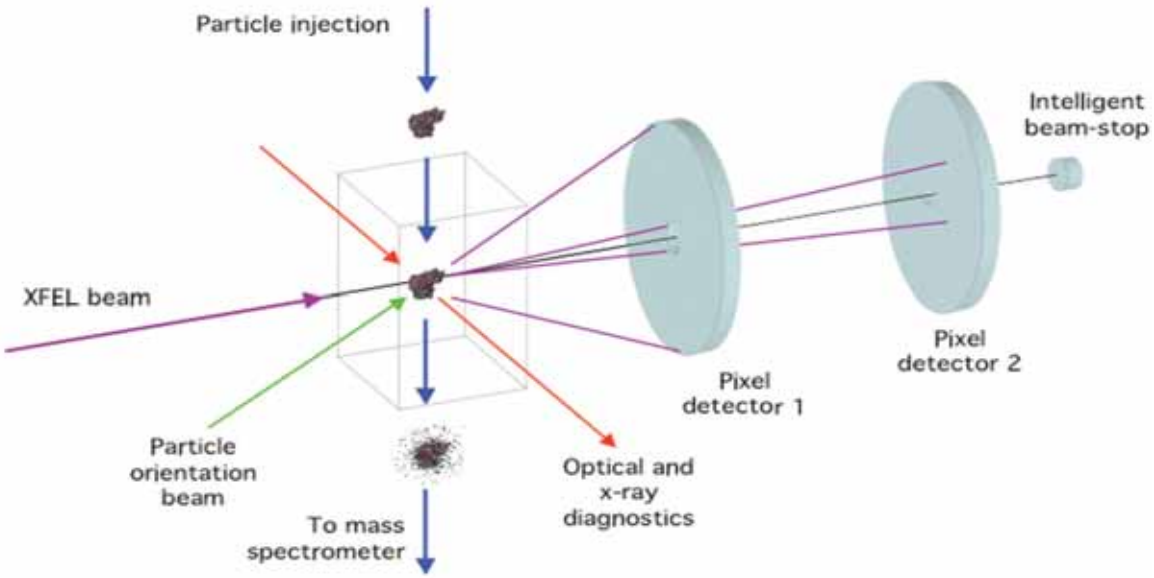


***Figure 6.4.75*** *Schematic diagram of the single-particle diffraction imaging experiment.*

We will use container-free methods based on spraying techniques to select and rapidly inject single hydrated molecules, nanoclusters of molecules, viruses and small living cells. Present sample injection and particle manipulation techniques will need to be improved significantly to achieve sufficient particle densities and injection precision. We will utilise electrospray ionisation (ESI) mass spectrometry and related ink-jet techniques as methods for introducing clusters, particles, viruses and cells with well controlled properties into the gas-phase **[6-376 – 6-380]**. We will explore techniques for trapping and aligning single particles in the focus, using optical, electrostatic, or electromagnetic methods. Sample diagnostics will be used to determine (a) if one or more of the particles were hit; (b) where the hits were along the beam path; and (c) how “good” were the individual hits. Such data can be obtained by measuring the UV-VIS light emission from the sample as it turns into a plasma, the electron and ion spectrum, and the fragmentation pattern at the end of the exposure. These data will be used in real time to veto bad shots.

In experiments on solid samples, the sample will be embedded into a thin layer of vitreous ice, positioned and manipulated in the beam using a cryogenic goniostat adopted from electron cryo-microscopy. Visual microscopy is used to manipulate the sample directly into the beam. The handling of these types of samples will be upgraded to be completely containerless by using a simple electrostatic system or special in-vacuum laser tweezers. This method would be ideal for diffraction imaging of membrane protein nanocrystals, but must be automated so that diffraction from thousands of individual crystals can be collected.

These two approaches require different detectors, and have different focusing requirements. Micron-sized objects will primarily be studied with the cryo-electromagnetic (EM) sample holder and experiments here will include studies on single cells, fibres (like Altzheimer fibres), organic and inorganic microstructures, micro- and nanocrystals, 2-D arrays, etc. Experiments using spraying techniques will be used to investigate nanometer-sized objects, including single virus particles, macromolecular complexes, and single biomolecules.

Initial experiments will use clouds of particles without stringent requirements, achievable with current methods, with and without alignment with a polarised laser. These will be improved upon, by first injecting short, concentrated bursts of particles into the beam focus area and relying on statistical positioning of individual particles. Such experiments require a focal spindle of about 5 mm length, shot-to-shot diagnostics to determine whether a particle was indeed hit by the x-ray beam and where the interaction happened along the focal spindle.

### Detector requirements

The diffraction pattern will be recorded on a pixelated detector subtending a solid angle dependent on the desired resolution, with a hole in the middle to avoid the direct beam. There must be sufficient pixels in the detector to oversample the diffraction pattern, which depends on the sample size and desired resolution, as described below. The scattering from the sample covers a large dynamic range: it is strong very close to the central core, and at high angles there will be much less than one photon per pixel. Since the technique relies upon classifying and averaging a large number of patterns, the read noise must be considerably less than the photon count per pixel averaged over these patterns. Estimates of the noise level and dynamic range are given below, after first listing the requirements of pixel count and sampling. For larger structures, e.g. virus particles and single cells, a finer sampling will be needed than for smaller objects (Figure 6.4.76).

The detector size should not be larger than approximately $100\times100$ mm$^2$, in order to reduce the beam path from sample to detector. At better vacuum levels, this distance could be increased without increasing the background. Other desired parameters are a read-out speed per frame matching the pulse rate of the x-ray laser; a dynamic range of $>10^6$ for the entire pattern (for large single particles such as viruses); a dynamic range locally of ~1,000 (a dynamic range of $10^{6\text{-}8}$ could be achievable with two detectors, each with smaller range where the response of the second detector measuring the strong forward scattering component is reduced by appropriate means). Diffraction data may be supplemented by a lower-resolution image of the sample obtained with a **zone plate** or a **wave-front sensor** as it could prove valuable in enhancing the robustness of the oversampling phasing algorithms.

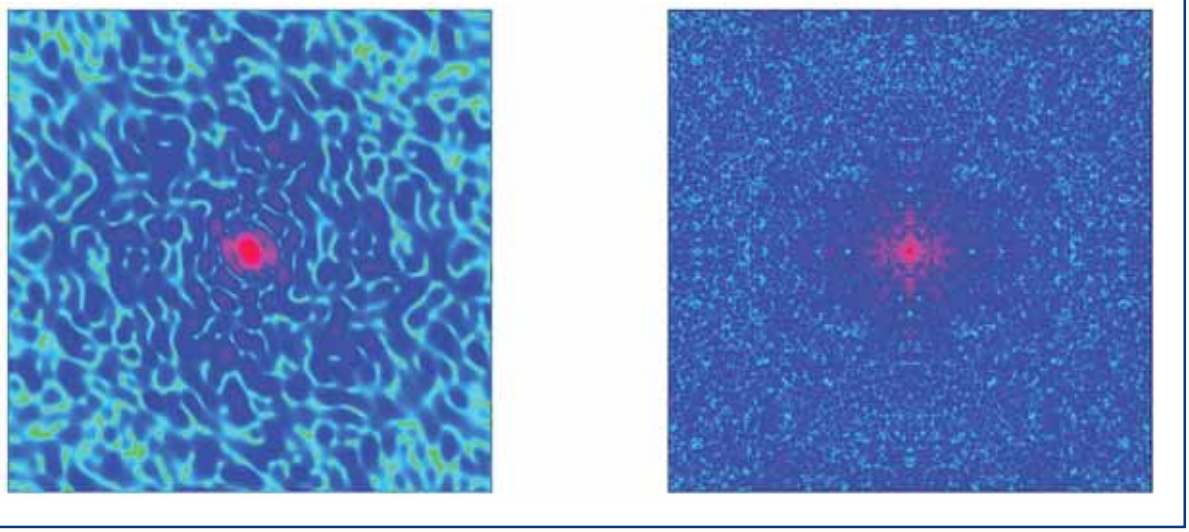

***Figure 6.4.76*** *Planar section through the centre of the molecular transform of a small protein molecule (lysozyme, left) and of a larger virus capsid (tomato bushy stunt virus, right) at similar maximal resolutions. The level of detail is significantly different in the two pictures, and detectors should be able to resolve details in the patterns of even larger objects than a virus particle.*

*Pixel requirements*

The pixel requirements simply depend on the number of resolution elements to sample the object of a given size at a given resolution, as described in Huldt et al. **[6-331]**, for example. To record to a resolution $f_{max} = 1/d$ requires a maximum scattering angle $2\theta$ given by $\sin \theta = \lambda f_{max}/2$. For an object of finite extent of width $D$, its molecular transform (in reciprocal space) is band limited. The Nyquist sampling rate of the transform is $1/D$ in each dimension. To measure this transform to a resolution $1/d$, in one dimension, requires samples from $-1/d$ to $+1/d$ or $2D/d$ samples. In real space this corresponds to samples at intervals $\Delta x = d/2$, which is the largest sufficient interval to measure periods larger than $d$. The detector measures the diffraction intensities, which are the modulus squared of the molecular transform, or equivalently, the Fourier transform of the object's autocorrelation function. For an object of extent $D$ the extent of its autocorrelation is $2D$, which means that the diffraction intensities are band limited with a Nyquist rate of $1/(2D)$. The phase retrieval algorithms do not necessarily require sampling at this rate but experimental experience shows better results with higher sampling. Note that sampling at a higher rate than $1/(2D)$ does not add any information to the measurement, but may improve the signal-to-noise ratio of the measurement. However, pixelated detectors do not sample at points but integrate over the active area of the pixels. This corresponds to a Modulation Transfer Function (MTF) that may decrease to zero at spatial frequencies (at the detector) of period $2p$, where $p$ is the pixel width. The effect of the MTF is to apply an envelope to the reconstructed real-space image, which should be no less than 0.7 at the largest radial extent of the object. As such, the detector's MTF influences the required pixel count. The number of pixels along the width of the detector is given by $N = 2Ds/d$, where $s$ is a sampling ratio per dimension (relative to the molecular transform Nyquist

rate), with $s$ = 2 in the case of maximum required sampling (for which the 0.7 MTF level should occur for pixel frequencies no lower than 1/(4 $p$)).

We estimate the maximum requirement for number of pixels is $N$ = 2,000, which corresponds to a particle size of 100 nm at a resolution of 1/(0.3 nm) and a sampling ratio of $s$ = 3, or a particle size of 200 nm at the same resolution and a sampling ratio of $s$ = 1.5. The larger sampling would be required if the detector MTF at 1/(2 $p$) is about 50%. These are likely parameters for imaging nanoparticles, and for the imaging of arrays of biological particles. For the cow-pea mosaic virus (CPMV) test object described below, which has $D$ = 32 nm, we require $N$ = 450 pixels for $s$=2 and a resolution of 1/(0.3 nm). This reduced pixel count will be sufficient for most small biological samples, and a larger pixel count detector will be needed for larger objects (Figure 6.4.76).

Image reconstruction can be achieved with considerable missing data due to a "beamstop" or corresponding hole in the middle of the detector. However, the larger this region, the larger the uncertainty of various components of the image, and the less quantitative the image. If the central blank area covers no more than the central speckle, then the only missing data is essentially $\mathrm{F}_{000}$. The speckle size for an object of width $D$ is $1/D$ or $2s$ pixels in width. The dynamic range values given below were based on patterns with the central $2s \times 2s$ pixels excluded.

*Simulations*

Detector signals were computed for a test sample of a CPMV, with labelling of nanoclusters of Gold **[6-381]**. This may be an early test sample for LCLS and XFEL experiments. The atomic coordinates of the virus capsid (1NY7) were obtained from the EMBL-EBI Macromolecular Structure Database **[6-382]**. The capsid structure is hollow (since the DNA structure inside is unknown), and this was filled in with Carbon atoms in random locations and average density of 1.3 g/cm$^3$ (less mass than DNA). When the Gold labelling was applied, clusters were attached to the 65 symmetry sites (CYS 295) as described by Wang et al. **[6-380]**. Each Gold cluster was spherical with a diameter of 1.4 nm diameter, and contained 82 Gold atoms (density of 18.8 g/cm$^3$). The Gold increases the total scattered photons by less than 10%. The CPMV has a diameter of 32 nm, and a total molecular mass of 14.8 MDalton (13.7 MDalton without the Gold labelling). Larger sized samples have been simulated by arraying the CPMV structure in ordered and disordered groups of particles. The incident beam was modelled as a single-mode coherent Gaussian beam, with a waist diameter of 0.1 or 0.2 micron and a total flux of $10^{12}$ photons. The diffraction patterns were computed for a wavelength of 0.15 nm, with a programme that computes the scattered intensity from a collection of atoms illuminated by a focused single Gaussian mode, in the Born approximation (and no atom motion or ionisation):

$$I(\mathbf{k}_{out}) = \Omega r_e^2 I_o \left| \sum_j f_j(\mathbf{q}) u(\mathbf{x}_j) \exp\{i\mathbf{k}_{out} \cdot \mathbf{x}_j\} \right|^2 \qquad (6.7)$$

where $f_j$ is the structure factor for the $j^{\text{th}}$ atom, $r_e$ the electron radius, $\Omega$ the solid angle of a pixel, and an incident field described by Siegman **[6-383]**

$$u(\mathbf{x}) = u(\mathbf{r}; z) = \sqrt{\frac{2}{\pi}} \frac{1}{w(z)} \exp\{-ikz + i\psi(z)\} \exp\{-r^2/w^2(z)\} \exp\{-ikr^2/(2R(z))\} \quad (6.8)$$

with $w(z) = w_0 \sqrt{1 + (z/z_R)^2}$ ; $R(z) = z + z_R^2/z$ ; $\psi(z) = \tan^{-1}(z/z_R)$ (6.9)

The parameter $w_0$ is the waist radius (radius at which intensity is $1/e^2$), and $z_R = kw_0^2/2$ is the Rayleigh range. The length $R(z)$ is the radius of curvature of the wavefront at a distance $z$, along the propagation axis, from the waist. The wave-vector magnitude is defined as $k = 2\pi/\lambda$, and the momentum transfer $\mathbf{q}$ is given by $\mathbf{q} = \mathbf{k}_{out} - \mathbf{k}_{in}$ with:

$$\mathbf{k}_{in} = [\mathbf{x}_j, -R(z_j)]\, k/\sqrt{\mathbf{x}_j^2 + R^2(z_j)} \quad (6.10)$$

Note that $\int_0^\infty 2\pi r u^2(r; z) dr = 1$, and thus the parameter $I_0$ is the total number of photons in the beam. In the simulations the intensity $I$ is quantised and photon noise added (normally distributed with standard deviation $\sqrt{I}$).

*Signal*

Results of simulations are shown in Figure 6.4.77. For these calculations, the centre of the particle was always positioned in the centre of the beam, at the $z$ location of minimum waist ($z$ = 0). For the calculations shown here we used $I_0 = 10^{12}$ and $w_0$ = 0.1 μm (0.2 μm diameter waist) and $w_0$ = 0.05 μm (0.1 μm diameter waist). The calculations were carried out for an x-ray wavelength of 0.15 nm. The simulated array size was 422×422 pixels, with $s$ = 2, corresponding to a resolution of 1/(0.3 nm). Most of the pixel values are zero or one photon, and the maximum and total photon counts (excluding the central 4×4 pixels) were 1,530 and $7.3\times10^4$, respectively, for the 0.2 μm diameter waist and 5,540 and $3.0\times10^5$, respectively, for the 0.1 μm diameter waist.

Note that larger samples do not necessarily give larger signals; there are a fixed number of photons per pulse and samples larger than the beam will require a proportionally larger beam and hence, lower fluence. Larger signals will be achieved with thicker objects and objects of higher-*Z*, and as such, the experiments of nanoscale inorganic samples will give stronger signals. Larger signals will also be achieved with arrays (2-D or 3-D) of particles, due to coherent addition in the Bragg directions.

Similarly, the imaging of large objects at low resolution (e.g. single-shot imaging of micrometre-sized cells beyond the radiation damage limit) will produce larger photons per pixel due to the coherent addition, in the forward direction, of scattering from atoms within a single resolution voxel **[6-384]**. For the case of crystals and arrays of identical unit cells, the photon count will increase in the Bragg peaks by a factor $n^2$, where $n$ is equal to the total number of unit cells illuminated.

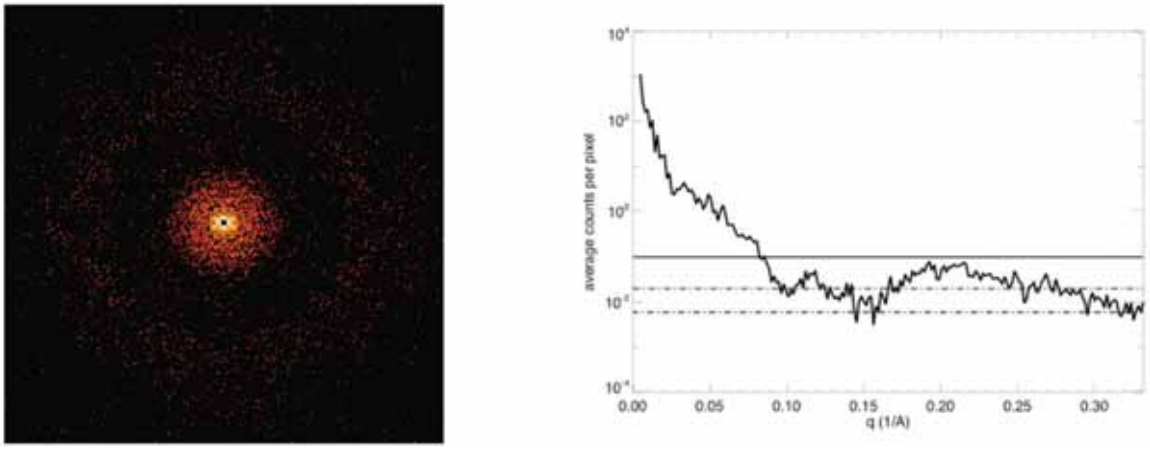


***Figure 6.4.77*** *Simulated diffraction data from the (CPMV test object, for a beam waist diameter of 0.2 μm. Total photon number in the incident beam was $10^{12}$. The array is 422×422 pixels, corresponding to s=2, and a resolution of 1/(0.3 nm). The central 4×4 pixels were blocked. Total integrated photons are $7.3\times10^4$. The intensities are displayed on a logarithmic greyscale. Away from the centre most pixels have one or no photons. The maximum photon count is 1,530. The plot shows the radial average of the photon counts. The solid line is at 0.1 counts, the minimum counts needed to classify* **[6-331]***, and the dotted lines denote the noise level for 10 and 100 averages, for a detector noise of 0.06.*

The signal between the Bragg peaks will only increase in proportion to $n$, but this signal can be built up by averaging, once classification has been achieved on the Bragg peaks. For a 2-D crystal with $n$ unit cells, if the beam size matches the object size then the incident fluence will be proportional to $1/n$ and the Bragg peaks will increase in photon count by $n$, not $n^2$. For the simulations we have run on 2-D and 3-D crystals of 5×5 and 5×5×5 unit cells, we typically see a factor <10 increase in photon count. In all these cases, the pattern is strongest near the zero frequency and locally (within a 10×10 pixel patch) the intensity changes by a factor of about 1,000.

*Noise*

Data sets will be assembled by classifying patterns into classes of like-orientation and averaging patterns within each class. Huldt et al. **[6-331]** showed that accurate classification could be performed with as little as 0.1 photon counts, on average, per pixel, at the highest resolution of the pattern. For the CPMV particle simulation, this means we can classify out to the full resolution of the simulation, of 1/(0.3 nm), for the case of a 0.1 μm diameter waist (Figure 6.4.78). This means that when we sum together ten diffraction patterns the accumulated noise must still be less than one photon. Choosing a noise level of 0.2 photon (SNR = 5, Rose criterion) in the ten-frame sum, the noise per pixel for each pattern should be no larger than $0.2/\sqrt{10} \sim 0.06$ photons per pixel.

Many of these requirements are in line with general directions currently driving the development of x-ray area detectors for synchrotrons and other experiments planned for the x-ray lasers. The detectors needed for our studies are relatively small, and that alleviates some of the difficulties in developing faster detectors for our studies.

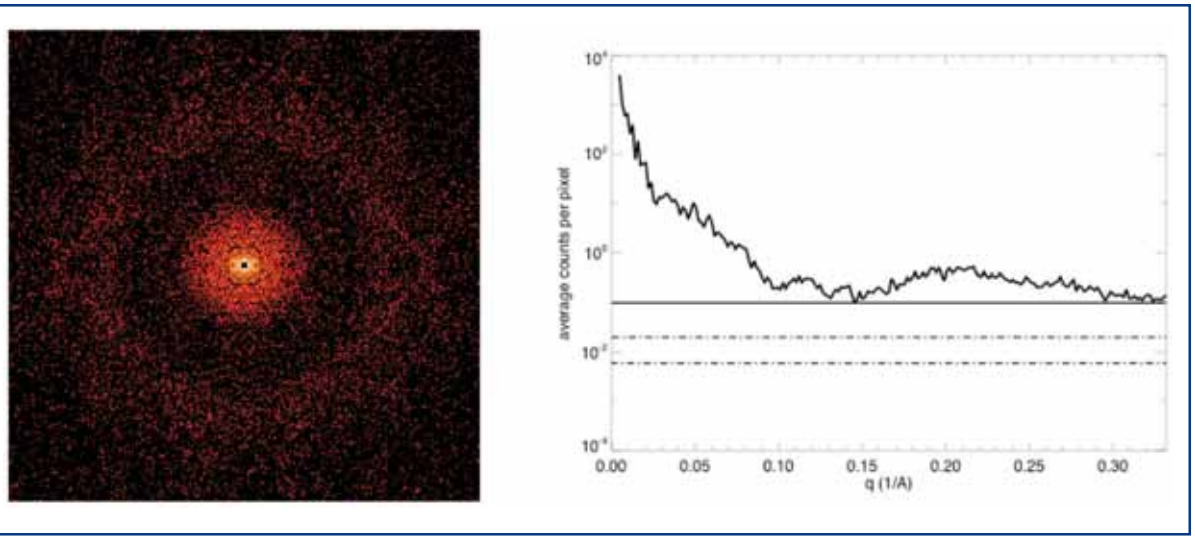


***Figure 6.4.78*** *Simulated diffraction data from the CPMV object, for a beam waist diameter of 0.1 µm, while all other parameters stayed the same as for Figure 6.4.77. The maximum photon count is 5,540, excluding the beamstop. The total integrated photons is $3.0 \times 10^5$. The plot shows the radial average of the photon counts. The solid line is at 0.1 counts, the minimum counts needed to classify, and the dotted lines denote the noise level for 10 and 100 averages, for a detector noise of 0.06 photons per pixel.*

*Channel optics for detector shielding*

We may find it necessary to shield the detector from scattering from gas or objects upstream from the sample, even with the judicious use of the apertures mentioned above. Ideally, the detector would only be sensitive to rays travelling in directions emanating from the sample position, so it would not detect scatter from any other object in the beam. Since downstream from the sample and off the axis of the direct beam, the x-ray intensity is very weak (the scattering from the sample) it may be feasible to use structures such as radial Soller slits (or, more precisely, square-pore capillary arrays) which accept only the diffracted light from a volume surrounding the sample (Figure 6.4.79).

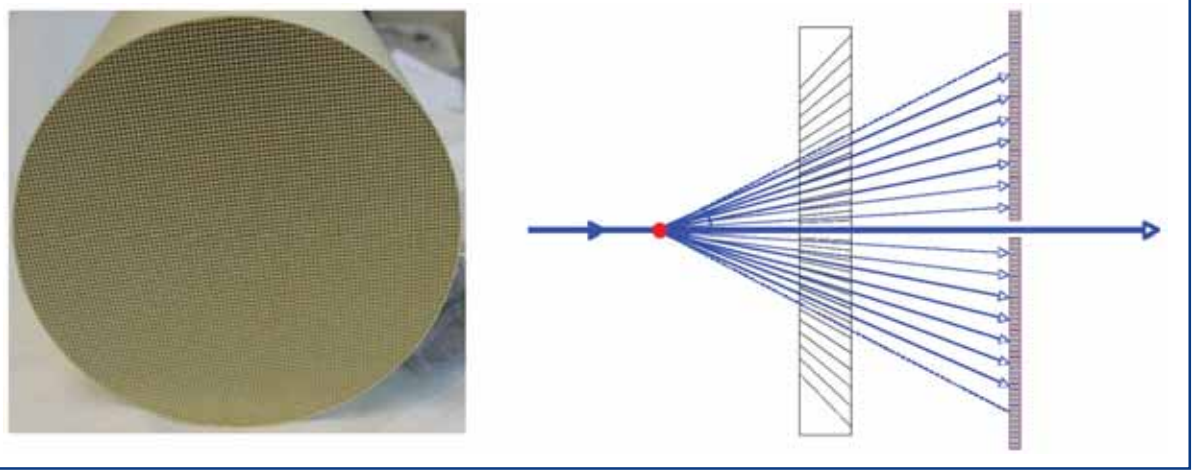

***Figure 6.4.79*** *Glass Soller collimator for filtering out stray light at the detector. These can be manufactured to conical shapes, and can have tapered channels with dimensions down to about $10 \times 10$ µm$^2$.*

### Visible laser requirements

No short-pulse laser for time-resolved pump-probe experiments is required to begin with. However, such experiments are likely to be carried out in the future and the design of the instrument must allow access to a state-of-the-art ultrashort pulse laser for UV-IR radiation. As discussed in Section 6.4.7.1, alignment of single particles or clouds of particles will be performed using a polarised near-infrared laser, focused to an intensity of about $10^9$ W/cm$^2$. For adiabatic alignment in the non-viscous environment of a pure vacuum, pulse durations longer than 100 ns are required. If the beam is focused down to 10 micron, this requires a laser with pulse energies of more than 100 µJ, or alternatively, a 1 kW continuous laser.

### Computer hardware and software for data acquisition and data processing

### Collecting, handling, and storing very large data sets

As in crystallography, the computer is a major component and algorithms are required to generate images from the measurements. Depending on the complexity of the molecule to be studied, the size of a diffraction pattern will be N×N pixels, with N = 100 to 1,000 (some applications may require N = 10,000). The need to build up a large enough signal to atomic resolution and to obtain full 3-D information may require about $10^5$ - $10^6$ diffraction patterns to be collected from a series of identical particles. This corresponds to about 40 Tb of data for N = 1,000. This volume of data could be collected in a day's operation and computing and data handling resources must be able to keep pace with this generation rate.

### Data processing

The processing of the non-crystalline diffraction data, with reconstructed electron density as the end result, consists of two distinct stages. In the first, a large number of noisy 2-D diffraction patterns must be given orientations in 3-D reciprocal space and merged into a single 3-D diffraction pattern. In the second stage, phases are derived from the 3-D diffraction pattern based on iterative phase-retrieval methods from the over-sampled diffraction data set.

*Image classification*

The patterns will be collected from particles at random and of unknown orientation, so these patterns must be aligned with each other and assembled into a 3-D data set. Due to the large number of images required for an adequate signal-to-noise ratio in coherent x-ray setting, it may also be necessary to significantly advance the power of the basic algorithms used, e.g. in EM studies. The standard approach has been to divide the merging stage into two operations: classification and orientation. Classification corresponds to applying criteria to establish which 2-D diffraction patterns have similar orientations and can, therefore, be averaged to improve the signal-to-noise ratio. Image classification can be done successively, starting at low resolution and performing finer groupings as the resolution increases. The requisite algorithms are easily parallellised. Once the diffraction data is classified and averaged to achieve the required signal-to-noise ratio, it must be assembled into an $N^3$ array (now about 16 Gb).

*Data reduction and merging*

The relative orientation of the averaged images may be determined through the method of common lines, a technique widely used in electron microscopy, where the micrographs represent planar sections through the centre of the molecular transform. Diffraction images are different in that they represent spherical sections of centric objects. Each pair of images will intersect in an arc that also passes through the origin of the molecular transform. If the signal is strong enough for the line of intersection to be found in two diffraction images, it will then be possible to establish the relative orientation of these images.

We note that due to the curvature of the sections, the common arc will provide a 3-D fix rather than a hinge-axis. Moreover, the centric symmetry of the modulus of the molecular transform ensures that we obtain 2 x 2 independent repeats of the common lines in the two images. This feature makes for determining sample orientation redundant, and is unique to the diffraction geometry. It can lead to a complete determination of the relative angles of the diffraction patterns.

The standard approach to merging, i.e. classification followed by orientation, suffers from some arbitrariness that can be circumvented without compromising performance. Primary among these is the need to establish, at the outset, the number of orientations that will be averaged and to choose criteria to define membership in the orientation classes (e.g. closeness to representatives).

In an alternative approach, each 2-D diffraction pattern will automatically be assigned a unique set of Euler angles determined by a pseudo energy functional defined on an associated “adjacency graph,” which is a natural encoding of the likelihood that two patterns are close in orientation given the applicable model of noise (e.g. Poisson counting statistics). Based on preliminary studies by Elser **[6-357]**, it appears that computationally the most challenging step in this approach is not the minimisation of the pseudo energy functional but rather, the initialisation of the minimisation, which corresponds to embedding the adjacency graph into the space of orientations so that the topology is correct.

The solution to this problem, and in effect the rate-limiting step of the entire approach, is to obtain the four lowest eigenvectors of the adjacency matrix using the Lanczos sparse matrix algorithm. A particularly attractive feature of this initial embedding step is that it simultaneously serves as a diagnostic for data acquisition. From the spectrum of the lowest eigenvalues one can readily assess the degree to which the collected data forms a quasi-continuum in the space of orientations, and assembly of the 3-D diffraction pattern can proceed. This diagnostic is fast because it acts on a relatively raw form of the collected data (adjacency graph) and could perhaps be used in “real time” during data collection.

*Phasing*

The 3-D structure is related to the measured amplitudes through a 3-D Fourier transform. Since only the Fourier magnitudes are measured, phase retrieval methods must be

employed to derive the phases and so determine the structure. The most promising approach is a method of generalised projections, in which known constraints are iteratively applied. This requires many thousands or tens of thousands of iterations, with two or more $N^3$ FFTs per iteration. The FFT is a demanding algorithm for parallel machines, and performance is usually limited by communication speeds. Efficient routines can be achieved when the number of nodes is equal to N, in which case two across-processor transposes are required. In general, the reconstruction problem requires $1{,}024^3$ FFTs to be performed in less than a second.

*Hardware*

A dedicated computer hardware configuration will be needed with large storage capacity. The primary objective will be to orient the patterns. Because the data rate in the experiments is very high (around 400 Tb/day near 100% hit rate), this will be a computing cluster where each node is responsible for either identifying members of particular orientation classes or establishing connectivity in the adjacency graph. A separate cluster will be used in the later steps of structure determination.

### *6.4.7.3 Realisation of the instrument*

The experiment requires an instrument at SASE 1 (SPB 1 – Hard XFEL radiation). For a description of the SASE 1 beamline see Section 6.2.4.1. All studies discussed in Section 6.4.7.1 will be carried out using this instrument. The experiments require highest achievable intensities. For large particles (>100 nm) the use of a perfect crystal monochromator (optional) is required to reduce the bandwidth. The SASE 1 beamline provides a double-mirror double-crystal setup, allowing both direct beam and monochromatised radiation to the instruments. All optics needs to be flat and preserve incident wavefronts as good as possible. Strong focusing will be achieved near the samples. The monochromator provides the opportunity to use third harmonic radiation.

**SPB 1: Hard XFEL radiation**

Since the preservation of the wavefront is crucial in these experiments the number of optical elements needs to be kept small. Therefore, the instrument will best be located in the forward direction of the beam coming from the double-mirror/double-crystal unit. The following elements belong to the SPB 1 instrument inside the experimental hall. They are depicted in the schematic layout of that instrument in Figure 6.4.80 and are described in Table 6.4.16. First optical element will be optional x-ray pulse compression optics. Apertures define the beam profile in front of two focusing optics for focal spots 1-10 µm diameter and for extreme focusing in the order 100 nm.

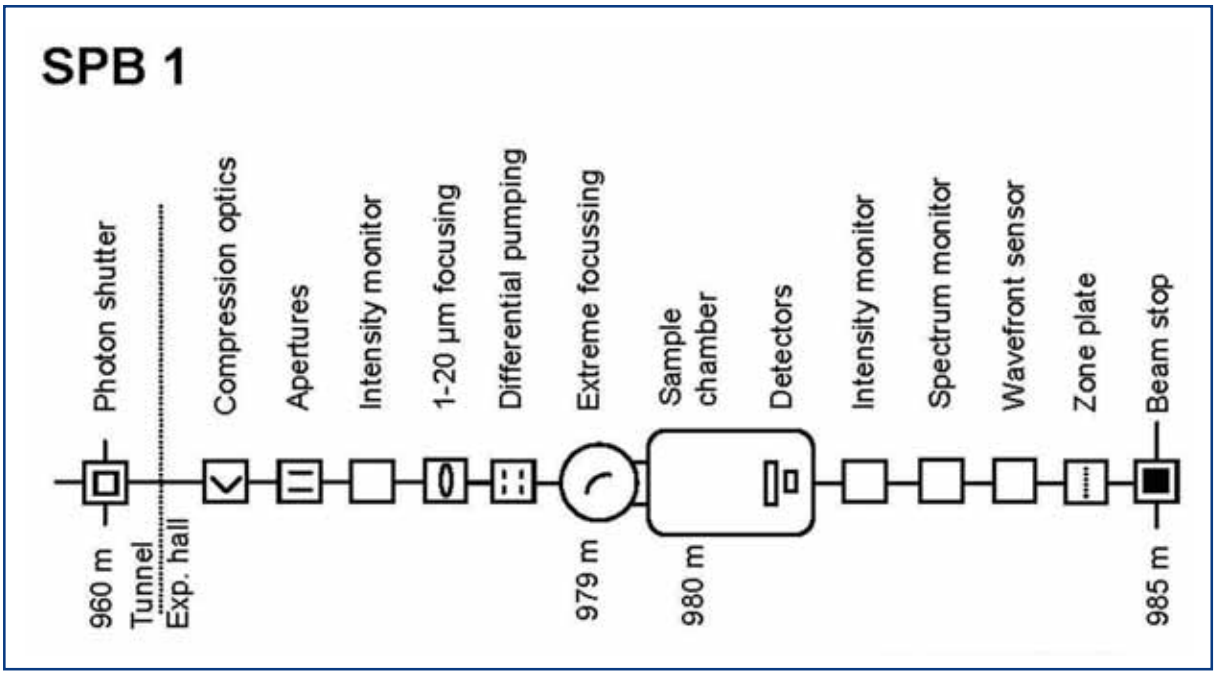


***Figure 6.4.80*** *Schematic layout of the SPB 1 instrument at the SASE 1 beamline. Distances are given in relation to the end of the undulator.*

For the larger focus, in-line optics would be ideal, but these are generally chromatic. Thus, the spatial performance at the focus is limited by chromatic blurring (compare Section 6.2.2). Reflecting optics, such as an ellipsoidal mirror, provide better performance but generate an angular deflection. For extreme focusing a pair of dynamically bent flat mirrors (K-B geometry) will be employed. This optic needs to be very close to the sample position. Apertures between the optics and the sample will both reduce background and provide shielding of the optics from debris. At the sample location the beam diameter is ~1 mm (FWHM; 12.4 keV) and mirrors need to operate at grazing angles of at least 4 mrad to accept 6$\sigma$ of the beam. The resulting mirror length is ~600 mm.

The vacuum system of the beam transport will be connected to the sample chamber by means of a differential pumping section. The sample chamber assembly includes the extreme focusing optics, the interaction area with access for spraying techniques, cryo-sampleholder and for diagnostics systems, and the in-vacuum detector system. Sample environment diagnostics include fluorescence monitors to position hits along the x-ray beam path, mass spectrometer to analyse fragmentation, electron spectrometer and a visible light microscope including CCD camera. Behind the detector diagnostics for photon flux, spectral distribution ($\Delta E/E$ ~ 1-2$\times 10^{-4}$) and spatial profile or wavefront is required. All diagnostics need to operate in the single-pulse mode.

At the instrument a laser system is available. This system will be used for sample alignment techniques first. Provision for future installation of an ultrashort pulse laser for pump-probe experiments will be made.

| Item | Purpose | Specification |
|---|---|---|
| Compression optics | Pulse compression to 5-10 fs with high reflectivity | Maintain x-ray duration, maintain wavefront |
| Slits/apertures | Beam definition, beam halo cleaning, apodising techniques to reduce scatter | 0.25 µm accuracy, 1 µm repeatability |
| Intensity monitor | Measurement of incident photon flux | Transmissive (<5% absorption), single pulse measurement, relative accuracy $<10^{-3}$ |
| Focusing optics | Generate 1-20 µm focus | Int. reflectivity ≥80%, stability 0.5 µm |
| Differential pumping | Separation of beamline and instrument | |
| Focusing optics | Generate 0.1 µm focus, K-B geometry | Int. reflectivity ≥80%, stability 0.1 µm |
| Sample chamber | Spraying techniques, cryo-sampleholder, sample diagnostics | UHV ($10^{-8}$-$10^{-6}$ mbar) |
| Detector | Two 2D detectors for low and high count rate | Size minimum 1K×1K, dynamic range $10^3$, in-vacuum opration, central hole maximum 4×4 pixel |
| Intensity monitor | Measurement of transmitted photon flux | Transmissive (<5% absorption), single pulse measurement, relative accuracy $<10^{-3}$ |
| Spectrum monitor | Measurement of distribution | Single pulse measurement, relative accuracy $<10^{-3}$ |
| Wavefront sensor | Measurement of spatial distribution at focal spot, adjustment of extreme focusing optics | λ/10 resolution |
| Zone plate | Beam profile measurement | |
| Alignment unit | Positioning and position verification | Permanently operating, accuracy ~100 µm |
| Lead hutch | Radiation protection, temperature stabilisation, laser protection | 4×10×3.5 $m^3$ (W×L×H), ±0.5° thermal stability |
| Control hutch | Operation of the instrument | Working environment (noise, temperature, light) |

***Table 6.4.16*** *Elements and specifications of the SPB 1 instrument.*

## 6.4.8 Research and development on x-ray instrumentation

Instrumentation for experiments using XFEL radiation creates new challenges in an area that has already witnessed an active development over the last decades driven by the synchrotron radiation community. To the already excellent properties of synchrotron radiation XFEL radiation adds the extremely high degree of transverse coherence, the thousand times shorter pulse duration and the high flux per pulse. Many measurements can be achieved in a single pulse exposure thus providing a tremendous advantage for time resolution. On the other side, single pulse measurements exclude averaging and will, thus, be determined by fluctuations.

The various experiments discussed before in this chapter are all based on the particular properties of XFEL radiation. The preservation and, eventually, the improvement of them is one of the challenges the new sources are facing. In this section a few fields are identified where the preservation and application of XFEL radiation properties will have a strong impact. Although current knowledge is advanced enough to design x-ray instrumentation for XFEL experiments, development will need to continue, once XFEL sources become available for experiments.

Obvious fields for continued development are the preservation of wavefronts using mirror or crystal optics and advanced optics schemes, e.g. for pulse compression, slicing or splitting. Also, the area of x-ray detection and diagnostics methods requires continued attention since the operation of XFEL sources is expected to lead to more sophisticated experiments with more challenging requirements. In the same direction, one expects that the particular properties of XFEL radiation lead to new advanced techniques, both for diagnostics and experimental schemes.

Although the properties of XFEL radiation and their application are the focus of interest, the following areas of research and development also require an experimental programme that, to a large extent, could use spontaneous synchrotron radiation. This radiation, albeit exhibiting less brilliance than the XFEL radiation, is still extremely well collimated, very intense per pulse and ultrashort in pulse duration. Parameters for spontaneous radiation, due to the high electron energy, do not vary significantly over a large photon energy range from ~10 keV up to ~100 keV (compare Section 5.3 and Table 5.3.2).

### *6.4.8.1 Scientific case*

**Experimental programme**

In the following we describe four exemplary areas of research and development. These areas are directly related to the key properties of XFEL radiation and the requirements of experiments with XFEL radiation. Firstly, the high degree of coherence of XFEL radiation and the high brilliance poses a challenge for optics development. Diffraction-limited optics for 0.1 nm radiation are difficult to achieve, and the development of optics that preserve and exploit the wavefront, in relation to the coherence of the radiation is needed.

Secondly, the exciting properties of XFEL radiation such as pulse duration and photon number lead to a desire to apply new schemes for x-ray optics, only applied in the optical regime as yet. Thirdly, the requirement for sophisticated detection and pulse-by-pulse diagnostics methods for XFEL experiments makes a development programme necessary to improve current methods and develop of new ones. This involves the development of x-ray detectors. Finally, completely new schemes for x-ray experimental techniques have been proposed.

## I. Wavefront preserving optics

The consequences of imperfection of optical surfaces on the properties of the x-ray pulse have been discussed in Section 6.2.2. Since current x-ray sources do not have a substantial coherent flux, the related issues cannot be solved yet and are of particular importance for XFEL instrumentation and research.

*Mirrors*

Surface roughness and slope error are important parameters affecting the performance of x-ray optics. The relation between both parameters and the consequences for the performance of x-ray optical elements is not yet understood **[6-386]**. Present metrology is near its resolution limit and new techniques need to be established or existing techniques reviewed to enhance the current understanding significantly.

Combining different laboratory metrology techniques in-situ with an x-ray beam of high coherence degree will provide new insights and lead to a better description of wavefront propagation by mirrors and other optical elements. In-depth understanding of the interplay between the shape function of an optical element and the variation in the propagation of a wavefront will lead to a new and better definition of these optics. This improved understanding might also lead to a reduction in some of the currently extremely challenging parameters.

*Crystal optics*

Perfect crystal optics is an important asset for the transport of radiation without disturbing wavefront properties. Single crystals with a high degree of perfection are available for Silicon. For reasons of energy dissipation and heat load, Diamond is an interesting alternative, however, its perfection is yet not high enough to reflect x-rays without damaging wavefront properties. The continued development and monitoring of newly grown Diamond crystals is, therefore, important.

In addition to the perfection of the crystal material, the preparation of the crystals must be very precise. Asymmetric orientation of reflecting planes leads to tilting wavefronts with respect to beam propagation which is important when trying to obtain the highest possible time resolution. Again, surface roughness of crystal needs to be considered in the full description. Investigation of wavefront properties after crystal reflection will firstly allow experimental validation of wavefront propagation codes and secondly, the measurement of crystal optics performance.

*Heat load*

Optical elements at the European XFEL undergo enormous heat load exposure in using the pulse train feature of electron acceleration. Temperature cycles of 50°C on surfaces in crystals or at mirror surfaces have been calculated. Several techniques have been proposed to solve this problem (see Section 6.2.2). Validation and further development will again require determining the performance of the optical system in terms of wavefront preservation.

## II. Advanced x-ray optic schemes

*Pulse compression*

Generation of x-ray pulses shorter than the design value of 100 fs would lead to improved capabilities for several experiments. Amongst the methods that have been proposed are x-ray optics methods using multilayers or crystals. Manipulation of wavefront orientation and bandwidth chirping are techniques with a high potential in this area. Experiments investigating the spatial-temporal properties of reflections provide the necessary information to verify and improve the various concepts. The experiments will investigate properties of x-ray pulses before and after reflection by these optical elements spatially and temporally resolved. In particular, the time domain diagnostics will require significant improvement compared to current technology.

*Beam-split-and-delay*

The high number of x-ray photons in a single XFEL pulse raises the interest in x-ray experiments. Pump-probe techniques will be of interest and require splitting one XFEL pulse into intense pump and weak probe pulses. Other experiments, e.g. auto-correlation measurements, require equal splitting. Furthermore, the pulses need to have an adjustable time delay. Also, the selection of the other radiation properties, e.g. the photon energy, bandwidth or harmonic number will be of interest. First x-ray optics for splitting into two equally strong pulses used in XPCS techniques (see Section 6.4.4.1) are currently under development. Advanced x-ray techniques (see IV. below) will be based on these developments.

*Phase modulation optics*

Due to the high degree of coherence, the propagation and reflection of the x-ray pulse will strongly depend on wavefront properties. The importance of preserving the wavefront was stressed before. Similar to techniques applied in the visible light optics domain, coherent x-ray radiation also offers the possibility of building phase modulating optics. For focusing, this technique is already in place, but other domains are very attractive. An example is the development of slit systems that do not have singularities on the density modulation, thus, reducing coherent scattering.

## III. X-ray detection and diagnostics methods

*Photon flux and spatial distribution*

Measurement of photon flux per pulse is an important diagnostic and will be required for XFEL experiments from the very beginning. It must allow operation in transmission and the simultaneous measurement of the spatial distribution of radiation will be a big asset. Currently proposed techniques use ionisation of gases. Although the current gas ionisation detectors provide the possibility of absolute calibration, a higher accuracy in the measurement of the photon number is desirable. Development of new monitors using gases or solids requires x-ray beams of well characterised properties that can be attenuated over a wide range.

*Coherence*

The degree of transverse and longitudinal coherence is crucial to many of the techniques and scientific applications. Many experimental methods determining coherence parameters have been proposed, but as yet, no real diagnostics monitors have been developed. In the long-term, monitoring of coherence properties should be possible on a pulse-by-pulse basis.

*Time*

Time domain diagnostics includes the measurement of the x-ray pulse arrival, its duration and eventually, its temporal distribution. For the optical domain these techniques are all well-established by now. However, for photon energies beyond the UV these techniques are not yet available. Many research projects are focusing on the different aspects of these measurements. Certainly, the measurement of the temporal distribution is very challenging, requiring for 12 keV x-rays a resolution of ~100 as to resolve the spike structure. Since this distribution is fluctuating for every pulse, the measurements need to be done pulse-resolved. Cross-correlation experiments using ultrashort pulse optical laser radiation (see below) are promising in this area.

***Wavefront techniques***

Using wavefront measurement techniques to diagnose the performance of the x-ray beam has been mentioned in Section 6.2.2 and before in this section. Many of the scientific experiments have further requested wavefront sensors in order to enable the alignment and characterisation of the focal spot at the sample location. Current developments have shown that wavefront sensors with high resolution in the order $\lambda/10$ at 0.1 nm can be realised. A major difficulty with the present designs is their limited dynamic range and the need to place the sensors into the direct beam. Therefore, in order to enhance the versatility and flexibility of these measurements, development of the sensors needs to be pursued.

*X-ray detectors*

The development programme for x-ray detectors for XFEL radiation is described in Section 6.5.4. It will include 0-D, 1-D and 2-D detectors. The response of the detectors to intense and ultrashort x-ray pulses needs to be analysed using lower intensity radiation of otherwise similar properties, and then XFEL radiation. Specific detector materials may also prove meaningful for diagnostics techniques for XFEL radiation, e.g. Diamond detectors are very promising for photon flux and beam profile measurements.

**IV. Advanced techniques**

*Large solid-angle optics for single-shot experiments*

For a signal to be meaningful for spectroscopy experiments investigating x-ray emission from atoms, plasma, liquids or solids, as much signal as possible for a single shot exposure will need to be collected. Typically, a spectroscopic resolution of $10^{-4}$ is required, thus, limiting the acceptance angles of standard spectrometers. Proposals for building systems with large acceptance angles using a series of crystals have been put forward and these will use either spherically or cylindrically curved analysers **[6-387]**.

*Auto- and cross-correlation techniques*

In particular for time domain studies and time domain diagnostics, the application of auto- and cross-correlation techniques will be required. While spontaneous radiation does have three orders of magnitude less flux then XFEL radiation, this flux will be rather similar to what can be used for diagnostics at the XFEL beamlines. Cross-correlation techniques using visible laser radiation are most promising due to the enhanced cross-sections compared to auto-correlation experiments. The latter experiments are feasible at full scale using XFEL radiation; spontaneous radiation will provide the possibility to do precursor studies.

*X-ray photon pulse echo experiments*

In investigating dynamics, inelastic scattering techniques probe the energy domain and direct techniques the time domain. While energy domain techniques benefit mainly from the increase in average brilliance of the European XFEL, time domain techniques will, in addition, profit from the ultra-short pulse duration. The development of a technique is proposed that makes use of the ultrashort pulse duration to study microscopic dynamics directly as a function of time. The idea is to transfer the scheme of the (resonant) neutron spin echo technique **[6-388]** to the x-ray case. Information on the sample dynamics is obtained by recombining two pulses which have been elastically scattered by the sample at an adjustable time delay and observing the interference pattern of the two pulses. As in the neutron case, information on the intermediate scattering function S(q,t) is obtained by a steady state experiment, without the need for fast detection.

The experiment consists of two x-ray delay lines located before and after the sample. The first part prepares two pulses, separated by an adjustable delay so that both pulses probe the sample structure at different times. The second delay line adds a second delay of exactly the same quantity so that the pulse delayed in the first optics and the one in the second optics overlap precisely. Consequently, three pulses arrive at the detector, where only the middle is the coherent sum of the two pulses with identical flight time. Only this pulse contains the information, whereas the pulses preceding and trailing provide only inherent background. The detector integrates all three pulses. Delay times from 100 fs up to the nanosecond regime are of interest here.

Possible applications of this technique will cover quasi-elastic scattering to probe diffusive motions or relaxation and inelastic measurements with high resolution. The wide time-interval offered by this technique is particularly valuable for systems showing non-exponential behaviour of the relaxation function, like glasses or bio-molecules. In the inelastic (short time, few picosecond) regime, the phonon density of states, in particular that of low-lying excitations, will be accessible.

*X-Ray Transient Grating Spectroscopy (XTGS)*

At an XFEL source the transient grating technique presently used for visible light studies **[6-389]** can be extended into the x-ray regime. With this technique the incoming beam is split into two transversely coherent beams which are crossed under an angle $s$ to produce a standing wave field with periodicity $d = k_0 sin(s/2)$, where $k_0$ is the wavevector of the

incident beams. The value of $d$ can be in the range from one to several hundred nanometres.

If a sample is placed in the standing wave field it will produce a periodic density modulation in the sample which has the same periodicity as the standing wave. If an XFEL is used, this modulation is formed during a single laser pulse, and after the pulse, relaxation will occur. A second pulse with a delay to the first one forming the standing wave pulse, can now be used to probe the periodic modulations within the sample by means of x-ray scattering. If the modulations relax, the scattered intensity will increase. Therefore, if the measurement is repeated for different time delays, the time course of the relaxation can be followed. This can reveal valuable information about the local dynamics within the sample on a nanometre length scale.

### *6.4.8.2 Requirements of the instrument*

The development projects for x-ray instrumentation require an instrument for R&D so that experiments needed to prepare specific projects and to validate the performance of XFEL-related x-ray instrumentation can be carried out. Once successful, the x-ray techniques will be available for all experiments at the European XFEL. Since many of the techniques use radiation much less intense than the XFEL radiation itself, the instrument could use the ultra-short and tunable spontaneous radiation from the U 1 undulator.

#### Spectral requirements

The experiments will require mirror-only and monochromatic radiation covering, in principle, all photon energies available at the European XFEL. However, we will restrict discussion in the following to the hard x-ray regime available at the U 1 beamline.

#### X-ray optics requirements

A versatile setup to insert various optical elements is requested. Since one of the main areas of work will be coherence properties, particular care has to be taken not to introduce wavefront errors by permanent optical elements. In-line optics will be used to focus the beam to approximately 100 µm spots.

#### Time domain requirements

Experiments will make use of single- and multi-pulse operations. The latter enhances the flux-per-pulse train considerably. In the timing experiment, the synchronisation between the x-ray pulse and optical laser needs to be accurate to well below the x-ray pulse duration.

#### Photon diagnostics requirements

Various detector systems for diagnostics of flux, spectral and temporal properties, and spatial distributions are needed. To begin with these will serve as references when developing new techniques and instrumentation.

### Sample manipulation and environment

No particular samples will be investigated using this instrument. However, very precise x-y-z translation and three rotational degrees of freedom will be required. For the in-situ measurement of mirror performance, high performance metrology tools such as long-trace profilers and near-field microscopes need to be installed.

### Detector requirements

Most experiments investigate intense reflection or diffraction spots. Therefore, point-like detectors can be applied in many of the experiments. These should be capable of reading at the 5 MHz repetition rate of the machine. A 1-D detector with sufficient spatial (10-50 µm) and/or angular resolution (10-50 µrad) in one direction is requested. Slow (10-50 Hz) 2-D detectors with CCD-like performance will be needed, too. Finally, for the performance of many optical systems an ultra-fast (~100 fs) x-ray streak camera will enable a lot of direct time domain measurements.

### Visible laser requirements

For the cross-correlation experiments, access to the ultra-short pulse laser system with the possibility of using frequency multiplying is needed. Synchronisation of laser and x-ray pulses better than the pulse duration is required. Otherwise the measurement of the relative arrival-time is required.

## *6.4.8.3 Realisation of the instrument*

The following describes an R&D instrument (RAD 1 – Hard tunable x-ray radiation) that will be located at the U 2 beamline. For a description of the U 2 beamline, see Section 6.2.4.5. This beamline cannot provide soft x-ray radiation, and experiments in these areas need to be carried out at other instruments. The instrument uses the double-mirror double-crystal system of beamline U 2. The collimating lens near the source increases flux and limits the beam size at the instrument. However, for experiments sensitive to coherence it has to be removed. A second, refocusing lens in 1:1 geometry provides a 100 µm focal spot at the instrument, thus, increasing intensity. The monochromator provides the opportunity to use third harmonic radiation.

### RAD 1: Hard tunable XFEL radiation

The RAD 1 instrument should be located in the forward direction of the beam coming from the double-mirror/double-crystal unit in U 2 so that coherence studies, which benefit from minimising the number of optical elements disturbing the wavefront parameters, can be carried out. The following elements belong to the RAD 1 instrument inside the experimental hall. They are depicted in the schematic layout of that instrument in Figure 6.4.81 and are described in Table 6.4.17. Beam-defining apertures, followed by an intensity monitor and a spatial beam profile monitor will precede the first sample mount that includes metrology instrumentation. Behind, a mount for an optional strong focusing optic and a second intensity monitor follow. At less than a metre distance the sample diffractometer provides versatile mounting. The diffractometer can be removed from the beam.

The vacuum system of the beam transport will end in front of the sample mounts. Beryllium windows are used at this instrument. Subsequent intensity monitors, using gas ionisation techniques, can also be capsulated using thin Beryllium windows. Behind the detector, diagnostics for intensity, spectral distribution ($\Delta E/E \sim 1\text{-}2\times10^{-4}$), spatial profile and wavefront is required. Single-pulse mode operation of the diagnostics is preferred. At the instrument an ultra-short pulse laser for pump-probe experiments could be used.

A specialty of the RAD 1 instrument is that the beam will be transferred to a second instrument mounted behind. It is not anticipated that both instruments will be operated at the same time and all RAD 1 instrumentation must be mounted so that it can be moved out of the beam. The beam-defining apertures and the intensity and spatial beam profile monitors can be used for both instruments.

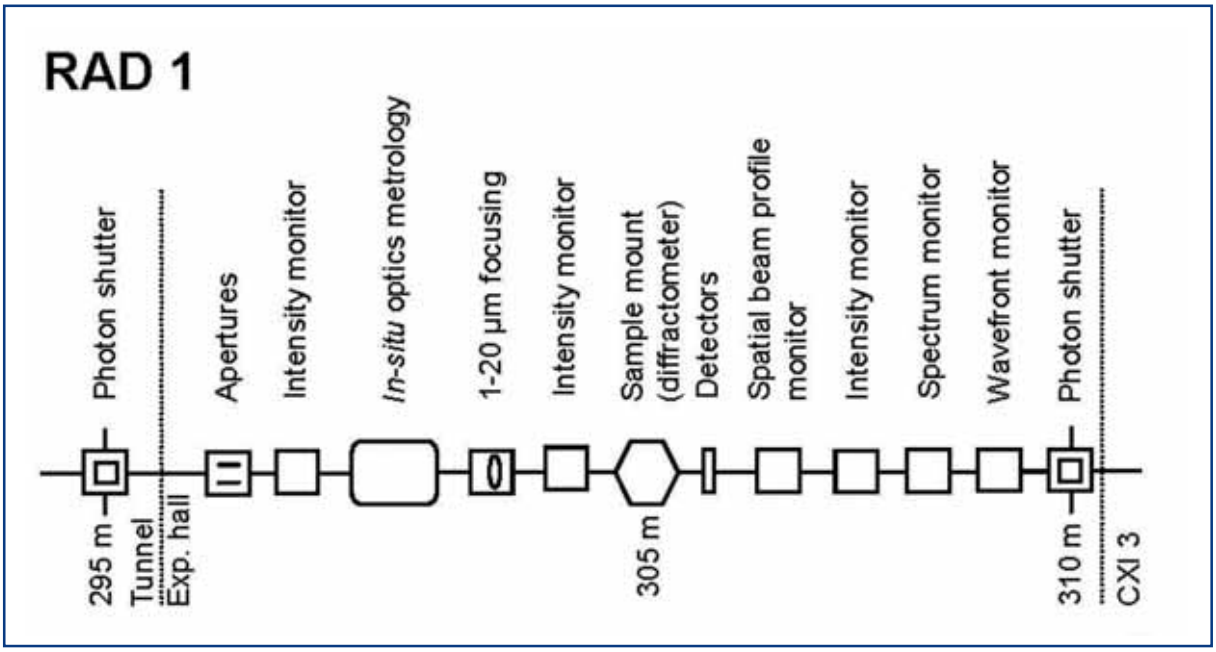


***Figure 6.4.81*** *Schematic layout of the RAD 1 instrument at the U 1 beamline. Distances are given in relation to the end of the undulator.*

| Item | Purpose | Specification |
|---|---|---|
| Slits/apertures | Beam definition,<br>beam halo cleaning,<br>apodising techniques to reduce scatter | 0.25 µm accuracy,<br>1 µm repeatability |
| Intensity monitor | Measurement of incident intensity | Transmissive (<5% absorption),<br>single pulse measurement,<br>relative accuracy $<10^{-3}$ |
| Sample mount | In-situ measurement of mirror using 'standard' metrology | x-y-z translation,<br>three rotations |
| Focusing optics | 1-5 µm focus, refractive lenses or K-B system | Integrated reflectivity ≥80%,<br>stability 0.1 µm |
| Intensity monitor | Measurement of incident intensity | Transmissive (<5% abs.),<br>single pulse measurement,<br>relative accuracy $<10^{-3}$ |
| Sample mount | Diffractometer | |
| Detector | 0-D,<br>1-D pixel detector (0.05×1mm2 pixel),<br>2-D CCD | 5 MHz,<br>10K, 1 MHz,<br>10-50 Hz |
| Intensity monitor | Measurement of transmitted intensity | Transmissive (<5% absorption),<br>single pulse measurement,<br>relative accuracy $<10^{-3}$ |
| Spatial beam profile monitor | Measurement of x-y distribution | Transmissive (<5% absorption),<br>single pulse measurement |
| Spectrum monitor | Measurement of photon energy (mean, distribution, harmonics) | Single pulse measurement,<br>relative accuracy $<10^{-3}$ |
| Wavefront sensor | Measurement of spatial distribution at focal spot,<br>Adjustment of extreme focusing optics | λ/10 resolution |
| Alignment unit | Positioning and position verification | Permanently operating,<br>accuracy ~100 µm |
| Lead hutch | Radiation protection,<br>temperature stabilisation,<br>laser protection | 5×10×3.5 $m^3$ (W×L×H),<br>±0.5° thermal stability |
| Control hutch | Operation of the instrument | Working environment<br>(noise, temperature, light) |

***Table 6.4.17*** *Elements and specifications of the RAD 1 instrument.*

## 6.5 Specific XFEL experiments instrumentation

Experiments using XFEL radiation will enter into domains of x-ray instrumentation where currently no experience exists. In addition, the proposed experimental programme (see Section 6.4) at the European XEL Facility and the operation of several beamlines and many scientific instruments (see Section 6.2) at this facility lead to specific requirements with respect to x-ray instrumentation. These require instrumentation of the soft and hard x-ray beamlines with specifications exceeding, in many cases, the existing technology, in particular the existing x-ray instrumentation at synchrotron radiation or laser facilities. Four specific areas of instrumentation have been identified and the R&D programme in these areas is described in the following sections.

### Sample environment and manipulation

Instrumentation issues related to sample preparation, positioning and exchange of solid samples, sample injection systems for non-solid samples and specific sample environments fall into this category. Due to the high intensity of the x-ray pulses, in particular for focused radiation, the damage and beam modification of samples needs to be considered. Using continuous sample replacement has been proposed for this reason. Techniques vary from moving solids samples, using liquid or gas jets, or preparing single particles. Another issue is related to precise sample alignment required for experiments with spatial resolution in the 0.1-1 μm regime.

### X-ray optics

The preservation of the x-ray beam properties using diffraction limited optics is important for all coherence applications and also for extreme focusing. The response of optical elements to the high peak power and to average power during pulse trains is a second obvious area of R&D in this category. Beam splitters and delay units are new optical elements in the x-ray domain to be employed by several of the instruments. In addition, specific optics using mirrors, crystals or grating will be required to provide the requested performance.

### Optical laser

The proposed experiments require optical lasers for time-resolved experiments and also for diagnostics purposes. These lasers in general need to be synchronised with the x-ray beam. The requirements towards laser radiation in terms of pulse duration, repetition rate, pulse energy, tunability, and availability are more complex than commercially available laser systems. A dedicated instrumentation programme is, therefore, required.

### Detectors and requirements

The specific needs of many of the instruments proposed in Section 6.4 lead to a requirement for 2-D x-ray detectors with specifications not available today. An R&D programme has to be implemented to develop, test, and install such detectors and a start has already been made by having had a dedicated workshop mentioned in the introduction to this chapter. Other specific detector developments, e.g. particle detectors and x-ray streak cameras, are considered too.

## 6.5.1 Sample environment and manipulation

### *6.5.1.1 Sample preparation*

Experiments investigating nano-particles have been proposed in the fields of physics, material sciences, or structural biology. The preparation and characterisation of nano-particles before inserting them at the x-ray instrument is important for an efficient use of the available beam time at the XFEL. Whereas in material sciences the samples are relatively stable and also brought by the users, in biology one wants to study rather fragile systems including membrane nanocrystals, arrays of particles, virus templates, pure protein samples, viruses and cells. In many cases, particles and more complicated sample structures need to be prepared on specific sample holders that allow insertion

into the instrument. The sample preparation includes the preparation of particles in dedicated laboratories, their characterisation by standard laboratory techniques, the preparation of samples on holders specific for insertion at the x-ray instruments and the pre-alignment and/or preparation for insertion. Since samples in many cases are sensitive to oxidation, the preparation and insertion under vacuum has to be possible.

Characterisation techniques such as high resolution microscopy, electron microscopy, atomic force microscopy, x-ray diffraction and small-angle scattering, visible laser spectroscopy are included here. Also, techniques for micromanipulation of nano-sized particles and inspection of samples after being used in the x-ray experiment are needed.

#### *6.5.1.2 Sample positioning, exchange and alignment*

After insertion at the x-ray instrument, the samples require exact positioning so that time is not wasted using XFEL radiation for alignment of samples. Having established a reference system for the sample area, the positioning occurs relative to this. The use of optical systems for online inspection is foreseen, in particular inside vacuum chambers. The accuracy of sample positioning is determined by the x-ray and visible laser beam sizes. Accuracy in the order 1 µm is required in all directions.

Experiments using solid samples will require concepts for exchanging samples at relatively high repetition. Sample exchange at the intra-bunchtrain repetition rate of ~1 MHz will require a sample speed of around 100 m/s (100 µm; 1 MHz) which is unlikely to be enabled for very complex structures. In focusing applications with extremely short depth of focus, one also needs to take into account that the sample remains in the same position along the x-ray beam after exchange.

An issue of specific interest to the XPCS experiments proposed is the stability of the samples in the x-ray beam. This needs to be known in order to prepare experiments. The issue of beam damage for different elements and materials as a function of intensity and photon energy, therefore, requires specific investigation.

In coherent diffraction experiments on intact cells and cell organelles using the unfocused, coherent beam of the XFEL, cryo-microscopic techniques could be suitable for tomography studies where a controlled sample rotation is necessary. Electron cryo-microscopy performs structural studies on hydrated samples at low temperatures in a high vacuum environment. Existing EM equipment can be adopted for similar studies in an x-ray beam. Sample molecules and particles may be embedded in a thin layer of vitreous ice of a few tens nanometres in thickness. Prior to an exposure, the sample(s) of interest may be located by UV/VIS fluorescence techniques, and once found, moved into the path of the x-ray pulse, using programmeable positioning devices. Such a technique requires excellent pointing stability from the XFEL, with minimal pulse-to-pulse creep. If this can be achieved, the complete repertoire of methods in electron cryo-microscopy will become available for x-ray experiments. Vitreous ice surrounding the sample will contribute to background. This method may, however, be the method of choice for large samples.

### *6.5.1.3 Sample injection systems*

These systems usually work indeterministically in that gases or liquids are injected into the vacuum, disperse following thermodynamical laws and get pumped away or collected in the case of fluids. Characterisation of the spatial density distribution at the interaction point with the x-ray beam is generally required. In these cases, samples are exchanged continuously and the speed at which the exchange occurs determines the repetition rate of the x-ray pulses. More sophisticated methods have been proposed for XFEL experiments on ions and single particles, clusters or biomolecules.

In atomic physics applications, the use of traps or ion beams provides the opportunity to prepare highly ionised and, in laser-cooled systems, ordered states of ions that can be investigated using the XFEL beams. The use of traps allows investigation of the ions in the excitation state and also determines the sample volume of interactions. Thereby, the scattering probability raises and enables these experiments. In a related, and more ambitious, version of these experiments one would install an ion beam, operated in either cross- or merged-beam geometry (compare Figure 6.4.4).

In materials science and structural biology applications on single particles, their controlled injection is needed. Particles are injected from the outside into the x-ray beam in such a way that single particles intersect with the brief XFEL pulses. Ideally, one fresh, single particle is injected into every focused pulse at the pulse rate of the XFEL. To achieve this, the trajectories of the particles must be controlled both in space (< 1 µm) and time (< 10 ns), so that each one of them will be well aligned with the focused x-ray pulse. Present sample injection and particle manipulation techniques need to be significantly refined in order to position individual particles with sufficient precision. The related R&D programme cannot be driven by the European XFEL project. However, close collaboration with the scientific community is anticipated in the field in order to design the scientific instrument for these applications according to the ongoing research. The next paragraph briefly describes the current approach in this area of R&D.

**Single particle injection**

Initial experiments will use clouds of particles without stringent requirements, achievable with current methods, with and without alignment with a polarised laser. These will be improved upon, by first injecting short, concentrated bursts of particles into the beam focus area and relying on the statistical positioning of individual particles. Such experiments require a focal spindle of about 5 mm length, shot-to-shot diagnostics to determine whether a particle was indeed hit by the x-ray beam and where the interaction along the focal spindle took place.

More advanced techniques of particle introduction and manipulation include the injection of a few or even a single particle into the beam at the proper time with well-controlled velocity, or trapping single particles at the XFEL beam focus using optical, electrostatic, or electromagnetic methods. ESI and related ink-jet spraying techniques will be used for introducing samples (like molecules or single particles, such as viruses) into the gas phase.

Spraying techniques have been refined in recent years for use in mass spectrometry of large proteins, supramolecular complexes, such as intact ribosomes **[6-390]**, and even whole viruses **[6-391]**. The charge imparted onto a particle by the ESI process is convenient for manipulating the particles in the gas phase by electrostatic forces. If necessary, a charge-reduction scheme based on the charge-reduction electrospray method, can be used to reduce the charge on electrosprayed molecular ions or particles to one or a few elementary charges in a controlled way. For the particle introduction into ultra-high vacuum, it is proposed that aerodynamic lens or nozzle techniques used for single-particle mass spectrometry and bioaerosol mass spectrometry will be applied. Also, techniques based on reverse micelles or Helium droplets to provide a protective coat for the sample molecules if necessary, will be explored.

An area with a direct bearing on the experiments is a technique to orientate particles using visible laser radiation. This method, applied to small molecules, is also part of the SQS experimental programme. The scaling of present techniques to larger molecules, or even to entire particles needs to be addressed. Another important area is the control of sample debris after the interaction with the intense XFEL beam. These techniques will be used in many of the experiments aiming for highest intensity. Diagnostics tools for determining where the particle was actually hit by the x-ray beam will improve the data quality. A possibility would be spatially resolved fluorescence that is emitted by the particles during x-ray induced heating.

## 6.5.2 X-ray optics

### *6.5.2.1 Preservation of XFEL radiation properties*

The high peak brilliance of the XFEL radiation follows from the ultra-short pulse duration and coherence of the x-ray beam. In particular, experiments applying time-resolved and coherence techniques make use of the properties. The x-ray transport to the scientific instruments must, therefore, preserve these properties. A particular challenge is the preservation of the wavefront here. The wavefront is important in many respects, as it governs the ability to focus to extremely small beam sizes, the possibility to retrieve structural data from coherent diffraction patterns and the time-smearing of the x-ray pulse. To fully understand and investigate the related phenomena, wavefront-propagation codes are required. Current codes must be extended to include x-ray diffraction theories in order to integrate time-dependent response of diffraction and must accept all kinds of x-ray optical elements.

#### Coherence

Most importantly, preservation of the coherence properties requires the specification of x-ray mirrors for the beam transport. At the European XFEL Facility mirrors have a central role in transporting the beam from the undulators to the experiments. The reason for using mirrors is that they are not chromatic and offer almost complete reflectivity. On the other hand for x-rays and low Z material, very small grazing angles are needed. In consequence, the mirrors become very long and the requirements to roughness and slope error are extremely high. The correlation of these two parameters and the consequences for x-ray diffraction are not fully understood yet and require further

research. The soft x-ray optics requirements for wavefront preservation have to be formulated and the monochromator design has to be verified in this respect. Related to the degree of coherence of an x-ray beam is the acceptance by the optical elements. Currently, the beam transport is designed to accept $6\sigma$ beam size for the highest photon energy. For smaller photon energies the divergence increases (see Table 5.2.2) and less beam size is accepted.

**Time domain**

For time-resolved experiments it is important to maintain, or even shorten, the x-ray pulse duration. The various optical elements, therefore, need to be analysed with respect to their effect on the pulse duration and wavefront inclination. In particular, the asymmetry of single crystals can give a contribution here. The accuracy to cut single crystals needs to be determined and, if needed, an instrument for verification needs to be set up. It was shown earlier **[6-392]** that double-crystal monochromators in asymmetric Bragg reflection can contribute substantially to pulse duration broadening. In the other direction, it has been proposed that the x-ray pulse be shortened or sliced using crystals **[6-393]** or multilayers **[6-394]** in specific configurations.

Splitting the x-ray pulse into two parts and delaying one of the pulses with respect to the other is requested for XPCS experiments, as well as for time-resolved experiments using the x-ray beam to induce an ultrafast change of sample properties. In XPCS, typically, two equally strong pulses and delay times of 1 ps to 200 ns are required. For pump-probe experiments, the first pulse excites the sample and therefore, the required intensity distribution between the split pulses may be very asymmetric. Here the range of delay time goes from 100 fs to few hundred picoseconds.

### *6.5.2.2 Power dissipation in optical elements*

The high photon number per x-ray pulse leads to very high peak power. Furthermore, the use of trains of x-ray pulses generates significant average power over the duration of the pulse train. An R&D programme must investigate the effect due to peak and average power dissipation to mirrors, monochromator crystals and beamline filters or windows. For peak power, the involved timescales are too short for thermal processes and the investigation of damage induced in the optics by single or accumulative effects needs to be investigated. First experiments have been carried out at the FLASH facility in the XUV regime and the scaling of the results towards the x-ray regime is of further interest.

In terms of average power, simulations have to be carried out to estimate the response of mirrors, crystals and window materials to the high average power during pulse trains. Specific schemes for preserving shape performance in mirrors include cryogenic cooling and active control mechanisms. For cryo-cooling of the long mirrors it has to be evaluated whether the extreme slope error tolerances can be preserved. Both schemes have to be integrated in the simulations in order to decide about the technology to be used.

### *6.5.2.3 Specific optical elements*

In the following a few optical systems are listed which have been requested by the various experiments. Although quite specific at present they may turn out to be very important in the future for more general classes of experiments.

**Focusing optics**

In nearly all focusing applications different focal spot sizes are requested for one scientific instrument. Focusing stronger than required is a disadvantage due to the increased intensity (W/cm$^2$). A design for the optics must, therefore, be quite flexible to change between different configurations. However, the number of optical elements is limited and an optimised design for the focusing optics must be developed. Specific aspects of focusing optics are listed below:

- The question how to achieve the smallest foci and the x-ray beam properties at the focal spot has to be solved. This extreme focusing requires coherent radiation and the techniques discussed in Section 6.2.2.4 above will work differently and lead to different consequences for the x-ray beam properties at the focus. This, in turn, is expected to influence the data in single particle imaging experiments.
- How to obtain extreme focusing in the very soft x-ray regime from 250-500 eV, so that, at the same instrument, beamline SASE 3, higher photon energy extreme focusing experiments can also be carried out. Is it also possible to use a second optics to achieve 10-20 µm focal spot size for the same experiment?
- How to enable focusing in the 1 µm regime for a wide bandwidth, both at SASE 2 and at SASE 3. Can compound refractive lenses be used for this application and is it possible to keep the focus and the focusing optics positions fixed. What will be the effect on the focal spot properties?

**Separation of first and third harmonics**

In pump-probe applications using the x-ray beam to excite the sample, it is foreseeable that probing can also be done at a different wavelength. This can be advantageous if, in this way, the cross-section for the pumping and probing processes can be better matched. For the XFELs, the third harmonics is expected to have in the order of 1% intensity and would, therefore, provide an excellent, less intense probe pulse. To enable these experiments one needs to split the initial beam into two monochromatic beams and then transport both beams to the scientific instrument. For these experiments a specific solution for the first double-mirror has to be found. The current mirror layout does not reflect photon energies higher than 15 keV so a different solution has to be found.

**Angular displacing monochromator**

In the proposed x-ray absorption experiments fast rotation of a monochromator crystal to displace the x-ray beam on the sample is a key element of a technique that allows the measurement of entire absorption spectra in the course of a single pulse train of 0.6 ms. The technique of rotating crystals for QEXAFS applications has been developed to a certain standard **[6-395]** and it needs to be investigated to what extent the angular speed

can be increased to match the requirements of this specific experiment. If successful, the technique will immediately be important in other experiments concerned with photon beam damage.

**Ultra-high resolution soft x-ray monochromator**

For precision spectroscopy on highly stripped ions, a bandwidth is required that is beyond the resolution a versatile monochromator, used by different applications, can provide. A resolution of $10^4$ up to $10^5$ will improve the precision of the proposed measurements significantly. The limitations of such a monochromator and whether it is possible to integrate it into the current beamline design for SASE 3 will be investigated.

**X-ray emission spectrometers**

For x-ray absorption spectroscopy, high energy density science and cluster research, the use of x-ray emission spectrometers has been proposed. For the XFEL experiments it is important to have efficient spectrometers covering a large solid angle. Such spectrometers have been proposed **[6-396]** and the effort required to build and the flexibility to operate such spectrometers need to be determined.

### 6.5.3 Optical lasers

To fully exploit the ultra-short pulse duration of the XFEL for time-resolved studies, synchronised ultra-short laser pulses in the optical regime are essential. Numerous optical/ x-ray pump-probe experiments have demonstrated that new insights in processes on the 0.1 nm length and femtosecond timescale can be explored **[6-397 – 6-400]** and many proposals to exploit XFEL envision scientific applications for these techniques (compare Section 6.4). Doubts whether two independent laser sources could be used for time-resolved experiments (due to the temporal jitter) with femtosecond time-resolution, were dispelled by groundbreaking progress in synchronising two lasers (e.g. **[6-401]**) and first experiments combining accelerator-generated femtosecond x-ray pulses with optical laser pulses at SPPS at Stanford **[6-402]**. By measuring the remaining temporal jitter precisely, the temporal resolution of the experiment was no longer determined by the timing jitter, but rather by the measurement precision itself.

Thus, an optical laser facility providing state-of-the-art laser technology (including synchronisation diagnostics) for all experimental end stations is strongly desired. The required specifications for such laser systems (see below) are extremely demanding, such that a permanent installation of the lasers, operated by experienced laser physicists, in the XFEL experimental area is absolutely necessary. For the vast majority of user groups it will not be possible to supply or support their own laser systems for these experiments.

Considering the user requirements and from general considerations, three different types of lasers for pump-probe experiments can be distinguished:

- lasers generating ultra-short pulses at medium to high pulse energy, 10 Hz;
- lasers generating ultra-short pulses at low pulse energy but high repetition rate;
- lasers generating highest possible pulse energy.

The following paragraph will outline the laser instrumentation programme for the European XFEL. The given specifications are meant to be available in the experimental chamber. Technical configurations to meet these specifications will be proposed in Section 6.5.3.2. Finally, auxiliary technical installations for the operation of the optical laser are described.

### *6.5.3.1 Types of lasers, technical specifications*

**Lasers generating ultra-short pulses at medium to high pulse energy**

This type of laser predominantly meets the requirement for pulse duration equal to or even shorter than the duration of the XFEL pulses in order to achieve highest time resolution in pump-probe experiments. For this laser type a required pulse duration ≤ 30 fs (FWHM) will be adequate.

Experiments requiring very high field strength for the optical laser can also be carried out with this type of laser. For this purpose it is important to provide pulse energies ranging from the upper millijoule to joule range, as requested by the experiments (1 mJ – 10 J). Due to the high pulse energies, the repetition rate will be limited to 10 Hz (upgradeable to ~ 30 Hz), i. e. equal to the burst repetition rate of the XFEL pulses. It should be noted that state-of-the-art laser technology allows generation of pulses with 30 fs pulse duration and 10 mJ energy with kHz repetition rate. But considering the temporal pulse pattern of the XFEL (see also Figure 6.1.1) a kHz repetition rate would not give any advantage over a 10 Hz rate. On the contrary it will be easier to obtain high pulse energies at 10 Hz.

**Lasers generating ultra-short pulses at high repetition rate and low pulse energy**

This type of laser is intended for pump-probe experiments where it is essential to repeat the measurement as often as possible. For example, a high repetition rate is important for effects demanding large statistics (with single bunch detection, e.g. single photon counting, detection of rare events, etc). Due to the particular time structure of the XFEL a laser with 1 MHz repetition rate gains a factor of 600 compared to a 10 Hz operation.

Assuming the timing stability of the laser to FEL pulses within a bunch train is better than the pulse duration, with a high repetition rate laser the pump-probe data can be summed over the bunch train and signal-to-noise can be enhanced for single bunch laser operations. Another method to enhance the signal relative to background or drifts is the “lock in” technique: e.g. the laser operates at 1 MHz repetition rate while the FEL produces pulses at 2 MHz, thus, only each second x-ray pulse is combined with a laser pulse, allowing detection of the difference between laser on and off – despite noise. Further, a high repetition rate allows (with a specially designed synchronisation unit) fast scanning of the delay within a bunch train (complete pump-probe experiment within one bunch train).

The requested parameters are: pulse duration: ≤50 fs (FWHM), pulse energy 0.1 to 3 mJ for a repetition rate ≥100 kHz, preferentially 1 – 5 MHz.

### *6.5.3.2 Creation of the optical laser systems*

**General considerations**

The laser systems should be based on commercially available solutions wherever possible. This provides reliable and well tested systems with the availability of fast assistance with severe hardware problems by service contracts with the vendor. Thus, downtimes can be minimised and the XFEL laser operating group can concentrate on the experiment support rather than laser repair. However, as shown below not all experimental requirements can be met by commercial laser systems. In particular, for the high repetition rate laser, an R&D project will be needed to enhance burst mode type lasers (as used at the FLASH facility, for example **[6-403]**).

**Technical configuration of the short pulse oscillator**

The front-end of the laser system will consist of an ultra-short-pulse laser oscillator meeting high synchronisation, stability (especially pointing stability) and reliability demands. The pulses from this oscillator will be used to seed two different amplifier chains (high repetition rate and high intensity). Since the demands on the synchronisation and stability require a considerable effort, it seems advisable to use only one well synchronised oscillator (for each laser laboratory, see below) to seed all amplifiers. It will be easier to tailor the oscillator parameters (bandwidth, beam diameter, etc.) to seed both amplifiers compared to the operation of two synchronised and stabilised oscillators.

The use of Titanium:Sapphire as laser material is a well established technique for the generation of ultra-short pulses – down to few-cycle pulses **[6-404]**. Using a piezo actuator in the cavity and appropriate feedback electronics, synchronisation to an RF-signal with a few femtoseconds accuracy can be achieved **[6-405]**. However, a Ti:Sapphire oscillator has several disadvantages: an expensive pump laser is needed and spatial drifts are observed since the cavity consists of many mechanical components. The upper level lifetime of Titanium:Sapphire is only 3 µs, thus, noise below 300 kHz will be amplified. However, the piezo control of the cavity length can only regulate up to several kHz. Therefore, in the frequency range from 10 to 200 kHz (currently) no control is possible.

The alternative to a Titanium:Sapphire oscillator is a fibre laser oscillator (e.g. Er-doped fibre) having several advantages over a Titanium:Sapphire oscillator: (i) high spatial stability (single mode fibre); (ii) no high quality pump laser needed; (iii) compact setup; (iv) long lifetime of upper laser level (Er: 8 ms), thus, it is less sensitive to noise. Using electro-optical modulators in the fibre laser oscillator, feedback frequencies up to 230 kHz were demonstrated **[6-406]**. Fibre lasers operating in the telecommunication band C have a wavelength in the range 1,530 – 1,560 nm. The second harmonic of such an oscillator can be directly used to seed a Titanium:Sapphire amplifier.

Currently, the bandwidth achieved with fibre lasers is not sufficient for the laser parameters demanded by the experiments, on the other hand, the development in the field is progressing extremely fast. Sub-50 fs oscillators can be purchased **[6-407]** and research is ongoing **[6-408]**. It is expected that in the next few years, fibre lasers with a

pulse duration of well below 30 fs will be available. However, R&D is necessary to adapt this kind of laser as the front-end of the pump-probe laser system.

**Technical configuration of ultra-fast medium high pulse energy amplifier**

For 10 Hz, high power TW-class laser systems a number of commercial solutions are available. Typical parameters of these lasers are 30 - 50 fs pulse duration with pulse energies between tens of millijoules and several joules (maximum commercially available pulse energy at the moment: 5 J **[6-409]**). Such laser systems are based on the principle of chirped pulse amplification. The short pulses from the oscillator are chirped in a grating arrangement, amplified first in a regenerative Titanium:Sapphire amplifier to millijoule energy level and subsequently amplified with a multipass Titanium:Sapphire amplifier to joule energy level. Finally, the pulses are compressed in a second grating arrangement to nearly their original pulse duration. In order to avoid self-focusing in air and non-linear effects while coupling the intense beam through a window flange into the experimental chamber, for pulses with peak powers exceeding ~10 TW, the compressor (spatial extent: ~ $3m^2$) will be located in vacuum close to the experimental chamber.

For the generation of pulses in the millijoule energy range, one can take advantage of the modular structure of the amplification chains and utilise pulses from the preamplifier stages. For that purpose it is recommended to have a separate, small compressor (in air). The modular construction of this kind of laser also permits the use of the uncompressed pulse which, in case of the 5 J/30 fs version, can provide up to 10 J with a pulse duration of roughly 1 ns (FWHM) for high energy density experiments.

Systems with the described architecture can provide pulse-to-pulse stabilities of 2% rms, pre-pulse contrast of $1:10^5$ and ASE $1:10^8$ for almost diffraction limited transversal beam profile (M2<1.5) **[6-409]**. For even better pre-pulse contrasts, OPCPA or SHG-stages might be added; however, these are no longer commercially available **[6-410]**.

**Technical configuration of the high repetition rate amplifier**

There is a strong user demand to use a highly repetitive laser system, capable of delivering more than one laser pulse during a bunch train. Commercial systems at repetition rates of up to 300 kHz providing 4 µJ pulses within 60 fs pulse duration are available **[6-411]**. However, the pulse energies as well as the repetition rate are rather far from the optimal specifications. It cannot be expected that the commercially available specifications will improve considerably in the next few years. Higher pulse energies are essential for many experiments. A system delivering 1 mJ pulse energies at 1 MHz repetition rate would result in 1 kW optical power which, even if technically feasible, causes tremendous operational expense; this is very hard to justify, since only 0.6% of the produced pulses can be used, as a result of the linac time structure. The problem can be elegantly approached using a laser system which operates in a pulsed burst mode. However, such a laser will not be commercially available. The pump-probe laser system at FLASH, designed and built by the Max-Born-Institute utilises an upgraded copy of the FLASH photocathode laser to pump two OPAs stages amplifying 100 fs pulses to pulse energies of 30 µJ at 1 MHz repetition rate (for a maximum of 800 pulses within 800 µs) **[6-403]**. The pulse energy can be significantly enhanced by reducing the repetition rate; thus, it is perfectly suitable for a large class of experiments.

Within an R&D project this type of laser could be redesigned and upgraded to provide sub-50 fs pulses with an energy of up to 1 mJ at 1 MHz. The pulse energy of the pump laser has to be increased (in comparison to the FLASH pump-probe (PP)-laser) and the amplified bandwidth has to be increased (e.g. by non-collinear OPA geometry **[6-412]**). Concepts utilising cavity-enhancement, relaxing the demands for pumping lasers, should also be pursued **[6-413]**.

### Technical configuration of the 100 J class laser

A laser generating sub-nanosecond pulses with 100 J energy is not commercially available at the moment. However, lasers with similar specifications are in operation or in development in research laboratories. The architecture of such laser systems consists of a front-end, generating femtosecond or picosecond pulses followed by a stretcher that brings the pulse duration to nanoseconds. In a preamplifier (regenerative and multipass amplifier) the energy of the pulses is increased into the upper millijoule range. With several single pass amplifiers separated by vacuum spatial filters the energy is finally brought to the final value. The technical effort for the power amplifier is considerable because of thermal problems in the laser medium. For the same reason a repetition rate of only some 10 mHz is possible. Based on reports of existing laser systems with similar specifications the space, requirement can be estimated to be more than 50 $m^2$.

In comparison to the above laser systems, a 100 J-class laser must be regarded as rather special equipment for a limited group of experiments. It will likely be used only in connection with one of the XFEL beamlines. Therefore, the optimal technical solution is to arrange the laser system in close proximity to the scientific instrument. This also has the benefit of an easier beam transport. In consequence, this laser system should be regarded as part of the instrument using this laser. In view of the effort and the related cost, a close connection with the user community will be required for design, R&D and commissioning of this laser system.

### Beam modification and frequency conversion modules

To widen the applicability of the laser for spectroscopic experiments, a wide spectral range will be offered. OPAs can provide a spectral range from 0.2 to 20 µm with pulse durations < 40 fs (FWHM) and conversion efficiencies of > 30% at incident 800 nm pulse energies of 2-3 mJ. To ease the laser beam transport (i.e. requirements on the mirrors and relay imaging), the 800 nm beam would be distributed to the experimental end station, generating the broad spectrum in the experimental area. The remote controllability via computers which is, therefore, needed is already included in commercial systems **[6-414]**.

With adaptive optics a spatial beam shaping can be performed to reach high optical beam quality in the experiment, e.g. focusing to diffraction-limited diameters. The module must be located before the power amplifier. Such a device, integrated in a laser system, is currently not commercially available so R&D efforts will be necessary.

To tailor the temporal shape of the laser pulses (e.g. for plasma physics or “femto-chemistry” **[6-415]**) the pulses can be shaped in the spectral domain using spatial light

modulators. Such a module must be located at a point with low pulse power, i. e. before the stretcher. All components are commercially available; however, its creation within an amplifier chain demands R&D efforts.

**Laser installation**

First experience at FLASH shows that it will not be sufficient to have only one laser system of each type (high repetition rate and 10 Hz medium to high pulse energy). In order to satisfy the requests for pump-probe experiments from five XFEL beamlines, two laser systems of each type will be necessary. To have at least two lasers of each type is also recommended to increase availability and as a security reserve in case of technical failure.

**Arrangement of laser hutches relative to experimental stations**

Two separate laser hutches are planned at the end of experimental areas corresponding to the SASE 1 and U 2 beamlines. Each laser hutch will deliver the laser beams to the three adjacent experimental areas. In addition, a beamline connection between both hutches will be required to increase flexibility of beam distribution and future upgrades. It is planned to equip each laser hutch with one high repetition rate system (0.1 - 1 MHz, 30 -50 fs, 0.1 to 3 mJ depending on repetition rate) and with one medium to high pulse energy system. For one laser hutch it is planned to provide highest pulse energies (20-100 TW e.g. 1-5 J, 30 fs) with a 10 Hz repetition rate, whereas in the second laser hutch a 1 TW laser system providing 30 mJ and 30 fs pulse duration seems sufficient. Due to the modular design of such systems a later upgrade for the second laser to several joules of pulse energy is feasible.

**Space requirement**

Laboratory space of between 80 to 90 $m^2$ is required for each laser room containing the ultrashort-pulse oscillator and two amplifier systems, including synchronisation, diagnostic, storage and spare capacity for future applications and/or lasers from users (for long-term experiments). Furthermore, about 20% of the area should be earmarked for future upgrades (e.g. few cycle-lasers, energy upgrades, etc.).

### *6.5.3.3 Synchronisation*

The temporal resolution of pump-probe experiments using x-ray and laser pulses should be limited rather by the pulse duration of the x-ray pulse than by the jitter between the independent sources. Thus, a level of synchronisation in the order of a few tens of femtoseconds between laser and XFEL is required. The task is challenging but feasible according to current technology. Jitter below a few tens of femtoseconds would ensure stable temporal overlap (once found) between x-ray and optical pulses. This would tremendously ease the alignment of the pump-probe experiments, most of all processes occurring only during temporal overlap (e.g. sidebands in photoelectron spectroscopy as discussed in Section 6.3.2.2). However, it has been shown that even for large jitter (several hundred femtoseconds) it is possible to reach ~ 50 fs time resolution by measuring the jitter for each shot and sorting the measured pump-probe data after the experiment according to the jitter data **[6-402]**.

The distributed master-laser oscillator frequencies (available as optical pulse train and electronic RF signals) are stable within 10 fs (rms between 1 kHz and 10 MHz) (see Section 4.8). It has been shown that femtosecond laser oscillators (Titanium:Sapphire as well as fibre lasers) can be synchronised to an external (electronic RF) master frequency by controlling the cavity length by a piezo element driven by a phase-locked loop circuit, with an rms jitter better than 20 fs **[6-405, 6-406]**. Using the optically distributed femtosecond pulse from the master-laser oscillator, the synchronisation can be improved **[6-401]**. The schematics are shown in Figure 6.5.1. In principle, current technology can provide the desired stability. To simplify the synchronisation scheme and omit electronic circuits (potential sources for noise and drift) in the feedback, it may be worthwhile exploring techniques that are not well established, such as seeding amplifiers directly with the distributed master-laser oscillator pulses, or use these pulses to injection lock the local oscillators in the laser rooms. However, for future application (e.g. attosecond pulse options of the XFEL) pursuing alternative synchronisation schemes to further decrease remaining temporal jitter is strongly recommended. One approach is the use of a 5 fs laser pulse to create attosecond x-ray pulses due to energy modulation of the electron bunch **[6-416]**. Synchronising another few-cycle laser in the experimental area to the laser initiating the modulation, the jitter of the accelerator ceases and the synchronisation of the two few-cycle pulses defines the degree of synchronisation (see Section 4.8). Such an operation could eventually allow pump-probe measurements with a few femtosecond temporal resolution. Sweeping the delay between the two lasers within a bunch train (different delay for each micropulse in the bunch, so that a whole pump-probe experiment within a single bunch train is performed) even sub-femtosecond resolution might be possible (since mechanical vibrations are negligible during the 0.6 ms bunch train).

Other concepts such as the direct amplification of optical light produced by the accelerator (e.g. undulator transition radiation **[6-417]** dipole radiation or similar) will be tested at the FLASH facility (Proposal by M. Drescher, University of Hamburg). These experiments might well result in new ideas for alternative synchronisation methods for the XFEL as well.

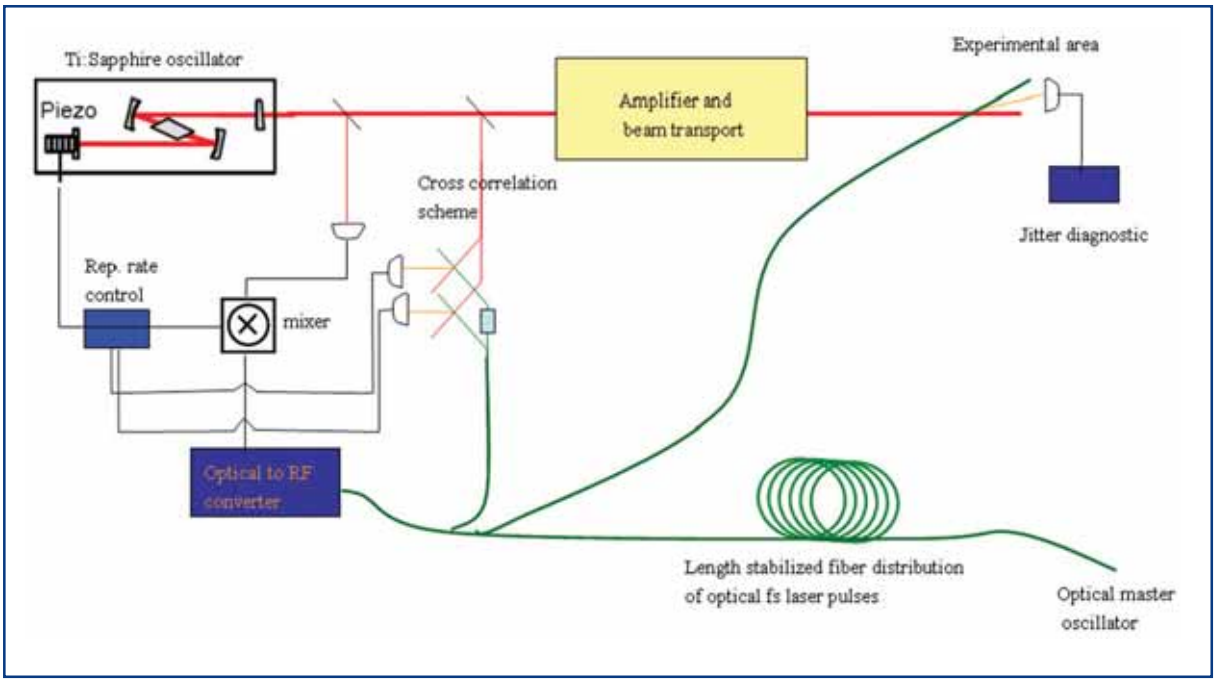


***Figure 6.5.1*** *The synchronisation scheme for the femtosecond-oscillator is shown, including jitter measurement at the experiment. Besides the basic RF-based synchronisation loop (left) the balanced cross-correlation scheme (middle; adapted from* **[6-401]***) is used to synchronise the repetition rate of the oscillator. The correlation setup in the experimental area (right) provides information about the jitter acquired by amplification and beam distribution.*

### Measurement of synchronisation

As observed at the FLASH facility, even if the laser used for pump-probe measurements is well synchronised with the master oscillator, timing drifts and even picosecond jumps might occur. Applying slight changes to the accelerator settings (e.g. RF-phases) results in significant changes in the arrival-time (several picoseconds) of the electron bunch at the undulator. Furthermore, timing jitter and drifts may occur during the amplification process within the laser system **[6-418]**, and due to the beam transport system from the laser hutch to the experimental end stations, located several tens of metres away (see Figure 6.5.1). Therefore, an online timing monitor is indispensable. To determine the contribution to the jitter due to the laser amplification and the beam transport, a single-shot cross-correlation setup is needed at the experimental end station. Here, the timing jitter between the master-laser oscillator pulses (a fibre distribution station located in the experimental hutches is envisaged) and the amplified laser pulses can be directly measured in the experimental area.

To determine the jitter between the electron bunches (which is a good measure of the arrival-time of the x-ray pulse within tens of femtoseconds **[6-402]**), a well established technique like the electro-optical sampling, correlating optical laser pulses with the electric field of the electron pulse, can be utilised. Results at FLASH and at SPPS at Stanford Linear Accelerator Center (SLAC) **[6-402]** show a time resolution of about 50 fs for the arrival-time of the electrons with respect to the laser pulses. At the XFEL, an electro-optic sampling station in front of the undulators, driven by the optical femtosecond

pulses from the master-laser oscillator will provide information on timing jitter between electron bunches and the master-laser oscillator. The timing difference between pump-probe laser and master-laser oscillator is continuously monitored and regulated as described above. In addition, phase pickup coils can provide timing information on the electron arrival-time with respect to the master-laser oscillator with a precision of ~20 fs (see Section 4.8.2.5) These two systems (electro-optical sampling and phase pickups) will provide timing information on a 50 fs level for the arrival-time of the electrons at the undulator in a non-invasive way for each electron bunch.

In addition, it is important to characterise the timing jitter of the pump-probe facility unambiguously between x-ray pulse and optical laser pulse in the experimental station for each pulse. A number of experiments can provide single-shot timing information between x-ray and optical pulses: non-thermal melting in single-shot geometry **[6-398]**, Auger electron sideband spectroscopy and spatially resolved photoelectron sideband spectroscopy (see Section 6.3.2.2). These experiments will be valuable tools in the commissioning and operation phases. Depending on the results, a permanent installation of such an experiment in the experimental area might be necessary.

### *6.5.3.4 Beam transport to instruments, characterisation and control*

**Laser beamlines**

An evacuated system of beamlines is needed to deliver the laser pulses from the laser hutch to the experimental hutches. Using relay imaging techniques to reduce spatial jitter of the laser beam at the experiment, intermediate focusing of the beam is required. As focusing optics, mirrors should be preferred because of the smaller B-integral. Focusing the intense beams in air, non-linear spectral broadening and self-focusing might occur. Thus, the beamlines should be evacuated at least to backing pressure. To avoid too many optical components in the experimental area, the pulse compression for the “low power” lasers will take place in the laser hutches. In order to keep the beam size in reasonable diameters (~ 30 mm FWHM) the 20-100 TW beam will be transported temporally stretched. The compression to 30 fs pulse duration will take place in a vacuum compressor located in the experimental area.

The space requirements for vacuum pipes (63 mm diameter), switching mirrors, supports etc. from the laser hutch to the adjacent three experimental areas has to be included in the early planning of the layout. One additional beamline connecting the two laser laboratories is also foreseen.

**Remote controllability**

The experience at the pump-probe laser of the FLASH facility shows that a high degree of remote controllability is necessary to provide the user with all necessary variable parameters (delay, pulse energy, pulse duration, polarisation, etc.) to be changed without the attendance of a laser operator.

**Diagnostics**

A profound characterisation of the laser parameters at the instruments is mandatory to perform well defined experiments. Thus, besides the online measurement of the pulse energy, spectrum and beam profile and position, devices will be required to monitor the pulse duration and pulse front tilt (e.g. using a GRENOUILLE **[6-419]**) as well as the synchronisation (see above).

**Safety installation**

For automatic safety surveillance, two separate monitoring systems will be used. One system ensures the compliance with laser safety regulations (personnel interlock) and the second monitors critical conditions or dangerous states in the laser system (technical safety interlock). Both systems are based on the SPS-technology. The interlock systems must be characterised by the following main features:

**Person interlock**:

- double door entrance, independent emergency exit;
- main power of all laser units is switched off in case of breaking any safety condition;
- laser safety installation at the experimental places and in beam distribution.

**Technical safety interlock**:

- prevention of faulty operation;
- interlock SPS is connected with the computer-based remote control system of the laser.

#### *6.5.3.5 Auxiliary requirements*

According to the experiences with FLASH, the laser hutches should be air-conditioned within 1K, and furthermore, flow boxes producing filtered dust-free and temperature-regulated air flow at the laser tables are required, at least for the oscillator and the amplifiers. They allow temperature stabilisation to 0.1 K on the laser tables and will supply a clean environment for the amplifiers (avoiding optical damages due to dust). The regulation of the temperature to 0.1 K at the laser table is required since larger temperature fluctuations cause thermal expansion which in turn induces temporal drifts.

Since the laser hutches at the experimental area are devoted to user experiments, it will be necessary to provide additional laser laboratories for maintenance work and small scale R&D.

### 6.5.4 Detectors and requirements

#### *6.5.4.1 Introduction*

It is clear that optimum use of the unprecedented capabilities of the European XFEL calls for a dedicated and substantial detector development programme. This was acknowledged by the Scientific and Technical Issues working group in its interim report of January 2005

(see its Annex 5.1: “Dedicated detector development programme”). The detector development programme for the XFEL will pursue various approaches, including (but not limited to) sub-picosecond x-ray streak cameras combined with crystal spectrometers, particle detectors (for electrons, ions and clusters) and 0-D, 1-D and 2-D x-ray photon detectors. Each system will be constructed in a dedicated project, while at the same time being an integral part of the overall detector development programme as well as an integral part of the scientific application development programme. Such a matrix-like approach will guarantee that the developed detectors will fulfil the requirements of the scientific applications, that there is cross-fertilisation between the projects and unnecessary duplication is avoided. To achieve this, the European XFEL project will have a sufficiently large detector group that takes upon itself a central coordinating role. It will be assisted and steered by an International Detector Advisory Board. This Detector Advisory Board will be convened at the earliest possible date.

One of the reasons to push the SASE process to 12 keV (0.1nm), is to be able to determine the structure of samples down to atomic resolution. This means that for the imaging experiments, one has to sample very finely (up to 4k×4k sampling points as explained below), and for scattering experiments one has to go to high scattering angles (up to $2\theta = \pm 60$ degrees). This means large detectors with many pixels. By using state-of-the technology art and dedicated, multi-national, development programmes, such detectors will be constructed over the next five years.

A number of further characteristics of the XFEL have direct consequences for the detectors to be used in the experiments. For example: the peak brilliance beyond $10^{33}$ ph/s/mrad$^2$/mm$^2$/0.1% BW will result in the fact that certain experiments are “single-shot” experiments. This means that all the data needed for the experiment has to be recorded for every pulse. A consequence is that “integrating” detectors is the only option (all photons arrive at once) and one cannot use “photon counting” nor “energy dispersive” detectors. Since one still needs “single photon sensitivity” (see below), special developments are called for. Furthermore, since every pulse is a new experiment, all the detectors involved in the experiment will have to be read out and the data stored before the next pulse arrives, very much like the mode of operation of High Energy Physics experiments. This means that to get the most from the high repetition rate enabled by the super-conducting technology of the linac, certain detectors will be constructed with sampling (framing) times down to 200 ns, and others with storage capacities of up to 3,000 samples (frames). It is clear that such detectors do not exist today. State of the art detector and micro-electronics technology will be used in dedicated detector development programmes, in order to construct such detectors within the next five years.

This section presents the requirements imposed by the experiments as well as an overview of the current detector technology that will be used to construct the detectors. It also contains the outcome of a two-day workshop on: “Detectors for the XFEL”, held in Abingdon, UK on the 28$^{th}$ and 29$^{th}$ of March 2006, and organised jointly between the CCLRC and the XFEL project team. This detector workshop was the fourth and last in a series of workshops. The three previous meetings were focused on scientific applications at the European XFEL. The requirements for detectors provided by these applications

workshops were then condensed into a document: “Draft Requirements for 2-D Detectors for the European XFEL”. A first draft of this document was circulated amongst German detector laboratories and discussed during a one-day workshop on the 17th February 2006. As a result a modified draft was produced and circulated to the participants of the workshop in Abingdon two weeks ahead of the meeting. In the preparation phase, a delegation from CCLRC, including detector experts, visited Hamburg on the 20th of September and the 15th of December 2005.

Since the biggest demand for new types of detectors is in the field of 2-D hard x-ray photon detectors, this was chosen as the main focus during the starting phase. However, it is well understood that a similar start-up process will be initiated before the end of 2006 for other systems as well. In particular, there is a need for fast x-ray streak cameras, new kinds of particle detectors (electrons, ions and clusters), soft energy detectors as well as generic detectors for all stations such as photon beam intensity, position and timing detectors. Any detector development for this project will be more widely applicable to other sources, particularly FELs, but also storage ring sources (see also section: “Links to other FEL projects”).

This section on detectors starts with a description of the detector requirements for each scientific application. Some of the requirements have already been mentioned in the specific sections on the applications. This is followed by an outline of the strategy foreseen for the developments, which consists of a two stage approach. The layout of phase one is then presented: the technology to be used for day-one operation and an outline of the research needed to reach optimum performance. At the end the preliminary programme for the start-up of phase-one and overall milestones are presented.

### *6.5.4.2 Experimental requirements*

**General**

In what follows, an overview is given of the major detector systems required for each scientific area. The first two areas, SQS and HED, require particle detectors and x-ray streak cameras, respectively. The area of x-ray absorption spectroscopy needs either a 0-D or a 1-D x-ray photon detector (depending on the mode of operation). The other areas (coherent x-ray diffraction, single particle and bio-molecules, femtosecond diffraction experiments and XPCS) all need 2-D x-ray photon detectors as their main detector. It is clear that the optimum detector differs from application to application, and the individual requirements will be discussed in the next sections. A few requirements are common to all 2-D x-ray photon detectors. They all need “photon-counting-statistics” (Poisson) limited resolution. This is very important for the low intensity regions in the image where the difference between zero and one photon can be crucial for the successful interpretation of the data. They all have to be sufficiently radiation hard to withstand the fluxes generated (integrated dose) for a few years. It is, at this moment, not possible to give hard numbers of the required radiation tolerances, since it depends, crucially, on the mode of operation of the experiments, but integrated doses at the SASE stations can be expected to be comparable to integrated doses at current day storage rings. It is obvious that Detective Quantum Efficiencies (DQE) should be as high as possible. Again, giving hard

numbers is not possible at the moment, since it depends on the details of the experiments. Some experiments will just take longer with a low DQE detector, whereas others become unfeasible. The x-ray photon energy range will be either between 8 and 12 keV for the hard x-ray SASE stations, or between 0.8 and 3 keV for the soft x-ray SASE station(s). Since the detectors will be operated in "integration mode", electronic pulse height analyses cannot be used to do harmonic rejection. If higher harmonic rejection is important, this has to be done by optical means, like mirrors or multi-layers.

An important issue for all detector systems is the number of frames per second and minimum framing time. The European XFEL will use superconducting linac technology, which allows for a high repetition rate, a characteristic that distinguishes the European XFEL from the other XFEL projects. For instance, the European XFEL will produce up to 30 000 pulses per second as compared to 120 for the LCLS. Therefore, for certain experiments, the crucial parameter will be to record as many images per second as possible, this would call for a "luminosity optimised" detector. For other experiments (for instance studies of exponentially decaying excited states) it is more important to be able to collect a limited number of frames, but with a minimum framing time of 200 ns (the minimum bunch spacing), at least at the beginning of the decay. Such experiments call for a "timing-optimised" detector. Ideally, the detector would record all 30,000 images per second.

A brief summary of the detector requirements per scientific application is given below. As stated above, in this first phase the focus is 2-D x-ray photon detectors. Subsequent phases will be needed to define in more detail the needs of other systems.

### Small quantum systems

The area of "small quantum systems" studies the interaction between the x-ray pulses and atoms, molecules and small clusters. The x-ray pulse will create highly charged particles and/or result in photo-fragmentation. After the interaction, the resulting particles are detected and their state analysed. Therefore, the main requirement is for fast particle detectors with drastically increased detection rates. The requirements for the detectors as well as the limitations of the existing detectors during the XFEL operation are difficult to extrapolate from existing experiments. A lot of experience is currently being gained at FLASH and the weak points of existing systems analysed. Since the initial focus is on 2D-x-ray photon detectors, the requirements for the particle detectors as well as the need for new developments will be detailed and analysed in the fourth quarter of 2006.

### High energy density

The HED community studies the plasmas produced through the interaction between a laser pulse (XFEL and/or visible light) and a specific target. The XFEL is used either as pump and probe via a beam-splitter or just as a probe. One of the main signals to detect is the time-dependent fluorescence of the plasma, which calls for the development of an ultra-fast XSC to be used in conjunction with an x-ray spectrometer. Such an XSC can also be used as a timing diagnostic tool of the XFEL beam itself. The XFEL will provide pulses with time durations of about 100 fs which would make it possible to study magnetisation dynamics. Therefore, one needs an XCS which has a time resolution of

100 fs or better. Nowadays, XSCs only have a time resolution of ~300 fs or worse and in addition are limited in detection efficiency due to their design **[6-420]**.

XCSs are based on photon-electron conversion where electrons emitted by a photocathode are extracted, then synchronously deflected by sweep plates, and finally are imaged by a suitable electron detector system. In this way the temporal information is transformed into spatial information.

In order to get a reliable and highly efficient XSC with time resolution of ≤100 fs, R&D in the following fields will be preformed:

- First, one has to understand how the photocathode limits the time resolution and the efficiency and how one can improve and optimise both properties. The main problem is that the secondary electrons emitted by the cathode have a finite non-zero energy width **[6-421]**.
- The second field is the question of electron optics and how this is limiting the time resolution of the camera. There are suggestions for an isochronous design **[6-422]** but this needs further investigation and up to now, no such camera has been built because of the complicated design.
- The question of space charge has to be investigated because it is the fundamental limit to the temporal resolution of streak cameras, especially when operated at high electron densities.
- Another field is the design of the sweep plates and the electrical sweep pulse which has to match the velocity of the electron beam in order to get high sweep sensitivity.
- The question of synchronisation and the jitter problem associated with the GaAs photo switch, which is primarily caused by laser intensity fluctuations has to be addressed **[6-423, 6-424]**.
- Last but not least one has to find the optimal detection system to 2-D image the electron beam. All these questions need to be solved in order to get a reliable and highly efficient XSC with time resolution of ≤100 fs.

The XFEL project will benefit from the fact that the comparable project LCLS at Stanford, USA, has the same requirement and need for such a camera system. The results of ongoing programmes in the USA will show if this path results in a detector system that shows the required performance. The XFEL project will initiate a similar detector development programme in Europe and join the American efforts of developing an ultra-fast x-ray detector with high efficiency which has the time resolution of ≤100 fs.

### Coherent x-ray diffraction imaging

In the experiment, the sample is illuminated by the coherent XFEL beam and diffraction images are recorded. The detector required to do this is a large 2-D x-ray photon detector.

In order to resolve structures down to an atomic resolution of 0.1 nm, using x-ray radiation of 0.1 nm, the detector has to span 120° (±60°). At the same time if one wants to study objects as large as 1,000 nm with a resolution of 0.2 nm we need 20,000 pixels in each direction (assuming a minimum over-sampling by a factor 2). This means an angular resolution of 120°/20,000 = 0.006°, or 0.1 mrad. An initial compromise could be a (movable) detector that only covers one quadrant of reciprocal space, giving a require-ment of 10,000×10,000 pixels. Since the detector area will only be sparsely populated with diffraction spots, a desirable mode of operation is to have the option of on the fly reconfigurable regions of interests (ROIs).

Single photon sensitivity is needed for the low flux regions of the image, for high flux regions the limitation should be counting statistics. It is expected that up to $10^4$ photons per pulse per pixel will be generated in the most intense parts, with an overall integrated count rate of $10^7$ photons per pulse.

It is foreseeable that certain experiments want a “luminosity-optimised” detector (as many images per second as possible) and others a “timing-optimised” detector (200 ns framing time).

### X-ray Photon Correlation Spectroscopy

Photon correlation spectroscopy analyses the temporal changes in a speckle pattern that are related to the sample’s equilibrium or non-equilibrium dynamics. The method operates in the far-field and takes advantage of the coherence properties of the beam. Data are taken in either sequential mode (with the accessible time windows determined by the time structure of the machine), in “split-pulse” mode giving access to fast (picosecond-nanosecond) dynamics (and requiring a delay-line device) or in “pump-probe” mode requiring a pump pulse. Experiments want to take advantage of as many bunches as possible.

The pixel size $D_p$ must be equal or smaller than the speckle size $D_s$ ($D_p \leq D_s$). The angular speckle size, $\theta_s$, is given by:

$$\theta_s = \frac{\lambda}{D_b}, \tag{6.11}$$

where $\lambda$ is the wavelength, and $D_b$ the size of the utilised (transversely coherent) beam. $D_b$ can, in principle, be chosen as big as the transverse coherence length $\xi_t$ and since the beam is expected to be spatially fully coherent, $\xi_t$ can be as big as the full uncollimated beam. The usable beam size is, however, limited by the ability to resolve the speckle pattern within a reasonable sample-to-detector distance $L$. To resolve the speckle, the incident beam size $D_b$ should not be larger than the speckle size at the detector. This yields:

$$D_b = \sqrt{\lambda L}, \tag{6.12}$$

For $\lambda$=0.1 nm and $L$ = 20 m the beam size should not exceed 45 µm. For these parameters the minimum speckle size is $D_s$ = 45 µm, and the required pixel size $D_p \leq D_s$. Larger pixel sizes would lead to lower contrast in the speckle pattern.

We see that the smaller the incident beam size, the larger the speckles. However, heat load and sampling volume put a lower limit on the focal spot sizes to be used. A realistic lower limit to the beam size is 25 μm. Using an x-ray wavelength, λ=0.1 nm, we get:

$$\theta_s = \frac{1\times10^{-10}}{25\times10^{-6}} = 4\mu rad\ , \tag{6.13}$$

For a detector distance of 20 m one finds a maximum pixel size of 80 μm. Taking this as an upper bound, one would require angular pixel sizes $(\lambda/L)^{1/2} \le \theta_p \le 4$ μrad. There are two types of experiments that have different requirements for the angular range of the detector: first, small angle scattering, looking at longer length scales, and second, single crystal diffraction, looking at the shorter length scales (down to atomic resolution).

In the case of single crystalline samples one gets distinct diffraction spots all the way out to a scattering angle of 60°. Since one might be interested in only a few diffraction spots one does not have to cover the full scattering range, which would mean 120 degrees at a distance of 20 m! However, one could move a smaller 2-D detector to the diffraction spots. It is foreseen that ten diffraction spots have to be covered simultaneously, thus, ten of these smaller area detectors are needed. The detector module defined for the small angle scattering experiment is then sufficient for the single crystal experiment.

The detector size needed for the small angle scattering experiment is determined by the minimum length scale we want to observe. If we want to see details down to 10 nm using 0.1 nm radiation, we need to go out to a scattering angle of 0.6 degrees, meaning 1.2° in total (21 mrad). With an angular resolution of 4 μrad, one would need 5,000 pixels in each direction.

However, if one does not use a monochromator to increase the monochromaticity and with that the longitudinal coherence length (see below) one will be limited in angular range by the fact that the Path Length Difference (PLD) of the various rays hitting a pixel has to be smaller than the longitudinal coherence length, which is given by:

$$\xi_1 = \frac{\lambda^2}{\Delta\lambda}. \tag{6.14}$$

The natural monochromaticity $\Delta\lambda=10^{-3}\times\lambda$, gives $\xi_l=10^3\times\lambda$ and for λ=0.1 nm radiation we get $\xi_l$=100 nm. It can be shown geometrically that the PLD is given by:

$$PLD = 2W\sin(\theta)^2 + D\sin(2\theta). \tag{6.15}$$

where W is the thickness of the sample and D is size of the beam. For typical values for sample thickness of 1 mm, beam size of 25 μm, longitudinal coherence length of 100 nm, maximum scattering angle of 0.10 degrees, corresponding to 0.2 degrees (3.5 mrad) detector coverage, with 4 μrad resolution leads to a requirement of 875 pixels. This means a 1K×1K detector, which should be the basic building block.

Tiling several of these 1K×1K detector modules together would allow one to cover SAXS pattern with length-scales down to 10 nm (in which case, one has to use a monochromator to increase the longitudinal coherence length). Therefore, a good strategy is to build a basic building block with 1K×1K pixels, to be tiled to a 5K×5K imager.

The maximum intensity per pixel per pulse is ≤1,000 photons. Single photon sensitivity is needed at low intensities; this means the counting statistics will be limited.

### X-ray absorption spectroscopy

The fast pulse structure of the electron beam of the XFEL accelerator makes it ideally suited to performing time-resolved x-ray spectroscopy. There are two possible modes of operation.

*Mode 1*

**Stepped energy scan.** With a suitable variable gap undulator and crystal monochromator it is possible to make "conventional" stepped scan spectroscopy measurements. Obviously, the system under study would have to be capable of being reproduced in its starting configuration for each point in the scan, e.g. in a pump-probe experiment. In this mode the sample could be extremely dilute and the fluorescence signal measured by an energy-dispersive detector array. Time-resolved measurements in the 1 ms to 100 ms regime can be done purely using the bunch structure; however, this domain can also be accessed by other SR sources. Timing measurements using the 100 fs bunches can still be made in this configuration if single pulse macro bunches are selected, and then the 100 fs-100 ms regime can be explored. This will require ionisation chambers that can deal with the instantaneous flux without losing linearity. For dilute samples, fluorescence detection or Auger electron detectors are required. The main challenges here centre on the instantaneous flux: conventional energy dispersive detectors will suffer massive pile-up; therefore, new and special signal processing electronics will be built to overcome these limitations.

*Mode 2*

**Energy dispersive.** A bent crystal monochromator can be used to produce a focused, but angularly dispersed, beam at the sample. The beam is transmitted through the sample on to a position sensitive detector which now records the entire range of energies simultaneously. The position sensitive detector would need 1,000 channels, be charge integrating and capable of being read out in the time between the 100 fs pulses, i.e. at 5 MHz. Again, it would be possible to have the pulse train incompletely filled: if one 100 fs pulse per bunch was selected, this would allow the 100 fs to 100 ms regime to be accessed and relax the readout time requirement of the detector. The best detectors currently available based on Silicon microstrip technology only operate at speeds up to 10 μs. Considerable development will take place to increase their speed, if this mode of operation is retained.

The advantage of the dispersive configuration is that all points in the spectrum are recorded simultaneously and time slices can be recorded at the maximum framing rate of the detector. This is a much more efficient means of data collection than the step-scanning mode, but requires a higher concentration of the element whose absorption edge is being studied, as the sample absorption is measured in transmission rather than by an indirect process such as x-ray fluorescence or Auger emission.

### Femtosecond diffraction experiments

From a detector perspective, this field can be separated into two domains which have very different requirements, especially concerning the spatial resolution: non-crystalline and crystalline samples.

### Pump-probe scattering experiments on non-crystalline samples

A sample, typically in solution, is promoted to a “pumped” state by a pump pulse (e.g. a visible laser, magnetic or electric field, XFEL or other pulse) and analysed after time $\Delta t$ with an XFEL bunch. Samples are in solution, which means that the scattered signal is (nearly) circularly symmetric, and the scattering intensity is slowly varying as a function of momentum transfer (scattering angle).

In this experiment, the form of the scattered signal is determined by the sample rather than by the source (except of course for the intensity). Therefore, we can base our requirements on existing experiments on storage ring sources.

In this pump-probe experiment one compares a pumped (excited) state with the un-pumped (ground) state. Simulations on for instance $I_2$ dissociation show that changes down to length scales of 0.065 nm are significant and can be measured. This means a scattering angle 2q=100° is needed (using 0.1 nm radiation) and the detector has to cover ±100°. In liquid scattering this is often expressed in a Q-range where, Q=4psin (q)/ $\lambda$, and the detector has to cover up to Q=10 $Å^{-1}$.

The experiments will look at the changes in only a few inter-atomic distances. One can show that for small changes in inter-atomic distance we get approximately five oscillations in the Q range between 0 and 10 $Å^{-1}$. For large changes (rupture of molecules) we get approximately 10 oscillations. Since we only probe a few changes, a sampling with 250 points over the entire Q range is sufficient, even if we get up to 20 oscillations. This gives 500 sampling points (positive and negative scattering angles) per direction. Corresponding to an angular resolution of 200/500=0.4° (=7 mrad).

We need to measure small changes in large signals. Therefore, counting statistics-limited resolution is needed. Based on the experience gained at the ESRF we can extrapolate to the European XFEL (which has $10^2$ times the number of x-rays per bunch), giving a maximum of $10^4$ photons per pixel per pulse, and an overall integrated flux of $10^7$ photons per pulse.

It is conceivable that experiments requiring as many pulses per second as possible to be recorded and thus, need a “luminosity” optimised detector. Other experiments will want to sample the time evolution of the system with a “timing optimised” detector (200 ns time resolution, at least in the beginning).

### Pump-probe scattering experiments on crystalline samples

Again, the sample, either a powder or a single crystal, is promoted to a “pumped” state and analysed after time $\Delta t$ with an XFEL pulse. Samples will give Bragg peaks, meaning localised intense spots on a low intensity background in the case of single crystals, or “Bragg-rings” (powder rings) meaning spotty (intense) rings on a low intensity background.

The angular resolution required is defined by both the size of the Bragg spots and the number of spots we want to measure (separation between the Bragg spots). The first one is independent of the distance between sample and detector (parallel beam), the second one scales linearly with detector distance.

The size of the Bragg spots is defined by a convolution of the mosaicity of the sample, the monochromaticity and divergence of the beam, and the size of the focal spot (or the size of the sample, whichever is the smallest). Assuming a static sample (in 100 fs, macroscopic matter cannot move), and $\Delta E/E=10^{-3}$ the Bragg spot size is basically defined by the beam size on the sample (divergence of the beam is a few µrad). Assume an intermediate focal spot size of a 100 µm (FWHM), then the Bragg spots will also be 100 µm (FWHM) on the detector, no matter what the detector distance is. This gives approximately 300 µm FW1%M. We want to be able to resolve 1,000 diffraction spots across the detector, giving a detector size of 300 mm. For 0.1 nm radiation, and a resolving power down to 0.1 nm, we have to measure out to $2\theta=\pm 60°$, which defines the sample to detector distance to be: L = 150/tan(60) = 85 mm. In summary: we need 3K×3K pixels of 100 µm. It is no surprise that detectors of this type are currently used at storage rings for protein crystallography.

Single photon sensitivity is needed for low flux; for high flux the limitation should be counting statistics. Based on the experience at the ESRF ($1.4\times10^{10}$ photons per pulse), we can estimate a maximum of $10^5$ photons per pulse per pixel at the European XFEL (~$10^{12}$ photons per pulse). The overall integrated intensity is expected to be in the order of $10^7$ photons per pulse.

It is conceivable that experiments requiring as many pulses per second to be recorded, or that experiments want to sample the time evolution of the system (200 ns time resolution, at least in the beginning), although in this case sample heating will be a major obstacle.

**Single particles and bio-molecules**

The so-called “single molecule diffraction” involves the recording of speckle patterns in the far field. Phase retrieval by “oversampling” requires very fine detector resolution, where the achievable structural resolution is determined by the maximum accessible momentum transfer (requiring a large detector).

Again, the detector has to span 120° (±60°). In order to solve structures as large as 100 nm (a large virus for example) down to atomic resolution, we need 4,000 pixels in each direction (assuming a minimum oversampling by a factor of 2). This means an angular resolution of 120°/4,000 = 0.03°, or 0.5 mrad. The sample to detector distance should be minimised and should be evacuated, since anything between the sample and the detector (even the residual molecules in a vacuum) will increase the background.

Another important aspect is the ability to collect scattering of even the very small angles, close to the primary beam. This means that for a small sample to detector distance. the primary beam stop might create too much shadowing. Therefore, the option to have two detectors has been discussed. The first, close to the sample, collects large angle scattering and has a central hole to let the small angle part of the scattering pattern pass

to the second detectors. This small angle part is then collected by a second detector at a much larger distance. The option of two detectors is also advantageous as it increases the dynamic range of the detector system.

Single photon sensitivity is needed for the low intensity regions of the image; for high intensity regions the limitation should be counting statistics. It is expected that up to $10^4$ photons per pulse per pixel will be generated in the most intense part (small angles). An overall scattered flux of $10^7$ photons per pulse is expected. Since the intense x-ray pulse will destroy the single particle (Coulomb explosion), time is needed for the residuals to be pumped away ("the smoke has to clear"), therefore, the foreseen repetition rate is 10 Hz. The detector has to be housed inside a vacuum chamber, although a thin entrance window could be considered for protection of the detector.

**Hard x-ray by spontaneous radiation**

The last field of applications is concerned with the use of hard x-rays up to 100 keV from spontaneous radiation. Two main advantages of this source over existing (SR) sources are the short pulse length and the low emittance. To fully exploit the potential of these sources, detectors with high efficiency at high energies will be constructed. It is clear that the main challenge will be in developing high-Z detector materials. Materials like GaAs and CdZnTe are promising candidates. Since the focus of the initial phase is one 2-D x-ray photon, detectors for the 8-12 keV range, the requirements and for the high energy detectors will be detailed in the first part of 2007.

### *6.5.4.3 Strategy*

**Two-phase approach**

The detector requirements imposed by the experiments, and listed above, present a major challenge for detector builders. At the same time, several potential solutions exist by using today's state-of-the-art technology, as will be shown further on. It is important to realise that Europe has a strong background and experience in building large scale detection systems, stimulated by high energy physics, space research as well as SR research. As a result, Europe holds a world leading position in many areas relevant to the detectors needed for the European XFEL, including, but not limited to, Silicon drift detectors, hybrid pixel detectors, monolithic active pixel sensors, high density inter-connects, and deep sub-micron chip design. There are various laboratories throughout Europe that have specialised in either specific detector components or complete detector systems. Also, there already exists a number of collaborations between laboratories providing complementary expertise. The European XFEL will stimulate the formation of consortia that will be able to supply detector systems on day one of the XFEL operation that meet most, if not all, of the requirements. Prototypes of such detectors will be ready when the LCLS is coming on-line. Besides starting the development and subsequent construction of the detectors for the first experiments using state-of-the-art technology as soon as possible, it is also crucial to initiate a research programme into detector technologies in order to arrive at uncompromised performances in the future.

Since the XFEL will produce SASE radiation in both the hard (8-12 keV) and the soft (0.8–3 keV) x-ray range, and since many applications intend to use both, it is mandatory that x-ray detectors are developed for both energy ranges. The situation is further complicated by the fact that the spontaneous emission undulators will produce very hard x-rays, well above 100 keV. An initial focus will be put on the 8-12 keV energy range, at the same time enough flexibility will be built into the detector systems, to make them applicable to the lower and higher x-ray energies as well, possibly with somewhat compromised performances. In a second phase, research will be initiated to optimise the detector systems for the lower and higher x-ray energies, this includes, but is not limited to, the development of detector materials different than Silicon, like GaAs and CdZnTe.

Experience has shown that both the planned experiments and the requirements quickly evolve in the first years of the project (new ideas, better defined ideas, etc.). We will, therefore, proceed in at least two phases (see also Table 6.5.1):

- **Phase 1:** Define, design and construct the detectors for day-one operation of the XFEL, using (optimised) current state-of-the-art technology, and based on the requirements imposed by the currently planned experiments.
- **Phase 2:** Define, design and construct the optimised (“ideal”) detectors using the experience gained from the construction and operation of day-one systems, using new detector technologies, using the experience gained at other sources (like FLASH and the LCLS) and based on new and better defined requirements (new experiments).

Phase 1 will advance in various steps (partly in parallel):

- Step one: 2-D x-ray photon detectors;
- Step two: 0-D and 1-D x-ray photon detectors;
- Step three: x-ray streak cameras;
- Step four: particle detectors (electrons, ions, atoms and clusters);
- Step five: generic detector research.

This phase has already started with the dedicated workshop on “Detectors for the XFEL”, following the three scientific application workshops. The first step of Phase 1 focuses on the requirement for 2-D x-ray detectors, judged to be the area requiring most efforts. As indicated at the end of this chapter, the requirements are currently being detailed via an interaction between detector builders and application scientists. A call for propositions to construct the required 2-D x-ray detectors will be launched before the summer of 2006. The exact format of the call (call for proposals, pre-proposals, letters of interest, etc.) is currently being decided upon. The deadline for replies will be 15 September 2006, after which a selection will be made before the end of 2006. The consortia retained in the selection will then be asked to prepare a detailed project plan. At this stage a strong interaction with the relevant application scientists will be needed. It is anticipated that the application scientists will be part of the consortium building the detector(s). To guide this process, a Detector Advisory Board will be convened as soon as possible.

**Link to other FEL projects**

Because the XFEL, operating at 5MHz, places the most severe demands on the detectors, the developed systems will naturally be applicable at many other FEL or SR x-ray sources. In addition, with appropriate modification, applications can be found for the XFEL detectors on other, lower energy XUV/VUV FELs, both existing and planned, elsewhere in the world.

It is important to consider the other major XFEL facility, LCLS, currently under development in the USA, which will be in operation before XFEL. The formal link already existing between the LCLS project and DESY will be extended to the XFEL GmbH once it comes into existence and starts detector activities. The European detector laboratories already have good informal links with the American project and access to this facility for detector testing will be available. Although LCLS will have a very different pulse structure, it will be an important test bed for XFEL detector systems. Appropriate detector technologies will be exchanged between the USA and Europe. It is worth pointing out that the ESRF running in 16-bunch mode produces 176 ns spaced x-ray pulses, close to the 200 ns of the XFEL. Therefore, access to the ESRF for timing issues-related studies will be very beneficial. Access to FLASH for testing components, in particular timing-related issues is foreseen at an early stage.

### *6.5.4.4 Design and construction of 2D-systems in Phase 1*

In what follows an overview is given of the technologies that will be used to construct the Phase 1 2-D x-ray detectors. As stated before, there exists a lot of experience within the European detector community in constructing such systems for real experiments, be it synchrotron radiation, particle physics or space research. Examples will be given of systems that have been developed or are under development and their shortcomings for the XFEL applications will be discussed, indicating the fields where developments are needed. The examples given are by no means exhaustive, and the omission of certain projects and developments means neither a judgement about their importance nor about their applicability to the XFEL requirements. Also, the fact that a specific project is quoted here indicates neither any pre-selection nor preference for the XFEL project. The selection of the most suited technologies and competitive consortia will be made via a fair and open competition.

**Hybrid pixel array detectors**

One of the technologies very likely to be used for one or more of the 2D-detector systems is hybrid pixel array detectors (PADs). A hybrid PAD consists of a detector layer which is an array of photo diodes that converts the incoming x-ray to electrons and holes. This detector layer is then coupled, via bump-bonds, to a pixellated readout chip (application specific integrated circuit, or ASIC). Each pixel contains its own signal processing electronics as well as a buffer to store the data. The device is schematically given in Figure 6.5.2.

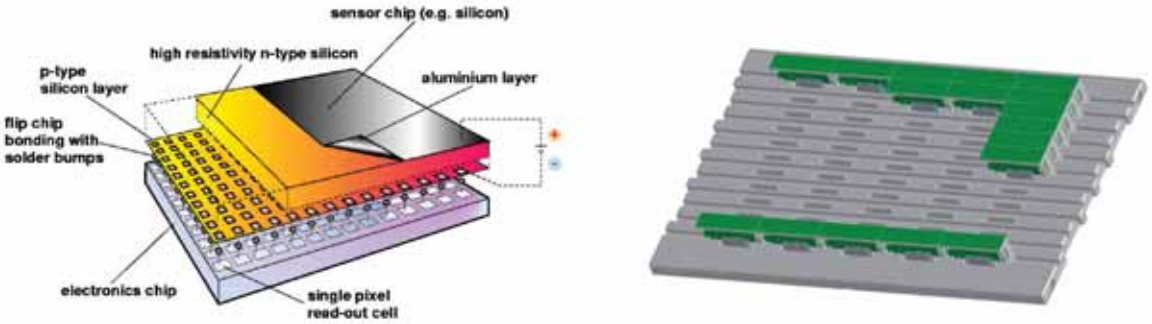


***Figure 6.5.2*** *Left: Schematic layout of a hybrid PAD (Courtesy: M. Campbell). Right: PILATUS 6M module containing 17 of total 60 modules. The total detector will have 6 million pixels, and will almost be 45×45 cm² (Courtesy of Ch. Broennimann* **[6-425]***).*

One of the advantages of hybrid PADs is that the sensor layer and the electronics chip can be optimised separately. In this way it is possible, for instance, to design a single electronic chip and to couple it to different sensor chips optimised for different x-ray energies, either by using different thicknesses of Silicon, or different materials like GaAs or CZT. A lot of experience for using these hybrid PADs has been gained over the past years through the various projects like: MEDIPIX, PILATUS, XPAD, APAD, etc. The first three are European projects and use photon counting. APAD is an American project (CHESS) using integrating chips. For the XFEL applications, new electronic chips will be designed, using very low-noise integrating electronics, with storage capacities of a few hundred frames or more. The APAD chip, for example, can store only eight consecutive frames. This will be done in the newest CMOS technologies (0.13 micron) and using radiation tolerant designs (like ring-gate transistors). The individual modules given in Figure 6.5.2 will then be assembled into large systems similar to the PILATUS project at SLS/PSI, (also shown).

### Silicon drift detectors (SDDs)

The semi-conductor drift chamber invented in 1984 by Gatti and Rehak, uses a sideward drift principle, which allows for the use of small read-out anodes, having small capacitance, even for large area detectors. This small capacitance results in a very low-noise device, with excellent spectroscopic performance. Many devices have since been constructed based on this drift principle, and Fano-limited performance has been reached in multi-element devices **[6-426]**. The very low noise performance of these systems can be used to obtain single photon sensitivity, an important requirement for the imaging experiments at the XFEL. Since all photons arrive in 100 fs, energy discrimination (spectroscopy) inside the detector is not possible. However, the spectroscopic performance of the detector can be used to tell the number of monochromatic photons absorbed, giving counting statistics limited performance. Furthermore, by keeping drift lengths small, 5 MHz framing rates are technically possible. A very promising system is the controlled drift detector (CDD) with DEPFET readout and running in continuous readout mode (non-controlled mode). A schematic layout is given in the Figure 6.5.3.

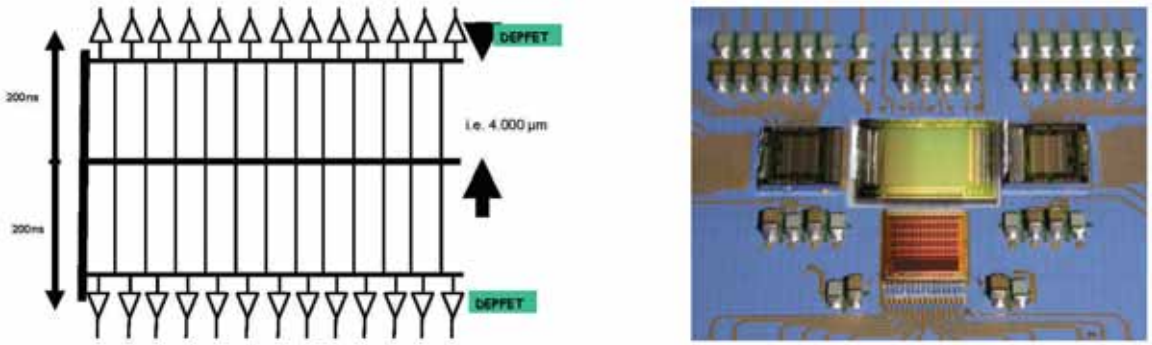


***Figure 6.5.3*** *Left: schematic layout of a CDD detector with DEPFET readout allowing 200 ns framing time. (Courtesy of L. Strüder). Right: operational CDD detector with front-end read-out electronics. (Courtesy of L. Strüder).*

Such detector modules will be coupled with ASICs for readout and frame storage. By using the most advanced CMOS technology (0.13 µm) and possible 3-D interconnects it looks possible to store ultimately 3,000 frames, although this might not be reachable for the day-one detectors. The drift detector principle described above has been used several times in detectors for high energy physics as well as for space research. A picture of an actually operational device is given in the right part of Figure 6.5.3.

**Column parallel CCDs**

Very fast CCDs are currently in development for particle physics applications such as the linear collider. There, customised CCDs are being developed that readout each column of the sensor in a parallel fashion, increasing the frame rate by orders of magnitude. Prototype custom CCDs have been built that bump-bond directly to high density readout ASICs down one readout edge of the CCD. This means that rather than read out the CCDs through one or more corner, each column has a dedicated output and is instrumented with its own amplifier and analogue to digital converters (ADC). In this arrangement charge is shifted from the CCD into the readout ASIC where it is measured and stored. The standard CMOS technology in the readout ASIC provides excellent matching and accurate charge-to-voltage conversion. Bump-bonding of the ASIC to the CCD means that the pitches of ~20 µm can easily be achieved and the low parasitic capacitance of the bonds minimises the noise performance penalty of interconnect load.

Figure 6.5.4 illustrates the concept. The picture on the left shows a schematic of the imaging surface of the CCD. Each column is clocked in parallel and samples converted at the bottom of each column. The image on the right shows a readout ASIC (in blue) bump-bonded to the CCD where the image is captured. These designs are currently highly optimised for the linear collider flavour identification (LCFI) application. If this concept is retained for one of the applications at the XFEL, they will be adapted to cope with increased dynamic range and modified to match the XFEL timing structure.

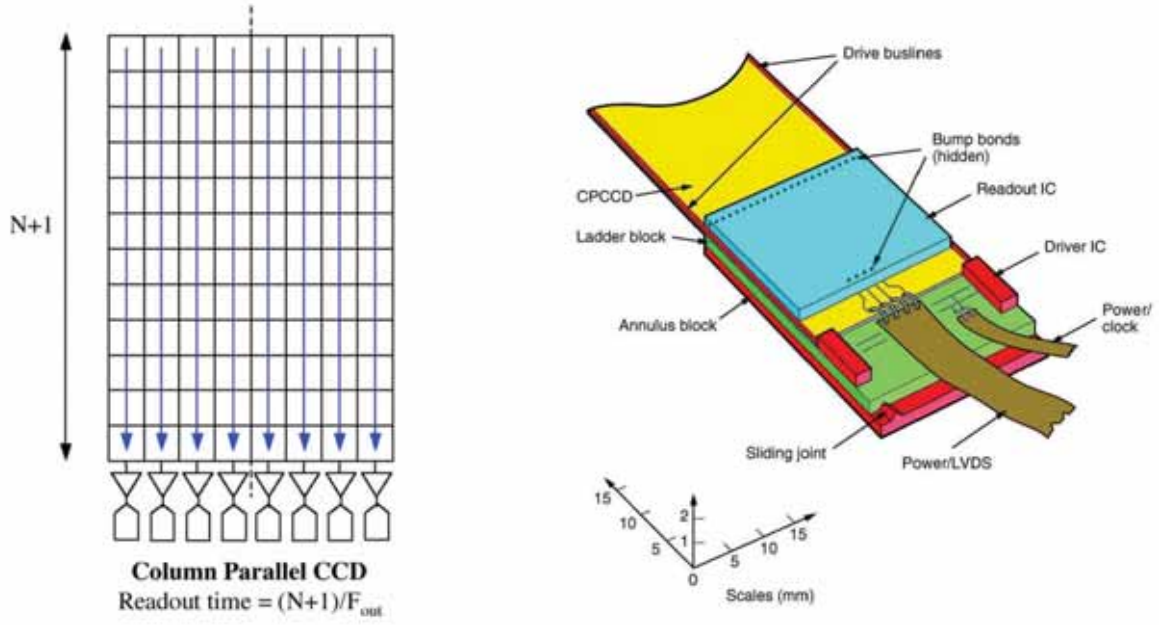


***Figure 6.5.4*** *Image showing a column parallel CCD (left) with bump-bonded readout (right) ASIC (courtesy of LCFI).*

### MAPS

Monolithic active pixel sensors (MAPS) were proposed as imaging devices over 10 years ago **[6-427, 6-428]**. They are manufactured in a standard microelectronics technology (mainly CMOS) and integrate the sensor elements in the readout ASIC. It was immediately recognised that they have several advantages with respect to existing imaging devices in terms of feature-size, integration of functionality, radiation resistance, power consumption, ease of use and low cost. Today, MAPS have overtaken CCDs as the main imaging devices for commercial applications and are now being adapted for x-ray detection, for example in intraoral dental sensors. The demonstration of their excellent performance as particle detectors triggered a world-wide development of MAPS for scientific applications. In the last few years a number of large sensors have been designed and manufactured, including a 12 million pixel device with 5 µm pixels for EUV detection and a 1 ½-D sensor with 32 µm pixels for x-ray detection **[6-429]** (Figure 6.5.5).

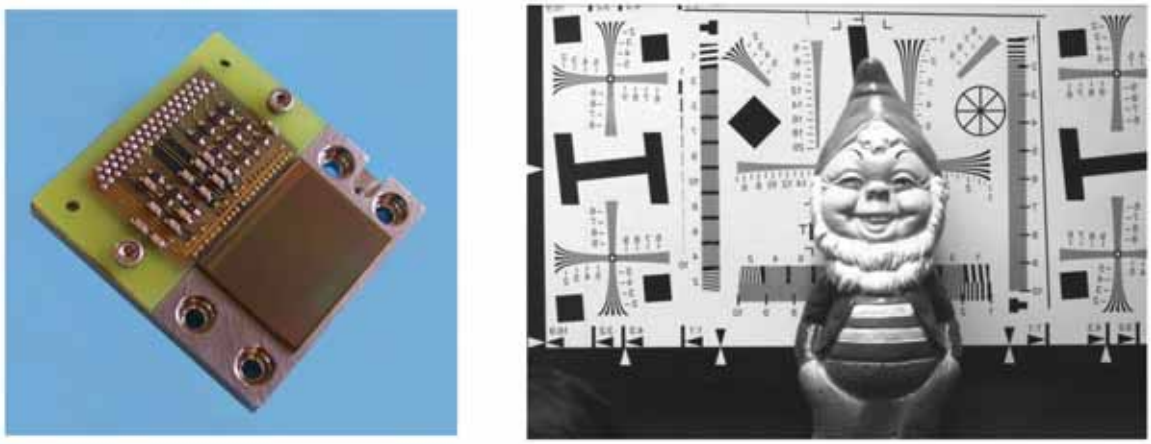

***Figure 6.5.5*** *Left: Photo of 12M-pixel MAPS mounted on invar block (for cooling). Right: Image taken with this sensor (courtesy of N. Waltham, M. Prydderch).*

For x-ray detection, high efficiency can be achieved by coupling to a scintillator or with a suitable directly deposited high-Z material. Alternatively, a stack of sensors can be arranged to achieve high efficiency together with energy information. High spatial resolution can then be achieved with small pixels and very high time resolution integrated by adopting architectures already developed for high-energy physics experiments: the flexible active pixel sensor (FAPS), capable of frame rates in excess of 10 MHz by storing signals inside the pixel **[6-430]**. Such a sensor with 20-µm pixel and 10 storage cells was already successfully demonstrated and the technology could be scaled up for the needs of XFEL (see Figure 6.5.6). The feasibility of this approach for the XFEL applications, as well as the advantages and disadvantages as compared to other technologies will be evaluated during the third quarter of 2006.

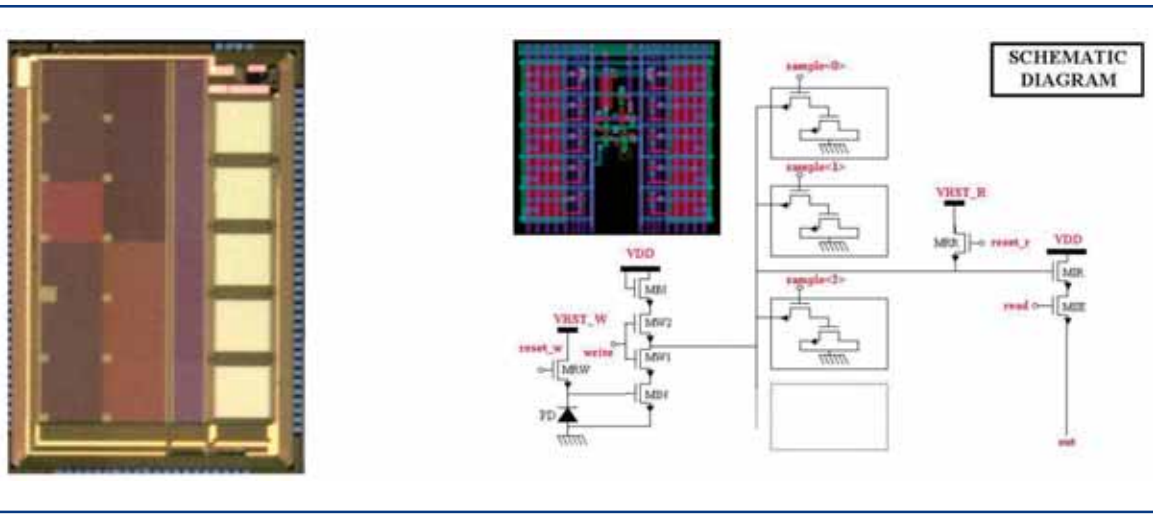


***Figure 6.5.6*** *Left: Photo of FAPS prototype. Right: schematic of the FAPS pixel (courtesy of R. Turchetta).*

### *6.5.4.5 R&D of new 2-D system components in Phase 1*

The above detectors for day-one operation will be built based around proven technologies and materials to keep risk levels at a manageable level and provide a reliable initial solution. However, to realise the full potential of the XFEL, a step change in sensor performance is required in many areas. This parallel programme of technology development is required to underpin the building activity and to develop ways of breaking through existing performance limits.

For most detector systems Silicon is likely to be the material of choice for the conversion of 5 keV to 15 keV photons. However, this choice raises some immediate concerns:

**Efficiency**

To be effective above 12 keV it must be used in thick layers (>500 μm) to achieve sufficient stopping power. This leads to parallax errors for tiled surfaces due to uncertainty in conversion depth for abnormal incident photons. This worsens the point spread function and will become severe at high angles.

**Radiation damage**

Whilst x-rays in this energy range will not cause any bulk damage to Silicon, interface layers on the detector surface and in the ASICs will give rise to problems. Charge build-up at these interfaces will disturb the ASIC transistors and, in the sensor material, will ultimately modulate the bias conditions of the sensor.

**Scattering**

One of Silicon's great strength is that high position resolution can be achieved by patterning the material with pixels and strips to achieve segmented layouts. However, scattering will occur at the ~0.01% level (for 1 keV photons in Silicon) and the scattered photons will stray from bright spots affecting data quality in low count rate regions.

**High signal flux**

At high energy densities, fields in Silicon will affect the usual charge collection process: Self-repulsion of the converted charge will broaden the signal image and possibly shield sensor areas, thereby disturbing the local detector bias conditions.

Other sensor materials offer ways of managing some of these issues but challenges exist in making these solutions useable. High-Z materials are one area that should be investigated. This is because high-Z direct conversion semiconductor materials are extremely efficient detectors in this spectral region. For example: 50 μm of CZT stops 98% of 12 keV photons, i.e. more than 10 times better than Silicon. This should deliver low parallax even in small pixel geometries (e.g. 50×50 $\mu m^2$) as well as providing excellent stopping power to protect ASIC electronics behind the detector. In addition, as these materials do not posses oxide interface layers of their own they should be extremely radiation hard in this environment. The potential for thinner layers also minimises the effects of photon scattering as the scattered photons will be efficiently stopped locally. Fields in the device, however, are still likely to be disturbed and this

remains a potentially serious problem. In summary, thin layers of materials such as CZT, GaAs, HgI and CdTe have the potential to be efficient, radiation hard detectors matching the performance requirements of the XFEL and high density readout electronics well.

Instrumentation of the sensor material, be it Silicon or high-Z in form, will always require ASICs matched to the detector substrates. These must sense, amplify and process the image data for handling in the DAQ system. Various groups building LHC particle physics detectors have demonstrated that radiation hard ASICs can be built using standard CMOS technology with a feature size of 0.25 µm and lower, provided various layout precautions are taken **[6-431]**. From a technology perspective solutions, therefore, exist. However, each new detector system still requires ASIC development as existing photon counting systems (e.g. Pilatus or Medipix) will not be appropriate because of the pulsed multi-photon structure of the machine. Specific designs suited to the XFEL sensors and tailored to the experiments will have to be developed. In addition, as the form of radiation differs significantly from that studied for particle physics, a qualification of technologies used for exposed environments will also be needed.

The sensor material must then connect via reliable interconnect technology to front-end ASICs that will form the first stage of the DAQ system. Depending on the format and geometry of the sensors, interconnects will either be wire- or bump-bond-based. Again, significant experience exists, particularly in particle physics and SR community. However, new developments enable so-called 3-D stacking or integration to allow stacking of multiple chips on top of each other. If applied, this technology will have to be mastered and adapted for the XFEL detectors.

Data processing in the front-end system raises further concerns as, for example, sensors of 4K×4K pixels, running at 30,000 frames per second with high dynamic range images will produce very large volumes of data. This will have to be processed efficiently and assembled into data sets for offline storage and analysis. Extensive use of fibre-optic systems will ease data transport, however, efficient computing systems will still be required to capture and analyse the experimental data. The bunched nature of the beam structure will necessitate on-detector storage to buffer the data flowing to DAQ.

Synchronising the detector systems to the FEL bunch structure also presents challenges. It is very important to be able to reliably separate the data from each 100 fs pulse so that records can be assembled from each detector system for combined experimental techniques. Systems such as the TTC system, developed at CERN **[6-432]** for the distribution of event clocks, can be used, but detectors that require accurate timing to better than 100 fs will still require local synchronisation. Local sensing of the pulse train, for example, from local beam monitors, will, therefore, be required to lock on to the data correctly. In addition, identifying ‘out-of-time’ events will also be needed to flag error data in the system for discarding.

Finally, because of the large volumes of data involved, data reduction is inevitable for the DAQ system. This means that frames of interest must be rapidly identified and tagged for transmission to off-line storage. The algorithms for achieving this are required as well as the hardware to deliver it. This will lead to complexities as, for example, fluorescence life-

time in scintillators (if significant compared to 200 ns) will have to be deconvolved from earlier data frames that might be rejected by the system (and therefore, impossible to reconstruct).

In summary there are several generic development areas which need to be addressed:

- Radiation damage studies of Silicon and high-Z direct conversion semiconductor detectors. This is required to establish the scale of the problem with modern Silicon technologies and define which materials can be used.
- Interconnection and deposition techniques for thin layers of high-Z materials. This is critical for delivering systems matched to the XFEL. Most high-Z materials are used in large volumes in thick blocks for high energy applications; here, the driver is for more efficient, thinner layers.
- The investigation of carrier transport in thin layers of high-Z materials. This will be required to develop accurate mathematical models of detector systems, so that replacements for Silicon systems can be modelled accurately and their relative benefits estimated.
- The investigation of high energy density deposition in materials and subsequent carrier transport, specifically looking at self shielding carrier drift (due to charge cloud repulsion), and diode and ohmic contact performance in high charge collection situations.
- Microelectronics design optimised for fine pixel geometries and integrating architectures. The performance of modern CMOS systems needs to be evaluated in the radiation environments expected at the XFEL.
- Some standardisation of the DAQ system must be defined with a view to understanding how the experiments will synchronise, process and transmit their data to offline storage.

#### *6.5.4.6 Data acquisition, handling and storage*

It is important to define clearly and at an early stage what comprises the detector system. Does the detector system includes everything up to the data storage, or only up to the digital output? No matter where the line between “detector” and “instrument control” is drawn, it is important to consider the detector as an integral part of the experiment. Therefore, a close and direct link between the detector builders and the experiment software control systems is important from the very first stages of the project. This is crucially important since the detectors will be capable of producing enormous amounts of data which have to be reduced, stored and ultimately processed. Equally important is the interfacing with the rest of the experiment, since a large fraction of the experiments will be triggered and single-shot measurements. Experience at large scale facilities has shown that a unified approach to instrument control, including detectors, greatly simplifies and improves the operation. This means, where possible, standardised interfaces and protocols.

### 6.5.4.7 *Preliminary programme for start up of Phase 1*

Table 6.5.1 below indicates a first draft of a timeline to start Phase 1 detector construction and research. This proposed timeline is to be considered as a first initiative to start discussions. Many issues, technical, financial and administrative, have to be clarified to a sufficient degree before actual calls can be issued. But since the first operation of the XFEL is only six years away, it is crucial not to delay the start of detector projects any further.

| | |
|---|---|
| Step 1: 2-D X-ray Detectors (two-step procedure) | |
| May-2006 | Detailed Requirements |
| Jun-2006 | Launch first call |
| Sep-2006 | Deadline first call |
| Nov-2006 | Evaluation and selection proposals |
| Q2-2007 | Start projects |
| Step 2: 0-D and 1-D x-ray detectors (one step procedure) | |
| Q3-2006 | Detailed requirements |
| Q4-2006 | Launch call |
| Q1-2007 | Evaluation and selection proposals |
| Q2-2007 | Start projects |
| Step 3: X-ray streak cameras (one-step procedure) | |
| Q3-2006 | Detailed requirements |
| Q4-2006 | Launch call |
| Q1-2007 | Evaluation and selection proposals |
| Q2-2007 | Start projects |
| Step 4: Particle detectors (one-step procedure) | |
| Q4-2006 | Detailed requirements |
| Q1-2007 | Launch call |
| Q2-2007 | Evaluation and selection proposals |
| Q3-2007 | Start projects |
| Step 5: Generic detector research | |
| Q1-2007 | Definition of research areas |

***Table 6.5.1*** *Time line for Phase 1 actvities*

**Overall milestones**

There are a number of identifiable milestones for the detector projects even at this early stage, mostly set by the progress of the construction of the XFEL machine and availability of the LCLS in the USA.

| | |
|---|---|
| Q3/2006 | Installation of a detector advisory board (DAC) |
| Q4/2006 | Selection of Phase 1 detector projects |
| Q1/2007 | Establishment of XFEL detector group |
| 2009 | LCLS becomes available for detector testing |
| 2013 | Initial operation of the European XFEL |

## 6.6 Summary of cost and manpower requirements

The capital investment and cost of the personnel necessary to build the photon beamlines and 10 scientific instruments as described in the previous sections of this chapter, are summarised in this section. The basis for the cost estimate is the system layout and the parameters specified here. For an overview about the total project cost, a description of the methodology of the performed estimate for capital investment, the determination of the cost for personnel and the expected uncertainties, see Chapter 10.

Table 6.6.1 gives a summary of the project cost in terms of capital investment and the cost for personnel for the photon beamlines and scientific instruments. The relative distribution of the full cost is shown in Figure 6.6.1. The photon beamlines and scientific instruments contribute about 13% to the overall capital investment and more than 16% to the full project cost. Integrated over the entire construction phase, 779.5 full-time equivalents (FTE) are required for the photon beam system.

| | Capital Investment [M€] | Personnel Cost [M€] | Full Cost [M€] |
|---|---|---|---|
| Photon beamlines | 22.41 | 20.58 | 42.99 |
| Scientific instruments | 73.20 | 41.12 | 114.32 |
| **Total** | 95.61 | 61.70 | 157.31 |

***Table 6.6.1*** *Capital investment, personnel cost and full cost in Million-Euro for the photon beamlines and scientific instruments. Values are given for capital investment, personnel cost and full cost in Million-Euro.*

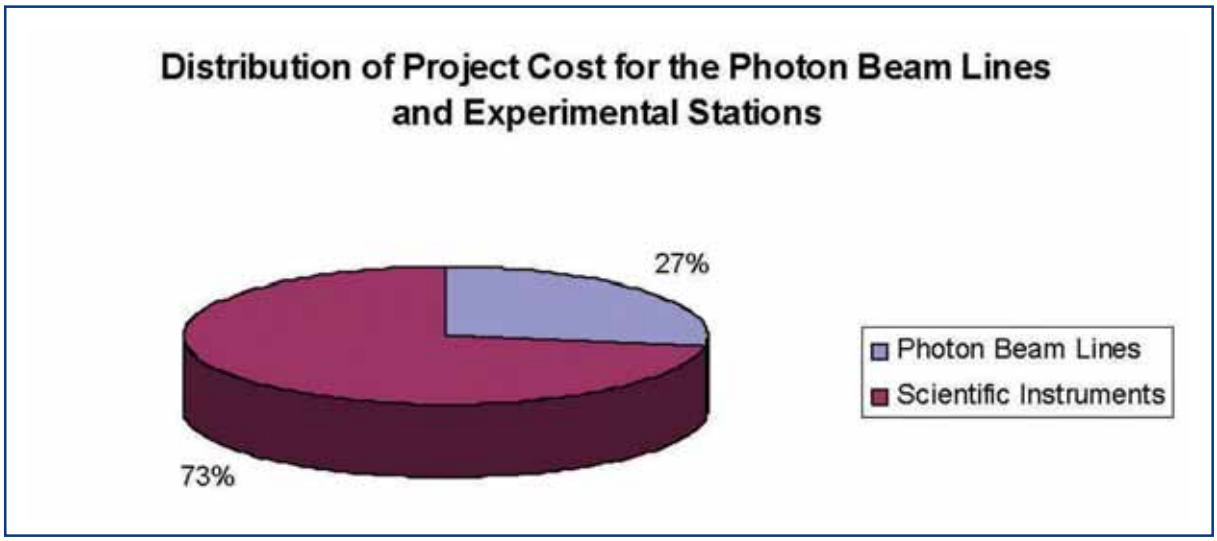


***Figure 6.6.1*** *Relative distribution of full project cost for the photon beamlines and scientific instruments.*

## Photon beamlines and scientific instruments

The cost summarised in Table 6.6.1 and Figure 6.6.1 include the cost and manpower of the following:

**Photon beamlines:** design, construction, installation and commissioning of the x-ray optics and vacuum systems installed in the photon beamlines; R&D for x-ray optics issues related to the experiment layout; design, construction, installation and commissioning of the photon beam diagnostic systems; R&D for photon diagnostics systems to be used at the scientific instruments;

**Scientific instruments:** design, construction, installation and commissioning of 10 scientific instruments in the experiments hall; R&D activities in the areas of sample environment and manipulation and optical laser installations; three full pixelated area detector systems; R&D on other detector systems (x-ray streak camera and particle detectors) and for conventional systems installed at the scientific instruments.

## References


**[6-1]** *LCLS-The First Experiments*, Stanford (2000), see also: http://www-ssrl.slac.stanford.edu/lcls/papers/LCLS_experiments_2.pdf

**[6-2]** TESLA Technical Design Report, eds. F. Richard et al., DESY 2001-011, DESY, Hamburg (2001).

**[6-3]** M.R. Howells, private communication (2006).

**[6-4]** M.R. Howells, *Optical designs and tolerances for the 8.3.1 protein crystallography beamline*, ALS technical note, LCBL-538, LBNL, Berkeley, (1999).

**[6-5]** S. Matsuyama et al., *Diffraction-limited two-dimensional hard-x-ray focusing at the 100 nm level using a Kirkpatrick-Baez mirror arrangement*, Rev. Sci. Instrum. 76 (2005) 083114.

**[6-6]** http://www-cxro.lbl.gov/

**[6-7]** J. Arthur et al., *Linac Coherent Light Source (LCLS) – Conceptual Design Report*, SLAC-R-593, SLAC, Stanford (2002).

**[6-8]** Workshop *Optics for x-ray FEL applications*, DESY, Hamburg, February (2006).

**[6-9]** G. Grübel, J. Als-Nielsen, A.K. Freund, *The TROIKA beamline at ESRF*, J. de Physique C9 (1994) C9-27.

**[6-10]** J. Hoszowska, A.K. Freund, E. Boller, J.P.F. Sellschop, G. Level, J. Härtwig, R.C. Burns, M. Rebak, J. Baruchel, *Characterization of synthetic diamond crystals by spatially resolved rocking curve measurements*, J. Phys. D: Appl. Phys. 34 (2001) A47.

**[6-11]** L. Zhang, A.K. Freund, T. Tschentscher, H. Schulte-Schrepping, *Performance studies of cryogenically cooled monochromator crystals for X-FELs*, SRI 2003 Conference, San Francisco, AIP Conf. Proc. 705 (2004) 639.

**[6-12]** D. Shastri, P. Zambianchi, D.M. Mills, *Femtosecond x-ray dynamical diffraction by perfect crystals*, SPIE proceedings Vol. 4143 (2000) 69.

**[6-13]** J.S. Wark, *Femtosecond X-ray diffraction: experiments and limits*, SPIE proceedings Vol. 4143 (2000) 26.

**[6-14]** W. Graeff, *Short X-ray pulses in a Laue-case crystal*, J. Synchrotron Rad. 9 (2002) 82.

**[6-15]** R. Follath, in *TESLA Technical Design Report Part V – The Free Electron Laser Laboratory*, G. Materlik, Th. Tschentscher (eds.), DESY 2001-011, DESY, Hamburg (2001) V-309.

**[6-16]** Jarre et al., *Two-Dimensional Hard X-Ray Beam Compression by Combined Focusing and Waveguide Optics*, Phys. Rev. Lett. 94 (2005) 074801.

**[6-17]** H. Mimura et al., *Hard X-ray diffraction-limited nanofocus with unprecedentedly accurate mirrors*, presented at the XRM2005 Conference, Himeji, Japan (2005).

**[6-18]** O. Hignette et al., *Focusing below 50 nm using dynamically-bent graded multilayers*, ESRF Highlights 2005, p. 108-109.

**[6-19]** C.G. Schroer et al., *Hard x-ray nanoprobe based on refractive x-ray lenses*, Appl. Phys. Lett. 87 (2005) 124103.

**[6-20]** W. Lun, B. Lai, Z. Cai, et al., *Nanometer focusing of hard x-rays by phase zone plates*, Rev. Sci. Instrum. 70 (1999) 2238.

**[6-21]** B. Nöhammer, C. David, M. Burghammer, C. Riekel, *Coherence-matched micro focusing of hard x-rays*, Applied Physics Letters 86 (2005) 163104.

**[6-22]** C.G. Schroer and B. Lengeler, *Focusing Hard X Rays to Nanometer Dimensions by Adiabatically Focusing Lenses*, Phys. Rev. Lett. 94 (2005) 054802.

**[6-23]** B. Nöhammer, J. Hoszowska, A.K. Freund, C. David, *Diamond planar refractive lenses for third- and fourth-generation X-ray sources*, J. Synchrotron Rad. 10 (2003) 168.

**[6-24]** C.G. Schroer, *Parabolic refractive lenses for the x-ray free-electron laser*, M. Kuhlmann, B. Benner, B. Lengeler, H. Schulte-Schrepping, A.A. Snigirev, I. Snigireva, SPIE proceedings Vol. 5534 (2004) 116.

**[6-25]** R. Bionta, in *Linac Coherent Light Source (LCLS) – Conceptual Design Report*, J. Arthur et al. (eds.), SLAC-R-593, SLAC, Stanford (2002), pages 9-3 – 9-5.

**[6-26]** Y.Y. Zhao, E.E. Alp, T.S. Toellner, W. Sturhahn, H. Sinn, D. Shu, *A water cooled compound refracting lens as a white beam collimator*, Rev. Sci. Instr. 73 (2002) 1611.

**[6-27]** B. Lengeler, *Coherence in X-ray physics*, Naturwissenschaften 88 (2001) 249.

**[6-28]** H.C. Kang, J. Maser, G. B. Stephenson, C. Liu, R. Conley, A. T. Macrander, S. Vogt, *Nanometer Linear Focusing of Hard X-Rays by a Multilayer Laue Lens*, Phys. Rev. Lett. 96 (2006) 127401.

**[6-29]** http://www.xradia.com/zpl_pd.htm

**[6-30]** E. DiFabrizio et al., *Differential Interference Contrast for X-ray Microscopy*, Surf. Rev. Lett. 9 (2002) 243.

**[6-31]** E. DiFabrizio et al., *Diffractive optical elements for differential interference contrast x-ray microscopy*, Optics Express 11 (2003) 2278.

**[6-32]** C. David, A. Souvorov, *High-efficiency Bragg–Fresnel lenses with 100 nm outermost zone width*, Rev. Sci. Instr. 70 (1999) 4168.

**[6-33]** U. Hahn, M. Rüter, *Hochleistungsstrahlverschluss- und Spaltsystem für Synchrotron-strahlung*, Deutsches Patent- und Markenamt, No. DE 101 35 307 C2, München (2001).

**[6-34]** R. Treusch et al., *Development of photon beam diagnostics for VUV radiation from a SASE FEL*, Nucl. Instr. Meth. A 445 (2000) 456.

**[6-35]** K. Tiedtke et al., *The SASE FEL at DESY: Photon Beam Diagnostics for the User Facility*, Proceedings SRI2003, San Francisco, AIP Conf. Proc. 705 (2004) 588.

**[6-36]** R. Treusch, *Photon Diagnostics for the VUV-FEL*, HASYLAB Annual Report 2005, DESY, Hamburg (2006) 159.

**[6-37]** A. Bytchkov et al., *Development of MCP-based photon diagnostics at the TESLA Test Facility at DESY*, Nucl. Instrum. and Meth. A 528 (2004) 254

**[6-38]** V. Ayvazyan et al., *Study of the statistical properties of the radiation from a VUV SASE FEL operating in the femtosecond regime*, Nucl. Instr. and Meth. A 507 (2003) 368.

**[6-39]** M. Wellhöfer, M. Martins, M. Richter, K. Tiedtke et al., *Photoelectron spectroscopy as non-invasive method to monitor SASE-FEL spectra*, in preparation.

**[6-40]** J. Feldhaus, E. Plönjes-Palm for the VUV-FEL team, *First user experiments at the VUV-FEL*, HASYLAB Annual Report 2005, DESY, Hamburg, (2006) 173.

**[6-41]** T. Weitkamp, B. Nöhammer, A. Diaz, C. David, E. Ziegler, *X-ray wavefront analysis and optics characterization with a grating interferometer*, Appl. Phys. Lett. 86 (2005) 054101.

**[6-42]** T. Weitkamp. J. Patommel, C. Schroer, et al., in preparation.

**[6-43]** L. Le Déroff, P. Salières, and B. Carré, *Beam-quality measurement of a focused high-order harmonic beam*, Opt. Lett. 23 (1998) 1544.

**[6-44]** D. Yoshitomi, T. Shimizu, T. Sekikawa, S. Watanabe, *Generation and focusing of submilliwatt-average-power 50-nm pulses by the fifth harmonic of a KrF laser*, Opt. Lett 27 (2002) 2170.

**[6-45]** C. Valentin et al., *Imaging and quality assessment of high-harmonic focal spots*, Opt. Lett. 28 (2003) 1049.

**[6-46]** H. Mashiko, A. Suda, K. Midorikawa, *Focusing coherent soft-x-ray radiation to a micrometer spot size with an intensity of $10^{14}$ W/cm$^2$*, Opt. Lett. 29 (2004) 1927.

**[6-47]** H. Mashiko, A. Suda and K. Midorikawa, *Focusing multiple high-order harmonics in the extreme-ultraviolet and soft-x-ray regions by a platinum coated ellipsoidal mirror*, Appl. Opt. 45 (2006) 573.

**[6-48]** A.A. Sorokin et al., *New method based on atomic photoionization for spot-size measurement on focused soft X-ray free-electron laser beams*, submitted for publication.

**[6-49]** M. Richter, A. Gottwald, U. Kroth, S.V. Bobashev, A.A. Sorokin, L.A. Shmaenok, J. Feldhaus, Ch. Gerth, and K. Tiedtke, Deutsches Patent- und Markenamt, No. 102 44 303.3, München (2002).

**[6-50]** M. Richter, A. Gottwald, U. Kroth, A.A. Sorokin, S.V. Bobashev, L.A. Shmaenok J. Feldhaus, Ch. Gerth, B. Steeg, K. Tiedtke, R. Treusch, *Measurement of gigawatt radiation pulses from a vacuum ultraviolet free electron laser*, Appl. Phys. Lett. 83 (2003) 2970.

**[6-51]** R. Klein et al., Synchrotron Radiation News 15 (2002) 23.

**[6-52]** K. Tiedtke, M. Richter, S. Moeller et al., in preparation.

**[6-53]** M. Krumrey and G. Ulm, Nucl. Instr. and Meth. A 467-468 (2001) 1175.

**[6-54]** A. Lindenberg et al., *Atomic-Scale Visualization of Inertial Dynamics*, Science 308 (2005) 392.

**[6-55]** M. Drescher, publication in preparation.

**[6-56]** R. Kienberger, to be published.

**[6-57]** F. Hornsta, *Residual gas ionization profile monitors for the HERA proton machines*, DESY HERA reports 87-25, DESY Hamburg (1987).

**[6-58]** P. Ilinski, U. Hahn, H. Schulte-Schrepping, K. Tiedtke, M. Sachwitz, *Residual Gas X-ray Beam Position Monitor for PETRA III*, HASYLAB Annual Report 2005, DESY, Hamburg (2006) 151.

**[6-59]** J.C. Weiskeit, Astrophys. J. 190 (1974) 785.

**[6-60]** R. Follath, *The versatility of collimated plane grating monochromators*, Nucl. Instr. Meth. A 467-468 (2001) 418.

**[6-61]** T. Ditmire et al., Nature 386 (1997) 54.

**[6-62]** Y.L. Shao, T. Ditmire, J.W.G. Tisch, E. Springate, J.P. Marangos, M.H.R. Hutchinson, *Multi-keV Electron Generation in the Interaction of Intense Laser Pulses with Xe Clusters*, Phys Rev Lett 77 (1996) 3343.

**[6-63]** V. Kumarappan, M. Krishnamurthy, D. Mathur, *Asymmetric emission of high-energy electrons in the two-dimensional hydrodynamic expansion of large xenon clusters irradiated by intense laser fields*, Phys. Rev. A 67 (2003) 043204.

**[6-64]** E. Springate, S.A. Aseyev, S. Zamith, M.J.J. Vrakking, *Electron kinetic energy measurements from laser irradiation of clusters*, Phys Rev A 68 (2003) 053201.

**[6-65]** H. Wabnitz et al., Nature 420 (2002) 486.

**[6-66]** S. Zamith, T. Martchenko, Y. Ni, S.A. Aseyev, H.G. Muller, M.J.J. Vrakking, *Control of the production of highly charged ions in femtosecond-laser cluster fragmentation*, Phys. Rev. A 70 (2002) 011201R.; C. Siedschlag, J.M. Rost, *Surface-plasma resonance in small rare-gas clusters by mixing ir and vuv laser pulses*, Phys. Rev. A 71 (2005) 031401R.

**[6-67]** P. Tzallas et al., *Direct Observation of Attosecond Light Bunching*, Nature 426 (2003) 267.

**[6-68]** P. Tzallas et al., *Second-order Autocorrelation Measurements of Attosecond XUV Pulse trains*, J. Mod. Opt. 52 (2005) 321.

**[6-69]** E. Goulielmakis et al., *A Dispersionless Michelson Interferometer for the Characterization of Attosecond Pulses*, Appl. Phys. B 74 (2002) 197.

**[6-70]** N.A. Papadogianis et al., *Temporal Characterization of Short-Pulse Third-Harmonic Generation in an Atomic Gas by a transmission Grating Michelson Interferometer*, Opt. Lett. 27 (2002) 1561.

**[6-71]** P. Emma et al., *Femtosecond and Subfemtosecond X-Ray Pulses from a Self-Amplified Spontaneous-Emission–Based Free-Electron Laser*, Phys. Rev. Lett. 92 (2004) 074801.

**[6-72]** H. Chapman, K. Nugent, *X-ray Pulse Compression Using Strained Crystals*, Optics Commun. 205 (2002) 351.

**[6-73]** U. Becker et al., reported at the Workshop on Ultrafast time-Resolved Soft X-ray Science, Berlin, 27-29 April (2005).

**[6-74]** *Connecting Quarks with the Cosmos: eleven science questions for the new century* National Academies Press (2003).

**[6-75]** *Frontiers in High energy density Physics - the X-games of contemporary science*, National Academies Press (2003).

**[6-76]** B. A. Remington, Plasma Phys. Control. Fusion 47 (2005) A191.

**[6-77]** P. Audebert, J.-P. Geindre, S. Rebibo, J.-C. Gauthier, *Direct observation of the ponderomotive force effects in short-scale-length laser plasmas by frequency-domain interferometry*, Phys. Rev. E 64 (2001) 056412.

**[6-78]** R. Shepherd et. al., JQSRT 71(2001) 711.

**[6-79]** M.W.C. Dharma-Wardana, F. Perrot, *Energy relaxation and the quasiequation of state of a dense two-temperature nonequilibrium plasma*, Phys. Rev. E 58 (1998) 3705.

**[6-80]** D. Riley, N.C. Woolsey, D. McSherry, I. Weaver, A. Djaoui, E. Nardi, *X-Ray Diffraction from a Dense Plasma*, Phys. Rev. Lett. 84 (2000) 1704.

**[6-81]** J.J. Angulo Gareta, D. Riley, submitted for publication (2006).

**[6-82]** S. Mazevet, J. Clerouin, V. Recoules, P.M. Anglade, G. Zerah, *Ab-Initio Simulations of the Optical Properties of Warm Dense Gold*, Phys. Rev. Lett. 95, 085002 (2005).

**[6-83]** M. Tabak et al., Phys. Plasmas 1 (1994) 1626.

**[6-84]** M. Tatarakis et. al., Nature 415 (2002) 6869.

**[6-85]** F.B. Rosmej, R.W. Lee, submitted for publication.

**[6-86]** D. Mihalas, *Stellar Atmospheres*, W. Freeman and Co., San Francisco, (1978).

**[6-87]** H.R. Griem, *Spectral Line Broadening by Plasmas*, Academic Press, New York (1974).

**[6-88]** H.R. Griem, *Principles of Plasma Spectroscopy*, Cambridge University Press (1997).

**[6-89]** J. Lindl, Phys. Plasmas 2 (1995) 3933.

**[6-90]** C. deMichelis, M. Mattioli, Nuclear Fusion 21 (1981) 677.

**[6-91]** D. Salzmann, H. Szichman, *Density dependence of the atomic transition probabilities in hot, dense plasmas*, Phys. Rev. A 35 (1987) 807.

**[6-92]** R.W. Lee et al., J. Opt. Soc. Am. B 20 (2003) 1.

**[6-93]** F.B. Rosmej et al. , Nucl. Instrum. Methods A 464 (2001) 257.

**[6-94]** F.B. Rosmej, J. Phys. B.: At. Mol. Opt. Phys. 30 (1997) L819.

**[6-95]** F.B. Rosmej et al., *Charge-exchange-induced two-electron satellite transitions from autoionizing levels in dense plasmas*, Phys. Rev. E 66 (2002) 056402.

**[6-96]** R. Loudon, *The Quantum Theory of Light*, Oxford Science Publications (1983).

**[6-97]** S.J. Gitomer et al., Phys. Fluids 29 (1986) 2679.

**[6-98]** E. Foord et al., JQSRT 99(2006) 712.

**[6-99]** T. Ditmire et al., Astrophysical Journal Supplement Series 127 (2000) 299.

**[6-100]** L.N. Gaier et al., J. Phys. B: At. Mol. Opt. Phys. 37(2004) L57.

**[6-101]** B.A. Remington et al., Metallurgical and Materials Transactions A-Physical Metallurgy and Materials Science 35A (2004) 2587.

**[6-102]** D. Kalantar et al., *Direct Observation of the a-e Transition in Shock-Compressed Iron via Nanosecond X-Ray Diffraction*, Phys. Rev. Lett. 95 (2005) 075502.

**[6-103]** E. Divall, P. Holligan Rutherford-Appleton Laboratory Report RAL-TR-2002-013, (2002) 187.

**[6-104]** A.J. Langley, W.J. Lester, J.M. Smith, Rutherford-Appleton Laboratory Report RAL-TR-2004-025, (2004) 187.

**[6-105]** T. Missalla et al., Rev. Sci. Instr. 70 (1999) 1288.

**[6-106]** D. Neely et al., Rutherford-Appleton Laboratory Report TR-95-025, (1995) 113.

**[6-107]** G. Chériaux, J-P. Chambaret, Meas. Sci. Technol. 12 (2001) 1769.

**[6-108]** D. Sayre, *Some implications of a theorem due to Shannon*, Acta Cryst. 5 (1952) 843.

**[6-109]** J. Miao, P. Charalambous, J. Kirz, D. Sayre, *Extending the methodology of X-ray crystallography to allow imaging of micrometer sized non-crystalline specimens*, Nature 400 (1999) 342.

**[6-110]** R.H.T. Bates., *Fourier phase problems are uniquely solvable in more than one dimension*, Optik 61 (1982) 247.

**[6-111]** M.H. Hayes, *The reconstruction of a multidimensional sequence from the phase or magnitude of its Fourier transform*, IEEE Trans. On Acoustics Speech and Signal Processing, 30 (1982) 140.

**[6-112]** J.R. Fienup, *Phase retrieval algorithms: a comparison*, Appl. Opt. 21 (1982) 2758.

**[6-113]** R. Henderson, *The potential and limitations of neutrons, electrons and X-rays for atomic resolution microscopy of unstained biological molecules*, Quart. Rev. Biophys. 28 (1995) 171.

**[6-114]** S. Eisebitt, J. Luning, W.F. Schlotter, M. Lorgen., O. Hellwig, W. Eberhardt, J. Stohr, *Lensless imaging of magnetic nanostructures by X-ray spectro-holography*, Nature 432 (2004) 885.

**[6-115]** E.L. Saldin, E.A. Schneidmiller, M.V. Yurkov, *Coherence properties of the radiation from X-ray free electron laser*, in press.

**[6-116]** I.K. Robinson, I.A. Vartanyants, G.J. Williams, M.A. Pfeifer, J.A. Pitney, *Reconstruction of the Shapes of Gold Nanocrystals using Coherent X-ray Diffraction*, Phys. Rev. Lett. 87 (2001) 195505.

**[6-117]** G.J. Williams, M.A. Pfeifer, I.A. Vartanyants, I.K. Robinson, *Three-Dimensional Imaging of Microstructure in Gold Nanocrystal*, Phys Rev. Lett., 90 (2003) 175501.

**[6-118]** H.W. Hayden, W.G. Moffat, J. Wulff, *Structure and Properties of Materials III*, Wiley, New York (1965).

**[6-119]** I.A. Vartanyants, I.K. Robinson, *Partial Coherence Effects on the Reconstruction of the Shape of Small Crystals from Coherent X-ray Diffraction Pattern*, J. Phys.: Condens. Matter 13 (2001) 10593.

**[6-120]** M.A. Pfeifer, G.J. Williams, I.A Vartanyants, R. Harder, I.K. Robinson, *Three-dimensional mapping of a deformation field inside a nanocrystal*, Nature 422 (2006) 63.

**[6-121]** I.A. Vartanyants, I.K. Robinson, J.D. Onken, M.A. Pfeifer, G.J. Williams, F. Pfeiffer, H. Metzger, Z. Zhong, G. Bauer, *Coherent x-ray diffraction from quantum dots*, Phys. Rev. B 71 (2005) 245302.

**[6-122]** I.A Vartanyants, I.K. Robinson, *Imaging of quantum array structures with coherent and partially coherent diffraction*, J. Synchrotron Rad. 10 (2003) 409.

**[6-123]** J. Miao, T. Ishikawa, B. Johnson, E.H. Anderson, B. Lai, K.O. Hodgson, *High Resolution 3D X-Ray Diffraction Microscopy*, Phys. Rev. Lett. 89 (2002) 088303.

**[6-124]** H.N. Chapman, A. Barty, S. Marchesini, A. Noy, C. Cui, M.R. Howells, R. Rosen, H. He, J.C.H. Spence, U. Weierstall, T. Beetz, C. Jacobsen, D. Shapiro, *High-resolution ab initio three-dimensional X-ray diffraction microscopy*, J. Opt. Soc. Am. in press (2006).

**[6-125]** J.E. Trebes et al., Science 238 (1987) 517.

**[6-126]** R.A. Bartels, et al., Science 297 (2002) 376.

**[6-127]** M.R. Howells, et al., Science 238 (1987) 514.

**[6-128]** C. Jacobsen, M. Howells, J. Kirz, S. Rothman, J. Opt. Soc. Am. A7 (1990) 1847.

**[6-129]** McNulty, J. Kirz, C. Jacobsen, E.H. Anderson, M.R. Howells, D.P. Kern, Science 256 (1992) 1009.

**[6-130]** S. Lindaas, M.R. Howells, C. Jacobsen, A. Kalinovsky, J. Opt. Soc. Am. A 13 (1996) 1788.

**[6-131]** P. Cloetens et al., Appl. Phys. Lett. 75 (1999) 2912.

**[6-132]** K.A. Nugent, A.G. Peele, H.N. Chapman, A.P. Mancuso, Phys. Rev. Lett. 91 (2003) 203902.

**[6-133]** W. Chao, B.D. Harteneck, J.A. Liddle, E.H. Anderson, D.T. Attwood, *Soft X-ray microscopy at a spatial resolution better than 15 nm*, Nature 435 (2005) 1210.

**[6-134]** H.C. Kang, J. Maser, G.B. Stephenson, C. Liu, R. Conley, A.T. Macrander, S. Vogt, *Nanometer Linear Focusing of Hard X Rays by a Multilayer Laue Lens*, Phys Rev. Lett. 96 (2006) 127401.

**[6-135]** H.M. Quiney, A.G. Peele, Z. Cai, D. Paterson, K.A. Nugent, Nature Physics 2 (2006) 101.

**[6-136]** H. He, et al., Appl. Phys. Lett. 85 (2004) 2454.

**[6-137]** H.J. Freund et al., *Metal Aggregates on Oxide Surfaces: Structure and Adsorption*, Crystal Research and Technology 33 (1998) 977.

**[6-138]** J.J. Finley et al., *Quantum-confined Stark Shift of Charged Exciton Complexes in Quantum Dots*, Phys. Rev. B 70 (2004) 201308(R).

**[6-139]** G. Bester et al., Phys.Rev. B 67 (2003) 161306.

**[6-140]** G.A. Narvaez et al., Phys. Rev. B 72 (2005) 245318.

**[6-141]** J. Stangl et al., Rev. Mod. Phys. 76 (2004) 725.

**[6-142]** A. Hesse, J. Stangl et al., Phys.Rev. B 66 (2002) 085321.

**[6-143]** Th. Wiebach et al., Phys.Rev. B 61 (2000) 5571.

**[6-144]** J. Stangl et al., Appl.Phys. Lett. 82 (2003) 2251.

**[6-145]** I. Kegel et al., Phys. Rev. B 63 (2001) 035318

**[6-146]** T.U. Schülli et al., Phys.Rev.Lett. 90 (2003) 066105.

**[6-147]** Malachias et al., Phys. Rev. Lett. 91 (2003) 176101.

**[6-148]** Malachias et al., Phys. Rev. B 72 (2005) 165316.

**[6-149]** C.G. Schroer et al., Appl.Phys. Lett. 82 (2003) 1485.

**[6-150]** C.G. Schroer, B. Lengeler, Phys.Rev.Lett. 94 (2005) 054802.

**[6-151]** Jarre et al., Phys. Rev. Lett. 94 (2005) 074801.

**[6-152]** C. David et al., Appl. Phys. Lett. 79 (2001) 1088.

**[6-153]** S. DiFonzo et al., *Non-destructive Determination of local strani with 100nm spatial resolution*, Nature 403 (2000) 638.

**[6-154]** Jarre et al., Appl. Phys. Lett. 85 (2004) 161.

**[6-155]** F. Pfeiffer et al., Science 297 (2002) 230.

**[6-156]** B.C. Larson, W. Yang, G.E. Ice, J.D. Budai, J.Z. Tischler, *Three-dimensional X-ray structural microscopy with submicrometer resolution*, Nature 415 (2002) 887.

**[6-157]** I.K. Robinson, J.L. Libbert, I.A. Vartanyants, J.A. Pitney, D.M. Smilgies, D.L. Abernathy, G. Grübel, *Coherent X-ray Diffraction Imaging of Silicon Oxide Growth*, Phys. Rev. B, 60 (1999) 9965.

**[6-158]** G. Rosenfeld et al., Phys. Rev. Lett. 69 (1992) 917.

**[6-159]** S. Alexander, J.P. McTague, Phys. Rev. Lett. 41 (1978) 702.

**[6-160]** Y.C. Shen, D.W. Oxtoby, Phys. Rev. Lett. 77 (1996) 3585.

**[6-161]** W. Klein, Phys. Rev. E 64 (2001) 056110.

**[6-162]** K. Mecke, private communication.

**[6-163]** H. Riedel, *Fracture mechanisms*, in Materials Science and Technology, Vol.6, R.W. Cahn, P. Haasen, E.J. Kramer (eds.), VCH, Weinheim (1992).

**[6-164]** B.C. Stuart et al., Phys. Rev. Lett. 74 (1995) 2248.

**[6-165]** B.C. Stuart et al., Phys. Rev. B 53 (1996) 1747.

**[6-166]** B.C. Stuart et al. Optical ablation by high-power short-pulse lasers. J.Opt.Soc.Am B 13 (1996) 459.

**[6-167]** J. Neev et al., IEEE, J. Selected Topics in Quan. Electron. 2 (1996) 790.

**[6-168]** M. Feil et al., Appl. Surface Science 127-129(1998)869.

**[6-169]** M.D. Perry et al., J. Appl. Phys. 85 (1999) 6803.

**[6-170]** For example, see Proc. 30th Ann.Conf. on Laser Damage in Optical Materials, SPIE proceedings Vol. 3578 (1999).

**[6-171]** C.W. Siders et al., Science 286 (1999) 1340.

**[6-172]** M. Rouhi, C&EN, Nov. 15, (1999).

**[6-173]** A. Plech, V. Kotaidis, M. Lorenc, J. Boneberg, *Femtosecond laser near-field ablation from Gold nanoparticles*, Nature Physics, 2(2006) 44.

**[6-174]** M.R. Howells et al., *An assessment of the resolution limitation due to radiation damage in x-ray diffraction microscopy*, in press.

**[6-175]** See e.g. G. Grübel, G.B. Stephenson, in *Proceedings of the 4th Generation Light Source Workshop*, Advanced Photon Source, Argonne National Laboratory, 10/27-29/97, and references therein.

**[6-176]** S. Brauer et al., Phys. Rev. Lett. 74 (1995) 2010; S.B. Dierker et al., Phys. Rev. Lett. 75 (1995) 449; T. Thurn-Albrecht et al., Phys. Rev. Lett. 77 (1996) 5437; S.G.J. Mochrie et al., Phys. Rev. Lett. 78 (1997) 1275; A. Malik et al., Phys. Rev. Lett. 81 (1998) 5832; A.C. Price et al., Phys. Rev. Lett. 82 (1999) 755; L.B. Lurio et al., Phys. Rev. Lett. 84 (2000) 785; D.O. Riese et al., Phys. Rev. Lett. 85 (2000) 5460; A. Fera et al., Phys. Rev. Lett. 85 (2000) 2316; D. Lumma et al., Phys. Rev. Lett. 86 (2001) 2042; I. Sikharulidze et al., Phys. Rev. Lett. 88 (2002) 115503; D. Pontoni et al., Phys. Rev. Lett. 90 (2003) 188301; H.J. Kim et al. Phys. Rev. Lett. 90 (2003) 068302; A. Madsen et al., Phys. Rev. Lett. 90 (2003) 085701; C. Gutt et al., Phys. Rev. Lett. 91 (2003) 076104; I. Sikharulidze et al., Phys. Rev. Lett. 91 (2003) 165504; A. Madsen et al., Phys. Rev. Lett. 92 (2004) 096104.

**[6-177]** http:// tesla.desy.de/new_pages/ TDR_CD/PartV/xfel.pdf); http://tesla.desy.de/new_pages/tdr_update/ supplement.html

**[6-178]** LCLS "*The First Experiments*", September 2000.

**[6-179]** L. Cipelletti, L. Ramos, J. Phys.: Condens. Matter 17 (2005) R253.

**[6-180]** W. Götze, L. Sjogren, Rep.Prog.Phys. 55 (1992) 241.

**[6-181]** R. Bergman et al., Phys. Rev. B 56 (1997) 11619.

**[6-182]** M. Grimsditch, M.L. Torell, in *Dynamics of Disordered Materials*, D. Richter et al. (eds.), Springer, Berlin (1989); M. Russina et al., Phys. Rev. Lett. 84 (2000) 3620; U. Buchenau et al., Phys. Rev. Lett. 77 (1996) 4035; C. Masciovecchio et al., Phys. Rev. Lett. 80 (1988) 544.

**[6-183]** R. Bruning, M. Sutton, Phys, Rev. B 49 (1994) 3124.

**[6-184]** A.K. Hassan et al., Phys. Rev. B 45 (1992) 12797.

**[6-185]** D. Engberg et al., Phys. Rev. B 59 (1999) 4053.

**[6-186]** H. Sinn, J. Phys.: Condens. Matter 13 (2001) 7525.

**[6-187]** S.K. Sinha et al., Phys. Rev. B 38 (1988) 2297.

**[6-188]** S. Mora, J. Daillant, Eur.Phys.J. B 27 (2002) 417.

**[6-189]** J.F. Peters, M.A. de Fries, J. Miguel, O. Toulemonde, J. Goedkoop,ESRF Newslett. 15 (2000) 34; F. Yakhou, A. Letoublon, F. Livet, M. de Boissieu, F. Bley, C. Vettier, ESRF Newslett. 32 (1999) 14; F. Yakhou, A. Létoublon, F. Livet, M. de Boissieu, F. Bley, J. Magnetism Magnetic Materials. 233 (2001) 119; K. Chesnel, M. Belakhovsky, F. Livet, S.P. Collins, G. van der Laan, S.S. Dhesi, J.P. Attane, A. Marty, Phys. Rev. Lett. 66 (2002) 172404.

**[6-190]** S. Eisebitt, J. Luning, W.F. Schlotter, M. Lorgen., O. Hellwig, W. Eberhardt, J. Stohr, *Lensless imaging of magnetic nanostructures by X-ray spectro-holography*, Nature 432 (2004) 885.

**[6-191]** A. Malik et al., Phys. Rev. Lett. 81 (1998) 5832.

**[6-192]** F. Livet et al., Phys. Rev. E 63 (2001) 036108.

**[6-193]** M. J. Rosker, M. Dantus, A.H. Zewail, J. Chem. Phys. 89 (1988) 6113.

**[6-194]** A.H. Zewail, J. Phys. Chem. A 104 (2000) 5660.

**[6-195]** T. Baumert, V. Engel, C. Rottgermann, W.T. Strunz, G. Gerber, Chem. Phys. Lett. 191 (1992) 639.

**[6-196]** S. Mukamel, *Principles of nonlinear optical spectroscopy*; Oxford University Press, New York (1995).

**[6-197]** J.-C. Diels, W. Rudolph, *Ultrashort laser pulse phenomena : fundamentals, techniques, and applications on a femtosecond time scale*; Academic Press: San Diego (1996).

**[6-198]** *Femtochemistry: Ultrafast chemical and physical processes in molecular systems*, Lausanne, M. Chergui (ed.), World Scientific,Singapore (1996).

**[6-199]** V.P.T. Sundström, R. van Grondelle, *Ultrafast spectroscopy in biology,* in Femtochemistry and femtobiology ultrafast reaction dynamics at atomic-scale resolution, Nobel Symposium 101, V. Sundström (ed.), Imperial College Press, London (1997) 319.

**[6-200]** *Femtochemistry and femtobiology ultrafast reaction dynamics at atomic-scale resolution*, Nobel Symposium 101, V. Sundström (ed.), Imperial College Press, London (1997).

**[6-201]** *Femtochemistry and femtobiology ultrafast dynamics in molecular science*, A. Douhal (ed.), World Scientific, New Jersey (2002).

**[6-202]** G.R. Fleming, T. Joo, M. Cho, A.H. Zewail, V.S. Letokhov, R.A. Marcus, E. Pollak, D.J. Tannor, S. Mukamel, Adv. Chem. Phys. 101 (1997) 141.

**[6-203]** L. Dhar, J.A. Rogers, K.A. Nelson, Chem. Rev. 94 (1994) 157.

**[6-204]** M. Chergui, Comptes Rendus de l'Academie des Sciences, Serie IV: Physique Astrophysique 2 (2001) 1453.

**[6-205]** M. Chergui, *Ultrafast structural dynamics in the condensed phase*, in Investigating extreme physical conditions with advanced optical techniques; B. Di Bartolo, O. Forte (eds.), Kluwer, Dordrecht, Vol. 168 (2005) 497.

**[6-206]** *Time-resolved electron and x-ray diffraction*, P.M. Rentzepis (ed.), SPIE: Bellingham, Washington (1995).

**[6-207]** J.R. Helliwell, P.M. Rentzepis, *Time-resolved diffraction*, Clarendon Press, Oxford (1997).

**[6-208]** K. Sokolowski-Tinten, J. Bialkowski, A. Cavalleri, D. von der Linde, A. Oparin, J. Meyer-ter-Vehn, S.I. Anisimov, Phys. Rev. Lett. 81 (1998) 224.

**[6-209]** K. Sokolowski-Tinten, D. von der Linde, Phys. Rev. B 61 (2000) 2643.

**[6-210]** K. Sokolowski-Tinten, W. Ziegler, D. von der Linde, M.P. Siegal, D.L. Overmyer, Appl. Phys. Lett. (2005) 86.

**[6-211]** L.X. Chen, J Electron Spectrosc. 119 (2001) 161.

**[6-212]** C. Bressler, M. Chergui, Chem. Rev. 104 (2004) 1781.

**[6-213]** *TESLA Technical Design Report Part V, The X-ray Free Electron Laser*, G. Materlik, T. Tschentscher (Eds.), DESY report 2001-011, DESY, Hamburg (2001), http://tesla.desy.de/new_pages/0000_TESLA_Project.html

**[6-214]** L.X. Chen, G. Jennings, T. Liu, D.J. Gosztola, J.P. Hessler, D.V. Scaltrito, G.J. Meyer, J. Am. Chem. Soc. 124 (2002) 10861.

**[6-215]** L.X. Chen, G.B. Shaw, I. Novozhilova, T. Liu, G. Jennings, K. Attenkofer, G.J. Meyer, P. Coppens, J. Am. Chem. Soc. 125 (2003) 7022.

**[6-216]** C. Bressler, M. Saes, M. Chergui, R. Abela, P. Pattison, Nucl. Instrum. Meth. A 467 (2001) 1444.

**[6-217]** M. Saes, C. Bressler, R. Abela, D. Grolimund, S.L. Johnson, P.A. Heimann, M. Chergui, Phys. Rev. Lett. 90 (2003) 047403.

**[6-218]** M. Saes, C. Bressler, F. van Mourik, W. Gawelda, M. Kaiser, M. Chergui, C. Bressler, D. Grolimund, R. Abela, T.E. Glover, P.A. Heimann, R.W. Schoenlein, S.L. Johnson, A.M. Lindenberg, R.W. Falcone, Rev. Sci. Instrum. 75 (2004) 24.

**[6-219]** S.L. Johnson, P.A. Heimann, A.M. Lindenberg, H.O. Jeschke, M.E. Garcia, Z. Chang, R.W. Lee, J.J. Rehr, R.W. Falcone, Phys. Rev. Lett. 91 (2003) 157403.

**[6-220]** M. Chergui, C. Bressler, R. Abela, Synchrotron Radiation News (2004).

**[6-221]** M. Chergui, S. Mukamel, Chem. Phys. 299 (2004) 155.

**[6-222]** S.L. Johnson, P.A. Heimann, A.G. MacPhee, A.M. Lindenberg, O.R. Monteiro, Z. Chang, R.W. Lee, R.W. Falcone, Phys. Rev. Lett. 94 (2005) 057407.

**[6-223]** W. Gawelda, M. Johnson, F.F.M. de Groot, R. Abela, C. Bressler, M. Chergui, J. Am. Chem. Soc. 128 (2006) 5001.

**[6-224]** M. Benfatto, S. Della Longa, K. Hatada, K. Hayakawa, W. Gawelda, C. Bressler, M. Chergui, submitted for publication.

**[6-225]** M.P. Hertlein, H. Adaniya, J. Amini, C. Bressler, B. Feinberg, M. Kaiser, N. Neumann, M.H. Prior, A. Belkacem, submitted for publication.

**[6-226]** U. Buontempo, A. Filipponi, P. Postorino, R. Zaccari, J. Chem. Phys. 108(1998)4131.

**[6-227]** U. Buontempo, A. DiCicco, A. Filipponi, M. Nardone, P. Postorino, J. Chem. Phys. 107 (1997) 5720.

**[6-228]** A. Filipponi, P.D. D'Angelo, J. Chem. Phys. 109 (1998) 5356.

**[6-229]** W. Gawelda, V.T. Pham, M. Kaiser, Y. Zaushytsin, S.L. Johnson, I. Iyas, C. Bressler, M. Chergui, to be published.

**[6-230]** D. Cubaynes, J.M. Bizau, F.J. Wuilleumier, B. Carré, F. Gounand, Phys. Rev. Lett. 63 (1989) 2460.

**[6-231]** A.S. Schlachter et al., J. Phys. B.: At. Mol. Opt. 37 (2004) L103.

**[6-232]** S.W. Scully et al., J. Phys. B.: At. Mol. Opt. 38 (2005) 1967.

**[6-233]** J. Workman, M. Nantel, A. Maksimchuk, D. Umstadter, Appl. Phys. Lett. 70 (1997) 312.

**[6-234]** L. Nugent-Glandorf, M. Scheer, D.A. Samuels, A.M. Mulhisen, E.R. Grant, X.M. Yang, V.M. Bierbaum, S.R. Leone, Phys. Rev. Lett. 87 (2001) 193002.

**[6-235]** L. Nugent-Glandorf, M. Scheer, D.A. Samuels, V.M. Bierbaum, S.R. Leone, J. Chem. Phys. 117 (2002) 6108.

**[6-236]** H. Lefebvre-Brion, R.W. Field, *Perturbations in the spectra of diatomic molecules*, Academic Press, Orlando (1986).

**[6-237]** J.T. Hynes, Ann. Rev. Phys. Chem. 36 (1985) 573.

**[6-238]** P. Barbara, W. Jarzeba, in *Advances in Photochemistry*; John Wiley & Sons, New York, Vol. 15 (1990) 1.

**[6-239]** R. Jimenez, G.R. Fleming, P.V. Kumar, M. Maroncelli, Nature 369 (1994) 471.

**[6-240]** M. Maroncelli, J. Mol. Liq. 57 (1993) 1.

**[6-241]** G.R. Fleming, M.H. Cho, Ann. Rev. Phys. Chem. 47 (1996) 109.

**[6-242]** N. Nandi, K. Bhattacharyya, B. Bagchi, Chem. Rev. 100 (2000) 2013.

**[6-243]** P. Larregaray, A. Cavina, M. Chergui, Chem. Phys. 308 (2005) 13.

**[6-244]** S.K. Pal, A.H. Zewail, Chem. Rev. 104 (2004) 2099.

**[6-245]** J.P. Bergsma, J.R. Reimers, K.R. Wilson, J.T. Hynes, J. Chem. Phys. 85(1986) 5625.

**[6-246]** J. Helbing, M. Chergui, J. Chem. Phys. 115 (2001) 6158.

**[6-247]** J. Helbing, M. Chergui, S. Fernandez-Alberti, J. Echave, N. Halberstadt, J.A. Beswick, Phys. Chem. Chem. Phys. 2 (2000) 4131.

**[6-248]** N. Winter, I. Chorny, J. Vieceli, I. Benjamin, J. Chem. Phys. 119 (2003) 2127.

**[6-249]** M.L. Horng, J.A. Gardecki, A. Papazyan, M. Maroncelli, J. Phys. Chem. 99 (1995) 17311.

**[6-250]** A.L. Harris, J.K. Brown, C.B. Harris, Ann. Rev. Phys. Chem. 39 (1988) 341.

**[6-251]** V.A. Apkarian, N. Schwentner, Chem. Rev. 99 (1999) 1481.

**[6-252]** J.M. Tour, Accounts Chem. Res. 33 (2000) 791.

**[6-253]** R.M. Metzger, Accounts Chem. Res. 32 (1999) 950.

**[6-254]** M. Gratzel, Nature 414 (2001) 338.

**[6-255]** S. Yasutomi, T. Morita, Y. Imanishi, S. Kimura, Science 304 (2004) 1944.

**[6-256]** J.Y. Jiao, G.J. Long, F. Grandjean, A.M. Beatty, T.P. Fehlner, J. Am. Chem. Soc. 125 (2003) 7522.

**[6-257]** K. Szacilowski, Chem. Eur. J. 10 (2004) 2520.

**[6-258]** C.G. Pierpont, Coordin. Chem. Rev. 219 (2001) 415.

**[6-259]** S. Schenkl, F. van Mourik, G. van der Zwan, S. Haacke, M. Chergui, Science 309 (2005) 917.

**[6-260]** W. Gawelda, C. Bressler, M. Saes, M. Kaiser, A. Tarnovsky, D. Grolimund, S.L. Johnson, R. Abela, M. Chergui, Physica Scripta T115 (2005) 102.

**[6-261]** N.H. Damrauer, G. Cerullo, A.T. Yeh, T.R. Boussie, C.V. Shank, J.K. McCusker, Science 275 (1997) 54.

**[6-262]** A.T. Yeh, C.V. Shank, J.K. McCusker, Science 289 (2000) 935.

**[6-263]** J.A. Weinstein, N.N. Zheligovskaya, M.Y. Mel'nikov, F. Hartl, J. Chem. Soc. Dalton (1998) 2459.

**[6-264]** J.A. Weinstein et al., Inorg. Chem. 42 (2003) 7077.

**[6-265]** J. Helbing et al., J. Biophys 87 (2004) 1881.

**[6-266]** H.Z. Yu, J.S. Baskin, B. Steiger, C.Z. Wan, F.C. Anson, A.H. Zewail, Chem. Phys. Lett. 293 (1998) 1.

**[6-267]** H.Z. Yu, J.S. Baskin, B. Steiger, F.C. Anson, A.H. Zewail, J. Am. Chem. Soc. 121 (1999) 484.

**[6-268]** H.Z. Yu, J.S. Baskin, A.H. Zewail, J. Phys. Chem. A 106 (2002) 9845.

**[6-269]** J.S. Baskin, H.Z. Yu, A.H. Zewail, J. Phys. Chem. A 106 (2002) 9837.

**[6-270]** F. Rosca, A.T.N. Kumar, X. Ye, T. Sjodin, A.A. Demidov, P.M. Champion, J. Phys. Chem. A 104 (2000) 4280.

**[6-271]** F. Rosca et al., J. Phys. Chem. A 106 (2002) 3540.

**[6-272]** S.K. Gayen, W.B. Wang, V. Petricevic, R. Dorsinville, R.R. Alfano, Appl. Phys. Lett., 47 (1985) 455.

**[6-273]** T. Matsuzawa, Y. Aoki, N. Takeuchi, Y. Murayama, J. Electrochem. Soc. 143 (1996) 2670.

**[6-274]** A.V. Kolobov, P. Fons, A.I. Frenkel, A.L. Ankudinov, J. Tominaga, T. Uruga, Nature Materials 3 (2004) 703.

**[6-275]** A.V. Kolobov, P. Fons, J. Tominaga, A.L. Ankudinov, S.N. Yannopoulos, K.S. Andrikopoulos, J. Phys. Condensed Mat. 16 (2004) S5103.

**[6-276]** A.V. Kolobov, P. Fons, J. Tominaga, A.I Frenkel, A.L. Ankudinov, S.N. Yannopoulos, K.S. Andrikopoulos, T. Uruga, Jpn. J. Appl. Phys. 44 (2005) 3345.

**[6-277]** H.W. Schumacher, C. Chappert, P. Crozat, R.C. Sousa, P.P. Freitas, J. Miltat, H.W. Fassbender, B. Hillebrands, Phys. Rev. Lett. 90 (2003) 017201.

**[6-278]** H.W. Schumacher, C. Chappert, R.C. Sousa, P.P. Freitas, J. Miltat, Phys. Rev. Lett. 90 (2003) 017204.

**[6-279]** A.V. Kimel, A. Kirilyuk, P.A. Usachev, R.V. Pisarev, A.M. Balbashov, T. Rasing, Nature 435 (2005) 655.

**[6-280]** F. Hansteen, A. Kimel, A. Kirilyuk, T. Rasing, Phys. Rev. Lett. 95 (2005) 047402.

**[6-281]** E. Beaurepaire, J.C. Merle, A. Daunois, J.Y. Bigot, Phys. Rev. Lett. 76 (1996) 4250.

**[6-282]** F. Sirotti, S. Girlando, P. Prieto, L. Floreano, G. Panaccione, G. Rossi, Phys. Rev. B 61 (2000) R9221.

**[6-283]** J. Vogel, W. Kuch, J. Camarero, K. Fukumoto, Y. Pennec, S. Pizzini, M. Bonfim, F. Petroff, A. Fontaine, J. Kirschner, Phys. Rev. B 71 (2005) 060404.

**[6-284]** A. Krasyuk, F. Wegelin, S.A. Nepijko, H.J. Elmers, G. Schonhense, M. Bolte, C.M. Schneider, Phys. Rev. Lett. 95 (2005) 207201.

**[6-285]** J. Raabe, C. Quitmann, C.H. Back, F. Nolting, S. Johnson, C. Buehler, Phys. Rev. Lett. 94 (2005) 217204.

**[6-286]** C. Bressler, M. Saes, M. Chergui, D. Grolimund, R. Abela, P. Pattison, J. Chem. Phys. 116 (2002) 2955.

**[6-287]** J.C. Willamson et al., *Clocking transient chemical changes by ultrafast electron diffraction*, Nature 386 (1997) 159.

**[6-288]** H. Ihee et al., *Direct imaging of transient molecular structures with ultrafast diffraction*, Science 291 (2001) 458.

**[6-289]** C.-Y. Ruan et al., *Ultrafast diffraction and structural dynamics: The nature of complex molecules far from equilibrium*, Proc. Nat. Acad. Sci. 98 (2001) 7117.

**[6-290]** M.H. Pirenne, *The diffraction of X-rays and electrons by free molecules*, The University Press, Cambridge (1946).

**[6-291]** I. Hargittai, M. Hargittai, *Stereochemical Applications of Gas-Phase Electron Diffraction*, VCH Publishers, New York (1988).

**[6-292]** H. Ihee, B.M. Goodson, R. Srinivasan, V.A. Lobastov, A.H. Zewail, *Ultrafast electron diffraction and structural dynamics: Transient intermediates in the elimination reaction of $C_2F_4I_2$*, J. Phys. Chem. A 106 (2002) 4087.

**[6-293]** J.C. Williamson, A.H. Zewail, *Ultrafast Electron Diffraction. 4. Molecular Structures and Coherent Dynamics*, J. Phys. Chem. 98 (1994) 2766.

**[6-294]** J.D. Geiser, P.M. Weber, *Pump-probe diffraction imaging of vibrational wave functions*, J. Chem. Phys. 108 (1998) 8004.

**[6-295]** T.S. Dibble, L.S. Bartell, *Electron Diffraction Studies of the Kinetics of Phase Changes in Molecular Clusters. 3. Solid-State Phase Transformations in $SeF_6$ and $(CH_3)_3CCl$*, J. Phys. Chem., 96 (1992) 8603.

**[6-296]** A. Plech et al., *Visualizing chemical reactions in solution by picosecond X-ray diffraction*, Phys. Rev. Lett. 92 (2004) 125506.

**[6-297]** J. Davidsson et al., *Structural Determination of Transient Isomer of $CH_2I_2$ by Picosecond X-ray Diffraction*, Phys. Rev. Lett. 94 (2005) 245503.

**[6-298]** S. Bratos, F. Mirloup, R. Vuilleumier, M. Wulff, A. Plech, *X-ray Filming of atomic motions in chemical reactions*, Chem. Phys. 304 (2004) 245.

**[6-299]** C. Rischel et al., *Femtosecond time-resolved X-ray diffraction from laser-heated organic films*, Nature 390 (1997) 490.

**[6-300]** A.M. Lindenberg et al., *Atomic-Scale Visualization of Intertial Dynamics*, Science 308 (2005) 392.

**[6-301]** R.M. Stratt, M. Maroncelli, *Nonreactive Dynamics in Solution: The Emerging Molecular View of Solvation Dynamics and Vibrational Relaxation*, J. Phys. Chem. 100 (1996) 12981.

**[6-302]** D.P. Millar, K.B. Eisenthal, *Picosecond dynamics of barrier crossing in solution: A study of the conformational change of excited state 1,1'-binaphthyl*, J. Chem. Phys. 83 (1985) 5076.

**[6-303]** F. Schotte et al., *Watching a protein as it functions with 150-ps time-resolved X-ray crystallography*, Science 300 (2003) 1944.

**[6-304]** F. Schotte et al., *Picosecond time-resolved X-ray crystallography: probing protein function in real time*, J. Struct. Biol. 147 (2004) 235.

**[6-305]** R.H. Austin et al., *Dynamics of ligand binding to myoglobin*, Biochemistry 14 (1975) 5355.

**[6-306]** E. Collet et al., Science 300 (2003) 612.

**[6-307]** K. Sokolowski-Tinten et al., Nature 422 (2003) 287.

**[6-308]** M. Chollet et al., Science 307 (2005) 86.

**[6-309]** E. Collet. M.-H. Lemée-Cailleau, M. Buron, H. Cailleau, S. Ravy, T. Luty, J.F. Bérar, P. Czarnecki, N. Karl, Europhys. Lett. 57 (2002) 67.

**[6-310]** J. B. Goodenough, Physical Review 100 (1955) 564.

**[6-311]** Y. Murakami, H. Kawada, H. Kawata, M. Tanaka, T. Arima, Y. Moritomo, Y. Tokura, Phys. Rev. Lett. 80 (1998) 1932.

**[6-312]** C.W. M. Castleton, M. Altarelli, Phys. Rev. B 62 (2000) 1033.

**[6-313]** S.B. Wilkins, P.D. Spencer, P.D. Hatton, S.P. Collins, M.D. Roper, D. Prabhakaran, A.T. Boothroyd, Phys. Rev. Lett. 91 (2003) 167205.

**[6-314]** S. Iwai, M. Ono, A. Maeda, H. Matsuzaki, H. Kishida, H. Okamoto, Y. Tokura, Phys. Rev. Lett. 91 (2003) 057401.

**[6-315]** A. Cavalleri, M. Rini, H. Chong, S. Formaux, T.E. Glover, P.A. Heimann, J.C. Kieffer, R.W. Schoenlein, Phys. Rev. Lett. 95 (2005) 067405.

**[6-316]** A. Cavalleri, C. Toth, C.W. Siders, J.A. Squier, F. Raksi, P. Forget, J.C. Kieffer, Phys. Rev. Lett. 87 (2001) 237401.

**[6-317]** A. Cavalleri, Th. Dekorsy, H. Chong, J.C. Kieffer, R.W. Schoenlein, Phys. Rev. B 70 (2004) 161102(R).

**[6-318]** A. Plech, V. Kotaidis, M. Lorenc, J. Boneberg, *Femtosecond laser near field ablation from gold nanoparticles*, Nature Physics (2006) 44.

**[6-319]** R. Neutze, R. Wouts, D. van der Spoel, E. Weckert, J. Hajdu, *Potential for biomolecular imaging with femtoscond X-ray pulses*, Nature 406 (2000) 752.

**[6-320]** Z. Jurek, G. Oszlanyi, G. Faigel, *Imaging atom-clusters by hard x-ray free electron lasers*, Europhys. Lett. 65 (2004) 491.

**[6-321]** S.P. Hau-Riege, H. Szoke, H.N. Chapman, A. Szoke, S. Marchesini, A. Noy, H. He, M.R. Howells, U. Weierstall, J.C.H. Spence, *SPEDEN: Reconstructing single particles from their diffraction patterns*, Acta Cryst. A 60 (2004) 294.

**[6-322]** M. Bergh, N. Timneanu, D. van der Spoel, *A Model for the Dynamics of a Water Cluster in an X-ray Free Electron Laser Beam*, Phys. Rev. E 70 (2004) 051904.

**[6-323]** R. H. T. Bates, *Fourier phase problems are uniquely solvable in more than one dimension: 1. Underlying theory*, Optik 61 (1982) 247.

**[6-324]** J.R. Fienup, *Phase retrieval algorithms-a comparison*, Appl. Opt. 21 (1982) 2758.

**[6-325]** D. Sayre, H.N. Chapman, J. Miao, *On the extendibility of x-ray crystallography to noncrystals*, Acta Cryst. A 54 (1998) 232.

**[6-326]** J. Miao, P. Charalambous, J. Kirz, D. Sayre, *Extending the methodology of x-ray crystallography to allow imaging of micrometre-sized non-crystalline specimens*, Nature 400 (1999) 342.

**[6-327]** I.K. Robinson, I.A. Vartanyants, G.J. Williams, M.A. Pfeifer, J.A. Pitney, *Reconstruction of the shapes of gold nanocrystals using coherent x-ray diffraction*, Phys. Rev. Lett. 87 (2001) 195505.

**[6-328]** S. Marchesini, H.N. Chapman, S.P. Hau-Riege, R.A. London, A. Szöke, *Coherent X-ray diffractive imaging: applications and limitations*, Opt. Express 11 (2003) 2344.

**[6-329]** S. Marchesini, H. He, H.N. Chapman, S.P. Hau-Riege, A. Noy, M.R. Howells, U. Weierstall, J.C.H. Spence, *X-ray image reconstruction from a diffraction pattern alone*, Phys. Rev. B 68 (2003) 140101.

**[6-330]** H.N. Chapman, J. Hajdu et al., Ultrafast coherent diffraction imaging with a soft X-ray free-electron laser, submitted for publication.

**[6-331]** G. Huldt, A. Szöke, J. Hajdu, *Diffraction imaging of single particles and biomolecules*, J. Struct. Biol. 144 (2003) 219.

**[6-332]** J. Hajdu, E. Weckert, *Life Sciences - Scientific applications of XFEL radiation*, in TESLA, the Superconducting Electron-Positron Linear Collider with an integrated X-ray Laser Laboratory. Technical Design Report., DESY, ISBN 3-935702-00-0, Volume 5 (2001) 150-168.

**[6-333]** J. Hajdu *Imaging the structure of single particles and biomolecules*, in TESLA XFEL, First stage of the X-Ray Laser Laboratory, P. Audebert et al. (eds.), DESY, Hamburg (2002) 16-22.

**[6-334]** R. Henderson, *Cryoprotection of protein crystals against radiation-damage in electron and X-ray diffraction*, Proc. R. Soc. 241 (1990) 6.

**[6-335]** C. Nave, *Radiation damage in protein crystallography*, Radiation Physics and Chemistry 45 (1995) 483.

**[6-336]** Z. Jurek, G. Faigel, M. Tegze, *Dynamics in a cluster under the influence of intense femtosecond hard x-ray pulses*, Euro. Phys. J. D 29 (2004) 217.

**[6-337]** S.P. Hau-Riege, R.A. London, A. Szöke, *Dynamics of X-Ray Irradiated Biological Molecules*, Phys. Rev. E 69 (2004) 051906.

**[6-338]** B. Ziaja, D. van der Spoel, A. Szoke, J. Hajdu, *Auger-electron cascades in diamond and amorphous carbon*, Phys. Rev. B 64 (2001) 214104.

**[6-339]** B. Ziaja, A. Szoke, D. van der Spoel, J. Hajdu, *Space-time evolution of electron cascades in diamond*, Phys. Rev. B 66 (2002) 024116.

**[6-340]** B. Ziaja, R.A. London, J. Hajdu, *Unified model of secondary electron cascades in diamond*, J. Appl. Phys. 97 (2005) 064905.

**[6-341]** B. Ziaja, R.A. London, J. Hajdu, *Ionization by impact electrons in solids: Electron mean free path fitted over a wide energy range*, J. Appl. Phys. 99 (2006) 033514.

**[6-342]** N. Timneanu, C. Caleman, J. Hajdu, D. van der Spoel, *Auger electron cascades in water and ice*, Chem. Phys. 299 (2004) 277.

**[6-343]** J. Frank, *Three-Dimensional Electron Microscopy of Macromolecular Assemblies*, Academic Press, San Diego (1996).

**[6-344]** M. van Heel et al., *Single-particle electron cryo-microscopy: towards atomic resolution*. Quart. Rev. Biophys. 33 (2000) 307.

**[6-345]** D. Sayre, *X-ray crystallography*, Struct. Chem. 13 (2002) 81.

**[6-346]** J. Miao, K.O. Hodgson, D. Sayre, A*n approach to three-dimensional structures of biomolecules by using single-molecule diffraction images*, Proc. Natl. Acad. Sci. USA 98 (2001) 6641.

**[6-347]** J. Miao, T. Ishikawa, B. Johnson, E.H. Anderson, B. Lai, K.O. Hodgson, *High resolution 3D X-ray diffraction microscopy*, Phys. Rev. 89 (2002) 088303.

**[6-348]** J. Miao, K.O. Hodgson, T. Ishikawa, C.A. Larabell, M.A. LeGros, Y. Nishino, *Imaging whole Escherichia coli bacteria by using single particle x-ray diffraction*, Proc. Natl. Acad. Sci. USA 100 (2003) 110.

**[6-349]** H.R. Reiss, *Physical basis for strong-field stabilization of atoms against ionization*, Laser Physics 7 (1997) 543.

**[6-350]** P. Persson, S. Lunell, A. Szoke, B. Ziaja, J. Hajdu, *Shake-up and shake-off excitations with associated electron losses in X-ray studies of proteins*, Protein Science 10 (2001) 2480.

**[6-351]** I. Andersson, *Large structures at high resolution: spinach ribulose-1, 5-bisphosphate carboxylase/oxygenase at 1.6 Å resolution*, J. Mol. Biol. 259 (1996) 160.

**[6-352]** S.P. Hau-Riege, R.A. London, G. Huldt, H.N. Chapman, *Pulse requirements for x-ray diffraction imaging of single biological molecules*. Phys. Rev. E 71 (2005) 061919.

**[6-353]** S.P. Hau-Riege, N. Timneanu, in preparation.

**[6-354]** D. Starodub et al., *Damped and thermal motion of laser-aligned hydrated macromolecule beams for diffraction*, J. Chem. Phys 123 (2005) 244304.

**[6-355]** J.J. Larsen, K. Hald, N. Bjerre, H. Stapelfeldt, T. Seidman, *Three Dimensional Alignment of Molecules Using Elliptically Polarized Laser Fields*, Phys. Rev. Lett. 85 (2000) 2470.

**[6-356]** G. Huldt et al., in preparation.

**[6-357]** V. Elser, *Reconstruction of an object from its symmetry-averaged diffraction pattern*, http://arxiv.org/pdf/physics/0505174 (2005).

**[6-358]** C.T. O'Konski, B.H. Zimm, Science 111 (1950) 113.

**[6-359]** D. Sayre, in Proceedings of the NATO Course, Erice, H. Schenk (ed.), (1990) 353-356.

**[6-360]** A. Szöke, *Time-resolved holographic diffraction at atomic resolution*, Chem. Phys. Lett. 313 (1999) 777.

**[6-361]** A. Szöke, *X-ray and electron holography using a local reference beam*, in Short Wavelength Coherent Radiation: Generation and Application, D.T. Attwood, J. Bokor (eds.), AIP Conf. Proc. 147 (1986).

**[6-362]** A. Szöke, *Holographic methods in X-ray crystallography. 2. Detailed theory and connection to other methods of crystallography*, Acta Cryst. A 49 (1993) 853.

**[6-363]** M. Tegze, G. Faigel, *Atomic-resolution X-ray holography*, Europhys. Lett. 16 (1991) 41.

**[6-364]** M. Tegze, G. Faigel, *X-ray holography with atomic resolution*, Nature 380 (1996) 49.

**[6-365]** A. Szöke, H. Szöke, J.R. Somoza, *Holographic methods in X-ray crystallography 5. Multiple isomorphous replacement, multiple anomalous dispersion and non- crystallographic symmetry*, Acta Cryst. A 53 (1997) 291.

**[6-366]** H.N. Chapman et al., *High resolution ab initio Three dimensional X-ray Diffraction Microscopy*, J. Opt. Soc. Am. A (2006) 1179.

**[6-367]** H. Haberland, *Clusters of Atoms and Molecules*, Springer, Berlin (1993).

**[6-368]** M. Maier-Borst et al., Phys. Rev. A 59 (1999) R3162.

**[6-369]** H. Wabnitz, et al., Nature 420 (2002) 482.

**[6-370]** R. Santra, C. Green, Phys. Rev. Lett. 91 (2003) 233401.

**[6-371]** C. Bostedt et al., to be published.

**[6-372]** R. Sobierajski et al., in preparation.

**[6-373]** L. Juha et al., in preparation.

**[6-374]** K. Sokolowski-Tinten et al., in preparation.

**[6-375]** H.N. Chapman, K. Nugent, *X-ray Pulse Compression Using Strained Crystals*, Optics Commun. 205 (2002) 351.

**[6-376]** G. Siuzdak et al., *Mass spectrometry and viral analysis*, Chem. Biol. 3 (1996) 45.

**[6-377]** M.A. Tito, K. Tars, K. Valegard, J. Hajdu, C.V. Robinson, *Electrospray Time-of-Flight Mass Spectrometry of the Intact MS2 Virus Capsid*, J. Am. Chem. Soc. 122 (2000) 3550.

**[6-378]** A.A. Rostom, P. Fucini, D.R. Benjamin, R. Juenemann, K.H. Nierhaus, F.U. Hartl, C.M. Dobson, C. V. Robinson, *Detection and selective dissociation of intact ribosomes in a mass spectrometer*, Proc. Natl. Acad. Sci. USA 97 (2000) 5185.

**[6-379]** B.T. Ruotolo, K. Giles, I. Campuzano, A.M. Sandercock, R.H. Bateman, C.V. Robinson, *Evidence for Macromolecular Protein Rings in the Absence of Bulk Water*, Science 310 (2005) 1658.

**[6-380]** S.H. Jayasinghe, P.A.M. Eagles, A.N. Qureshi, *Electric field driven jetting: an emerging approach for processing living cells*, Biotechnol. J. 1 (2006) 86.

**[6-381]** Q. Wang et al., *Icosahedral virus particles as addressable nanoscale building blocks*, Angew. Chem. 41 (2002) 459.

**[6-382]** http://pqs.ebi.ac.uk/pqs-bin/macmol.pl?filename=1ny7

**[6-383]** A.E. Siegman, *Lasers*, University Science Books (1986).

**[6-384]** D. Sayre, H.N. Chapman, *X-ray microscopy*, Acta Cryst. A 51 (1995) 237.

**[6-385]** R. Henderson, *The potential and limitations of neutrons, electrons and X-rays for atomic resolution microscopy of unstained biological molecules*, Quart. Rev. Biophys. 28 (1995) 171.

**[6-386]** M.R. Howells, in preparation

**[6-387]** U. Bergman, in *Technical Design Report TESLA Part V – The X-ray Free Electron Laser*, G. Materlik, Th. Tschentscher (eds.), DESY 2001-011, DESY, Hamburg (2001) V-307 ff.

**[6-388]** R. Gähler, R. Golub, Z. Phys. B 65 (1987) 269.

**[6-389]** Y.-X. Yan, K.A Nelson, J. Chem. Phys. 87 (1987) 6240.

**[6-390]** A.A. Rostom et al., *Detection and selective dissociation of intact ribosomes in a mass spectrometer*, Proc. Natl. Acad. Sci. USA 97 (2000) 5185.

**[6-391]** M.A. Tito et al., *Electrospray Time of Flight Mass Spectrometry of the Intact MS2 Virus Capsid*, J. Am. Chem. Soc. 122 (2000) 3150.

**[6-392]** S. Brauer et al., Phys. Rev. Lett. 74 (1995) 2010.

**[6-393]** H.N. Chapman, K. Nugent, *X-ray Pulse Compression Using Strained Crystals*, Opt. Commun. 205 (2002) 351.

**[6-394]** R. Tatchyn, R. Bionta, *Performance studies of a multilayer-based radiation pulse slicer for Linac Coherent Light Source applications*, SPIE proceedings 4143 (2001) 89.

**[6-395]** M. Richwin, R. Zaeper, D. Lützenkirchen-Hecht, R. Frahm, *Piezo-QEXAFS: advances in time-resolved X-ray absorption spectroscopy*, J. Synchrotron Rad. 8 (2001) 354.

**[6-396]** U. Bergman, in Technical Design Report TESLA Part V – The X-ray Free Electron Laser, G. Materlik, Th. Tschentscher (eds.), DESY 2001-011, DESY, Hamburg, (2001) V-307ff.

**[6-397]** A. Rousse et al., *Non-thermal melting in semiconductors measured at femtosecond resolution*, Nature 410 (2001) 65.

**[6-398]** A.M. Lindenberg et al., *Atomic-Scale Visualization of Inertial Dynamics*, Science 308 (2005) 392.

**[6-399]** K. Sokolowski-Tinten et al., *Femtosecond X-ray measurement of coherent lattice vibrations near the Lindemann stability limit*, Nature 422 (2003) 287.

**[6-400]** F. Schotte et al., *Watching a protein as it functions with 150-ps time-resolved X-ray crystallography*, Science 300 (2003) 1944.

**[6-401]** T.R. Schibli et al., *Attosecond active synchronization of passively mode-locked lasers by balanced cross correlation*, Opt. Letters. 28 (2003) 947.

**[6-402]** A.L. Cavalieri et al., *Clocking Femtosecond X-Rays*, Phys. Rev. Lett. 94 (2005) 114801.

**[6-403]** H. Redlin et al., *Ultrafast-OPCPA burst mode laser synchronized to the VUV-FEL*, to be published.

**[6-404]** T. Brabec, F. Krausz, *Intense few-cycle laser fields: Frontiers of nonlinear optics*, Rev. Mod. Phys 72 (2000) 545.

**[6-405]** Kiewiet et al., *Femtosecond synchronization of a 3 GHz RF oscillator to a mode-locked Ti:sapphire laser*, Nucl. Instrum. Methods A 484 (2002) 619.

**[6-406]** D. Hudson et al., *Modelocked-fiber laser frequency-controlled with an intracavity electro-optic modulator*, Opt. Lett. 30 (2005) 2948.

**[6-407]** Datasheet for FFS fs fibre laser from Toptica Photonics AG (2006).

**[6-408]** F. Tauser, F. Adler, A. Leitenstorfer, *Widely tuneable sub-30-fs pulses from a compact erbium-doped fiber source*, Opt. Lett 29 (2004) 516.

**[6-409]** Datasheet “Alpha10” system by Thales Laser (2006).

**[6-410]** Kiriyama et al., *Prepulse-free, multi-terawatt, sub-30-fs laser system*, Opt. Express 14 (2006) 438.

**[6-411]** Datasheet RegA 9050 by Coherent, Inc. (2006).

**[6-412]** I.N. Ross, P. Matousek, G.H.C. New, K. Osvay, *Analysis and optimization of optical parametric chirped pulse amplification*, J. Opt. Soc. Am. B 19 (2002) 2945.

**[6-413]** F. Ilday, F. Kärntner, *Cavity-enhanced optical parametric chirped-pulse amplification*, Opt. Lett. 31 (2006) 637.

**[6-414]** Datasheet “TOPAS” by Quantronix (2006).

**[6-415]** T. Brixner, G. Gerber, *Quantum control of gas-phase and liquid-phase femtochemistry*, Chem. Phys. Chem. 4 (2003) 418.

**[6-416]** E.L. Saldin, E.A. Schneidmiller, M.V. Yurkov, *Terawatt-scale sub-10-fs laser techno-logy - key to generation of GW-level attosecond pulses in X-ray free electron laser*, Opt. Comm. 239 (2004) 161.

**[6-417]** B.W. Adams, *Femtosecond synchronism of x-rays to visible light in an x-ray free-electron laser*, Rev Sci. Inst 76 (2005) 063304.

**[6-418]** T. Miura et al., *Timing jitter in a kilohertz regenerative amplifier of a femtosecond-pulse Ti : Al2O3 laser*, Opt. Lett. 25 (2000) 1795.

**[6-419]** P. O'Shea, M. Kimmel, X. Gu, R. Trebino, *Highly simplified device for ultrashort-pulse measurement*, Opt. Lett. 26 (2001) 932.

**[6-420]** M.M. Shakya et al., Appl. Phys. Lett. 87 (2005) 041103.

**[6-421]** B. Henke et al., J. Appl. Phys. 52 (1981) 1509.

**[6-422]** P.A. Jaanimagi, *Fourth-Generation X-Ray Sources and Ultrafast X-Ray Detectors*, SPIE proceedings Vol. 5194 (2004).

**[6-423]** C. Belzile et al., Rev. Sci. Instr. 73 (2002) 1617.

**[6-424]** J. Liu, Appl. Phys. Lett. 82 (2003) 3553.

**[6-425]** Ch. Broennimann et al., J. Synchrotron Rad. 13 (2006) 120.

**[6-426]** G. Lutz, J. Synchrotron Rad. 13 (2006) 99.

**[6-427]** E.R. Fossum et al., Proceeding of SPIE 1949 (1993) 256-265.

**[6-428]** B. Dierickx et al., Proceedings of 1997 IEEE CCD & Advanced Image Sensors Workshop, Brugge, Belgium.

**[6-429]** A. Fant et al.: presented at PSD7, to be published in NIM A.

**[6-430]** R. Turchetta, J. Velthuis et al., NIM A 560 (2006) 102-108.

**[6-431]** G. Anelli et al., *Radiation tolerant VLSI circuits in standard deep submicron CMOS technologies for the LHC experiments: Practical design aspects*, IEEE Trans. Nucl. Sci. 45 (1999) 1690-1696.

**[6-432]** B.G. Taylor, *TTC Distribution for LHC Detectors*, IEEE Trans. Nuclear Science 45 (1998) 821.

# 7 Infrastructure and auxiliary systems

## 7.1 Site layout and civil construction

### 7.1.1 Overall site layout

The overall layout of the X-Ray Free-Electron Lasers (XFEL) is shown in Figure 7.1.1. It will be realised in two steps.

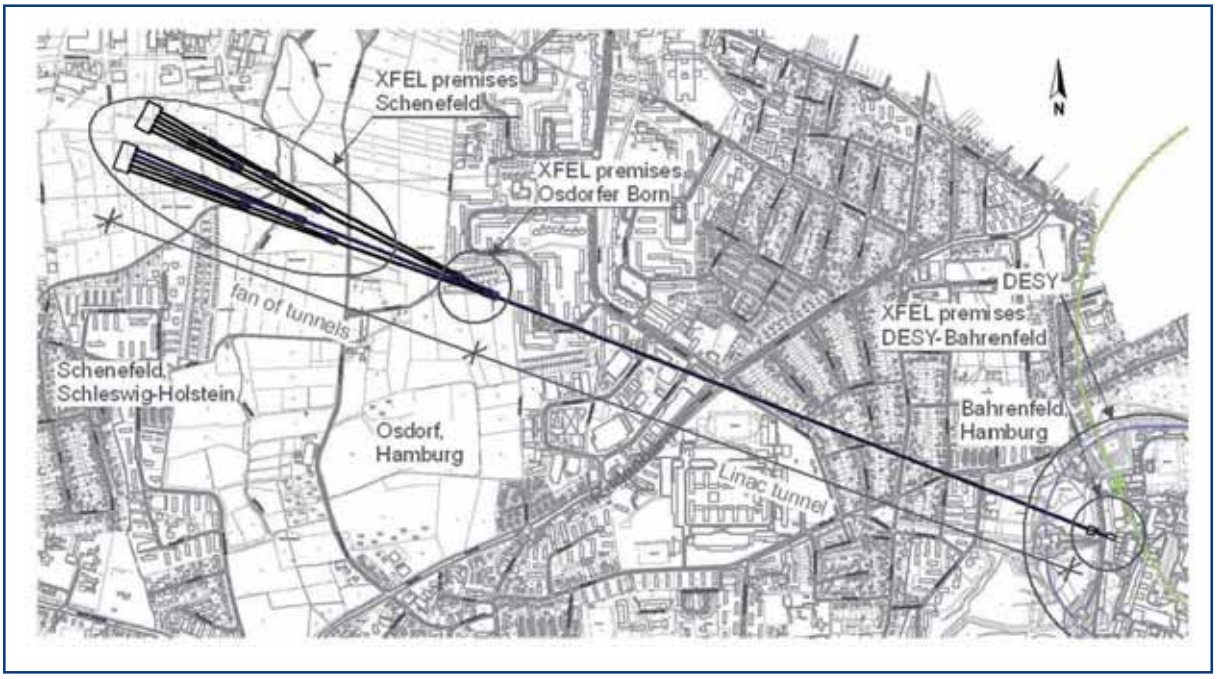


***Figure 7.1.1*** *Topographical layout of the XFEL.*

The facility stretches from the Deutsches Elektronen-Synchrotron (DESY) Laboratory site in Hamburg-Bahrenfeld in north-west direction to an area south of the city of Schenefeld (district Pinneberg). The facility predominantly consists of tunnels that run underground. The buildings at the surface are concentrated on three sites:

#### *7.1.1.1 DESY-Bahrenfeld*

This is where the injector is located and the tunnel for the linear accelerator (linac) starts. The cryogenic supply, power, water and climate are provided via access shafts that are also used for the insertion and removal of the tunnel drilling machine. On top of the shafts there exist halls that are provided with cranes for the transport of components into the injector building and the tunnel.

### *7.1.1.2 Osdorfer Born*

After acceleration in the linac, the electron beam is at this position distributed into two undulator tunnels and into the first tunnel of the second building phase of the XFEL. The division of one incoming tunnel into three outgoing tunnels necessitates the construction of a large distribution shaft that is also used to accommodate the tunnel drilling machine and to transport the components of the machine and undulator beamlines into the tunnel buildings. In addition, the linac commissioning electron dump is positioned here. Only the underground part of phase two will be realised initially. This way the interference of the later phase two construction with the operation of the existing facility can be minimised.

### *7.1.1.3 Schenefeld*

The undulator tunnels split up into photon tunnels and further undulator tunnels. Thus, a distribution fan of photon and undulator tunnels is generated, producing five photon beamlines that end in the experimental hall. Further shafts are located where the tunnels divide. They will also be used for the transport of the tunnel drilling machine and the beamline components. The experimental hall and the accompanying buildings (office and laboratory space, canteen, warehouses, etc.) form the centre of the experimental activities of the XFEL Facility.

Figure 7.1.2 shows a side view of the XFEL tunnels and shafts. The depth of the position of the tunnels underground is determined by several factors. For cryogenic reasons, the tunnel for the linear accelerator is positioned with its longitudinal centre (at a distance of 1,000 m from the start of the linac) tangential to an equipotential plane of the Earth's gravitational field. The distribution tunnels (undulator tunnels and photon tunnels) are positioned so that the experimental hall (at a distance of approximately 3,350 m from the start of the XFEL) is also tangential to the equipotential surface. Thus, the linac tunnel and the plane in which the distribution tunnels lie form an angle of approx. 0.02°. Their intersection lies approximately 200 m before the end of the linac tunnel.

To reach the radiation safety goals, the minimum depth of coverage of the tunnel with earth amounts to approximately 6 m. Thus, the shallowest surface area along the length of the tunnel determines the depth of the entire building complex. This occurs near the small river Düpenau at a distance of approximately 2,800 m from the start of the XFEL.

The tunnel and shaft buildings will be realised in a depth from 12 m up to 44 m below the surface. The foundation of the buildings will, thus, be situated below the groundwater table and the buildings will lie up to 20 m inside the groundwater.

The tunnels will most probably be constructed using a tunnel drilling machine using a supported-tunnel-shield method with segmented concrete lining. This will mean minimum interference with the groundwater level and flow.

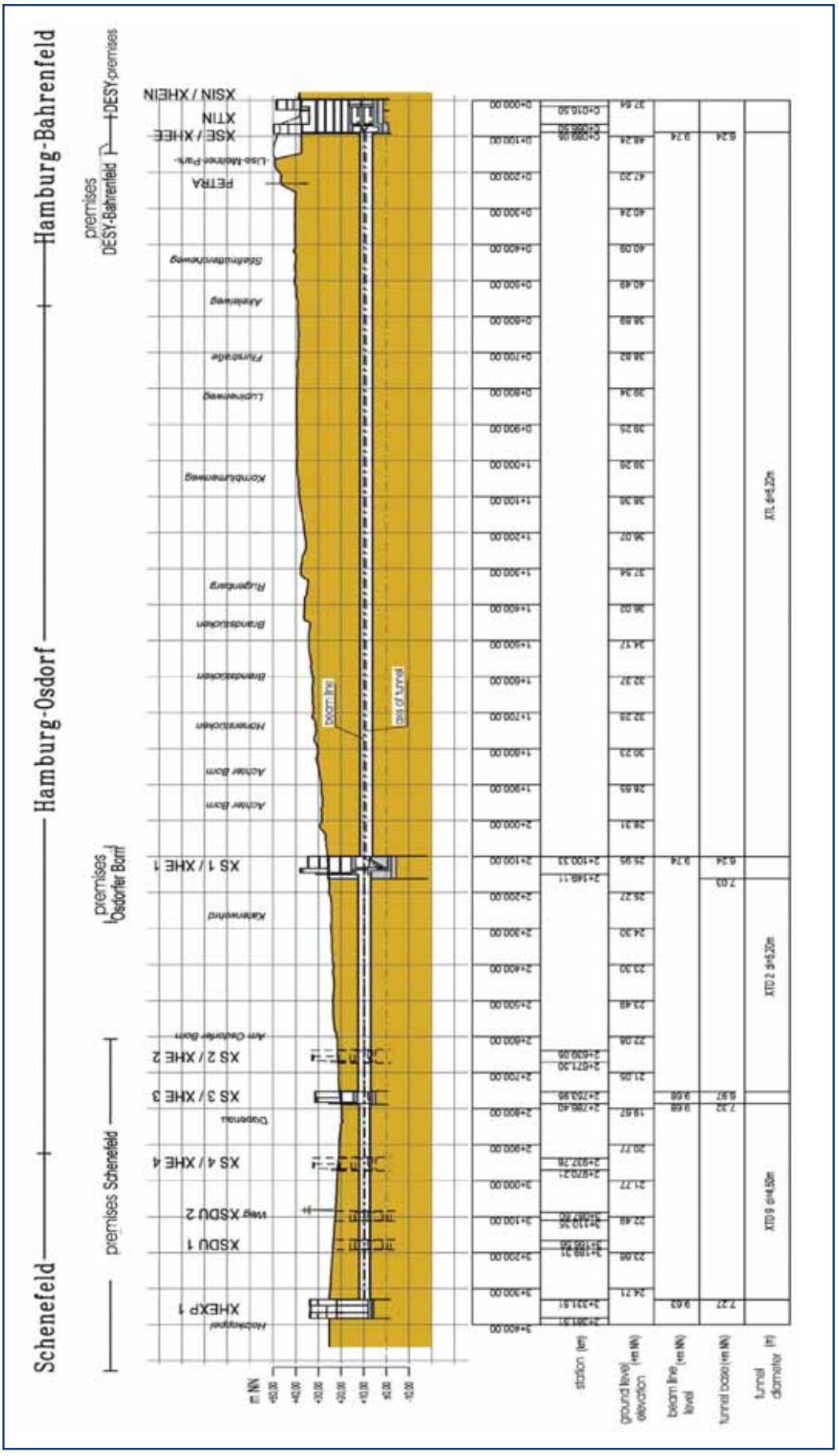


***Figure 7.1.2*** *Side view of the XFEL tunnels and shafts.*

The main parameters for the layout of the XFEL civil construction are listed in Table 7.1.1.

| | |
|---|---|
| Length of injector building (XSIN+XTIN+XSE) | 89.5 m |
| Length of the preaccelerating section 1 (130 - 500 MeV) | 80.5 m |
| Length of bunch compressor 1 | 63 m |
| Length of the booster accelerating section (500 - 2000 MeV) | 150 m |
| Length of bunch compressor 2 | 84 m |
| Length of main accelerating section (2 – 20 GeV) | 1221 m |
| Length of collimation section | 207 m |
| Length of distribution tunnel building | 1230 m |
| Overall length of the facility | 3400 m |
| Range of earth coverage of tunnels below surface | 6 to 38 m |

***Table 7.1.1*** *Main layout parameters for the XFEL civil construction.*

Figure 7.1.3 shows the nomenclature for the main buildings of the XFEL Facility for the two building phases, both above and below the surface. The individual buildings will be described in the following sections, organised according to their topographical position. In this report only the first building step will be described further.

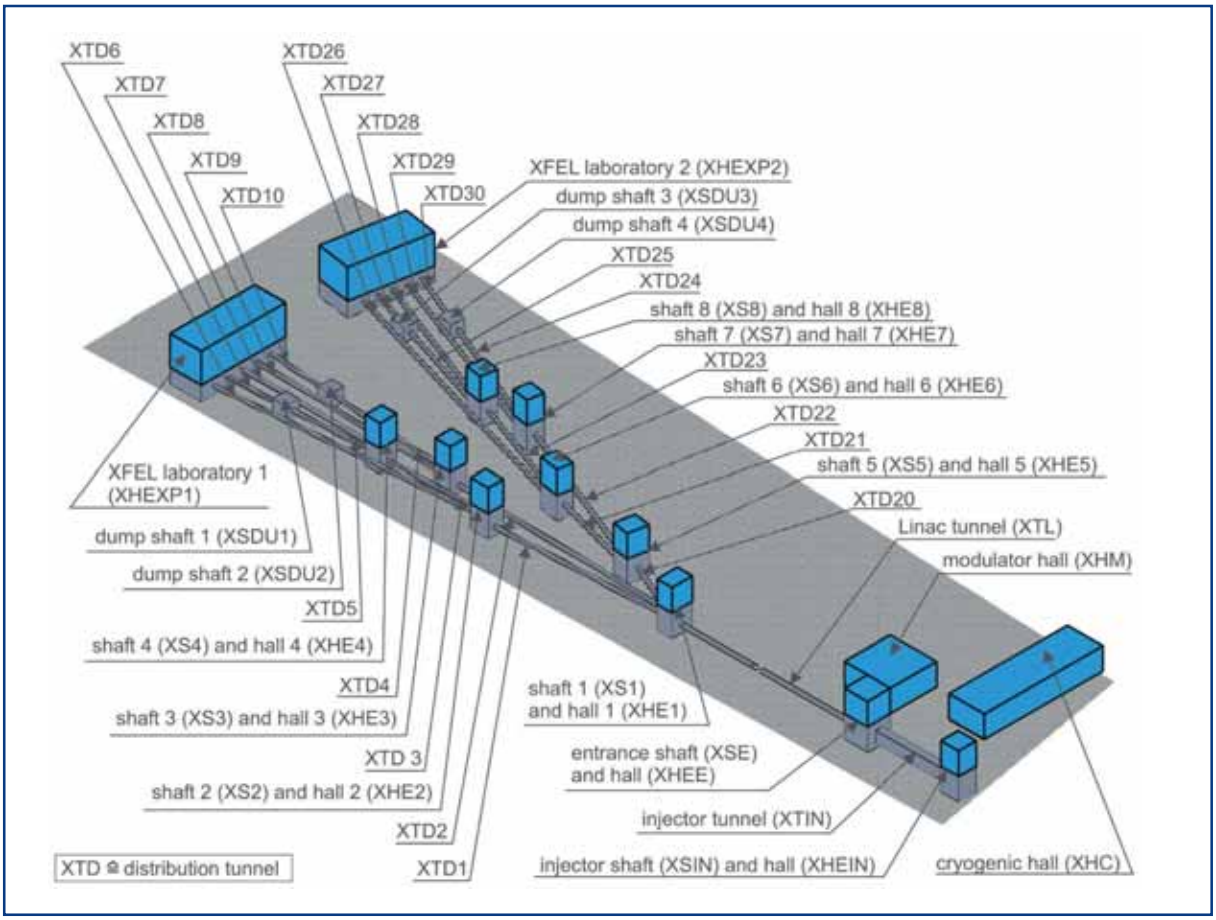


***Figure 7.1.3*** *Nomenclature for the main buildings of the XFEL Facility for the two building phases, both above and below the surface.*

## 7.1.2 Civil construction

### *7.1.2.1 XFEL site DESY-Bahrenfeld*

Figure 7.1.4 shows an overview of the DESY site in Hamburg-Bahrenfeld. Figure 7.1.5 shows the new buildings that have to be constructed for the XFEL in the north-western area of the DESY site. This is where the tunnel XTL for the acceleration of the electron bunches starts with the injector complex.

The installation of components into the tunnel XTL is performed using the tunnel entrance building (XHEE). The pulsed radio frequency for the accelerating structures in the injector building and the tunnel XTL is produced in the modulator hall XHM and fed with pulse cables into the tunnels. The liquid Helium for the superconducting accelerating structures is provided by the cryogenic facility located mainly in the cryogenics hall XHC.

The technical infrastructure on the XFEL site DESY-Bahrenfeld is complemented by buildings for transformers and pumps, storage tanks for excess liquid Helium and heat exchangers.

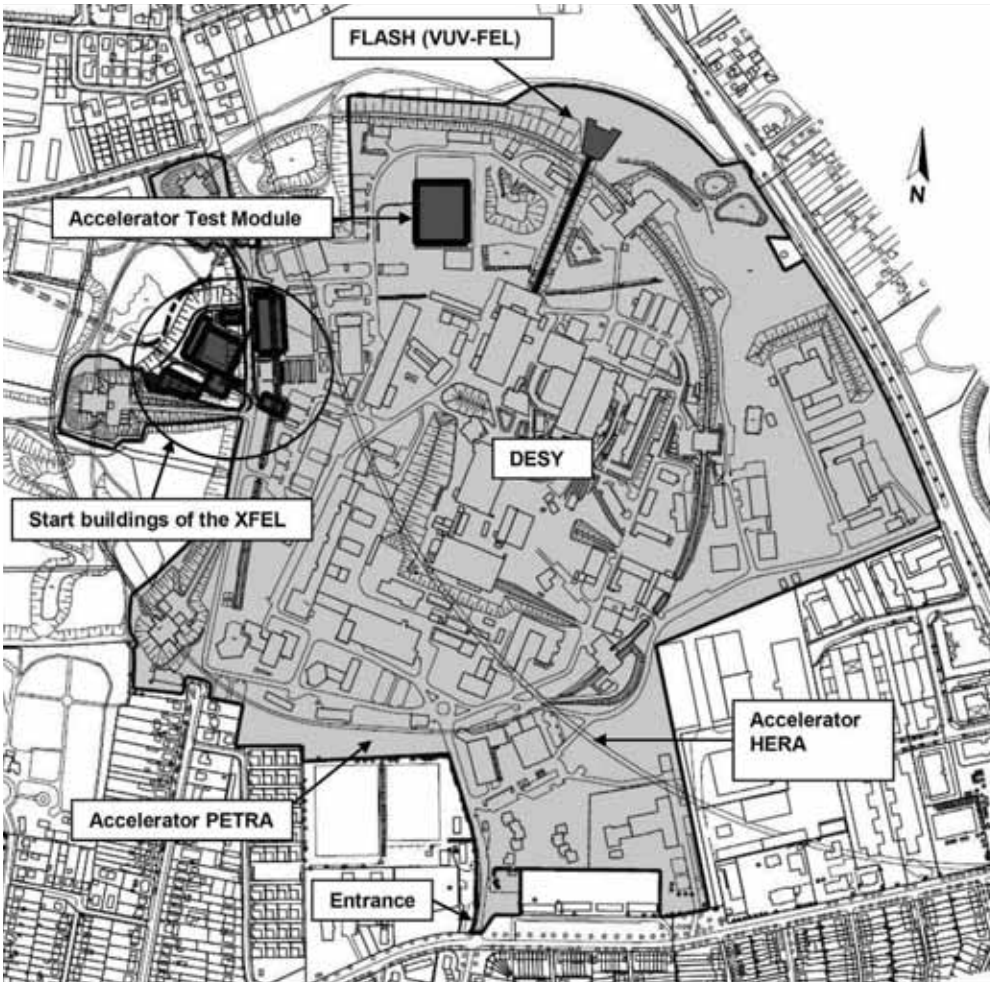


***Figure 7.1.4*** *Overview of the DESY site in Hamburg-Bahrenfeld.*

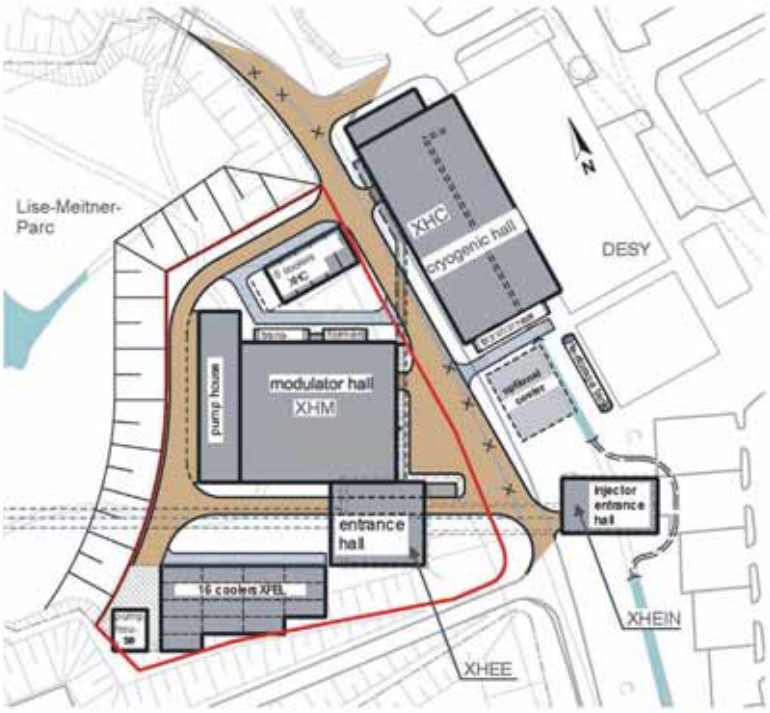


***Figure 7.1.5*** *Overview of the civil construction for the XFEL on the DESY site Hamburg-Bahrenfeld. The necessary enlargement of the existing DESY site is marked in red.*

The acceptance tests of the accelerating modules will take place in a newly erected building called Accelerator Module Test Facility (AMTF). Its position on the DESY site can be seen in Figure 7.1.4. For completeness its description is included in this report (Section 7.2.5).

Figure 7.1.6 shows a longitudinal cross-section of the injector building and the adjacent shaft XSE. The two injectors are located on the two lowest floors of the building XTIN. The remaining floors of the building XTIN are occupied by klystrons including electric power equipment and a cold box for the distribution of the liquid Helium to the superconducting accelerator modules of the two injectors and the main accelerator. In addition, they house the photo cathode laser system, cabinets for electronics and diagnostics hardware, and power supplies for the beamline magnets of the injector and the main accelerator.

During the construction phase, the shaft XSE serves as target shaft for the drilling of the tunnel XTL and as emergency exit. During the installation and operation phases, the shaft is used to gain access to the injector tunnel XTIN, the accelerator tunnel XTL and as emergency exit. In addition it is used as an installation shaft for all supply media for these buildings, including the liquid Helium.

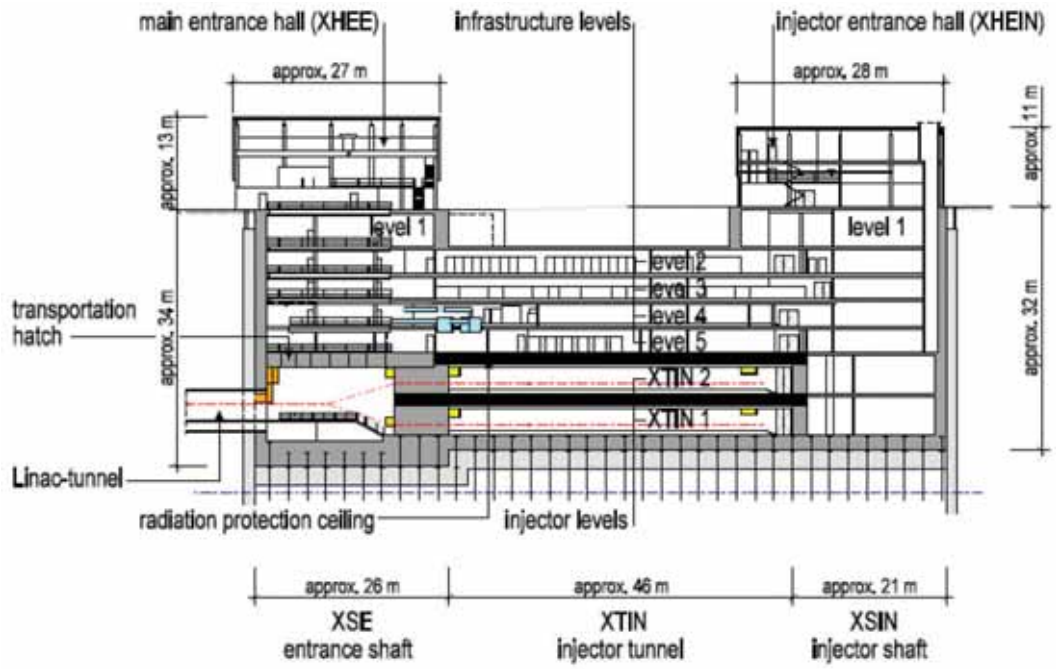


***Figure 7.1.6*** *Longitudinal cross-section of the injector buildings XTIN and XSIN and the adjacent shaft XSE. The dash-dotted red lines indicate the direction of the electron beam axes in the two injectors and the linac tunnel.*

Figure 7.1.7 shows a three-dimensional view of the injector complex including the underground facilities.

***Figure 7.1.7*** *Three-dimensional view of the injector complex at the XFEL site DESY-Bahrenfeld.*

The cryogenics hall will be built directly adjacent to the existing HERA cryogenics hall. To store the Helium the existing Helium gas tanks of the HERA cryogenics plus a storage tank for liquid Helium will be used. The HERA cryogenics hall and the new XFEL cryogenics hall XHC, to be built, will be connected using the cold box in the XFEL hall. Thus, the HERA cryogenics facility can be used to cool the injectors and/or linear accelerator when the XFEL cryogenics facility is down or being serviced.

Figure 7.1.8 shows the ground plan of the cryogenics hall for the XFEL Facility.

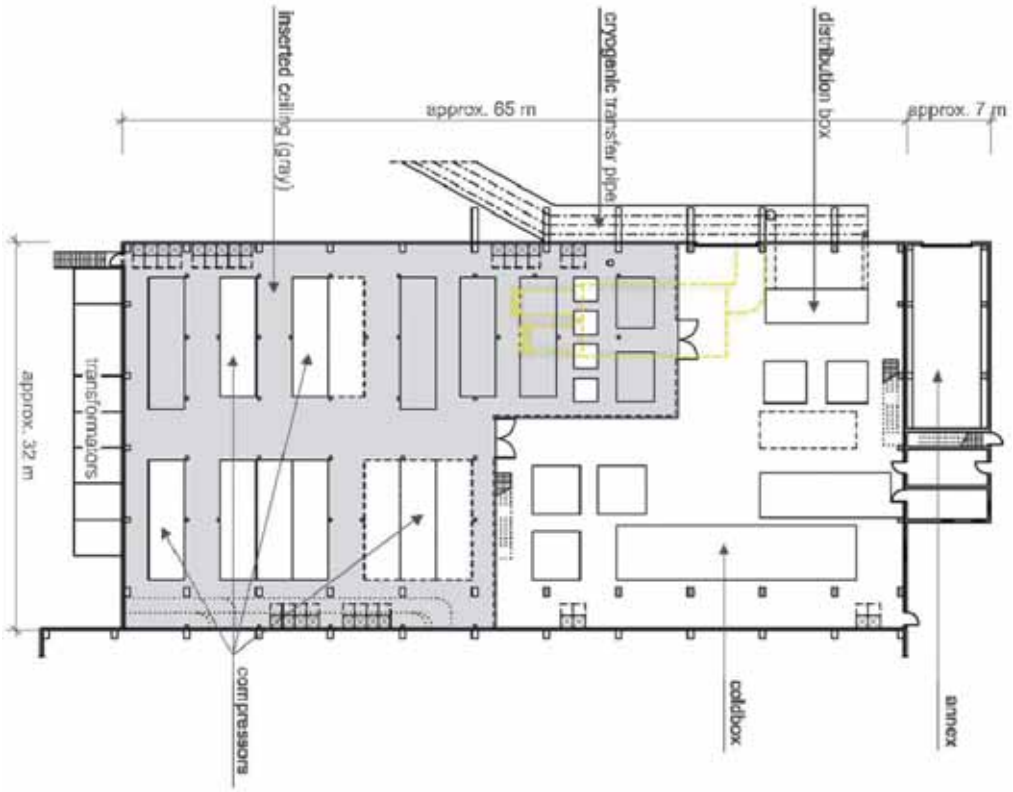


***Figure 7.1.8*** *Ground plan of the XFEL cryogenics hall. The dimensions of the hall are about 72 m × 32 m with a height of about 14 m.*

The modulator hall XHM is located next to the supply shaft XSE. It is designed to house up to 35 modulator stations (including the second injector and two reserves). Control and pulse cables are routed from the modulator hall via the shaft XSE to the tunnel sections of the injector building XTIN and the linear accelerator XTL where they will be connected to the pulse transformers of the corresponding radio frequency (RF) station. The size of the modulator hall is about 46 m × 41 m.

Figure 7.1.9 shows an aerial visualisation/simulation of the XFEL site DESY-Bahrenfeld.

***Figure 7.1.9*** *Aerial visualisation/simulation of the XFEL site DESY-Bahrenfeld.*

### *7.1.2.2 Accelerator tunnel XTL*

The tunnel building XTL starts at the shaft XSE on the DESY-Bahrenfeld site and contains the booster linac, the bunch compressor sections, the superconducting linear accelerator structures and a collimation section. The tunnel XTL ends in the shaft XS1 on the XFEL site Osdorf. Here, the electron beam is distributed to the different undulator beamlines in the tunnel building XTD. The overall length of the tunnel XTL is 2,010 m.

The diameter of the tunnel XTL is 5.2 m. It is the result of an optimisation process with the space requirement and cost aspects as important boundary conditions.

Figure 7.1.10 shows a cross-sectional view of the tunnel XTL with basic dimensions.

A detailed analysis of the space requirements in the tunnel showed that the suspension of the accelerator modules from the top is advantageous, especially for servicing of the installed components.

Starting at the top right are located the return line for the warm Helium gas, followed in a clockwise direction by the cable trays for signal cables and cooling water pipes. The cable trays beneath the floor are used for the RF pulse cables to the klystrons, cooling water supply lines for the experimental hall and pipes for pumping back possible leakage water. The pipes above the floor to the left are used for compressed air and Nitrogen. The big pipe on the top left side is used as an air duct for rapidly removing smoke in case of a fire.

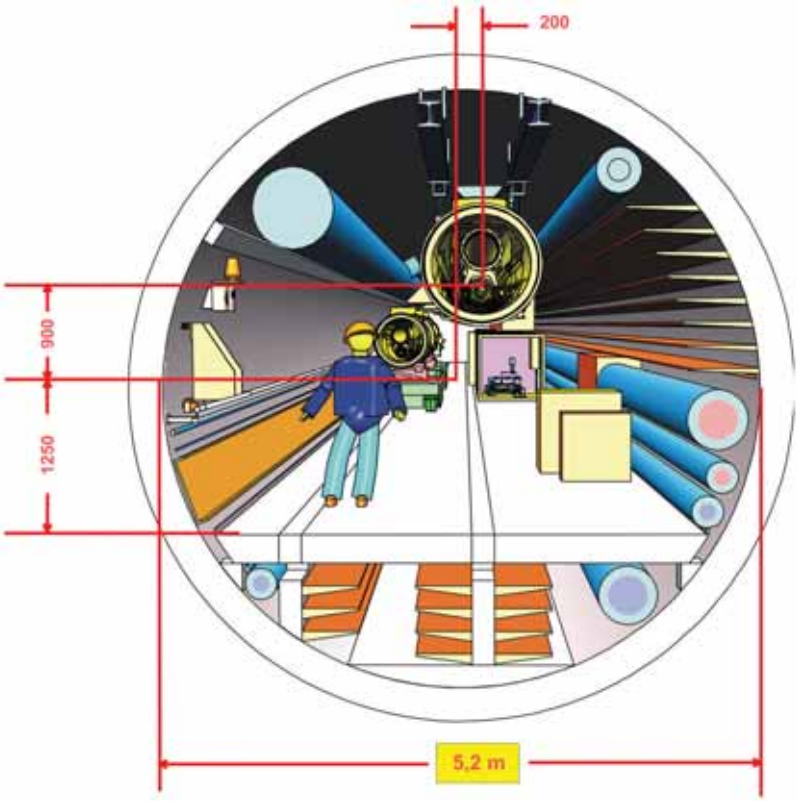


***Figure 7.1.10*** *Cross-sectional view of the tunnel XTL in the region of the accelerator modules including its basic dimensions. The beam axis of the accelerator is shifted from the tunnel centre by 200 mm to the right and 900 mm to the top (as viewed in the direction of beam acceleration). In the background the transport of another accelerator module is shown.*

Concerning the RF system, four superconducting accelerator modules of length 12.2 m each will be connected to become a unit of approximately 50 m length. Several other supply facilities will be grouped accordingly.

Figure 7.1.11 shows the same tunnel section as in Figure 7.1.10, but viewed from the other direction. Here one can see the infrastructure needed to supply the group of four accelerator modules: the klystron with pulse transformer and interface network and the electronics cabinets that contain the control systems and diagnostics hardware.

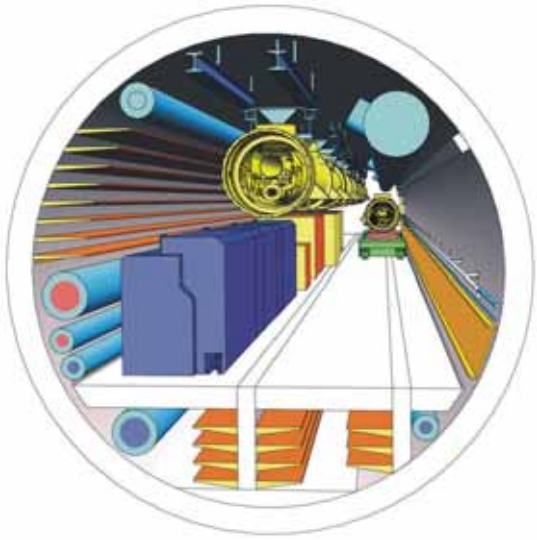

***Figure 7.1.11*** *Cross-sectional view of the tunnel XTL in the region of the accelerator modules (line of sight opposite to that of Figure 7.1.10).*

Figure 7.1.12 shows the same tunnel section in a longitudinal view. The free space of approximately 15 m in front of the supply section serves as a reserve space for the future installation of a second RF system to provide the possibility of a continuous wave (CW) mode for the operation of the accelerator.

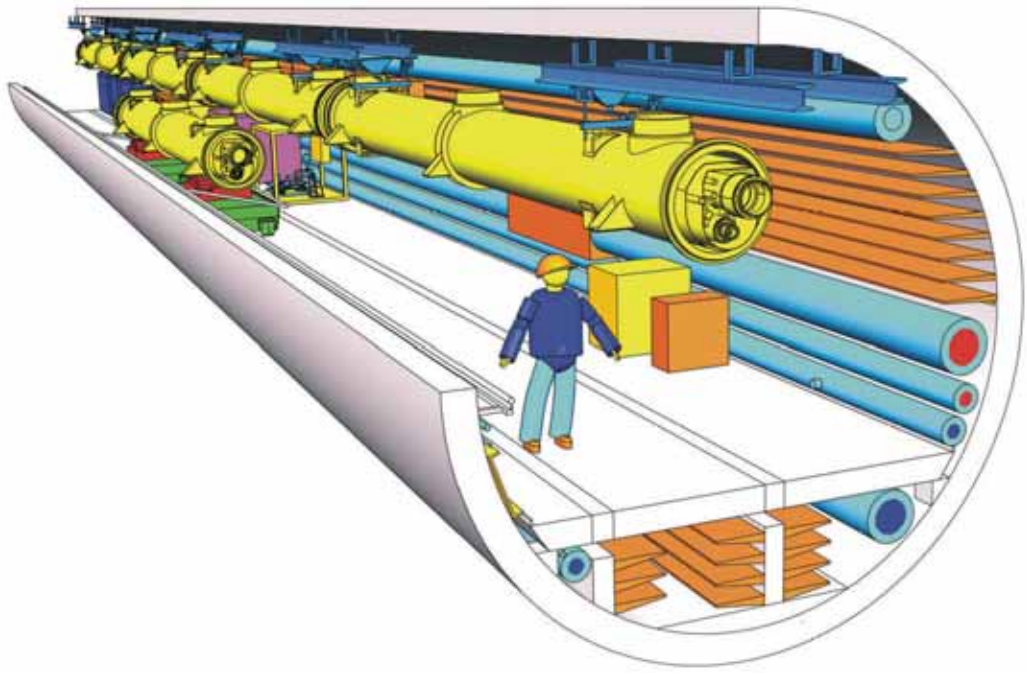

***Figure 7.1.12*** *Longitudinal view of the same tunnel section as shown in Figure 7.1.10. The entire section of approximately 50 m in length will be supplied with one RF system.*

Figure 7.1.13 shows the region of the electron beam distribution at the end of the linac tunnel XTL into the two undulator tunnels (and the tunnel XTD20, for a possible construction phase two of the XFEL Facility construction) at the shaft XS1. In addition, one can see a fourth beamline that is led downward through the shaft floor, where the beam dump for the commissioning of the linac is located.

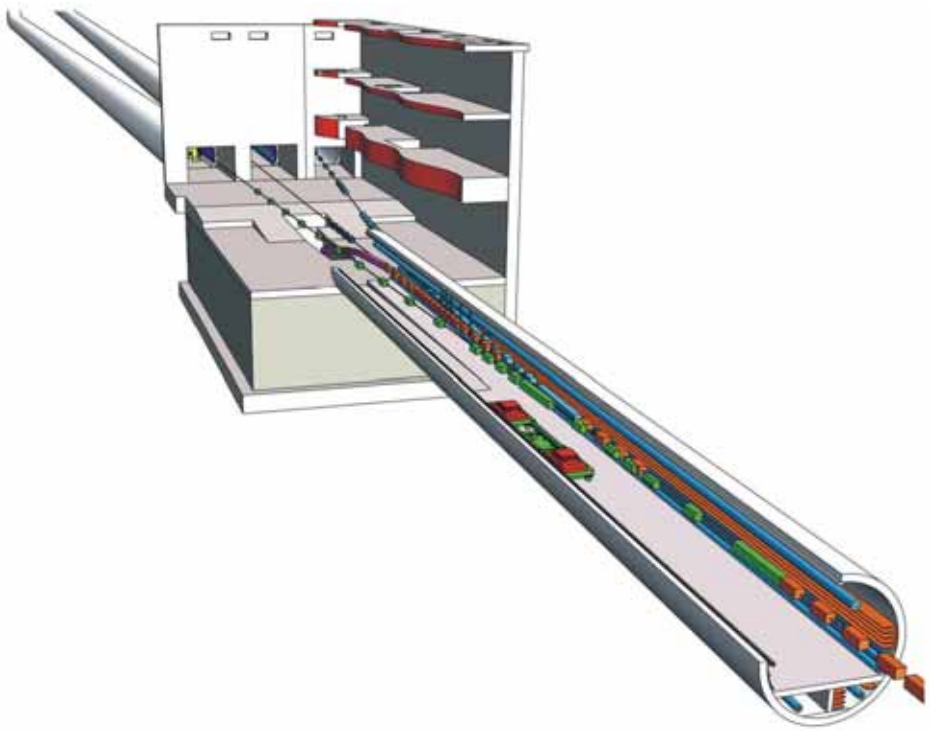

***Figure 7.1.13*** *Beam distribution at the end of the tunnel XTL. The three-dimensional drawing shows the distribution of the electron beam to the three distribution tunnels XTD1, XTD2 and XTD20 in the horizontal plane. In addition, the vertical deflection of the beam down to the emergency and commissioning beam dump is shown.*

### *7.1.2.2 Distribution tunnel system XTD*

Figure 7.1.14 shows a schematic overview and Figure 7.1.15 shows the actual layout of the distribution tunnel building XTD for the first construction phase.

An electron bunch after acceleration in the linac, can go through the following states on its way towards the beam dump (see Figure 7.1.15):

- distribution by pulsed magnets alternatively to one or the other of two branches of undulator tunnels (I);
- passage through SASE 1 and SASE 2 undulator sections for the generation of intense photon beams with high energy (II);
- horizontal deflection to the next (Self-Amplified Sponteneous Emission (SASE) or spontaneous) undulator section by long magnet sections (III);
- generation of a photon beam of lower (SASE)/higher (spontaneous) energy in these undulator sections (IV);

- horizontal deflection to the next spontaneous undulator section by long magnet sections (III') (branch 1, only);
- generation of a photon beam of higher energy in this undulator section (branch 1, only);
- vertical deflection to the beam dump absorber (V).

The layout of the distribution tunnel building is determined by this sequence. For each separation of the beams, a new shaft building is needed into which the incoming beam enters and from which two new tunnels exit.

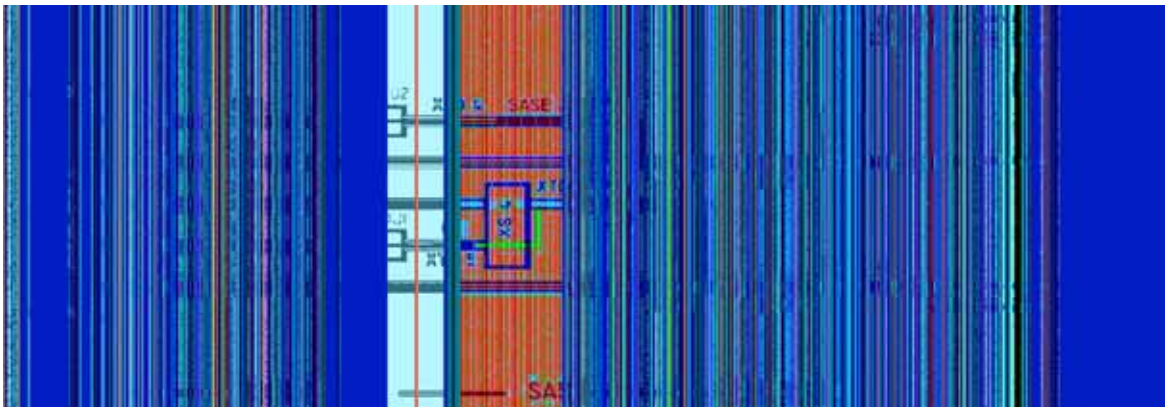


***Figure 7.1.14*** *Schematic view of the XFEL distribution tunnel system XTD (construction phase 1).*

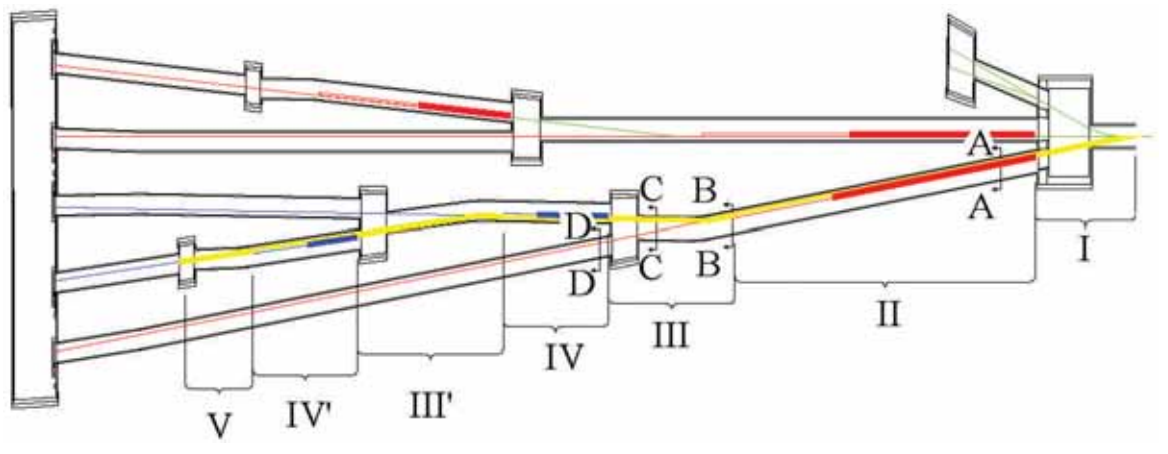


***Figure 7.1.15*** *Top view of the distribution tunnel building XTD (construction phase 1, distorted view in the ratio 5:1 for the horizontal to the vertical dimension). The sections labelled with Roman numerals indicate the various states that an electron bunch can be in while travelling through the structure. Letters indicate the position of the tunnel sections that are shown in cross sectional view in Figures 7.1.16 to 7.1.18. The electron trajectories are drawn in green, the trajectories of the photon beams generated in the SASE undulators are drawn in red and those generated in the spontaneous undulators are drawn in blue. Where electron and photon beam directions coincide, the colour of the photon beam is taken.*

The tunnel diameter in the two largest SASE undulator sections is determined by the high packing density of components and the optional placement of additional undulators in the future. The diameter of the photon tunnels that lead into the experimental hall is determined by the space requirements of the monochromator sections and the requirement that it must be possible, in the future, to accommodate additional photon beamlines. The tunnels XTD1-2 have an inner diameter of 5.2 m, identical to the tunnel for the linear accelerator, XTL. All other tunnels in the distribution building XTD have an inner diameter of 4.5 m. In this way only two different tunnel drilling machines are needed.

The basic dimensions of the tunnels of the tunnel distribution building XTD for construction phase 1 are listed in Table 7.1.2.

| Name | Ø [m] | Length [m] | Function |
|---|---|---|---|
| XTD1 | 5.2 | 480 | Undulator tunnel SASE 2 |
| XTD2 | 5.2 | 594 | Undulator tunnel SASE 1 |
| XTD3 | 4.5 | 263 | Undulator tunnel U1 |
| XTD4 | 4.5 | 302 | Undulator tunnel SASE 3 |
| XTD5 | 4.5 | 205 | Undulator tunnel U2 |
| XTD6 | 4.5 | 660 | Photon tunnel |
| XTD7 | 4.5 | 137 | Photon tunnel |
| XTD8 | 4.5 | 365 | Photon tunnel |
| XTD9 | 4.5 | 545 | Photon tunnel |
| XTD10 | 4.5 | 221 | Photon tunnel |
| XTD20 | 4.5 (w)× 4.3 (h) | 61 | e- Transfer tunnel to construction phase 2 (rectangular cross-section) |

***Table 7.1.2*** *Basic dimensions of the tunnels of the tunnel distribution building XTD for construction phase 1.*

Figures 7.1.16 to 7.1.18 show cross-sectional views of representative tunnel sections in the tunnel distribution building XTD, including the technical infrastructure at those positions (undulator tunnel, beam distribution region, photon tunnel (gas filter section)). The relative positions of the selected sections in XTD have been indicated by letters in Figure 7.1.15.

The shaft buildings serve not only to accommodate the beam distribution but also as access points to the tunnels for personnel and material and for the routing of the supply lines for power, water, air conditioning, etc. to and from the tunnels. During the construction phase they serve as start and target shafts for the tunnel drilling machine.

The dimensions of the shafts are largely determined by the parameters for the beam deflection geometries:

- radius of deflection for the electron beam;
- geometrical size of the components for the beamline optics;
- minimum distance of the beamline components to the tunnel walls.

In addition, the length of the shafts is affected by the requirement to allow access to each tunnel while the neighbouring tunnel is in operation.

Figure 7.1.19 and Figure 7.1.20 show the layout of the lowest floor and a side view of the shaft XS2 which is analogous with XS3 to XS5.

***Figure 7.1.16*** *Cross sectional view of the tunnel in the region of the SASE undulators as viewed in the beam direction. The diameter of the tunnel is determined by the transport path for a replacement undulator module and the necessary emergency pathway (see position A-A in Figure 7.1.15).*

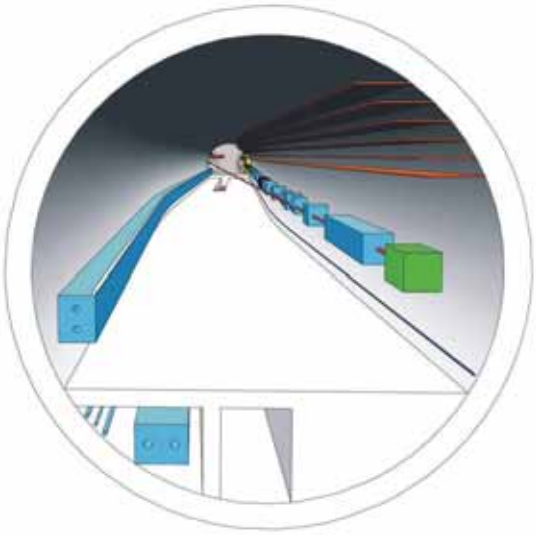

***Figure 7.1.17*** *Cross-sectional view of the tunnel distribution region as viewed from the incoming tunnel. (see position B-B in Figure 7.1.15).*

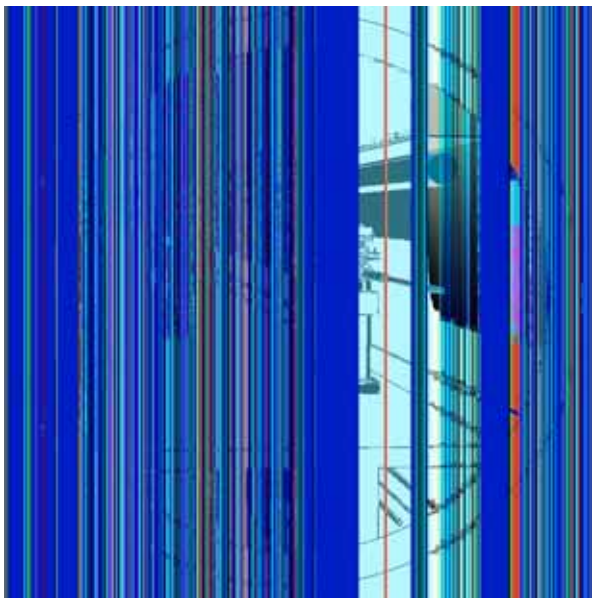

***Figure 7.1.18*** *Cross-sectional view in the region of the gas filter section (see position D-D in Figure 7.1.15 as viewed along the beam direction).*

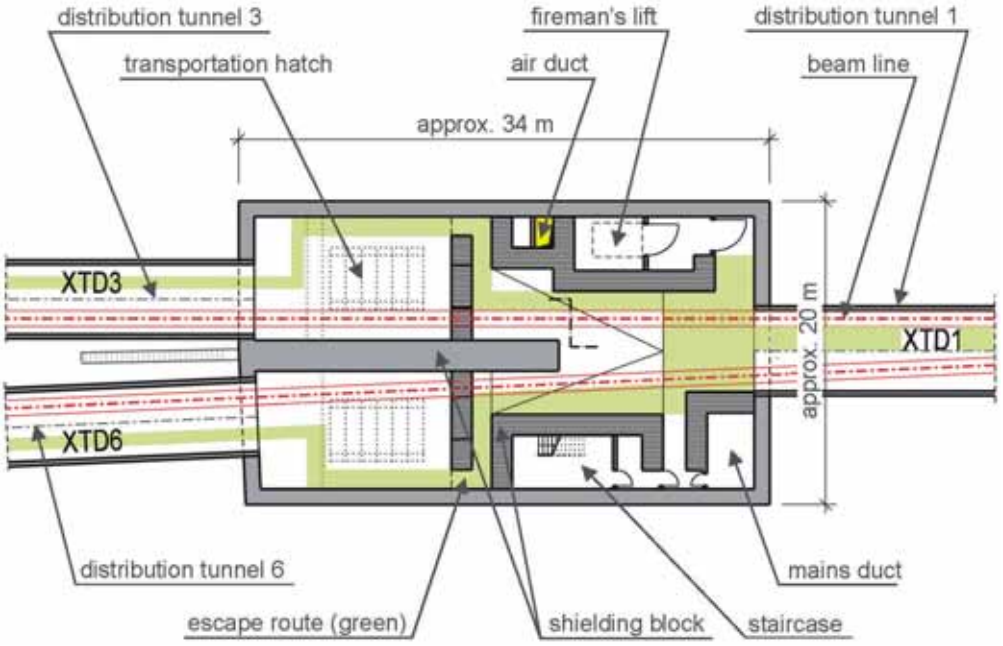


***Figure 7.1.19*** *Layout of the lowest floor of the shaft XS2.*

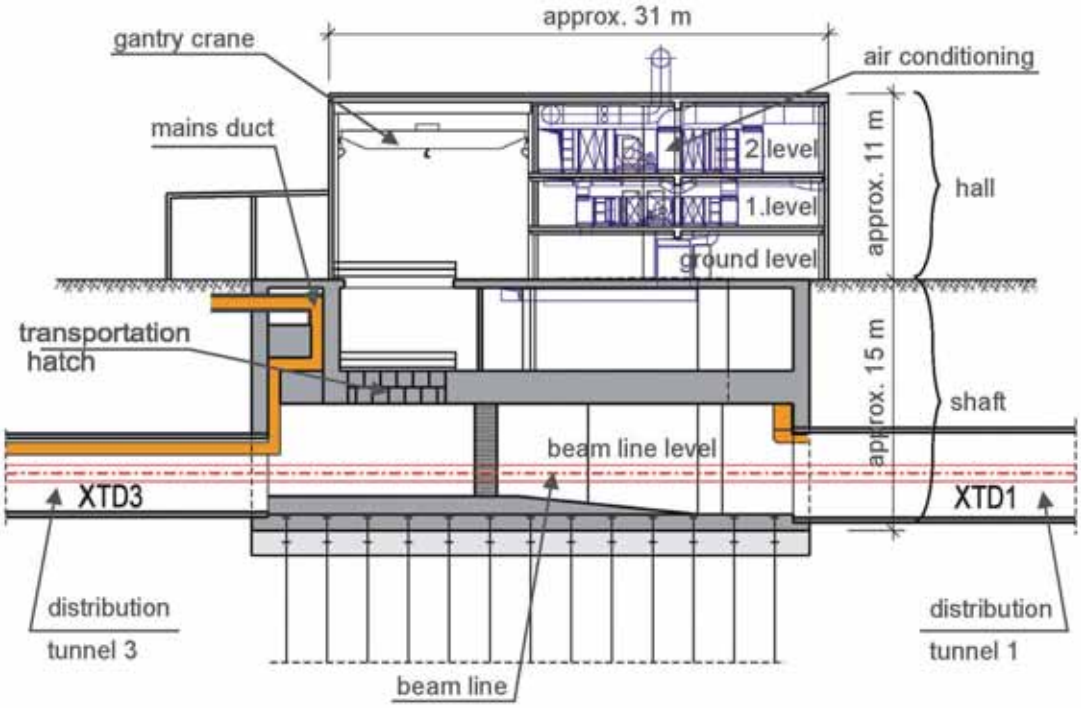


***Figure 7.1.20*** *Side view of the underground floors and the entrance hall of the shaft XS2.*

Figure 7.1.21 shows a side view of the absorber shaft building XSDU2.

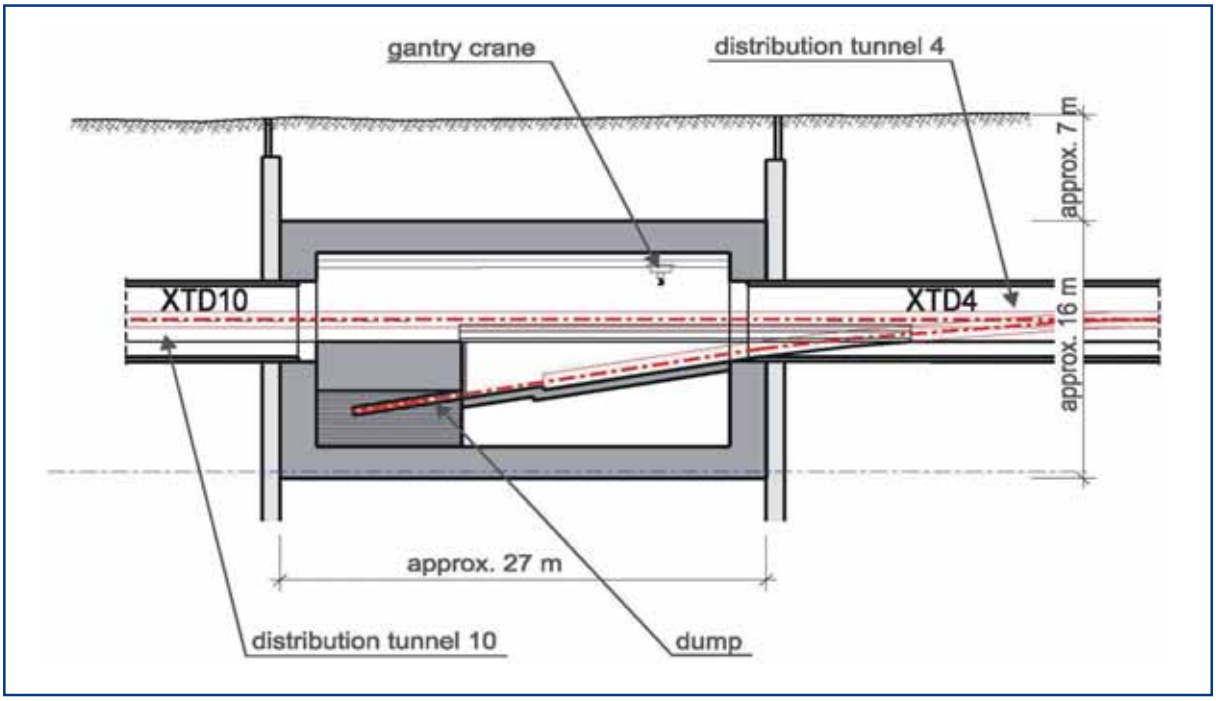


***Figure 7.1.21*** *Side view of the beam absorber shaft building XSDU2. The electron beam is deflected downwards, the photon beam is unaffected and travels towards the experimental hall. In addition, the crane facility and the local concrete shielding of the absorber are shown.*

### *7.1.2.4 XFEL site Osdorfer Born*

Figure 7.1.22 shows an overview of the XFEL site Osdorfer Born.

The linac tunnel XTL ends here and the electron beam is distributed to the undulator sections in the tunnel system XTD and/or to the connection tunnel XTD20 that will feed the undulator tunnel fan for the second construction phase of the XFEL.

Figure 7.1.23 shows the layout for the ground floor of the distribution shaft building XS1. This shaft is considerably larger than the other shaft buildings as it is the only one that has to accommodate three outgoing tunnels.

The outer dimensions of the shaft XS1 are about 51 m × 23 m (length x width), at the beam level even 63 m × 23 m. The depth of the underground part is approximately 28 m because of the commissioning dump below the beam level. The entrance hall XHE1 has two stories with a height of about 8 m. The region of the installation crane is about 12 m high. The outer dimensions of the shaft XS5 for the distribution of the beam into the undulator tunnels for the second construction phase are about 38 m × 18 m (length x width). The depth of the underground part is approximately 18 m.

Figure 7.1.24 shows a three-dimensional view of the shaft complex XS1 and XS5 at the XFEL site Osdorfer Born.

Figure 7.1.25 shows an aerial visualisation/simulation of the XFEL site Osdorfer Born. The entrance hall XHE5 that covers the shaft XS5 will only be realised in the second construction phase of the XFEL Facility.

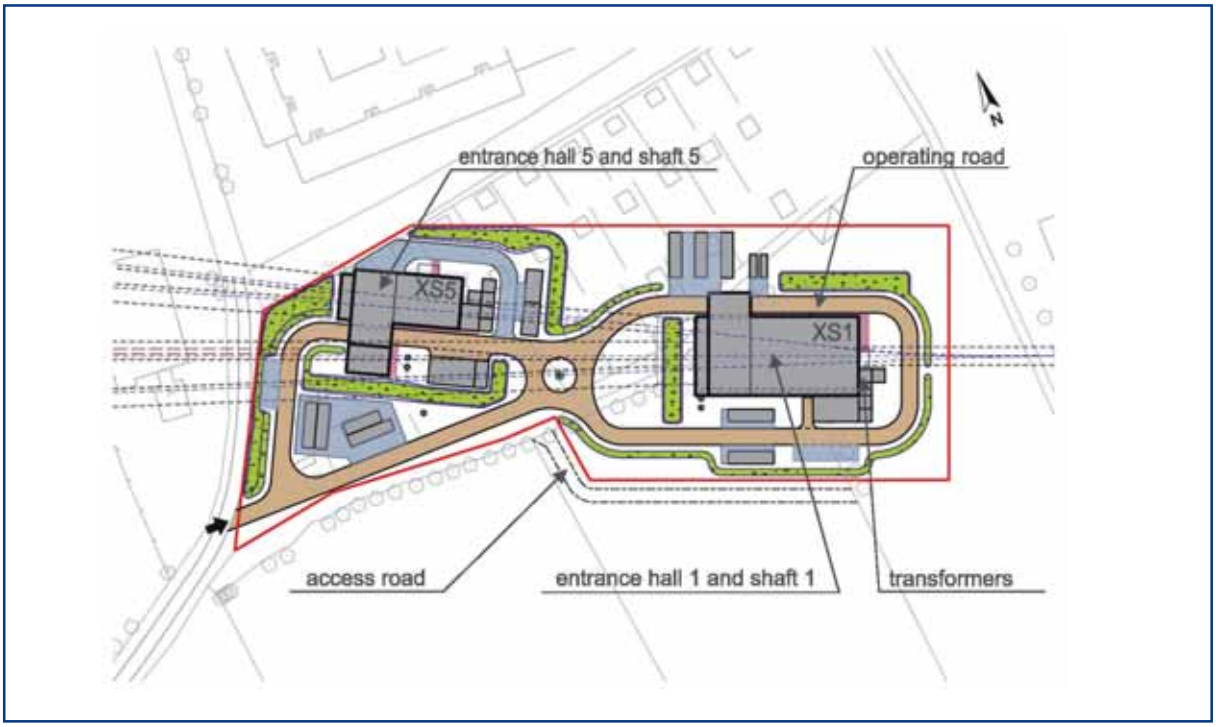


***Figure 7.1.22*** *The XFEL site Osdorfer Born. The accelerated electron beam is distributed to the undulator tunnels and to the connection tunnel XTD20 that will feed the undulator tunnel fan for the second construction phase of the XFEL Facility.*

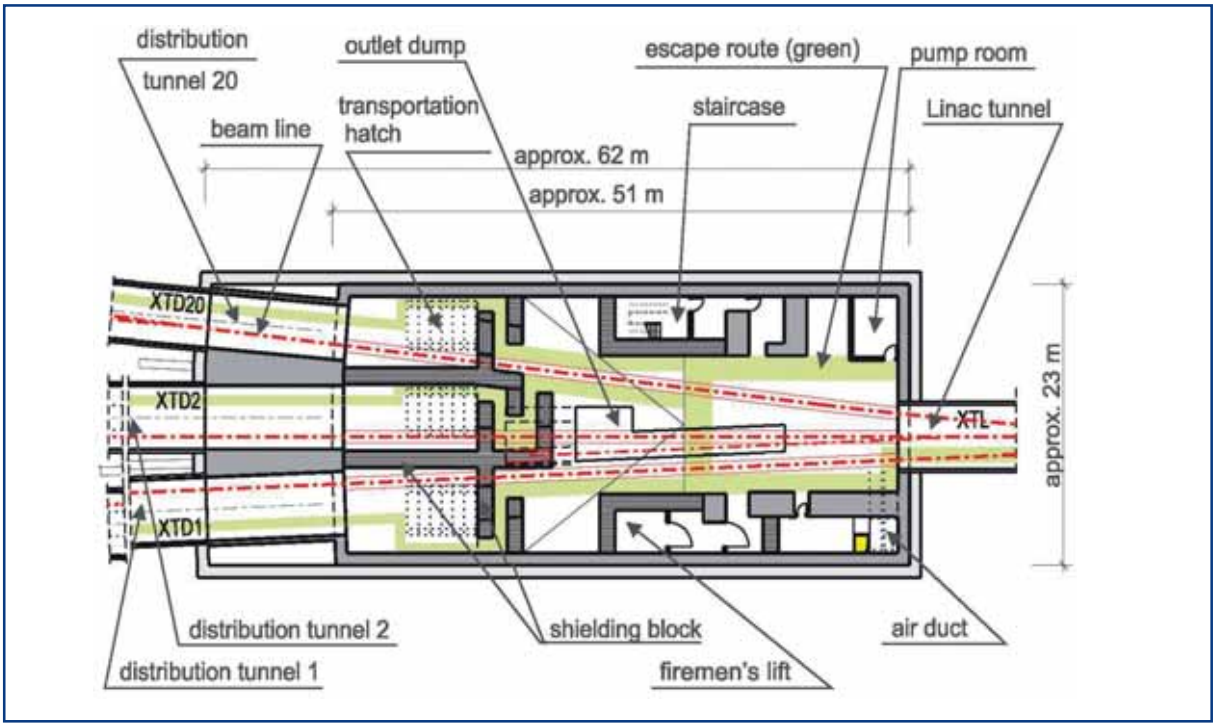


***Figure 7.1.23*** *Layout for the ground floor of the distribution shaft building XS1.*

***Figure 7.1.24*** *Three-dimensional view of the shaft complex XS1 and XS5 at the XFEL site Osdorfer Born.*


***Figure 7.1.25*** *Aerial visualisation/simulation of the XFEL site Osdorfer Born.*

### *7.1.2.5 XFEL site Schenefeld (Campus)*

The XFEL site Schenefeld (also called “Campus”) ranges from the street “Am Osdorfer Born” in the north-west to an area south of the street “Holzkoppel” in Schenefeld. Figure 7.1.26 shows an overview of the position of the individual buildings on the Campus site for the first construction phase.

The Campus can be divided into two separate areas: The western part constitutes the heart of the facility. The underground experimental hall and the laboratory and office complex for the scientists and technical personnel are located here. In addition to the research in the experimental hall facilities to hold meetings, workshops, lectures and seminars are provided.

The civil construction in the eastern part of the Schenefeld site is concentrated largely on the access halls (XHE2 + XHE4) for the distribution and access shafts XS2-4 and the accompanying infrastructure and supply facilities. Both parts of the Campus are connected via a central road.

It is expected that there will be considerable interest from external institutes in building outstations on the Schenefeld site in order to get maximum benefit from the intensive scientific interplay on the campus. For this purpose a central area of approximately 4,500 $m^2$ has been planned in the southwest part next to the experimental hall XHEXP1.

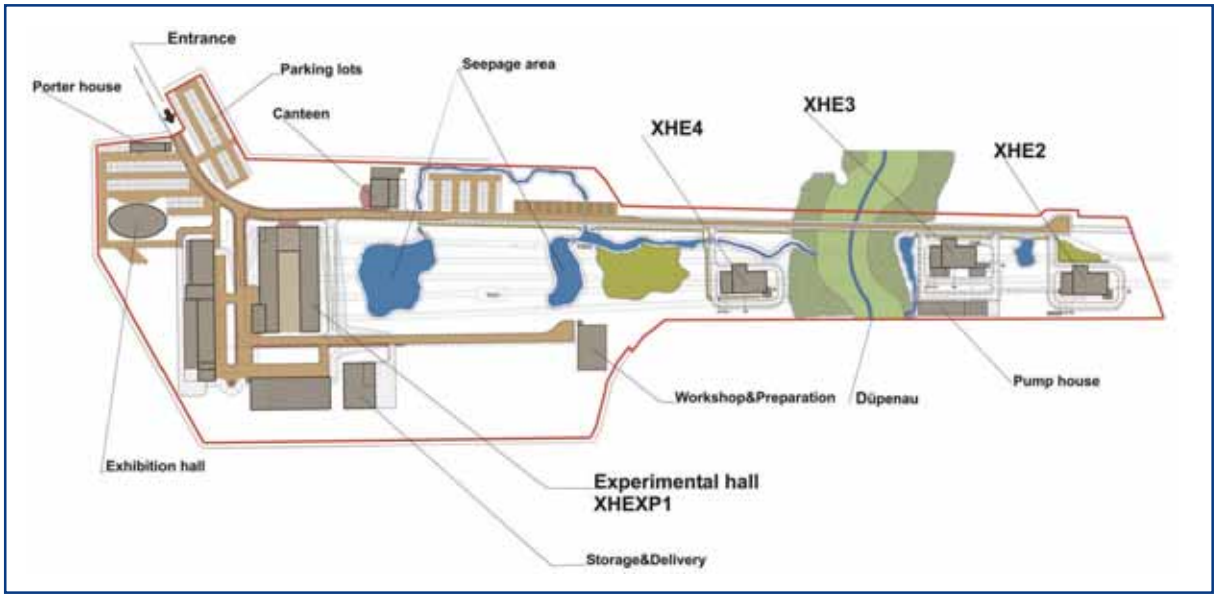


***Figure 7.1.26*** *Overview of the XFEL site Schenefeld for the first construction phase.*

Figure 7.1.27 shows the layout of the ground floor of the experimental hall XHEXP1 at the level of the five photon beamlines. It contains five separate areas for experiments that are positioned in line with the incoming photon tunnels. Also shown are the transport pathways and staircases. The experimental hall covers an area of 50 m × 90 m.

Two cranes are planned for the front and middle area of the hall to allow for the transport and installation of large components. The available height of the hall amounts to 14 m with considerable space above the cranes to accommodate ducts for supply media.

Figure 7.1.28 shows a three-dimensional view of the experimental hall and laboratory complex, as viewed from the incoming photon tunnels XTD6-XTD10.

The laboratory and office space for the technical and scientific staff includes seminar rooms and an auditorium for 200 people. It is located above the experimental hall. The office space is laid out for 350 staff. In addition, the building contains social rooms, transport pathways and rooms for the infrastructure needed for heating, power distribution and air conditioning. The laboratory and office building complex has an elevation of about 12 m above ground. Figure 7.1.29 shows the front view of the entrance region.

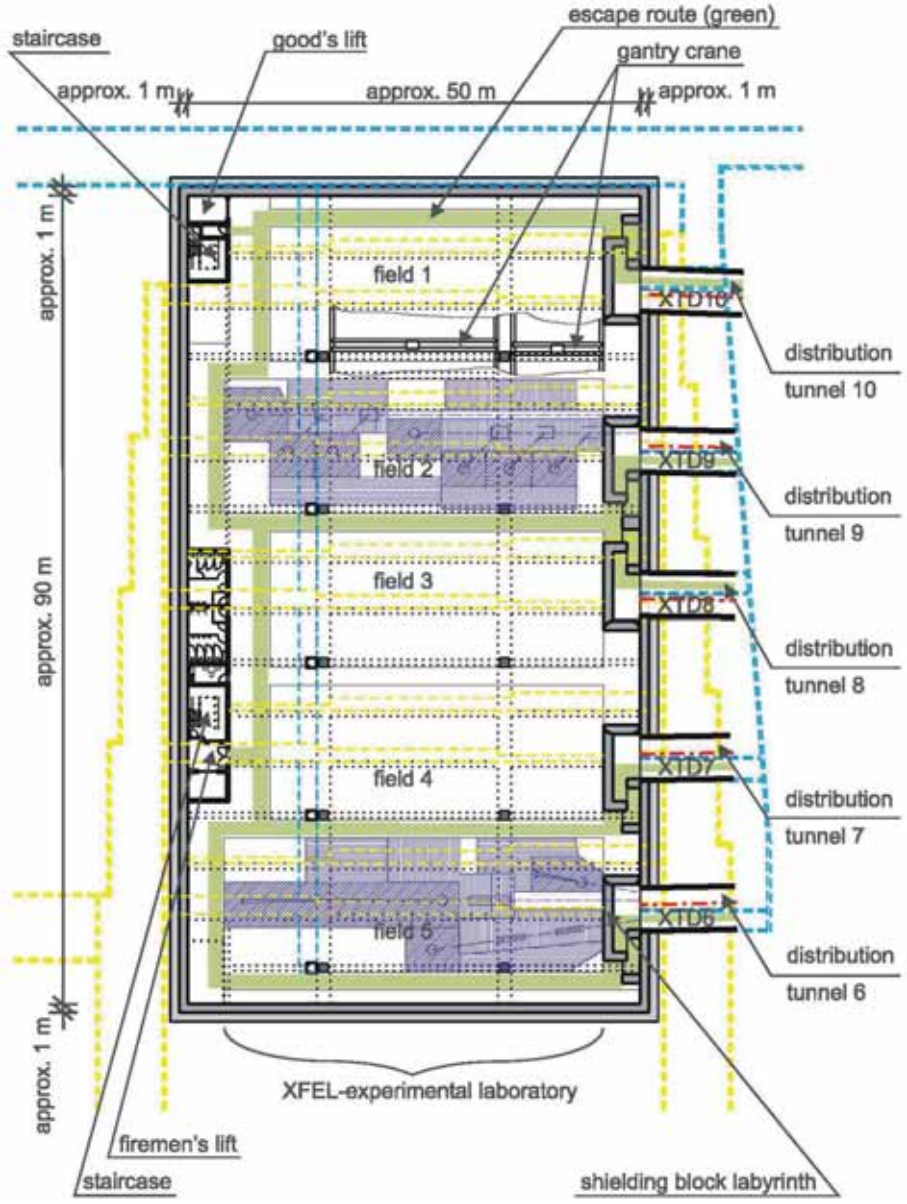


***Figure 7.1.27*** *Layout of the ground floor of the experimental hall XHEXP1. It contains five separate areas for experiments that are positioned in line with the incoming photon tunnels. Also shown are the transport pathways and staircases.*

***Figure 7.1.28*** *Three-dimensional view of the experimental hall and laboratory complex as viewed from the incoming photon tunnels XTD6-10.*


***Figure 7.1.29*** *Front view of the entrance region of the laboratory and office building that will be built on top of the underground experimental hall.*

In the vicinity of the laboratory and office complex a canteen, workshop, delivery area and exhibition hall for the general public are planned. For a capacity of 300 meals per day, a canteen of about 800 $m^2$ is needed.

In the workshop of approximately 1,000 $m^2$ small components can be produced or repaired, and experiments can be prepared. The long distance to the central DESY workshop makes such a facility mandatory. A small workshop for the technical services of 96 $m^2$ is also planned.

Besides the delivery of goods, a storage hall of 1,080 $m^2$ is foreseen for voluminous parts such as entire undulator modules.

The exhibition hall lies close to the entrance and is approximately 1,000 $m^2$ in size. It contains long-term future and current information about the ongoing experiments to visitors. This is important as many of these experiments are not directly accessible due to radiation protection or great sensitivity to vibrations induced by large visitor groups. In this area, the majority of the parking space for the XFEL campus is located.

The infrastructure for the supply of the experimental hall and the incoming photon tunnels (power supplies, transformers, emergency power, pump huts and heat exchangers, central heating and exhaust ventilation), is located next to the experiment complex. Air, water and electricity are routed to the experimental hall and the tunnels via underground channels.

Figure 7.1.30 shows an aerial visualisation/simulation of the XFEL site Schenefeld for the first construction phase.

***Figure 7.1.30*** *Aerial visualisation/simulation of the XFEL site Schenefeld for the first construction phase.*

## 7.2 Conventional technical infrastructure

### 7.2.1 Power distribution and power supplies

The electrical power for the XFEL Facility will be supplied from the DESY site. The power consumption will be approximately 9 MVA on the DESY site and 10 MVA on the Osdorfer Born and Schenefeld sites. This power requires a connection to the 110 kV network. The distribution on the DESY/XFEL sites will be done at the 10 kV-medium voltage level. The 110 kV-connection of the HERA storage ring provides 2 x 31.5 MVA at the 10 kV level. After the shut-down of HERA in July 2007, the existing 10 kV substation HST C can be used for the XFEL power supply.

The scheme of the 10 kV mains is shown in Figure 7.2.1. The switchboard of the substation HST C has to be expanded to feed the new transformers for the cryogenic plant XHC, the modulator hall XHM, the injector XTIN and the linac tunnel XTL. The transformers will be placed close to the consumers in order to lower the costs of the low-voltage AC cables (230 V/400 V/690 V). The input to the transformers will run directly from the 10 kV substation HST C via high-voltage cables.

The electrical supply for the Osdorfer Born and Schenefeld sites is planned to lay in the linac tunnel XTL. Therefore, four cable systems consisting each of 3 x 240 mm² Copper cables will be installed in cable trays beneath the tunnel floor. Every two cable systems will be connected together to a circuit, building a ring line. For service and maintenance purposes, a cable system or a substation can be disconnected and the power feed will still guaranteed.

Each 10 kV cable system will be twisted in order to reduce magnetic stray fields. This means sensitive monitors and electronic equipment will not be disturbed.

There are three central 10 kV substations foreseen near the halls XHE1, XHE3 and XHEXP1. The 10 kV substations will be installed above the surface in order to have direct access in case of a hazardous situation. The 10 kV power cables and the control cables run underground from the XFEL hall to the substations. A group of transformers is located adjacent to each service building.

#### *7.2.1.1 Cables in service rooms, shafts and tunnels*

All power cables are flame retardant and non-corrosive, so called “fire retardent and non-corrosive (FRNC)” cables. This applies for the 10 kV power cable and modulator pulse cables as well. The AC cables run on trays under the tunnel floor and in the shafts between the tunnel and the service rooms. The DC, control and signal cables are placed on separate cable trays and routes.

#### *7.2.1.2 Distribution of the low voltage mains*

The levels of the low voltage loads are:

- 690 V/400 V for the modulators and power supplies; and
- 400 V/230 V for heating, ventilation and air conditioning (HVAC), water pumps and lighting.

The 10 kV transformers provide the applied voltages. The low voltage energy will be distributed in switchboards located in separate service rooms.

The loads in the tunnel are: auxiliaries of the klystrons, electronics cupboards, magnet power supplies, diagnostics, magnet movers, etc. Here, 400 V/230 V are needed. Therefore, sub-distributions and mobile distribution panels will be placed at regular intervals in the tunnel.

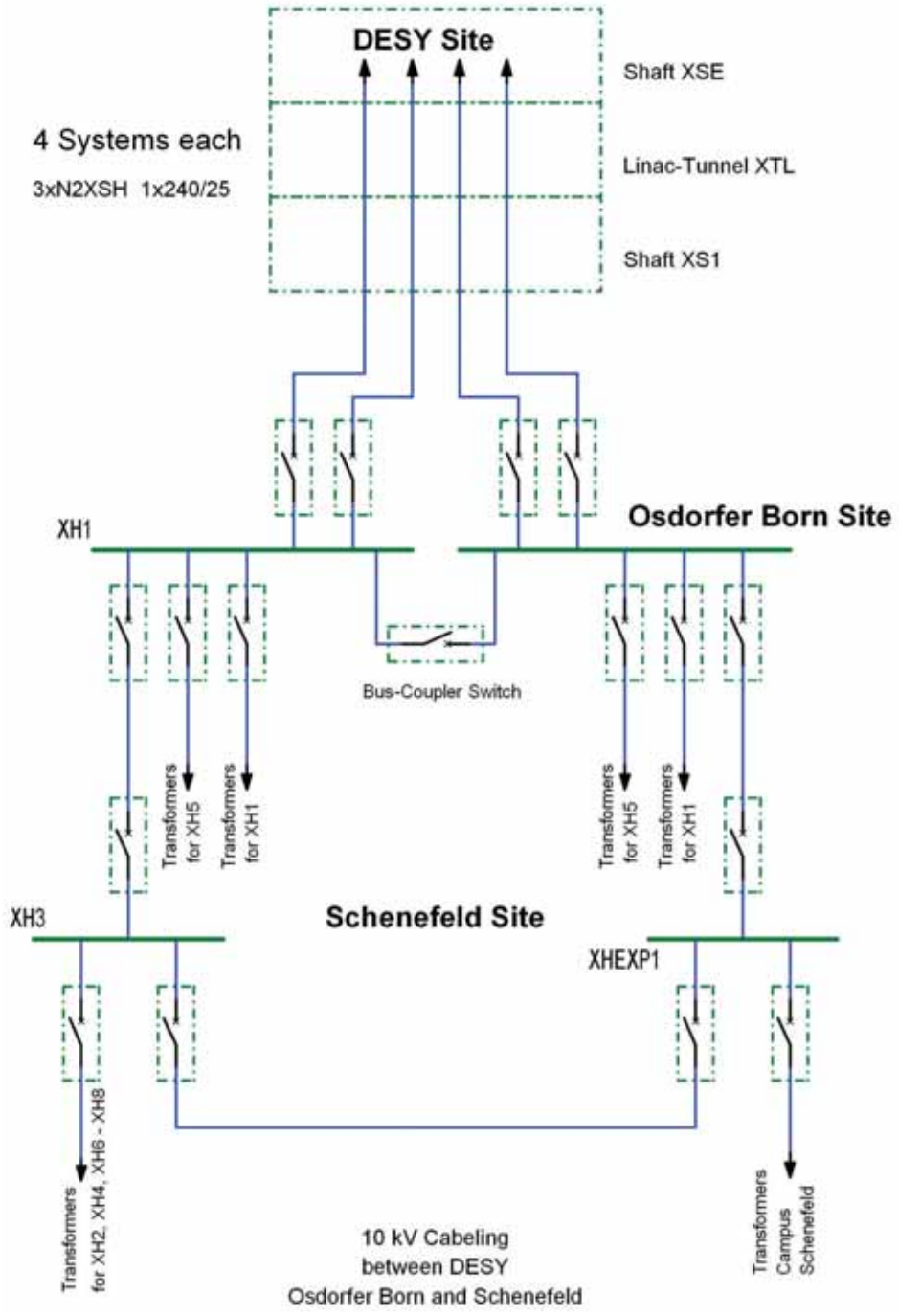


***Figure 7.2.1*** *10 kV mains of the XFEL.*

#### *7.2.1.3 Tunnel lighting*

The tunnels will be lit by fluorescent lamps installed under the tunnel ceiling above the walkway. The planned illumination is sufficient for a walkway but not for a workplace. For the illumination of a workplace for temporary work, portable lamps or spotlights have to be used.

#### *7.2.1.4 Emergency and auxiliary power*

The security relevant loads will have a back-up system such as an emergency power diesel generator, an uninterruptible power supply or DC batteries. The emergency generators will power the illumination of escape routes, stairways and the smoke extractors. They will be installed above the surface near the buildings XHE1, XHE3 and XHEXP1.

### 7.2.2 Magnet power supplies

Electromagnets are used to guide and focus the electron beams in the vacuum chambers. Their power supplies will be installed in different locations according to their purpose.

#### *7.2.2.1 Power supplies in the linac tunnel XTL*

In the cryomodules the magnets are superconducting. This means high current and low voltage. The cables between the magnets and the power supply have to be short, therefore, the power supplies in the linac tunnel XTL will be located close to the magnets.

Power supplies are also needed for the klystrons. The power supplies for the cryomodule magnets and for the klystrons are grouped into rack units every 48 m. In this way, cable losses and the number and length of cables are drastically reduced in the tunnel. Every rack unit has one redundant spare power supply which can be engaged by remote control.

The heat losses from the power supplies are transferred to the cooling water. The semiconductors and chokes are cooled using water with a temperature of 30°C. The cabinet air is cooled by an air/water cooler using 18°C water. The ventilation circuit of the cabinet works in a closed loop and is separated from the tunnel air. In this way the heating of the tunnel air by the power supplies is reduced.

#### *7.2.2.2 Power supplies for the mormal conducting magnets in the beamlines*

Due to their size, the power supplies for the normal conducting magnets are located outside the tunnel in service rooms that are ventilated and air conditioned to assure optimal efficiency. The DC cables between the power supplies and the magnets in the tunnel run on cable trays through the shafts and the tunnel. The cables will be installed in one piece to prevent overheating by bad connections. These cables are FRNC.

The steering and correction power supplies with power up to 10 kW are mostly cooled by air. The power supplies above 10 kW are cooled by 30°C cooling water. This reduces the heating of the ambient air. The semiconductors, chokes and transformers are directly

water cooled. The electronic racks for regulation and controls are cooled by the ambient air. The power supplies will not be equipped with fans. This increases reliability and reduces the time and effort for maintenance.

The power supplies will have a grounding system. By this the magnets inside the tunnel are short-circuited and grounded during a maintenance phase. Due to this safety measure it is possible to perform work inside the tunnel by non-electrician staff.

The power supplies will have a redundancy system, which allows the switching-in of a spare power supply in case of a failure of the running power supply.

The location of the power supplies and the electrical power consumption under typical operating conditions at a beam energy of 17 GeV are listed in Table 7.2.1.

| Location | Name | Power consumption [kW] |
|---|---|---|
| Cryogenics hall | XHC | 2,300 |
| Modulator hall | XHM | 6,960 |
| Access shaft “Osdorfer Born” | XS1 | 2,880 |
| Access shafts “Schenefeld Campus” | XS2-4 | 2,210 |
| Experimental hall and auxiliary buildings on “Schenefeld Campus” | XHEXP1 | 4,410 |
| **Total** | | **17,760** |

***Table 7.2.1*** *The location of the power supplies and the electrical power consumption under typical operating conditions at a beam energy of 17 GeV. Locations and number of power supplies.*

## 7.2.3 Magnet water cooling and air conditioning

### *7.2.3.1 Water cooling*

Extensive water cooling systems are needed for the XFEL Facility. The cooling water circulates in a closed loop. The recooling of the cooling water occurs by so-called hybrid dry coolers (see Figure 7.2.2). Three locations are foreseen: on the DESY site near the shaft XSE, on the Schenefeld site near the shaft XHE3 and near the experimental hall XHEXP1.

The hybrid dry cooler normally works dry by releasing the heat directly to the air. Only in the summer seasons are the coolers wetted with water to guarantee the supply temperature of 30°C. This way, a lot of auxiliary water and costs can be saved. An additional advantage is that the hybrid dry cooler does not create wafts of mist. It is a closed single loop circuit system without heat exchangers between hybrid dry coolers and water cooling circuits.

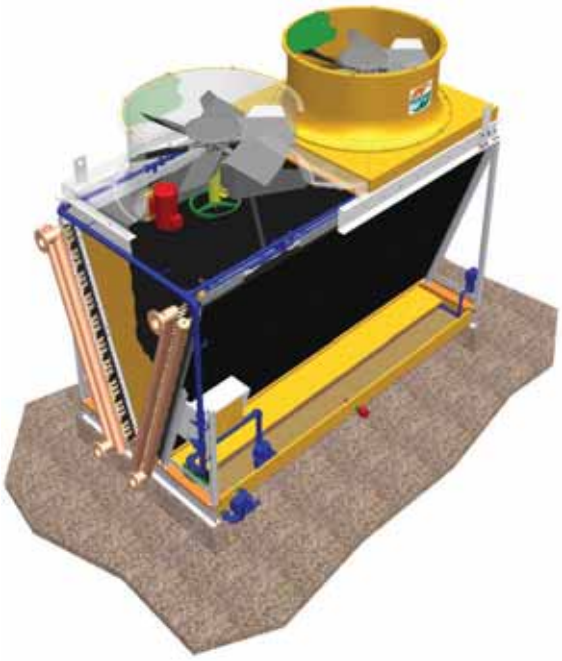

***Figure 7.2.2*** *Hybrid dry cooler.*

The auxiliary water is taken from the water of the wells. About 60,000 m³ per year are needed which can be supplied on the DESY site.

For the cooling of the air condition systems and the electronic racks, chilled water is foreseen. The chillers are located in the pump rooms and are, in turn, cooled by the hybrid dry coolers. The chilled water flows in a closed water circuit.

### *7.2.3.2 General requirements of the cooling water*

The cooling water absorbs the heat of the loads in the tunnels and the modulator hall. It is in direct contact with electrical components. Therefore, the water is deionised. Due to the deionised water, only Copper, stainless steel and red brass are acceptable for materials which are in direct contact with the water. For flexible connections only, reinforced EPDM hoses and stainless steel corrugated pipes are allowed.

The supply temperature of the cooling water is 30°C. The return temperature should be higher than 50°C to reduce the amount of water that has to be circulated. This saves pumping power and reduces the number of coolers and the amount of outside installation area. The maximum pressure difference for all loads is 4 bar. The nominal pressure of the whole system is 10 bar. Each component must withstand a test pressure of 16 bar.

The water used to wet hybrid dry coolers must be deionised in order to prevent calcification. During frosty weather the coolers must be protected by Venetian blinds as the water in the coolers is not frost-protected. During hard frost and shutdown the coolants and the water pipes have to be drained. The deionised cooling water should be saved in a tank.

For cooling the electronic racks in the tunnel, chilled water is needed. The supply temperature is 18°C in order to prevent condensation in the electronic racks. The dew point of the tunnel air may not exceed 16°C. Again, the return temperature should be higher than 26°C to reduce the amount of water that has to be circulated. Electric parts in the cold water circuit should be only Copper or stainless steel for parts with direct water contact, to avoid corrosion and pitting. For flexible connections EPDM-tubes and/or stainless steel corrugated pipes are allowed.

Also for the air conditioning, chilled water is required. The water temperature is 6°C in the supply pipe and 12°C in the return pipe. The requirements for the pressures are the same as for the other water systems.

#### *7.2.3.3 Pump rooms*

Each pump room contains the main water pumps, the chillers, the deionised water treatment, the compressed air machines and their associated control panels. For maintenance, a 5 t crane is foreseen. There are also buffer tanks for the pressure maintenance and the sprinkler water for the hybrid dry coolers. The water pipes between the pump room and the outside hybrid coolers run underground.

#### *7.2.3.4 Water cooling pipes*

The water cooling pipes are designed according to the heat load that has to be transported. The height difference between the tunnel floor and the pump rooms is up to 30 m. In order to keep the return pressure in the tunnel pipe above 0.5 bar, booster pumps are foreseen to push the water to the pump room level. One booster pump is on standby. The booster pumps need a space of 4 m x 3 m. A crane of 1 t is necessary to exchange a pump.

For the leakage water in the tunnel, a pipe is installed. The leakage water pipe will have access every 50 m.

The return pipe will be thermally insulated to reduce the heating of the tunnel air. All pipes need sliding supports and axial expansion joints. All expansion joints and outlets will be accessible for maintenance. The components are connected directly or via sub-distribution to the pipes.

The dimensions of the main pipes, the space needed and the forces for fixed and intermediate fixed points are listed in Table 7.2.2.

| Tunnel | Pipes cooling water | Space needed [mm] x [mm] | FP force [kN] | SP force [kN] | Pipes chilled water | Space needed [mm] x [mm] | FP force [kN] | SP force [kN] |
|---|---|---|---|---|---|---|---|---|
| XTL | DN 300 | 1 050 x 700 | 250 | 110 | DN 100 | 610 x 460 | 90 | 72 |
| XTD1 XTD2 | DN 80 | 530 x 420 | 73 | 63 | DN 50 | 480 x 390 | 47 | 43 |
| XTD3 | DN 100 | 610 x 460 | 80 | 65 | DN 65 | 530 x 405 | 56 | 46 |
| XTD4 XTD5 | DN 80 | 530 x 420 | 73 | 63 | DN 50 | 480 x 390 | 47 | 43 |
| XTD6 | | 530 x 420 | 73 | 63 | DN 50 | 480 x 390 | 47 | 43 |
| XTD7 | DN 150 | 730 x 530 | 125 | 90 | DN 50 | 480 x 390 | 47 | 43 |
| XTD8 XTD9 | DN 80 | 530 x 420 | 73 | 63 | DN 40 | 480 x 380 | 47 | 43 |
| XTD10 | DN 150 | 730 x 530 | 125 | 90 | DN 50 | 480 x 390 | 47 | 43 |

***Table 7.2.2*** *The dimensions of the main pipes, the space needed and the forces for fixed and intermediate fixed points. Cooling water: 30°C supply temperature, 50°C return temperature; chilled water: 18°C supply temperature, 26°C return temperature, FP: fixed point, SP: intermediate fixed point.*

### 7.2.4 Heating, ventilation and air conditioning

For each of the buildings (shafts, halls and tunnels), heating, ventilation and exhaust systems are foreseen. The total number of systems is approximately 100. The air-handling systems are equipped with air filter, heater, ventilation and extractor fans as well as silencers. They are steered by digital data controllers which control the operating state, the interlocks, and the temperature and communicate with a global control system.

During operation of the XFEL, the tunnels are ventilated continuously to remove the humidity generated by water diffusion through the tunnel walls, leakages through cracks and cooling water losses. The air injected into the tunnel is dried prior to injection so that it can absorb the additional humidity.

The air conditioning appliances for the tunnels are located close to the shafts to keep the air ducts short. For the air drying chilled water of 6/12°C is required. In winter the outside air must be heated. The temperatures of the hot water for the heaters are 30/50°C. Hot water is produced by a natural gas-powered central-heating boiler. On the DESY site, the heating, ventilation and air conditioning units are connected to the DESY long-distance heating.

Special air conditioning is required for the tunnel sections accommodating the SASE undulators where the ambient temperature has to be kept constant to within ±0.1°C. These sections will be equipped with local air conditioning systems that are installed in the tunnels. Detailed simulations are presently being carried out to establish an optimal solution for the layout.

In case of a fire in the linac tunnel XTL, the smoke is removed by two smoke extractors which operate independently from each other. The smoke is extracted by a dedicated smoke extraction duct which is installed above the walkway under the tunnel ceiling. About 25,000 m³ of air have to be transported per hour. The smoke extraction occurs close to the origin of the fire and is organised in sections using flaps in the smoke extraction duct. The flaps are controlled by smoke detectors. The supply air unit supplies the tunnel with fresh air in the case of fire. The smoke extraction system is backed up by an emergency power generator.

The air conditioning and the smoke extraction are performed by separate units. The outside air is treated before entering the tunnel at the shaft XSE. The air flows from the shaft XSE to the shaft XS1. At XS1 the tunnel air is released. The air exhaust ducts conduct beyond the roof of the building to keep the access roads to the halls smoke free.

In the tunnels that contain the photon beamlines (XTD6-10), the smoke is extracted through longitudinal ventilation. After detecting smoke or fire in the tunnel by smoke detectors, the ventilation is activated. The air moves from the experimental hall XHEXP1 to the access shafts located in the upstream direction (XS2-4). A ventilation fan presses the outside air into the tunnel and an extractor fan sucks the air and smoke out of the tunnel at the upstream shaft.

| | **Equipment** | **Location of HVAC systems** |
|---|---|---|
| XHC | Cryo plant | Roof of the cryo plant |
| XTIN | Floors of the injector building | HVAC units on each floor |
| XTIN | Injector tunnel | First upper floor XHEIN |
| XHM | Modulator hall | First upper floor XHM |
| XSE | Entrance shaft under the radiation shielding ceiling | First upper floor XHM |
| XTL | Linac tunnel | Supply unit in First upper floor of XHM<br>Extraction ventilator in shaft of XS1 |
| XTL | Smoke extractor 1 | First upper floor of XHM |
| XTL | Smoke extractor 2 | Supply unit and smoke extractor in second basement |
| XS1 to XS4 | Power supplies | Several locations at the shafts XS1-4 and entrance to the tunnels at XHEXP1 |
| XS1 to XS4 | Staircase overpressure unit | Shafts XS1 to XS4 under the radiation shielding ceiling to the tunnels XTD1 to XTD10 |
| XHEP1 | Experimental hall | HVAC building near XHEXP1 with nine air-conditioning systems and six smoke extraction units |
| XHEP1 | Laboratories in office building | HVAC rooms in office building |
| | Canteen and kitchen | HVAC room near canteen |

***Table 7.2.3*** *The specific location of the HVAC systems for selected buildings of the XFEL Facility.*

The access halls and shafts are used for personal access and for material transport. They receive the cables, water pipes and air ducts. Access via staircases or elevators is separated from the shaft. In case of smoke or a fire they are ventilated with overpressure to keep the escape routes smoke-free. The shaft and the tunnel itself are separated by a partitioning wall.

The experimental hall XHEXP1 is equipped with nine air conditioner units and six smoke extractors. The heating, ventilation and air conditioning systems are located in a separate building near the hall. This minimises body and ground vibration from the fans near the experimental areas. An underground channel connects this building with the experimental hall. The air channels inside the hall are located under the ceiling and above the crane. Air nozzles distribute the air inside the hall. The temperature requirements are moderate but the volume of the hall determines the large number of units and requires big channel cross-sections. The experimental hutches have their own air conditioning or ventilation. They take the air from the ambient air of the hall.

In case of smoke or a fire alarm, the smoke extractors are activated. They remove the smoke accumulating at the ceiling and blow it outside, above the roof of the office building. Fans blow outside air into the hall to keep the floor and the escape routes smoke-free.

Table 7.2.3 lists the specific location of the HVAC systems for selected buildings of the XFEL Facility.

### 7.2.5 Cryogenics

In general, the concepts for the cryogenic supply, which were developed for the superconducting Tera-Electronvolt Superconducting Linear Accelerator (TESLA) linear collider **[7-1]**, will be applied for the XFEL linear accelerator **[7-2 – 7-4]**. These concepts have been validated during long-term runs of the TTF1 and FLASH linacs.

The XFEL linear accelerator will consist of 944 superconducting-Niobium 1.3 GHz 9 cell cavities, which will be cooled in a liquid-Helium bath at a temperature of 2 K, to achieve a cavity quality factor $Q_0=10^{10}$ at an accelerating gradient of 23.6 MV/m. A Helium bath cooling at 2 K will make use of the Helium II heat conduction properties and is a technically safe and economically reasonable choice **[7-5]**. Eight cavities and one superconducting magnet package will be assembled in cryomodules of about 12.2 m length. The 2-K cryostat will be protected against heat radiation by means of two thermal shields cooled to temperatures from 5 K to 8 K and from 40 K to 80 K, respectively (for details see Section 4.2.2.4).

The cryogenic supply of the injector cryomodules is separated from the supply of the cryomodules in the main tunnel. From the cryogenic point of view the cryomodules, in the low-energy section (separated by bunch compressors), the third harmonic (3.9 GHz) system and the main linac cryomodules, are treated as one unit of about 1.7 km length. The 2-K cryogenic supply of the main linac will be separated in parallel cryogenic sections of 12 cryomodules each. These sections are called “strings.” The string sections are connected by string connection boxes (SCBs).

The cryogenic supply of the linac has to be maintained continuously 24 hours a day/ seven days a week for run periods in the order of two to three years without scheduled breaks or shut-down of the cryogenic system at an availability in the order of 99% or better.

In addition to the linac cryogenics, in a large accelerator module test facility (AMTF) for serial production tests of all XFEL superconducting RF-cavities and cryomodules has to be operated during the series production of the linac components (see Section 7.2.6). The Helium supply for the TESLA Test Facility (TTF) and the Free-electron LASer in Hamburg (FLASH) linac also has to be maintained in parallel to the operation of the XFEL facilities. As a consequence, the new XFEL cryogenic installations have to be integrated into the already existing cryogenic infrastructures at DESY, consisting of the HERA and the TTF cryogenic plants. These detailed requirements have been defined in **[7-3]**.

### *7.2.5.1 Cryogenic components of the linac*

Figure 7.2.3 summarises the cryogenic components of the linac: 116 cryomodules of the main linac, two 3.9 GHz cryomodules, 11 valve-boxes of the SCB type, two bunch compressor sections and three end boxes (connection boxes without valves) will be installed in the main tunnel. The design of the XFEL cryomodules is based on the latest step in the development of the TTF cryomodules (see Section 4.2.2.4) In addition to the cavities, a superconducting magnet package is cooled by the 2-K Helium circuit (for details, see Section 4.2.2.5). Two injectors, consisting of one cryomodule each, have to be supplied separately from the main linac as well as from each other for the final installation of the XFEL-linac. For the start of the project, only one injector will be installed, but the Helium distribution system will already be prepared for the integration of the second injector. In addition, the distribution system will allow the exchange of the cryomodule of one injector during the operation of the main linac and the second injector.

A new XFEL refrigerator, suited for the demands of the XFEL linac, will be connected to a main distribution box. One HERA refrigerator will also be connected to the distribution box to serve as a limited capacity back-up. The distribution box manifolds the different cryogenic circuits to the main linac and to an injector valve-box. A set of multiple-staged cold-compressors will be attached to the distribution box. The injector valve-box branches to individual feed-boxes of the injector cryomodules.

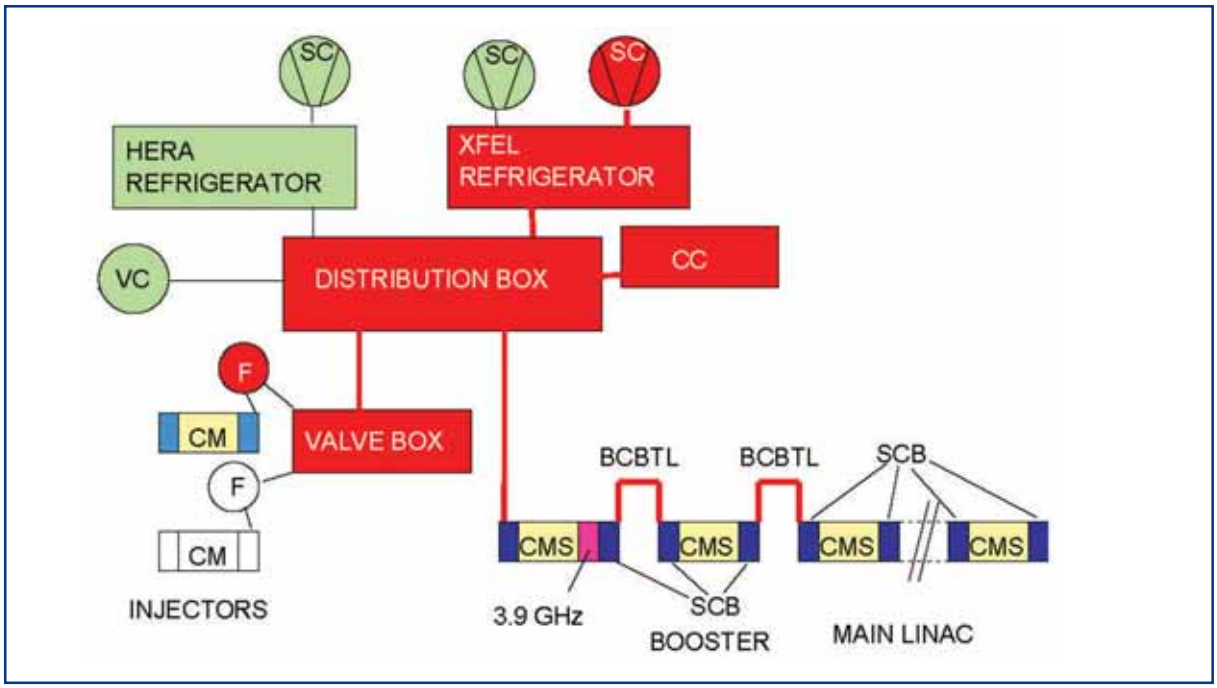


***Figure 7.2.3*** *The cryogenic components of the XFEL linac. SC= screw compressor, CC=cold compressor, VC= warm vacuum compressor, F=feed box, CM= cryomodule, CMS= cryomodules in a string, BCBTL= bunch compressor bypass transfer-line, SCB= string connection box. Colour code: red = main installations, light green = redundant installations, general coloured = installations at the start of the XFEL linac operation.*

The “regular” arrangement of cryogenic strings is disturbed at the booster- and bunch-compressor sections. At the bunch-compressor sections the warm linac components have to be bypassed by transfer lines of 68 m and 92 m length, respectively. The transfer lines will contain the 2.2 K forward, the 2 K gas return and the 5-8 K and 40-80 K supply and return tubes of the cryomodules.

In addition, the two-phase liquid-Helium II supply of the cavities has to deal with the fact that the linac will be installed “laser-straight” and not on a gravity equipotential surface. The minimum level is at about 900 m behind the start of the XTL tunnel and approximately 5 cm lower than the maximum level at the beginning of the linac. The string connection boxes, containing, among other things, the Joule-Thomson valves (JT-valves) for the 2-K liquid-Helium supply and warm-up/cool-down bypass valves (BP-valves), will be installed in a way that only liquid-Helium downhill flow will result. The arrangement also avoids two-phase liquid-Helium flow in the bunch-compressor bypass transfer-line sections (BCBTL). As a result, the BCBTLs can be installed at the top or the bottom of the warm bunch compressor components.

### *7.2.5.2 Cryogenic operation and control*

The superconducting cavities and magnet packages can be operated as long as the cavity vessels and magnet cryostats are sufficiently filled with liquid-Helium at a temperature of 2 K, corresponding to a Helium vapour pressure of about 31 mbar. As a consequence, the control of the 2-K Helium liquid level and the 2-K vapour pressure is mandatory for the safe operation of the linac.

Figure 7.2.4 shows the scheme of the cryogenic 2-K string supply. The Helium vessels of the cryomodules (cavity vessels and magnet cryostats) are connected by a two-phase supply tube. At the end of each string of 12 cryomodules, the two-phase tube is connected to a Helium reservoir, equipped with a liquid level probe and a pressure sensor. During steady state operation, the two-phase tube is filled with liquid to about 1/3 of the diameter. This liquid level is monitored by means of the level probe in the reservoir. Helium from the 2.2-K forward tube of the cryomodules is expanded from 1.2 bar to 31 mbar through a JT-valve in each SCB. The Helium supply through the JT-valve in the two-phase supply tube of the string is regulated by the level signal in a control loop.

Thus, the JT-valve reacts on any changes of the 2-K cryogenic load within the string by keeping the liquid level constant. In addition, extra cryogenic load can be generated by means of electrical heaters in the liquid reservoirs, in order to compensate for fast changes of the dynamic load. The electrical heaters will buffer the fast load changes and will give the refrigerator (in particular the cold compressors) time to adapt. A redundant unit will be installed for each liquid Helium level probe and for each heater in the reservoir.

The Helium vapour pressure of 31 mbar will be regulated to a variation of smaller than +/-1 mbar by the operation of the cold compressors and by means of a control valve in the 2 K return to the refrigerator.

If the 2-K Helium liquid level drops below a lower limit or if the level increases above an upper limit, which could indicate cavity quenches in the string, a hardware interlock is triggered, which switches off the RF for the affected string of cryomodules and inhibits the beam injection into the linac. A trigger signal is also generated, if an increase of the pressure in the 2-K areas is detected. (In addition, cavity quenches will be detected by the low level RF-controls independently from the cryogenic controls.)

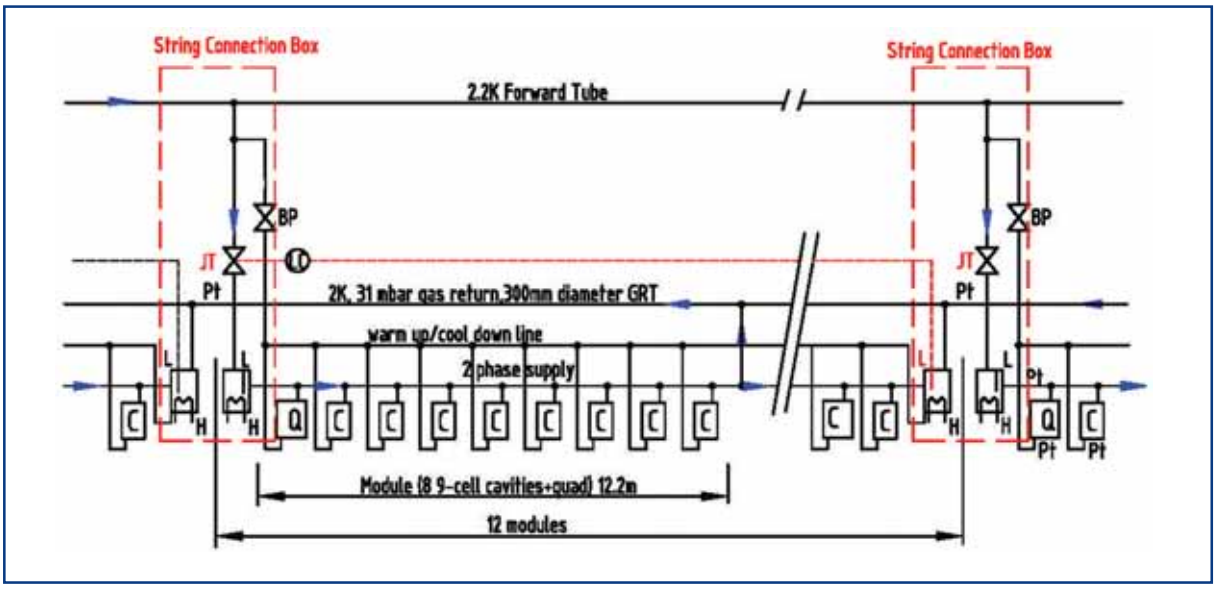


***Figure 7.2.4*** *A simplified flow scheme of the 2 K cooling loop of a cryogenic string. JT = Joule-Thomson valve, BP = bypass valve for cool-down/warm-up, L = Level probe, H = electrical heater, C = cavity vessel, Q = quadrupole (magnet package).*

### *7.2.5.3 Transient and fault condition operations*

The cool-down/warm-up procedures for the XFEL linac were reported in detail **[7-6]**. To avoid a misalignment of the cavities and the magnet packages, the cool down/warm-up rates are limited. All cavities of the linac will be cooled-down/warmed-up in parallel in about four days. Another day will be required to fill the Helium vessels with liquid. It is expected that the superconducting cavities will show no performance decrease due to Hydrogen diffusion at the Niobium surface (so called “Q-disease”). Therefore, no fast-cooling procedures from about 150 K to 4 K are foreseen.

Precautions against loss of insulation or beam vacuum in the cryostats are derived from studies for cryo-units of the TESLA linac **[7-7]**. Some SCBs are equipped with vacuum barriers resulting in vacuum sections of about 300 m in length, to limit the impact of insulation vacuum breakdown. Fast acting vacuum valves at the beam tube in each SCB will prevent the venting of the cavities. The 2-K and 40-80-K cryogenic circuits will be equipped with safety valves at both ends of the linac. At the SCBs, safety valves for the 5-8-K circuit and the 2.2-K forward tube will be installed. The safety valves in the tunnel will vent into a DN200 warm gas tube. The relief for this tube will be installed close to the cryo-hall (XHC) and the shaft XS1. Fault conditions in the cryogenic shield circuits can be tolerated to some extent, as long as the 2-K liquid Helium level and the vapour pressure are kept constant. In general, we know from the FLASH linac operation that short interruptions in the cryogenic supply (e.g. trips of turbines in the cold box) will not necessarily cause an interruption of beam operation.

### *7.2.5.4 Heat loads*

Table 7.2.4 summarises the static and dynamic heat loads of one XFEL linac cryomodule at the nominal operating conditions of the XFEL-linac at the different temperature levels.

Table 7.2.5 summarises the complete heat loads of the XFEL main linac, the injectors and the related Helium distribution systems. The calculated values of the different heat loads have to be converted into values, which can serve as a safe basis for the design of the cryogenic plant by means of a “design factor” of 1.5.

The use of the design factor is a general demand in the cryogenic community; it includes a margin for plant regulation, a buffer for transient operating conditions, a buffer for performance decreases during operation and a buffer for general design risks. As a result, the design factor adds to the general availability and reliability of the cryogenic operation of the facility.

| Source | 2K static | 2K dynamic | 5K-8K static | 5K-8K dynamic | 40K-80K static | 40K-80K dynamic |
|---|---|---|---|---|---|---|
| RF load | 0.00 | 6.47 | 0.00 | 0.00 | 0.00 | 0.00 |
| Radiation | 0.00 | 0.00 | 1.39 | 0.00 | 32.09 | 0.00 |
| Supports | 0.60 | 0.00 | 2.40 | 0.00 | 6.00 | 0.00 |
| Input coupler | 0.24 | 0.19 | 2.56 | 0.86 | 18.00 | 15.16 |
| HOM coupler | 0.01 | 0.38 | 4.27 | 3.47 | 1.70 | 17.64 |
| HOM absorber | 0.15 | 0.06 | 1.50 | 0.25 | 0.00 | 2.50 |
| Beam tube bellows | 0.00 | 0.32 | 0.00 | 0.00 | 0.00 | 0.00 |
| Current leads | 0.20 | 0.10 | 1.80 | 1.44 | 7.80 | 7.56 |
| HOM to structure | 0.00 | 0.94 | 0.00 | 0.00 | 0.00 | 0.00 |
| Cables | 0.13 | 0.00 | 1.39 | 0.00 | 5.38 | 0.00 |
| Sum | 1.33 | 8.45 | 11.04 | 6.01 | 70.97 | 42.86 |
| Sum static + dynamic | | 9.78 | | 17.05 | | 113.83 |

***Table 7.2.4*** *The static and dynamic heat loads (in W) of one cryomodule consisting of eight 1.3 GHz superconducting cavities and a magnet package at an accelerating field gradient of 23.6 MV/m, $Q_0 = 10^{10}$, RF-repetition rate of 10 Hz and the nominal XFEL beam parameters.*

### *7.2.5.5 Refrigerator*

The XFEL-project heat loads shown in Table 7.2.5 result in the specification of the Helium refrigerator plant presented in Table 7.2.6. The design of the refrigerator will follow the concepts, which were already outlined for the TESLA Model Refrigerator (TMR) **[7-1, 7-8]**. The TMR had been designed with valuable advice from Conseil Européen pour la Recherche Nucléaire (CERN) and from industry. For the XFEL project the concept is adapted to the smaller loads of the XFEL linac, corresponding to a 4.4 K equivalent capacity of about 12 kW (about 22 kW for the TMR). The overall size, as well as the technology, of this refrigerator comes close to that of the existing refrigerators for the LHC project at CERN. As a consequence, all components of the XFEL refrigerator are already developed and available from industry.

Figure 7.2.5 shows a simplified flow scheme of the XFEL refrigerator. The refrigerator processes are almost identical to the TMR and have been reported in detail already **[7-1, 7-8]**. Helium is compressed at ambient temperature by a two-stage screw compressor group (LP 1,2,3 and HP 1 in Figure 7.2.5) to a pressure in the 20 bar range. After recooling to ambient temperature and careful oil removal and drying from residual water vapour, the high pressure Helium is cooled in a cascade of counter-flow heat exchangers and expansion turbines. At the 40-K and 5-K temperature levels, Helium flows are directed to the thermal shields of the linac cryomodules, respectively. The corresponding return flows are fed back to the refrigerator at suited temperature levels. Inside the refrigerator cold-box, the Helium is purified from residual air and Neon and Hydrogen by switchable adsorbers (AD1 and AD5) at the 80-K and 20-K temperature levels, respectively.

| Source | 2K static | 2K dynamic | 5-8K static | 5-8K dynamic | 40-80K static | 40-80K dynamic |
|---|---|---|---|---|---|---|
| Main linac cryomodules | 154 | 879 | 1281 | 625 | 8233 | 4457 |
| 3.9 GHz cryomodules | 3 | 43 | 19 | 11 | 126 | 55 |
| Main linac distribution | 322 | | 472 | | 2279 | |
| Injector cryomodules | 3 | 17 | 22 | 12 | 142 | 86 |
| Injector distribution | 212 | | 208 | | 1807 | |
| | | | | | | |
| Sum | 694 | 939 | 2002 | 648 | 12587 | 4598 |
| Design sum | 1041 | 1409 | 3003 | 972 | 18880 | 6897 |
| Total design | | 2450 | | 3975 | | 25777 |

***Table 7.2.5*** *The heat loads (in W) of the main linac cryomodules (104 modules RF operated, 12 in cold standby) under nominal operating conditions with reference to Table 7.2.4, the third harmonic cryomodules, the linac Helium distribution system, two injector cryomodules and the related injector Helium distribution system. The design sum results from the multiplication of the calculated loads by a factor of 1.5 ("design-factor"). The total design heat loads result from the addition of the static and dynamic design loads.*

A part of the 5-K flow is expanded from about 5 bar via a JT-valve into a liquid reservoir (LRS in Figure 7.2.5) to about 1.2 bar, corresponding to a temperature of 4.4 K. This liquid is sub-cooled to about 2.2 K in the JT counter-flow heat exchanger HXJT and enters the 2.2-K forward tube of the linac cryomodules. At each SCB, the Helium is expanded to 31 mbar via a JT-valve, resulting in a mass fraction of 91% Helium II liquid at 2 K (see Section 2.3.4). The heat dissipation of the linac cavities causes evaporation of the Helium. The low pressure Helium vapour returns to the refrigerator through the 300-mm gas return tube (GRT) in the cryomodules. After superheating to about 3.5 K in HXJT, the gas is compressed in a multiple-stage cold compression system to a pressure in the 0.5 to 0.9 bar range, depending on the operating conditions. This stream is separately warmed up to the ambient temperature in exchangers 4, 3, 2 and 1 and enters its own sub-atmospheric pressure screw compressor LP 3. The combination of cold compressors and an adjustable sub-atmospheric suction pressure of a screw compressor ("mixed compression cycle") can accommodate a large dynamic range and is very useful during transient operation modes **[7-9]**. DESY has a long time operational experience with the screw compressors of the HERA plant running at sub-atmospheric conditions.

The design flow rates, pressures and power requirements of the refrigerator are summarised in Table 7.2.6. The coefficients of performance (COPs) (the inverse of the overall refrigerator efficiency) at the different temperature levels, correspond to measured values of the LHC plants **[7-9]**, assuming lower efficiencies than specified for the TMR, because of the smaller plant size of the XFEL refrigerator.

| | | Mass flow | Outlet | Return |
|---|---|---|---|---|
| 2K load | 2450 W | 117 g/s | 1.1 bar<br>2.2 K | 0.0275 bar<br>3.5 K |
| 5-8K shield | 4000 W | 142 g/s | 5.5 bar<br>5.16 K | 5.4 bar<br>8.2 K |
| 40-80K shield | 30000 W | 142 g/s | 18 bar<br>40 K | 17 bar<br>80 K |
| Compressors | | | | |
| LP 3 | | 117 g/s | floating | 0.5 – 0.9 bar<br>295 K |
| LP 1+2 | | 1045 g/s | floating | 1.2 bar<br>295 K |
| HP 1 | | 1162 g/s | 20 bar<br>295 K | floating |

| Power consumption | Refrigeration | COP | Specific load | % of power |
|---|---|---|---|---|
| 2K | 2.45 KW | ≤ 870 W/W | 2.13 MW | 59 |
| 5-8K | 4.00 KW | ≤ 220 W/W | 0.88 MW | 24 |
| 40-80K | 30.00 KW | ≤ 20 W/W | 0.60 MW | 17 |
| total | | | ≤ 3.61 MW | 100 |

***Table 7.2.6*** *Process parameters of the XFEL refrigerator. The requirements for the XFEL linac are marked in red. The other parameters depend on the final layout of the refrigerator, which will be left to industry, to achieve the most economical results. The COPs (the inverse of the overall refrigerator efficiency for the different temperature levels) correspond to the measured values of the existing LHC plants.*

The XFEL cryogenic system will contain about 4.5 t of Helium. Suitable storage capacities for liquid and gaseous Helium will be provided. The refrigerator infrastructure is described in reference **[7-4]**.

### *7.2.5.6 Use of the HERA cryogenic plant*

The HERA cryogenic plant consists of three parallel Helium refrigerators, each of an equivalent cooling capacity of about 8 kW at 4.4 K. One of the refrigerators will be used for the supply of the FLASH linac and the AMTF. The remaining two refrigerators will be available for the XFEL after the end of the operation of the HERA accelerator in June 2007. Among other things, two cold-boxes of the HERA plant would have to be modified, to meet the capacity requirements of the XFEL project (see Table 7.2.6) **[7-10]**. In addition, out-dated equipment would have to be replaced to ensure the required availability for the operation of the XFEL linac **[7-2]**. An industrial study has been launched, to investigate these aspects in detail.

In any case, an unmodified HERA refrigerator will be used as a low-capacity back-up, as already outlined (see Figure 7.2.3). Specific components, like the warm gas storage tanks, a 10-m3 liquid storage dewar and the Helium purifiers will be adapted to the XFEL cryogenic system with minor changes.

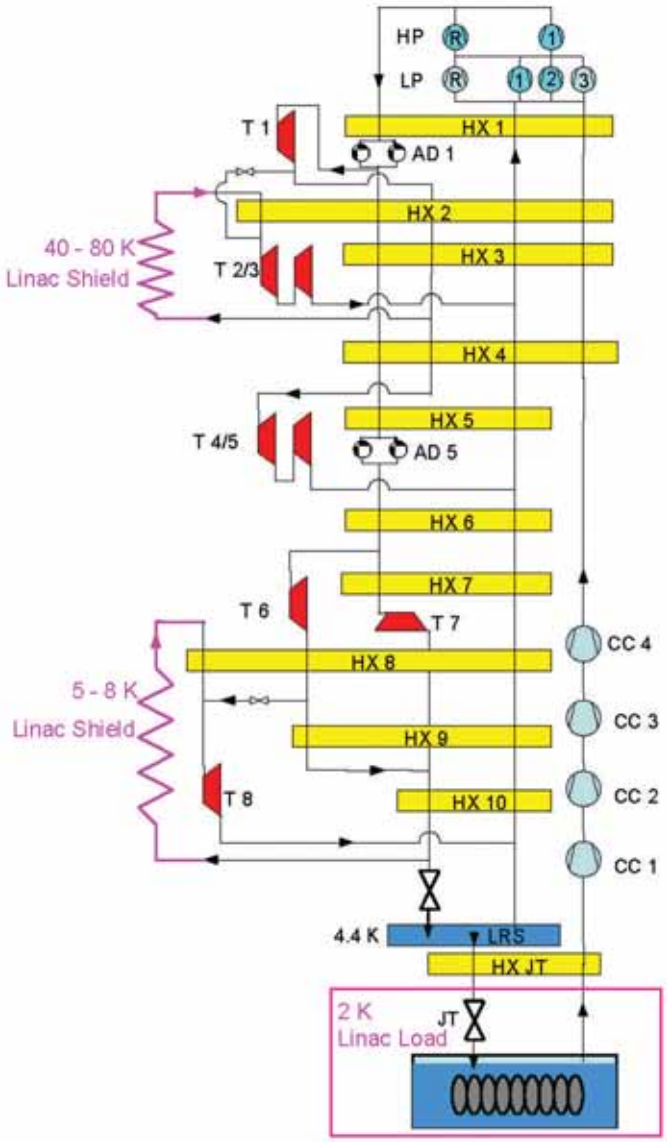


***Figure 7.2.5*** *Flow diagram of the XFEL refrigerator. LP 1,2,3 = low pressure screw compressors, LP R = redundant low pressure screw compressor, HP 1 = high pressure screw compressor, HP R = redundant high pressure screw compressor, HX = heat exchangers, T = expansion turbines, AD = impurity adsorbers, LRS = liquid Helium reservoir, JT = Joule-Thomson-valve, CC 1,2 = cold compressor stage. Specifying the final number of turbines, heat exchangers and CC stages will be left to industry, to achieve the most economical result. The flow scheme corresponds to the TMR* **[7-1, 7-8]**.

### *7.2.5.7 Redundancy and availability*

The continuous operation of the linac depends on the availability of the cryogenic supply. Hence, highest availability at reasonable costs has priority in all design considerations, aiming at an availability in the order of 99% or better. For the TMR, the sources of unavailability have been carefully investigated [**7-1, 7-8]**. As a result, the required availability can be achieved by means of a single refrigerator, if adequate built-in component redundancy is foreseen and a clear strategy to fight impurities exists. The availability of the process controls is mandatory for the overall availability (see Section 7.2.5.8).

The design of the XFEL-refrigerator includes redundant screw compressors for the low and high pressure stages. Turbines as well as cold compressor cartridges can be exchanged easily. The cold box contains switchable gas adsorbers.

In the baseline concept, the existing HERA refrigerator will be used as a low-capacity back-up for the main XFEL refrigerator. The HERA refrigerator can operate as a 4-K Helium liquefier with warm Helium compressors (from the CMTF) connected to the 2 K return circuit to maintain the XFEL linac at 2 K with static heat-loads only. By this operation, maintenance periods for the main XFEL refrigerator can be bridged.

### *7.2.5.8 Cryogenic process controls*

A highly available cryogenic process control system is required for widely distributed cryogenic components and the continuous cryogenic plant operation **[7-11]**. A high degree of automation of the cryogenic processes will contribute to the reliability.

Basic real-time process control functions like functional process control blocks and supervisory programmes written in state notation language (SNL) are mandatory for controlling the cryogenic processes. Process control databases, device specific data, asset properties as well as maintenance data, will be stored in a set of relational databases implemented in Oracle.

The control system has to integrate local Programmable Logic Controllers (PLC) controls of the screw compressors, the cold compressors and other sub-systems as well as state-of-the-art microprocessor-controlled valve actuators and transmitters. In general, standard industrial components will be used as far as possible.

The environmental conditions in the XFEL tunnel demand special precautions to protect the electronics against radiation damage. Redundant process controllers and a comprehensive redundancy scheme will provide high availability and a reliable failover of damaged components. Redundant I/O components in the XFEL tunnel will extend the mean time to repair for cryogenic operation.

Precise timing of control loops and diskless operation require real-time operating systems like vxWorks on the process controllers. The operator interface applications will have to run natively on multiple platforms. These applications will be implemented in a rich client platform (RCP), preferably written in Java. This approach will allow maximum flexibility and platform independence.

The EPICS toolkit will meet all the requirements within the XFEL project timeframe. It provides reliability, stability, a rich functionality, extensibility, and has a powerful user base within the European partner states of the XFEL collaboration.

## 7.2.6 Accelerator Module Test Facility

### *7.2.6.1 Objectives of the Accelerator Module Test Facility*

All main components constituting the accelerator modules, e.g. cavity, magnets and RF coupler, will have to be tested before the module assembly. Nevertheless, the completed accelerator modules also have to be qualified after the assembly and before their installation in the XFEL tunnel. The qualification includes a check of the general mechanical dimensions, the determination of the RF properties, and the measurement of the cryogenic performance of all systems, in particular, the gradient performance of the cavities. All the test results from the test facility will be used as a fast feedback into the series production, in order to avoid failures and guarantee the performance.

In addition to the cavities, magnets and accelerator modules, some RF components will also have to be tested. This includes testing the waveguide systems and the klystrons.

### *7.2.6.2 Test programme for single accelerating cavities*

The maximum accelerating field and the corresponding unloaded quality factor $Q_0$ of each single cavity will be measured at a temperature of 2 K in a vertical bath cryostat. To increase the throughput of the vertical test stands, four cavities are assembled in one cryostat insert. The design of the cryostats can be scaled from the vertical test dewars of the TTF **[7-12, 7-13]**. Each cavity will be equipped with a fixed coupler antenna ($Q_{ext}=1\times10^{10}$) and a pick up probe ($Q_{ext}=1\times10^{13}$). The cavities will be operated in the accelerating $\pi$-mode. The accelerator field will be increased to its maximum value in steps. At each step the cavities will be powered for 20 s in CW-operation mode. In total about 40 hours are needed for one complete test run with four cavities, including the assembly and disassembly of the insert to the cryostat, and the cool-down and warm-up procedures.

The inserts will be assembled at the cavity manufacturer's site and delivered to the test facility. Qualified cavities will be sent to the accelerator module manufacturer. Close to 1,000 single cavities have to be tested at a rate of about 12 cavities per week. Spot tests of the cavities already welded into their Helium-tanks will also have to be carried out in order to reveal systematic manufacturing errors caused by the assembly procedure. The tests will be carried out at 2 K in a CHECHIA **[7-14]** like cryostat. The tests include coupler processing and tests of the tuning system. About two weeks are needed for one complete test.

### *7.2.6.3 Test programme for the magnets*

The performance of the superconducting magnets will be tested at 4.5 K in a horizontal bath cryostat. A so-called "anti-cryostat" allows accessing the bore of the magnet at room temperature with harmonic coils and a stretched wire system. Thus, the test programme

includes measuring the magnetic field quality, saturation effects due to the Iron, and magnetic axis as well as roll angle measurements. In the cryostat one magnet will be tested at a time. In total, about 120 packages of superconducting magnets have to be tested within the total module series production of about two years.

#### *7.2.6.4 Test programme for the accelerator modules*

The performance of the accelerator modules will be tested at module test benches. The tests include cryogenic performance tests, and performance tests of the cavities. Preliminary tests will be done outside the test stands and comprise a reception control. The cryogenic tests include the integral leak check of all vacuum systems, cryogenic process tubes and the current leads, the test of the instrumentation and measurements of the static heat load at different temperatures. The final check of the magnet package together with the current leads will also be carried out.

During the performance tests of the cavities, the maximum accelerating field of the cavities and the corresponding unloaded quality factor $Q_0$ as well as the X-ray radiation and the related dark currents, will be measured. The quality factor will be monitored by means of cryogenic measurements of the dynamic heat load.

The pre-conditioned RF couplers will be further conditioned. The RF phase will be adjusted within +/- 20 degrees. There will also be a possibility to process the cavities.

Twelve days are needed for the complete test of one accelerator module, including the mechanical assembly and disassembly on the test bench. In total, approximately 120 modules have to be tested within two years.

#### *7.2.6.5 Test programme for the klystrons*

The performance of the XFEL klystrons will be checked at a klystron test stand. Each klystron will be checked together with its auxiliaries and pulse transformer. The assembled unit will then be lowered into the XFEL tunnel. In total, 31 klystrons have to be tested at a rate of two klystrons per month.

#### *7.2.6.6 Test programme for the waveguides*

The waveguide system for the individual accelerator modules will be completely mounted, checked, tuned and conditioned at full power. About 120 waveguide systems have to be tested within two years.

#### *7.2.6.7 Layout of the Accelerator Module Test Facility*

The given test rates and the estimates for the test schedules mean the following test stands need to be installed in the test hall:

- three test benches for complete accelerator modules;
- two vertical cryostats for cavities;
- one CHECHIA-like horizontal cryostat for cavities embedded in the Helium-tank;
- one horizontal bath cryostat for testing the magnets;

- one test stand for testing the klystrons;
- one test stand for testing the wave guides.

The number of test benches and vertical cryostats includes an overcapacity to compensate for shutdown periods, maintenance, repairs and repetition of tests. The Test Facility will be located on the DESY site and will comprise an experimental hall, a pump house, a Helium compressor station, and an office building.

**The test facility hall** houses all test stands, transport areas, accelerator modules' baking-out areas, and areas for intermediate storage of modules, cavity test inserts, magnets, etc. The hall will have an overall size of 70 m × 60 m ground area and a height of about 11 m. Two parallel hall cranes, each with a capacity of 20 t, a span of 30 m and a hook height of 8 m will be installed (see Figure 7.2.6).

Each individual module test bench including the CHECHIA-like cryostat has to be surrounded by a concrete shielding of 0.8 m thickness and covered by a roof shielding of 0.8 m thickness in order to establish radiation safety in all parts of the test hall. The front door of each shielding can be moved horizontally on rails in order to allow access to the cavity in the CHECHIA-like cryostat, or to shift the module, together with its support structure, into the mounting area.

For the installation of an accelerator module on a test bench, the module will be moved by the hall crane from the storage area to the front of one test bench and installed on a support structure. After installation, the support structure will be moved back into the shielding of the test bench. During the installations inside the shielding, the front door can be shifted relative to the support and will stay open.

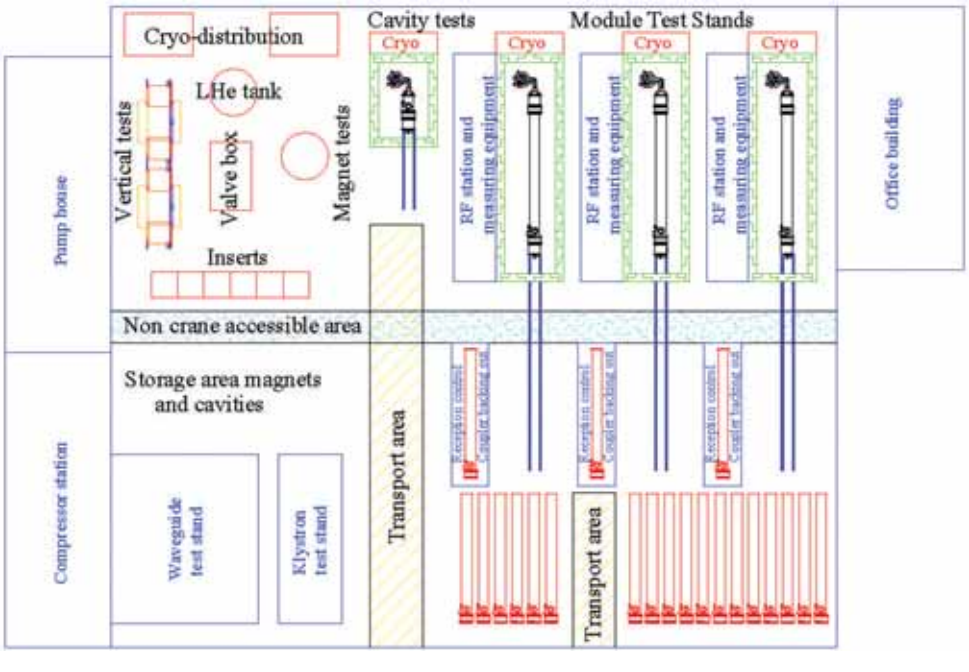


***Figure 7.2.6*** *Ground plan of the Accelerator Module Test Facility.*

The vertical cryostats will be inserted into the ground and covered with movable concrete shielding blocks of 1.2 m thickness. The cryostat inserts will be moved from the storage area into the cryostats using the hall crane.

**The pump house** is placed in the immediate proximity of the HERA water towers and contains water cooling and air compressing equipment.

**The Helium compressors' station** houses a set of compressors needed to lower the vapour pressure of the Helium baths to 30 mbar **[7-13]**. The walls of the compressors' station and the pump house will be sound protected.

**The office building** will comprise a workshop, control rooms, offices and social rooms.

### *7.2.6.8 Cryogenic system*

The cryogenic system of the test facility will be supplied with cold Helium from the HERA refrigerator. For the continuous operation of the test hall, cooling capacities of about 10 kW at 40/80 K, 1.0 kW at 4.5 K and 0.6 kW at 2.0 K are needed. In order to reduce the strain on the Helium distribution system, only the 40/80 K and 4.5 K circuits will be branched to the cryogenic stands via a ~200 m long transfer line connecting the HERA refrigerator with the test facility. The 2 K liquid Helium will be supplied there by isenthalpic expansion of the 4.5 K Helium, which will be sub-cooled to 2.2 K before the expansion by means of counter-flow heat exchangers. A distributed warm compressor system will, therefore, be used to lower the Helium vapour pressure to 30 mbar. This will result in a required Helium liquefaction rate of about 50 g/s to be supplied on average from the Helium plant. Peak liquefaction rates will be levelled by means of a 10 $m^3$ liquid Helium tank.

The cryogenic system of the test facility will be designed as a modular structure (see Figure 7.2.7) and will basically consist of two sub-systems. The first one will be in charge of the cryogenic supply for the three module test benches and the CHECHIA-like cryostat, whereas all bath cryostats will be supplied from the second sub-system. Inside each sub-system the cryogenic supply is in turn subdivided into two "layers" in order to operate the test stands independently from each other, to avoid air condensation on cryogenic valves during exchange and installation of modules, or cavities or magnets, and to reduce the consequences of leaky valves. For each sub-system the corresponding valve box represents the first layer while the feed boxes of the accelerator module test benches and the CHECHIA like cryostat, together with the valves of the vertical and horizontal bath cryostats, form the second layer. As a result, all cryogenic supply and return tubes are separated by two cryogenic valves in series from each test stand.

The valve box in each sub-system will be supplied from the test hall distribution box. In order to compensate for heat loss in the connecting transfer lines, sub-coolers will be provided in the feed and valve boxes and the liquid Helium tank.

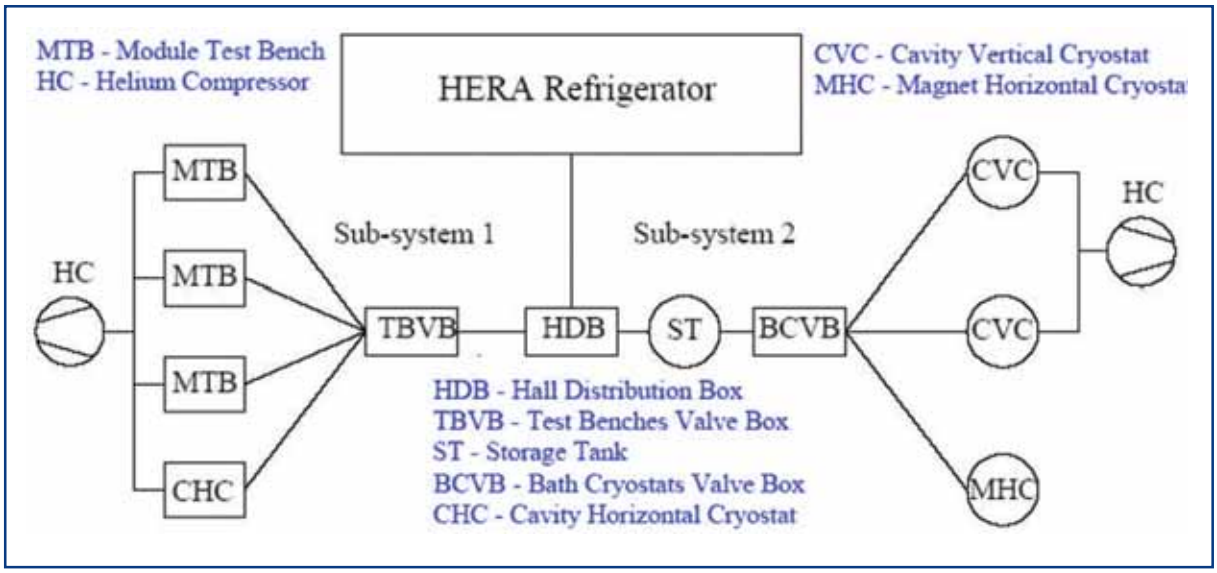


***Figure 7.2.7*** Block diagram of the cryogenic system.

Each test stand will be equipped with a 2 K vapour return tube. The return tubes in each sub-system will be connected to one 300 K Helium compressor unit. One additional Helium compressor unit will provide backup for both sub-systems. Before being processed by the compressor, the cold Helium will be warmed to ambient temperature in a heat exchanger. In the exhaust of the compressor unit, the pumped mass flow can be measured by warm gas flow meters for accurate measurement of the heat load in the 2 K circuit.

### *7.2.6.9 RF systems*

Since one accelerator module test bench is mainly intended to compensate for maintenance, repairs, etc., and only spot checking of the cavities embedded into the Helium-tank will be carried out on the CHECHIA-like test stand only, three RF stations, each equipped with a 10 MW klystron and a modulator set, will be installed. The two RF stations will be permanently connected to the test bench. The third RF station can be switched between one test bench and the CHECHIA-like test stand. It is supposed that RF power can simultaneously be supplied to the test stands in parallel and independently from each other for conditioning the couplers.

Two additional RF stations will be installed for testing waveguides and klystrons. The RF station for testing the klystrons will be designed so as to allow a trouble-free installation of each klystron to be tested.

### *7.2.6.10 Vacuum system*

For the insulation vacuum of the cryogenic system, standard turbo-molecular pump units will be provided. Each accelerator module test bench will get two such units allocated to the insulation vacuum of the modules.

The main RF couplers of one accelerator module will be equipped with one pumping tube to which one getter pump and one Ti-sublimation pump will be connected without individual valves. There will be only one manual valve at the pumping tube. The pumps and pumping tube will stay at each individual accelerator module from the assembly during the tests, until installation in the XFEL tunnel.

The cavity vacuum will mainly be created by means of oil-free turbo-molecular pump units. Each unit contains an integrated Helium leak detector. The accelerator module test benches and the CHECHIA-like stand will also get getter pumps to reach ultra high vacuum (UHV) conditions for the cavity vacuum. There will be also oil-free pumps, clean rooms, leak detectors and turbo-molecular pumps which can be moved according to requirements.

#### *7.2.6.11 Controls*

There will be different sub-control systems for the RF, vacuum and cryogenic systems, which have to be integrated by an industrial visualisation and data management system. In general, standard industrial components will be used as far as possible. The transfer of data between the different systems and data management will be mandatory for the operation of the test facility.

#### *7.2.6.12 Infrastructure*

Operation of the test facility will require 5 MVA of electrical primary power, 2.5 MW equivalent of water-cooling capacity, and about 330 $m^3/h$ of instrument air (operation of the HERA refrigerator is not included in these numbers).

### 7.2.7 Survey and alignment of XFEL

Planning and assembly of the whole facility will be assisted by the DESY survey group from the first peg-out of buildings via control survey during construction of buildings and the tunnel, installation of components, alignment of the accelerator components up to maintenance work and inspection survey. In order to realise the high accuracy demands on the alignment of the accelerator and the experiments, special survey methods are being applied which may have an impact on buildings or operating procedures at certain places.

Geodetic reference networks serve as fundamentals for all survey methods. The technical design of the respective reference systems depends on the accuracy required.

#### *7.2.7.1 Basic networks*

In order to mark any installation of the facility, a basic network has to be established. Coordinates of aboveground reference points along the accelerator axis have to be determined in relation to the existing coordinate system at the respective site. In case of the XFEL, this will be the DESY site coordinate system with respect to HERA/PETRA.

### Primary reference network

The primary reference network ensures the correct location and orientation of the various buildings, the tunnel, the accelerator and accelerator subsystems to each other. It is essential to install stable reference monuments (see Figure 7.2.8) at every site and at selected stations along the trace of the accelerator. These monuments are suitable to serve as a reference for position (GPS) measurements, height and gravity.

***Figure 7.2.8*** Survey reference monument.

At the Schenefeld site, approximately 10 survey reference monuments will be installed. At the other premises four of these pillars will be installed, which can be removed after construction work is done. Their role in the primary reference network will then be taken over by the survey pillars on the roofs of the buildings.

In order to enable the connection between the XFEL and the existing accelerators at the DESY site, the new reference monuments will be surveyed, together with existing survey monuments at the DESY site. The coordinates aboveground will be determined by using geodetic receivers of the GPS satellites. The required global precision of every reference point in the XFEL area has to be in the range of 5 mm (one standard deviation). The precise vertical network has to be established by precision levelling. The coordinates of the primary reference network have to be transferred to the subterranean reference network via sounding.

### Secondary reference network

The (subterranean) secondary reference network ensures the global positioning of the components of the accelerator. The network has to be established with wall-mounted target marks (see Figure 7.2.9) at intervals of approximately 10 m. The complete survey

system consists of these target marks and a wall-mounted rail on which the measuring instrument can be mounted and transported to every designated position. The target marks have to be installed at variable heights from floor level to top. Wherever possible, additional target marks have to be installed at the wall opposite the measuring instrument. The existing plumbing points in the shafts have to be included in this reference grid. With this setup, an accuracy of 0.2 mm over a section of 150 m length can be achieved.


***Figure 7.2.9*** *An example of wall mounted target marks (reference points) for the secondary reference network.*

### *7.2.7.2 Survey and alignment methods*

With an initial survey, the coordinates of the target marks will be determined with regard to the primary reference network. After this, the target marks can serve as a reference used to peg out every machine component such as pillars, pedestals, mounts, magnets, modules, undulators and so on. For this, the survey instrument is placed on a carriage mounted to a transport rail (see Figure 7.2.10) and fixed to the concrete wall for the time of the measurement. By surveying a given number of reference points the position of the instrument is calculated (free stationing) and then any user-defined points, can be pegged out (see Figure 7.2.11). The lines of sight from the instrument to the reference points and to the target marks on the machine components have to be kept free at all times.

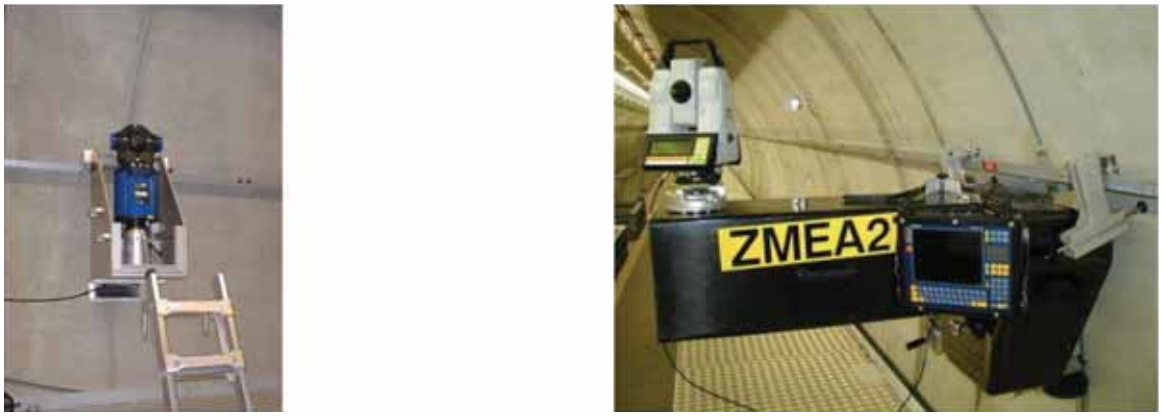


***Figure 7.2.10*** *Carriages for laser tracker and tachymeter.*

The survey methods for the reference system and machine components vary depending on the demands on the alignment accuracy of the machine.

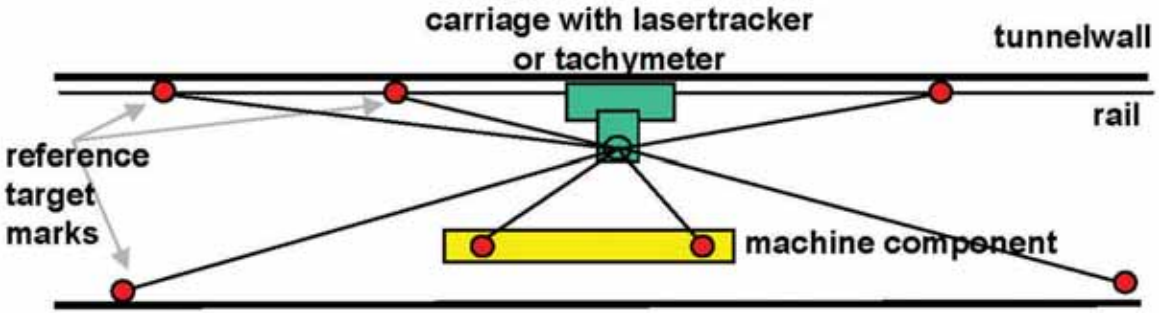


***Figure 7.2.11*** *The principle of the "free stationing" peg-out (see text).*

### Injector and linac sections

The injector and linac sections can both be surveyed with classical optical methods. Thus, the demanded accuracy for this part of the XFEL – which is 0.3 mm over any 150 m range – can be reached.

There has to be a line of sight equipped with removable radiation shielding.

### Start and distribution shafts

At the start shaft and at the distribution shafts, the coordinates are transferred from the aboveground primary reference grid down to the subterranean secondary reference grid. At the roof of the respective buildings there have to be survey pillars securely connected to the support structure of the building. These pillars are part of the primary reference network and their coordinates can be determined by geodetic GPS survey. During the construction phase there will be four of these pillars at every building, one at each corner of the shaft. For the plumbing measurements, four tubes (300 mm bore each) will be installed from the survey pillars down to the tunnel level. Underneath these

ducts, a survey bracket at tunnel level will be mounted to ensure the transfer measurements. After completion of the construction phase three of the four survey monuments can be removed.

Since there are significant temperature gradients between the tunnel sections and the shafts it is impossible to continue the reference system through the shafts with classical optical survey methods. Therefore, the connection of the tunnel sections on both sides of a shaft is accomplished by means of a laser alignment system (LAS). This setup is implemented into a vacuum pipe (300 mm bore) which overlaps each tunnel section by the length of the crossed shaft (see Figure 7.2.12).

The diverging distribution tunnels are connected to the reference system via cross cuts and precise distance measurements (see Figure 7.2.12).

**Photon beamlines and experiments**

Since there are components at the end of the photon beamlines (e.g. Beryllium lenses and monochromators) which have to be aligned to 0.5 mm accuracy for the undulator section and since some photon beamlines are up to 1 km long, the demands for the initial installation can only be met by an LAS. The LAS will provide an accuracy of 25 µm over a 300 m range and ~100 µm over the range of 1 km. This will be installed in addition to the classical optical survey system and will be routed through the radiation shielding into the experimental area to ensure the correct geometrical connection of the experiments to the beamline. For the survey and alignment of the experiments, wall- and floor-mounted reference points as well as brackets for instruments at the pillars of the experimental hall, will be installed.

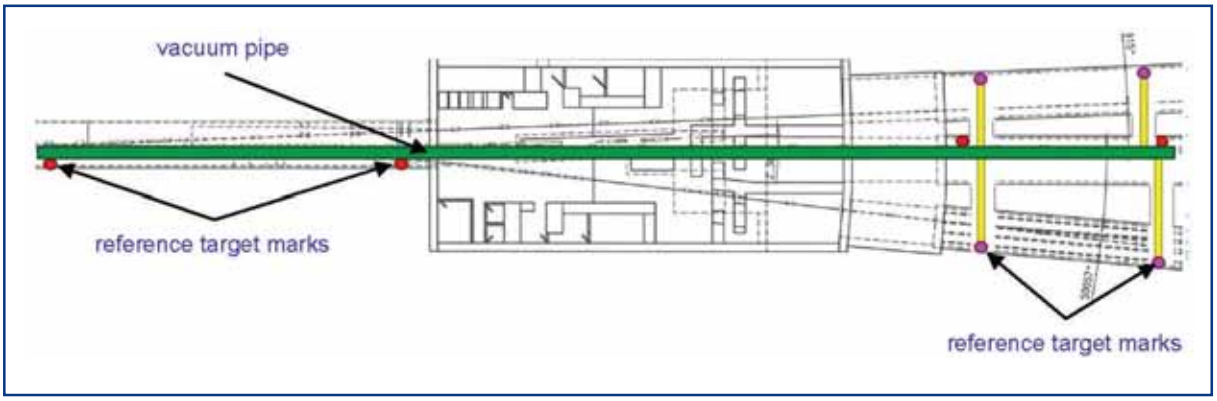


***Figure 7.2.12*** *Crossing the shafts with an LAS.*

### *7.2.7.3 Accuracy demands and performance*

The demanded accuracy for the reference points of the primary reference network has been specified as 5 mm. This demand can easily be reached by a combination of GPS measurements with geodetic receivers for the 2-D-position and precise levelling methods for the height.

The accuracy of the secondary reference network is determined by the demands of the initial alignment of the accelerator parts. The demands of the injector and linac section are 0.3 mm over a 150 m range. An accuracy of 0.2 mm over 150 m can be reached by using laser trackers and a dedicated layout of the reference grid. The machine components can then be aligned to the desired accuracy.

Any higher accuracy demands can't be reached with classical optical methods. For the above mentioned photon beamlines and experiments, the demands stay in a range of 0.5 mm over 1 km length. The chosen laser alignment system will be capable of delivering a resolution of 25 µm over 300 m length or ~100 µm over 1 km which qualifies the system both for the crossing of the shafts and for the (survey of the) photon beamlines.

## 7.2.8 Installation of components

### *7.2.8.1 Installation procedures and vehicles*

All transports in the tunnel have to pass through a shaft or the experimental hall. All shafts and the experimental hall are equipped with a freight elevator, staircase and, except for the injector shaft, with a crane and crane shaft. The big injector components will be installed via the shaft XSE. This shaft is the only one where the 12 m long accelerating modules can be let down. The other shafts XS1-4 are designed to allow the 5 m long undulators to pass through.

A large part of the shaft and tunnel walls will be equipped with in-profile rails that allow a fast and proper mounting of most of the installations.

In the linac tunnel (XTL), where all accelerator components are suspended from the tunnel ceiling, the top tubbing segments will have two in-cast channels to take the load and the longitudinal vacuum forces. A mock-up of the XTL tunnel will be constructed to allow tests of the module suspension, alignment, installation and connection, to verify the space requirements, test vehicles, train the installation crews and so on.

Most of the installation and underground transportation work will be done with standard vehicles (forklifts, scissor lifts, electric carts, trailers, etc.). A special vehicle is needed to transport, lift and install the modules and other heavy components in the XTL tunnel. Figure 7.2.13 shows the conceptual design of the accelerator module transportation and installation vehicle.

Another special vehicle will be developed to transport and install the undulator modules in the undulator tunnels. It will be based on standard air cushions supplied from compressed air outlets at the tunnel wall.

For the transport of the electron beam dumps from the installation shaft to their final position in the dump shafts XSDU1-2, a special trailer will be designed. The installation will be done with the underground crane and a special tool will slide it into the bore of the shielding.

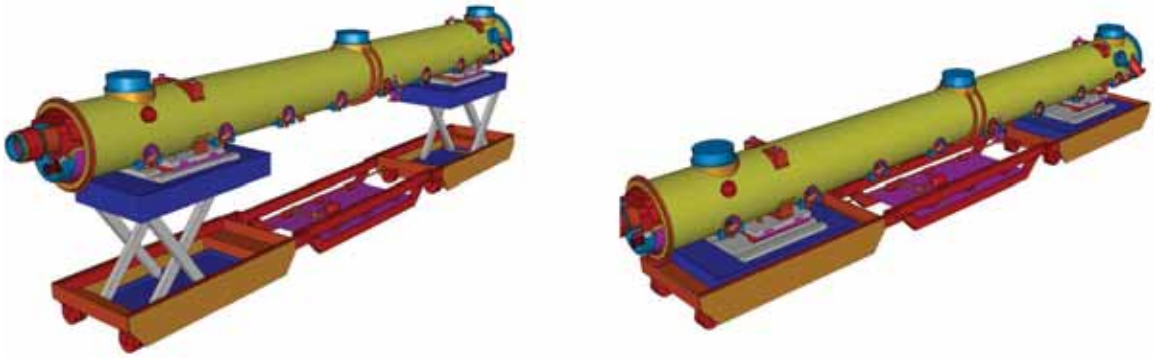

***Figure 7.2.13*** *The conceptual design of the accelerator module transportation and installation vehicle.*

**Installation sequence**

It is assumed that the work on the injector, the linac tunnel, the beam distribution and the undulator tunnels and in the experimental hall will run in parallel. The injector installation has a high priority, because it can, and should be, commissioned before the linac.

After the construction of a tunnel section is finished, the survey group will immediately measure the tunnel shape and place a rough longitudinal (and vertical) scale (10 m ticks) to allow an easy orientation for the workers.

In all buildings, except the linac tunnel (XTL), the installation of the basic infrastructure like light, power, phone and safety installation will start after the survey. This will be followed by the installation of cable trays and cables, water and gas pipes and other services. Because of the underfloor installation in the linac tunnel (XTL) the installation of the basic infrastructure has to wait for these parts and the floor plates to have been put into place.

### *7.2.8.2 Linac tunnel (XTL)*

The installation of the pulse cables from the modulator locations to the klystron positions in the tunnel is very time consuming and has to start immediately after the civil construction of the linac tunnel (XTL), the first access shaft (XSE) and the modulator hall (XHM) has been finished. The cable trays will be mounted and then each cable will be pulled. The longest cable has to be installed first.

In parallel, the installation of the other underfloor services (pipes, power cables, etc.) in the XTL tunnel can start from both ends (shafts XSE and XS1). The transport of tools and material will be done by installation vehicles that run on the centre wall and the console at one side of the tunnel.

It is assumed that the far (XS1) end will be ready earlier, so one can start to place the floor plates from this side. They will be sized so that they can be handled with standard forklifts. In the range of the superconducting linac, the pulse cables have to be carefully guided through the gaps foreseen in the plates.

This task will be followed by the installation of the basic infrastructure: the smoke exhaust pipe, the fire protection walls, emergency guidance rail, communication services and the support rail for the survey equipment.

Next, the installation of the I-beams to suspend the linac components from the tunnel ceiling will start. The 4-5 m long beams will be lifted and mounted with scissor lifts (see Figure 7.2.13). The I-beam will be bolted to two in-cast channels in the top tubbing segments. The alignment will be assured by adjusted laser beams and targets attached to the I-beams. The position of the beams will then be checked by the survey group and the positions of the suspensions will be marked. After this preparation, the installation of the accelerator components can start.

The installation of the linac will start from the shaft XSE. The first element will be a 2 m long cryo-box followed by the first accelerator module. The waveguide distribution has to be placed before the module can be installed. After alignment the module will be connected to the next module or cryo-box in a clean room that will be set up locally. After several checks, the pulse forming network, pulse transformer, klystron, and several racks with shielding, water distribution, and power outlet box will be installed.

When the module installation has passed the region of the bunch compressors, the cryo bypass line will be installed, followed by the bunch compressor sections that are pre-assembled in ~12 m units. This is followed by the racks with shielding.

The components of collimation/beam distribution section will also be suspended from the tunnel ceiling. Their installation will start from the end of the linac in the direction of the shaft XS1.

#### *7.2.8.3 Injector, undulator and photon tunnels*

All magnets, undulators, photon optics, gun, module and cryo-boxes in the injector and the undulator/photon section, will rest on aligned and tamped bases bolted to the floor.

In the undulator sections, special supports for the vacuum chamber are needed and the vacuum chamber has to be installed before the undulator. All vacuum connections will be done using temporary local clean rooms. At the same time the installation of electronic racks can start.

## 7.3 Controls and operation

### 7.3.1 Control systems

The XFEL requires a complex control system with many I/O devices, computers and software modules. The design of the control system incorporates strategies to keep the system modular, simple and well structured with loose coupling and adequate and robust interfaces between its components. On a smaller scale, the required technologies for the XFEL were successfully demonstrated in the TTF vacuum ultraviolet (VUV)-FEL with the DOOCS control system. Since the framework for TTF is the basis of the development for the XFEL, further improvements will be tested in FLASH before the commissioning of the XFEL.

The XFEL will be built as a collaborative effort and therefore, the control system has to be able to integrate contributions from partners. In TTF a lot of experience has been gained to smoothly integrate various different systems into the common DOOCS environment. A homogeneous system is, of course, easier to setup and maintain and therefore, a discussion of how to implement individual systems with a balance of effort on all partners and benefits for the final system, is required.

From the experience of FLASH it has been learnt that a single electron bunch resolution of all monitoring devices, including the storage of the data, is required. This data can be used for offline analysis to improve the machine, correlate accelerator and user experiments and for slow feedback systems. The current implementation of such a high performance data acquisition system (DAQ) is described in **[7-15]**, further developments are foreseen.

#### *7.3.1.1 Architecture*

As shown in Figure 7.3.1, the overall architecture consists of three layers: A top level with display or client programmes as a presentation layer; a front-end level with device servers and I/O as a connection to the hardware and a middle layer with powerful data servers. The upper layer is the interface to the operators. These upper services, with the application programmes, are available to the consoles in the control room, the experts working at the machine or in their offices. For remote operations, all these applications are provided via secure links to the remote shifts or experts.

Examples of applications in the presentation layer are: archive viewer, synoptic displays with a graphic representation of the subsystems, alarm panel, save and restore tool, plotting and measurement and simulation tools.

Client programmes often require information from a group of devices or need to operate on such a group. Middle-layer servers can provide such collective reports and controls. An example of an implementation is a Finite State Machine (FSM) server. This server keeps track of several devices and is able to initiate state dependent control actions. A hierarchical grouping of servers is a better way of structuring the system. These kinds of servers are usually implemented in the middle layer. Databases, file servers, machine physics simulation servers, name servers, the DAQ system, slow feedbacks and other automation as well as Web services, and in general services without a direct device connection, are placed in the middle layer.

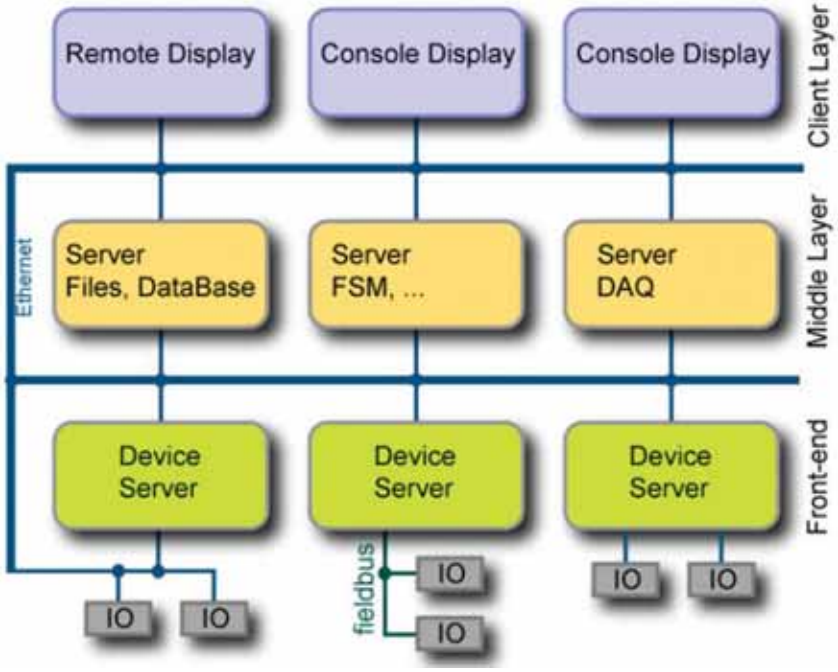


***Figure 7.3.1*** *Control system architecture.*

The front-ends are distributed and placed close to the hardware (accelerator components, undulators, beamline components and experiments), most of them inside the tunnel in cooled and radiation-shielded racks. Industry standards are used whenever possible so that most of the required electronic modules can be bought.

### *7.3.1.2 Hardware*

Robust hardware for the front-ends with a high reliability is foreseen. VME and Advanced Telecom Computing Architecture (ATCA or µTCA) are the two options for crate systems. The VME standard has been successfully used in many accelerators, including TTF. The market share is expected to be constant over the next few years. With the optional VXS on the VME, bus, modern Gigabit serial communications are useable. ATCA and µTCA are new standards from the telecom industry for future crate systems and should be considered as an alternative to the VME bus. ATCA is a pure Gigabit serial communication system that allows redundant connections. Redundant power supplies are also used as well as the standard supports, full hot-swap support as well as crate monitoring and software interfaces to manage failures.

The crate systems are used for fast acquisitions and feedbacks. Slow and reliable tasks are better implemented in PLCs. The control system is preferably connected to the PLC by an Ethernet link, but a fieldbus link like CAN or ProfiBus is possible too. A further category of I/O devices are stepper motor controllers, temperature sensors, digital I/O and slow analogue to digital converters (ADCs). These devices are housed in DIN-Rail-Modules with an Ethernet bus coupler for a group of I/O devices.

### *7.3.1.3 Network*

The front-ends are connected mainly by Ethernet, or if Ethernet is not available, by a fieldbus (CAN or ProfiBus) and digital cameras are attached by FireWire. All the other communication runs on Ethernet via switches and routers. The Ethernet speeds used in the field are 100 and 1,000Mbit/second or higher which results in a maximum data rate of about 10 or 100MB per second, respectively. The backbones of the switches are being connected with higher speeds and by fibre optical links. The control system is decoupled from the outside intranet and internet by a firewall to secure the control system network from attacks or viruses. Remote operations or maintenance will be foreseen. This includes access from a remote expert at home to reduce the downtime in case of failures.

The tunnels and halls are equipped with wireless networks. Maintenance work on the electronics and front-end devices usually requires access to the control system data. Wireless Local Area Network (WLAN) infrastructure will be used for maintenance tasks with mobile devices.

### *7.3.1.4 Software*

The control system software covers the whole range from server programmes, communication protocols, applications and some Web services. The whole control system will run several thousand processes on distributed computers. Self-healing technologies will be applied to keep services running. Automated procedures are required to manage software upgrades and to keep the system consistent.

Operating systems on the servers and front-ends will be UNIX flavours (LINUX or Solaris). Object-orientation is the main paradigm of the control system to get a well structured and modular architecture that is easier to maintain and improve. The main part of the control system will be based on modular libraries to allow easy upgrades.

Programming languages will be mainly based on the languages C++ and Java.

The growing complexity of the software requires adequate tools: Integrated Development Environments (IDEs) for the complete design cycle from editors, Graphical User Interface (GUI) designers, compilers, debuggers, performance analysers, documentation generation and code repositories. A centralised repository like Concurrent Versions System (CVS) is mandatory for developers working in a team or in collaboration with members in different institutes. Access to this system will be provided from the Web.

The commercial software MATLAB for mathematical processing, will be fully integrated. Whenever possible, mature “open source” products will be integrated too.

It is planned to provide controlled access for remote operations or maintenance. Single sign-on for the users of Web services and controls applications is foreseen.

### *7.3.1.5 Operation*

The demands on the control system from XFEL operation are:

- automated procedures to hardware setup (e.g. the RF systems);
- procedures to switch to a spare module section in case of a failure (e.g. to keep the linac energy constant);
- various slow feedback systems;
- handling of different electron bunch patterns;
- full access to all parameters of the diagnostic devices with a single bunch resolution.

Beside the “traditional” control system applications, some further tools are required for the operation of the XFEL. It is planned to continue the development of the TTF electronic logbook and similar technologies for this.

A control system demands manpower during the whole lifetime of the accelerator. It needs bug-fixes, improvements, extensions, security patches and also hardware repairs. The operability and availability of the entire facility is, to a great extent, influenced by the control system. Automated operation, fast detection of problems and reasons for faults and good error recovery are important for reliable operation.

In order to reduce downtimes caused by the control system and central hardware, the “Mean Time Between Failures (MTBF)” has to be increased and single points of failure avoided. Some examples of MTBF in hours are: PC motherboard $5\times10^4$, VME central processing un it (CPU) 18×104, Fan $5\times10^4$, SCSI disk $10^6$, IDE disk $3\times10^5$, power supply $4\times10^4$... $10^5$, integrated circuit $3\times10^7$. These values vary considerably with temperature, radiation dose, power dissipation or operation close to, for example, voltage ratings. The conclusions from these numbers are:

- the electronics will be installed in cooled racks;
- the racks need radiation protection;
- central systems like timing and network are connected in a star-shaped topology;
- the central network is operated by two redundant switches;
- systems should depend on a minimum of other systems;
- fans and power supplies should be redundant when possible;
- self-healing by automated processes and error reporting should be implemented.

### *7.3.1.6 Timing*

The purpose of the timing system is to trigger devices like the gun, kickers, klystrons and data acquisition modules with configurable delays on certain events of the machine operation, to provide synchronised clocks for ADC sampling and to distribute further reliable information. For the trigger, a jitter in the order of a nanosecond is sufficient while ADC clocks might require a much better stability (well below 100 ps). The timing signals

have to be stable and therefore, are programmed into the hardware, with all parameters controllable and readable by the control system. The system is planned on the basis of serial optical links with a transmission frequency of about 2.6 GHz which is synchronised with the RF master oscillator as a stable frequency reference. A timing resolution up to about 400 ps has been achieved.

A star topology of the optical links is aimed at, to have a system with a maximum redundancy. All optical fibres of the links will have the same lengths (about 3 – 4 km). Sender and receiver modules will be based on the same design with a Field Programmable Gate Array (FPGA) as the CPU. To reduce the number of sender modules it is planned to equip the modules with up to four transceivers. The optical links will be bidirectional to implement a temperature compensation of the link timing as well as to provide the possibility of a feedback from the subsystems to the CPU.

From the coded events transmitted over the links, variable gates and trigger signals with programmable delays are derived in the receiver modules to allow the subsystems to adjust the timing events most flexibly to their required needs. In addition, information about, for example, bunch patterns can be transferred by the system.

#### *7.3.1.7 Machine protection system*

The complete accelerator has to be equipped with a machine protection system (MPS) to prevent beam operation, e.g. in case of technical failures. The MPS is an independent, fast alarm system that allows the beam and subsystems, e.g. Laser and RF, to be switched off within microseconds. The system will be based on fast distributed interlock logic. Decentralised boxes with interlock inputs and some inhibit outputs are linked by fibre optic cables in the upstream and downstream directions. Each box gets an interface to the control system for the readout of the status and interrupt sources. The control system is not involved in the fast protection process, but in the configuration of the whole system.

### 7.3.2 Radiation safety

#### *7.3.2.1 Radiation protection considerations*

This section describes the radiation safety requirements for the XFEL. The main emphasis has been placed on the impact of the XFEL operation on the public (local population) and the environment. Most important here is the limitation of the radiation level (doses) to the public, coming directly from stray radiation or indirectly through a potential activation of soil and groundwater or air and coolants released from the facility.

Following the German regulation **[7-16]** and the As Low As Reasonably Achievable (ALARA) principle, planning goals in terms of dose limits for the public have been set. According to the German regulation, the maximum allowed personal dose due to direct radiation and radiation from radioactive release (activated air, water, etc.) is 1 mSv/a, and for radiation from radioactive release alone 0.3 mSv/a. Considering the ALARA principle, our planning goals for the XFEL are 1/10 of the above given limits. This results in 0.1 mSv/ per person for the public from direct radiation and radiation from radioactive release and

0.03 mSv/a from radiation from radioactive release alone. The corresponding limits for staff members are higher according to their surveillance status. The limit for the public is, therefore, the more demanding requirement. For comparison, the natural doses in the northern part of Germany are about 1-2 mSv/a. Most of the single dose contributions given below occur at different locations along the facility. One, therefore, has to keep in mind that these single dose contributions do not have to be added. To be conservative, however, this has been done to estimate the maximum dose.

The studies of the radiological impact on the public and the environment carried out by the DESY radiation protection group (summarised in **[7-17]** and **[7-18]**) have been evaluated by an independent German institute, the Öko-Institut e.V. Darmstadt **[7-19]**. The Öko-Institut e.V. Darmstadt agreed with our basic assumptions and calculations and found no missing items or problems for an implementation of the XFEL in the foreseen way.

The basic parameters and main assumptions for beam losses in the cold and warm machine can be found in Table 7.3.1. The earth coverage of the tunnels will be on average about 12 m and at minimum 6 m.

| | | |
|---|---|---|
| Maximum beam energy | 20 | GeV |
| Maximum beam power | 1.2 | MW |
| Maximum beam power/dump | 0.3 | MW |
| Maximum rate (0.3 MW) | $9.4 \times 10^{13}$ | e/s |
| Operation time/year | 5000 | hours |
| Cold machine: | | |
| Maximum local beam loss (0.4 W/m'"8 m=3.2 W) | $1.0 \times 10^{9}$ | e/s |
| Maximum time of loss/year | 5000 | hours |
| Maximum lost particles/year | $1.8 \times 10^{16}$ | e |
| Warm machine: | | |
| Maximum beam loss (0.3 MW) | $9.4 \times 10^{13}$ | e/s |
| Maximum time of loss/year | 1 | hour |
| Maximum lost particles/year (0.3 MW) | $3.4 \times 10^{17}$ | E |

***Table 7.3.1*** *The basic parameters and main assumptions for beam losses in the cold and warm machine.*

### *7.3.2.2 Stray radiation due to neutrons and muons*

There are two different kinds of secondary radiation capable of penetrating thick material layers: high energetic neutrons and muons. At three locations, high energetic neutrons have to be investigated: The cold part of the machine with permanent losses, the warm part of the machine with exceptional losses and the beam dumps with permanent losses (**[7-20]** and **[7-21]**).

The annual dose for the public living above the cold part of the linac is based on the inherent safety mechanism which means that more than ¾ of the lost power is absorbed

by the cold mass. This results in a dramatic pressure rise in the 2 K cooling circuit and therefore, superconductivity is lost and the acceleration is stopped immediately. At the cryogenic limit, with an average power loss of 0.4 W/m for the cold part of the main linac, an annual dose of 0.002 mSv will be created for the public, assuming a minimum earth coverage of 6 m and 5,000 h of operation per year. Concerning the above given beam losses for the warm part of the machine, the annual dose will be 0.041 mSv assuming again a minimum earth coverage of 6 m. Local loss points such as emergency dumps and collimator sections can be additionally shielded inside the tunnel according to their power loss and the thickness of the soil layer above.

For the shielding of the dumps, two options have been worked out **[7-18]**. The baseline design consists of 4 m ordinary concrete and 5.5 m sand, leading to a maximum annual dose of 0.038 mSv on the earth surface directly above the dump shafts, which is located on the XFEL site.

Muons with maximum energies of 20 GeV are capable of penetrating 60 m of soil but have a strong forward characteristic. Those muons can hardly be shielded artificially (**[7-22]** and **[7-23]**). The most intense muon sources are the beam dumps with maximum doses of about 0.0001 mSv per year on the surface **[7-18]**.

#### *7.3.2.3 Activation of soil and groundwater*

Around the beam dumps, the activation of soil and groundwater has been estimated by Monte Carlo simulations with FLUKA (**[7-24]** and **[7-25]**). For soil and groundwater activation behind the 4 m thick concrete shielding of the dump shafts, a realistic model of transformation of soil and groundwater activation in the first 1 m around the dump shielding into activation concentration of drinking water and doses for the public, were used (details can be found in **[7-26]** and **[7-27]**). It has been shown that the production of radionuclides in the soil leads, in the first 1 m near the dump shielding, to a maximum annual dose of 0.012 mSv **[7-18]**. The content of $^{3}H$ (Hydrogen) and $^{22}Na$ (Sodium) in groundwater after 20 years of operation was found to be 0.024 Bq/g and 0.0025 Bq/g, respectively. This leads, under the assumption that a person is taking all of their drinking water (700 litres per year) from the above described location, to a maximum annual dose of 0.008 mSv **[7-18]**.

#### *7.3.2.4 Activation of air*

For the XFEL, one expects a higher activation of the tunnel air at three different locations:

**1** tunnel air close to areas with collimation systems;

**2** tunnel air which passes the beam dump area;

**3** enclosed air near the beam dump system which will escape if access is needed to this area.

Taking into account the above ventilation concept described, one can calculate the air activation concentration at the nearest air outlets for the activation area. Calculations **[7-18]** lead to a relative release factor (in comparison to the release numbers from the

German Strahlenschutzverordnung **[7-16]**) of 0.32 which results in an annual dose of 0.096 mSv directly at the air outlet due to air from group 1. One has to keep in mind that this air will be released on the existing DESY site so this dose cannot directly be transformed to a dose for the public. For groups 2 and 3, the corresponding numbers are 0.0035 as the relative release factor which results in an annual dose of 0.001 mSv directly at the air outlet due to air from groups 2 and 3. This air will be released at the corresponding access shafts and can, therefore, easily be used as the maximum dose for the public due to activated air from groups 2 and 3 **[7-18]**. The average dose due to activation of released air was calculated to be 0.010 mSv per year at maximum **[7-18]**. More details about the method of calculating the air activation can be found in the studies **[7-28]** and **[7-29]**.

### *7.3.2.5 Activation of coolants*

The highest activity concentration of cooling water is expected in the dump cooling water **[7-27]**. It circulates in a closed loop (see Section 4.7.4). Two long-living radioactive isotopes have to be considered: Tritium and Beryllium-7. Their activities in the primary cooling circuit after one year of operation are 20 MBq and 2 MBq, respectively, which results in activity concentrations of $1.0 \times 10^7$ Bq/m$^3$ and $1.1 \times 10^6$ Bq/m$^3$, respectively **[7-18]**. These numbers are well below the corresponding release numbers for “uneingeschränkte Freigabe” of the German Strahlenschutzverordnung **[7-16]** and, therefore, the activation of cooling water implies no special risk at the XFEL.

The superconductive cavities are cooled with liquid Helium. The coolant is continuously transported within a loop consisting of accelerator structures in the tunnel and a cooling plant outside. In shutdown periods, storage outside the tunnel must also be possible and therefore, the activation of Helium may be of radiological interest. The only activation product is Tritium. Similar to the calculations in **[7-30]**, under the assumption of operation at the cryogenic limit of 0.4 W/m over the whole accelerator and an operation of 5,000 hours per year, one gets a total activity of 2.2 GBq and an activity concentration of 250 Bq/g after a total operation time of 20 years. This is well below the release number for “uneingeschränkte Freigabe” of the German Strahlenschutzverordnung **[7-16]** and, therefore, implies no special risk at the XFEL.

### *7.3.2.6 Summary and other studies*

In Table 7.3.2 , a summary of all maximum exposures and the sum of all these sources can be found, keeping in mind that these doses arise at different locations. The planning goal of 0.1 mSv/a personal dose for the public from direct radiation and radiation from radioactive release, and 0.03 mSv/a from radiation from radioactive release alone, has been met and realistic doses to the public are safely more than two orders of magnitude lower because of the very conservative assumptions used in the calculations of the above numbers.

| Exposure path | Maximum exposure |
|---|---|
| Stray radiation, warm part | 0.041 mSv/year |
| Stray radiation, beam dumps | 0.038 mSv/year |
| Stray radiation, muons | 0.0001 mSv/year |
| Activation of soil | 0.012 mSv/year |
| Activation of groundwater | 0.008 mSv/year |
| Mean activation of air | 0.010 mSv/year |
| **Sum** | **0.11 mSv/year** |

***Table 7.3.2*** *A summary of all maximum exposures and the sum of these sources.*

As is the case for the HERA accelerator, the XFEL will have a radiation monitoring system installed to survey online dose rates at several locations along the beamline. Therefore, studies have been started to design new radiation monitoring detectors to handle the special timing conditions. In addition, a lot of detailed studies were done to optimise the shielding of the XFEL shaft buildings (similar to **[7-31]**) to ensure a minimum of controlled areas.

The interlock system used at DESY including all the maintenance and testing procedures is described elsewhere (**[7-32]** and **[7-33]** and also in Section 7.3.4). A similar system, with state of the art components, will be installed at the XFEL to ensure a safe operation and a variety of combinations of access and machine operation. Details of the expected activation of materials can be found in **[7-34]**, **[7-35]** and **[7-36]**, procedures for beam dump handling, environmental and personal monitoring, potential failure scenarios and dismantling issues, are described in **[7-18]**.

## 7.3.3 General safety

### *7.3.3.1 Fire safety and emergency response*

**General**

The following rules underline the general safety requirements.

Fire safety measures in the tunnels and the buildings have to be provided during construction, shutdown, maintenance and operation of the XFEL. During all of these phases, access to the tunnels is restricted to trained and instructed personnel. Tunnels and buildings are designed so that people can safely manage to escape to a safe area in case of a fire. For this purpose, the XTL tunnel is divided into segments with an individual length of approximately 600 m. Segments are separated by fire-resistant walls in combination with water curtains. The length of each of the other tunnels does not exceed 700 m. All tunnels are separated from the shafts by fire-resistant walls with a fire-resistance time of 30 minutes.

The underground experimental hall is equipped with automatic fire detection and smoke extraction systems. Supporting structures are built with fire-resistant construction materials with a fire-resistance time of 90 minutes. The maximum escape route from this area is 40 m.

Fire loads in all underground areas are kept as low as possible. Specifically, only flame retardant cables are used in the underground areas. The storage of flammable materials in underground areas is prohibited.

In addition to these primary measures, fire detection and extinguishing systems as well as organisational and technical measures for emergency response will be installed, as detailed below.

### Fire detection, alarm and extinguishing systems

All tunnels and underground buildings are equipped with a fire detection and localisation system. The XTL tunnel and two of the XTDs with a comparatively high fire load have a smoke extraction system. The other buildings are equipped with a fire detection and localisation system with an automatic evacuation alarm (siren).

The tunnels are connected to a fire water supply comprising a fire water pipe with connections at least every 50 m. The experimental hall and the buildings are also connected to a fire water supply.

During the installation phase, mobile water curtains are installed in the linac tunnel (XTL). Electronic racks are equipped with local inert gas extinguishing systems integrated into the racks which are triggered automatically in case smoke is detected. Transformers in the tunnels have water mist extinguishing systems.

### Communication system for tunnel and buildings

Communication booths are installed in all tunnels with a maximum distance of 50 m. The installed communication systems will allow communication by radio, mobile phone and fire brigade radio.

### Emergency power supply and emergency lighting

All tunnels and buildings will be equipped with emergency lighting. In addition, all tunnels will be equipped with an emergency power supply to maintain the operability of installations relevant for safety in case of failures of the main power supply. The emergency supply will cover the smoke extraction system, the communication system, the emergency lighting and the signposting of escape routes.

### Access monitoring system

The tunnels and shafts are equipped with an access monitoring system with personal separation.

**Organisational requirements for fire safety and emergency preparedness**

The following organisational fire safety precautions will be implemented:

- emergency escape plans and fire safety regulations (Brandschutzordnung Teile A,B,C) as well as emergency plans for the fire brigade will be established and employees will be regularly instructed in fire safety regulations;
- a welding permit defining specific fire safety precautions will be required for hot works in all buildings;
- smoking will be prohibited in the tunnels and shafts during all phases (construction, installation, commissioning, maintenance and operation);
- emergency preparedness measures will include:
  - an emergency response system which ensures that first aid by a qualified paramedic can be provided to all areas within the XFEL installations within a response period of 15 minutes;
  - specific response measures for the evacuation of employees with restricted mobility including the use of stretchers and rescue chairs in areas where such employees are present;
  - a specific wheeled stretcher carrier for the evacuation of injured persons to be provided in the tunnels.

### *7.3.3.2 Safety of equipment and accident prevention*

**Design considerations**

The design of the equipment will incorporate various safety measures including:

- the use of non-halogenated cable and insulation materials in line with the DESY cable specification. Flame-retardant cable materials will be used in the tunnels and underground areas;
- the design of pressure vessels and pressure lines will be in accordance with the requirements of the European Pressure Vessel Directive, or implementation of a similar safety standard;
- the design of machines, mobile equipment, transport vehicles and lifting equipment will be in accordance with the requirements of the European Machine Directive and the harmonised European norms;
- the design of electrical equipment and installations will be in line with the requirements of the European Low Voltage Directive and the applicable standards (EN, VDE, IEC, etc.);
- transport vehicles used within the tunnels will have safety features such as headlights illuminating narrowed areas of emergency escape routes and safety railings for guidance in case of narrowed escape routes;

- installations containing substances hazardous to water will be designed in accordance with the regulations for such installations. This includes the use of double-walled equipment or appropriate secondary containment as well as technical or organisational leak detection measures for equipment holding significant amounts of substances hazardous to water, such as pulse transformers.

**Requirements for the safe operation of equipment**

The following measures will be implemented to ensure safe operation of the equipment:

- prior to commissioning, initial inspections will be performed of all fixed electrical equipment as well as of installations requiring supervision under German and/or EU law. This specifically includes pressure vessels, cranes, elevators and transport vehicles. All equipment will be included in the existing inspection database and regular follow-up inspections will also be performed;
- for other types of equipment (including mobile electrical equipment, gates, safety cabinets, emergency lighting, fire alarm systems) regular inspections will be performed based on the German Ordinance on the Safe Operation of Equipment;
- for all workplaces, hazard analyses will be performed in accordance with the German and European legal requirements.

**Organisational Health & Safety requirements for the construction phase**

The specific safety precautions during the construction phase will be established in the form of a Health & Safety Coordination Plans (SiGe-Plan) for each construction site. Health & Safety Coordinators will also be appointed to supervise the implementation of the safety requirements during the construction phase.

### 7.3.4 Personnel interlock

#### *7.3.4.1 General*

The personnel interlock system is an active part of the accelerator radiation safety system to secure radiation restricted areas which are established due to beam operation. The main task of the system is to switch off all relevant radiation producing devices in case of danger and so prevent accidental exposure of people to radiation.

For this purpose, installations such as emergency off-switches, access doors, safety key boxes or beam shutters are equipped with electrical contacts and switches. Their signals are processed in a central interlock logic unit where a beam operation permission is generated after a warning procedure. This permission of the interlock system is necessary to operate accelerator components like klystrons, kickers, septa or magnets, or to open beam shutters and absorbers. If one of the safety input signals disappears, these components must be switched off in a safe way or beam shutters must be closed.

At DESY, there exists more than 40 years of experience with the conceptual and technical design and building of reliable complex personnel interlock systems. For XFEL, a technology will be used, which has been developed at DESY in the past five years and

is working successfully at the complete interlock system for the FLASH facility and at subsystems of other DESY accelerator interlocks. Also for PETRA3 and its experiments and pre-accelerators this technology will be used. The general concept of the new technology has been approved by experts of the German TÜV (Technischer Überwachungs-Verein).

### *7.3.4.2 Design features*

All functions of high safety relevance are based on two independent redundant systems: The contacts and switches at local installations are doubled, each with its own cabling. Their signals are parallel-processed in logic units and the approval of both systems is required to start a warning procedure. For switching off beam generating devices, two different redundant methods are always chosen, each triggered by a separate system of the beam operation permission interlock.

Another important design feature is the fail-safety of the system. In case of failures or damages, a safe state must be achieved. For example, beam shutters are installed in a way that they close at lack of pressure; or power failures or broken cables and contacts interrupt a signal chain.

A tree structure of modular subsystems is chosen to achieve a transparent signal flow within the system and to allow flexibility for upgrades and changes. In the signal paths, interrupt buttons are installed to allow easy testing procedures. According to the law, official interlock test procedures have to be performed at least once a year.

For the system to operate successfully a stable operation of all components is necessary and in case of a failure, easy repair or replacement must be possible. Uninterruptable power supplies are also used to keep the interlock system working in case of main power failures.

For a large accelerator like XFEL with many remote interlock subsystems, information about the status must be available in the main accelerator control room. The new interlock technology provides a computer connection which is used by the accelerator control system to enable surveillance, event logging and the operation of some functions at an interlock console.

### *7.3.4.3 Basic technology*

All high safety level systems are working with hard-wired 60 V powered relay technology using modern special relays with forcible guided contacts.

The logic units are housed in modules. Only a few standard modules are required to fulfil many purposes. Additionally, the modules themselves are constructed in a modular way; circuits for certain functions are located on plugged boards for easy replacement or redesign in case some industrial hardware is no longer available. Figure 7.3.2 shows an electronic module which is used for an interlock door.

To enable a continuous remote supervision during operation, the logic status of each relay in a module is read out by an opto coupler and the information is processed by a local interface board.

Each module is equipped with a standard interface board which connects the interlock electronics on the main board with a commercial CANopen bus controller. The interfaces of all modules of a system are connected by a CANopen bus line with an embedded Linux computer module. This local interlock server has a protected separate local area network (LAN) connection to the control system's computers.

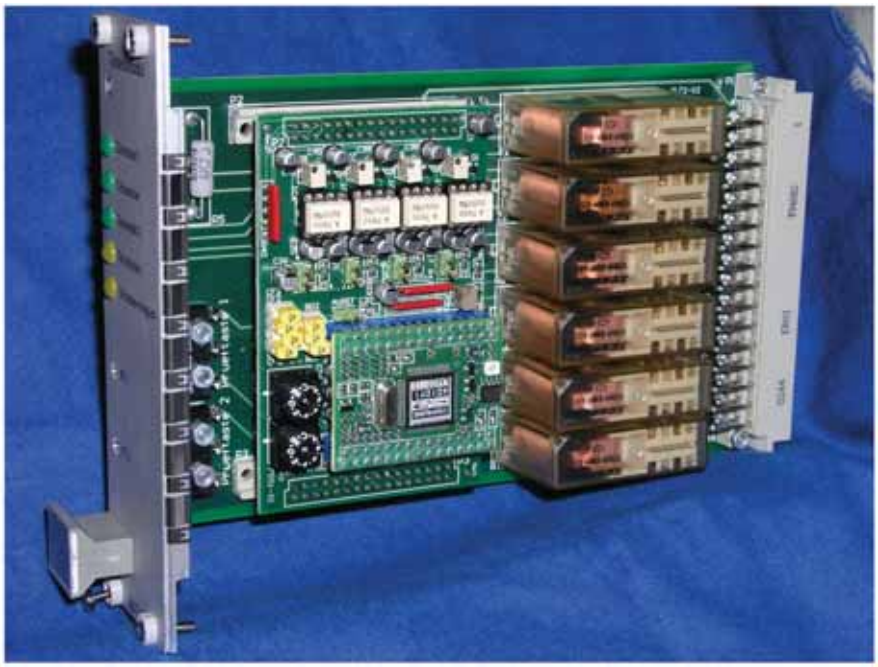

***Figure 7.3.2*** *Door interlock module with plugged interface board.*

For some tasks of lower safety relevance, a computer-controlled operation is foreseen. For example, warning panels and blinking lamps are operated with local bus driven switches at the accelerator doors.

### *7.3.4.4 Subsystems*

**Door interlock**

Before beam operation is possible, all interlock areas concerned have to be searched. Everyone must leave the area and all interlock doors have to be shut. The area search is supported by the door interlock system using a start/interrupt function, an acoustic announcement, set buttons at the doors and search buttons in the area. The order in which doors and search buttons must be set is computer-controlled. When the search is completed, a sum signal for the interlock area is generated in an additional third relay safety path. If a door to a searched area is opened, the 60 V signal lines are interrupted in both systems by the two door contacts and the sum signal "area searched" disappears.

For large accelerator tunnels, a controlled access procedure to searched areas is supported by the door interlock system. For this purpose it is possible to override the “searched” signal in the third safety path during the opening of the door whilst the door contacts remain active. This procedure, under the control of the operators in the accelerator control room, is allowed under several safety conditions: a video and audio communication system between door and control room is necessary, the names of the persons entering the area must be registered, each person has to take a safety key and the override procedure is only active as long as a button is pressed by the operator.

The XFEL tunnels have a total length of about 6 km. If long tunnels like XTL, XTD1 and XTD2 are split into two interlock areas, there will be 15 accelerator interlock areas. The main interlock doors of each area will be equipped for controlled access procedures. An area search has to be performed by at least two people.

For each of the five photon beamlines three experimental interlock areas are foreseen. The door interlock system is different to enable an area search by a single person. Controlled access to searched areas is not possible.

### Safety keys

Interlock safety keys are housed in modules. All modules are equipped with switches to detect the presence of a key in two systems. All keys have to be in their modules for a beam operation permission. The keys are used to inhibit beam operation, they are needed for a controlled access to searched areas.

### Emergency-off system

Each emergency off-button in an interlock area is part of the personnel interlock system and inhibits any beam operation when pressed. The buttons are installed in such numbers and distances, that it is always possible to reach one of them within the beam warning time.

An emergency off-button has two internal switches, one for each system. The buttons are connected with the CANopen bus system to give information about their location and status.

In case other sources of danger in the area must also be switched off, interfaces are provided which allow shutdown across the system or by single buttons.

### Beam operation permissions

At the presence of all safety relevant input signals, a beam warning procedure can be started at a central logic interlock unit. Afterwards, a beam operation permission can be given. Typical input signals originate from the door interlocks of all areas involved, the key modules and the emergency-off system. Signals from all other essential safety installations can also be processed as required.

*Accelerator*

Before generating an electron beam in XFEL, it must be ensured that the beam will be dumped in one of the absorbers. The dump safety system will be a combination of active and passive elements. The function of active components such as bending magnets has to be checked by the personnel interlock system.

Depending on the operation mode (Injector test, Commissioning, FEL beam 1-3, FEL beam 4-5) the electrons must go to the appropriate dump. This is essential to permit access to some tunnel areas during beam operation in other tunnels. To enable access in one of the photon tunnels XTD6-XT10 whilst the neighbouring photon beamlines are in operation, beam shutters are required in the photon beam sections of XTD1-XTD5. Their contacts indicating the “closed” position must be checked by the interlock system.

*Experiments*

For an experimental area, the personnel interlock system must provide permission to open a beam shutter in the photon beamline. Therefore, all safety input signals of the experimental area must be present. If this operation permission disappears whilst the beam shutter is open, the electron beam operation has to be interrupted. Only closing the beam shutter is not sufficient because this process is too slow to guarantee personnel safety.

#### *7.3.4.5 Klystron interlocks*

The 35 klystrons for operating the accelerator modules are located in the tunnels XTIN and XTL. Connected to the cavities, these are the main beam generating devices and must be switched off in two independent ways if required by the personnel interlock system as it is realised at FLASH.

## 7.4 Summary of costs and manpower requirements

The capital investment and cost of the personnel needed for the technical and conventional infrastructure and the civil constructions of all buildings of the XFEL facility as described in the previous sections of this chapter are summarised in this section. The basis for the cost estimate is the site layout and the buildings specified here. For an overview about the total project cost, a description of the methodology of the performed estimate for capital investment, the determination of the costs for personnel and the expected uncertainties, see Chapter 10.

Table 7.4.1 gives a summary of the project cost in terms of capital investment and the cost of personnel for the technical and conventional infrastructure and the civil constructions of the XFEL Facility. The civil construction cost is shown separately for the different sites of the facility. The relative distribution of the full costs for the civil construction is shown in Figure 7.4.1. The civil construction and the infrastructure contribute about 20% each to the to the overall project cost. In terms of personnel cost, the contribution is about 35%. The personnel cost for the civil construction amount to only about 1% of the total personnel cost since manpower is only needed to supervise the construction. Integrated

over the entire construction phase, 996.7 full-time equivalents (FTE) are required for the technical and conventional infrastructure and the civil construction.

| | Capital investment [M€] | Personnel cost [M€] | Full cost [M€] |
|---|---|---|---|
| Linac building | 21.12 | | 21.12 |
| Desy site buildings | 35.34 | | 35.34 |
| Osdorfer Born site buildings | 18.40 | | 18.40 |
| Schenefeld site buildings | 86.52 | | 86.52 |
| Global Infrastructure | 5.07 | 2.18 | 7.25 |
| Utilities | 75.93 | 13.93 | 89.85 |
| Cryogenic system | 34.35 | 4.39 | 38.74 |
| Module test facility | 23.83 | 14.34 | 38.17 |
| Installation and alignment | 8.56 | 13.99 | 22.55 |
| Control system and operability | 5.23 | 20.16 | 25.39 |
| Safety and interlock | 8.96 | 5.03 | 13.99 |
| **Total** | **323.30** | **74.02** | **397.32** |

***Table 7.4.1*** *Project cost distribution civil construction and the infrastructure of the XFEL Facility. Values are given for capital investment, personnel costs and full costs in Million-Euro.*

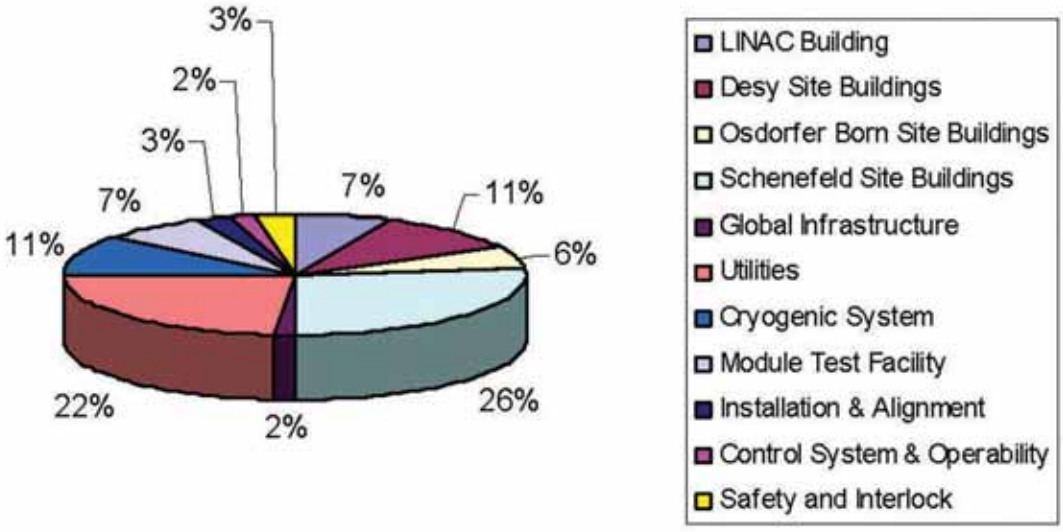


***Figure 7.4.1*** *Relative distribution of full project costs for civil construction and infrastructure.*

## Infrastructure and auxiliary systems

The costs summarised in Table 7.4.1 and Figure 7.4.1 include the costs and manpower of the following:

**Civil construction (first five entries in Table 7.4.1):** site preparation, tunnels, underground halls and shafts, technical surface buildings, office buildings and auxiliary buildings of the site at DESY, Osdorfer Born and Schenefeld; a list and locations of all buildings can seen in Figure 7.1.3.

**Utilities:** power distribution from the DESY site with cables, transformers and sub-stations, magnet power supplies, cooling and fresh water, air conditioning, heating and ventilation, undulator section temperature stabilisation, smoke extraction system, emergency power and water lines for fire extinguishing system.

**Cryogenic system:** refrigerator for the liquid Helium, Helium distribution box, multiple-stage cold compressors, valve boxes and feed boxes to the accelerator modules, Helium transfer lines to bypass warm sections in the linac and costs for modification of the HERA Helium plant as limited back-up.

**Module test facility:** test benches for complete accelerator modules, horizontal and vertical cryostats for cavity test, horizontal cryostats for magnet test and infrastructure (power supplies, RF system, cryogenic systems, etc.) to operate the test stands.

**Installation and alignment:** mock-up tunnel for test and training of the installation crews, regular and specialised (modules, undulators, dumps) transport vehicles, installation of all auxiliary systems and support structures, installation of the components of the superconducting linac, undulators, photon beamlines and the experimental hall, set-up of a surface and a sub-terrain reference system with reference monuments and points, laser-based tracking system, survey assistance during the entire construction phase for sites, buildings, accelerator components, beamlines, undulators and experiments.

**Control system and operability:** device, middle-layer and application server, DAQ system, archive system, electronic racks and front-end electronics, networks based on Ethernet, optical fibres and bus systems, machine protection system, definition of start-up and operation modes, failure handling and recovery procedures.

**Safety and interlock:** radiation protection monitoring system, radiation surveillance, simulations and preparation of legal permissions, legal permission fees, fire detection, alarm and extinguishing systems, smoke detection and alarm system, communication systems, access monitoring system, on-site emergency response staff, emergency equipment, door interlock, safety key system, emergency switches, electronic racks and electronics boards for two independent redundant systems.

## References


**[7-1]** *TESLA Technical Design Report, Part II The Accelerator*, edited by R.Brinkmann et al., Deutsches Elektronen Synchrotron, Hamburg, March 2001.

**[7-2]** H. Lierl, B. Petersen, and A. Zolotov, *Conceptual Layout of the European XFEL Linear Accelerator Cryogenic Supply*, Proceedings XXII International Linear Accelerator Conference, LINAC 2004, Luebeck, Germany, August 2004, pp. 225-227, http://www.linac2004.de

**[7-3]** Y. Bozhko, H. Lierl, B. Petersen, D. Sellmann, A. Zolotov, *Requirements for the Cryogenic Supply of the European XFEL-Project at DESY*, to be published in the Advances of Cryogenic Engineering, Vol.51, Proceedings of the CEC/ ICMC, Keystone, Colorado, USA, August 29 – September 2, 2005.

**[7-4]** H. Lierl, for the plan-approval group at DESY, *The Planning of the Cryogenic Supply Infrastructure for the Superconducting Cavities of the European XFEL Linear Accelerator*, to be published in Advances of Cryogenic Engineering, Vol.51, Proceedings of the CEC/ICMC, Keystone, Colorado, USA, August 29 – September 2, 2005.

**[7-5]** B. Petersen, *Some Aspects of the Layout and Optimization for the Cryogenic Supply of Superconducting Linacs*, submitted for publication in the proceedings of the 32nd ICFA Beam Dynamics Workshops on Energy Recovering Linacs ERL2005 at Jefferson Lab, Newport News, USA, 2005, in Nuclear Inst. and Methods in Physics Research, A. Elsevier.

**[7-6]** K. Jensch, R. Lange, B. Petersen, *Numerical Simulations for the Cool-Down of the XFEL and TTF Superconducting Accelerators*, Advances in Cryogenic Engineering 49 A, edited by J. Waynert et al., AIP Conference Proceedings, Melville, New York, (2004) 371-378.

**[7-7]** B. Petersen, S. Wolff, *Numerical Simulations of Possible Fault Conditions in the Operation of the TTF/FEL and TESLA Linear Accelerators*, Proceedings of the 18th International Cryogenic Engineering Conference ICEC18, edited by K.G. Narayankhedkar, Narosa Publ., Mumbai (2000) 67-70.

**[7-8]** H. Quack, C. Haberstroh, M. Kauschke, H. Lierl, B. Petersen, S. Wolff, *The TESLA Cryo plants*, DESY report: TESLA 2001-38, Hamburg, December 2001.

**[7-9]** S. Claudet, *Recent Progress in Power Refrigeration Below 2 K for superconducting Accelerators*, Invited paper at Particle Accelerator Conference, Knoxville,USA, 2005.

**[7-10]** H. Quack, A. Kutschbach, *Über die Möglichkeit des Umbaus der HERA-Kälteanlage für TESLA*, internal report DESY/TU Dresden, in German, Dresden/Hamburg, 2002.

**[7-11]** M. Clausen et al., *The XFEL Cryogenic Control System , XFEL- Report*, Deutsches Elektronen Synchrotron, Hamburg, to be published.

**[7-12]** T.H. Nicol et al., *TESLA Vertical Test Dewar Cryogenic and Mechanical Design*, IEEE Proceedings of the 1993 Particle Accelerator Conference, Vol. 2, (1993) .989-991, Piscataway, N.J.

**[7-13]** G. Grygiel et al., *Status of the TTF Cryogenic System*, Adv. in Cryogenic Engineering, Plenum Press, New York, Vol. 41 a (1996) 847-854.

**[7-14]** P. Clay et al., *Cryogenic and Electrical Test Cryostat for Instrumented Superconductive RF Cavities (CHECHIA)*, Adv. in Cryogenic Engineering, Plenum Press, New York (1996), Vol. 41 a, pp. 905-910.

**[7-15]** A. Agababyan et al., *Data Acquisition System for a VUV-FEL Linac*, PCaPAC 2005, Hayama, Japan.

**[7-16]** *Verordnung über den Schutz vor Schäden durch ionisierende Strahlen* (Strahlenschutzverordnung - StrlSchV), Stand 20.7.2001, Bundesanzeiger Verlagsgesellschaft mbH, Köln (2001).

**[7-17]** N. Tesch, *Radiologische Auswirkungen auf die Umwelt beim Betrieb des Röntgenlasers XFEL*, Laborbericht DESY D3-119/2 (2005).

**[7-18]** N. Tesch, A. Leuschner, Sicherheitsbericht zum Strahlenschutz für das Planfeststellungsverfahren des europäischen Röntgenlasers XFEL, Internal Report, 13.04.2005.

**[7-19]** Öko-Institut e.V., *Bewertung des Berichts "Radiologische Auswirkungen auf die Umwelt beim Betrieb des Röntgenlasers XFEL" des Deutschen Elektronen-Synchrotrons (DESY)*, Darmstadt, 15.03.2005.

**[7-20]** H. Dinter, A. Leuschner, K. Tesch, D. Dworak, J. Loskiewicz, *Calculation of hadron yield around thick targets and doses behind concrete shielding of high energy electron accelerators*, Internal Report DESY D3-95 (1999).

**[7-21]** K. Tesch, *Shielding against high energy neutrons from electron accelerators - A review*, Radiation Protection Dosimetry 22 (1988) 27.

**[7-22]** A. Leuschner, K. Tesch*, Muon doses at earth surface above the Linear Collide*r, Internal Report DESY D3-89 (1998).

**[7-23]** G. Baur, A. Leuschner, K. Tesch, *Muon doses at earth surface above the Linear Collider: Improved calculations*, Internal Report DESY D3-91 (1998).

**[7-24]** A. Fasso, A. Ferrari, P.R. Sala, *Electron-photon transport in FLUKA: Status*, Proceedings of the MonteCarlo 2000 Conference, Lisbon, October 23-26 2000, Springer-Verlag Berlin, (2001) 159-164.

**[7-25]** A. Fasso, A. Ferrari, J. Ranft, P.R. Sala, *FLUKA: Status and Prospective for Hadronic Applications*, Proceedings of the MonteCarlo 2000 Conference, Lisbon, October 23-26 2000, Springer-Verlag Berlin, (2001) 955-960.

**[7-26]** K. Tesch, *Production of radioactive nuclides in soil and groundwater near the beam dump of a Linear Collider*, Internal Report DESY D3-86 (1997).

**[7-27]** N. Tesch, *Soil, Groundwater and Cooling Water Activation at the TESLA Beam Dump*, Laborbericht DESY D3-114 (2001).

**[7-28]** K. Tesch, H. Dinter, *Production of radioactive nuclides in air inside the collider tunnel and associated doses in the environment*, Internal Report DESY D3-88 (1998).

**[7-29]** A. Leuschner, B. Racky, *A Ventilation Concept for Activated Air in the TESLA Tunnel*, Laborbericht DESY D3-104a (2001).

**[7-30]** A. Leuschner, K. Tesch, *Production of tritium in the liquid helium of the TESLA Linear Collider*, Laborbericht DESY D3-101 (1999).

**[7-31]** H. Dinter, *Abschirmung des Linear Colliders TESLA im Bereich der Kryohallen*, Laborbericht DESY D3-99 (1999).

**[7-32]** B. Racky, *Das Personen-Interlocksystem des VUV-FEL*, DESY Internal Report, February 2005.

**[7-33]** A. Leuschner, *Vorschrift für die Prüfung der Interlocksysteme von TTF2*, DESY Internal Report, February 2005.

**[7-34]** A. Leuschner, K. Tesch, *The residual radioactivity of a water-copper beam dump for the TESLA Test Facility*, Internal Report DESY D3-92 (1998).

**[7-35]** H. Dinter, A. Leuschner, *Induced radioactivity and dose rates in the vicinity of a collimator at the Linear Collider TESLA*, Laborbericht DESY D3-104 (1999).

**[7-36]** A. Leuschner, S. Simrock, *Radiation field inside the tunnel of the Linear Collider TESLA*, Laborbericht DESY D3-113 (2000).

# 8 Commissioning and operation

In the following, general aspects of commissioning and operation are discussed, the transition from construction to operation is outlined and the resources required during this transition, as well as for full operation of the facility, are summarised.

## 8.1 General considerations

A detailed plan for beam commissioning of the European X-ray Free-Electron Laser (XFEL) Facility with a week-to-week or even day-to-day schedule will be worked out in due course when construction work has progressed and first beam operation is in sight. Nevertheless, several essential aspects of the commissioning process can already be assessed:

- A careful and thorough check of all technical components is an indispensable prerequisite for an efficient and successful start-up of beam operation. For example, reliable operation of all radio frequency (RF) stations has to be verified, RF coupling and phasing of the cavities have to be pre-adjusted, polarities and excitation currents of all magnets have to be checked, etc. The functionality of diagnostics devices should be checked as far as possible without a beam in the machine (e.g. using test signals). The control system has to be setup well in advance and software has to be de-bugged, including, for example, using simulated data to test data acquisition and higher level application programmes. In the undulator sections, a precise determination of the magnetic field quality and a pre-alignment of the magnets and diagnostics elements with best possible accuracy is mandatory to facilitate and speed up the later process of electron and photon beam-based alignment.
- A crew, well trained and experienced in accelerator and photon beamline operation, has to be available from the start. The experience already gained at the Free-electron LASer in Hamburg (FLASH) (vacuum ultraviolet (VUV)-FEL) facility and still to be gained in years to come is an extremely valuable asset in this context. Training of XFEL personnel by participation in the operation of FLASH will help to guarantee having a well prepared team available when the XFEL becomes ready for beam commissioning. Furthermore, the experience from the Linac Coherent Light Source (LCLS) commissioning will be particularly invaluable when setting up the Self-Amplified Spontaneous Emission (SASE) FEL process in the challenging x-ray wavelength regime.
- The availability of an already commissioned injector, delivering a good quality, stable beam, will be particularly helpful for an efficient commissioning of the accelerator complex. The layout of the facility with the injector in an enclosure separate from the linac tunnel permits an early start of injector operation, while the linac is still under construction.

- As a general rule, early commissioning of **all** sections of the facility, from beginning of the linac to photon diagnostics, with relaxed beam parameters (energy, number of bunches, emittance, etc.) should be given priority in comparison to pushing **parts of the machine** to the design specifications. This will not only help to discover unexpected technical problems in all sub-systems as quickly as possible, but will also allow the SASE process to be set up with less stringent requirements on beam stability and steering accuracy. Once a SASE signal has been established and stabilised at longer wavelength, a stepwise optimisation towards the performance goals can take place.

In the later phase of routine operation for users, high reliability and availability of the machine are of particular importance. All sub-systems are laid out with a considerable margin when operated at the baseline design parameters. This de-rated way of operating the components will reduce failure rates. In addition, a linac energy overhead of 10% is built-in to be able to handle RF system failures without the need for frequent tunnel access for repair. Failures of single magnet power supplies in the linac do not make access necessary, since the beam-optics can be re-matched. A flexible control system with well-prepared failure handling procedures is essential for being able to resume beam operation quickly in such cases. Another example of technical detail in the reliability context is the cold water cooling system for all electronics racks in the tunnel, which is expected to reduce the failure rate and improve the lifetime of these systems.

Efficient usage and optimum performance of the XFEL Facility will require a close relationship between operating the machine and the photon beamlines/experiments. This does not necessarily require a common control room, but continuous good cooperation and information exchange between the accelerator operation crew, the photon beamline and instruments operation crew and the user teams is vital and must be established. The layout of the control systems has to take into account the need for fast and well organised data exchange (e.g. concerning photon and electron beam diagnostics, timing, etc.), as well as common standards for parts of the hardware and software.

## 8.2 Transition phase

When, after installation and technical commissioning have been completed, beam commissioning of the linac begins, there will still be installation work ongoing in other sections (second branch of electron beamline, photon beamlines and scientific instruments). Likewise, when the first photon beamline (SASE 1) starts operation, others are still being commissioned. During this transition phase, construction, commissioning and operation will take place in parallel. This phase will last about 2.5 years, until all five photon beamlines can be expected to be operational. The situation is sketched in Figure 8.2.1, using a relative timescale (on an absolute scale, this phase starts with the third quarter of 2013, under the assumption that construction on the project will start in January 2007, see Chapter 10).

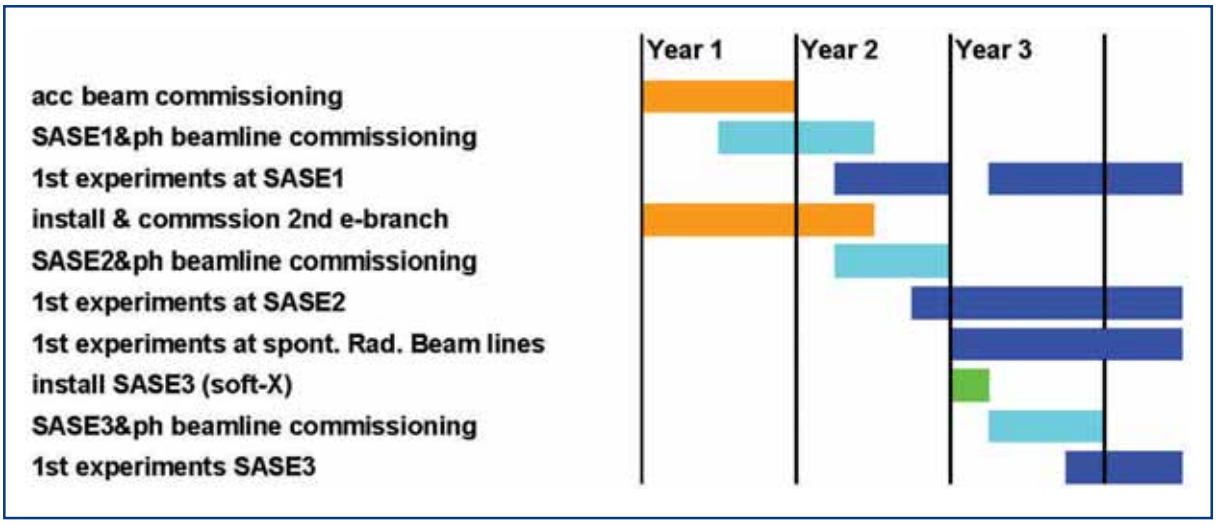


***Figure 8.2.1*** *Sketch of the transition phase, indicating the sequence in which the different parts of the facility will be brought into operation.*

The definition for the start of the operation phase of the accelerator and the first beamline (SASE 1) has been chosen so that an intermediate performance goal (relaxed with respect to the design specification, but already with a FEL beam quality sufficient to start first experiments) is reached. This performance goal is shown in Table 8.2.1. It is assumed that this goal will be reached approximately one year after the first beam has been injected into the linac. Likewise, the other FEL beamlines will then enter the operation phase once similar performance goals are reached (at wavelengths of 0.2 - 0.4 nm and 2 - 6 nm for SASE 2 and 3, respectively).

| | |
|---|---|
| Wavelength [nm] | 0.2 |
| Peak Brilliance [photons/s/mm$^2$/mrad$^2$/0.1% BW] | > $10^{30}$ |
| Photon beam size at sample [mm$^2$ FWHM] (no optics) | < 1 |
| Photon beam position stability [% of rms size] | 50 |
| Electron beam energy stability [% rms] | 0.1 |
| Photon pulse intensity fluctuation [peak-to-peak] | Factor 10 |

***Table 8.2.1*** *Initial performance goal for the SASE 1 radiator. Reaching this milestone defines the start of operation phase for the accelerator complex and for the SASE 1 beamline.*

## 8.3 User operation

The European XFEL is conceived as a multi-user facility. External user groups will come to the facility for a short period of time to carry out experiments at the various beamlines and experimental stations, suited to their specific project. As is practice at synchrotron radiation facilities, the XFEL will regularly (probably twice a year) invite proposals for research projects. Beam time will be allocated by the XFEL management according to scientific excellence. Priorities will be decided by peer review committees composed of highly qualified scientists, mainly from the contracting party countries. Sufficient flexibility

will be incorporated into the beam time allocation scheme to allow rapid access to beamlines for promising urgent work or to guarantee long term access to scientifically excellent projects which require beam time over a longer period. Up to a certain number of users (affiliated to universities or publicly funded laboratories of contracting party countries) per selected experiment will be reimbursed or funded by the XFEL for travel and subsistence expenses directly related to the execution of the approved experiment. Many proposals are likely to come from larger collaborations. If more scientists than those supported from the XFEL budget (see Section 8.4) participate in the selected experiment, they will have to be funded from their home institutes. The described procedure refers to the allocation of beam time for non-proprietary research where the results are open for publication. Non-refereed access to beam time, e.g. for proprietary research, will be possible but will have to be paid for.

Scheduling the experiments will be an important task since the time structure, energy range and, to some extent, quality of the photon beams in the various beamlines are not totally independent from each other, i.e. attention will have to be paid as to which experiments are best suited to run in parallel. A seven-days per week, round-the-clock beamline support for the users will be provided to help them make the most efficient use of the beam time allocated.

The total amount of scheduled user beam time per year is expected to be 4,800 hours. This includes the time necessary to set up and re-tune the machine to accommodate changing user requirements (e.g. variation of electron beam energy or bunch train time structure). Using the operation of the FLASH facility as a guideline, it is assumed that one day per week is needed for maintenance. In total, two months per year are foreseen for machine studies and improvements of the FEL performance. The remaining time per year will be allocated to a longer (approximately two months, plus appropriate time for re-start) shutdown, where more time consuming maintenance, refurbishment and additional installations can take place.

The complexity of the installation and of the proposed experiments requires an active and cutting-edge research and development programme to continuously improve the performance of the European XFEL Facility. A strong and highly visible in-house research programme is, therefore, considered important for the overall success of this installation. Topics of in-house research could range from FEL techniques over x-ray optics to scientific applications of FEL radiation. The in-house research programme will further enable staff scientists to promote their scientific careers and will, therefore, render positions at the European XFEL attractive.

## 8.4 Operation budget

The budget required to operate the XFEL Facility (not escalated, i.e. in year 2005 Euros) is summarised in Table 8.4.1 and its different components are briefly described in the following sections. Note that this will be the yearly budget for the XFEL from when all beamlines have come into operation. During the transition phase, the budget has three components: construction, commissioning (accounted as construction) and operation

(see Chapter 10). The ramp-up of the operation part of the budget during this phase has been determined according to the sequence of commissioning the different parts of the facility described in the previous sections.

| | |
|---|---|
| Consumables | 11.5 M€ |
| Maintenance and refurbishment | 22 M€ |
| Research and development | 11 M€ |
| Personnel accelerator and technical infrastructure | 19.8 M€ |
| Personnel photon beamlines and experiments | 13.8 M€ |
| User support (including overhead) | 1.8 M€ |
| Visitor and student programme | 1.7 M€ |
| **Total yearly operation cost** | **81.1 M€** |

***Table 8.4.1*** *Overview of operations costs (in year 2005 Euros).*

**Consumables** include the cost for electricity, fluids (Helium, water) and the exchange/ repair of klystrons. For electricity cost, a power consumption of 18 MW (approximately 80% for accelerator/infrastructure and 20% for the experimental facility) has been assumed (corresponding to operation at 17.5 GeV energy and baseline design parameters for the duty cycle), except for the maintenance/shutdown breaks where the power will be significantly reduced. In the transition phase, an initial, somewhat lower, power consumption has been assumed, reflecting the expectation that one would start with reduced electron beam energy and that downtime periods will be longer than later during routine user operation. The cost for fluids has been estimated on the basis of experience at HERA and FLASH. The repair/exchange rate for klystrons has been deduced from the assumption of an average lifetime of 40,000 hours.

**Maintenance and refurbishment** costs correspond to approximately 4% of the initial capital investment for all technical components, which is a reasonable assumption based on the experience from other large accelerator and synchrotron radiation facilities.

The **Research and development (R&D) budget** is appropriate since it can be expected that for this new type of facility a continuous development of new ideas, concepts and improvements and extensions of the experimental possibilities will take place.

The **personnel** requirment for the **accelerator** complex **and technical infrastructure** has been estimated from the Deutsches Elektronen-Synchrotron (DESY) Laboratory experience of operating large accelerator facilities. About 30% of the estimated total 251 full-time equivalents (FTEs) are needed for the round-the-clock shift crew (including safety and technical emergency services). The distribution of FTEs over the different technical sub-systems and tasks is shown in Table 8.4.2. The costs per FTE (different for the different categories in Table 8.4.2) were, similarly as for the construction phase, derived from the salary structure in the technical groups of the DESY-M division, including an overhead also determined at DESY.

| Subsystem/task | FTE |
|---|---|
| Coordination | 3 |
| Linear Accelerator | 50 |
| Cryogenics | 20 |
| Utilities | 35 |
| Vacuum system | 23 |
| Beam diagnostics | 25 |
| Injector | 6 |
| Control system | 25 |
| Beam Physics | 20 |
| Installation/survey | 10 |
| Radiation safety/Personnel interlock | 9 |
| General safety | 25 |
| **Total FTEs per operation year** | **251** |

***Table 8.4.2*** *Distribution of personnel for accelerator and infrastructure in the operation phase.*

The **personnel** requirement for the **photon beamlines and experiments** has been estimated by starting from experience at synchrotron radiation facilities, but taking into account the substantially higher complexity and technical challenges of the XFEL Facility. About one quarter of the estimated total 172 FTEs are needed for the round-the-clock shift crew. The permanent presence of experts from the beamline group will guarantee optimum support for the user groups, enabling them to conduct their experiments in the most efficient and successful fashion. The distribution of FTEs over the different technical sub-systems and tasks is shown in Table 8.4.3 (see also Chapter 9). The costs per FTE were, similarly as for the construction phase, derived from the salary structure in the DESY-HASYLAB division, including an overhead also determined at DESY.

| Sub-system/task | FTE |
|---|---|
| Undulators | 13 |
| Operation of scientific instruments/In-house research | 45 |
| Photon diagnostics and photon transport/x-ray optics | 23 |
| Detectors | 12 |
| Laser systems | 8 |
| Computing | 16 |
| Preparation laboratories | 10 |
| Beamline/instrument design | 5 |
| Vacuum system | 11 |
| Mechanics and electronics | 23 |
| User administration | 4 |
| Public relations | 2 |
| **Total FTEs per operation year** | **172** |

***Table 8.4.3*** *Distribution of personnel for photon beamlines and experiments in the operation phase.*

The budget for **User support** covers direct funding of user group expenses (travel, accommodation and meals) as well as an additional overhead related to administrative and logistics expenses. It is assumed that on average eight (out of 10) experiments are operated in parallel, in total 200 experiments per year are performed, and typically a user group of six scientists spends 10 days at the facility per visit. With 360**€** per travel and 60**€** per user day on site, a total amount of direct user support of 1,080 k**€** results. Based on the DESY model of FTE-related overhead, another 670 k**€** have to be added to this.

The **visitor and student programme** is included in the operation budget to enhance the scientific exploitation of the XFEL Facility. It is directly related to the in-house research programme. The proposed budget provides the salaries for 10 longer-term visiting scientists and 20 PhD students.

The budget summarised in Table 8.4.1 corresponds to the “steady state” situation when the facility is fully operational. During the transition phase, different parts of the operation budget are assumed to ramp-up in a reasonable fashion. For example, the electricity consumption will initially be somewhat lower, because operation will probably start at reduced electron beam energy and the yearly time integral of operation hours will be lower than in the later phase of routine operation. The R&D programme, the funding required for user support and the visitor/student programme will start at a lower level and increase in steps towards the “steady state”. This has been included when putting together the yearly budget and its operation component to derive the budget profile for the transition phase (see Chapter 10). It should also be noted that the personnel in the operation phase will, to a large extent, be the same as in the late part of the construction phase – meaning that what changes during the transition phase is essentially how the personnel costs are accounted for.

It should be noted that in the definition of the staff required for operation, the same approach was followed as for the construction phase, i.e. applying the DESY-model with an overhead, covering expenses for management and support and workplace-related expenses. The relation between DESY and the XFEL GmbH, sharing the responsibilities for operating the facility, are discussed in Chapter 9 and the particularities of the XFEL GmbH personnel costs are discussed in Chapters 9 and 10.

# 9 Project management and organisation

## 9.1 Introduction

In accordance with the draft X-Ray Free-Electron Laser (XFEL) legal texts (Convention and Articles of Association):

- the construction and operation of the European X-ray FEL Facility shall be entrusted to a limited liability company, the XFEL GmbH;
- the XFEL GmbH and Deutsches Elektronen Synchrotron (DESY) in Hamburg will collaborate on construction, commissioning and operation of the XFEL on the basis of a long-term agreement;
- the shareholders contribute to construction costs either in cash or in kind, where the in-kind contributions are defined and decided in accordance with rules laid down in Annex 5[8] to the XFEL Convention.

While implementing these objectives, it has to be ensured that:

- the XFEL GmbH is provided with the appropriate resources and tools to assume the responsibility for construction and operation;
- the collaboration between the XFEL GmbH and DESY is transparent, with clearly defined roles, no duplication of structures and no conflicts of interest;
- reasonable and adequate consideration is given to the international partners' interests to contribute to the project, with equal conditions and opportunities for DESY and other interested institutes.

The intended set-up of the future XFEL GmbH and the structure of the relationship of the XFEL GmbH with all contributing institutions during the construction period is set out in the following sections, with special consideration of the relationship between the XFEL GmbH and DESY. Section 9.2 deals with the structure of the XFEL GmbH itself, first the internal organisation foreseen for the steady state in about ten years, then the steps to attain this objective. Section 9.3 describes the project management structure and the general procedures concerning tasks, work packages and in-kind contributions, while Section 9.4 focuses on the special aspects of the corresponding collaboration agreement between the XFEL GmbH and DESY. This refers, on the one hand, to DESY's role as contributor to the XFEL project, and on the other, to DESY's role as host of the XFEL GmbH. Section 9.5 sets out the management tools to be applied, largely inspired by the well-proven practice of DESY.

[8] See the basic rules and procedures in Section 9.3.2.

## 9.2 Internal organisation of the XFEL GmbH

### 9.2.1 General aspects

Once the XFEL legal texts (Convention, Final Act and Articles of Association) are signed and the XFEL GmbH is registered, the responsibility for advancing the project, so far borne by DESY, will lie with the XFEL GmbH, the cash contributions will flow through its accounts, and it will have to oversee all in-kind contributions. The appointment of Managing Directors (forming the Management Board) is one of the preconditions for registering the company. One of the directors will assume the function of the project leader. In addition, a core team will be necessary from the start, even if many components are provided as contributions in-kind and many tasks, especially in the beginning, are handled by DESY through power of attorney. The coordination and management of the construction of the XFEL facility requires a technically competent team as part of the XFEL GmbH, to assist the XFEL Project Leader, with experience in the following fields: Accelerator Physics, Civil Engineering, Infrastructure (electrical, fluids, cryogenics, communication networks), Photon Beamlines and Instrumentation, Project Management and Administrative Procedures (Accounting, Purchasing, Contract Management).

The XFEL GmbH must also be ready to take over those work packages or tasks, which will not be assigned to collaborating institutes. In particular, the build-up of a Scientific Experiments Division must start as soon as possible and grow in a few years to a staff of about 200 people.

### 9.2.2 Primary tasks and internal structure of the XFEL GmbH

The XFEL GmbH with its organs (Council, Management Board), supported by various advisory committees (Science, Machine, Administration and Finance), will, in particular, be in charge of the:

- coordination and monitoring of the construction activities;
- scientific policy and strategy;
- build-up of five beamlines with ten experiment stations and associated infrastructure;
- operation of the beamlines and the implementation of the user programme;
- further development of the facility based on a vigorous research and development (R&D) programme;

and, related to the aforementioned tasks;

- management, supervision and controlling of all financial and other resources made available by the shareholders or through collaboration contracts.

The internal structure of the XFEL GmbH, aimed at in the long-term, is illustrated in Figure 9.2.1. It shows the organs of the company (Council and Management Board), the Advisory Committees (Machine, Science, Administration and Finance) and the distribution of the personnel among, essentially, three divisions (Technical, Experiments and

Administration) and some services directly assigned to the Director General (Safety, Communication and Internal Audit). This structure refers to the operation phase and has, for the time being, to be considered as a best guess, which needs further fine tuning during the years to come.

The relationship with the in-kind contributors and, in particular, with DESY during the construction period is further expanded in Section 9.3.

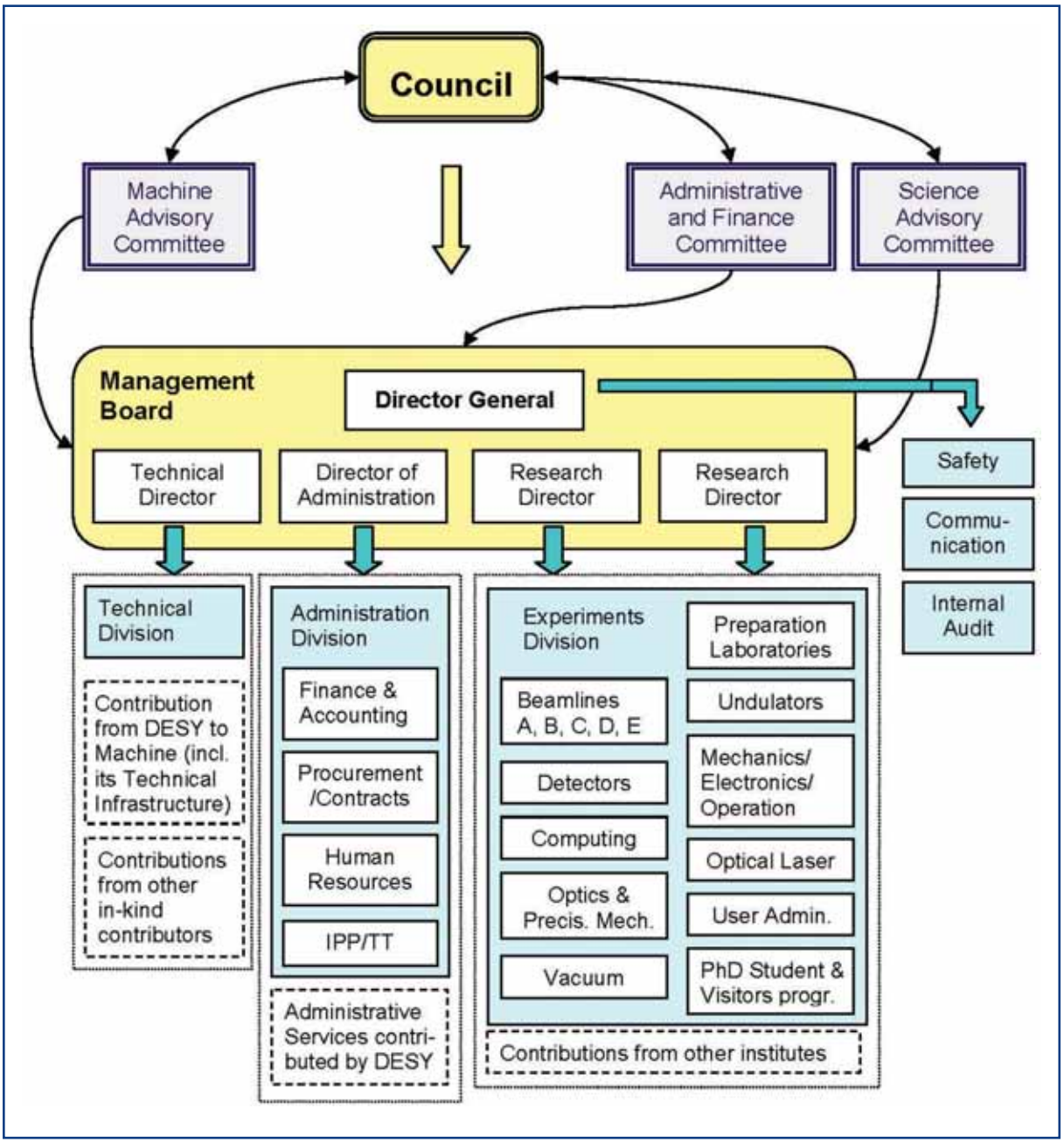


***Figure 9.2.1*** *Organisation chart of the XFEL GmbH for the operation phase.*

Certain tasks will be “contracted out” to DESY, on the basis of a long-term collaboration agreement. This will, in particular, apply for the accelerators and for the technical infrastructure. Although the extent is not fully specified, it seems very likely that for these two areas the staffing on the side of the XFEL GmbH can be restricted to people:

- working on very specific XFEL-related tasks; or
- coordinating and liaising with personnel from DESY and other in-kind contributors.

For the time being we assume that about 10% of the 251 full-time equivalents (FTEs) foreseen in the costing of the operation under accelerators/infrastructure will be represented by XFEL GmbH personnel. In Figure 9.2.1 they appear under Technical Division and Safety Group. This item is further developed in Section 9.2.3.

On the other hand, the photon beamlines and the ten experiment set-ups are expected to be constructed and operated essentially by XFEL personnel, albeit in close contact with interested user groups. The Experiments Division will, therefore, make up the main part of the XFEL GmbH’s staff with a complement of 203, out of which 115 (5 × 23) staff directly assigned to the five beamlines (ten stations), 51 to the various beamline support groups, four for user administration, 20 posts for thesis students and 10 posts to accommodate scientific visitors collaborating temporarily on specific projects. A tentative distribution by specific areas is given in Table 9.2.1.

The **Administration** will be in charge of all financial matters, all procurements not carried out in the framework of in-kind contributions, follow-up of contracts and all personnel matters such as recruitment, salaries, and staff development. While these core activities need to be under the close control of the XFEL Management, for other, more peripheral, administrative tasks (such as works doctor, guest services and site security), sharing of resources with DESY appears appropriate. The staff complement required for the Administration is estimated at about 34 persons.

Management of the XFEL GmbH will be under the responsibility of the **Board of Managing Directors** chaired by a Director General. Given the variety of disciplines concerned and the complexity of instrumentation, two Research Directors are foreseen for the operation phase. The five directors, one assistant and several secretaries together with Public Relations and Internal Audit make up a complement of 15 persons.

The aforementioned tentative staff distribution is based on our present overview of the project. However, the XFEL GmbH must retain a wide degree of flexibility in its organisation. The proposal outlined above may well be revised in the light of future experience and following the exact definition of the role of DESY in the long-term operation and development of the XFEL Facility.

| | | Specific fields of activity (tentatively) | | | | | | | | | |
|---|---|---|---|---|---|---|---|---|---|---|---|
| | | **Experiments** | **Detectors** | **Computing** | **Optics/ diagnostics/ beam transport** | **Optical laser systems** | **Preparation labs** | **Vacuum** | **Mechanics/ electronics/ operation** | **Undulators** | **Total** |
| Per each of the five **beamlines** (with **two** stations each) | | **9** | **2** | **2** | **3** | **1** | **2** | **1** | **3** | | **23** |
| out of which | scientists | 5 | 1 | 1 | 1 | | 1 | | | | 9 |
| | engineers | 2 | 1 | 1 | 1 | 1 | | 1 | 1 | | 8 |
| | technicians | 2 | | | 1 | | 1 | | 2 | | 6 |
| BL support groups | | **5** | **2** | **6** | **8** | **3** | | **6** | **8** | **13** | **51** |
| out of which | scientists | 5 | 2 | 1 | 2 | 2 | | | | 3 | 15 |
| | engineers | | | 5 | 3 | 1 | | 2 | 4 | 4 | 19 |
| | technicians | | | | 3 | | | 4 | 4 | 6 | 17 |
| BL operation total | | **50** | **12** | **16** | **23** | **8** | **10** | **11** | **23** | **13** | **166** |
| out of which | scientists | 30 | 7 | 6 | 7 | 2 | 5 | | | 3 | 60 |
| | engineers | 10 | 5 | 10 | 8 | 6 | | 7 | 9 | 4 | 59 |
| | technicians | 10 | | | 8 | | 5 | 4 | 14 | 6 | 47 |
| | | | | | | | | | **User Administration** | | **4** |
| | | | | | | | | | **PhD student programme** | | **20** |
| | | | | | | | | | **Visitors programme** | | **10** |
| | | | | | | | | | **Secretariat** | | **3** |
| | | | | | | | | | **Experiments Division Total** | | **203** |

***Table 9.2.1*** *Planned staff complement of the Experiments Division.*

### 9.2.3 Operation of the accelerator complex

During its period of usage, i.e. after the commissioning phase, the XFEL will run in continuous around-the-clock operation for long periods in order to obtain stable conditions and to make the best benefit from the large investment made. The objectives of:

- high availability and reliability of the accelerator complex;
- adjusting the beam parameters to the specific requirements of the users;
- keeping the beam parameters extremely stable during the experimental sessions; and
- achieving this with an efficient use of the available resources;

put strong demands on the organisation of operation. Those people who are involved in this task must:

- have the adequate know-how of the technical systems and the functionality of the accelerator in order to be able to react appropriately in case of problems;
- communicate effectively about the performance of the technical systems, limitations and problems, needs for developing new tools, etc; and
- be highly motivated to achieve the optimum performance of the accelerator complex.

There are various technical systems mandatory for reliable operation, which have to be fixed as quickly as possible in the event of failures. For some systems such as cryogenics or power supplies, experts must either belong to each shift crew or be available on very short notice. For other systems such as vacuum systems, on-call duty might be sufficient.

The DESY Machine Group, which is likely to be strongly involved in the construction and commissioning of the accelerator complex, is, due to its intimate knowledge of all systems, also best suited to assume the operation tasks. Joining forces with the operation of the other accelerators at DESY (DORIS III, PETRA III, and especially FLASH) brings additional benefits. By bundling the service for the systems of all accelerators, it will become feasible to ensure shift service for systems which otherwise could only be covered by on-call duty.

For the time being, it is, therefore, proposed that, in the framework of the long-term cooperation agreement between the XFEL GmbH and DESY, the operation of the accelerator complex and the associated technical infrastructure be entrusted to DESY. Nevertheless, the XFEL GmbH should not remain totally bare of any involvement in operation, let alone to enable the full understanding of all problems which might arise and of any further development work proposed. The small machine-oriented technical team of the XFEL GmbH will essentially pursue R&D projects, but also participate in the XFEL operation alongside their colleagues of DESY.

### 9.2.4 Build-up of the XFEL staff complement

As indicated at the end of Section 9.2.2, the staff requirements detailed hereafter should be treated as a tentative proposal. They are shown, as a function of time, in Tables 9.2.2 to 9.2.6 with a breakdown by grade and type of work. The numbers represent the positions to be filled **at the end** of each corresponding year (and as such, should not be confused with the FTEs needed **during** the year). At the end of year 2016, a total complement of 281 people is planned. Of these, 135 will be of category K1 (scientists, senior engineers and administrators) and 126 of category K2 (technicians, junior engineers[9] and administrators and secretaries), and 20 will be thesis students. It is expected that there will be more thesis students working at the XFEL Facility, but funded from other sources (e.g. EU grants or national grants in the framework of collaboration contracts).

Although in the long term, the XFEL activity will possibly grow beyond the current target specifications and might well be expanded to a second fan of beamlines, the present estimates are based on the assumption that beyond 2015, the x-ray source and the ten experimental stations are run in a steady-state mode. This explains the flattening out of the staff evolution in the later years (apart from the visitors and students programme added from 2016 on). Obviously, this will have to be revised if the second fan of beamlines is to be implemented.

Figure 9.2.2 illustrates the planned evolution of the personnel of the XFEL GmbH, as summarised in Table 9.2.6. Specific posts for PhD students appear here only once the facility is in full operation. This does not exclude that beforehand, posts of the planned general staff complement are opened for thesis students working on tasks related to construction and commissioning.

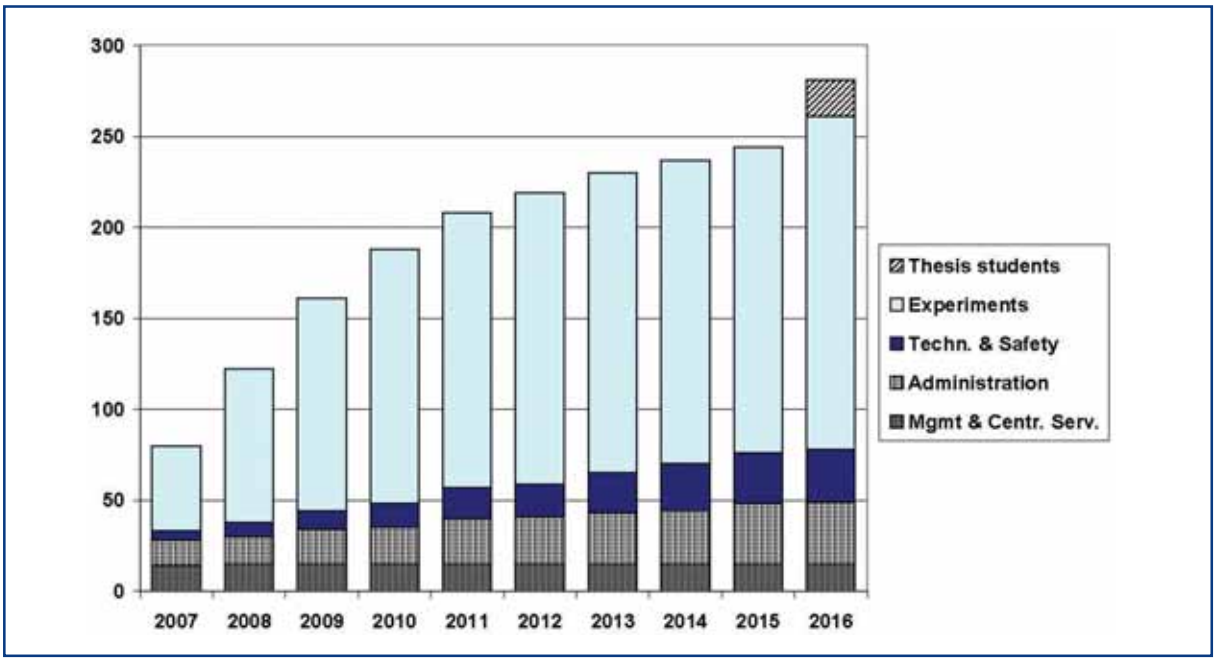


***Figure 9.2.2*** *Evolution of personnel of XFEL GmbH.*

[9] About half of the engineer positions were assigned to K1 and half to K2.

| | 2007 | | 2008 | | 2009 | | 2010 | | 2011 | | 2012 | | 2013 | | 2014 | | 2015 | | 2016 | |
|---|---|---|---|---|---|---|---|---|---|---|---|---|---|---|---|---|---|---|---|---|
| **ExperimentsDdivision** | **K1** | **K2** | **K1** | **K2** | **K1** | **K2** | **K1** | **K2** | **K1** | **K2** | **K1** | **K2** | **K1** | **K2** | **K1** | **K2** | **K1** | **K2** | **K1** | **K2** |
| Experiments | 10 | 5 | 20 | 7 | 30 | 10 | 33 | 12 | 34 | 13 | 34 | 14 | 35 | 15 | 35 | 15 | 35 | 15 | 35 | 15 |
| Detectors, computing | 8 | 2 | 15 | 5 | 18 | 7 | 20 | 8 | 20 | 8 | 20 | 8 | 20 | 8 | 20 | 8 | 20 | 8 | 20 | 8 |
| Optics/diagnostics/beam transport | 3 | 2 | 5 | 5 | 8 | 8 | 10 | 11 | 10 | 12 | 11 | 12 | 11 | 12 | 11 | 12 | 11 | 12 | 11 | 12 |
| Laser systems/Preparation labs/vacuum | 2 | 2 | 3 | 4 | 4 | 6 | 7 | 8 | 8 | 13 | 11 | 14 | 11 | 15 | 12 | 15 | 12 | 15 | 13 | 16 |
| Mechanics/electronics/operation | 2 | 3 | 4 | 5 | 4 | 8 | 5 | 11 | 5 | 13 | 5 | 16 | 5 | 16 | 5 | 16 | 5 | 16 | 5 | 18 |
| Undulators | 5 | 2 | 6 | 4 | 7 | 6 | 7 | 6 | 7 | 6 | 7 | 6 | 7 | 6 | 7 | 6 | 7 | 6 | 7 | 6 |
| Secretariat | | 1 | | 1 | | 1 | | 2 | | 2 | | 2 | | 2 | | 3 | | 3 | | 3 |
| User administration | | | | | | | | | | | | | 1 | 1 | 1 | 1 | 1 | 2 | 1 | 3 |
| Visitor programme | | | | | | | | | | | | | | | | | | | 10 | |
| **Subtotal** | 30 | 17 | 53 | 31 | 71 | 46 | 82 | 58 | 84 | 67 | 88 | 72 | 90 | 75 | 91 | 76 | 91 | 77 | 102 | 81 |
| | 47 | | 84 | | 117 | | 140 | | 151 | | 160 | | 165 | | 167 | | 168 | | 183 | |
| Thesis Students (½ K1) | | | | | | | | | | | | | | | | | | | 20 | |
| **Total** | | | | | | | | | | | | | | | | | | | 203 | |

***Table 9.2.2*** *Evolution of Experiments Division Personnel (excluding thesis students), in number of posts to be filled at the end of the corresponding year.*

| | 2007 | | 2008 | | 2009 | | 2010 | | 2011 | | 2012 | | 2013 | | 2014 | | 2015 | | 2016 | |
|---|---|---|---|---|---|---|---|---|---|---|---|---|---|---|---|---|---|---|---|---|
| **Technical Division & Safety Group** | **K1** | **K2** | **K1** | **K2** | **K1** | **K2** | **K1** | **K2** | **K1** | **K2** | **K1** | **K2** | **K1** | **K2** | **K1** | **K2** | **K1** | **K2** | **K1** | **K2** |
| **Total** | 4 | 1 | 6 | 2 | 7 | 3 | 8 | 5 | 9 | 8 | 9 | 9 | 11 | 11 | 12 | 14 | 13 | 15 | 13 | 16 |
| | 5 | | 8 | | 10 | | 13 | | 17 | | 18 | | 22 | | 26 | | 28 | | 29 | |

***Table 9.2.3*** *Evolution of Technical Division and Safety Group personnel, in number of posts to be filled at the end of the corresponding year.*

| Administration Division | 2007 | | 2008 | | 2009 | | 2010 | | 2011 | | 2012 | | 2013 | | 2014 | | 2015 | | 2016 | |
|---|---|---|---|---|---|---|---|---|---|---|---|---|---|---|---|---|---|---|---|---|
| | K1 | K2 | K1 | K2 | K1 | K2 | K1 | K2 | K1 | K2 | K1 | K2 | K1 | K2 | K1 | K2 | K1 | K2 | K1 | K2 |
| Finance (budget, accounts) | 1 | 3 | 1 | 3 | 2 | 3 | 2 | 3 | 3 | 4 | 3 | 4 | 3 | 4 | 3 | 4 | 3 | 4 | 3 | 4 |
| Procurement, contracts, stores | 1 | 3 | 1 | 3 | 1 | 4 | 1 | 5 | 2 | 6 | 2 | 6 | 2 | 7 | 2 | 7 | 2 | 8 | 2 | 8 |
| Personnel (recruitment, pay, etc.) | 1 | 3 | 1 | 3 | 2 | 3 | 2 | 3 | 3 | 3 | 3 | 4 | 3 | 4 | 3 | 4 | 4 | 4 | 4 | 4 |
| General (reception, travel, library, etc.) | | 2 | | 3 | | 4 | | 4 | | 4 | | 4 | 1 | 4 | 1 | 5 | 2 | 6 | 2 | 7 |
| **Total** | 3 | 11 | 3 | 12 | 5 | 14 | 5 | 15 | 8 | 17 | 8 | 18 | 9 | 19 | 9 | 20 | 11 | 22 | 11 | 23 |
| | 14 | | 15 | | 19 | | 20 | | 25 | | 26 | | 28 | | 29 | | 33 | | 34 | |

***Table 9.2.4*** *Evolution of Administration Division personnel, in number of posts to be filled at the end of the corresponding year.*

| Management Board | 2007 | | 2008 | | 2009 | | 2010 | | 2011 | | 2012 | | 2013 | | 2014 | | 2015 | | 2016 | |
|---|---|---|---|---|---|---|---|---|---|---|---|---|---|---|---|---|---|---|---|---|
| | K1 | K2 | K1 | K2 | K1 | K2 | K1 | K2 | K1 | K2 | K1 | K2 | K1 | K2 | K1 | K2 | K1 | K2 | K1 | K2 |
| Directors and assistants/secretariat | 6 | 5 | 6 | 5 | 6 | 5 | 6 | 5 | 6 | 5 | 6 | 5 | 6 | 5 | 6 | 5 | 6 | 5 | 6 | 5 |
| PR, Communications, Web | 2 | 1 | 2 | 1 | 2 | 1 | 2 | 1 | 2 | 1 | 2 | 1 | 2 | 1 | 2 | 1 | 2 | 1 | 2 | 1 |
| Internal Audit | | | 1 | | 1 | | 1 | | 1 | | 1 | | 1 | | 1 | | 1 | | 1 | |
| **Total** | 8 | 6 | 9 | 6 | 9 | 6 | 9 | 6 | 9 | 6 | 9 | 6 | 9 | 6 | 9 | 6 | 9 | 6 | 9 | 6 |
| | 14 | | 15 | | 15 | | 15 | | 15 | | 15 | | 15 | | 15 | | 15 | | 15 | |

***Table 9.2.5*** *Evolution of Management Board and associated personnel, in number of posts to be filled at the end of the corresponding year.*

| | 2007 | | 2008 | | 2009 | | 2010 | | 2011 | | 2012 | | 2013 | | 2014 | | 2015 | | 2016 | |
|---|---|---|---|---|---|---|---|---|---|---|---|---|---|---|---|---|---|---|---|---|
| **XFEL GmbH** | **K1** | **K2** | **K1** | **K2** | **K1** | **K2** | **K1** | **K2** | **K1** | **K2** | **K1** | **K2** | **K1** | **K2** | **K1** | **K2** | **K1** | **K2** | **K1** | **K2** |
| Experiments | 30 | 17 | 53 | 31 | 71 | 46 | 82 | 58 | 84 | 67 | 88 | 72 | 90 | 75 | 91 | 76 | 91 | 77 | 102 | 81 |
| Technical Division and Safety Group | 4 | 1 | 6 | 2 | 7 | 3 | 8 | 5 | 9 | 8 | 9 | 9 | 11 | 11 | 12 | 14 | 13 | 15 | 13 | 16 |
| Administration | 3 | 11 | 3 | 12 | 5 | 14 | 5 | 15 | 8 | 17 | 8 | 18 | 9 | 19 | 9 | 20 | 11 | 22 | 11 | 23 |
| Management and associated services | 8 | 6 | 9 | 6 | 9 | 6 | 9 | 6 | 9 | 6 | 9 | 6 | 9 | 6 | 9 | 6 | 9 | 6 | 9 | 6 |
| **Subtotal** | 45 | 35 | 71 | 51 | 92 | 69 | 104 | 84 | 110 | 98 | 114 | 105 | 119 | 111 | 121 | 116 | 124 | 120 | 135 | 126 |
| Students (½ K1) | | | | | | | | | | | | | | | | | | | 20 | |
| **Total** | 80 | | 122 | | 161 | | 188 | | 208 | | 219 | | 230 | | 237 | | 244 | | 281 | |

***Table 9.2.6*** *Summary of evolution of XFEL GmbH Personnel, in number of posts to be filled at the end of the corresponding year.*

### 9.2.5 Status of personnel and recruitment policy

The XFEL GmbH's personnel management and salaries policy depend on the legal framework. As a private company under German law, the XFEL GmbH will be subject to German legislation, including the current labour legislation. Salary scales and working times similar to those paid in the public sector (and thus, not too different from those at DESY and at other German research centres) are anticipated. Nevertheless, some positive features available to employees of public service-like organisations such as DESY (employment security, additional pension scheme, etc.) will have to be compensated for by some extra payment in order to render the XFEL GmbH competitive in the labour market, especially for scientists and engineers.

As far as possible the aim of the recruitment policy will be to produce a balanced staff structure with respect to nationality. Where reasonable, the posts will be advertised in all the member countries. As with other comparable international organisations, people hired from abroad will receive settling-in, adaptation and expatriation allowances, and their removal expenses will be refunded. The allowances for transfer to the Hamburg area and the expatriation allowance will be set to attract good candidates from all Contracting Party countries.

During construction of the facility, the XFEL GmbH will only recruit people who will continue to be needed for its operation, improvements and developments. The engineers and technicians who have worked on the construction of the machine and the instruments will have an intimate understanding of it. They are the best people to operate the source and the experimental equipment efficiently. Additional "peak" effort possibly required during construction will, therefore, be "bought in" by subcontracting and will be quoted under Capital Costs.

Personnel directly involved in the operation of the facility such as engineers, technicians, other support staff and at least one scientist per beamline could be offered permanent contracts.

Directors and most junior scientists will have fixed-term contracts, normally for five years. Nevertheless, contracts for staff engaged in the early design and construction phase of the project might be extended for a certain period. They should have the opportunity of following up commissioning and the early stages of operation. Research posts (normally three years) will be available for thesis students.

Specific in-house provisions will be set up for:

- shift work, staggered working hours and on-call duty (in the context of the permanent operation of the installations);
- personnel from outside firms and temporary workers;
- visitors and consultants.

## 9.3 General project structure and procedures for the construction period

### 9.3.1 Principles

The whole XFEL construction project has been structured according to work packages or tasks, combined into groups as follows:

| | | | |
|---|---|---|---|
| **Group 1: Linac** | 01 RF system<br>04 SC cavities<br>07 Frequency tuner<br>11 Cold magnets | 02 Low level RF<br>05 Power coupler<br>08 Cold vacuum | 03 Accelerator modules<br>06 HOM coupler<br>09 Strings |
| **Group 2: Accelerator Subsystems** | 12 Warm magnets<br>16 Lattice<br>19 Warm vacuum | 14 Injector<br>17 Standard Beam Diagnostics<br>20 Beam Dump | 15 Bunch compressor<br>18 Specific Beam Diagnostics |
| **Group 3: Photon Beamlines** | 21 Undulators<br>24 Photon diagnostic<br>27 FEL concepts | 22 Hard photons<br>25 Experiment areas | 23 Medium photons<br>26 Detector developmt |
| **Group 4: Control and Operation** | 28 Control systems<br>36 General safety | 29 Operability<br>38 Personnel interlock | 35 Radiation safety<br>39 EM interference |
| **Group 5: Infrastructure** | 10 Module test facility<br>33 Tunnel installation | 13 Cryogenic<br>34 Utilities | 32 Survey |
| **Group 6: Site and Buildings** | 31 Site and civil construction | 37 Plan approval procedure | |

Preparatory work has been carried out on this scheme for about three years, pushed forward almost exclusively by DESY's XFEL Project Group. For the construction, commissioning and operation, a broader participation is expected. The procedures for the distribution of these tasks have to ensure that for tasks which are not performed by the XFEL GmbH itself, individual institutes have the opportunity to contribute to the project according to their capacities and with their contributions being visible as such.

From the funding point of view, there are basically two different options for institutes from the Contracting Party countries to get involved in the construction and operation of the XFEL Facility:

- a contract with the XFEL GmbH on the supply of equipment and/or services, paid from the XFEL's budget; and
- the contribution in kind, for which some basic rules and procedures are laid down in Annex 5 to the XFEL Convention.

All other supplies, not provided by institutes from the Contracting Party countries, will be procured by the XFEL from industrial or commercial suppliers.

### 9.3.2 Collaboration agreements between contributing institutes and the XFEL GmbH

In both cases mentioned under Section 9.3.1, institutes which are interested in contributing to the realisation of the European XFEL project conclude a collaboration agreement with the XFEL GmbH. The agreement specifies the obligations and responsibilities of both partners and sets out whether or not the collaboration constitutes an in-kind contribution.

The assignment of in-kind contributions requires the approval by the XFEL Council, given that the in-flow and scheduling of cash contributions is affected. For other collaboration agreements there will be certain levels set out in the financial and/or purchasing rules, above which the Administrative and Finance Committee or even the Council might intervene.

In line with the basic rules for in-kind contributions (see below), the agreement for each task describes the cost, the schedule, the deliverables, the milestones, the acceptance procedures, etc., for the whole duration, i.e. until the final delivery. It will also contain a work plan to be updated on a yearly basis. This means that, at the time of signature, as an integral part of each contract, there will be a work plan for the whole period of the task, which is particularly detailed for the first year, agreed and signed by the XFEL Director General and the equivalent person (Director General) of the other institute(s). The work plan stipulates, among other things, the manpower assigned to the XFEL project, as well as the other resources (e.g. use of special labs, clean rooms and assembly halls). Once a year, this work plan has to be updated for the remaining period, and these updates, also signed by the Director Generals, also become integral parts of the contract.

The management of each institute, which concludes a collaboration agreement with the XFEL GmbH, appoints a person responsible for handling all tasks for the XFEL project within the institute.

**Basic rules and procedures for in-kind contributions**

(proposed as Annex 5 to the XFEL Convention)

1 In-kind contribution might cover:

- a technical component as well as personnel needed for its installation and integration on site; or
- personnel made available for specific tasks during the construction phase.

2 Special attention has to be paid to the allocation of responsibility, the calculation of the monetary/financial value of the contribution, the problem of under- and over-spending, and the resolution of disputes.

Continued

3 The in-kind contribution agreement for each task will contain *inter alia*:

- a technical description and specifications;
- time schedules and milestones;
- deliverables;
- quality control issues;
- performance testing, acceptance and commissioning;
- technical and financial control systems;
- appointment of responsible technical personnel;
- intellectual property right issues.

4 An In-kind Review Committee is set up, composed of one representative per Contracting Party and the Project Team, to propose to the XFEL management the allocation of in-kind tasks to specific partner institutes for decision by Council.

5 The Review Committee seeks to take the best profit of available expertise at DESY and throughout Europe and identifies to this end the possible/potential work packages for in-kind contributions as a function of the available expertise and independent of the location.

6 The Review Committee, when evaluating possible allocations of in-kind contributions, will take into account the willingness of the partner institute to make available personnel and experts for the installation and integration of the delivered system as well as for its operation. The conclusion of long-term maintenance contracts may be envisaged.

7 The Review Committee will define very early in the process the necessary interface specifications and common standards, in order to extend the field of potential in-kind contributions to any task which has a clear interface with another task, element or component.

Central coordination for each of the elements is essential and will have to be located where the relevant expertise is available.

### 9.3.3 Project management structure and oversight

The Managing Directors of the XFEL GmbH, together with the persons responsible in the various institutes involved, form the **XFEL Executive Board**. The Executive Board is the main coordination and communication body for the execution of the XFEL project. It monitors the execution of individual work packages or tasks and discusses matters involving several of them. The Executive Board meets regularly (probably once per month, also in the form of video conferences). It is chaired by the XFEL Project Leader, i.e. the Director General of the XFEL GmbH or a person designated by them to fulfil this role.

On request of the XFEL Project Leader experts from the institutes involved may be appointed as members of the Executive Committee.

Personnel employed by the participating institutes and assigned to the XFEL project according to the corresponding contract and approved work plan, remain under the regulations of their employer, in particular as far as their supervision is concerned, whether working in their home laboratory or at the DESY site, unless explicit detachment to the XFEL GmbH is foreseen as part of the contract or a separate agreement.

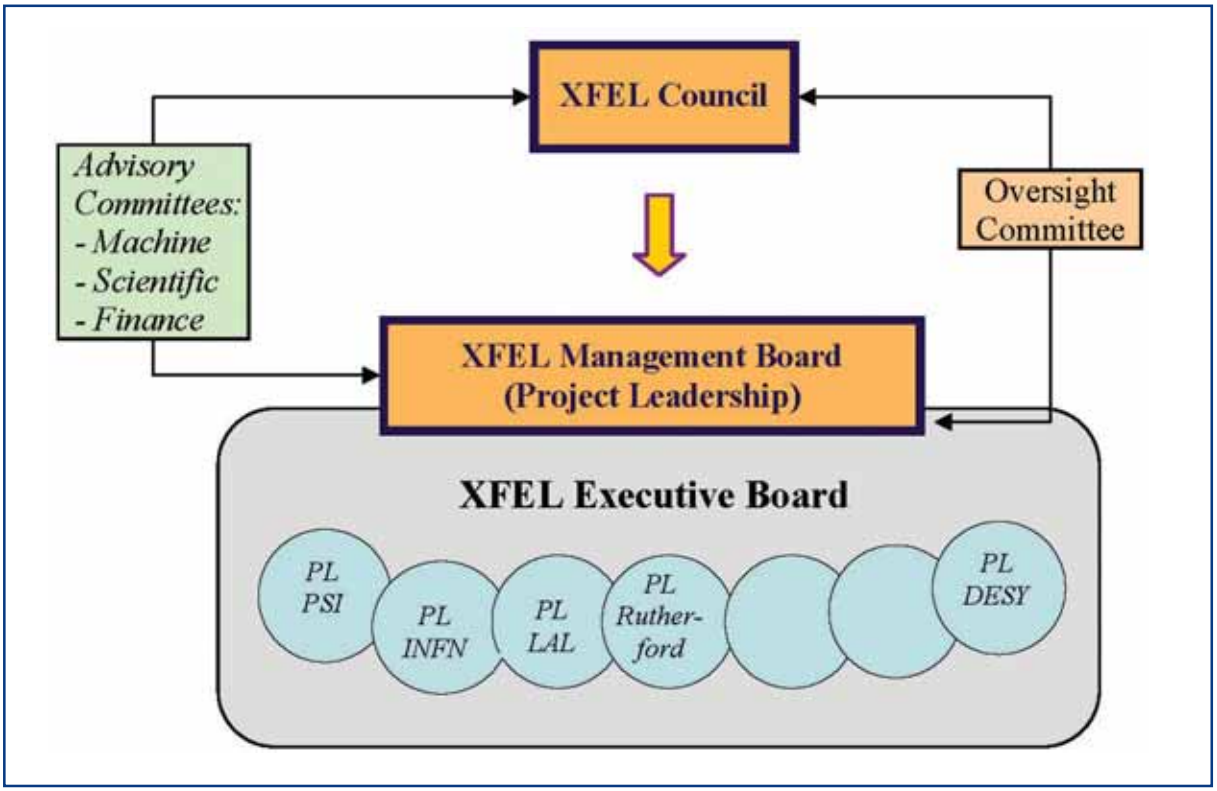


***Figure 9.3.1*** *Relationship between XFEL GmbH and collaborating institutes during the construction period.*

During the construction period, an **Overseeing Committee** nominated by, and reporting to, the XFEL Council regularly monitors the overall management of the project and the partners' adherence to the agreements. The committee is composed of independent experts on management of scientific projects. The Overseeing Committee will be in a position to identify problems in the implementation of the foreseen work plans, to examine any proposed remedial action and, if needed, suggest alternative action by the managements of the institutes, by the XFEL management and, if necessary, by the XFEL Council.

### 9.3.4 Later operation of the equipment contributed in kind

For all components and systems produced for the XFEL project it is essential that the corresponding know-how is available for the operation of the facility. It would be desirable that institutes, which have taken the responsibility for the construction of a component or

system, are also responsible for it during operation (see item 6 of the “Basic Rules and procedures for in-kind contributions”, reproduced in Section 9.3.2). Therefore, the XFEL GmbH has to clarify the responsibility for all in-kind systems during operation when an agreement is signed.

## 9.4 Special relationship between the XFEL GmbH and DESY

### 9.4.1 DESY as contributor to the construction, commissioning and operation of the XFEL Facility

#### *9.4.1.1 Volume of DESY involvement*

The DESY involvement is significantly different from that of other partners, since tasks entrusted to DESY are likely to correspond to a very large fraction of the total project costs during the early years of the construction period.

In fact, out of the work packages of the whole XFEL construction project (see Section 9.3.1), DESY is expected to play a major role in Groups 1 (Linac), 2 (Accelerator Sub-systems) and 5 (Infrastructure), and possibly, at least partially, in Work Package Groups 3 (Undulators, Photon beamlines), 4 (Control and Operation) and 6 (Site and Buildings).

All work package groups, apart perhaps from Group 3, will, already in the early stages of the project, get strongly involved in commitments, expenditure and recruitment. Therefore, mechanisms must be set up so that the XFEL GmbH can retain the responsibility and therefore, full control of its activities and budget. Consequently, in the special case of DESY, the general model for all in-kind contribution contracts will have to be supplemented by special provisions in order to assure the aforementioned responsibility and transparency. This will mean very close communication (much more intense than possible during the monthly meetings of the Executive Board) on all aspects of management, schedule and funding. These provisions will ensure the participation of the XFEL Managing Directors all decisions concerning major purchases, in the recruitment of personnel, etc.

#### *9.4.1.2 Power of attorney*

For some special aspects of the project, for instance obtaining the building permit (“*Planfeststellungsverfahren*”), DESY acted even before the XFEL GmbH was founded. In these cases and in others that are likely to emerge in the course of time, such as the:

- preparation of technical documents and engineering drawings for project implementation;
- preparing/obtaining permits including permit management; and
- other administrative services;

a “power of attorney” might be granted by the XFEL GmbH to DESY, for the necessary procedures, negotiations, and legal actions. The contract should specify the power of attorney granted to DESY and its limitations, for example, from the financial point of view.

Where DESY is granted power of attorney by the XFEL GmbH, the extent of the liability of DESY will have to be clearly defined. It could be stipulated that DESY should be liable only for wilful intent or gross negligence, except where this would be inconsistent with statute law. Moreover, a limitation of liability and the conclusion of a third party liability insurance contract by DESY should be considered.

#### *9.4.1.3 Long-term involvement*

DESY is strongly interested in providing its longstanding experience in the operation of accelerators, especially the vacuum ultraviolet (VUV)-FEL FLASH, to ensure optimal operation and upgrades of the XFEL. DESY is willing to stay responsible for all components and systems it supplies and guarantees a long-term commitment to provide the necessary know-how and services (including for upgrades of the facility), for the lifetime of the project . As mentioned in Section 9.2.3, it is planned to meet this interest by entrusting the operation of the accelerator complex to DESY.

### 9.4.2 DESY as host for the XFEL GmbH

The XFEL-DESY relationship has two basically different aspects: Besides contributing to the construction and operation of the XFEL, DESY plays the role of the host for the XFEL GmbH, and provides not only buildings but also site and infrastructural services, at least as long as the XFEL GmbH does not have its own campus in Schenefeld. The services mentioned here include, for example, services to ensure supplies and disposals, access to the canteen, security and safety, use of DESY's IT and communications infrastructure, use of the scientific infrastructure (e.g. library), etc.

For reasons of principle and practical convenience, these services on the one hand and the implementation of work packages on the other, are to be regulated by two different contracts:

- From a principle point of view, it is hardly possible, as far as site services are concerned, to respect the principle that DESY should be given the same chances and treatment as any other laboratory. Some measure of competition may be possible with local private companies providing similar services, but not with institutes located in different countries.
- From a practical point of view, two separate contracts are helpful to ensure complete cost transparency, and also for tax reasons.

The contract for site services has to reflect a usual tenant-landlord relationship or a customer service provider relationship and to specify a fair and transparent accounting procedure. The contract with the European Molecular Biology Laboratory (EMBL), an international organisation which has operated an outstation on the DESY site for many years, will be taken as model.

Given the size of the XFEL-related activities and their impact on the site management, the directorates of DESY and of the XFEL GmbH will meet regularly, to exchange information and to solve all possible interferences and conflicts between the various activities. Obviously, once the Schenefeld site becomes operational, the amount and type of the services provided by DESY will change.

## 9.5 Project management

The project management for the XFEL construction phase will follow well established and proven best practice techniques as described in standard handbooks for project management, for example **[9-1]** and Annexes 15 and 16 of the administrative and financial issue (AFI) FCI report **[9-2]**. An overview is given in Section 9.5.1. The detailed implementation of these best practises is to be defined by the XFEL Project Leader (see Section 9.5.2). The project management will be supported by tools for scheduling, resource planning and progress tracking, as set out in Section 9.5.3.

### 9.5.1 Overview

Following, by and large, the “Guide for planning and control procedures for large scale DESY Projects”, the XFEL Management Board will set up and keep updated a project plan comprising, in particular the:

- project structure plan;
- project schedule;
- project costing plan (financial planning with chronological profile);
- resource planning.

The **project structure plan** contains all activities pertaining to the construction and commissioning of the XFEL Facility. Related tasks form **work packages**; related work packages form **work package groups**. Work Package Leaders are responsible for the implementation of their work packages.

The planned completion time of the elements of the project structure plan and the relationship between these elements result in the **project schedule**. It is represented as a network plan (PERT chart) and as a bar diagram (Gantt chart) where the interrelations between various work steps are visible, and the critical path of the project schedule is established. The project schedule contains applicable milestones. The project schedule will be updated at reasonable intervals and indicates the degree of completion of the elements of the project structure plan.

The **project costing plan** specifies planned expenses and funding as a function of time for the overall project and for the individual elements of the project structure plan. A summary is set out in Chapter 10 of this report. During implementation of the project, budgeted costs and actual expenditure as well as corresponding funding are continuously tracked and trend analyses generated, if required.

In the event of a deviation in the project schedule or the project costing plan from the base plan, the required resources must, if necessary, be re-coordinated with the participating divisions (XFEL and/or DESY) and, if appropriate, with the in-kind contributors.

Labour requirements are also determined from the project structure plan. The work packages in the project structure plan include investments, **labour and technical**

**resources**. The assignment of XFEL groups to work packages is set out in an internal project assignment document; the assignment of DESY groups or of groups from other institutes are regulated in the corresponding agreements on in-kind contributions.

**Quality standards** for the final facility and its major components are established in this report. Following completion of an interim product, a work package or other work steps, the result is compared with the quality standards and documented. If a quality standard is not attained or work is completed late, the consequences to the project will be analysed and documented. This documentation is an integral part of the project plan.

The Executive Board will develop a plan that specifies the authorisation for undertaking **changes to the project**, including how changes will be documented and communicated within the project. Fundamental changes to the project plan, in particular to the project structure plan, schedule and costing, must be confirmed in writing by the XFEL Management Board, after approval of the XFEL Council, if appropriate. This authorisation plan is an integral part of the project plan.

Internal project **communication**, as well as reporting to external bodies and committees, is supported by the programming system for project management. Every project member should have access to the information in their field of activity, in particular with regard to the project schedule, cost base plan and resource planning. A specific communication scheme governs who may view larger areas of the project and access standardised reports and who will be informed of changes in the project and in what manner. Communication within the project includes the management of project documents. For each element of the project structure plan the related documents (e.g. planning documentation, production documentation and protocols for quality controls) must be easily retrievable.

The risk analysis consists of the identification of risks, their quantification with respect to the likelihood of the incidence of events and their consequences for the project. Risk analyses should be updated and documented at appropriate intervals. These documents become part of the project plan.

The Overseeing Committee assesses the progress of a project at least twice a year. The progress report contains at least the following updated information, as generated by the programming system for project management:

- a network plan with critical path;
- a schedule in the form of a bar diagram with milestones;
- a milestone analysis;
- an earned value analysis;
- a resource plan showing the utilisation of planned resources;
- an updated risk analysis.

Assessment dates should, where possible, be coordinated with the other reports to be produced.

### 9.5.2 Roles and responsibilities within the XFEL project

According to the general structure of the XFEL project in terms of Work Package Groups and work packages, as described in Section 9.3, the main roles and responsibilities for the project team are as follows:

The **XFEL Project Leader** coordinates, instructs, leads and motivates the project team, releases the overall project plan and approves the work plan of the work packages within the context of the overall project plan, ensures the overall technical and scientific progress of the project according to the released project plan and develops solutions in case of problems. The project leader assigns financial and personnel resources to the individual work packages; tracks the project schedule by establishing and monitoring project relevant milestones; and reports to the Overseeing Committee (see Section 9.3.3).

The **Work Package Leader** fulfils the same responsibilities as the project leader for the tasks within their work package. They establish the work package plan with scheduling and resource planning for the tasks in their work package. This plan is approved by the project leader and then released for the overall project plan. The Work Package Leader is responsible for the execution of the tasks according to the approved plan. The progress of their work package is recorded appropriately in the project plan by updating it with actual values. The Work Package Leader reports regularly to the project leader on the status of their work package.

The XFEL Project Leader and the project team are supported by a **Project Management Office**. The Project Management Office establishes planning and reporting guidelines for the XFEL project and provides the necessary tools (see Section 9.5.3). It ensures that the individual work package plans follow those guidelines formally and can, therefore, be (upon approval by the Project Leader) incorporated to create a consistent overall project plan. The Project Management Office coordinates the status reporting within the project and composes an overall project status for the XFEL Project Leader; keeps track of the financial status of the project and provides this information for the project team; supports the Work Package Leaders in planning and other management and administrative tasks where necessary; and is assigned directly to the XFEL Project Leader.

### 9.5.3 Project management tools

The approach of project planning currently carried out by the XFEL project group at DESY, which will also be adopted for the XFEL construction project, is a system of bottom-up project plans created by the Work Package Leaders linked together by cross-work package milestones in an overall project plan. The individual work package plans are maintained by the Work Package Leader but (in case of changes) released for the overall project schedule by the XFEL Project Leader. The project plan contains the scheduling, and personnel, financial and equipment resource allocation. Maintenance of the plan includes updates in case of necessary changes (to be handled by the change management) and for actual values for personnel, finances and equipment usage. Since the XFEL project is a European effort with work packages being managed by partners not located at the XFEL site, the central project management software should be easily

available for all partners. Since it will also be the central tool for progress tracking, there should be opportunities to import actual financial data from various Enterprise Resource Planning (ERP) software packages used in the XFEL partners' administration. At DESY, this is the SAP system.

Microsoft Project Enterprise **[9-3]** with the Microsoft Project Web-access is the most widely used project management software and fulfils most, if not all, of the requirements, and will, therefore, be the central planning and tracking tool for the XFEL Project Team. Financial data will be imported automatically for cost controlling whenever possible. The Web-access will be used for online project progress tracking information for the project management and the entire project team.

Tracking and controlling of the project will be performed using project management best practise techniques such as milestone trend analysis and earned value-analysis.

## References

**[9-1]** *A Guide to the Project Management Body of Knowledge*, Project Management Institute, Newtown Square, PA 19073-3299 USA.

**[9-2]** Final Report of the Sub Group of Full Cost Issues (FCI) in respect of the European Free-Electron Laser Facility XFEL.

**[9-3]** Microsoft Project Enterprise, Microsoft Cooperation, http://office.microsoft.com/en-us/FX011204851033.aspx

# 10 Cost and time schedule

In this chapter, a summary of the complete project cost is given, the basic schedule from start of construction until end of commissioning is discussed and the resulting budget profile over all phases of the project is described.

## 10.1 Total project cost

All costs from the project preparation to the commissioning phase (i.e. prior to the start of operation) have to be summed up in order to determine the total project cost (TPC, which is covered by the construction budget). As explained in Chapter 8, there will be a period of about 2.5 years during which an overlap of construction and commissioning (which are covered by the construction budget), on the one hand, and operation (which is covered by the operation budget), on the other, will occur (see also the discussion of time schedule and budget profile below). The contributions to the TPC, summarised in Table 10.1.1, are:

- The project preparation costs. These are the expenses since the X-Ray Free-Electron Laser (XFEL) Memorandum of Understanding (MOU) came into effect (end of 2004) between Deutsches Elektronen Synchrotron (DESY) Laboratory and those institutes which have concluded collaboration contracts with DESY.
- The project construction costs in the proper sense, as described at the end of Chapters 4 to 7.
- The cost for commissioning the facility with beam, as described in Chapter 8.
- An addition to the personnel cost, to take into account allowances for personnel moving from their home country to work at the XFEL company.
- An addition to the XFEL company personnel cost overhead for management and support.

Recurrent costs during the construction phase (electricity, water and Helium) are not included in the TPC since they will be covered by the DESY operation budget free of charge to the XFEL project. Costs related to land acquisition are also not included in the TPC.

| | |
|---|---|
| Project preparation | 38.8 M€ |
| *Project construction, capital investment* | *736.3 M€* |
| *Project construction, personnel* | *250.1 M€* |
| **Total construction cost** | **986.4 M€** |
| Beam commissioning | 56.4 M€ |
| **Total project construction cost** | **1,081.6 M€** |

***Table 10.1.1*** *Total project cost, including preparation – commissioning phases. All cost figures are on the price basis of the year 2005. - The original Table 10.1.1 of the TDR has been slightly re-arranged: the additional personnel cost (allowances) and the additional management overhead of the XFEL GmbH, initially shown in separate lines of the table, are now included in the cost for construction and commissioning.*

Using the present organisational structure of the project (see Chapter 9) with six groups of work packages and 38 work packages in total, a breakdown of the construction costs is shown in Figure 10.1.1. The relation between the work package groups and the chapters in this report is shown in Table 10.1.2.

| Work package group | Chapter 4 | Chapter 5 | Chapter 6 | Chapter 7 |
|---|---|---|---|---|
| WPG1 linac | X | | | |
| WPG2 Accelerator sub-systems | X | | | |
| WPG3 Undulator and photon | | X | X | |
| WPG4 Controls and operation | | | | X |
| WPG5 Infrastructure | | | | X |
| WPG6 Site and civil | | | | X |

***Table 10.1.2*** *Relation between chapters in this report and work package groups in the present organisational structure of the project.*

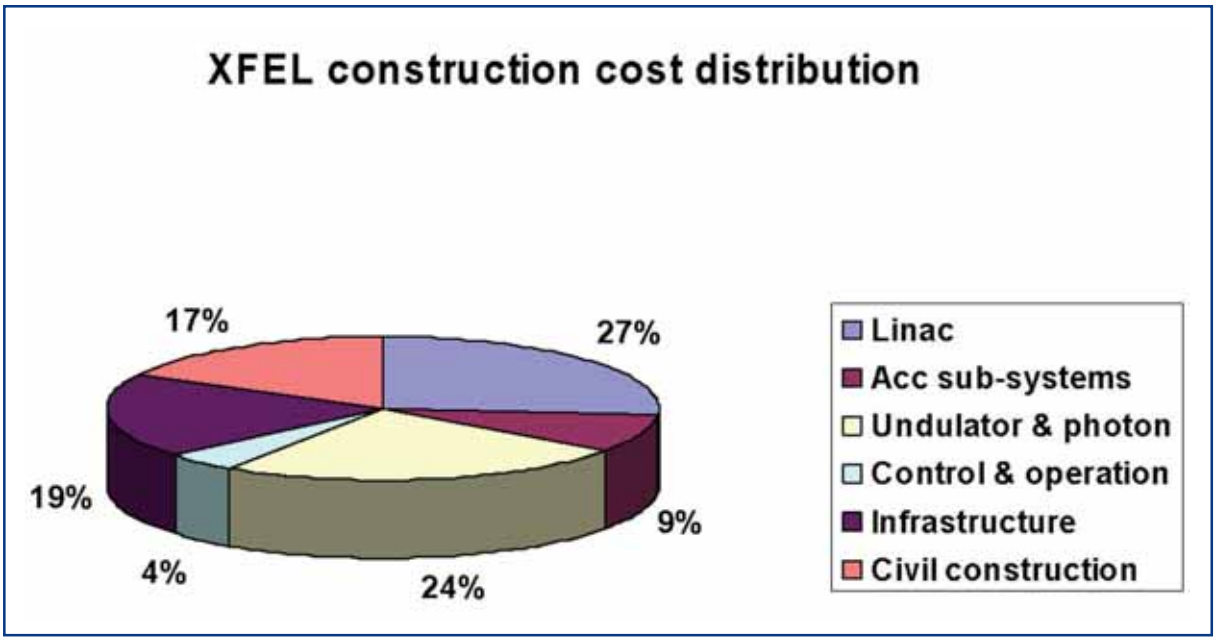


***Figure 10.1.1*** *Breakdown of project construction cost (sum of capital investment and personnel cost) into the work package groups.*

The evaluation of personnel costs has been performed in accord with the rules approved by the XFEL Working Group on Administrative and Funding Issues (AFI) **[10-1]**. The salary structure (2005 basis) of the different technical groups in the DESY Divisions has been used to determine the cost per full-time equivalent (FTE) for each of the 38 work packages in the XFEL project, depending on the percentages of scientific and technical personnel in each work package. To this an overhead of 13k€ per FTE, also derived at DESY, has been added. This approach, which was also used for the earlier cost estimations since 2002, has so far been maintained in order to permit a better follow-up and comparison of the various updates of the project costs, related to scientific and technical issues or to external economic parameters. However, two items are not, or not sufficiently, taken into account by this procedure.

The Administrative and Financial Issues Working Group (AFI) "Guidelines for establishing the XFEL cost estimates and control tools" indicate that *"the transformation of...FTE into personnel costs may, in the first instance, be based on salaries and social charges according to the German Public Service. The amount has to be revised once the actual employment conditions for the XFEL personnel are specified."* This question is not yet fully settled, however, one aspect is relatively clear: in view of being able to attract personnel from partner countries, underlining the international character of the project, an addition to the salaries as defined above should be taken into account for personnel moving from their home country to work at the XFEL company. Based on the practice at the European Synchrotron Radiation Facility (ESRF), such allowances are assumed to amount to 16% of the salaries (without overhead) which have been derived from the salary structure at DESY. As a model to estimate the total amount of these additional personnel costs (see Chapter 9), it is assumed that the XFEL company's personnel ramps up continuously from the beginning of 2007 to its full "steady state" staff in 2016

(see Chapter 9) and that, on average, half of the company's personnel receive the allowances.

The other item concerns the way the cost for general expenditure is taken into account. This includes all staff posts not directly related to the accelerator and beamline work packages, such as Management, Administration and other central services. Their costs enter the calculation exclusively through overheads on the costs per FTE. The previous cost estimates have used the overheads calculated for DESY. However, in the XFEL company, due to its much smaller amount of staff, the relative part of management and support is significantly higher than at DESY. This is all the more the case, if the accelerator part were to be constructed, to a large extent, by DESY personnel, as a contribution in kind. In addition, the XFEL Management, essential parts of the XFEL Administration and some other general services need to be in place well before the major part of the personnel of the Experiments Division. Treating their costs only as part of the overhead of the Experiments Division staff would result in a wrong cost profile. This discrepancy has been solved by adding a global overhead of 1.5 M€ per year. For the first years this simply corresponds to advancing by one year the recruitment of about 20 staff under management and general support, when compared to the cost profile resulting from the overhead view. In the transition phase, this figure of 1.5 M€ per year is accounted partially as TPC, partially as operation cost, in proportion to the amount of personnel allocated to construction/commissioning and operation, respectively.

## 10.2 Risk analysis

As part of the construction cost evaluation, every item in the budget book is estimated with an expected lowest and highest price based on the current knowledge about the component or system. Using these price ranges, a statistical probability distribution of the project construction cost can be derived. According to the AFI recommendations **[10-1]**, the estimated prices were chosen such that the estimated construction cost is in the centre of this probability distribution, i.e. at 50% probability.

In order to generate an estimate of maximum cost risk for the project, for several large cost items, the upper limit of the cost range was increased using more pessimistic assumptions. In particular, it was assumed that the expected cost reduction in going from present prototype manufacturing to later industrial series fabrication cannot be achieved as planned – only half of this reduction can be realised. Using these artificially extended cost variation ranges, a statistical analysis of the construction cost was again performed. The result of this analysis is a curve which gives a probability value for a given budget that the project can be completed successfully within that budget. From this probability curve a risk budget can be derived, which is needed to guarantee a high probability (98% as recommended by AFI) to complete the project in budget (= estimated cost + risk budget). From the construction of this **maximum risk** analysis, it is clear that the estimated (i.e. **most likely**) construction cost is at a point well below 50% in the probability curve.

The statistical analysis was performed using Monte Carlo methods implemented in the commercial risk analysis tool @Risk for Excel **[10-2]**. The price range for each cost item

is given by three values: the lowest and highest expected price and the central value which is used to calculate the project cost. A typical random distribution used in financial mathematics is the log-normal distribution:

$$C = C_0 e^{aZ}$$

where $Z$ is the standard normal distribution and $C_0$ and $a$ are the parameters. This distribution finds its application in processes where the variation of prices is multiplicative, i.e. the prices vary in percentages rather than in absolute units **[10-3]**. For the statistical analysis it was therefore assumed, that the price distribution follows a log-normal distribution. The parameters $C_0$ and $a$ were chosen in a way that the expectation value and the variance of the log-normal distribution are equal to the expectation value and variance of a triangular risk function defined by the three cost values of each item as suggested by **[10-3]**.

Not all of the more than 2,500 cost items can be considered independent of each other. Therefore, it is necessary to include correlations between items in the statistical analysis. Correlations were defined on the work package level. Three correlation classes are defined:

- **fully uncorrelated cost items in a work package**: all costing items can be considered independent of each other, so that each item is included with its own log-normal random distribution in the analysis; an example for a fully uncorrelated group of cost items is the accelerator module;
- **fully correlated cost items in a work package**: the majority of the items in a work package are subject to the same cost uncertainty, so that only the total sum of the correlated items with its uncertainty is included in the analysis; an example of a fully correlated group of cost items are the normal conducting magnets;
- **partially correlated cost items in a work package**: big blocks of cost items within a work package are subject to the same cost uncertainty; these blocks of cost items within a work package are then taken to be fully correlated; an example are the costs for electric power, air conditioning and water supplies, respectively, of the utilities work package.

The statistical analysis of the project costs was performed by means of Monte Carlo methods. In a Monte Carlo experiment, a random price value distributed according to the log-normal distribution discussed above was generated for the cost item taking into account the three correlation classes. A total (or sub-total) price corresponding to these randomly distributed values was calculated. After performing many such Monte Carlo simulations, a distribution of expected total project costs was obtained. Integrating this distribution and normalising it to the number of performed Monte Carlo experiments then yielded the probability curve discussed already (see Figure 10.2.1). As the final result, a risk budget of 6% of the estimated construction cost has to be allocated in order to provide a 98% probability of completing the project within budget even with the pessimistic assumptions on cost variations already described.

An additional cost risk results from possible delays, caused, for example, by companies being over-committed or, as an extreme case, going into bankruptcy. Delays due to such events can, to a certain extent, be mitigated by re-scheduling other parts of the project (e.g. rearranging the sequence of component installation), but additional cost resulting from project personnel not being able to continue the work as efficiently as planned will be hard to avoid. The cost risk due to delays has been estimated as half a year of personnel cost in the middle of the construction phase, corresponding to 2% of the project constructions cost.

In summary, the estimated risk budget amounts to 8% of the construction cost (78 M€).

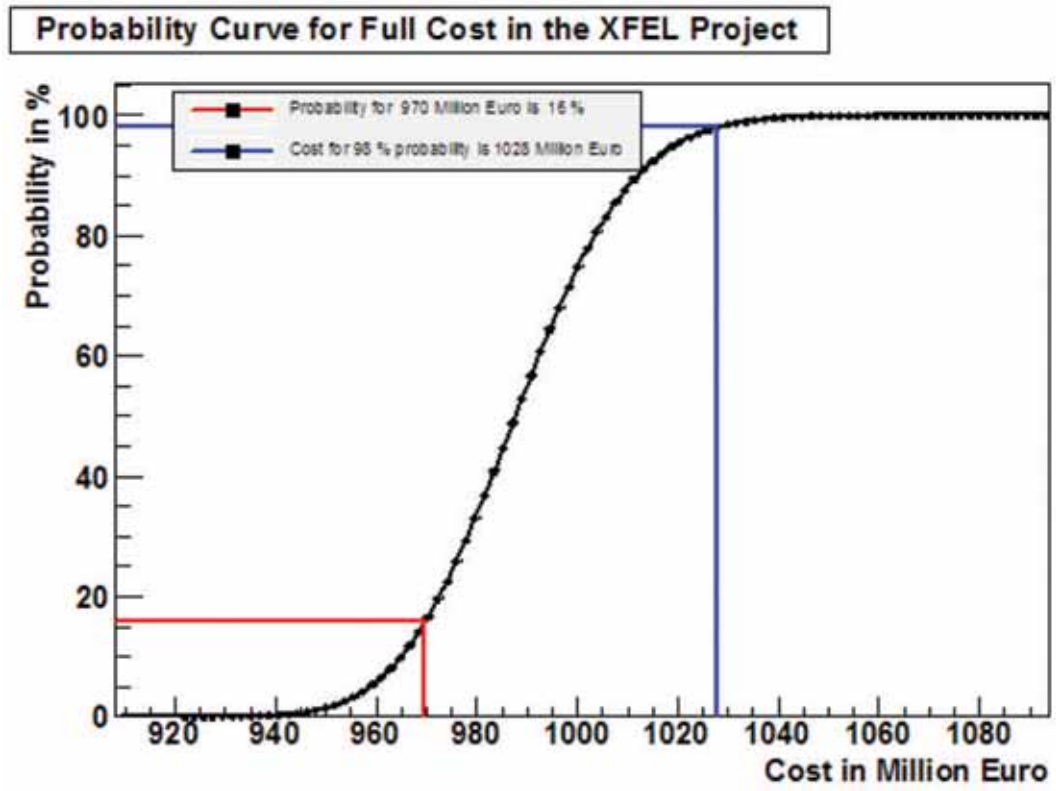


***Figure 10.2.1*** *Result of the statistical construction cost risk analysis (see text).*

## 10.3 Operation cost

The yearly costs for operating the facility, as explained in more detail in Chapter 8, are reproduced here in Table 10.3.1. As in the construction phase, budget items have been added here to cover allowances for GmbH personnel and overhead for the GmbH management and support (see Section 10.1). This budget represents the “steady state” value when the facility is fully operational. During the transition phase, the budget ramps-up in a way following the sequence in which the different parts of the facility are put into operation, as described in Chapter 8. The resulting evolution of the operation part of the yearly budget with time is shown in Section 10.5.

| | |
|---|---|
| Consumables | 11.5 M€ |
| Maintenance and refurbishment | 22.0 M€ |
| Research and development | 11.0 M€ |
| Personnel accelerator and technical infrastructure | 19.8 M€ |
| Personnel photon beamlines and experiments | 13.8 M€ |
| User support | 1.8 M€ |
| Visitor and student programme | 1.7 M€ |
| Additional personnel cost (allowances) GmbH | 1.0 M€ |
| Global management and support overhead GmbH | 1.5 M€ |
| **Total yearly operation cost** | **83.6 M€** |

***Table 10.3.1*** *Overview of operations costs (in year 2005 Euros), including allowances and overhead for the GmbH management and support.*

## 10.4 Time schedule

At the time of completing this report, the project preparation has advanced to a state which, from the point of view of project planning and technical readiness, allows the construction phase to begin without delay. In order to put the schedule on a realistic absolute time scale, it is assumed that the official start of project construction will be January 2007.

A description of the fully detailed scheduling for all technical components and sub-systems of the facility, including complex inter-relations between them, is beyond the scope of this report. In the following, a simplified overview of how the project will proceed from start of construction to beginning of operation is given. For each of the major parts of the facility, phases during construction (which can partially overlap in time) can be defined as:

- design, prototyping and industrialisation;
- fabrication (including pre-series);
- installation;
- commissioning (technical and with beam).

A schematic view of these phases for each of the six work package groups is shown in Figure 10.4.1. The beginning of operation and its partial overlap with ongoing construction, as discussed in Chapter 8, is also shown.

**Civil construction** is scheduled to start very soon after the project receives the official go-ahead. Based on very advanced planning, the call for the bids procedure on the underground part of construction work can already be completed by the time of the official project start. Excavations of shafts and underground halls will go in parallel on the DESY site and at the user facility (Schenefeld/Osdorfer Born). Installation work on the accelerator tunnel, access shafts and injector building will be ready to start in autumn 2009. Civil construction, including all surface buildings, will be completed after four years.

## Cost and time schedule

For the **linear accelerator/linac**, the ongoing work on industrialisation of its main components will continue until approximately the middle of 2008, by which time first orders on series fabrication can be placed. About one year is foreseen for the companies to set up fabrication. In total, three years are foreseen to manufacture all linac components, including a low-rate start-up of pre-series fabrication. The existing infrastructure at DESY (clean rooms and treatment facilities, test stands, etc.) will be used to help setting up industrial production in an efficient, time-saving fashion. While series fabrication and component testing is ongoing, installation and technical commissioning work in the tunnel will proceed in parallel. The linac is scheduled to be ready for acceleration of a first beam up to the commissioning dump at the end of the linac tunnel in the middle of 2013.

For the **accelerator sub-systems**, the design phase stretches out over a longer period in time. This results from the expected research and development (R&D) work closely linked with the experience to be gained at the Free-electron LASer in Hamburg (FLASH) facility over the next years in certain areas of challenging special beam diagnostics, beam stabilisation and femtosecond-synchronisation systems. Furthermore, installation of the second electron beamline will take place while the first is already commissioned with beam. While, therefore, accelerator sub-system construction extends over a relatively long time, certain parts are scheduled to be completed early. This applies in particular to the injector, which will be installed and commissioned already in 2010-2012, which has the advantage of having a stable beam of good quality available at the time when linac beam commissioning begins.

Realisation of the **technical infrastructure** has to start early in the process, since the schedule of other work package groups often depends on having completed certain parts of infrastructure work. For example, the cavity and module test facility has to be completed and operational when the series production of linac components starts. Another example is infrastructure in the tunnel (cables, water pipes, etc.) which has to be installed before the first radio frequency (RF) systems and accelerator modules can be installed.

The schedule for **operation and control** systems naturally reflects that the completion of this part of the facility is required relatively late in the construction phase. A considerable amount of time can be allocated to working out the final design.

**Undulators and photon beamlines** are the parts of the facility which come latest in the commissioning sequence. Consequently, the schedule foresees an appreciable amount of R&D time. The fabrication and installation of the components stretches out over several years, in accord with the plan of building up and commissioning the beamlines in a sequential fashion.

In summary, construction has been scheduled to meet the milestone of first beam through the linac 6.5 years after construction start. At this point in time, the first branch of beamlines with the SASE 1 undulator will also have been installed. As described in Chapter 8, beam commissioning will then progress until the performance milestone of SASE 1 radiation is reached. This beamline will then become operational for first experiments. Commissioning of the other beamlines follows in the sequence described in Chapter 8.

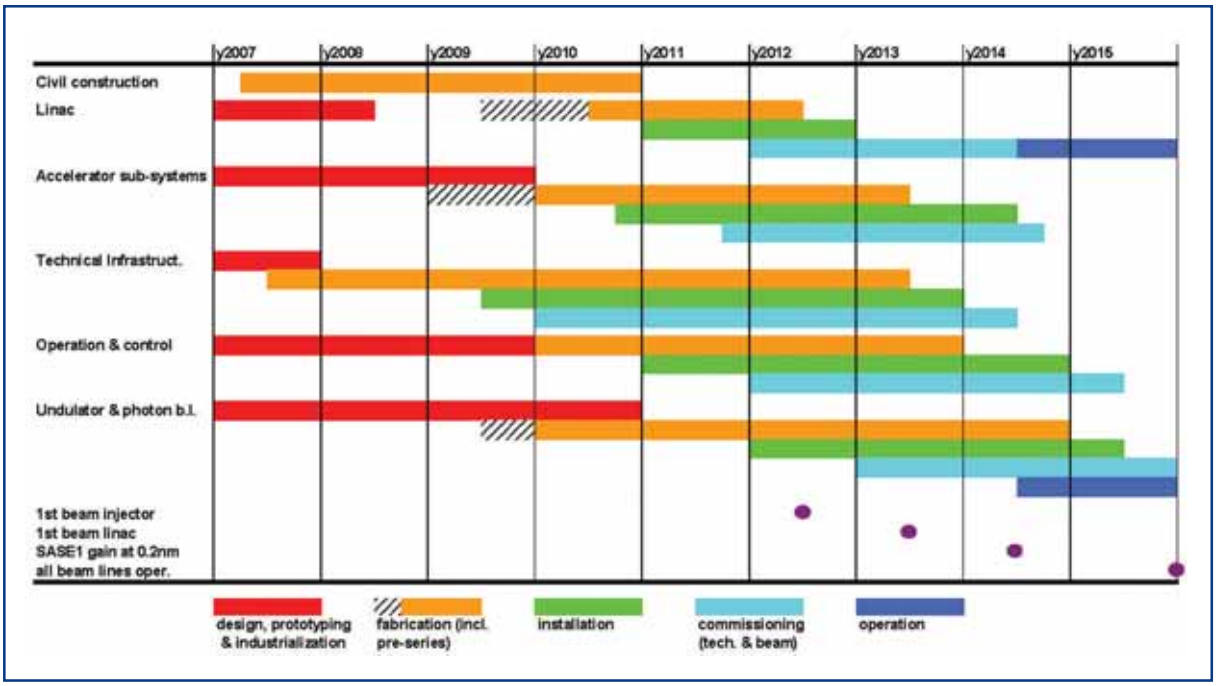


***Figure 10.4.1*** *Sketch of the schedule for the six work package groups from start of construction to beginning of operation.*

## 10.5 Budget profile

With the different contributions to the TPC as summarised above, the construction time schedule and the operation costs as described in Chapter 8, a complete budget profile for all phases from preparation to operation can be constructed. The result is displayed in Figure 10.5.1 and Table 10.5.1, showing the yearly budget from 2005-2016 on the price basis of 2005 (i.e. without applying an escalation to take into account inflation).

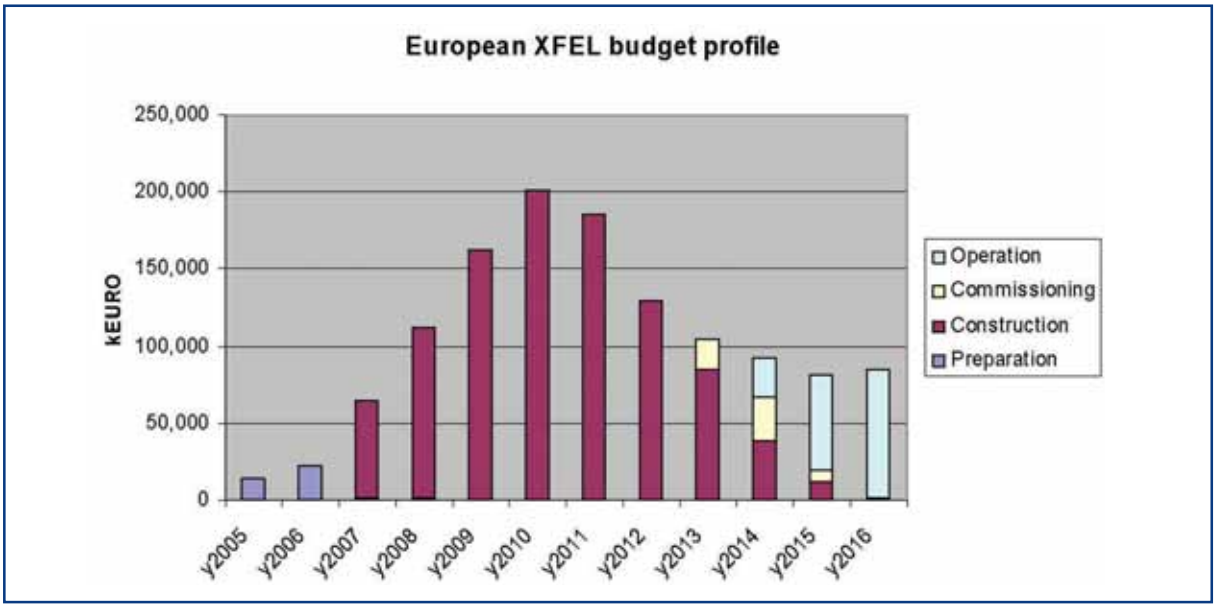


***Figure 10.5.1*** *Budget profile (sum of capital investment and personnel cost on year 2005 price basis) from preparation to operation phase of the project.*

## Cost and time schedule

| | Preparation | Construction | Commissioning | Operation | Sum | |
|---|---|---|---|---|---|---|
| **2005** | 14.2 | | | | 14.2 | M€ |
| **2006** | 22.5 | | | | 22.5 | M€ |
| **2007** | 1.0 | 63.6 | | | 64.6 | M€ |
| **2008** | 1.2 | 110.9 | | | 112.0 | M€ |
| **2009** | | 161.9 | | | 161.9 | M€ |
| **2010** | | 200.8 | | | 200.8 | M€ |
| **2011** | | 185.3 | | | 185.3 | M€ |
| **2012** | | 128.7 | | | 128.7 | M€ |
| **2013** | | 84.9 | 20.1 | | 105.0 | M€ |
| **2014** | | 38.3 | 28.0 | 25.4 | 91.7 | M€ |
| **2015** | | 12.0 | 7.1 | 62.9 | 82.0 | M€ |
| **2016** | | | 1.2 | 83.4 | 84.6 | M€ |

***Table 10.3.1*** *Yearly budget of the European XFEL through all phases from preparation to operation (in year 2005 Euros), including GmbH personnel allowances and overhead for management and support (16.7 M€ under construction and 1.5 M€ under commissioning).*

In Figure 10.5.2, the distribution of capital investment (construction phase) over the six work package groups as a function of time is displayed. The differences with which the cost contributions from the six work package groups evolve with time are clearly recognisable.

Figure 10.5.3 shows the evolution of personnel for the accelerator/infrastructure and photon beamline/experiments parts of the project, respectively. While the latter evolves in a rather smooth way into the “steady state” staff required for operation, a “peak” occurs for the accelerator/infrastructure part, which is essentially related to the test facility operation and installation work going on in parallel. Such a situation may be somewhat difficult to handle. One way could be to temporarily detach personnel from collaborating institutes to the project, another one to avoid this “peak” in project staff by involving the industry which is manufacturing the technical components in the testing and installation procedures as well.

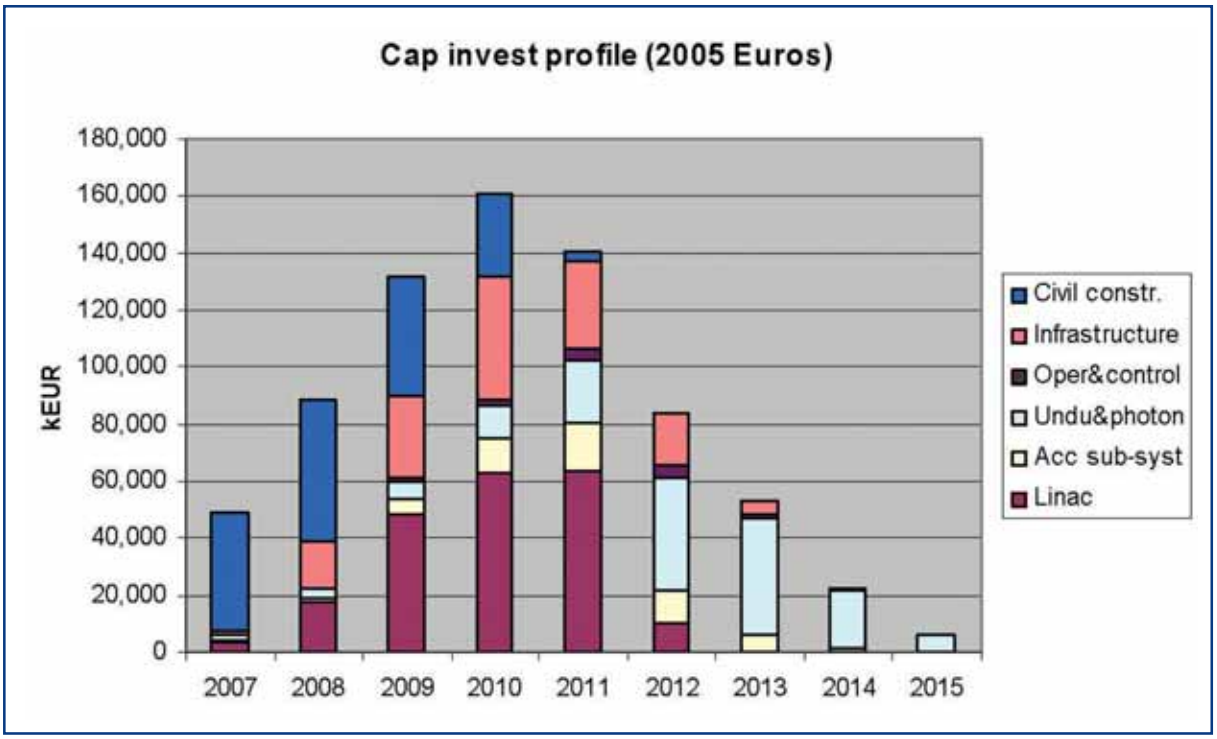


***Figure 10.5.2*** *Yearly capital investment for the six work package groups during the construction phase.*

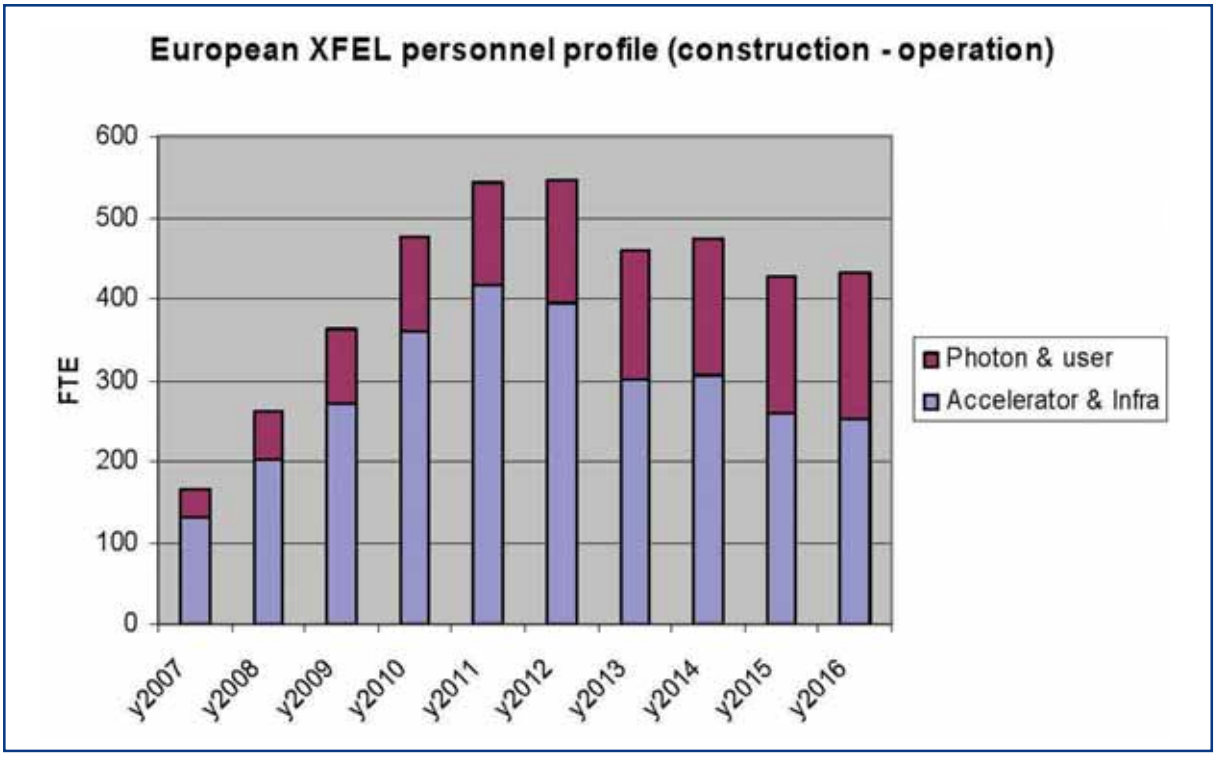


***Figure10.5.3*** *Personnel profile from start of construction to operation phase of the project.*

# References

**[10-1]** Final Report of the Sub Group of Full Cost Issues (FCI) in respect of the European Free-Electron Laser Facility XFEL.

**[10-2]** Microsoft Excel Add-on @Risk4.5 for Excel (Standard Edition), Palisade Corporation Europe, Middlesex, UK, http://www.palisade-europe.com

**[10-3]** A. Bovier, A. Schied, *Probabilistic evaluation of cost risks in large scale projects*, report to the XFEL project team, TU Berlin, 15. Nov. 2005.